

Surender Kumar Sharma *Editor*

Dalip Singh Verma

Latif Ullah Khan

Shalendra Kumar

Sher Bahadar Khan *Associate Editors*

Handbook of Materials Characterization

 Springer

Handbook of Materials Characterization

Surender Kumar Sharma

Editor

Dalip Singh Verma • Latif Ullah Khan
Shalendra Kumar • Sher Bahadar Khan

Associate Editors

Handbook of Materials Characterization



Springer

Editor

Surender Kumar Sharma
Department of Physics
Federal University of Maranhão
São Luis, Maranhão, Brazil

Associate Editors

Dalip Singh Verma
Department of Physics & Astronomical
Science
Central University of Himachal Pradesh
Dharamshala, Kangra
Himachal Pradesh, India

Latif Ullah Khan
Brazilian Nanotechnology National
Laboratory (LNNano)
Brazilian Center for Research in
Energy and Materials (CNPEM)
Campinas, São Paulo, Brazil

Shalendra Kumar
Department of Applied Physics
Amity School of Applied Sciences
Amity University Haryana
Gurgaon, India

Sher Bahadar Khan
Center of Excellence for
Advanced Materials Research
King Abdulaziz University
Jeddah, Saudi Arabia

Chemistry Department
Faculty of Science
King Abdulaziz University
Jeddah, Saudi Arabia

ISBN 978-3-319-92954-5 ISBN 978-3-319-92955-2 (eBook)
<https://doi.org/10.1007/978-3-319-92955-2>

Library of Congress Control Number: 2018951223

© Springer International Publishing AG, part of Springer Nature 2018

This work is subject to copyright. All rights are reserved by the Publisher, whether the whole or part of the material is concerned, specifically the rights of translation, reprinting, reuse of illustrations, recitation, broadcasting, reproduction on microfilms or in any other physical way, and transmission or information storage and retrieval, electronic adaptation, computer software, or by similar or dissimilar methodology now known or hereafter developed.

The use of general descriptive names, registered names, trademarks, service marks, etc. in this publication does not imply, even in the absence of a specific statement, that such names are exempt from the relevant protective laws and regulations and therefore free for general use.

The publisher, the authors and the editors are safe to assume that the advice and information in this book are believed to be true and accurate at the date of publication. Neither the publisher nor the authors or the editors give a warranty, express or implied, with respect to the material contained herein or for any errors or omissions that may have been made. The publisher remains neutral with regard to jurisdictional claims in published maps and institutional affiliations.

Printed on acid-free paper

This Springer imprint is published by the registered company Springer Nature Switzerland AG
The registered company address is: Gewerbestrasse 11, 6330 Cham, Switzerland

Preface

One of the significant aspects of materials-based research is the characterization tools. Today, there is an immense range of scientific techniques available that enables us to study physiochemical properties of the materials. This book focuses on the utmost effective and widely used techniques available for structural, morphological, and spectroscopic characterizations of materials. Three important aspects of characterization namely materials structures, morphology, and chemical analysis are included in the present volume. The developments in wide range of techniques and their application to the quantification of the materials properties are essential sides of the book.

The principal objective is to provide a concise reading material on both practical and theoretical description of the techniques used to characterize a wide variety of materials. Our approach is focused on fundamental understanding, basic instrumentation, experimental strategy, analyses, and application part. Most of the characterization techniques are used throughout undergraduate courses; however, the background of these methods will not be provided in the standard textbooks. This book will serve as an overview of characterization of materials for a wide audience: from beginners and graduate-level students up to advanced specialists in both academic and industrial sectors. The authors of each chapter have been encouraged to present the highlights from the extensive literature on the topic including latest cutting-edge research using both conventional and nonconventional characterization tools.

São Luis, Brazil

Surender Kumar Sharma

Contents

1	Neutron Diffraction: A tool for the Magnetic Properties	1
	Pablo Leite Bernardo and Helio Salim de Amorim	
2	Small-Angle X-Ray Scattering to Analyze the Morphological Properties of Nanoparticulated Systems	37
	Oscar Moscoso Londoño, Pablo Tancredi, Patricia Rivas, Diego Muraca, Leandro M. Socolovsky, and Marcelo Knobel	
3	Dynamic Light Scattering: Effective Sizing Technique for Characterization of Magnetic Nanoparticles	77
	Sim Siong Leong, Wei Ming Ng, JitKang Lim, and Swee Pin Yeap	
4	Scanning Electron Microscopy: Principle and Applications in Nanomaterials Characterization	113
	Kalsoom Akhtar, Shahid Ali Khan, Sher Bahadar Khan, and Abdullah M. Asiri	
5	TEM for Atomic-Scale Study: Fundamental, Instrumentation, and Applications in Nanotechnology	147
	Yasir Javed, Khuram Ali, Kanwal Akhtar, Jawaria, M. Irfan Hussain, Gulzar Ahmad, and Taskeen Arif	
6	Materials Characterization Using Scanning Tunneling Microscopy: From Fundamentals to Advanced Applications	217
	Suryakanti Debata, Trupti R. Das, Rashmi Madhuri, and Prashant K. Sharma	
7	Atomic and Magnetic Force Studies of Co Thin Films and Nanoparticles: Understanding the Surface Correlation Using Fractal Studies	263
	Indra Sulania, R. P. Yadav, and Ranjeet Kumar Karn	

8	Optical Spectroscopy and Its Applications in Inorganic Materials ...	293
	Marcio Aurélio Pinheiro Almeida and Adeilton Pereira Maciel	
9	Fourier Transform Infrared Spectroscopy: Fundamentals and Application in Functional Groups and Nanomaterials Characterization	317
	Shahid Ali Khan, Sher Bahadar Khan, Latif Ullah Khan, Aliya Farooq, Kalsoom Akhtar, and Abdullah M. Asiri	
10	Rare Earth Luminescence: Electronic Spectroscopy and Applications	345
	Latif Ullah Khan and Zahid U. Khan	
11	Raman Spectroscopy: A Potential Characterization Tool for Carbon Materials	405
	Padmnabh Rai and Satish Kumar Dubey	
12	Photoelectron Spectroscopy: Fundamental Principles and Applications	435
	Jagdish Kumar	
13	Introduction to X-Ray Absorption Spectroscopy and Its Applications in Material Science	497
	Aditya Sharma, Jitendra Pal Singh, Sung Ok Won, Keun Hwa Chae, Surender Kumar Sharma, and Shalendra Kumar	
14	³¹P Solid-State NMR Spectroscopy of Adsorbed Phosphorous Probe Molecules: Acidity Characterization of Solid Acid Carbonaceous Materials for Catalytic Applications	549
	Bhaskar Garg	
	Index	597

Chapter 1

Neutron Diffraction: A tool for the Magnetic Properties



Pablo Leite Bernardo and Helio Salim de Amorim

1.1 Introduction

Experimental techniques based on neutron scattering have a special relevance in the study of new materials due to some basic aspects of the neutrons as particles in free state, that is, outside the atomic nucleus. They are relatively stable, with a mean lifetime of about 14 min; as indicated in their own name, do not have a net electric charge, that is, they are neutral; have no measurable electrical dipole moment; but have a relevant magnetic dipole moment associated with an intrinsic angular momentum or spin.

Because they do not have an electric charge, or an electric dipole, they do not electrically interact directly with atoms, ions, or molecules that make up matter. In general, they are poorly absorbed in direct interaction with matter when compared to other charged particles or even with X- and gamma-type photons. The predominant interaction is with the atomic nuclei. The exact form of the interaction between neutrons and nuclei is not known, but it is possible to theoretically treat the problem with Fermi's pseudo-potential. We will detail this later. This interaction can occur in an elastic regime where the kinetic energy of the neutron is conserved in the collision with the nucleus. We usually call the elastic scattering regime as neutron diffraction, and the phenomenon of the collective neutron scattering of a set of atoms can be treated in wave bases, involving notions, such as constructive and destructive interference.

P. L. Bernardo (✉)

Centro Brasileiro de Pesquisas Físicas (CBPF), Rio de Janeiro, Brazil
e-mail: pablo81@cbpf.br

H. S. de Amorim

Universidade Federal do Rio de Janeiro (UFRJ), Rio de Janeiro, Brazil
e-mail: hsalim@if.ufrj.br

Neutron diffraction experiments are widely used for the determination, and refinement, of crystalline structures. They are applied in materials in the form of monocrystals or polycrystals (powder) through experimental methods, and analysis procedures, that are completely similar to those used in X-ray diffraction. This correspondence can be appreciated with the use of structural refinement programs of polycrystalline materials by the Rietveld method, such as FullProf and GSAS where, in general, it is possible to process neutron diffraction and X-ray diffraction data on the same platform and with the same algorithms.

An important feature in neutron diffraction is that there is not much contrast in the efficiency of scattering, if so we can express it, among the various chemical elements in the periodic table. In X-ray diffraction, the scattering efficiency, as depicted by the atomic scattering factor, increases with the number of electrons in the atom. This fact allows it to be much easier to locate light atoms in association with heavy atoms through neutron diffraction experiments than X-ray diffraction. The advantages of neutron diffraction in relation to X-ray diffraction in the location of hydrogen atoms present, for example, in organic materials or in hydrated materials, are well-known.

In the inelastic scattering regime, neutrons can transfer momentum to the atoms in the lattice. In a nuclear reactor, we can produce neutrons with energy very close to the vibrational energy of the atoms (thermal neutrons) and yet with wavelength of the order of the interatomic distances. In this way, an expressive interaction with normal crystal vibration modes (phonons) is possible, and the result of the scattering can be very informative. Because they work with very close energies between neutrons and phonons, neutron diffraction is a very skillful technique for the study of lattice dynamics.

Another form of the interaction of neutrons with matter is the magnetic interaction. Whenever atoms with permanent magnetic dipole moments are present, an interaction between the atomic magnetic dipole and the magnetic dipole of the neutron is established. Particularly important is the result of this interaction when we have materials with some sort of magnetic ordering. The result of a neutron diffraction experiment, mediated by magnetic interaction, has the potential to reveal the spatial arrangement of the magnetic dipoles of the magnetic sublattice present in the material. On the other hand, in the inelastic scattering regime intermediated by the magnetic interaction, we can observe energy transfers between neutrons and spin waves present in the material in a manner analogous to that occurring in the inelastic nuclear scattering with the lattice phonons.

In this chapter, we intend to give some practical information on how this characterization can be achieved through a case study. We begin with a simple description of the scattering of neutrons with nuclei where we try to give an overview of the most important concepts involved, and then we will discuss the magnetic scattering. Naturally, it would be far from the scope of this chapter to attempt to synthesize all the details of the theoretical modeling of the neutron scattering process, and for those who would appreciate a greater depth, we remember that there are good texts that develop all the treatment from the first principles [1, 2].

1.2 Nuclear Scattering

Shortly after the discovery of the neutron by Chadwick in 1932, the first studies on the possibility of the diffraction of a beam of neutrons by crystals, in the same way that occurs with an electron or X-ray beams, appeared. The analogy is very direct and very plausible. Neutrons are very massive particles with mass comparable to the hydrogen atom, and because they do not have a net electric charge, they have a remarkable ability to penetrate the solid matter. According to the quantum mechanics, each particle of momentum $\mathbf{p} = m\mathbf{v}$ (m – mass, \mathbf{v} – velocity) a wave of wavelength λ given by the relation of de Broglie,

$$\lambda = \frac{h}{p} \quad (1.1)$$

where h is the Planck constant. If we consider a beam of neutrons generated by a radioactive source incident on a paraffin-moderating target, we will have a dispersion of the kinetic energy of the neutrons by elastic collisions with the hydrogen atoms, abundant in paraffin. This dispersion closely follows the distribution of Maxwell–Boltzmann velocities for an ideal gas. If the absolute temperature of the moderating target is T , the average kinetic energy of the neutrons (\mathbf{k}) is given by

$$K = \frac{p^2}{2m} = \frac{3}{2}kT \quad (1.2)$$

where k is the Boltzmann constant. For a paraffin-moderating target at room temperature (~ 300 K), the average kinetic energy of the neutrons is about 0.04 eV with a De Broglie wavelength of approximately 1.5 Å. This value closely approximates the average wavelength of the $K\alpha$ doublet of an X-ray tube with copper anode, widely used in the X-ray diffractometers of polycrystals for structural characterization of the most diverse materials.

In 1930s the first evidence of neutron diffraction [3–5] emerged through experimental assemblies based on low intensity radioactive sources. The applications of neutron diffraction in crystallography as an accessory technique in the structural characterization of materials had their great impetus in the post-II War period with the advent of nuclear reactors and accelerators of particles.

With the new sources, it is possible to obtain beams with abundant thermal neutrons. These neutron beams have a continuous spectrum of kinetic energy, which is to say, in wavy terms, a “white” radiation. From a white beam of neutrons, we can obtain a monochromatic beam using monocrystals exactly as we proceed with X-rays. Monocrystals of Be, Si, Ge, Cu, Pb, or even laminar pyrolytic graphite are used for this purpose. Figure 1.1 shows, schematically, an experimental setup using a monochromatic beam for the study of a polycrystalline sample, in a configuration equivalent to Debye–Scherrer geometry used by X-ray diffractometers for polycrystals. The differences are more related to the dimensions: the neutron diffractometers are significantly larger than their equivalents for X-rays. In part,

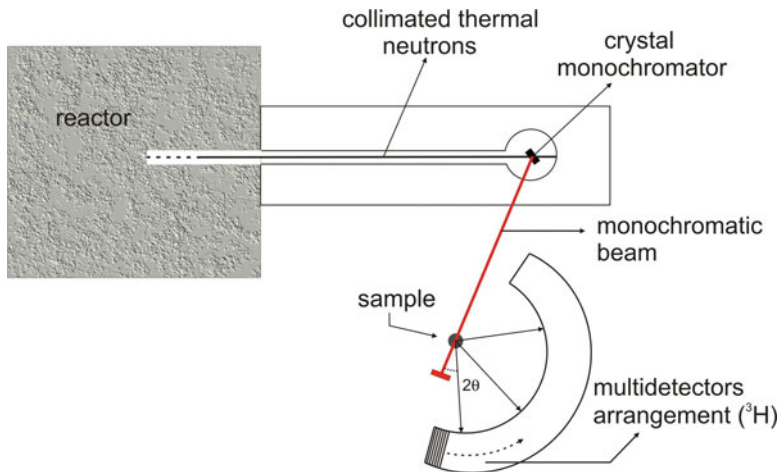


Fig. 1.1 Schematic representation of the typical experimental configuration of a neutron diffractometer for polycrystalline samples

this is due to the dimensions of the monochromatic neutron beam and the neutron scattering cross section itself which are smaller than that of X-photons, requiring larger amounts of sample. The neutron diffractometer installations are also larger due to the need to provide safety for users and technical personnel.

The most efficient experimental setup makes use of position-sensitive detectors as the arrangement of multiple detectors aligned in an arc concentric with the sample, as indicated in Fig. 1.1. As detection units for thermal neutrons (low energy), proportional gas detectors containing ^3He or BF_3 are used. Both ^3He and B have high cross section of shock for thermal neutrons, and by absorbing a neutron, they decay in ionized particles that are detected by the proportional detector [1].

Other processes that do not involve a nuclear reactor can also produce neutrons. High-energy charged particles obtained from particle accelerators are used for the production of neutrons by collision with solid targets. Usually, because they are more efficient, proton beams are used instead of electrons, which when they collide against a solid target produce high-energy neutrons. These neutrons need to be moderate to energies in the range of a few tens of meV, so they can be applied in a useful way in the structural analysis of materials. As in the case of the reactors, the moderators are materials consisting of chemical elements with expressive section of shock to collision with the neutrons. It is common to use water maintained at controlled temperatures with a common cooling system. The neutron diffractometers based on accelerators bring some advantages due, among other things, to the characteristics of the primary neutron beam. Unlike the nuclear reactor where the neutron beam is continuous, in the particle accelerators, the beam is pulsed, discontinuous. Since the pulses have very short duration, it is possible to measure the flight time from the moderator to the detector with a very high precision, which allows to measure the speed of the neutrons (typically of a few kilometers

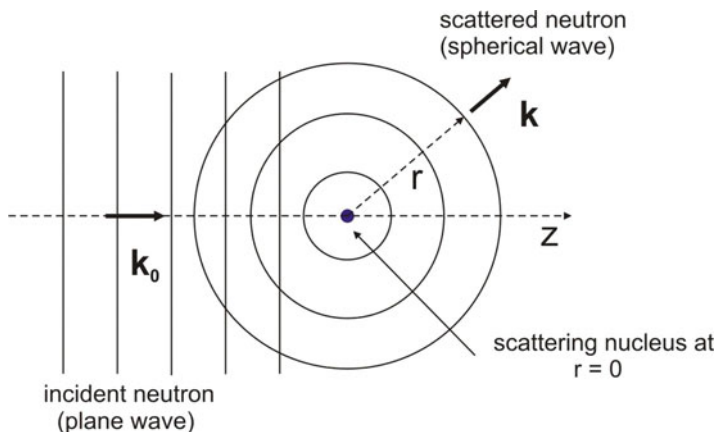


Fig. 1.2 The atomic nucleus behaves like a point scattering center for neutrons. The incident neutron can be described as a plane wave with wave vector k_0 . The scattered neutron is well described as a spherical wave

per second) and, consequently, its wavelength, through de Broglie's equation, very accurately. In this case monochromators are not used which allows the use of all produced neutrons.

Because it is a neutral particle, not carrying liquid electric charge, the interaction of the neutron with the atoms is mainly with the atomic nucleus. If we consider thermal neutrons with de Broglie wavelengths of the order 1 \AA (10^{-10} m) compared to the dimensions of the atomic nucleus of the order of 10^{-14} m , we can conclude that the atomic nuclei are basically punctiform scattering centers. If the energy of the incident beam of neutrons is different from the energy of the excited states of the target nuclei, resonance does not occur, and the scattering is essentially elastic. Thus, in this context, we can describe the wave function for the incident neutron beam as a plane wave of the type $e^{(-ik_0 \cdot z)}$, and we can describe the scattering wave by an atomic nucleus as $-b/r \cdot e^{(-ik \cdot r)}$,¹ where k_0 is the incident wave vector, $k_0 = k = 2\pi/\lambda$, and λ is the associated wavelength (Fig. 1.2). The parameter b is a constant for each nuclide and is called scattering length.

Since there is no theory about the interaction between the nucleus and the neutron, it is not possible to determine b from the first principles, and its measurement is strictly obtained experimentally. To describe the scattering, a phenomenological approach is used where a potential interaction function $V(\mathbf{r})$ between neutron and atomic nucleus is introduced, which only simulates the main characteristics of this interaction, such as short range, centrality, and high intensity. This potential is known as Fermi's pseudo-potential,

¹The minus sign is purely conventional.

$$V(\mathbf{r}) = \frac{2\pi\hbar^2}{m} b\delta(\mathbf{r}) \quad (1.3)$$

where m is the mass of the neutron and $\delta(\mathbf{r})$ is the Dirac delta function for three dimensions,

$$\int \delta(\mathbf{r})dV = 1 \quad (1.4)$$

The formalism that describes the scattering is too extensive to be summarized here, and we refer the interested reader to other sources [1, 6]. It is possible to show that if we produce the neutron collision with a fixed nucleus at the origin of a coordinate system, the fraction of the total number of neutrons scattered at a solid angle $d\Omega$, in the direction given by the angles θ and φ in spherical coordinates, is given by

$$\frac{d\sigma}{d\Omega} = \left(\frac{m}{2\pi\hbar^2}\right)^2 \left| \int V(\mathbf{r}) \cdot e^{i\mathbf{k}\cdot\mathbf{r}} dV \right|^2 \quad (1.5)$$

where $\frac{d\sigma}{d\Omega}$ is the so-called differential cross section. If we substitute pseudo-potential in this expression, we obtain

$$\frac{d\sigma}{d\Omega} = b^2 \quad (1.6)$$

i.e., a constant for any direction of scattering. This picture is very peculiar to neutron scattering, and a rapid comparison with what occurs in X-ray diffraction might be useful.

In X-ray scattering, we have an electromagnetic plane wave that interacts with the N electrons of an atom. The atomic electrosphere has dimensions much greater than the size of the nucleus being of the same order of the wavelength of the X-rays. The general approach to treat this scattering is to take an elemental partition of electronic cloud. In the quantum-mechanical description, each infinitesimal volume dV , at position \mathbf{R} of the electronic cloud, contains a charge dq mediated by the probability density of finding an electron in this position and given by

$$dq = \rho dV = -e \cdot \sum_{j=1}^N |\Psi_j(\mathbf{R})|^2 \cdot dV \quad (1.7)$$

where ρ is the density of electrons at point \mathbf{R} , e is charge of the electron, and $\Psi_j(\mathbf{R})$ is the wave function of the electron- j . Each charge element dq oscillates under the action of the incident wave and forms an elemental electric dipole that consequently emits radiation at the same frequency of the incident wave (Thomson scattering). The wave scattered by the atom is a superposition of each elemental wave. Figure 1.3

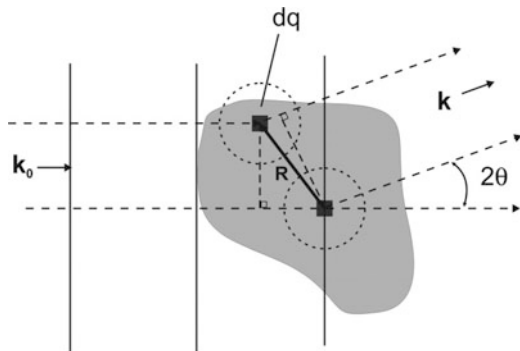


Fig. 1.3 To compute the X-ray scattering by the electron cloud of the atom, we must consider the contribution of each charge element $dq = \rho dV$ of an infinitesimal volume partition dV . Each charge element forms a small dipole that generates an elemental spherical wave. The interference of these waves generates an anisotropic scattering that varies according to the 2θ angle

shows schematically how we should add the contributions, where a phase difference between the elementary waves has to be taken into account. If we consider the wave amplitude $A(\theta)$ (electric field or magnetic field) at a point far from the atom,

$$A(\theta) = \left(\int_{\text{atom}} dq \cdot e^{i[\mathbf{k}-\mathbf{k}_0] \cdot \mathbf{R}} \right) \cdot A_0(\vartheta) = f(\theta) \cdot A_0(\theta) \quad (1.8)$$

$$f(\theta) = \int_{\text{atom}} \rho e^{i[\mathbf{k}-\mathbf{k}_0] \cdot \mathbf{R}} \cdot dV \quad (1.9)$$

$A_0(\theta)$ represents the amplitude of the wave scattered by an oscillating electron supposedly placed at the origin of the reference system. Thus, in a closer view of the Huygens principle for wave propagation, the function $f(\theta)$ measures the interference of the elementary waves emitted by the different parts of the electron cloud of the atom and is called the atomic scattering factor. Figure 1.4 shows the behavior of $f(\theta)$ for the cobalt atom ($N = 27$). We see a noticeable attenuation of the scattering intensity of the X-rays with the scattering angle θ , due to the interference in the electronic cloud. As we have seen, the same effect does not occur with the neutron–nucleus interaction. In the same plot, we represent the behavior of scattering length for the nuclide ^{59}Co .

For certain nuclides b is a complex number that varies strongly with the energy of the incident neutron. For these cases, in the interaction between the neutron and the nuclide occurs the formation of a new nucleus, involving the original nucleus and the incident neutron, with energy close to an excited state of the new system. This interaction is strongly dependent on neutron energy. The imaginary part of parameter b is linked to the absorption of the neutron. Under these conditions, b can assume significant values. Examples of nuclides where these resonant effects occur

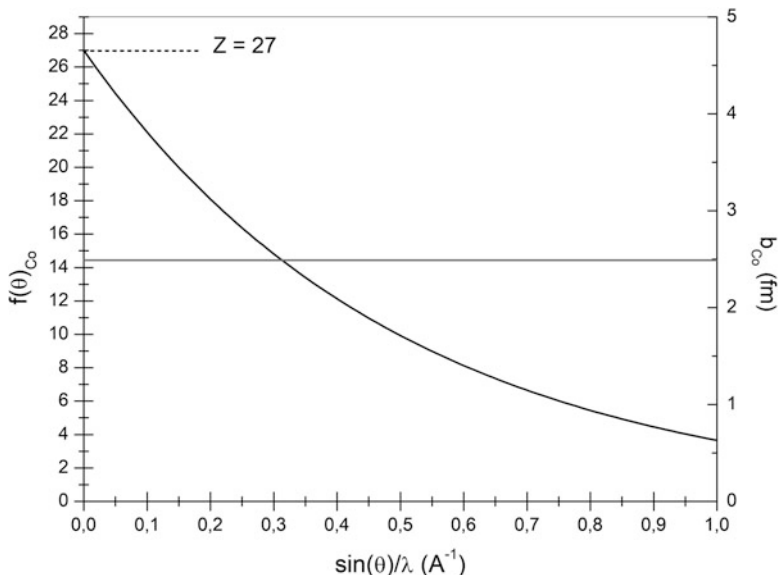


Fig. 1.4 Schematic chart showing the behavior of the atomic scattering factor for X-rays and the scattering length for neutron scattering of element ^{59}Co ($Z = 27$). We can see that for X-rays the intensity of scattered radiation decreases sharply with the scattering angle (θ), while the scattering length remains constant

Table 1.1 Values of b for the interaction between the neutron and some nuclides [7, 8]

Nuclide	Total spin (neutron + nuclide)	$b(\text{fm})$
^1H	1	10.817
	0	-47.42
^2H	3/2	9.53
	1/2	0.975
^6Li	3/2	0.67
	1/2	4.67
^{59}Co	4	-9.21
	3	3.58

are ^{103}Rh , ^{113}Cd , ^{157}Gd , and ^{176}Lu [1]. For most cases the parameter b does not depend on the energy.

Since the neutron has spin $1/2$, in the condition that the nuclide has a spin $I \neq 0$, the integrated neutron + nuclide system will have two possible states for the total spin, $I + 1/2$ and $I - 1/2$, and for each of these states we will have a value of b . Table 1.1 presents some values. If the spin of the nuclide is zero, only one value of b occurs.

In Fig. 1.5 we see the absolute value of b as a function of the atomic mass of the chemical elements. As we see, the behavior of b is unpredictable. For each isotope

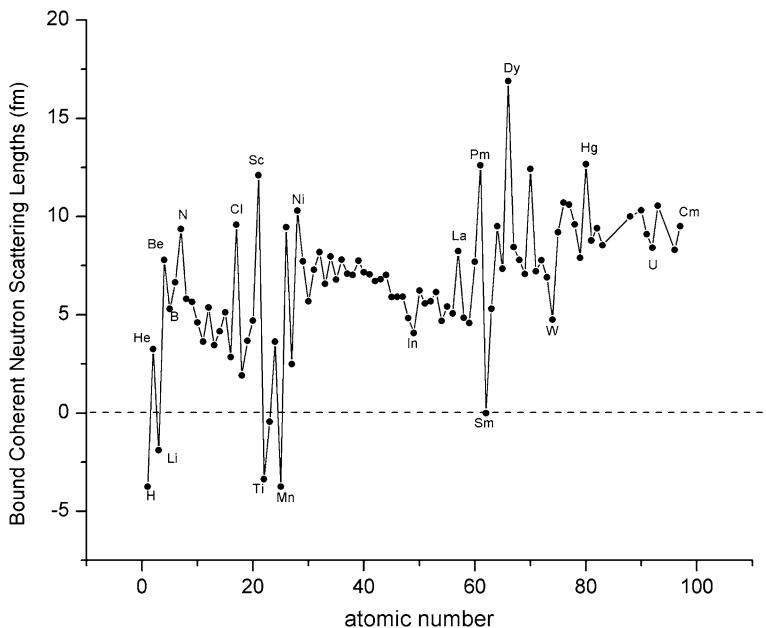


Fig. 1.5 Variation of the scattering length (b) with the atomic number for the most stable isotopes. The measurements are based on experimental results. Variation with atomic number is not smooth and predictable

Table 1.2 The values of b for the different isotopes of the iron element [7, 8]

	Spin	%	$b(\text{fm})$
^{26}Fe			9.45
$^{26}\text{Fe}, A = 54$	0	5.8	4.2
$^{26}\text{Fe}, A = 56$	0	91.7	9.94
$^{26}\text{Fe}, A = 57$	1/2	2.2	2.3
$^{26}\text{Fe}, A = 58$	0	0.3	15

of a given element, other values of b are found. In Table 1.2 we see the values of b for the different isotopes of the iron element.

From Fig. 1.5 we can conclude that there is no big variation between the values of b and the atomic number, with the majority of values being in the range of 5 to 10 fm. This result contrasts sharply with what occurs in X-ray diffraction where the diffracted intensities are regulated by the number of electrons in the atoms. The consequence of this phenomenon is clear when we try to determine or refine, by XRD, a structure where very different atomic number elements occur, for example, in the superconducting ceramic YBACU where oxygen contributes very little compared to the cations, Y, Ba, and Cu. Only with the diffraction of neutrons, a correct determination of the structure of this material was possible. This same property shows why neutron diffraction is the most appropriate technique when it is necessary to locate hydrogen atoms in the crystal lattice with higher precision.

1.3 Elastic Neutron Scattering by Polycrystals

The applications of neutron scattering in the structural characterization of materials are similar to the applications of X-ray scattering. In a sense, we can say that both techniques present many conceptual similarities and, in what they have specifically, they complement each other. In elastic scattering the neutrons collide with the nuclei without losing their kinetic energy. In X-ray scattering we also observe the elastic scattering of photons, and in this condition, in both cases, we say that a diffraction phenomenon occurs. However, in the case of thermal neutrons, the typical energy is of the order of some meV, and in this case the neutron energies are of the same order of magnitude of the thermal vibrations of the atoms in the crystalline lattice. It is thus possible for efficient energy exchange interactions between neutrons and network phonons. In this interaction, the neutron can receive or donate energy. This interaction path gives rise to an inelastic scattering, which does not preserve the energy (wavelength) of the neutron and does not give rise to constructive interference formation (Bragg lines). In turn, neutron inelastic scattering has been used, among other things, to characterize the phonon spectrum of a given material of enormous importance to materials science and solid-state physics [9].

In the case of crystalline materials, one of the most widely used methods of neutron diffraction is the polycrystalline method where the sample is reduced to a very fine granulation powder and subjected to a well-known neutron beam, that is, wave determined. This is the experimental setup discussed in the introduction and illustrated in Fig. 1.1. The formation of elastically scattered beams in precise directions can be predicted through the Bragg equation, just as in X-ray diffraction,

$$2d.\sin(\theta) = n\lambda \quad (1.10)$$

where 2θ is the scattering angle, n is an integer, d is the distance between planes of a given family of crystallographic planes, and λ is the wavelength of the neutron beam. With the randomly distributed powder sample on the target, we ensure that an appropriate amount of small grains of the material will be conveniently oriented at the angle θ that satisfies the strict condition established by the Bragg equation. The scattered beams, also called Bragg lines or reflections, have intensities that relate to crystalline symmetries and the distribution of atoms in the crystal lattice. Each atom of the structure gives rise to a spherical wave, and the observed result is a superposition of these waves:

$$\sum_{i=1}^N \left(\frac{b_i}{r} \right) e^{ik.r} . e^{i\mathbf{R}_i \cdot (\mathbf{k} - \mathbf{k}_0)} \quad (1.11)$$

In this expression the exponential term $e^{i\mathbf{R}_i \cdot (\mathbf{k} - \mathbf{k}_0)}$ takes into account the phase difference between the spherical waves emitted by the N atoms because they are in different positions of the crystal. \mathbf{R}_i is the position vector of the atom- i in

relation to an origin taken in the crystalline lattice. The intensity of the Bragg line is proportional to the square of the wave amplitude and depends in some way on the square of the scattering lengths of the atoms involved.

For the crystalline structures, where the atoms are distributed periodically, the sum in (1.11) can be rearranged. We can show that in the Bragg condition, constructive interference maxima can be written as

$$\frac{d\sigma}{d\Omega} \propto |F_N(hkl)|^2 \quad (1.12)$$

$$F_N(hkl) = \sum_{i=1} b_i e^{i\mathbf{R}_i \cdot (\mathbf{k} - \mathbf{k}_0)} \quad (1.13)$$

where F_N is called the nuclear structure factor for the family of planes hkl . The sum in (1.13) extends over all atoms in a unit cell of the crystal lattice. The nuclear structure factor is completely analogous to the structure factor used in the X-ray diffraction. As we know, due to the translational symmetries present in the crystal lattice, the sum (1.13) can cancel. The symmetry conditions for the extinctions of certain reflections are the same in the neutron and X-ray diffraction.

The difference we find with neutrons when compared to X-rays is that for the same chemical element, we have different values of b due to their natural isotopic composition and also with respect to the state of the spin of the nucleus which, as we have seen, non-zero nuclear spin implies two values, b_+ and b_- . Taking into account the influence of a given chemical element on the intensity of the Bragg reflection, we have to use a kind of average between the values of b of the different isotopes present and different spin states. This average is represented as b_i in the Eq. (1.13). If we consider that nuclei of the different natural isotopic varieties of a given chemical element are distributed randomly in the crystalline lattice, we can show that this gives rise to an incoherent component of the elastic scattering. This radiation spreads in all directions and contributes to the background. The effect of background increase on hydrogen samples due to their characteristic two spin states is well-known. In Table 1.1, we see that for the two states of total spin, the values of b are very different. Depending on the hydrogen content in a sample, this significant difference between b_+ and b_- may lead to a significant increase of background in the powder diffractograms. In these cases, one way to soften the influence of this incoherent spin component is to replace the hydrogen by deuterium in the synthesis of these compounds, because as indicated in Table 1.1 the component b_- is small compared to b_+ .

1.4 Magnetic Scattering

Another form of interaction between neutrons and atoms of enormous practical importance is the magnetic interaction. As we know, neutrons have a magnetic

dipole μ_n associated with spin I given by

$$\mu_n = -\gamma_n \mu_N I \quad (1.14)$$

where $\gamma_n = 1.913$ is a constant and μ_N is the nuclear magneton, given by

$$\mu_N = \frac{e\hbar}{2m_p} \quad (1.15)$$

where m_p is the mass of the proton. The magnetic dipole of the neutron interacts with the magnetic field \mathbf{B} produced by a permanent atomic magnetic dipole. This dipole, in turn, is associated with the orbital motion and the spin of the electrons. The magnetic dipole moment due to the orbital motion of the electron is given by

$$\mu_{\text{orbital}} = \frac{-e}{2m_e} L \quad (1.16)$$

where L is the angular momentum and m_e is the mass of the electron. The magnetic dipole moment due to spin is given by

$$\mu_{\text{spin}} = -2\mu_B S \quad (1.17)$$

$$\mu_B = \frac{e\hbar}{2m_e} \quad (1.18)$$

where μ_B is the magneton of Bohr and S is the spin of the electron. It is convenient to calculate separately the contributions to the total magnetic field due to electronic spin and orbital motion and to study the interaction of the magnetic dipole of the neutron with each of the components separately. Particularly when the atomic dipoles are oriented and ordered in the crystalline lattice, forming a kind of magnetic subnetwork, constructive interference beams (Bragg reflections) can be formed based on this interaction. This magnetic ordering is observed in ferromagnetic, antiferromagnetic, and ferrimagnetic materials to name but three well-known examples. The presence of new reflections will indicate a change of symmetry of the scattering system that starts to incorporate the distribution of magnetic dipoles and not just the spatial distribution of the nuclei. In Fig. 1.9 we can see the neutron diffractogram of a substance in the paramagnetic state and the diffractogram of the same sample after transit to the magnetic state. We can see the emergence of new Bragg lines and a change in the intensities of lines that were already present in the paramagnetic state. The characterization of the magnetic structure of materials has in the neutron diffraction technique its greatest experimental tool.

The potential V , which describes the magnetic interaction of the neutron with the magnetic field B of the atom, is given by

$$V = -\mu_n \cdot B \quad (1.19)$$

which differs greatly from the potential governing interaction with the nucleus. While the interaction with the nucleus is restricted to a very limited region, the magnetic interaction is a long-range interaction. In turn, it results from a superposition of contributions to the atomic magnetic field that comes from the entire electronic cloud. For these reasons, in the nuclear magnetic interaction, we cannot treat the atom as a particle, as a punctiform scattering object. The magnetic field originates in the magnetic dipoles associated with the spin and the orbital motion of the unpaired electrons, that is, we can write that

$$B(r) = B_{\text{spin}}(r, S) + B_{\text{orbital}}(r, L) \quad (1.20)$$

Using Eqs. (1.14) and (1.15) and using the same procedure that allowed the derivation of Eq. (1.5), we obtain the expression of the differential cross section for the magnetic scattering. We are omitting the details (see [1]), but we can add that B is calculated from the atomic model of quantum mechanics and the formalism of classical electrodynamics.

A similar behavior to X-ray scattering is observed in the magnetic interaction. A term analogous to the atomic scattering factor $f(\theta)$, now of magnetic origin, most commonly termed magnetic form factor is used to describe the contribution of each atom:

$$f(\theta) = \frac{\langle q | \int_{\text{atom}} M \cdot e^{-i(k-k_0)R} d^3r | q \rangle}{\langle q | \int_{\text{atom}} M d^3r | q \rangle} \quad (1.21)$$

The letter q symbolizes the fundamental state of the atom, the brackets represent the spatial averaged value, and M represents the magnetization operator. The magnetization can be separated with origin in the spin and orbital motion of electrons:

$$M = M_{\text{spin}} + M_{\text{orbital}} \quad (1.22)$$

Magnetization is a measure of the amount of magnetic dipole moment per unit volume and can be separated by contributions due to spin and orbital motion of the electrons. The calculation of magnetization takes into account all the electrons, but it turns out that the relevant contributions come from the unpaired electrons. For transition metals, for example, the electrons of the 3d-orbital are those relevant [10]. Figure 1.6 shows the behavior of the magnetic form factor for the Nd^{3+} obtained by values provided by International Tables of Crystallography, Vol. C. The graph shows separately the contributions due to the spin magnetic dipole and the magnetic dipole associated with the orbital movement of the unpaired electrons.

The nuclear interaction is completely isotropic and the dipole–dipole magnetic interaction is strongly anisotropic. However, both interactions are, basically, of the same magnitude. As a consequence of the anisotropy of the magnetic interaction, it

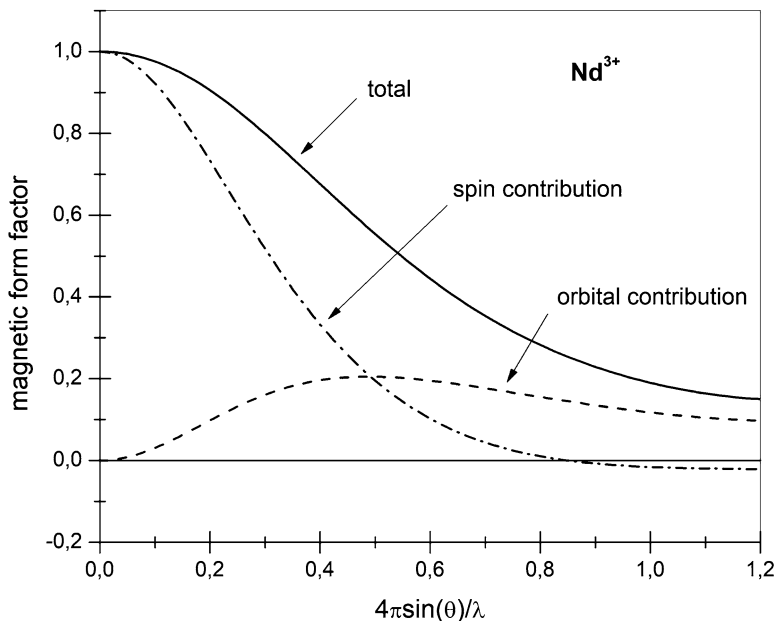


Fig. 1.6 Magnetic form factor of the Nd^{3+} with partial contributions due to spin and orbital motion of the unpaired electrons

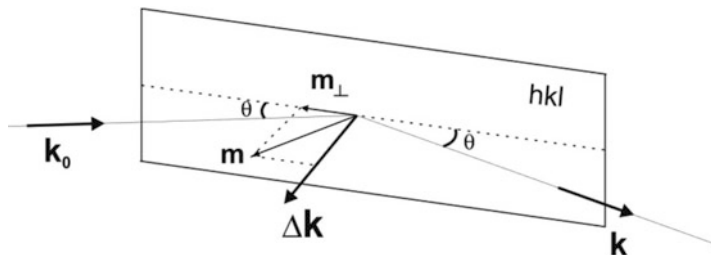


Fig. 1.7 In the magnetic scattering, the intensity of the diffracted beam depends on the component of the magnetization vector perpendicular to the scattering vector Δk

is verified that only the parallel component of the magnetic dipole moment of the atom at a given crystallographic plane of indices hkl contributes to the magnetic scattering (“reflection”). In other words, for those cases where magnetization is perpendicular to a given plane hkl , a magnetic contribution does not result to the scattering by this plane. This is an intrinsic extinction condition, different from the extinction conditions due to the symmetries of the crystalline lattice and is a very important factor to determine the orientation of the magnetic dipoles in relation to the crystallographic axes. Figure 1.7 schematically shows this arrangement.

The intensity of the Bragg reflections due to magnetic interaction can be calculated in a similar way to the way we calculate for nuclear scattering. In this

case, the differential cross section is directly proportional to the square of the magnetic structure factor (F_M). The most important difference is that the magnetic structure factor is a vector quantity, as opposed to a nuclear structure factor that is scalar. This property is also related to the anisotropic nature of magnetic interaction. The magnetic structure factor, in the Bragg condition, for a simple magnetic structure in which the magnetic ordering is entirely defined in a unit cell of the crystal can be written as

$$F_M(hkl) = p \sum_i^{\text{cell}} f_i(\theta_{hkl}) \cdot \mu_i e^{-i R_i(k-k_0)} \quad (1.23)$$

where p is a constant and μ_i is the magnetic dipole moment of the atom- i .

Other forms of magnetic structures, such as helical magnetic structures, cannot be described by a simple translation of the magnetic arrangement contained in a unit cell. These cases can be analyzed using propagation vectors (\mathbf{k}). The idea is based on the fact that if there is a periodic ordering in the spatial distribution of the atomic magnetic dipoles, these can be described as a Fourier series expansion as

$$\mu_{ji} = \sum_k C_{k,i} e^{-2\pi i k \cdot R_j} \quad (1.24)$$

where μ_{ji} is the magnetic dipole moment of the l -atom in the j -cell. $C_{k,i}$ are complex vector coefficients, \mathbf{k} are vectors defined in the reciprocal space, called propagation vectors, and R_j are position vectors of the origin of the unit j -cell. A similar procedure is used in the description of modulated structures, where instead of μ_{ji} , we will have, for example, a vector that measures the displacement of the l -atom in the j -cell in relation to the position of these atoms in an original cell, taken as reference. As in modulated structures, these magnetic structures need few propagation vectors, typically no more than three. The simplest situation is that in which there is only one propagation vector $\mathbf{k} = 0$. In this situation $C_{0,i} = \mu_{ji}$ for all cells. This is the case described by Eq. (1.23).

In the case of magnetic structures, the scattering of neutrons is given by the sum of the nuclear and magnetic contributions. In the situation where a beam of neutrons with non-polarized spins, that is, not aligned in a particular direction, which impinges on a crystal with magnetic ordering, it can be shown that the intensity of the interference maxima is given as

$$\frac{d\sigma}{d\Omega} \propto |F_N|^2 + |(F_M)_{\perp}|^2 \quad (1.25)$$

In the magnetic part of (1.25), we take into account the perpendicular component of the magnetic structure factor to the scattering vector, defined as $\Delta\mathbf{k} = \mathbf{k} - \mathbf{k}_0$. In the Bragg condition, the scattering vector is parallel to the normal direction to the plane hkl considered.

In vector notation, the Bragg condition given by Eq. (1.10) can be written as

$$\Delta \mathbf{k} = \mathbf{h} \quad (1.26)$$

where \mathbf{h} is a vector of the reciprocal lattice representing a family of hkl planes. For the case of magnetic structures, the formalism with the propagation vectors allows us to write a more general Bragg condition,

$$\Delta \mathbf{k} = \mathbf{h} + \mathbf{k} \quad (1.27)$$

In the case where $\mathbf{k} = 0$ (1.26), the reflections correspond to the points of the reciprocal lattice, and the magnetic contribution overlap with the nuclear contribution. In the case where $\mathbf{k} \neq 0$ (1.27), new lines are observed close to the points of the reciprocal lattice. These lines are generally called satellite lines.

1.5 Applications

Neutron diffraction is the application of neutron scattering to the determination of the atomic and/or magnetic structure of a material. As we have already seen, neutrons are uncharged and carry a spin and therefore interact with magnetic moments, including those arising from the electron cloud around an atom. Neutron diffraction can therefore reveal the microscopic magnetic structure of a material [2].

Magnetic scattering does require an atomic form factor as it is caused by the much larger electron cloud around the tiny nucleus. The intensity of the magnetic contribution to the diffraction peaks will therefore decrease toward higher angles. The use of neutrons as research tools gives scientists unprecedented insight into the structure and properties of materials important in biology, chemistry, physics, and engineering. Neutron scattering shows directly where atoms are and what they are doing. It allows researchers to see in real time how the structure of a material shifts with changes in temperature, pressure, and magnetic or electronic fields. It also traces the atomic motions and electron states that give materials properties such as magnetism or the ability to conduct electricity – essential information in the pursuit of energy savings.

Neutrons have wavelengths ranging from 0.1 to 1000 Å, and they have the power to reveal what cannot be seen using other types of radiation. The specific properties of neutrons to behave as particles or as microscopic magnetic dipoles enable them to give us some information which is often impossible to obtain using other techniques. For instance, the neutrons scattering off gases, liquids, and solid matter give us information about the structure and magnetism of these materials.

Neutrons are nondestructive radiation and can penetrate deep into matter. For this reason, they are ideal for applications in biological materials and samples under extreme conditions of pressure, temperature, and magnetic field. Furthermore, neutrons are sensitive to hydrogen atoms. It is a powerful tool for analyzing

hydrogen storage materials, organic molecular materials, and biomolecular samples or polymers. Some applications of neutrons in different fields of research are [11]:

Condensed-matter physics, materials science, and chemistry:

- Examination of the structure of new materials, for example, new ceramic high-temperature superconductors or magnetic materials (important for electronic and electrical applications).
- Clarification of still unknown phenomena in processes such as the recharging of electric batteries.
- Storing of hydrogen in metals, an important feature for the development of renewable energy sources.
- Analysis of important parameters (e.g., elasticity) in polymers (e.g., plastic material).
- Colloid research gives new information on such diverse subjects as the extraction of oil, cosmetics, pharmaceuticals, food industry, and medicine.

Biosciences:

- Biological materials, naturally rich in hydrogen and other light elements, are ideal samples for analysis with neutrons.
- Cell membranes and proteins
- Virus investigations
- Photosynthesis in plants

Nuclear and elementary particle physics:

- Experiments on the physical properties of the neutron and the neutrino.
- Production of extremely slow neutrons down to 5 m/s (the velocity of the neutrons which leave the reactor is generally about 2200 m/s).
- Experiments on atomic fission and the structure of nuclei.

Engineering sciences:

- Since neutron diffraction is nondestructive, it is ideal for the analysis of different technical phenomena in materials.
- Visualization of residual stress in materials.
- Hardening and corrosion phenomena in concrete.
- Inhomogeneity and trace elements in materials.

1.6 Instrumental

1.6.1 *Institut Laue-Langevin (ILL)*

The Institut Laue-Langevin (France) provides scientists with a very high flux of neutrons feeding some 40 state-of-the-art instruments, which are constantly being developed and upgraded. As a service institute, the ILL makes its facilities and expertise available to visiting scientists. Every year, some 1400 researchers from over 40 countries visit the ILL. More than 800 experiments selected by a scientific review committee are performed annually. Research focuses primarily on fundamental science in a variety of fields: condensed matter physics, chemistry, biology, nuclear physics and materials science, etc. ILL can specially tailor its neutron beams to probe the fundamental processes that help to explain how our universe came into being, why it looks the way it does today, and how it can sustain life. ILL is funded and managed by France, Germany, and the United Kingdom, in partnership with 10 other countries.

The ILL's powder diffraction instruments are D2B, D20, D1B (CRG), D4, SALSA and D7. All of our measurements were performed in the D1B instrument. It uses a large crystal monochromator to select a particular neutron wavelength, just as the different wavelengths of light can be separated using a prism or fine grating. The material to be studied is placed in this monochromatic neutron beam, and the scattered neutrons are collected on a large 2D detector. The sample can be a liquid, a bunch of fibers, a crystal, or a polycrystal. A polycrystal is the usual form of solid matter, such as a lump of metal or ceramic, and is made up of millions of tiny crystals. (site)

Neutron diffraction experiments at ILL are thus really quite simple and available to a wide variety of users – materials scientists, chemists, physicists, and biologists. The simplest is called “powder diffraction,” when a polycrystalline lump of material, often ground to a fine powder, is placed in the beam. Neutrons are scattered at specific angles, corresponding to the spacing between atomic planes, and by measuring these angles and intensities, the atomic structure of the material can be deduced. If instead of a crystalline powder an amorphous or liquid sample is used, there are only broad peaks at specific angles corresponding to average interatomic distances.

To obtain more data, short neutron wavelengths are used, and sometimes one type of atom is replaced by its isotope – chemically identical, but with a different nucleus and different neutron scattering power. This difference then gives information specific to that atom.

D1B (Fig. 1.8) is a high intensity powder diffractometer with a PSD covering the angular range 0.8° to 128° . A cryostat 1.6–320 K or even a dilution cryostat can be mounted on the D1B diffractometer enabling to investigate magnetic structures on powder samples. It has always been in very high demand for real-time experiments and for very small samples because of its high-efficiency position-sensitive detector (PSD). The new PSD makes it an even more valuable tool. Run as a CRG-A instrument by a CNRS/CSIC team, it is available 50% of the time for scheduled ILL experiments (Fig. 1.8).

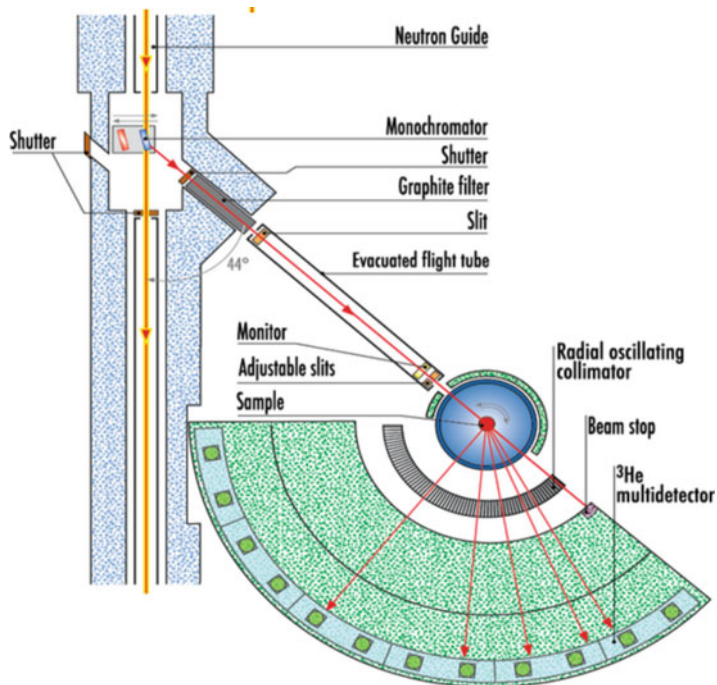


Fig. 1.8 This layout shows the new D1B (ILL) setup with the new position-sensitive detector (PSD) with 1280 cells covering a total of 128° and the radial oscillating collimator (ROC) (Figure taken from [<https://www.ill.eu/instruments-support/instruments-groups/instruments/d1b/description/instrument-layout/>])

1.7 Magnetic Pattern

The magnetic structure for the most of magnetic compounds can be determined using neutron powder diffraction (NPD) data and complementary magnetic measures. In this chapter, we will determine the magnetic structure of the double perovskite Sr_2YRuO_6 using FullProf Suite [12], a crystallographic program developed for Rietveld analysis (structure profile refinement) of neutron (constant wavelength, time of flight, nuclear and magnetic scattering) or X-ray powder diffraction data collected at constant or variable step in scattering angle 2θ . The NPD measurements were performed in Institut Laue-Langevin (ILL), and the basic steps for determining the magnetic structure were based on a tutorial made by Juan Carvajal [13]. This procedure will be easier if the reader has experience with crystallography and structure profile refinement using X-ray powder diffraction and/or neutron diffraction through Rietveld analysis. For determining the magnetic structure of Sr_2YRuO_6 , we will take the following steps:

- The first step is to perform a NPD measure of the sample in paramagnetic state (in general, at room temperature if you do not know the magnetic transition

temperature). The data must be refined in order to obtain the sample structural parameters and check if any impurities are present.

- Perform a NPD measure of the sample in magnetic state; in other words, we have to know the magnetic transition temperature (T_C or T_N). Below this temperature, additional magnetic peaks will appear, specially for lower 2θ values (if additional peaks are not observed, go to the next step). Refine with the same PCR file used in the paramagnetic state. Using WinPLOTR-2006, open both diffraction pattern data, and save the additional peaks in a K_Search Format.
- At this point, we have to determine the propagation vectors (\mathbf{K}) of the magnetic structure (more details about \mathbf{K} vector can be found in the references [13, 14]). If additional peaks are not observed in magnetic state, the magnetic structure has a $\mathbf{K} = (\mathbf{0}, \mathbf{0}, \mathbf{0})$. Otherwise, we will use the program K_Search to calculate the propagation vector. The propagation vectors must be tested with Le Bail fit mode [12, 15].
- After the determination of the propagation vector, the program BasIreps is used to calculate the basis vector of the irreducible representations (irreps). It is a basic information about the magnetic structure symmetry that we have to insert in the PCR file (for more details, see [13]).
- Finally, we can refine the magnetic structure and get all the possible magnetic informations about the sample given by the Rietveld method.

1.7.1 Magnetic Structure of the Double Perovskite $A_2BB'O_6$

NPD measurements of the sample Sr_2YRuO_6 were performed for various temperatures at the D1B instrument in ILL with $\lambda = 2, 52\text{\AA}$. For determining the magnetic structure of this compound, we will use just two powder diffraction patterns, one in the paramagnetic state (40 K) and another in the magnetic state (1.6 K). All the basic informations about the magnetic and structural state of this compound were obtained in the references [16–19]. Initially, we will use the monoclinic $P2_1/n$ space group and lattice parameters with $a = 5.7698(2)$, $b = 5.7814(1)$, and $c = 8.1646(4)$, along with $\beta = 90.21(1)$ [16]. The data obtained at 1.6 K and 40 K corresponds to the format *XY SIGMA* (Ins =10), Fig. 1.9.

In order to obtain the sample structural parameters and check if any impurities are present, we refined the crystal structure of Sr_2YRuO_6 at 40 K in a folder called Temp40K. The complete PCR file (Sr2YRuO6_40K.pcr) is shown in Fig. 1.10, and the calculated and observed patterns are shown in Fig. 1.11. Also, we put $Pcr = 2$ (a new input file is generated conserving the old one) to generate Sr2YRuO6_40K.new.

After creating a folder called test, we can observe the magnetic peaks using the PCR file (Sr2YRuO6_40K.pcr) at 40 K (after the refinement) into a test PCR file (test.pcr) and refine the data at 1.6 K. At this moment, we can just leave zero, background coefficients, and scale to be refined. All the other parameters must be fixed. Also, we can put $Nba = -3$ (read 6 additional polynomial background

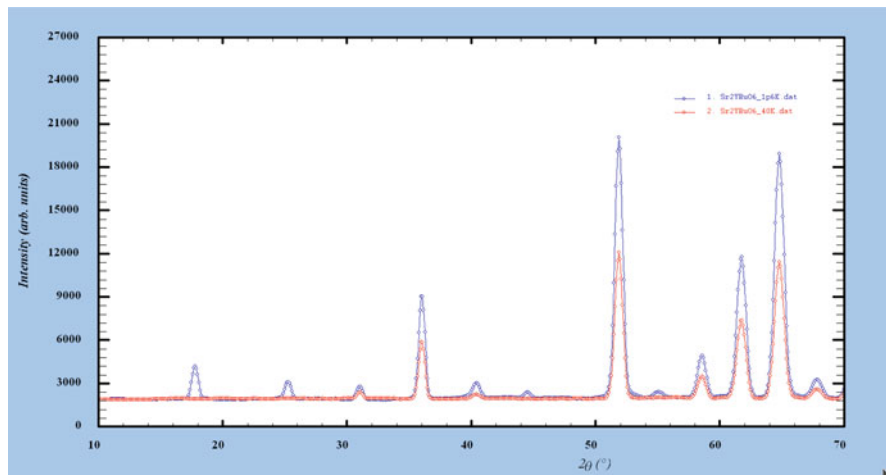


Fig. 1.9 Powder diffraction patterns at 1.6 K (blue line) and 40 K (red line)

```
Sr2YRu06_40K
! Current global Ch2 (Bragg contrib.) = 25.53
UNIT 1 ! Flags for patterns (1:refined, 0: excluded)
W.PAT 1.000
! Nph Dun Iso Nre Cry Cut Aut
! 0 0 0 0 0 0 0 1
! Job Npr Nba Nbc Nbr Nw Ilo Res Site Uni Cor Ann Int
! 1 7 3 2 0 0 0 0 0 0 0 0 1 -> Pattern: 1
! File names of data(patterns) files
Sr2YRu06_40K.dat
!
! Mat Pcr Nli Rpa Svm Sho
! 0 2 0 0 0 0
! Ipr Pfl Ioc Ls1 Ls2 Ls3 Prf Irs Nkl Fou Ana
! 0 0 2 0 4 0 3 10 0 0 0 1 -> Pattern: 1
!
! Lambda Lambda1 Ratio Hpos HET Ctho hnk AsyLin Npolar1 2nd-mkr -> Pattern: 1
! 2.522984 1.261452 0.00100 20.000 12.0000 0.0000 0.0000 30.00 0.0000 0.0000
!
! NCV Eps R_at R_an R_pr R_rl
! 10 0.01 1.00 1.00 1.00
! Theta Step Theta PSD Scaled -> Pattern: 1
! 0.7000 0.100078 128.6700 0.000 0.000
! Excluded regions (LowT HIGHT) for Pattern# 1
! 0.00 29.00
! 128.00 180.00
!
! 0 Number of refined parameters
!
! Zern Code Sylan Code Sylin Code Lambda Code MORE ->Pattern: 1
! -0.03647 41.0 0.00000 0.0 0.00000 0.0 0.000000 0.00 0
! Background coefficients/codes for Pattern: 1 (Polynomial of 9th degree = terms 1/1, 1/1^2, and 1/1^3)
! 1463.228 -221.505 5.484 6.000 0.000 0.000
! 21.00 31.00 41.00 0.00 0.00 0.00
! 0.000 0.000 0.000 0.000 0.000 0.000
! 0.00 0.00 0.00 0.00 0.00 0.00
!
!-----> Profile Parameters for Pattern # 1
! Scale Shift Rev Str1 Str2 Str3 Strain-Model
! 21.731 0.00000 -0.22123 0.00000 0.00000 0.00000 0
! 11.00000 0.000 0.000 0.000 0.000 0.000
! 1.961933 -0.81558 0.48705 0.000000 0.000000 0.000000 0.000 0.000
! 0.000 0.000 0.000 0.000 0.000 0.000 0.000 0.000
! 5.754833 5.707660 8.160513 90.128454 90.128454 90.000000
! 13.00000 61.00000 71.00000 alpha beta gamma Kcell Info
! Pref1 Pref2 Asy1 Asy2 Asy3 Asy4 S.L. D.L
! 0.0000 0.0000 0.01116 0.01153 0.00000 0.00000 0.0000 0.0000
! 0.00 0.00 0.00 0.00 0.00 0.00 0.00 0.00
! 2Th1/2F1 2Th2/2F2 Pattern to plot
! 29.000 128.000
! 1
```

Fig. 1.10 PCR file at 40 K for the structural pattern of the Sr_2YRuO_6

coefficients). After the refinement, we can see the magnetic peaks, not calculated by the refinement, at low angles (Fig. 1.12). Now we are able to calculate the propagation vector \mathbf{K} that represents the magnetic peaks observed.

1.7.2 Magnetic Peaks Identification and Propagation Vector \mathbf{K}

The next step is to open the last PRF file (test.prf) using the WinPLOTR-2006 program. This file is generated using Prf=1 or 3, into PCR file. Then, we can select the most salient peaks and save them in K_Search Format. For this, first go in the menu Calculation – Peak detection – Enable. Then, Calculation – Peak detection –

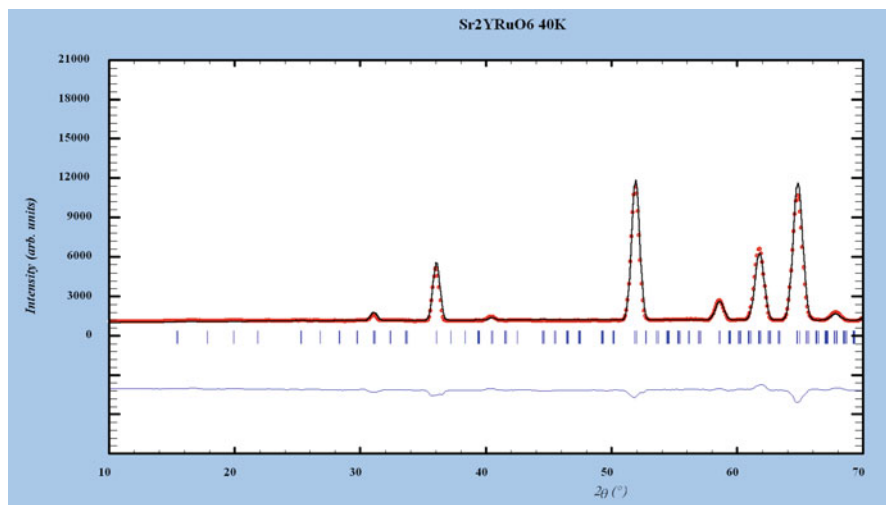


Fig. 1.11 Calculated (red line) and observed (black line) patterns at 40 K

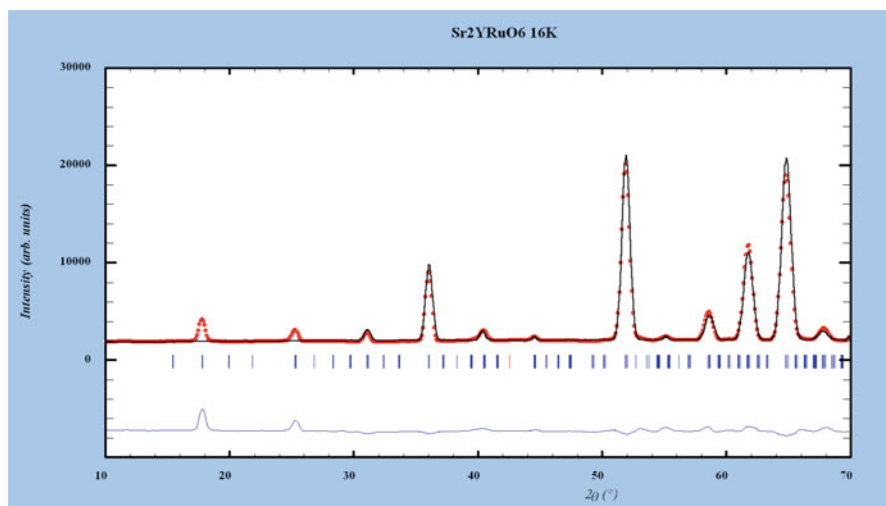


Fig. 1.12 Magnetic peaks at low angles not calculated by the refinement

Insert peak. After insert the magnetic peaks (two in this case), and go in the menu Calculation – Peak detection – Save peaks – K_Search format (Fig. 1.13).

After selecting the K_Search format menu, open a dialog for the input parameters. If you are working with the refined pattern, the parameters will be introduced automatically (Fig. 1.14a). We can start selecting Short Output and Search only special K-vectors options. The magnetic peaks will be saved in a file called K-search.sat. Then, we have to run the K_Search program in order to get the solutions for the possible propagation vectors (Fig. 1.14b). If you want to select more peaks,

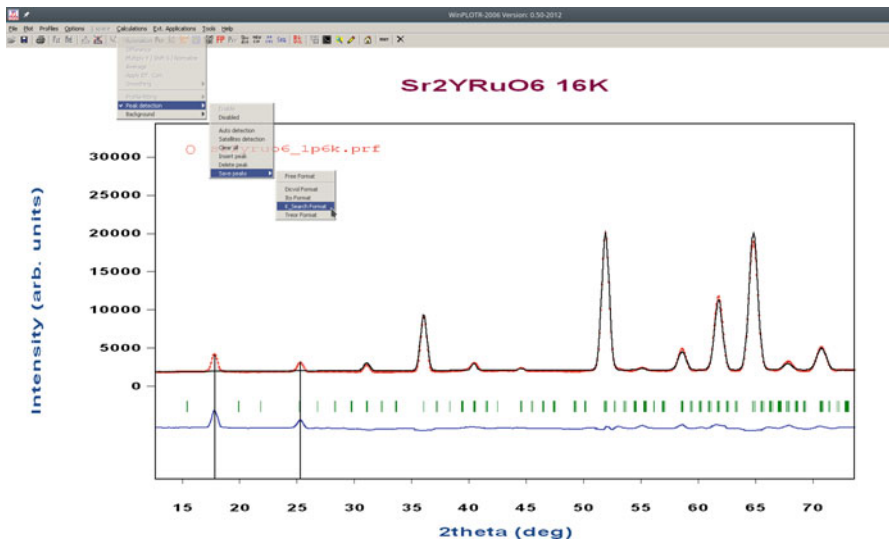


Fig. 1.13 Using the WinPLOTR-2006 program to save the magnetic peaks in K_Search format

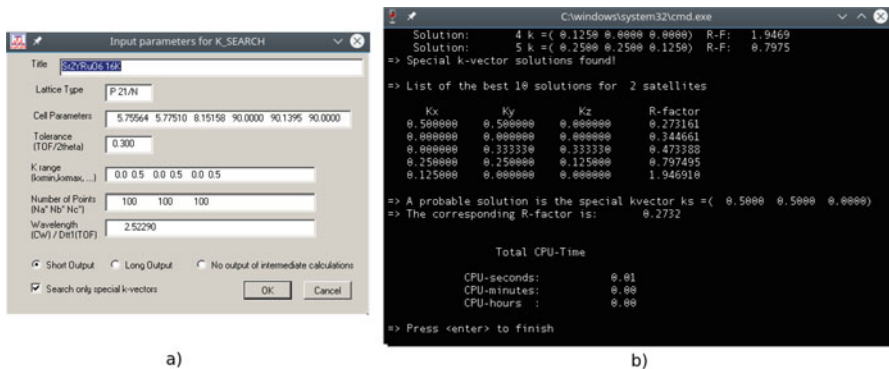


Fig. 1.14 (a) Is the dialog for the input parameters for K_Search program, and in (b) we can see the solutions for the possible propagation vectors \mathbf{K} calculated by K_Search program

delete peaks, or just rerun the program, press the *enter* key (\leftrightarrow) to close the program.

In Fig. 1.14b, we can see that $\mathbf{K} = (0.5 \ 0.5 \ 0.0)$ is the best solution, followed by $\mathbf{K} = (0 \ 0 \ 0)$. If the magnetic cell is the same as the nuclear cell, then the propagation vector $\mathbf{K} = (0 \ 0 \ 0)$. In our case, $\mathbf{K} = (0.5 \ 0.5 \ 0.0)$ is commensurate with magnetic cell $2a \times 2b \times c$ (compared with the nuclear unit cell a, b and c) [20]. At this time, we must be careful with a possible small shift in positioning when we insert the magnetic peaks. When it takes place, a wrong solution can be found for a better R-factor. However, we can check the propagations vectors by doing Le Bail fit method [12, 15].

1.7.3 *Le Bail Method*

In this chapter, we will just use the Le Bail method to check if it is possible to use the propagation vectors calculated by `K_Search` program. If a specific propagation vector generates the correct satellites (compared with the observed data), this propagation vector can be used to describe the magnetic structure of the compound. In the Le Bail method, we have to introduce a magnetic phase, with a propagation vector, into the PCR file at 1.6 K (`test.pcr`). For this, we can create a folder called `LeBail`, copy the data at 1.6 K, and make a copy of the file `test.pcr` into the file `trestLE.pcr`.

At this point, we have to be careful when we introduce the magnetic phase due to the large number of parameters we have to consider. Open the `testLE.pcr` file with a text editor and put `Nph = 2` (two phases), and duplicate the description of the phase 1 to include it as phase 2. Change the phase 2 nome (Magnetic LeBail), remove the atoms, and put `Nat = 0` and `Jbt = 2`.

After that, we recommend to open this file with `FullProf PCR Editor`, and in the phase 2, change the symmetry to P-1. Once the magnetic structure is unknown, we can use the space group P-1 for generating the fundamental reflections. Next, add a propagation vector, and to create a line with `!Jvi [13]`, go in the menu `Output – Phase Output Information – Overlapped peaks List(INT)` and mark phase 2. Open again the `testeLE.pcr` file with a text editor. You will observe that the `Nvk = 1`, `More = 1` and a line with `Jvi = 11`. Put `Aut = 0` (the maximum number of parameters to be refined is fixed manually) and do not forget to put all parameters fixed, put `Irf = -1`, and now you can start the Le Bail method running `FullProf` with the `testLE.pcr` file (Fig. 1.15).

Observing Fig. 1.14b, we have a list of the five best solutions for the magnetic peaks. After testing $\mathbf{K} = (0.5 \ 0.5 \ 0.0)$ and $\mathbf{K} = (0 \ 0 \ 0)$, we obtained the observed and calculated patterns shown in Fig. 1.16. We can observe that the magnetic peaks are described for both propagation vectors. Therefore, both $\mathbf{K} = (0.5 \ 0.5 \ 0.0)$ and $\mathbf{K} = (0 \ 0 \ 0)$ can be used to describe the magnetic structure.

The program has produced a file called `testLEcltr.int` due to `Jvi = 11`, and if we put `Ipr = -1`, the program will generate a file called `testLE.spr`. Both files can be used for doing a simulated annealing for determining the magnetic structure in more complicated cases. For more details, we recommend the tutorials [13, 15, 21].

Although the two propagation vectors can be used to describe the magnetic structure, we have to be careful for choosing the correct propagation vector. In this case, we can use a trial and error method and previous information about the macroscopic magnetic results of the sample. Anticipating the result, we were able to refine the data using both propagation vectors. However, we obtained the lowest R-factor for $\mathbf{K} = (0.5 \ 0.5 \ 0.0)$. Furthermore, for the propagation vector $\mathbf{K} = (0 \ 0 \ 0)$, we observed some divergence conditions after running the program.

The next step is to calculate the basis vector of the irreducible representations (irreps) using the program `BasIreps` [12, 13, 22] for the best propagation vector. The program `BasIreps` calculates the irreducible representations (irreps) of the so-called little groups from which the full irreducible representations of space groups can be calculated using the induction formula [22].

```

!-----
! Data for PHASE number: 2 ==> Current R Bragg for Pattern# 1: 0.71
!-----
Magnetic Le Bail
!
!Nat Dis Ang Jbt Isy Str Furth ATZ Nvk More
0 0 0 2 0 0 0 922.4247 1 1
!Jvi Jdi Hel Sol Mom Ter N_Domains
11 0 0 0 0 0 0
!Contributions (0/1) of this phase to the 1 patterns
1
!Irf Npr Jtyp Nsp_Ref Ph_Shift for Pattern# 1
-1 7 1 0 0
! Pr1 Pr2 Pr3 Brind. Rmua Rmub Rmuc for Pattern# 1
0.000 0.000 1.000 3.000 0.000 0.000 0.000
!
!
P -1 <--Space group symbol
!----->> Profile Parameters for Pattern # 1
! Scale Shape1 Bov Str1 Str2 Str3 Strain-Model
104.13 0.00000 -0.22123 0.00000 0.00000 0.00000 0
0.00000 0.000 0.000 0.000 0.000 0.000
! U V W X Y GauSiz LorSiz Size-Model
1.961933 -0.851558 0.485795 0.000000 0.000000 0.000000 0.000000 0
0.000 0.000 0.000 0.000 0.000 0.000 0.000
! a b c alpha beta gamma #Cell Info
5.754436 5.770562 8.160518 90.000000 90.139580 90.000000
0.00000 0.00000 0.00000 0.00000 0.00000 0.00000
! Pref1 Pref2 Asy1 Asy2 Asy3 Asy4 S L D L
0.00000 0.00000 0.03116 0.01155 0.00000 0.00000 0.00000 0.00000
0.00 0.00 0.00 0.00 0.00 0.00 0.00 0.00
! Propagation vectors:
0.5000000 0.5000000 0.0000000 Propagation Vector 1
0.0000000 0.0000000 0.0000000
! 2Th1/TOF1 2Th2/TOF2 Pattern to plot
10.000 80.000 1

```

Fig. 1.15 Part of the testLE.pcr file for the Le Bail method to run in the FullProf program

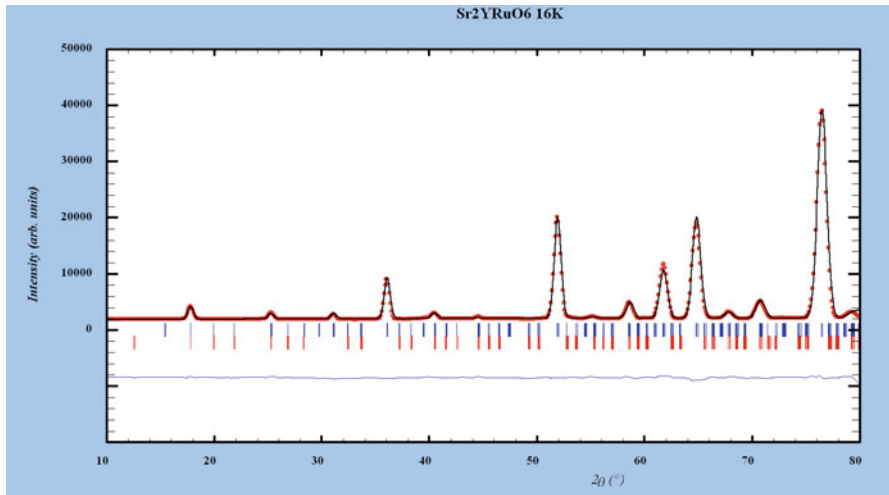


Fig. 1.16 The observed (red line) and calculated (black line) patterns obtained by Le Bail method

1.7.4 Irreducible Representation of Space Groups (*BasIrreps*)

In this chapter, we are going to use the *BasIrreps* program to obtain the information about the magnetic structure symmetry of the compound. Few information is required to calculate the irreducible representations using *BasIrrep*, as shown in Fig. 1.17. More details about representation analysis for magnetic structures can be found in the references [13, 22].

In *BasIrreps*, we will need the space group ($P2_1/n$), the propagation vector \mathbf{K} (in Fig. 1.17 we used $K_{1/2}$), and Wyckoff sites for the magnetic atom. The Ru atoms are in Wyckoff position 2c with two sublattices for this space group in $(1/2, 0, 1/2)$ and $(0, 1/2, 0)$. Axial vector or polar vector will select the behavior of the symmetry operators upon acting on vectors [22]. When explicit sublattice is marked, the “number of atoms” is the total number of atoms in the unit cell. For a particular site, they must share the same atom code, and the different sublattices are distinguished by an added underscore “_” followed by the number of the sublattice [22].

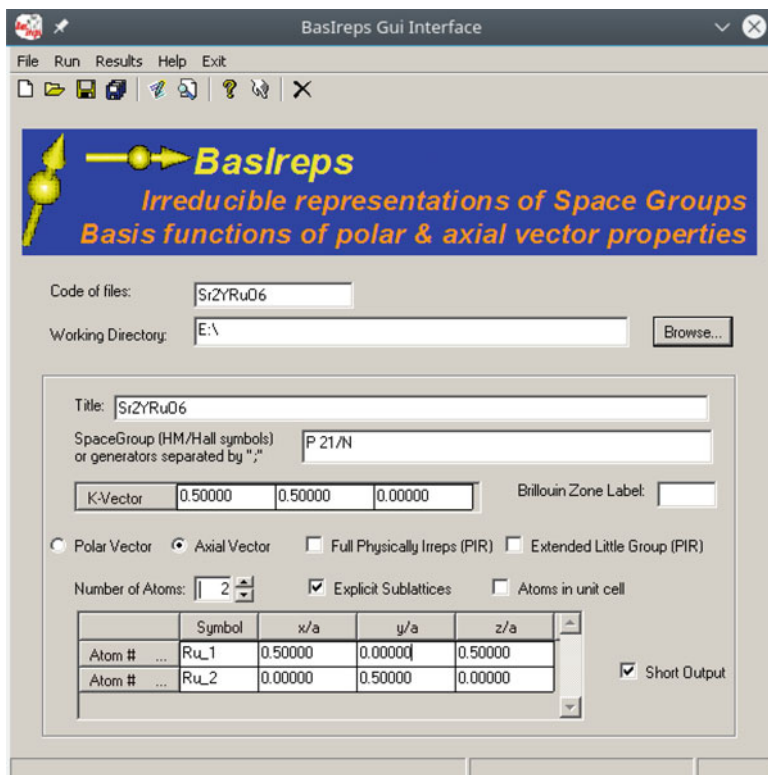


Fig. 1.17 *BasIrreps* window: basic information is required to calculate the irreducible representations

```

-----
Output of BasIREPS for FullProf
-----
The group of lines starting with the symbol of space groups and
finishing with the last keyword BASI, may be pasted into the PCR file

=> Basis functions of Representation IRrep( 2) of dimension 1 contained 3 times in GAMMA
Representation number : 2 for Site: 1
Number of basis functions: 3

----- Block-of-lines for PCR start just below this line
P -1 <--Space group symbol for hkl generation
! Nsym Cen Laue Ireps N_Bas
  2 1 1 -1 3
! Real(0)-Imaginary(1) indicator for Ci
  0 0 0
SYMM x,y,z
BASR 1 0 0 0 1 0 0 0 1
BASI 0 0 0 0 0 0 0 0 0
SYMM -x+1/2,y+1/2,-z+1/2
BASR 0 0 0 0 0 0 0 0 0
BASI 1 0 0 0 -1 0 0 0 1
----- End-of-block of lines for PCR

=> Basis functions of Representation IRrep( 4) of dimension 1 contained 3 times in GAMMA
Representation number : 4 for Site: 1
Number of basis functions: 3

----- Block-of-lines for PCR start just below this line
P -1 <--Space group symbol for hkl generation
! Nsym Cen Laue Ireps N_Bas
  2 1 1 -1 3
! Real(0)-Imaginary(1) indicator for Ci
  0 0 0
SYMM x,y,z
BASR 1 0 0 0 1 0 0 0 1
BASI 0 0 0 0 0 0 0 0 0
SYMM -x+1/2,y+1/2,-z+1/2
BASR 0 0 0 0 0 0 0 0 0
BASI -1 0 0 0 1 0 0 0 -1
----- End-of-block of lines for PCR

```

Fig. 1.18 Part of the output file Sr2YRuO6.fp with a list for the possible irreducible representations IRrep(2) and IRrep(4)

After run, the program will generate an output file called Sr2YRuO6.fp with a list for the possible irreducible representations (Fig. 1.18), two in this case, IRrep(2) and IRrep(4). In this way, we can describe the magnetic structure using directly the basis vectors.

1.7.5 Magnetic Structure Description Using the Coefficients of the Basis Functions

Now we can use a trial and error method applying the symmetry information of the output file. For this, we will complete the magnetic phase in testLE.pcr file (Fig. 1.19) and save the file with a different name (Mag.pcr). After that, put More = 0 and delete the line with Jvi = 11. Copy the block of lines from Sr2YRuO6.pf into Mag.pcr file and add the magnetic atoms.

```

-----
! Data for PHASE number: 2 ==> Current R_Bragg for Pattern# 1: 74.21
-----
Magnetic
! Nat Dis Ang Jbt Isy Str Furth ATZ Nvk More
  1  0  0  1 -2  0  0          922.4247  1  0
! Contributions (0/1) of this phase to the 1 patterns
  1
! Irf Npr Jtyp Nsp_Ref Ph_Shift for Pattern# 1
  -1  7  1          0          0
! Pr1 Pr2 Pr3 Brind. Rmua Rmub Rmuc for Pattern# 1
  0.000 0.000 1.000 3.000 0.000 0.000 0.000
!
!
P -1 <-Space group symbol for hkl generation
! Nsym Cen Laue Ireps N_Bas
  2  1  1 -1  3
! Real(0)-Imaginary(1) indicator for Ci
  0  0  0
!
SYMM x,y,z
BASR  1  0  0  0  1  0  0  0  1
BASR  0  0  0  0  0  0  0  0  0
SYMM -x+1/2,y+1/2,-z+1/2
BASR  0  0  0  0  0  0  0  0  0
BASR  1  0  0  0 -1  0  0  0  1
!
! Atom Typ Mag Vek X Y Z Biso Occ C1 C2 C3
! Ru1 MRU1 1 0 0.50000 0.00000 0.50000 0.50000 1.00000
! 0.000 0.000 0.000 0.000 0.000 0.000 0.000 0.000
! 0.000 0.000 0.000 0.000 0.000 0.000 0.000
! # color blue

```

Fig. 1.19 The magnetic phase in testLE.pcr file with the irreducible representations IRrep(2)

In the PCR file, the parameter Typ is used for identifying the name of the magnetic form factor. For transition metals the symbol is given by MCSV, CS is the chemical symbol, and V is a number corresponding to the valence of the magnetic ion [13]. For V, we used the magnetic form factor of the Ru^{+1} ion due to the absence of the magnetic form factor of the Ru^{+5} in the FullProf program. It is a good approximation once the difference between the magnetic form factors is very small [23].

When we put Jbt = 1, the phase is treated with the Rietveld method, and it is considered as pure magnetic (only magnetic atoms are required). Jbt = -1, we have extra parameters in spherical coordinates. Isy = -1, the program will read symmetry instructions, and Isy = -2, we use the basis functions of irreducible representations of propagation vector group instead of symmetry operators.

Finally, we have to use reasonable values of the coefficients of the basis functions C1, C2, and C3 to run the program. If we run the program with all parameters fixed and using any symmetry, IRrep(2) or IRrep(4), we will see a poor agreement between the magnetic peaks in the observed and calculated pattern.

After that, we can try to refine the coefficients of the basis functions C1, C2, and C3. If a divergence condition appears at some cycle, the symmetry used is wrong, and we have to change it. In the case of Mag.pcr file, both symmetries worked fine; however the best solution is IRrep(2), with the lowest R-factor. From this point, we are able to refine all parameters and the background, obtaining the pattern shown in Fig. 1.20.

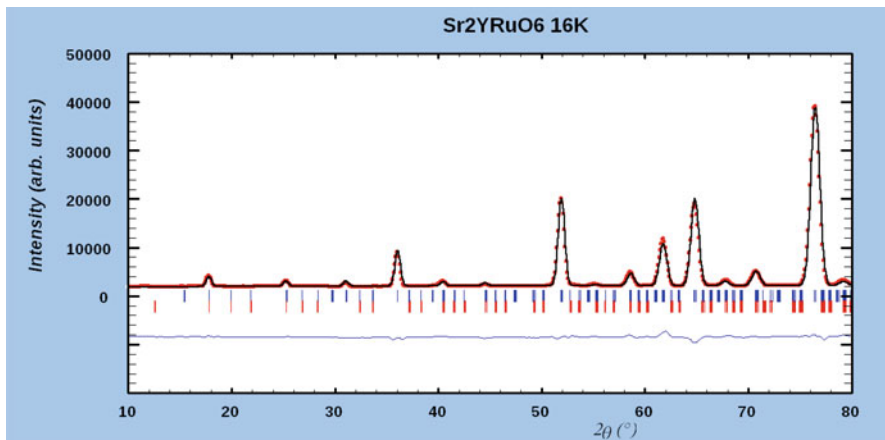


Fig. 1.20 Observed (red line) and calculated (black line) patterns with all parameters refined after completing the information for the Mag.pcr file

1.7.6 Magnetic Structure Description in Cartesian Components or Spherical Components

Instead of describing the magnetic structure using the coefficients of the basis functions, we can describe it using the Cartesian components or the spherical components. Using $J_{bt} = 1$, $I_{sy} = -1$, and a small change in the block of symmetry, we can refine the Cartesian components of the magnetic moments R_x , R_y , and R_z (Fig. 1.21a). If $J_{bt} = -1$, we can use spherical components and refine the magnetic moments R_m , R_{phi} , and R_{theta} (Fig. 1.21b).

Also, the symmetry block and the magnetic parameters in the Mag.pcr file can be easily edited using EdPCR program. For this, select Phase – Next – Symmetry, and put User defined in Symmetry Operators to refine the Cartesian components. For spherical components, just change Calculation to “Magnetic Phase with magnetic moments in spherical mode (Rietveld Method).”

From Fig. 1.21a, we can see the magnetic component R_x is larger than the other components and R_z is close to zero. For this reason, in spherical coordinates, we can start by putting $R_{phi} = 180^\circ$ and $R_{theta} = 90^\circ$ before running the program.

Previous informations about the magnetic state of any sample is very important to conduct the magnetic refinement properly. Sr_2YRuO_6 has two peaks in the magnetic contribution to the specific heat, at $T_{N1} = 28$ K and $T_{N2} = 24$ K [16, 19]. For a long time, this compound was described as having a collinear type-I AFM order with $\mathbf{K} = (0,0,0)$. Furthermore, for this compound, the emergence of a canted spin state from the temperature dependence of the coercive field H_C (Fig. 1.22) is observed, which exhibits a maximum of about 2 kOe close to T_{N1} followed by an abrupt decrease down to a few Oe near T_{N2} [16, 19]. The collinear type-I AFM order cannot account for the $H_C(T)$ behavior.

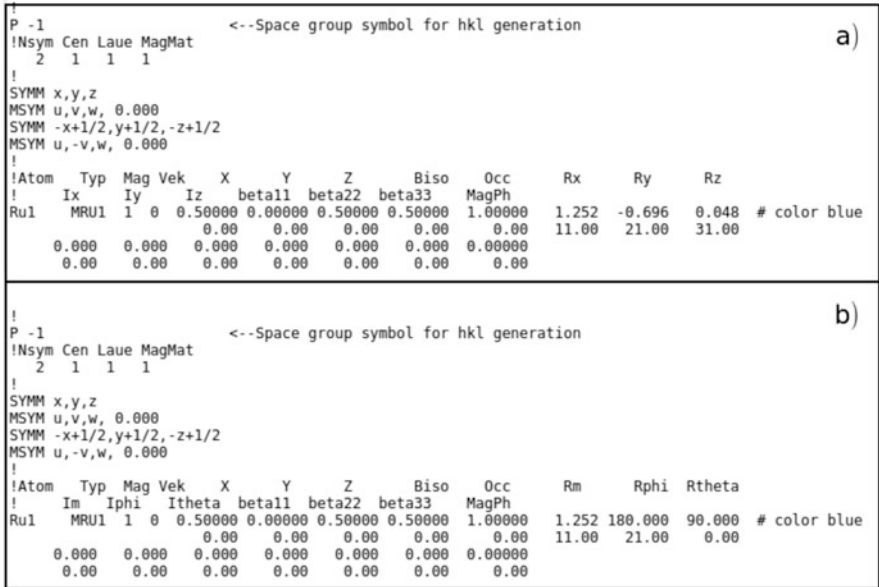
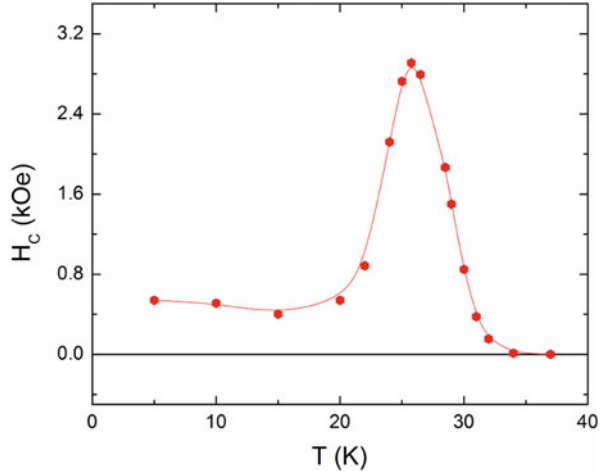


Fig. 1.21 (a) Is the information for the pcr file in Cartesian components of the magnetic moments R_x , R_y , and R_z . (b) Is the information in spherical components with the parameters R_m , R_{phi} , and R_{theta}

Fig. 1.22 The temperature dependence of the coercive field H_C [24]



Anticipating the result, if we refine the magnetic structure with just one magnetic ion (Fig. 1.19), only collinear structures will appear. For this reason, once the program generates the sublattices by applying the symmetry operators of the space group [13], in spherical coordinate, we can use the Wyckoff position 2c with two sublattices and a small block of magnetic symmetry operator (Fig. 1.23). Thereby, the program is able to generate a magnetic structure with canted spin state.

```

-----
! Data for PHASE number: 2 ==> Current R_Bragg for Pattern# 1: 0.00
-----
Magnetic
!
!Nat Dis Mom Jbt Isy Str Furth ATZ Nvk More
2 0 0 -1 -1 0 0 922.4247 1 0
!Contributions (0/1) of this phase to the 1 patterns
1
!Irf Npr Jtyp Nsp_Ref Ph_Shift for Pattern# 1
-1 7 1 0 0
! Pr1 Pr2 Pr3 Brind. Rmua Rmub Rmuc for Pattern# 1
0.000 0.000 1.000 3.000 0.000 0.000 0.000
!
!
P -1 <--Space group symbol for hkl generation
!Nsym Cen Laue MagMat
1 1 1 1
!
SYMM x,y,z
MSYM u,v,w, 0.000
!
!Atom Typ Mag Vek X Y Z Biso Occ Rm Rphi Rtheta
! Im Iphi Itheta beta11 beta22 beta33 MagPh
Ru1 MRU1 1 0 0.50000 0.00000 0.50000 0.50000 1.00000 1.252 180.000 90.000 # color blue
0.000 0.000 0.000 0.000 0.000 0.000 0.000 0.000000
0.00 0.00 0.00 0.00 0.00 0.00 0.00 0.00
Ru2 MRU1 1 0 0.00000 0.50000 0.00000 0.50000 1.00000 1.252 180.000 90.000 # color blue
0.000 0.000 0.000 0.000 0.000 0.000 0.000 0.000000
0.00 0.00 0.00 0.00 0.00 0.00 0.00 0.00

```

Fig. 1.23 Magnetic phase in spherical coordinate with two sublattices and a small block of magnetic symmetry operator

Table 1.3 Results for the refinement of magnetic ions Ru1 and Ru2 using spherical coordinates

Atom	Rm (μ_B)	Rphi	Rtheta
Ru1	2.213	170.5°	90°
Ru2	2.213	58.1°	90°

After completing the Mag.pcr file in spherical coordinate and refining all the parameters, we obtained Table 1.3 with the factors $\chi^2 = 1.46$.

1.7.7 FullProf Studio

The program FullProf Studio has been developed for visualizing crystal and magnetic structures [25]. After refining the magnetic structure, we can open the Mag.pcr file and put the keyword magphn, being n the number of the magnetic phase ($n = 2$), in the line with the name of the crystallographic phase (1). By doing this, we are able to plot the magnetic structure together with the crystal structure [13]. Then, in Fig. 1.10, instead of **Sr2YRuO6** in the name of the phase 1, we put **Sr2YRuO6 magph2**. The FullProf program generates an output file called Mag.fst, and the result of the magnetic structure description observed using FullProf Studio is shown in Fig. 1.24, which is a spin structure of the K_2NiF_4 – type [17, 26].

Top view from the c-axis is showing the orientation of the magnetic moments of the Ru ions for the canted spin state in Fig. 1.25. The canting angle $\eta = |Rphi_1 -$

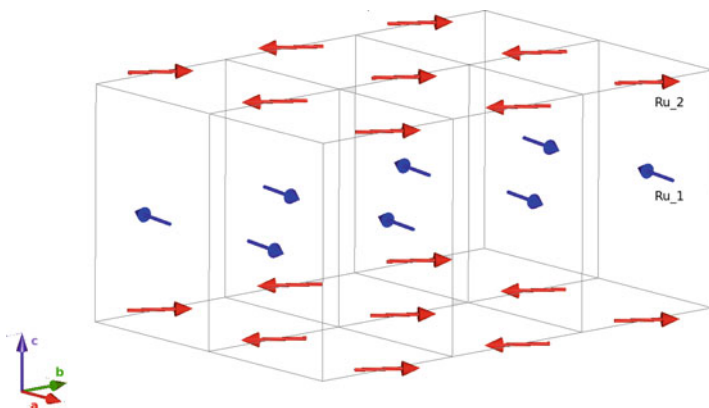


Fig. 1.24 Magnetic structure observed using FullProf Studio. Spin structure of the K_2NiF_4 -type

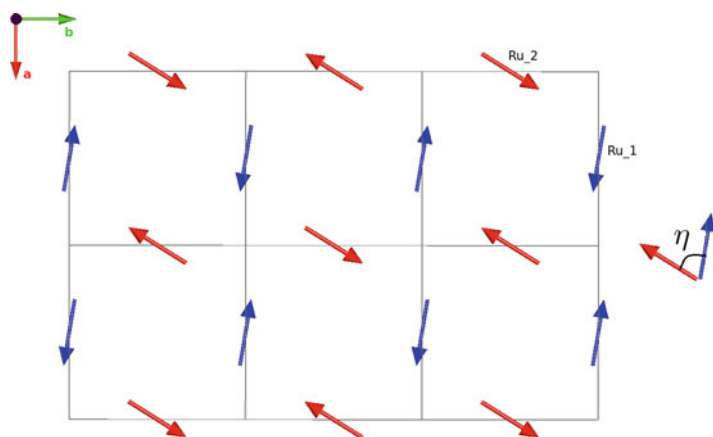


Fig. 1.25 Top view from the c-axis showing the orientation of the magnetic moments of the Ru ions for the canted spin state. η is the canting angle

$|R\phi_{i2} - 180^\circ| = 67.6^\circ$ is defined as the deviation from the AFM alignment of the magnetic moments for neighboring Ru(1) and Ru(2) ions along the c-axis.

For Figs. 1.24 and 1.25, we are showing just the magnetic moments of the Ru ions. For this, in FullProf Studio, go in the menu Crystal Structure – Atoms – Display, and uncheck the box Show atom for all atoms. In Fig. 1.26a, we checked the box for the Ru and Y atoms, and then it is possible to see the atomic positions for these atoms. Also, if we uncheck all the atoms and edit the Mag.fst file, adding the line CONN Y O 0.000 2.500 RADIUS 1.000, after the list of atoms, and the line POLY Y COLOR 0.000 1.000 0.000 1.000, after the list of magnetic moments, we will obtain Fig. 1.26b showing a polyhedral representation with Y in the center of the octahedron.

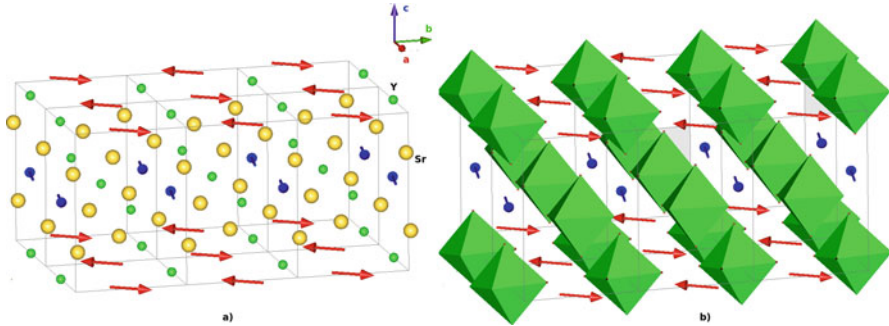


Fig. 1.26 In addition to the positions of the magnetic moments of the Ru ions, figure (a) shows the Sr and Y atoms, and the figure (b) shows a polyhedral representation with Y in the center of the octahedron

1.8 Conclusions

After using some programs for the analysis of neutron diffraction data, we observed a spin canting structure like K_2NiF_4 -type for the magnetic structure of the double perovskite Sr_2YRuO_6 . We found the propagation vector $\mathbf{K} = (0.5 \ 0.5 \ 0.0)$ as being the best solution for the two magnetic peaks observed at low angles. Although we confirmed, using the Le Bail method, that the $\mathbf{K} = (0 \ 0 \ 0)$ can describe the magnetic structure, we were able to refine the magnetic structure just in the case when we put one magnetic Ru sublattice. This description is not convenient for the spin canting structure previously observed.

The BasIreps program is an easy tool to obtain the information about the magnetic structure symmetry of the compound. This program gives us a list with the possible irreducible representations and the basis vectors to be used directly in the pcr file. In this case, we have to be careful with the values of the coefficients of the basis functions C1, C2, and C3 if a divergence condition appears at some cycle.

The easiest way to obtain the magnetic parameters of the compounds is to refine the magnetic structure using the Cartesian components or the spherical components. The first one is better for analyzing the magnetic moment on each axis, in which we can refine more accurately if we have some information about the magnetic behavior of a single crystal of the compound. On the other hand, the second is fundamental to describe a magnetic structure with spin canting and gives us a global magnetic moment.

FullProf Studio is a program for visualizing crystal and magnetic structures using the output files from refinement. In this program we can easily see the magnetic moments direction and the atoms' position. We should keep in mind that this chapter is just a basic way to describe a magnetic structure. We tried to approach the magnetic structure description as easily as we could. In more complicated cases, we should use the simulated annealing (SAnn) procedure in FullProf.

Acknowledgements This research was supported by the Brazilian agencies CNPq and CAPES. Research at Institut Laue-Langevin, D1B (CRG) – High resolution neutron two-axis powder diffractometer – was sponsored by the Scientific User Facilities Division, European scientific research organizations. We would like to thank Dr. Claire Colin (ILL) for the assistance with NPD measurements and Dr. John Neumeier (MSU–USA), Dr. Luis Ghivelder, and Dr. Sergio Garcia (UFRJ–Brazil) for the assistance with sample synthesis.

References

1. Izyumov, Y. A., Naish, V. E., & Ozerov, R. P. (1981). *Neutron diffraction of magnetic materials*. Moscow: Atomizdat (New York: Consultants Bureau, 1991. Google Scholar).
2. Elsasser, W. M. (1936). Comptes rendus. *Academy of Science of Paris*, 202, 1029–1030.
3. von Halban, H., Jr., & Preiswerk, P. (1936). Comptes rendus. *Academy of Science of Paris*, 203, 73.
4. Mitchell, D. P., & Powers, P. N. (1936). Bragg reflection of slow neutrons. *Physical Review*, 50(5), 486.
5. Squires, G. L. (1996). *Introduction to the theory of thermal neutron scattering*. Mineola: Dover Publications.
6. Merzbacher, E. (1970). *Quantum mechanics* (2nd ed.). New York: Wiley.
7. Koester, L., Rauch, H., & Seymann, E. (1991). Neutron scattering lengths: A survey of experimental data and methods. *Atomic Data and Nuclear Data Tables*, 49(1), 65–120.
8. Zamyatin, Y. S., & Konovalov, V. Y. (2000). Probability of nuclear fission and effective fission cross sections. In Y. A. Alexandrov (Ed.), *Low energy neutrons and their interaction with nuclei and matter* (Part 1, pp. 1–49). Berlin: Springer.
9. Schwartz, L. H., & Cohen, J. B. (1977). *Diffraction from materials*. New York: Academic.
10. Edward Prince and Arthur James Cochran Wilson. International tables for crystallography. 2004.
11. Institut Laue-Langevin. The neutron. <https://www.ill.eu/en/html/science-technology/the-neutron/what-are-neutrons-used-for/>.
12. Rodriguez-Carvajal T. Roisnel. (2006). Fullprof suite. <https://www.ill.eu/sites/fullprof/index.html>
13. Juan Rodríguez-Carvajal. (2014). Tutorial on magnetic structure determination and refinement using neutron powder diffraction and fullprof. http://neutrons2.ornl.gov/conf/2014/magstr/docs/tutorial_magnetic_structures.pdf
14. Ressouche, E. (2014). Reminder: Magnetic structures description and determination by neutron diffraction. *École thématique de la Société Française de la Neutronique*, 13, 02001.
15. Le Bail, A. (1988). H Duroy, and JL Fourquet. Ab-initio structure determination of LiSbWO₆ by x-ray powder diffraction. *Materials Research Bulletin*, 23(3), 447–452.
16. Bernardo, P. L., Ghivelder, L., Eslava, G. G., Amorim, H. S., Sinnecker, E. H. C., Felner, I., Neumeier, J. J., & García, S. (2012). Magnetic and thermal responses triggered by structural changes in the double perovskite Sr₂YRuO₆. *Journal of Physics: Condensed Matter*, 24(48), 486001.
17. Bernardo, P. L., Ghivelder, L., Amorim, H. S., Neumeier, J. J., & García, S. (2015). Magnetic structure driven by monoclinic distortions in the double perovskite Sr₂YRuO₆. *New Journal of Physics*, 17(10), 103007.
18. Bernardo, P. L., Ghivelder, L., Eslava, G. G., Amorim, H. S., Felner, I., & Garcia, S. (2014). Monoclinic distortion and magnetic coupling in the double perovskite Sr_{2-x}Cax/RuO₆. *Journal of Solid State Chemistry*, 220, 270–276.
19. Ravi, P. (2008). Singh and CV Tomy. Anomalous magnetic properties of Sr₂YRuO₆. *Physical Review B*, 78(2), 024432.
20. Chatterji, T. (2005). *Neutron scattering from magnetic materials*. Gulf Professional Publishing.

21. Rodriguez-Carvajal, J. (2013). How to work with symmetry modes using fullprof and amplimodes. two simple examples: CaTiO₃ and LaMnO₃ <http://www.cryst.ehu.es/cryst/tutorials/FullProf-Tutorial-Symmetry-Modes.pdf>.
22. The FullProf Team. (2014). Basireps. <http://www.ccp14.ac.uk/ccp/web-mirrors/plotr/tutorials&documents/basireps.pdf>.
23. Parkinson, N. G., Hatton, P. D., Howard, J. A. K., Ritter, C., Chien, F. Z., & Wu, M.-K. (2003). Crystal and magnetic structures of A₂YRu_{1-x}Cu_xO₆ with A = SR, BA and x = 0.05 to 0.15. *Journal of Materials Chemistry*, 13(6), 1468–1474.
24. Bernardo, P. L. (2013). *Structural, magnetic and thermal proprieties of doble perovskites with Ru*. Dissetation, Instituto de Física – Universidade Federal do Rio de Janeiro. Brazil.
25. The FullProf Team. (2015). Fullprof studio. http://www.ccp14.ac.uk/ccp/web-mirrors/plotr/fp_studio/windows/manual_fullprof_studio.pdf
26. Christopher, S., Knee, & Weller, M. T. (2004). Neutron diffraction study of crystal structure and antiferromagnetic order in Sr₂CoO₂X₂ (X = Cl, Br). *Physical Review B*, 70(14), 144406.

Chapter 2

Small-Angle X-Ray Scattering to Analyze the Morphological Properties of Nanoparticulated Systems



Oscar Moscoso Londoño, Pablo Tancredi, Patricia Rivas, Diego Muraca,
Leandro M. Socolovsky, and Marcelo Knobel

2.1 Introduction

This chapter provides a global overview of the small-angle X-ray scattering (SAXS) theory and related concepts. The main goal of this document is to provide useful tools to analyze, fit, and simulate the SAXS data obtained from sets of different nanoparticulated systems. The emphasis will be placed on systems composed by single nanoparticles, as well as on those with a more complex morphology, standing out how the scattering intensity changes with nanoparticle size, with interparticle distance, or with nanoparticle morphology.

The structural nature of nanoscale materials can be studied by different techniques, including electron microscopy, X-ray diffraction, scattering, electron energy-loss spectroscopy, or neutron scattering, among others. All of these techniques are based on the scattering, absorption, or diffraction processes due to the interaction of an incoming radiation with matter. Basically, the structural information depends on the radiation source and its wavelength; for example,

O. Moscoso Londoño (✉)

Gleb Wataghin Institute of Physics, University of Campinas, Campinas, SP, Brazil

Faculty of Engineering, Autonomous University of Manizales, Manizales, Colombia

e-mail: omoscoso@ifi.unicamp.br; oscar.moscosol@autonoma.edu.co

P. Tancredi · P. Rivas

Laboratory of Amorphous Solids, Faculty of Engineering, University of Buenos Aires, Buenos Aires, Argentina

D. Muraca · M. Knobel

Gleb Wataghin Institute of Physics, University of Campinas, Campinas, SP, Brazil

L. M. Socolovsky

Santa Cruz Regional Faculty, National Technological University – CIT-Santa Cruz (CONICET), Rio Gallegos, Argentina

the use of radiation beams of X-rays, electrons, or neutrons, with wavelengths around 0.1 nm, permits the study of matter down to atomic resolution [1]. At these wavelengths it is possible to determine the crystal structure or the interplanar spacing of crystalline materials. By using neutron diffraction techniques, the atomic and magnetic structure of a material can also be studied. However, for a complete structural characterization, the study of the structure at the atomic level must be accompanied with morphological information. In this case, it is necessary to use X-ray or neutrons beams with wavelengths from 1 nm to thousands or even more [1]. Especially, for nanoscale systems composed by nanoparticles with size ranging between a few nanometers and ~ 100 nm, the knowledge of the shape, the interparticle distance, the size nanoparticle distribution, the arrangement into a host matrix, as well as other information at superatomic scale are extremely relevant in order to obtain a complete picture of the structural features of the studied material. Fundamental morphological information can be accomplished by using the small-angle X-ray scattering (SAXS) technique. In nanoparticle research, a suitable data processing obtained from a SAXS measurement allows obtaining an overall picture of the nanoparticle sizes, shapes, and/or relative position of nanoparticles [2, 3]. In SAXS data treatment for a nanoparticulated system, it is generally assumed that each nanoparticle has a simple geometrical shape, such as sphere, ellipse, or rod, among others. Despite this simple geometric assumption, the SAXS technique has proven to be a powerful tool to determine the mean size of the nanoparticle, its size distribution, the shape, and the surface structure [3]; it is even possible to define the pair potential if the relative positions of the nanoparticles are known [4]. For other shapes, it is possible to compute a form factor that can be used in the SAXS equations.

The framework behind the SAXS technique is exploited in both scientific and industrial fields. These studies involve several branches, covering the metal alloys, polymers, biological macromolecules, emulsions, or porous materials, among others [2].

2.2 Small-Angle X-Ray Scattering

2.2.1 General Phenomenology

Small-angle X-ray scattering (SAXS) is a technique where the elastic scattering of X-rays by a sample is recorded at very low angles (typically $0.1\text{--}10^\circ$ measured from the beam axes). This angular range contains information regarding the structure of scatterer entities, like nanoparticles and micro- and macromolecules, among others. Depending of the studied systems, SAXS technique could provide information of the distances between partially ordered materials, pore sizes, as well as other data [5]. Besides, depending on the experimental setup, SAXS is capable of delivering structural information of objects whose size ranges between ~ 0.5 and ~ 100 nm.

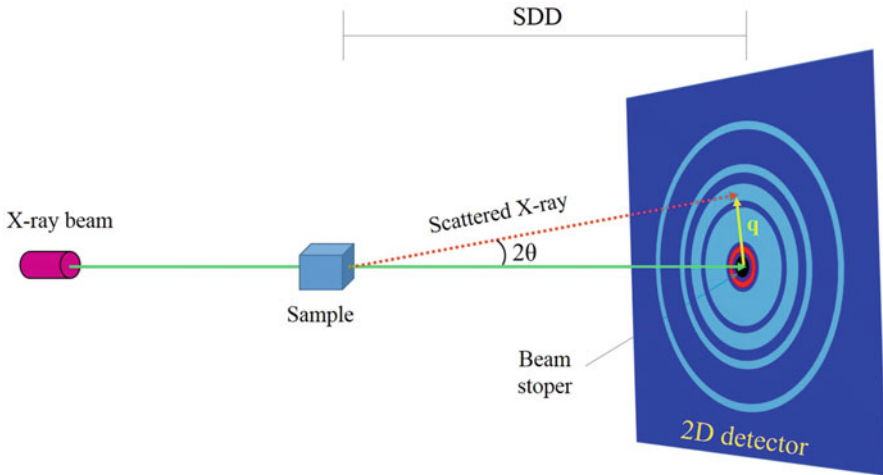


Fig. 2.1 Basic schematic SAXS setup

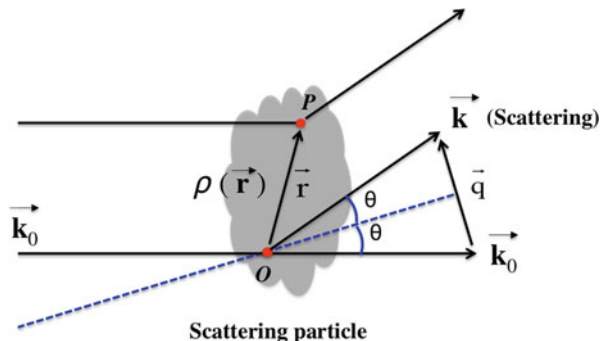
The limits depend on the photon energy, sample-to-detector distance (SDD), the pixel size and geometry of the X-ray detector, and size of the beam stopper (a SAXS setup is shown in Fig. 2.1) [6]. For example, larger objects, whose size is around $\sim 1 \mu\text{m}$, just produce perceptible scattering only at extremely small angles that means that the beam stopper size must be as small as possible; if not, the scattering waves hit the stopper and are not recorded by the detector [6].

To understand how the X-ray is scattered at low angles by a particle, it is necessary to know what happens when the X-rays irradiate a particle. In a very general way, it is possible to say that two phenomena occur: absorption and scattering. At the moment in which the X-rays hit the particle, one part of these will pass through the sample. Another part will be absorbed and transformed into heat and/or fluorescence radiation. The remaining fraction will be scattered into another direction of propagation [2]. The absorption processes occur with more probability at the absorption edges. At these edges, the electrons of the materials can be expelled leaving the atoms in an unstable state (with a hole). When the atom recovers its natural configuration, fluorescence radiation is emitted, with a given wavelength. The scattering processes can take place with or without energy loss, i.e., the scattered waves can have similar or different wavelength, compared to the incident radiation.

To analyze a scattering experiment, it is suitable to start assuming a fixed entity (or particle), with an arbitrary structure that can be represented by an electronic density function $\rho(\vec{r})$. Assuming that a monochromatic radiation beam, with \vec{k}_0 as wave vector, hits this particle, the scattered wave direction will be defined by wave vector \vec{k} , as shown in Fig. 2.2.

Since scattering is assumed as an elastic process, the scattered wave has the same modulus of the incident wave, whose absolute value, in both cases, is given by $2\pi/\lambda$,

Fig. 2.2 Representation of the scattering process by a fixed particle



being λ the wavelength of the used radiation. This fact makes possible to establish the difference between the incident and scattered beams, which is given by:

$$\vec{q} = \vec{k} - \vec{k}_0, \quad (2.1)$$

where \vec{q} is the scattering vector. Rewriting the scattering vector can be defined as $\vec{q} = 2\pi/\lambda (\vec{u} - \vec{u}_0)$, being \vec{u}_0 and \vec{u} the unitary vectors defining the incident and scatter beam directions, respectively. Since 2θ is the angle formed by the incident and scattered beams, then the magnitude of the scattering vector is:

$$q = 4\pi/\lambda \sin \theta \quad (2.2)$$

In a SAXS experiment, the scattering intensity I is measured as a function of q . It is well known that $I(\vec{q})$ can be obtained by calculating the quadratic modulus of the amplitude function, defined in the reciprocal space (q space), of those waves scattered over the whole volume [6], i.e., $I(\vec{q}) = A(\vec{q}) \cdot A(\vec{q})^*/V = |A(\vec{q})|^2/V$. The scattering amplitude $A(\vec{q})$ is given by the Fourier transform of the electronic density, $\rho(\vec{r})$:

$$A(\vec{q}) = \int_V \rho(\vec{r}) \exp(-i\vec{q} \cdot \vec{r}) d\vec{r} \quad (2.3)$$

Consequently, applying the inverse Fourier transformation on Eq. 2.3, the electron density can be derived.

$$\rho(\vec{r}) = 1/(2\pi)^3 \int A(\vec{q}) \exp(i\vec{q} \cdot \vec{r}) dq \quad (2.4)$$

Notice that $-i\vec{q} \cdot \vec{r}$ is proportional to the phase shift $\Delta\varphi = 2\pi\Delta S/\lambda = -(\vec{k} \cdot \vec{r} - \vec{k}_0 \cdot \vec{r})$, being ΔS the optical paths of two waves scattered by two volume elements, which in our case are represented by point O and P shown in Fig. 2.2. Using Eq. 2.1, the phase shift can be written as $\Delta\varphi = -\vec{q} \cdot \vec{r}$. Additional details of this procedure can be found in a recent chapter [6].

Once $A(\vec{q})$ is determined, the dispersion intensity can be written as:

$$I(\vec{q}) = \int_V^0 a \int_V^0 \rho(\vec{r}') \rho(\vec{r}' - \vec{r}) \exp(-i\vec{q} \cdot \vec{r}) dr dr' \quad (2.5)$$

Here, it is possible to introduce the so-called correlation function, $\gamma(\vec{r})$ [7], which is particularly important in non-particulated systems, such as microemulsions or metal alloys, since it describes the variation of density as a function of the distance measured from a reference point. This function is defined as:

$$\gamma(\vec{r}) = \frac{1}{V} \int_V^0 \rho(\vec{r}') \rho(\vec{r}' - \vec{r}) dr = \frac{1}{V} P(r), \quad (2.6)$$

where $P(r)$ is a similar function to those obtained from crystallographic methods, which is called the Patterson function. Crystallographically speaking it is basically a map of all atom-to-atom vectors in a crystal, which can be expressed as. $P(u, v, w) = \int \rho(x, y, z) \rho(x + u, y + v, z + w) dx dy dz$, being \vec{u} , \vec{v} , and \vec{w} the vectors formed between positions x and $x + u$, y and $y + v$, and z and $z + w$, respectively. This function contains information regarding all vectors between every two atoms of all the molecules within the crystal [8]. In a scattering experiment of a macromolecule, for example, the $P(r)$ function takes the name of pair-density distribution function or simply pair-distribution function. In this case, $P(r)$ provides information of the electron distances of the scattering entities; in others words, it is the probability of finding another scatterer entity at a position \vec{r} with respect to the one placed at the origin [9]. The main difference between the Patterson function and the pair-distribution function lies on that $P(r)$ provides a radial average and does not give rise to vectors between scattering entities. In that sense, $P(r)$ can be determined if the electronic density $\rho(\vec{r})$ is known. Therefore, $P(r) = r^2 \left\langle \int_V^0 \Delta\rho(\vec{r}) \Delta\rho(\vec{r} + \vec{r}') d\vec{r}' \right\rangle$ [8]. The brackets $\langle \rangle$ represent an average over the analyzed sample volume V , and $\Delta\rho(\vec{r})$ is the average electron density, which can be defined as $\Delta\rho(\vec{r}) = \rho(\vec{r}) - \rho_S$. Here, $\rho(\vec{r})$ is the electron density of the molecules of interest, and ρ_S is assumed to be constant that represents the electron density of the host medium, which can be, for example, pure water ($\sim 0.33 \text{ e}^- \text{ \AA}^{-3}$).

Then, using Eqs. 2.5 and 2.6, the scattering intensity can be rewritten as:

$$I(\vec{q}) = \int_V \gamma(\vec{r}) \exp(-i\vec{q} \cdot \vec{r}) dr = \frac{1}{V} \int_V P(\vec{r}) \exp(-i\vec{q} \cdot \vec{r}) dr \quad (2.7)$$

As can be noted, $\gamma(\vec{r})$ can be indirectly determined by the inverse Fourier transformation of the experimental scattering function:

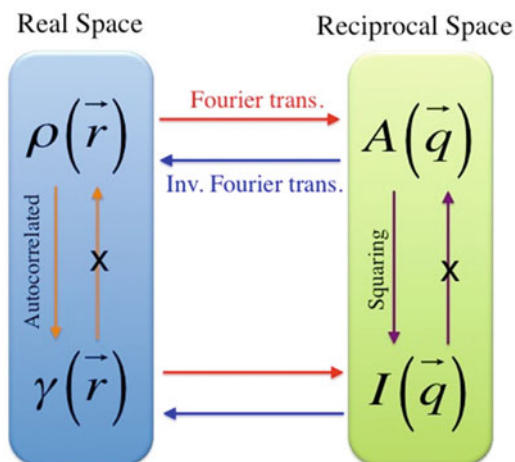
$$\gamma(\vec{r}) = \frac{1}{(2\pi)^3 V} \int I(\vec{q}) \exp(i\vec{q} \cdot \vec{r}) d\vec{q} \quad (2.8)$$

This procedure is regularly used in order to avoid problems of the discrete sampling of the scattering intensity curve over a finite range [10].

In this first section, the main concepts related to the scattering processes from non-particulated entities have been introduced. Some of them are defined in the real space, such as electron density $\rho(\vec{r})$, which is directly linked to the correlation function $\gamma(\vec{r})$, as well as with the pair-distribution function $P(r)$. While, in the reciprocal space, the scattering amplitude $A(\vec{q})$ and the scattering intensity $I(\vec{q})$ were defined. Some of these parameters can be connected mathematically by the Fourier transformations. For example, the electron density $\rho(\vec{r})$ with the scattering amplitude $A(\vec{q})$ as well as the autocorrelation function $\gamma(\vec{r})$ with the scattering intensity $I(\vec{q})$ (see Fig. 2.3). However, there are a series of facts/restrictions, whether mathematical or instrumental, that must be taken into account in order to correctly determine and connect the mentioned quantities, for instance, the function $\gamma(\vec{r})$ can be determined from $\rho(\vec{r})$ (Eq. 2.5), but inversely $\rho(\vec{r})$ cannot be calculated [6]. Similarly situation happens with $A(\vec{q})$ and $I(\vec{q})$, where the scattering intensity can be determined by squaring the scattering amplitude, but not in the opposite direction, as shown in Fig. 2.3. On the other hand, the mathematical properties of the Fourier transformations allow to connect the expressions of the real space with the reciprocal ones, as mentioned above. Here, the challenge lies on choosing the suitable reciprocal resolution for the desired scattering experiment. For instance, it is well known that in a scattering experiment at low angles (SAXS), the scattering amplitude $A(\vec{q})$ is obtained for a small volume in the q space [6], and hence, the structural features that can be extracted from $\rho(\vec{r})$ will be restricted to those at *low resolution*.¹ On the other hand, if $A(\vec{q})$ is determined for a large volume in the q space and the structure of the studied material is sufficiently ordered, then it is possible to obtain an expression for the electron density, containing structural information of *high resolution*.¹

¹Notice that *high* or *low resolution* refers to those structural properties at atomic or superatomic level, respectively.

Fig. 2.3 Pathways between the main expressions derived from a scattering framework. (Graph adapted from Amemiya and Shinohara [11])



In a SAXS experiment, a one- or two-dimensional (1-D or 2-D) detector collects the experimental information by counting the scattered photons as a function of the distance to the beam axes, measured as an angular position to subsequently form a 1-D or 2-D scattering pattern. It can be expressed as a function of the scattering vector q , or by using Eq. 2.2, it is also possible to express the position of each pixel in terms of the scattering angle (2θ). In isotropic systems, a 2-D graph can be azimuthally averaged to give a one-dimensional scattering curve. Especially, for colloidal systems containing randomly oriented nanoparticles, the majority of the obtained 2-D patterns have isotropic scattering features, which can be azimuthally averaged [3]. Anisotropic systems, such as lamellar structures or ordered polymers [12], among others, cannot be azimuthally averaged because the 2-D pattern is not isotropic along the azimuthal direction [3]. On these cases, the scattering profiles can be represented using other coordination systems.

As can be noticed, the scattering intensity $I(\vec{q})$ is obtained instead of the scattering amplitude² $A(\vec{q})$. This condition implies that Eq. 2.4 cannot be applied in order to determine the electron density function, which, in fact, contains the structural information. To obtain accurate *low-resolution* structural features of nanosystems, including nanoparticles, nanowires, and nanopillars, among others, this obstacle is often overcome by proposing a model that includes shapes, sizes and its distributions, distances between nanoparticles, as well as other features at superatomic level, whose initial conditions can be refined by means of a SAS software package. Depending on the studied systems or if the scattering entities are interacting, it will be necessary to introduce a function to correlate them.

²Experimentally it is not possible to obtain the amplitude and phase of the scattering amplitude $A(\vec{q})$. Experimental SAXS data allows determining the modulus of $A(\vec{q})$, but the phase remains unknown.

This procedure requires a previous knowledge of the system. Some of these features can be initially determined using other techniques, as, for example, X-ray diffraction (XRD) and scanning or transmission electron microscopy (SEM/TEM).

2.2.2 *Small-Angle X-Ray Scattering from Isotropic and Non-fixed Nano-objects*

Considering a centrosymmetric, randomly oriented and non-fixed particle and assuming a constant electron density within the particle ($\gamma(\vec{r}) = \gamma(r)$) and null outside it, then the obtained scattering intensity will be isotropic, and it will contain the scattering information of all possible orientations. Under these assumptions, the factor $\exp(-i\vec{q} \cdot \vec{r})$ can be averaged as $\langle \exp(-i\vec{q} \cdot \vec{r}) \rangle = \frac{\sin(qr)}{qr}$ [1, 6]. Thus, the scattering intensity for this particle (Eq. 2.7) becomes:

$$I_p(\vec{q}) = 4\pi V \int_0^\infty \gamma(r) \frac{\sin qr}{qr} r^2 dr, \quad (2.9)$$

being V the particle volume. From this result, it is possible to infer that for a set of identical and uncorrelated particles, the total scattering intensity can be expressed as:

$$I(q) = NI_p(q) \quad (2.10)$$

where N is the number of particles per unit volume and $I_p(q)$ is the scattering intensity produced by a single particle. Notice that the solution of Eq. 2.10 depends on the q range. For example, when solving this equation at low- q range, the so-called Guinier law is obtained, sometimes expressed as Guinier approximation [13]. While at high- q values, the solution takes the name of Porod law [14].

2.2.2.1 **Low- q Regime: Guinier Law**

According to the Guinier approximation, the scattering intensity at low- q depends on the radius of gyration of the particle. To develop the solution for Eq. 2.10 at small- q values, it is necessary to look back to Eq. 2.3, which describes the scattering amplitude in terms of the electron density function. Thus, expanding the exponential factor of this equation, it becomes:

$$A(q) = \int \rho(r) dV - i \int qr \rho(r) dV - \frac{1}{2!} \int (qr)^2 \rho(r) dV \dots \quad (2.11)$$

Assuming an isotropic system ($\rho(r) = \rho_0$) with r taken from the center of the mass, then the first integral becomes $\rho_0 V$, and the second one will be null. Therefore, Eq. 2.11 can be rewritten as $A(q) = \rho_0 V - \frac{1}{2}(qr)^2 \int \rho(r) dV \dots$ or also:

$$A(q) = \rho_0 V \left[1 - \frac{1}{2}(qr)^2 \dots \right] \quad (2.12)$$

Remembering that the scattering intensity can be obtained by squaring $A(q)$, then:

$$I(q) = (\rho_0 V)^2 \left[1 - (qr)^2 + \frac{1}{2}(qr)^4 \dots \right] \quad (2.13)$$

At low- q values, it is clear that $(qr)^2 \gg (qr)^4$, whereby the scattering intensity at low- q turns into:

$$I(q \rightarrow 0) \cong (\rho_0 V)^2 \left[1 - (qr)^2 \dots \right] \quad (2.14)$$

A simple way to relate r with the radius of gyration R_g is bearing in mind that vector r written in the Cartesian coordinate system is $r = \vec{x}^2 + \vec{y}^2 + \vec{z}^2 + 2\vec{x}\vec{y} + 2\vec{x}\vec{z} + 2\vec{y}\vec{z}$ and then $(qr)^2 = q_x^2 \vec{x}^2 + q_y^2 \vec{y}^2 + q_z^2 \vec{z}^2 + 2q_x^2 q_y^2 \vec{x}\vec{y} + 2q_x^2 q_z^2 \vec{x}\vec{z} + 2q_y^2 q_z^2 \vec{y}\vec{z}$. As the system was assumed to be isotropic, then $\vec{x}\vec{y} = \vec{x}\vec{z} = \vec{y}\vec{z} = 0$ and $\vec{x}^2 + \vec{y}^2 + \vec{z}^2 = \frac{1}{3}R_g^2$ [15]. With this tools at hand, the scattering intensity acquires the form of $I(q \rightarrow 0) \cong (\rho_0 V)^2 \left[1 - q^2 \frac{1}{3}R_g^2 \dots \right]$ or well, reduced to an exponential form, $I(q \rightarrow 0)$:

$$I(q \rightarrow 0) \cong (\rho_0 V)^2 \exp\left(-q^2 \frac{1}{3}R_g^2\right) \quad (2.15)$$

The latter equation is known as the Guinier law, which for ideal particle systems provides the most simple and accurate method to determine the size of a particle using SAXS [3]. Notice that this equation can be applied on experimental data to obtain the radius of gyration of the scattered objects. Basically, the procedure consists in plotting the $\log[I(q)]$ against q^2 for the data obtained at low- q values and whose trend is more or less linear. However, when determining R_g from the Guinier plot, the accuracy of R_g is limited by the minimum q value, which in fact is determined by the minimum scattering angle at which the scattering radiation is detected [1]. The nonlinearity of $I(q)$ against q^2 at low- q can be mainly attributed to two factors, the measured q range and possible interference effects of those

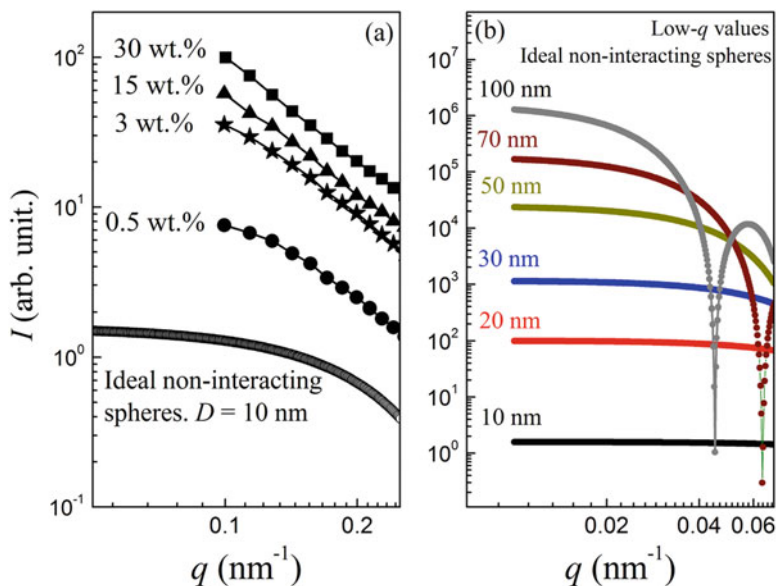


Fig. 2.4 (a) Comparison between four experimental SAXS curves at low- q for a set of 10 nm nanoparticles loaded in four different concentrations in a non-conductive polymer matrix and the simulated SAXS curve for a set of noninteracting and monodisperse 10 nm nanoparticles. (b) Simulated SAXS curves for ideal systems composed for spherical nanoparticles with different diameters

waves scattered by neighboring particles. The first case commonly occurs on particle systems whose size ranges around 100 nm; for these kinds of objects, it is necessary to record the experimental scattering intensities at extremely low- q values. On the other hand, if the studied system is composed of densely packed particles, such as concentrated nanoparticle solution or percolated samples, the relative distances between the scattering particles will be in the same order of the particle size, or it could even be smaller. On these materials, interference effects between the scattered waves take place, producing deviations of the Guinier trend. To model these interference effects, a structure factor $S(q)$ must be added to the scattering intensity, whose framework will be discussed in the next sections.

Figure 2.4 presents the experimental and simulated SAXS curves at low- q representing the effects of size and agglomeration on the Guinier law. From Fig. 2.4a it is possible to appreciate the effects of the nanoparticle concentration on the SAXS pattern linearity at low- q . Here, four experimental SAXS curves are shown, which correspond to systems composed of nanoparticles of mean size ~ 10 nm, loaded in a polymer matrix with concentrations of 0.5 wt%, 3 wt%, 15 wt%, and 30 wt%. As can be noticed, the increase in the nanoparticle concentration generates a greater deviation from the Guinier behavior. For comparison purposes it is also presented the simulated SAXS curve for a system composed by noninteracting and monodisperse spherical nanoparticles of 10 nm of diameter, where the linearity of

Table 2.1 Radius of gyration for particles of known geometry

Sphere of radius R	$R_g^2 = \frac{3}{5} R^2$	[1]
Thin rod with length L	$R_g^2 = \frac{L^2}{12}$	[15]
Thin circular disk with radius R	$R_g^2 = \frac{R^2}{2}$	[15]
Spherical shell with inner radius R_A and outer radius R_B	$R_g^2 = \frac{3}{5} \frac{R_B^5 - R_A^5}{R_B^3 - R_A^3}$	[1]
Ellipse with semiaxes a and b	$R_g^2 = \frac{a^2 + b^2}{4}$	[1]
Ellipsoid with semiaxes a , b , and c	$R_g^2 = \frac{a^2 + b^2 + c^2}{5}$	[1]
Circular cylinder with radius R and height L	$R_g^2 = \frac{L^2}{12} + \frac{R^2}{2}$	[16]
Hollow circular cylinder with inner radius R_A , outer radius R_B , and height L	$R_g^2 = \frac{R_A^2 + R_B^2}{2} + \frac{L^2}{12}$	[1]
Elliptical cylinder with semiaxes a and b and height L	$R_g^2 = \frac{a^2 + b^2}{4} + \frac{L^2}{12}$	[1]
Squared platelets with thickness T and length L	$R_g^2 = \frac{L^2}{6} + \frac{T^2}{12}$	[16]
Gaussian chain of $N+1$ segments connected by N bonds of fixed length l	$R_g^2 = \frac{Nl^2}{6}$	[15]

the SAXS pattern is clearly observed at low- q . In Fig. 2.4b, the scenario is different; here six simulated SAXS curves for ideal spheres with diameters ranging between 10 and 150 nm are presented. Each curve represents the SAXS intensity behavior at the Guinier zone; from these curves it is clear that the Guinier trend is lost at lower- q values as the size of the scattering objects is greater; hence the Guinier approximation is only valid for the interval q_{MIN} to q in which the linear dependence is followed [1]. Summarizing, it must be noticed that for a correct estimation of the radius of gyration, it is necessary to take into account effects like the aggregation. Also it is crucial to propose a precise ratio between the measuring q range and the particle size.

Assuming the most typical case, in which the scattering objects are considered solid spheres, the radius of gyration can be directly estimated by determining R_g from the slope of the $\log[I(q)]$ vs. q^2 plot, which is equal to $R_g^2/3$. For non-spherical particles but of known geometric like cylinders, ellipses, or platelets, for example, the employment of a generalized Guinier plot, it is also useful to determine the radius of gyration of these objects [5]. Some expressions to derive the radius of gyration through the geometric dimensions of their bodies are listed in Table 2.1.

The previous expressions were developed for highly ideal systems, i.e., they neglect features existing in any real sample, such as particle size distribution effects. In order to consider the distributed properties found in almost all of the real samples, it is necessary to consider the individual contribution of each scattering object. If the studied sample is composed of particles with a narrow size distribution, the distributed properties can be taken into account by considering the averaged parameters at the Guinier law (Eq. 2.15). Then, the Guinier law becomes $I(q \rightarrow 0) \cong \rho_0^2 \langle V^2 \rangle \exp\left(-q^2 \frac{1}{3} \langle R_g^2 \rangle\right)$, where $\langle V \rangle$ is the volume average of all

scattered particles contained in the sample and $\langle R_g \rangle$ is the so-called Guinier average approach (weighted average [6]), which is defined as:

$$\langle R_g \rangle^2 = \frac{\int (V R_g)^2 dR_g}{\int V^2 dR_g}, \quad (2.16)$$

Solving Eq. 2.16 for a set of spherical uncorrelated nanoparticles with a narrow size distribution, the radius of gyration can be determined by $\langle R_g \rangle^2 = \langle R^8 \rangle / \langle R^6 \rangle$. It is extremely important to keep in mind that the above expression comes from averaging operations, where the statistical weight of those larger particles will be greater in comparison to the small ones. In that sense, if the studied sample is highly polydisperse or if this is composed by several sets of particles, each one with different mean size, then the estimation of the radius of gyration will be biased toward R_g values linked with larger scattering particles. This effect is commonly attended by proposing different sets of scattering contributions as necessary. For example, if we have a sample composed of n_i sets of particles, each one with mean size $\langle D \rangle_i$, then, the total scattering intensity can be expressed as the sum of all contributions; therefore $I(q) = N_1 I_1(q) + N_2 I_2(q) + \dots$, being N_i the number of particles belonging to each family.

2.2.2.2 High- q Regime: Porod Law

The Porod law describes the behavior of the scattering intensity at the high- q region. As mentioned in the previous section, the scattering intensity ($I(q)$) and the correlation function ($\gamma(\vec{r})$) are mathematically connected by the Fourier transform properties. Analyzing the properties of these functions, one can establish that for high- q values ($q \rightarrow \infty$), the smallest values of r have prevalence in $\gamma(\vec{r})$. Mathematically speaking, it means that for small r , the correlation function can be expanded in Taylor series [13], obtaining the following equivalence:

$$\gamma(r) = \gamma(0) \left[1 + \frac{1}{4} \frac{S}{V} r + \dots \right] \quad (2.17)$$

being S the specific surface of the scattering particle in the illuminated sample volume V' or well S/V' can be interpreted as the illuminated area per unit volume. Replacing the expanded expression for the correlation function ($\gamma(\vec{r})$) in Eq. 2.9 and solving the integral for $q \rightarrow \infty$, the scattering intensity expression becomes:

$$I(q \rightarrow \infty) = \frac{2\pi\rho^2 S}{q^4} \quad (2.18)$$

Then, it can be noticed that Eq. 2.18, named the Porod law, indicates the asymptotic behavior of $I(q)$ when the scattering vector q tends to be large values. As an important point to highlight, the dependence of $I(q \rightarrow \infty)$ with S can be harnessed to examine the surface of those particles illuminated in a SAXS experiment. As

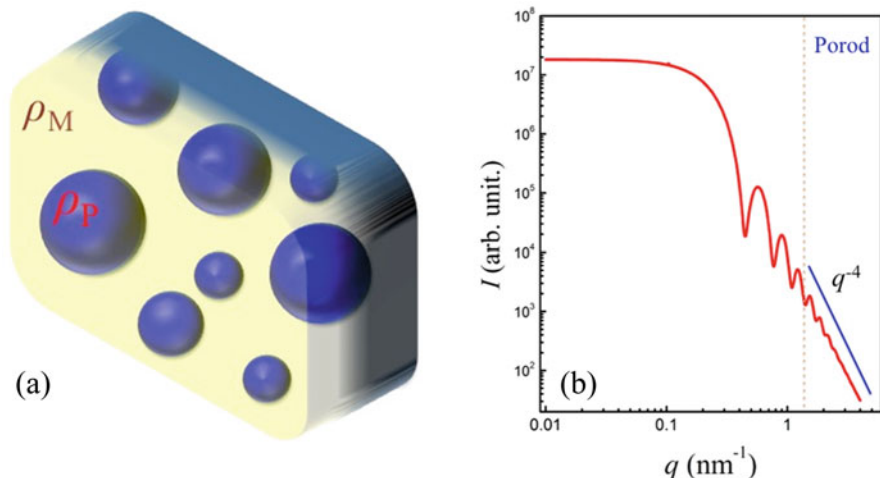


Fig. 2.5 (a) Schematic representation of a set of polydisperse and uncorrelated particles loaded in a matrix with a constant electron density. (b) SAXS-simulated spectra for a set of polydisperse particles with 10 nm as the mean size. Here, a lognormal size distribution was proposed ($\sigma = 0.05$)

in any real sample, the scattering particles are surrounded by a specific medium (as is shown in Fig. 2.5), with a different electronic density; due to this fact, it is convenient to express the Porod law taking into account both electron densities. Then, assuming that both the electron densities of the particles and surrounding media are isotropic, the Porod law is rewritten as $I(q \rightarrow \infty) = 2\pi(\rho_P - \rho_M)^2 S/q^4$, being ρ_P and ρ_M the constant electronic densities of the scattering particles and the surrounding medium, respectively. Additional details of this procedure are found in a recent chapter book [6].

The Porod law can also be applied for systems composed of nanobodies with other simpler geometric shapes, for example, cylinders or planar objects. Independently of the shape of the scattering particles, the Porod law is applicable if a sharp interface between the particle and the medium is present.

2.2.2.3 Intermediate- q Regime: The Role of the Polydispersity

The supposition that a sample is constituted by a set of identical particles is rarely real. In most real samples, naturally occurring or lab synthesized, there is a combination of particles with different sizes and shapes. In these cases, SAXS is a powerful technique from which information as regards the shape and/or the size distribution can be obtained [17, 18]. We are going to start proposing a sample composed by N particles of the same shape and isotropic electronic density but whose sizes oscillates moderately around a mean value, to then analyze the main alterations on a set of SAXS patterns produced by ensembles of spherical particles with different polydispersities. Despite in this section, we focus the discussion on

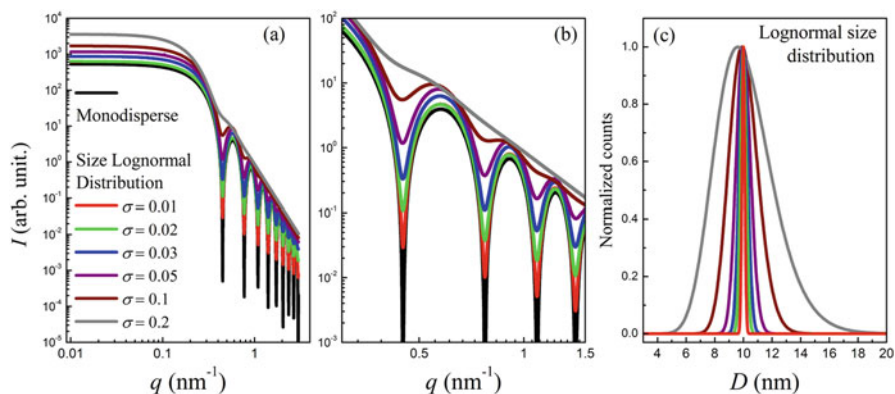


Fig. 2.6 (a) Simulated SAXS curves for spherical particles varying the degree of polydispersity. These simulations were carried out proposing a size distribution that follows a lognormal function. (b) Representative zoom of the intermediate- q region. (c) Simulated lognormal-type size distributions

particles with the simplest shape (spheres); one of the main challenges derived from a SAXS study is to determine the particle shape, an issue that can be overcome employing shape-independent modeling methods [19, 20].

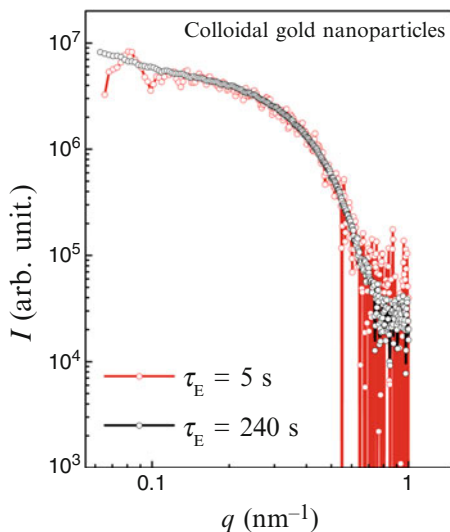
Figure 2.6 shows seven simulated SAXS curves; these curves were constructed assuming a scattering entity of known shape, spheres in this case (form factors will be introduced in next section). Each scattering intensity curve is related to a set of particles with mean diameter of 10 nm whose size distribution follows a lognormal-type size distribution $f(d)$, except for that curve representing a monodisperse system (black curve). As can be noted in Fig. 2.6a, b, the curve silhouette is extremely sensitive to the polydispersity degree (controlled via the lognormal standard deviation σ), especially on the oscillatory behavior of the curve at intermediate- q values. Here one can also note that for monodisperse samples, as well as for those samples with low polydispersity ($\sigma < 0.05$), the oscillatory behavior is perfectly perceived at intermediate- q values.

Despite that in this example a lognormal function was adopted to represent the particle polydispersity, there are other functions which depend on the polydispersity nature of the studied sample and can represent this feature very well. Some of these are the Schultz-Zimm and the Gaussian distributions, among many others. A few expressions often used to represent the polydispersity in samples composed by nanoparticles are listed in Table. 2.2.

As discussed for previous regions (Guinier and Porod regimes), there are a series of cautions that necessarily need to be considered in order to correctly determine the polydispersity of a real sample from an experimental SAXS pattern. For instance, if the studied sample is highly diluted, the collected scattered intensities coming from the smallest particles will have poor data statistics, especially at intermediate- and high- q values [3, 21, 22]. As a consequence statistical weight will be skewed to those

Table 2.2 Most commonly used probability density functions to represent the polydispersity in nanoparticulate samples

Lognormal	$f(r) = \frac{1}{\sigma r \sqrt{2\pi}} e^{-\ln(r/r_0)^2/2\sigma^2}$	Being σ the lognormal standard deviation and r_0 the mean particle radius
Gaussian	$g(r) = \frac{1}{\sigma \sqrt{2\pi}} e^{-(r-r_0)^2/2\sigma^2}$	Being σ the standard deviation and r_0 the mean particle radius
Schultz-Zimm	$n(r) = \frac{[(z+1)/r_0]^{(z+1)} r^z}{\Gamma(z+1)} e^{-[(z+1)/r_0]r}$	Being $z = (r/\sigma)^2 - 1$, r_0 the number-averaged radius, and σ the root-mean-square deviation. Γ being the gamma function

Fig. 2.7 Experimental scattering curves from non-aggregate gold nanoparticles recorded at exposure times of 5 s (red curve) and 240 s (black curve)

particles of larger sizes. Experimentally, this obstacle can be addressed by increasing the exposure time (τ_E), i.e., the time in which the X-ray beam illuminates the sample and the detectors are counting photons. However, one needs to be cautious with the increase of τ_E ; larger values of this could lead to saturation of the detectors,³ thereby losing information or inducing serious damage to them [23]. Figure 2.7 presents two experimental SAXS patterns collected from colloidal gold nanoparticles (of spherical shape and ~ 5 nm as the mean size). As can be perceived, the scattering intensity curve recorded with an exposure time of 5 s is noisier in almost the whole measuring range. However, by increasing the exposure time, until 240 s in this case, the statistical quality of the scattered signal was improved, making this curve a better candidate to be modeled.

Data collection time must be adjusted based on the nature of the sample and taking into account the radiation source. For instance, to examine the superatomic

³Every detector has a specific saturation value expressed in counts [2].

structure of biological samples, such as proteins, it is required to use radiation sources with high photon flux. If the X-ray radiation is extremely intense, as those coming from a synchrotron source ($\sim 10^{11}$ photons per second), exposure times ranging between few seconds and 1 or 2 min are used. If the SAXS experiment is performed employing X-ray sources with smaller photon flux instead (benchtop devices or as those sources placed on crystallography laboratories), it will be necessary to increase the data collection time in order to obtain an optimal SAXS pattern.

2.3 Diluted Sets of Nano-objects: Experimental Data Modeling Assuming a Known Particle Shape

From a SAXS point of view, to catalog a system as diluted, it is necessary to ensure that the relative distances between particles are greater than their diameter. On the contrary case, the scattering intensity is affected by interference effects, and it will therefore contain contributions from neighboring particles. The simplest way to confirm that a system is diluted is to examine the scattering pattern linearity at the Guinier region (Sect. 2.2.2.1). If the diluted condition is satisfied, one can say that spatially uncorrelated objects compose the sample. Under this condition the total scattering intensity is given by $I(q) = NI_p(q)$; recalling Eq. 2.10, here N represents the number of particles per unit volume, and $I_p(q)$ is the scattering intensity of a single particle.

2.3.1 Dilute Sets of Uncorrelated Spherical Nanoparticles

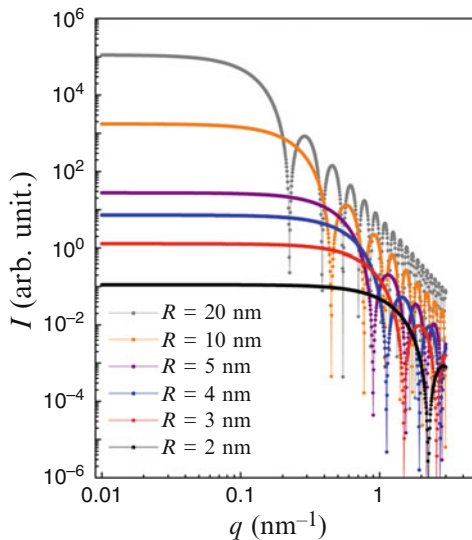
The simplest case is to assume a set of monodisperse spherical particles of radius R with constant electronic density ρ_P , which are embedded in a homogeneous matrix (e.g., colloidal, solid dispersion, or polymeric matrices), whose electronic density is also constant (ρ_M). In this context, the total scattering intensity ($I(q)$) can be obtained by solving the following equation:

$$I(q) = N \left[\Delta\rho \int_0^R 4\pi r^2 \frac{\sin(qr)}{qr} dr \right]^2, \quad (2.19)$$

whose solution for the particular case of monodisperse spheres, according to several references, including [17, 18], is:

$$I(q) = N(\Delta\rho)^2 V_P^2 3 \left[\frac{\sin(qR) - qr \cos(qR)}{(qR)^3} \right]^2 \quad (2.20)$$

Fig. 2.8 Simulated SAXS curves for monodisperse spherical particles constructed following Eq. 2.20 and varying radius



Here, the factor $3 \left[\frac{\sin(qR) - qR \cos(qR)}{(qR)^3} \right]^2$ is the form factor or the amplitude form factor for particles with spherical morphology $P(q)$, $\Delta\rho$ is the electronic density difference between the particles and the surrounding medium ($\rho_P - \rho_M$), and V_P is the particle volume. Figure 2.8 displays a series of simulated SAXS curves constructed following Eq. 2.20 and assuming different radius ranging between 2 and 20 nm. In all curves the same tendency is evidenced, a linear trend at the Guinier region followed by an oscillatory behavior at intermediate- q values.

As already mentioned, a nanoparticulate system can rarely be classified as monodisperse. On the contrary, most of the times, it presents polydispersity. This behavior can be examined knowing the polydispersity nature (lognormal, Gaussian, among others) or proposing a distribution function to model it. Under this circumstance, the total scattering intensity cannot be expressed as the sum of the individual contribution of each identical particle; rather particles with different size must be considered. Thus, the total scattering from a set of polydisperse particles is given by $I(q) = \int N(r)I_p(q, r)dr$, where $N(r)$ symbolizes a proper distribution function (some of these are listed in Table 2.2). Notice that the scattering intensity of a single particle not only depends on q (or the angle) but also of their specific size. Following the same protocol used for monodisperse spheres, an expression to determine the total scattering can be achieved, resulting in:

$$I(q) = N(\Delta\rho)^2 \int_0^{\infty} V_P^2 \left[3 \frac{\sin(qr) - qr \cos(qr)}{(qr)^3} \right]^2 N(r) dr \quad (2.21)$$

2.3.1.1 Application of the Model That Describes the Scattering Intensity of Uncorrelated Spherical Nanoparticles: Gold Nanoparticles Diluted on Organic Solvents

Following the model discussed above, we have fitted two experimental SAXS curves obtained from a set of non-aggregated gold nanoparticles. Experimental (black curve) and fitted (red curve) results are presented in Fig. 2.9a, d. To test the scope of this model, none of the parameters involved in the model was restricted. Those structure parameters, derived from the SAXS fitted results, show an excellent agreement to those obtained by a direct method, like the transmission electron microscopy (TEM) (Fig. 2.9b, e). The small differences in the mean size as well as in the standard deviation can be linked to several causes, for example, the statistical contribution associated to each technique. While from TEM the counts are limited to hundreds or in the best of the cases to a few thousands of particles, from SAXS the illuminated portion of the sample may contain $\sim 10^{12}$ particles or even more. The quality of the SAXS data, especially at high- q values may generate errors in the obtained distribution. Furthermore, polydispersity errors are extremely sensitive to increasing particle interaction [24].

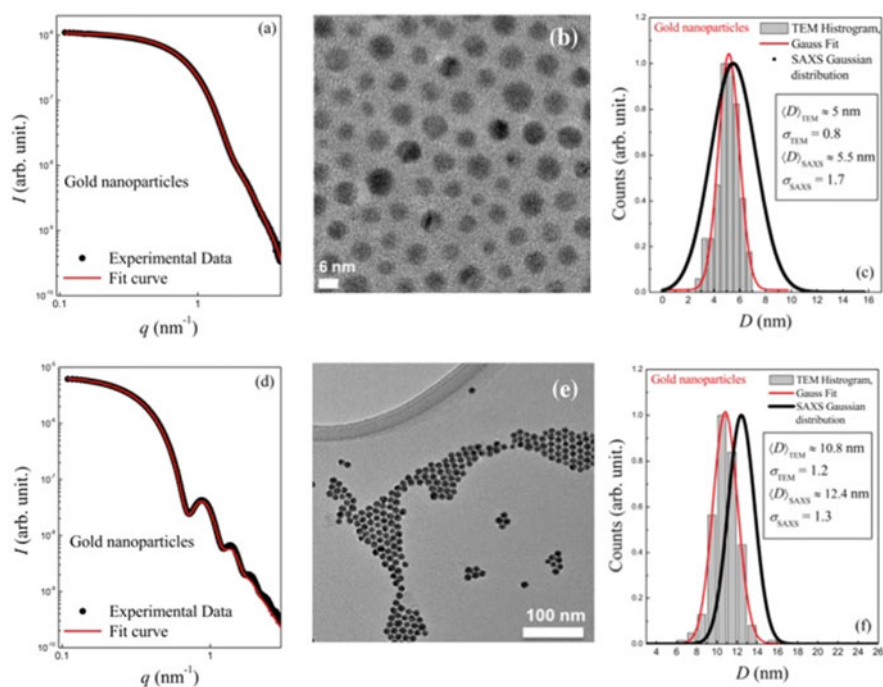


Fig. 2.9 Experimental SAXS curves, TEM images, SAXS and TEM size distribution functions from non-aggregate gold nanoparticles with diameters of ~ 5 nm (a-c) and ~ 12 nm. SAXS fitted curves are presented as red continuous lines. Both TEM histograms were obtained by counting more than 500 particles from several TEM images

2.3.2 Dilute Sets of Uncorrelated Nanoparticles of Simple Geometrical Shape

A direct and simple approach to model a scattering curve is by starting from the knowledge or assumption of the particle shape. In Table. 2.3 some expressions for scattering intensity of particles with simple shapes are listed. Also, simulated SAXS patterns under specific geometrical considerations are displayed.

As can be noted, this approach is very useful if the shape of the scattering objects is known. Also, with this approach, it is possible to combine contributions from particles of different shapes, e.g., if the studied sample contains more than one family of objects with different shapes. Moreover, there are several form factors for complex morphologies, including core/shell spheres, bilayered or multilayered vesicle, and core/shell structures of elliptical or cylindrical shape [25, 26], among others. Some of this form factors have been successfully employed to characterize the growth of rare earth multilayers in magnetic nanoparticles [27] or well to analyze the size and shape effects on several physicochemical properties of the iron oxide nanoparticles [28]. The use of an analytical expression has numerous advantages; perhaps one of the most relevant is the reduced number of parameters, which make this approach a convenient tool to fit experimental data at low computational cost.

There are several cases where the irregular geometry of the scattering objects is difficult in the analytical calculation and the fitting process. Under this circumstance it is possible to use a method to approximate the particle geometry using subparticle units, whose shape may be spherical, elliptical, or cylindrical [29]. This approach packs small simple geometrical subunits to construct more complex ones [30]. For instance, the construction of these complex structures from spherical subunits can be done from finite element methods, to use then the Debye formulation to determine the intensity [5]:


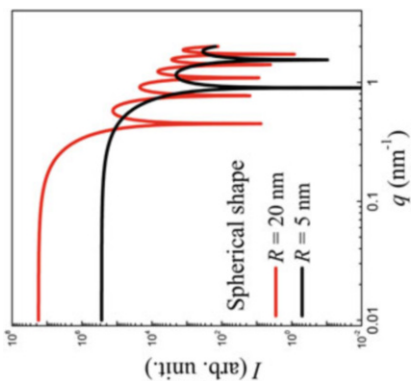
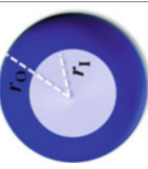
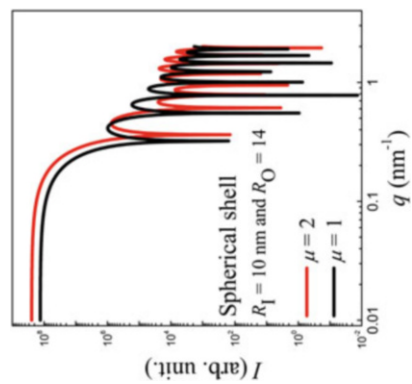
$$I(q) = \sum_{i,j=1}^N f_i(q)f_j(q) \frac{\sin(qr_{ij})}{qr_{ij}} \quad (2.22)$$


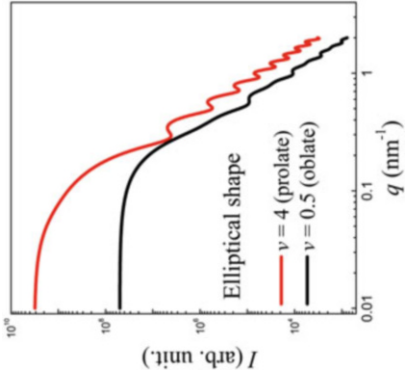

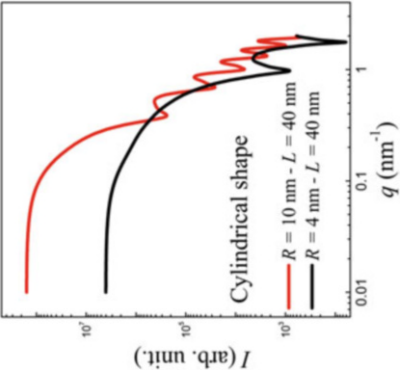
where N is the number of scattering particles, r_{ij} is the distance between atoms i and j , and $f_i(q)$ is the scattering factor for atom i . This approach allows the calculation and optimization of complex systems admitting, if necessary, the use of additional terms to take into account possible particle interaction effects [31, 32].

2.4 Densely Packed Sets of Particles: Correlated Particles

The approaches discussed in the previous section have been founded on a common underlying assumption, which is that the investigated system is composed by diluted particles hosted in a matrix. Fundamentally, this means that the particle spatial

Table 2.3 Expressions for the scattering intensity determined from particles of simple geometrical shape

Shape	Scattering intensity	Calculated SAXS pattern
Sphere of radius R	 $I(q) = N(\Delta\rho)^2 V_p^2 \left[\frac{\sin(qR) - qR \cos(qR)}{(qR)^3} \right]^2$	 <p style="text-align: center;">Spherical shape</p> <p style="text-align: center;">— $R = 20$ nm — $R = 5$ nm</p>
Spherical shell with an inner radius r_1 and outer radius r_0	 $I(q) = [P(q, r_0, \Delta\eta) - P(q, r_1, \Delta\eta(1 - \mu))]^2$ <p>with</p> $P(q, r, \Delta\eta) = \frac{4}{3} \pi r^3 \Delta\eta^3 \left[\frac{\sin(qr) - qr \cos(qr)}{(qr)^3} \right]$	 <p style="text-align: center;">Spherical shell</p> <p style="text-align: center;">$R_1 = 10$ nm and $R_0 = 14$</p> <p style="text-align: center;">— $\mu = 2$ — $\mu = 1$</p>

<p>Ellipsoid of two equal semiaxis of length r and semiprincipal axis of length νr</p>		$I(q) = (\Delta\rho)^2 \left(\frac{4}{3}\pi R^3\right)^{2\pi/2} \int_0^{2\pi/2} P^2(q, r(\nu^2 \cos^2\vartheta + \sin^2\vartheta)^{1/2}) \sin\vartheta d\vartheta$	
<p>Cylinder of radius r and length L</p>		$I(q) = \frac{16(\pi R^2 L)^2 (\Delta\rho)^2 \int_0^{qR\sqrt{1-x^2}} \frac{\sin(qLx/2)}{q^2 R\sqrt{1-x^2} Lx} dx}{}$	

Spherical shell, scattering length difference between core and matrix relative to the shell contrast μ . Ellipsoid, if $\nu < 1$ the ellipse is oblate, and for $\nu > 1$ the ellipse is prolate. Cylinder, J is the cylindrical Bessel function. All of the patterns were constructed assuming a monodisperse system. The expression listed here were adapted from reference [25]

arrangement effect on the total scattering intensity is negligible. However, in a densely packed system, the positions and orientations of their particles can be ordered or aligned following a preferential configuration, i.e., they can interact with each other [2]. Also, interacting particles can form clusters with a particular shape. Commonly, these systems are simply called *interacting* or *correlated*. A good example of these kinds of systems is those composed of magnetic or metallic nanoparticles, where the large surface/volume ratio plus intrinsic magnetic and/or ionic forces promotes the formation of clusters, as it is shown in these references [33–35]. The scattering intensity from this kind of systems not only carries the scattered information coming from a single particle but also contains the effects produced by the interference of those waves scattered by neighboring particles. To consider this additional interference, it is necessary to modify the scattering intensity expression determined from a set of non-correlated particles by adding the structure factor⁴ $S(q)$, which contains the information about the spatial position of the particles.

The total scattering intensity for a system composed of N spatially correlated particles is given by:

$$I(q) = NI_p(q)S(q) \quad (2.23)$$

Recalling that $I_p(q) = (\Delta\rho)^2 V_p^2 P(q)$, with $P(q)$ being the form factor (associated to the scattering amplitude $A(q)$), then Eq. 2.23 can be rewritten as:

$$I(q) = NP(q)S(q) \quad (2.24)$$

Assuming that the particles are close to each other but non-percolated, the structure factor $S(q)$ for a monodisperse system is given by [29]:

$$S(q) = 1 + \frac{N}{V} \int_0^\infty 4\pi r^2 (P(r) - 1) \frac{\sin(qr)}{qr} dr, \quad (2.25)$$

where $P(r)$ is the pair-distribution function mentioned above and the integral $\int_0^\infty 4\pi r^2 (P(r) - 1) \frac{\sin(qr)}{qr} dr$ is the Ornstein-Zernike integral, which is in fact the expression that carries the information of the pair distance among the particles in a system.

As mentioned before, the correlated effects between nanoparticles are particularly appreciable at the Guinier region (low- q values) as shown in Fig. 2.4a. This can be analyzed well from the asymptotic behavior of $S(q)$. For instance, at high- q values, this factor tends to be 1, while at low- q values, $S(q)$ exclusively depends on the nature of the interaction. Furthermore, it can be noticed that for a set of non-correlated particles, $S(q)$ takes a value of 1, and thus Eq. 2.25 turns into Eq. 2.10.

⁴In crystallography it is known as the lattice factor.

The solution of Eq. 2.25 depends on the nature of the interactions as well as on the type of the formed aggregate, i.e., of $P(r)$. When a structure factor is introduced in the scattering intensity equation, one tries to establish what kind of interaction potential is present in the sample. Some of the most used interaction potentials, developed for globular particles, are the hard sphere, the sticky hard sphere [36], the squared-well potential, or the rescaled mean spherical approximation (based on spheres with Coulomb interaction) [37]. To solve the Ornstein-Zernike integral, there must be a closure relationship between the correlation function and the potential [29]. Some of the most common closure relationships are the Percus-Yevick approximations [38], which have been successfully used to find an analytical solution for the Ornstein-Zernike integral for a hard sphere and sticky hard sphere potentials. There are several closure relations reported to solve the Ornstein-Zernike integral, such as the mean spherical approximation, the Roger-Young (RY) closure [39], and the zero separation theorem-based closure (ZSEP) [40], among others. A complete list can be consulted in reference [25]. Once it is determined, which potential will be employed and the respective closure relation, the Ornstein-Zernike integral equation can be solved, and thus the correlation function can be obtained. Then, the structure factor is determined by using Eq. 2.25. This methodology can be followed to introduce other interaction forms as well as to insert, if necessary, suitable size distribution functions.

In this chapter, our objective is not focused on analyzing the solutions of the Ornstein-Zernike integral from different closure relations or demonstrating how some structure factors are obtained; rather we will focus our efforts on two particular approaches often employed to obtain valuable information from experimental data obtained from a nanoparticulate system. These are the fractal aggregate model and the unified exponential power law model (Beaucage model).

2.4.1 Fractal Aggregate Model

The fractal aggregate model (FA) was postulated by Chen and Teixeira in the mid-1980s [41], since then it has been widely applied to investigate structural features of diverse systems, including biological and nanoparticulated systems. Particularly speaking of nanoparticulated materials, the aggregation dynamics is related to the nature of the nanoparticle components. For example, metallic nanoparticles, such as silver or gold, hosted in water tend to form aggregates due to ionic forces, while for magnetic nanostructures, including nanoparticles of iron, cobalt, nickel, or their respective oxides, magnetic interaction can promote the formation of aggregates [42]. In these two cases, the interacting forces depend on several factors, such as the size of the nanoparticles, the polarity of the host solvent, and the nanoparticle functionalization, among others.

The application of the FA model for correlated nanoparticles has been founded assuming that N primary nanoparticles (of radius r_0) can be spatially arranged

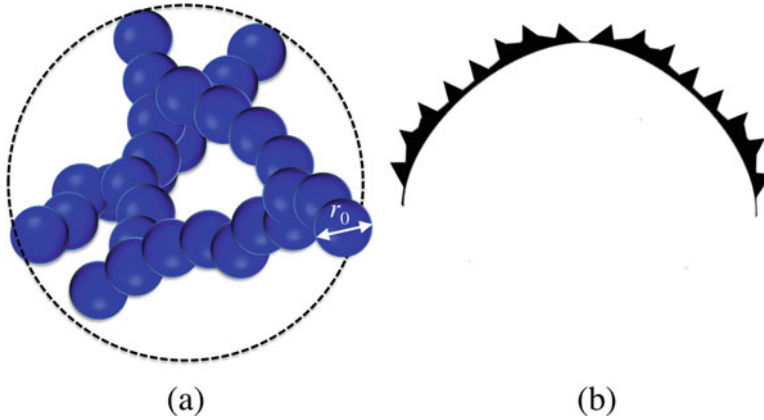


Fig. 2.10 (a) Schematic representation of a mass fractal structure. This structure is made out of primary particles of radius r_0 that are aggregated. (b) Schematic representation of a surface fractal structure of moderated roughness

forming aggregates of mass M and size ξ . These quantities are directly related through a power law, as follows:

$$M \sim \xi^{D_F} \quad (2.26)$$

where D_F is the fractal dimension that depends on the nature of the aggregation mechanism [6]. Those aggregates whose mass increase follows Eq. 2.26 are known as *mass fractals* [43]. A mass fractal aggregate can be understood as a large structure with branches cross-linked by the effect of certain forces, as is shown in Fig. 2.10a. Notice that the concept behind D_F is consistent with the common notion of Euclidean objects, i.e., for objects with homogeneous shapes, such as globular, planar, or elongated 1-D objects, D_F takes values of 3, 2, and 1 [44], respectively. While, for objects with mass fractal features, D_F takes semi-integer values. On the other hand, the surface of the aggregates can also have fractal topographies, in this case referred as *surface fractals* (see Fig. 2.10b). Here, the proportional relationship between fractal surface S and aggregate size ξ is given by:

$$S \sim \xi^{D_S} \quad (2.27)$$

where the exponent D_S carries the aggregate roughness information, being 2 for smooth surfaces and taking values ranging between 2 and 3 for surfaces with fractal topographies [9].

Using the above information, one can generalize the Porod law, which becomes:

$$I(q \rightarrow \infty) \sim q^{-2D_F + D_S} \quad (2.28)$$

Notice that for a globular aggregate ($D_F = 3$) with smooth surface ($D_F = 2$), the Porod law keeps its power dependence with q^{-4} .

Remembering, the structure factor $S(q)$ for a set of correlated monodisperse nanoparticles can be determined by solving Eq. 2.25. Certainly this implies determining first a suitable pair-distribution function $P(r)$. Thus, one can start from the fact that the primary particle number density inside a sphere of radius r is given by [6, 9].

$$N(r) = (r/r_0)^{D_F} \quad (2.29)$$

Note that Eq. 2.29 is valid if the number of primary particles is calculated from the center of the mass fractal aggregate. Moreover, from the pair-distribution function definition, it is also possible to determine the primary particle number density [45], as follows:

$$N(r) = \frac{N}{V} \int_0^{\infty} 4\pi r^2 P(r) dr \quad (2.30)$$

From Eqs. 2.29 and 2.30, the following equivalence is reached:

$$(r/r_0)^{D_F} = \frac{N}{V} \int_0^{\infty} 4\pi r^2 P(r) dr \quad (2.31)$$

Then, Eq. 2.31 can be solved to find the expression for the pair-distribution function:

$$P(r) = \frac{1}{r_0^{D_F}} \frac{1}{4\pi N} D_F r^{D_F-3} \quad (2.32)$$

Finally, introducing the obtained result from the Eq. 2.32 into Eq. 2.25, and then solving it, the structure function for a fractal object is given by [45]:

$$S(q) = 1 + \frac{1}{(qr)^{D_F}} \frac{D_F \Gamma(D_F - 1)}{[1 + 1/(q\xi)^2]^{(D_F-1)/2}} \sin \left[(D_F - 1) \tan^{-1}(q\xi) \right] \quad (2.33)$$

From the asymptotic behavior of Eq. 2.33, one can also find valuable information. For example, analyzing the expression at the Guinier region ($S(q \rightarrow 0)$), one can find an expression for the radius of gyration of the mass fractal aggregate:

$$R_g^2 = \frac{D_F (D_F + 1) \xi^2}{2} \quad (2.34)$$

A complete procedure to obtain the radius of gyration of the mass fractal is available in [9, 45].

In the case of a system composed by monodisperse correlated nanoparticles, one can select the sphere form factor (listed in Table. 2.3) and thus apply Eq. 2.24 ($I(q) \sim P(q)S(q)$) to finally determinate an expression for the scattering intensity produced by a system with fractal aggregate architecture, which is:

$$I(q) = N(\Delta\rho)^2 V_P^2 3 \left[\frac{\sin(qr_0) - qr_0 \cos(qr_0)}{(qr_0)^3} \right]^2 \left\{ 1 + \frac{1}{(qr_0)^{D_F}} \frac{D_F \Gamma(D_F - 1)}{[1 + 1/(q\xi)^2]^{(D_F-1)/2}} \sin[(D_F - 1) \tan^{-1}(q\xi)] \right\} \quad (2.35)$$

being Γ the gamma function. For systems composed by polydisperse correlated nanoparticles, it is necessary to introduce a suitable distribution function $f(r)$ to then integrate the expression $I(q) \sim \int P(q)S(q)f(r)dr$.

In Fig. 2.11 we present a series of representative SAXS curves of fractal structures composed by primary particles of spherical shape. To construct Fig. 2.11a, we decided to carry out the simulation keeping constant two of the structural parameters, r_0 and ξ , but varying the fractal dimension D_F . On simulation displayed in Fig. 2.11b, a Gaussian size distribution $g(r)$ was introduced in order to consider the polydispersity effect. Also, r_0 and ξ were kept constant, while D_F was changed, choosing values ranging between 1.1 and 3. On these figures, one can see different characteristic regions. Notice that for the fractal structures constructed with monodisperse spheres, the Porod trend (at high- q values) is screened, because the SAXS intensity exhibits the oscillatory behavior even at large- q values. Each region carries specific information. This means:

1. The first region, defined for the small- q range ($q \ll \xi$), is known as the Guinier region for the aggregate. For this q range, $I(q)$ behaves accordingly to the Guinier law. Note that depending on the aggregate size, it becomes necessary to record the scattering intensity at extremely small- q values, which from an experimental point of view represents a big challenge. From this region it is possible to determine the aggregate size as well as their radius of gyration (Eq. 2.34).
2. The second region is described over the intermediate- q region and can be defined when $1/\xi < q < 1/r_0$. In this region the scattering intensity falls, following a power

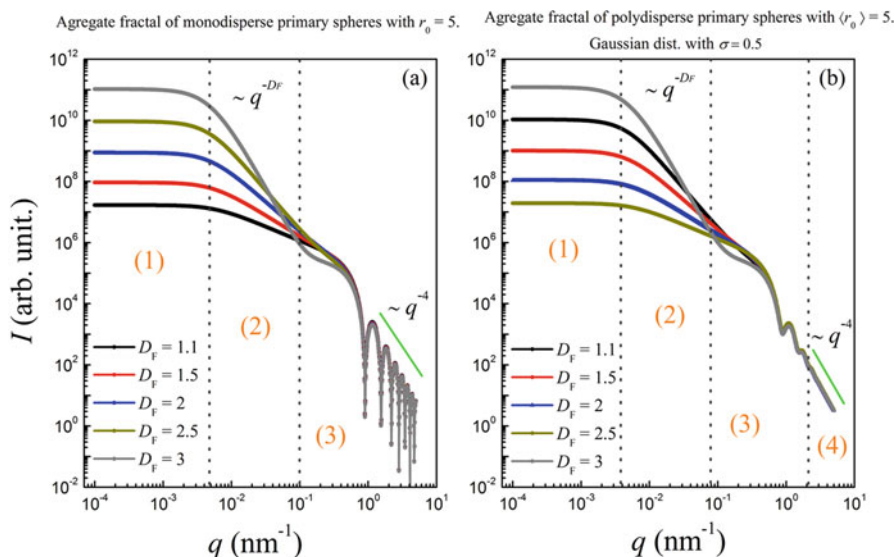


Fig. 2.11 Simulated SAXS curves according to the FA model for a set of (a) monodisperse and (b) polydisperse nanoparticles. For each five SAXS curves were simulated varying the fractal dimension

law of $I(q) \sim q^{D_F}$. Since this region comprises the aggregated Porod zone and the primary particle Guinier zone, then the fractal dimension of the aggregate and the size of the primary particles can be determined.

3. The third region or the oscillatory one is defined at $q > 2/r_0$. Since this oscillatory behavior is related to the size distribution of the primary particles, one can determine the degree of polydispersity of the primary particles.
4. Finally, the last region, better defined in Fig. 2.11b, describes the scattering intensity behavior at large- q values. This is associated to the Porod zone of the primary particles, which means that the scattering intensity decreases following a power law of $I(q) \sim q^{-4}$.

There are several papers where this model is applied in order to determine the most important structural parameters linked to the formation of aggregates. Specially, when working with magnetic nanoparticles, it is extremely important to take them into account, since their degree of aggregation and the aggregate features can modify the macroscopic magnetic response of the system. Some examples of this behavior can be found in these references [27, 33–35, 46].

On Sect. 2.4.3 we will present some examples where this model is applied in order to structurally characterize nanoparticulated systems.

2.4.2 Unified Exponential/Power Law Model (Beaucage Model Based on Hierarchical Structures)

The unified exponential/power law model postulated by Beaucage describes the scattering intensity produced by an aggregate of fractal dimension D_F and radius of gyration R_g [47]. Basically, this model combines the Guinier and Porod regimes into a unified expression to describe the scattering intensity behavior of any morphology of complex systems containing multiple levels of related structural features [34, 35, 47, 48]. As in the FA model, the aggregates are considered as constituted by single subunits (primary particles), which has a radius of gyration r_S . This model establishes a semiempirical expression for $I(q)$. For two structural levels (aggregates and single subunits), the equation for $I(q)$ is given by:

$$I(q) = G \exp \left[-\frac{q^2 R_g^2}{3} \right] + B \exp \left[-\frac{q^2 r_S^2}{3} \right] \left(\left[\operatorname{erf} \left(\frac{q R_g}{\sqrt{6}} \right) \right]^3 / q \right)^{D_F} + G_S \exp \left[-\frac{q^2 r_S^2}{3} \right] + B_S \left(\left[\operatorname{erf} \left(\frac{q r_S}{\sqrt{6}} \right) \right]^3 / q \right)^P \quad (2.36)$$

where erf is the error function and P is the Porod exponent, which usually takes a value of 4. G and B are, respectively, the Guinier and Porod pre-factors for the aggregate, while G_S and B_S are the respective pre-factors for the primary particles. Thus, the first term describes the aggregate structure, while the second one carries the information of the mass fractal structure [25]. The last two terms contain the structural information of the single subunits. For aggregates formed by solid particles of globular form, the mentioned pre-factors are given by [34, 44]:

$$G = N_\xi \Delta \eta^2 \left(\frac{4\pi}{3} \right)^2 \left(\frac{\xi}{2} \right)^6 \quad (2.37)$$

$$B = 2\pi N_{PP} \Delta \eta^2 S \quad (2.38)$$

$$G_S = N_{PP} \Delta \eta^2 \left(\frac{4\pi}{3} \right)^2 r_S^6 \quad (2.39)$$

$$B_S = 8\pi N_{PP} \Delta \eta^2 r_S^2 \quad (2.40)$$

being N_ξ the number of aggregates per unit volume, $\Delta\eta$ the scattering length density difference between the particles and the host matrix, N_{pp} the number of small subunits within each aggregate, and S the specific surface. For a set of experimental SAXS data, one can use Eq. 2.36 to fit the data and obtain the three parameters of importance, being these ξ , r_s , and D_F . With these information, other valuable structural information can be indirectly obtained, for example, the number of aggregates per unit volume N_ξ [34]:

$$N_\xi = \frac{G}{\Delta\eta^2 \left(\frac{4\pi}{3}\right)^2 \left(\frac{\xi}{2}\right)^6} \quad (2.41)$$

Besides, if the aggregate is composed by polydisperse single primary particles, the structural parameters involved in Eqs. 2.37–2.40 can be replaced by their averaged expressions, i.e., ξ and r_s can be substituted by $\langle\xi\rangle$ and $\langle r_s\rangle$, respectively. According to Ref. [44], the averaged expressions can be merged to determine the polydispersity index (PI) of the primary particles, resulting in:

$$PI = \frac{B_S r_S^4}{1.62 G_S} \quad (2.42)$$

being $PI = 1$ for monodisperse primary particles.

As can be noted, the approach above discussed has been founded on the assumption that the investigated system contains two structural levels (aggregates and primary particles). However, the Beaucage model can also be extended to describe the scattering intensity of an arbitrary number or structural levels [25]; thus Eq. 2.36 becomes:

$$I(q) \approx \sum_i^n \left[G_i \exp \left[-\frac{q^2 R_{g,i}^2}{3} \right] + B_i \exp \left[-\frac{q^2 R_{g,i+1}^2}{3} \right] \left(\left[\operatorname{erf} \left(\frac{q R_{g,i}}{\sqrt{6}} \right) \right]^3 / q \right)^{P_i} \right] \quad (2.43)$$

where n is related to the number of structural levels and being $i = 1$ for the largest one.

In the next section, we will present some examples where the Beaucage model is applied to structurally characterize systems conformed by nanoparticles hosted in colloids or in solid polymeric matrices.

2.4.3 *Application of the Fractal Aggregate and Beaucage Models on Specific Systems with Correlated Nanoparticles*

In this section we will show the application of the FA and Beaucage models on particular samples. The samples presented here were synthesized by our research group. For the first example (colloidal silver nanoparticles), the SAXS patterns were recorded in the Brazilian Synchrotron Light Laboratory while for the second example (Fe oxide nanoparticles loaded in polymeric matrices) already published in [34]. Essentially, we will focus in analyzing the most important regions of the SAXS pattern, as well as in briefly discussing the most interesting results.

2.4.3.1 **Correlated Nanoparticles: Silver Nanoparticles Diluted on Organic Solvent**

The Ag nanoparticles studied here were prepared following the thermal-assisted reduction procedure. According to TEM images (not shown here), the nanoparticles present a moderate aggregation degree, and their sizes are framed in a lognormal-type distribution with a mean diameter of ~ 4 nm. According to the experimental SAXS pattern, displayed in Fig. 2.12 (black symbols), the scattering intensity follows a power-law behavior for the low- q range instead of the Guinier behavior; this is a first signal of the existence of nanometric scale aggregates. In the intermediate- q region ($0.16 \text{ nm}^{-1} < q < 0.26 \text{ nm}^{-1}$), the scattering intensity seems to follow a power law dependence with $\sim q^\alpha$ (with $\alpha = 2$) suggesting the presence of aggregates with a fractal structure. After this region, the absence of an oscillatory behavior confirms the existence of a size distribution of moderate width. For the high- q values (Porod region), the scattering intensity falls according to a power law of $\sim q^{-4}$, characteristic of elementary particles with smooth surface. This first semiquantitative analysis leads us to think that a model of correlated particles must be applied in order to get the suitable structural information. In that sense, we decide to use the previously discussed model to fit the experimental data. Figure 2.12a, b shows the fitting results by following the FA and Beaucage models. According to the results, from the FA model, a mean primary diameter of ~ 4.1 nm and a fractal dimension D_F of ~ 1.90 were obtained, while following the Beaucage expression, values of 4.4 nm and 1.92 were calculated for primary particle diameter and fractal dimension, respectively. Comparing the values obtained from both models, one can note that the slight differences are in the same magnitude order than the experimental error. Thus, it can be concluded that the two employed models are suitable to obtain the desired morphological information. It is noteworthy that the primary particle size determined from both approaches is in good agreement to those obtained from microscopy techniques. These results suggest the formation of aggregates with a two-dimensional structure. The size of this structure was directly obtained from the FA model, being $\xi \approx 14$ nm. Despite that from the

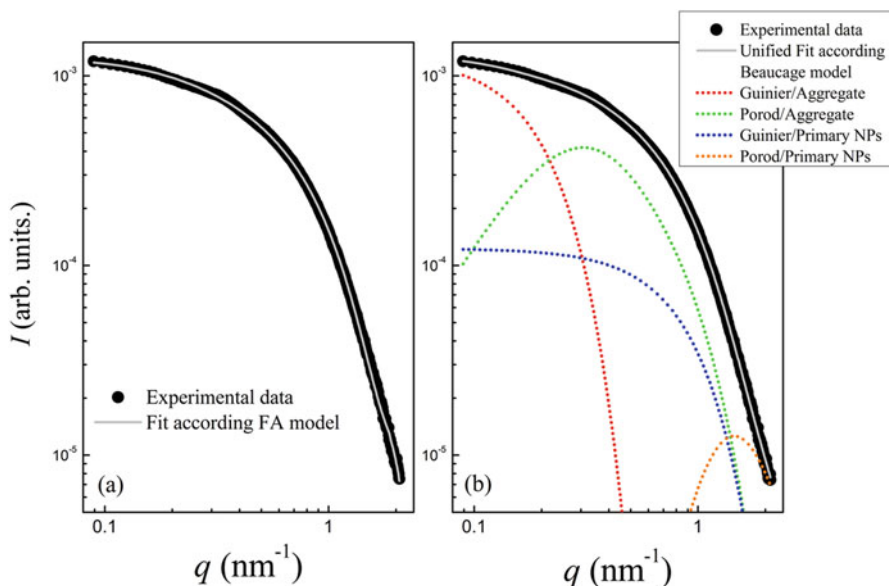


Fig. 2.12 Experimental SAXS pattern (black symbols) obtained from a set of silver colloidal nanoparticles. (a) Best fitting results according to the fractal aggregate model. (b) Best fitting result following the extended Beaucage expression described in the text. Contribution of the Guinier and Porod for aggregates and primary particles are presented as dotted lines

Table 2.4 Structural information derived from the fitting procedure according to the FA and Beaucage models

FA model				Beaucage model			
$\langle D \rangle$ (nm)	σ	ξ (nm)	D_F	D_S (nm)	D_F	R_g (nm)	D_{Agg} (nm)
~ 4.1	0.2	~ 14	1.96	~ 4.4	2.01	~ 14.8	~ 11

D_S was calculated using $D_S = 2r_s$. D_{Agg} is the aggregate diameter; this was indirectly determined using the radii of gyration (R_g) of the aggregates and assuming their 2-D morphology as something close to a thin circular disk with radius R ($R_g^2 = \frac{R^2}{2}$), i.e., $\frac{D_{Agg}}{2} = (2R_g)^{1/2}$

Beaucage model the aggregate size cannot be directly obtained, we assume a 2-D structure, with a morphology similar to a thin circular disk. Under this assumption the aggregate size was determined, obtaining a value of approximately 11 nm. A complete list with the fitting results is presented in Table 2.4.

2.4.3.2 Correlated Iron Oxide Nanoparticles Loaded in Nonconducting Polymeric Matrices: The Role of the Nanoparticle Concentration

With this example we show how the previously discussed models (Sects. 2.4.1 and 2.4.2) can be applied to follow the nanoparticle agglomeration degree on

magnetic polymer nanocomposites. With this intention we have retaken part of a work already published [34] but solely focused the discussion on the most relevant information obtained from the SAXS technique. According to the mentioned work, the studied samples are prepared by loading four different concentrations of iron oxide nanoparticles (0.5 wt.%, 3 wt.%, 15 wt.%, and 30 wt.%) on polymeric matrices of polyvinyl alcohol (PVA). Synthesis details can be consulted on [34].

Regarding the cited work, the SAXS intensities were well fitted following the extended Beaucage expression for two structural levels (Eq. 2.36). Among the most important results, this work stresses that the aggregate size (ξ) and the fractal dimension (D_F) increase as the nanoparticle concentration rises, indicating the formation of larger and most compact aggregates for those systems with larger amounts of Fe oxide nanoparticles. These features are reflected also on their magnetic properties [49] (Fig. 2.13).

2.5 Small-Angle X-Ray Scattering Instrumentation

An X-ray source, a collimation system, a sample holder, a beam stopper, and a detection system basically compose every SAXS instrument. In a typical experiment, the sample is irradiated by a very narrow, collimated beam of fixed diameter, and the elastic, coherent scattered radiation is detected at very low angles, requiring in first

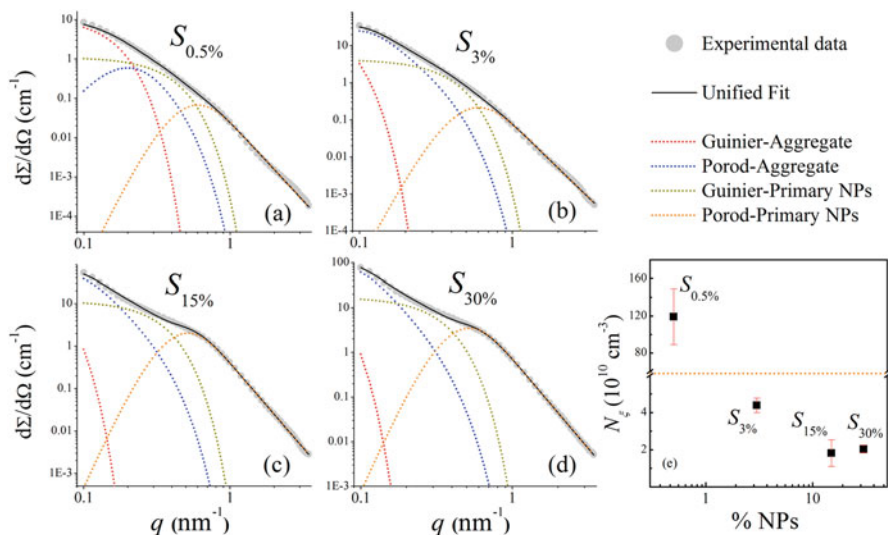


Fig. 2.13 (a–d) SAXS curves of the magnetic composites. The experimental data represented by symbols. Guinier and Porod contributions for the two structural levels are presented as dotted lines. (e) Number density of magnetic aggregates (N_ξ) as a function of nanoparticle concentration (Figure reprinted with permission from [34])

instance that the detector is placed a few meters away from the sample, since the scattered intensity decays as the inverse of the squared distance. It is noteworthy that the main instrumental challenge is separating the weak scattered radiation from the strong main beam, which travels through the sample and reaches the detector directly, making the beam stop indispensable.

The *X-ray source* constrains the entire equipment design and construction; it divides the instruments in two big groups, the laboratory or benchtop SAXS instruments, equipped with conventional X-ray sources, e.g., X-ray tubes of the characteristic wavelength of the anode material [5]. Secondly, the synchrotron SAXS instruments obtain X-rays from the electromagnetic radiation emitted from charges accelerated at relativistic velocities, usually electrons or positrons. These instruments combine great advantages like high intensity, narrow angular divergence, and broad spectral range, extending the possibilities of SAXS applications [1], e.g., time-resolved and anomalous SAXS measurements.

A second classification of the instruments can be done regarding the collimation mechanism, which must contemplate two main challenges: the beam size, directly related to the resolution, which must be balanced by larger divergence to ensure sufficient intensity and the parasitic scattering caused by the process of beam reduction, which must be minimized. A high-power density of an incident X-ray beam will be a waste if these aspects are ignored [50]. Three main classes of instruments can be defined:

- (a) Slit-collimated instruments: using parallel slits is the simplest and reasonably the first historically employed solution to collimate a SAXS instrument beam. The resolution can be improved with narrower slits and longer inter-slit distances, but it is limited by the parasitic scattering emitted at low angles. The latter can be avoided introducing additional slits in the appropriate configuration. In these instruments, also known as Kratky cameras, the primary beam is usually emitted with a line-shaped cross section; hence the superposition of intensity contributions from various scattering points along the line-shaped beam can occur, causing distorted or blurred patterns that must be properly corrected before being analyzed.
- (b) Pinhole-collimated instruments: the growing technological development of point-source X-ray generators as well as 2-D focusing optics augmented the popularity of these instruments over slit-collimated, due to sample versatility and easy availability of data reduction and analysis procedures. In a pinhole-collimated instrument, the pinhole selects a highly coherent part of the beam and produces a finite illumination area, with a circular or elliptical shape. Thus, the scattering pattern is a centrosymmetrical distribution formed by concentric circles around the illuminated spot of the primary beam, useful for investigations on orientation distributions.

Compared to slit-collimated instruments, the illuminated volume in the sample is small and so will be the scattered intensity, comprising the resolution. The latter can be improved increasing the sample-to-detector distance, resulting

in larger instruments (up to few meters) and lower intensity at the detector, increasing the needed measurement time up to hours.

- (c) Bonse-Hart instruments: taking advantage of the high angular selectivity of crystalline reflections, an intense, large cross-sectional X-ray beam, with very small angular divergence, can be obtained. For this purpose a first fixed crystal is placed between the source and the sample to collimate the incident beam, so that the radiation from the source strikes it at the Bragg angle. A second rotatable crystal placed after the sample is responsible for the analysis of the angular distribution of the scattered radiation, since the highest reflectivity is only for radiation impinging upon it at the Bragg angle [51]. The novelty introduced by Bonse and Hart was an increase in the angular resolution by increasing the number of reflections in each of the crystals, preserving the main beam intensity and reducing its tails [52]. With conventional X-ray sources, these instruments have low efficiency in the mid- q range, because the point-taking technique excludes the use of position-sensitive detectors, limiting these instruments to systems of rather large scatterers. Conversely, the point-by-point measurement limitations can be compensated using higher flux synchrotron radiation [53]. A third crystal may be added parallel to the second, expecting to diminish even more the beam tails.

The *sample holder* is a key component of the instrument; it must be versatile enough to adapt to many sample preparations and SAXS modes, i.e., transmission mode and reflection/grazing angle (GISAXS). The sample-to-detector beam path should be free of scatterers to minimize background scattering, this includes air molecules, and hence vacuum is required ideally. In most experiments, samples are destroyed when subjected to vacuum conditions and require control over parameters such as temperature, pressure, flow/shear rate, humidity, strain, projection angle, etc. As a consequence, completely homemade or variants of commercially available sample holders are often used. Most common sample preparations are described in [2]:

- (a) Liquids are usually measured in transmission mode in thin-walled capillaries of variable thickness, according to the absorbance of the solvents, i.e., heavy atoms composed of solvents require thinner walls. Suspensions must be stable over time and sufficiently diluted.
- (b) Pastes, rubbers, powders, and vacuum-sensitive materials are usually mounted on sample holders of removable windows. A commonly used window material is a polyimide or a beryllium film, characterized for being transparent to X-rays, with high mechanical and thermal stability.
- (c) Solids can be fixed to frames; the same film can be used for protection and stabilization. Thickness must be controlled to ensure sufficient transmittance for the measurement.
- (d) Materials on a substrate can be measured on transmission mode if the substrate is sufficiently thin and X-ray transparent; otherwise it must be measured in reflection mode, as long as the thin film material scattering is stronger than the scattering of the substrate.

In many cases if samples require a controlled atmosphere or are sensitive to vacuum, they are placed in a small compartment that is inserted into the vacuum. It must be kept in mind that the windows and air or gas volume of this compartment can contribute to background scattering.

The *beam stop* is responsible for protecting the detection system of the direct intense main beam or the possible overhanding of the scattered signal caused by strong backscatter from the detector material when reached by the intense beam.

The main beam can be completely blocked with an opaque, dense material like lead or tungsten or attenuated with a transparent material to a manageable intensity. When attenuated, the main beam profile and the zero-angle position can be acquired directly in each measurement, but possible background scattering caused by the beam stop material must be taken into account. A third option is to substitute or condition the beam stop with a PIN diode in order to characterize the transmitted beam.

In X-ray free-electron lasers (XFEL), the focused primary X-ray beam has sufficient energy to ablate most materials; small primary beam stops cannot be used in front of the detectors, as is customary at storage ring sources. Therefore, the X-ray imaging detectors in the forward scattering direction need to have a central hole to let the direct beam through.

SAXS parameters of interest are the flux and position of the incident photons. The detection system employs a mechanism that absorbs the energy from an X-ray photon and transforms it into an electrical signal. Some of these mechanisms are the ionization of a gas, liquid, or solid; the excitation of optical states, known as scintillation; and the excitation of lattice vibrations (phonons).

To this aim, the most commonly employed detectors are [2]:

Wire detectors consist of one or an array of parallel wires to produce a 1-D or 2-D scattering patterns, respectively, placed inside an absorbing gas atmosphere (Xe or Ar/methane) in the presence of an applied high voltage bias. An entering X-ray photon ejects an electron from the gas molecules, which accelerates toward a wire and induces an electrical pulse that propagates in both directions of the wire. The arrival of the pulse to both of the wire ends is recorded, and the time difference can be related to the position where the impulse was generated. This technique has a rather poor spatial resolution but a high sensitivity to different wavelengths.

- (a) Charge-coupled device (CCD) detectors, like conventional cameras, detect visible light which is emitted from a fluorescence screen when an X-ray photon impacts. A glass fiber plate is placed between the screen and the video chip to conduce the light with minor distortions. Each pixel consists of a capacitor that charges with the incident radiation; hence no pulses can be filtered. The resolution and quality of the acquisition will be dependent on the number, size, and quality of the chips, on an efficient cooling system, and on the ability of on-chip binning, which interconnects chip information to increase the precision.
- (b) Imaging plates detectors consist of photostimulable composite structures (e.g., BaF(Br,I) Eu²⁺ micrometer-sized crystals coating a plastic plate) capable of storing a fraction of the absorbed X-ray energy as excited electrons. Posterior

exposure to visible light liberates the stored energy as luminescence, proportional to the absorbed X-ray intensity. The photostimulated luminescence wavelength differs from that of the stimulating radiation and can be collected with photomultiplier tubes or avalanche photodiodes, amplified and converted to a digital image. The plate can be reused after exposed to visible light to remove any residual stored energy [54]. The resolution mainly depends on the readout system.

- (c) Solid-state detectors or CMOS (complementary metal-oxide-semiconductor) are based on a semiconductor crystal, commonly silicon or germanium, subjected to a bias. When an X-ray photon is absorbed, a number of electron-hole pairs are created proportional to the energy of the incident X-ray photon divided by the energy required to produce an electron-hole pair, reflected in high-energy resolution. The applied bias induces a current by the movement of the positive and negative charge carriers, and the charge, proportional to the energy of the incident photon, is collected.

The whole instrumental selection and design must be engineered to maximize the achievable resolution, defined by the length of the flight tube, the beam size and divergence, and the point spread function of the detector. It must be kept in mind that each of the components can originate pattern smearing as a consequence of effects like finite collimation, finite detector resolution, and wavelength spread. Equilibrium can be looked for between high-quality equipment (costs/facilities) and manageable data analysis.

2.5.1 Small-Angle X-Ray Scattering and Transmission Electron Microscopy

In the last section of this chapter, we want to highlight the importance of microscopy experiments as a complementary technique to determine the structure features in nanoparticulate systems. Both transmission electron microscopy (TEM) and small-angle X-ray scattering (SAXS) are the most used techniques to determine the morphology features of a set of nanoparticles. Both techniques (as well as others that use radiation) create an output signal by taking advantage of the electron density function difference between the studied objects and surrounding medium. Basically SAXS and TEM techniques are based on the same physical principle, but, at the end, the obtained information is recorded in a different way. For example, in microscopy the scattering pattern is treated by a set of lens, from which the image is reconstructed. Instead, in a SAXS experiment, the scattering pattern is recorded, and a potential image must be reconstructed mathematically.

Certainly TEM and SAXS have advantages and disadvantages. It is clear that the greatest advantage of TEM is the direct generation of real images of the studied object. However, this technique is restricted to a small portion of the sample, a fact that, for example, can limit the construction of an accuracy size distribution curve.

For nanoparticles composed of atoms of low molecular weight (such as carbon, sulfur, phosphorous, among others), it is also common to have problems identifying the nanoparticle boundaries. On the other hand, in the SAXS technique, a larger volume of the sample can be illuminated, a fact that leads to the estimation of more precisely average values. Despite that the SAXS pattern is obtained from over all particles oriented in all directions, the structural features are determined in an indirect way, an issue that could lead to ambiguous results and wrong interpretations. The previous facts indicate that in order to obtain a complete picture of the structural features at superatomic scale, it is recommendable to combine both TEM and SAXS.

Acknowledgment O. M. L., D. M., and M. K. acknowledge FAPESP, Brazil (2014/26672-8, 2011/01235-6 and 2011/02356-11), P. T., P. R., and L. M. S. Thanks to CONICET (Argentina). LNLS/CNPEM is acknowledged for SAXS measurements. LNNano/CNPEM is acknowledged for the use of TEM microscopes. All the authors want to especially thank the developers of the SASfit software, which was used to simulate the SAXS curves presented here.

References

1. Feigin, L. A., & Svergun, D. I. (1989). *Structure analysis by small-angle X-ray and neutron scattering*. New York: Plenum Press.
2. Schnablegger, H., & Singh, Y. (2013). *The SAXS guide*. Austria: Anton Paar GmbH.
3. Li, T., Senesi, A. J., & Lee, B. (2016). Small angle A-ray scattering for nanoparticle research. *Chemical Reviews*, 116(18), 11128–11180.
4. Thiele, E. (1963). Equation of state for hard spheres. *The Journal of Chemical Physics*, 39(2), 474–479.
5. Glatter, O., & Kratky, O. (1982). *Small-angle X-ray scattering*. London: Academic.
6. Craievich, A. F. (2016). Small-angle X-ray scattering by nanostructured materials. In L. Klein, M. Aparicio, & A. Jitianu (Eds.), *Handbook of sol-gel science and technology*. Cham: Springer.
7. Debye, P., & Bueche, A. M. (1949). Scattering by an inhomogeneous solid. *Journal of Applied Physics*, 20, 51525.
8. Putnam, C. D., Hammel, M., Hura, G. L., & Tainer, J. A. (2007). X-ray solution scattering (SAXS) combined with crystallography and computation: Defining accurate macromolecular structures, conformations and assemblies in solution. *Quarterly Reviews of Biophysics*, 40(3), 191–285.
9. Hammouda, B. (2008). *Probing nanoscale structures – the SANS toolbox*. Maryland: Gaithersburg.
10. Glatter, O. (1977). A new method for the evaluation of small angle scattering data. *Journal of Applied Crystallography*, 10, 415–421.
11. Amemiya, Y., & Shinohara, Y. *Oral presentation at Cheiron School 2011: Small-angle X-ray scattering basics & applications*. Japan: Graduate School of Frontier Sciences, The University of Tokyo.
12. Sanjeeva Murthy, N. (2016). X-ray diffractions from polymers. In Q. Guo (Ed.), *Polymer morphology: Principles, characterization and processing* (pp. 29–31). Hoboken: Wiley.
13. Guinier, A., & Fournet, G. (1955). *Small-angle scattering of X-rays*. New York: Wiley.
14. Porod, G. (1982). Chapter 2: General theory. In O. Glatter & O. Kratky (Eds.), *Small-angle X-ray scattering*. London: Academic.

15. Roe, R.-J. (2000). *Methods of X-ray and neutron scattering in polymer science*. Oxford: Oxford University Press.
16. Hammouda, B. (2010). Analysis of the Beaucage model. *Journal of Applied Crystallography*, *43*, 1474–1478.
17. Rivas Rojas, P. C., Tancredi, P., Moscoso Londoño, O., Knobel, M., & Socolovsky, L. M. (2018). Tuning dipolar magnetic interactions by controlling individual silica coating of iron oxide nanoparticles. *Journal of Magnetism and Magnetic Materials*, *451*, 688–696.
18. Tancredi, P., Rivas Rojas, P. C., Moscoso-Londoño, O., Wolff, U., Neu, V., Damm, C., Rellinghaus, B., Knobel, M., & Socolovsky, L. M. (2017). Synthesis process, size and composition effects of spherical Fe₃O₄ and FeO@Fe₃O₄ core/shell nanoparticles. *New Journal of Chemistry*, *41*, 15033–15041.
19. Xu, R., Jiang, H., Song, C., Rodriguez, J. A., Huang, Z., Chen, C.-C., Nam, D., Park, J., et al. (2014). Single-shot three-dimensional structure determination of nanocrystals with femtosecond X-ray free-electron laser pulses. *Nature Communications*, *5*, 4061.
20. Barke, I., Hartmann, H., Rupp, D., Flückiger, L., Sauppe, M., Adolph, M., Schorb, S., Bostedt, C., et al. (2015). The 3D-architecture of individual free silver nanoparticles captured by X-ray scattering. *Nature Communications*, *6*, 6187.
21. Pedersen, J. (1994). Determination of size distribution from small-angle scattering data for systems with effective hard-sphere interactions. *Journal of Applied Crystallography*, *27*, 595–608.
22. Nakamura, K., Kawabata, T., & Mori, Y. (2003). Size distribution analysis of colloidal gold by small angle X-ray scattering and light absorbance. *Powder Technology*, *131*, 120–128.
23. Skou, S., Gillilan, R. E., & Ando, N. (2014). Synchrotron-based small-angle X-ray scattering of proteins in solution. *Nature Protocols*, *9*, 1727–1739.
24. Goertz, V., Dingenouts, N., Nirschl, H., et al. (2009). *Particle & Particle Systems Characterization*, *26*, 17–24.
25. Kohlbrecher, J. (2014). *SASfit: A program for fitting simple structural models to small angle scattering data*. Paul Scherrer Institute.
26. Pedersen, J. S. (1997). Analysis of small-angle data from colloids and polymer solutions: Modeling and least-squares fitting. *Advance in Colloid and Interface Science*, *70*, 171–210.
27. Khan, L. U., Muraca, D., Brito, H. F., Moscoso-Londono, O., Felinto, M. C. F. C., Pirota, K. R., Teotonio, E. E. S., & Malta, O. L. (2016). *Journal of Alloys and Compounds*, *686*, 453–466.
28. Orozco-Henao, J. M., Coral, D. F., Muraca, D., Moscoso-Londono, O., Mendoza Zelis, P., Fernandez van Raap, M. B., Sharma, S. K., Pirota, K. R., & Knobel, M. (2016). *The Journal of Physical Chemistry C*, *120*, 12796–12809.
29. Agbabiaka, A., Wiltfong, M., & Park, C. (2013). Small angle X-ray scattering technique for the particle size distribution of nonporous nanoparticles. *Journal of Nanoparticles*, *2013*, 640436.
30. Müller, J. J., Damaschun, G., & Hübner, G. (1979). Small angle X-ray scattering studies on the structure and symmetry of yeast pyruvate decarboxylase in solution. *Acta Biologica et Medica Germanica*, *38*(1), 1–10.
31. Pedersen, J. S., Oliveira, C. L. P., Hübschmann, H. B., Arleth, L., Manniche, S., Kirkby, N., & Nielsen, H. M. Structure of immune stimulating complex matrices and immune stimulating complexes in suspension determined by small-angle X-ray scattering. *Biophysical Journal*, *102*(10), 2372–2380.
32. Oliveira, C. L. P., Behrens, M. A., Pedersen, J. S., Erlacher, K., Otzen, D., & Pedersen, J. S. *Journal of Molecular Biology*, *387*(1), 147–161.
33. Moscoso-Londoño, O., Gonzalez, J. S., Muraca, D., Hoppe, C. E., Alvarez, V. A., López-Quintela, A., Socolovsky, L. M., & Pirota, K. R. (2013). *European Polymer Journal*, *49*(2), 279–289.
34. Moscoso-Londoño, O., Tancredi, P., Muraca, D., Mendoza Zélis, P., Coral, D., Fernández van Raap, M. B., Wolff, U., Neu, V., Damm, C., de Oliveira, C. L. P., Pirota, K. R., Knobel, M., & Socolovsky, L. M. (2017). Different approaches to analyze the dipolar interaction effects on diluted and concentrated granular superparamagnetic systems. *Journal of Magnetism and Magnetic Materials*, *428*, 105–118.

35. Meiorin, C., Moscoso-Londoño, O., Muraca, D., Socolovsky, L. M., Pirota, K. R., Aranguren, M. I., Knobel, M., & Mosiewicki, M. A. *Materials Chemistry and Physics*, 175, 81–91.
36. Baxter, R. J. (1968). Percus-Yevick equation for hard spheres with surface adhesion. *The Journal of Chemical Physics*, 49(6), 2770–2774.
37. Hansen, J. P., & Hayter, J. B. (1982). A rescaled mean spherical approximation structure factor for dilute charged colloidal dispersion. *Molecular Physics*, 46, 651–656.
38. Percus, J. K., & Yevick, G. J. (1958). Analysis of classical statistical mechanics by means of collective coordinates. *Physical Review*, 110(1), 1–13.
39. Rogers, F. J., & Young, D. A. (1984). New, thermodynamically consistent, integral equation for simple fluids. *Physical Review A*, 30, 999–1007.
40. Lee, L. L. (1995). An accurate integral equation theory for hard spheres: Role of the zero-separation theorems in the closure relation. *The Journal of Chemical Physics*, 103(21), 9388–9396.
41. Chen, S.-H., & Teixeira, J. (1986). Structure and fractal dimension of protein-detergent complexes. *Physical Review Letters*, 57, 2583.
42. Moscoso-Londono, O., Carriao, M. S., Cosio-Castaneda, C., Bilovol, V., Martinez Sanchez, R., Lede, E. J., Socolovsky, L. M., & Martinez-Garcia, R. (2013). *Materials Research Bulletin*, 48, 3474–3478.
43. Schaefer, D. W. (1989). Polymers, fractals, and ceramic materials. *Science*, 243, 1023–1027.
44. Thesis. Physics Institute, University of La Plata. (2015).
45. Teixeira, J. (1988). Small-angle scattering by fractal systems. *Journal of Applied Crystallography*, 21, 781–785.
46. Moscoso-Londono, O., Muraca, D., Tancredi, P., Cosio-Castaneda, C., Pirota, K. R., & Socolovsky, L. M. (2014). Physicochemical studies of complex silver–magnetite nanoheterodimers with controlled morphology. *The Journal of Physics Chemistry C*, 118, 13168–13176.
47. Beaucage, G. (1995). Approximations leading to a unified exponential/power-law approach to small-angle scattering. *Journal of Applied Crystallography*, 28, 717–728.
48. Hernández, R., Sacristán, J., Nogales, A., Ezquerro, T. A., & Mijangos, C. (2009). Structural organization of iron oxide nanoparticles synthesized inside hybrid polymer gels derived from alginate studied with small-angle X-ray scattering. *Langmuir*, 25, 13212–13218.
49. Socolovsky, L. M., & Moscoso Londoño, O. (2017). Consequences of magnetic interaction phenomena in granular systems. In S. Sharma (Ed.), *Complex magnetic nanostructures*. Cham: Springer.
50. Chu, B., & Hsiao, B. S. (2001). Small-angle X-ray scattering of polymers. *Chemical Reviews*, 101(6), 1727–1762.
51. Ritland, H. N., Kaesberg, P., & Beeman, W. W. (1950). Double crystal and slit methods in small angle X-ray scattering. *Journal of Applied Physics*, 21(8), 838.
52. Bonse, U., & Hart, M. (1966). Small angle X-ray scattering by spherical particles of polystyrene and Polyvinyltoluene. *Zeitschrift Für Physikalische*, 189, 151–162.
53. Chu, B., Li, Y., Gao, T., Chua, B., & Ao, T. G. (1992). A Bonse–Hart ultrasmall angle x-ray scattering instrument employing synchrotron and conventional x-ray sources. *Review Scientific Instruments*, 63, 4128.
54. Amemiya, Y. (1997). X-Ray storage-phosphor imaging-plate detectors: High-sensitivity X-ray area detector, In: Academic Press (Ed.), *Methods enzymol.* 276th ed., Elsevier, (pp. 233–243).

Chapter 3

Dynamic Light Scattering: Effective Sizing Technique for Characterization of Magnetic Nanoparticles



Sim Siong Leong, Wei Ming Ng, JitKang Lim, and Swee Pin Yeap

3.1 Introduction

Measurement of particle size is an essential step in research dealing with magnetic nanoparticles (MNPs). This necessity is ascribed to the unique features of MNP, such as magnetism and magnetic responsiveness, which change with respect to its size. For instance, the saturation magnetization, M_s , and the coercivity, H_c , of MNPs change as a function of the particle size. Gong et al. showed that the M_s of ultrafine Fe, Co, and Ni particles decreased with the decrease of particle diameter [1]. Meanwhile, H_c increased with the decrease of particle diameter; after reaching its maximum value, the H_c decreases with the decrease of particle diameter [1, 2]. In addition, below a critical size, MNPs exhibit zero H_c and zero remanence characteristics, an indication of superparamagnetic behavior [3, 4]. In terms of magnetic responsiveness, larger MNPs are more magnetically responsive and thus can be magnetophoretically separated from the smaller counterparts [5].

S. S. Leong

School of Chemical Engineering, Universiti Sains Malaysia, Penang, Malaysia

Faculty of Engineering and Built Environment, SEGi University, 47810, Selangor, Malaysia

W. M. Ng

School of Chemical Engineering, Universiti Sains Malaysia, Penang, Malaysia

J. Lim

School of Chemical Engineering, Universiti Sains Malaysia, Penang, Malaysia

Department of Physics, Carnegie Mellon University, Pittsburgh, PA, USA

S. P. Yeap (✉)

Department of Chemical & Petroleum Engineering, Faculty of Engineering, Technology and Built Environment, UCSI University, Kuala Lumpur, Malaysia

e-mail: yeapsw@ucsiuniversity.edu.my

In view of the direct correlation between MNP's size and its magnetic properties, there is a practical need to standardize the technique used for sizing of MNPs. This chapter focuses on dynamic light scattering (DLS), a powerful technique to characterize particle size, specifically for quantifying hydrodynamic size of particle in suspension form. Applying light scattering as the working principle, DLS is noninvasive, and thus the sample can be reused for other purposes after the DLS analysis. In addition, no specific modification is needed (except dilution) [6], and a small sample volume (1–1.5 mL) is sufficient for the analysis. The main data generated by DLS is Z-average size (mean size) [7]; meanwhile, certain models are also ready to translate the sizing results into distribution form [6]. Basically, size distribution based on intensity percentage, volume percentage, and number percentage can be generated from the DLS analysis for the user's perusal.

In pace with the advancement in nanotechnology development, DLS analysis is further simplified with the incorporation of user-friendly instrument and software. With such advantage in hand, DLS sizing can be conducted through a simple three steps, which are *step 1*, insert sample into the instrument; *step 2*, allocate proper setting on the software; and *step 3*, press START button to begin the measurement. After that, the user just needs to wait for the measurement results. These simplified steps have greatly reduced the proper technical training required to conduct DLS measurement, leading to the high popularity of this technique, but at the same time making DLS a “black-box” tool/technique. No any prior knowledge on scattering theory is needed to conduct the measurement or even getting “good” results. However, challenge arose from the correct interpretation of the obtained data. For instance, despite the various statistical information generated from DLS analysis, there is inconsistency selection of the types of size distributions for reporting purpose in current published accounts. It was found that some published works on MNPs research reported intensity-weighted size distribution [5, 8, 9]; meanwhile, there are also numerous published works that reported the volume-weighted [10, 11] or the number-weighted size distribution [12, 13]. It should be alerted that the three types of size distributions often provide different size values which could be vastly deviated. This scenario is mainly due to the different principles and assumptions taken in obtaining these size distributions. Furthermore, questions regarding the deviation of particle size from DLS and those from transmission electron microscopic (TEM) measurement, the suitable particle concentration for DLS measurement, etc., were also often asked by DLS users via online platform (e.g., *ResearchGate* [14]).

To address the concerns stated above, understanding the fundamental concept and working principle of DLS is therefore needed for effective and correct utilization of this sizing approach. More importantly, extra care should be allocated when interpreting the DLS data for strongly interacting nanoparticles, such as MNPs, which tend to agglomerate into clusters form. Henceforth, this chapter is dedicated to provide (i) an overview on the working principle of DLS and (ii) correlation between different types of size distributions, to discuss (iii) the practical uses of DLS in MNP-based researches with the experiment strategies, as well as to disclose (iv) several important considerations in DLS analysis.

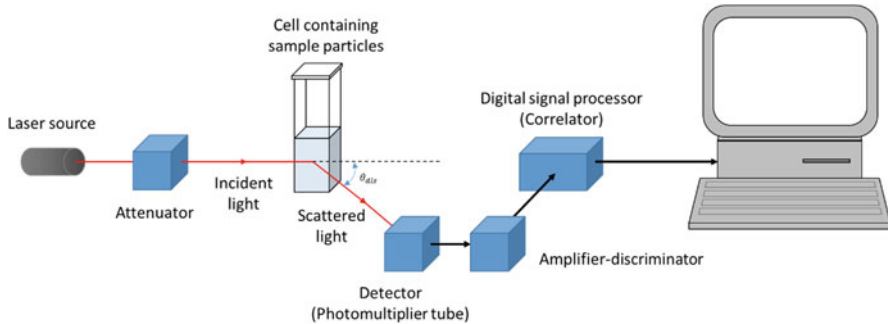


Fig. 3.1 Optical configuration of a typical experimental setup for dynamic light scattering measurement. The detector, which is usually a photomultiplier tube, measures the intensity of the scattered light in the form of rate modulated pulse train. These pulses are then passed through an electronic module called an amplifier-discriminator before entering to the correlator. The amplifier-discriminator is used to amplify the weak signals appearing from the detector output, suppress the background noise, and standardize the pulses making them suitable for processing by a correlator. The correlator performs autocorrelation of the rate modulated pulse trains by comparing the scattering intensity for a given period of time t_k in discrete steps Δt

3.2 Working Principle of DLS

3.2.1 Theory

During the operation of dynamic light scattering, light from a laser source passes through an attenuator which is used to define the polarization of the incident beam [15]. The polarized light beam is then illuminated onto a sample (particles in suspension) within a cuvette (see Fig. 3.1). Note that the directional stability of optical beam is crucial here as light beam that shifts direction with time might illuminate the location outside the sample zone. As the incident light interacts with the particles inside the sample solution, a certain portion of light is scattered away, while most of the light beam passes straight through the sample [16]. The scattering light intensity is measured by a detector, which is located at a particular angle θ_{dls} with respect to the outgoing light beam, such that the intensity profile of the scattering light can be recorded. The light intensity fluctuation given by smaller particles is relatively faster than the larger particles owing to their faster dynamics (more significant Brownian motion) within the suspension. Figure 3.2 shows the comparison between the intensity profiles of the light scattered by large and small particles. Henceforth, for sample with smaller particles, the scattered light correlation function $C(q, \tau)$ decays more rapidly with respect to the delay time τ between two intensity signals, $I(q, t)$ and $I(q, t + \tau)$ [17]:

$$C(q, \tau) = \frac{1}{t_k} \int_0^{t_k} I(q, t) \cdot I(q, t + \tau) dt \quad (3.1)$$

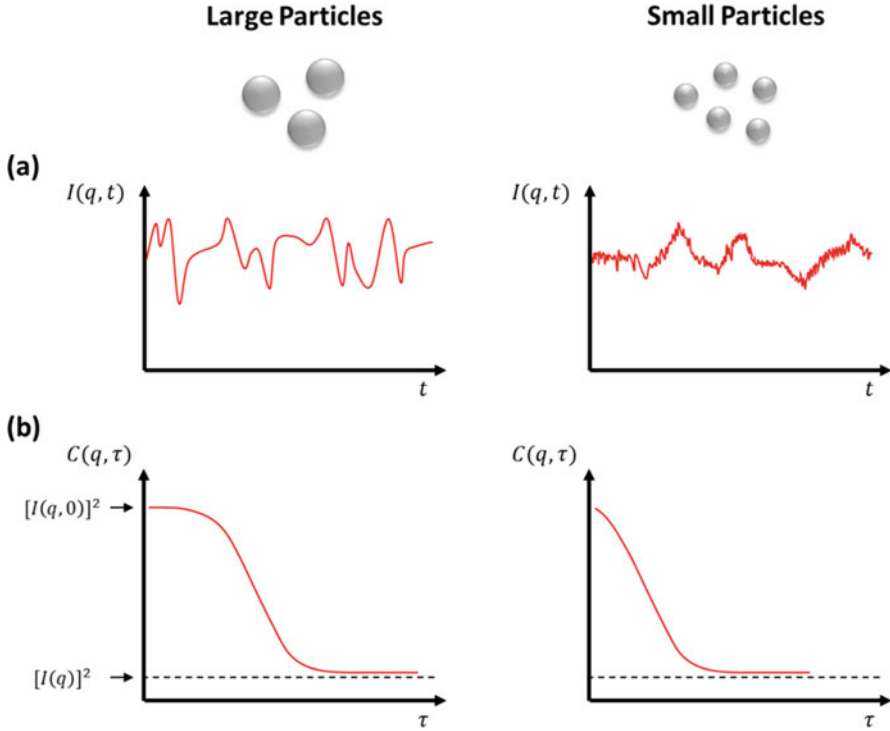


Fig. 3.2 Schematic illustration of (a) fluctuation of scattered light intensity and (b) the corresponding autocorrelation function in dynamic light scattering. (Redrawn from Lim et al. [21])

Here, t_k is the overall measurement time, while q is the magnitude of the scattered light wave vector which is the function of θ_{dls} , refractive index of the sample n , and the wavelength of the incident light λ , as given by the following equation [18]:

$$q = \frac{4\pi n}{\lambda} \sin(\theta_{\text{dls}}/2) \quad (3.2)$$

Upon division by the square of time-averaged intensity $\langle I(q) \rangle$, Eq. (3.1) becomes [19]

$$\frac{C(q, \tau)}{\langle I(q) \rangle^2} = G_2(q, \tau) = \frac{\frac{1}{t_k} \int_0^{t_k} I(q, t) \cdot I(q, t + \tau) dt}{\langle I(q) \rangle^2} \quad (3.3)$$

where $G_2(q, \tau)$ is the normalized intensity correlation function and the time-averaged intensity $\langle I(q) \rangle$ is given by [20]

$$\langle I(q) \rangle = \frac{1}{t_k} \int_0^{t_k} I(q, t) dt \quad (3.4)$$

The normalized intensity correlation function is related to another correlation function known as the normalized electric field correlation function. Both the intensity and the electric field fluctuations contain important information regarding the particle motion [22]. Similar to Eq. (3.3) for normalized intensity correlation function, the normalized electric field correlation function $G_1(q, \tau)$ is given as follows:

$$G_1(q, \tau) = \frac{\frac{1}{t_k} \int_0^{t_k} E(q, t) \cdot E(q, t + \tau) dt}{\langle E(q) \rangle^2} \quad (3.5)$$

where $E(q, t)$ is the electric field (which is the function of t and q) and $\langle E(q) \rangle$ is the time-averaged electric field. For a particle system which is undergoing Brownian motion, $G_1(q, \tau)$ decays exponentially with the delay time τ [21]:

$$G_1(q, \tau) = \exp(-\Gamma\tau) \quad (3.6)$$

where Γ is the decay constant given by

$$\Gamma = Dq^2 \quad (3.7)$$

Here, D is the diffusivity of the particles in the solution. For spherical particles, the particles' hydrodynamic diameter d_h is related to their diffusivity by Stokes-Einstein equation which is given by [23]

$$d_h = \frac{kT}{3\pi\eta D} \quad (3.8)$$

where k is Boltzmann constant, T is the absolute temperature of the system, and η is the viscosity of the solution. Both normalized intensity correlation function $G_2(q, \tau)$ and normalized electric field correlation function $G_1(q, \tau)$ can be related by Seigert equation as shown below [24]:

$$G_2(q, \tau) = 1 + \xi |G_1(q, \tau)|^2 \quad (3.9)$$

where ξ is the instrument constant. The left-hand side of Eq. (3.9) shows the normalized intensity correlation function $G_2(q, \tau)$ which can be obtained from experimental measurement, while the function $G_1(q, \tau)$ in the right-hand side of Eq. (3.9) reflects the dynamical behavior and Brownian motion (and hence hydrodynamic diameter) of the particles in the solution. In this regard, Seigert equation portrays a bridging role which relates the light scattering measurement to the hydrodynamic diameter of the particles, and it is the principal governing equation to be solved in DLS instrument.

3.2.2 Computation and Analysis of Experimental Data

In DLS instrument, the scattered light intensity is measured by the detector at every time interval of Δt . The measured signal is sent to a digital signal processor (also known as correlator) which computes the normalized intensity correlation function $G_2(q, \tau)$ based on the measurement data. Here, the normalized intensity correlation function $G_2(q, \tau)$ is computed according to the discretized form of Eqs. (3.3) and (3.4), as demonstrated in the following equation:

$$G_2(q, \tau) = \frac{\frac{1}{k} \sum_{i=1}^k I(q, i \Delta t) \cdot I(q, (i + j) \Delta t)}{\left[\frac{1}{k} \sum_{i=1}^k I(q, i \Delta t) \right]^2} \quad (3.10)$$

where $j = \tau/\Delta t$. The function $C(q, \tau)$ correlates the intensity at time $t_1(I(q, t_1))$ and the intensity after a time delay $\tau(I(q, t_1 + \tau))$ and is obtained for a series of τ by taking $j = 0, 1, 2, 3, \dots$, etc. [25]. During the measurement, it is important to ensure the overall measurement time t_k and number of discrete time step k are sufficiently large such that the calculated $G_2(q, \tau)$ is accurate and not far deviated from the real value.

There are several methods to analyze the value of $(G_2(q, \tau))$ and calculate the hydrodynamic diameter of the particles according to Eq. (3.9). Here, we are going to discuss three methods in details, namely, (1) linear fit, (2) cumulant method, and (3) CONTIN regularization.

3.2.2.1 Linear Fit

This is the simplest method to obtain the hydrodynamic diameter of the suspended particles by analyzing the normalized intensity correlation function $G_2(q, \tau)$. Upon rearrangement and taking logarithm of Eq. (3.9), the following equation was resulted:

$$\ln [G_2(q, \tau) - 1] = \ln \xi + 2 \ln G_1(q, \tau) \quad (3.11)$$

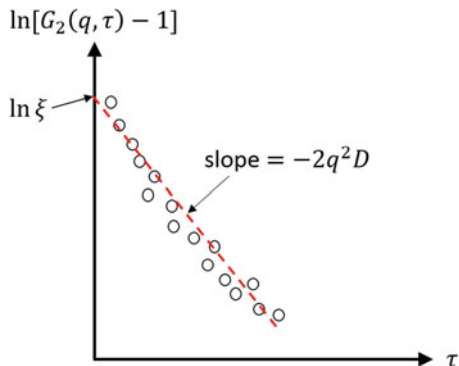
Substituting Eqs. (3.6) and (3.7) into Eq. (3.11) gives

$$\ln [G_2(q, \tau) - 1] = \ln \xi - 2q^2 D \tau \quad (3.12)$$

Henceforth, by inserting a linear fit into the tabulation of $\ln[G_2(q, \tau) - 1]$ against τ , the slope of the linear fit m is obtained, and it is then used to infer the diffusivity of the particles D as shown in the following equation (see Fig. 3.3):

$$m = -2q^2 D \quad (3.13)$$

Fig. 3.3 The plot of $\ln[G_2(q, \tau) - 1]$ versus τ for linear fit method. The red dotted line is the straight line that is fitted into the experimental data



Based on the diffusivity D , the hydrodynamic diameter of particles d_h can be calculated by using Stokes-Einstein equation as shown in Eq. (3.8).

However, this calculation is based on the assumption that all particles in the solution have the same diffusivity (and hence hydrodynamic diameter). Therefore, despite its simplicity, this analysis method is only limited to particle system which is highly monodispersed. In addition, there is no any information related to the polydispersity of the particle system if this analysis scheme is adopted.

3.2.2.2 Cumulant Method

Since all particle systems exhibit certain degree of polydispersity (even for highly monodispersed system), it is useful to consider the particle solution consists of the mixture of particles with different sizes [26]. In cumulant method, it is assumed that the particle size distribution in the solution obeys Gaussian distribution, in which the probability density function is maximum at the mean value and decays to the both ends. In accordance to this situation, the normalized electric field correlation function $G_1(q, \tau)$ of a given particle solution is resulted from the superposition of the individual electric field correlation function that is caused by each particle in the solution (Fig. 3.4):

$$G_1(q, \tau) = \int_0^{\infty} G(\Gamma) e^{-\Gamma\tau} d\Gamma \quad (3.14)$$

Here, $G(\Gamma)$ is the probability density function of particles according to decay constant Γ (recalled that particles with different hydrodynamic diameters give different decay constants Γ , as shown in Eqs. (3.7) and (3.8)). The exponential term in the integral of Eq. (3.14) is the electric field correlation function caused by particles with decay constant Γ (see Eq. (3.6)), which can be further divided into two exponential terms as below:

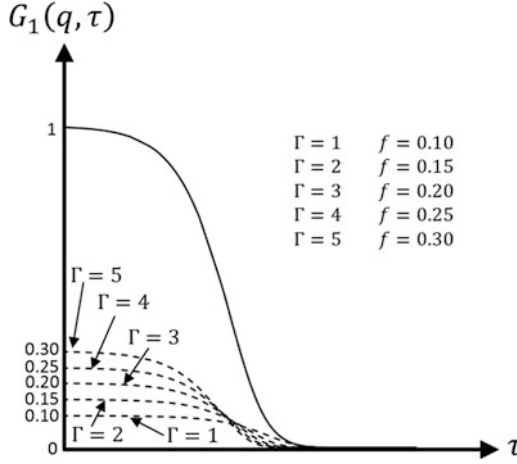


Fig. 3.4 The plot of $G_1(q, \tau)$ against τ . The dotted lines are normalized electric field correlation function contributed by particles with decay constants of 1, 2, 3, 4, and 5. In this particular illustration, the fractions of particle with decay constants of 1, 2, 3, 4, and 5 are given by 0.10, 0.15, 0.20, 0.25, and 0.30, respectively. The solid line represents the sum of normalized electric field correlation function contributed by particles with different decay constants (as the summation of all dotted lines in the plot)

$$e^{-\Gamma\tau} = e^{-\bar{\Gamma}\tau} e^{-(\Gamma-\bar{\Gamma})\tau} \quad (3.15)$$

where $\bar{\Gamma}$ is the mean decay rate. The second exponential term on the right-hand side of Eq. (3.15) can be expanded according to Maclaurin series:

$$e^{-\Gamma\tau} = e^{-\bar{\Gamma}\tau} \left[1 - (\Gamma - \bar{\Gamma})\tau + \frac{(\Gamma - \bar{\Gamma})^2}{2!}\tau^2 - \frac{(\Gamma - \bar{\Gamma})^3}{3!}\tau^3 + \dots \right] \quad (3.16)$$

By substituting Eq. (3.16) into Eq. (3.14),

$$\begin{aligned} G_1(q, \tau) &= \int_0^\infty G(\Gamma) e^{-\bar{\Gamma}\tau} \left[1 - (\Gamma - \bar{\Gamma})\tau + \frac{(\Gamma - \bar{\Gamma})^2}{2!}\tau^2 - \frac{(\Gamma - \bar{\Gamma})^3}{3!}\tau^3 + \dots \right] d\Gamma \\ &= e^{-\bar{\Gamma}\tau} \int_0^\infty G(\Gamma) \left[1 - (\Gamma - \bar{\Gamma})\tau + \frac{(\Gamma - \bar{\Gamma})^2}{2!}\tau^2 - \frac{(\Gamma - \bar{\Gamma})^3}{3!}\tau^3 + \dots \right] d\Gamma \\ &= e^{-\bar{\Gamma}\tau} \left(1 - 0 + \frac{k_2}{2!}\tau^2 - \frac{k_3}{3!}\tau^3 + \dots \right) \end{aligned} \quad (3.17)$$

where $k_n = \int_0^\infty G(\Gamma) (\Gamma - \bar{\Gamma})^n d\Gamma$. The unity in the first term in the blanket of Eq. (3.17) is emerged from the integration of probability density function $G(\Gamma)$ with the limit from $\Gamma = 0$ to $\Gamma \rightarrow \infty$:

$$\int_0^{\infty} G(\Gamma) d\Gamma = 1 \quad (3.18)$$

while the zero in the second term is resulted from the assumption that the probability density function $G(\Gamma)$ obeys Gaussian distribution which is symmetry about its mean value:

$$\int_0^{\infty} G(\Gamma) (\Gamma - \bar{\Gamma}) d\Gamma = 0 \quad (3.19)$$

By inserting Eq. (3.17) into Eq. (3.11), we obtained

$$\begin{aligned} \ln[G_2(q, \tau) - 1] &= \ln \xi + 2 \ln \left[e^{-\bar{\Gamma}\tau} \left(1 - 0 + \frac{k_2}{2!} \tau^2 - \frac{k_3}{3!} \tau^3 + \dots \right) \right] \\ &= \ln \xi - 2\bar{\Gamma}\tau + 2 \ln \left(1 - 0 + \frac{k_2}{2!} \tau^2 - \frac{k_3}{3!} \tau^3 + \dots \right) \\ &= \ln \xi - 2\bar{\Gamma}\tau + 2 \left(\frac{k_2}{2!} \tau^2 - \frac{k_3}{3!} \tau^3 + \dots \right) \\ &= \ln \xi - 2\bar{\Gamma}\tau + k_2 \tau^2 - \frac{k_3}{3} \tau^3 + \dots \end{aligned} \quad (3.20)$$

(The simplification of second line to third line is done by using the Maclaurin approximation of $\ln(1+x) = x - \frac{x^2}{2} + \frac{x^3}{3} + \dots$. Due to the small delay time, usually of the order of microsecond to millisecond, x^2 and higher order terms can be neglected.)

By taking the expansion up to τ term, Eq. (3.12) is regained, and it gives the result exactly the same with the linear fit method. However, by taking the expansion up to τ^2 term (neglecting the τ^3 and higher order terms), the following expression is resulted:

$$\ln[G_2(q, \tau) - 1] = \ln \xi - 2\bar{\Gamma}\tau + k_2 \tau^2 \quad (3.21)$$

In such a case, the polydispersity index PDI of the particle system is defined as

$$\text{PDI} = \frac{k_2}{\bar{\Gamma}^2} \quad (3.22)$$

Therefore, by fitting the experimental data into Eq. (3.21), the particle size distribution and the polydispersity of the particle system can be evaluated. This computational scheme is particularly advantageous to analyze monomodal particle system which can be approximated by Gaussian distribution. However, this method is inappropriate to analyze non-monomodal particle system in which the particle distribution contains two or more peaks. Therefore, CONTIN regularization is introduced to cope with this particle system.

3.2.2.3 CONTIN Regularization

Similar to cumulant method, the particle system is considered as the mixture of particles with different sizes (and hence consisted of different decay constants Γ) with probability density function $G(\Gamma)$, in which the normalized electric field correlation function $G_1(q, \tau)$ is also given by Eq. (3.14). It should be noted that Eq. (3.14) has the similar form of Laplace transform formula:

$$F(s) = \mathcal{L}[f(t)] = \int_0^{\infty} f(t)e^{-st} dt \quad (3.23)$$

By comparing Eqs. (3.14) and (3.23), it can be deduced that

$$G_1(q, \tau) = \mathcal{L}[G(\Gamma)] = \int_0^{\infty} G(\Gamma) e^{-\Gamma\tau} d\Gamma \quad (3.24)$$

Hence, probability density function can be obtained by inverse Laplace transformation of the normalized electric field correlation function $G_1(q, \tau)$, which is related to the experimentally measured $G_2(q, \tau)$ by Siegert Equation (see Eq. (3.9)):

$$\begin{aligned} G(\Gamma) &= \mathcal{L}^{(-1)}[G_1(q, \tau)] \\ &= \mathcal{L}^{(-1)}\left[\frac{(G_2(q, \tau)-1)}{\xi}\right] \end{aligned} \quad (3.25)$$

CONTIN algorithm is developed to solve the inverse Laplace transformation (Eq. 3.25) numerically [27]. This method is ideal for solving multimodal particle system (which has particle distribution with two or more peaks) that cannot be approximated by cumulant method.

3.3 Interpretation of Data from DLS Analysis

3.3.1 Z-Average

Generally, the DLS results are often reported in the term of the Z-average. The Z-average is defined as the harmonic intensity-averaged hydrodynamic size of the sample particles measured by DLS. It is also known as the ‘‘cumulant mean’’ as it arises in the analysis of DLS data through the use of the cumulant method [17]. For particle dispersion with discrete size distribution, the Z-average of an arbitrary property y is given by [19]

$$Z_y = \frac{\sum n_i v_i^2 y_i}{\sum n_i v_i^2} \quad (3.26)$$

where n_i is the number of particles of class i having volume v_i and property y_i .

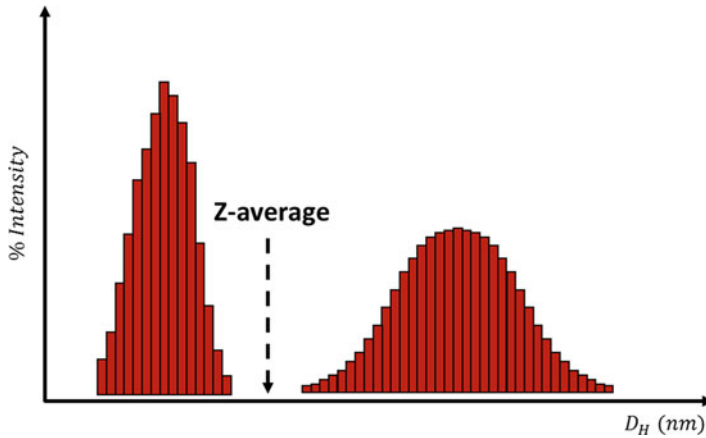


Fig. 3.5 Z-average (cumulant) size for particle system with bimodal distribution. (Redrawn from Lim et al. [21])

However, it should be noted that the Z-average is a hydrodynamic parameter which is only applicable to particles in a dispersion or molecules in solution. The Z-average should only be reported if the sample is monomodal (only one peak), spherical, and monodisperse. As shown in Fig. 3.5, for a bimodal system, the Z-average carries irrelevant size information because it will still be a single size even though there are significant segregated size distributions present in the sample [21].

3.3.2 Polydispersity Index (PDI)

Generally, polydispersity index (PDI) is defined as the quotient of variance σ^2 to the square of the mean value for a particular parameter x (such as decay constant Γ , diffusivity D , hydrodynamic diameter d_h , etc.) of a particle system [28]:

$$\text{PDI} = \frac{\sigma^2}{\bar{x}^2} \quad (3.27)$$

In physical perspective, PDI represents the degree of heterogeneity in the hydrodynamic diameter of the particles within a particular system. The greater PDI value indicates the more significant nonuniformity in the particles' hydrodynamic diameter and higher polydispersity of the particle system.

By taking decay constant Γ as the parameter which is involved in the PDI analysis, the variance σ^2 can be written as

$$\sigma^2 = \langle \Gamma^2 \rangle - \langle \Gamma \rangle^2 \quad (3.28)$$

Table 3.1 Description of particle system with different range of PDI value

PDI	Description
0	Uniform (or monodispersed) particle system. All particles are having the same size
0–0.1	Nearly monodispersed particle system. The dispersion are narrow and still can be considered as “monodispersed” throughout result analysis
0.1–0.4	Polydispersed particle system. Particle distribution should be considered in data analysis
> 0.4	Highly polydispersed particle system. Particle distribution might be multimodal and multiple particle species might present

In particular, for cumulant method with Maclaurin expansion up to τ^2 term, the variance (of decay rate constant Γ) is given by $\sigma^2 = k_2$, and PDI is exactly equal to the expression as shown in Eq. (3.22). Contrastingly, for CONTIN algorithm, the analytical form for PDI is nonexistence, and it is computed numerically according to Eq. (3.27).

Particle system with zero PDI means all particles in the system have exactly the same size. In such a case, the probability density function (or particle distribution function) has the same form with delta function, in which the density function is infinity about the mean value and drops to zero for other values. Particle system, with PDI within the range of 0–0.1, can still be considered as “monodispersed” as the polydispersity is insignificant under this context [29]. Typically, particle systems which fulfill this criterion ($\text{PDI} < 0.1$) can be assumed to be uniform about its mean value in the data analysis and calculation. On the other hand, for particle system with PDI within the range of 0.1–0.4, the polydispersity effect is dominant, and it is crucial to take the size distribution into account throughout the data analysis [28]. Lastly, for particle system with PDI value greater than 0.4, further analysis or other characterization method should be conducted to ensure the result obtained from DLS measurement is reliable. This is owing to the fact that high PDI might be resulted by other factors (such as multi-peaks, intervention of other species, etc.). Table 3.1 demonstrates the description of particle systems according to their range of PDI value.

It should be emphasized that PDI value is only representative for monomodal particle system (particle distribution with only one peak) as similar to Z-average discussed in the previous section. For multimodal particle system, PDI value lost its significance as the measure of particle dispersion and additional analysis should be conducted to obtain an accurate picture on the dispersity of the particle sample.

3.3.3 Correlation Between Different Types of Size Distributions

Decay rates can be extracted from the correlation function for a number of size classes to produce particle size distribution. Three types of particle size distribution can be generated from a DLS measurement, namely, number distribution, volume

distribution, and intensity distribution. Consider a particle dispersion consists of exactly two sizes of particles 1 and 2; there are n_1 particles 1 with size d_1 and n_2 particles 2 with size d_2 . Their relative contributions in terms of number compared to the other particle are

$$\%n_1 = \frac{100n_1}{n_1 + n_2} \quad (3.29)$$

where $\%n_1$ is the relative number of the particle 1 [30]. Since the particle volume is proportional to the cube of the size, the relative contribution of particle 1 can be expressed in terms of volume as

$$\%v_1 = \frac{100n_1d_1^3}{n_1d_1^3 + n_2d_2^3} \quad (3.30)$$

where $\%v_1$ is the relative volume of the particle 1 with size d_1 . Here, it is assumed that all particles are spherical. For small and isotropic particles, the intensity of light scattered by a spherical particle is proportional to the size raised to the power of six according to Rayleigh scattering. Thus, the relative contribution of particle 1 is given in terms of intensity as

$$\%I_1 = \frac{100n_1d_1^6}{n_1d_1^6 + n_2d_2^6} \quad (3.31)$$

where $\%I_1$ is the relative intensity of the particle 1 with size d_1 . It is clearly shown that the intensity distribution is more sensitive to the size of particles than that of volume distribution and number distribution.

The primary size distribution obtained from a DLS measurement is the intensity-weighted distribution. The intensity distribution describes the amount of light scattered by the particles in the different size bins. Thus, it is sensitive to the presence of large particles or aggregations of small particles. Viscosity and refractive index of the dispersing medium are required in producing an intensity size distribution.

The volume-weighted size distribution can be derived from the intensity distribution using Mie theory. The volume distribution shows the total volume of particles in the different size bins. It is also equivalent to the mass-weighted size distribution. The optical properties of the particles such as refractive index and absorption are required to convert the intensity distribution to volume distribution.

Finally, this volume distribution can be further converted to a number distribution as shown in Fig. 3.6. The number distribution shows the number of particles in the different size bins. For these transformations from intensity distribution to volume distribution or number distribution, it is assumed that all particles are spherical and have a homogenous and equivalent density [30].

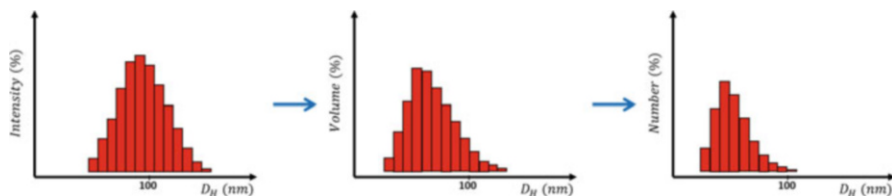


Fig. 3.6 Conversion of intensity distribution to volume distribution and then to number distribution. (Redrawn from Malvern Instruments Ltd. [30])

Keep in mind that from scattering theory, the scattered light is directly proportional to the sixth power of particle radius (Rayleigh's approximation). So in a simple linearized view, the scattered intensity of a single 10 μm particle is equivalent to the scattered intensity of 10^{18} particles of size 10 nm. As such, the intensity % of larger-size particles will be higher than the intensity % of smaller-size particles; even the number of larger-size particle in the sample is lesser. However, in most cases, the intensity distribution is always the best choice to report the particle size measured by DLS as it is the primary distribution (or, raw data) used to generate all other distributions. Furthermore, DLS tends to over-amplify small noise in the intensity distribution and leads to erroneous results in the transformation to volume distribution and hence number distribution.

3.4 Practical Uses of DLS in MNP-Based Researches

3.4.1 Characterizing Layer Thickness of Functionalized MNPs

For application in environmental purification and in biomedical processes, the MNPs normally need to be surface functionalized with a polymer layer. Ultimately, the nanoparticles form a core-shell structure with MNPs acted as *core* surrounded by polymer layer(s) as *shell*. Surface functionalization of MNPs with polymer is necessary to impart steric stabilization which can prevent occurrence of particle aggregation [31–33]. Moreover, the polymer coating is also needed to tailor specific functionalities to the MNPs [34, 35]. For instance, in environmental remediation, Madrakian et al. adopted synthetic mercaptoethylaminohomo polymer (which has chelating functional groups) on their MNPs for adsorption of heavy metal ions [36]. While in biomedical diagnostic application, Chen et al. showed that their antibody-conjugated MNPs specifically bound to *Salmonella enterica* over other species of bacteria via the antibody-antigen recognition feature [37].

For the case to determine the *shell* thickness [38], as well as to verify successful surface functionalization of nanoparticle, DLS always come as a useful analytical technique. Theoretically, it is expected that the hydrodynamic size of the surface-functionalized nanoparticles is larger than that of the bare nanoparticles.

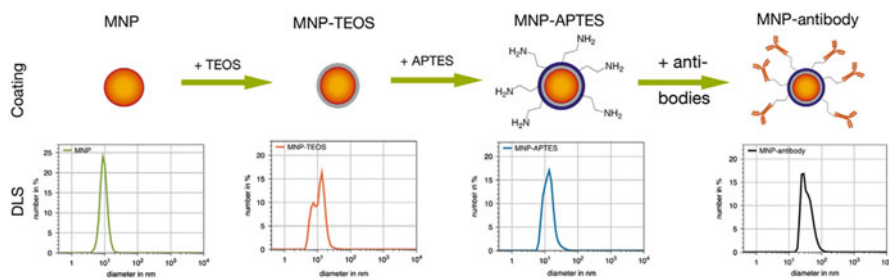


Fig. 3.7 Layer-by-layer functionalization of MNP with TEOS, APTES, and antibody. DLS analysis was conducted to track the change in hydrodynamic size after each step of functionalization. (Reprinted with permission from Rumenapp et al. [40], copyright 2015 Elsevier)

Thus, the thickness of functionalized layer can be estimated by comparing the hydrodynamic size of the nanoparticle before and after functionalization [39]. For instance, Rumenapp et al. documented an increase in hydrodynamic size of their MNPs after being layer-by-layer surface functionalized [40]. They found that the hydrodynamic size of the MNPs was originally 9.7 nm and it increased to 11.8 nm after encapsulated with TEOS shell. The MNP-TEOS was then functionalized with APTES and resulted in 13.7 nm diameter. The hydrodynamic size further increased to 30.14 nm after final functionalization with an antibody layer (see Table 3.2, row 1). Figure 3.7 shows the corresponding number-weighted size distribution obtained from their DLS analysis. Similarly, Stone et al. reported that the hydrodynamic diameters of the magnetic nanoparticles before and after modification with alkyne-PEO-NitroDOPA(6) were 29.2 nm and 77.3 nm, respectively (see Table 3.2, row 2)~[41].

However, utilization of DLS analysis as an approach to characterize layer thickness is not without limitation; particularly, it is restricted to nanoparticles having (1) narrow size distribution (monodispersed) and (2) good colloidal stability which can show a clear increment in hydrodynamic size after surface functionalization. On the other hand, for bare nanoparticles that tend to aggregate into polydisperse suspension, usage of DLS analysis for layer thickness estimation becomes challenging (or even impossible). In fact, besides the anticipated increase in hydrodynamic size after surface functionalization, it is also commonly found that hydrodynamic size of the functionalized MNPs is smaller than the bare MNPs (as listed in Row 5–Row 9 of Table 3.2). Chai et al. analyzed the hydrodynamic size of iron (II, III) oxide nanoparticles and found that the particles modified with different molecular weights of poly(diallyldimethylammonium chloride) (PDDA) have smaller hydrodynamic sizes (195.87–317.07 nm) as compared to the particles without functionalization (327.6 nm) [44]. Similarly, Tiraferri et al. reported hydrodynamic diameter of reactive bare iron nanoparticles was >1000 nm and it reduced to <400 nm after 0.5 g/L of guar gum was added as stabilizer [47]. In most likelihood, the larger hydrodynamic size of the bare nanoparticles is ascribed to their self-aggregation into large clusters during the interval between sample preparation (sonication) and DLS

Table 3.2 Hydrodynamic size of MNPs before and after surface functionalization

MNPs	Surface functionalization	Hydrodynamic diameter (nm) before surface functionalization	Hydrodynamic diameter (nm) after surface functionalization	References
Iron-based nanoparticles	–	9.7		[40]
	TEOS shell		11.8	
	TEOS shell + APTES		13.7	
Oleylamine-coated iron oxide nanoparticles	TEOS shell + APTES + antibody		30.14	
	–	29.2		[41]
Modified magnetite nanoparticles with APTES	Alkyne-PEO-nitroDOPA(6)		77.3	
	–	100		[42]
Iron oxide nanoparticles (mixture of magnetite and maghemite)	Chitosan		500–600	
	–	16		[43]
Iron(II, III) oxide <i>From Sigma-Aldrich</i>	POEGA- <i>b</i> -PMAEP		44	
	–	327.6		[44]
	PDDA (100,000 g/mol)		195.87	
	PDDA (100,000–200,000 g/mol)		202.07	
Fe_3O_4 <i>From nanostructured and amorphous materials</i>	PDDA (200,000–350,000 g/mol)		250.40	
	PDDA (400,000–500,000 g/mol)		317.07	
	–	331.2		[45]
	PSS (70, 000 g/mol)		220.7	
	PSS (1000, 000 g/mol)		387.3	

Fe ₂ O ₃ From Aldrich	–	> 600		[46]
	SDS		462.8	
	PSS		381.4	
Reactive bare iron nanoparticles From Toda Kogyo Corp.	–	> 1000		[47]
	0.05 g/L guar gum		Over 600	
	0.5 g/L guar gum		<400	
Palladium-doped nano-sized zero-valent iron (Pd-NZVI) in 10 mM NaHCO ₃	–	1370		[48]
	CMC		911	
	JBR215 rhamnolipid		62	
	R95 rhamnolipid		78	
	Soy flour		310	
	Soy protein		177	
	Soy milk		101	

TEOS tetraethoxysilane, *APTES* 3-aminopropyltriethoxysilane, *PDDA* poly(diallyldimethylammonium chloride), *PSS* poly(sodium 4-styrenesulfonate), *PEO* polyethylene oxide, *POEGA-b-PMAEP* poly((oligo(ethylene glycol) methyl ether acrylate)-*b*-*block*-poly(monoacryloxy ethyl phosphate)), *SDS* sodium dodecyl sulfate, *CMC* carboxymethyl cellulose

data acquisition. While for functionalized nanoparticles with enhanced colloidal stability, the self-aggregation is prevented during DLS analysis and thus gave a smaller hydrodynamic size as compared to the bare counterpart. In such occasion, assigning the size difference to adsorbed layer thickness is impossible.

3.4.2 *Time Lapse DLS Measurement for particle's Colloidal Stability and Aggregation Kinetic Studies*

One of the practical usages of DLS is on the tracking of particle's colloidal stability, as well as the aggregation profile of the particles under various surrounding medium. This kind of study is possible by assigning proper setting on the DLS software. In particular, manual setting needs to be done by increasing both (1) the number of measurements and (2) the delay time between measurements. For instance, by setting 50 numbers of measurements and 300 s of delay time, the DLS analysis will be automatically conducted on the sample for 50 times with an interval stop time of 300 s. By this way, changes in hydrodynamic size of the particles over a long period can be traced. The delay time can be adjusted into a more constrict time gap depending on the study requirement.

DLS analysis is very sensitive to the presence of large particles; this unique feature allows the rapid detection of particle aggregates in a suspension [5]. Tanapon et al. utilized time lapse DLS analysis to monitor changes in hydrodynamic size of reactive nanoscale iron particles (RNIP) (Toda Kyogo, Japan) and magnetite and hematite nanoparticles (Nanostructured and Amorphous Materials Inc., Los Alamos, NM) over a time frame of >30 min (see Fig. 3.8a) [49]. Bare MNPs are fond toward aggregation due to the existence of both van der Waals and magnetic dipole-dipole attraction [45]. As shown in Fig. 3.8a, result from DLS analysis showed that RNIP at 60 mg/L experiences a greater extent of aggregation as compared to RNIP at 2 mg/L. It was also found that both 60 mg/L RNIP and 69 mg/L magnetite experience gelation of aggregates at the last measurement point. Such observation indicates that DLS analysis is possible to describe the aggregation behavior of MNPs.

On the other hand, we have also conducted a series of time-dependent DLS measurement to monitor the disruption in colloidal stability of poly(sodium 4-styrenesulfonate)-coated Fe_3O_4 MNPs (*denoted as PSS 70K/Fe₃O₄*) upon addition of monovalent electrolyte [45]. As delineated in Fig. 3.8b, the PSS 70K/Fe₃O₄ does not show any size increment when it was being dispersed in salt-free deionized water. Here, the electrosteric stabilization contributed from the PSS 70K adlayer prevents the particle from aggregation. However, with the addition of 5 mM NaCl, increment in hydrodynamic size over time (indication of particle aggregation) was observed. The extent of particle agglomeration increased with the increase of NaCl concentration. Addition of NaCl induces suppression in electrostatic double layer as well as weakens the electrosteric repulsion which subsequently causes particle

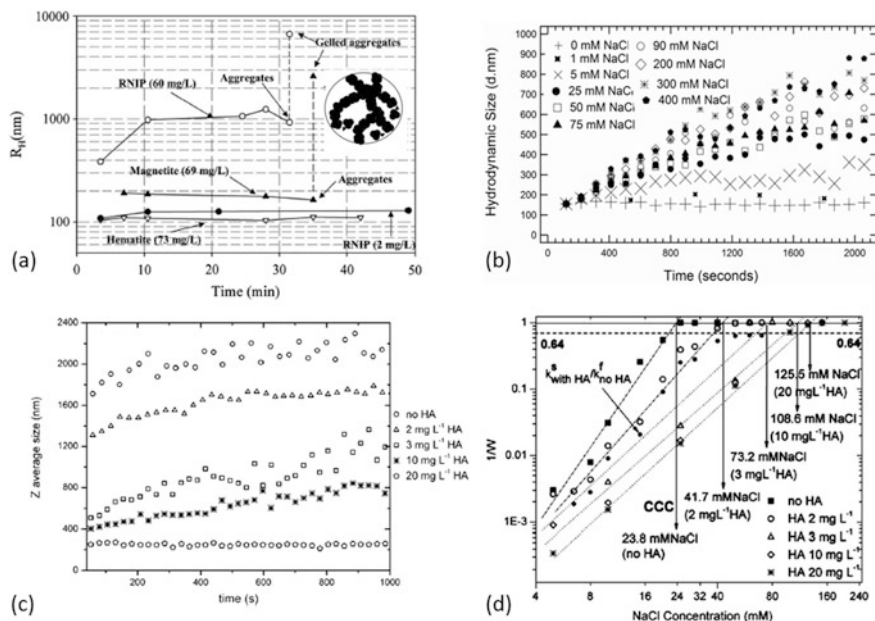


Fig. 3.8 (a) Evaluation on changes in hydrodynamic size of RNIP, magnetite, and hematite over time using time-lapse DLS analysis. The insert diagram illustrates gelled aggregates formed by individual particles. (Reprinted with permission from Phenrat et al. [49], copyright 2007 American Chemical Society). (b) Time-lapse tracking on the growth in hydrodynamic size of PSS 70K/Fe₃O₄ MNPs upon addition of different amount of NaCl. (Reprinted with permission from Yeap et al. [45], copyright 2012 American Chemical Society). (c) Time-dependent changes in hydrodynamic size of MNPs at 50 mM NaCl, pH 9.8 with the absence and the presence of HA. (d) The stability ratio and c.c.c value of MNPs as a function of NaCl concentration at pH 9.8 under the absence and the presence of HA (2 mg/L, 3 mg/L, 10 mg/L, 20 mg/L). (Reprinted with permission from Yu et al. [51], copyright 2010 Elsevier)

aggregation [50]. Nevertheless, the aggregation profile starts to overlap each other when the concentration of NaCl is ≥ 200 mM implying that the critical coagulation concentration (c.c.c) of PSS 70K/Fe₃O₄ MNPs is at ~ 200 mM NaCl [45].

For a more detailed environmental science and technology research, the particle aggregation profile under the presence of dissolved organic matters (DOMs) is evaluated by DLS. Hu et al. assessed time-dependent changes in hydrodynamic size of MNPs as a function of NaCl concentration at pH 9.8 under the presence of humic acid (HA), a naturally abundant DOM [51]. According to their observation, the aggregation level of MNPs notably lessened in the presence of HA due to stabilization effect induced by HA that have attached onto the particle surface (see Fig. 3.8c). The authors later on reinterpreted the particle aggregation profile in the form of stability ratio (W) profile in which W was calculated by taking the ratio of fast aggregation rate to the slow aggregation rate (Fig. 3.8d). Based on the stability ratio profile, the shift in c.c.c of the MNPs upon increase in HA loading can be

determined. By having those information, the colloidal stability and thus fate and transport of engineered nanoparticles upon their deliberate or accidental release into the environment can then be predicted.

3.4.3 *Detecting Size Evolution of Thermoresponsive MNPs*

Another interesting usage of DLS in MNP research is on the evaluation of changes in particle size of thermoresponsive MNPs. Thermoresponsive MNPs is a type of smart nanomaterials that experience a change in size upon change in surrounding temperature. Owing to its responsiveness toward both temperature and magnetic field, the synthesis and application of this hybrid nanomaterial have gained much attention in recent years [52]. Generally, thermoresponsive MNP is designed by capping MNPs with thermoresponsive polymer. Poly(N-isopropylacrylamide) (PNIPAAm) [53], poly(N-vinylcaprolactam) (PNVCL) [54], and poly(oligo(ethylene glycol)-methacrylate) (POEGMA) [55, 56] are example of polymer with thermoresponsive characteristic. The main feature of thermoresponsive polymers is their ability to change from an extended and hydrophilic structure to a globular and hydrophobic structure upon heating above a specific temperature known as lower critical solution temperature (LCST) [52, 57]. Therefore, the polymer is expected to be soluble in water at temperature < LCST and form precipitate at temperature > LCST [58].

For DLS analysis system incorporated with tunable temperature setting, the hydrodynamic size of the thermoresponsive MNPs can be closely monitored as a function of solution temperature. Zhao et al. synthesized Fe_3O_4 MNPs surface modified with poly(sodium styrene-4-sulfonate)-co-poly(N-isopropylacrylamide) (PSS-PNIPAM) [53]. The particles were employed for seawater desalination. After the application, the sample was heated to temperature > LCST in order to induce clustering of the particles (as illustrated in Fig. 3.9a.i). This heat-mediated clustering effect is crucial to improve the subsequent magnetic separation rate as magnetophoresis of aggregated particles is faster than magnetophoresis of single particle. As shown in Fig. 3.9a.ii, the hydrodynamic size of the thermoresponsive MNPs was ~ 25 nm at room temperature and grew to ~ 100 nm when the temperature increased to 32°C . On the other hand, in biomedical application, Hoshino et al. prepared antibody-conjugated thermoresponsive MNPs for the separation of murine neutrophils and macrophages [59]. The particles were first incubated in a suspension containing mixture of cells in which the conjugated antibody directed the particles to specifically bind to the unwanted cells. Later on, heat was applied to increase the temperature to $>30^\circ\text{C}$ to initiate particle aggregation. Here, DLS was employed to trace the aggregation level and found that the particles which were 167.6 nm in chilled condition (10°C) successfully aggregated to 1470.0 nm upon heated to 40°C (see Fig. 3.9b). Again, such aggregation is needed to promote fast magnetic separation of the particles-bound unwanted cells from the suspension.

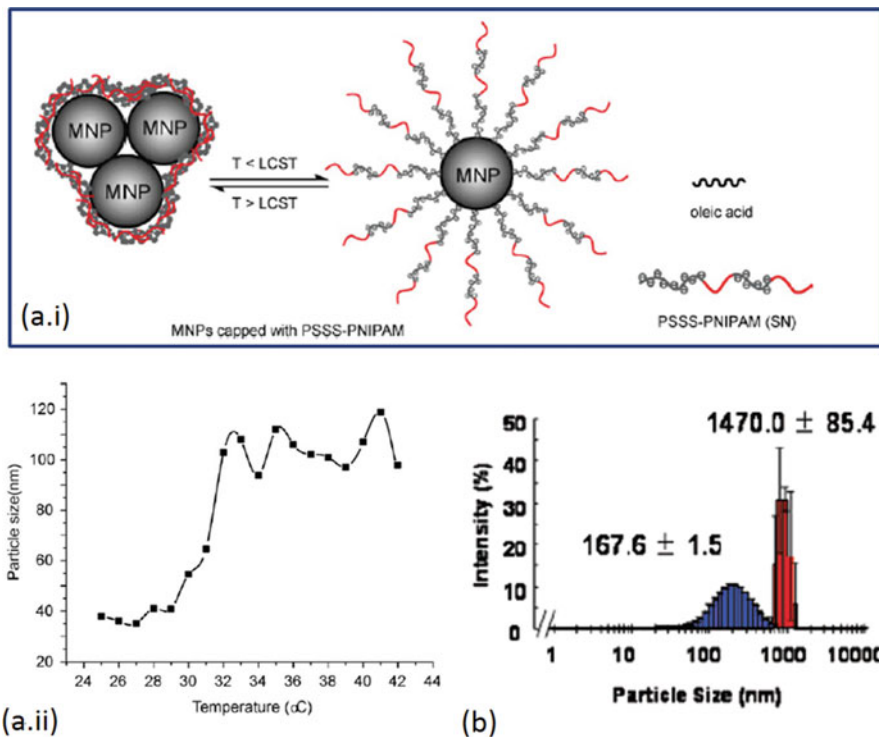


Fig. 3.9 (a.i) Schematic diagram shows swelling of the polymer chains when temperature is < LCST and shrinkage of the polymer chains when temperature is > LCST which subsequently cause particle aggregation. (a.ii) shows changes in hydrodynamic size of the PSS-PNIPAM copolymer-encapsulated MNPs with the increase of surrounding temperature. (Reprinted with permission from Zhao et al. [53], copyright 2013 American Chemical Society). (b) Size distribution by intensity percentage of antibody-conjugated thermoresponsive MNPs at 10 °C (blue bar) and at 40 °C (red bar). (Reprinted with permission from Hoshino et al. [59], copyright 2008 John Wiley and Sons)

3.4.4 DLS as an Innovative Tool to Determine Particle Concentration

Interestingly, DLS is not limited to size measurement only; it is also feasible as particle concentration determination tool. Even though there are less report on this specific use of DLS, but discussion related to this topic can still be found in current literature [60–63]. This fascinating feature of DLS arises from the linear relationship between the photon count rate (in unit of kCPS) with the particle concentration [61]. Such relationship is applicable in certain concentration range in which the photon count rate, P , is proportional to the scattered light intensity, I , of the particle suspension [60, 64]. If the particle size is smaller than the wavelength of the incident

light, Rayleigh law is applicable to further describe the correlation between I and particle concentration, C , [60, 64]

$$I = I_0 \frac{\pi^4 (1 + \cos^2\theta)}{8R^2\lambda^4} \left(\frac{m^2 - 1}{m^2 + 2} \right)^2 d^6 C$$

where I_0 is the intensity of the incident light, λ is the wavelength of the incident light, θ is the scattering angle, R is the distance between the point of observation and the particle, m is the particle-to-medium refractive index ratio, C is the number concentration of nanoparticles, and d is the particle diameter. This relationship is valid for monodisperse systems [60].

In order to use DLS for determination of particle concentration, there are few criteria to be fulfilled. First, a standard nanoparticle solution is needed for calibration purpose; this standard should have the same nanoparticles and solvent with the unknown sample. Second, the attenuation factor and the measurement position must be the same for both the standard and the unknown sample [64]. If this approach is to apply to determine concentration of MNPs, firstly, the MNPs must be free of aggregation. This is because particle aggregation and sedimentation would respectively induce increase and decrease in count rate over the analysis duration [7, 61]. Thus, stable superparamagnetic MNPs (which possess no magnetic attraction in absence of external magnetic field) or stabilized MNPs should be feasible for this specific usage of DLS.

3.4.5 Other Potential Uses of DLS in MNP Research

Recently de Kanter et al. reported their work on in-line DLS measurement of particle suspension under continuous stirring [65]. The in-line measurement requires a device which consists of (1) a commercialized Nanotrac 250 (Particle Metrix/Microtrac Europe GmbH, Germany) and (2) a customized probe head. The Nanotrac 250 is a robust DLS device with DLS probe employing fiber-optic quasi-elastic light scattering (FOQELS) measurement principle (see Fig. 3.10a), while the probe head was custom designed with few detachable parts (see Fig. 3.10b). The customized probe head was attached onto the DLS probe of the DLS device and being dipped into a beaker filled with particle suspension. The probe head was used to isolate a small portion of the particle suspension from the bulk (a process called compartmentalization), which was then used for DLS measurement. The authors used this setup to measure size of microgel sample under 1000 rpm stirring (result shown in Fig. 3.10c). Experiment was firstly done on unstirred suspension and without the incorporation of the customized probe head; after that, stirring is provided, and it was found that the measured size distorted to a smaller range. This was mainly due to superposition of Brownian motion and forced convection. However, such effect was successfully omitted after compartmentalization by the customized probe head.

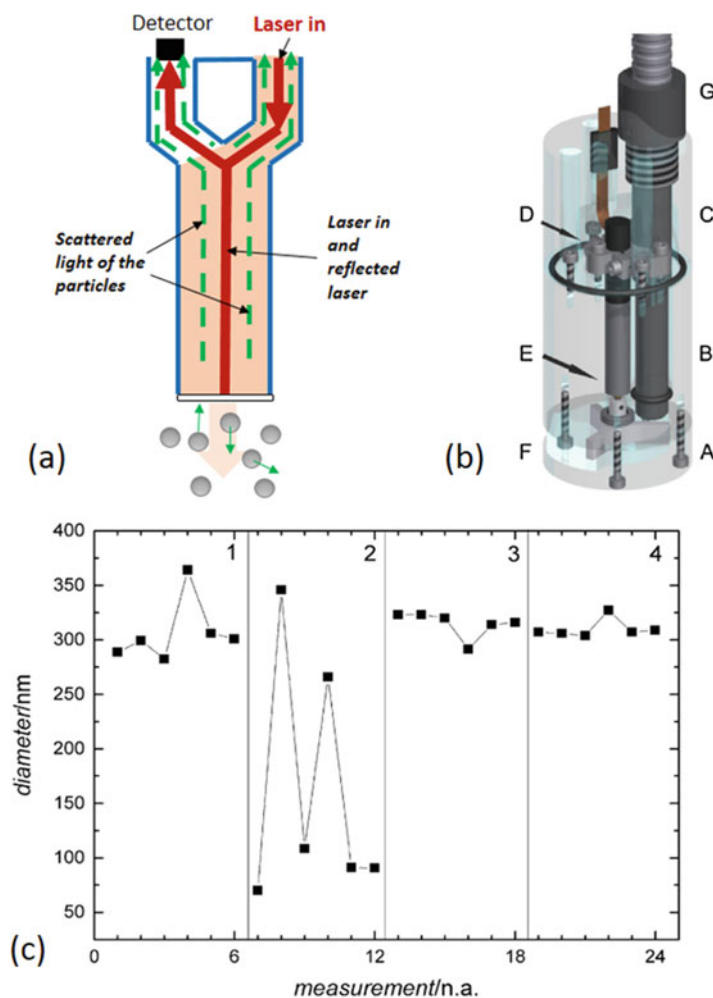


Fig. 3.10 (a) Illustration on measurement principle of the DLS device: laser is guided by an optical fiber and focused to the target sample close to the sapphire window. The 180° backscattered light as well as the laser light that reflected by the window are then collected by the detector. (Redrawn from [65, 66]). (b) Design of the optical DLS probe (G) surrounded by detachable probe head (A–C) customized by the authors. This setup is designed to cope with the need to measure particle size in either laboratory or industrial reactors, which are usually in stirring mode. (c) Size measurement on microgel suspension under four different conditions. Condition 1, not stirred, bare DLS probe; Condition 2, stirred, bare DLS probe; Condition 3, not stirred, DLS probe + customized probe head; Condition 4, stirred, DLS probe + customized probe head. (Reprinted from de Kanter et al. [65])

The in-line DLS measurement mentioned above serves as an alternative route to the normal off-line DLS measurement which requires portion of the sample to be drawn and diluted for DLS analysis. One of the potential future uses of this novel design is to track the self-aggregation and/or magnetic field-induced aggregation of MNPs under stirred system. Such study is imperative to reveal whether the stirring enhances the particle aggregation or induces aggregate breakage. Those information are crucial as it is known that self-aggregation and magnetic field-induced aggregation are the criteria for rapid magnetophoresis of MNPs [5]. However, MNPs might attract to the magnetic stirrer upon magnetic attraction; thus, proper modification still needs to be done on the design.

3.5 Considerations in DLS Analysis

There are several important considerations that need to be taken into account for correct interpretation of the DLS data. In particular, (1) the correlation between particle sizes acquired from DLS analysis and particle sizes acquired from electron microscopy analysis and (2) the effect of particle concentration on DLS analysis, as well as (3) the effect of particle sedimentation during DLS analysis on the sizing result, must be clarified.

3.5.1 *DLS Size Versus Electron Microscopy's Size*

Transmission electron microscopy (TEM) and scanning electron microscopy (SEM) are imaging type of sizing techniques that are useful on examining the size and the morphology of nanoparticles. In TEM analysis, electrons are emitted by electron source and being accelerated toward the sample. Image is formed based on the electrons that transmitted through the sample [67, 68]. On the other hand, in SEM analysis, a focused beam of electrons is scanned over the sample's surface, and the backscattered or secondary electrons produced upon interaction of the electrons with the sample are collected as signal readout [69, 70]. These signals are used to form image of the sample [70]. From the electron microscopy images, size of individual nanoparticles can be measured, and its corresponding number-weighted size distribution can be constructed.

Unlike DLS, TEM and SEM analysis requires the nanoparticle sample to be dried on a substrate. For instance, a common practice in preparation of sample for TEM analysis is to drop a droplet of a nanoparticle suspension on a Cu TEM grid (coated with carbon film) and letting the sample suspension to evaporate in order to get a dry sample [5, 71]. Similarly, nanoparticle suspension was dried out before visualized with SEM [72–74]. Both TEM and SEM are operated under high vacuum condition, and thus sample drying is needed to ensure it remains stable under vacuum condition [69, 75]. However, the deposited nanoparticles are

subjected to further aggregation which was artificially induced by the drying step [76]. This drying artifact occurs due the flow of liquid from the interior of the droplet to the edge of the droplet when the liquid at the edge is evaporated [77] and sharing the same physics origin of a coffee stain formation. This outward flow subsequently accumulates and aggregates the nanoparticles at the perimeter of the dried droplet [78]. Under this circumstance, the particle aggregation information obtained from TEM imaging, which has suffered from drying artifact, is less reliable to represent the real situation when the particles are in the suspended form. On the other hand, DLS technique does not requires the drying step (avoid drying artifact) and can be conducted in the original dispersion state during sizing analysis. Hence, for research that aims to investigate aggregation behavior/applications of magnetic nanoparticles dispersed in different liquid mediums (e.g., pure water [45], PBS [8], seawater [79], and other environmental-related media [80]), DLS definitely can provide more meaningful data compared to TEM or SEM.

The particle size determined from TEM and SEM images are the core size of the nanoparticles. Meanwhile, the particle size obtained from DLS analysis is termed as hydrodynamic size which includes not only the particle's core size but also the contribution from the hydration layer. Furthermore, for nanoparticles that have been surface modified with steric layer, the residing molecule also contributes to the increment in hydrodynamic size (see Fig. 3.11a for hydrodynamic size). Thus, it is commonly found that the particle size measured by DLS analysis is larger than the particle size determined from electron microscopy. Liu et al. [81] synthesized two different batches of MnFe_2O_4 magnetic nanoparticles of mean size 6 nm and 18 nm, as per determined from TEM analysis. However, the hydrodynamic size of the same nanoparticles from DLS analysis were 13 nm and 28 nm, respectively. The larger size determined from DLS could be attributed to the oleic acid ligands of MnFe_2O_4 nanoparticles. Similarly, Shanmuga et al. [82] reported that the average size of their carrageenan-coated magnetic nanoparticles is around 70–100 nm when measured via SEM, while DLS analysis gave a larger value (i.e., 140.5 nm). This discrepancy arises from the reason that the molecule layer is invisible in electron micrographs. In fact, one of the limitations associated to the electron microscopy analysis is that the quality of imaging is strongly dependent on the interaction between the electron beam and the specimen. In this case, polymer molecules, which mainly consist of the same light elements (carbon, hydrogen, oxygen, etc.) that weakly interact with the electron beam, have low contrast between structural details [83]. Nguyen et al. synthesized block copolymer poly((oligo(ethylene glycol) methyl ether acrylate)-*block*-poly(monoacryloxy ethyl phosphate)-coated iron oxide nanoparticles for hyperthermia application [43]. They found that the polymer layer cannot be seen in the TEM image (Fig. 3.11b) but its presence can be verified from the increment in hydrodynamic size (Fig. 3.11c). Even though the contrast of the polymer layer can be enhanced via chemical staining method, the polymer layer may still suffer from shrinkage effect upon dehydration [84, 85]. The drying and contrasting processes also might alter properties of the particles [86]. Thus the thickness of the adlayer observed in TEM was unable to correctly represent the “real” thickness when the polymer-coated nanoparticles are dispersed in suspension form.

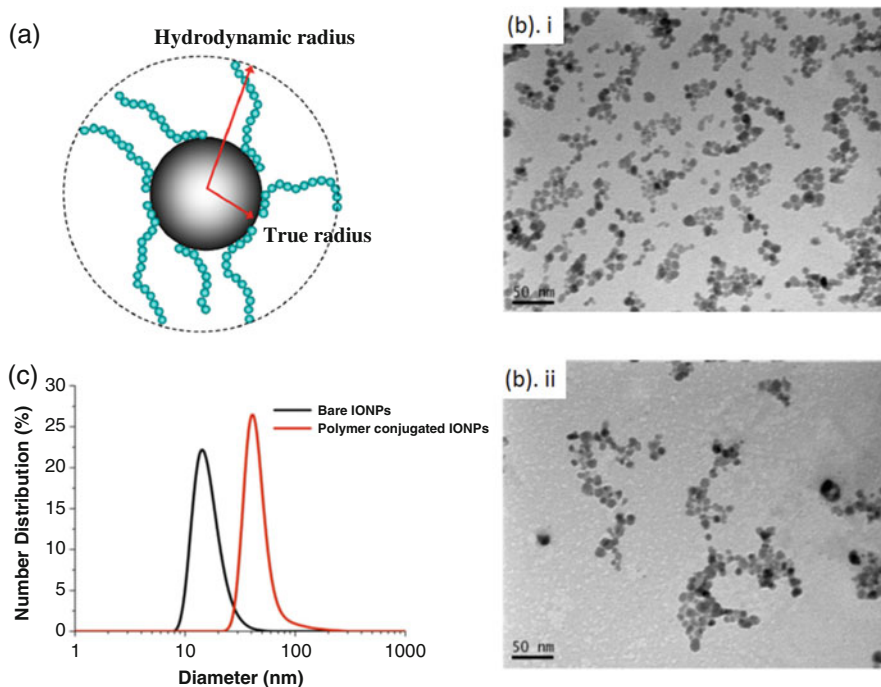


Fig. 3.11 (a) Image indicates hydrodynamic size of a particle (Reprinted from Lim et al. [21]). (b) TEM images of iron oxide nanoparticles (i) before and (ii) after conjugated with polymer. (c) Number-weighted size distribution of the iron oxide nanoparticles measured using DLS. (Reprinted from Nguyen et al. [43])

Apparently, different sample preparation protocols and different working principles have imposed substantial deviation in sizing outcomes from DLS and those from electron microscopy analysis. Proper justification includes discussion on aggregation level and hydration layer, and presence of polymer adlayer must be allocated when comparing sizing results from DLS to TEM and/or SEM.

3.5.2 Role of Particle Concentration

Perhaps, the most frequently asked question among DLS users is regarding the suitable particle concentration for the DLS analysis. In general, there is no standardized particle concentration to be followed in the sample preparation, yet it is undeniable that particle concentration does affect the sizing quality. For instance, sample with too high concentration could induce multiple scattering in which the light scattered by a particle is being re-scattered by neighboring particles (as shown in Fig. 3.12a) before arriving in the detector. Multiple scattering caused the intensity of the detected scattered light to fluctuate more rapidly and thus distorted the

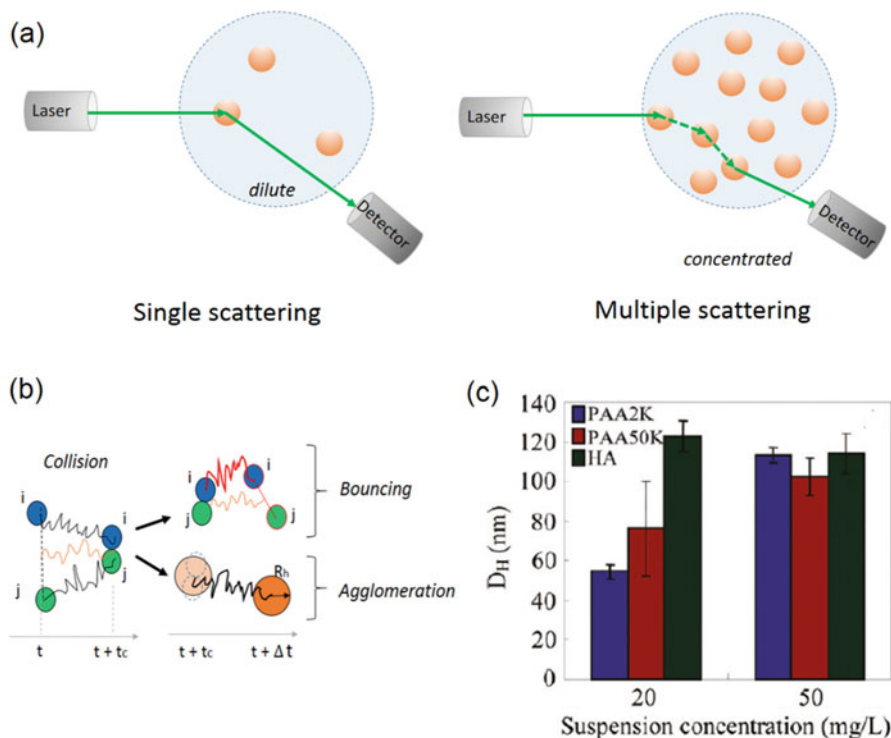


Fig. 3.12 (a) Illustration on single scattering effect occurred in diluted sample, and multiple scattering effects occurred in concentrated sample. (b) Collision of particles occurred due to Brownian motion (zigzag motion). The collision could be resulting in aggregation or bouncing [88]. (c) Effect of particle concentration on hydrodynamic diameter of γ -Fe₂O₃ MNPs surface functionalized with short-chain polyacrylic acid (PAA 2K), long-chain polyacrylic acid (PAA 50K), and humic acid (HA). (Reprinted with permission from Ghosh et al. [80], copyright 2011 American Chemical Society)

measurement outcome to a lower size range [87]. Therefore, sample dilution is normally needed for DLS analysis [65]. It should be noted that over-dilution might cause insufficient light scattered to make a measurement as well.

A more critical impact of particle concentration is on the occurrence of particle-particle interaction. An increase in particle concentration reduces the interparticle distance which subsequently enhances the collision frequency among the particles. Upon collision, the particles might experience aggregation or bouncing (as illustrated in Fig. 3.12b) depending on the balance between both the attractive energies, U_A , and the repulsive energies, U_R . The balance between both types of energies creates an energy barrier, E_{barr} . The E_{barr} is high if U_R is larger than U_A , and E_{barr} is low if U_A is larger than U_R . Aggregation occurred when the relative kinetic energy of collision, E_{kin} , is high enough to overcome the magnitude of E_{barr} [88]. For the case of U_A dominating over U_R , bare MNPs are fond of

aggregation [31, 45]. Moreover, magnetic attraction is stronger as the interparticle distance decreases [80]. Thus, aggregation of MNPs is somehow unavoidable. Phenrat et al. conducted DLS analysis on bare RNIP at two different concentrations (i.e., 2 mg/L and 60 mg/L) and found that the obtained hydrodynamic radius were ~ 100 nm and ~ 400 nm, respectively, due to larger extent of aggregation experienced by the particles at higher concentration (refer Fig. 3.8a) [49]. On the other hand, Ghosh et al. investigated the influence of particle concentration on the hydrodynamic diameter of polyelectrolyte-coated γ -Fe₂O₃ MNPs [80]. As delineated in Fig. 3.12c, γ -Fe₂O₃ surface coated with short-chain polyacrylic acid (PAA 2K) showed a drastic increase in hydrodynamic size (from ~ 60 to ~ 120 nm) when the particle concentration increase from 20 to 50 mg/L. This outcome was ascribed to the weaker stabilization effect of the short-chain PAA which was insufficient to counteract the magnetic attraction. γ -Fe₂O₃ surface coated with long-chain polyacrylic acid (PAA 50K) showed the same increment but to a lesser extent. On the contrary, such effect was not observed for humic acid (HA)-coated γ -Fe₂O₃ MNPs. HA formed a thicker adsorbed layer on the particles and thus much effective in preventing the particles from aggregation at higher particle concentration.

To avoid biases in DLS analysis upon the concentration-dependent effect, it is suggested that the same particle concentration is employed for the analysis in the aim of comparing particle size of two or more independent samples.

3.5.3 Differential Sedimentation During Measurement

A suspended particle will settle out if the sedimentation energy, $(\rho - \rho_o)V_{pt}gh$, is larger than the thermal energy, $k_B T$ [89], where V_{pt} is particle volume, g is acceleration due to gravity, and h is the height of the particle, while ρ and ρ_o are the particle density and the liquid density, respectively. Considering the stationary-state sedimentation velocity of spherical particles described by $v = \frac{2}{9} \frac{R^2(\rho - \rho_o)g}{\eta}$ [89], the corresponding sedimentation time is thus shortened for particles of larger dimension. For instance, given an iron oxide magnetic particle of diameter 10 nm with density 5200 kg/m³ dispersed in water of viscosity 1.002 mPa.s, the estimated time for the particle to settle through a distance of 3 cm is 36,478 h. On the other hand, the estimated settling time shorten to 3.65 h for the same magnetic particle of 1 μ m size. Since the measurement principle of DLS is based on particle diffusion (Brownian motion), occurrence of particle sedimentation (downward motion due to gravity pulling) will affect the measurement outcome. Thus, it is not advisable to employ DLS for sizing particles with size more than a few microns [90].

To avoid/reduce the effect of particle sedimentation, the DLS analysis needs to be done immediately after preparation of the nanoparticle dispersion (normally via ultrasonication). However, it should be noted that prolonging the duration of DLS analysis is needed in some occasions. For instance, in the attempt to assess long-term colloidal stability of the nanoparticle dispersion (Sect. 3.4.2). Here, occurrence

of particle sedimentation over the DLS measurement time is expected for particles of larger sizes. For dispersion consists of wide particle size distribution, the DLS analysis will detect only the smaller particles which remain suspended after the settlement of the larger particles, as illustrated in Fig. 3.13a. Thus, there will be a reduction in Z-average size with the progress in DLS analysis time. From our previous DLS analysis over a duration of 12 h on PSS 70K/Fe₃O₄ MNPs of initial Z-average size 458.7 nm [91], we found that the Z-average size reduced by time and reached 272.7 nm after 12 h (see Fig. 3.13b). The same phenomenon was observed for the particles of initial Z-average sizes 194.2, 245.8, and 309.9, which respectively reduced to 171.9, 191.1, and 258.1 nm after 12 h. Such evidence has indicated the significant contribution of particle sedimentation on the interpretation of DLS data. It is worth to highlight that the occurrence of sedimentation during DLS measurement also can be evidenced from the decrease in count rate [7].

3.6 Summary

The present chapter covers the detailed description on the working principle as well as theoretical background of DLS technique. Discussion was done on how the Z-average, the three types of size distribution (i.e., intensity-weighted distribution, volume-weighted distribution, and number-weighted distribution), and the PDI value are calculated from DLS measurement. Understanding the origin of the DLS data is important in order to avoid misinterpretation. Current applications and potential future applications of DLS in MNPs-based research are also reviewed in this chapter. In particular, besides serving as a common particle sizing technique, DLS offers analytical capability beyond this conventional purpose. For instance, it is useful in the investigation of particle aggregation kinetic, which can be used to describe the extent of particle-particle interactions in fundamental research studies. Furthermore, some innovative uses of DLS (such as *(i)* for detecting size evolution of thermoresponsive particles due to temperature change, *(ii)* as particle concentration determination tools based on the photon count rate, or *(iii)* in-line measurement on a stirring sample) further extend the applicability of DLS in research study. However, it should be noted that hydrodynamic size obtained from DLS should not be directly compared to size obtained from electron microscopy due to the different working principles of both sizing techniques. DLS size is concentration dependent especially for particles that tend to aggregate; thus, we suggest the same particle concentration is prepared for DLS analysis in the aim of comparing particle size of two or more independent samples. In addition, occurrence of differential sedimentation during long-term DLS measurement is possible and thus should be accounted in the interpretation of DLS data. After all, DLS is still a non-imaging type of sizing technique that provides hydrodynamic size and aggregate size of particles; thus, for the aim to reveal morphology and core size of the particles, electron microscopy analysis (such as TEM and/or SEM) needs to be added into the report in conjunction with DLS analysis. Lastly, it is noteworthy to be

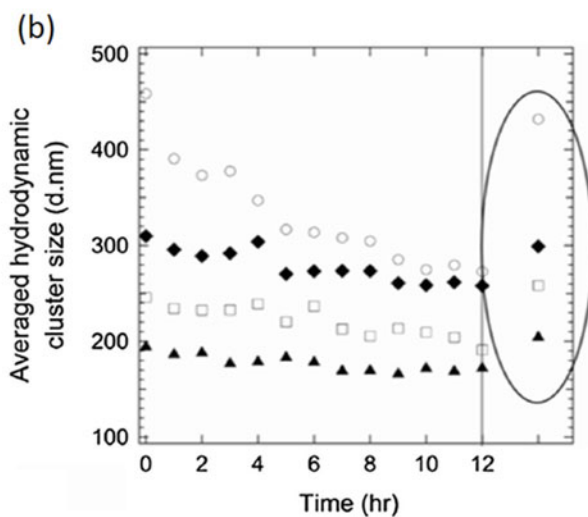
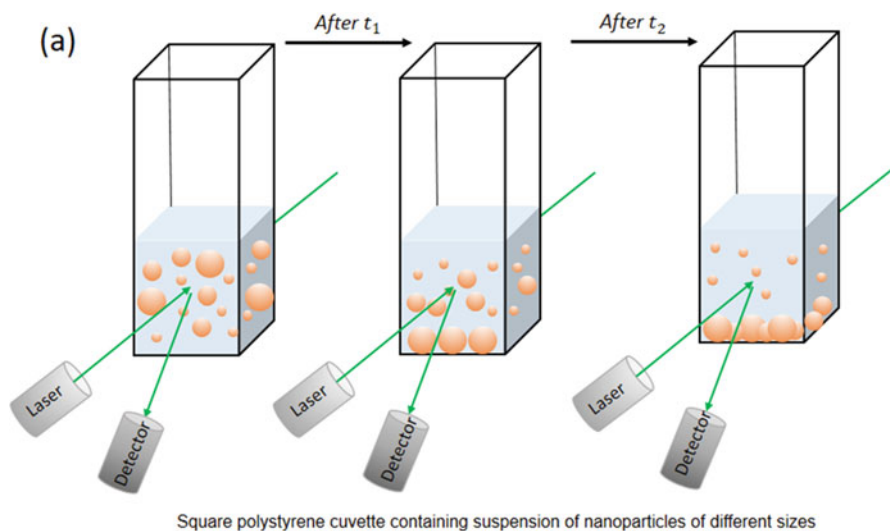


Fig. 3.13 (a) Suspension containing nanoparticles of different sizes under DLS analysis. When time passes, larger particles (which is heavier) precipitate to the cuvette bottom, while the smaller particles remain suspended and being detected by the system. (b) Time lapse DLS measurement on four PSS 70K/Fe₃O₄ MNPs suspensions with different initial average cluster sizes (194.2, 245.8, 309.9, and 458.7 nm) showing reduction in size when time progresses. (Reprinted with permission from Yeap et al. [91], copyright 2015 Springer). The circled data were obtained by gently turning over the cuvette to resuspend the settled particles

reminded that the laser light of the DLS equipment might not be suitable to perform size measurement for all types of material. One of the major limitations of laser light

in DLS is that some fluorescent materials have higher tendency to absorb the light generated by laser (with particular wavelength in the light spectrum) which might significantly alter the light scattering process and subsequently lead to the error in size distribution measurement. Thus, it is crucial to identify the optical property of the material being measured to ensure the accuracy of size distribution measurement by using DLS technique.

References

1. Gong, W., Li, H., Zhao, Z., & Chen, J. (1991). Ultrafine particles of Fe, Co, and Ni ferromagnetic metals. *Journal of Applied Physics*, *69*, 5119–5121.
2. Kolhatkar, A. G., Jamison, A. C., Litvinov, D., Willson, R. C., & Lee, T. R. (2013). Tuning the magnetic properties of nanoparticles. *International Journal of Molecular Sciences*, *14*, 15977–16009.
3. Qu, Y., Yang, H., Yang, N., Fan, Y., Zhu, H., & Zou, G. (2006). The effect of reaction temperature on the particle size, structure and magnetic properties of coprecipitated CoFe₂O₄ nanoparticles. *Materials Letters*, *60*, 3548–3552.
4. Mody Vicky, V., Singh, A., & Wesley, B. (2013). Basics of magnetic nanoparticles for their application in the field of magnetic fluid hyperthermia. *European Journal of Nanomedicine*, *5*, 11–21.
5. Yeap, S. P., Leong, S. S., Ahmad, A. L., Ooi, B. S., & Lim, J. (2014). On size fractionation of iron oxide nanoclusters by low magnetic field gradient. *The Journal of Physical Chemistry C*, *118*, 24042–24054.
6. Alexander, M., & Dalgleish, D. G. (2006). Dynamic light scattering techniques and their applications in food science. *Food Biophysics*, *1*, 2–13.
7. Malvern Instruments. (2013). Zetasizer nano user manual: MAN0485 Issue 1.1.
8. Lim, J. K., Majetich, S. A., & Tilton, R. D. (2009). Stabilization of superparamagnetic iron oxide core-gold shell nanoparticles in high ionic strength media. *Langmuir*, *25*, 13384–13393.
9. Saville, S. L., Woodward, R. C., House, M. J., Tokarev, A., Hammers, J., Qi, B., Shaw, J., Saunders, M., Varsani, R. R., St Pierre, T. G., et al. (2013). The effect of magnetically induced linear aggregates on proton transverse relaxation rates of aqueous suspensions of polymer coated magnetic nanoparticles. *Nanoscale*, *5*, 2152–2163.
10. Majeed, M. I., Lu, Q., Yan, W., Li, Z., Hussain, I., Tahir, M. N., Tremel, W., & Tan, B. (2013). Highly water-soluble magnetic iron oxide (Fe₃O₄) nanoparticles for drug delivery: Enhanced in vitro therapeutic efficacy of doxorubicin and MION conjugates. *Journal of Materials Chemistry B*, *1*, 2874–2884.
11. Huang, X., Bronstein, L. M., Retrum, J., Dufort, C., Tsvetkova, I., Aniagyei, S., Stein, B., Stucky, G., McKenna, B., Remmes, N., et al. (2007). Self-assembled virus-like particles with magnetic cores. *Nano Letters*, *7*, 2407–2416.
12. Toh, P. Y., Ng, B. W., Ahmad, A. L., Chieh, D. C. J., & Lim, J. (2014). Magnetophoretic separation of *Chlorella* sp.: Role of cationic polymer binder. *Process Safety and Environmental Protection*, *92*, 515–521.
13. Kleine, A., Altan, C. L., Yarar, U. E., Sommerdijk, N. A. J. M., Bucak, S., & Holder, S. J. (2014). The polymerisation of oligo(ethylene glycol methyl ether) methacrylate from a multifunctional poly(ethylene imine) derived amide: A stabiliser for the synthesis and dispersion of magnetite nanoparticles. *Polymer Chemistry*, *5*, 524–534.
14. ResearchGate: Research Gate (2015). https://www.researchgate.net/post/Can_anyone_help_with_lognormal_Size_Distribution_and_Multimodal_Size_Distribution_by_Dynamic_Light_Scattering_DLS_measurement. Accessed 3 June 2017. ResearchGate (2015) https://www.researchgate.net/post/Why_does_the_particle_size_differ_in_TEM_and_DLS_measure

- ments. Accessed 3 June 2017. ResearchGate (2014) https://www.researchgate.net/post/Why_am_I_getting_different_measurements_of_particle_size_by_dynamic_light_scattering_laser_diffraction_and_TEM. Accessed 3 June 2017. ResearchGate (2015) https://www.researchgate.net/post/Why_does_dynamic_light_scattering_provide_larger_size_value_than_transmission_electron_microscope. Accessed 3 June 2017. ResearchGate (2014) https://www.researchgate.net/post/What_should_be_reported_as_a_nano_particle_size_Intensity_volume_or_number. Accessed 3 June 2017. ResearchGate (2016) https://www.researchgate.net/post/What_is_the_accurate_value_i_should_use_from_DLS_measurement. Accessed 3 June 2017. ResearchGate (2015) https://www.researchgate.net/post/What_is_the_lowest_particle_number_or_concentration_for_dynamic_light_scattering_to_detect. Accessed 3 June 2017.
15. Goldburg, W. (1999). Dynamic light scattering. *American Journal of Physics*, 67, 1152–1160.
 16. Van de Hulst, H. C. (2012). *Light scattering by small particles*. New York: Dover Publications.
 17. Koppel, D. E. (1972). Analysis of macromolecular polydispersity in intensity correlation spectroscopy: The method of cumulants. *The Journal of Chemical Physics*, 57, 4814–4820.
 18. Pecora, R. (2013). *Dynamic light scattering: Applications of photon correlation spectroscopy*. New York: Plenum Press
 19. Min, G. K., Bevan, M. A., Prieve, D. C., & Patterson, G. D. (2002). Light scattering characterization of polystyrene latex with and without adsorbed polymer. *Colloids and Surfaces A: Physicochemical and Engineering Aspects*, 202, 9–21.
 20. Berne, B. J., & Pecora, R. (2000). *Dynamic light scattering: With applications to chemistry, biology, and physics*. New York: Dover Publications.
 21. Lim, J., Yeap, S. P., Che, H. X., & Low, S. C. (2013). Characterization of magnetic nanoparticle by dynamic light scattering. *Nanoscale Research Letters*, 8, 381.
 22. Yu, G., Durduran, T., Zhou, C., Cheng, R., & Yodh, A. G. (2011). Near-infrared diffuse correlation spectroscopy for assessment of tissue blood flow. In D. A. Boas, C. Pitris, & N. Ramanujam (Eds.), *Handbook of biomedical optics* (pp. 195–216). Boca Raton: CRC Press.
 23. Bird, R. B., Stewart, W. E., & Lightfoot, E. N. (2007). *Transport phenomena*. New York: Wiley.
 24. Ingle, J. D. J., & Crouch, S. R. (1988). *Spectrochemical analysis*. Old Tappan: Prentice Hall College Book Division None.
 25. Hiemenz, P. C., & Rajagopalan, R. (1997). *Principles of colloid and surface chemistry, Third Edition, Revised and Expanded*. New York: Marcel Dekker, Inc.
 26. Chu, B. (1974). *Laser light scattering*. New York: Elsevier Science.
 27. Xu, R., Winnik, M. A., Hallett, F. R., Riess, G., & Croucher, M. D. (1991). Light-scattering study of the association behavior of styrene-ethylene oxide block copolymers in aqueous solution. *Macromolecules*, 24, 87–93.
 28. Nobbmann, U. (2014). Polydispersity – what does it mean for DLS and chromatography? [Online]. Available: <http://www.materials-talks.com/blog/2014/10/23/polydispersity-what-does-it-mean-for-dls-and-chromatography/>.
 29. Nobbmann, U., & Morfesis, A. (2009). Light scattering and nanoparticles. *Materials Today*, 12, 52–54.
 30. Malvern Instruments Ltd. (2009). Intensity-volume-number which size is correct? Malvern Technical Notes.
 31. Phenrat, T., Saleh, N., Sirk, K., Kim, H.-J., Tilton, R. D., & Lowry, G. V. (2008). Stabilization of aqueous nanoscale zerovalent iron dispersions by anionic polyelectrolytes: Adsorbed anionic polyelectrolyte layer properties and their effect on aggregation and sedimentation. *Journal of Nanoparticle Research*, 10, 795–814.
 32. Ditsch, A., Laibinis, P. E., Wang, D. I. C., & Hatton, A. (2005). Controlled clustering and enhanced stability of polymer-coated magnetic nanoparticles. *Langmuir*, 21, 6006–6018.
 33. Zhu, A., Yuan, L., & Dai, S. (2008). Preparation of well-dispersed superparamagnetic iron oxide nanoparticles in aqueous solution with biocompatible N-succinyl-O-carboxymethylchitosan. *The Journal of Physical Chemistry C*, 112, 5432–5438. <https://doi.org/10.1021/jp711319a>.

34. Tang, S. C. N., & Lo, I. M. C. (2013). Magnetic nanoparticles: Essential factors for sustainable environmental applications. *Water Research*, *47*, 2613–2632.
35. Mahdavian, A. R., & Mirrahimi, M. A.-S. (2010). Efficient separation of heavy metal cations by anchoring polyacrylic acid on superparamagnetic magnetite nanoparticles through surface modification. *Chemical Engineering Journal*, *159*, 264–271.
36. Madrakian, T., Afkhami, A., Zadpour, B., & Ahmadi, M. (2015). New synthetic mercaptoethylaminohomopolymer-modified maghemite nanoparticles for effective removal of some heavy metal ions from aqueous solution. *Journal of Industrial and Engineering Chemistry*, *21*, 1160–1166.
37. Chen, Y., Xianyu, Y., Wang, Y., Zhang, X., Cha, R., Sun, J., & Jiang, X. (2015). One-step detection of pathogens and viruses: Combining magnetic relaxation switching and magnetic separation. *ACS Nano*, *9*, 3184–3191.
38. Oberdisse, J. (2007). Adsorption and grafting on colloidal interfaces studied by scattering techniques. *Current Opinion in Colloid & Interface Science*, *12*, 3–8.
39. Van der Beek, G. P., & Cohen Stuart, M. A. (1988). The hydrodynamic thickness of adsorbed polymer layers measured by dynamic light scattering: Effects of polymer concentration and segmental binding strength. *Journal of Physics France*, *49*, 1449–1454.
40. Rümennapp, C., Gleich, B., Mannherz, H. G., & Haase, A. (2015). Detection of molecules and cells using nuclear magnetic resonance with magnetic nanoparticles. *Journal of Magnetism and Magnetic Materials*, *380*, 271–275.
41. Stone, R. C., Qi, B., Trebatoski, D., Jetli, R., Bandera, Y. P., Foulger, S. H., & Mefford, O. T. (2014). A versatile stable platform for multifunctional applications: Synthesis of a nitroDOPA-PEO-alkyne scaffold for iron oxide nanoparticles. *Journal of Materials Chemistry B*, *2*, 4789–4793.
42. Roveimiab, Z., Mahdavian, A. R., Biazar, E., & Heidari, K. S. (2012). Preparation of magnetic chitosan nanocomposite particles and their susceptibility for cellular separation applications. *Journal of Colloid Science and Biotechnology*, *1*, 82–88.
43. Nguyen, T.-K., Duong, H. T. T., Selvanayagam, R., Boyer, C., & Barraud, N. (2015). Iron oxide nanoparticle-mediated hyperthermia stimulates dispersal in bacterial biofilms and enhances antibiotic efficacy. *Scientific Reports*, *5*, 18385.
44. Chai, C. C., Lee, Z. H., Toh, P. Y., Chieh, D. C. J., Ahmad, A. L., & Lim, J. K. (2015). Effects of dissolved organic matter and suspended solids on the magnetophoretic separation of microalgal cells from an aqueous environment. *Chemical Engineering Journal*, *281*, 523–530.
45. Yeap, S. P., Ahmad, A. L., Ooi, B. S., & Lim, J. K. (2012). Electrosteric stabilization and its role in cooperative magnetophoresis of colloidal magnetic nanoparticles. *Langmuir*, *28*, 14878–14891.
46. Choi, Y.-W., Lee, H., Song, Y., & Sohn, D. (2015). Colloidal stability of iron oxide nanoparticles with multivalent polymer surfactants. *Journal of Colloid and Interface Science*, *443*, 8–12.
47. Tiraferri, A., Chen, K. L., Sethi, R., & Elimelech, M. (2008). Reduced aggregation and sedimentation of zero-valent iron nanoparticles in the presence of guar gum. *Journal of Colloid and Interface Science*, *324*, 71–79.
48. Basnet, M., Ghoshal, S., & Tufenkji, N. (2013). Rhamnolipidbiosurfactant and soy protein act as effective stabilizers in the aggregation and transport of palladium-doped zerovalent iron nanoparticles in saturated porous media. *Environmental Science & Technology*, *47*, 13355–13364.
49. Phenrat, T., Saleh, N., Sirk, K., Tilton, R. D., & Lowry, G. V. (2007). Aggregation and sedimentation of aqueous nanoscale zero-valent iron dispersions. *Environmental Science & Technology*, *41*, 284–290.
50. Golas, P. L., Louie, S., Lowry, G. V., Matyjaszewski, K., & Tilton, R. D. (2010). Comparative study of polymeric stabilizers for magnetite nanoparticles using ATRP. *Langmuir*, *26*, 16890–16900.
51. Hu, J.-D., Zevi, Y., Kou, X.-M., Xiao, J., Wang, X.-J., & Jin, Y. (2010). Effect of dissolved organic matter on the stability of magnetite nanoparticles under different pH and ionic strength conditions. *Science of the Total Environment*, *408*, 3477–3489.

52. Yildiz, I., & SizericiYildiz, B. (2015). Applications of thermoresponsive magnetic nanoparticles. *Journal of Nanomaterials*, 2015, 12.
53. Zhao, Q., Chen, N., Zhao, D., & Lu, X. (2013). Thermoresponsive magnetic nanoparticles for seawater desalination. *ACS Applied Materials & Interfaces*, 5, 11453–11461.
54. Cortez-Lemus, N. A., & Licea-Claverie, A. (2016). Poly(N-vinylcaprolactam), a comprehensive review on a thermoresponsive polymer becoming popular. *Progress in Polymer Science*, 53, 1–51.
55. Soeriyadi, A. H., Li, G.-Z., Slavin, S., Jones, M. W., Amos, C. M., Becer, C. R., Whittaker, M. R., Haddleton, D. M., Boyer, C., & Davis, T. P. (2011). Synthesis and modification of thermoresponsive poly(oligo(ethylene glycol) methacrylate) via catalytic chain transfer polymerization and thiol-ene Michael addition. *Polymer Chemistry*, 2, 815–822.
56. Lutz, J.-F. (2008). Polymerization of oligo(ethylene glycol) (meth)acrylates: Toward new generations of smart biocompatible materials. *Journal of Polymer Science Part A: Polymer Chemistry*, 46, 3459–3470.
57. Wang, X., Qiu, X., & Wu, C. (1998). Comparison of the coil-to-globule and the globule-to-coil transitions of a single poly(N-isopropylacrylamide) homopolymer chain in water. *Macromolecules*, 31, 2972–2976.
58. Dong, H., & Matyjaszewski, K. (2010). Thermally responsive P(M(EO)2MA-co-OEOMA) copolymers via AGET ATRP in miniemulsion. *Macromolecules*, 43, 4623–4628.
59. Hoshino, A., Ohnishi, N., Yasuhara, M., Yamamoto, K., & Kondo, A. (2007). Separation of murine neutrophils and macrophages by thermoresponsive magnetic nanoparticles. *Biotechnology Progress*, 23, 1513–1516.
60. Vysotskii, V. V., Uryupina, O. Y., Gusel'nikova, A. V., & Roldugin, V. I. (2009). On the feasibility of determining nanoparticle concentration by the dynamic light scattering method. *Colloid Journal*, 71, 739.
61. Smeraldi, J., Ganesh, R., Safarik, J., & Rosso, D. (2012). Statistical evaluation of photon count rate data for nanoscale particle measurement in wastewaters. *Journal of Environmental Monitoring*, 14, 79–84.
62. Makra, I., Terejanszky, P., & Gyurcsanyi, R. E. (2015). A method based on light scattering to estimate the concentration of virus particles without the need for virus particle standards. *MethodsX*, 2, 91–99.
63. Liu, X., Dai, Q., Austin, L., Coutts, J., Knowles, G., Zou, J., Chen, H., & Huo, Q. (2008). A one-step homogeneous immunoassay for cancer biomarker detection using gold nanoparticle probes coupled with dynamic light scattering. *Journal of the American Chemical Society*, 130, 2780–2782.
64. Shang, J., & Gao, X. (2014). Nanoparticle counting: Towards accurate determination of the molar concentration. *Chemical Society Reviews*, 43, 7267–7278.
65. de Kanter, M., Meyer-Kirschner, J., Viell, J., Mitsos, A., Kather, M., Pich, A., & Janzen, C. (2016). Enabling the measurement of particle sizes in stirred colloidal suspensions by embedding dynamic light scattering into an automated probe head. *Measurement*, 80, 92–98.
66. Particle Matrix: <https://www.particle-matrix.de/en/products/nano-flex-180-dls-size.html#c280>.
67. Kikuchi, J.-I., & Yasuhara, K. (2012). Transmission electron microscopy (TEM). In *Supramolecular chemistry*. Chichester: Wiley
68. Egerton, R. F. (2005). *Physical principles of electron microscopy: An introduction to TEM, SEM, and AEM*. New York: Springer Science & Business Media.
69. de Jonge, N., & Ross, F. M. (2011). Electron microscopy specimens in liquid. *Nature Nanotechnology*, 6, 695–704.
70. Vernon-Parry, K. D. (2000). Scanning electron microscopy: An introduction. *III-Vs Review*, 13, 40–44.
71. Ito, T., Sun, L., Bevan, M. A., & Crooks, R. M. (2004). Comparison of nanoparticle size and electrophoretic mobility measurements using a carbon-nanotube-based coulter counter, dynamic light scattering, transmission electron microscopy, and phase analysis light scattering. *Langmuir*, 20, 6940–6945.

72. Alwan, R. M., Kadhim, Q. A., Sahan, K. M., Ali, R. A., Mahdi, R. J., Kassim, N. A., & Jassim, A. N. (2015). Synthesis of zinc oxide nanoparticles via sol-gel route and their characterization. *Nanoscience and Nanotechnology*, 5, 1–6.
73. Vijayakumar, M., Priya, K., Nancy, F. T., Noorlidah, A., & Ahmed, A. B. A. (2013). Biosynthesis, characterisation and anti-bacterial effect of plant-mediated silver nanoparticles using *Artemisia nilagirica*. *Industrial Crops and Products*, 41, 235–240.
74. Fissan, H., Ristig, S., Kaminski, H., Asbach, C., & Epple, M. (2014). Comparison of different characterization methods for nanoparticle dispersions before and after aerosolization. *Analytical Methods*, 6, 7324–7334.
75. Stadtländer, C. (2007). Scanning electron microscopy and transmission electron microscopy of molluscs: Challenges and opportunities. *Modern Research and Educational Topics in Microscopy*, 1, 122–131.
76. Hall, J. B., Dobrovolskaia, M. A., Patri, A. K., & McNeil, S. E. (2007). Characterization of nanoparticles for therapeutics. *Nanomedicine*, 2, 789–803.
77. Deegan, R. D., Bakajin, O., Dupont, T. F., Huber, G., Nagel, S. R., & Witten, T. A. (1997). Capillary flow as the cause of ring stains from dried liquid drops. *Nature*, 389, 827–829.
78. Michen, B., Geers, C., Vanhecke, D., Endes, C., Rothen-Rutishauser, B., Balog, S., & Petri-Fink, A. (2015). Avoiding drying-artifacts in transmission electron microscopy: Characterizing the size and colloidal state of nanoparticles. *Scientific Reports*, 5, 9793.
79. Kadar, E., Batalha, Í. L., Fisher, A., & Roque, A. C. A. (2014). The interaction of polymer-coated magnetic nanoparticles with seawater. *Science of the Total Environment*, 487, 771–777.
80. Ghosh, S., Jiang, W., McClements, J. D., & Xing, B. (2011). Colloidal stability of magnetic iron oxide nanoparticles: Influence of natural organic matter and synthetic polyelectrolytes. *Langmuir*, 27, 8036–8043.
81. Liu, X. L., Choo, E. S. G., Ahmed, A. S., Zhao, L. Y., Yang, Y., Ramanujan, R. V., Xue, J. M., Fan, D. D., Fan, H. M., & Ding, J. (2014). Magnetic nanoparticle-loaded polymer nanospheres as magnetic hyperthermia agents. *Journal of Materials Chemistry B*, 2, 120–128.
82. Shanmuga, S., Singhal, M., & Sen, S. (2015). Synthesis and characterization of carrageenan coated Ma. *Translational Biomedicine*, 6.
83. Michler, G. H. (2008). *Electron microscopy of polymers*. Heidelberg: Springer.
84. Yu, W. W., Chang, E., Falkner, J. C., Zhang, J., Al-Somali, A. M., Sayes, C. M., Johns, J., Drezek, R., & Colvin, V. L. (2007). Forming biocompatible and nonaggregated nanocrystals in water using amphiphilic polymers. *Journal of the American Chemical Society*, 129, 2871–2879.
85. Lee, S., Kim, K., Shon, H. K., Kim, S. D., & Cho, J. (2011). Biototoxicity of nanoparticles: Effect of natural organic matter. *Journal of Nanoparticle Research*, 13, 3051–3061.
86. Bootz, A., Vogel, V., Schubert, D., & Kreuter, J. (2004). Comparison of scanning electron microscopy, dynamic light scattering and analytical ultracentrifugation for the sizing of poly(butyl cyanoacrylate) nanoparticles. *European Journal of Pharmaceutics and Biopharmaceutics*, 57, 369–375.
87. Lu, R. (2016). *Light scattering technology for food property, quality and safety assessment*. Boca Raton: CRC Press.
88. Henry, C., Minier, J.-P., Pozorski, J., & Lefèvre, G. (2013). A new stochastic approach for the simulation of agglomeration between colloidal particles. *Langmuir*, 29, 13694–13707.
89. Yeap, S. P., Toh, P. Y., Ahmad, A. L., Low, S. C., Majetich, S. A., & Lim, J. (2012). Colloidal stability and magnetophoresis of gold-coated iron oxide nanorods in biological media. *Journal of Physical Chemistry C*, 116, 22561–22569.
90. Hassan, P. A., Rana, S., & Verma, G. (2015). Making sense of Brownian motion: Colloid characterization by dynamic light scattering. *Langmuir*, 31(1), 3–12.
91. Yeap, S. P., Ahmad, A. L., Ooi, B. S., & Lim, J. (2015). Manipulating cluster size of polyanion-stabilized Fe₃O₄ magnetic nanoparticle clusters via electrostatic-mediated assembly for tunable magnetophoresis behavior. *Journal of Nanoparticle Research*, 17, 1–22.

Chapter 4

Scanning Electron Microscopy: Principle and Applications in Nanomaterials Characterization



**Kalsoom Akhtar, Shahid Ali Khan, Sher Bahadar Khan,
and Abdullah M. Asiri**

4.1 Introduction

The human eyes have some limit and are able to resolve two points that are 0.2 mm apart from each other, called as the resolution power of the human eye. However, by the addition of lens or group of lenses (aided eye), the human eye is enabled for high resolution and can resolve the two dots that are closer than 0.1–0.2 mm from each other. Anything below 0.1–0.2 mm requires some sort of magnification; therefore, to overcome these limitations of human eyesight, the microscope was developed and used as an efficient magnifying tool. Microscope has a much higher resolution and has been used as a powerful tool for studying and characterizing a wide range of materials.

The microscope resolving power not only depends on the quality and number of the lenses used, but also the light wavelength or source to produce image is highly considered. Therefore, microscope can be divided into two categories on the basis

K. Akhtar
Division of Nano Sciences and Department of Chemistry, Ewha Womans University, Seoul,
South Korea

S. A. Khan
Department of Chemistry, University of Swabi, Anbar-23561, Khyber Pakhtunkhwa, Pakistan
Center of Excellence for Advanced Materials Research, King Abdulaziz University, Jeddah,
Saudi Arabia

Chemistry Department, Faculty of Science, King Abdulaziz University, Jeddah, Saudi Arabia

S. B. Khan (✉) · A. M. Asiri
Center of Excellence for Advanced Materials Research, King Abdulaziz University, Jeddah,
Saudi Arabia

Chemistry Department, Faculty of Science, King Abdulaziz University, Jeddah, Saudi Arabia
e-mail: sbkhan@kau.edu.sa

of source to produce image, i.e. optical or light microscope (OM) and electron microscope (EM). Both OM and EM have the same working principle, but the major difference is the source, i.e. OM uses visible light as a source while EM uses focused accelerated electrons beam. Surface investigation of the materials can be achieved through both microscopes. However, the resolution of optical microscope is very limited by diffraction properties. Instead, a much higher resolution data can be attained by using one of the electron microscopic methods. Because electrons have shorter wavelength than visible light and thus are more energetic than visible light photon, a beam of highly accelerated electrons are focused on the surface of materials, thus creating the image. EM is an imaging tool with much better imaging resolution as compared to OM.

The use of the accelerated electrons beam in EM featured by short wavelength causes the diffraction effects to occur at much smaller physical dimension, which in turn helps resolve atomic features ranging from nanometre to micrometre particle size. In the case of EM, focused accelerated electrons are used to see through the sample and scan materials on a fine and very small scale. As a result, it gives images of higher magnification with better resolution. The main reason for the development of electron microscopes was the precincts and limitation of OM. Two main types of EM are available, scanning electron microscope (SEM) and transmission electron microscope (TEM) [1, 2]. The first EM, i.e. TEM, was invented in 1931 by Knoll and Ruska in Germany, and ever since it was considered as a valuable instrument that has been used to understand scientific phenomena in diverse fields, such as nanotechnology, science, medicine and many others [1, 2]. The SEM was first introduced in 1938 (Von Ardenne), and in 1965 the first SEM instrument came into market.

4.2 Comparison Between Optical Microscope and Electron Microscope

Optical microscope (OM) and electron microscope (EM) are analogous in many ways; however, they also show differences. Both types of microscopes exhibit certain similarities as follows:

- (i) EM and OM are identical both fundamentally and functionally.
- (ii) Magnify those objects which normally cannot be seen to the naked eyes.
- (iii) Present similar component terminology and overall design.
- (iv) Contain a source of illumination and condenser lens system which direct parallel radiation onto the specimen.
- (v) Contain a series of imaging lenses which form the image of the specimen.

In addition, the EM and OM also show dissimilarities:

- (i) Illumination beams are different; the EM uses very energetic electrons as a source instead of visible light used in the OM, i.e. a lamp produces the light

beam (including UV rays) in the OM while an electron gun produces electron beam in EM.

- (ii) Optical lens in OM while electron lens (magnetic or electrostatic) in EM.
- (iii) Accelerated electrons used in EM have very short wavelength ($0.859\text{--}0.037\text{ \AA}$, $20\text{--}100\text{ kV}$) and thus give a high resolution which is the limitation of OM ($\lambda = 7500\text{--}2000\text{ \AA}$) and thus make it possible to see very small features.
- (iv) EM needs high vacuum while OM can operate in any atmosphere.
- (v) EM has a capability of higher magnification ($90\text{--}800,000\times$) which can be varied continuously as compared to OM ($10\text{--}2000\times$) which can be varied by exchange of lenses.
- (vi) EM has higher resolving power (point to point: 3 \AA , lattice: 1.4 \AA), while OM has lower resolution (visible: 3000 \AA , UV: 1000 \AA).
- (vii) EM has a larger depth of field and has better depth of focus than OM, making EM suitable for studying rough surfaces.
- (viii) Focusing can be done electrically in EM while it is mechanically by OM. Thus, EM has higher magnification and lower depth of focus.
- (ix) In an EM, the contrast is either by scattering absorption (SEM) or diffraction (TEM); while in an OM, it is by either absorption or reflection.
- (x) EM gives information about composition and crystallography which are not possible by OM. Similarly, SEM and TEM are both electron microscopes but still have certain differences.

4.3 Difference Between SEM and TEM

There are certain differences between a scanning electron microscope (SEM) and transmission electron microscope (TEM), which are given as below:

- (i) SEM detects scattered electrons emitted from the surface of the sample, while TEM detects transmitted electrons.
- (ii) SEM provides information about surface morphology and composition of materials while TEM gives details about internal composition of materials. Thus, TEM can illustrate several characters of a material (morphology, crystallization, stress or even magnetic domains).
- (iii) Both need electrically conductive materials to be tested. Non-conductive materials should be coated with a conductive layer of metal or carbon.
- (iv) The accelerated voltage ranges from $10\text{ to }40\text{ kV}$ for the SEM, while for TEM, it is $>100\text{ kV}$.
- (v) SEM requires a very easy preparation technique, while TEM needs skill to prepare a very thin sample. The thickness of the specimen is not important in SEM, while specimen thickness is very important in TEM. The thickness of the specimens to be examined under TEM should be less than 100 nm . SEM is a better tool for surface characterization as compared to TEM which is better for internal structure analysis.

- (vi) The resolution is much higher in TEM as compared to SEM.
- (vii) TEM is used for high magnification compared to SEM.
- (viii) In the case of SEM, the electron beam scans over the surface of the sample, while in the case of TEM, the electron beam passes through the sample.
- (ix) SEM has a comparatively low resolution than TEM, while TEM has high resolution.
- (x) SEM has a high depth of field, while TEM has moderate.
- (xi) SEM has lower magnifying power, while TEM has high magnifying power.
- (xii) In SEM, the specimen contrast is by electron absorption, while it is by electron scattering in TEM.
- (xiii) SEM produces three-dimensional black and white images, while TEM produces two-dimensional black and white images.

4.4 Scanning Electron Microscope (SEM)

SEM is a versatile advanced instrument which is largely employed to observe the surface phenomena of the materials. The sample is shot in a SEM using high-energy electron, and the outcoming electrons/X-rays are analysed. These outcoming electrons/X-rays give information about topography, morphology, composition, orientation of grains, crystallographic information, etc. of a material. Morphology indicates the shape and size, while topography indicates the surface features of an object or “how it looks”, its texture, smoothness or roughness. Likewise, composition means elements and compounds that constitute the material, while crystallography means the arrangement of atoms in the materials. SEM is the leading apparatus that is capable of achieving a detailed visual image of a particle with high-quality and spatial resolution of 1 nm [3–5]. Magnifications of this kind of apparatus can extend up to 300,000 times. Although SEM is used just to visualize surface images of a material and does not give any internal information [2], it is still considered as a powerful instrument that can be used in characterizing crystallographic, magnetic and electrical features of the sample and in determining if any morphological changes of the particle has occurred after modifying the sample surface with other molecules [3].

SEM is able to provide several qualitative information of the specimen including its topography, morphology, composition and crystallographic information. In other words, it provides information about the surface features and texture, shape, size and arrangement of the particles lying on the sample’s surface. The type of elements and compounds the sample consists of and their relative ratios as well as the arrangement of atoms in the single crystal particles and their degree of order can also be provided [2, 6]. Thus, SEM is a multipurpose instrument which is able to examine and analyse the materials with high resolution.

4.5 Importance of Electron Beam in SEM

Let's suppose two objects are there that can be easily recognized as separate objects if they are separate and far away from each other. Let's take two Airy discs having a small spot surrounded by halos, and the radius of the halo is $1.22 F\lambda/d$ (see Fig. 4.1). If they are close in such a way where the maximum of the first Airy disc coincides with the first minimum of the second Airy disc, the separation between the two peaks is $1.22 F\lambda/d$. The images are too close and overlap but still can be distinguished where the human eye can still see the two separate points. Then a limit point is reached where lesser separation would result in formation of a continuous blur and this limit is referred to as the Rayleigh criterion. The Rayleigh criterion for the resolution of an optical system states that two points can be resolved if the maximum of the intensity of the Airy disc from one of them coincides with the first minimum intensity of the Airy disc of the other [7]. According to Abbe the minimum resolvable separation d_0 or resolution ρ (the resolving power) is given by:

$$d_0 = \rho = 1.22\lambda/2 (n \sin \alpha) = 0.61\lambda / (n \sin \alpha) = 0.61\lambda/NA \quad (4.1)$$

where λ is the wavelength, n is the refractive index and α is the semiangle of the specimen; $NA = n \sin \alpha$ is the numerical aperture. According to Eq. (4.1), the resolving power will be limited by several factors, and λ is the most important factor if we want to raise resolving power.

According to de Broglie, λ of electrons is determined by the accelerating voltage on the filament from which they are emitted. A moving electron has a dual character as a moving charged particle or as a radiation with associated wavelength, and λ of an electron is inversely proportional to the momentum $p = mv$ of the electron by:

$$\lambda \propto 1/p$$

$$\lambda = h/p$$

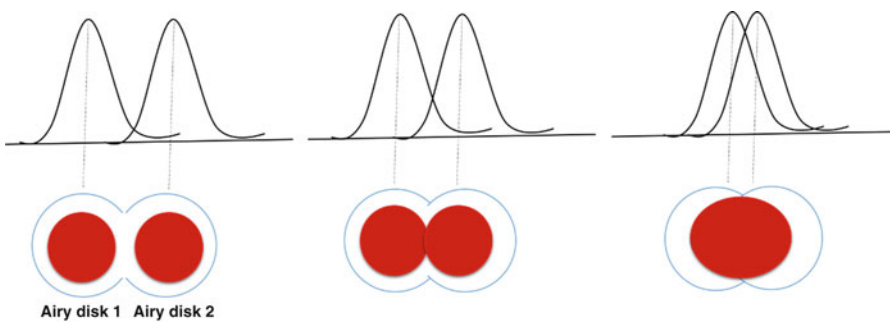


Fig. 4.1 Airy patterns and Rayleigh criterion

$$\lambda = h/mv$$

where λ is the de Broglie wavelength of the electrons, h Planck constant, m mass of electron and v velocity of the electron. So, if electron beam is used as a source, the wavelength will be very short and can be calculated by the following relation:

$$\lambda = 1.22 / (v) \frac{1}{2}$$

Therefore, electron beam as an illuminate is important for high resolution. Basically, SEM is utilized to image the sample surface through detecting different signals generated from the impact of focused highly energetic electrons (primary electrons) at the sample surface [5]. These electrons have very short wavelength (λ) which can vary as per the applied high voltage.

4.6 Fundamental Principles of SEM

SEM has a specific sample holder where the stub should be fixed containing the sample on the surface. Generally, carbon tap is used for sticking the sample to the stub. First two-sided carbon tap should fix on the stub and then a thin layer or a small amount of material will be placed on the carbon tap because the thin layer properly sticks with the carbon tap which reduces the charging problem and help in getting a good image. Some requirements are needed when operating SEM analysis. Additionally, when using SEM, the samples have to be electrically conductive to avoid overcharging on the surface. This overcharging may introduce extreme brightness and poor images. Thus, non-conductive samples like polymers are usually sputter coated [4] with a thin layer of carbon [1] or metal that readily reflects electrons and provides a conductive surface for electrons, e.g. gold and platinum [2, 8]. The non-conductive materials must be sputtered in order to reduce the charging problem. After that the sample-covering stub will be fixed in the sample holder and should be put in the sample-holding chamber or specimen chamber. In contrast to TEM, relatively thick samples can be examined by scanning electron microscopy.

The SEM instrument is based on the principle that the primary electrons released from the source provide energy to the atomic electrons of the specimen which can then release as the secondary electrons (SEs) and an image can be formed by collecting these secondary electrons from each point of the specimen, the basic requirement for SEM to operate under a vacuum to avoid interactions of electrons with gas molecules in order to obtain high resolution. In addition, the primary electrons produced and emitted from the electron gun are accelerated by heating or applying high energy in the range of 1–40 keV [2, 4]. These emitted electrons are focused and confined to a monochromatic beam (to a diameter of 100 nm or less)

by magnetic field lenses and metal slits within a vacuumed column. The confined primary electrons are scanned across the sample surface by scanning coils in a raster pattern [1, 2]. Once the primary electron beam hits the sample surface, it will interact with the near-surface area of the sample to a certain depth in many different ways [4]. The impinging electrons accelerated towards the specimens have substantial quantities of kinetic energy, which lose their energy inside the sample by generating several signals from the interactions of electrons with specimen. It scattered both elastically and inelastically in the sample.

The scattering of electrons and interaction volume depends on the atomic number, concentration of atoms of the analysed sample and the incoming electron energy (accelerating voltage). Increasing the electron energy (accelerating voltage) will increase the interaction volume and scattering process, and if the concentration of atoms and atomic number of the element is high, then the interaction volume and scattering will be low. Similarly, angle of incidence of the electron beam also play an important role in the interaction volume and scattering process. Thus the angle of incidence of the electron beam, atomic number of the material under examination and accelerating voltage are the main factors for the volume inside the specimen in which interactions occur. The materials having higher atomic number absorb or stop more electrons and will thus generate smaller interaction volume. Similarly, if high voltages are applied, it will generate electrons with high energy and will thus penetrate farther into the sample and generate a larger interaction volume. Similarly, the greater the angle of incidence (further from normal), the smaller will be the interaction volume.

In consequence, it will emit a variety of signals due to Coulomb (electric charge) field interaction of incoming electrons with specimen nucleus and electrons, such as secondary electrons (SEs), backscattered electrons (BSEs), photons (X-rays used for elemental analysis) and visible light (cathodoluminescence – CL) [1, 8]. The signals are gathered by electron collectors (detectors), which are then manipulated by the computer to form the required image. According to the detected signal (secondary electrons, backscattered electrons or X-rays), different information about the sample could be observed [2]. The two routinely used electrons for sample image creation are the backscattered and secondary electrons. However, secondary electrons are considered the most important electrons, indicating sample morphology and topography, while backscattered electrons are used for demonstrating the contrasts in multiphase samples composition (i.e. for prompt phase judgement). Similarly, X-rays are generated by the inflexible impacts of the incident electrons with the electrons available in the orbitals of sample atoms. After this the electrons are excited to the higher energy levels; when it comes back to the lower energy levels, it emits X-rays, having a specified wavelength, depending on the difference in energy level of various elements. In this way each element generated a characteristic X-ray after the impinging of electrons beam. SEM is non-destructive, as the generation of X-rays does not lead to any loss in the volume of the specimen; therefore, one can repeatedly analyse the same material (Fig. 4.2).

Generally, there are two types of interaction such as inelastic interaction and elastic interaction. Inelastic interactions are those in which interaction takes place

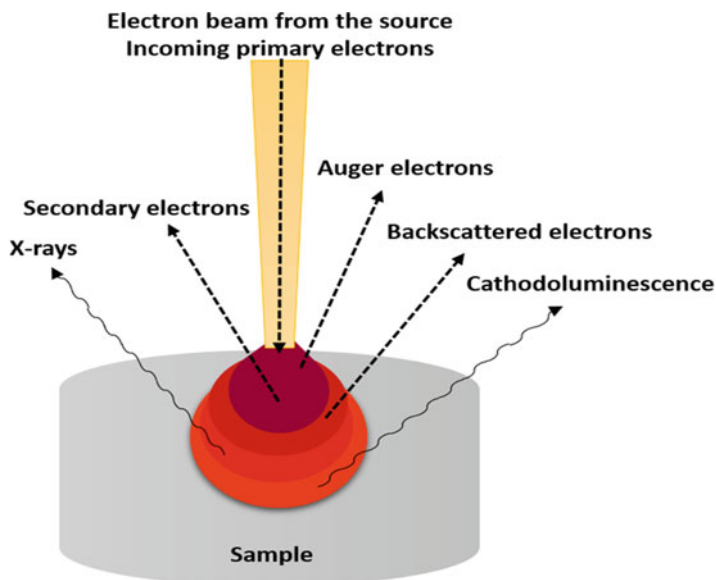


Fig. 4.2 The interaction of electron beam with specimen and the signal emitted from the sample

between the beam electron and electric field of a specimen atom electron, where transfer of energy from the beam electron to the specimen atom takes place which results in potential ejection of an electron from that atom as SEs have usually energy less than 50 eV. The vacancy created by the emission of a secondary electron is filled from a higher-level orbital, and an X-ray characteristic of that energy transition is produced [8].

Elastic interactions are those interactions that take place between the primary electrons and electric field of the nucleus of a specimen atom, and due to these interactions, the direction of the primary electrons changes without a significant change in the energy of the primary electron (<1 eV) [9]. If these elastically scattered electrons deflect back out of the specimen, these electrons are called BSEs, having energy from 50 eV \sim to energy almost equal to the incident beam electrons. Usually, mainly BSEs maintain a minimum of 50% of the incident beam energy. Thus, the beam electron distributes due to these elastic and inelastic interactions over a three-dimensional “interaction volume”. Secondary and backscattered electrons escape from different depths of the sample, and therefore their energy remains different. SEs generally escape from the depth of approximately 5–50 nm, while BSEs escape from a depth of several times greater than the depth of SEs, and X-rays greater yet [9]. Thus, greater escape depths generally translate to wider lateral dimension from which the signal can generate and thus lower potential resolutions, but the real size and shape of the interaction volume depend upon accelerating voltage, atomic number and tilt.

4.6.1 Accelerating Voltage

The accelerating voltages control the dimensions of the interaction volume. The increase in accelerating voltage helps in increasing the size of interaction volume. The increase in beam energy reduces the energy loss rate in the specimen, and as a result the beam electrons enter deeply into the specimen. Moreover, if the elastic scattering is less, the beam paths close to the specimen surface become straight and the beam electrons enter more deeply [9]. Ultimately, several elastic scattering collectively push some electrons back towards the surface of the specimen and as a result increasing the interaction volume.

4.6.2 Atomic Number

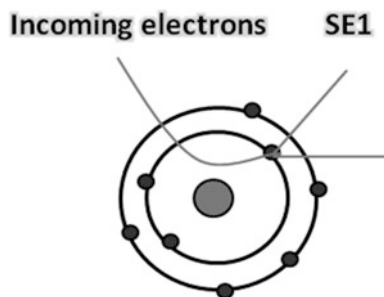
Atomic number is another factor which affects the interaction volume. The higher the atomic number of the elements, the lower will be the interaction volume, because if the atomic number is higher, the rate of energy loss of the electron beam will be higher, and as a result electrons will not penetrate deeply into the specimen. Also, the probability for elastic scattering and the average scattering angle increase with atomic number – causing the interaction volume to widen [8].

4.6.3 Tilt

After tilting the sample, the incident beam electrons move along greater distances in the region near the surface. Due to this occurrence more SEs are produced in this area as compared to areas which are normal to the beam, and these SE signal-produced images reveal the so-called edge effect. Edges and ridges of the sample due to emission of more SEs look brighter in the image.

Secondary electrons are stated as the electrons that escaped from the sample surface (only electrons ~ 10 nm near to the surface) when some of the energy (~ 5 eV) is transferred from the primary electrons to the specimen electrons, mostly in the K-shell. These electrons can be used to image the topography and morphology of the sample [1, 2]. After striking the electrons on the surface of the material emerging from the primary electron probe, electrons emit from the materials surface; these electrons are called secondary electrons. These secondary electrons are set free to the detector, where it forms the surface image of the materials. The secondary electrons interact with the surface of the materials by creating a different signal, providing the information about the morphology and composition of the materials. Secondary electrons and backscattered electrons are usually utilized for material imaging: secondary electrons are mainly important

Fig. 4.3 The secondary electrons (SE1) emitted from the sample



for screening morphology and topography of materials [1–11]. Thus, secondary electrons are those which are generated by:

- (i) Collision among the primary electrons and the weakly bonded outer electrons.
- (ii) These are low energy electrons (less than 50 eV but mostly in the range of 2–5 eV).
- (iii) SEs are produced near the surface and thus give information about topography.
- (iv) The number of SEs remains higher as compared to the number of incoming electrons.
- (v) SE coefficient (δ) which is the ratio of the number of SE to the number of primary electrons which strike the specimen is comparatively insensitive to atomic number.
- (vi) SE coefficient (δ) increases with decrease in beam energy (accelerating voltage) which is due to the decrease in interaction volume.
- (vii) SEs have very low escape depth because of their low energies.

Secondary electrons (SEs) are produced by two mechanisms and can be further differentiated as SE1 and SE2:

SE1 are those secondary electrons which are produced by the primary electron beam. Once the primary electrons enter the surface of materials, some of the energy is transferred to the specimen electrons and gives high-resolution signal limited by the electron beam diameter (Fig. 4.3).

SE2 are those secondary electrons which are produced by those electrons that first undergo several inelastic scatterings and then come to the surface. SE2 generate from a surface area greater than the incoming electrons' spot. SE1 resolution remains stronger than for SE2. Electron beam energy, electron beam current, atomic number, local curvature of the surface and work function of the surface are the factors which disturb and affect SE emission. Higher atomic number creates more SE2. The effect of atomic number is much more prominent at lower beam energies [9] (Fig. 4.4).

Backscattered electrons (BSEs) are referred as primary electrons that are reflected back from the atoms surface. The energy of BSEs differs according to the atoms density from which these electrons are reflected. Therefore, they are used in visualizing the contrast variation in surface composition, showing brighter images for atoms with higher atomic number. If the scattered electrons maintained

Fig. 4.4 The secondary electrons (SE2) emitted from the sample

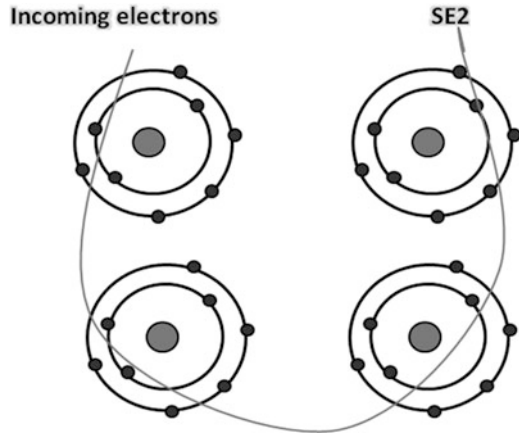
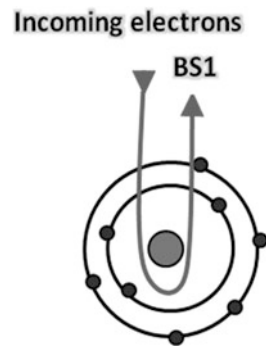


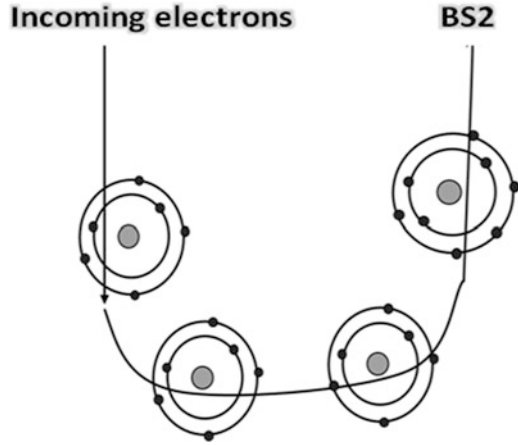
Fig. 4.5 The backscattered electrons (BS1) emitted from the sample



their energy, they are called elastic scattered electrons. These electrons are useful in getting information about orientation and arrangement of atoms. Transmitted electrons are stated when the primary electrons pass through the sample without interacting with their atoms. They are used to develop an image of thin samples. Backscattered electrons are mainly important for showing discrimination of phases and composition of any multiphase samples. BSEs are the incident electrons which are repelled and escaped from the surface by the electromagnetic field of the nucleus. These are elastically scattered high-energy electrons which are less than SEs [9] (Fig. 4.5).

Backscatter coefficient (η) which is the ratio of the number of BSEs to the number of primary electrons that strike the specimen is sensitive to atomic number. It increases with increase in atomic number. Materials possessing higher atomic number elements discharge more backscatter signal and thus appear brighter in the image. Accelerating voltage has less effect on η and slightly changes it. η increases in case of tilted surface but in a direction away from the incident beam. With no tilt, η follows a distribution that approximates a cosine expression. What this means is that the maximum number of backscattered electrons travel back along the incident beam [9] (Fig. 4.6).

Fig. 4.6 The backscattered electrons (BS2) emitted from the sample



Other interactions such as Auger electrons and X-rays occur to release the excess energy gained after hitting and exciting the atoms with incident beam. Auger electrons can be used in chemical analysis, while X-rays are used in energy-dispersive X-ray (EDX) analysis to identify the elements and their concentrations in the sample [1]. X-rays are generated by inelastic interaction of the incident electrons with electrons in discrete orbitals (shells). These are photons, not electrons. Each element has its own special X-ray signal *fingerprint*.

4.7 Instrumentation

SEM is an electronic and optical system which consists of the following components:

- (i) Electron gun
- (ii) Vacuum
- (iii) Column: condenser lens, scanning coil, objective lens, stigmator, sample holder and detector

In principle, first the gun emits the electron beam which is held within a vacuum which follows a vertical travel path through electromagnetic fields and lenses. The electron beam is focussed by objective lens on the specimen. Then the focussed beam scans over a specific area of the specimen surface where the focussed beam is rastered across the surface of the materials with help of deflector coils, which is controlled by the scan generator. Magnification controls the size of the rastering pattern. The changes in magnification change the size of the rastered area on the sample. When the electron beam hits the material, this strike produces a huge number of signals, i.e. electrons and X-rays are emitted from the specimen. These signals are detected by the detector (depending on the

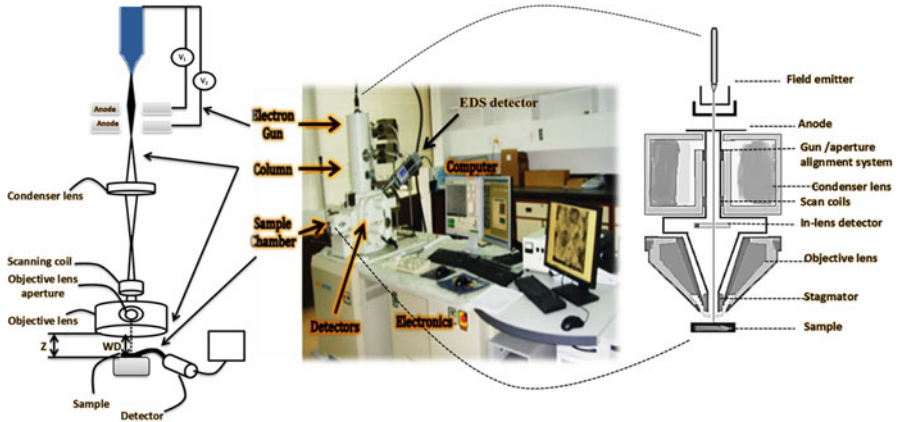


Fig. 4.7 The external and internal configuration of FESEM

type of detector) and converted to signals where images are produced from the signals. The signal that originates from electron-sample interaction gives detailed information about the material such as external morphology (texture), chemical composition and crystalline structure and orientation of materials making up the sample. The scanning electron microscope has several advantages because it has a big profundity of field which permits to focus more specimens at one time. The SEM also has much superior resolution, so narrowly spaced specimens can be magnified at many advanced levels. The bigger advantage of SEM is that it provides the researcher much more control in the degree of magnification as lenses are replaced by electromagnets. The permutation of enhanced magnification, bigger depth of focus, superior resolution and ease of sample surveillance make the SEM one of the most profoundly used instruments in research areas nowadays [1–11] (Fig. 4.7).

4.7.1 *Electron Gun*

Electron gun provides the electron beam whose energy can vary as per need of material to get an image with the best resolution with minimum sample charging and damage. The function of the electron gun is to provide a large and stable current in a small beam. The electron gun or emission source is of two types, i.e. thermionic emitter and field emitter [11]. The main difference between SEM and FESEM is the type of emitter, i.e. thermionic emitter is used in SEM while field emitter is the electron gun utilized in FESEM.

4.7.1.1 Thermionic Emitters

In this case, a filament made up of tungsten (W) and lanthanum hexaboride (LaB_6) is heated up using electrical current. When the heat is enough to overcome the work function of the filament material, the electrons escape from the material itself. Thermionic sources have relatively low brightness, evaporation of cathode material and thermal drift during operation [11]. The source of electron is a tungsten filament with diameter of about 0.1 mm and electrically heated to about 2700 K. The Wehnelt cylinder is potentially more negative than the filament and helps to emit the electron from one point. This point is also called crossover, and the Wehnelt cylinder helps to control the diameter of crossover and also control the number of emitting electrons. Lanthanum or cerium hexaboride are high brightness electron sources, but higher vacuum is required. To produce vacuum in the chamber, a vane-type rotary pump and a turbo molecular pump are used to produce a vacuum of 10^{-5} mbar.

4.7.1.2 Field Emitters

Field emission gun (FEG) generates electrons without heating and thus avoids the heating problem. Therefore, FEG is also called a cold cathode field emitter. In FEG, a wire of tungsten with a sharp point (tip, radius = less than 100 nm) is used as filament where the emission of electron takes place by employing the filament in a huge electrical potential gradient. The significance of the small tip radius (~ 100 nm) is that an electric field can be concentrated to an extreme level, becoming so big that the work function of the material is lowered and electrons can leave the cathode [11]. Field emission electron microscope (FESEM) thus introduced a different electron gun design. In this technology, field emission cathode releases the electrons by applying a high electric field near the filament tip. The speed with which the electrons are ejected from the electron reservoir in the filament is organized by the degree and proximity of the electric field to the reservoir. This technology can tolerate high current and offer higher stability by producing finer beams with emission $1000\times$ the emission of a traditional tungsten wire. This design required considerably higher vacuum conditions. As a result, an improved spatial resolution and minimal sample charging is provided. Therefore, FESEM offers high performance, i.e. high resolution which means large probe current and small diameter electron probes over a wide energy range (1–30 keV).

FESEM uses a field emission gun to produce a cleaner image, less electrostatic distortions and spatial resolution <2 nm (that means three or six times better than SEM). The FESEM has two anodes for electrostatic focusing. A voltage (0–5 kV) between the field emission tip and the first anode (anode 1), called the extraction voltage, controls the current emission (1–20 μA). The potential difference V_1 which are applied between anode 1 and emission tip generated an electric field which results in the emission of electrons (emission current). The velocity at which the electrons move into the column is determined by the beam energy. A voltage (1–30 kV), called the accelerating voltage (V_0), when applied between the cathode and

the second anode (anode 2) increases the beam energy. The higher the V_0 , the faster the electrons travel down the column and the higher the penetrating power. This voltage combined with the beam diameter determines the resolution (capacity to resolves two closely spaced point as two separates entities), which increases with increase in voltage [11].

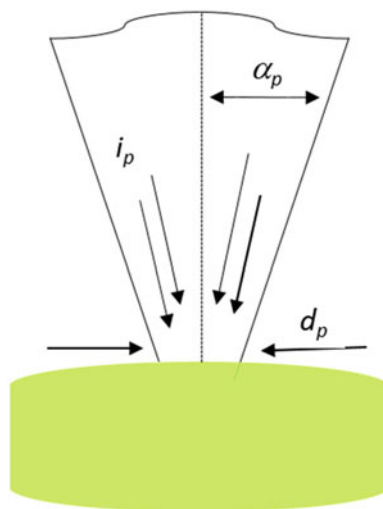
In FESEM, electrons are emitted from the field emission cathode by applying a high electric field near the filament tip. The degree to which electrons are expelled out of the electron reservoir in the filament is controlled by the magnitude and proximity of the electric field to the reservoir. Even though this design required considerably higher vacuum conditions [1], it has greater stability, can tolerate higher current and hence produces finer beams [5] with $1000\times$ the emission of a traditional tungsten wire [1]. As a result, an improved spatial resolution and minimal sample charging is provided [5]. There are different types of FEGs such as cold FEG (JEOL 6700) and thermally assisted FEG (JEOL 6500). In the cold FEG, the electric field produced by the extraction voltage lowers the work function barrier and allows electrons to directly tunnel through it – thus facilitating emission. The thermally assisted FEG (Schottky field emitter) uses heat in addition to voltage to overcome the potential barrier level [9].

Three parameters, i.e. brightness, source size and energy spread, are important in electron emitters and can be compared for various types of electron emitters. Although the FEG has a moderate emission current, its brightness is higher than the thermionic tungsten and LaB_6 sources (Table 4.1). Brightness is dependent on accelerating voltage, which increases linearly with accelerating voltage [9]. The high brightness value of FEGs is also due to the small source size. In FEGs, the source size is in nanometre while it is in micron in other emission sources, and thus the current emission in FEGs takes place in an extremely small source size as the beam leaves the gun. Thus, sufficient probe current in a small diameter probe lets the FEGSEM get a better resolution. The ability to achieve a small probe diameter is directly related to the source size or the diameter of the electron beam exiting the gun. An electron beam emanating from a small source size is said to have high spatial coherency. Electron beams can also be characterized in terms of temporal coherency. A beam with high temporal coherency will have electrons of the same wavelength. There is a certain “Energy Spread” associated with the beam. As we will see, lower energy spreads result in better resolution and are particularly important in low accelerating voltage imaging [9].

In addition, proper vacuum, lifetime, cost and expected mode of use are also important factors for SEM. Source size is the apparent size of the disc from which the electrons come. A small source size is good for high resolution and less demagnification. A large source size is sometimes good. For example, for large probe sizes and high beam current, electrons leave guns with an energy spread that depends on the cathode type. Lens focus varies with energy, so energy spread spoils high-resolution and low-energy images. The cold field emission gun offers the best performance parameters in all three categories for most purposes. Field emission guns are best for high-resolution and low-voltage operation. Thermionic emitters have advantages when very high-beam current and large spot sizes are required. At

Table 4.1 Different parameters in electron emitters and their comparison with others

	Tungsten	LaB ₆	Thermal FEG	Cold FEG
Brightness (A/cm ² str)	10 ⁵	10 ⁶	10 ⁸	10 ⁸
Lifetime (hrs)	40–100	200–1000	>1000	>1000
Source size	30–100 μm	5–50 μm	<5 nm	<5 nm
Energy spread (eV)	1–3	1–2	1.0	0.3
Current stability (%hr)	1	1	5.0	5
Vacuum (Torr)	10 ⁻⁸	10 ⁻⁷	10 ⁻¹¹	10 ⁻¹¹

Fig. 4.8 The electron beam parameters which has impact on sharpness, resolution and visibility of SEM images

a typical imaging current, FEGSEM spot size is set only by lens quality. Lower brightness guns must use bigger spots to give the same beam. This is brightness-limited imaging. The best resolution is always obtained at the smallest working distance (WD), but the minimum WD value varies with beam energy. The sharpness, contrast and depth of field depends upon three major electron beam parameters, i.e. electron probe size (d_p), electron probe current (i_p) and electron probe convergence angle (α_p) (Fig. 4.8).

The beam diameter (d_p) should be as small as possible for highest resolution. The emission current (i_p) must be as large as possible for the best image quality and X-ray analysis. For the best depth of field, the convergence angle (α_p) must be as small as possible.

FESEM is a high vacuum instrument and the vacuum allocates movement of electrons along the column devoid of scattering and spreading and avoids discharge in the interior gun zone. SEM requires operating under a vacuum to avoid interactions of electrons with gas molecules in order to obtain high resolution. The microscope must have vacuum system in order to achieve the required vacuum. The vacuum keeps the column free of molecules, and thus the beam will not interact with any molecules on the path down the column. The gun level of the column needs

vacuum in the range of 10^{-10} – 10^{-11} Torr, while the specimen chamber requires vacuum in the range of 10^{-5} – 10^{-6} Torr.

4.7.2 Column with Lenses and Apertures

Condenser lens, scanning coils, stigmator coils and objective lens and the apertures in the column focus the electron beam onto the surface of specimen. Each lens consists of copper wire carrying direct current surrounded by an iron shroud. Thus, electromagnetic lens contains copper wire coil within an iron pole piece. These coils create magnetic field when applying current through the coils, and this magnetic field converge the electron beam. Once an electron passes through an electromagnetic lens, it faces two vector forces at any particular moment [9]:

- (i) A force parallel to the Z-axis of the lens and therefore is represented by Hz that causes spiralling of the electrons while passing through the lens
- (ii) A force parallel to the radius of the lens and therefore is represented as HR, which causes focusing of the electrons while passing through the lens

When an electron is passing through the lens, it will experience a force parallel to the Z-axis, and this force will urge the electron to spiral through the lens. This spiralling causes the electron to experience another force parallel to the radius of the lens, and this force compress the beam towards the Z-axis. The magnetic field does not remain homogeneous. It remains strong close to the bore while weak in the centre of the gap. Thus, those electrons which pass close to the centre experience less force and are less strongly deflected, while those electrons which are passing the lens far from the axis experience more force and are more strongly deflected. Thus, electromagnetic lens produces electromagnetic fields which have axial and radial parts. The radial component keeps the electrons in helix path. If the beam diameter is smaller than the feature, in such a case, feature on the specimen surface can be resolved, and for this purpose, it is a must to condense the electron beam. Therefore, electromagnetic lenses are utilized to support in the demagnification of the beam. Field emission source has small crossover diameter, and therefore the beam condensation to a lower level is necessary because in such a case the probe will be valuable for image processing, and that is why the FESEM is the highest resolution instrument [9].

4.7.3 Condenser Lens

The condenser lens converges the cone of the electron beam to a spot below it, before the cone flares out again and is converged back again by the objective lens and down onto the sample. This initial convergence can be at different heights, i.e.

close to the lens or further away. The closer it is to the lens, the smaller the spot diameter at the point of convergence. The further away, the larger the diameter of this point. Therefore, the condenser lens currently controls this initial spot size and is referred to as the spot-size control. The diameter of this initial convergence (also called a crossover point) affects the final diameter of the spot the beam makes on the sample. The condenser lens reduces the diameter of the probe. Changing the current in the condenser lens will result in changing the diameter of the beam and can get a beam with a small diameter. A smaller probe diameter and narrow beam will enable better resolution. However, the drawback of a narrow beam is worse signal-to-noise ratio, while in the case of beam with large diameter, the signal-to-noise ratio will be better. The source size of the FEG is comparatively small so that the amount of demagnification necessary to produce small probe sizes is less than that of other electron sources [9–12].

4.7.4 Scanning Coils

Scanning coils which are also called beam deflection coils are used to scan the sample surface, and the current in these coils is increased in order to get a higher magnification. The role of the scanning coils is to deflect the electron beam above the object in a zigzag pattern, and with help of this scan movement, the creation of the image occurs on the monitor in synchrony. The refreshing rate on the screen and amount of noise in the image depends on the scan velocity. In case of slow scan, the refreshing will be slow; the signal will be high while the noise will be low. On the other hand, if the scan is fast, the refreshing will be fast, the signal will be low while the noise will be high. Scanning coils mostly contain upper and lower coils, which avoid the creation of a circular shadow at low magnification [9–12].

4.7.5 Objective Lens

The objective lens is the lowest lens in the column which focuses the probe on the sample. The objective lens is used to focus the beam on the specimen. Coarse focusing of the specimen can be done by choosing the working distance (WD = distance between the bottom of the objective lens and the specimen), focusing the objective lens to coincide with this value and then changing the physical height of the specimen to bring it into focus. Fine focusing can be subsequently done solely with the objective lens. WD needs to be decreased for a specimen to be well focused. If the WD is less, it means that the sample is at a higher position and close to the objective lens. Therefore, greater force is needed to deflect the electron beam by objective lens. The shortest WD generates beam with the smallest diameter and gives the poorest depth of field thus getting an image with the best resolution [9–12].

4.7.6 Stigmator Coils

The stigmator coils are utilized to correct irregularities in the x and y deflection of the beam and thus to obtain a perfectly round-shaped beam. When the beam is not circular, but ellipsoidal, the image looks blurred and stretched [9–12].

4.7.7 Apertures

For refinement of the beam, different size apertures are utilized. The aperture with small size produces a very fine beam. Small objective aperture sizes will produce better resolution, good depth of field and minimal charging. The selection of correct aperture size depends on the requirement of sample and user. The choice and selection of accurate aperture size is the responsibility of the user. Apertures are circular holes in metal discs on the micron scale. The net effect of the aperture is to reduce the effects of spherical aberration. Highest working distance (which is the distance between the sample surface and the objective lens) and small aperture produces images that look in focus over a big change in Z -axis [9–12] (Fig. 4.9).

4.7.8 Specimen Chamber

SEM has a specific sample holder where the stub should be fixed containing the sample on the surface. Generally, carbon tape, silver paste, copper tape, etc. are used for sticking the sample to the stub. If the sample is electrically conductive,

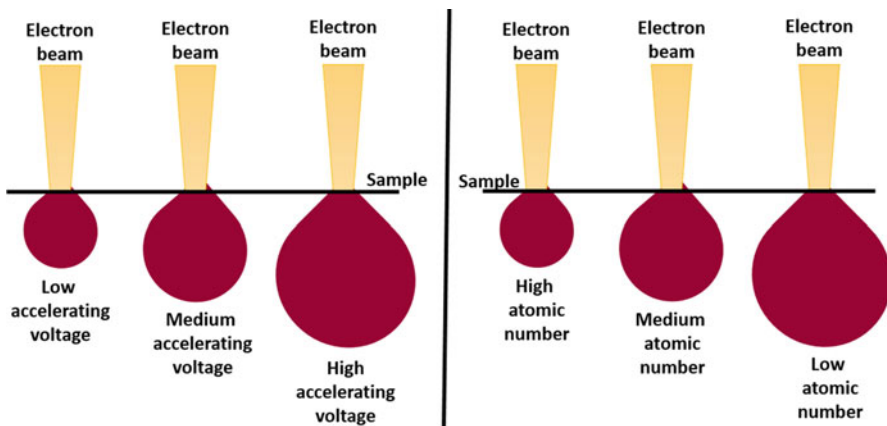


Fig. 4.9 Schematic dependency of interaction volume and penetration depth on the accelerating voltage of the beam and atomic number of the sample

then it can avoid overcharging on the surface. This overcharging may introduce extreme brightness and poor images. Thus, non-conductive samples like polymers are usually sputter coated with a thin layer of carbon or metal that readily reflects electrons and provides a conductive surface for electrons, e.g. gold and platinum. The non-conductive materials must be sputtered in order to reduce the charging problem. After that the sample-covering stub will be fixed in the sample holder and should be put in the sample-holding chamber or specimen chamber. Then vacuum should be generated and ensure that FESEM is at good vacuum level, and proper vacuum level is attained. The sample can be moved in horizontal and vertical directions in FESEM. The position of the specimen can easily be adjusted by using a joy stick that steers in the left-right axis, or forward and backward. Similarly, the sample can be tilted, rotated and moved in Z-direction. By this movement, the sample can bring close or keep away from the objective lens. The “secondary electron emission” detector is located at the rear of the object holder in the chamber.

4.8 FESEM Operation

The instrument should be properly checked before systematic operation. Gun vacuum, filament current, emission current and voltage should be checked. If all the things are in order, then prepare the sample. The sample should be dry and free of excessive outgassing. SEM has a specific sample holder where the stub should be fixed containing the sample on the surface. Generally, carbon tape, silver paste, copper tape, etc. are used for sticking the sample to the stub. First two-sided carbon tape should be fixed on the stub, and then a thin layer or a small amount of material will be placed on the carbon tape because the thin layer properly sticks with the carbon tape which reduces the charging problem and helps in getting a good image. Some requirements are needed when operating SEM analysis. Additionally, when using SEM, the samples have to be electrically conductive to avoid overcharging on the surface. This overcharging may introduce extreme brightness and poor images. Thus, non-conductive samples like polymers are usually sputter coated [4] with a thin layer of carbon [1] or metal that readily reflects electrons and provides a conductive surface for electrons, e.g. gold [2] and platinum [8]. The non-conductive materials must be sputtered in order to reduce the charging problem. After that the sample-covering stub will be fixed in the sample holder and should be put in the sample-holding chamber or specimen chamber. The stage height which is working distance and specimen surface offset must be properly adjusted to avoid the contact of the specimen with lens column and thus avoid specimen and stage damage. For the correct stage height estimation, the sample height must be correctly estimated, which is the distance between the top surface of the sample holder and surface of the specimen. Gun valve should be closed during sample exchange. The gun valve separates the upper column from the rest of the microscope [9]. Then vacuum should be generated and ensure that *microscope is at good vacuum level and proper vacuum level is attained.*

Once pressure in the main chamber reaches to 9.6×10^{-5} Pa (JEOL JSm-7600F), then set the accelerating voltage (0.5–30 kV) while keeping in mind that high voltage can give better resolution, but at the same time, it also causes charging problems for non-conductive materials. Thus, it will be better to select high accelerating voltage for conductive materials, but lower voltage should be selected for non-conductive materials in order to avoid charging issues. Also select better working distance (WD) which is the distance between the sample surface and the objective lens. The stage height (Z) will also be set and the stage will rise to the set Z depending on the specimen surface offset. A better resolution will be achieved through smaller WD, but keep in mind that very small WD may cause accident of the sample with the lens column, and therefore WD between 6 and 8 mm are usually suggested. After setting all these things, switch on the gun and the focused beam is rastered across the surface of the sample with the help of deflector coils which is controlled by the scan generator. The size of the rastering pattern is under magnification control. Once the beam is focused on the surface of the sample, the magnification should be changed in order to change the size of the rastered area on the sample. The size of the monitor raster pattern is constant. Magnification will increase if we reduce the size of the area scanned on the specimen [9], which can be represented as:

$$\text{Magnification} = \text{area scanned on the monitor} / \text{area scanned on the specimen}$$

Electron gun alignment is important in all the electronic microscopes, which must be aligned in SEM. The image should remain stationary during changing focus. If the object is moving during focusing, this indicates that the beam (electron gun) is not aligned. Similarly, astigmatism correction is important which is caused by different focal lengths for rays of various orientations, resulting in a directional image blur.

During SEM analysis, one has to keep a suitable probe current (i_p) (the applied current to specimen which produce numerous imaging signals) in a small probe diameter (d_p) (the diameter of the final beam at the surface of the specimen) which would increase the probe convergence angle (α_p) (the half-angle of the cone of electrons converging onto the specimen). But this is not the case due to aberrations in the optic system (more details are given later). A small probe diameter always comes with a decrease in probe current. These parameters are interrelated in other ways. For example, a decrease in accelerating voltage (kV) (the voltage with which the electrons are accelerated down the column) will result in a decrease in probe current as well as an increase in probe size [9].

Electromagnetic lenses, i.e. condenser lenses, are involved in demagnification; the objective lens focuses on the specimen as well as demagnifies. A smaller probe diameter will enable better resolution. The source size of the FEG is comparatively small so that the amount of demagnification necessary to produce small probe sizes is less than that of other electron sources. The objective lens is used to focus the beam on the specimen. Coarse focusing of the specimen is done by choosing the

working distance (WD = distance between the bottom of the objective lens and the specimen), focusing the objective lens to coincide with this value and then changing the physical height of the specimen to bring it into focus [9]. Fine focusing is subsequently done solely with the objective lens.

A: Specimen in focus.

B: Working distance needs to be decreased for specimen to be in focus.

4.9 Operator Control

4.9.1 Accelerating Voltage

The sample can be checked at different accelerating voltages (1–30 kV) depending on its nature. The high accelerating voltage causes reduction in lens aberrations which result in a smaller probe diameter and enhance resolution. The high accelerating voltage enhances the probe current at the sample. For an image of good contrast and high signal-to-noise ratio, a least probe current is required. The high accelerating voltage also causes charging of a sample especially non-conductive and beam-sensitive material. Thus, it is important to control accelerating voltage which can charge up and ultimately damage the material. High accelerating voltage increases the electron penetration more into the sample which ultimately obscures, making the surface features vague [1–12].

4.9.2 Emission Current

Different emission currents can be applied during the checking of materials. The increase in emission current enhances the probe current at the sample which causes charging of a sample, especially of non-conductive and beam-sensitive material. Thus, it is important to control the emission current which can charge up and ultimately damage the material [1–12].

4.9.3 Probe Diameter

The probe diameter or spot size could be varied by altering the current to the condenser lens. The decrease in probe diameter will cause increase in resolution while a decrease in lens aberration and probe current. The image with large spot size will be less sharp but look smooth, while lower probe size will result in sharp but coarser image appearance because of lower signal-to-noise ratios related to a lower beam current. In all types of guns, the smaller probe diameter can be obtained

with higher accelerating voltage. In the case of a tungsten thermionic gun, the source size of the gun is larger and thus has a larger minimum probe diameter. Similarly, in the case of a tungsten thermionic gun, there is a dramatic increase of spot size with increasing probe current, while it is relatively small in FEGs. The spot size is small at high accelerating voltages while it starts to enhance as the accelerating voltage decreases. The probe diameter can determine the sizes of the sample area from which the signal is produced [1–12].

4.9.4 Objective Aperture Size

The objective apertures have a range of sizes that can be selected. Reducing the diameter of the aperture causes decrease in lens aberrations and thus increases the resolution. The decrease in the diameter of the aperture causes

- Decrease in probe current
- Decrease in the convergence angle of the beam and thus increase the depth of focus

The larger diameter of the aperture results in a larger beam convergence angle and thus a reduced depth of focus. However, when using the same working distance but with a narrower diameter aperture, an increased depth of focus results [1–12].

4.9.5 Working Distance

Working distance (WD) which is the distance between the sample surface and the objective lens is adjustable. The enhancement of working distance causes increase in depth of focus and probe size and thus decreases the resolution [1–12].

4.9.6 Focus and Alignment

For better result, the focus and alignment are important, and for the alignment of the microscope, the apertures must be centred. If the microscope is not aligned and trying to focus the beam on the material in order to take image, the image will move because the objective aperture is not centred. For correcting of this, one needs to wobble the current to the objective lens and align the aperture to minimize movement in both the X and Y plane. This adjustment can be done consecutively at higher magnifications [1–12].

4.9.7 Astigmatism

Adjustment of objective lens astigmatism is also crucial which can be done at higher magnifications. In case of high astigmatism, the image is streaking on either side of focus. When extreme, astigmatism displays itself as a streaking of the image even if streaking is not clear, astigmatism should be fine-tuned to acquire quality images [1–12]. An operator turns for objective lens astigmatism by using current differentially to a ring of stigmator coils surrounding the objective lens. The compensating field in the image is responsible for a more circular (symmetric) form of the beam. The objective lens is used primarily to focus and initially magnify the image. It is needed to do fine focusing at high magnifications because increase in magnification relates to a smaller rastered area on the specimen. When the magnification decreases, the focus gets better. During experiment, first estimate the highest magnification for obtaining images and then double that magnification value and conduct final aperture alignment and astigmatism correction, and focus there to get your required images. Alignment must be done upon any change in accelerating voltage, spot size, etc. [1–12].

4.9.8 Tilt

After tilting the sample, the incident beam electrons move along greater distances in the region near the surface. Due to this occurrence, more SEs are produced in this area as compared to areas which are normal to the beam, and these SE signal-produced images reveal the so-called edge effect. Edges and ridges of the sample due to emission of more SEs look brighter in the image [1–12].

4.9.9 High-Resolution Imaging

The resolution means minimum space at which two specimen features can be distinguished as distinct or separate. To obtain high-resolution images, the probe diameter should be adjusted to the scale of interest and make sure that a minimum level of contrast occurs between the appropriate probe current and scan rate settings. SEs give a high-resolution signal and the interaction volume will be quite large even with small probe diameters, and thus at very small magnifications, the pixel overlap will take place. The high resolution can be achieved at low and high voltage, but at low voltage, contamination will be a serious problem which results from the interaction of the electron beam with residual gases and hydrocarbons on the specimen surface [1–12].

For low atomic number samples, it is difficult to get high-resolution images because it produces low SEs and thus poor signal-to-noise ratio. In such a case,

ultrathin metal coating can increase the SE yield while thicker coatings can also produce high SE yield, but in case of thicker coating, the metal particles may appear in the image at high magnification. The uncoated sample image is quite blurry, having no defined edges. Considering the coated sample, the rapid change in metal thickness changes as the beam strikes on the sample which leads to SE signal maxima that allows the size and shape of the feature to be clearly resolved. The coating process acts as a remedy for the charging under the beam considering non-conductive samples [1–12].

4.9.10 Charging

Charging is one of the most important problems in SEM analysis. During charging process, when the electron beam hits the sample surface, it (sample) cannot conduct the beam energy. The possible reason is that the electrons lose all initial energy and are held by the specimen. If a specimen is a conductor, then this charge flows to ground in case of suitable connection. If the ground path is broken, in such a case the conductive specimen collects charge, thus raising its surface potential. Non-conductive specimens will evidently amass charge. The subsequent image will “glow” or show general distortion in the image with enhancement in electron production [1–12].

Conductive tapes or paints bind both conductive and non-conductive samples to their holders. Non-conductive samples contain the thin conductive films (carbon, gold, platinum, etc.) to make the electron flow easy [1–12].

4.9.11 Scan-Square Method of Testing the Conductivity of a Specimen

- (i) Focus should be on an area at a high magnification.
- (ii) Wait for a few seconds, allowing the beam to irradiate the particular area.
- (iii) The magnification should be reduced, and then observe the sample.
- (iv) If a bright square is shown, it means negative charging is probable. To avoid it, lower the voltage.
- (v) Positive charging is probable only when the dark square appears then rapidly disappears. So, raise the voltage. Note: if the dark square is still there, contamination is most likely responsible for it.
- (vi) The effect of charging is intensified at higher magnifications, so make sure to clear these conditions at levels near or at the highest magnification you wish to use.
- (vii) To reduce charging in thin metal coatings, the following approaches can be utilized to reduce charging: (a) the probe current should be reduced; (b) the

accelerating voltage should be lowered; (c) the specimen should be tilted to discover a balanced point between the amount of incident electrons and the electrons that escape out of the specimen; (d) imaging should be done with BSEs; (e) rapid scan rates and frame integration should be used; (f) insulator's E2 value should be determined.

E2 Value While calculating the sum of the BSE and SE coefficient at very low kV, an energy range is found where this sum is positive. The presence of this positive form of charging shows that more electrons are emitted from the sample as compared to a primary electron beam. Apart from glowing, a dark box (from the scan footprint) will appear as secondary electrons are discharged. E1 and E2 are the charge balance achieved at voltages near the area of positive charging. Considering each material, E1 and E2 are constants. E2 is obtained at a higher accelerating voltage for uncoated observation, thus using a higher resolution condition of the SEM [1–12].

4.9.12 Specimen Damage by Electron Beam

Mostly the loss of electron beam energy takes place at the irradiated point in the form of heat generation. Polymer materials and biological specimens due to their low heat conductivity are easily damaged using the electron beam [1–12].

The following approaches can be applied to avoid this damage:

- (i) The electron beam intensity should be decreased.
- (ii) The exposure time should be shortened.
- (iii) Low magnifications should be used for imaging large scanning areas.
- (iv) The thickness of coating metal should be controlled on the specimen surface.

4.10 Development in SEM

Over the past years, SEM has been developed and equipped with several electron emitters, detectors and systems to increase the microscope liability and overcome some of its disadvantages. For example, SEMs have been frequently equipped with an energy-dispersive X-ray (EDX) analysis system to perform the elemental analysis of certain materials [1–12]. The electron emitter of the microscope has also passed through several improvements, from traditional tungsten and carbon wire to higher performance lanthanum hexaboride (LaB₆) to field emission (FE) gun. Field emission scanning electron microscope (FESEM) has been further developed into cold gun FESEM and Schottky in-lens thermal FESEM [5]. In addition, the invention of environmental SEM enables many natural samples such as polymers, food, drugs and biological and forensic materials to be studied at ambient conditions and without any pretreatment. Thus, the need of pretreating the samples to obtain

a solid, dry and electrically conductive material became no longer a requirement. Furthermore, Hitachi was able to substitute the traditional backscattered and secondary electron detectors by producing a new detector, environmental secondary electron detector (ESED), which is able to detect ions in addition to electrons and provide better surface information [2]. Additionally, we can conduct SEM-based scanning transmission electron microscope (STEM) imaging, that is, STEM can be carried out in a SEM by adding different detectors. A fine, highly focused beam of electrons is scanned over a thin specimen, and the electrons that pass through the thin sample are collected on a detector placed beneath the sample, yielding the desired bright-field images. The bright-field image in the STEM looks quite similar to that observed from the same specimen in the normal TEM measurements. FE-STEM measurements have become important for some reasons, for example, suitability for the observations of carbon-based nanomaterials where high beam energy is not always required, since light atom-based material is easily penetrated by less energetic electrons. The FE source reasonably combines with scanning electron microscopes (SEMs) whose development has been supported by advances in secondary electron detector technology [1–12].

4.11 Difference Between SEM and FESEM

- (i) Emitter type is the main difference between the SEM and FESEM. SEM uses tungsten filament and crystal of LaB_6 as electron guns which produce or generate electrons by “heating”, while in the case of FESEM, no heating but a so-called “cold” source is employed. Field emission is the emission of electrons from the surface of a conductor caused by a strong electric field. Thermionic emitters use electrical current to heat up a filament; the two most common materials used for filaments are tungsten (W) and lanthanum hexaboride (LaB_6). When the heat is enough to overcome the work function of the filament material, the electrons can escape from the material itself. Thermionic sources have relatively low brightness, evaporation of cathode material and thermal drift during operation. Field emission is one way of generating electrons that avoids these problems. A field emission gun (FEG), also called a cold cathode field emitter, does not heat the filament. The emission is reached by placing the filament in a huge electrical potential gradient. The FEG is usually a wire of tungsten (W) fashioned into a sharp point.
- (ii) FESEM needs high vacuum as compared to SEM.
- (iii) FESEM needs high acceleration voltage as compared to SEM.
- (iv) The electron beam produced by the FE source is about 1000 times smaller than that in a standard microscope with a thermal electron gun.
- (v) FESEM is high-resolution surface-imaging tool as compared to SEM.
- (vi) Clear and well-focused images of particles/surfaces are possible by FESEM at higher magnifications as compared to SEM.

- (vii) The resolution of a SEM is basically given by the minimal spot size which can be formed and then rastered over your sample. This probe is formed by demagnifying the image of your gun. A field emission gun emits the electrons from a much smaller area than a thermionic gun. Therefore, the probe will principally be smaller for a FEG instrument compared to a W or a LaB₆ instrument. Additionally, the coherency is much higher and the energy spread smaller. This again allows to more perfectly focus the beam. FESEM has more intensive and at SEM.
- (viii) FE gun has the following advantages over the others (W or LaB₆). Crossover diameter is less. Spot diameter is also less compared to thermionic emission. It is more coherent and energy spread is very low.
- (ix) The brightness will be very high compared to other thermionic source.
- (x) All these will make FESEM give better resolution than SEM.
- (xi) Crossover diameter – the point at which the electrons are focused when leaving the electron gun, virtual electron source. For SEM a smaller crossover gives smaller final electron spot, i.e. higher resolution.
- (xii) Crossover-free beam pathway of forming beam without crossover is implemented by some manufacturers. It theoretically eliminates some aberrations caused by electron-electron interactions in a crossover spot. Since it is not supported by all manufacturers, we can assume that other ways of increasing resolution are at least as good as that one.

4.12 Applications of SEM

SEM can measure and analyse the following parameters:

- (i) Thickness of films and thin coatings
- (ii) Surface morphology and appearance
- (iii) Size and size distribution
- (iv) Shape and dispersion of particles, fibres, nanomaterials or any other additives in composites and blends
- (v) Height and lateral dimensions of nanometre-sized materials
- (vi) Cell size and size distribution in foam materials
- (vii) Chemical composition and elemental analysis of nano- and micro-materials
- (viii) Fracture and structural defects analysis

4.13 Application of SEM in Nanomaterials Characterization

SEM is a multipurpose, non-destructive tool which tells the comprehensive information about the morphology, arrangement and composition of nanomaterials. Especially, FESEM has the ability to supply clear and high-quality images and

information about the composition of nanomaterials which is required for various demanding applications in the field of nanotechnology. SEM has been utilized to study the surface morphology of nanomaterials and nanoparticles. Nanotechnology has intensely motivated the development and improvement of recent electron microscopy with many demands, especially for increasing resolution and to achieve more information about nanomaterials. Generally, the nanomaterials have size in the range typically from hundreds of nanometres down to the atomic level (approximately 0.2 nm), and the properties of nanomaterials largely depend on their size. Nanomaterials can have diverse or higher chemical/physical properties as compared to the bulk size of the same material [13–17]. High relative surface area and dominant quantum effects are the main reason and key origins for these features and size. Chemical reactivity of nanomaterials is highly dependent on the surface area of nanomaterials, and thus rise in specific surface area increases chemical reactivity, thus making nanomaterials suitable for many demanding applications.

The high reactivity of nanomaterials makes them useful catalyst in photocatalysis as well as electrocatalysis. Quantum effects play an important role in improving various properties of nanomaterials, and it starts to play role as the size of matter is reduced to tens of nanometres or less. Quantum effects significantly alter the optical, magnetic or electrical properties of materials [15]. For example, gold nanoparticles can appear blue, red or yellow in colour as a function of their size. The main problem in nanoscience is the uniform growth of nanomaterials especially nanoparticles of the same size and size distribution. The growth of nanoparticles with same size is important for specific intended applications. Thus, the growth of nanoparticles with uniform size is one of the crucial challenges [14]. Another challenge is to control the shape of nanomaterials and grow nanomaterials with uniform shape [14]. Shape control of nanomaterials has been emphasized because specific shapes of nanomaterial tune the properties with a greater versatility than can be achieved otherwise [18–20]. In face-centred cubic (fcc) metal particles, for example, the crystallographic {111} and {100} surfaces are different not only in the surface atom densities but also in surface energies, so that single-crystalline silver or gold nanoparticles with sizes smaller than ~ 10 nm show intriguing particle shapes such as truncated octahedron or cuboctahedron [21, 22]. In addition, twinned metal particles are found [21, 22]. Twinning is the result of two subgrains sharing a common crystallographic plane, and thus multiple twinning on alternate coplanar planes produces cyclic twinned polyhedron (decahedron and icosahedron) where the twinned tetrahedral subunits are arranged around a fivefold axes [23].

Furthermore, construction of superstructures (ordered assemblies or super lattices) of nanomaterials is of recent key interest not only in future electronics applications but also in fundamental nanoscience [24–29]. Metal (gold and/or silver) nanoparticles are ideal “building blocks” for two- and three-dimensional super lattice structures. Preparation of ordered assemblies often requires surface passivation of the building blocks to protect against modifications of their properties by their environment, as well as to inhibit sintering. The organic surface protection of nanoparticles enables to self-assemble into their super lattices, so that controlling the chemical functionality of the organic monolayer allows the collective properties

of the nanoparticle super lattices to be engineered [24]. Since FESEM utilizes a beam of very energetic electrons to scrutinize materials on an extremely fine scale [9], therefore, FESEM is the highest resolution instrument and extremely useful tool to analyse surface morphology, shape, features, size, composition and crystalline structure with high-resolution surface imaging in the area of nanoscience.

FESEM has been used to identify the surface morphologies of a variety of materials. Here, we explain some of the images of various materials such as metal oxide, polymer and metal oxide-based polymer materials. In an embodiment, the co-doped CuO/ZnO nanomaterials were examined through high-resolution FESEM indicating a nanostructure ingredient with nanorods shape for the chemical sensor application. However, the rod morphology was due to zinc oxide, and the aggregated rod shapes were displayed by copper oxide. The average morphology of ZnO rods was 530 nm, and the aggregated rod shape due to CuO was 8 μm ; however, these aggregated rods also consist of other sub-nanorods whose morphologies were 183 nm [13]. ZnO nanoparticles were grown in the form of dense particles with smooth surface for the environmental remediation and methanol sensor [20]. In one of our recent works, we supported the ZnO nanomaterials onto the cellulose acetate polymer for the synthesis of coumarin where it displayed the flower shape morphology under the FESEM imaging. A close look showed that these nanomaterials have flower shape morphologies; however, on aggregation it displayed sheet morphology [14].

The Co_3O_4 -based nanomaterials were synthesized for the electrochemical water splitting, where the $\text{CeO}_2/\text{Co}_3\text{O}_4$ and calcined $\text{CeO}_2/\text{Co}_3\text{O}_4$ as well as $\text{TiO}_2/\text{Co}_3\text{O}_4$ and $\text{Fe}_2\text{O}_3/\text{Co}_3\text{O}_4$ were grown in the form of particle morphologies [15]. Other Co-based nanomaterials Co-Al and Co-Ni were grown in the form of spherical particles; however, the Co-NiAl have sheet-like morphology after the FESEM imaging. Other Co-based materials were evaluated for the electrochemical water splitting, such Co_3O_4 , $\text{Co}_3\text{O}_4@ \text{SiO}_2$, $\text{ZnO}@ \text{SiO}_2$ and $\text{Fe}_2\text{O}_3/\text{Co}_3\text{O}_4$, which were grown in the form of spherical particles; only $\text{Fe}_2\text{O}_3/\text{Co}_3\text{O}_4$ were grown in mixed particle and fibre morphologies. The $\text{Co}_3\text{O}_4@ \text{SiO}_2$ showed the mesoporous morphology with an unprecedented surface area. The Zn-Al/C and Zn-Cr/C nanocatalyst were grown in layered double hydroxide morphologies and applied for the photocatalytic reduction of various cationic and anionic dyes. The FESEM images showed the sheet-like shape and morphology for both the catalysts; however, these sheets were made of small particles; therefore, it can suggest that the aggregation of the particle makes sheet-like shape of the corresponding catalysts [17]. Another sheet morphology was examined under the FESEM for the Cd-based materials (Cd-Al/C and Cd-Sb/C), where the Cd-Al/C was grown in the form of layered double hydroxide and the Cd-Sn/C in the form of nanomaterials, although both displayed the sheet morphology. The Cd-AL/C was indicating strong catalytic performance in the decolouration of organic dyes as compared to Cd-Sb/C due to its layered double hydroxide morphologies [18]. The uniform morphology particles were observed for CoSb_2O_6 under the FESEM for the chemical sensor and environmental remediation [19]. Similarly, aggregated nanosheets were observed for CuO- TiO_2 [21]. Ag_2O were synthesized in the form of spherical particle with uniform size for 4-nitrophenol

sensing [22]. Cage-like mesoporous core-shell composites with H-type ZSM-5 are synthesized and then encapsulated Pt nanoparticles for the toluene oxidation [23].

FESEM is an extremely important tool for the determination and investigation of inorganic-organic interaction or dispersion. The dispersion of inorganic materials inside the polymer host materials is important, because it controls many characteristics of the synthesized materials. The FESEM are largely used for the polymer and composite materials characterization. The FESEM images of poly(propylene carbonate)/ZnO composite materials displayed spots of ZnO in the polymer host materials. No aggregation was observed below 5% of ZnO content; however, on increasing the agglomeration, it was observed in the polymer host materials. These composite materials are used for the packaging application [24]. Similarly, poly(urethane acrylate) (PUA) and tetrapod ZnO whisker (TZnO-W) composite films displayed homogenous dispersion of TZnO [25]. In our group an efficient adsorbent material $\text{Co}_3\text{O}_4@\text{SiO}_2$ embedded in the chitosan polymer host materials was synthesized for the adsorption of organic dyes. The white spot in the FESEM images indicates the $\text{Co}_3\text{O}_4@\text{SiO}_2$ materials in the polymer host materials. These films were extremely active for the adsorption of organic dyes and indicate an extremely high antibacterial activity [26]. Similarly, in another embodiment, the Ni/Al nanostructured materials were incorporated to the chitosan material in the form of sphere and sheets, indicating high antibacterial and high adsorption performance [27]. Polyethersulfone-based spherical materials were synthesized and incorporated different materials such as SiO_2 , carbon black and cellulose acetate-CB. All these spherical materials displayed antibacterial activity and adsorption of nitrophenols. The FESEM displayed the rough nature of the PES polymer with about 2.26–2.45 μm and incorporation of SiO_2 , cellulose acetate and carbon black. Then Cu^0 nanoparticles were grown on the surface of PES-cellulose acetate-carbon black materials because of its high catalytic activity. The Cu^0 nanoparticles show strong performance for the reduction of 4-nitrophenol [28]. Similarly, PES-CA- Ag_2O membrane was synthesized and evaluated for their water permeability, mechanical strength, and porosity and contact angle. Cu^0 nanoparticles were grown on the surface of these membranes and then applied for the reduction of 4-nitrophenols. All the membranes and Cu nanoparticle-supported membranes indicated good antibacterial activity. The FESEM images of the Ag_2O indicated the agglomerate morphology of the particles, while the pure PES and PES-CA displayed a dense rough porous nature; while with the addition of Ag_2O nanoparticles to the PES and PES-CA, a well-dispersed nature of the membrane was observed. The Cu nanoparticles are supported on the PES-CA and PES-CA- Ag_2O indicating uniform particles [29]. Besides the aforementioned description, FESEM is used to investigate the particle size, morphology and textural characteristics of a number of materials.

4.14 Summary

FESEM is a useful and leading machine that is capable of achieving a detailed visual image of a particle with high-quality and spatial resolution. It can provide information about the morphology, composition and structure of the materials, especially nanomaterials. A special care is needed during the operation and material analysis. This chapter discussed briefly about SEM techniques, their utilization, principle, their advancement, operation, samples preparation and applications in materials science.

Acknowledgement The authors are grateful to the Department of Chemistry and the Center of Excellence for Advanced Materials Research (CEAMR) at King Abdulaziz University for providing research facilities.

References

1. Alyamani, A., & Lemine, O. M. (2012). FE-SEM characterization of some nanomaterial. In V. Kazmiruk (Ed.), *Scanning electron microscopy*. InTech. London
2. McMahon, G. (2007). *Analytical instrumentation: A guide to laboratory, portable and miniaturized instruments* (1st ed.p. 296). Chichester: Wiley.
3. Goldstein, J. K., & Yakowitz, H. (1975). *Practical scanning electron microscopy: Electron and ion microprobe analysis* (p. 582). New York: Plenum Press.
4. Goldstein, J. I., Newbury, D. E., Echlin, P., & Joy, D. C. (1992). *Scanning electron microscopy and x-ray microanalysis* (2nd ed.). New York: Plenum Press.
5. Brabazon, D., & Raffer, A. (2010). 3 – advanced characterization techniques for nanostructures. In W. Ahmed & M. J. Jackson (Eds.), *Emerging nanotechnologies for manufacturing* (pp. 59–91). Boston: William Andrew Publishing.
6. McMahon. (2007, November 11). Imaging instruments. *Analytical Instrumentation*.
7. Ram, S., Ward, E. S., & Ober, R. J. (2006). Beyond Rayleigh's criterion: A resolution measure with application to single-molecule microscopy. *PNAS*, 103(12), 4457–4462.
8. Bondeson, D. (2007). Biopolymer-based nanocomposites: Processing and properties. In *Department of engineering design and materials* (p. 114). Trondheim: Norwegian University of Science and Technology.
9. Zhou, W., Apkarian, R. P., Wang, Z. L., & Joy, D. (2006). Fundamentals of scanning electron microscopy. In *Scanning microscopy for nanotechnology* (pp. 1–40). New York: Springer.
10. Hayes, T. L., & Pease, R. F. W. (1968). The scanning electron microscope: Principles and applications in biology and medicine. *Advances in biological and medical physics*, 12, 85–137.
11. Sant'Anna, C., Campanati, L., Gadelha, C., Lourenco, D., Labati-Terra, L., Bittencourt-Silvestre, J., Benchimol, M., Cunha-e-Silva, N. L., & De Souza, W. (2005). Improvement on the visualization of cytoskeletal structures of protozoan parasites using high-resolution field emission scanning electron microscopy (FESEM). *Histochemistry and Cell Biology*, 124(1), 87–95.
12. Lloyd, G. E. (1987). Atomic number and crystallographic contrast images with the SEM: A review of backscattered electron techniques. *Mineralogical Magazine*, 51(359), 3–19.
13. Rahman, M. M., Jamal, A., Khan, S. B., & Faisal, M. (2011). CuO codoped ZnO based nanostructured materials for sensitive chemical sensor applications. *ACS Applied Materials & Interfaces*, 3, 1346–1351.

14. Khan, S. A., Khan, S. B., Asiri, A. M., & Ahmad, I. (2016). Zirconia-based catalyst for the one-pot synthesis of coumarin through Pechmann reaction. *Nanoscale Research Letters*, *11*, 345–353.
15. Khan, S. A., Khan, S. B., & Asiri, A. M. (2016). Electro-catalyst based on cerium doped cobalt oxide for oxygen evolution reaction in electrochemical water splitting. *Journal of Materials Science: Materials in Electronics*, *27*, 5294–5302.
16. Khan, S. B., Khan, S. A., & Asiri, A. M. (2016). A fascinating combination of Co, Ni and Al nanomaterial for oxygen evolution reaction. *Applied Surface Science*, *370*, 445–451.
17. Khan, S. A., Khan, S. B., & Asiri, A. M. (2016). Toward the design of Zn–Al and Zn–Cr LDH wrapped in activated carbon for the solar assisted de-coloration of organic dyes. *RSC Advances*, *6*, 83196–83208.
18. Khan, S. A., Khan, S. B., & Asiri, A. M. (2016). Layered double hydroxide of Cd–Al/C for the mineralization and de-coloration of dyes in solar and visible light exposure. *Scientific Reports*, *6*, 35107.
19. Jamal, A., Rahman, M. M., Khan, S. B., Faisal, M., Akhtar, K., Abdul Rub, M., Asiri, A. M., & Al-Youbi, A. O. (2012). Cobalt doped antimony oxide nano-particles based chemical sensor and photo-catalyst for environmental pollutants. *Applied Surface Science*, *261*, 52–58.
20. Faisal, M., Khan, S. B., Rahman, M. M., Jamal, A., & Abdullah, M. M. (2012). Fabrication of ZnO nanoparticles based sensitive methanol sensor and efficient photocatalyst. *Applied Surface Science*, *258*, 7515–7522.
21. Rahman, M. M., Khan, S. B., Marwani, H. M., Asiri, A. M., & Alamry, K. A. (2012). Selective iron (III) ion uptake using CuO–TiO₂ nanostructure by inductively coupled plasma-optical emission spectrometry. *Chemistry Central Journal*, *6*, 158.
22. Rahman, M. M., Khan, S. B., Asiri, A. M., & Al-Sehemi, A. G. (2013). Chemical sensor development based on polycrystalline gold electrode embedded low-dimensional Ag₂O nanoparticles. *Electrochimica Acta*, *112*, 422–430.
23. Qian, X., Xiong, D., Asiri, A. M., Khan, S. B., Rahman, M. M., Xu, H., & Zhao, D. (2013). A facile route to cage-like mesoporous silica coated ZSM-5 combined with Pt immobilization. *Journal of Materials Chemistry A*, *1*, 7525–7532.
24. Seo, J., Jeon, G., Jang, E. S., Khan, S. B., & Han, H. (2011). Preparation and properties of poly(propylene carbonate) and nanosized ZnO composite films for packaging applications. *Journal of Applied Polymer Science*, *122*, 1101–1108.
25. Kim, D., Lee, Y., Seo, J., Han, H., & Khan, S. B. (2013). Preparation and properties of poly(urethane acrylate) (PUA) and tetrapod ZnO whisker (TZnO-W) composite films. *Polymer International*, *62*, 257–265.
26. Khan, S. A., Khan, S. B., Kamal, T., Yasir, M., & Asiri, A. M. (2016). Antibacterial nanocomposites based on chitosan/Co-MCM as a selective and efficient adsorbent for organic dyes. *International Journal of Biological Macromolecules*, *91*, 744–751.
27. Ahmed, M. S., Kamal, T., Khan, S. A., Anwar, Y., Saeed, M. T., Asiri, A. M., & Khan, S. B. (2016). Assessment of anti-bacterial Ni–Al/chitosan composite spheres for adsorption assisted photo-degradation of organic pollutants. *Current Nanoscience*, *12*, 569–575.
28. Khan, S. B., Khan, S. A., Marwani, H. M., Bakhsh, E. M., Anwar, Y., Kamal, T., Asiri, A. M., & Akhtar, K. (2016). Anti-bacterial PES-cellulose composite spheres: Dual character toward extraction and catalytic reduction of nitrophenol. *RSC Advances*, *6*, 110077–110090.
29. Gul, S., Rehan, Z. A., Khan, S. A., Akhtar, K., Khan, M. A., Khan, M. I., Rashid, M. I., Asiri, A. M., & Khan, S. B. (2017). Antibacterial PES-CA–Ag₂O nanocomposite supported Cu nanoparticles membrane toward ultrafiltration, BSA rejection and reduction of nitrophenol. *Journal of Molecular Liquids*, *230*, 616–624.

Chapter 5

TEM for Atomic-Scale Study: Fundamental, Instrumentation, and Applications in Nanotechnology



Yasir Javed, Khuram Ali, Kanwal Akhtar, Jawaria, M. Irfan Hussain,
Gulzar Ahmad, and Taskeen Arif

5.1 Introduction

5.1.1 TEM Overview

Recent developments in science have unveiled many unthinkable and amazing techniques for characterization. Many things that were just a figment of our imagination have now become reality, and transmission electron microscope (TEM) is one of those few wonders. TEM is one of the most advanced and versatile characterization techniques [1]. The best thing about this technique is its focus on detail, and consequently, we can characterize almost any material in depth with the help of TEM. TEM brought a revolution in the research areas of physics, chemistry, medical sciences, steel industry, etc. After its invention, it has been considered as one of the most widely used techniques for characterization till date. Electron microscopes replaced light microscope because of better magnification and resolution powers [2, 3]. Light microscope cannot provide in-depth information about observing object because it utilizes light as an illumination source, having very large wavelength with almost no penetration. On the other hand, electron microscope can provide excellent images because of the shorter wavelength and better interaction power of electrons. Earlier, electrons were utilized in electron microscope specifically due to their elastic interactions, but later their other benefits were also utilized (inelastic interactions, X-ray emission, etc.). A lot of developments have been made since the invention of TEM. Its predecessors have improved its features enormously, although the basic idea remained same throughout the time [4, 5]. Many new types of microscopic and spectroscopic modes have been introduced, e.g.,

Y. Javed (✉) · K. Ali · K. Akhtar · Jawaria · M. Irfan Hussain · G. Ahmad · T. Arif
Department of Physics, University of Agriculture, Faisalabad, Pakistan
e-mail: yasir.javed@uaf.edu.pk

high-resolution transmission electron microscopy (HRTEM), scanning transmission electron microscopy (STEM) [6], electron energy-loss spectroscopy (EELS) [7], energy-dispersive X-ray spectroscopy (EDX) [8], etc. Nanotechnology is probably one of the major beneficiaries of all the advancements in TEM. It is an important field of research in recent times and has caused a lot of hype all around the world due to its applications in all fields of life. TEM is the best technique for the characterization of nanoparticles due to its very high resolving power and precision for analytical measurements. The specimen of TEM should be lean with specific length (typical thickness ~ 100 to 200 nm) [9, 10]. In this chapter, we have covered different topics related to TEM: the historical developments, layout and various components, and microscopy and spectroscopy measurements that can be performed by using TEM [11, 12].

5.1.2 Historical Development of Modern TEM

The history of TEM starts way back with the discovery of electrons. It all started with Thomas Young's double-slit experiment in which he discovered the dual behavior of light, shortly after J. J. Thomson discovered negatively charged particles in the sea of positive charges with greater charge-to-mass ratio than protons [13, 14]. He named those particles "electrons." This discovery was the beginning of a whole new chapter in the history of science. After this discovery, electrons were subjected to different experiments to study their nature and behavior. In 1930, de Broglie made the remarkable discovery of the dual behavior of electrons, and later Davisson and Germer conducted a diffraction experiment to prove this theory [15–18]. It was discovered that not only electrons have dual nature, but their wavelength is much shorter than visible light. These properties of electrons opened new gateways in the research field [19, 20]. It was around that time a scientist named Hans Busch discovered that electrons can be disciplined or focused under the influence of magnetic field. This idea formulated the concept of electron lenses, and it was not long until two scientists named Knoll and Ruska put forth a substantial theory about electron microscope [21, 22]. They made electron lenses and observed that electrons can provide better and magnified image than light. This technique has reached many milestones on the way including atomic resolution, and it is still progressing as many wonders are yet to be unveiled. On commercial scale, first TEM named EM-1 was manufactured in short time of 4 years after Knoll and Ruska's idea. EM-1 was built by a British company named Metropolitan-Vickers, and the credit for its invention goes to Professor L. C. Martin. The most difficult part about manufacturing process is that when we produce something from our imagination, it does not always end up as planned. No matter how many scenarios we think about along with their solutions, there is always a chance of error. This is what separates theoretical and practical work. Similar thing happened with EM-1; it did not work properly unlike the theory presented by Knoll and Ruska. After omission of major errors, worldwide production and sale of TEM was started in 1939 with the

Table 5.1 Timeline of TEM development

Scientist/company	Experiment/development	Year
Thomas Young	Experimental proof of dual nature of light	1801
J.J. Thompson	Discovery of electron	1897
De Broglie	Postulates for dual nature of electron	1925
Davisson and Germer [25]	Experimental proof of dual nature of electron	1927
Hans Busch	Electron optics	1926
Knoll and Ruska	Prototype of electron microscope	1931
Professor L.C Martin	EM-1 first commercial Electron microscope	1936
Siemens and Halske	Improved model of TEM	1939
	Ultrahigh voltage	1980
	Aberration correction	2008

help of Siemens and Halske in Germany. After that many other companies such as Hitachi, Philips, Japan Electron Optics Laboratory (JEOL), and Radio Corporation of America (RCA) started manufacturing TEM [23, 24]. Complete timeline of TEM development is presented in Table 5.1.

Over the years, many developments took place that not only improved the resolution but also added spectroscopic methods in the instrument. The 10 nm resolution of TEM in 1930 was reduced to 2 nm by the end of 1944 due to higher acceleration voltages and sophisticated lenses. After its invention, TEM conquered all the major fields gradually by the major contributions of many peoples. The early research work with TEM was completely based on samples containing minute particles like pigments and carbon black, but the results were only limited to the shape and structure of particle. When TEM was first developed, the characterization of biological sample was not possible. In 1941, due to the hard work of Ruska's brother Helmut, the first image of viruses was produced, and after that TEM took over the biological research. In the mid-1950s, Bollman in Switzerland and a Cambridge group consisting of Hirsch and his co-workers individually used metal foil as test subject by making them thin so that electrons can easily pass through them. The Cambridge research group also invented a diffraction contrast method to study all kinds of defects in a crystal including dislocations, phase changes, etc. Later, Thomas in the USA discovered the use of TEM for solving material problems. Many other major instrumental changes also took place from 1940 to 1950. The lenses got better in resolution with more stability, the electron beam got brighter and faster, and the instrument became more sleek and advanced with the passage of time. In the 1960s, new TEM was introduced with ultrahigh voltage capable of deeper penetration with more visible images and in-depth characterization. Basically, smaller wavelengths correspond to high energies, and thus, high accelerating voltages are necessary to get high-energy electrons. After this, the real limitation was intrinsic imperfections in electron lenses: spherical and chromatic aberrations. To overcome these constraints, Field Electron and Ion (FEI) and Corrected Electron Optical Systems (CEOS) companies along with US Department of Energy started a collaborative research

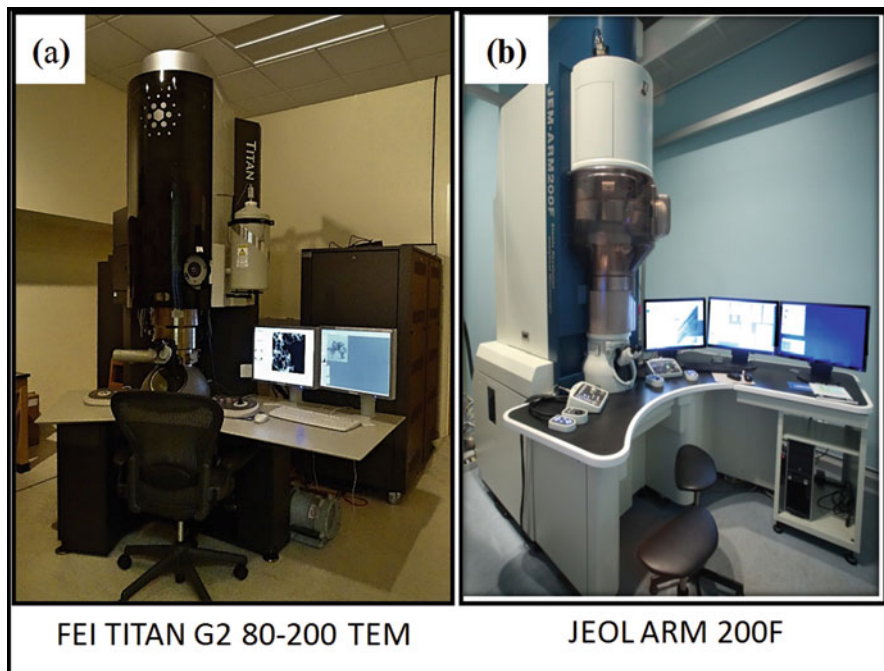


Fig. 5.1 Aberration correction model of TEM produced by FEI and JEOL companies

project with three research laboratories from the USA in 2004. The aim was to design TEM with spatial resolution below 0.5 nm. As a result, first aberration-corrected TEM started its operation in 2008, and target resolution was achieved in 2009. Later on, many major TEM-inspired characterization tools including electron energy-loss spectroscopy (EELS), scanning TEM (STEM), environmental electron microscopy, energy-filtered TEM (EFTEM), etc. are incorporated in TEM which make this machine a combination of microscopy and spectroscopy [26]. Latest TEM models manufactured by FEI and JEOL are shown in Fig. 5.1. One of the latest developments is liquid-cell TEM, where in situ observations can be made directly in the microscope. In short, the innovative technique named TEM has brought a revolution in the research world with its countless applications and amazing features [27].

5.1.3 What Can We Do?

The primary purpose of TEM is to examine the structure, chemical composition, and morphological and electrical properties at the nanoscale. Although major area of interest is material science for TEM, it is also being used in geology

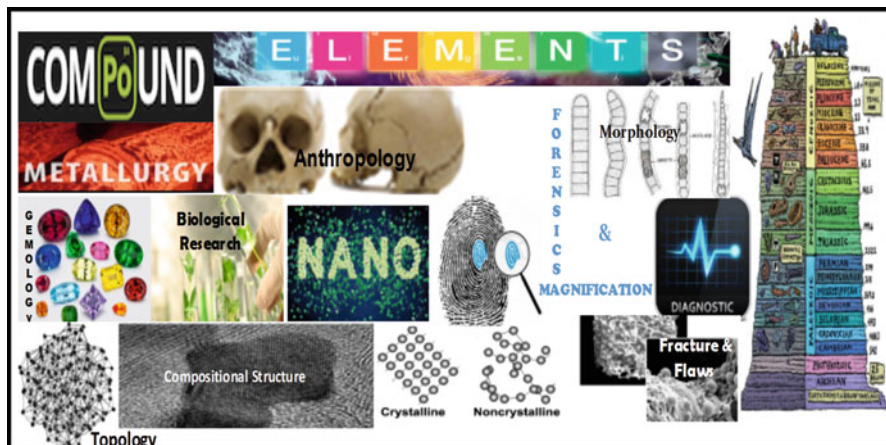


Fig. 5.2 Applications of transmission electron microscopy in different research areas

and environmental, agricultural, biological, and medical sciences (Fig. 5.2). The analyses of morphology, size, size distribution, structure, and local chemistry of nano-objects are important points in today's nanotechnology, because along with synthesis and other aspects, changes in morphology drastically affect the efficacy of the objects at the nanoscale. Today we are able to investigate bimetallic nanomaterials, their crystal structure, orientations, chemistry of phases, precipitates, stacking faults, dislocations, and contaminants by using electron diffraction, energy-dispersive spectroscopy, and electron energy-loss spectroscopy [28].

TEM can be utilized for:

- Morphology of nanomaterials from different parts of specimen and particle's statistics. Specimen can be colloidal suspensions, hydrated organs (the spleen, liver, lungs, etc.), viruses, bacteria, etc.
- Nanomaterials-polymer interface through HRTEM.
- Microanalysis by characteristic X-rays.
- Localized chemical composition of nanomaterial or thin film by STEM-EDX.
- Electron diffraction patterns.
- In situ temperature changes in the sample.
- Differentiating phases of nanomaterials by using electron energy-loss spectroscopy.
- Chemical mapping of an area of interest of the sample.
- Live dynamics of the nanomaterials in liquid phase by using latest liquid-cell TEM holder.

5.2 Basic Background and Principles

5.2.1 *Light Versus Electron Microscope*

Microscopes are very important part for all the research fields because objects and their dynamics are needed to understand that are beyond the limit of a naked eye. Whether impurities in a particle, surface defects in a material, internal structure of organisms, or changes in soil due to waste materials, microscope always comes in handy. The basic and key component of a microscope is its illumination source. When we think of a natural source with good and less damaging features, sunlight immediately comes to our mind. Moreover, it is easy to focus and operate. Visible-light microscope uses ordinary light for illumination and is considered very successful for the characterization of small organisms. When it comes to microscopes, both light and electron microscopes are very famous in the research area [29, 30]. Both microscopes have certain benefits as well as limitations. Light microscope utilizes light as illumination source. The objective lens in optical microscope is always bigger than other microscopes to capture as much light as possible. The more light it captures, the clearer will be the image. Due to bigger lens size, image is always at a distance. This is the basic reason that telescopes are designed to cover as much length as possible. Light microscopes are different from telescopes because small specimens are used as test subject instead of stars. Light falls on different parts of an object in a different manner, thus forming an image depending on scattering of light. The basic drawback of visible light is its large wavelength. The minimum wavelength 400 nm of visible region is very large for micro-/nanoscale characterization because it can't resolve small objects [31, 32].

Let's compare some of the basic features of both microscopes. When it comes to hardware, optical microscope is light, simple, and easy to handle. It does not have a lot of complicated features and functions. Anyone can operate it easily. On the other hand, electron microscope is huge and complicated, which makes it challenging to operate for beginners. Light microscope is economical; that's why it is available in many and a lot of regular schools and educational institutes (Fig. 5.3), whereas TEM costs up to 10\$ per eV, and typical beam energy is in the range 1×10^5 – 4×10^5 eV, so cost is extremely high; consequently, strong scientific justification is required to invest so much money in TEM. High vacuum is an essential condition for electron microscope so that electrons gain longer mean free path and can interact with the sample with maximum energy, whereas there is no such condition for compound microscope. Both alive and frozen specimens can be studied by the help of light microscope [33]. On the other hand, electron microscope requires a lot of preparation to make samples electron transparent so that electrons can easily pass through them. Now, only frozen specimen can be studied with the help of electron microscopes because electrons are difficult to handle and living sample will not be able to survive under the influence of vacuum and electrons. Also, biological samples can damage the vacuum of the electron microscopy, so, it must be frozen. The specimen of light microscope should be 5 μm or bulkier,

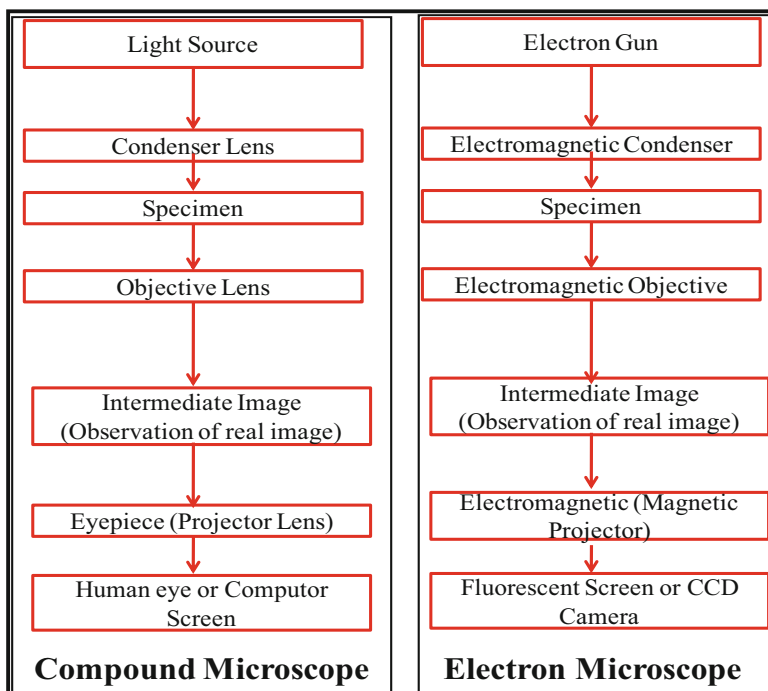


Fig. 5.3 Block diagram comparison of optical and electron microscope

but electron microscope can only handle 500 nm or thinner samples. Sample should be fixed and stable to bear the electron beam. If you want to study dynamics of living organisms, then light microscope is a good option, but to get information from microorganisms, nanoparticles, or subcellular level, electron microscope is usually used. Sample of electron microscope can be viewed on fluorescent screen; computer screens and images can also be saved for post-analysis. Specimen preparation of electron microscope requires heavy metal coating for reflecting electrons in biological samples. Light microscope, on the other hand, requires colored dyes. Light microscope has resolution power ranging from 1 to 100 nm with magnification power up to 1000 \times . Contrary to this, electron microscope has resolving power of 1 μm to 0.05 nm with magnification power up to five million times [34–39]. Table 5.2 provides the comparison of different features of light and electron microscope.

In short, optical microscope is safe, economical, easy to handle, and time saving, but it does not provide detailed information about the sample at nanoscale. On the other hand, electron microscope provides excellent images and structural and analytical information about the observed sample for analysis. So, optical microscope is a better option for simple experiments and where overall analysis of object is required, but electron microscope is preferable for detailed characterization

Table 5.2 Comparison of specifications between optical and electron microscope

Feature	Light microscope	Electron microscope
Radiation source [44]	Tungsten or quartz lamp	High voltage (50 kV) Tungsten lamp
Type of radiation	Visible light rays	Electron beam
Max. resolution	200 nm	0.2 nm
Max. magnification [45]	1000–1500 \times	500,000 \times
Sample type	Living or dead	Dead
Sample preparation	Quick and easy	Time-consuming and complex
Focused by [46–49]	Glass lenses	Electromagnetic lenses
Cost	Cheap	Expensive

of micro- and nano-objects. That is why electron microscope has emerged as a powerful technique to observe samples at nanoscale which is not possible by its counterpart optical microscope [40–43].

5.2.2 Resolution and Its Limitations

Resolving power is the ability of an optical instrument to distinguish or separate two points. The better the resolving power, the finer the image obtained through microscope. According to Bragg's law, interplanar spacing depends on λ wavelength of the illumination source and refractive index.

The minimum distance that a normal human eye can resolve is about 0.1–0.2 mm. Microscope is an instrument that displays objects when distance between two points is less than 0.1–0.2 mm. Resolving power is highly dependent on the interacting source. The resolution of a microscope should be large enough to distinguish two nearby objects to form a fine image [50, 51].

TEM is specialized in deep visualization, through electron beam sources, objective lenses, and aberration corrections, of very small objects or a specific portion of an object. One of the major limitations of resolution comes from electron's wave nature associated with its high speed (close to speed of light). This causes the phenomenon of diffraction and interference which makes absolute focus impossible to achieve. Diffraction is observed when a wave front interacts with any object. In case of TEM, edge of the lens or aperture can play the role of object; this produces diffraction which suppresses the resolution. Even for perfect optical system, electron beam cannot be focused in the form of perfect dot. In fact, image of the electron beam appeared as a disk comprised of concentric circles, called Airy disk. This Airy disk generates primary, secondary, and tertiary wave fronts. Wave fronts further arise to higher orders, but their importance reduces for optical phenomenon. The resolution is usually estimated by the distance between first-order peaks and its trough, denoted by " r " in Fig. 5.4. If distance between two points is

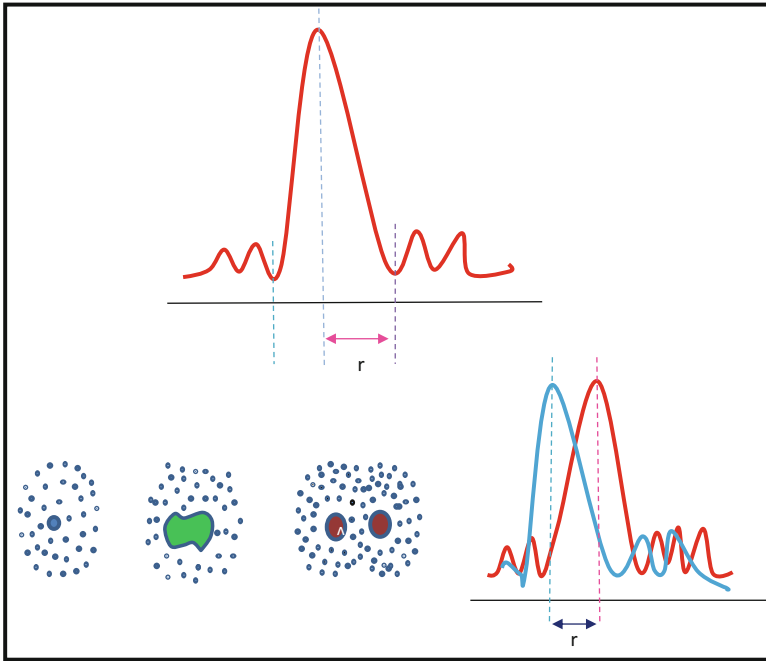


Fig. 5.4 Different aspects of resolution limits. (Reproduced with permission from Schmolze et al. [56])

more than “*r*,” then peaks observed by the two points will emerge as single point (Fig. 5.4) [52–55]. Abbe’s equation provides mathematical expression for resolution of a perfect optical system:

$$d = \frac{0.612 * \lambda}{n \sin \alpha} \tag{5.1}$$

d, resolution.

λ , wavelength of incident radiation.

n, refractive index of atmosphere between point source and lens with respect to free space.

α , half aperture angle in radians.

$n \sin \alpha$ is also called the numerical aperture (NA).

If we overcome all the aberrations and distortions in the optical system, even then resolution is limited by diffraction factor [57–60]. We know that wavelength associated with moving objects can be calculated by using de Broglie relation:

$$\lambda = \frac{h}{m * v} \tag{5.2}$$

When an accelerating voltage is applied on an electron, its kinetic energy will be equal to eV , energy of the field. Therefore,

$$eV = \frac{1}{2}mv^2 \quad (5.3)$$

By substituting the values from Eqs. (5.3) to (5.2) and putting values of h , e , and m , we obtained

$$\lambda = \frac{1.23 \text{ nm}}{V^{\frac{1}{2}}} \quad (5.4)$$

This equation is valid until speed of electron is comparatively low but as soon as speed approaches to speed of light, relativistic effects must also be considered in the equation for more accuracy.

We can obtain equation for resolution in TEM by substituting Eq. (5.4) in (5.1). Since α is very small, $\sin\alpha \approx \alpha$, refractive index, $n = 1$, and final equation becomes

$$d = \frac{0.753}{\alpha V^{\frac{1}{2}}}$$

Here,

d , resolution in nm

α , half aperture angle

V , accelerating voltage

We can determine the resolution of the TEM by using accelerating voltages, e.g., for 100 kV, the result will be 0.24 nm. Higher voltages improve the resolutions and hamper by low accelerating voltages. If we want to know practical limit of resolution, we need to consider relativistic effects, aberrations, and distortions that arise by each lens and aperture [61].

Past few years have been very significant for the improvements in the resolution of electron microscopes. Many limitations of resolution were removed, but it is still an ongoing process. The basic component used in early microscope to discipline and focus electrons is electromagnetic lens causing positive spherical aberration. These lenses focus electrons at large angles rather than the ones with short angles, and thus the image produced is blurry. On the other hand, the implemented wavelength is very short in the range of 0.02–0.03 Å, but it was impossible to attain the perfect resolution by using this wavelength due to the limited spherical aberration. The use of imperfect lenses is just like trying to see outside from a foggy window [62].

Multipole lenses were the next big thing for the formation of negative spherical aberration. Multipole lenses set the magnetic field lines perpendicular to the electron beams, while round lenses set them parallel to the direction of beam. The basic complication in this technique is the control and stability of all the constituents simultaneously. The computer controls were later introduced to solve this issue.

Another big limitation was chromatic aberration in TEM, but this problem is also now solved by introducing new simulation software and lenses [63].

The use of aberration-corrected instruments caused another problem named thermal magnetic noise. As the name indicates, this problem arises due to the thermal activation. To solve this problem, aberration correctors were replaced with stainless steel and permalloy tubes with the ability to maintain lower temperature [64].

TEM contains a lot of metal parts for the flow of current or other purposes. They can cause problems due to dislocations, phases, or other defects. Any fluctuation in the current can mess up magnetic field. These fluctuations can seriously affect the resolution [65].

5.2.3 Electrons and Other Radiation Sources: Pros and Cons

The discussion in the above section indicates that resolution limitation of optical microscope was the main reason for the development of TEM. There exist other radiation sources besides electrons. The most common source of radiations is X-rays, which have very short wavelength of approximately 1.5 Å. It seems that our short wavelength requirement has been perfectly met, and another advantage is that our body lets them pass through it, but X-rays have other several issues of their own. Firstly, X-rays are very hard to focus because refractive index of glass is not enough to guide X-rays. Zone plates have been often used to discipline these rays, but they have many other technical issues [66, 67]. Another disadvantage of X-rays is that they can damage the sample badly, and thus it can't be used in the microscopes. One of the main advantages of electrons is their small wavelength which can guarantee a good resolution. Another benefit is their easy alignment and focusing by using electromagnetic lenses. The number of interactions of electrons with the sample is very high (few of those interactions are shown in Fig. 5.5). Electrons also have few limitations, but these can be tackled. Major limitation is its low penetration in the samples; that's why very thin samples (~500 nm or less) are being observed in TEM. Electrons can be harmful for hydrated biological samples; therefore, some material coating has been used (usually carbon). This can degrade the imaging to some extent, but still useful information can be extracted from the sample. Neutrons also have wavelength in the range of picometer, with less damaging effects for samples than electrons. However, the existence of neutron source and its focusing are the questions still need to be resolved [68].

5.2.4 Properties of Electrons

The electron is one of the subatomic particles of atom which belongs to lepton family having negative charge. J.J. Thomson discovered electron in 1897 (Nobel Prize 1904), and Stoney gave the name of electron. Where other subatomic particles are packed together in the core (nucleus) of the atom, electrons are distributed in

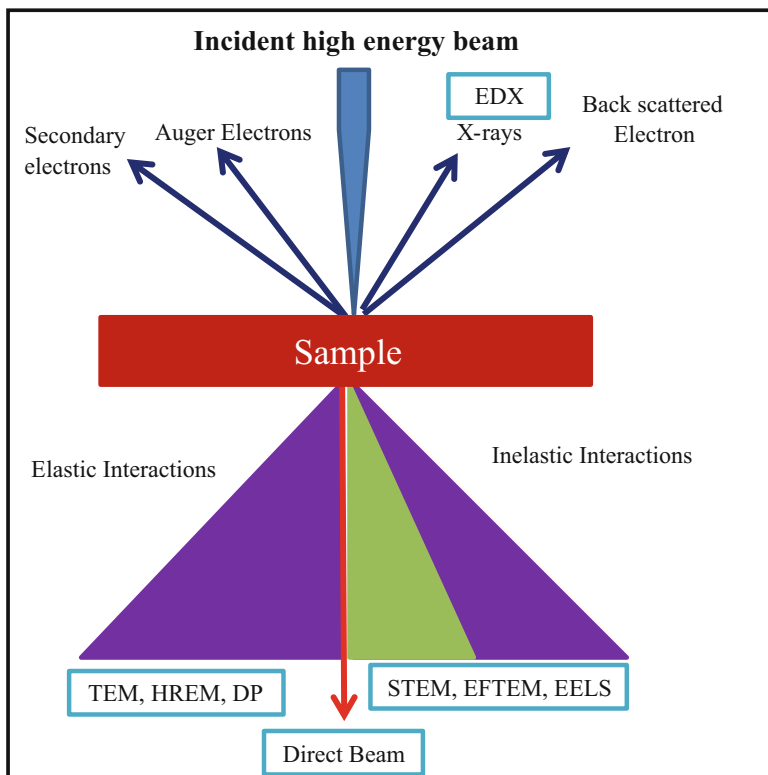


Fig. 5.5 Schematic of different electron interactions with matter and corresponding techniques in TEM using specific interaction

specified shells in the exterior of the nucleus. The mass of electron is nearly 1/1836 times of the mass of proton and 1000 times less than the mass of hydrogen. Electrons also have dual nature as all other moving matter possess [69]. This property is vital for electron microscopy because this shows that accelerated electrons will also show wave nature at higher speed which results in different wave phenomena in the TEM such as diffraction, interference, etc. [70–72]. These wave nature phenomena are responsible for contrast arising during the image formation, i.e., diffraction contrast and phase contrast [73]. The wavelength of the electrons can be calculated from the equation given below:

$$\lambda = \frac{h}{\left(2m_0eU \left[1 + \frac{eU}{2m_0C^2}\right]\right)^{1/2}}$$

h = Planck constant, 6.626×10^{-34} m² kg/s

m_0 = rest mass of electrons, 9.109×10^{-31} kg

U = accelerating voltages

C = speed of light in vacuum, 2.998×10^8 m/s

e = charge of electron, -1.602×10^{-19} C

5.2.5 *Imaging Contrast Mechanisms*

The essential parts of a transmission electron microscopy will be described in the following sections. In general, electron gun comprises the illumination system; electromagnetic lenses are used to control electron beam (condenser lens) and to form images (objective lens). The remaining necessary components are a viewing screen and a charge-coupled device (CCD) to record the images. The optical system is important for magnification, depth of field, and focus, but it is essentially useless for understanding obtained images. That's why it is necessary to realize all the possible contrast arising phenomena. In this way, we can determine whether a characteristic will turn out to be bright or dark in the image [74]. These contrast mechanisms can be categorized into three types, i.e., mass thickness, diffraction, and phase-contrast mechanisms. In an image, one or more mechanisms can induce considerable contribution for image formation. For example, in amorphous materials, mass thickness contrast can be more dominant mechanism than other two mechanisms. Similarly, diffraction contrast plays a vital role in low-magnification images, and phase contrast appears as major contributor in high magnification, along with other factors. Final image formation in any case depends largely on the electrons that are allowed to pass through the objective aperture because electrons blocked by the aperture do not contribute in image-forming process. That's why size and position of the aperture are very important for the contrast observed in the image. The position of the objective aperture decides about the imaging mode whether it is bright field (if aperture is at the center and allows unscattered beam to pass) or dark field (if aperture is positioned at the scattered electron beam) (Fig. 5.6) [75]. The abovementioned factors will be observed when we discuss each contrast mechanism separately below:

(i) Mass Thickness Contrast

This is the basic contrast arising mechanism that will be observed, when we introduce a sample into sample chamber. This contrast can arise from any type of sample such as organic, inorganic, biological, amorphous, and crystalline. In other words, any sample from which electrons can transmit will give you some contrast depending on its thickness. This contrast mainly arises when our objective aperture is positioned at the optical center, i.e., bright-field imaging. Sections of the sample with different thickness will show distinct contrast. Thicker or higher density parts will appear more dark as compare to thin sections [74]. This is because incident electron beam will be scattered more by thicker or high-density parts and thus produce darker contrast in the image (Fig. 5.7a). Example of such contrast can be seen in Fig. 5.7a. We can observe nanostructures on a commercial lacey carbon-

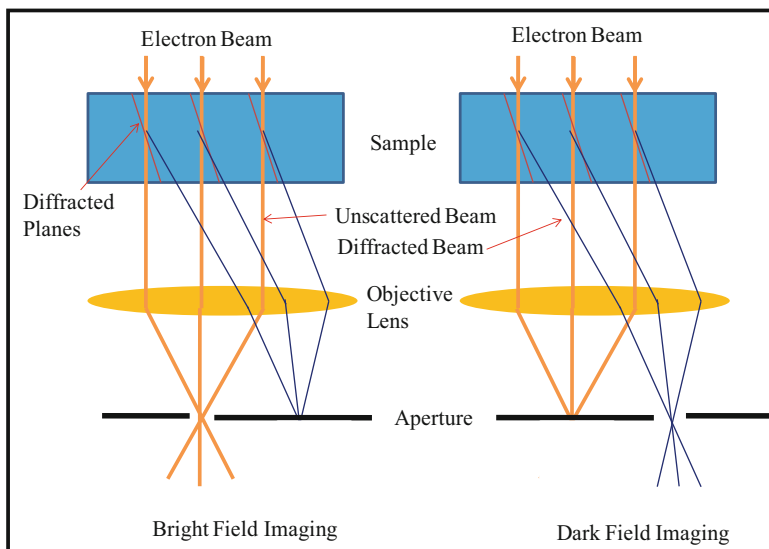


Fig. 5.6 Ray diagrams of bright-field imaging and dark-field imaging

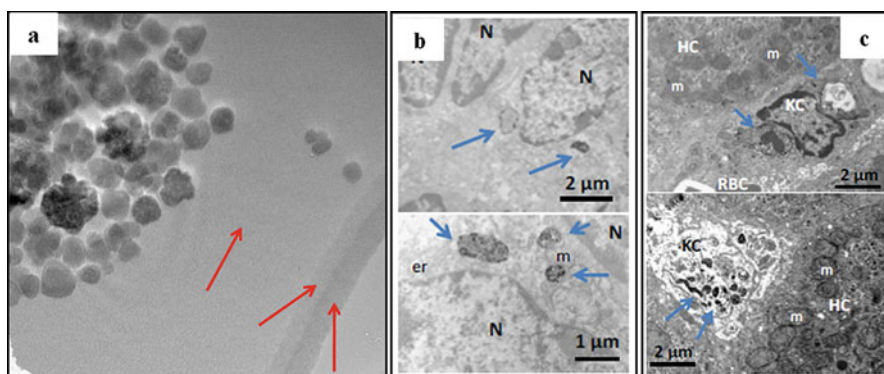


Fig. 5.7 Mass thickness contrast, (a) arrows showing different contrast of carbon film on the Cu TEM grid. (b) Low-resolution bright-field images of different organelles of the spleen, N nucleus, m mitochondria, er endoplasmic reticulum, (c) low-resolution bright-field images of different organelles of the liver, RBC red blood cells, HC hepatocytes, m mitochondria, KC Kupffer cells. (Reproduced with permission from Kolosnjaj-Tabi et al. [78] Copyright (2015) American Chemical Society)

coated Cu grid. As amorphous carbon is used for coating, we can observe different contrasts for three different sections of the carbon film (arrows indicating different dark sections). This difference in contrast is only due to different thickness of the carbon film [76].

As mentioned earlier, this type of contrast emerges in all type of samples, but it is mostly utilized in biological samples. Hydrated biological samples such

as different organs, the spleen, liver, and lungs, and their organelles are almost transparent to electrons (weak-phase object) (Fig. 5.7b, c). Therefore, this type of samples is coated or stained with a heavy metal such as osmium, lead, or uranium. Mass thickness contrast is more important in all type of samples; other types of mechanisms can add to it or can be more prominent in specific samples [77].

(ii) Diffraction Contrast/Amplitude Contrast

For crystalline samples, an additional contrast is developed, i.e., diffraction contrast. Diffraction is the property of wave nature in which waves spread out when passed through a narrow slit or opening. In crystalline samples, atoms are arranged in specific order, and spacing between them works as slits for electron waves. The intensity of scattering can be significantly affected by diffraction at specific orientations of the sample. In diffraction contrast, amplitude of the incident electron beam is affected in actual; that's why sometimes it is also called amplitude contrast. Extinction distance is one of the important factors that help in producing sharp imaging. Diffraction contrast largely depends on the atomic number of the material. Materials with high atomic number will appear darker as compare to low atomic number elements [79]. One of the examples is shown in Fig. 5.8 (Fig. 5.8c) where gold, due to its high atomic number, emerged as darker, whereas iron oxide evolved as bright. But at low magnification, diffraction contrast is not the only mechanism that produces contrast; there are other factors that can arise the contrast, and one can be misled by the conclusion. When talking about nanomaterials, particles from the same material can show different contrast due to their alignment with the electron beam (Fig. 5.8b). Particles or part of the particle that will be oriented exactly with the electron beam will appear dark. Figure 5.8b shows such contrast where iron oxide nanostructures can be seen with different contrasts. In conclusion, nature, thickness, and orientation with the electron beam can produce contrast in low-magnification images [80].

(iii) Phase Contrast

Phase contrast arises when electrons of different phases interfere with each other after passing through the objective aperture. When electrons behave as wave, there exist both the properties of wave behavior, i.e., amplitude and phase. As electron scattering involves both amplitude and phase change, therefore, amplitude contrast (more useful at low-magnification images) as well as phase contrast present in every image. Since we usually use very small objective aperture, even then at higher magnifications, phase-contrast component becomes noticeable. But we can make this phase contrast useful, if we allow interfering two or more diffracted beams after passing through the objective aperture. Therefore, a relatively larger aperture is used to obtain phase contrast. This can also be called interference contrast because here diffracted beams interfere constructively or destructively to produce the contrast [81]. Higher-resolution images of iron oxide nanocubes can be observed in Fig. 5.8d. Here contrast arises due to the interference of diffracted beams.

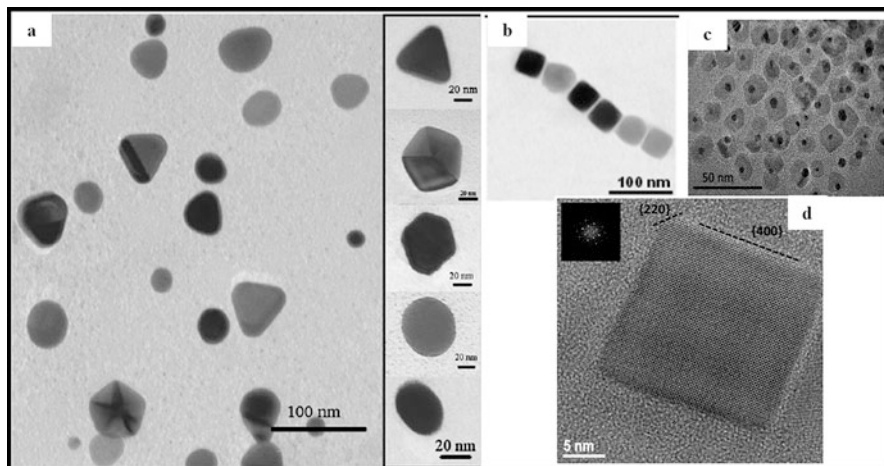


Fig. 5.8 Bright-field images, (a) different morphologies of nanoparticles. (Reproduced with permission from [82]), (b) different contrast of iron oxide nanoparticles due to alignment with the e beam. (c) Iron oxide-gold heterostructures; dark contrast belongs to high atomic number, and bright contrast belongs to iron oxide. (d) High-resolution iron oxide nanocubes where phase contrast is the dominant phenomena (inset showing fast Fourier transform (FFT) of the image). (Reproduced with permission from Kolosnjaj-Tabi et al. [78] Copyright (2015) American Chemical Society)

5.3 Instrumentation

5.3.1 Basic Layout and Components

Transmission electron microscope is an advanced scientific tool used for detailed imaging of very small objects by using electrons as illumination source. An intense electron beam is focused to irradiate the sample and the interaction between the electrons and atoms of test subject form a detailed and high-resolution image, with the help of which characteristics like size, quality, crystal structure, defects, and chemical composition can be observed. Electrons are very small and can be easily distracted from their path by contaminants and gases; that is why it is necessary to always use this source in vacuum. Various vacuum pumps are used to establish vacuum in TEM. Rotary pump, also known as roughing pump, is used to establish low vacuum range, and it is also used as a backing pump for other ultrahigh vacuum pumps, e.g., diffusion pump, turbo or cryopump, etc. The electron gun, used for extracting and controlling electron beam in illumination system, is of two types, i.e., thermionic emission and field emission. Field emission source is preferred for high-resolution imaging. After extraction of electron from the source, the electron beam is focused by lenses onto the sample, and extra electrons are filtered out by apertures. The condenser lens is used for focusing the beam and illuminating the test subject under observation. The objective lens, on the other hand, is used for

image formation. A CCD camera is set right below the screen to capture and store the image. In the next section, we will discuss these different parts in more detail.

5.3.1.1 Electron Sources

The basic purpose of a microscope is to present a clear and detailed image of the specimen, and it highly depends on the quality of source used for its illumination. The choice of the right source depends on many factors including type of material, requirement of image quality and resolution, etc. Two basic electron sources/electron guns are available for transmission electron microscope, thermionic emission gun, and field emission gun. In electron microscope, image is formed by focusing the beam of electron onto the specimen, and their resultant interaction is then transformed into an image showcasing the properties of that specimen. For the use of electron as a source, it is very important to have it completely under control. At the upper part of the TEM, an electron gun is located which basically serves as a source for electron supply. The beam of electron is energized to suitable high energy and then carefully bombarded onto the sample with the help of condenser lens, aperture, and diaphragm.

Thermionic Emission Source

One of the abovementioned sources of electron is based on thermionic emission. As the name depicts, it involves a heated source. For electrons to escape from a material, they need to have enough energy to escape the barrier known as work function. So, one way to provide that energy is to heat electrons. To simplify all the physics behind this thermionic emission, Richardson's law is used which shows a relationship between current density J (number of electrons per unit area per unit time) to the temperature of operation T :

$$J = AT^2 e^{-\phi/kT}$$

Here k is Boltzmann constant with value 8.6×10^{-5} eV/K, and A is Richardson's constant whose value varies with the type of material.

The equation shows that electrons are required to be heated more than work function (ϕ) to make them escape, but the energy supply of even few eV to the electrons of most materials usually initiates melting or vaporization. This limits the materials for thermionic emission process to only those with high melting point or low work function (ϕ).

For this purpose, materials mostly used are heated filament of tungsten or lanthanum hexaboride (LaB₆). For the former, a heated metal tungsten filament with melting point 3660 K is implemented which works similar to a bulb. High voltage is provided to the filament which in turn provides energy and helps the electrons to escape from the filament. On the other hand, LaB₆ crystals are also used for the

similar purpose. They have high efficiency and less energy is required for electrons to escape. The disadvantage of using this material is that it is prone to thermal shocks due to its thermal nature. Both heated filament and LaB₆ crystals work as cathode in the electron gun.

Field Emission Source

In the second source, the electrons are generated by field emission process. In this process, a needle-like tip is used as a source. Electrons are pulled out by creating a large electric field around the sharp tip. It is accomplished by reshaping a tungsten wire to a fine tip usually smaller than 0.1 μm and providing voltage of 1 kV. This results an electric field of 10¹⁰ Am⁻¹ which reduces the ϕ for extracting electron out of the sample. It can be shown in the following relation:

$$E = V/r$$

The type of material and its orientation matters a lot because production of high-intensity electric fields puts a lot of pressure on the tip and it can damage it easily. In the case of tungsten, <310> orientation is considered to be best so far. The surface should be free of any contamination and oxidation for this source to work efficiently.

Electron Guns

Thermionic Emission Guns

Nowadays for thermionic emission source, a triode gun is used in most of the TEMs consisting of electron source as a cathode, Wehnelt cylinder as a grid, and an anode with an opening in the middle. In case of thermionic source, LaB₆ crystal is attached with a wire attached to a high voltage supply, and due to this, the electrons that leave the cathode possess high energy and velocity. To control the beam of electron, a DC supply is added to the Wehnelt cylinder to bias it negatively so that electron can converge after they leave the cathode. The negative biasing and cathode heating can be controlled separately, or a self-biased gun can be used in which when the emission current increases, bias increases automatically. This goes on until the emission current attains saturation. The electron source is operated at or below saturation level (Fig. 5.9).

Field Emission Guns (FEG)

The working of field emission guns is way simpler than thermionic emission guns with field emission source as a cathode and two anodes. The first positively charged anode provides the voltage required for electrons to escape out of the tip, while

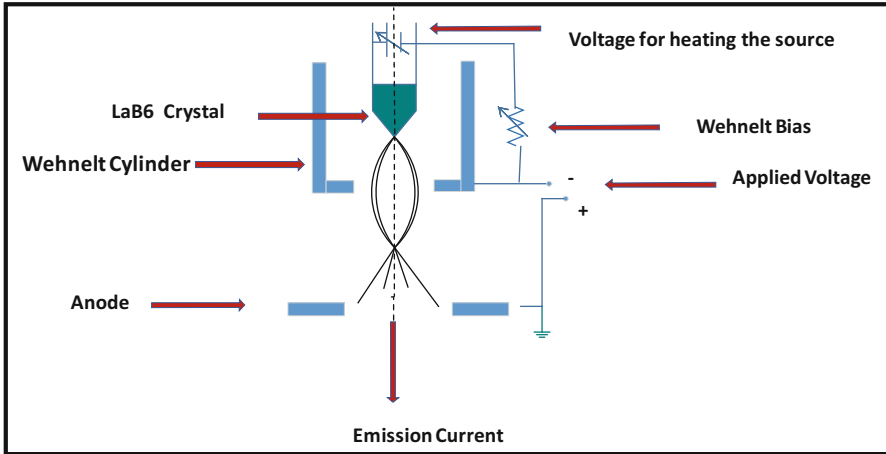


Fig. 5.9 Schematic of thermionic gun. (Reproduced with permission from Oshima et al. [83])

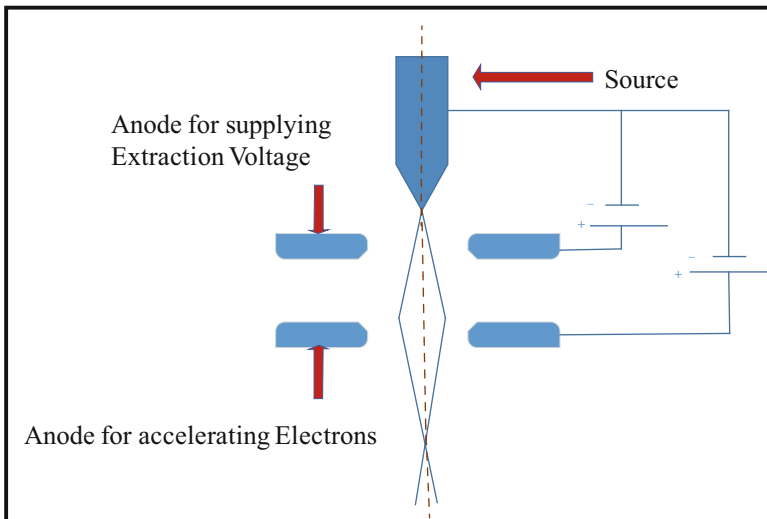


Fig. 5.10 Schematic of field emission gun. (Reproduced with permission from Williams and Carter [84])

the second anode accelerates them with high voltage. The supply voltage should be increased slowly to prevent any shocks (Fig. 5.10).

Comparison: LaB₆ crystal is the best thermionic source for many reasons including low work function, long life, high brightness, current density, and coherency. This super source also requires more precautionary measures and care because extra heating or saturation can destroy it.

Field emission sources are more monochromatic and give bright electrons, high coherency, and greater brightness than thermionic emission source which makes it a better option for applications like HRTEM, holography, etc.

In field emission, there is a significant difference between cold-field emission and hot-field emission source. The beam produced due to cold-field emission gun is spatially coherent as compare to hot-field emission gun (Schottky FEG), but hot-field emission provides more stability and less noise. Also, the setup for cold emission gun is expensive and requires high maintenance. In short, cold-field emission gun is best for high-resolution imaging, but for regular use hot-field emission gun is preferred because it is easy to operate and maintain.

5.3.1.2 Electromagnetic Lens

In transmission electron microscope, all the basic operations or functions are executed with the help of lenses. An aperture is used in lenses to control the current beam and converge the beam to hit the specimen. The main purpose of electromagnetic lens is to focus the electrons. In 1927, Busch successfully focused electrons by using electromagnetic lens. These lenses are very commonly used because of high-voltage susceptibility.

The formation of the electromagnetic lenses depends on two factors: one is the cylindrical core of soft iron with hole in it, called pole piece, and second is coil of copper wire wound over it. In most electromagnetic lenses, there are two pole pieces, and distance between pole pieces is called gap. The ratio of the hole in the pole piece and gap is critical factor to control the focusing action of the lens. The flow of electric current in the coil of copper wire develops magnetic field in the hole of the pole piece. As we know, copper coils produce heat due its resistivity increment; thus, water circulation system is essential to cool down lenses. It is a characteristic part of TEM lenses (Fig. 5.11) [85].

Several types of lenses are used depending on their function in TEM. The objective lenses in which upper and lower pole pieces have their separated coil system are more flexible. Due to separated pole piece coil system, the other instruments (e.g. X-ray spectrometers) can easily access the specimen. There are multiple characteristics of split pole-piece lens for specimen holders in TEM such as rotation, tilting, cooling, heating, and straining which increase the versatility of instrument. These split pole-piece lenses produce broad and fine beam of electrons for TEM and STEM, respectively. For the high-resolution TEM, there are some limitations such as we cannot tilt above its restricted range, e.g., snorkel lens. The strong lens is used for high resolution and their focal length is shorter for object. This is the essential part of high-resolution lens [87].

Electromagnetic lenses of different materials are being used depending on their characteristics and advantages in TEM. The ferromagnetic lens is less flexible rather than superconducting lens. There are some positive features of superconducting lenses.

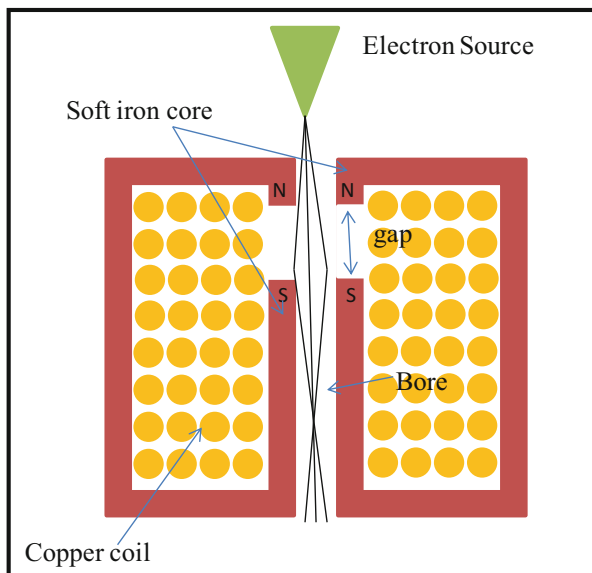


Fig. 5.11 Schematic of magnetic lens. (Reproduced with permission from Williams and Carter [86])

- These are very small and efficient.
- No need of any water cooling.
- These lenses cool the area around the specimen.
- These lenses generate fix field.

Some lenses are specifically used for electron spectrometer, and these lenses cannot be used in TEM. Such lenses are known as quadra-pole and octa-pole in which four and eight pole pieces are adjusted, respectively. These types of lenses are used to highlight the other lens defects. One of the major advantages of these lenses is that they use less power and do not induce rotation in the images [88]. There are four types of lenses generally used in the TEM for different purposes:

- (i) Condenser lens
- (ii) Objective lens
- (iii) Intermediate lenses
- (iv) Projector lenses

5.3.1.3 Vacuum Systems

Apart from the basic components, many other factors take part in the smooth execution of this technique, and vacuum pumps are one of the most crucial factors. A low vacuum level drastically affects the electron beam and ultimately the images

produced by TEM. Ultrahigh vacuum is necessary for longer mean free path and lesser collisions with the species present in the path between electron gun and sample. Another benefit of using high vacuum is that it keeps the test subjects clean and well-preserved. Therefore, to use TEM properly, it is essential to have complete knowledge about vacuum pumps and their working [10, 89].

The word “vacuum” literally means “space devoid of matter.” It is a Latin word which means “empty.” The definition of vacuum in other words is “create low pressure in an enclosed object as compare to surrounding pressure” [90, 91].

In quantum mechanics, vacuum is the space filled with gas having molecular density lower than 2.5×10^{19} molecules per centimeter cube at room temperature. It creates around 19 orders of magnitude of pressure less than atmospheric pressure [92, 93]. Few principle purposes for vacuum creation are:

- (i) To avoid molecular collisions
- (ii) To remove the effect of energy transferring
- (iii) To achieve pressure difference
- (iv) To produce clean environment in an isolated system

Brief history: The history of vacuum started from the Greek. In the fifth century (B.C.), the most famous philosopher “Empedocles” said that air is a substance by describing the concept of water clock [94, 95]. He concluded that air as a substance resisted the water flow inside the vessel. Aristotle declared in the next century that empty space can’t exist in nature. Later, the invention of syringes (Heron) and water pumps (Ctesibius) led to the physical concept of vacuum (empty space) [96, 97]. The credit for the invention of barometer goes to Torricelli (1644). Robert Boyle (1659) placed a bell in evacuated vessel of glass and proved that sound could not cross in vacuum. However, magnetism, light, and heat can pass through the vacuum [97–102].

Boyle (1662) formulated the pressure volume law of ideal gases. However, before the nineteenth century, vacuum technology was becoming a famous topic in scientific inventions. But in the nineteenth century, vacuum pump was the focusing invention in industrial development. Faraday investigation of conduction of electricity through vacuum led to the invention of tube lights and electric bulb. In the twentieth century, Wolfgang Gaede (German physicist) invented vapor diffusion pump and rotary vane mechanical pump [103, 104].

Vacuum Units

There are different vacuum units used for the description of vacuum level. The normal atmospheric pressure on the surface is 760 mmHg. In 1958, the term “mm Hg” was replaced by “Torr” by the honor of Torricelli [5, 105]. The basic unit of pressure in system international (SI) units is Nm^{-2} . This is also named as “pascal.” In CGS, the “dynes cm^{-2} ” unit is used for pressure. This is also called microbar. In French literature, the “barye” is used for microbar. For the units “mill bar,” the

name “vac” was proposed. In MKS, the Newton per meter square (pascal) is used for pressure.

$$1 \text{ pascal (Pa)} = 1 \text{ Nm}^{-2}$$

In British system of units, the pound-force per square inch (Psi or lb-in⁻²) and in MTS (meter-tonne-second), the unit of pressure is called “pieze” (1pz = 10³ pa) [5, 106, 107].

So,

$$1 \text{ atm} = 760 \text{ torr} = 1.013 \times 10^5 \text{ Nm}^{-2}$$

And

$$1 \text{ torr} = 1 \text{ mbar} = 1.333 \times 10^3 \text{ dynes cm}^{-2} = 133.32 \text{ Nm}^{-2}$$

Types of Vacuum

The working technology in three different vacuum regions is distinguishable. These regions are described as follows:

1. Low vacuum
2. High vacuum
3. Ultrahigh vacuum

We know the atmospheric pressure is equivalent to 760 Torr. In low vacuum, we can achieve pressure lower than 760 Torr [108]. The particle number density in this region is greater than 10¹³ cm⁻³, and mean free path is less than 10¹ cm. Collision frequency per cm³ is above 10¹⁷ s⁻¹. Roughing or rotary pumps are used to obtain this vacuum level. The quality of vacuum pumps enhances to achieve lower pressures. In high vacuum region, the particles in the vacuum vessel can travel without colliding with each other [109–112]. The range of this region is 10⁻³–10⁻⁷ Torr. The particle density range is 10¹³–10⁹ cm⁻³. In this range, the nature of gas flow is molecular in which mean free path is less than 10³ cm. The collision frequency per cm³ is 10¹⁷–10⁹ s⁻¹. However, in ultrahigh vacuum, the formation of monolayer takes more time, and the range of pressure is 10⁻⁷–10⁻¹⁸ Torr. The density of particles in this vacuum range is less than 10⁹ cm⁻³. The mean free path is greater than 10³ cm in this region. The nature of gas flow is also molecular, and the collision frequency per cm³ is less than 10⁹ s⁻¹ [113]. Vacuum pumps with their vacuum range are shown in Table 5.3.

The most common roughing pumps used these days are mechanical rotary vane pumps. The basic components of this pump are rotor, vane, inlet valve, and working chamber. This is divided into two parts due to rotor and vanes. The eccentric motion of the pump creates a vacuum in the right-hand side when it rotates and the vacuum sucks air into the inlet valve. As the cylinder rotates further, it cuts off the inlet and

Table 5.3 Different vacuum pumps and their ranges

Pumps category	Range of operation (Torr)
Single-stage gas ballast pumps (oil sealed) [114]	$<10^{-2}$
Two-stage gas ballast (oil sealed) [115]	$<10^{-4}$
Roots	10^1-10^{-4}
Mercury vapor pumps [116]	10^0-10^{-6}
Sublimation pumps [117, 118]	$10^{-2}-10^{-5}$
Turbo-molecular pumps [119]	$10^{-1}-10^{-9}$
Mercury diffusion pumps [120, 121]	$10^{-3}-10^{-10}$
Sputter-ion pump [122, 123]	$10^{-3}-10^{-11}$
Cryopumps [124]	$10^{-3}-10^{-12}$

forces the air through the outlet on the left-hand side, creating a vacuum again on the inlet side as it does so. Because of the constant contact between the rotating cylinder and the inside of the pump, oil is needed to reduce frictional heating. Some of the benefits of using these pumps are low cost and easy to operate, but they are unhygienic to some extent, and the risk of contamination is very high due to the use of hydrocarbons. The pump and the exhaust line should be secured properly for safely using these pumps. There is also another option of using the dry pumps instead of oil ones to avoid contamination, but these pumps cost a lot. The roughing pump is usually used as a backing pump for the diffusion pump to achieve low pressure of approximately 10^{-4} Torr [111, 125, 126].

The diffusion pumps are used to attain high vacuum. The gas molecules are transferred from inlet to outlet. This pump incorporates a hot plate to heat up oil, and the resulting vapors are dragged upward by means of jets or nozzles. These vapors fall onto the cool pump walls and condense due to low temperature which leads to the withdrawal of air molecules by the backing pump (roughing pump). The diffusion pump apparatus is simple and easy to use, plus it is capable of transferring hundred liters of air in an hour which makes it more suitable for TEM. The working of these pumps mainly depends on the hot plate and the cooling mechanism, so as long as these two things work perfectly, diffusion pump remains in excellent condition.

Another type of pump, known as turbo-molecular pump, can also be used in TEM [127–129]. This pump uses a turbine for the transfer of the molecules. This pump works at about 20,000–50,000 rpm speed, but the pump achieves the high speed gradually after starting, and the speed keeps increasing and pressure keeps on getting low, and after some time ultrahigh vacuum is achieved. It is safe to use because it does not distort the image quality due to negligible lens vibrations [129–135].

Ion pumps are also considered to be a wise option for achieving ultrahigh vacuum. As the name indicates, they depend solely on the process of ionization, so the risk of contamination can be eliminated completely [135, 136]. In this type of pump, electrons are emitted from a titanium cathode which spread these ions across the magnetic field, and in return ionization of gas and other molecules takes place [137–139]. After ionization, these molecules lead to the cathode to lay them rest by

using kinetic energy. On the other hand, active molecules are chemisorbed (a form of adsorption with chemical bonds) by titanium deposited on anode. The quality of vacuum depends on the current between electrodes. Ion pumps are especially known for ultrahigh vacuum, and it works efficiently in the range of 10^{-11} Torr [140–144].

Cryopumps are being widely used for removing air molecules in TEM. The working of these pumps depends entirely on the condensation process, and excess of liquid nitrogen is required to lower the temperature to 20 K or below. These pumps can be used to achieve a low pressure of about 10^{-12} Torr. They are mostly used for backing ion pumps and for eliminating contamination risks due to their oil-free nature. These pumps are also used to increase the vacuum quality in TEM without ultrahigh vacuum. These pumps are excellent for use because of low-temperature operating conditions and keep other contaminants at bay by condensation. Table 5.4 provides information about different vacuum pumps according to their requirements [145, 146].

TEM requires multiple vacuum pumps because the requirement of vacuum is different for different sections. In simple TEM, one type of pump is required specifically for the evacuation of column, and other pumps are required for creating the vacuum for camera and screen chamber. Illumination system of TEM always remains in ultrahigh vacuum, while only sample insertion part is exposed to atmospheric pressure [147, 148].

5.3.1.4 Electron Detectors

TEM employs electrons as interacting source to display images of the test subjects. So, the resultant images are nothing but mere conversion of electron intensity to the visible light because electrons are invisible to the naked eyes. After preparation of sample and then passing it through TEM, the final and most important step is to record and store the sample information in the form of image or spectrum [149, 150].

The first step, i.e., electron detection, is performed by using electron detectors. Several types of detectors are available with different specifications. It is very important to study the nature and requirement of TEM in detail before selecting the right detector. In conventional TEM, it is easy to focus the image on the screen within the required area due to the static nature of incident beam. As a result, fixed analog image is obtained which rules out any chance of manipulation of image during the detection. Viewing screen holds a great importance in this regard, and it can lead to various changes in the image itself [30].

The electron can never be in static condition, and our eyes can never see electrons without a phenomenon called cathodeluminescence (CL). So, instead of the naked eye, cathodeluminescence is the electron display system which depends on the physical existence of electron. Then the screen displays the emission of light spot due to intensity of an electron or more than one electron falling on it [151].

Table 5.4 Vacuum pumps and their attributes

Attribute	Pump type	Dry roughing pump	Diffusion pump	Turbo-molecular pump	Cryopump	Ion pump
Basic component	Oil rotary pump	Dry roughing pump	Diffusion pump	Turbo-molecular pump	Cryopump	Ion pump
Main part	Hydrocarbon oil	Oil or fluid free	Vapors	Oil or fluid free	Liquid nitrogen	Ions
Reliability	Rotary vane	Self-lubricating rotary vane	Hot plates	Turbines	Molecular sieves	Ion pumps
Type of pump	Reliable	Unreliable	Reliable	Unreliable	Reliable	Reliable
Type of vacuum	Exhaust pump	Exhaust pump	Exhaust pump	Exhaust pump	Trapping pump	Trapping pump
Max. pressure	Rough	Rough	Ultrahigh	Ultrahigh	Low	Low
Pumping speed	10^{-4} Torr	10^{-1} Torr	10^{-1} – 10^{-9} Torr	10^{-2} – 10^{-8} Torr	10^{-6} Torr	10^{-3} – 10^{-5} Torr
	0.7–275 m ³ /h	0.6–10 m ³ /h	50–5000 l/s	10–50,000 l/s	1200–4200 l/s	1000 l/s

The three effects imply, given as follows:

- (i) Emission of light is caused by the scintillation of ionizing radiations.
- (ii) The fluorescence process implies due to rapid emission.
- (iii) The wavelength and delay time both are greater for phosphorescence rather than fluorescence.

The detector which is used for the detection of electrons might be linear in its response; then its “Detection Quantum Efficiency (DQE)” can be defined as

$$\text{DQE} = \frac{(S/N)_{\text{out}}^2}{(S/N)_{\text{in}}^2}$$

“S/N” is the signal-to-noise ratio for output and input signals.

- (i) The perfect detectors have their DQE equal to one, which is also the maximum value.

$$\text{DQE}_{\text{perfect}} = 1$$

- (ii) All practical detectors have DQE less than one.

$$\text{DQE}_{\text{practical}} < 1$$

The electron detectors also play an important role in STEM and scanning electron microscope (SEM). There are several detectors which are being alternatives to fluorescent screen detectors.

There are two major types of electron detectors:

- (i) Semiconductor (Si p-n junction) detectors
- (ii) Scintillator-photomultiplier detectors

These detectors are also known as charge-coupled device (CCD) [152]. It was first introduced in 1970 by Boyle and Smith as a first charge-coupled semiconductor “BS70.” Its structure depends on the silicon substrate in which $\sim 10^{15}$ acceptor atoms per cm^3 are added by lightly doping. This substrate acts as a p-type semiconductor. The silicon dioxide layer of 100 nm is added on the top of substrate which relates the voltage “V” with metal gate [153].

Modern CCD consists of 4096×4096 detector elements, and each element dynamic has a range of 12, 14, or 16 bits. Single image of modern CCD detectors can occupy 32 Mb of memory or even more. As mentioned above, many types of electron detectors are available apart from fluorescent screens for the detection purpose. All the detectors available in market right now are either made of semiconductors or scintillator-photomultiplier systems [155, 156].

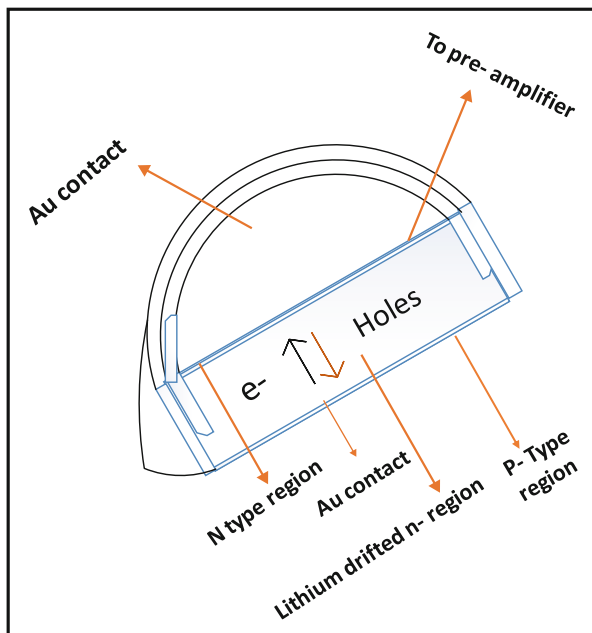


Fig. 5.12 Schematic of semiconductor detectors. (Reproduced with permission from Williams and Carter [154])

Semiconductor Detectors

Semiconductor detectors are made up of silicon and transform it into an electron detector by creating a p-n junction which takes place as a result of doping of silicon with impurities. Another type of detector named as surface barrier detector is formed by slight dispersing gold onto the p-type silicon or aluminum onto the n-type silicon. This dispersion acts as a key for the formation of p-n junction (Fig. 5.12) [157].

When this detector comes under an electron beam, it energizes the electrons in the valence band and transfers it to the conduction band. As a result, electron-hole pairs are formed which are then separated by applying reverse bias potential. However, it is usually not necessary in TEM because of the abundance of the electron-hole pairs in TEM, and their internal potential is more than enough for the division of electrons and holes. This detector quickly responds toward the electron beam and amplifies it. About 3.6 keV are required to create one electron-hole pair, and as a result 100 keV can create 28,000 electron-hole pairs, thus providing overall gain of 3×10^3 ideally [158, 159]. These detectors don't respond well to any change in the signal. So, overall semiconductor detectors are simple, cheap, and easily available, but they have many disadvantages too. Due to light falling or thermal activities, dark current arises in case of uncoated metal. Under this condition, these detectors work in TEM as an Ohmic conductor. Therefore, liquid nitrogen temperature reduction becomes

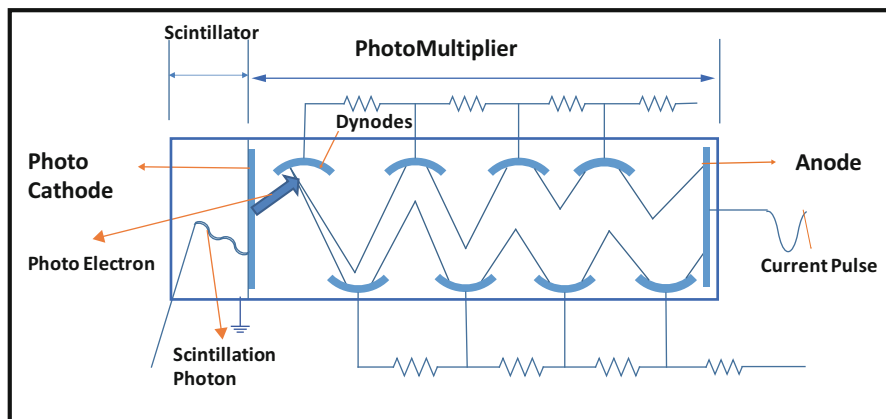


Fig. 5.13 Schematic diagram of scintillator-photomultiplier detector. (Reproduced with permission from Williams and Carter [154])

essential to remove thermal effect. Its DQE is very poor for low-intensity signals and maximum for high-intensity signals. These detectors are very sensitive to electron beam which can damage it due to deeper depletion region in silicon. These detectors are not sensitive to low-energy electrons also called secondary electron [160, 161].

Scintillator-Photomultiplier Detector

A scintillator is a material that emits light when bombarded with electrons. Scintillator detector works on the same basic principle. A good detector is one which produces light continuously and responds immediately to the changes in the signals (Fig. 5.13). Both inorganic and organic material-based detectors are available. In inorganic materials, Ce-doped yttrium aluminum garnet with decay time approximately nanoseconds is preferred for these detectors. After the conversion into visible light, the signal is further amplified by using photomultipliers. This type of detectors is used for the detection of secondary electrons in TEM and primary electrons in STEM. An additional coating of aluminum on the photomultipliers is used to stop the light from wandering around and causing noise. Scintillator has high gain, low noise, and high bandwidth which means it is capable of producing low-intensity images easily. On the other hand, it is not very durable and can easily be damaged by radiation. Also, it may cost more than the semiconductor detector and a bit hard to fit inside TEM because of its shape and size, while its efficiency to convert energy is lower than semiconductor detector. Scintillator detector is used more widely than the semiconductor detector, but high-intensity signals must be avoided to refrain it from damage [162, 163].

Unlike the abovementioned detectors, in TEM, the use of fluorescent screen becomes minimal because television (TV) cameras are taking their place gradually.

TV cameras are preferred because of their easy transmission and recording options. Both analog and digital TV cameras are used in TEM. CCD are one of the most exceptional examples of the abovementioned TV cameras. These cameras are metal insulator silicon piece of equipment implementing millions of pixels made up of electrically separated capacitors. They store the charge emitted by light or electron beam solely based on its intensity. These CCD detectors are used in telescope, very large in size and expensive with giga pixels. For TEM, CCD can be as big as 4000×4000 -pixel size. The size of one cell can be as small as $6 \mu\text{m}$ and mostly it lies in the range of $10\text{--}15 \mu\text{m}$. The size of the image and the nature of the system used for interpreting the signal play an important role in determining the frame time. One of their major drawback is called blooming which is caused by storage of many signals in one pixel. Overall, it is one of the best options to detect and store signals for TEM [164, 165].

5.3.1.5 Filters

When a specimen is subjected to a beam of electrons, most of them succeed in passing through it unaffected, whereas others scatter elastically or inelastically. Many electrons suffer from energy loss and change in momentum due to inelastic scattering. These inelastic electrons tend to cause a lot of problems in the final image including noise and damaging the contrast effect. The type of specimen is very important in this regard. Bulky specimens are preferred in TEM for their ability to increase vibrant effect in the pattern, but the disadvantage of their use is that the inelastic electrons cover the contrast effect in their presence. The importance of thick specimens couldn't be denied, so, scientists decided to find a way to get rid of the inelastic electrons, and that is where energy filters came in. Energy filters are used to remove inelastic effects when working in TEM mode. Two types of energy filters, named as in-column filter and post-column filter, are used for sorting out electrons of required energy [30, 166]. In TEM, in-column filter is usually sandwiched between intermediate and projector lens so that the detector will only receive electrons of required energy approved from the filter or succeeded in passing through the filter. We can turn it on or off per our requirement. These filters can also be used for developing a spectrum apart from imaging and diffraction patterns. In-column filters are effective in order to get better contrast images; that's why they are contemporary part of modern TEMs. On the other hand, post-column GIF (Gatan¹ Imaging Filter) is placed after the viewing screen, and the position of this filter permits us to perform energy-filtered microscopy called EFTEM. Omega filter is a magnetic filter with magnetic prisms arranged in the shape of alphabet O. The omega filters require specific balance of voltage between mirror and gun to operate. This type of arrangement was first implemented in a TEM by Zeiss², and now

¹Manufacturer of instruments and softwares for TEM.

²TEM manufacturing company.

JEOL³ is also using this arrangement. The magnetic prisms in the filter scatter electron away from axis and fetch them back before the electrons go through the projector lens. The specific electrons that can pass through the slit of spectrometer are used to produce the image [167].

5.3.1.6 Apertures

Apertures are holes made of thick metallic disks called diaphragms. Both aperture and diaphragm act as a team that can easily stop the electrons from passing through them. Only the required axial electrons are allowed to pass because apertures minimize their intensity to save the sample from excessive irradiation. Apertures allow us to choose specific electrons, i.e., elastic or inelastic electrons according to their imaging modes, i.e., bright-field imaging or dark-field imaging. This setup also prevents contaminants from reaching the specimen. These contaminants are collected on the diaphragm and often results in ruining the aperture boundary. So, it is very important to clean the aperture and diaphragm regularly or use a foil on the surface to remove these contaminants by heating up. This heat can also end up destroying the surface of diaphragm or making gaps in it. The image resolution, intensity, and other major factors highly depend on the correct use of aperture and diaphragm. Diaphragms come in various shapes and sizes. Some diaphragms are equipped with one aperture, while other diaphragms are seen to contain various apertures. The most commonly used diaphragms with one aperture are made of Mo or Pt with 25–50 μm thickness [168, 169].

5.3.2 *Functional and Operational Procedures*

Although functioning and operational procedures can differ according to model and manufacturing company, basic alignment steps and procedure remain nearly similar. Alignment of the TEMs starts from top to bottom approach, i.e., gun alignment, beam alignment, etc. The operational and alignment procedures which will be presented here are based on JEOL company-based TEM.

Procedures before starting alignment:

- Vacuum check of the TEM, vacuum should be under 10^{-5} Torr.
- Confirm operating voltage, 80–200 KV.
- Fill the dewar of EDX detector with liquid nitrogen.
- Turn ON electron gun (flash high) (use this option only once at the start of the work for specific day).
- Check vacuum level of illumination part and it should be less than 10^{-9} Torr.

³TEM manufacturing company.

TEM Alignment Part

For microscope alignment, a clean and unused copper grid can be used. Put the TEM grid in the sample holder:

- Sample insertion.
- Introduce sample holder.
- Press pump and wait for yellow light to turn ON (primary pumping).
- Further insertion of sample and wait for good vacuum, i.e., less than 5×10^{-5} Torr in sample chamber.
- Emission controller.
- Emission ON.
- Load C if image is out of focus.
- Open Gatan digital micrograph (interface to observe produced images).
- Insert condenser aperture.
- Alignment.
 - Gun alignment.
 - At 100 k magnification, Anode wobbler, go to Anode = gun align tilt (use Def button or function from the TEM interface to set).
 - Gun shift.
 - Move to Spot 5 (use Gun shift) for beam align.
 - Move to Spot 1 (use Gun shift) for gun align.
 - Repeat process until beam is not stable.
 - Remove condenser astigmatism.
 - Go to 800 k or maximum magnification.
 - Make the beam spherical; then focus the beam (make the intensity of the arms of the beam symmetrical).
- HT wobbler.
 - Find a detail (group of nanoparticles, etc.) on the grid.
 - Press standard focus button twice (STD focus).
 - Set x and y and then set HT wobbler.
 - Magnification ~ 200 to 250 k.
 - Find right z position.
- α detector.
 - TEM-L mode
- Pivot point.
 - At 150 k.
 - Set tilt x .
 - Set tilt y .
 - Beam spread should be clockwise.

This completes the initial alignment procedure for conventional TEM. The next steps will describe the alignment of diffraction.

- For diffraction
 - Spread the beam completely.
 - Shift to diffraction mode.
 - Go slightly underfocus. Two triangles will be observed (use IL STIG button to overlap the two triangles).
 - Check HT wobbler again. Set HT wobbler and triangle overlapping simultaneously.

Now your TEM is ready for observation of microscopy and diffraction. There are additional settings associated with TEM if we have aberration-corrected TEM. Further settings are associated with Cs-corrected TEM from JEOL.

- Cs correction.
 - At 800 k, select a contamination-free carbon area on the grid.
 - Shift to “screen” mode.
 - From correction software, go to process-live FFT,
 - To set astigmatism, diffractograms at different tilt angles should be the same, and rings should be circular (for adjustment use OBJ STG setting should be STAG A1).
 - At standard focus, use z position at zero focus to set rings.
 - For circular rings, beam should be underfocus.
 - !!! Stop digital micrograph camera; otherwise system will be crashed.
- Go to CEOS corrector software.
 - Confirm that you are at the same magnification on the corrector software as on machine.
 - Go to Dialogue-Config-Check magnification of corrector software,
 - If magnification does not match, then there is a bug (this happens sometimes).
 - Communication Problem: go to My Computer – Manage – Services and applications – Service – Microhandler (restart)
 - Press A1 and then press tableau.
- Correction values for different variables:
 - $C1 \sim -150$ to -250 nm (this value should be between half and one third of the maximum value of C1 showing on the screen)
 - $A1 \sim 1$ nm
 - $A2 < 100$ nm or better under 50 nm
 - $B2 < 100$ nm or better under 50 nm
 - $C3 < 1-3 \mu\text{m}$ (if -ve value is observed, then there will be reverse imaging)
- Second-order corrections.
 - $A3 < 1 \mu\text{m}$
 - $S3 < 1 \mu\text{m}$

- Tilt angle should be greater than 18 mrad.

At the end, check rings again.

Precautions!!!

- Never go to low magnification, when EDX detector is inserted.
- Never close the CEOS corrector window.

For taking a diffraction image

- Inset SA aperture.
- Camera length 25–30 cm (this length is already set during installation and calibration of microscope; therefore, you will not do anything with this, but you should know this value).
- Use PL align to center the diffraction.
- Binning should be 4.
- Exposure time should be very less ~ 0.05 s.
- Stop beam by beam stopper.
- Use beam align to center the beam under beam stopper.
- Spot size should be 5.
- Take the image.

After finishing the work:

- Close the valve (i.e., beam).
- Emission off.
- Stage neutral.
- EDX retracted.
- At weekend, set voltage to 160 KV or set at standby (only do one thing).
- If liquid nitrogen is used, go to maintenance and press ACD heat (do this after removing the sample).
- Inset the resistance in the nitrogen chamber.

5.3.3 Sample Preparation

Sample preparation is a very critical part of TEM and it must be done with precision. This segment is dedicated to the suggested methodology. In specific, it presents the approach to select the appropriate method considering the available material, its type, construction, and properties. The study of the physical and chemical processes which evolved during different types of preparation methods allows us to detect the artifacts that might be left behind otherwise. When highly accelerated electrons move in a high vacuum, they transmit very small sample thickness. The aim of the sample preparation is to solve both of these problems: the sample stability under vacuum and its thickness (order of 100 nm) [170].

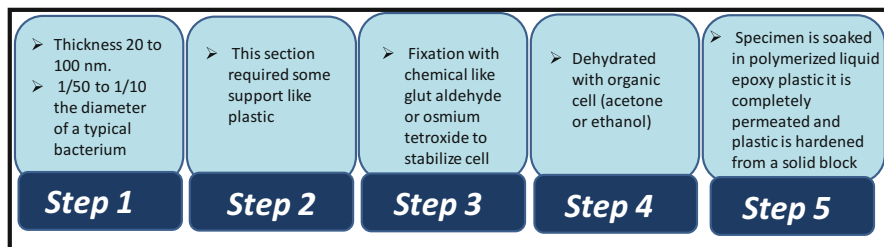


Fig. 5.14 Typical steps for a biological sample preparation

However, this is not the case for hydrated samples because most of the materials are solid and stable under vacuum. For biological samples, water must be restrained by converting it into ice or removed (Fig. 5.14). In order to prevent variation in original construction by transformation, it requires a complex technique. The classical preparation methods for samples studied in TEM require thin elements or a fine powder made up of discrete particles with thickness in the range of few nanometers [171].

5.3.3.1 Basic Criterion for Successful TEM Sample

For obtaining a thin slice, numerous preparation methods comprising different interaction mechanisms have been devised to make them visible in the TEM. In some mechanisms, only disruption of material is involved, or sample remains close to its initial state, while others involve the abrasion or termination of the material. Physical, chemical, and mechanical variations take place in some cases, while in others, it is essential to vary the properties of material or physical state or involved ionic movements.

In order to acquire a thin slice, usually different types of actions are combined during the preparation stages (Fig. 5.15). The mechanical movements contain actions like rupture or abrasion. Abrasion of the material surface by ionized particles is called an ionic action. Other actions are chemical action, which have two kinds: dissolution and bridging reactions. One mechanism for restraining the structure includes adjustment of its physical state with the help of freezing. And final mechanism, either physical or chemical, contains additional particles to allow topographical investigations or contrast development. These actions can vary the construction and can go as far as to convert its physical state and organization of the material.

One of the major limitations is sample thickness. In case of high-resolution imaging, the optimum thickness for energy-loss analysis is 50 nm, whereas thickness can extend up to 200 nm for bright-field and dark-field imaging. For high-voltage microscopes, optimum range is between 5 and 20 nm. In case of light elements, sample thickness can be between 50 and 100 nm for bright-field imaging mode. Excessively thin samples suppress contrast, while excessively thick sections lack description.

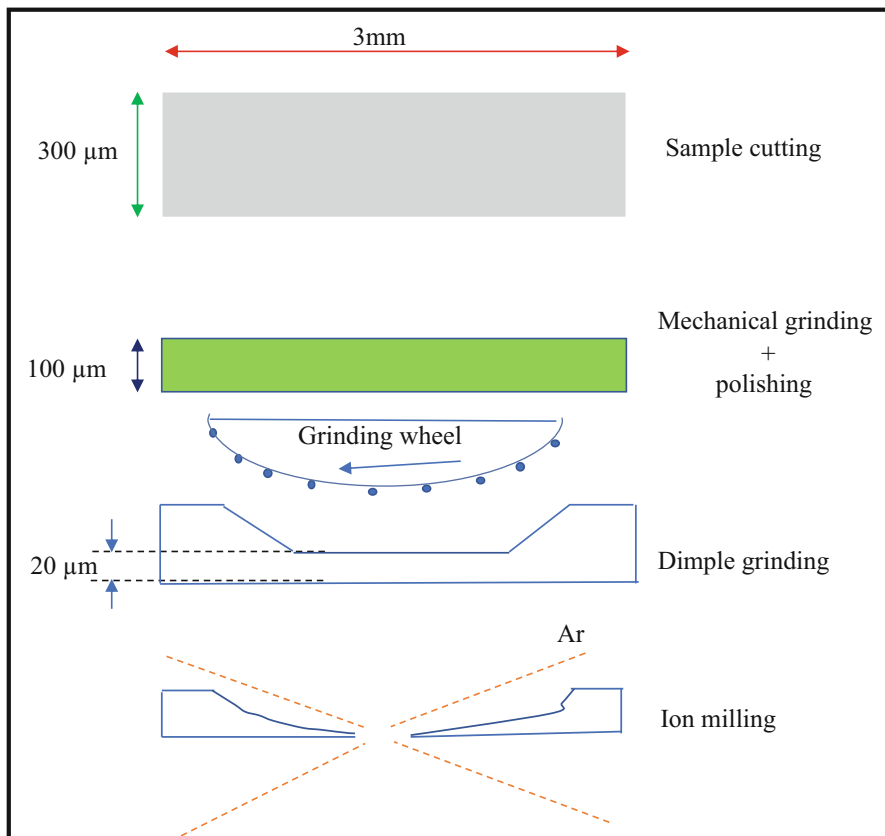


Fig. 5.15 Schematic of different sample preparation steps for bulk sample. (Reproduced with permission from Bakhsh et al. [182])

5.3.3.2 Different Preparation Methods

TEM specimens obtained from different sources can be prepared by the following techniques.

Mechanical Action

Abrasion Principle

Abrasion causes the removal of matter associated with substance. Loss of matter can be induced from microcracks or fissures or by a tool. There are three components involved in this preparation method: the material, the abrasion, and the emollient.

This physical action depends on applied stress, rate of erosion, and tool nature. The abrasion mechanism can induce different depths in the sample depending on its mechanical properties. This change is more prominent in ductile as compare to brittle materials. Different stress applied during this process can produce various defects: dislocations, twinnings, microcracks, etc. Thermal effects produced can also cause localized re-fusion, transformation, or phase change. In this following section, we will discuss different techniques where mechanical abrasion is involved. Techniques which involve cutting by means of mechanical abrasion are discussed below [172, 173].

Abrasive Techniques' Initial Step: Sawing and Grinding

Abrasion involves directional cutting of the material into two or more parts. This includes sawing, use of cutting tool, ultrasonic grinding, and machining by electrical discharge. The stresses originate cracks in the material at different depth which leads to complete cutting [174]. Sawing uses a disk or wire having abrasive grains of different kinds (diamond, carbides, etc.) and variable gratings. Water or oil is used as lubricant to reduce temperature and eliminate abraded grains [175]. Ultrasonic cutting is achieved by using hollow cutting tool of required form. An ultrasonic generator is attached to form wave. By placing the abrasive grains on the sample surface, the ultra-sonicator vibrates the tool and applied pressure. This pressure is used to cut the sample [176].

The selection of experimental parameters varies with the attributes of the tool and nature of material. This initial cutting process produces defects and must be eradicated by making sample thinner. On the other hand, this process creates more defects and is difficult to remove during final preparation stages [177].

Abrasive Techniques' Final Steps: Mechanical Polishing, Dimpling, and Tripod Polishing

The abrasion grains of reduced size up to $0.025\ \mu\text{m}$ are used to control surface roughness. Polishing disks with carbide grains of different sites ($60\text{--}7\ \mu\text{m}$) are being used in mechanical polishing. This is followed by diamond abrasion of reduce grain size ($6\text{--}0.1\ \mu\text{m}$) diamond paste [178].

Similar diamond paste is used for dimpling process; however, final polishing is performed by using some colloids, e.g., silica. In tripod, diamond (alumina) grains are fixed in the support and cannot move. This is good for unidirectional polishing. Even with best conditions used for mechanical polishing, there are always leftover microcracks at the final stages of polishing. These can be removed by using additional ionic and chemical polishing so that defect free thin slice can be observed in TEM [179].

Chemical Action

Principle of Chemical and Electrochemical Dissolution

This method involves dissolution by redox reaction of the sample in the chemical solution. An electrical voltage is established on the liquid sample interface which induces dissolution process [180]. This process is similar to electrochemical polishing due to interplay of ions and electrons at the surface. Dissolution in this method is very fast (50–500 $\mu\text{m}/\text{min}$). Electroplating is anodic dissolution of the material using controlled voltage. Its dissolution processes can be divided based on complexity and many other factors [181].

Chemical and Electrochemical Dissolution

Preliminary Chemical Polishing Preparation and Chemical Thinning Technique

This preparation method is used for electrical insulator material, e.g., oxides, glass, etc., and conductive material have the ability to dissolve chemically [183]. This method is useful for multiphase materials due to poor control on the process. Elevated temperature and highly reactive solutions are needed as compare to electropolishing. It is employed to polish surface to reduce surface roughness and remove microcracks [184].

Preliminary Electropolishing Preparation and Electrochemical Thinning Technique

This method is used for electrically conductive samples. It is performed in low temperature to avoid explosion or fire threat. However, low temperature influences thickness of layer, rate of polishing, and quality. The sample is usually placed in the solution or between two nozzles. These nozzles direct the electrolyte solution to both sides of the samples [185].

The surface of the sample achieves equilibrium voltage in the absence of external action. A potentiostat or electrical generator is used for controlling the potential during electrochemical process. With constant potential increase, a fixed dissolution current is established for each value, and current/voltage curve can be drawn [186].

Ionic Action

Ionic Abrasion Principles

This action is based on the interaction between sample material and ionic species. An electrical discharge is used to produce ions which then accelerated by applying acceleration voltage and directed toward the required part of the sample. The ions strike the atoms of the sample and displace them with sufficient energy. These atoms further collide and tore atoms from the surface. This process is called pulverization. The ratio of total atoms displaced to the total ion incident gives the output of the

pulverization. Generally, output relies on the minimum threshold energy (>40 eV) of the incident ions to expel the atoms [187].

In the voltage range (2–30 keV), the output reaches to maximum where an ion can tear 1–50 atoms. But if energy is too high, ions absorb into the material. This happens usually with light atomic weight materials [188].

Techniques Involving Ion Abrasion

Ion Beam Thinning and Focused Ion Beam Thinning (FIB)

Ionic action carries out in vacuum range 10^{-4} – 10^{-5} Pa. Ion guns consist of an ionization source chamber and acceleration voltage. Specific area of the sample can be thinned by focusing the produced ion beam [189–192].

An inert gas is generally used to avoid any chemical reaction with the sample. The gas with high atomic weight such as argon is used so that it can pulverize heavy atoms. Gas used should also be not the part of the sample material so that implantation can be identified. Sometimes, a mixture of an inert and a reactive gas is used so expedite abrasion or minimize artifacts [184]. The typical acceleration voltage lies in the range of 100 eV to 10 keV [193–195]. The higher voltage can abrade material more rapidly, but this causes high percentage of artifacts. Therefore, lower voltage is a better option for ionic action. Liquid nitrogen cooling is used to reduce the temperature of the sample during the process [171, 196, 197]. Figure 5.16 is showing optical images of different steps for TEM sample preparation.

Nanoparticles

The sample preparation for nanostructures is relatively easy. Nowadays, commercial grids are available in the market. We just need to buy those grids and deposit a drop of colloidal suspension (typically few microliters) on it and can observe in TEM. These commercial grids are made of copper, nickel, or gold mesh with coated film on it [170, 199]. This coated film can be continuous or have holes in it (Fig. 5.17) depending on the requirement of the sample. Coating films can be amorphous (carbon) or crystalline (silicon). For nanoparticles' suspensions, continuous coatings are more useful, whereas holey carbon grids are best alternative for thin films due to large scattering which can produce more noise toward imaging in normal grids.

Once a group of images is obtained from different portions of the TEM grid, the next step is to count as many particles as possible. Higher number of particles can give more reliable statistics on the size, size distribution, and polydispersity. This technique is called “by eye and by hand” having limitations such as human mistakes and biasness but still acceptable among scientific community. Due to these limitations, computer-based image processing received more attention these days where comparatively large number of particles can be counted with better objectivity. However, particle-size calculations by using image processing software have limitations too when dealing with high polydispersity. Higher polydispersity

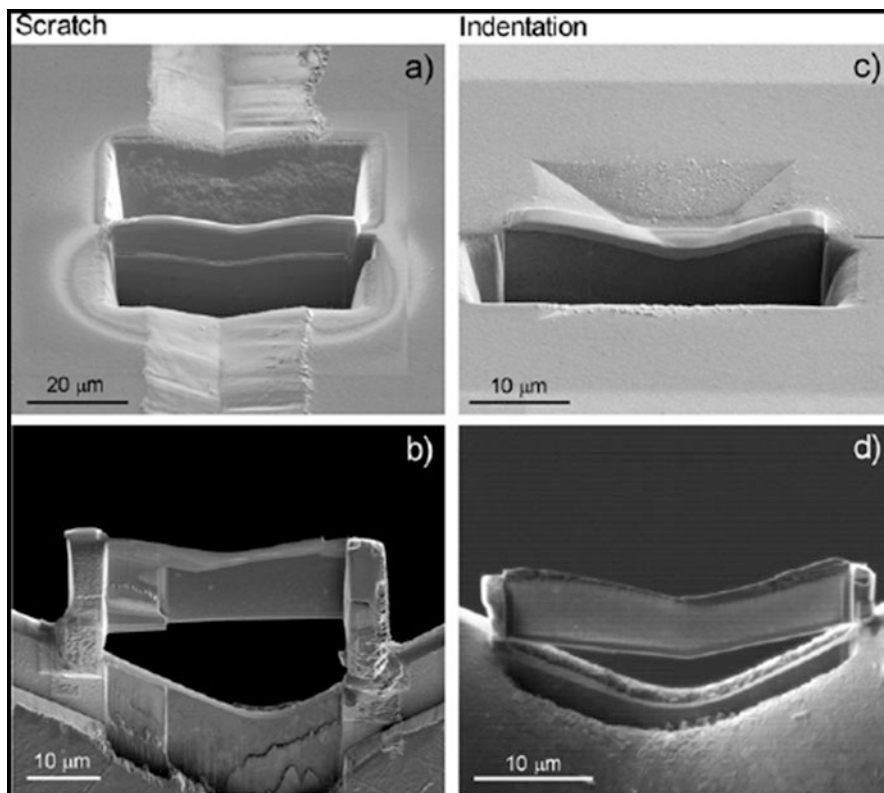


Fig. 5.16 Images of different steps of TEM sample preparation. (Reproduced with permission from Munoz-Tabares et al. [198])

limits the homogenous selection of the particles from specific area of the sample image. In brief, both the methods are being used for size distribution of the nanomaterials and admissible in the scientific journals.

5.3.3.3 Artifact Eliminations

Artifacts are the changes or damages induced in the sample at different stages of TEM observations and can be confusing with the microstructure of the sample. These artifacts can induce primarily during the sample preparation process or later during irradiation of sample by electron beam. All types of material can be affected by the development of artifacts to a certain extent with respect to their type and chemical bonding.

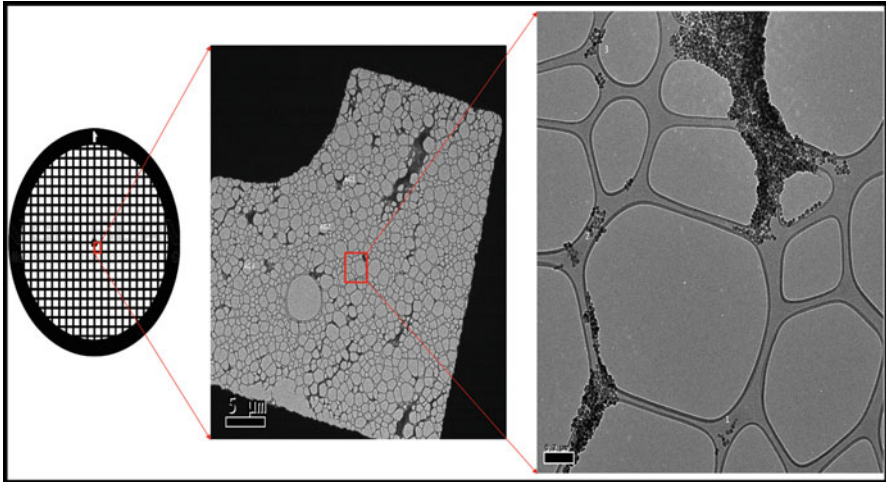


Fig. 5.17 Commercial TEM grid (left), one square selected from the grid by low magnification (middle image), further selection of the specific area from the selected square (right)

Artifacts which emerged during sample preparation result in deformation, matter displacement, material tearing, cracks, fractures, dislocations, glide planes, twinning, etc. The cause of these artifacts is sample preparation methods discussed in the previous section. There are some artifacts due to thermal damage of the electronic beam. These include fusion, phase transformations, loss of chemical electrons, amorphization, and demixing. Thermal artifacts can be minimized by cooling down sample holder under liquid nitrogen during the observation. Similarly, biological samples might have certain alterations such as volume change, transformations in proteins, and denaturing of different components.

There are also some artifacts that are not associated with the thermal damages. First is the dehydration of the biological samples that happened due to the ultrahigh vacuum in the microscopy column. Therefore, liquid must be in frozen form, or liquid must be extracted from the sample before observations. Second artifact is charging of the sample which induces instability in the sample. This effect is more prominent when beam is focused and material is insulator. This effect can be minimized by using the carbon coating on the sample. Sample destruction is the third effect that can be aroused in biological samples due to electron irradiation and temperature increase together. Contamination is also another important factor that hinders the observations of the sample. This is caused by the interaction of electron beam with the hydrocarbons present in the microscope column. An anti-contamination cold trap is introduced near the sample to cope with this effect. But if one still observes this effect, it is irreversible and will be a big problem. This can also be reduced by increasing vacuum level in the column.

5.4 Imaging and Spectroscopy: A Brief Overview

The first thing that comes into mind with the name of TEM is imaging and structural analysis of nanomaterials and other samples. In fact, this was the initial idea of the TEM, but with the passage of time, tremendous progress has been made, and availability of detectors for signals, other than elastic signals, has made TEM a complete analytical tool which can provide both structure and chemical information [200]. In the following section, we will discuss briefly different imaging and spectroscopy options available in TEM.

5.4.1 *Imaging*

Imaging is a primary function of TEM. As it produces images of the electrons that interact with the sample, both elastic (conventional TEM) and inelastic (STEM) signals are used for imaging in conventional TEM and STEM, respectively. There are three major imaging portions, conventional TEM, HRTEM, and STEM [201]. Diffraction will also be discussed in this section.

5.4.2 *Conventional Imaging*

In conventional TEM, a thin transparent specimen is irradiated with an electron beam of unvarying current density and direct image is recorded on image plane with objective lens by calculating the scattered amplitudes in specified direction. These wave amplitudes are conglomerated to form image intensity and amplitude [202]. Image is produced by combining the diffracted beam which emerged from the sample in the Gaussian plane. Conventional TEM usually works at an acceleration voltage of 100–200 kV. To provide better resolution and transmission, an accelerating voltage in the range of 200–500 kV can be applied [203–205]. Conventional TEM imaging mode can be changed into diffraction mode easily by simple commutation which represents different currents in the projector lenses. Therefore, conventional TEM has three modes: low magnification, high magnification, and diffraction mode. These modes and their contrast mechanisms are discussed previously. In conventional TEM mode, beam is widespread and covers the whole sample at the same time. This situation makes this imaging mode versatile and, therefore, can be used for bright-field imaging, dark-field imaging, selected area electron diffraction, micro- and nano-diffraction, and high-resolution imaging. Each imaging mode has distinct beam geometry. Conventional TEM provides two-dimensional projection of three-dimensional objects with clear information of size, shape, and structure [206–208]. Examples are shown in Fig. 5.18. In conventional

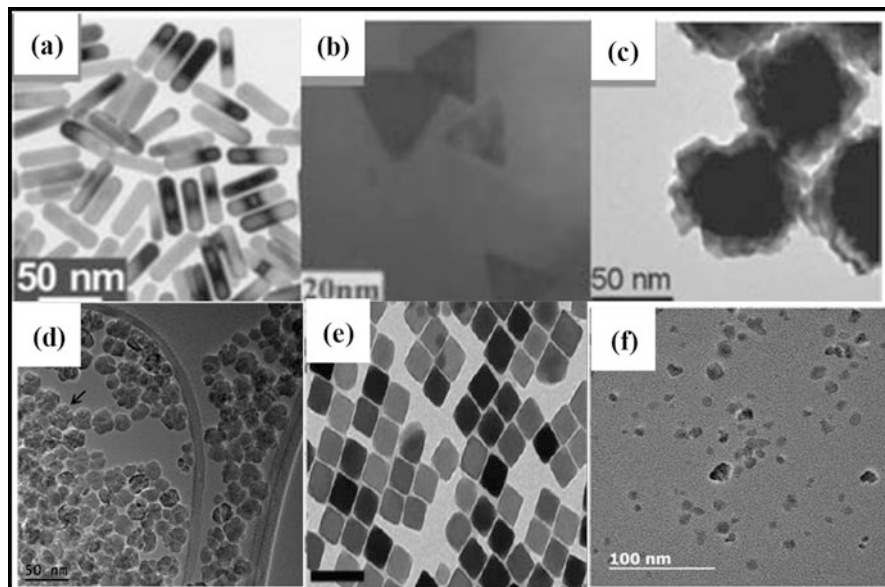


Fig. 5.18 TEM images of different shapes of shape nanoparticles: (a) gold nanorods. (Reproduced with permission from [211] Copyright (2013) American Chemical Society), (b) gold nanoprisms, (c) gold nanoflowers. (Reproduced with permission from Xie et al. and Hugounenq et al. [212, 213] Copyright (2008) American Chemical Society), (d) iron oxide nanoflowers. (Reproduced with permission from Hugounenq et al. [213] Copyright (2012) American Chemical Society), (e) iron oxide nanocubes. (Reproduced with permission from Guardia et al. [214] Copyright (2012) American Chemical Society), (f) cobalt ferrite spherical nanoparticles

TEM, electrons are expelled by thermionic, Schottky, or field emission. Field emission is ideal when coherence and high brightness are requisite [209].

Tuning of contrast transfer function accurately based on high precise aberration coefficient measurements is very important for attaining resolution up to 50 pm. While recording a TEM micrograph, due to imprecise imaging techniques, residual aberration comes back even after the correction of aberration. By recording both amplitude and phase, coherent aberration can be corrected. However, during recording of micrograph, phase is usually lost, while intensity of the image is always recorded. Loss of phase is actually loss of qualitative information related to structure of object which results in uncertainty in micrograph interpretation [210]. Nanoparticles of different morphologies have been presented in Fig. 5.18 produced by conventional TEM in bright-field imaging mode.

Major limitation of conventional TEM is the problem during characterization of magnetic materials; even with the use of corrected TEM that results in high band pass, filtering situation of phase information makes the situation worse by suppressing long-range phase modulation. So corrected conventional TEM is

considered blind for magnetic field and coarse phase modulation out of electric potentials. Zero-dimensional point defects (impurities and vacancies) are invisible through conventional TEM [205, 210].

5.4.3 *High-Resolution Transmission Electron Microscopy*

High-resolution TEM is a versatile powerful imaging technique that is used to provide micrographs of crystal surfaces at atomic resolution with chemical composition at 1 nm spatial resolution. HRTEM is not only used in solving complex material science problems but also for the improvement of computational stimulation and processing data analysis. Other uses of high-resolution TEM include crystal structure information and real-space imaging at atomic-scale resolution to local structure of thin specimens [215, 216].

HRTEM with resolving power of approximately 0.05 nm can be obtained nowadays with the development of aberration correctors, controlled sample environment, electron, and digital detector sources [217, 218]. Suitable micrograph processing with quantitative recording leads to the accurate and reliable determination of defects and homogeneities [219, 220].

Image formation process in HRTEM is perceived to occur in two stages. Interaction between incident and incoming electrons with atoms of specimen results in elastic and inelastic scattering. Electrons that are scattered elastically play a major role in the formation of high-resolution bright-field micrographs. Therefore, HR imaging always perform in the bright-field imaging mode. On the other hand, electrons that are scattered inelastically give irrational sample compositional information using electron energy-loss spectroscopy (EELS) techniques and imaging information through STEM [221].

Electrons are focused by magnetic lenses in HRTEM that leads toward the intuitive and direct representation in real space [217, 221]. A bladed layer of crystal is tilted in such a way that it comes perpendicular to electronic beam. Lattice plane that comes parallel to electronic beam will come near to Bragg position, and as a result primary beam will diffract. Diffraction spots of periodically arranged diffraction pattern in two dimensions are explained by Fourier transform. Electron optical system is used to obtain enlarge image at screen with five million times magnification. Such type of imaging process is called high-resolution imaging or phase-contrast imaging [222]. Examples of different high-resolution images are shown in Fig. 5.19.

HRTEM images are created by interference of both scattered and transmitted beams. This phase-contrast image is small like the unit cell of crystal, so HRTEM is used successfully for the determination of stacking faults, interference, dislocations, point defects, surface structure, and precipitates [223]. Major limitation of HRTEM is its inability to differentiate between core and shell even combining electron and X-ray diffraction techniques. In case of epitaxial growth of core on shell with two

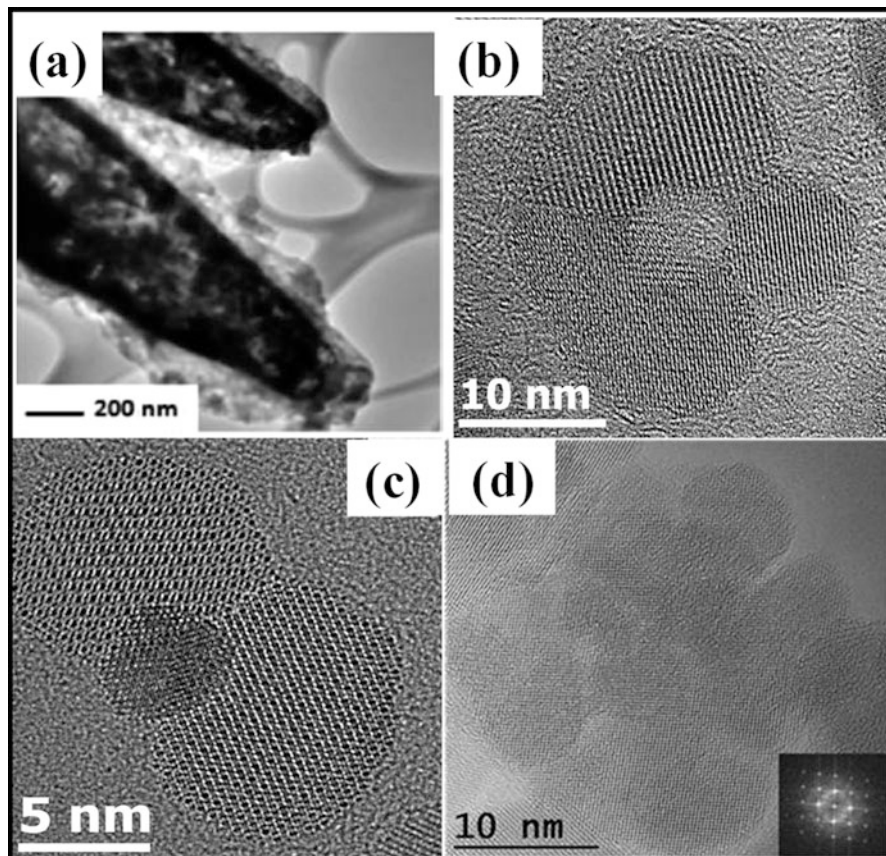


Fig. 5.19 High-resolution images of different morphologies; (a) MoO₃ hollow nanorods. (Reproduced with permission from Deepak et al. [223]). (b) Iron oxide hollow structures. (c) Iron oxide-gold nanodimers. (d) Iron oxide nanoflowers

different types of metals having slight difference in lattice constant and the same crystal structure, precise structure can't be determined by using HRTEM [215] (Fig. 5.20).

5.4.4 Scanning Transmission Electron Microscopy

In addition to above microscopic techniques where elastic signals are preferred for imaging, inelastic signals are now also being utilized for imaging, and this mode is named as scanning TEM. In this mode, the widespread beam is transformed into focused beam and acts as an optical probe that can be scanned over the sample similar to atomic force microscopy. STEM mode is mostly operated in dark-field

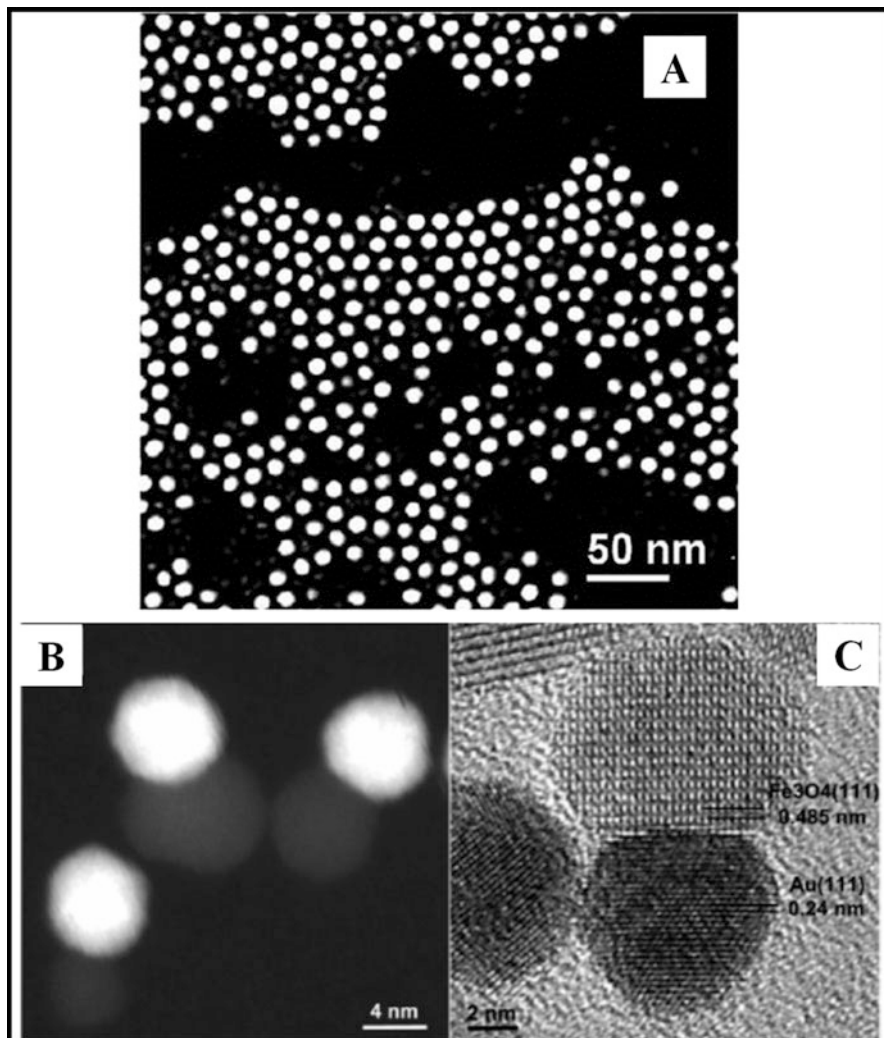


Fig. 5.20 (a) HAADF-STEM images of iron oxide nanoparticles [229], (b, c) STEM and TEM images of Au-iron oxide heterostructures. (Reproduced with permission from Yu et al. [230]. Copyright (2005) American Chemical Society)

imaging mode. STEM mode is useful for microanalysis, and contrast, in this mode, depends solely on atomic number, Z^α , in which α is greater than 1. All types of signals, i.e., elastic, inelastic, scattered, and unscattered, are emitted and detected by using an annular detector position below the sample [135, 224–226]. That's why this mode is also named as high-angle annular dark-field scanning transmission electron microscopy (HAADF-STEM) (Figs. 5.21 and 5.22). STEM mode is more efficient for energy-dispersive spectroscopy (EDS) analysis at nanoscale. This can

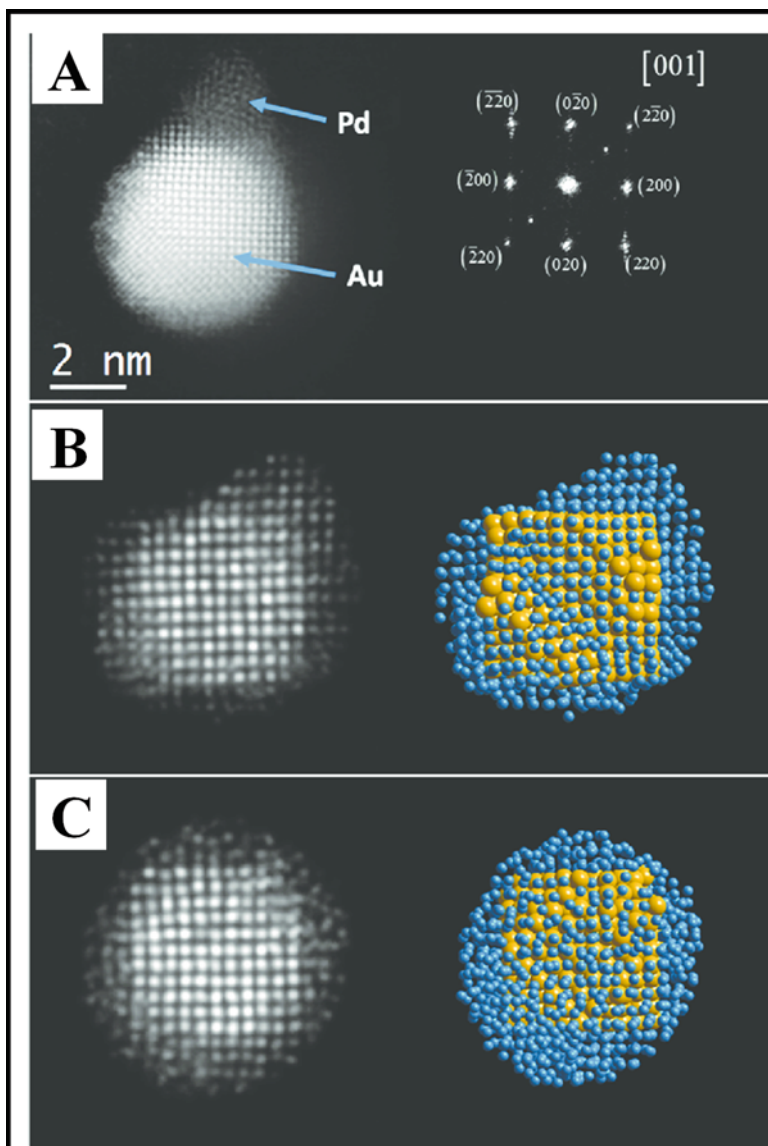


Fig. 5.21 (a) STEM image of Au nanoparticles with segregated Pd (right side shows the calculated FFT). (b, c) Simulated images obtained by inverse FFT and corresponding atomic model. (Reproduced with permission from Esparza et al. [231] Copyright (2014) American Chemical Society)

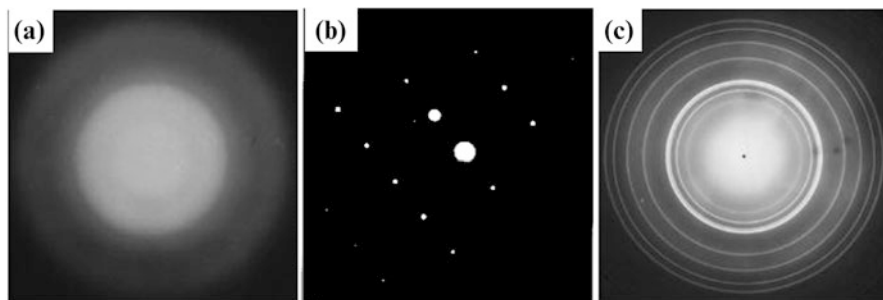


Fig. 5.22 Electron diffraction patterns of (a) amorphous, (b) single crystalline, and (c) polycrystalline materials

also provide concentration profiles by using EELS in imaging spectrum mode. The spatial resolution can reach up to the probe size. Currently probe-corrected STEM is also available. Localized chemical analysis (point, line, or area) can be performed by using STEM mode [227, 228].

5.4.5 Selected Area Electron Diffraction (SAED)

As we have discussed in contrast mechanism section (Sect. 5.2.5), due to very small wavelength of high-energy electrons, distance between atoms in the material sample acts as diffraction gratings which can diffract electrons. This phenomenon is used for conventional imaging in TEM mode because diffraction contrast mechanism is very significant in the crystalline materials. In addition to this, diffraction patterns of the sample can also be obtained just as X-ray diffractometer. These patterns are very useful for structure analysis and to study crystal defects. In diffraction mode, the intermediate lens is focused in the back focal plane of the objective lens; as a result, both transmitted and all the diffracted beams can be imaged. Then an aperture is introduced in the image plane of the objective lens which allows us to obtain diffraction pattern of selected area of the sample; that's why this is called selected area electron diffraction (SAED).

To take a diffraction pattern, first step is to examine the sample in the image mode and locate specific part or group of nanoparticles of interest and then fully spread the beam so that maximum electrons remain parallel to the sample. Next, intermediate aperture is inserted and fixed at the specific feature. By switching from imaging to diffraction mode, diffraction pattern in the form of spots or circles can be observed on the viewing screen. A beam stopper is introduced in the path of the diffracted beam to avoid camera damage during the observations. These obtained diffraction patterns can then be analyzed and indexed according to their d spacing. The emergence of the diffraction spots can be understood by constructing the Ewald sphere which provides lattice planes for a particular wavelength of incident

radiations. The spots apparent on the diffraction pattern belong to the nodes of the reciprocal lattice intercepted by the Ewald sphere. The radius of this hypothetical sphere is inversely proportional to the wavelength of the incident beam. Due to this reason, electron (wavelength in the range of picometer) diffraction becomes more prominent than X-ray (approximately 0.1 nm) diffraction where fewer nodes are observed at the tangent of the Ewald sphere. This phenomenon is further enhanced by introducing the diffraction volumes so that spots remain visible even when the Bragg condition is not completely fulfilled.

The diffraction pattern depends mainly on the orientation of the nanoparticles in the sample. In case of monocrystalline sample, distinct diffraction spots which correspond to specific planes can be observed, but the condition is that all parts of the sample (nanoparticles) selected by aperture should align with the electron beam (Fig. 5.22). This is the case when nanoparticles are grown on a substrate by vapor deposition method or electrodeposition method (Fig. 5.23b). But in case of nanoparticles, they all can be oriented in different directions; as a result, distance from the direct beam remains the same for spots, but angle is changed for every nanoparticle, and finally bright circles are obtained in place of spots (Fig. 5.23a). Similarly, for polycrystalline materials, circles are obtained (Fig. 5.22c). Each circle corresponds to specific planes that can be determined from the d spacing. Interplanar distance (d spacing) can be calculated by the formula:

$$d_{hkl} = \frac{L\lambda}{R_{hkl}}$$

where,

L , camera length.

λ , wavelength of electrons.

$L\lambda$ is also called camera constant and has units \AA cm .

R_{hkl} , distance of spot or circle from the direct beam.

5.4.5.1 Spectroscopic Techniques Available in TEM

Energy-Dispersive Spectroscopy (EDS/EDX)

Energy-dispersive spectroscopy (EDS) is considered as one of the auspicious characterization technique that is used for chemical analyzing purposes in TEM. It is referred as simple technique used for compositional analysis with TEM. When inelastic transition occurs, electrons from inner shells can knockout and result into a transition from higher levels to core level with the emission of an X-ray. The energy of these characteristic X-rays can tell the chemical nature of the material [234–236]. The emission spectrum of the X-ray is relatively easy to analyze than counterpart

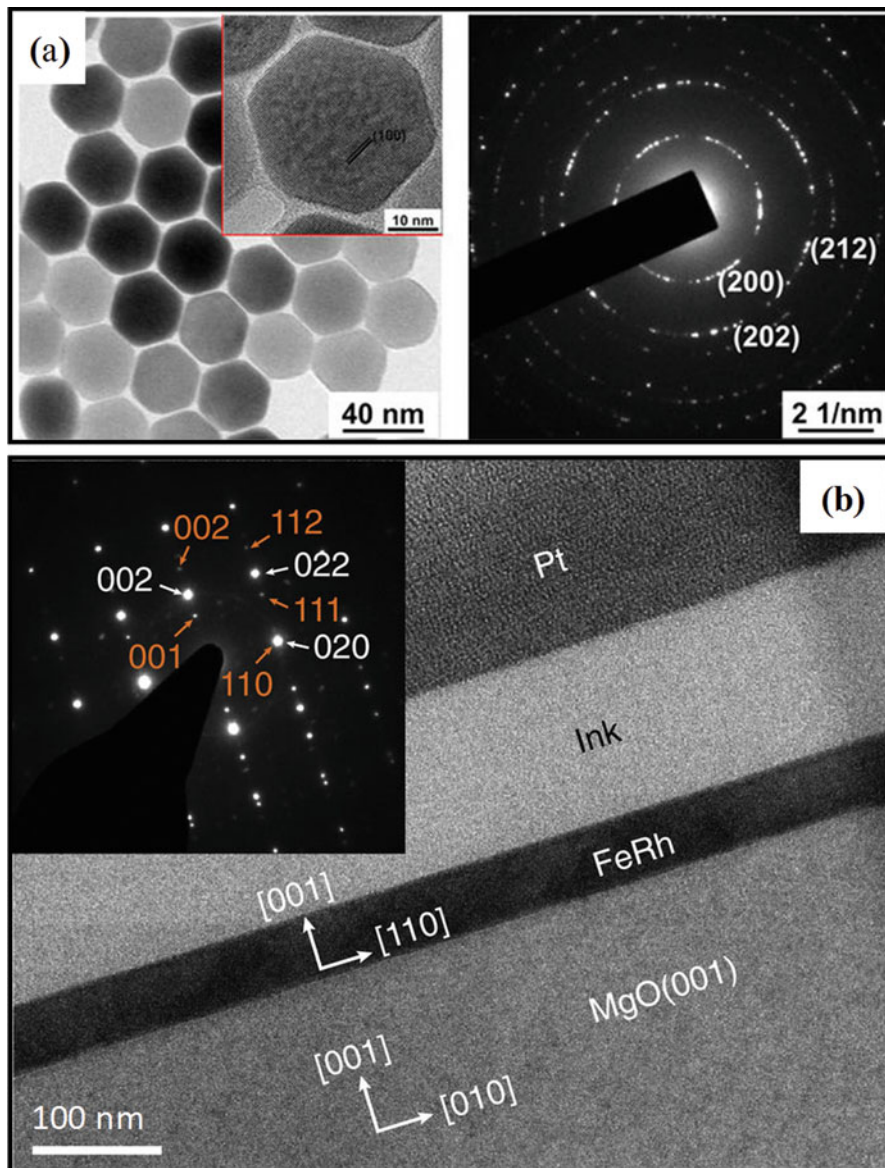


Fig. 5.23 (a) TEM image of lanthanum-doped upconversion nanoparticles (left), HRTEM image (inset), and electron diffraction pattern of nanoparticles (right). (Reproduced with permission from Feng et al. [232]). (b) TEM image (main panel) of FeRh film grown epitaxially on a MgO (001) substrate by DC sputtering and diffraction pattern (inset) of the area. Diffraction pattern is indexed for FeRh (orange) layer and MgO (white) substrate. (Reproduced with permission from Gatel et al. [233])

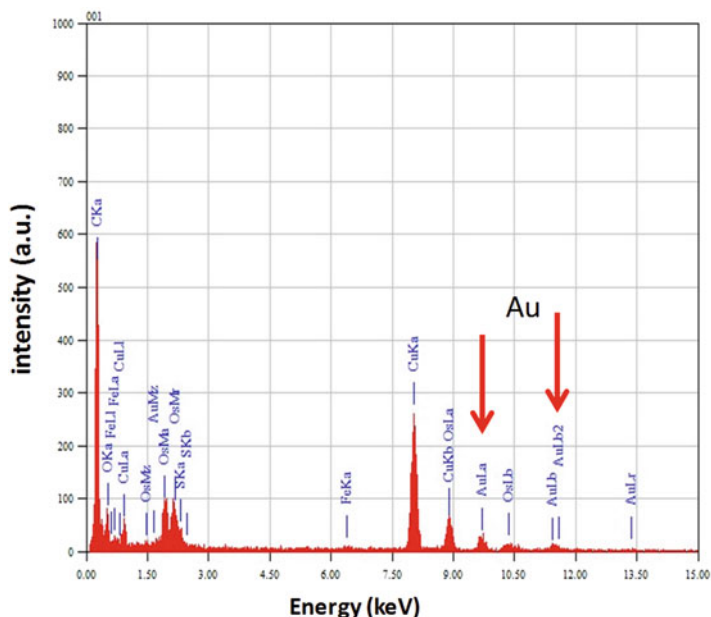


Fig. 5.24 Typical EDX spectrum of hydrated spleen with gold nanoparticles

energy loss in EELS. X-ray energy-dispersive detectors are available commercially which can collect the X-ray signals and display in the form of spectrum (Fig. 5.24). Although the process looks very simple, there are certain limitations associated with these spectra. For example, signal collection efficiency is very poor due to small solid angle between detector and sample. EDX diode present in the detector can heat up very quickly; therefore, liquid nitrogen is maintained in the detector dewar. In addition, it only provides qualitative information about the sample when used in TEM mode. Internal design of detectors and TEM is optimized to reduce artifacts in spectrum of energy-dispersive spectroscopy; however, abdicable signals negatively affect the elemental analysis [236, 237].

Dispersive device in energy-dispersive spectroscopy is fictitious of semiconductor diode that is fabricated with single crystal of silicon/germanium. When photons enter and go through the process of penetration in transition region (formed by n-type and p-type doped materials), it results in the release of energy due to valance electron confinement to atomic nucleus. This is an equivalent process to excite electrons from valance to conduction shell that ignites electrical conduction because of electron-hole pair formation for specified period. Electron energy for energy-dispersive spectroscopy in TEM is set to 200 keV [238–240].

5.4.6 *Electron Energy-Loss Spectroscopy (EELS)*

Fast-moving electrons lost energy during interaction with sample and provide extensive information about the sample. Consequently, electron energy-loss spectroscopy (EELS) is valuable for probing chemical, physical, and optical characteristics of the sample material. There are two approaches presented on EELS. In first approach, filtered images are obtained by using a fixed and widespread beam, whereas second approach presented EELS spectrum by scanning the focused beam on each pixel of the given image. This is also called spectrum imaging mode in EELS [30, 241–243].

An EELS spectrum typically consists of three parts: zero-loss region, low-loss region, and core-loss region. Zero-loss region belongs to elastic electrons, and very intense peak in the EELS spectrum can be observed. In this region, there is no loss and peak is located at 0 eV. Low-loss region gives information about the optical properties of the sample. This region spans from 0 to 50 eV. This region presents inter-band transitions, i.e., transition from valence to conduction band. The information obtained from low-loss spectrum is grouped in three parts, bulk, surface and *begrenzung*, and combination of these components provides full EELS spectrum. Core-loss region belongs to energy loss of core electrons, and energy of this region is greater than 50 eV. This region belongs to excitation of electrons from the inner shells [244–246].

For comprehensive analysis on chemical and local atomic level as well as for characterization of electronic structures, diffraction data and image obtained with TEM are preferred to combine with analytical information provided by EELS. Combination of EELS with TEM leads toward the advantage of unifying the high spatial resolution with acceptable energy resolution. Combination of TEM and EELS rendered chemical and physical information with energy-filtered and energy-loss spectral images (Fig. 5.25) [248, 249].

EELS edges of heavy elements at high energy-loss region having low intensities are arduous to detect due to low signal-to-noise ratio by EELS spectrum. Major drawback is that EELS is used to find excellent relations for spatial resolution as compared to other techniques, but it is not considered as promising measuring technique for low atomic concentration [250, 251].

5.4.7 *Energy-Filtered Transmission Electron Microscope (EFTEM)*

EFTEM is used for spectral imaging of electron energy-loss information and recording purpose of elemental distribution maps [252]. This allows electrons with peculiar energy loss to make image. In TEM, energy filtering is performed by two approaches. One approach is in-column Ω -type filter, while other approach is post-column approach [253]. In first approach, Castaing-Henry filter is used. This filter consists of two 90° magnetic prisms usually named as Castaing and Henry. It is

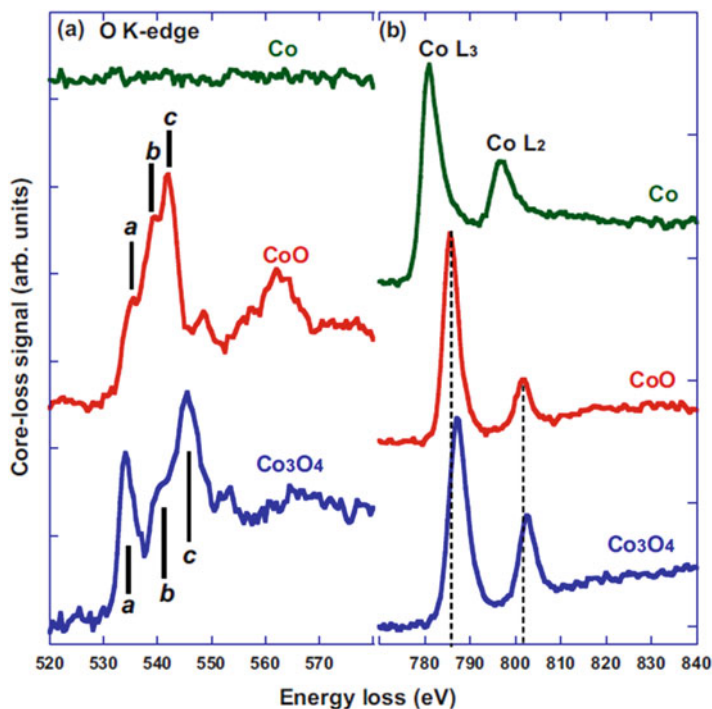


Fig. 5.25 Comparison of K-edge and L-edge of O, Co, CoO, and Co₃O₄. (Reproduced with permission from Zhao et al. [247])

situated between intermediate lens and objective lens; a slit is placed before them to control electrons on the basis of specified energy losses. Electrons are transmitted to 90° electromagnetic sector; as a result, these electrons are reflected back by electrostatic mirrors and dispersed on the basis of different energies. Electrons are deflected back by the second 90° magnetic prism onto optical axis [254]. Major advantage of omega-type filter is in energy filtering diffraction as well as in EFTEM imaging [253]. For post-column approach, the detector is positioned below the sample. Electrons after inelastic interactions are subject to an orthogonal magnetic field, where electrons experience centripetal force and distribute according to their speed. This speed distribution is directly linked to their energy. A filter or window is placed in front of the detector to select electrons of specific energy (eV). In this method, two pre-threshold windows are used to collect background signals, whereas one window with exact energy value is used to get actual electron signal (Fig. 5.26).

EFTEM is considered as an essential technique for characterization of biological samples and in materials science. It can be used to determine the distribution of polymer layer on the surface of the nanoparticles (Fig. 5.27). It can also be used to unambiguously identify core-shell nanoparticles because it can show both moieties of the nano-entity separately on the basis of their chemical nature. EFTEM is

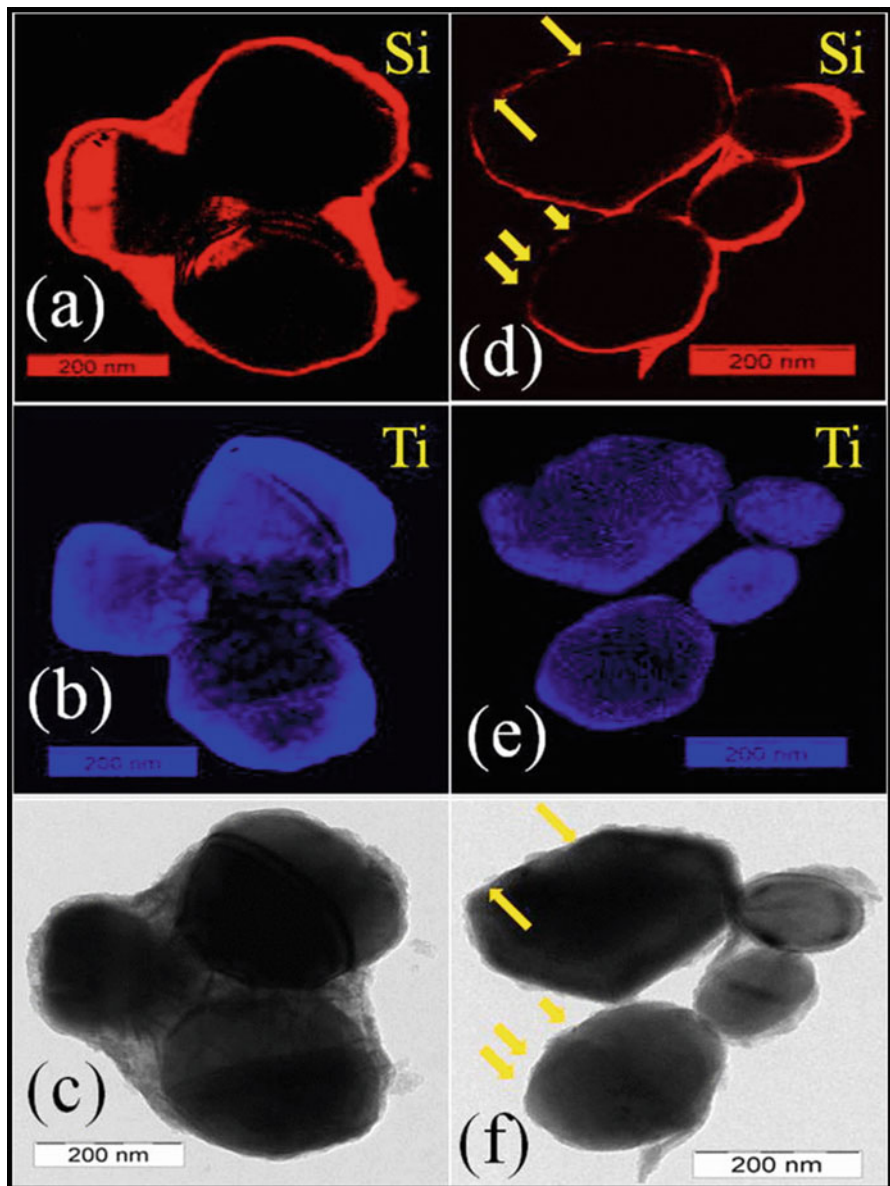
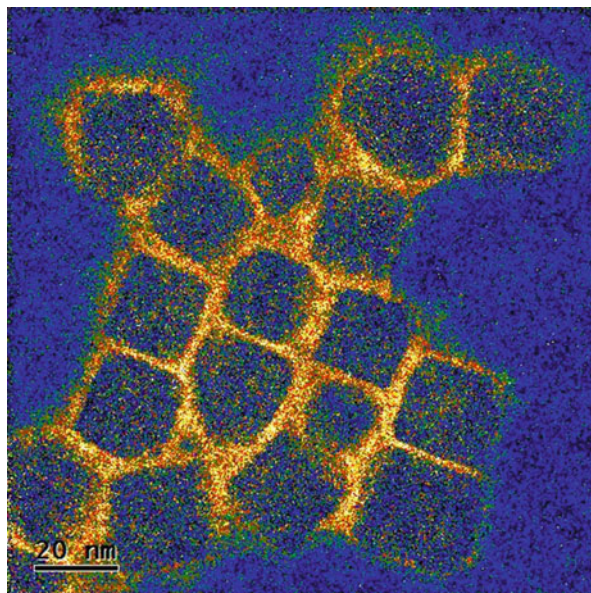


Fig. 5.26 EELS-based EFTEM chemical mapping images of $\text{TiO}_2@Si$ core-shell nanoparticles, (a, d) showing Si distribution on the nanoparticles, (b, e) represent the presence of Ti contents, (c, f) bright-field image of $\text{TiO}_2@Si$ core-shell nanoparticles. (Reproduced with permission from Jimenez-Villar et al. [255])

Fig. 5.27 EFTEM imaging of polymer distribution on the nanoparticles' surface. Image is acquired at carbon K-edge (284 eV). (Reproduced with permission from Lartigue et al. [259] Copyright (2013) American Chemical Society)



used to ameliorate the contrast of inhomogeneous specimens and 2-D display for distribution of elemental mapping with very narrow electron probe [252, 256].

One of the most promising applications of EFTEM is determination of the compositional information in the form of maps by using specified element ionization edges. Possible spatial resolution of such maps comes in nanometer range that can be easily acquired around an edge with series filtered energy images [252]. A 2-D image of elemental distribution with a collection of large number of loss images around featuring of ionized core-loss edges with specified energy loss in very short time (5–60 s) is formed. It is possible to retrace an elementally distributed 3-D map [257].

Elementally distributed 3-D quantitative imaging with EFTEM renders new approach in frozen substituted cells for localization of specific components. EFTEM tomography expectedly provides important information about intrinsic elements of cells. EFTEM reconstruction methods and techniques are used for improving those results with minimum detectable number of atoms that can access theoretical limits [258].

5.4.8 Chemical Mapping

Chemical imaging is used for analyzing the compositional changes of a subset of atomic lattice at atomic occupancy that can be achieved by proper recording of angle of reflection for diffracted electrons in TEM. Chemical mapping is considered

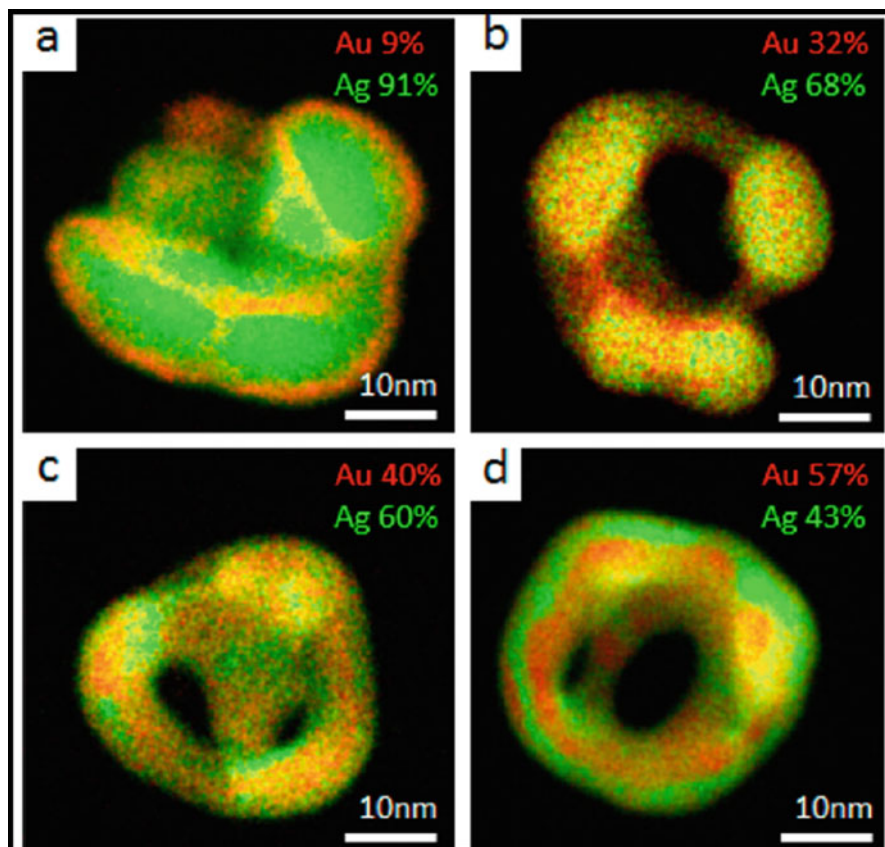


Fig. 5.28 STEM-EDX chemical mapping of gold and silver distribution in the particles. Increasing gold concentration can be seen by inverting the colors in the map. (Reproduced with permission from Slater et al. [265] Copyright (2014) American Chemical Society)

as an ideal technique for characterization of sharpness of interfaces among hetero-epitaxial layers as well as structural analysis. Chemical mapping is the most obvious and suitable technique for characterizing the interface modifications because of annealing and ion implantation. X-rays are used not only for qualitative or quantitative analysis but also for chemical mapping [216, 260, 261].

Chemical mapping for surface analysis is possible in special mode that can characterize exact location of specified elements in samples (Figs. 5.28 and 5.29). Chemical mapping is done in STEM mode where optical probe scans over the sample or specific part of the sample. During this process, optical probe stays for a certain time on each pixel and extracts chemical information. Each scan box is called a data cube. Information obtained through chemical mapping can be manipulated later according to requirements for chemical distribution of elements. Maps are required for chemical characterization of quantitative minor/major analysis of microfossils, cements, glasses, and minerals. Each microfossil should have well-

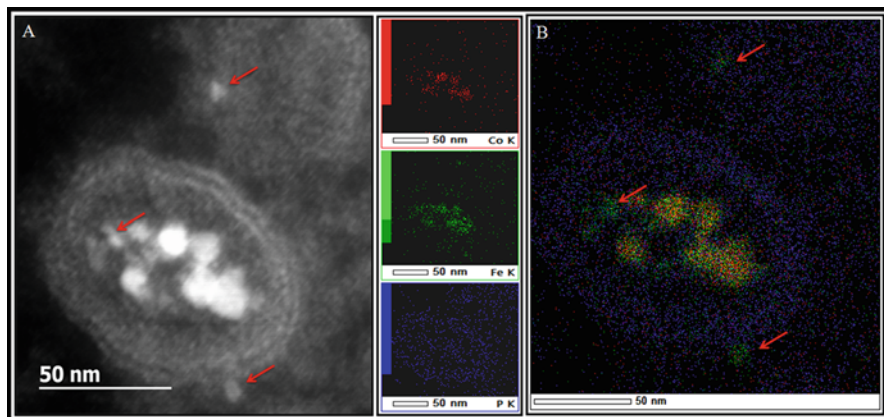


Fig. 5.29 EDX chemical mapping of cobalt ferrite nanoparticles confine in the vesicle. Representing colors for cobalt, iron, and phosphorus are red, green, and blue, respectively. Ferritins with only iron can be observed inside and outside the vesicle with pure green and blue, respectively. Ferritins with only iron can be observed inside and outside the vesicle with pure green signal (iron) indicated by arrows. **(a)** STEM-HAADF image. **(b)** Overlay of three chemical signals

defined fabric, texture, quantitative chemistry, morphology, and feature in 2-D or 3-D and chemical maps that show major and minor variations [225, 239, 240].

Quantitative chemical imaging by TEM of individual nanostructures is rivetingly potential application not only for environment and safety purposes, but it is also considered as potentially exciting option for applications in microelectronic devices (helpful in understanding interfaces of Si/high k-dielectric). Mutual relation of chemical mapping with cracks in concrete and desorption mass spectrometry by chemical mapping are two major representative topics that were demonstrated by surface and microanalysis science division. Major drawback lies in complexity during sample preparation [262–264].

5.4.9 Three-Dimensional (3-D) Tomography in TEM

3-D tomography is a reconstruction technique of obtaining 3-D images from series of 2-D projections. For this type of imaging, double-tilt holders are used which can tilt the sample to certain angle (approx $\pm 60^\circ$) (Fig. 5.30). Then series of images are taken and reconstruct in 3-D by using software. With reappearance of automatic microscopic control, newly formed reconstructive algorithm, high-power computed techniques/capabilities, and computerized tomography, rendering of 3-D images becomes a promising perspective for future applications. By using TEM, electron tomography greatly offers representation for 3-D nanostructures. Reconstruction of 3-D TEM images is being widely applied not only for biological purposes as well as material science [266, 267].

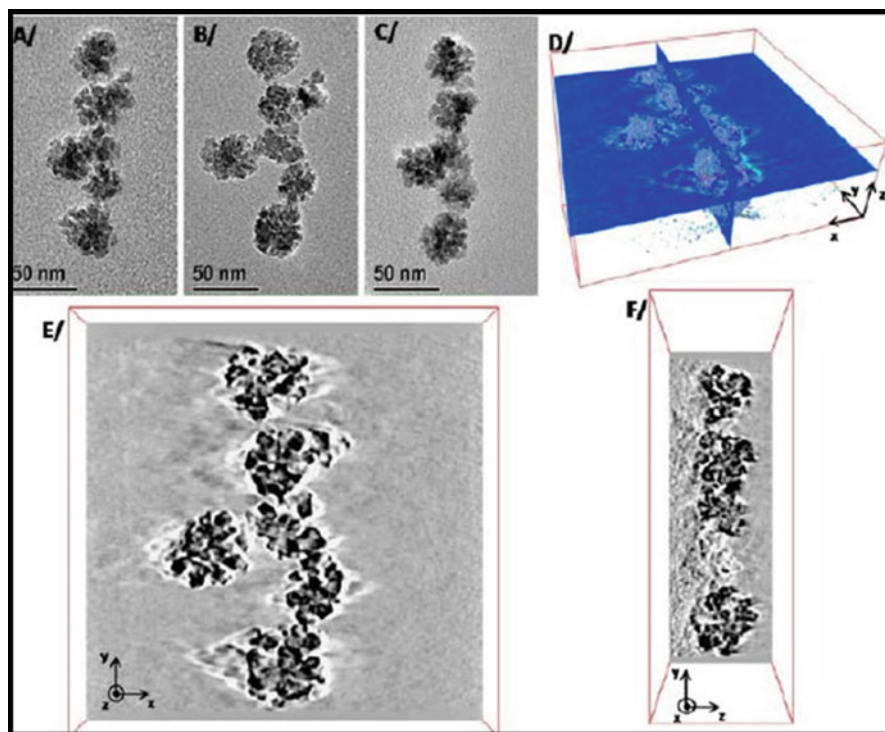


Fig. 5.30 Three-dimensional analysis of iron oxide nanoflowers, tomography TEM images taken at tilt angle of (a) 60, (b) 0, and (c) -60° . (d) Three-dimensional tomogram of the particle. (e, f) 2-D slice corresponding to (x, y) and (y,z) planes, respectively. (Reproduced with permission from Hugouenq et al. [213] Copyright (2012) American Chemical Society)

Computerized tomography is processed for slice images to construct 3-D image with resolution till range of nanometers. With bright-field method at 200 kV, 3-D images have been constructed without sample staining [268, 269]. Bright-field electron tomography is much suitable for three components: carbon black (grade HAF), silica, and matrix NR [270].

5.5 Conclusion and Future Perspectives

This chapter is intended to give an overview of instrumentation, working, imaging, and analytical techniques involved in TEM with the intention to highlight its applications in the field of nanotechnology for beginners. TEM already have huge impact in different research areas due to its capabilities to determine atomic structure and analytical facilities. By removing spherical and chromatic aberrations, the resolution of different TEM imaging modes has been improved in the range of

picometer. Chromatic aberration correction is important for high-resolution imaging in TEM mode, whereas probe correction is essential for STEM mode to observe objects at the atomic resolution. Addition of different analytical tools, e.g., EDX, EELS, EFTEM, chemical mapping, etc., makes TEM a complete technique to analyze material or biological sample extensively. Localized EELS analysis has been significantly improved due to advancement in energy resolution and signal-to-noise ratio. The enhanced sensitivity and decrease record time of chemical maps have been realized with new silicon-based drift detectors.

In material science, synthesis of nanoparticles is a key part, and understanding of nucleation and growth mechanisms at the solid-liquid interface is very crucial to get control over shape and size of the nanoparticles. The elaboration of mechanisms requires the visualization of reaction kinetics, and this was the missing part of the story. With the advancements in micro-electromechanical system (MEMS) technology, an innovative liquid-cell TEM has been emerged to track the dynamical processes in liquid phase. This in situ technique can image the dynamics of nano-objects encapsulated in solution form through an electron transparent window micro-fabricated in the closed cell. This new setup will certainly reduce the gap between liquid and solid interface reactions and allow to observe live biological samples that were not possible before due to ultrahigh vacuum in the TEM column. STEM mode is the main beneficiary of liquid-cell TEM due to control over electron beam because dose rate can affect the reaction kinetics. Another development which arises with MEMS technology is gas holder. This is also called environmental specimen holder. Environmental TEM is very important to study performance of many nano-devices, e.g., fuel cells and batteries. These two new approaches will certainly improve the TEM applications in chemistry, physics, and material science. In addition, orbital and spin angular momentum of electrons have not been used in electron microscopy generally. These electrons employed for dislocation identification. The studies based on these properties are at initial stages and likely to mature for actual applications in near future. EELS and X-ray absorption spectroscopy explore the same mechanism of transition from core state to empty states above the fermi level. Therefore, both techniques can be applied to the identical physical phenomena such as dichroism. Dichroism is the dependency of certain materials' photon absorption spectrum on polarization of incident radiation. The polarization vector of the photon performs similar role as the momentum transfer in electron scattering. That's why new TEM technique and electron energy-loss magnetic chiral dichroism (EMCD) have been proposed with high spatial resolution than X-ray magnetic circular dichroism (XMCD). There are certain obstacles that hamper the EMCD such as low signal and precise scattering conditions to observe chiral dichroic signal. All these prospects will certainly provide new developments and dimensions in TEM.

References

1. Zocco, T., & Schwartz, A. (2003). A brief history of TEM observations of plutonium and its alloys. *JOM Journal of the Minerals, Metals and Materials Society*, 55(9), 24–27.
2. Shen, Z., & Wei, C. (2010). TEM tests: Past, present and future [J]. *Foreign Language World*, 6, 004.
3. Liu, Z., et al. (2000). TEM studies of platinum nanowires fabricated in mesoporous silica MCM-41. *Angewandte Chemie International Edition*, 39(17), 3107–3110.
4. Pedersen, B. G., et al. (2003). Colonoscopy and multidetector-array computed-tomographic colonography: Detection rates and feasibility. *Endoscopy*, 35(09), 736–742.
5. Nakhosteen, C. B., & Jousten, K. (2016). *Handbook of vacuum technology*. Wiley.
6. Bertram, F., et al. (2016). Nanoscale imaging of structural and optical properties using helium temperature scanning transmission electron microscopy cathodoluminescence of nitride based nanostructures. *Microscopy and Microanalysis*, 22(S3), 600–601.
7. Davoisne, C., et al. (2017). MnO conversion reaction: TEM and EELS investigation of the instability under electron irradiation. *Journal of the Electrochemical Society*, 164(7), A1520–A1525.
8. Nishimura, T., et al. (2016). *Structural, electrical, and compositional analysis of surface and grain boundary for Cu (In, Ga) Se₂ solar cells by EBSD/SSRM/TEM-EDX*. Structural, Electrical, and Compositional Analysis of Surface and Grain Boundary for Cu (In, Ga) Se₂ Solar Cells by EBSD/SSRM/TEM-EDX.
9. Sun, W., et al. (2016). Communication—multi-layer boron nitride nanosheets as corrosion-protective coating fillers. *Journal of the Electrochemical Society*, 163(2), C16–C18.
10. Egerton, R., Li, P., & Malac, M. (2004). Radiation damage in the TEM and SEM. *Micron*, 35(6), 399–409.
11. Jacobsen, C. J., et al. (2000). Mesoporous zeolite single crystals. *Journal of the American Chemical Society*, 122(29), 7116–7117.
12. Talapin, D. V., et al. (2002). Synthesis and surface modification of amino-stabilized CdSe, CdTe and InP nanocrystals. *Colloids and Surfaces A: Physicochemical and Engineering Aspects*, 202(2), 145–154.
13. Navarro, J. (2012). *A history of the electron: J. J. and G. P. Thomson*. Cambridge: Cambridge University Press.
14. Melissinos, A. C., & Napolitano, J. (2003). *Experiments in modern physics*. Academic.
15. Born, M., & Wolf, E. (2013). *Principles of optics: Electromagnetic theory of propagation, interference and diffraction of light*. Elsevier.
16. Kleppner, D., & Jackiw, R. (2000). One hundred years of quantum physics. *Science*, 289(5481), 893–898.
17. Gan, Y., & Wang, W. (2007). A self-consistent picture of wave-particle duality of light. In *Optical engineering+ applications*. International Society for Optics and Photonics.
18. Logiurato, F. (2012). *Relativistic derivations of de Broglie and Planck-Einstein equations*. arXiv preprint arXiv:1208.0119.
19. Yoshimura, N. (2013). *Historical evolution toward achieving ultrahigh vacuum in JEOL electron microscopes*. Japan: Springer.
20. Williams, D. B., & Carter, C. B. (1996). *Transmission electron microscopy: A textbook for materials science. Diffraction. II*. Springer.
21. Eichmeier, J. A., & Thumm, M. (2008). *Vacuum electronics: Components and devices*. Berlin: Springer.
22. Williams, D. B., & Carter, C. B. (2009). *Transmission electron microscopy: A textbook for materials science*. New York: Springer.
23. Reimer, L. (2000). *Scanning electron microscopy: Physics of image formation and microanalysis*. Bristol: IOP Publishing.
24. Wiesen, S. J. (2003). *West German industry and the challenge of the Nazi Past, 1945–1955*. Chapel Hill: University of North Carolina Press.

25. VanHove, M. A., & Weinberg, W. H., Chan, C.-M. (2012). *Low-energy electron diffraction: Experiment, theory and surface structure determination*. Vol. 6. Springer Science & Business Media.
26. Leapman, R. D. (2017). Application of EELS and EFTEM to the life sciences enabled by the contributions of Ondrej Krivanek. *Ultramicroscopy*, 180, 180.
27. Waitz, T., Kazykhanov, V., & Karnthaler, H. (2004). Martensitic phase transformations in nanocrystalline NiTi studied by TEM. *Acta Materialia*, 52(1), 137–147.
28. Hofmann, T. (2001). Unsupervised learning by probabilistic latent semantic analysis. *Machine Learning*, 42(1), 177–196.
29. Denk, W., & Horstmann, H. (2004). Serial block-face scanning electron microscopy to reconstruct three-dimensional tissue nanostructure. *PLoS Biology*, 2(11), e329.
30. Egerton, R. F. (2011). *Electron energy-loss spectroscopy in the electron microscope*. Springer Science & Business Media.
31. Gaietta, G., et al. (2002). Multicolor and electron microscopic imaging of connexin trafficking. *Science*, 296(5567), 503–507.
32. Goldstein, J., et al. (2012). *Scanning electron microscopy and X-ray microanalysis: A text for biologists, materials scientists, and geologists*. Berlin: Springer Science & Business Media.
33. Goldstein, J. (2012). *Practical scanning electron microscopy: Electron and ion microprobe analysis*. Springer Science & Business Media.
34. Zewail, A. H. (2010). Four-dimensional electron microscopy. *Science*, 328(5975), 187–193.
35. Bayram, M., et al. (2005). Light and electron microscope examination of the effects of methotrexate on the endosalpinx. *European Journal of Obstetrics, Gynecology, and Reproductive Biology*, 120(1), 96–103.
36. Zonneville, A., et al. (2013). Integration of a high-NA light microscope in a scanning electron microscope. *Journal of Microscopy*, 252(1), 58–70.
37. Amenta, F., et al. (2001). Age-related changes of dopamine receptors in the rat hippocampus: A light microscope autoradiography study. *Mechanisms of Ageing and Development*, 122(16), 2071–2083.
38. Westphal, V., & Hell, S. W. (2005). Nanoscale resolution in the focal plane of an optical microscope. *Physical Review Letters*, 94(14), 143903.
39. Gustafsson, M. G. (2005). Nonlinear structured-illumination microscopy: Wide-field fluorescence imaging with theoretically unlimited resolution. *Proceedings of the National Academy of Sciences of the United States of America*, 102(37), 13081–13086.
40. Klar, T. A., et al. (2000). Fluorescence microscopy with diffraction resolution barrier broken by stimulated emission. *Proceedings of the National Academy of Sciences*, 97(15), 8206–8210.
41. Kawata, S. (2001). Near-field microscope probes utilizing surface plasmon polaritons. In *Near-field optics and surface plasmon polaritons* (pp. 15–27). Springer.
42. Chen, B.-C., et al. (2014). Lattice light-sheet microscopy: Imaging molecules to embryos at high spatiotemporal resolution. *Science*, 346(6208), 1257998.
43. Bolte, S., & Cordelières, F. (2006). A guided tour into subcellular colocalization analysis in light microscopy. *Journal of Microscopy*, 224(3), 213–232.
44. Wen, D. (2010). *Tungsten-halogen quartz lamp*. Google Patents.
45. Vladar, A. E., Postek Jr, M. T., & Vane, R. (2001). Active monitoring and control of electron-beam-induced contamination. In *26th Annual International Symposium on Microlithography*. International Society for Optics and Photonics.
46. Murphy, D. B. (2002). *Fundamentals of light microscopy and electronic imaging*. Wiley.
47. Batson, P., Dellby, N., & Krivanek, O. (2002). Sub-angstrom resolution using aberration corrected electron optics. *Nature*, 418(6898), 617.
48. Bajt, S., et al. (2000). Quantitative phase-sensitive imaging in a transmission electron microscope. *Ultramicroscopy*, 83(1), 67–73.
49. Kaynig, V., et al. (2010). Fully automatic stitching and distortion correction of transmission electron microscope images. *Journal of Structural Biology*, 171(2), 163–173.

50. Kumar, S., et al. (2008). A structural resolution cryo-TEM study of the early stages of MFI growth. *Journal of the American Chemical Society*, *130*(51), 17284–17286.
51. Tiemeijer, P., et al. (2012). Using a monochromator to improve the resolution in TEM to below 0.5 Å. Part I: Creating highly coherent monochromated illumination. *Ultramicroscopy*, *114*, 72–81.
52. Suenaga, K., et al. (2007). Imaging active topological defects in carbon nanotubes. *Nature Nanotechnology*, *2*(6), 358–360.
53. Soldati, A. L., et al. (2011). High resolution FIB-TEM and FIB-SEM characterization of electrode/electrolyte interfaces in solid oxide fuel cells materials. *International Journal of Hydrogen Energy*, *36*(15), 9180–9188.
54. Takeda, S., & Yoshida, H. (2013). Atomic-resolution environmental TEM for quantitative in-situ microscopy in materials science. *Microscopy*, *62*(1), 193–203.
55. den Dekker, A., et al. (2013). Estimation of unknown structure parameters from high-resolution (S) TEM images: What are the limits? *Ultramicroscopy*, *134*, 34–43.
56. Schmolze, D. B., et al. (2011). Advances in microscopy techniques. *Archives of Pathology & Laboratory Medicine*, *135*(2), 255–263.
57. Meyer, L., et al. (2008). Dual-color STED microscopy at 30-nm focal-plane resolution. *Small*, *4*(8), 1095–1100.
58. Benaissa, A., & Messaoudi, S. A. (2002). Blow-up of solutions for the Kirchoff equation of $\Delta u = \lambda u - u^3$ -Laplacian type with nonlinear dissipation. In *Colloquium Mathematicum*. Instytut Matematyczny Polskiej Akademii Nauk.
59. Hell, S. W., Dyba, M., & Jakobs, S. (2004). Concepts for nanoscale resolution in fluorescence microscopy. *Current Opinion in Neurobiology*, *14*(5), 599–609.
60. Smith, M. L., et al. (2003). Near-wall μ -PIV reveals a hydrodynamically relevant endothelial surface layer in venules in vivo. *Biophysical Journal*, *85*(1), 637–645.
61. Sasaki, T., et al. (2010). Performance of low-voltage STEM/TEM with delta corrector and cold field emission gun. *Journal of Electron Microscopy*, *59*(S1), S7–S13.
62. Suenaga, K., et al. (2009). Visualizing and identifying single atoms using electron energy-loss spectroscopy with low accelerating voltage. *Nature Chemistry*, *1*(5), 415.
63. Walther, T., et al. (2006). First experimental test of a new monochromated and aberration-corrected 200kV field-emission scanning transmission electron microscope. *Ultramicroscopy*, *106*(11), 963–969.
64. Terada, S., Taniguchi, Y., & Kaji K. (2011). *Electron microscope with electron spectrometer*. Google Patents.
65. Hughes, D., & Hansen, N. (2001). Graded nanostructures produced by sliding and exhibiting universal behavior. *Physical Review Letters*, *87*(13), 135503.
66. Watanabe, M., et al. (2002). The pros and cons of apoptosis assays for use in the study of cells, tissues, and organs. *Microscopy and Microanalysis*, *8*(05), 375–391.
67. Liu, J., et al. (2013). PEGylation and Zwitterionization: Pros and cons in the renal clearance and tumor targeting of near-IR-emitting gold nanoparticles. *Angewandte Chemie International Edition*, *52*(48), 12572–12576.
68. Porter, S. R. (2004). Pros and cons of paper and electronic surveys. *New Directions for Institutional Research*, *2004*(121), 91–97.
69. Jin, Z., et al. (2014). Intrinsic transport properties of electrons and holes in monolayer transition-metal dichalcogenides. *Physical Review B*, *90*(4), 045422.
70. Yannouleas, C., & Landman, U. (2004). Structural properties of electrons in quantum dots in high magnetic fields: Crystalline character of cusp states and excitation spectra. *Physical Review B*, *70*(23), 235319.
71. Mauriz, P., Vasconcelos, M., & Albuquerque, E. (2003). Specific heat properties of electrons in generalized Fibonacci quasicrystals. *Physica A: Statistical Mechanics and its Applications*, *329*(1), 101–113.
72. Krumeich, F. (2011). *Properties of electrons, their interactions with matter and applications in electron microscopy*. Laboratory of Inorganic Chemistry, disponível em <http://www.microscopy.ethz.ch/downloads/Interactions.pdf>, consultado em, (pp. 3–08).

73. Caldwell, T., et al. (2009) *Transport properties of electrons in CF4*. arXiv preprint arXiv:0905.2549.
74. Kim, J. S., et al. (2008). Imaging of transient structures using nanosecond in situ TEM. *Science*, 321(5895), 1472–1475.
75. Betzig, E., et al. (2006). Imaging intracellular fluorescent proteins at nanometer resolution. *Science*, 313(5793), 1642–1645.
76. Midgley, P., & Weyland, M. (2003). 3D electron microscopy in the physical sciences: The development of Z-contrast and EFTEM tomography. *Ultramicroscopy*, 96(3), 413–431.
77. Klein, K. L., Anderson, I. M., & De Jonge, N. (2011). Transmission electron microscopy with a liquid flow cell. *Journal of Microscopy*, 242(2), 117–123.
78. Kolosnjaj-Tabi, J., et al. (2015). The one year fate of iron oxide coated gold nanoparticles in mice. *ACS Nano*, 9(8), 7925–7939.
79. Phillips, P., et al. (2011). Diffraction contrast STEM of dislocations: Imaging and simulations. *Ultramicroscopy*, 111(9), 1483–1487.
80. Herzing, A. A., Richter, L. J., & Anderson, I. M. (2010). 3D nanoscale characterization of thin-film organic photovoltaic device structures via spectroscopic contrast in the TEM 1. *The Journal of Physical Chemistry C*, 114(41), 17501–17508.
81. Bai, J., et al. (2010). Graphene nanomesh. *Nature Nanotechnology*, 5(3), 190.
82. Trandafilovic, L. V., et al. (2012). Formation of nano-plate silver particles in the presence of polyampholyte copolymer. *Colloids and Surfaces A: Physicochemical and Engineering Aspects*, 414, 17–25.
83. Oshima, C., et al. (1980). Thermionic emission from single-crystal LaB6 tips with [100],[110],[111], and [210] orientations. *Journal of Applied Physics*, 51(2), 1201–1206.
84. Williams, D. B., & Carter, C. B. (2009). Electron sources. In *Transmission electron microscopy: A textbook for materials science* (pp. 73–89). Boston: Springer US.
85. Baumann, C. E., Carin, L., & Stone, A. P. (2013). *Ultra-wideband, short-pulse electromagnetics 3*. Springer Science & Business Media.
86. Williams, D. B., & Carter, C. B. (2009). Lenses, apertures, and resolution. In *Transmission electron microscopy: A textbook for materials science* (pp. 91–114). Boston: Springer US.
87. Dehm, G., Howe, J. M., & Zweck, J. (2012). *In-situ electron microscopy: Applications in physics, chemistry and materials science*. Wiley.
88. Cheng, Q., Ma, H., & Cui, T. (2010). A complementary lens based on broadband metamaterials. *Journal of Electromagnetic Waves and Applications*, 24(1), 93–101.
89. Yuan, Y., et al. (2014). Ultra-high mobility transparent organic thin film transistors grown by an off-centre spin-coating method. *Nature Communications*, 5, 3005.
90. Binns, C., et al. (2012). Preparation of hydrosol suspensions of elemental and core–shell nanoparticles by co-deposition with water vapour from the gas-phase in ultra-high vacuum conditions. *Journal of Nanoparticle Research*, 14(9), 1136.
91. Somorjai, G. A., & Park, J. Y. (2008). Molecular surface chemistry by metal single crystals and nanoparticles from vacuum to high pressure. *Chemical Society Reviews*, 37(10), 2155–2162.
92. Laity, G., et al. (2014). A passive measurement of dissociated atom densities in atmospheric pressure air discharge plasmas using vacuum ultraviolet self-absorption spectroscopy. *Journal of Applied Physics*, 115(12), 123302.
93. Davis, A. B., & Marshak, A. (2004). Photon propagation in heterogeneous optical media with spatial correlations: Enhanced mean-free-paths and wider-than-exponential free-path distributions. *Journal of Quantitative Spectroscopy and Radiative Transfer*, 84(1), 3–34.
94. Homma, M., et al. (2006). History of vacuum circuit breakers and recent developments in Japan. *IEEE Transactions on Dielectrics and Electrical Insulation*, 13(1), 85–92.
95. Boxman, R. L. (2001). Early history of vacuum arc deposition. *IEEE Transactions on Plasma Science*, 29(5), 759–761.
96. Moniruzzaman, M. (2015). A study on dealers preference towards water pumps with special reference to beacon pump in Chennai City. *Global Journal of Management And Business Research*, 15(1).

97. Reinemann, D. J. (2005). The history of vacuum regulation technology. In *Proceedings of the 44th Annual meeting of the National Mastitis Council*. Citeseer.
98. Principe, L. M. (2000). *The aspiring adept: Robert Boyle and his alchemical quest*. Princeton University Press.
99. Hunter, M. (2003). *Robert Boyle reconsidered*. Cambridge University Press.
100. Anstey, P. R. (2002). *The philosophy of Robert Boyle*. Routledge.
101. Pisano, R., & Capecchi, D. (2010). On Archimedean roots in Torricelli's mechanics. In *The genius of Archimedes—23 centuries of influence on mathematics, science and engineering* (pp. 17–27). Springer.
102. Palmieri, P. (2009). Radical mathematical Thomism: Beings of reason and divine decrees in Torricelli's philosophy of mathematics. *Studies in History and Philosophy of Science Part A*, 40(2), 131–142.
103. Shapin, S., & Schaffer, S. (2011). *Leviathan and the air-pump: Hobbes, Boyle, and the experimental life (New in paper)*. Princeton University Press.
104. Hunter, M., Clericuzio, A., & Principe, L. M. (2001). *The correspondence of Robert Boyle* (Vol. 6). London: Pickering & Chatto.
105. Brewster, B. D. (2001). *Vacuum pumping systems*. Google Patents.
106. Zohuri, B., & McDaniel, P. (2015). Definitions and basic principles. In *Thermodynamics in nuclear power plant systems* (pp. 1–23). Springer.
107. Hucknall, D. J. (2013). *Vacuum technology and applications*. Elsevier.
108. Dong, L., et al. (2005). Observation of spiral pattern and spiral defect chaos in dielectric barrier discharge in argon/air at atmospheric pressure. *Physical Review E*, 72(4), 046215.
109. Smith, E. F., et al. (2006). Ionic liquids in vacuo: Analysis of liquid surfaces using ultra-high-vacuum techniques. *Langmuir*, 22(22), 9386–9392.
110. Day, C., & Giegerich, T. (2014). Development of advanced exhaust pumping technology for a DT fusion power plant. *IEEE Transactions on Plasma Science*, 42(4), 1058–1071.
111. Moazami, N., et al. (2013). Axial and centrifugal continuous-flow rotary pumps: A translation from pump mechanics to clinical practice. *The Journal of Heart and Lung Transplantation*, 32(1), 1–11.
112. Houzeaux, G., & Codina, R. (2007). A finite element method for the solution of rotary pumps. *Computers & Fluids*, 36(4), 667–679.
113. Holland, L. (2012). *Vacuum manual*. Springer Science & Business Media.
114. Bernhardt, K.-H. (2000). *Gas ballast system for a multi-stage positive displacement pump*. Google Patents.
115. Hucknall, D. J., & Morris, A. (2003). *Vacuum technology: Calculations in chemistry*. Cambridge: Royal Society of Chemistry.
116. Yu, Y.-L., et al. (2007). Coating of a thin layer of NaBH₄ solution for mercury vapor generation coupled to atomic fluorescence spectrometry. *Journal of Analytical Atomic Spectrometry*, 22(7), 800–806.
117. Carlisle, C., et al. (2000). Atomic imaging of the transition between oxygen chemisorption and oxide film growth on Ag {111}. *Surface Science*, 470(1), 15–31.
118. Tanabe, T., et al. (2002). An electrostatic storage ring for atomic and molecular science. *Nuclear Instruments and Methods in Physics Research Section A: Accelerators, Spectrometers, Detectors and Associated Equipment*, 482(3), 595–605.
119. Yamauchi, A. (2002). *Turbo molecular pump*. Google Patents.
120. Uhrig, D., & Mays, J. W. (2005). Experimental techniques in high-vacuum anionic polymerization. *Journal of Polymer Science Part A: Polymer Chemistry*, 43(24), 6179–6222.
121. Hadjichristidis, N., et al. (2000). Anionic polymerization: High vacuum techniques. *Journal of Polymer Science Part A: Polymer Chemistry*, 38(18), 3211–3234.
122. Spagnol, M. (2001). *Sputter ion pump*. Google Patents.
123. Qian, L., et al. (2010). *Sputter ion pump*. Google Patents.
124. Glugla, M., et al. (2006). ITER fuel cycle R&D: Consequences for the design. *Fusion Engineering and Design*, 81(1), 733–744.

125. Keefer, B. G., & McLean, C. R. (2000). *High frequency rotary pressure swing adsorption apparatus*. Google Patents.
126. Inaguma, Y., & Hibi, A. (2005). Vane pump theory for mechanical efficiency. *Proceedings of the Institution of Mechanical Engineers, Part C: Journal of Mechanical Engineering Science*, 219(11), 1269–1278.
127. Sakaguchi, Y., Miwata, T., & Wada, A. (2016). *Turbo-molecular pump*. Google Patents.
128. Tsutsui, S. (2017). *Turbo-molecular pump*. Google Patents.
129. Tsutsui, S. (2016). *Turbo-molecular pump*. Google Patents.
130. Tsutsui, S., & Tsubokawa, T. (2015). *Turbo-molecular pump*. Google Patents.
131. Yamaguchi, T. (2013). *Turbo-molecular pump*. Google Patents.
132. Jeong, J., Lee, I., & Joo, J. (2015). A destruction pattern analysis of a Turbo-molecular pump according to the Foreline clamp damage in an ICP dry etcher for 300 mm wafers. *Applied Science and Convergence Technology*, 24(2), 27–32.
133. Moriya, T., Sugawara, E., & Matsui, H. (2015). Observation and elimination of recoil particles from Turbo molecular pumps. *IEEE Transactions on Semiconductor Manufacturing*, 28(3), 253–259.
134. Tsutsui, S. (2015). *Turbo molecular pump device*. Google Patents.
135. Dellby, N., et al. (2001). Progress in aberration-corrected scanning transmission electron microscopy. *Journal of Electron Microscopy*, 50(3), 177–185.
136. Gadsby, D. C. (2009). Ion channels versus ion pumps: The principal difference, in principle. *Nature Reviews Molecular Cell Biology*, 10(5), 344–352.
137. Weston, G. F. (2013). *Ultrahigh vacuum practice*. New York: Elsevier Science.
138. Shimizu, T. (2004). *Construction of a low temperature ultra high vacuum scanning tunneling/atomic force microscope*. Berkeley: University of California.
139. Malyshev, O. B. (2018). *Charged particle accelerators – Design and modelling of ultra-high vacuum (UHV) systems*. Wiley-VCH Verlag GmbH.
140. Chakradhar, A., et al. (2015). Support effects in the adsorption of water on CVD graphene: An ultra-high vacuum adsorption study. *Chemical Communications*, 51(57), 11463–11466.
141. Frankevich, V., et al. (2014). Fluorescence resonance energy transfer of gas-phase ions under ultra high vacuum and ambient conditions. *Physical Chemistry Chemical Physics*, 16(19), 8911–8920.
142. Bora, D. K., et al. (2014). An ultra-high vacuum electrochemical flow cell for in situ/operando soft X-ray spectroscopy study. *Review of Scientific Instruments*, 85(4), 043106.
143. Ren, W., et al. (2015). Development of an ultra-high vacuum system for space cold atom clock. *Vacuum*, 116, 54–59.
144. Miyase, T., et al. (2014). Roles of hydrogen in amorphous oxide semiconductor In-Ga-Zn-O: Comparison of conventional and ultra-high-vacuum sputtering. *ECS Journal of Solid State Science and Technology*, 3(9), Q3085–Q3090.
145. Matthews, G., & Contributors, J. E. (2013). Plasma operation with an all metal first-wall: Comparison of an ITER-like wall with a carbon wall in JET. *Journal of Nuclear Materials*, 438, S2–S10.
146. Williams, D. B., & Carter, C. B. (2009). Pumps and holders. *Transmission electron microscopy* (pp. 127–140). Boston: Springer US.
147. Quirk, M., & Serda, J. (2001). *Semiconductor manufacturing technology* (Vol. 1). Upper Saddle River: Prentice Hall.
148. Lessard, P. A. (2000). Dry vacuum pumps for semiconductor processes: Guidelines for primary pump selection. *Journal of Vacuum Science & Technology, A: Vacuum, Surfaces, and Films*, 18(4), 1777–1781.
149. Ruskin, R. S., Yu, Z., & Grigorieff, N. (2013). Quantitative characterization of electron detectors for transmission electron microscopy. *Journal of Structural Biology*, 184(3), 385–393.
150. McMullan, G., et al. (2014). Comparison of optimal performance at 300keV of three direct electron detectors for use in low dose electron microscopy. *Ultramicroscopy*, 147, 156–163.

151. Meyer, R. R., & Kirkland, A. I. (2000). Characterisation of the signal and noise transfer of CCD cameras for electron detection. *Microscopy Research and Technique*, 49(3), 269–280.
152. Gruner, S. M., Tate, M. W., & Eikenberry, E. F. (2002). Charge-coupled device area X-ray detectors. *Review of Scientific Instruments*, 73(8), 2815–2842.
153. Janesick, J. R. (2001). *Scientific charge-coupled devices* (Vol. 83). Bellingham: SPIE press.
154. Williams, D. B., & Carter, C. B. (2009). How to see electrons. In *Transmission electron microscopy: A textbook for materials science* (pp. 115–126). Boston: Springer US.
155. Sermanet, P., et al. (2013). *Overfeat: Integrated recognition, localization and detection using convolutional networks*. arXiv preprint arXiv:1312.6229.
156. Dopita, M., et al. (2007). The wide field spectrograph (WiFeS). *Astrophysics and Space Science*, 310(3–4), 255–268.
157. Buechel, R. R., et al. (2010). Ultrafast nuclear myocardial perfusion imaging on a new gamma camera with semiconductor detector technique: First clinical validation. *European Journal of Nuclear Medicine and Molecular Imaging*, 37(4), 773–778.
158. Popovic, Z., et al. (2000). Life extension of organic LED's by doping of a hole transport layer. *Thin Solid Films*, 363(1), 6–8.
159. Van Oudheusden, T., et al. (2007). Electron source concept for single-shot sub-100 fs electron diffraction in the 100 keV range. *Journal of Applied Physics*, 102(9), 093501.
160. Che, W.-Q., et al. (2007). Investigation on the ohmic conductor losses in substrate-integrated waveguide and equivalent rectangular waveguide. *Journal of Electromagnetic Waves and Applications*, 21(6), 769–780.
161. Zybtshev, S., et al. (2012). Growth, crystal structure and transport properties of quasi one-dimensional conductors NbS₃. *Physica B: Condensed Matter*, 407(11), 1696–1699.
162. Van Eijk, C. W. (2001). Inorganic-scintillator development. *Nuclear Instruments and Methods in Physics Research Section A: Accelerators, Spectrometers, Detectors and Associated Equipment*, 460(1), 1–14.
163. Castillo-Mejía, F., et al. (2001). Small plasma focus studied as a source of hard X-ray. *IEEE Transactions on Plasma Science*, 29(6), 921–926.
164. Milazzo, A.-C., et al. (2005). Active pixel sensor array as a detector for electron microscopy. *Ultramicroscopy*, 104(2), 152–159.
165. Wiedenheft, B., et al. (2011). Structures of the RNA-guided surveillance complex from a bacterial immune system. *Nature*, 477(7365), 486–489.
166. Hutchison, J. L., et al. (2005). A versatile double aberration-corrected, energy filtered HREM/STEM for materials science. *Ultramicroscopy*, 103(1), 7–15.
167. Egerton, R., & Malac, M. (2005). EELS in the TEM. *Journal of Electron Spectroscopy and Related Phenomena*, 143(2), 43–50.
168. Poland, C. A., et al. (2008). Carbon nanotubes introduced into the abdominal cavity of mice show asbestos-like pathogenicity in a pilot study. *Nature Nanotechnology*, 3(7), 423.
169. Baldwin, C. E., Paratz, J. D., & Bersten, A. D. (2011). Diaphragm and peripheral muscle thickness on ultrasound: Intra-rater reliability and variability of a methodology using non-standard recumbent positions. *Respirology*, 16(7), 1136–1143.
170. Mayer, J., et al. (2007). TEM sample preparation and FIB-induced damage. *MRS Bulletin*, 32(05), 400–407.
171. Giannuzzi, L. A. (2006). *Introduction to focused ion beams: Instrumentation, theory, techniques and practice*. Springer Science & Business Media.
172. Gant, A., & Gee, M. (2011). A review of micro-scale abrasion testing. *Journal of Physics D: Applied Physics*, 44(7), 073001.
173. Heymann, J. A., et al. (2009). 3D imaging of mammalian cells with ion-abrasion scanning electron microscopy. *Journal of Structural Biology*, 166(1), 1–7.
174. Malkin, S., & Guo, C. (2008). *Grinding technology: Theory and application of machining with abrasives*. New York: Industrial Press.
175. Kalpakjian, S., Schmid, S. R., & Sekar, K. V. (2014). *Manufacturing engineering and technology*. Upper Saddle River: Pearson.

176. Webster, J., & Tricard, M. (2004). Innovations in abrasive products for precision grinding. *CIRP Annals – Manufacturing Technology*, 53(2), 597–617.
177. Ersoy, A., Buyuksagic, S., & Atici, U. (2005). Wear characteristics of circular diamond saws in the cutting of different hard abrasive rocks. *Wear*, 258(9), 1422–1436.
178. Mitchell, D., et al. (2003). Characterisation of PI 3 and RF plasma nitrided austenitic stainless steels using plan and cross-sectional TEM techniques. *Surface and Coatings Technology*, 165(2), 107–118.
179. Mukhopadhyay, S. M. (2003). Sample preparation for microscopic and spectroscopic characterization of solid surfaces and films. *Sample Preparation Techniques in Analytical Chemistry*, 162(9), 377–411.
180. Bockris, J. O. M., & Reddy, A. K. (2000). *Modern electrochemistry 2B: Electrodicts in chemistry, engineering, biology and environmental science*. Vol. 2. Springer Science & Business Media.
181. Greeley, J., & Nørskov, J. K. (2007). Electrochemical dissolution of surface alloys in acids: Thermodynamic trends from first-principles calculations. *Electrochimica Acta*, 52(19), 5829–5836.
182. Bakhsh, T. A., Sadr, A., & Tagami, J. (2015). Focused ion beam processing for transmission electron microscopy of composite/adhesive interfaces. *Journal of Adhesion Science and Technology*, 29(3), 232–243.
183. Perdu, P., Desplats, R., & Beaudoin, F. (2000). A review of sample backside preparation techniques for VLSI. *Microelectronics Reliability*, 40(8), 1431–1436.
184. Ayache, J., et al. (2010). *Sample preparation handbook for transmission electron microscopy: Techniques*. Vol. 2. Springer Science & Business Media.
185. Alam, S. N., et al. *Sample preparation techniques for electron microscopy 50 years of SEM and beyond!*
186. Cooke, K. O. (2016). Parametric analysis of electrodeposited nano-composite coatings for abrasive wear resistance. In *Electrodeposition of composite materials*. InTech.
187. Odian, G. (2004). *Principles of polymerization*. Wiley.
188. Predel, T., et al. (2007). Ionic liquids as operating fluids in high pressure applications. *Chemical Engineering & Technology*, 30(11), 1475–1480.
189. Chan, L., Hiller, J. M., & Giannuzzi, L. A. (2014). Ex situ lift out of plasma focused ion beam prepared site specific specimens. In *ISTFA 2014: Conference Proceedings from the 40th International Symposium for Testing and Failure Analysis*. ASM International.
190. Mahamid, J., et al. (2015). A focused ion beam milling and lift-out approach for site-specific preparation of frozen-hydrated lamellas from multicellular organisms. *Journal of Structural Biology*, 192(2), 262–269.
191. Cui, A., et al. (2015). Single grain boundary break junction for suspended nanogap electrodes with gapwidth down to 1–2 nm by focused ion beam milling. *Advanced Materials*, 27(19), 3002–3006.
192. Villa, E., et al. (2013). Opening windows into the cell: Focused-ion-beam milling for cryo-electron tomography. *Current Opinion in Structural Biology*, 23(5), 771–777.
193. Fukuda, Y., et al. (2014). Coordinate transformation based cryo-correlative methods for electron tomography and focused ion beam milling. *Ultramicroscopy*, 143, 15–23.
194. Hsieh, C., et al. (2014). Practical workflow for cryo focused-ion-beam milling of tissues and cells for cryo-TEM tomography. *Journal of Structural Biology*, 185(1), 32–41.
195. Schaffer, M., et al. (2015). Cryo-focused ion beam sample preparation for imaging vitreous cells by cryo-electron tomography. *Bio-protocol*, 5(17), e1575.
196. Buchheim, J., et al. (2016). Understanding the interaction between energetic ions and freestanding graphene towards practical 2D perforation. *Nanoscale*, 8(15), 8345–8354.
197. Dykstra, M. J., & Reuss, L. E. (2003). *Biological electron microscopy: Theory, techniques, and troubleshooting*. New York: Springer US.
198. Munoz-Tabares, J. A., et al. Microstructural changes in 3Y-TZP induced by scratching and indentation. *Journal of the European Ceramic Society*, 32(15), 3919–3927.
199. Mitra, S. (2004). *Sample preparation techniques in analytical chemistry*. Vol. 237. Wiley.

200. Smalley, R. E., et al. (2003). *Carbon nanotubes: Synthesis, structure, properties, and applications*. Vol. 80. Springer Science & Business Media.
201. Stankovich, S., et al. (2006). Graphene-based composite materials. *Nature*, 442(7100), 282.
202. Joy, D. C., & Romig Jr, A. D. (1986). *Principles of analytical electron microscopy*. Springer Science & Business Media.
203. Nellist, P., & Pennycook, S. (1998). Subangstrom resolution by underfocused incoherent transmission electron microscopy. *Physical Review Letters*, 81(19), 4156.
204. Reimer, L., & Kohl, H. (2008). *Transmission electron microscopy: Physics of image formation*. New York: Springer.
205. Rosenauer, A., et al. (2014). Conventional transmission electron microscopy imaging beyond the diffraction and information limits. *Physical Review Letters*, 113(9), 096101.
206. Cejka, J., Corma, A., & Zones, S. (2010). *Zeolites and catalysis: Synthesis, reactions and applications*. Weinheim: Wiley.
207. Bals, S., et al. (2007). High-quality sample preparation by low kV FIB thinning for analytical TEM measurements. *Microscopy and Microanalysis*, 13(02), 80–86.
208. Sun, B., et al. (2005). Artifacts induced in metallic glasses during TEM sample preparation. *Scripta Materialia*, 53(7), 805–809.
209. Caplovicova, M., et al. (2007). An alternative approach to carbon nanotube sample preparation for TEM investigation. *Ultramicroscopy*, 107(8), 692–697.
210. Carter, C. B., & Williams, D. B. (2016). *Transmission electron microscopy: Diffraction, imaging, and spectrometry*. Springer International Publishing.
211. Joo, J. H., & Lee, J.-S. (2013). Library approach for reliable synthesis and properties of DNA–gold nanorod conjugates. *Analytical Chemistry*, 85(14), 6580–6586.
212. Xie, J., et al. (2008). The synthesis of SERS-active gold nanoflower tags for in vivo applications. *ACS Nano*, 2(12), 2473–2480.
213. Hugounenq, P., et al. (2012). Iron oxide monocrystalline nanoflowers for highly efficient magnetic hyperthermia. *The Journal of Physical Chemistry C*, 116(29), 15702–15712.
214. Guardia, P., et al. (2012). Water-soluble iron oxide nanocubes with high values of specific absorption rate for cancer cell hyperthermia treatment. *ACS Nano*, 6(4), 3080–3091.
215. Corain, B., Schmid, G., & Toshima, N. (2011). *Metal nanoclusters in catalysis and materials science: The issue of size control*. Elsevier Science.
216. Wang, Z. (2000). *Transmission electron microscopy of shape-controlled nanocrystals and their assemblies*. ACS Publications.
217. García-Martínez, J., Li, K., & Davis, M. E. (2015). *Mesoporous zeolites: Preparation, characterization and applications*. Weinheim: Wiley.
218. Kirkland, A., & Young, N. (2012). Advances in high-resolution transmission electron microscopy for materials science. *Microscopy and Analysis*, 26(6), 19–24.
219. Yao, N., & Wang, Z. L. (2006). *Handbook of microscopy for nanotechnology*. Springer US.
220. Gusev, E. P., et al. (2000). High-resolution depth profiling in ultrathin Al₂O₃ films on Si. *Applied Physics Letters*, 76(2), 176–178.
221. 纳米技术中的显微学手册：电子显微学。第2卷。2005：清华大学出版社。
222. Egerton, R. (2011). *Physical principles of electron microscopy: An introduction to TEM, SEM, and AEM*. Springer US.
223. Deepak, F. L., Mayoral, A., & Arenal R. (2015). *Advanced transmission electron microscopy: Applications to nanomaterials*. Springer International Publishing.
224. LeBeau, J. M., et al. (2008). Quantitative atomic resolution scanning transmission electron microscopy. *Physical Review Letters*, 100(20), 206101.
225. Muller, D. A. (2009). Structure and bonding at the atomic scale by scanning transmission electron microscopy. *Nature Materials*, 8(4), 263–270.
226. Pennycook, S. J. (2011). A scan through the history of STEM. In *Scanning transmission electron microscopy* (pp. 1–90). Springer.
227. Buban, J. P., et al. (2010). High-resolution low-dose scanning transmission electron microscopy. *Journal of Electron Microscopy*, 59(2), 103–112.

228. Hawkes, P., et al. (2013). *Energy-filtering transmission electron microscopy*. Vol. 71. Springer.
229. Torre, B., et al. (2011). Magnetic force microscopy and energy loss imaging of superparamagnetic iron oxide nanoparticles. *Scientific Reports*, 1, 202.
230. Yu, H., et al. (2005). Dumbbell-like bifunctional Au⁺ Fe₃O₄ nanoparticles. *Nano Letters*, 5(2), 379–382.
231. Esparza, R., et al. (2014). Atomic structure characterization of Au–Pd bimetallic nanoparticles by aberration-corrected scanning transmission electron microscopy. *The Journal of Physical Chemistry C*, 118(38), 22383–22388.
232. Feng, A. L., et al. (2015). Distance-dependent plasmon-enhanced fluorescence of upconversion nanoparticles using polyelectrolyte multilayers as tunable spacers. *Scientific Reports*, 5, 7779.
233. Gatel, C., et al. (2017). Inhomogeneous spatial distribution of the magnetic transition in an iron-rhodium thin film. *Nature Communications*, 8, 15703.
234. Saleh, I. M., et al. (2003). Adhesion of endodontic sealers: Scanning electron microscopy and energy dispersive spectroscopy. *Journal of Endodontics*, 29(9), 595–601.
235. Martins, R., Bahia, M., & Buono, V. (2002). Surface analysis of ProFile instruments by scanning electron microscopy and X-ray energy-dispersive spectroscopy: A preliminary study. *International Endodontic Journal*, 35(10), 848–853.
236. Brodowski, S., et al. (2005). Morphological and chemical properties of black carbon in physical soil fractions as revealed by scanning electron microscopy and energy-dispersive X-ray spectroscopy. *Geoderma*, 128(1), 116–129.
237. d'Alfonso, A., et al. (2010). Atomic-resolution chemical mapping using energy-dispersive x-ray spectroscopy. *Physical Review B*, 81(10), 100101.
238. Pascarelli, S., et al. (2006). Energy-dispersive absorption spectroscopy for hard-X-ray micro-XAS applications. *Journal of Synchrotron Radiation*, 13(5), 351–358.
239. Herzing, A. A., et al. (2008). Energy dispersive X-ray spectroscopy of bimetallic nanoparticles in an aberration corrected scanning transmission electron microscope. *Faraday Discussions*, 138, 337–351.
240. Chu, M.-W., et al. (2010). Emergent chemical mapping at atomic-column resolution by energy-dispersive X-ray spectroscopy in an aberration-corrected electron microscope. *Physical Review Letters*, 104(19), 196101.
241. Ferrari, A. C., et al. (2000). Density, sp³ fraction, and cross-sectional structure of amorphous carbon films determined by X-ray reflectivity and electron energy-loss spectroscopy. *Physical Review B*, 62(16), 11089.
242. Egerton, R. (2008). Electron energy-loss spectroscopy in the TEM. *Reports on Progress in Physics*, 72(1), 016502.
243. Laffont, L., et al. (2006). Study of the LiFePO₄/FePO₄ two-phase system by high-resolution electron energy loss spectroscopy. *Chemistry of Materials*, 18(23), 5520–5529.
244. Tan, H., et al. (2011). 2D atomic mapping of oxidation states in transition metal oxides by scanning transmission electron microscopy and electron energy-loss spectroscopy. *Physical Review Letters*, 107(10), 107602.
245. Madsen, S. J., et al. (2017). Observing plasmon damping due to adhesion layers in gold nanostructures using electron energy loss spectroscopy. *ACS Photonics*, 4(2), 268–274.
246. Williams, R. P., Hart, R. D., & Van Riessen, A. (2011). Quantification of the extent of reaction of metakaolin-based geopolymers using X-ray diffraction, scanning electron microscopy, and energy-dispersive spectroscopy. *Journal of the American Ceramic Society*, 94(8), 2663–2670.
247. Zhao, Y., et al. (2010). In situ electron energy loss spectroscopy study of metallic Co and Co oxides. *Journal of Applied Physics*, 108(6), 063704.
248. Titantah, J., & Lamoen, D. (2005). sp³/sp² characterization of carbon materials from first-principles calculations: X-ray photoelectron versus high energy electron energy-loss spectroscopy techniques. *Carbon*, 43(6), 1311–1316.
249. Daniels, H., et al. (2003). Experimental and theoretical evidence for the magic angle in transmission electron energy loss spectroscopy. *Ultramicroscopy*, 96(3), 523–534.

250. Morello, M., et al. (2008). Sub-cellular localization of manganese in the basal ganglia of normal and manganese-treated rats: An electron spectroscopy imaging and electron energy-loss spectroscopy study. *Neurotoxicology*, 29(1), 60–72.
251. Holtz, M. E., et al. (2013). In situ electron energy-loss spectroscopy in liquids. *Microscopy and Microanalysis*, 19(4), 1027–1035.
252. Kiely, C. J. (1999). *Electron microscopy and analysis 1999: Proceedings of the institute of physics electron microscopy and analysis group conference, University of Sheffield, 24–27 August 1999*. Taylor & Francis.
253. Sardela, M. (2014). *Practical materials characterization*. New York: Springer.
254. Zhang, X. F., & Zhang, Z. (2001). *Progress in transmission electron microscopy 1: Concepts and techniques*. Berlin: Springer.
255. Jimenez-Villar, E., et al. (2014). TiO₂@ Silica nanoparticles in a random laser: Strong relationship of silica shell thickness on scattering medium properties and random laser performance. *Applied Physics Letters*, 104(8), 081909.
256. Ernst, F., & Rühle, M. (2013). *High-resolution imaging and spectrometry of materials*. Berlin: Springer.
257. Kirkland, A. I., & Haigh, S. J. (2015). *Nanocharacterisation: 2nd edition*. Cambridge, UK: Royal Society of Chemistry.
258. McIntosh, J. R. (2011). *Cellular electron microscopy*. Elsevier Science.
259. Lartigue, L., et al. (2013). Biodegradation of iron oxide nanocubes: High-resolution in situ monitoring. *ACS Nano*, 7(5), 3939–3952.
260. Muller, D., et al. (2008). Atomic-scale chemical imaging of composition and bonding by aberration-corrected microscopy. *Science*, 319(5866), 1073–1076.
261. Lawrence, J., et al. (2003). Scanning transmission X-ray, laser scanning, and transmission electron microscopy mapping of the exopolymeric matrix of microbial biofilms. *Applied and Environmental Microbiology*, 69(9), 5543–5554.
262. Urban, K. W. (2008). Studying atomic structures by aberration-corrected transmission electron microscopy. *Science*, 321(5888), 506–510.
263. Bosman, M., et al. (2007). Two-dimensional mapping of chemical information at atomic resolution. *Physical Review Letters*, 99(8), 086102.
264. De Angelis, F., et al. (2010). Nanoscale chemical mapping using three-dimensional adiabatic compression of surface plasmon polaritons. *Nature Nanotechnology*, 5(1), 67–72.
265. Slater, T. J. A., et al. (2014). Correlating catalytic activity of Ag–Au nanoparticles with 3D compositional variations. *Nano Letters*, 14(4), 1921–1926.
266. Midgley, P. A., & Dunin-Borkowski, R. E. (2009). Electron tomography and holography in materials science. *Nature Materials*, 8(4), 271.
267. Koster, A., et al. (2000). Development and application of 3-dimensional transmission electron microscopy (3D-TEM) for the characterization of metal-zeolite catalyst systems. *Studies in Surface Science and Catalysis*, 130, 329–334.
268. Shearing, P., et al. (2010). Characterization of the 3-dimensional microstructure of a graphite negative electrode from a Li-ion battery. *Electrochemistry Communications*, 12(3), 374–377.
269. Chang, L. K., et al. (2008). Ultrastructural correlation of spectral-domain optical coherence tomographic findings in vitreomacular traction syndrome. *American Journal of Ophthalmology*, 146(1), 121–127.
270. Kübel, C., et al. (2005). Recent advances in electron tomography: TEM and HAADF-STEM tomography for materials science and semiconductor applications. *Microscopy and Microanalysis*, 11(05), 378–400.

Chapter 6

Materials Characterization Using Scanning Tunneling Microscopy: From Fundamentals to Advanced Applications



Suryakanti Debata, Trupti R. Das, Rashmi Madhuri, and Prashant K. Sharma

6.1 Introduction

Dealing with the objects at the nanoscale is currently most fascinating in condensed matter physics. With the advancement of technology and with the development of many experimental tools, the study of materials at the nanoscale has become practicable. Surface scanning at high resolution has become possible with the help of scanning probe microscopy, in which a nanodimensional probe is brought in close proximity to the surface and the physical processes happening due to the tip-sample interaction are recorded. In scanning tunneling microscopy (STM), a lateral resolution of few angstroms and a resolution of less than 1 Å are achieved along the perpendicular direction to the surface. The earliest arrival of the probe microscopic techniques to the world is STM. The invention of STM by Gerd Binnig and Heinrich Rohrer in the year 1982 astonished the surface science community [1]. This pioneering contrivance of imaging the materials in their atomic scale on real surface brought them the Nobel Prize in Physics 1986. They have used this surface imaging technique to inspect the surface features of the conducting substrates. Thereafter so many developments have been made in the field of surface science to vividly raise its application in multiple fields like surface analysis of nonconducting inorganic materials, organic frameworks, semiconductors, biological molecules, superconductors, atomic-scale manipulation, phonon detection, the study of charge density waves, and many more.

S. Debata · T. R. Das · P. K. Sharma (✉)

Functional Nanomaterials Research Laboratory, Department of Applied Physics, Indian Institute of Technology (Indian School of Mines), Dhanbad, Jharkhand, India
e-mail: prashant@iitism.ac.in

R. Madhuri

Department of Applied Chemistry, Indian Institute of Technology (Indian School of Mines), Dhanbad, Jharkhand, India

The working principle of this versatile instrument STM can be described by a simple quantum mechanical phenomenon, known as “quantum tunneling.” When a sharp conducting tip ending approximately at one atomic dimension is kept very close ($\sim 10 \text{ \AA}$) to a conducting surface, the tunneling current flows between the tip and the surface through a vacuum barrier, when a potential difference is applied between the two. As the tunneling current is exponentially dependent on the width of the barrier, even a small change in the distance of separation between the tip and the surface can be detected. The tip is generally made up of metals like W or Pt-Ir alloy, and it is operated by a piezo drive, consisting of three mutually perpendicular piezoelectric transducers (P_x , P_y , and P_z). A feedback circuit is connected in order to maintain an appropriate distance between the tip and sample. By applying an appropriate bias voltage (V) to the sample, the flow of electrons is controlled. If $V > 0$, the electrons from the occupied states of the tip will acquire the unoccupied states of the sample by tunneling through the potential barrier and the process is reversed for the case of $V < 0$. By scanning the tip over the entire surface, we can take the topographical images of the material under interest. Earlier STM needed vacuum environment for its operation. But as the technology developed, the researchers tried to scan the surface in normal conditions, i.e., in liquid and gaseous media, to resolve the problem of vacuum requirement in many of the electron microscopes. Another essential application of STM is the manipulation of atoms/molecules over the substrates. This can be achieved by several techniques like tip crash, changing the polarity of the electric field, vertical and lateral manipulation, etc. In a brief, we can say that STM is a versatile tool to touch, transfer, and hear the voice of the individual atoms and nanoscale structures present on the surface of the material.

6.2 Basic Theory of Scanning Tunneling Microscope (STM)

6.2.1 Physics of Tunneling

According to the classical theory, a particle moving with energy less than the energy of a potential barrier will reflect back to the same region. The possibility of the particle crossing the barrier cannot be explained by the laws of classical mechanics. However quantum mechanics can better explain the probability of the particle penetrating the potential barrier. Thus the working of STM can be well explained by the quantum mechanical phenomenon, known as “tunneling.” In a conventional STM, the metallic tip placed over the extended sample at a distance of $\sim 1 \text{ nm}$ forms a vacuum potential barrier for the electrons in between the tip and sample.

To understand the tunneling effect, let us consider a one-dimensional case, where a beam of electrons of energy E and mass m is incident from the left of the potential barrier of height V_0 (Fig. 6.1). The system can be divided into three regions as,

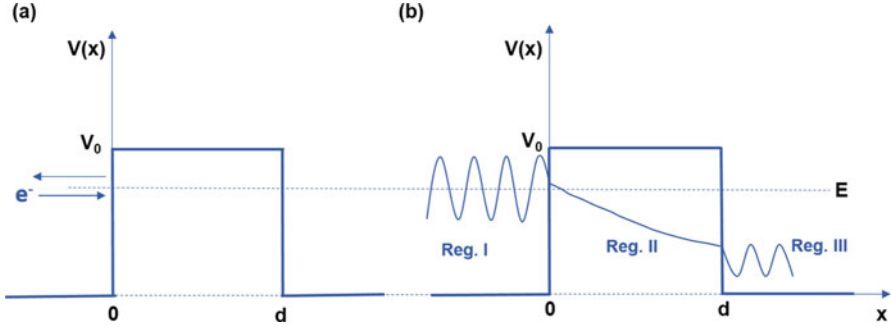


Fig. 6.1 Tunneling of electron through one-dimensional potential barrier. (a) According to classical mechanics, the electron should reflect back if the energy (E) is less than the height of the barrier (V_0). (b) In quantum mechanics there is a finite probability of the electron to cross the potential barrier

$$V = \begin{cases} 0, & x < 0 & \text{(Region I)} \\ V_0, & 0 < x < d & \text{(Region II)} \\ 0, & x > 0 & \text{(Region III)} \end{cases} \quad (6.1)$$

As the electrons are the quantum particles represented by the wave function $\Psi(x)$, they must obey the Schrödinger's equation represented by

$$-\frac{\hbar^2}{2m} \frac{\partial^2 \Psi(x)}{\partial x^2} + V(x)\Psi(x) = E\Psi(x) \quad (6.2)$$

where \hbar is the reduced Planck's constant, $\Psi(x)$ is the spatial wave function, and E is the energy of the electron beam.

The solution of Schrödinger's equation of the electron beam in the three different regions gives the nature of the wave function represented by

$$\Psi(x) = \begin{cases} Ae^{iK_1x} + Be^{-ik_1x}, & \text{Region I} \\ Ce^{k_2x} + De^{-k_2x}, & \text{Region II} \\ Ee^{ik_1x}, & \text{Region III} \end{cases} \quad (6.3)$$

where, A , B , C , D , and E are four arbitrary constants, k_1 is the wave vector in Regions I and III, and k_2 is the wave vector in Region II. $k_1 = \sqrt{\frac{2mE}{\hbar^2}}$ and $k_2 = \sqrt{\frac{2m(V_0-E)}{\hbar^2}}$.

The probability density corresponding to the wave functions in Regions I and III is oscillatory, and in Region II, the probability density of the electrons is exponentially decaying in nature.

From the continuity conditions of the wave functions and their first derivatives at the boundaries $x = 0$ and $x = d$, the transmission coefficient can be derived as,

$$T = \frac{1}{1 + \frac{1}{4} \left(\frac{K_1^2 + K_2^2}{K_1 K_2} \right)^2 \sin^2 h^2 (K_2 d)} \quad (6.4)$$

Since the transmission coefficient T has a finite value, the probability of finding the electrons in the region $x > d$ is finite. This is a pure quantum mechanical phenomenon, in which the particle with energy less than the potential barrier can penetrate through it, known as “tunneling.”

Electrons are filled in the densely packed energy levels of both tip and the sample. Obeying the Pauli’s exclusion principle, no more than two electrons occupy the same energy level. For the lowest energy state of the metal (at 0 K), the electrons are filled up to the Fermi level (E_F). Even at room temperature, a feeble number of electrons are excited to the higher energy states, which is negligible. To bring the electrons out of the metal surface, some energy is required from the external influences like temperature, photon irradiation, and externally applied electric field. This extra energy is known as “work function” of the metal (W), which brings the electrons out of the metal surface from the Fermi level.

The tunneling effect can be well understood by looking at the three situations represented in Fig. 6.2. The ideal case is taken, where it is assumed that the work function of the tip is same as that of the sample. Before applying the field, the energy states are completely filled in both sides of the barrier. As the electrons do not see any vacant state in the opposite side, there is no flow of e^- from one side to the other. Under the influence of the external potential V_a , the work function W is decreased to $(W - eV_a)$, where e represents the charge of the electron. This results in the lowering of the Fermi energy level in one side of the potential barrier, thereby introducing new vacant energy states in that region. This effect also changes the shape of the potential barrier, as can be observed in the slanted portion of the barriers in Fig. 6.2b, c. Now the bound electrons can tunnel from one side to the other through the vacuum, producing a measurable electrical current.

The tunneling current can be expressed by

$$I = A \exp \left\{ - \left(B \sqrt{W} d \right) \right\} \quad (6.5)$$

where A and B are two constants and d is the width of the potential barrier. The constant A is dependent on the density of electrons in the tip and sample. From the above equation, it is worth noting that the tunneling current is exponentially decreasing with the width of the potential barrier. Thus, even a small change in the gap between tip and sample can be detected by observing the change in the value of the tunneling current. When the work function of the tip and sample is different, the average value of the both is taken ($W = \frac{1}{2} (W_T + W_S)$) [2].

Depending on the polarity of the applied potential, the electrons can either tunnel from tip to sample or from sample to tip as represented in Fig. 6.2b, c. The situation is better realizable by looking at the diagrams shown in Fig. 6.2. Before the potential is applied to the system, the Fermi levels of the sample (E_S) and tip (E_T) are located at their original positions. When the external potential is applied to it, the position of

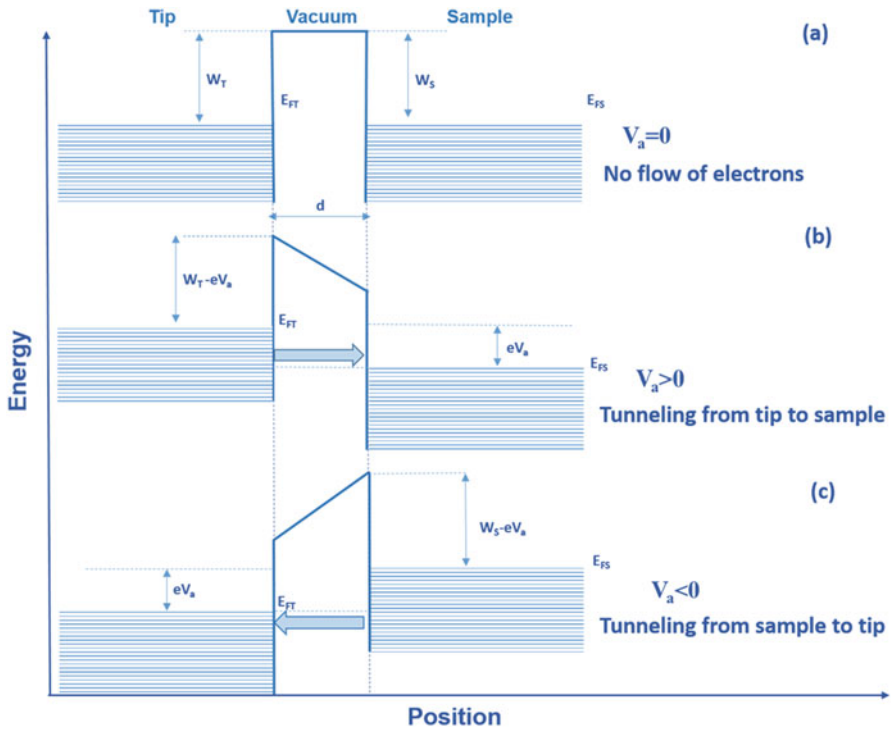


Fig. 6.2 (a) Energy level diagram of tip and sample separated by a potential barrier of width d . E_{FS} and E_{FT} represent the Fermi levels and W_S and W_T are the work functions of sample and tip, respectively. None of the electrons tunnel from either side of the barrier when there is no potential difference across them. (b) Tunneling of electrons from tip to sample and (c) from sample to tip, with the applied potential V

the Fermi levels is changed. If the sample is given with a positive potential ($V_S > 0$), the position of E_{FS} goes down and provides empty states for the tip electrons. Similarly, the positive potential applied to the tip lowers the position of E_{FT} in the tip side. The electrons acquiring energy from the applied potential are excited to the higher energy states. Thus the work functions of the tip and the sample are decreased to $(W_T - eV_a)$ and $(W_S - eV_a)$, respectively. When the energy of the electrons in one side becomes greater than the other, tunneling of electrons takes place from the region with higher energy to the lower [3].

The theoretical formulation of tunneling effect in one dimension is much simpler, but bringing this concept into real experiment as in STM is quite demanding. In order to get the description of the entire process, a more pragmatic modeling is needed. As in an STM, the tunneling process takes place between tip and sample, and the exact geometry and the choice of the tip material must be taken care of. It must be kept in mind that the electron wave function in an STM is not the same as that of a free electron in a one-dimensional system. We must deal with the three-dimensional model for getting the electronic structure of the tip electrons.

6.2.2 Instrumentation

According to the theory established before, the tunneling of electrons from tip to sample depends on the Fermi level electron density of states of the sample at the locality of the tip. The tunneling current due to the overlapping of the wave functions of tip and sample becomes the measurable parameter in the surface study. Therefore the fundamental understanding of the geometry of STM tip is very essential. J. Tersoff and D. R. Hamann proposed a model to describe the microscopic structure of STM tip. When the tip is brought very close to the sample, the system (apex of tip) is assumed to be a spherical potential well of radius R . The center of curvature of the tip is represented by r_0 and d represents the distance of closest approach of the tip and sample (Fig. 6.3a). As the experiment is generally carried out in ambient environmental conditions with very low tip-sample separation, taking the first-order time-dependent perturbation theory, the tunneling current is represented by

$$I \propto \int_0^{eV} \rho_t(E) \rho_s(E, eV) T(E, eV) dE \quad (6.6)$$

where $T(E, eV)$ is the probability of the electrons tunneling through the potential barrier, represented as

$$T(E, eV) = \exp \left\{ -d \sqrt{\frac{4m}{\hbar^2} (W_T + W_S + eV - 2E)} \right\} \quad (6.7)$$

The symbols $\rho_t(E)$ and $\rho_s(E, eV)$ in Eq. (6.6) correspond to the density of states of tip and sample, respectively. The tunneling current through the vacuum potential barrier is proportional to the density of states of tip and sample and the probability of electrons passing through the barrier.

The lateral resolution of STM image depends on the radius of curvature of the tip (R) and the gap between the sample and tip (d), and this can be measured by using the formula $\{(2A^0)(R+d)\}^{\frac{1}{2}}$ [4]. Thus the important step toward obtaining a high-resolution image is to develop a tip of appropriate geometry. As realized by Binnig and Rohrer, a very sharp tip of diameter less than 1 nm is required to achieve the atomic-scale resolution. In the beginning the two scientists tried to develop the tip by mechanically grinding the pure metal wire W or Mo. This manual process of grinding resulted in the formation of many sharper mini-tips, which on close proximity of the sample initiate the tunneling process. This results in the formation of multiple images of the surface at a time, which is undesirable. There are many reports relying on other tip-sharpening processes which include electrochemical etching [5], ion milling [6], pulsed alternating current etching [7], cathode sputtering [8], annealing, field emission method, cutting, and others. Out of these sharpening techniques, electrochemical etching is serving as the most preferable technique in fabricating the sharp STM tip of radius of 10–100 nm.

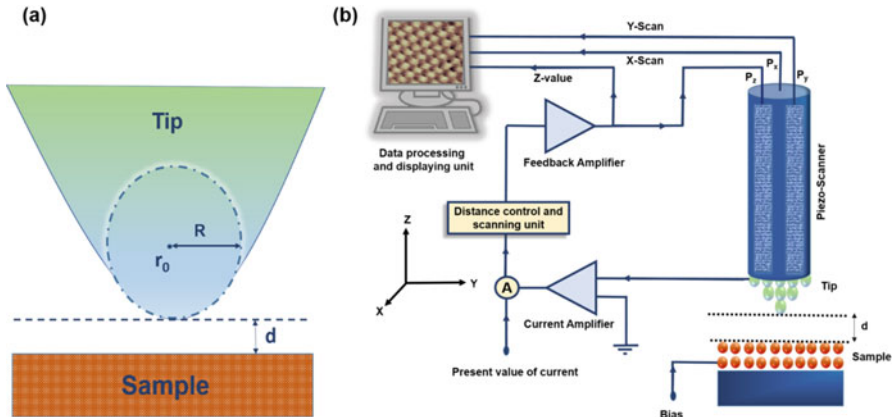


Fig. 6.3 Schematic representation of (a) geometry of STM tip as described by *Tersoff-Hamann* model. The apex of STM tip is assumed to be a sphere of radius R when brought very close to the sample. The distance of closest approach is d and the center of curvature of the tip is represented by r_0 . (b) Instrumental operation of STM

The detailed operation of STM is represented in Fig. 6.3b. The width of the potential barrier and the XY position of the tip can be controlled by an actuator consisting of a piezoelectric ceramic material (P_x , P_y , P_z). A control unit is stationed to supply the constant voltage to the piezo drive P_z , such that the tunneling current (I) is maintained at a constant value while scanning the tip along X and Y directions. Now with a constant work function, the topography of the sample $z(x, y)$ is recorded directly by measuring V_z . A feedback circuit is equipped with the piezo-scanner for regulating the position of the tip at a constant current level over the sample. For communicating the atomic world to the STM operator, a computer system is provided, which not only displays the control over the tip position but also displays the phenomena happening in the atomic scale by recording the data and converting the data into a clear image [9, 10].

6.2.3 Different Operational Modes of STM

6.2.3.1 Topography

The sharp metallic tip scans the surface “line by line” in all directions, producing tunneling current corresponding to the tunneling electrons. Since the tunneling current is an exponential function of tip height, in order to linearize the measurable current, it is advisable to use a logarithmic amplifier after the current amplifier in Fig. 6.3b.

Constant Current Mode

In most of the topographic mode of STM operation, the tunneling current is held constant with constant applied potential between the tip and sample (Fig. 6.4a). A feedback circuit is used to adjust the height of the tip over the surface with a continuously variable gap, such that any change in the tunneling current is compensated by the feedback loop during the surface analysis. Before each experiment, the feedback parameters need to be optimized to achieve the optimum gain. There are various factors including the preamplifier gain, tip distance, high voltage gain of the amplifier, and the intrinsic property of the microscope itself, which may affect the overall gain of the loop. Ziegler-Nichols method [11] is a suitable way of optimizing the feedback parameters, in which a PI feedback is used in such a way that the P-part (i.e., proportional gain) is increased until small oscillations of the current are detected. Then the P-part is reduced to 0.45 times the P_{crit} , and the I-part (integration with a characteristic time constant) is set to 0.85 times the oscillation period (T_{crit}). Both the P-part and I-part are combined and fed to the piezo-scanner. The voltage of the piezo-scanner can be recorded and the tunneling current is maintained constant accordingly. This topographic constant current mode is very much useful for the analysis of rough surfaces. Since the tunneling current is obtained by integrating over the states above and below E_F up to the energy corresponding to the applied potential, the topographic constant current mode presents the information of integrated density of states (DOS) of electrons on the surface. For the homogeneous metals, the tip-sample gap remains constant, and the position-dependent tip height ($z = z(x, y)$) provides the topographical information of the surface. The topographical image of the sample is thus obtained by continuously digitizing the feedback signal, which is the conventional parameter for measuring the height z of the tip from the surface.

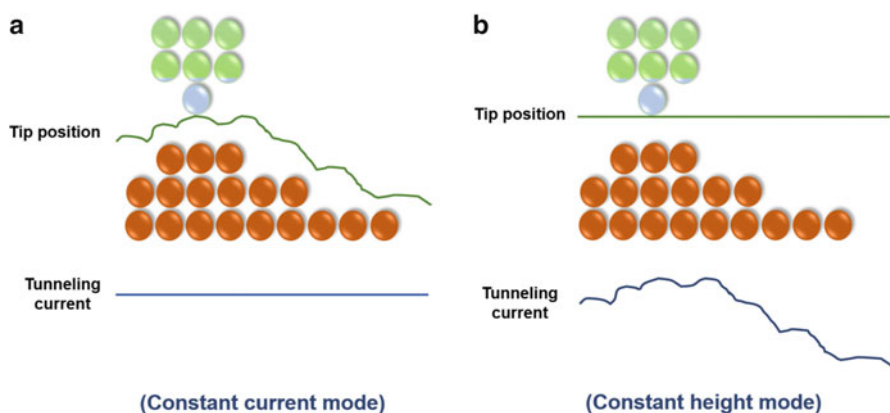


Fig. 6.4 Different operational modes of STM for surface analysis. (a) Constant current mode, (b) constant height mode

Constant Height Mode

The scan speed is quite less in the case of constant current mode as the tip is continuously adjusted to a certain height from the surface each time. This scan rate can be increased if this tip adjustment problem is avoided, therefore providing the opportunity to record the real-time video of the flat sample surface. This mode of topography is known as constant height mode or “skating mode,” for which a flat enough surface is preferably chosen. The surface for which the corrugation is greater than the sample-tip gap (few angstroms); there always remains a chance of tip crash [12]. The feedback circuit is also used in this mode, but the time constant of the feedback is more than the scan rate, so as to maintain the tip at a constant average height during each scan. The STM reported by D. Sarid et al. works in real time with a scan rate of four frames per second, in which a sinusoidal signal of frequency 1 kHz was used instead of triangular signal, which enables the raster scanning at a faster rate, and the tunneling current produced during the scan is fed to an Arlunya image processor to convert the scan rate into video rate. During the experiment, they have obtained both the geometric and spectroscopic information of BiI_3 cluster deposited on a graphite substrate [13]. The same research group has obtained the atomic-scale image of hexagonal MoS_2 at constant height mode in an air medium. They have used both positive and negative sample-tip biasing and obtained the image with high resolution for both the cases [14].

6.2.3.2 Spectroscopy

STM, a versatile tool for surface imaging, is not limited only to the imaging purpose; rather the application of STM is extended to surface tunneling spectroscopy. Overlapping of wave functions of tip and sample results in the tunneling current. If the applied potential is varied, the overlap of the wave functions is also changed and hence leads to the variation of tunneling current. This change in current w.r.t the applied voltage provides the spectroscopic information, making STM a multi-skilled instrument in surface science.

The earliest spectroscopic mode developed by Becker et al. [15] was helpful in generating and monitoring the electron standing waves between the tip and metal surface operated with a blunt tip with the apex greater than 20 \AA . The feedback circuit, which controls the tip-sample separation, was a DC integrating type feedback, and the bias voltage was taken by mixing a small AC component with the DC voltage. At a low-frequency voltage of 1–20 V, the tip-sample gap is adjusted to maintain the tunneling current at 1 nA and the in-phase modulation in tunneling current is recorded by a lock-in amplifier, which is operated at high-frequency voltage. This high-frequency AC signal was chosen such that the feedback circuit could not respond to it. With the continuous variation of V , the AC tunneling conductances (dI/dV) were measured. In the same year, G. Binnig et al. proposed that the surface states could be assumed as the hydrogen-like states and the applied tip-sample bias causes a stark shift in the hydrogenic spectrum. They extended

this concept to study the tunneling spectra for pure and oxygen-covered Ni (100) surface. The image-type surface electronic states result in the oscillatory behavior of dI/dV [16]. The shape of probing tip matters a lot in spectroscopic measurement. An atomically sharp tip is used to obtain the high-resolution spectrum, while the blunt tips have less position specific and observe the surface density of states averaged over the unit cell of the crystal.

As the transmission probability is dependent on the biasing voltage V (Eq. 6.7), the increasing background data with the increase in V is contained in dI/dV curves. However, several problems are associated with this method. (i) As the tip-sample separation varies with the applied potential V keeping I constant by the feedback loop, the lateral resolution is lost with the increase in voltage and the tip-sample gap. (ii) Since I is kept constant, the DC tunneling conductance is varied with V . With an extremely low bias voltage (~ 1 V), dI/dV approaches to infinity, which results in the loss of many useful data. (iii) In the case of semiconductors, it is very hard to control the tunneling current to a constant value. For a bias voltage lying within the bandgap of semiconductor, the stable current value is not maintained and hence the tip-sample gap decreases, which leads to a serious damage of the tip. In order to resolve all these discrepancies, the dynamic conductance dI/dV was divided by the DC conductance I/V , resulting in a dimensionless quantity providing the information about the tunneling spectroscopy [17]. Stroscio et al. reported for the first time that STM does not image the atomic positions in the sample, but it images the surface wave functions. The spectroscopic normalization $\frac{(dI/dV)}{(I/V)}$ or $d(\ln I)/d(\ln V)$ avoids the distance and energy dependency of transmission probability from the images. So this parameter becomes useful for getting information about the local density of states (LDOS) of electrons on the surface [18]. F. D. Natterer et al. have reported the scanning tunneling spectroscopic measurement of graphene-superconductor (GS) interface. Superconducting Al layers were grown on the multilayer graphene on the SiC substrate to form the GS junction. By measuring the tunneling differential conductance dI/dV , the decrease of the superconducting energy gap with the increase in the separation between graphene and the superconducting material was observed [19].

6.2.3.3 Work Function Measurement

The work function is affected by several bulk and surface features of the material under interest. The elemental composition and the electron density of the material change the work function, which is undergoing the bulk properties of the material. Among the surface features, the surface flatness, the surface dipole moment arising due to the split of an electron from the surface, surface adsorption, and atomic density of the surface affect the work function of the material significantly. The surface adsorbates like alkali metals decrease the work function, while it increases

with the exposure to oxygen environment. The work function of the material can be measured from the very conventional microscopic method, which includes the detection of surface electron emission and measurement of contact potential. But the spatial resolution is very less and the averaged information of the work function is disclosed at the probed area of the surface. For the measurement of mesoscopic work function, which relates the macroscopic work function with the atomic-scale surface potential, probes are kept very close to the surface ($<10 \text{ \AA}$). By using PAX (photoemission from absorbed xenon) technique, the potential seen by the absorbed xenon atom probes at the substrate can be measured. The image states can also be used to measure the mesoscopic work function. But the spatial resolution is still lower in these two methods of measuring the mesoscopic work function. By using STM, the spatial variation of mesoscopic work function can be estimated [20]. Before doing the surface scanning, Bennig et al. [1] described the work-function profile of the substrate. The work function (W) can be measured experimentally by modulating the tip-sample gap (Δs) by applying a sinusoidal potential through the piezo drive (P_z) during the scan. The modulation frequency is chosen far above the cutoff frequency of the feedback system, so that the measured current modulation is not affected. Again, this modulation frequency must be less than the response frequency of the current amplifier equipped with STM.

As represented in Eq. 6.5, the tunneling current is dependent on W ; thus by eliminating the other parameters from the expression of tunneling current, the work function can be measured. Payne et al. [21] have proposed two simpler techniques for the measurement of work function of metals using STM. One is by measuring the tunneling current $I(s)$ with constant applied potential, and the other technique is to measure the voltage $V(s)$ by maintaining constant tunneling current, where $I(s)$ and $V(s)$ represent the tunneling current and voltage as the functions of tip-sample separation (s), respectively. Experimentally the values of $d(\ln I)/ds$ and $d(\ln V)/ds$ can be measured to calculate the average value of work function. They have used the results of Simmons' calculation of tunneling current through the image-reduced potential barrier to compare between the theoretical and experimental findings [22]. The relation of $\ln j$ and $\ln V$ with s produced those curves, for which the gradient of their straight line portions is used for the derivation of effective work functions, representing the height of the potential barriers. $d(\ln I)/ds$ at small applied potential results in the accurate average work function, while the accuracy is less from the measurement of $d(\ln V)/ds$. Since the work function is sensitive to the surface features at atomic and nanometer scales, it is quite difficult to measure it directly.

S. Joshi et al. have characterized the hexagonal boron nitride (h-BN) grown on Cu (111) surface. The spatial inhomogeneity in the h-BN layer due to the presence of Moiré features was studied by measuring the tunneling current, which provides the information of local work function. The adsorption sites like "Hills" and "Valleys" of the slightly stretched h-BN monolayer result in the spatial variations in the local work function. As a result, the surface potential of the sample is also varied [23]. L. Vitali et al. have introduced the measurement of spatial variation in the local work function of a single molecule-metal contact [24].

6.2.3.4 Potentiometry

Another extension of STM application is scanning tunneling potentiometry (STP), which simultaneously provides the information about the topography and electric potential distribution on the surface with microscopic resolution. With the help of potentiometry technique, the problem with electrical conduction through granular structures can be resolved. For example, P. Muralt et al. have applied STP on a granular gold sheet. They have used a normal STM setup, with two electrodes attached to the substrate so that a potential difference $\Delta U = U_2 - U_1$ can be applied across it, where U_1 and U_2 are two electrode potentials. Thus a position-dependent potential $U(x, U_1, U_2)$ is distributed over the surface of the sample. In order to distinguish the tunneling voltage from this surface potential difference, the STM is operated with AC tunneling potential. The linear and symmetric IV -characteristic curves were emerged from the STP measurement, which is the case of metallic surfaces [25].

Soon after this achievement, the same research group has implemented the STM potentiometry technique to measure the microscopic potential distribution of semiconductors. A laser diode consisting of 100-nm-thick GaAs layer, sandwiched between two thin layers of $\text{Al}_{0.4}\text{Ga}_{0.6}\text{As}$, was used for this study. The STM was set with an ultrahigh vacuum high-resolution scanning electron microscope (SEM). The tunnel potential (V_t) used for the potentiometry was a combination of AC and DC components, which were applied to the tip and sample, respectively. A feedback circuit was also used to adjust the AC component of V_t , so that a constant tip-sample gap was maintained. The topography was found to be almost flat, but potential data of the semiconductor was obtained to be a waterfall-like characteristic, where the potential falls from the n-region to the p-region. The asymmetric region in the potential distribution indicates the less favorable electron injection from sample to tip, which is obvious in the case of a p-type semiconductor. In a p-type material, the number of electrons in the conduction band is very less, and the electrons from the valence band suffer a high-potential barrier, resulting in asymmetric potential distribution. However, the asymmetry was removed in a certain extent by the irradiation of electron beams of the SEM [26]. The potentiometric technique is analogous to the macroscopic four-probe method of measuring electrical charge transport, in which both of the inner tips are replaced by STM tips. Since the tip voltage is a known parameter, the surface voltage mapping can be obtained from the tunneling current as a measure of local tip-sample potential difference [27].

6.2.4 Tip-Material Influence

The atomic positions and electronic states on the tip apex play an important role in the lateral resolution of STM. A very sharp tip, which apex ends with only one atom, is necessary to get the atomic resolution of the surface. But obtaining such a

tip is highly challenging, and also it is very difficult to maintain it unharmed. Due to the strong tip-sample interaction and irregular surfaces of both sample and the tip, there always remains a chance of tip crash during the surface scan. Tungsten polycrystalline wire is the most commonly used material for fabricating STM tip. Apart from this, several transition metals like platinum, ruthenium, iridium, cobalt, nickel, and their alloys have been used as the tip materials. The methods of preparing such sharp tips include electrochemical etching, field evaporation method, annealing, sputtering mechanical cutting, grinding, and many more [28]. For example, HW Fink et al. have in situ developed a single-atom tip by adding an extra W atom on the top of W (111) pyramidal tip. The tip was constructed by removing the atoms in a stratified manner by field evaporation process [29]. As discussed by WA Hofer et al., the atomic resolution of the sample can also be obtained by using a tip covered by the atoms of the sample itself [30]. Electrochemical polishing is one of the preferred techniques for converting a metallic wire into a sharp tip. In this technique, a thin metal wire is dipped in an electrolyte with a counter electrode to supply an external AC or DC voltage between the two, so that the wire undergoes chemical dissolution to generate a sharp edge [31]. In a review by A. J. Melmed, few such methods for making sharp tips have been discussed in detail. A simple electrochemical approach involves the narrowing of the wire in presence of an applied potential. In floating-layer technique, a thin layer of the electrolyte solution is floated over a dense inert liquid base. After immersing the metal wire in the solution, the diameter of the small part immersed in the liquid is reduced gradually, and finally, the bottom of the specimen drops, forming two sharp tips. By using different shields, only a selected portion of the specimen is exposed to the electrolyte for etching purpose. Loop technique is also a kind of electrochemical etching method, in which the wire is protruded through the inert metal loop containing the active electrolyte [32]. The chemical modification in the STM tip brings the new opportunity of identifying different functional groups like hydroxyl (-OH), carboxyl (-COOH), ethers (-C-O-C-), and esters (-C(=O)-O-) present on the surface [33, 34].

The surface feature of the sample is as important as the structure of an STM tip for obtaining high-resolution images. A uniform, flat, and clean surface is needed for this purpose. If the roughness of the surface exceeds few atomic dimensions, then there remains a chance of accidental tip crash on the surface. Therefore the surface treatment by cleaning is a primary requirement before doing the STM measurement. The defect that reaches substrates can be cleaned and reconstructed by high-temperature annealing, cleaving, and sputtering techniques [35]. If the preliminary idea about the surface structure can be obtained, then STM can be directly used for the surface topography. If in case there is no previous knowledge about the surface structure, the combination of some experimental and theoretical methods becomes helpful for obtaining the structure explicitly [36]. Among the experimental tools, atomic probe microscopy, electron diffraction, ion scattering, Auger spectroscopy, infrared spectroscopy, and photoelectron emission methods are used for obtaining the preliminary idea of the surface features as well as for the surface preparation. The theoretical approaches including density functional theory

(DFT) [37, 38] and tight-binding model [39] are useful for computing the electronic structures of the surface.

As discussed by H. Ness et al., the influence of the whole tip-sample junction acts on the STM image. The interaction between tip and sample takes place by means of two types of forces. One is the microscopic chemical interaction between the atoms sitting on the surface of the sample and the tip edge, and the second one is the macroscopic forces, including van der Waals and electrostatic forces [40]. The electronic and atomic structures of the tip and surface are highly distorted by the close contact between them. This distortion generates the images which cannot be understood by the Tersoff-Hamann approach [4]. The electronic structure is also affected by the long-range electric field involved when the tip-sample separation is more than the range of forming the tip-sample chemical bonding. The microscopic forces are generally involved for obtaining the high-resolution images [41].

6.3 Imaging Process of STM

6.3.1 Topographical Process

The topographic image of a substrate provides the information about the surface nanostructure of that particular material. Topographic measurement is the fundamental experiment performed with an STM. The surface electronic structure of the material provides the way to interpret the STM topographic images. The electrons present on the sample surface can be represented by means of wave functions. According to Tersoff-Hamann model, the local density of states (LDOS) of the surface at the Fermi level in the locality of the tip decides the tunneling of an electron in an STM [4]. Depending on the penetration depth of the probing particles, a certain thickness of the sample surface can be explored. This thickness ranges up to few nanometers. The contours of the surface $z(x)$, maintaining constant LDOS (i.e., the constant electric conductance), determine the topographic image of the STM. These contours are represented by $z(x_i) = \langle z \rangle + \Delta(x_i, \langle z \rangle)$, where $\langle z \rangle$ represents the average separation between the tip and the surface and $\Delta(x_i, \langle z \rangle)$ represents the convolution of a surface profile function ($h(x_i)$) [42]. The image contrast depends on the sample bias voltage. At low applied potential, the tip follows a contour corresponding to the constant Fermi level density of states. However the semiconductors require the potential of the order of several volts, which violate the assumptions made by Tersoff and Hamann. Therefore the WKB theory of planar tunneling was emerged, according to which the tunneling current is written as represented in Eq. 6.6. S. Heinze et al. have discussed the corrugation reversal in STM images of bcc(110) transition metals (W(110), Ta(110), and Fe(110)), which depends on the bias voltage. The change in bias voltage results in the inversion of the surface corrugation, i.e., the protruding atoms appear like the interstices and the interstices appear as the atoms. The stripe-like topographical image appears

in the voltage range where this image inversion occurs. This results when the corrugation and anti-corrugation electronic states encounter [43]. G.M. Rutter et al. have captured the STM image of the interface of graphene and SiC substrate. They have discussed the bias-dependent surface imaging of single-layer graphene. At low applied bias, the graphene lattices are observed, while at higher bias, the adatoms at the interface are observed [44].

According to the polarity of the bias voltage, the positive bias ($V > 0$) given to the sample directs the electrons to tunnel from the tip to the substrate. Thus the vacant states of the sample are filled by the electrons which are previously occupying the energy states of the tip. Thus the contour followed by the STM tip is dependent on the spatial distribution of the electrons over the sample. When the sample is applied with a negative bias ($V < 0$), the electrons tunnel in a reverse direction and the tip follows the contour, which is dependent on the spatial distribution of the empty states of the sample. The tunneling probability is more for the electrons at the Fermi level of the electrode which is negatively biased [45].

The topographic image can also be dependent on the distance between the tip and the surface (d). The strength of the tip-surface interaction changes with a change in the gap between them, which sometimes cause the image variation. This kind of image variation can be attributed to the surface consisting of several orbitals, having the wave functions of different decay length. The d -dependency of the image comes from the shifting of the dominant surface orbital, which contributes the tunneling process. For example, Y. Takahashi et al. have reported the topographic image of Fe₂N layer. From the first-principle LDOS calculations, they have found that Fe 3d states change to s/p states with an increase in the tip-surface gap [46].

6.3.2 Spectroscopic Imaging

In scanning tunneling spectroscopic measurement, we get the information complementary to that obtained in topographic measurement. When applied bias exceeds the energy corresponding to Fermi level, more electronic states are involved in the imaging process. The LDOS of the surface as a function of lateral position (x, y) can be obtained from scanning tunneling spectroscopy (STS). For a particular bias voltage, the LDOS can be obtained from the dynamic conductance, dI/dV [47]. A. Selloni et al. have extended the Tersoff-Hamann model to generalize the expression for tunneling current for the moderate voltages. The expression for the tunneling current can be represented as

$$I \propto \int_{E_F}^{E_F + eV} \rho(E) T(E, V) dE \quad (6.8)$$

where $\rho(E)$ represents the local electron density of states of the sample at the locality of the tip and at energy $E = E_F + V$. The transmission coefficient $T(E, V)$ is the correction factor, which is accounted for the potential drop in the vacuum region [48]. This model is still unable to interpret the tunneling spectrum directly as the dynamic conductance dI/dV has no direct relationship with the density of states. However it provides a direct comparison of the band structure calculations with the STM image.

Most of the tunneling spectroscopic measurements are carried out in constant height mode. Thus a feedback circuit plays an important role in the spectroscopic measurement in an appropriate voltage range and the tunneling current is simultaneously measured. By adopting the method in a straightforward manner, we can obtain the low-resolution outcomes. The high-resolution spectra can be obtained from the simultaneous topography and $I-V$ measurements of the surface, which were first proposed by RJ Hamers et al. [49]. The electronic structures of the surface are measured by matching the $I-V$ characteristics at every spatial location of the surface.

By recording the differential conductance (dI/dV) spectra, O. Deniz et al. have demonstrated the electronic structure of armchair graphene nanoribbons (GNR). The graphene nanoribbons were grown on Au (111) and silicon was intercalated in between the GNR and Au substrate, so that the electronic band gap of GNR can be determined by using STS. Because of the silicon intercalation, the Au (111) surface states are suppressed, and the spectra of gold silicide-supported GNR reveal a well-defined bandgap of 2.7 eV [50].

6.4 Applications of STM in Various Fields

6.4.1 *STM in Single-Atom/Single-Molecule Manipulation and Its Application to Nanoscience and Nanotechnology*

Perturbation occurs at tip-sample interface when STM tip is at distance of less than 1 nm range from the sample surface. Such perturbation technique has influenced the researchers about the manipulation of atoms and molecules on the sample surface. Construction of quantum structures on the sample surfaces is based on this manipulation technique. The quantum structures are in atom-by-atom basis. Similarly, molecules are synthesized by one-molecule-at-a-time basis method [51–58]. Atomically a clean surface and high stable tip-sample junction lead to manipulating single atom and molecules. Pressures below 4×10^{-11} torr maintain an atomically clean sample condition for a long period of time. Polycrystalline tungsten wires are used tips in most cases.

In STM, tip crash technique is used for applying nanoindentation to measure hardness of material surface and to form nanowire between tip and sample [59–62]. For manipulation experiment, atomically sharp tip apex is much necessary. Initially the tip is dipped inside a metallic substrate for few nanometer at high voltage (>4 V). Then the tip apex is turned into sharper profile by the thermal energy produced due to the tip crash. The extraction of individual atoms from the native substrate is performed at a low tunneling bias condition. At the end of the experiment, the scattered individual atoms are found at tip-surface contact area. While using a silver-coated tungsten tip on Ag surface, mostly Ag atoms are extracted [63]. These atoms can be used as basic building block in atomistic construction. Lateral manipulation procedure is used to relocate atoms and molecules across the surface.

In 1990 Eigler and Schweizer demonstrated the lateral manipulation (LM) while writing the logo of IBM company with Xe atom on Ni substrate [64]. LM includes three steps, i.e., vertical approach of the tip toward the manipulated atom, scanning the tip parallel to the surface, and retracting the tip back to the normal image height. Tunneling resistance is used to analyze the tip-atom interaction strength. Their minimum distance between the tip and the atom is calculated by measuring the tunneling current for moving the atom at a fixed bias. A slope is calculated from the current and bias voltage plot, which corresponds to resistance. That resistance corresponds to distance between the tip and atom. There are three basic modes to analyze the nature of force between the tip and the atom, i.e., pushing, pulling, and sliding [65]. Due to tip-atom interaction, the atom follows the tip in pulling. There is a repulsive tip-atom interaction that arises in case of pushing. In atom manipulation process, the STM is set in constant current scanning mode. As the tip is placed vertically on the atom surface, there is a vertical force component that exists. Due to the unavailability of lateral force, the atom will not transfer to the tip or not move to the next adsorption site. When the tips move in parallel, the lateral force component increases and vertical force component decreases and there will be hopping of atoms to the next adsorption site under the tip. STM feedback retracts the tip to maintain a constant current causing an abrupt increase in tip height. In pushing mode, an abrupt decreasing in tip height occurs. The pushing and pulling signals are recorded at constant scanning mode. The manipulation signal here corresponds to the tunneling current intensity. Vertical manipulation is another technique which involves the transfer of atoms and molecules between the tip and surface [66–68]. Here the transfer is controlled by the electric field between the tip and the sample, exciting with inelastic tunneling electron and making a mechanical contact between tip atom and molecule. Here the basic mechanism is based on double potential well model. Surface and the tip apex are two stable positions for the manipulated atoms/molecules.

6.4.2 Application of STM in Surface Science

6.4.2.1 Graphite

STM is a fastest growing topic for the characterization of surfaces. Highly oriented pyrolytic graphite (HOPG) acts as a bench mark for STM instrumental test and calibration due to its large atomically flat area which is relatively clean and inert [69, 70]. Researchers have investigated many anomalous behavior of graphite surface. RJ Colton et al. have studied about the role of tip in imaging graphite in air by scanning tunneling microscope [69]. For imaging HOPG, a functioning tip is necessary. RJ Colton et al. have worked on pencil graphite lead and tungsten tip coated with graphite as working tip for better atomic resolution. By using ac or dc electrochemical etching procedure, tungsten tip was prepared, and for graphite coating, the tungsten tip was placed inside a colloidal graphite suspension. The graphite present in the tungsten tip leads to an oxide-free tip and resistant to further oxidation. During the imaging of HOPG, the tip provides high contact area along with more rigidity and better image quality. Tip has several structures consisting single and multiple atoms. The multiple-atom tip shows a trigonally symmetric graphitic plane where the center atom of the tip is 0.142 nm away from three outer atoms. During the scanning of graphite surface, the tip atom goes into or out of the registry with the surface atom. A surface image of hexagonal ring was observed through a single-atom tip or three-atom tip. The six atoms in the hexagonal ring have equal electron density, whereas in case of four-atom tip, three carbon atoms of the ring have the same electron density.

In case of graphene, STM observes honeycomb and triangular lattice for monolayer and bilayer films, respectively. HS Wong et al. have tried to determine the basic reason for the origin of triangular/honeycomb lattice transition in graphite [70]. They have solved the controversies regarding the mechanism of triangular/honeycomb lattice transition along with the origin of super lattice. The groups have also produced graphene nanoribbon by STM manipulation. During the imaging of HOPG, the sample under the tip was wrapped. By optimizing the scanning condition, graphene layers are decoupled from the underlying layers. STM tip is scanned over the graphene layers of HOPG through the zigzag termination. Later the graphene ribbons are successfully manipulated. The resulted superstructure is due to the misorientation between the layers. ME Stawasz et al. have investigated the ordered structure of dialkylamino hydroxylated squaraines adsorbed on HOPG [71]. The three-dimensional squaraines affect the generation and transportation abilities of charge in photoreceptor device, and also the n-alkyl substituent disturbs the intermolecular charge transport interaction. For such reason STM is useful in studying the ordered structure of organic molecule on solid substrate. JI Paredes et al. have investigated the plasma oxidation process of HOPG by combination atomic force microscope and STM and STM tip starching of HOPG substrate [72]. TG Gopakumar et al. have used STM and LEED for adsorption of planar palladium phthalocyanine (PdPc) molecules on the basal plane

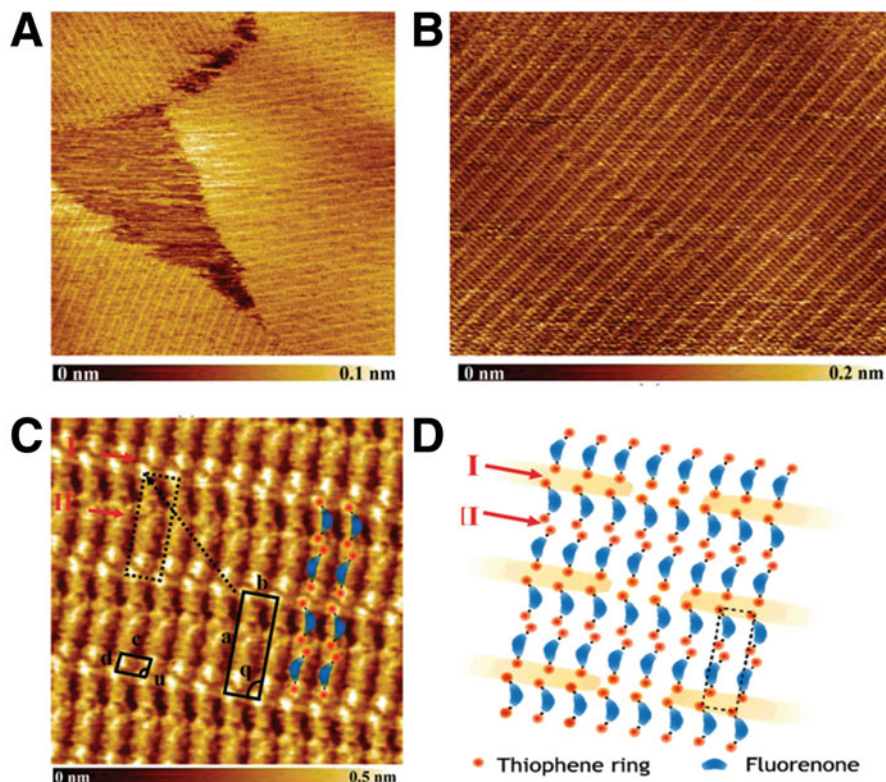


Fig. 6.5 STM images of B4OTF molecules assembled on graphite. (a) Three domains rotated by 120° with respect to each other, according to graphite axis; (b) magnified image of a mono domain, demonstrating the regular arrangement of B4OTF; (c) high-resolution STM images of B4OTF, showing two elementary cells (enclosed in dotted and solid black lines), shifted from each other by $4b$; (d) schematic representation of arrangement of B4OTF molecules on graphite surface. (This figure is adapted from Linares et al. [74])

of graphite [73]. M. Linares et al. have studied the self-assembled monolayer of bithiophene-fluorenone conjugated oligomers 2,7-bis-(4-octyl-thien-2-yl)-fluorene-9-one (B4OTF) and 2,7-bis-(5-octyl-thien-2-yl)-fluorene-9-one (B5OTF) on HOPG through STM technique [74].

Figure 6.5 represents STM images of B4OTF assembled on graphite. In Fig. 6.5a, three domains are found to be rotated by 120° with respect to each other. Figure 6.5b is the higher-resolution view of a single domain which shows a regular arrangement for B4OTF. In Fig. 6.5c slightly curved elongated objects are observed. The length of such elongated objects was found to be 1.4 nm. The molecule lies flat on the surface of graphite due to the π - π interactions with the substrate. Figure 6.5d shows the sketch of the organization of B4OTF molecules on the graphite surface.

B. Chilukuri et al. have studied about the self-assembly of cyclic trinuclear Au(I) complexes on HOPG at the solution-solid interface through STM technique [75]. The gold cyclotrimers form epitaxial nanostructure on HOPG surface. The first morphology shown in Fig. 6.6a, b involves a monolayer of Au_3Cb_3 molecule separated from its neighbor by 1.48 ± 0.05 nm. In the second morphology (Fig. 6.6c, d), Au_3Cb_3 molecules are assembled in form of hexagons wherein the center of each gold trimer is located at each vertex of hexagon and the center of hexagon has a vacant space, overall giving rise to a porous structure with a pore diameter 9.5 Å. The gold trimers are separated from its nearest neighbor at a center to center distance of 1.00 ± 0.02 n. For a simplicity and comparison, the first morphology is named as “open structure (OS),” and the second morphology is named as “closed structure (CS).”

6.4.2.2 Semiconductors

Processing of semiconductor devices is based on two types, i.e., additive process and subtractive process. In additive process, materials are added to the wafer through deposition, growth implantation, and chemical reaction. Subtractive process includes removal of unwanted material by mechanical and chemical means. Such process must be compatible with situations like pattern definition, submicron lateral dimension, and atomic level vertical dimension. To realize the phenomenon, surface and interface characterization is required. STM have special impact in characterizing the surface of sample. Better quality of semiconductor material depends on substrate, on which the materials are to be deposited. STM provides information about the defects and contaminants on substrate surface. Thickness of the semiconductor will be also provided by STM technique. Information regarding dopant segregations and diffusion properties are collected from the electronic study. Such electrical characterization of wafer depends on STM study. The voltages and electrostatic potentials in chips are mapped through spatial and electronic resolutions of STM at the electrical characterization of the semiconductor.

The spatial resolution of STM is also used to investigate the nature of epitaxial growth of metals, semiconductors, and insulators. The mechanism like nucleation and role of particulates in silicides are obtained through surface characterizations [76]. For STM application, a clean defined surface in air and solution is necessary. But in case of semiconductor electrodes, the surface of the semiconductors are generally covered with oxides, which is a major drawback. K. Uosaki et al. have applied STM microscopy to semiconductor/electrolyte interfaces and suggested about the inhibition of STM measurement at some specific potential. This is due to the more positive and negative potential than that of middle region [77]. The tip current in case of an etched n-gallium arsenide (GaAs) electrode was maintained at a preset value when the potential on n-GaAs was more negative than -250 mV and more positive than that of $+700$ mV. STM images at the two different potential regions explain the possibility of imaging at that region. The surface, after treatment

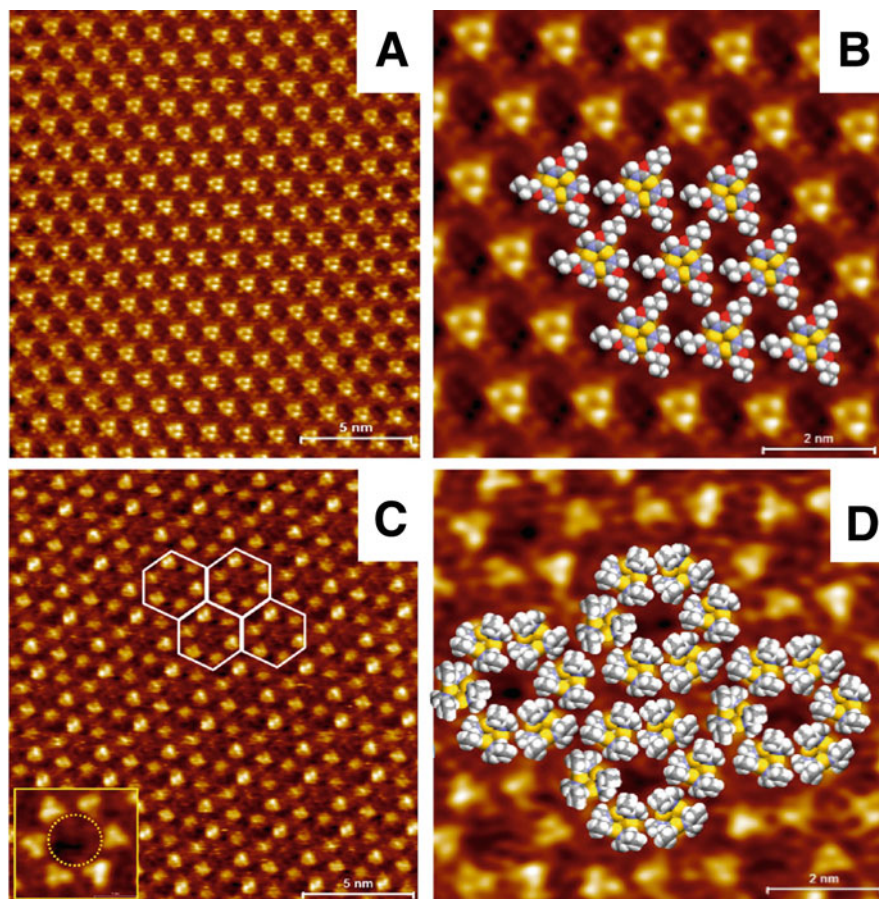


Fig. 6.6 (a) STM image of an open structure (OS) Au_3Cb_3 monolayer on HOPG. (b) Correlation-averaged OS STM image with models of Au_3Cb_3 laid on top. (c) STM image of a closed structure (CS) Au_3Cb_3 monolayer on HOPG. The white hexagons represent each unit cell; the inset at the bottom left corner represents a high-resolution image of each CS while the dotted circle represents a nanopore. (d) Correlation-averaged CS STM image with models of Au_3Cb_3 laid on top. Empty pores can be clearly seen at the center of each CS. (This figure is adapted from Chilukuri et al. [75])

of RuCl_3 solution, enables a flow of preset tip current with a condition that, the potential must be more negative than -100 mV and more positive than $+100$ mV. STM-fabricated devices have attained a special position. STM-fabricated devices at GHz frequencies enable the excited-state spectroscopy and measurement of the excited-state lifetime. For large-scale quantum devices, the practical bottom-up construction is enabled by STM lithography [78]. C. Volder et al. have developed an alternative way to synthesize silicon by reconstructing the surface of hexagonal MoSi_2 crystallites [79].

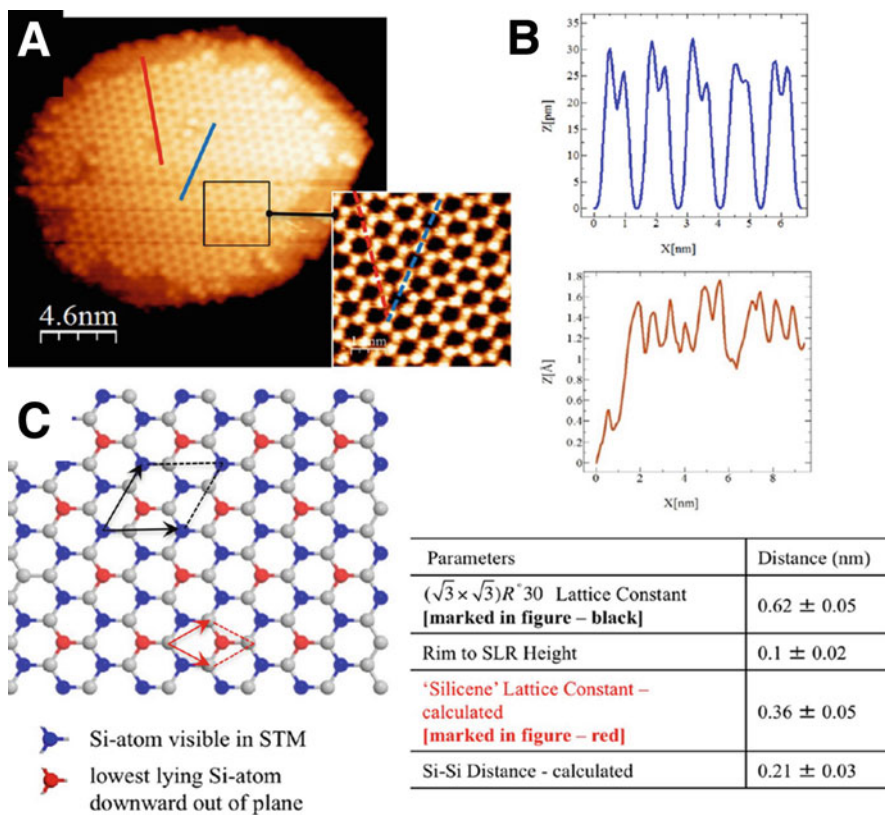


Fig. 6.7 (a) STM image of a representative crystallite, which shows the SLR; (b) line scans along high symmetry lines on the surface as marked in the image. The equivalent directions of the line scan are illustrated in a high-resolution image. (c) Model of the SLR reconstruction. (This figure is adapted from Volders et al. [79])

Silicene is a two-dimensional material like graphene. The band structure in silicene is Dirac type. In a typical process, silicene is synthesized by depositing monolayer amount of silicon on heated Ag surface. Later the Ir and ZrB_2 substrates are studied. Surface reconstruction of h-MoSi₂ nanocrystallites was performed at high temperature for synthesizing silicene. Solid-state epitaxy process is used to synthesize MoSi₂ nanocrystals on Si (001). The process leads to synthesis of silicone-like reconstruction (SLR) on MoSi₂ surface. STM is used to study the geometric and electronic structure of the SLR. Detailed description about SLR structure is studied in Fig. 6.7a; the inset atomically resolved STM image explains the honeycomb pattern where, as in Fig. 6.7c, the surface structure of SLR is provided. Figure 6.7b shows the line scans along high symmetry lines on the surface as marked in the corresponding image. With the help of line scan, the lattice constants are calculated and shown in the table inserted in Fig. 6.7. The equivalent

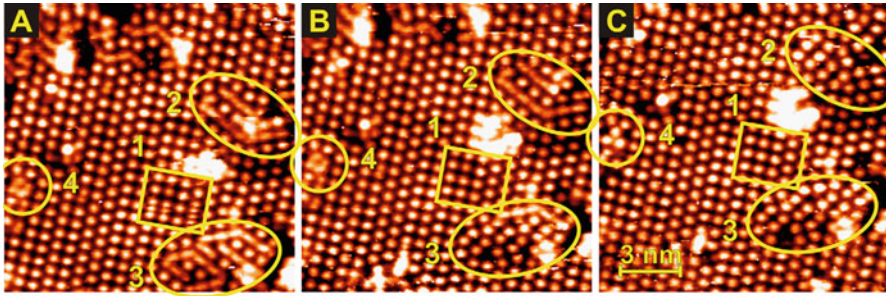


Fig. 6.8 A sequence of images of Ge(111) recorded with a conventional STM at room temperature. Time lapse between the images is 2 min. The images show different dynamic processes caused by mobile Ge adatoms. (This figure is adapted from Saedi et al. [80])

directions of the line scan are illustrated in a high-resolution image. The dimension of lattice constant was measured to be 0.62 ± 0.05 nm by the atoms visible in the STM image. SLR is due to the surface reconstruction of the h-MoSi₂ plane. Si atom decoupled from the underlying surface and adopts the honeycomb structure reducing the Si-Si bond length at the same time. The constructed honeycomb is formed with two Si atoms out of every Si hexagon buckled upward out of plane, and one Si atom is buckled downward into the plane. In STM, all Si atoms are not visible and only the third Si atom can be visualized.

A. Saedi et al. have studied the dynamic process on semiconductor, i.e., Ge(100), surface by using time-resolved STM [80]. The sample was subsequently annealed at a temperature of 1100 K and cooled down at room temperature. The sequences of empty-state STM images (Fig. 6.8a–c) of the sample on Ge surface were recorded at room temperature. The time required to take each frame is 2 min. Many defects like absence of adatoms and adatom islands were observed. The regions on the vicinity of defect or phase boundary are responsible for showing dynamics.

6.4.2.3 Metals

Precise control of the quantum state of a single molecule on a surface depends on the development of new functional materials and nanoscale electronics. Combination of STM with first-principle simulations helps to reach that level of understanding. Z. Li et al. have described about the recent research on the characterization and control adsorption and electronic state of metal phthalocyanine (MPc) molecule on noble metal surface. The electronic and magnetic properties of aMPc molecule largely depend on the type of metal ion within the phthalocyanine ligand and surface nature on which the molecule is adsorbed. STM study is used to manipulate the structure and properties of the molecule. There is a dehydrogenation reaction of MPc induced by STM study. This dehydrogenation explains the spin polarization of the molecule and its interaction with complex environment [81]. P. Miao et al.

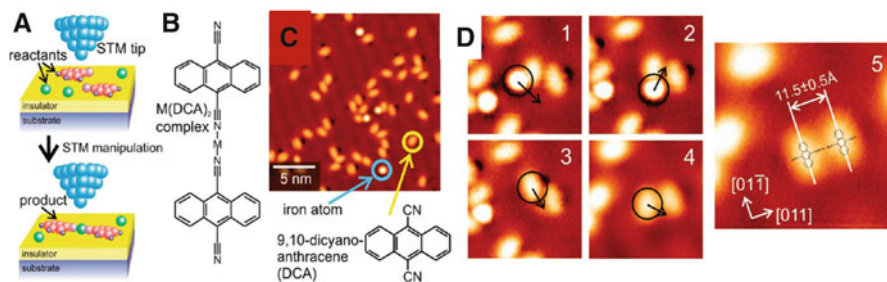


Fig. 6.9 Formation of a metal-ligand complex on an ultrathin insulating film by STM manipulation. (a) Schematic of the experiment. (b) The target molecule, linear $M(\text{DCA})_2$ complex. (c) Large-scale STM topography of DCA molecules and iron atoms deposited on NaCl bilayer on Cu (111). (d) Series of lateral manipulation steps resulting in the formation of a linear $\text{Fe}(\text{DCA})_2$ complexes (all images are $50 \times 50 \text{ \AA}^2$). (This figure is adapted from Liljeroth et al. [83])

have studied the structural properties of the organosilicon macromolecular films through STM study. The deposition of silicon phthalocyanine dichloride (SiPcCl_2) on the H-passivated surface was investigated through STM study. STM provides a direct view of molecular structure as well as the adsorption geometry on several substrates. Metal phthalocyanines like copper (CuPc), iron (FePc), cobalt (CoPc), and lead (PbPc) have been studied vigorously [82].

P. Liljeroth et al. have reported the STM-based single molecule synthesis of linear metal-ligand complex from atoms and organic molecules (9,10-dicyanoanthracene) deposited on an ultrathin insulating film. The frontier molecule orbitals are directly visualized by STM orbital imaging. STM-based synthesis emphasizes on structure of the single molecules having implementation in molecular electronics and molecular spintronics [83]. Figure 6.9a explains the schematic representation of the experiment where the organic molecules and metal atoms are deposited on an ultrathin insulating film and laterally manipulated by STM to form the target complex. Figure 6.9b shows the synthesis of target complex, metal-di-9 and 10-dicyanoanthracene (DCA), directly on NaCl bilayer on Cu surface by the lateral manipulation of coevaporated metal atoms and organic molecules in low-temperature STM. In Fig. 6.9c, the adsorption of DCA molecules in different orientation is shown. The interaction between the molecules with the NaCl film is very weak. A linear $M(\text{DCA})_2$ complex was formed in a stepwise fashion (Fig. 6.9d). The $M(\text{DCA})_2$ complexes are found to be oriented along the polar $[01\bar{1}]$ direction of the underlying NaCl film, and the distance between the anthracene moieties ($11.5 \pm 0.5 \text{ \AA}$) corresponds to the calculated geometry of an isolated complex (11.6 \AA). Metal string complex study is an important subject for understanding the fundamental research of metal-metal interaction.

The complex has wide potential application as a molecular metal wire. S-Y Lin et al. have demonstrated the electron transfer properties of the molecular wire by designing and fine-tuning metal-metal interactions [84]. J. Li et al. have studied the self-assembly of 1,3,5-benzenetribenzoic acid (BTB) molecules on both Cu and

epitaxial graphene grown on Cu with the help of STM at a high vacuum condition [85]. The BTB molecules on Cu surface were found to be arranged in a closed pack structure through hydrogen bonding. Here the H-bond arises between the deprotonated carboxylic acid groups. On graphene grown on Cu surface, the BTB molecule forms porous structure accompanied by small patches of disordered close-pack structure. The molecular self-assembly behavior is highly dependent on first substrate layer that was concluded from the annealing treatment.

6.4.2.4 Irregular Structures

Many surface sensitive techniques are available for studying periodic and regular structures. But STM has an advantage of studying small features like defects and monatomic steps. Here in case of step, the desired information was obtained from the height of steps. X. Han et al. have studied the morphologies of films spin coated from dilute block copolymer solution onto a mica substrate through atomic force microscopy (AFM). The concentration of a predominant factor for determining the shape of the aggregates displayed from the sphere and rods to irregular patches with increasing concentration [86]. R. Dabirian et al. have developed single-component and mixed self-assembled monolayers (SAMs) of one- and three-ring semirigid tetrahydro-4*H*-thiopyran end-capped oligo (cyclohexylidenes), i.e., (1), 4-(4-cyclohexylidencyclohexylidene)tetrahydro-4*H*-thiopyran (2) and 4-(tetrahydro-4*H*-thiopyran-4-cyclohexylidene-4-ylidene)- tetrahydro-4*H*-thiopyran (3), on Au (111) substrate by cyclic voltammetry, atomic force microscopy, and STM technique. STM imaging has revealed that domains of molecules of 2 or 3 amidst a monolayer of 1 are formed in both cases, where, as in the mixed SAM of 1 and 2, the domains are irregularly shaped and circular islands of uniform size are found in the mixed SAM of 1 and 3 [87]. B. Baubet et al. have developed cobalt promoted and non-promoted MoS₂ nanolayers supported on alumina. Various sulfidation conditions, such as the flow of pure H₂S and H₂/15% H₂S at different temperatures help in the formation of nanolayers of MoS₂ with two-dimensional morphology. The observed shapes are found to be more irregular in STM study [88].

6.4.2.5 Adsorbate Covered Surface

Different types of interactions like physical and chemical interactions support to the various adsorption process. Surface can act as a catalyst and speed up the chemical reactions by lowering its activation energy. A small deposition or coverage of adsorbate is sufficient for the reconstruction in the surface [89]. The image of STM is due to the electronic structure at the Fermi level energy. A perturbation in electronic structure is offered by the adsorbate, and the STM current in their vicinity is compared with the bare surface, which results in a specific pattern in the image [90]. AJ Mayne et al. have studied the chemisorptions of ethylene (C₂H₂)

on Si (001) (2×1) surface through STM technique. The adsorption of individual molecules and change in local structure can be observed. The C_2H_2 molecule normally prefers to adsorb on alternate dimer sites at low coverage. The removal of relatively weak π -bond is confirmed from the scanning tunneling spectroscopy study performed on the adsorbate covered surface [91]. P. Avouris et al. have studied that the scattering of surface electron step by step and adsorbate leads to long-range oscillation in local density of state through STM technique [92]. J. Yang et al. have vertically manipulated native In adatom in a semiconductor of InAs surface through atomic precession in STM. The vertical manipulation implies about the reversible transfer of individual adatom between the surface and STM tip. Stepwise vibrational excitation of the adsorbate-surface bond helps for transferring the atom from surface to tip. Such vibrational excitation is achieved from the inelastic electron tunneling and the electron tunneling is achieved by the tip induced electric field [93]. S. Hong et al. have given a theoretical study about the change in surface phonon frequency and surface stress for a selected light gas adsorbed on Ni and Cu surface. When the study was compared with the experimental data, the surface information and electronic structures were recorded [94]. A. Kiejna et al. have studied the surface properties of clean and Au- or Pd-covered hematite (α -Fe $2O_3$) (0001) [95]. Q Chen et al. have uncovered the structural evolution of CO adsorption on Ru (0001) at different coverage through high-resolution STM [96]. STM studies of Ru (0001) sample exposed to 0.5 and 1 L CO at room temperature were shown in Fig. 6.10a, b. Then the sample was cooled to 4.3 K. The small number of distributed molecules and densely packed island exist on the surface. Figure 6.10c, d represents the zoom version of the STM images, and it revealed ($\sqrt{3}$) superstructure of the CO islands. Such structure attributes to CO molecule sitting at the top site of Ru (0001) surface (termed as T-CO). T-CO species are normally imaged as round protrusion or depressions when a metallic tip was used. From the STM image, a donut-like morphology was observed when the tip moved closer to the surface.

As shown in Fig. 6.10c, each donut-like CO molecules are found to be centered at the top site by simply overlapping the Ru (0001) lattice grid onto the CO islands. There are some small numbers of isolated species observed which appear as round protrusions having no depletion in the center. As shown in Fig. 6.10c, d, such features reside on the hollow portion of the Ru (0001) lattice and assigned as CO molecules binding at the hollow sites (termed as H-CO). The coverage of H-CO decrease with the increase of the total CO coverage, indicating that the phenomenon is due to the nonequilibrium effect by rapid cooling treatment.

RE Tanner et al. have studied the adsorption of formic acid on anatase TiO $_2$ (001)-(1×4) thin film through STM analysis [97]. The combination of high-resolution STM image and noncontact AFM reveals the highest point of the ridge of the (1×4) structures consisting of single row of atoms. Formate gets adsorbed at coordinated Ti sites in the added row with a minimum separation of $2a_0$ and never adsorbs in the channels even though the channels also likely expose under coordinated Ti atoms.

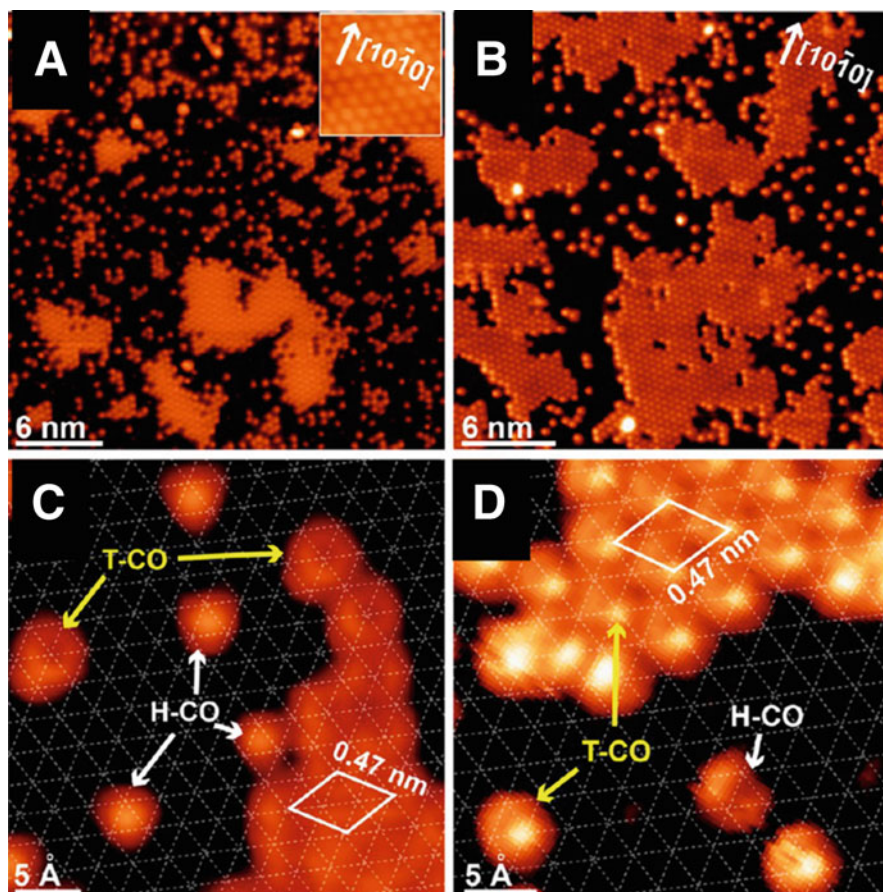


Fig. 6.10 STM images of Ru(0001) exposed to (a) 0.5 L and (b) 1 L CO at 300 K and observed at 4.5 K.). Inset in (a) is the atomic resolution image of the Ru(0001) lattice ($2.14 \times 2.14 \text{ nm}^2$). (c, d) are the zoom version of the STM images. (This figure is adapted from Chen et al. [96])

6.4.2.6 Charge Density Wave

Charge density wave (CDW) is the ground state of metal in which the conduction electron charge density is sinusoidally modulated in space [89]. Electron-phonon interaction induces the Fermi surface instabilities in metallic crystal resulting in formation of CDW [98]. AL Tchougreff et al. have treated the graphite monolayer with the tight-binding approximation. By describing the π electrons with extended Hubbard model, they have produced the charge density wave of graphite monolayer. Different unsymmetrical states in the extended conjugated system were described by the Hubbard model. The data observed on STM was interpreted by considering the electronic structure of graphite monolayer, which was represented through extended

Hubbard model [99]. The STM pattern provides a result where only three of six carbon atoms of each carbon hexagon were visible. They have constructed a phase diagram of graphite in space defined by the magnitude of on-site and nearest-neighbor repulsion. Conditions regarding the charge and spin-density wave were solved through a diagram. A. Tomic et al. have studied the nature of the surface charge distribution in case of metallic compound like CeTe_3 [100]. CeTe_3 is a cleavable layered material. STM technique is applied on the exposed area of cleaved single crystal. Fourier transformations of STM data have explained the Te square lattice peak. Peaks related to the charge density wave are oriented at 45° to the lattice peak. Low-temperature topographic and spectroscopic studies have been performed on CeTe_3 crystals for characterizing the CDW states. For STM study, the crystals were cleaved carefully through adhesive tape and placed inside the vacuum chamber. W. Sacks et al. have studied the dependence of voltage on contrasting STM images of materials which shows CDWs [101]. Presence of many bands at Fermi level of layered, i.e., two-dimensional material and incomplete band gapping makes the problem complicated. By making a simple perturbation, the amplitude and phase of the CDWs can be related to the features of the band structure. W. Sacks et al. have focused on characteristic energies where the CDW has a large contribution from the K points of Brillouin zone which gives different modulations of STM images. The voltage-dependent contrast STM image for NbSe_3 was recorded. The phase and amplitude of CDW changed as function of energy or voltage. R. V. Coleman et al. have performed the STM studies on the surfaces of different transition metal di- and tri-chalcogenides to explore the contribution of CDW toward the surface charge modulation. In case of 1T-TaSe₂ and TaS₂, the amplitude of CDWs were found to be very high, while the 2H-phase dichalcogenides support the less amplitude CDWs. The superimposed CDW charge modulation could be detected with high sensitivity STM scans. The CDW charge modulation for NbSe_3 was detected at 4.2 K with 80% gap at Fermi surface [98]. C. Brun et al. have studied the CDW transition in NbSe_3 by STM study on an in situ cleaved (b, c) plane [102].

Figure 6.11 shows the STM images on large atomically flat terrace at different temperatures like 78, 63, and 5 K with their 2D Fourier transform (2DFT). Inset shows the smaller portion of the image at higher scale. At 78 K the q_1 CDW superlattice is clearly seen, whereas the q_{2p} superlattice spots are diffused. At 63 K, i.e., 4 K above the bulk transition temperature, the q_{2p} CDW superlattice spots are already well defined, their amplitude being larger than the one of the q_1 spots. At 5 K the ratio of the q_{2p} to q_1 amplitude is slightly larger than that at 63 K.

Q. Fan et al. have performed low-temperature STM study on quasi-one-dimensional $\text{Ta}_4\text{Pd}_3\text{Te}_{16}$ crystal [103]. Figure 6.12a shows the typical topography of the cleaved surface, corresponding to the $(\bar{1}03)$ plane of $\text{Ta}_4\text{Pd}_3\text{Te}_{16}$. The imaged surface is found to be atomically flat, featured by regular stripes with a spacing of 2.7 nm (Fig. 6.12b). The corrugations of these modulations are less than 0.05 Å. For their clear identification, 2D Fourier transform of Fig. 6.12c was performed as shown in Fig. 6.12d.

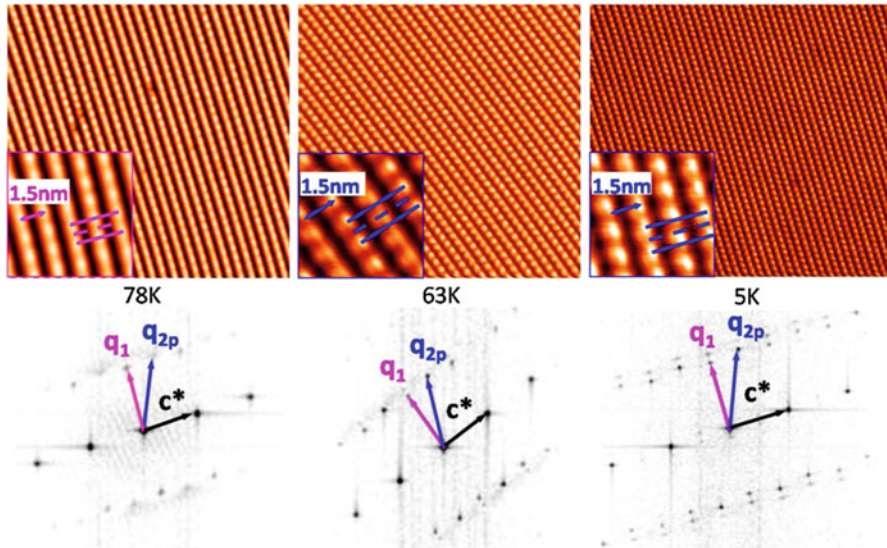


Fig. 6.11 STM images of the in situ cleaved surface of NbSe_3 measured at $T = 78, 63,$ and 5 K. Insets: smaller portion of the image at larger scale. Below each image, its 2D Fourier transform shows the lattice Bragg spots (indicated by c^* normal to the chains) and the q_1 and q_{2p} superlattice spots. (This figure is adapted from Brun et al. [102])

6.4.2.7 Superconductors

Superconductivity is one of the most remarkable phenomena observed in physics. Tunneling spectroscopy is a better solution for understanding high-temperature superconductors (HTS). STM has become an important advantage for tunneling spectroscopy. Initially the difficulty of reproducible data on cuprates is due to the poor control of the tunnel barrier and due to material inhomogeneities. Use of STM demonstrates the reproducible spectra and identifies the essential intrinsic features of tunneling spectra on HTS [104]. Superconductivity in HTS cuprates appears due to the itinerant carrier doping of localized electrons of a Mott insulator. Such superconductivity in cuprates arises from the atomically localized electrons and shows disorder at nanolevel. For describing such phenomenon, a purely momentum-dependent description is required. J. Lee et al. have developed spectroscopic imaging STM which probes the real-space electronic structure along with momentum space electronic structure at nanolevel [105]. J.G Rodrigo et al. have reported the high-quality local tunnel spectroscopy measurements in superconductors using in situ fabricated superconducting tips as counter electrode. The experiment was conducted at very low temperature using a dilution refrigerator and ^3He cryostat [106]. Q. Zou et al. have given a combined STM and local barrier height (LBH) studies of low temperature cleaved optimally doped BaFe_2As_2 superconductors. Zou have concluded that the Ba and As dominated surface can be identified by

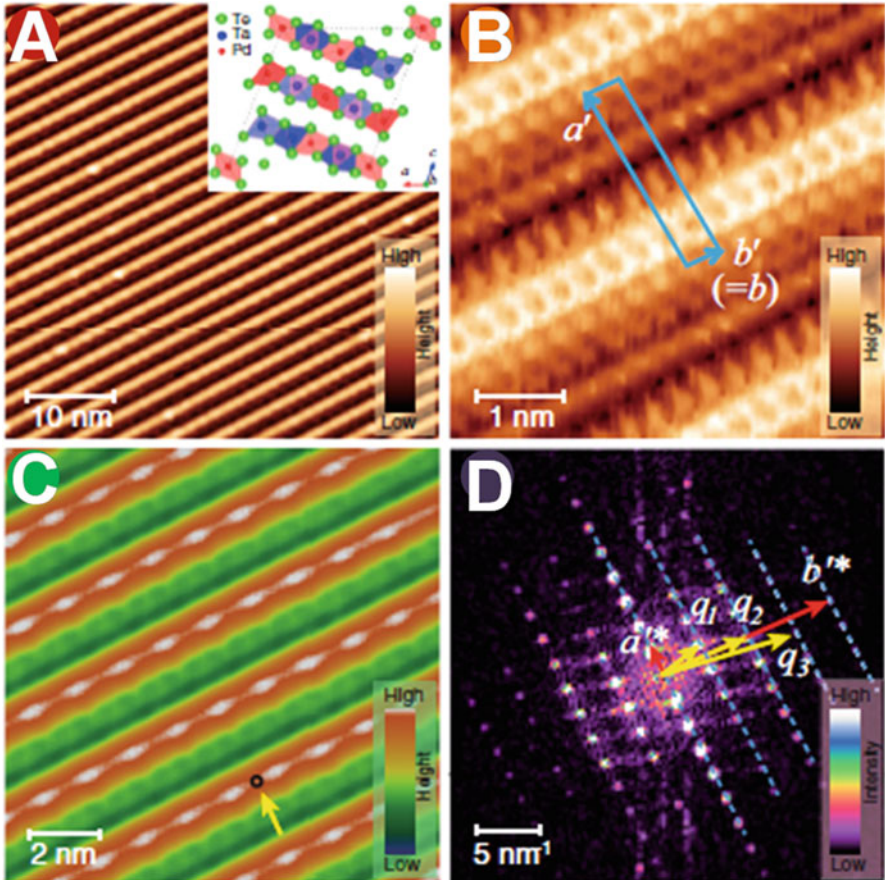


Fig. 6.12 (a) STM topography of $\text{Ta}_4\text{Pd}_3\text{Te}_{16}$ and CDW-like modulations. (a) 50×50 nm STM image ($V_{\text{bias}} = 1.0$ V, $I = 30$ pA). Inset: Crystal structure of $\text{Ta}_4\text{Pd}_3\text{Te}_{16}$ projected along the [010] directions. (b) Atomically resolved STM image (5×5 nm, $V_{\text{bias}} = 10$ meV, $I = 50$ pA). (c) STM image showing additional modulations (12×12 nm, $V_{\text{bias}} = -100$ meV, $I = 50$ pA). (d) The Fourier transformation of (c). (This figure is adapted from Fan et al. [103])

combining the information obtained from STM, STS, and LBH analysis [107]. Q. Fan et al. have performed STM study on quasi-one-dimensional structured material, i.e., $\text{Ta}_4\text{Pd}_3\text{Te}_{16}$. The tunneling conductance was measured at 0.4 K within ± 3 mV around E_F . Superconducting gap with coherence peak was observed and the tunneling conductance in the gap bottom reaches zero [103].

6.4.2.8 Inhomogeneous Material

In electron material, the Coulomb's repulsion between electrons hinders the formation of a homogeneous Fermi liquid. Normally the high-temperature superconductor exhibits nanoscale inhomogeneity. W.D Wise et al. have studied Fourier transform STM for probing the Fermi surface of Bi-based cuprate superconductors. The cuprate Fermi surface varies at a nanometer scale, and its local geometry was found to be correlated with the size of large inhomogeneous gap [108]. The inhomogeneity in a material can corrupt itself but such defects are advantageous. Normally in case of superconductor the non-stoichiometric dopants achieve high temperature. I. Zeljkovic et al. have given a STM study on the chemical disorder in the superconductors and discussed about the use of dopants, impurities, and adatoms in probe and how they enhance the intrinsic electronic properties of the material [109]. H. Wang et al. have performed a low-temperature STM study on the defect-rich 2H-NbSe₂ single crystal superstructure, developed either by the sudden change in bias voltage or by superimposing a voltage pulse with the bias voltage [110]. Charge density wave is also observed at the vicinity of the defect. A defected image with diameter 120 ± 10 nm and depth of 13 nm was observed after a voltage drop as shown in Fig. 6.13a. The layered structure of 2H-NbSe was exposed, and the new modulations were found in the rough area on the edges and inside of the defect from Fig. 6.9b–d. N. Liu et al. have studied the structural properties of heterogeneous InGaAs quantum dots, grown by heterogeneous droplet epitaxy method through STM technique [111].

6.4.2.9 Phonon Detection

I. Altfeder et al. have observed phonon oscillation on atomic scale due to the quantum tunneling of electron into the vibrating surface atom. The result explains about the dependence of effective radius of the phonon quasi-bound state, the scattering phase shift, the real-space distribution of phonon standing wave amplitude, and the nonlinear inter-mode coupling on defect-induced scattering resonance [112].

Altfeder et al. have performed STM study on WSe₂, which grown above graphene sheets. Phonon standing wave pattern was observed on the quasi-free-standing one monolayer island which is in triangular shape (Fig. 6.14a). STM images of WSe₂ spiral pyramid are shown in Fig. 6.14b. The band structure of graphene is modified by many body interactions, such as electron-electron, electron-plasmon, and electron-phonon interactions. Phonons are excited by the tunneling electron from the tip of a STM. The electron-phonon coupling is due to the increases of electron tunneling to the graphene state at larger energy than that of phonon energy. HW Kim et al. have given a nanoscale control of phonon excitation in graphene [113]. Initially graphene nanoisland is grown on the surface of Pt. The controlled irradiation of Ar⁺ ion modifies graphene rather than Pt.

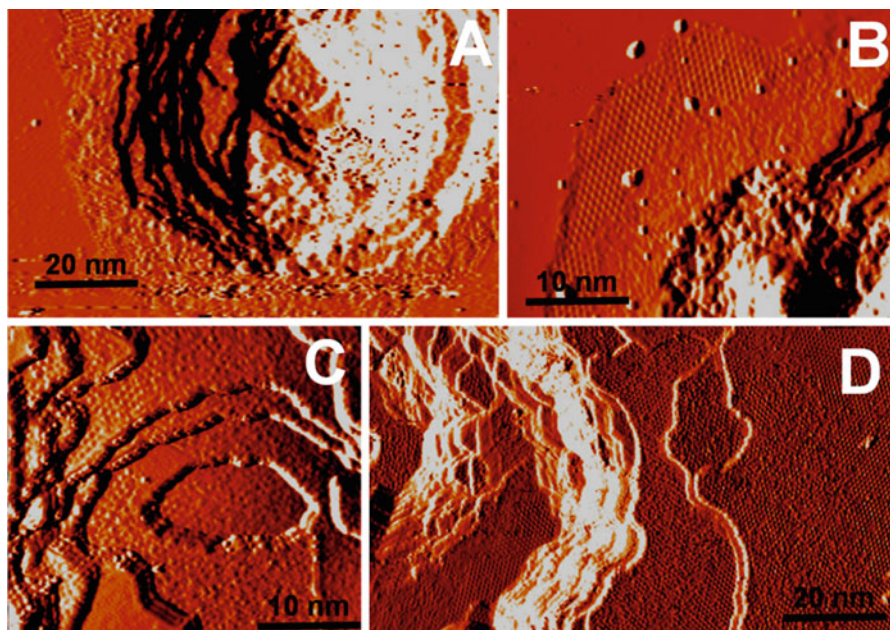


Fig. 6.13 (a) Example shows the typical topographic profile of the defects and its vicinity. (b) Zoomed view of a corner of a defect, and the regular lattice structure on the side shows a new modulation. (c) Topographic profile on the side of another defect where the CDW on each sandwich layer is exposed. (d) The topographic image of the bottom of a defect and new modulations appeared on various layers. (This figure is adapted from Wang et al. [110])

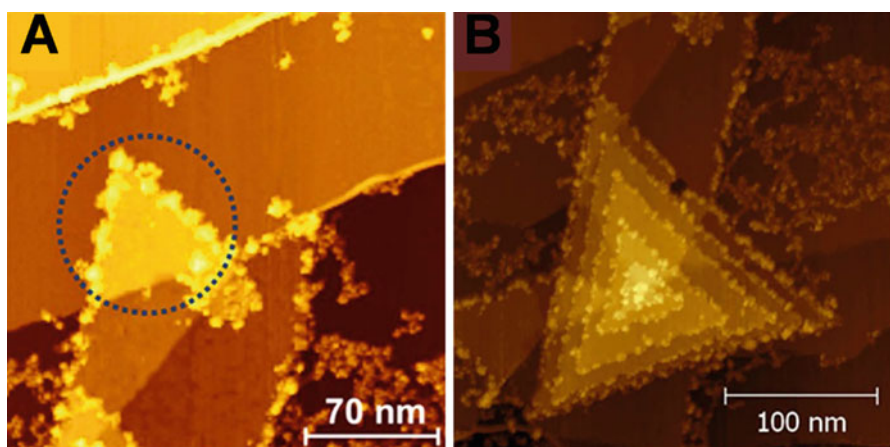


Fig. 6.14 STM image and cross-section WSe_2 nanostructures. (a) The dotted line surrounding the triangle-shaped one monolayer WSe_2 island and (b) STM image of WSe_2 spiral pyramid. Observed particles at the edges of WSe_2 domain in both A and B are tungsten oxide phase. (This figure is adapted from Altfeder et al. [112])

6.4.2.10 Spin-Polarized Tunneling

In case of spin-polarized scanning tunneling microscope (SP-STM), the working principle relies on the tunneling of spin-polarized electron between the tip and sample across the vacuum barrier. D. Wortman et al. have introduced a method of operating SP-STM at constant current mode. The magnetic structure of one monolayer Cr on Ag was resolved through the potential of SP-STM in constant current mode [114]. W. Wulfhekel et al. have studied the magneto-tunnel effect between a ferromagnetic tip and a ferromagnetic sample basing on SP-STM [115]. The magnetization of the tip was changed periodically which separated the topographic and spin-dependent parts of tunnel current. Simultaneously the topography and magnetic structures of the samples were recorded. M. Kleiber et al. have studied the spin disturbance on antiferromagnetic bulk crystal Cr (001) surface by SP-STM [116]. M. Bode et al. have demonstrated the spin-polarized tunneling on Gd (0001) thin film by using ferromagnetic probe tip in a low-temperature STM. Spin-polarized tunneling was demonstrated by measuring asymmetry of differential tunneling conductivity. The nanomagnetic domain structure of Gd (0001) thin film was observed by mapping the vibration of asymmetry parameter [117]. M. Eltschka et al. have introduced a spin-polarized STM by employing Zeeman splitting in superconducting tip. The STM combines the probing capability of absolute values of spin polarization with precise control at atomic scale. The technique was implemented to resolve spin polarization of magnetic Co nanoislands on Cu (111). The spin polarization was enhanced by 65% with the increasing of the width of the tunnel barrier by only 2.3 Å [118].

6.4.3 Exotic Applications of STM in Physics

STM has various field of application basing on its physics. STM acts as a sensing device which can detect the width of tunnel gap. STM has a very high sensitivity along with reduced back action. The back action of STM consists of the impulse of tunneling electron and the force due to opposite charge on the tip and sample. U. Durig et al. have studied the sensing of force through STM and also observed the adhesion force on clean metal surface [119]. STM are also used as a detector and mixer. Electron spin resonance is another aspect of STM application. Y. Manassen et al. have performed electron spin resonance STM study on a thermally oxidized Si (111). Initially the experiment was performed in a magnetic field of 139 G which measured through Gauss meter. The predicted Larmor frequency and detection band width were measured to be 389.2 MHz and 100 Hz, respectively [120].

6.4.4 Applications of STM for Nonconducting Materials

Many reports basing on imaging of the nonconductive biomolecules have been published, which includes nucleic acids, proteins, lipids, polysaccharides, lipid membranes, etc. Thick molecules were very difficult to recognize through the STM, but the smaller molecules like fatty acids, liquid crystal molecules, aromatic molecules, and hydrocarbons are imaged through STM in a vacuum or at solid-liquid interfaces. The investigations of material with STM are limited to conducting materials. Thus, another method permitting high-resolution examination of nonconducting specimens was developed in 1986. This technique was named atomic force microscopy (AFM) or, by analogy with STM, scanning force microscopy (SFM) [121]. Samples for STM analysis need to be prepared or undergo some treatment. Contact SFM images provide easy view of the structure without depending on their conductivity.

6.4.5 Application of STM in Biology and Organic Chemistry

Before studying the STM and AFM biological specimen except bulk sample, some preparation techniques are necessary. The preparation technique involves about the adsorption of molecule on substrate. Small field of view of STM is a major problem in biological application. Due to the inhomogeneous nature biological specimen, one has to focus on large area. To identify the sample, STM can be combined or incorporated to techniques like transmission electron microscopy (TEM) and scanning electron microscopy (SEM) [122]. Due to the inhomogeneous nature of biological specimen, the work function varies strongly. Another problem is the rigidity of the sample. The force between the tip and sample easily deforms the sample. To solve the problems related to the conductivity and rigidity, the sample needs to be coated with metallic layer which will act as a replica of the sample. There are different sample preparation techniques used for conducting the STM study. Crystal of an organic material can be a good conductor and its surface can be studied through STM. While growing the specimen on substrate, we must be aware of about the rigidity and flat, inert, sticking, and conducting nature of the substrate. Different possible substrates like Au (111), graphite, PtC film on mica, amorphous carbon film on a finder grid, etc. are widely used in STM study of biological and organic samples [123]. NJ Tao et al. have reported the nucleation, growth, and molecular packing structure of monolayer guanine and adenine on graphite surface by using AFM and STM method. Guanine and adenine were condensed into monolayer film on graphite spontaneously. Complex features like super-periodic structure superimposed on guanine lattice were observed through STM study [124]. M. Smerieri et al. have investigated the self-assembly of S-glutamic acid on Ag (100) surface by utilizing the low-temperature STM study. The S-glutamic acid was found to be arranged in a square fashion [125]. Figure 6.15a shows the STM image

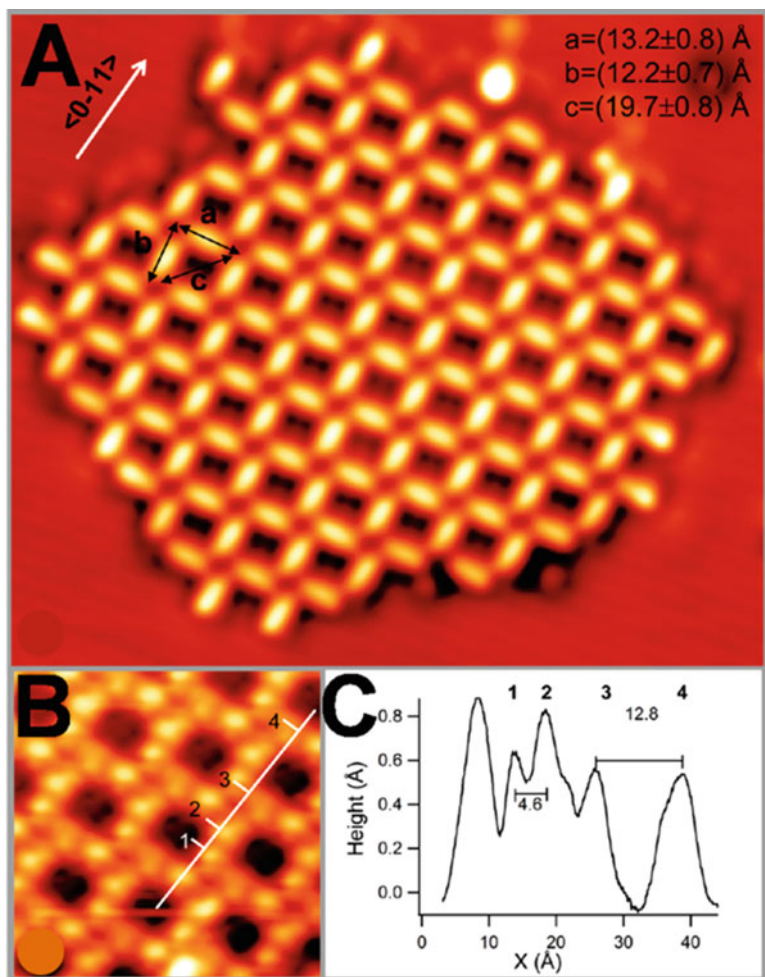


Fig. 6.15 (a) STM image of a (S)-Glu island produced upon Glu evaporation on Ag(100) at $T = 350 \text{ K}$. (b) High-resolution image of a portion of the same layer, (c) height profile along the white line reported in panel B. (This is figure is adapted from Smerieri et al. [125])

of a (S)-Glu island produced upon Glu evaporation on Ag (100) at $T = 350 \text{ K}$. The measured molecular dimensions are generally larger than that actual one due to the convolution with the tip. The high-resolution image as shown in Fig. 6.15b explains the submolecular units of the glue molecules. In Fig. 6.15b, c, each amino acid appears formed by two bright lobes at a distance of $(4.6 \pm 0.2) \text{ \AA}$, corresponding to the head and tail of the molecule.

6.4.6 Application of STM in Electrochemistry

The electrochemical reaction, at solid-liquid interface, is a very important study. The structure of electrical double layer and roughness characteristic can be measured through STM study. Again STM has a wide application in determining the topography of metal surface at early stage of corrosion, organic film formation and structure determination, mechanism of passive layer growth, and aging effect on passive layers [89, 126]. M.D. Lay et al. have given an electrochemical STM study of the growth of CdTe on Au surface [127]. Y. Kou et al. have used voltammetry and in situ STM technique to examine electrodeposition of cobalt (Co) on a stationary Pt(111) electrode [128].

Figure 6.16a shows the deposition of Co adlayer ended with an organized monolayer on the Pt(111) electrode. The degree of ordering depends on the quality of Pt substrate and the electrochemical environment. The ordered structure appears as honeycomb form defined by two sets of mounds exhibiting slightly different corrugation height (Fig. 6.16b). STM appearance of these structures varies with the imaging condition. Figure 6.16b shows an imaging condition of 200 mV and 1 nA, whereas in Fig. 6.16c the imaging condition was 250 mV and 2 nA. With the change of imaging condition, the depression of honeycomb became less pronounced. Y-C Yang et al. have used cyclic voltammetry and STM technique for examining adsorption of dithiol molecules on well-ordered Pt(111) electrodes in 0.1 M HClO₄ [129]. M. Gurub et al. have described about the adsorption and identification of the binding site of [Ru(NH)₃]³⁺ (RuHex) molecules in a closely packed monolayer of a 13 base ssDNA on Au(111) electrodes by electrochemical in situ STM study [130].

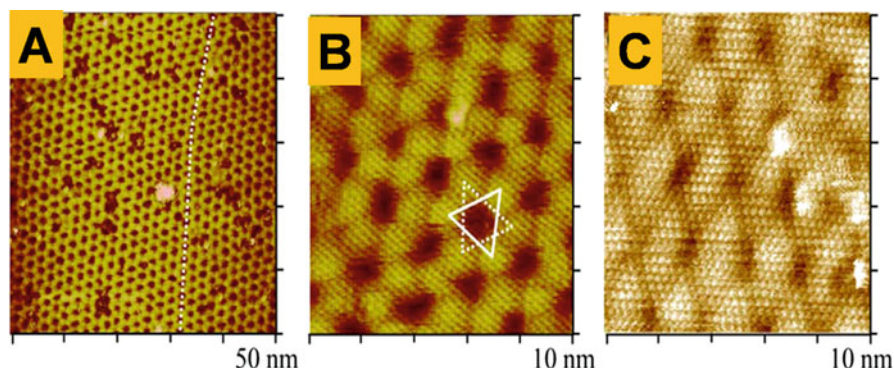


Fig. 6.16 (a) The spatial structure of the first monolayer of cobalt deposited on the Pt electrode. (b, c) Atomic resolution STM images of the Co monolayer. The bias voltages and set point currents were 200 mV and 1 nA for (b) and 250 mV and 2 nA for (c), respectively. (This figure is adapted from Kuo et al. [128])

6.4.7 Technological Applications of STM

6.4.7.1 Tribology: Wear and Friction

The basic understanding on the atomic process occurring at the interface of two materials have some typical technological problems, which include, adhesion, contact formation, friction, wear, lubrication, nanoindentation, fractures, and matching [131]. STM provides information on the microscopic roughness of a damaged surface. The direct measurement of lateral force occurs by the dragging of tip along the surface. Y-H Ding et al. have studied the intrinsic structure and frictional properties of graphene and graphene oxide nanosheets by using scanning probe microscopy [132].

6.4.7.2 Nanolithography and Nanomachining

The surface of a material is modified by the STM tip and the material gets transported from one place to another place through the STM tip. The proper study of such activity results in some new aspects like information storage device, nanometer patterning technique, X-ray optics on electron localization, manipulation of big molecule, and building of small devices. For machining a surface through STM, the easier way is to push the tip into the surface, which results in a hole with a small mount. The hole is due to the adhering of the surface material to the retracting tip. With the help of this technique, thin insulator layer present on the conductor surface can be easily removed in a controlled way. RC Jaklevic have studied the time-lapse topography on a clean annealed Au(111) surface by using scanning tunneling microscope which shows the effect of surface diffusion of Au atoms at room temperature [133]. W. E. Pakard et al. have given a study about the STM for machining the surface. The STM tip can be used as a micro-mechanical tool-bit to shave off resist material from surfaces and also to deform region of surfaces by point contact between the tip and surface. Formation of hillocks and/or holes on gold surfaces by increasing the bias potential between the STM tip and the surface, explains the versatile application of STM. Again STM is used in organo-metallic gases to write metallic features on surfaces and also can create text character on a Si substrate by using contamination resist [134].

6.5 Advantages and Drawbacks of STM Over Other Imaging Techniques

Curiosity in human being leads to the development of advanced techniques for making everything as simpler as possible. The invention of STM is an epitome of the level of human curiosity to see the atoms in the nanometer scale, hear

their vibrations, and transfer the atoms from one surface to the other. Optical microscopes are being primarily used for investigating the microstructures of the materials, but it is not possible to reach a very high magnification with these microscopes. However the electron microscopes like scanning electron microscopes (SEM) and transmission electron microscopes (TEM) use the electrons as the source of illumination, whose wavelength is $\sim 10^4$ times shorter than that of the visible light. Thus the images with very high magnification and high resolution are generated, which provide the ultrafine features of the material microstructures. But the instruments are only operated in high vacuum environment. However the gradual progress in technology makes STM capable of operating in vacuum, liquid, as well as ambient air conditions, which are mostly beneficial for the biological and electrochemical applications [126, 135]. Atomic-scale resolution of the probing surfaces and manipulation of the single atoms/molecules are the exciting aspects of STM technology [53, 136, 137]. In a report by P. Xu et al., the modulated manipulation of graphene sheets was achieved by controlling the tunneling current and bias voltage. The graphene sheet suffers a displacement toward the tip when the bias voltage increases and it moves away from the tip with the increase in tunneling current [138]. The greatest drawback of STM is that the surface of insulating materials is difficult to analyze due to the large bandgap and lack of vacant energy states available for the tunneling process. Another major difficulty in applying STM in real world arises from the delicate STM tips. Due to the tip-surface interaction, the tip may be attracted toward the surface and finally gets crashed over it, which leads to a severe loss. Thus, care must be taken while scanning the tip in a raster manner over the surface to avoid this damage. Controlled preparation of STM tip is another major task. If the tip is not properly prepared, then the presence of several mini-tips, contaminants, or the oxides on the surface causes the distortion in the STM imaging and in STS. Also the scanning process is quite slow in probe microscopes, which is another shortcoming of STM. Instead of these few difficulties in STM operation, this instrument provides a very good platform for investigating the surface features in atomic resolution and provides the facility of real-space surface imaging of the desired material.

6.6 Conclusions

In this chapter, we have tried to shed some light on the detailed features of STM, starting from the basic principles to the application of STM in different areas including surface science, solid-state physics, electrochemistry, biology, and manipulation of single atoms/molecules. The facility of work function determination and scanning tunneling spectroscopy makes this instrument a versatile tool for surface science. Different modes of operation and imaging techniques of STM have been detailed. Now, both the surface scanning and nanofabrication are combined together in STM, which makes STM easily operable and less time-consuming.

Acknowledgments Authors are thankful to the Department of Science and Technology, Government of India, for sanction of Fast Track Research Project for Young Scientists to Dr. Prashant K. Sharma (Ref. No.: SR/FTP/PS-157/2011) and Dr. Rashmi Madhuri (Ref. No.: SB/FT/CS-155/2012). Dr. Sharma (FRS/34/2012-2013/APH) and Dr. Madhuri (FRS/43/2013-2014/AC) are also thankful to the Indian Institute of Technology (Indian School of Mines), Dhanbad, for grant of Major Research Project under Faculty Research Scheme. We are also thankful to the Board of Research in Nuclear Sciences (BRNS), Department of Atomic Energy, Government of India, for major research project (Sanction No. 34/14/21/2014-BRNS/0295). Suryakanti and Trupti are also thankful to the Indian Institute of Technology (Indian School of Mines), Dhanbad, for Fellowship.

References

1. Binnig, G., Rohrer, H., Gerber, C., & Weibel, E. (1982). Surface studies by scanning tunneling microscopy. *Physical Review Letters*, *49*, 57.
2. Gasiorowicz, S. (2003). *Quantum physics*. New York: Wiley.
3. Sun, X. (2010). *Engineering supramolecular architectures on insulating and metal surfaces studied by scanning tunneling microscopy*. Doctor of Philosophy. Groningen.
4. Tersoff, J., & Hamann, D. R. (1985). Theory of the scanning tunneling microscope. *Physical Review B*, *31*(2), 805.
5. Ekvall, I., Wahlstrom, E., Claesson, D., Olin, H., & Olsson, E. (1999). Preparation and characterization of electrochemically etched W tips for STM. *Science and Technology*, *10*, 11–18.
6. Biegelsen, D. K., Ponce, F. A., & Tramontana, J. C. (1987). Ion mined tips for scanning tunneling microscopy. *Applied Physics Letters*, *50*, 696.
7. Valencia, V. A., Thaker, A. A., Derouin, J., Valencia, D. N., Farber, R. G., Gebel, D. A., & Killelea, D. R. (2014). Preparation of scanning tunneling microscopy tips using pulsed alternating current etching. *Journal of Vacuum Science and Technology A*, *33*, 023001.
8. Albrektsen, O., Salemink, H. W. M., Morch, K. A., & Tholen, A. R. (1994). Reliable tip preparation for high-resolution scanning tunneling microscopy. *Journal of Vacuum Science and Technology B*, *12*, 3187.
9. Leng, Y. (2008). *Materials characterization: Introduction to microscopic and spectroscopic methods*. Singapore: Wiley.
10. Oura, K., Lifshits, V. G., Saranin, A. A., Zotov, A. V., & Katayama, M. (2003). *Surface science: An introduction*. Berlin: Springer.
11. Ziegler, J. G., & Nichols, N. B. (1993). Optimum settings for automatic controllers. *The Journal of Dynamic Systems, Measurement, and Control*, *115*, 220–222.
12. Sarid, D., Henson, T., Bell, L. S., & Sandroff, C. J. (1988). Scanning tunneling microscopy of semiconductor clusters. *Journal of Vacuum Science & Technology, A: Vacuum, Surfaces, and Films*, *6*, 424.
13. Sand, D., McGinnis, B. P., & Henson, D. (1988). Four-wave mixing and scanning tunneling microscopy of semiconductor clusters. Proc. SPIE 0881, Optical Computing and Nonlinear Materials 114.
14. Sarid, D., Henson, T. D., Armstrong, N. R., & Bell, L. S. (1988). Probing of basal planes of MoS₂ by scanning tunneling microscopy. *Applied Physics Letters*, *52*, 2252.
15. Becker, R. S., Golovchenko, J. A., & Swartzentruber, B. S. (1985). Electron interferometry at crystal surfaces. *Physical Review Letters*, *55*, 987.
16. Binnig, G., Frank, K. H., Fuchs, H., Garcia, N., Reihl, B., Rohrer, H., Salvan, F., & Williams, A. R. (1985). Tunneling spectroscopy and inverse photoemission: Image and field states. *Physical Review Letters*, *55*, 991–994.
17. Tromp, R. M. (1989). Spectroscopy with the scanning tunnelling microscope: A critical review. *Journal of Physics: Condensed Matter*, *1*, 10211–10228.

18. Stroschio, J. A., Feenstra, R. M., Newns, D. M., & Fein, A. P. (1988). Voltage-dependent scanning tunneling microscopy imaging of semiconductor surfaces. *Journal of Vacuum Science & Technology, A: Vacuum, Surfaces, and Films*, 6, 499.
19. Natterer, F. D., Ha, J., Baek, H., Zhang, D., Cullen, W. G., Zhitenev, N. B., Kuk, Y., & Stroschio, J. A. (2016). Scanning tunneling spectroscopy of proximity superconductivity in epitaxial multilayer grapheme. *Physical Review B*, 93, 045406.
20. Sakurai, T., & Wille, L. (Eds.). (2000). *Advances in scanning probe microscopy*. Berlin: Springer.
21. Payne, M. C., & Inkson, J. C. (1985). Measurement of work functions by tunneling and the effect of the image potential. *Surface Science*, 159, 485–495.
22. Simmons, J. G. (1963). Generalized formula for the electric tunnel effect between similar electrodes separated by a thin insulating film. *Journal of Applied Physics*, 34, 1793.
23. Joshi, S., Ecija, D., Koitz, R., Iannuzzi, M., Seitsonen, A. P., Hutter, J., Sachdev, H., Vijayaraghavan, S., Bischoff, F., Seufert, K., Barth, J. V., & Auwärter, W. (2012). Boron nitride on Cu(111): An electronically corrugated monolayer. *Nano Letters*, 12, 5821–5828.
24. Vitali, L., Levita, G., Ohmann, R., Comisso, A., De Vita, A., & Kern, K. (2010). Portrait of the potential barrier at metal–organic nanocontacts. *Nature Materials*, 9, 320–323.
25. Muralt, P., & Pohl, D. W. (1986). Scanning tunneling potentiometry. *Applied Physics Letters*, 48, 514.
26. Muralt, P., Meier, H., Pohl, D. W., & Saleminck, H. W. M. (1987). Scanning tunneling microscopy and potentiometry on a semiconductor heterojunction. *Applied Physics Letters*, 50, 1352.
27. Baddorf, A. P. (2007). Scanning tunneling potentiometry: The power of STM applied to electrical transport. In S. Kalinin & A. Gruverman (Eds.), *Scanning probe microscopy* (pp. 11–30). New York: Springer.
28. Meyer, E., Hug, H. J., & Bennewitz, R. (2004). *Scanning probe microscopy: The lab on a tip*. New York: Springer.
29. Fink, H.-W. (1986). Mono-atomic tips for scanning tunneling microscopy. *IBM Journal of Research and Development*, 30, 460–465.
30. Hofer, W. A., & Redinger, J. (2000). Scanning tunneling microscopy of binary alloys: First principles calculation of the current for PtX (100) surfaces. *Surface Science*, 447, 51–61.
31. Lucier, A.-S. (2004). *Preparation and characterization of tungsten tips suitable for molecular electronics studies*. Master's thesis. McGill University.
32. Melmed, A. J. (1991). The art and science and other aspects of making sharp tips. *Journal of Vacuum Science and Technology B*, 9, 601.
33. Volcke, C. (2010). Chemical modification of scanning tunneling microscopy tips for identification of functional groups in self-assembled monolayers. In A. Mendez-Vilas & J. Diaz (Eds.), *Microscopy: Science, technology, applications and education* (pp. 1293–1301). Spain: Formatex.
34. Hahn, J. R., & Ho, W. (2001). Single molecule imaging and vibrational spectroscopy with a chemically modified tip of a scanning tunneling microscope. *Physical Review Letters*, 87, 196102.
35. Kuk, Y., & Silverman, P. J. (1989). Scanning tunneling microscope instrumentation. *The Review of Scientific Instruments*, 60, 165.
36. Hofer, W. A., Fisher, A. J., Wolkow, R. A., & Grutter, P. (2001). Surface relaxations, current enhancements, and absolute distances in high resolution scanning tunneling microscopy. *Physical Review Letters*, 87, 236104.
37. Kresse, G., & Hafner, J. (1993). Ab initio molecular dynamics for liquid metals. *Physical Review B*, 47, 558.
38. Kohn, W., Becke, A. D., & Parr, R. G. (1996). Density functional theory of electronic structure. *The Journal of Physical Chemistry*, 100, 12974–12980.
39. Turchi, P. E. A., Gonis, A., & Colombo, L. (Eds.). (1998). *Tight-binding approach to computational materials science*. Pennsylvania: Materials Research Society.

40. Ness, H., & Fisher, A. J. (1997). Influence of the tip-induced electric field on the STM contrast of chemisorbed C₂H₄ on the Si(001) surface. *Physical Review B*, *55*, 10081–10093.
41. Hofer, W. A. (2003). Challenges and errors: Interpreting high resolution images in scanning tunneling microscopy. *Progress in Surface Science*, *71*, 147–183.
42. Sacks, W., Gauthier, S., Rousset, S., Klein, J., & Esrick, M. A. (1987). Surface topography in scanning tunneling microscopy: A free-electron model. *Physical Review B*, *36*, 961.
43. Heinze, S., Blugel, S., Pascal, R., Bode, M., & Wiesendanger, R. (1998). Prediction of bias-voltage-dependent corrugation reversal for STM images of bcc (110) surfaces: W(110), Ta(110), and Fe(110). *Physical Review B*, *58*, 16432.
44. Rutter, G. M., Guisinger, N. P., Crain, J. N., Jarvis, E. A. A., Stiles, M. D., Li, T., First, P. N., & Stroscio, J. A. (2007). Imaging the interface of epitaxial graphene with silicon carbide via scanning tunneling microscopy. *Physical Review B*, *76*, 235416.
45. Chen, C. J. (2008). *Introduction to scanning tunneling microscopy*. New York: Oxford University Press.
46. Takahashi, Y., Miyamachi, T., Ienaga, I., Kawamura, N., Ernst, A., & Komori, F. (2016). Orbital selectivity in scanning tunneling microscopy: Distance-dependent tunneling process observed in iron nitride. *Physical Review Letters*, *116*, 056802.
47. Präser, H. (2015). *Scanning tunneling spectroscopy of magnetic bulk impurities: From a single kondo atom towards a coupled system*. Switzerland: Springer International Publishing.
48. Selloni, A., Carnevali, P., Tosatti, E., & Chen, C. D. (1986). Voltage-dependent scanning-tunneling microscopy of a crystal surface: Graphite. *Physical Review B*, *34*, 7406.
49. Hamers, R. J., Tromp, R. M., & Demuth, J. E. (1986). Surface electronic structure of Si(111)-(7 × 7) resolved in real space. *Physical Review Letters*, *56*, 1972.
50. Deniz, O., Sanchez-Sanchez, C., Dumsclaff, T., Feng, X., Narita, A., Mullen, K., Kharche, N., Meunier, V., Fasel, R., & Ruffieux, P. (2017). Revealing the electronic structure of silicon intercalated armchair graphene nanoribbons by scanning tunneling spectroscopy. *Nano Letters*, *17*, 2197–2203.
51. Braun, K.-F., & Hla, S.-W. (2005). Probing the conformation of physisorbed molecules at the atomic scale using STM manipulation. *Nano Letters*, *5*, 73–76.
52. Crommie, M. F., Lutz, C. P., & Eigler, D. M. (1993). Confinement of electrons to quantum corrals on a metal surface. *Science*, *262*, 218.
53. Hla, S.-W., Braun, K.-F., Wassermann, B., & Rieder, K.-H. (2004). Controlled low-temperature molecular manipulation of sexiphenyl molecules on Ag(111) using scanning tunneling microscopy. *Physical Review Letters*, *93*, 208302.
54. Heinrich, J. A., Gupta, J. A., Lutz, C. P., & Eigler, D. M. (2004). Singleatom spin-flip spectroscopy. *Science*, *306*, 466.
55. Jamneala, T., Madhavan, V., & Crommie, M. F. (2001). Kondo response of a single antiferromagnetic chromium trimer. *Physical Review Letters*, *87*, 256804.
56. Hla, S. W., Bartels, L., Meyer, G., & Rieder, K.-H. (2000). Inducing all steps of a chemical reaction with the scanning tunneling microscope tip: Towards single molecule engineering. *Physical Review Letters*, *85*, 2777.
57. Komeda, T., Kim, Y., Fujita, Y., Sainoo, Y., & Kawai, M. (2004). Local chemical reaction of benzene on Cu(110) via STM-induced excitation. *The Journal of Chemical Physics*, *120*, 5347.
58. Lauhon, L. J., & Ho, W. (2000). Control and characterization of a multistep unimolecular reaction. *Physical Review Letters*, *84*, 1527.
59. Corcoran, S. G., Colton, R. J., Lilleodden, E. T., & Gerberich, W. W. (1997). Anomalous plastic deformation at surfaces: Nanoindentation of gold single crystals. *Physical Review B*, *55*, R16057.
60. de la Fuente, O. R., Zimmerman, J. A., González, M. A., de la Figuera, J., Hamilton, J. C., Pai, W. W., & Rojo, J. M. Dislocation emission around nanoindentations on a (001) fcc metal surface studied by scanning tunneling microscopy and atomistic simulations. *Physical Review Letters*, *88*, 036101.

61. Kondo, Y., & Takayanagi, K. (2000). Synthesis and characterization of helical multi-shell gold nanowires. *Science*, 289, 606.
62. Tosatti, E., & Prestipino, S. (2000). Weird gold nanowires. *Science*, 289, 561.
63. Hla, S.-W., Braun, K.-F., Iancu, V., & Deshpande, A. (2004). Single atom extraction by scanning tunneling microscope tip-crash and nanoscale surface engineering. *Nano Letters*, 4, 1997.
64. Eigler, D. M., & Schweizer, E. K. (1990). Positioning single atoms with a scanning tunneling microscope. *Nature*, 344, 524.
65. Bartels, L., Meyer, G., & Rieder, K.-H. (1997). Basic steps of lateral manipulation of single atoms and diatomic clusters with a scanning tunneling microscope tip. *Physical Review Letters*, 79, 697.
66. Lyo, I.-W., & Avouris, P. (1991). Field-induced nanometer- to atomic-scale manipulation of silicon surfaces with the STM. *Science*, 253, 173.
67. Meyer, G., Zöphel, S., & Rieder, K.-H. (1996). Manipulation of atoms and molecules with a low temperature scanning tunneling microscope. *Applied Physics A: Materials Science & Processing*, 63, 557.
68. Tilinin, I. S., Van Hove, M. A., & Salmeron, M. (1998). Tip-surface transfer of adatoms in AFM/STM: Effect of quantum oscillations. *Applied Surface Science*, 676, 130–132.
69. Colton, R. J., Baker, S. M., Driscoll, R. J., Youngquist, M. G., Baldeschwieler, J. D., & Kaiser, W. J. (1988). Imaging graphite in air by scanning tunneling microscopy: Role of the tip. *Journal of Vacuum Science and Technology A*, 6(2), 349.
70. Wong, H. S., Durkan, C., & Chandrasekhar, N. (2009). Tailoring the local interaction between graphene layers in graphite at the atomic scale and above using scanning tunneling microscopy. *ACS Nano*, 3, 3455–3462.
71. Stawasz, M. E., Sampson, D. L., & Parkinson, B. A. (2000). Scanning tunneling microscopy investigation of the ordered structures of dialkylamino hydroxylated squaraines adsorbed on highly oriented pyrolytic graphite. *Langmuir*, 16, 2326–2342.
72. Paredes, J. I., Martinez-Alonso, A., & Tascon, J. M. D. (2007). Multiscale imaging and tip-scratch studies reveal insight into the plasma oxidation of graphite. *Langmuir*, 23, 8932–8943.
73. Gopakumar, T. G., Lackinger, M., Hackert, M., Muller, F., & Hietschold, M. (2004). Adsorption of palladium phthalocyanine on graphite: STM and LEED study. *The Journal of Physical Chemistry B*, 108, 7839–7843.
74. Linares, M., Scifo, L., Demadrille, R., Brocens, P., Beljonne, D., Lazzaroni, R., & Grevin, B. (2008). Two-dimensional self-assemblies of thiophene-fluorenone conjugated oligomers on graphite: A joint STM and molecular modeling study. *Journal of Physical Chemistry C*, 112, 6850–6859.
75. Chilukuri, B., McDougald, R. N., Jr., Ghimire, M. M., Nesterov, V. N., Mazur, U., Omary, M. A., & Hips, K. W. (2015). Polymorphic, porous, and host-guest nanostructures directed by monolayer-substrate interactions: Epitaxial self-assembly study of cyclic trinuclear Au(I) complexes on HOPG at the solution–solid interface. *Journal of Physical Chemistry C*, 119, 24844–24858.
76. Lipari, N. O. (1987). STM applications for semiconductor materials and devices. *Surface Science*, 181, 285–294.
77. Uosaki, K., & Koinuma, M. (1992). Application of scanning tunnelling microscopy to semiconductor electrolyte interfaces. *Faraday Discussions*, 94, 361–368.
78. Petta, J. R. (2017). Atom-by-atom construction of a quantum device., 11, 2382–2386.
79. Volders, C., Monazami, E., Ramalingam, G., & Reinke, P. (2016). Alternative route to silicene synthesis via surface reconstruction on h-MoSi₂ crystallites. *Nano Letters*, 17, 299–307.
80. Saedi, A., Poelsema, B., & Zandvliet, H. J. W. (2010). Study of dynamic processes on semiconductor surfaces using time-resolved scanning tunneling microscopy. *Journal of Physics: Condensed Matter*, 22, 264007.
81. Li, Z., Li, B., Yang, J., & Hou, J. G. (2010). Single-molecule chemistry of metal phthalocyanine on noble metal surfaces. *Accounts of Chemical Research*, 43, 954–962.

82. Miao, P., Robinson, A. W., & Palmer, R. E. (2000). Structural properties of self-organized organo-silicon macromolecular films investigated by scanning tunneling microscopy and X-ray diffraction. *The Journal of Physical Chemistry B*, *104*, 1285–1291.
83. Liljeroth, P., Swart, I., Paavilainen, S., Repp, J., & Meyer, G. (2010). Single-molecule synthesis and characterization of metal-ligand complexes by low-temperature STM. *Nano Letters*, *10*, 2475–2479.
84. Lin, S.-Y., Chen I-W, P., Chen, C.-H., Hsieh, M.-H., Yeh, C.-Y., Lin, T.-W., Chen, Y.-H. G., & Peng, S.-M. (2004). Effect of metal-metal interactions on electron transfer: An STM study of one-dimensional metal string complexes. *The Journal of Physical Chemistry B*, *108*, 959–964.
85. Li, J., Gottardi, S., Solianyk, L., Moreno-Lopez, J. C., & Stohr, M. (2016). 1,3,5-benzenetribenzoic acid on Cu(111) and graphene/Cu(111): A comparative STM study. *Journal of Physical Chemistry C*, *120*, 18093–18098.
86. Han, X., Hu, J., Liu, H., & Hu, Y. (2006). SEBS aggregate patterning at a surface studied by atomic force microscopy. *Langmuir*, *22*, 3428–3433.
87. Dabirian, R., Zdravkova, A. N., Liljeroth, P., van Walree, C. A., & Jennekens, L. W. (2005). Mixed self-assembled monolayers of semirigid tetrahydro-4H-thiopyran end-capped oligo (cyclohexylidenes). *Langmuir*, *21*, 10497–10503.
88. Baubet, B., Girleanu, M., Gay, A.-S., Taleb, A.-L., Moreaud, M., Wahl, F. O., Delattre, V., Devers, E., Hugon, A., Ersen, O., Afanasiev, P., & Raybaud, P. (2016). Quantitative two-dimensional (2D) morphology–selectivity relationship of CoMoS nanolayers: A combined high-resolution high-angle annular dark field scanning transmission electron microscopy (HR HAADF-STEM) and density functional theory (DFT) study. *ACS Catalysis*, *6*, 1081–1092.
89. van de Leemput, L. E. C., & Kempen, H. V. (1992). Scanning tunnelling microscopy. *Report on Png Physics*, *55*, 1165–1240.
90. Sumi, H. (1998). V-I characteristics of STM processes as a probe detecting vibronic interactions at a redox state in large molecular adsorbates such as electron-transfer metalloproteins. *The Journal of Physical Chemistry B*, *102*, 1833–1844.
91. Mayne, A. J., Avery, A. R., Knall, J., Jones, T. S., GAD, B., & Weinberg, W. H. (1993). An STM study of the chemisorption of C,H, on Si(OO1)(2x 1). *Surface Science*, *284*, 247–256.
92. Avow-is, P., Lyo, I.-W., & Molinas-Mata, P. (1995). STM studies of the interaction of surface state electrons on metals with steps and adsorbates. *Chemical Physics Letters*, *240*, 423–428.
93. Yang, J., Nacci, C., Martinez-Blanco, J., Kanisawa, K., & Folsch, S. (2012). Vertical manipulation of native adatoms on the InAs(111)A surface. *Journal of Physics: Condensed Matter*, *24*, 354008.
94. Hong, S., & Rahman, T. S. (2008). Adsorbate induced changes in surface stress and phonon dispersion curves of chemisorbed systems. *Journal of Physics: Condensed Matter*, *20*, 224005.
95. Kiejna, A., & Pabisiak, T. (2012). Surface properties of clean and Au or Pd covered hematite (α -Fe₂O₃) (0001).
96. Chen, Q., Liu, J., Zhou, X., Shang, J., Zhang, Y., Shao, X., Wang, Y., Li, J., Chen, W., Xu, G., & Wu, K. (2015). Unveiling structural evolution of CO adsorption on Ru(0001) with high-resolution STM. *Journal of Physical Chemistry C*, *119*, 8626–8633.
97. Majzik, Z., Drevniok, B., Kaminski, W., Ondracek, M., AB, M. L., & Jehnek, P. (2013). Room temperature discrimination of adsorbed molecules and attachment sites on the Si(111)-7×7 surface using a q-plus sensor. *ACS Nano*, *7*, 2686–2692.
98. Coleman, R. V., Drake, B., Giambattista, B., Johnson, A., Hansma, P. K., McNairy, W. W., & Slough, G. (1988). Applications of scanning tunneling microscopy to the study of charge density waves. *Physica Scripta*, *38*, 235–243.
99. Tcbougreeff, A. L., & Hoffmann, R. (1992). Charge and spin density waves in the electronic structure of graphlte. Application to analysis of STM images. *The Journal of Physical Chemistry*, *96*, 8993–8998.
100. Tomic, A., Rak, Z., Veazey, J. P., Mahanti, S. D., & Tessmer, S. H. (2009). Scanning tunneling microscopy study of the CeTe₃ charge density wave. *Physical Review B*, *79*, 085422.

101. Sacks, W., Roditchev, D., & Klein, J. (1998). Voltage-dependent STM image of a charge density wave. *Physical Review B*, *57*, 1920.
102. Brun, C., Wang, Z.-Z., Monceau, P., & Brazovskii, S. (2010). Surface charge density wave phase transition in NbSe₃. *Physical Review Letters*, *104*, 256403.
103. Fan, Q., Zhang, W. H., Liu, X., Yan, Y. J., Ren, M. Q., Xia, M., Chen, H. Y., Xu, D. F., Ye, Z. R., Jiao, W. H., & Cao, G. H. (2015). Scanning tunneling microscopy study of superconductivity, magnetic vortices, and possible charge-density wave in Ta₄Pd₃Te₁₆. *Physical Review B*, *91*, 104506.
104. Fischer, O., Kugler, M., Maggio-Aprile, I., & Berthod, C. (2007). Scanning tunneling spectroscopy of high-temperature superconductors. *Reviews of Modern Physics*, *79*, 353.
105. Lee, J., Slezak, J. A., & Davis, J. C. (2005). Spectroscopic imaging STM studies of high-TC superconductivity. *Journal of Physics and Chemistry of Solids*, *66*, 1370–1375.
106. Rodrigo, J. G., Suderow, H., & Vieira, S. (2004). On the use of STM superconducting tips at very low temperatures. <https://doi.org/10.1140/epjbe2004-00273-y>.
107. Zou, Q., Wu, Z., Fu, M., Zhang, C., Rajput, S., Wu, Y., Li, L., Parker, D. S., Kang, J., Sefat, A. S., & Gai, Z. (2017). Effect of surface morphology and magnetic impurities on the electronic structure in cobalt-doped BaFe₂As₂ superconductors. *Nano Letters*, *17*, 1642–1647.
108. Wise, W. D., Chatterjee, K., Boyer, M. C., Kondo, T., Takeuchi, T., Ikuta, H., Xu, Z., Wen, J., Gu, G. D., Wang, Y., & Hudson, E. W. (2009). Imaging nanoscale Fermi surface variations in an inhomogeneous superconductor. *Nature Physics*, *5*, 213–216 2009.
109. Zeljkovic, I., & Hoffman, J. E. (2013). Interplay of chemical disorder and electronic inhomogeneity in unconventional superconductors. *Physical Chemistry*, *15*, 13462–13478.
110. Wang, H., Lee, J., Dreyer, M., & Barker, B. I. (2009). A scanning tunneling microscopy study of a new superstructure around defects created by tip-sample interaction on 2H-NbSe₂. *Journal of Physics: Condensed Matter*, *21*, 265005.
111. Liu, N., Lyeo, H. K., Shih, C. K., Oshima, M., Mano, T., & Koguchi, N. (2002). Cross-sectional scanning tunneling microscopy study of InGaAs quantum dots on GaAs(001) grown by heterogeneous droplet epitaxy. *Applied Physics Letters*, *80*, 4345.
112. Altfeder, I., Voevodin, A. A., Check, M. H., Eichfeld, S. M., Robinson, J. A., & Balatsky, A. V. (2017). *Scientific Reports*, *7*, 43214.
113. Kim, H. W., Ko, W., Ku, J. Y., Jeon, I., Kim, D., Kwon, H., Oh, Y., Ryu, S., Kuk, Y., Hwang, S. W., & Suh, H. (2015). Nanoscale control of phonon excitations in graphene. *Nature Communications*, *6*, 7528.
114. Wortmann, D., Heinze, S., Kurz, P., Bihlmayer, G., & Blügel, S. (2001). Resolving complex atomic-scale spin structures by spin-polarized scanning tunneling microscopy. *Physical Review Letters*, *n86*, 4132.
115. Wulfhekela, W., & Kirschner, J. (1999). Spin-polarized scanning tunneling microscopy on ferromagnets. *Applied Physics Letters*, *75*, 1944.
116. Kleiber, M., Bode, M., Ravlic, R., & Wiesendanger, R. (2000). Topology-induced spin frustrations at the Cr(001) surface studied by spin-polarized scanning tunneling spectroscopy. *Physical Review Letters*, *85*, 4606.
117. Bode, M., Getzlaff, M., & Wiesendanger, R. (1998). Spin-polarized vacuum tunneling into the exchange-split surface state of Gd(0001). *Physical Review Letters*, *81*, 4256.
118. Eltschka, M., Jack, B., Assig, M., Kondrashov, O. V., Skvortsov, M. A., Etzkorn, M., Ast, C. R., & Kern, K. (2014). Probing absolute spin polarization at the nanoscale. *Nano Letters*, *14*, 7171–7174.
119. Dorig, U., Zoger, O., & Pohl, D. W. (1988). Force sensing in scanning tunnelling microscopy: Observation of adhesion forces on clean metal surfaces. *Journal of Microscopy*, *152*, 259–267.
120. Manassen, Y., Ter-Ovanesyan, E., Shachal, D., & Richter, S. (1993). Electron spin resonance-scanning tunneling microscopy experiments on thermally oxidized Si(111). *Physical Review B*, *48*, 4887.

121. Zhdan, P. A. (2002). Nanoscale surface characterization of conducting and non-conducting materials with STM and contact SFM: Some problems and solutions. *Surface and Interface Analysis*, 33, 879–893.
122. Guckenberger, R., Kosslinger, C., Gatz, R., Breu, H., Levai, N., & Baumeister, W. (1988). A scanning tunneling microscope (STM) for biological applications: Design and performance. *Ultramicroscopy*, 25, 111–122.
123. Wilson, R. J., Johnson, K. E., Chambliss, D. D., & Melior, B. (1993). Scanning tunneling microscopy of biological molecules on Pt(111): From 100 to 5×10^6 Da. *Langmuir*, 9, 3478–3490.
124. Tao, N. J., & Shi, Z. (1994). Monolayer guanine and adenine on graphite in NaCl solution: A comparative STM and AFM study. *The Journal of Physical Chemistry*, 98, 1464–1471.
125. Smerieri, M., Vattuone, L., Costa, D., Tielens, F., & Savio, L. (2010). Self-assembly of (S)-glutamic acid on Ag(100): A combined LT-STM and Ab initio investigation. *Langmuir*, 26(10), 7208–7215.
126. Tao, N. J., Li, C. Z., & He, H. X. (2000). Scanning tunneling microscopy applications in electrochemistry -beyond imaging. *Journal of Electroanalytical Chemistry*, 492, 81–93.
127. Lay, M. D., Sorenson, T. A., & Stickney, J. L. (2003). High-resolution electrochemical scanning tunneling microscopy (EC-STM) flow-cell studies. *The Journal of Physical Chemistry B*, 107, 10598–10602.
128. Kuo, Y., Liao, W., & Yau, S. L. (2014). Effects of anions on the electrodeposition of cobalt on Pt(111) electrode. *Langmuir*, 30, 13890–13897.
129. Yang, Y.-C., Lee, Y.-L., Ou Yang, L.-Y., & Yau, S.-L. (2006). In situ scanning tunneling microscopy of 1,6-hexanedithiol, 1,9-nonanedithiol, 1,2-benzenedithiol, and 1,3-benzenedithiol adsorbed on Pt(111) electrodes. *Langmuir*, 22, 5189–5195.
130. Grubb, M., Wackerbarth, H., Jesper, W., & Jens, U. (2007). Direct imaging of Hexamine-ruthenium(III) in domain boundaries in monolayers of single-stranded DNA. *Langmuir*, 23, 1410–1413.
131. Bhusan, B., Israelachvili, J. N., & Lndman, U. (1995). Nanotribology: Friction, wear and lubrication at the atomic scale. *Nature*, 374, 607.
132. Ding, Y. H., Ren, H.-M., Chang, F.-H., Zhang, P., & Jiang, Y. (2013). Intrinsic structure and friction properties of graphene and graphene oxide nanosheets studied by scanning probe microscopy. *Bulletin of Materials Science*, 36, 1073–1077.
133. Jaklevic, R. C., & Elie, L. (1998). Scanning-tunneling-microscope observation of surface diffusion on an atomic scale: Au on Au(111). *Physical Review Letters*, 60, 120.
134. Packard, W. E., Liang, Y., Dai, N., Dow, J. D., Nicolides, R., Jaklevic, R. C., & Kaise, W. J. (1988). Nano-machining of gold and semiconductor surfaces. *Journal of Microscopy*, 152, 715–725.
135. Williams, P. M., Cheema, M. S., Davies, M. C., Jackson, D. E., & Tandler, S. J. B. (1994). Biological applications of scanning tunneling microscopy. In C. Jones, B. Mulloy, & A. H. Thomas (Eds.), *Microscopy, optical spectroscopy, and macroscopic techniques* (pp. 25–37). Totowa: Humana Press.
136. Stegemann, B., Bernhardt, T. M., Kaiser, B., & Rademann, K. (2002). STM investigation of surface alloy formation and thin film growth by Sb₄ deposition on Au (111). *Surface Science*, 511, 153–162.
137. Biegelsen, D. K., Bringans, R. D., Northrup, J. E., & Swartz, L.-E. (1990). Reconstructions of GaAs(111) surfaces observed by scanning tunneling microscopy. *Physical Review Letters*, 65.
138. Xu, P., Barber, S. D., Ackerman, M. L., Schoelz, J. K., & Thibado, P. M. (2013). Role of bias voltage and tunneling current in the perpendicular displacements of freestanding graphene via scanning tunneling microscopy. *Journal of Vacuum Science and Technology B*, 31, 04D103.

Chapter 7

Atomic and Magnetic Force Studies of Co Thin Films and Nanoparticles: Understanding the Surface Correlation Using Fractal Studies



Indra Sulania, R. P. Yadav, and Ranjeet Kumar Karn

7.1 Introduction

Microscopy is a technique used for viewing those objects which cannot be seen with naked eyes. Zacharias Jansen and his father Hans were the persons who invented the first compound microscope in the late sixteenth century which enables us to look into the micrometer-scaled structures. Since then, many developments have happened that had made it possible for us to observe the structures in atomic scales. There are three well-known branches of microscopy: (i) *optical microscopy*, (ii) *electron microscopy*, and (iii) *scanning probe microscopy*. Optical microscopy (OM) is based upon the principles of reflection and refraction of light. In electron microscopy (EM), scattered electrons are collected to form the image of an object, whereas, in scanning probe microscopy (SPM), there is a physical interaction of a fine probe/tip with the surface of the sample which is capable of giving out the topography of a sample in three dimensions. Therefore, one can say it is the physical scanning of objects/samples with the help of a very small probe [1–3].

Scanning probe microscope is an instrument used for studying the surfaces at nanoscale regime. It forms images of surfaces using a physical probe that touches the sample's surface to scan it and collect data, typically obtained as a two-dimensional grid of data points and displayed as a computer image. The first SPM

I. Sulania (✉)

Inter University Accelerator Centre, New Delhi, India

e-mail: indra@iuac.res.in

R. P. Yadav

Department of Physics, Motilal Nehru National Institute of Technology Allahabad, Allahabad, India

R. K. Karn

University Department of Physics, Kolhan University, Chaibasa, India

© Springer International Publishing AG, part of Springer Nature 2018

S. K. Sharma (ed.), *Handbook of Materials Characterization*,

https://doi.org/10.1007/978-3-319-92955-2_7

instrument was developed in 1982 at the IBM Research Laboratory in Zurich by Gerd Binnig and Heinrich Rohrer and known as scanning tunneling microscope (STM) [4, 5]. It was the first technology to be recognized as having atomic resolution capability. It uses an electrical current between the microscope's scanning tip and the sample to image the surface of the sample. Unfortunately, the surface of the sample must be conductive or semiconductive, hence limiting the materials that can be studied using STMs [4]. These limitations drove the invention of the first atomic force microscope (AFM) [1, 3], and later magnetic force microscopy (MFM), electric field microscopy (EFM), conductive AFM, and AFM for liquid samples, which mainly find application in biological systems, etc., were developed together with STM in a single unit. Such instruments are called multimode, as they can be used to scan the samples in various modes, as per the requirement, using a proper interface between the software and hardware. AFM uses a very sharp tip to probe and map the morphology of a surface. However, AFM neither poses any requirement from the sample's side to be conductive, nor is it necessary to measure a current between the tip and sample to produce an image. AFM employs the tip or probe, at the end of a micro-fabricated cantilever with a low stiffness constant (spring constant) to measure the tip-sample forces as the tip presses (either continuously or intermittently) against the sample. Forces between the tip and the sample surface cause the cantilever to bend, or deflect, as the tip is scanned over the sample. The cantilever deflection is measured, and the measurements generate a map of surface topography. The details will be discussed in later sections.

In this chapter the basic principles of operation of an AFM will be presented, outlining the utmost common imaging modes and describing the attainment of force-distance measurements and techniques to calibrate cantilever spring constants. Further, we discuss the surface features such as shape and dimensions of the nano- and micron-sized particles, roughness of the surfaces, three-dimensional information of the surfaces and magnetic strength of the samples, biological sample scanning with the help of fluid cells to know the stiffness of the cell membranes, adhesion properties using the force-distance spectra, conducting properties with IV curves using conducting mode AFM, etc. Therefore, we can say that since the invention of AFM in 1986, it has become one of the most important tools for imaging the surfaces of samples at nanometric-scale resolution. Thus, it is considered to be a strong competitor to conventional methods, which are used to obtain the morphology of the samples and to investigate the structures, such as in electron microscopy, X-ray scattering, etc. In the beginning, atomic force microscopy (AFM) was applied almost exclusively to characterize the surfaces of non-biological materials. But we have cited few examples where the role of AFMs in imaging of biological samples is also highlighted. In the end, a few experimental examples are included to show the versatility of the techniques of AFM for the variety of samples. We will start our discussion briefly with scanning tunneling microscope. The detail about the STM is covered in another chapter of this book.

7.1.1 Scanning Tunneling Microscope

Scanning tunneling microscopy is a microscopy technique which helps us to investigate the electrically conducting surfaces down to the atomic scales, as it requires the tunneling of electrons from a conducting tip to the sample and vice versa depending upon the density of states of the electrons in the two. Here, quantum mechanical tunneling allows the particles to tunnel through a potential barrier which they could not do according to the classical laws of physics. Moreover, the probability of tunneling is exponentially dependent upon the distance of separation between the tip and surface, making the technique even more sensitive to investigate in atomistic levels.

7.1.1.1 Basic Working Principles of STM

The basic principle behind this instrument is the quantum mechanical tunneling of electrons when the tip and the samples are separated by a very small distance and a bias voltage is applied between them. The tunneling current flows across the small gap that separates the tip from the sample, a case that is forbidden in classical physics but that can be explained by the better approach of quantum mechanics: the electrons are “tunneling” across the gap. The tunneling current, “ I ,” exhibits an exponentially decaying behavior with the separation between the tip and the sample. The relation is given by $I \propto U \exp(-kd)$, where k is a constant, U is the bias applied, and d is the tip-sample separation [2, 4, 5].

It is to be noted here that a very small change in the tip-sample separation induces large changes in the tunneling current. This behavior enables us to control the tip-sample separation very precisely. Furthermore, the tunneling current is mainly a contribution from the outermost atom of the tip, i.e., the atoms that are second nearest carry only a negligible amount of the current. Therefore, one can say that the sample surface is scanned with a single atom, which gives out the atomic resolution. As shown in the schematic in Fig. 7.1, the STM setup basically consists of a sharp conducting tip or probe, which is within angstrom distance from the sample, piezo scanners, and electronic control modules. Tip is attached with piezoelectric transducer. By applying a bias voltage between the tip and the sample, a “tunneling current” is generated. Tunneling current is converted into voltage by current amplifier which is then compared with reference value. The difference is amplified to derive z piezo. If absolute value of tunneling current is larger than the reference value, the voltage applied to z piezo tends to withdraw tip from sample surface and vice versa. The direction of current flow is determined by the polarity of the bias. If the sample is biased positive with respect to the tip, then electrons will flow from the tip to the surface and vice versa, as shown in Fig. 7.2.

Generally, the imaging of the surface topology can be carried out in two ways, either you keep the distance constant or you keep the current constant. This is described in details below:

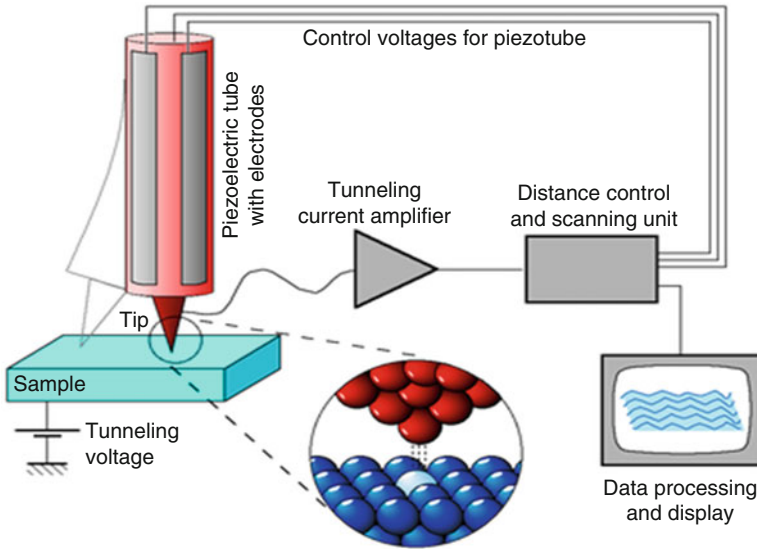


Fig. 7.1 Schematic of STM [Michael Schmid, TU Wien; adapted from the IAPTU Wien STM Gallery]

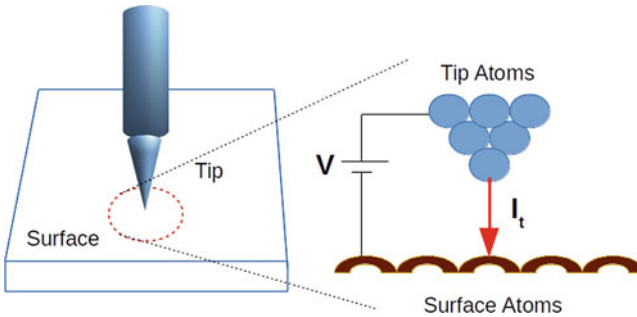


Fig. 7.2 Sample bias and flow of tunneling current

7.1.1.2 Working Modes of STM

There are two main modes of working of STM – constant height mode and constant current mode.

Constant Height Mode

In constant height mode, the tunneling current is monitored as the tip is scanned parallel to the surface. If the tip is scanned at constant height above the surface (Fig. 7.3a), there is a periodic variation in the separation distance between the tip and

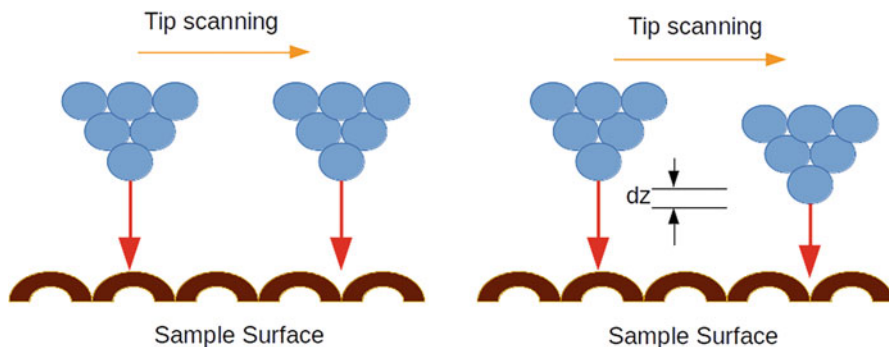


Fig. 7.3 Constant (a-left panel) height mode and (b-right panel) current mode

surface atoms. At one point the tip will be directly above a surface atom, and the tunneling current will be large, while at other points the tip will be above hollow sites and the tunneling current will be much smaller. Therefore, variation between tunneling current to tip's position gives the image of the surface.

Constant Current Mode

In constant current mode, the tunneling current is maintained constant as the tip is scanned across the surface. Generally, the normal way of imaging the surface is to maintain the constant tunneling current. This is done by adjusting the tip's height above the surface so that the tunneling current does not vary with the lateral tip position (Fig. 7.3b). Therefore, the tip will move slightly upward as it passes over a surface atom and, conversely, slightly in toward the surface as it passes over a hollow. The image is formed by plotting the tip height versus the tip position.

Limitation Although STM is capable of giving out the images in atomic scales, it could only be helpful for the conducting surfaces; this limitation led to the invention of atomic force microscopy (AFM) in 1986.

7.1.2 Atomic Force Microscopy

Atomic force microscope (AFM) is based on the sensing of the van der Waals interactions between the tip and the sample. AFM is used to investigate the samples by measuring forces between a sharp probe (<10 nm) and surface at very narrow distances (probe-sample separation) typical in the order of ~ 0.2 to 10 nm. It was invented in 1986 by Binnig et al.; since then, it has undergone many developments. The first AFMs were operated in contact mode (see Binnig et al. [5]).

7.1.2.1 Basic Working Principles of AFM

In AFM, a probe is supported on a flexible cantilever analogous to tip attached to a spring as shown in Fig. 7.4. The force exerted by the tip onto the sample is given by Hooke's law. Therefore, by observing the deflection of the probe due to various forces acting between the tip and the sample (separated at a distance of 0.1–100 nm), the topography of the sample can be obtained in the form of two- or three-dimensional information [6–10].

These forces can be broadly classified into attractive and repulsive forces. The attractive forces are mainly van der Waals forces, electrostatic forces, chemical forces, etc. The repulsive forces are mainly electrostatic Coulombic interactions, capillary forces, covalent forces, etc. In general, the repulsive forces are very short-range forces and have an exponential decaying or show inverse power-law behavior which hugely depends upon the separation distance.

Van der Waals forces are the weakest forces which exist between the atoms and molecules and cumulatively hold atoms and molecules together. Their importance follows from two unique properties. Firstly, they are universal forces, which exist everywhere. All atoms and molecules attract one another through these interactions. They are responsible for cohesion of the inert gases in the solid and liquid states, and physical adsorption of molecules to solid surfaces, where no normal chemical bonds are formed. Secondly, the force is still significant when the molecules are comparatively far apart, and it is additive for large numbers of molecules. Van der Waals forces affect various properties of gases and also give rise to an attractive force between two solid objects separated by a small gap, which is important in adhesion and thus provides stability to colloids. To acquire the image resolution, AFMs can generally measure the vertical and lateral deflections of cantilever by using an optical lever as shown in Fig. 7.5.

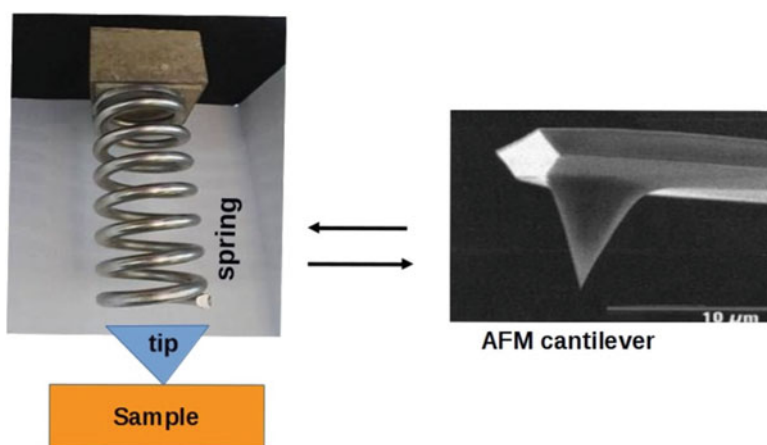


Fig. 7.4 AFM probe/tip attached to a flexible cantilever

Fig. 7.5 Schematic of the optical lever (adapted from [8]).

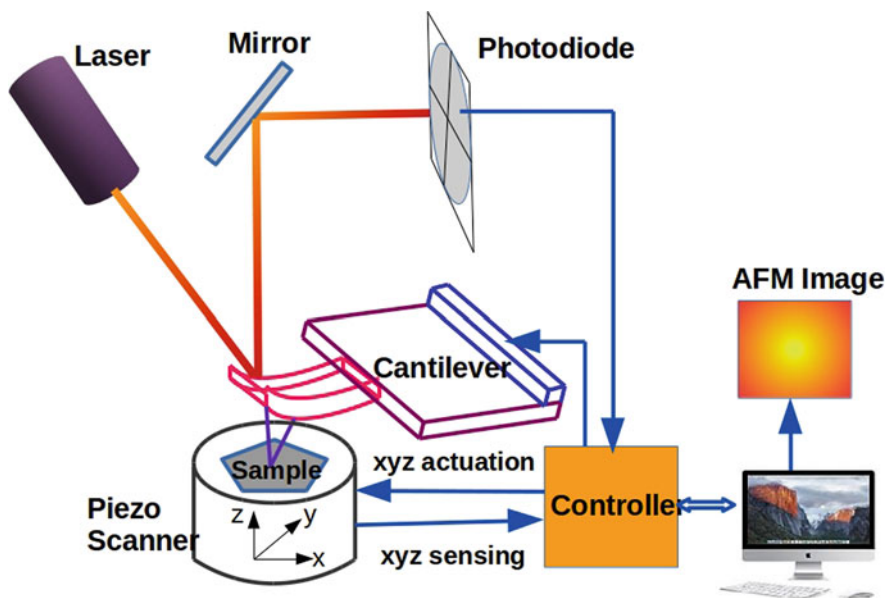
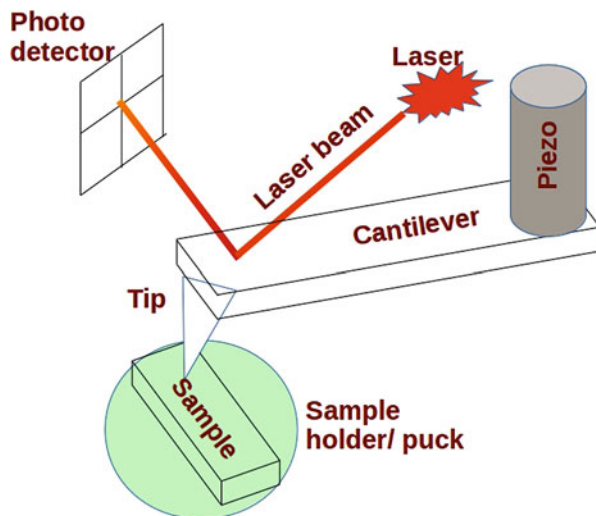


Fig. 7.6 Schematic of atomic force microscope (adapted from <https://www.techbriefs.com/component/content/article/tb/supplements/pit/applications/27833>).

The optical lever operates by reflecting a laser beam off the cantilever. The AFM consists of four major parts, a cantilever with a sharp tip, normally made of silicon or silicon nitride, mounted on a piezo scanner that drives the cantilever; a laser diode; and a position-sensitive detector, as shown in Fig. 7.6. As the tip scans over the sample's surface, the interactions between the AFM tip and the features on

the surface cause displacement of the cantilever. The reflected laser beam strikes a position-sensitive photodetector consisting of four segmented photodetector. The difference between the signals obtained from various segments of photodetector indicate the position of the laser spot onto the detector and, thereby the angular deflections of the cantilever (Fig. 7.5). When tip and specimen are brought close to each other, the force between them led to deflection of cantilever. The atomic force microscope creates topographic images of the surface by plotting the laser beam deflection as its tip scans over the surface. This design greatly improved the sensitivity of the design of the microscope as cantilever displacement can easily be amplified by the light path. Atomic resolution images of a variety of surfaces have been achieved with this design. However, the most important point of this design for biomedical purposes is that it makes operation of the atomic force microscope possible in ambient environments or in aqueous solutions at room temperature or at 37 °C. These conditions are required for imaging native biological samples in their functional and physiological environments.

By using AFM, one cannot only image the surface in atomic resolution but also measure the force at nanonewton (nN) scale. Therefore, one can obtain the force-distance curves and calculate the spring constant of the samples, various polymeric samples and biological membranes. AFM consists of a cantilever with a sharp tip/probe that is used to scan the specimen surface. The deflection of the cantilever is measured using a laser spot reflected from the top of the surface of cantilever into the photodiode. If tip is scanned at constant height, due to local curvature of the surfaces, the tip may collide with the sample surface causing damage to the tip or the samples. Hence, *feedback mechanism* is employed to adjust the tip-to-sample distance to maintain a constant force between the tip and the sample surface as shown in the schematic in Fig. 7.6. Traditionally, the sample is mounted on piezoelectric tube scanner that can move the sample in z direction for maintaining a constant force and the x and y direction to scan the sample. AFM can be operated in a number of modes depending on the application. The basic modes are the static mode and dynamic mode.

7.1.2.2 Different Working Modes of AFM

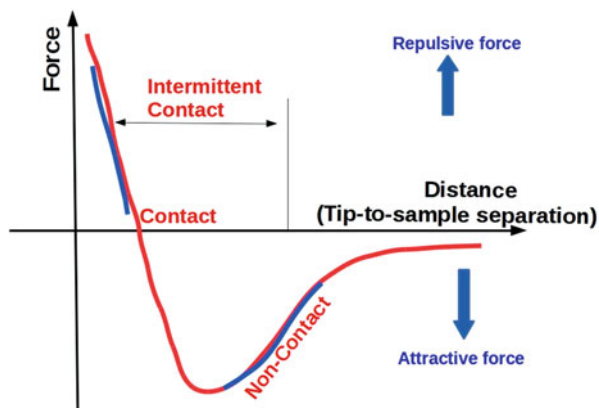
There are three primary imaging modes of operation in AFM [1, 3, 6, 7]:

- (i) Contact AFM: **<0.5 nm** probe-surface separation
- (ii) Intermittent contact (tapping mode AFM): **0.5–2 nm** probe-surface separation
- (iii) Non-contact AFM: **0.1–10 nm** probe-surface separation

Contact Mode AFM

The static mode is performed in “contact” with the sample surface, where the overall force is repulsive in nature. The cantilever tip is dragged over the substrate main-

Fig. 7.7 Force versus probe-sample separation curve



taining the deflection at a constant order. In contact mode, tip/probe experiences a repulsive force with the sample surface. As the tip traces the sample, force on the tip is repulsive; thus, cantilever bends away from sample to accommodate changes in topography. To examine this force, we refer to force-distance curve in Fig. 7.7.

At larger distances, the atoms experience the attractive forces between them. As the distance decreases, they weakly attract each other, on further approach of the tip toward the sample; electron clouds begin to repel each other electrostatically, and the atoms experience the repulsive forces. When the van der Waals force becomes positive (repulsive), the atoms are in contact. Force between tip and sample is determined by measuring the deflection of a spring cantilever. The force is calculated by Hooke's law $F = -kX$, where "k" is the "spring constant" and "X" is the displacement of the cantilever. The deflection of cantilever is used as the input to feedback circuit that moves the scanner up and down in "z" direction. The cantilever deflection constant (using the feedback loops) the force between the probe and the sample remains constant and an image of the surface is obtained as shown in schematic in Fig. 7.6.

The SPM controller is the heart of the instrument. It collects the signal and converts it to height information using control electronics. The control system performs two main functions:

- (i) It generates drive voltage to control X-Y scans of the piezoelectric transducer.
- (ii) It maintains incoming analog signal from microscope detection simultaneously at a constant value through a feedback loop. The computer reads voltage from comparator circuit through A/D converter. It is programmed to keep the two inputs of the comparator circuit equal to 0 volts. An output voltage generated by the computer continuously moves the piezoelectric transducer in the z direction to correct for differences read into the A/D converter. This closed-loop feedback control is the heart of the imaging portion of the control station.

Advantages: This mode provides fast scanning, and it is good for rough samples and can be used in friction analysis.

Disadvantages: At times, forces can damage/deform soft samples.

Tapping (Intermittent) Mode AFM

In tapping mode, imaging is similar to contact; however, in this mode the cantilever is oscillated at its resonant frequency to avoid dragging the tip across the surface. The probe lightly “taps” on the sample surface during scanning, contacting the surface at the bottom of its swing (as in contact mode) and collects the data. Then go back at certain distance (as in non-contact mode). Cantilever amplitude is made constant in this mode. When tip passes over a bump surface, the amplitude oscillation decreases, and when tip passes over a depression, the amplitude increases. Amplitude oscillation is measured by the detection and used as input to controller electronics. The digital feedback loop then adjusts the tip separation to maintain constant amplitude and force on sample.

Advantages: Allows high resolution of samples that are easily damaged, good to use for biological samples

Disadvantages: More challenging to image in liquids, slower scan speeds needed

Non-contact Mode AFM

The non-contact mode is the dynamic mode since the cantilever is deliberately vibrated at or close to its resonance frequency. The resonance of the cantilever is characterized by amplitude, phase, and frequency. The variation of these three indicators, due to the interaction force, can be measured and generates an image. Obtaining atomic resolution in the dynamic mode is difficult in ambient conditions. In this mode, the probe does not contact the sample surface, but oscillates above the adsorbed fluid layer on the surface during scanning. Cantilevers used in this mode are stiffer than those used in contact mode. In non-contact AFM (NC-AFM), cantilever is oscillated slightly near its resonant frequency; change in frequency acts as input in feedback circuit to move scanner up and down. Feedback loop maintains constant frequency by maintaining tip-to-sample distance.

Advantages: As a very low force exerted on the sample (10–12 nN), the lifespan of the probe is increased.

Disadvantages: Generally gives lower resolution. The contaminant layer on surface can interfere with oscillation; therefore, it usually needs ultrahigh vacuum (UHV) to have the best imaging.

Limitations of AFM The AFM can be used to study a wide variety of samples (i.e., plastic, metals, glasses, semiconductors, and biological samples such as the walls of cells and bacteria). Unlike STM or scanning electron microscopy, it does not require a conductive sample. However there are limitations in achieving atomic resolution. The physical probe used in AFM imaging is not ideally sharp. As a consequence,

an AFM image does not reflect the true sample topography, but rather represents the interaction of the probe with the sample surface. This is called tip convolution.

7.1.2.3 Magnetic Force Microscopy (MFM)

Magnetic force microscopy (MFM) is a special mode of operation of the scanning probe microscope (SPM). The technique employs a magnetic probe, which is brought close to a sample and interacts with the magnetic stray fields near the surface. MFM was introduced shortly after the invention of the AFM (Martin and Wickramasinghe [12]) and became popular as a technique that offers high imaging resolution without the need for special sample preparation or environmental conditions. Since then, it has been extensively used in the fundamental research of magnetic materials, as well as the development of magnetic recording components.

7.1.2.4 Basic Working Principles of MFM

With the help of MFM, one can detect the magnetic domains within the sample. It is performed in lift mode, and it detects the phase change in the tip's oscillation due to magnetic strength of the domains lying in the sample. The operating principle of MFM is the same as in AFM, but it requires an additional lock-in amplifier to compare the phase and amplitude changes of the signal which arises due to sample's stray magnetic field as shown in Fig. 7.8.

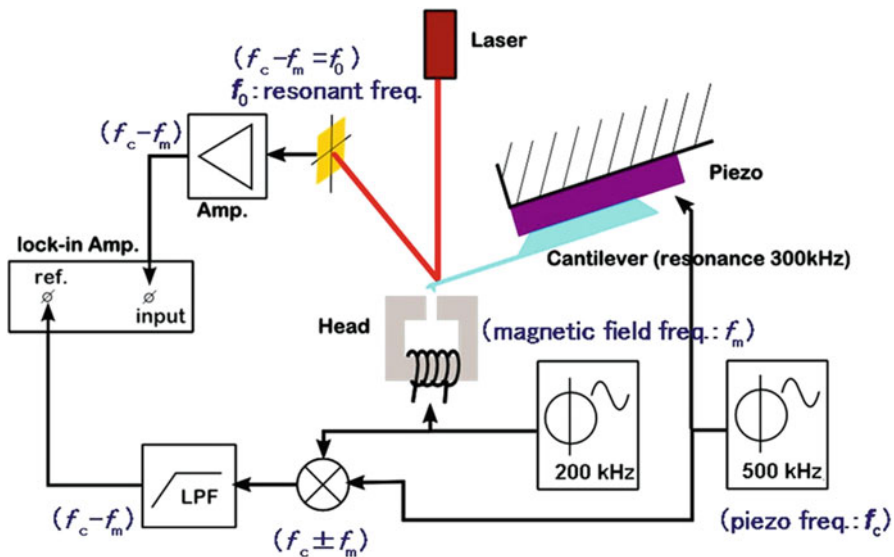


Fig. 7.8 Schematic of magnetic force microscopy setup (adapted from [13])

MFM images can be taken at different lift heights by lifting the tip at a certain distance above the sample in the lift mode. The scan is taken four times on the same line; magnetic interactions are taken during the second pass, where the topographic effect is subtracted from the MFM contrast. Both static and dynamic detection modes can be used for operation, but mainly the dynamic mode is considered as it can detect poor signals as well as, therefore, offers more sensitivity. More details are available in [13].

Here, the cantilever is oscillated by a piezoelectric element at an oscillation frequency, f_c , while the alternating magnetic field (driving frequency f_m) from the sample's stray field periodically modulates the effective spring constant of the cantilever. The frequency-modulated signals ($f = f_c - f_m$) are auto-selected by the mechanically oscillated tip. The driving voltages of the piezo and the sample are processed by a multiplier and low-pass filter. The processed signal is used as a reference for lock-in amplifier. The total signals due to magnetic field gradients, such as amplitude and phase, in-phase, and out-of-phase signals, can be detected simultaneously by the lock-in technique. The oscillation frequency (f_c) of the piezoelectric element is higher than the resonant frequency (f_0) of the tip. Therefore, one can get the information about the sample's magnetic strength by detecting the phase shift in the signals. The tip used in MFM mode is single-crystal Si coated with alloy of Co-Cr. The strength of the local magnetostatic interaction determines the vertical motion of the tip as it scans across the sample. The tip is magnetized every time before taking the measurements in the direction perpendicular to the plane of the film using a small permanent magnet to keep the directions of the spins same in the tip. Simultaneously, we obtained the topographic as well as magnetic images of the sample on the same spot locally. One can scan the samples at multiple points to get overall information about the sample's magnetic behavior [14–18].

7.1.2.5 Working Modes of MFM

The information about the sample's magnetic stray field can only be derived from MFM images when topographic signal contributions are not included. This is especially important when the tip is brought very close to the sample (in order to improve resolution), since nonmagnetic forces become increasingly stronger. The solution to this problem is to keep the topography influence constant by letting the tip follow the surface height profile [19]. This constant distance mode places higher demands on instrument stability, because it is sensitive to drift.

Therefore, one uses the specific method employed to separate signal contributions which is called lift mode (Fig. 7.9). It involves measuring the topography on each scan line in a first scan (left diagram), and the magnetic information in a second scan of the same line (right diagram).

The difference in height ∂h between the two scans is the lift height; it is selected by the user. Topography is measured in dynamic AM mode and the data is recorded to one image. This height data is also used to move the tip at a constant local distance above the surface during the second (magnetic) scan line, during which the feedback

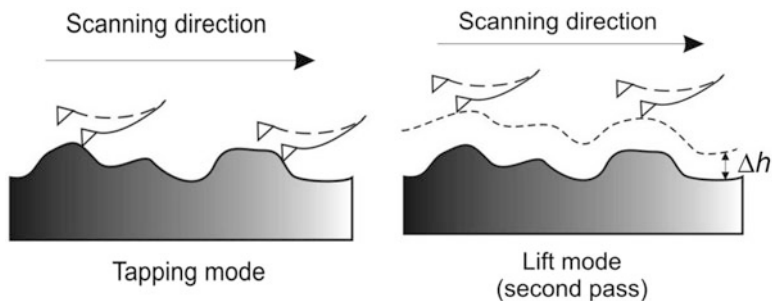


Fig. 7.9 Scanning the sample using lift mode in MFM. Magnetic information is recorded during the second pass in lift mode (adapted from [14])

is turned off. In theory, topographic contributions should be eliminated in the second image. Magnetic data can be recorded either as variations in amplitude, frequency, or phase of the cantilever oscillation. Therefore, MFM allows the imaging of relatively weak but long-range magnetic interactions. This measurement is unique as it gives us the idea about the localized magnetic domains within the magnetic films which no other technique can provide. All other techniques are used to detect magnetic strength of the films in bulk level or overall system. Especially, in the case of ion irradiation experiments, we get help to know how the ions have changed the magnetization locally as the ion beam is falling statistically onto the samples.

7.2 Applications

In the last few decades, extensive research has been done by our group to understand diversifying phenomena of the various materials using scanning probe microscopes in various modes such as STM, MFM, tapping AFM, IV spectroscopy in C-AFM, F-D curves using contact AFM, and many more [20–24]. In the next section, we are highlighting some of the important results.

7.2.1 AFM and MFM Studies on Co Nanoparticles

7.2.1.1 For Pristine Films

Thin films of Co with thickness ~ 4 nm have been deposited on Si using thermal evaporation technique. The films were further irradiated with 120 MeV Ag ions at various ion fluences. Here, we are discussing only the example of the sample irradiated with a fluence of 1×10^{14} ions/cm². We have characterized the sample with Co-Cr-coated Si crystal tip in tapping mode. Upon scanning the pristine film of

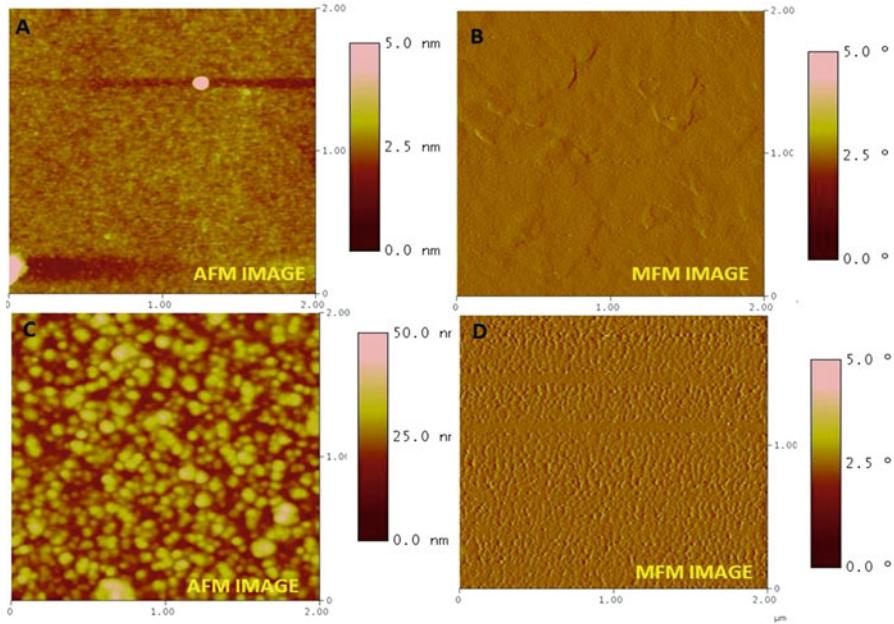


Fig. 7.10 AFM micrographs of pristine (a) and irradiated (c) thin-film (4 nm) samples of Co. MFM micrographs of pristine (b) and irradiated (d) thin-film (4 nm) samples of Co taken at a lift height of 50 nm

4 nm in MFM/lift mode, we could observe the smooth film with roughness 0.42 nm (given in Fig. 7.10a). Figure 7.10 is showing the AFM (a) and MFM (b) (topographic and the phase images, respectively) of the pristine sample at a lift height 50 nm.

In contrast to the AFM images, the MFM image shows good phase contrasts; the right side MFM/phase image shows the formation of domain/Bloch walls in the thin films, suggesting the magnetic nature of the cobalt is retained even after depositing in the form of a thinner layer of ~ 4 nm. Although there is no magnetic cluster of particle formation, the overall film is magnetic in nature (Fig. 7.10b) with no preferred orientation or alignment. The domain walls can be seen with dark and bright contrast which is due to magnetic spin interaction of the sample and the tip. Bright reflects the alignment of the spins in the same direction (upward), and dark represents in opposite (downward). The intermediate or mean color contrast is due to the cancelation of spin up and down interaction between sample and the tip.

Apart from looking at the topography of the films, one can determine the size, height, and shape of the features too. Similarly we can find out the surface roughness of the films. Roughness is an important parameter for device applications and sensors. Figure 7.11 shows the sectional analysis of the pristine film with corresponding 3D view.

The AFM image shows a smoother film with smaller particle sizes ~ 39 nm, as represented by red cursor (as shown in Fig. 7.11a, horizontal distance). The

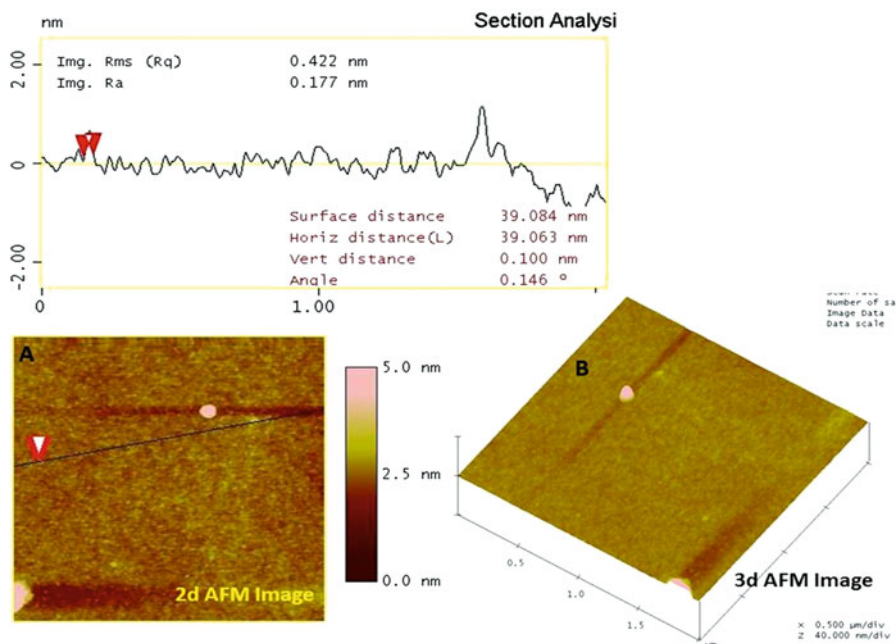


Fig. 7.11 (a) Section analysis of the pristine thin-film (~ 4 nm) samples of Co and (b) 3D view of the pristine sample

corresponding rms value of the image was found to be ~ 0.42 nm. Figure 7.11b represents a three-dimensional view of the pristine film to further confirm the formation of smoother films with not much height differences. Studies on Co thin-film samples after irradiation are given in the next section.

7.2.1.2 For Irradiated Films

The 4 nm thin-film sample of Co was irradiated with Ag 120 MeV swift heavy ions (SHI). The purpose of the irradiation was to form Co nanoparticles with uniform size distribution due to the impact of SHI with energy 120 MeV. The AFM and MFM images of the irradiated thin-film samples are shown in Fig. 7.10c, d, respectively. As can be observed, the irradiated films show granular morphology. However, this is only applicable for sample irradiated at 1×10^{14} ions/cm² in terms of uniformity of the structure sizes. The right panel (of Fig. 7.10d) shows that phase contrast is uniformly visible with no particular orientation. This is due to the fact that the irradiation dispersed Co grains with uniform magnetization on the surface.

Figure 7.12 shows the sectional analysis (a) of the irradiated film with corresponding 3D view (b). The AFM image shows a smoother film with smaller particle

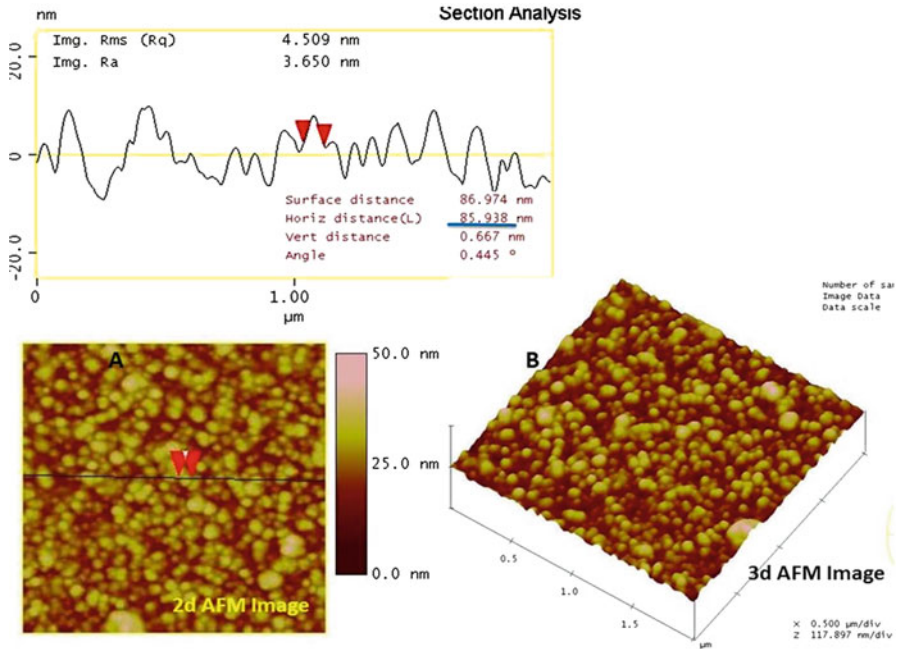


Fig. 7.12 (a) Section analysis of the irradiated thin-film (4 nm) samples of Co and (b) three-dimensional view of the irradiated sample

sizes ~ 85.9 nm, as represented by red cursor (as shown in Fig. 7.12a, horizontal distance).

The corresponding rms roughness value of the image was found to be ~ 3.7 nm. Figure 7.12b represents a 3D view of the irradiated film to further confirm the formation of uniform grains or nanoparticles with increased surface roughness. Further, in Fig. 7.11, we tried to find out the strength of magnetization in the pristine and irradiated thin-film samples through phase shift using section analysis. Figure 7.13a shows the phase shift due to magnetization as 0.53° , given by the peak-to-peak distance in vertical direction in the phase image captured in lift/MFM mode. The strength of magnetization has increased to 0.99° in the irradiated film as shown in Fig. 7.13b. This indicates that irradiation has resulted further into uniform Co nanoparticles formation; moreover, the magnetization has increased due to the effect of ion irradiation.

From the above study, one can say that due to irradiation the uniformly deposited thin film has resulted into well-ordered granular film of Co with an average size of ~ 90 nm. The magnetic strength of the film has increased upon irradiation. The granular film obtained after irradiation is uniform with uniform magnetization. In general, AFM and MFM provide a good morphological and phase contrast to the magnetic clusters.

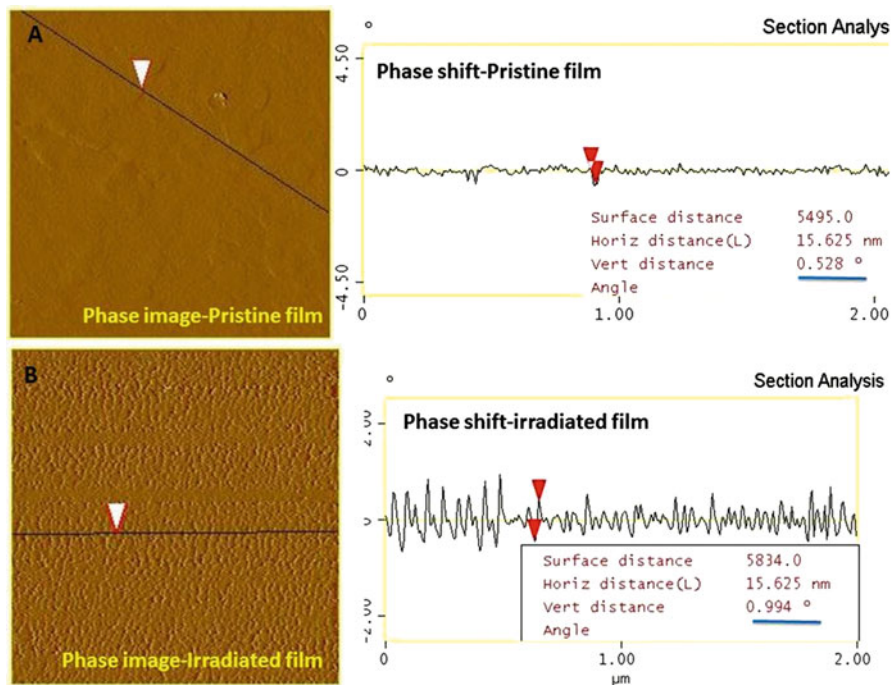


Fig. 7.13 Section analysis of MFM micrographs of pristine and irradiated Co 4 nm thin film

7.2.2 More Interesting Results Obtained from SPM in Various Modes

For more than a decade now, we have been using a multimode SPM with nanoscope IIIa controller acquired from Digital/Veeco Instruments Inc. (now Bruker, Singapore) installed at Inter University Accelerator Centre, New Delhi, in the following modes of operation in the user experiments: contact/tapping AFM, STM, MFM, and C-AFM. The areas of research include ion-induced surface morphology, SHI-induced modification in the size distribution, SHI-induced modification in magnetic domains, SHI-induced plastic flow of materials, and characterization of ion tracks in terms of size and number density. This system is actively being used by almost 70 institutes across India. Four of the illustrative images are taken in lift (tapping) mode MFM (Fig. 7.14), contact mode AFM (Fig. 7.15) tapping mode AFM (Fig. 7.16), and conducting mode (C-AFM) mode (Fig. 7.17). Tapping mode AFM for biological samples (Fig. 7.18) is given in the next section.

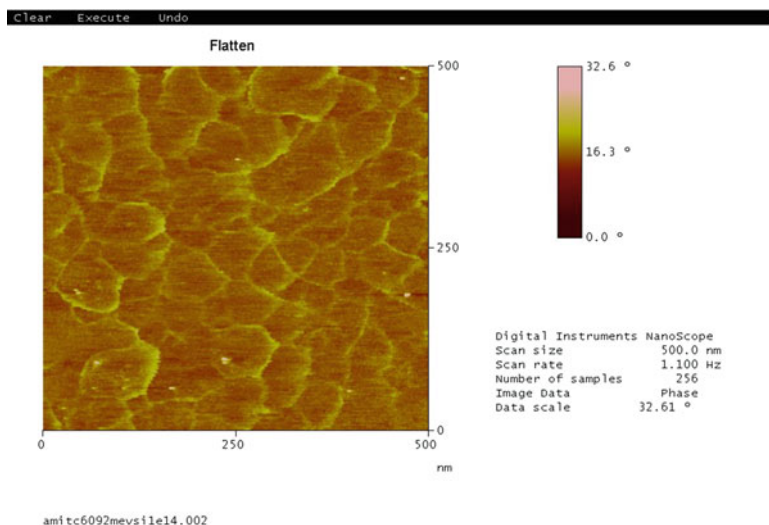
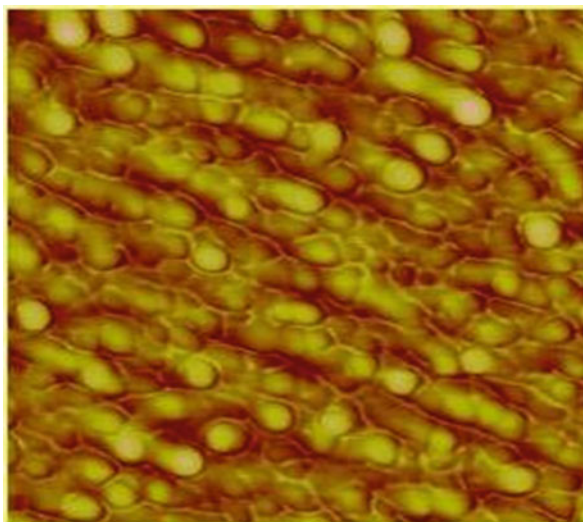


Fig. 7.14 Magnetic domains in fullerene films using MFM

Fig. 7.15 1.5 keV Ar beam-induced ripple formation on InP surface using contact mode AFM



7.2.2.1 Magnetic Force Microscope

MFM image shows the phase contrast between the grain boundaries due to the influence of magnetic force (see Fig. 7.14). The image is taken at the lift mode where the van der Waals force (2–10 nm) diminishes and magnetic forces are active at a height (>10 nm). The sample was C-60 film and irradiated at 90 MeV Si ions at a fluence of 1×10^{14} ions/cm². Here, we would like to mention that the as-deposited film was not showing any magnetic signal. Due to irradiation some

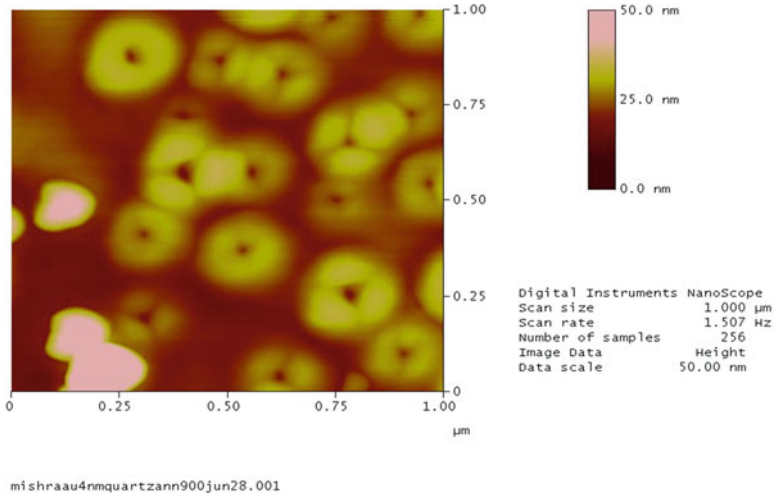


Fig. 7.16 Nanoring formations in Au thin films after annealing at 900 °C

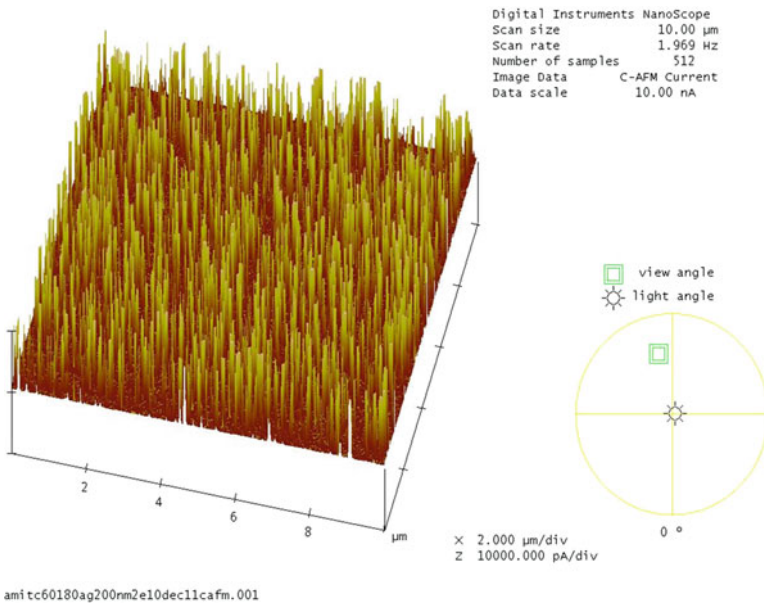


Fig. 7.17 Conducting tracks in fullerene films by conducting AFM (C-AFM)

unpaired electrons have been generated at the grain boundaries and hence giving magnetic contrast. The track diameter was around 50 nm. This is a clear example of swift heavy ion (SHI)-induced magnetization of nonmagnetic film [17].

7.2.2.2 Contact Mode AFM

The AFM image performed in contact mode shows clearly the formation of ripple (Fig. 7.15). The sample was InP(100) substrate and bombarded with 1.5 keV Ar atoms. Due to high nuclear energy loss (S_n), it leads to displacement of atoms from their sites through collision cascades, and as the range of these atoms at this energy is about 40 nm so it will create modifications just below the surface and rippling is observed. The basics of ion-matter interaction can be read elsewhere. The main mechanism involved in such kind of pattern formation on the surface of any material is the interplay between the ion-induced sputtering or roughening and diffusion-induced smoothing of the surfaces.

Figure 7.16 is showing an example of nanoring formation in gold films, of thickness 4 nm deposited on quartz in UHV chamber at a base pressure of 10^{-8} Torr, obtained using the AFM image taken in tapping mode. The films were then annealed at 900 °C in Ar atmosphere. Interestingly, the films have shown the formation of nanorings. It was observed that at lower annealing temperatures, Au has agglomerated into clusters, whereas at 900 °C, three of such clusters have come together to form the ring (Fig. 7.16).

The above example shows that not only imaging but one can get the idea about how the agglomeration happen in certain kind of films (especially metallic films). These nanorings are formed to minimize the surface energies. Further annealing at higher temperatures may damage the ring formation.

7.2.2.3 Conducting Atomic Force Microscopy (C-AFM)

C-AFM image for C-60 film irradiated at 180 MeV Ag ions at 2×10^{10} ions/cm² showing the formation of ion tracks (see Fig. 7.17). Conducting ion tracks (~ 50 nm in diameter) were formed in the films due to the passage of the ions through it. In C-AFM, we apply the bias to the sample, and the conducting path is obtained as we increase the bias voltage.

The above figure is not the topography image but is the current image [17]. The three-dimensional view gives the idea about how much conducting the sample is in particular regions where the track formation has happened due to ion irradiation.

One can say that SPMs have been used on almost all kind of samples and in different modes to fulfill the user requirements as per need [20–24]. Conventional AFM can be routinely utilized to observe the topological features as well as to analyze the surface roughness to fabricate good device for reflectivity estimation, sensing, etc. On the other hand, MFM can be very useful to study the magnetic domains of the magnetic thin films. C-AFM is another important tool which helps to determine the local conductivity of the samples and is very important in the field of ion irradiation experiments as the ion falls statistically onto the samples and locally modifies the surface conductivity. Moreover there are fluid cells available as an attachment which helps us to study the live cell under AFM to determine the elasticity, etc. of the cell membrane.

7.2.2.4 Application in Imaging of Biological Samples

The atomic force microscope is an important tool to explore the area of imaging in biomolecules. Modifications and improvements to the atomic force microscope in the past two decades have enabled the observation of biological samples from large structures, such as hair and whole cells, down to individual molecules of nucleic acids and proteins with submolecular resolution as shown by Chang et al. [25] and Ushiki et al. [26]. The AFM image shown in Fig. 7.18 reveals the image of the human chromosomes.

The images of the chromosomes were obtained by AFM and SEM techniques and are compared here. The height of the specimens in the AFM image is displayed as color gradations. The AFM image corresponds well to the SEM image but has the advantage in giving height information of non-coated samples unlike as in scanning electron microscopy. Generally, AFM is considered to be a superior tool to explore these biomolecules as mostly they are in the order of few microns in length scales. Moreover, AFM has the unique ability to measure molecular forces with high sensitivity. These applications have been exploited to reveal structural details and define the molecular forces involved in a variety of biological systems.

Measurements of electrostatic characteristics are also among the emerging advances that can facilitate the analysis of biological and biomedical samples. The need for detailed imaging at the molecular level and for monitoring dynamic biological processes will continue. AFM is, therefore, likely to play an important and enduring role in biological and biomedical research. Nowadays, a large number of AFM applications in mammalian cell studies are related to cancer cells, while the mechanical properties of cancer cells have been measured by AFM and their use has been proposed for cancer cell identification.

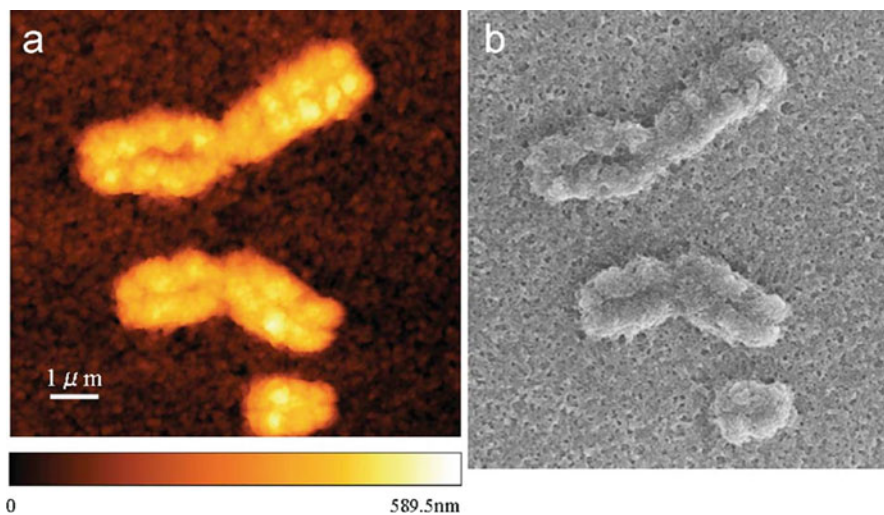


Fig. 7.18 (a) AFM and (b) SEM images of human metaphase chromosomes

7.3 Understanding the Surface Correlation for Co Nanoparticles

In this section, we will discuss how one can analyze the results obtained from AFM images using the correlation length, surface roughness, autocorrelation functions, and its importance to draw useful information for the samples using AFM images of Co thin-film samples.

Here, it is to be noted that the deposited thin films or ion-irradiated surfaces are not perfectly uniform. The surface height varies from point to point due to random elements in the growth process or after ion beam irradiation. Conventional statistical measures to characterize this height variation are measures of deviation like the mean deviation and the root mean square (rms) deviation. The mean deviation of the surface heights is called the average roughness, whereas the rms deviation is called the interface width. Interface width is the most important characteristic that describes the roughness of a surface.

However, interface width is not sufficient to describe the surface profile of a thin film because it does not provide any information about the observed correlation in surface heights. If the surface height is more than the average height at one point, it is very likely that the surface height in the neighborhood of the point is also more than the average height. Autocorrelation function, height-height correlation function, and lateral correlation length are used extensively to characterize these correlation properties. In recent times fluctuations in surface heights have been shown to exhibit self-affinity properties which are best characterized by techniques that have been developed for exploration of fractal objects. In this section, we introduce a set of useful statistical functions and techniques that have been used extensively in the literature to characterize the abovementioned properties of height fluctuations in thin film or ion-irradiated surfaces.

7.3.1 Surface Roughness

The root mean square value of the surface height, also known as interface width (w), and average roughness (R_a) of the surface are important parameters in quantitatively analyzing the characteristics of the surface morphology of thin films. Experimentally, the surface height is measured over a discrete lattice. From this discrete data, the interface width is computed as

$$w = \frac{1}{N} \sqrt{\sum_{i=1}^N \sum_{j=1}^N [h(i, j) - \langle h(i, j) \rangle]^2} \quad (7.1)$$

whereas the average roughness R_a of the surface is computed as

$$R_a = \frac{1}{N^2} \sum_{i=1}^N \sum_{j=1}^N |h(i, j) - \langle h(i, j) \rangle| \quad (7.2)$$

where $h(i, j)$ denotes height of the surface measured using the AFM at the point (i, j) and $\langle h(i, j) \rangle$ is their overall average over a total number of $N \times N$ points, which is given by

$$\langle h(i, j) \rangle = \frac{1}{N^2} \sum_{i=1}^N \sum_{j=1}^N h(i, j) \quad (7.3)$$

7.3.2 Correlation Functions

Average roughness and interface width characterize global roughness of a surface [27–29]. They do not characterize surface correlation, which is an important characteristic of the surface. Since correlation functions relate height fluctuations at different points, in defining correlation functions, it is very common to redefine the surface height profile such that $\langle h(i, j) \rangle = 0$ by choosing a suitable reference height. Unless otherwise stated, the mean height is taken to be zero at all times by replacing $h(i, j)$ with $(h(i, j) - \langle h(i, j) \rangle)$.

7.3.2.1 Autocorrelation Function

Autocorrelation function is very frequently used to characterize correlation properties. The one-dimensional autocorrelation function along the fast-scan direction x is usually evaluated from the height profiles $h(i, j)$ as

$$A(r = md) = \frac{1}{N(N-m)w^2} \sum_{j=1}^N \sum_{i=1}^{N-m} h(i+m, j) h(i, j) \quad (7.4)$$

where d is the horizontal distance between two adjacent pixels.

From Eqs. (7.1) and (7.3), it follows that $A(0) = 1$. Also we expect that the correlation decreases as r increases and becomes negligible for sufficiently large r . For thin-film surfaces, the autocorrelation function $A(r)$ is often found to have an exponentially decreasing behavior, and it approaches zero for large r . The value of r at which $A(r)$ decreases to $1/e$ is known as the lateral correlation length ξ . Thus,

$$A(\xi) \cong \frac{1}{e} \quad (7.5)$$

Therefore, the lateral correlation length ξ is defined as the length beyond which the surface heights are not significantly correlated.

7.3.2.2 Exponential Correlation Model

Several analytic expressions have been proposed for the autocorrelation function. A particularly simple form as

$$A(r) = \exp \left[- \left(\frac{r}{\xi} \right)^{2\alpha} \right] \quad (7.6)$$

where α is called the roughness exponent. The exponential correlation model (Eq. 7.6) does not work for $\alpha \rightarrow 0$ because the autocorrelation function becomes constant at $\alpha = 0$.

7.3.2.3 Height-Height Correlation Function

Another function used for characterizing correlation is the height-height correlation function H , which is calculated along the fast-scan direction x as

$$H(r) = \frac{1}{N(N-m)} \sum_{j=1}^N \sum_{i=1}^{N-m} [h(i+m, j) - h(i, j)]^2 \quad (7.7)$$

This function is especially useful for characterizing self-affine surfaces.

The relationship between the height-height correlation function and the autocorrelation function can be derived as follows:

$$\begin{aligned} H(r) &= \langle [h(i+m, j) - h(i, j)]^2 \rangle \\ &= \langle [h(i+m, j)]^2 \rangle + \langle [h(i, j)]^2 \rangle - 2 \langle h(i+m, j) h(i, j) \rangle \\ &= w^2 + w^2 - 2(w^2 A(r)) \\ &= 2w^2 - 2w^2 A(r) \\ &= 2w^2 [1 - A(r)] \end{aligned} \quad (7.8)$$

Using Eq. (7.5), we have

$$H(\xi) = 2w^2 (1 - 1/e) \quad (7.9)$$

In other words, we can say that the value of r at which $H(r)$ increases to $(1 - 1/e)$ is identified as the lateral correlation length ξ .

For surfaces which are self-affine on a short scale and for which the autocorrelation function vanishes for large separation, the height-height correlation function

$H(r)$ takes the scaling form

$$H(r) = \begin{cases} 2w^2, & \text{for } r \gg \xi \\ r^{2\alpha}, & \text{for } r \ll \xi \end{cases} \quad (7.10)$$

For the exponential correlation model [30],

$$H(r) = 2w^2 \left[1 - \exp\left(-\left(\frac{r}{\xi}\right)^{2\alpha}\right) \right] \quad (7.11)$$

This form is consistent with Eq. (7.10), because for $r \ll \xi$,

$$H(r) \approx 2w^2 \left[1 - \left(1 - \left(\frac{r}{\xi}\right)^{2\alpha} \right) \right] \approx 2w^2 \frac{r^{2\alpha}}{\xi^{2\alpha}} \sim r^{2\alpha} \quad (7.12)$$

and for $r \gg \xi$, it gives

$$H(r) \approx 2w^2 \quad (7.13)$$

For example, Fig. 7.10a, c shows AFM images of pristine and ion-irradiated thin films deposited for 4-nm-thick Co layer onto Si substrates by electron beam evaporation method at room temperature. The granules of various scales are present in the films, which have irregular shapes, different sizes, and separations. In quantitative analyses, the height roughness (R_a) and interface width (w) have been employed to describe the surface morphology. Here R_a is defined as the mean value of surface height relative to the center plane, and w is the root mean square (rms) value of the surface height. The roughness (R_a and w) is calculated using the method described in Sect. 5.2. The computed values for R_a and w are 0.7527 and 3.7341 nm and 1.0059 and 4.6570 nm corresponding to pristine and ion-irradiated surface, respectively. It is found that these values are increased with ion irradiation. The roughness parameters based on conventional theories depend on the sampling interval of measuring instrument. These parameters do not provide the complete outline like the shape of peaks and valleys of the thin-film surfaces. Average roughness (R_a) and interface width (w) are global measures of roughness but fail to describe the short-range variation of the surface roughness. These parameters are only sensitive to the peak values of surface profile. But, these parameters do not give information about irregularity/complexity of a surface.

The normalized autocorrelation function is computed to investigate the self-affine nature of thin-film surfaces applying the method described by Eq. (7.4). Figure 7.19 shows $A(r)$ versus r plot for pristine and ion-irradiated film. The $A(r)$ shows exponentially decreasing behavior of the surface which confirms that the surface under investigation has self-affine nature. The value of r at which $A(r)$ decreases to $1/e$ is known as the lateral correlation length ξ . We find that for pristine thin film, $A(r)$ do not decrease to $1/e$, while after irradiation it drops $1/e$ as depicted in Fig.

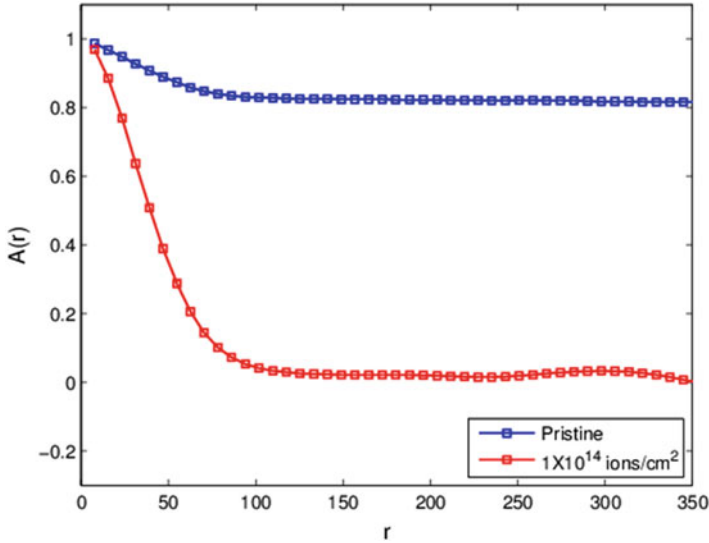


Fig. 7.19 Autocorrelation function for pristine and ion-irradiated 4 nm Co thin-film surfaces

7.19. The value of ξ for ion-irradiated Co thin-film surface is computed 48.6680 nm as shown in Fig. 7.20. It is found that the best-fit curve used to represent $A(r)$ for an isotropic self-affine surface may be written by Eq. (7.6). e provides vertical as well as lateral information about the surfaces. Here, ξ is the measure of length beyond the surface heights which are not significantly correlated.

The height-height correlation function $H(r)$ gives the same information as autocorrelation function $A(r)$. It is straightforward to show that the $H(r)$ and $A(r)$ are related by Eq. (7.8). The two clearly distinct regions are observed in $\log H(r)$ versus $\log r$, which marks the transition between power-law regime and the saturation regime. The turning point determines the value of ξ . Surface heights at points separated by a distance much larger than the lateral correlation length can be considered uncorrelated. Surface heights often exhibit self-affinity properties. The saturation value of $H(r)$, i.e., the value of $H(r)$ at which it forms a plateau, is very close to the value of $2w^2$ corresponding to that thin film as depicted in Fig. 7.21. The roughness exponent (α) is determined from a fit to the linear portion of the log-log plot of $H(r)$ versus r . The lateral correlation length ξ marks the transition between power-law region and the saturation region. Surface heights at points separated by a distance much larger than the lateral correlation length can be considered uncorrelated. Surface heights often exhibit self-affinity properties. For thin-film surfaces, self-affinity holds only for small r . Therefore, α characterizes only the short-range roughness of the surface. The roughness exponent α signifies the height fluctuation which corresponds to vertical growth of the thin film [31].

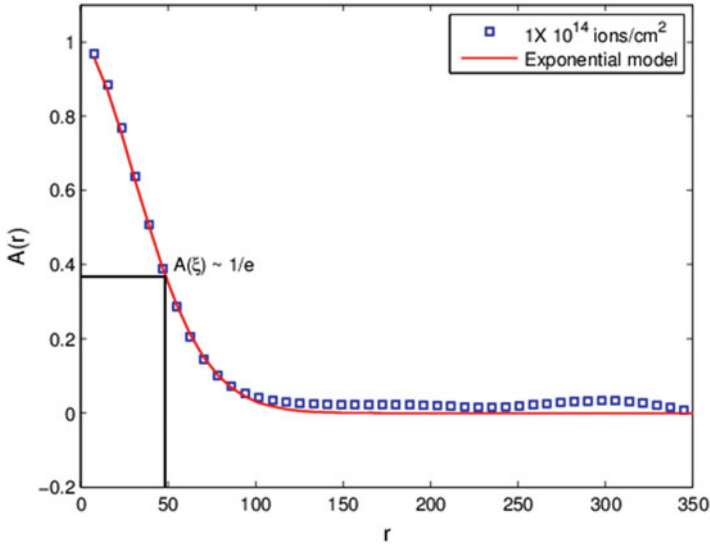


Fig. 7.20 Autocorrelation function A versus r

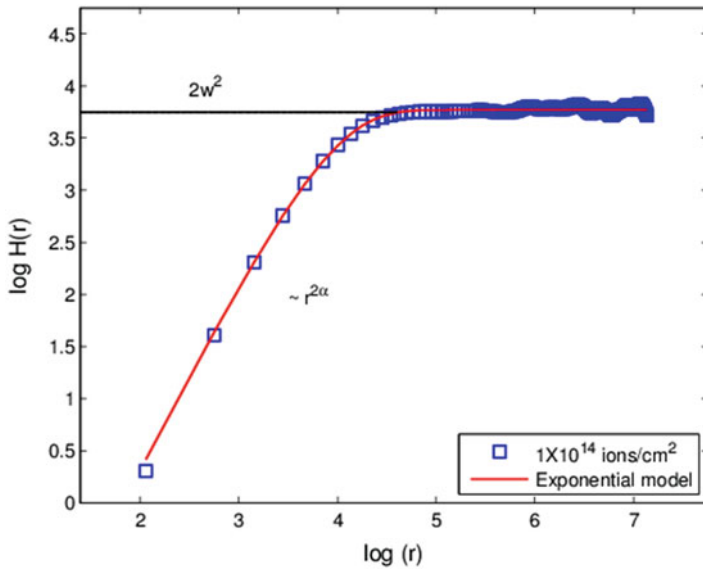


Fig. 7.21 $\log H$ as a function of $\log r$ for each thickness. The solid lines are best-fit curves

7.4 Conclusion

It is concluded that the invention of AFM is indeed a boon to the researchers worldwide, to determine the surface topography of the variety of samples such as polymers, magnetic films, metals, glasses, semiconductors, and biological samples such as the walls of cells and bacteria, etc. It has become one of the most important tools for imaging the surfaces of samples at nanometric-scale resolution. Thus, it is considered to be a strong competitor to conventional methods, which are used to obtain the morphology of the samples and to investigate the structures, such as in electron microscopy, X-ray scattering, etc. Unlike STM or scanning electron microscopy, it does not require a conductive sample. However, limitations in achieving atomic resolution arise due to the use of physical probe which may not be ideally sharp. As a consequence, an AFM image does not reflect the true sample topography, but rather represents the interaction of the probe with the sample surface. Further, with MFM we came to know that the information about the sample's magnetic stray field can only be derived from MFM images when topographic signal contributions are not included. This is especially important when the tip is brought very close to the sample. Therefore, MFM allows the imaging of relatively weak but long-range magnetic interactions. This measurement is unique as it gives us the idea about the localized magnetic domains within the magnetic films which no other technique can provide. All other techniques are used to detect magnetic strength of the films in bulk level or overall system. Further, we understood that using the correlation lengths of the surface features, one can find out if the structures are self-affine or not. For thin-film surfaces, self-affinity holds only for small distances, r . Therefore, roughness exponent, α , characterizes only the short-range roughness of the surface; α signifies the height fluctuation which corresponds to vertical growth of the thin film.

References

1. Giessibl, F. J. (2003). Advances in atomic force microscopy. *Reviews of Modern Physics*, 75, 949.
2. Julian Chen, C. (2007). *Introduction to scanning tunneling microscopy* (2nd edn). Oxford University Press. Oxford Scholarship Online
3. Wiesendanger, R. (1994). *Scanning probe microscopy and spectroscopy: Methods and applications*. Cambridge, UK: Cambridge University Press.
4. *Scanning tunneling microscopy. Perspectives in condensed matter physics (a critical reprint series)* (Vol. 6). Dordrecht: Springer.
5. Binning G, Rohrer H. (1986) *Scanning Tunneling Microscopy*, *IBM Journal of Research and Development* 30(4), 355–369.
6. <http://www.chembiouoguelph.ca/educmat/chm729/afm/detail.htm#tapping>.
7. <http://en.wikipedia.org/wiki/Atomic-force-microscopy>.
8. A. Yacoot and L. Koenders (2008), Aspects of scanning force microscope probes and their effects on dimensional measurement, *J. Phys. D: Appl. Phys.*, 41, 103001.

9. <https://www.techbriefs.com/component/content/article/tb/supplements/pit/applications/27833>.
10. <http://www.nanoscience.gatech.edu/zwang/research/afm.html>.
11. <http://ipc.iisc.ernet.in/~ipcafms/about%20us.html>.
12. New, R., Martin, Y., & Wickramasinghe H. K. (1987). Magnetic imaging by “force microscopy” with 1000 Angstrom resolution. *Applied Physics Letters*, 50, 1455(1987). <https://doi.org/10.1063/1.97800 Y>.
13. Zhenghua, L., Xiang, L., Dong, D., Dongping, L., Saito, H., & Ishio, S. (2014). AC driven magnetic domain quantification with 5 nm resolution *Scientific Reports*, 4, 5594.
14. Gomez, R. D., et al. (1998). Quantification of magnetic force microscopy images using combined electrostatic and magnetostatic imaging *Journal of Applied Physics*, 83, 6226.
15. Gomez, R. D., et al. (1996). Switching characteristics of submicron cobalt islands *Journal of Applied Physics*, 80(1), 342.
16. Landis, S., et al. (1999). Domain structure of magnetic layers deposited on patterned silicon *Applied Physics Letters*, 75, 2473.
17. Kumar, A., Avasthi, D. K., Pivin, J. C., Papaléo, R. M., Tripathi, A., Singh, F., & Sulania, I. (2007). Magnetic Force Microscopy of Nano-Size Magnetic Domain Ordering in Heavy Ion Irradiated Fullerene Films *Journal of Nanoscience and Nanotechnology*, 7(6), 2201.
18. Hartmann, U. (1999). MAGNETIC FORCE MICROSCOPY *Annual Review of Materials Research*, 29, 53–87.
19. Porthun, S., Abelmann, L., & Lodder, C. (1998). Magnetic force microscopy of thin film media for high density magnetic recording *Journal Magnetism Magnetic Materials*, 182, 238–273.
20. Sulania, I., Agarwal, D. C., Kumar, M., Kumar, S., & Kumar, P. (2016). Topography evolution of 500 keV Ar⁴⁺ ion beam irradiated InP(100) surfaces - formation of self-organized In-rich nano-dots and scaling laws *Physical Chemistry Chemical Physics*, 18(30), 20363–20370.
21. Sulania, I., Agarwal, D., Husain, M., & Avasthi, D. K. (2016). Investigations of ripple pattern formation on Germanium surfaces using 100-keV Ar⁺ ions *Nanoscale Research Letters*, 10(88), 1–8.
22. Sulania, I., Agarwal, D., Kumar, M., & Avasthi, M. (2013). Low energy bombardment induced formation of Ge nanoparticles *Advanced Materials Letters*, 4(6), 402.
23. Sulania, I., Tripathi, A., Kabiraj, D., Varma, S., & Avasthi, D. K. (2008). keV Ion-Induced Effective Surface Modifications on InP *Journal Nanoscience Nanotechnology*, 8(8), 4163–4167.
24. Mishra, Y. K., Kabiraj, D., Sulania, I., Pivin, J. C., & Avasthi, D. K. (2007). Synthesis and Characterization of Gold Nanorings *Journal Nanoscience Nanotechnology*, 7(6), 1878–1881.
25. Chang, K.-C., Chiang, Y.-W., Yang, C.-H., Liou, J.-W., & Chi, T. (2012). Atomic force microscopy in biology and biomedicine. *Medical Journal*, 24, 162–169.
26. Ushiki, T., & Hoshi, O. (2008). Atomic force microscopy for imaging human metaphase chromosomes. *Chromosome Research*, 16, 383–396.
27. Yadav, R. P., Kumar, T., Mittal, A. K., Dwivedi, S., & Kanjilal, D. (2015). Fractal characterization of the silicon surfaces produced by ion beam irradiation of varying fluences *Applied Surface Science*, 347, 706–712.
28. Yadav, R. P., Dwivedi, S., Mittal, A. K., Kumar, M., & Pandey, A. C. (2012). Fractal and multifractal analysis of LiF thin film surface *Applied Surface Science*, 261, 547–553.
29. Yadav, R. P., Kumar, M., Mittal, A. K., & Pandey, A. C. (2015). Fractal and multifractal characteristics of swift heavy ion induced self-affine nanostructured BaF₂ thin film surfaces *Chaos*, 25, 083115.
30. Pelliccione, M., & Lu, T. M. (2008). *Evolution of thin film morphology: Modeling and simulations*. Berlin: Springer.
31. Yadav, R. P., Kumar, M., Mittal, A. K., Dwivedi, S., & Pandey, A. C. (2014). On the scaling law analysis of nanodimensional LiF thin film surfaces *Materials Letters*, 126, 123–125.

Chapter 8

Optical Spectroscopy and Its Applications in Inorganic Materials



Marcio Aurélio Pinheiro Almeida and Adeilton Pereira Maciel

8.1 Electromagnetic Spectrum

It is consensus that technology is closely related to electromagnetic spectrum understanding levels. The electromagnetic field results from magnetic and electric waves outspreading throughout the space at speed $c = 2.99792458 \times 10^8 \text{ m}\cdot\text{s}^{-1}$ and at different wavelengths. Such wavelengths can be very long (low frequency), such as the radio, infrared, and visible waves, and very short (high frequency) such as the X-ray and gamma rays. The gamma ray corresponds to a high energy of approximate 100 keV, which is equal to the atom size [1].

Almost all wavelengths are emitted by sunlight, approximately 44% of the emitted energy concentrates in the visible region (from 400 to 700 nm), followed by 37% of infrared radiation (>1500 nm). Ultraviolet radiation accounts for 7% of the wavelength, and other radiations such as microwaves, radio waves, X-rays, and gamma rays respond for the remaining 1%. Many daily life activities are based on the knowledge about electromagnetic radiation. Radio waves used in telecommunication systems, infrared in night vision and remote systems (TV, garage door), passing through visible radiation (sensible to the human eyes) until high energy radiation such as X-ray used in medicine and the gamma radiation employed in research, electromagnetic waves are used to develop new technologies (Fig. 8.1) [2].

The radiation-matter interaction is an object of study since the nineteenth century. Several ideas about electromagnetic radiation derive from warm body observations, the so-called blackbody effect, which was explained by Max Planck. He suggested that radiation frequency ν could only be generated if an oscillator at the same frequency has minimum energy enough to start oscillating, $E = h\nu$ [3]. Thus, he

M. A. P. Almeida (✉) · A. P. Maciel
Universidade Federal do Maranhão, São Luis, MA, Brazil

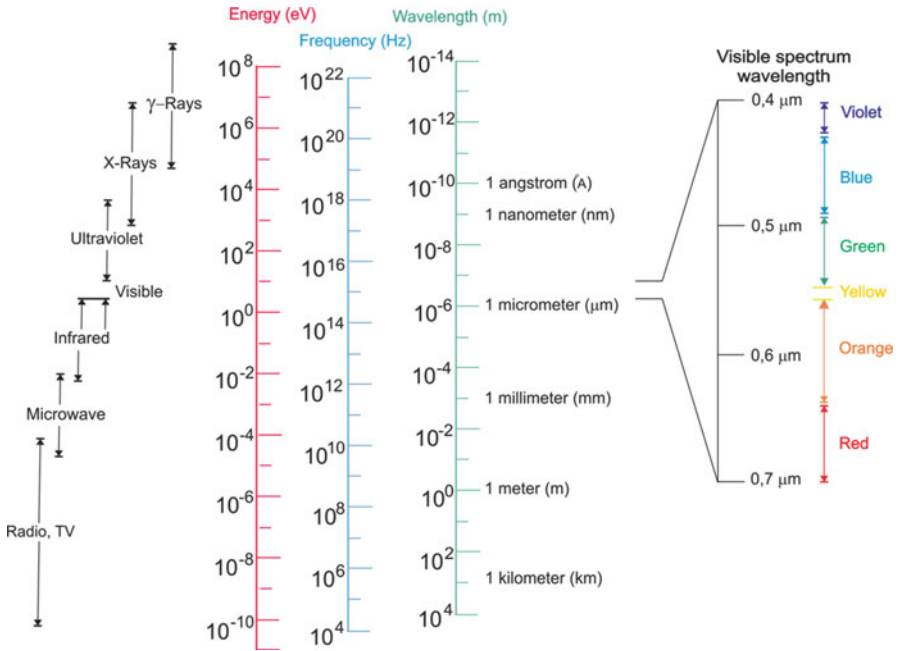


Fig. 8.1 The electromagnetic spectrum. Wavelengths in the spectrum range, from cosmic ray to the very long infrasonic wave. (Reproduced from William et al. [2] with permission)

established that maximum spectral radiance associated with spectral distribution could be emitted by a body in thermodynamic equilibrium at a specific temperature:

$$E = hv = \frac{hc}{\lambda}$$

wherein

c = light speed in vacuum ($2.99792458 \times 10^8 \text{ m.s}^{-1} \approx 3 \times 10^8 \text{ m/s}$)

h = Planck constant ($6.6262 \times 10^{-34} \text{ J.s}$)

λ = Wavelength (meters, m)

Therefore, the energy emitted by the blackbody depends on its temperature and wavelength:

$$\varnothing(\lambda, T) = \frac{a_1}{\lambda^5} \left[\exp \frac{a_2}{\lambda T} - 1 \right]^{-1}$$

wherein

$a_1 = 2\pi hc^2 \approx 3.75 \times 10^{-16} \text{ Jm}^2/\text{s}$

$a_2 = hc/k_B \approx 1.44 \times 10^{-2} \text{ mK}$

k_B is the Boltzmann constant $1.38 \times 10^{-23} \text{ J/K}$.

8.2 Optical Properties of Materials

Three basic phenomena can happen when radiation strikes a sample, namely, absorption, reflection, and transmission [4] (Fig. 8.2). Studies in this field are often performed at a wavelength range from 200 nm to approximately 3000 nm, which is known as the optical range.

The *absorption* process takes place when the incident radiation is absorbed and it leads the molecules to several electronic excitement states. Overall, a fraction of the absorbed radiation (I_e) is emitted at a frequency lower than the incident radiation, and other intensity fractions are lost through nonradioactive processes (heat). The *reflection* process happens when part of the incident radiation reflects (I_R) from the external and internal surfaces. Finally, *transmittance* occurs when part of the radiation passes through the material [1].

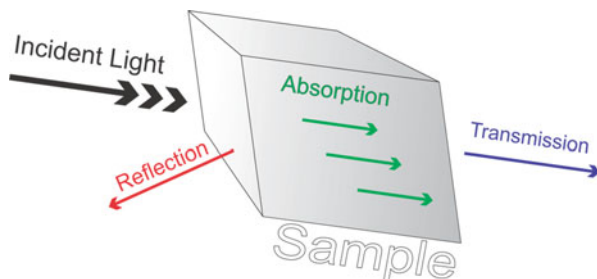
8.2.1 Absorption

When light crosses a medium (Fig. 8.2), part of this light is absorbed this medium. The quantitative measurements taken to find how much light was absorbed by the medium can be calculated through the absorption coefficient, α . Therefore, light intensity $I_{(z)}$ after crossing material thickness z , compared to the incident light, I_0 , can be described as:

$$I_{(z)} = I_0 e^{-\alpha \cdot z}$$

wherein I_0 is the optical intensity at $z = 0$, $I_{(z)}$ is the light intensity after crossing thickness z , and α is the absorption coefficient [5]. It is essential measuring the absorption coefficient to study the optical properties of materials and their application in different fields. Electronic transitions between the valence (VB) and the conduction bands (CB), which are known as direct and indirect transitions, can happen when radiation is absorbed by the medium. Moreover, the direct transition can be of the allowed and forbidden type [1, 6].

Fig. 8.2 Illustration of possible beams emerging from a solid sample illuminated with beam intensity I_0



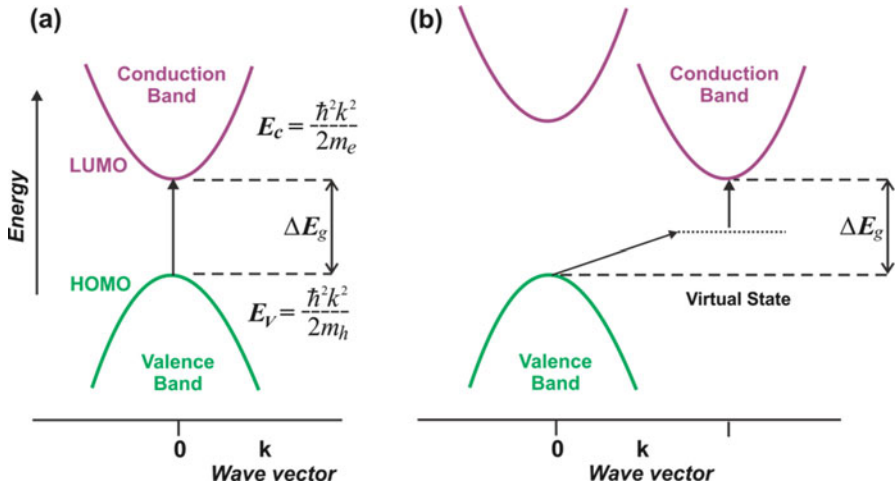


Fig. 8.3 (a) Direct transition from the valence band (VB) to the conduction band (CB) by means of photon absorption. (Reproduced from Kitai [7] with permission)

The photoexcitation process in direct transitions does not involve phonons and does not change the electron's \mathbf{k} -vector ($\mathbf{k} = 2\pi/\lambda$) (Fig. 8.3) [1]. Thus, the absorption coefficient of amorphous, polycrystalline, and crystalline materials can be described as:

$$\alpha_{AD} = C_{AD}(\hbar\omega - E_g)^{\frac{1}{2}}$$

This equation (above) is limited, since it is only valid for direct absorption, which allows electrical dipole. Those types of transitions take place between states of band edges of the Γ point with conservation (\mathbf{k} -vector) vertical transitions. There are cases wherein transition is allowed at $k \neq 0$ and forbidden at $k = 0$, which is called direct forbidden. Its absorption coefficient is expressed through $\alpha_{FD} = C_{FD}(\hbar\omega - E_g)^{\frac{3}{2}}$ [6] (Fig. 8.3).

Indirect transition, or indirect absorption, happens when the photoexcitation process involved phonons. Such transition forbids the electric dipole; absorption takes place at different \mathbf{k} values (from VB to CB). Thus, this absorption coefficient follows $\alpha_{AI} = (E - E_g \pm \hbar\omega_{ph})^2$, wherein $\hbar\omega_{ph}$ is the phonon energy [6].

8.2.2 Reflectance

Absorption studies are performed through the absorption coefficient (α); however, they can only be conducted in high-absorption samples (10^5 – 10^6 cm $^{-1}$) [8]. Such

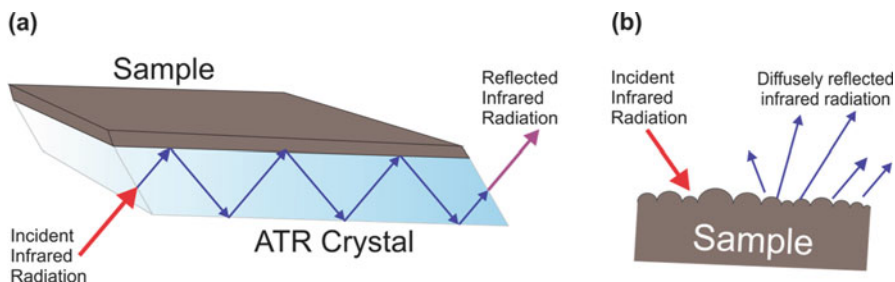


Fig. 8.4 (a) Attenuated total reflectance phenomenon (ATR) and (b) diffuse reflectance from a rough surface

high absorption is achieved in thin samples, in other words, in thin films. Reflectance can be advantageous to bulk sample studies, since it is the ratio between the reflected and the incident radiation.

There is the internal and the external reflectance [9]. The first one is represented by the attenuated total reflectance (ATR), in which an infrared radiation beam passes through of a crystal that is in contact with the sample (Fig. 8.4a). This technique demands the crystal to have higher refractive index than the sample. Deeper penetrations into the sample depend on several factors such as incident angle and the refractive index of the sample. On the other hand, the external reflectance can be subdivided in two categories, namely, specular and diffuse [10, 11].

The incident radiation in the specular reflectance focused onto the sample can be directly reflected by its smooth surface – similar to a mirror. This technique is a powerful tool to work with thin films, whereas the diffuse reflectance is the most commonly used technique in rough surfaces (Fig. 8.4b).

The Kubelka and Munk (1931) theory is a powerful tool for diffuse reflectance studies. It can be described through the equation below [12–15]:

$$F(R_{\infty}) = \frac{(1 - R_{\infty})^2}{2R_{\infty}} = \frac{K}{s}$$

wherein R_{∞} is the relative diffuse reflectance and K and s are the absorption and scattering coefficients of the sample, respectively. In theory, the Kubelka-Munk function can neglect the scattering coefficient since it slowly changes depending on the wavelength, $F(R_{\infty}) = K F(R_{\infty}) = K$. K is the absorption constant previously described as α and followed by the K - M function. It is also possible estimating the band gap values through the equation below [16–19]:

$$F(R_{\infty}) h\nu = C(h\nu - E_g)^{\frac{m}{2}}$$

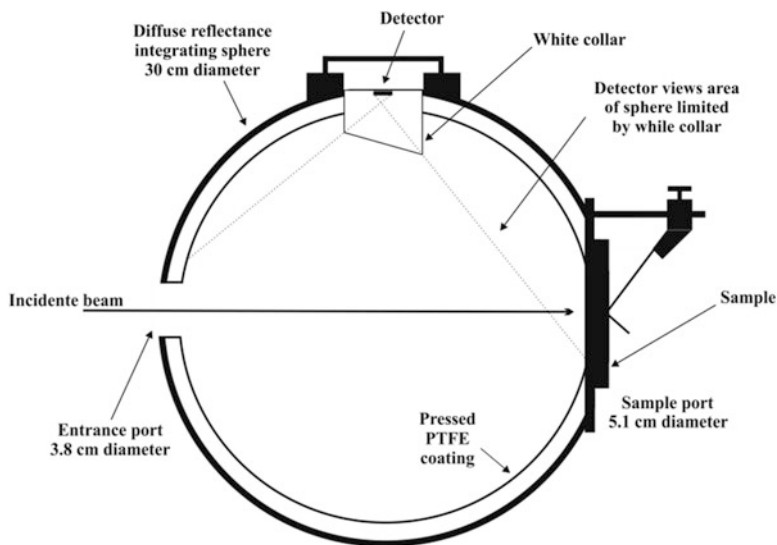


Fig. 8.5 Illustration of an integrating sphere. (Reproduced from Barnes et al. [10] with permission)

Thus, one can intercept the plot $(F(R_{\infty}).hv)^2$ versus hv to calculate the band gap for a direct allowed transition, whereas the indirect allowed transition $(F(R_{\infty}).hv)^{1/2}$ versus hv is found when the linear region is extrapolated to the zero ordinate.

8.2.2.1 Diffuse Reflectance Measurements

Diffuse reflectance measurements are taken in UV-vis spectrophotometers coupled to an accessory integrating sphere (Fig. 8.5), which is capable of collecting the reflected light flux. All the radiation reaches the detector in the integrating sphere after repeating reflections. Also known as Ulbricht sphere, the integrating sphere diameter is of approximately 50–250 mm; it is hollow and internally coated with a diffuse reflectance material close to 1 [11]. Magnesium oxide (MgO) is often used because its reflectance is approximately 0.98, although other materials such as barium sulfate and polytetrafluoroethylene (PTFE) are also used [20].

8.2.3 Transmittance

Measurements of light transmission through specific materials (solids, liquids, or gases) are essential to the design of new materials for optics.

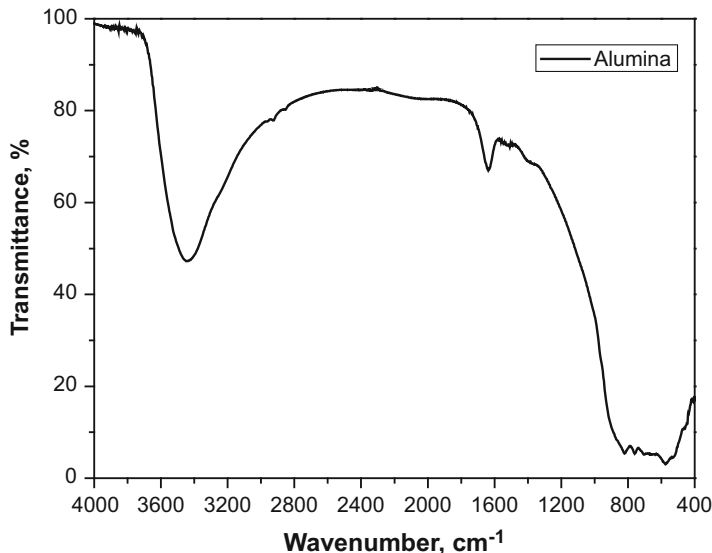


Fig. 8.6 Fourier transforms infrared of the alumina sample

Figure 8.6 shows the transmission phenomenon happening when the incident light, I_0 , leaves the sample through the opposite side, I_t . In this case, the sample transmittance can be calculated as $\tau = \frac{I_t}{I_0}$. Thus, sample transmittance is the simple ratio from the transmitted light to the incident light.

According to Palmer [21], sample transmittance can be usually carried out in commercial spectrophotometers.

Figure 8.6 displays a typical transmittance spectrum in the infrared region.

It shows the transmittance percentage, which is ($\% \tau$), calculated by multiplying the transmittance by 100:

$$\% \tau = \frac{I_t}{I_0} 100$$

thus, $0 \leq \% \tau \leq 100$.

Transmittance percentage is equal to 100% when all the incident light is transmitted, whereas it is equal to 0% when no light is transmitted. Transmittance can turn into absorbance, A , through logarithmic transformation. A is the common logarithm of τ^{-1} [22].

$$A = \log_{10} (\tau^{-1}) = \log_{10} \left(\frac{I_0}{I_t} \right)$$

Gottfries et al. [23] used vibrational spectrometry to assess the active substance in metoprolol tablets and found that sample transmittance was more efficient than

diffuse reflectance. They believe that “the main reason for such outcome lies on the fact that NIR spectrometry is very sensitive to material non-homogeneity in the reflectance mode, whereas such problem is less severe in the transmission mode. It happens due to the larger volume of material scanned in the transmission mode than in the diffuse reflectance.”

It is worth pointing out that sample transmittance can be geometrically classified according to the direction of the transmitted light [21]. There is specular transmittance, τ_{specular} , when the transmitted light leaves the sample in parallel to the incident light. All the light transmitted by the sample, except for that parallel to the incident light, represents the diffuse transmittance, τ_{diffuse} . The total transmittance, τ_{total} , is the sum of the specular and the diffuse transmittances:

$$\tau_{\text{total}} = \tau_{\text{specular}} + \tau_{\text{diffuse}}$$

Transmittance measurements are largely used to control the manufacture of optimum-quality materials for optics. Haze is a measurement used to determine sample transparency. Mathematically speaking, haze, H , can be calculated as:

$$H = \frac{\tau_{\text{diffuse}}}{\tau_{\text{total}}}$$

Haze is applied to samples presenting impurities or other structural disorders such as low crystallinity. Minimum haze values imply high-clarity samples [24].

8.3 Applications

Optical spectroscopy techniques are largely employed to characterize nanomaterials. They are powerful tools to the development of materials used in photovoltaic devices, in catalytic applications and in the manufacture of electronic devices.

8.3.1 Solar Cell Applications

Solar cells stand out among the mostly studied promising technologies in the world [25, 26]. Understanding the electronic process is crucial to develop better photovoltaic devices. Semiconductors with the potential to be used in the development of solar cells have the basic condition to provide strong visible-range absorption [27]. Thus, optical-absorption experimental measurements can be carried out in ultraviolet-visible spectrophotometers. Moreover, other measurements such as the transmittance and diffuse ones, which are also important to the construction of photovoltaic devices, can be taken in UV-vis spectrophotometers.

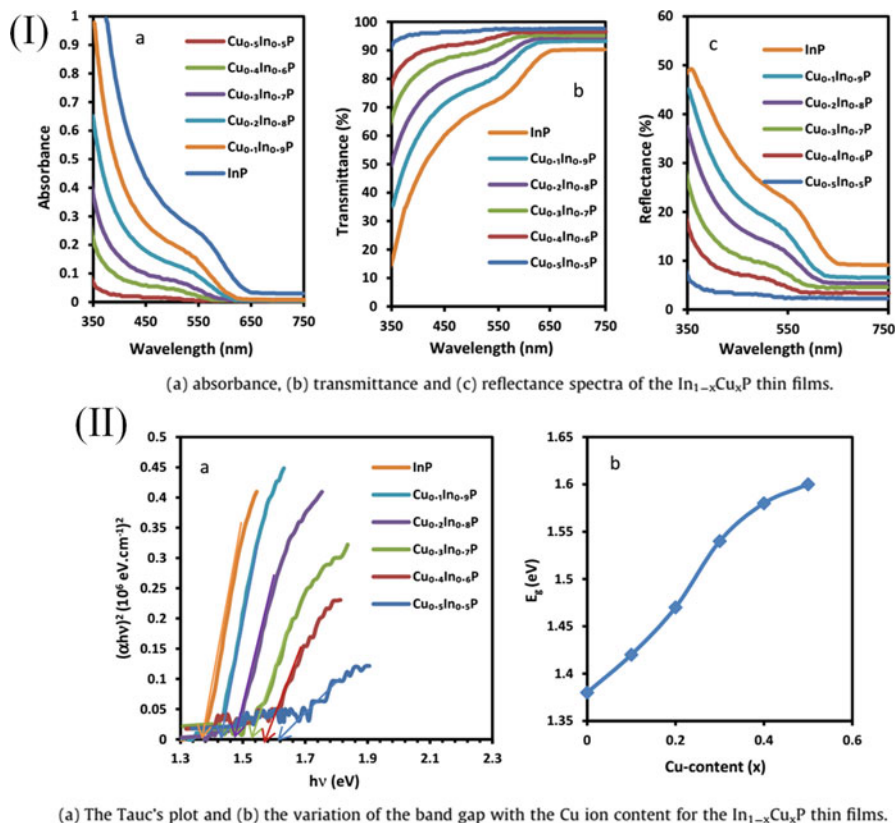


Fig. 8.7 (I) (a) Absorbance, (b) transmittance, and (c) reflectance spectra of $\text{In}_{1-x}\text{Cu}_x\text{P}$ thin films. (II) Tauc's plot and (b) band gap variation in the Cu ion content of $\text{In}_{1-x}\text{Cu}_x\text{P}$ thin films. (Reproduced from Alshahrie et al. [29] with permission)

The literature describes several studies about solar cells, which are based on UV-vis spectroscopy analysis. Perovskite has proven to be an excellent material among most of those used in solar cells [28]. The optical characteristics of perovskite and of other materials can change drastically depending on the adopted obtainment method. Their results are shown through the absorbance, transmittance, and reflectance spectra (Fig. 8.7) [29].

Nowadays, the efficiency of photovoltaic device designs is limited by several factors [30], among them is the band gap energy, which must be within the solar spectrum range 1.1–1.5 eV [31, 32]. Lead perovskite presenting different bromide (Br^-), iodide (I^-), and mixed halides ratio can record band gap 1.58–2.2 eV [33]; on the other hand, the mixed Sn and Pd band gap value ranges from 1.17 to 1.55 eV [3]. Therefore, the absorbance measurements based on the absorption coefficient, on specular (to thin film) or diffuse (powder) reflectance concepts, allow observing the absorbance, as well as estimating the band gap values of several semiconductors.

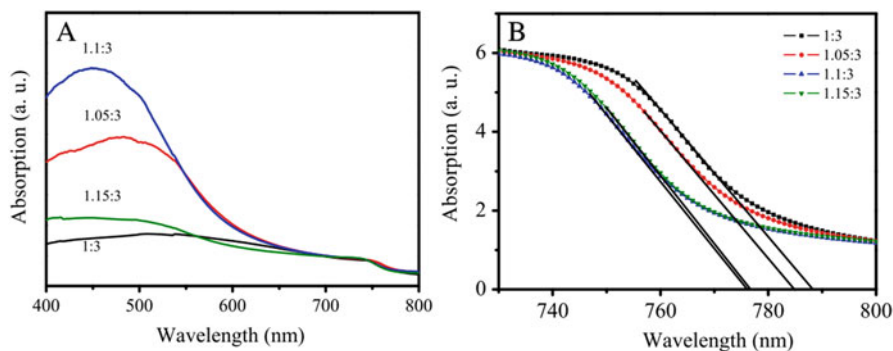


Fig. 8.8 UV-vis absorption spectra of MAPbI₃-xCl_x films presenting different mole ratios at the (a) 400–800 nm and (b) 730–800 nm. (Reproduced from Zhang et al. [34] with permission)

Zhang and coworkers [34] showed that the absorbance intensity of the perovskite at formulation PbCl₂:CH₃NH₃I is directly related to the CH₃NH₃I concentration in the structure, which is clearly shown by the absorbance spectra reflecting on the band gap (Fig. 8.8). Sample 1.1:3 recorded the best absorbance and PCE (11.3%) in this process possibly due to the insertion of high PbCl₂ concentration in the perovskite structure. Sample 1.15:3 showed reduced absorbance intensity, which could have been caused by the quenching effect.

Eperon and coworkers [35] recently showed that perovskite structure types CsPbI₃, MAPbI₃, and FAPbI₃ recorded different band gap values: 1.73, 1.57, and 1.48 eV, respectively, which were attributed to the cation size. Thus, assumingly, new perovskite structures at formulation FAPbI_yBr_{3-y} led to $y = 0.1, 0.2, 0.3, 0.4, 0.8, 0.9,$ and 1; increased visible-range absorption with shift-red was observed in the new perovskite (Fig. 8.9a). Increasing band gap values from 1.48 to 2.23 eV – with y increase – was also observed in this compound. Band gap values 1.48, 1.55, and 2.23 eV were observed in sample presenting $y = 0, 0.8,$ and 1. The properties of photovoltaic devices made out of these perovskites showed J_{sc} increase and V_{oc} reduction, fact that resulted in PCE increase from 1.9% to 14% (Fig. 8.9b).

Besides the material to provide great absorption at visible range, narrow band gaps are of extreme importance to the development of photovoltaic devices. Therefore, photovoltaic property investigations, such as absorbance, transmittance, or even reflectance diffuse measurements, are powerful tools.

8.3.2 Catalytic Applications

The photocatalytic properties of metal oxides have been largely studied since 1921 [36, 37]. Metal oxides (semiconducting) can be activated by light and used to develop technology to be employed in water splitting, to treat environmental

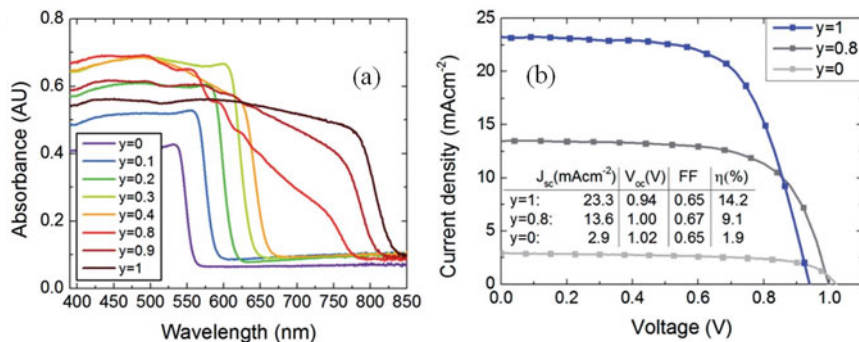


Fig. 8.9 Tunability of the FAPbI_yBr_{3-y} perovskite system. (a) UV-vis absorbance of FAPbI_yBr_{3-y} perovskites presenting varying y through integrating sphere measurements. (b) Current-voltage characteristics of FAPbI_yBr_{3-y} planar heterojunction solar cells under 100 mW cm⁻² AM1.5, illumination showing devices recording $y = 0.8$ and $y = 0$ in comparison to the champion FAPbI₃ solar cell. Performance parameters are expressed as inset. (Reproduced from Eperon et al. [35] with permission)

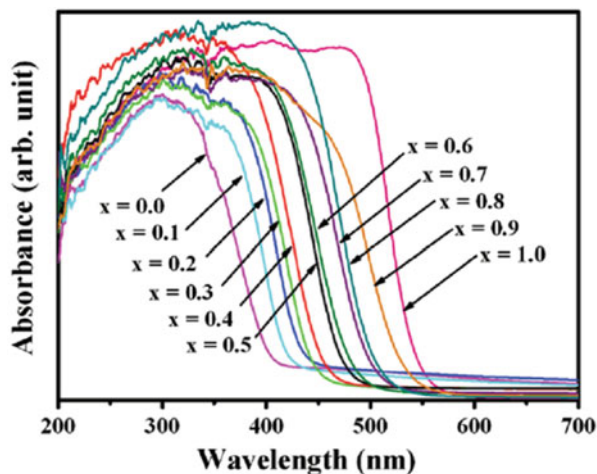
pollution, and disinfection processes, among others [37–39]. The catalytic applications of metal oxides result in their surface physical-chemical properties [39]. An improvement in the surface of physical-chemical properties can be achieved by several synthesis methods such as doping, which is able of changing the electronic properties [40].

Researchers worldwide have joined efforts to develop materials capable of efficiently absorbing visible light and exhibiting catalytic properties [41]. Catalyst-photoactivated engineering, which is the science of materials, has made the strongest efforts to feature energy band aiming at finding narrow band gap materials and lower electron-hole recombination, since they facilitate the photoinduced charge process in photocatalysts. Therefore, the formation of active species [42, 43] plays a significant role in both water splitting and photodegradation process.

It is essential developing new technology active under visible light in order to better understand the relation between catalytic-optical properties such as the UV-vis absorption, reflectance (diffuse and specular), and photoluminescence spectra aiming at obtaining optically active catalysts. TiO₂ is the mostly studied material in this scientific field given its strong absorption in UV wavelength [44]. However, catalysts capable of absorbing sunlight irradiation are currently desired for catalytic applications. Tungstate and molybdate metals (MWO₄, M = metals) [45, 46], titanates, TiO₂ (and their derivatives) [47], and bismuth oxyhalides (BiOX, X = halides) are some examples of such materials [48].

Literature reports several studies about great absorption bismuth tungstate under visible range [45]. Such characteristic gives the material a great potential for catalysis applications. Amano et al. [49] reported that different Bi₂WO₆ band gap values can be achieved (2.77 and 2.82 eV) depending on the molar ratio W/Bi (1 and 0.55). It happens due to the formation of different crystalline structures that

Fig. 8.10 UV-visible absorption spectra of β - $\text{AgAl}_{1-x}\text{Ga}_x\text{O}_2$ solid solutions. (Reproduced from Ouyang and Ye [51] with permission)



alter surface properties. Catalytic activities completely different from acetaldehyde oxidative decomposition were observed in these structures. ZnWO_4 presented a band gap between 4.6 and 4.9 eV when ZnO/ZnWO_4 band gap was close to 3.62 eV. These structures showed better catalytic activity in rhodamine B and methyl orange when they were compared to ZnWO_4 [50]. AgAlO_2 has an orthorhombic crystal system. Ouyang et al. [51] showed different gallium ion composition in $\text{AgAl}_{1-x}\text{Ga}_x\text{O}$, which led to the absorption band shift. Consequently, different band gap values at range 2.83–2.19 eV were observed (Fig. 8.10). These materials presented different catalytic properties in acetone under visible light irradiation, and such outcome can be attributed to the optimized band structure.

In order to build photocatalysts to photodegradation, it is necessary to know if the material has absorption in the visible range, as well as its electronic properties. For the absorption studies in the visible range, the technique of ultraviolet-visible spectroscopy (UV-vis) is a powerful tool. While for studies of electronic properties, photoluminescence measurements, band structure calculus, and estimate of band gap values, these are data of much importance. The band gap value can be carried out using diffuse (to powder) or specular reflectance, being this last one concerning film.

Geng et al. [52] found narrow band gap BiVO_4 structure through doping it with Co^{2+} , a fact that led to an increased absorption and to a reduced band gap value (from 2.47 to 2.44 eV). Co/BiVO_4 showed improved catalytic activity in methylene blue degradation under visible light irradiation, with emphasis to $\text{Co}^{2+}:\text{BiVO}_4$ at ratio 0.06.

With regard to low band gap value compounds, bismuth oxyhalides (BiOX , $X = \text{F}^-$, Cl^- , Br^- , and I^-) have been largely studied as an attempt to find new photocatalysts [48, 53]. Bismuth oxyhalides display their band gap value with a strong dependence of atomic size, which decreases from fluorine to iodine [54, 55]. Saraf et al. [56] studied the catalytic properties of $\text{Bi}_{1-x}\text{Eu}_x\text{OCl}$ at RhB under visible

light and observed a band gap reduction from 2.92 to 2.86 eV when they used Eu^{3+} ions to narrow the band gap. Such band gap value decreased drastically influenced the catalytic activity, mainly in $\text{Bi}_{0.95}\text{Eu}_{0.05}\text{OCl}$ (band gap 2.86 eV). It degraded the RhB dye under visible light for 30 min, and the process was faster than BiOCl (band gap 2.92 eV), which lasted 45 min.

BiOI recorded better catalytic activity in the series BiOX through methyl orange degradation under visible light. This outcome can be attributed to the lower band gap value [57], although it is not often observed. Ying-ying et al. [58] used the same series (BiOX , $X = \text{Cl}^-$, Br^- , I^-), but the BiOBr presented a lower band gap than other series in their study; moreover, it showed a great RhB kinetic degradation under visible light. The decreased catalytic activity may have resulted in the high recombination rate (e^-/h^+), which can be proved by photoluminescent measurements, since high PL spectra mean greater recombination rate (e^-/h^+) and, consequently, lower photocatalysis [59–61].

Band gap and absorption measurements can be employed to characterize the catalysts to be used for water splitting purposes [62, 63]. Fujishima and Honda [64] reported electrochemical photolysis after using TiO_2 . Researchers around the world have been making strong efforts to find photoactive catalysts under sunshine light to extract H_2 and O_2 from water.

It is the consensus that for a catalyst to have a good catalytic activity for water splitting, its bottom conduction band must be more negative than the water reduction potential (H_2 production) and the top of the valence band must be more positive than the water oxidation potential (O_2 production) (Fig. 8.11). The catalyst must have a band gap of approximately 1.23 eV [65–67].

Similar to the photocatalysis process used for environmental remediation, two factors related to band gap narrowing need to be overcome in order to develop catalysts capable of producing H_2 and O_2 , namely, (1) the lowest recombination

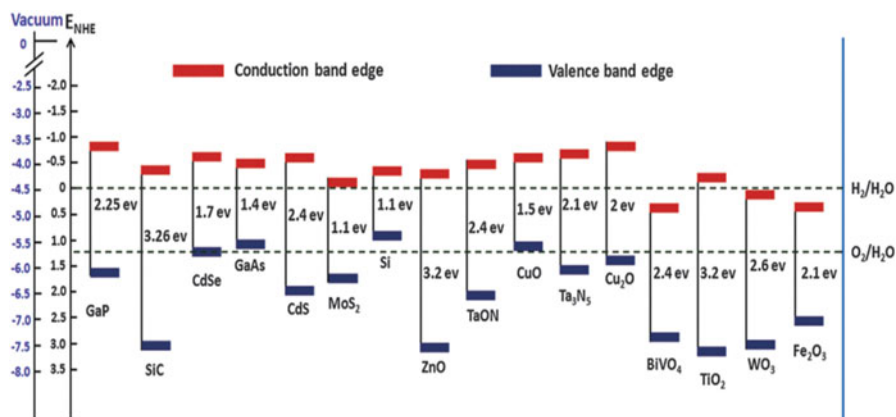


Fig. 8.11 Band structure of different semiconductors to depict water splitting redox potential. (Reproduced from Tamirat et al. [68] with permission)

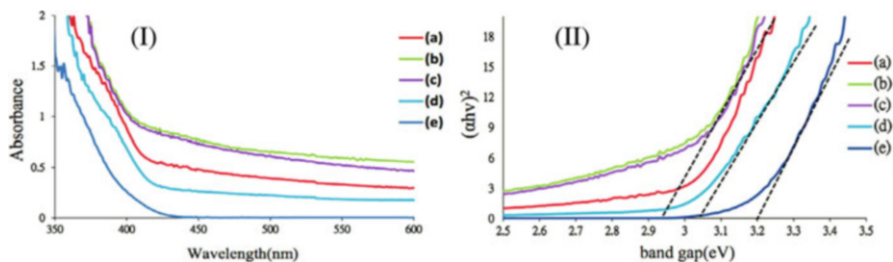


Fig. 8.12 (I) UV-vis patterns of (a) 0.5 wt% Pt/C-HS-TiO₂, (b) 1.0 wt% Pt/C-HS-TiO₂, (c) 1.5 wt% Pt/C-HS-TiO₂, (d) C-HS-TiO₂, and (e) commercial P25. (II) Band gap patterns of (a) 0.5 wt% Pt/C-HS-TiO₂, (b) 1.0 wt% Pt/C-HS-TiO₂, (c) 1.5 wt% Pt/C-HS-TiO₂, (d) C-HS-TiO₂, and (e) commercial P25. (Reproduced from Zhu et al. [71] with permission)

Table 8.1 Hydrogen yield and band gap of different photocatalysts [71]

Photocatalysts	H ₂ yield (μmol/h)	Band gap
P25-TiO ₂	10.6	3.20
C-HS-TiO ₂	80.3	3.04
0.5 wt% Pt/C-HS-TiO ₂	1943.4	2.98
1.0 wt% Pt/C-HS-TiO ₂	2856.8	2.94
1.5 wt% Pt/C-HS-TiO ₂	1632.7	2.95

Reproduced from Zhu et al. [71] with permission

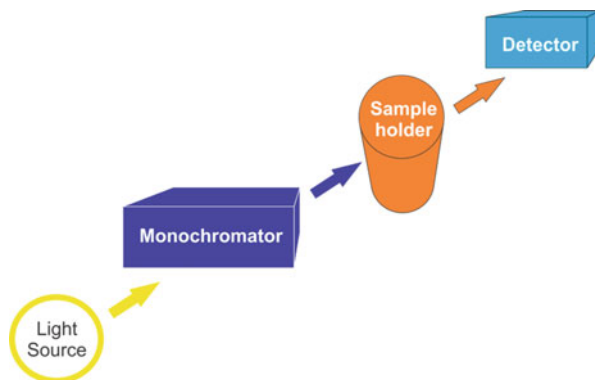
Table 8.2 Continuum sources in optical spectrophotometer

Source	Wavelength region (nm)
Xenon arc lamp	250–600
H ₂ and D2 lamp	160–380
Tungsten lamp-halogen lamp	240–2500
Tungsten lamp	350–2200

pair rate e^-/h^+ and (2) high absorption at visible range, which is related to band gap narrowing.

Many studies have been reporting water splitting under visible light [43, 66, 69, 70]. They show that depending on the synthesis method used, changes in the structural and electronic properties can be achieved. Material crystallinity can be achieved by decreasing the density defects, since they are responsible for the recombination of the photogenerated electron-hole pairs [69]. Zhu et al. [71] obtained different C-HC-TiO₂ compounds through Pt deposit at C-HS-TiO₂, and it increased the water splitting activity (Table 8.2). When their optical properties were investigated, a decrease of band gap value was observed for the increase of the Pt deposited, Fig. 8.12. Such outcome suggested increased crystallinity, which was proved by the XDR patterns (Table 8.1) [71].

Fig. 8.13 Basic spectrophotometer construction



8.4 Instrumentation

Spectrophotometers basically consist of four components: light source, sample holder (liquid or solid samples), dispersion element (monochromator), and detector (Fig. 8.13).

8.4.1 Radiation Source

The most commonly used radiation sources for the UV region are the deuterium or hydrogen arc lamps (180–350 nm), besides the xenon arc lamp (Fig. 8.14a), which is less used because its radiation is not as stable as the radiation of the other lamps. Light intensity in this radiation type often decreases steadily over time; thus, the tungsten filament lamp is the most used to achieve half-life 1000 h under visible range 350–2500 nm (Fig. 8.14b). Other types of source to the visible region such as carbon arc, quartz-iodine, and tungsten-halogen lamps are also available in the market but in smaller number than the tungsten filament lamps, for example.

8.4.2 Dispersion Device

The herein addressed energy source emits a continuous radiation over a wide range of wavelengths. It is necessary using filters (dispersion) to achieve better radiation absorption and adherence to the Beer's law. These devices are capable of dispersing the electromagnetic spectra at narrower bands that stay quite close to each other. Dispersion such as prism and holographic grating are used for such purpose (Fig. 8.15).

Similar to the rainbow, the prism is able of dispersing the polychromatic light from the source to a different wavelength extent; however, the most modern

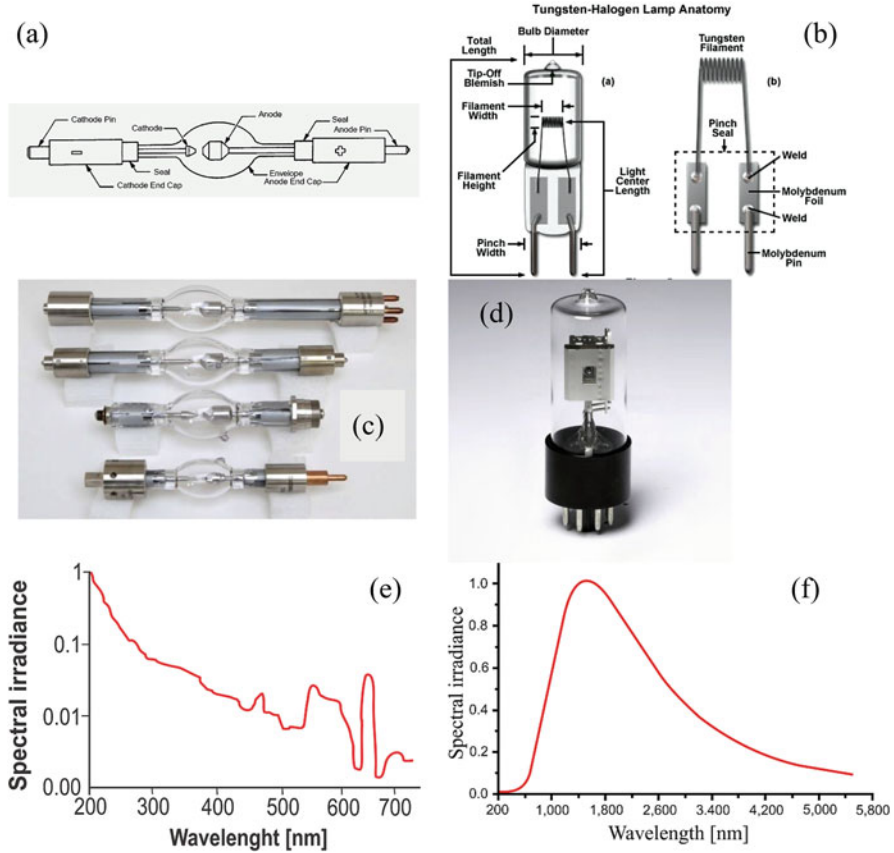


Fig. 8.14 Source types: (a) deuterium arc lamp, (b) tungsten-halogen lamp, (c) deuterium lamps found in the market, (d) tungsten-halogen lamp found in the market, (e) spectrum of the deuterium arc lamp, and (f) spectrum of the tungsten halogen lamp

spectrophotometers use holographic grating as a dispersion device. Despite having nonlinear angular dispersion, prism dispersion angles are temperature sensitive. Therefore, the holographic grating is the option other than the prism, since it has a linear angular dispersion wavelength and is temperature insensitive.

The herein described filters belong to the monochromator system. They are basically composed of (1) one entrance slit, (2) one collimating lens, (3) one dispersing device (prism or grating), (4) focusing lens, and (5) one exit lens (Fig. 8.15).

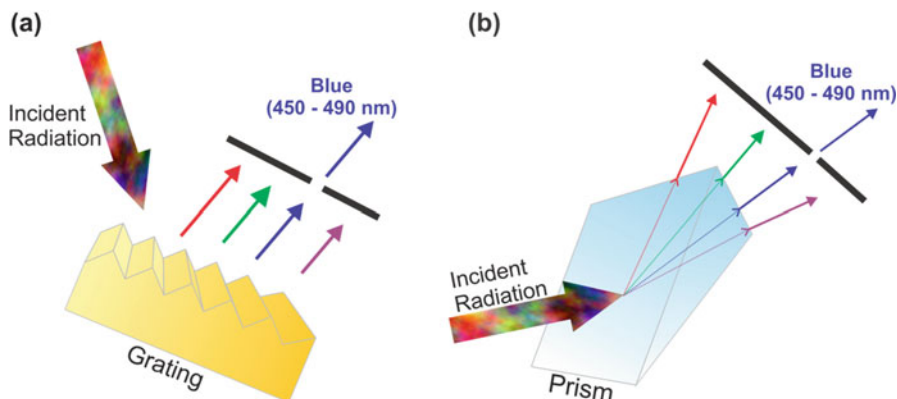


Fig. 8.15 Monochromator types: (a) grating and (b) prism

8.4.3 UV-Vis Spectrophotometer Configuration

There are several UV-vis spectrophotometer configuration types in the market, the single-beam (including diode array) and the double-beam varieties, and the dual wavelength types stand out among them [72–74] (Fig. 8.16). In the single-beam design, there is only one optical pathway from the source to the detector. The beam passes through the sample and reaches the detector after crossing the entrance slit, the monochromator, and the exit slit. Monochromators are used in this system, but such configuration only allows a narrow wavelength track to reach the detector at the time. However, when the option is made to use a polychromator, first, the radiation passes through the sample and only searches the diode array after crossing the entrance slit, the prism or the grating. Such configuration is somehow advantageous, since the wavelength is simultaneously recorded, fact that makes the spectral acquisition faster (Fig. 8.16).

For the double-beam spectrophotometer, differently from other configurations, the energy from the source after passing through monochromatic slit exit, two designs of spectrophotometers are possible, (1) double-beam using a chopper instrument Fig. 8.16c and (2) double-beam using a slit-beam instrument Fig. 8.16d [74]. Both instruments have the function of directing the two beams, one for the reference cell and the other for the sample. In both cases, the two beams simultaneously pass through the sample and the reference cell, reaching a single detector (using mechanical chopper) or different ones, when using slit-beam.

There is a special spectrophotometer, which has two wavelength types completely different crossing the same sample, the so-called dual wavelength [75] (Fig. 8.17). Only a single detector is used in this configuration type, often the photomultiplier one. This spectrophotometer type is only adopted for coordination compound samples, which have absorption bands of free ligands and complexes completely different. Such technique is ideal for studies focused on two concurrent reactions in a single sample.

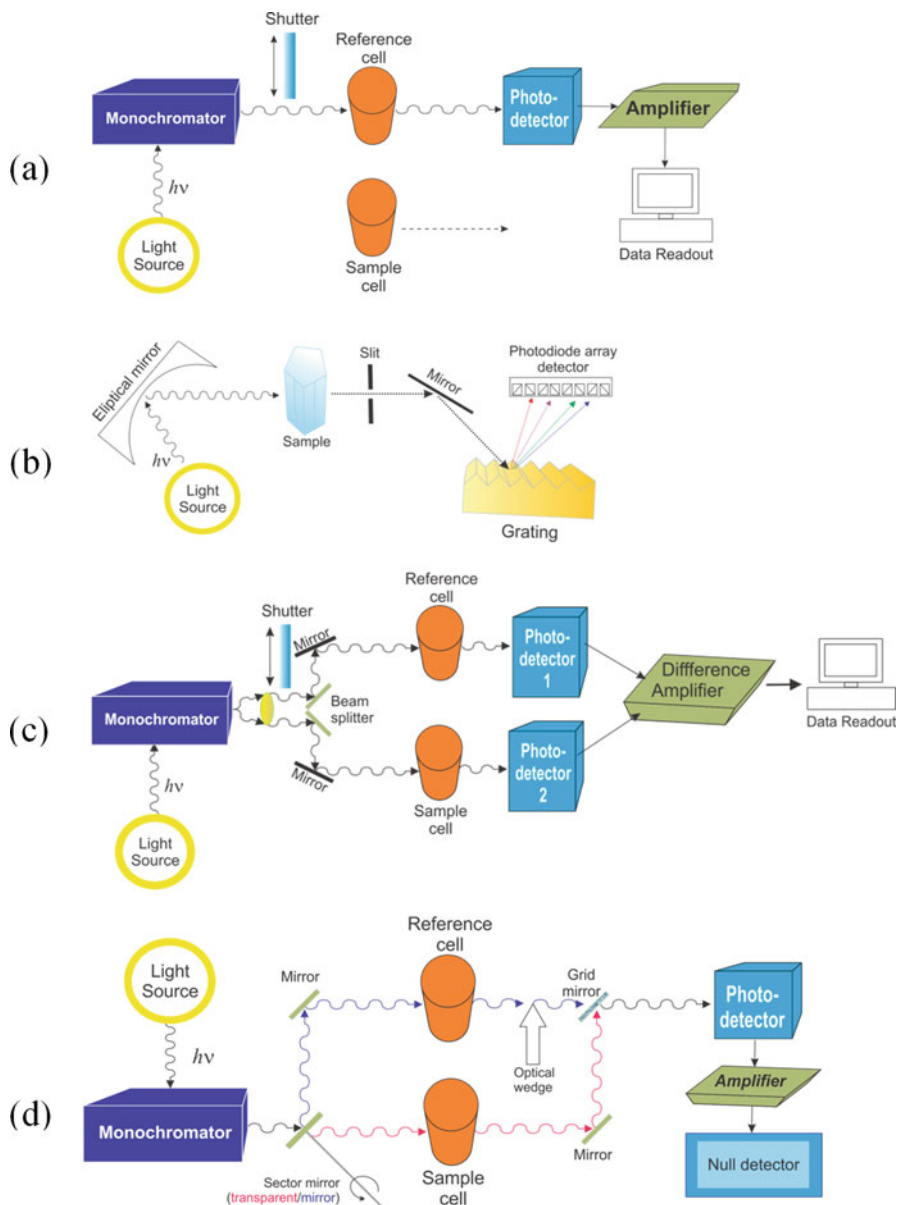


Fig. 8.16 UV-vis spectrophotometer designs. (a) One single-beam instrument, (b) diode array spectrophotometer, (c) double-beam-in-space instrument with two photodetectors, and (d) double-beam-in-space instrument with a single photodetector

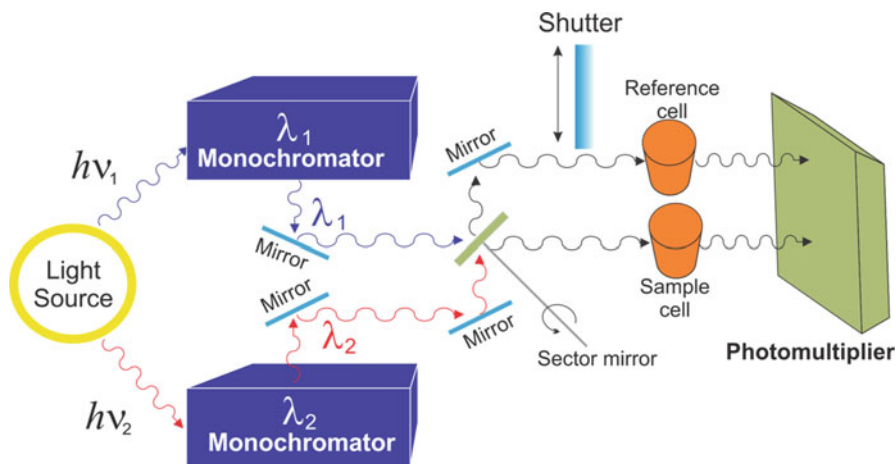


Fig. 8.17 Double-wavelength instrument design

8.4.4 Detectors

Detectors are devices capable of converting photons into electric signs. Overall, when the visible light or the ultraviolet radiation reaches the negatively charged surface (the so-called cathode), the electrons are emitted to a positively charged collector (called anode), which is proportional to the radiation intensity. This process is an application of the photoelectrical effect. There are four main spectrophotometer detector types in the market: (1) phototube, (2) photomultiplier, (3) silicon diode, and (4) diode array [73] (Fig. 8.18).

Phototubes are basically composed of light-sensitive cathodes and of one anode in the sealed tube. The operation of this detector happens in three stages:

1. Potential difference of approximately 90 V between the two electrodes (cathode and anode), one photon reaches the anode and the electrons reach the cathode surface.
2. The electrons are collected by the anode.
3. Current flow (Fig. 8.18).

The number of electrons ejected from the cathode surface at the time is directly proportional to the radiation striking the cathode surface. This process amplifies the current, which is also measured.

A process similar to that of the phototube takes place in the photomultiplier. The cathode surface emits photoelectrons when it is struck by the radiant power. The photoelectrons are emitted toward the first dynode, which ejects several electrons toward the second dynode. The process flows to the third dynode and keeps going until 10^5 or 10^7 electrons that are produced in each incident photon. Finally, the

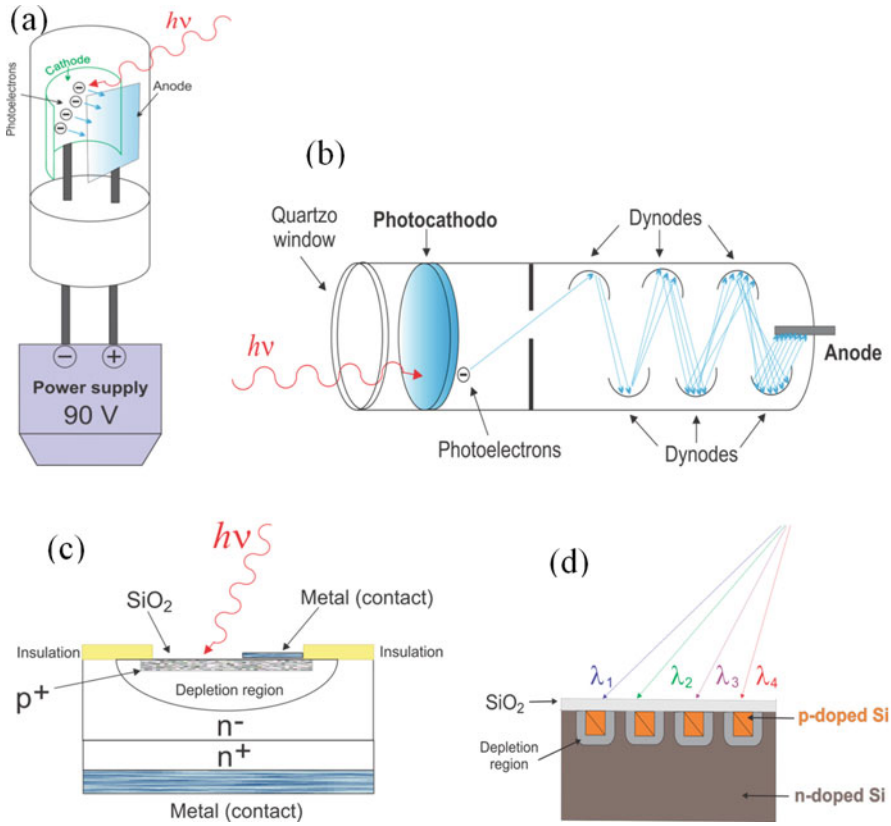


Fig. 8.18 Detector design. (a) Phototube, (b) photomultiplier tube, (c) silicon diode, and (d) diode array

electrons are collected by the photoanode and generate the current, which is further amplified and measured (Fig. 8.18).

Silicon diodes are devices made of *pn* junction semiconductors, (Fig. 8.18). Electrons and hole migrate to opposite directions and create a depletion layer when a voltage is applied in the silicon diode; this layer has less electrons and hole. Thus, more electrons and holes are created when the ultraviolet and visible radiation reach the silicon photodiode; these electrons strike the depletion layer of the *pn* junction. Such outcome increases the current, which is directly proportional to the radiation, and can be measured. While in the silicon diode only has one diode, a single silicon chip has silicon photodiodes in the diode array (1024), fact that allows simultaneously measuring different wavelengths (Fig. 8.18).

8.5 Conclusions

We have shown the potential that some techniques of optical spectroscopy such as absorbance, reflectance, and transmittance have in the characterizations and interpretations of data to inorganic nanostructured materials. Such tools are of fundamental importance to forward development of new technologies such as catalysts, which have several applications, and photovoltaic devices as well, used for creating solar cells.

Acknowledgments We are grateful to the Fundação de Amparo à Pesquisa e ao Desenvolvimento Científico e Tecnológico do Maranhão (FAPEMA) for the substantial financial support in the research projects Proc. INFRA-03965/15 and Proc. UNIVERSAL-00656/15.

References

1. Solé, J. G., Bausá, L. E., & Jaque, D. (2005). *An introduction to the optical spectroscopy of inorganic solids*. New Jersey: Wiley.
2. William, J., Callister, D., & Rethwisch, D. G. (2013). *Materials science and engineering: An introduction* (9th ed.). New York: Wiley.
3. Housecroft, C. E., & Sharpe, A. G. (2008). *Inorganic chemistry* (3th ed.). London: Pearson Education.
4. Fox, M. (2007). *Optical properties of solids*. New York: Oxford University Press.
5. Tilley, R. J. D. (2004). *Understand solids: The science of materials*. New York: Wiley.
6. Grundmann, M. (2010). *The physics of semiconductors: An introduction including nanophysics and applications* (2th ed.). New York: Springer.
7. Kitai, A. (2008). *Luminescent materials and applications*. Chichester: Wiley.
8. Bergman, L., & McHale, J. L. (2012). *Handbook of luminescent semiconductor materials*. New York: CCR Press.
9. Gauglitz, G., & Vo-Dinh, T. (2003). *Handbook of spectroscopy*. Weinheim: WILEY-VCH.
10. Barnes, P. Y., Early, E. A., & Parr, A. C. (1998). *Spectral reflectance*. Washington: NIST PUBLICATIONS.
11. Torrent, J., & Barrón, V. (2008). Diffuse reflectance spectroscopy. In M.o.S.A.P.M. Methods (Ed.), (pp. 367–385). Madison: Soil Science Society of America.
12. Wood, B. J., & Strens, R. G. J. (1979). *Mineralogical Magazine*, 43, 509–518.
13. Dzimbeg-Malcic, V., Barbaric-Mikocevic, Z., & Itric, K. (2011). *Technical Gazette*, 18, 117–124.
14. Morales, A. E., Mora, E. S., & Pal, U. (2007). *Revista Mexicana de Física*, 53, 18–22.
15. Sardela, M. (2014). *Practical materials characterization*. New York: Spriger.
16. Kofenstein, R., Jager, L., & Ebbinghaus, S. G. (2013). *Solid State Ionics*, 249, 1–5.
17. Mehmood, M. S., Siddiqui, N., Maqbool, S. A., Baluch, M. A., Mukhtar, S. S., & Yasin, T. (2017). *Optik*, 144, 387–392.
18. Eberl, J., & Kisch, H. (2008). *Photochemical & Photobiological Sciences*, 7, 1400–1406.
19. Bellardita, M., Addamo, M., Di Paola, A., Palmisano, L., & Venezia, A. M. (2009). *Physical Chemistry Chemical Physics*, 11, 4084–4093.
20. Khoshhesab, Z. M. (2012). *Infrared spectroscopy – materials science, engineering and technology*. Croatia: InTech.
21. Palmer, J. M. (1995). The measurement of transmission, absorption, emission, and reflection. In J. M. Palmer (Ed.), *Handbook of optics* (p. 25.21). New York: McGraw-Hill Professional.

22. Toft, J., & Kvalheim, O. M. (1993). *Chemometrics and Intelligent Laboratory Systems*, 19, 65–73.
23. Gottfries, J., Depui, H., Fransson, M., Jongeneelen, M., Josefson, M., Langkilde, F. W., & Witte, D. T. (1996). *Journal of Pharmaceutical and Biomedical Analysis*, 14, 1495–1503.
24. Nasser, H., Ozkol, E., Bek, A., & Turan, R. (2015). *Optical Materials Express*, 5, 932–942.
25. Sampaio, P. G. V., & González, M. O. A. (2017). *Renewable and Sustainable Energy Reviews*, 74, 590–601.
26. Gong, J. W., Sumathy, K., Qiao, Q. Q., & Zhou, Z. P. (2017). *Renewable and Sustainable Energy Reviews*, 68, 234–246.
27. Snaith, H. J. (2010). *Advanced Functional Materials*, 20, 13–19.
28. Zuo, C. T., Bolink, H. J., Han, H. W., Huang, J. S., Cahen, D., & Ding, L. M. (2016). *Advancement of Science*, 3, 1500324–1500324.
29. Alshahrie, A., Juodkakis, S., Al-Ghamdi, A. A., Hafez, M., & Bronstein, L. M. (2017). *Optics and Laser Technology*, 95, 29–35.
30. Conibeer, G. J., & Willoughby, A. (2014). *Solar cell materials: Developing technologies*. UK: Wiley.
31. Niv, A., Abrams, Z. R., Gharghi, M., Gladden, C., & Zhang, X. (2012). *Applied Physics Letters*, 100, 083901.
32. Polman, A., Knight, M., Garnett, E. C., Ehrler, B., & Sinke, W. C. (2016). *Science*, 352, 307.
33. Liao, W. Q., Zhao, D. W., Yu, Y., Shrestha, N., Ghimire, K., Grice, C. R., Wang, C. L., Xiao, Y. Q., Cimaroli, A. J., Ellingson, R. J., Podraza, N. J., Zhu, K., Xiong, R. G., & Yan, Y. F. (2016). *Journal of the American Chemical Society*, 138, 12360–12363.
34. Zhang, Z. L., Men, B. Q., Liu, Y. F., Gao, H. P., & Mao, Y. L. (2017). *Nanoscale Research Letters*, 12, 84.
35. Eperon, G. E., Stranks, S. D., Menelaou, C., Johnston, M. B., Herz, L. M., & Snaith, H. J. (2014). *Energy & Environmental Science*, 7, 982–988.
36. Renz, C. (1921). *Helvetica Chimica Acta*, 4, 961–968.
37. Coronado, J. M., Fresno, F., Hernández-Alonso, M. D., & Portela, R. (2013). *Design of advanced photocatalytic materials for energy and environmental applications: Green energy and technology*. London: Springer.
38. Reddy, P. V. L., Kavitha, B., Reddy, P. A. K., & Kim, K. H. (2017). *Environmental Research*, 154, 296–303.
39. Fujishima, A., Zhang, X. T., & Tryk, D. A. (2008). *Surface Science Reports*, 63, 515–582.
40. Hernández-Ramírez, A., & Medina-Ramírez, I. (2015). *Photocatalytic semiconductors: Synthesis, characterization, and environmental applications*. London: Springer.
41. Bora, L. V., & Mewada, R. K. (2017). *Renewable and Sustainable Energy Reviews*, 76, 1393–1421.
42. Tong, H., Ouyang, S. X., Bi, Y. P., Umezawa, N., Oshikiri, M., & Ye, J. H. (2012). *Advanced Materials*, 24, 229–251.
43. Abe, R. (2010). *Journal of Photochemistry Photobiology C-Photochemistry Reviews*, 11, 179–209.
44. Coronado, J. M., Fresno, F., Hernández-Alonso, M. D., & Portela, R. (2013). *Design of advanced photocatalytic materials for energy and environmental applications*. London: Springer.
45. Luevano-Hipolito, E., & Martinez-de la Cruz, A. (2017). *Advanced Powder Technology*, 28, 1511–1518.
46. Shan, Z. C., Wang, Y. M., Ding, H. M., & Huang, F. Q. (2009). *Journal of Molecular Catalysis A-Chemical*, 302, 54–58.
47. Bian, Z. F., Zhu, J., & Li, H. X. (2016). *Journal of Photochemistry Photobiology C-Photochemistry Reviews*, 28, 72–86.
48. Cheng, H. F., Huang, B. B., & Dai, Y. (2014). *Nanoscale*, 6, 2009–2026.
49. Amano, F., Nogami, K., & Ohtani, B. (2012). *Catalysis Communications*, 20, 12–16.
50. Hao, Y. Y., Zhang, L. Y., Zhang, Y., Zhao, L., & Zhang, B. S. (2017). *RSC Advances*, 7, 26179–26184.

51. Ouyang, S. X., & Ye, J. H. (2011). *Journal of the American Chemical Society*, *133*, 7757–7763.
52. Geng, Y., Zhang, P., Li, N., Sun, Z., & Alloys, J. (2015). *Compounds*, *651*, 744–748.
53. An, H., Du, Y., Wang, T., Wang, C., Hao, W., & Zhang, J. (2008). *Rare Metals*, *27*, 243–250.
54. Zhao, Z. Y., & Dai, W. W. (2014). *Inorganic Chemistry*, *53*, 13001–13011.
55. Ganose, A. M., Cuff, M., Butler, K. T., Walsh, A., & Scanlon, D. O. (2016). *Chemistry of Materials*, *28*, 1980–1984.
56. Saraf, R., Shivakumara, C., Behera, S., Nagabhushana, H., & Dhananjaya, N. (2015). *RSC Advances*, *5*, 4109–4120.
57. Liu, Y., Xu, J., Wang, L., Zhang, H., Xu, P., Duan, X., Sun, H., & Wang, S. (2017). *Nanomaterials*, *7*, 64.
58. Gu, Y.-y., Zhao, L., Yang, M.-y., Xiong, Y.-q., Wu, Z., Zhou, M.-j., Yan, J., & Cent, J. (2017). *South University*, *24*, 754–765.
59. Liqiang, J., Yichun, Q., Baiqi, W., Shudan, L., Baojiang, J., Libin, Y., Wei, F., Honggang, F., & Jiazhong, S. (2006). *Solar Energy Materials & Solar Cells*, *90*, 1773–1787.
60. Yu, J.-G., Yu, H.-G., Cheng, B., Zhao, X.-J., Yu, J. C., Ho, W.-K., & Phys, J. (2003). *Chemistry B*, *107*, 13871–13879.
61. Li, F. B., & Li, X. Z. (2002). *Applied Catalysis A-General*, *228*, 15–27.
62. Ismail, A. A., & Bahnemann, D. W. (2014). *Solar Energy Materials & Solar Cells*, *128*, 85–101.
63. Walter, M. G., Warren, E. L., McKone, J. R., Boettcher, S. W., Mi, Q. X., Santori, E. A., & Lewis, N. S. (2010). *Chemical Reviews*, *110*, 6446–6473.
64. Fujishima, A., & Honda, K. (1972). *Nature*, *238*, 37–+.
65. Yamashita, H., & Li, H. (2016). In H. Yamashita & H. Li (Eds.), *Nanostructure science and technology* (p. 544). Switzerland: Springer.
66. Jafari, T., Moharreri, E., Amin, A. S., Miao, R., Song, W. Q., & Suib, S. L. (2016). *Molecules*, *21*, 900.
67. Noureldine, D., & Takanabe, K. (2016). *Catalysis Science & Technology*, *6*, 7656–7670.
68. Tamirat, A. G., Rick, J., Dubale, A. A., Su, W. N., & Hwang, B. J. (2016). *Nanoscale Horizons*, *1*, 243–267.
69. Maeda, K. (2013). *ACS Catalysis*, *3*, 1486–1503.
70. Ong, W. J., Tan, L. L., Ng, Y. H., Yong, S. T., & Chai, S. P. (2016). *Chemical Reviews*, *116*, 7159–7329.
71. Zhu, Z., Chen, J. Y., Su, K. Y., Wu, R. J., & Taiwan Inst, J. (2016). *Chemical Engineer*, *60*, 222–228.
72. Harris, D. C. (2010). *Quantitative chemistry analysis* (8th ed.). New York: W. H. Freeman.
73. Skoog, D. A., West, D. M., Holler, F. J., & Crouch, S. R. (2014). *Fundamentals of analytical chemistry* (9th ed.). Australia: BROOKS/COLE, Cengage Learning.
74. Willard, H. H., Merritt, L. L., & Dean, J. A. (1988). *Instrumental methods of analysis* (6th ed.). New York: Wadsworth Publishing Company.
75. Nath, U. U. (2009). *Biophysical chemistry: Principle and techniques*. Mumbai: Himalaya Publishing House.

Chapter 9

Fourier Transform Infrared Spectroscopy: Fundamentals and Application in Functional Groups and Nanomaterials Characterization



Shahid Ali Khan, Sher Bahadar Khan, Latif Ullah Khan, Aliya Farooq, Kalsoom Akhtar, and Abdullah M. Asiri

9.1 Introduction

Fourier transform infrared spectroscopy (FTIR) is a largely used technique to identify the functional groups in the materials (gas, liquid, and solid) by using the beam of infrared radiations. An infrared spectroscopy measured the absorption of IR radiation made by each bond in the molecule and as a result gives spectrum which is commonly designated as % transmittance versus wavenumber (cm^{-1}). A diverse range of materials containing the covalent bond absorbed electromagnetic radiation

S. A. Khan (✉)

Department of Chemistry, University of Swabi, Anbar-23561, Khyber Pakhtunkhwa, Pakistan

Center of Excellence for Advanced Materials Research, King Abdulaziz University, Jeddah, Saudi Arabia

Chemistry Department, Faculty of Science, King Abdulaziz University, Jeddah, Saudi Arabia

e-mail: skhan0034@stu.kau.edu.sa

S. B. Khan (✉) · A. M. Asiri

Center of Excellence for Advanced Materials Research, King Abdulaziz University, Jeddah, Saudi Arabia

Chemistry Department, Faculty of Science, King Abdulaziz University, Jeddah, Saudi Arabia

e-mail: sbkhan@kau.edu.sa

L. U. Khan

Brazilian Nanotechnology National Laboratory (LNNano), Brazilian Center for Research in Energy and Materials (CNPEM), Campinas, São Paulo, Brazil

A. Farooq

Department of Chemistry, Shaheed Benazir Bhutto Women University, Peshawar, Pakistan

K. Akhtar

Division of Nano Sciences and Department of Chemistry, Ewha Womans University, Seoul, South Korea

in the IR region. The IR region is at lower energy and higher wavelength than the UV-visible light and has higher energy or shorter wavelength than the microwave radiations. For the determination of functional groups in a molecule, it must be IR active. An IR active molecule is the one which has dipole moment. When the IR radiation interacts with the covalent bond of the materials having an electric dipole, the molecule absorbed energy, and the bond starts back and forth oscillation. Therefore, the oscillation which caused the change in the net dipole moment of the molecule should absorbed IR radiations.

A single atom doesn't absorb IR radiation as it has no chemical bond. Symmetrical molecules also do not absorb IR radiation, because of zero dipole moment. For instance, H₂ molecule has two H atoms; both canceled the effect of each other and giving zero dipole moment to H₂ molecule. Therefore, H₂ molecule is not an IR active molecule. On other hand, H-F (hydrogen fluoride) is an IR active molecule, because when IR radiation interacts with H-F molecule, the charge transferred toward the fluorine atom and as a result fluorine becomes partial negative and hydrogen becomes partial positive, giving net dipole moment to H-F molecule.

It should be noted here that a particular IR radiation (frequency) will be absorbed by a particular bond in the molecule, because every bond has their particular natural vibrational frequency. For instance, a molecule such as acetic acid (CH₃COOH) containing various bonds (C-C, C-H, C-O, O-H, and C=O), all these bonds are absorbed at specific wavelength and are not affected by other bond. We can say that two molecules with different structures don't have the same infrared spectrum, although some of the frequencies might be same.

9.1.1 Electromagnetic Spectrum

The interaction of matter with any part of the electromagnetic spectrum is called spectroscopy, which is an instrumentally assisted study between matter and electromagnetic radiation of any range. Electromagnetic spectrum is composed of various radiations containing different wavelengths, which is a type of radiant energy, ranging from gamma rays to X-rays via visible light to radio waves, each of which can be considered as a wave or particle traveling at the speed of light. Electromagnetic radiations have a broad range of spectrum starting from the highest energy cosmic rays via X-rays, UV, Vis, infrared, micro-, and radio waves (Table 9.1). They propagate in vacuum with the speed of light. The electromagnetic radiations are described by the parameters like frequency, wavelength, and energy. The relationship between the frequency, wavelength, and energy is given as:

$$\begin{aligned} E &\propto f \\ E &= hf \end{aligned} \tag{9.1}$$

where E is the energy, f is the frequency of the electromagnetic radiations, and h is the Planck's constant which is equal to 6.634×10^{-34} J. s. The frequency and energy have direct relation, while both have indirect relation with the wavelength.

Table 9.1 Electromagnetic spectrum and molecular effects

Radiation	Wavelength (cm)	Energy (Kcal/mol)	Molecular effects	Approximate range of wavelength
Gamma rays	10^{-9}	10^6	Ionization	Atomic nuclei
X-ray	10^{-7}	10^4	Ionization	Atoms
Vacuum UV	10^{-5}	10^{-9}	Ionization	Molecules
Near UV	10^{-4}	10^2	Electronic transition	Protozoans
Visible	10^{-3}	10	Electronic transition	Needle point
Infrared	10^{-1}	10^{-2}	Molecular vibration	Butterfly
Microwaves	10^2	10^{-4}	Rotational motion	Human
Radio wave	10^4	10^{-6}	Nuclear spin transition	Buildings

$$f \propto \frac{1}{\lambda}$$

$$E = \frac{hc}{\lambda} \quad (9.2)$$

where c is the speed of light which is equal to 3×10^8 m/s and λ is the wavelength of light.

Chemists used selectively the electromagnetic radiations to explore the complete structural, chemical, and physical properties of the molecules.

9.1.2 Infrared

The IR region is lying between visible and microwave end of the electromagnetic radiation spectrum. It is basically divided into three main portions: near IR ($14000\text{--}4000\text{ cm}^{-1}$), mid-IR ($4000\text{--}400\text{ cm}^{-1}$), and far IR ($400\text{--}40\text{ cm}^{-1}$). IR spectroscopy is an advanced and extensively used analytical tool that investigates the structural chemistry of the sample by irradiating with IR radiations. The molecules or sample absorbed the IR radiations and displayed an absorption spectrum. IR measured the amount of radiations absorbed by the molecule and their intensity. The absorption of the IR radiations causes various molecular motions in the molecule, which create a net dipole moment. Therefore, a molecule is said to be IR active if the molecule has a net dipole moment (e.g., CH_4 , C_2H_6 , NO_2 , TiO_2), otherwise it will be IR inactive (e.g., H_2 , O_2 , etc.). One of main advantages of FTIR spectroscopy is its capability to identify functional groups such as C=O, C-H, or N-H. FTIR spectroscopy enables by measuring all types of samples: solids, liquids, and gases.

9.1.3 Infrared Spectrum

The plot of measured infrared light intensity (absorbance or % transmittance) versus its property, such as energy range expressed in wavenumber (cm^{-1}), is called an infrared spectrum. The infrared spectrum is conventionally plotted with high wavenumber to the left and low wavenumber to the right in its x -axis. Plots of the typical FTIR spectra should always follow this convention. However, in certain articles the contrary profile of FTIR spectra are also reported (Fig. 9.1). The IR spectrum is recorded in absorbance mode, which measures the amount of light absorbed by a sample, and its intensity at y -axis is plotted in absorbance unit. As shown in Fig. 9.1, the absorption band of each characteristic functional group in compound is pointed up, and their tops represent wavenumbers at which significant amounts of IR light were absorbed by the sample. The absorbance spectrum of a sample is calculated from the following relation:

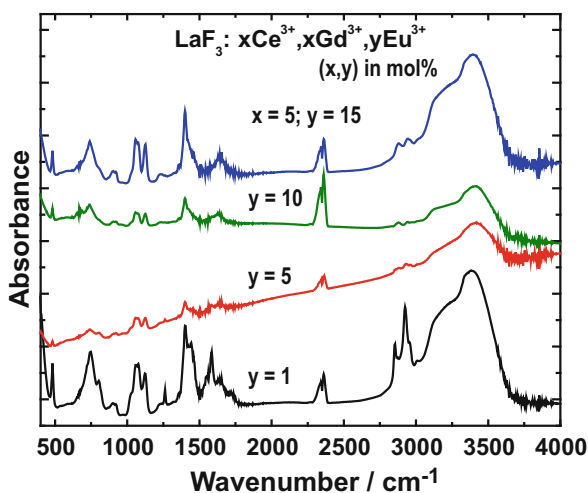
$$A = \log(I_0/I) \quad (9.3)$$

where A , absorbance; I_0 , intensity in the background spectrum; and I , intensity in the spectrum of sample. The absorbance can be also correlated with the concentration of molecules in a sample through the equation called as Beer's law:

$$A = \epsilon lc \quad (9.4)$$

where, A absorbance; ϵ , molar absorptivity; l , path length; and c , concentration of the sample. The height or area of a peak in an absorbance spectrum is proportional to concentration; therefore Beer's law can be used to determine the concentrations of molecules in samples.

Fig. 9.1 FTIR spectra of $\text{LaF}_3:x\text{Ce}^{3+}$, $x\text{Gd}^{3+},y\text{Eu}^{3+}$ ($x = 5; y = 1, 5, 10$ and 15 mol%) nanomaterials functionalized with oleic acid [1]



In the given example (Fig. 9.1), we have explained the FTIR spectra of oleic acid coated $\text{LaF}_3:x\text{Ce}^{3+}$, $x\text{Gd}^{3+}$, $y\text{Eu}^{3+}$ NPs [1] for the sake of understanding of the nonspecialized readers. The FTIR spectra of these nanomaterials are dominated by broad and intensive absorption band at 3400 cm^{-1} corresponding to the O-H stretching vibrations (asymmetric and symmetric) of the adsorbed water molecules with the existence of O-H deformation (σ) vibrational around 1640 cm^{-1} . The absorption bands around 2930 and 1390 cm^{-1} are attributed to the $\nu_{\text{C-H}}$ of CH_2 groups present in oleic acid, revealing the presence of organic surfactant on surface of $\text{LaF}_3:x\text{Ce}^{3+}$, $x\text{Gd}^{3+}$, $y\text{Eu}^{3+}$ NPs. A closer look revealed the appearance of two absorption peaks around 1582 and 1546 cm^{-1} , which is attributed to the characteristic of the asymmetric (COO^-) stretching and the symmetric (COO^-) stretching. However, this analysis gives no information about the presence of LaF_3 phase, because $\nu_{\text{Ln-F}}$ is generally observed below 400 cm^{-1} .

On the other hand, the y -axis of an infrared spectrum can be also plotted in unit called percent transmittance (% T), which measures the percentage of light transmitted by the compound and can be calculated as follows:

$$\%T = 100 \times (I/I_0) \quad (9.5)$$

where % T , percent transmittance; I_0 , intensity in the background spectrum; and I , intensity in the sample spectrum.

It is noteworthy that in the % T spectrum, the band of each characteristic functional group of the compound is pointed down, as shown in Fig. 9.2. Absorbance and % T are mathematically related to each other, and they are interconvertible using FTIR software. This conversion causes change of the y -axis, but the peak positions are not affected. In the scientific literature, the FTIR spectra are usually plotted in both absorbance and % T units.

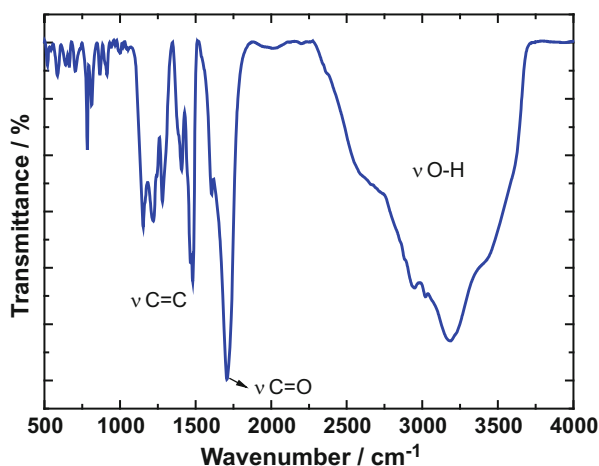


Fig. 9.2 FTIR absorption spectrum of p-tetrakis (carboxymethyl)calix-4-arene tetrol macrocycle ligand [2]

9.2 Brief History of FTIR

The development of spectroscopy in non-visual wavelengths (IR region) was advanced simultaneously with the development of visual spectroscopy. Infrared light was first discovered by Sir Frederick William Herschel during his experiment, which was performed with mercury-in-glass thermometers illuminated by sunlight dispersed through a glass prism (Herschel 1800). He was really surprised when he found that not only the thermometers register heat beyond the red end of the visible spectrum, but the greatest amount of heat was found in this region [3]. Later on, various scientists, including William Herschel's son, Sir John Frederick William Herschel, contribute to the infrared spectroscopy very effectively to measure the infrared spectrum practically. Jacquinet [4], Fellgett [5], and Connes [6] are the famous researchers along with other known scientists for their work in the early history of spectroscopy [7, 8]. The work of Rubens and Wood on FTIR interferogram [9] and Rubens and von Baeyer in spectroscopy [10] was known before the advent of Michelson interferometer [11]. However, before 1980 some domestic high-resolution FTIR spectrometers were also reported [12–14].

In the mid-1960s, progress has been made in the infrared microscopy and developed techniques which enhanced the signal-to-noise ratio. In the late 1970s, the infrared microscope systems were introduced in the market and in the early stages of 1980s by Digilab and Spectra-Tech Company.

However, the real advancement was made in FTIR spectroscopy with the availability of commercially accessible high-resolution instruments. Later on, the scientists focused their attention on innovation, queries, and evolutions of the essential theoretical and spectroscopic procedures. Erstwhile to 1980, the FTIR spectrometers resolution was 0.04 cm^{-1} which is inadequate and less efficient than the old-fashioned grating apparatuses. Revolution attained with the Bomem instruments having a maximum optical path difference ($d_{\text{MOPD}} = 250 \text{ cm}^{-1}$), associated to the unapodized resolution which is $\Delta\tilde{\nu} = 0.61 d_{\text{MOPD}}^{-1} = 0.0024 \text{ cm}^{-1}$.

In the traditional IR spectroscopy, specific IR radiations are selected for the analysis, which is a tedious and time-consuming process. For example, a molecule containing O-H and C=O functional groups, different ranges of IR radiation were applied for the determination of O-H and C=O functional groups. This problem was solved with the advent of Fourier transform infrared spectroscopy (FTIR), where a pulse (burst of energy) is bombarded on molecules; as a result, different parts of the same molecules received its characteristics IR radiation and displayed a time domain spectrum called interferogram. The time domain spectrum (interferogram) is converted to frequency domain spectrum by the application of mathematical procedure known as Fourier transform.

9.3 Matter-Energy Interaction

When electromagnetic radiation interacts with a material, for example, UV-Vis light, the excitation of electrons occurs from the highest occupied molecular orbital (HOMO) to lowest unoccupied molecular orbital (LUMO). This movement of an electron from a lower energy level to a higher energy level is known as a *transition*, as depicted in Fig. 9.3. Generally, the infrared spectroscopy is principally similar as the other absorption spectroscopy. The lower energy radiation in the infrared (IR) region of the electromagnetic spectrum can interact with atoms, and molecules can produce changes within these entities. This type of radiation is not energetic enough to excite electrons, but it can cause the chemical bonds in molecules to vibrate in different ways. The absorption of IR radiation is also quantized like other absorption process. In a quantized process, the molecule absorbed only selected frequency. The energy changes in the infrared radiation are in the order of 8–40 KJ/mole (1.9–9.5 KCal/mol). The energy in this range covers the stretching and bending vibrations of various bonds in covalent molecules.

During an absorption process, the molecule absorbed only those frequencies of IR radiation which matched with the natural vibrational frequency of the bonds and hence increases the amplitude of vibrational modes of the molecules. However, all the bonds in a molecule cannot absorb the IR radiation irrespective to the matching frequency of IR radiations, until and unless it has a net dipole moment.

9.3.1 Modes of Vibrations

Organic molecules mostly contain covalent bonds between the atoms, which are not stiff but rather behave like springs and always agitating at room temperature. This movement of the bonds in molecule gives various modes of vibration. There are two modes of vibrations: stretching and bending vibration. These two are the simplest vibrations in IR active molecules, for instance, the diatomic linear molecule

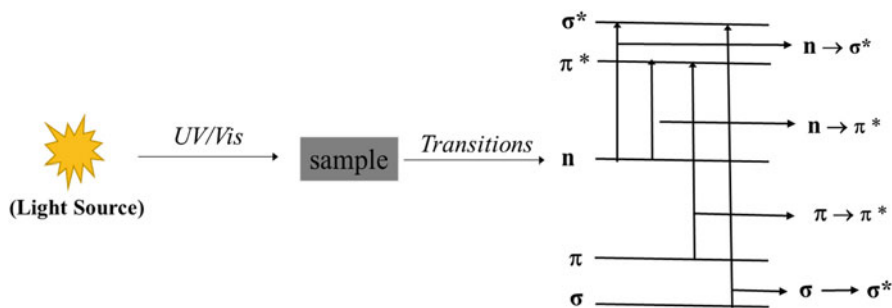


Fig. 9.3 Typical diagram of UV-Vis and electronic transitions under UV-Vis light illuminations

Fig. 9.4 Representation of stretching vibration in diatomic linear molecule hydrogen fluoride (H-F) and bending vibration in triatomic molecule water (H_2O)

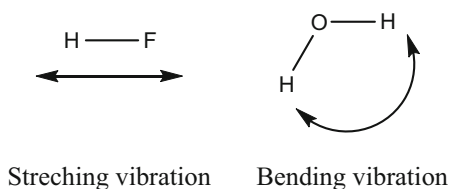
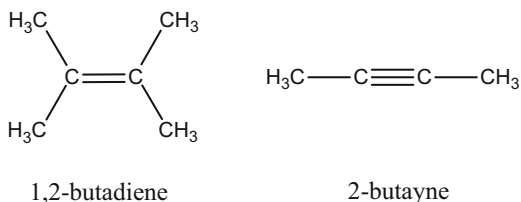


Fig. 9.5 IR inactive molecules with double and triple bond



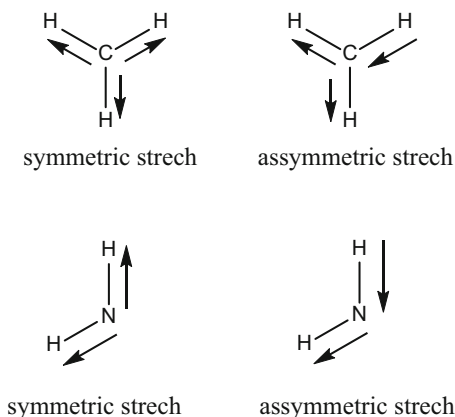
H-F showing stretching vibration and triatomic H_2O molecule showing bending vibration as depicted in the inset of Fig. 9.4.

However, other complex types of stretching and bending vibration also occurred in IR active molecules. Symmetric and asymmetric vibrations are the types of stretching vibration, while wagging, rocking, twisting, and scissoring are the characteristic types of bending vibrations. It is noteworthy that the stretching vibrations usually occurred at higher energy when compared to the bending vibrations. Similarly, among the stretching vibrations, asymmetric stretching vibrations are aroused at higher energy than the symmetric one. Furthermore, this absorption process is quantized; therefore, stretching and bending vibration take place at specific allowed energy levels. However, some molecules absorbed strongly as compared to others, and some even do not absorb at all. Those which absorb IR radiations are called IR active, and those which not absorb IR radiation are called IR inactive molecules. The absorption and strength of absorption depend on the dipole moment of the molecules. For instance, the amplitude of carbonyl group ($\text{C}=\text{O}$) stretching frequency is much intense as compared to alkyne ($\text{C}\equiv\text{C}$), because of the fact that the polarity of ($\text{C}=\text{O}$) is higher than ($\text{C}\equiv\text{C}$). Some IR inactive vibrations of the molecules containing double and triple bonds are depicted in Fig. 9.5.

9.3.1.1 Stretching Vibration

If a molecule contain at least two or three identical groups, then symmetric and asymmetric stretching arises, for instance, CH_2 , CH_3 , CCl_2 , anhydride, NO_2 , and NH_2 groups. The asymmetric stretching has higher energy than the symmetric stretching. In symmetric stretch, the bond lengths of the participating atoms either increase or decrease simultaneously, while in asymmetric stretch one of the bond length increases, while the other decreases. For instance, the CH_3 symmetric stretch arises at approximately 2872 cm^{-1} , while its counterpart asymmetric stretch occurs

Fig. 9.6 Symmetric stretching and asymmetric stretching vibration of CH_3 and NH_2 groups, where the asymmetric stretch appeared at higher energy



at higher energy (2962 cm^{-1}). Similarly, the symmetric stretch of NH_2 group appears at 3300 cm^{-1} while its asymmetric stretch at 3400 cm^{-1} (Fig. 9.6).

9.3.1.2 Bending Vibration

This type of vibration is also called deformation vibration and causes change in the bond length; however, the bond angle remains the same. There are two types of bending vibrations: (i) in-plane bending and (ii) out-plane bending.

In-plane bending vibration – Scissoring and rocking vibrations are the two types of in-plane bending vibrations. In scissoring vibration both atoms are moving toward each other or away from each other. While in rocking vibration, the bond angles are unchanged due to moments of participating atoms in the same direction, as shown in Fig. 9.7.

Out of plane bending vibration – This vibration includes wagging and twisting vibrations, where the bond angle is changed. In wagging vibration, both the atoms move toward a common side of the plane. While in twisting vibration, both the atoms go opposite to each other. These different types of bending vibrations are presented in Fig. 9.7a, for instance, CH_2 group [15].

9.4 Basic Principle of FTIR

When infrared radiation is bombarded on a sample, it absorbs the light and creates various vibration modes. This absorption relates precisely to the nature of bonds in the molecule. The frequency ranges are measured as wavenumbers typically over the range of $4000\text{--}600\text{ cm}^{-1}$. The FTIR spectrum is measured as wavenumber because wavenumber is directly related to the energy and frequency, thus providing an easy

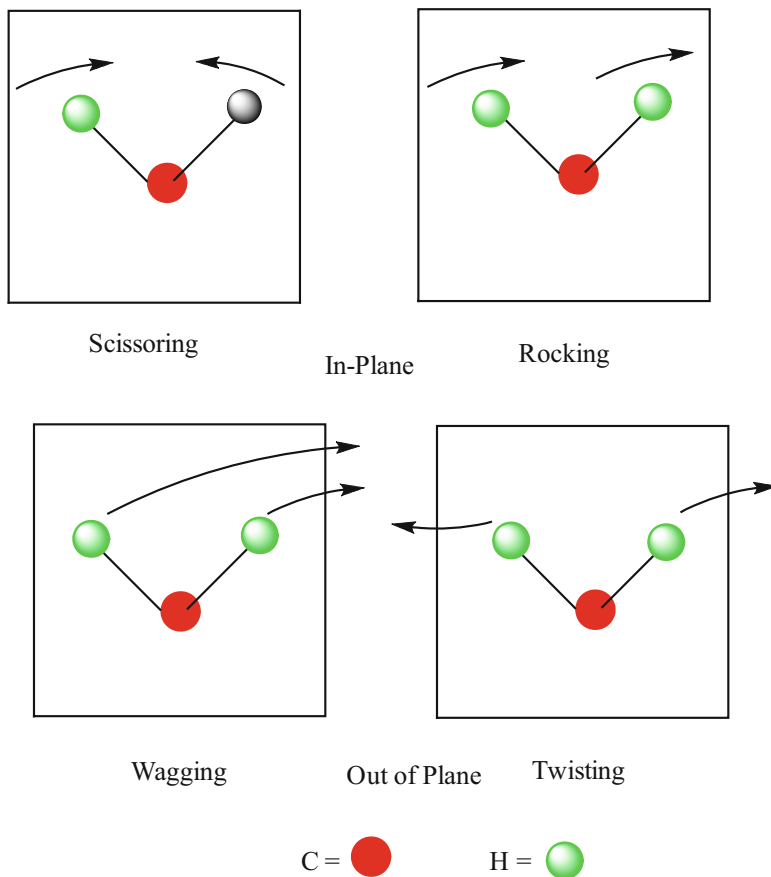


Fig. 9.7 Various modes of bending vibration in methylene group (CH_2). The in-plane comprises the scissoring and rocking vibrations, while the out of plane bending vibrations consist of wagging and twisting

way for interpreting the spectrum. Prior to the sample analysis, the background is recorded, to avoid air and water vapor contamination peaks. The proportion of the background and the sample spectrum are directly related to the absorption spectrum of the sample. The absorption spectrum indicating various vibrations of the bonds presents in the sample molecule. Several modes arise due to the various bond vibrations. So, in this way one can easily identify the functional group in a molecule.

9.5 Instrumentation

The typical FTIR spectrometer consists of an IR light source, interferometer, sample compartment, detector, amplifier, and computer. The light source generates radiation which strikes the sample passing through the interferometer and reaches the detector. Then the signal is amplified and converted to digital signal (interferogram) by the amplifier and analog-to-digital converter, respectively. Eventually, the interferogram is translated to spectrum through the fast Fourier transform algorithm. Michelson interferometer is the main core of FTIR spectrometer and is shown in Fig. 9.8 [12, 16]. The interferometer consists of a beam splitter, fixed mirror, and a moveable mirror that translates back and forth, very precisely. The beam splitter is made of a special material that transmits half of the radiation striking it and reflects the rest half of the radiation. It works on the basis of principle that the light from the source is collected by collimating mirror and made its rays parallel, which strikes beam splitter and consequently splits into two beams. One beam is transmitted through the beam splitter to the fixed mirror, and the second is reflected off the beam splitter to the moving mirror. The fixed and moving mirrors reflect the radiation back to the beam splitter. Accordingly, both of these reflected radiations are recombined at the beam splitter, resulting in one beam that leaves the interferometer and interacts with the sample and strikes the detector, as shown in Fig. 9.8.

Principally, FTIR (Fourier transform infrared) is a method of obtaining infrared spectra, which includes initially the collection of an interferogram of a sample signal using an interferometer and then performance of a Fourier transform (FT) on the

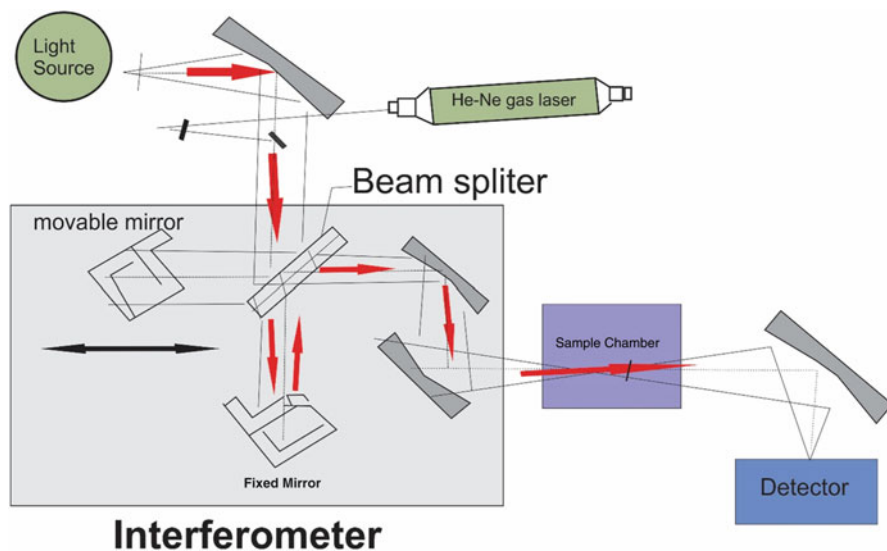


Fig. 9.8 Instrumentation of the double-beam (top) and single-beam (bottom) IR spectrophotometers

interferogram to obtain the spectrum. An FTIR spectrometer collects and digitizes the interferogram, performs the FT function, and displays the spectrum.

9.5.1 Interferometer and Interferogram

The interferometer or interference meter, an optical device, is an important part of the FTIR instrument, which is diagrammatically shown in Fig. 9.8. Principally, the light coming from an infrared source entered the interferometer, where the single light beam splits into two light beams. The interferometer makes these two light beams to travel at different paths, which are denoted by d_1 for beam 1 and d_2 for beam 2, respectively. The optical path difference (OPD) of an interferometer is denoted by the Greek letter small delta (δ), which is the difference in distance traveled by the two light beams. For instance, if the path d_1 is 4 cm long and d_2 is 10 cm long, the optical path difference is $10 - 4 \text{ cm} = 6 \text{ cm}$. If the distances of the two light beams travel in the interferometer are identical, then $\delta = 0$, the condition is called zero path difference (ZPD), which occurred when the moving and fixed mirrors are at the same distance from the beam splitter. After traveling of these two beams at their different paths, they recombined into one beam, and then the light beam leaves the interferometer (Fig. 9.8).

The most common type of interferometer used in FTIR nowadays is the Michelson interferometer, named after Albert Abraham Michelson (1852–1931), who first designed this interferometer in the 1880s [17] and won the Nobel Prize in Physics for his discoveries made with it. The Michelson interferometer has already been explained above in the same experimental Sect. 9.5. However, it is important to mention here that how the two light beams recombine into one at the beam splitter. It is usually a characteristic of the waves; they interfere with each other, when they superposed, which means their amplitudes add together to form a single wave. In a Michelson interferometer, the light beams reflected from the fixed and moving mirrors undergo interference, which may be constructive or destructive. If the final amplitude of the resultant beam after interference is greater than the amplitudes of the fixed mirror beam and moving mirror beam, this means that the two beams undergo *constructive interference*. If the final amplitude of the resultant beam is less than the amplitude of either of the two beams, a *destructive interference* has taken place. The square of the amplitude of a light beam is proportional to its intensity. This phenomenon can be explained by a simple example, a candle is usually dim because it gives visible light of low amplitude, and the sun is intense because it gives visible light with high amplitude. When the two light beams in an interferometer interfere with each other (meaning of the word interferometer), the resulting signal pattern obtained called as interferogram.

We are going to explain in a simple understandable way how this interferogram is formed in a Michelson interferometer. It is noteworthy that in case of constructive interference, the optical path difference (OPD) between the fixed mirror and moving mirror beams is $\delta = n\lambda$ ($n = 0, 1, 2, \dots$ integral numbers), means that waves

of both beams are in phase with each other and their crests and troughs are overlapped. Therefore, the final amplitude of the resulting interfere wave is greater than the amplitude of either beam wave by itself. Whereas, in case of destructive interference, the OPD between the fixed mirror and moving mirror beams is $\delta = 1/2\lambda$, which means that waves of both beams are out of phase with each other and the crests of the one beam wave are overlapped with troughs of the other one. Therefore, their amplitudes cancel, and the final amplitude is less than the amplitude of either beam wave by itself. Similar phenomenon occurred during the formation of interferogram in the Michelson interferometer.

We simply assume here that a single wavelength light beam passed the interferometer, splits by beam splitter, and undergoes interference to give interferogram. At zero path difference ($\delta = 0\lambda = 0$), the intensity is large because the fixed mirror and moving mirror beams are in phase and constructive interference takes place. As we gradually move ($\delta = 1/2\lambda$) the moving mirror away from the beam splitter, the two beams (fixed and moving beams) grow out of phase with each other, and the resultant beam becomes dimmer due to destructive interference and gives minimum intensity (Fig. 9.9). As the moving mirror continues to move ($\delta = \lambda$), the beams become more in phase, and the resultant beam gains its intensity

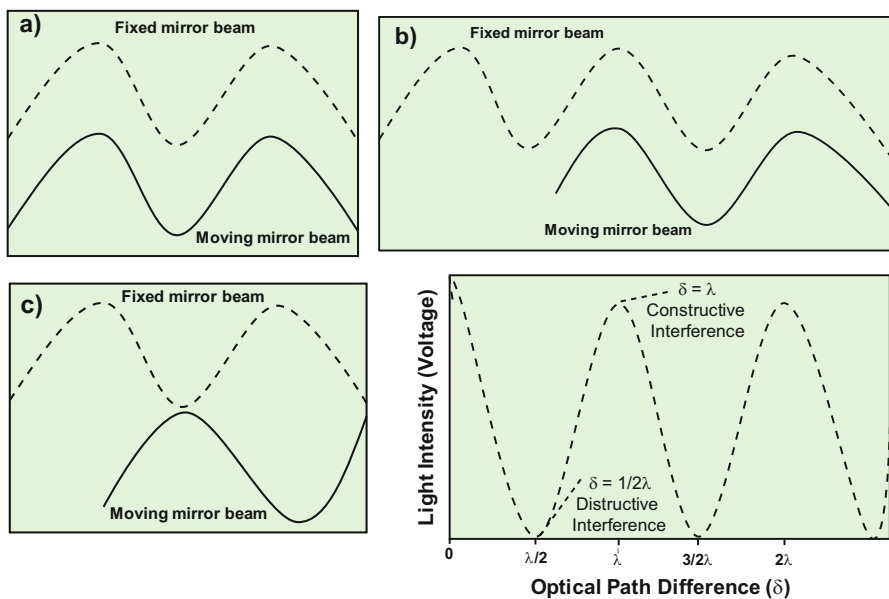
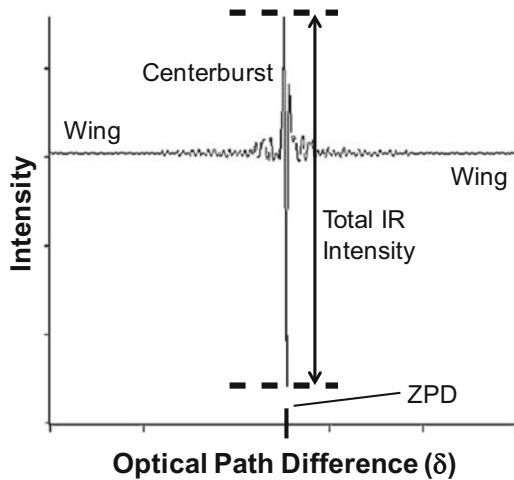


Fig. 9.9 Schematic illustrations of the fixed mirror and moving mirror beams that are present at (a) zero optical path distance ($\delta = 0$), in phase and undergoing constructive interference, (b) optical path distance of $\delta = \lambda$, undergoing constructive interference, and (c) optical path distance of $\delta = 1/2\lambda$, undergoing destructive interference as well as (d) interferogram for a single wavelength of light passing through the interferometer, showing a plot of light intensity (or detector signal) versus optical path difference for a mirror moving in a Michelson interferometer [18]

Fig. 9.10 Schematic illustration of the real case interferogram obtained when many wavenumbers of IR light pass through the interferometer together [18]



again. Consequently, the resultant beam intensity grows dimmer and brighter and passes through maxima and minima, as the moving mirror continuously moves. If the measured light intensity versus optical path difference is plotted, the graph obtained is called an *interferogram* (Fig. 9.9), which means “interference writing.”

It should be notified that the shape of the interferogram as shown in Fig. 9.10 is a cosine wave and it looks like a light wave, but the interferogram is the electrical signal coming out from the detector. Therefore, the y-axis unit in this Figure is presented in voltage. Remember that we have assumed only one wavelength of light passing through the interferometer and making the interferogram. The IR light source through an IR beam containing large number of wavelengths (wavenumbers) passes through the interferometer together. For each of these wavenumbers, there exists an interferogram with a unique Fourier frequency. The detector measures the sum of these individual interferograms, as shown in Fig. 9.10.

It is noteworthy that a large burst of infrared intensity at zero path difference can be observed that is called as *centerburst*. At ZPD all the wavelengths of light are in phase and constructively interfere, consequently giving high-intensity centerburst, which size is proportional to the total amount of infrared light striking the detector. In addition, it can be observed in Fig. 9.10 that as the optical path difference changes, the infrared intensity falls off quickly on both sides of the interferogram called as *wings*. The low intensity of the wings might be due to the increasingly out of phase of the various Fourier frequencies [19] with each other and consequently their destructively interference because of the increasing the optical path difference.

9.5.2 Fourier Transform of Interferogram to Spectrum

Fourier transform, named in the honor of French mathematician and physicist Jean Baptiste Joseph Fourier (1768–1830). It is a mathematical method to transform a function into a new function. Fourier transform contains a complicated discussion of mathematics; here we demonstrate to the readers a simple picture that how Fourier transform works qualitatively to convert an interferogram to its spectrum. Please, recall from the above discussion in Sect. 9.5.1 that an interferogram is a superposition of cosine waves. Therefore, when we Fourier transform an interferogram, a new mathematical function is obtained that corresponds to the interferogram. This function is the spectrum of the infrared beam that hits the detector.

It is important to know, when a Fourier transform is applied to a function, the crucial changes that occur are the inversion of the x -axis units of that function. For instance, an interferogram is a plot of infrared intensity versus optical path difference (OPD), which can be measured in centimeters as discussed earlier in Sect. 9.5.1. When an interferogram is Fourier transformed, a function is obtained that is a plot of infrared intensity versus cm^{-1} . The unit of wavenumber is cm^{-1} ; therefore, a plot of infrared intensity versus wavenumber is an FTIR spectrum as shown in Fig. 9.11. The Fourier transform of any interferogram produces a *single-beam spectrum*, which is a plot of arbitrary infrared intensity versus wavenumber (Fig. 9.11). The term “single beam” is from the fact that there is only one infrared beam used in an FTIR. However, there are some other types of infrared spectrometers, which use two beams.

A single-beam spectrum obtained without a sample is called a background spectrum, which is the characteristic of the instrument and the measuring environment. In this spectrum the characteristic bands around 3500 cm^{-1} and 1630 cm^{-1} are attributed to the atmospheric water vapor, and the bands at 2350 cm^{-1} and 667 cm^{-1} are ascribed to atmospheric carbon dioxide. Therefore, background spectrum must always be run when analyzing sample by FTIR. The single-beam spectrum of the sample obtained after Fourier transformation of interferogram looks similar to the background spectrum except that the peaks of the sample are superimposed upon the instrumental and atmospheric bands. To eliminate these characteristic bands contributed from instrument and atmosphere, the spectrum of the sample must be normalized against the background spectrum. Consequently, a transmittance

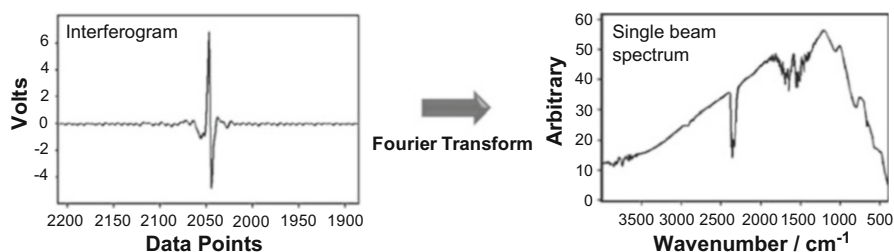


Fig. 9.11 Fourier transform of interferogram to produce a single-beam spectrum [18]

spectrum is obtained as follows:

$$\%T = I/I_0 \quad (9.6)$$

where $\%T$, transmittance; I , intensity of the measured sample in the beam (single-beam spectrum); and I_0 , intensity of the background spectrum.

The absorbance spectrum can be calculated from the transmittance spectrum by the following relation:

$$A = -\log_{10} T \quad (9.7)$$

where A is the absorbance.

Therefore, the final transmittance/absorbance spectrum should be devoid of all instrumental and environmental contributions and shows only the characteristic absorption bands of the sample.

9.5.3 Detectors

Detectors convert the thermal or light energy into electrical signal. Thermal and photodetectors are the two main types of detectors used in the FTIR spectrophotometer.

9.5.3.1 Photon Detectors

Semiconductor IR detectors are the most sensitive detectors in the IR spectrometer, which convert photon energy into electrical charge by the internal photoelectric effect. Liquid nitrogen cooled HgCdTe (MCT), InSb, and In(Ga) detectors are a few examples of quantum detectors, which are designed to achieve good performance in FTIR spectrometers. In this class of detectors, the radiation is absorbed within the material which promote the electrons from valence band to the conduction band of the materials resulting in observed electrical output signal. The higher sensitivity is the major advantage of quantum detectors. However, narrower spectral range is the major limitation in quantum detectors. HgCdTe detectors work from 8 to 13 μm of the spectral range. Similarly, PbS and PbSe detectors are sensitive from 1 to 3 μm and 1 to 6 μm , respectively, while the InSb from 1 to 5.5 μm and InAs from 1 to 3.5 μm spectral ranges, respectively.

9.5.3.2 Thermal Detectors

This type of detector measures a change in temperature of a material by absorbing the incident electromagnetic radiations. Thermal detectors transformed thermal

energy to electrical signals. Bolometers, thermopiles, thermocouples, pyroelectric, photoacoustic, and pneumatic detectors are some of the most common thermal detectors. Thermal detectors usually used a broad spectral range.

9.5.3.3 Pyroelectric Detectors

Pyroelectric effect is the variation in the spontaneous polarization of a piezoelectric crystal with change in temperature. As compared to the other thermal detectors, the pyroelectric detectors are robust and inexpensive and have comparatively constant sensitivity range through the whole spectral range. Triglycine sulfate (TGS) and deuterated TGS (DTGS) detectors are common example of pyroelectric detectors. The TGS and DTGS detectors measure the voltage due to the change in temperature by changing their capacitance; however, less sensitivity makes them less efficient.

9.5.3.4 Bolometers

Bolometers detect the change in temperature by changing their resistance. For instance, Si- and Sb-doped Ge semiconductors are the example of bolometer detectors. Bolometers are quite sensitive, but their main disadvantage is the requirement of liquid He as well as their slow process.

Cryogenic bolometers are the most sensitive detectors which can detect from 100 to 1000 μm wavelength range. Such type of detectors converts the light to electric current. Photodiode is the most common high-speed semiconductor detector, which absorbs light and converts it into electrical signals. The signal power limit of the device is resolute by its capacitance and by its junction area. HgCdTe and PbSnTe photodiodes are the examples of high-speed detectors.

9.5.4 *Infrared Red Radiation Sources*

Different types of lamps are generally used in FTIR with different ranges. For the mid-IR radiation, the silicon carbide is heated to approximately 1200 K. Higher temperature source like tungsten-halogen lamp is used for the near-IR range (shorter wavelengths). The long wavelength output of these is limited to about 5 μm (2000 cm^{-1}) by the absorption of the quartz envelope. For the far-IR, especially at wavelengths beyond 50 μm (200 cm^{-1}), a mercury discharge lamp gives higher output than a thermal source.

9.5.5 Sample Holders in FTIR

There are several types of sample holders used in the FTIR spectrometer as explained below:

Universal sample holder – It is constructed in a spring-loaded mechanism that easily placed KBr pellets, salt plates, films, and other materials. The holder's aperture is 10–20 mm with high sample mounting controllability.

Heavy-duty magnetic film holder – This type of holder is made up of polymer materials. This holder has 20 mm hole with big size steel plate and magnet.

Magnetic film/pellet holder – This type of holder is designed to keep thin polymer films having 0.5 mm size and KBr pellets with 13 mm thickness, comprising of an elastic magnetic strip and steel plate.

Press-on demountable cell holders – It is used for the investigation of mull and smears. 25 mm and 38 mm versions are available and both form containing pressure cap and mounting plate.

Single-pellet holder – This type sample holder is more convenient as compared to dual-pellet holder in virtue of its 7 mm pellets. The PIKE Technologies Hand Press and Pixie Hydraulic Press used this technology.

Dual-pellet holder – Its features are 1, 3, and 7 mm KBr pellet semicircular supports with holes and are helpful in the specified size pellets. The PIKE Technologies Sampling Cards are low-cost sample holders for the examination of polymers, films, and KBr pellets (13 mm). The cards deal with compressed and a suitable means of sample storage.

Bolt press and gas cell holders – These holders are used to mount large sample and salt plate. Three different forms of these holders are available with supported rods having different sized fixtures and are easily separable.

9.5.6 Sample Preparation

The sample preparation is very important for IR spectra analysis where the sample is placed in the cell or in the holder. It is very problematic because IR radiations are strongly absorbed by glass and plastic materials throughout the entire IR range. The cell is constructed of ionic materials, such as KBr or NaCl. The KBr plates are expensive, but they have advantages over NaCl, as they can record IR spectra from 400 to 4000 cm^{-1} . However, NaCl plate is also largely used due to its low cost and recorded spectra from 650 to 4000 cm^{-1} . NaCl is absorbed at 650 cm^{-1} , and very few bands are supposed to absorb in this region; therefore, it is commonly used in the routine experiment. The CO_2 and H_2O from the atmosphere usually appeared in the compound spectrum which causes problem during the interpretation of the spectrum. Therefore, it is very important to run background spectrum so that it is automatically subtracted from the compound spectrum. Between the polished NaCl or KBr plates, a drop of liquid is placed, known as salt plate. After pressing

the plates, a thin film is formed. The pair of plates is inserted in the holders. The spectrum obtained during this method is called as neat spectrum because it is free of solvent. Moreover, being ionic in nature, these salt plates are easily soluble in water; therefore, it is recommended that the compounds must be free of water.

Three methods are available for solid sample. In the first method, the compounds are finely grounded with KBr salt and then pressed at high pressure to form pellets called KBr pellets. However, KBr absorb water which gives water peaks in the spectrum and hindered the peaks originated from the compounds. Nevertheless, if KBr plates are prepared carefully by avoiding the absorption of moisture, no peak will appear in the spectrum. The other advantage is that KBr is transparent below 400 cm^{-1} .

In another method called Nujol mull, the compound is finely grounded with the mineral oil called Nujol, as a result a thick suspension is formed which is placed between the plates. The main drawbacks of this method are the Nujol peaks which appeared at 2924 , 1462 , and 1377 cm^{-1} that might interfere with for compounds having peak in these regions. In the third method, the compound is dissolved in solvent. Chloroform (CCl_4) is mostly used, because it dissolves most of the organic compounds; however, like Nujol the CCl_4 peaks appeared and interfere with the compounds peak at approximately 700 cm^{-1} .

9.6 IR-ATR (Attenuated Total Reflection)

Due to the drawbacks associated with KBr pellets and liquid cells method, FTIR measurements are largely achieved in attenuated total reflection (ATR) mode because of its simplicity as compared to the conventional transmission mode. Various samples such as liquids, solids, pastes, fiber pellets, powders, slurries, and many other are placed without any treatment on the ATR crystal. It is a fast technique and the data is obtained in a few seconds. This can be achieved practically without any major sample preparation. IR-ATR provided an advantage that the sample can be investigated without interruption. Thus, biofilm removal from its support, which modifies its structure significantly from its natural form, can be avoided. Additionally, very thin films and surface coverings can be examined, which are not available to normal chemical approaches. Particularly ATR is an extremely good technique for polymer and membrane science. The key advantage of ATR is its aptitude for the measurement of varieties of samples such as solid and liquid samples without the need of complex steps.

In this approach, the IR ray enters the ATR crystal at 45° relative to the crystal surface and is entirely reflected at the crystal to sample interface. Because of its wavelike properties, the light is not reflected directly by the boundary surface but by a computer-generated layer within the optically less dense sample. Evanescent wave is a fraction of light which reached to the sample. The penetration depth depends on the wavelength, the refractive indices of the ATR crystal and the sample, as well as the angle of the incident light. Characteristically, it is of the order of a few microns

(0.5–3 μm). The evanescent wave is attenuated in the spectral regions, where the sample absorbs energy. After one or numerous internal reflections, the IR beam exits the ATR crystal and is directed to the IR detector.

9.6.1 Instrumentation of ATR-FTIR

The ATR units are designed as horizontal crystals with a type of fastening usefulness that guarantees good contact between sample and solids. In case of liquid or viscous material, a small drop of the sample is sufficient for its measurement. Crystal constituents are mostly made up of zinc selenide (ZnSe), diamond, and germanium.

For liquid and “soft” samples analysis, ZnSe is appropriate because it is an inexpensive material; however, scratches are made on ZnSe and can only be used between pH 5 and pH 9. For the study of highly absorbing colored samples such as rubbers and carbon black, germanium material is the choice due to its high refractive index. Similarly, for high-surface sensitivity, like thin layers, Ge is perfect because of its low penetration depth. Diamond is chemically inert and also an ideal substance for the manufacturing of crystal surface materials. Although making the crystal material from diamond is quite expensive, however, the reliability of the instrument due to the high resistance of diamond to cut and scrap and its complete insolubility make diamond an ideal material for ATR-FTIR crystal formation. The stepwise procedure for an ATR is as follow: (i) clean the crystal (e.g., with a cellulose tissue and isopropanol); (ii) then measure the instrument background within the ATR unit; and (iii) after that place the sample on the crystal confirming the good contact, record the sample, and save the document.

9.7 FTIR for Materials Characterization

FTIR is an efficient spectroscopic technique to characterize the structure of the following materials.

9.7.1 Organic Compounds

FTIR is largely used for the study of organic molecules, which brought mainly two types of changes in the molecules: stretching vibration causes of change in the bond length and bending vibration causes of change in the bond angle. Change in the bond length usually occurred at higher frequency or energy because stretching required higher energy as compared to bending vibrations. According to Hooke’s law, increasing the mass of the atoms will vibrate the atoms at lower frequency or lower energy. For instance, in organic molecules the most common bonds in the

Table 9.2 Range in wavenumber (cm^{-1}) of various functional groups

Range (cm^{-1})	Functional group
3200–3550	O-H stretching
2500–3000	Carboxylic O-H
3300–3500	N-H stretch, primary amine gives two, secondary one, while tertiary amine gives no peak
3500–3500	O=C-N-H stretch
2260–2220	Nitrile (CN)
2950–2850	C-H stretch
3010–3100	=C-H stretch
1620–1680	C=C stretch
1740–1690	Aldehyde C=O
1750–1680	Ketone C=O
1750–1735	Ester C=O
1780–1710	Carboxylic acid C=O
1690–1630	Amide C=O
2800–2700	Aldehyde C-H stretch

molecule are C-C, C-H, C-X, C-O, C-N, etc. While dealing the FTIR spectrum of compounds containing C-H, C-D, and C-C bonds, the stretching vibration of C-H (2900 cm^{-1}) appeared at higher frequency as compared to C-D (2100 cm^{-1}) and C-C at (1200 cm^{-1}); the same order is true for bending vibrations. If the molecule has C-F, C-Cl, C-Br, and C-I, the stretching vibration will appear as C-F > C-Cl > C-Br > C-I (descending order of energy). The molecule containing multiple different bonds, for instance, C-C, C=C, and C \equiv C, the absorption will occur according to the strength of bonds, for example, triple bond is more stronger as compared to double and single, so the C \equiv C stretching vibration will appear at 2200 cm^{-1} , C=C at 1600 cm^{-1} , and C-C bond at 1200 cm^{-1} , respectively.

For the organic molecule, the infrared spectrum can be usually divided into four parts (Table 9.2):

- (i) $4000\text{--}2500 \text{ cm}^{-1}$: Single bonds absorption of hydrogen with other elements, e.g., O-H, N-H, and C-H.
- (ii) $2000\text{--}2500 \text{ cm}^{-1}$: Triple bonds absorption, C \equiv C and C \equiv N.
- (iii) $1500\text{--}2000 \text{ cm}^{-1}$: Double bonds absorption, e.g., C=C and C=O.
- (iv) $400\text{--}1500 \text{ cm}^{-1}$: The region from 1000 to 1500 cm^{-1} is usually used for C-O and C-C and other bending vibrations. The region $700\text{--}400 \text{ cm}^{-1}$ is usually called the fingerprint region which is unique for various compounds and rarely used for the identification of functional groups.

The H-X bonds are more prominent in the organic molecules. For instance, the C-H asymmetric stretching vibrations appeared at approximately 2900 cm^{-1} . There are different types of C-H stretching vibration, for instance, in case of unsaturated vibrations, the C-H sp (H-C \equiv C) will appear at approximately 3300 cm^{-1} due to the higher bond strength of sp bond, while C-H sp² (H-C=C) are above 3000 cm^{-1} ,

and C-H sp^3 are below 3000 cm^{-1} . The different bond strengths and absorptions are explained on the basis of their bond strength, which is due to the increase in s character of these bonds. The aldehyde exhibited two weak bands at 2850 and 2750 cm^{-1} . The C=C of the benzene ring appeared at 1600 – 1500 cm^{-1} , and the bending vibration of aromatic hydrogen Ar-H appeared at the range of 700 cm^{-1} . Similarly, the CH_3 bending vibrations appeared at 1460 and 1375 cm^{-1} , while the bending vibration of CH_2 appeared at 1465 cm^{-1} . The bending vibrations of CH_3 (asymmetric) and CH_2 are not mostly resolved and overlapped with each other. The O-H vibrations appeared at 3300 – 3600 cm^{-1} . If the O-H group makes hydrogen bonding to any other group inter- or intramolecular, the bond becomes weak, and a broadband will appear at lower frequency at approximately 3300 cm^{-1} . In case of free O-H (no hydrogen bonding), a sharp peak will appear at approximately 3600 cm^{-1} . The N-H appeared at 3300 – 3400 cm^{-1} . There are three types of N-H bonds: primary, secondary, and tertiary. The primary N-H gives two peaks, secondary one and tertiary indicating no peak at all.

9.7.2 Nanomaterials

Any solid materials with one of its dimension fewer than about 100 nm are known as nanoscale materials or nanomaterials. Nano is one billionth 10^{-9} and is one millionth of a millimeter. It was revealed that a nanomaterial is almost $100,000$ times lesser than the human hair. Nanomaterials size is lying somewhere between the atoms or molecules size and a bulk structure of the molecules [13]. This small size of the particle (one millionth of a millimeter), abruptly, increases the surface/volume ratio, and, therefore, many vital physical and chemical characteristics are expressively improved, which are completely different from their bulk counterparts. Although, nanomaterials and their bulk counterparts organize the same materials, but smaller particles indicate absolutely diverse physicochemical or electromagnetic properties from their bulk counterparts [20]. FTIR spectra of various metal oxide and doped metal oxide are discussed below:

FTIR spectrum of zinc oxide – For ZnO, the absorption peak at 1050 cm^{-1} indicated the presence of Zn-O bond, whereas the peaks at 1406 and 1575 cm^{-1} exhibited the presence of carbonate anion. Moreover, the absorption peak at 3408 cm^{-1} is indicative of O-H stretching vibration. When ZnO is mixed with graphene oxide (GO), some characteristic peak appeared for the GO along with ZnO at 1050 , 1621 , 1735 , and 3436 cm^{-1} due to the C-O bond, carboxyl groups, aromatic structure, and O-H groups, respectively [21]. The general FTIR spectrum for nanomaterials is depicted in the inset of Fig. 9.12.

FTIR spectrum of cobalt oxide – The Co_3O_4 exhibited absorption bands for M-O at 567 cm^{-1} , M-O-M, stretching at 655 cm^{-1} , whereas the absorption peak at 1374 cm^{-1} is indicative of the presence of carbonate (CO_3^{-2}) anions. If we look at the core-shell structure of $\text{Co}_3\text{O}_4/\text{SiO}_2$, it displayed various absorption bands at 1605 cm^{-1} for the O-H bond and absorptions from 1086 – 1320 cm^{-1} due to the presence of SiO_2 [22] as depicted in Fig. 9.12.

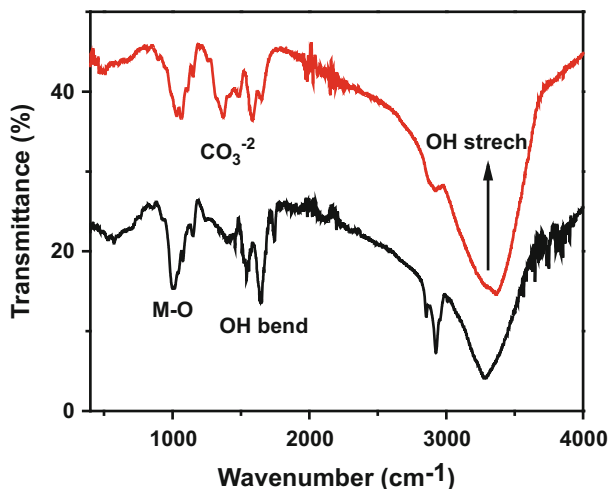


Fig. 9.12 Generalized FTIR spectra of various M-O bond, CO_3^{-2} , and O-H stretching and bending vibration

FTIR spectrum of titanium oxide – The Ti-O bond usually shows absorption band at 818 cm^{-1} in the TiO_2 catalyst, while a sharp band may be observed at 3747 cm^{-1} indicating the O-H group. When TiO_2 is mixed with polyaniline (PANI), some characteristics absorption bands of PANI at 1308, 1494, 1567, 3268, and 3747 cm^{-1} appeared in their FTIR spectrum [23].

FTIR spectrum of iron oxide – The iron oxide displayed absorption peaks at 431 and 525 cm^{-1} which clearly indicated the metal oxide bond in the sample. In the doped $\text{Co}_3\text{O}_4/\text{Fe}_2\text{O}_3$, peaks for M-O appeared along with the presence of carbonate group [22].

FTIR spectrum of cadmium oxide – The CdO absorbance appeared in the FIR spectrum at 462, 542, 780, and 1107 cm^{-1} . A sharp peak at 3435 cm^{-1} in CdO_2 exhibited the stretching vibration of water molecule. The sharp peak indicated the absence of hydrogen bonding, while the bending vibration of H_2O in CdO_2 nanomaterial appeared 1623 cm^{-1} [24] as depicted in Fig. 9.12.

9.8 Applications

9.8.1 FTIR in Biomedical Imaging

FTIR spectroscopic imaging is a chemical imaging technique which is very important to investigate the biological samples. For characterizing the biomedical sample, FTIR spectroscopy has advantages over other imaging techniques because

it detects specific molecular vibrations in the chemical bonds of molecules. FTIR imaging technique does not require the dyes for labeling or visualization in various samples, and its application is largely reported in medical imaging samples [25]. There are several examples which indicate the application of FTIR in medical imaging techniques. For instance, it is used in human colorectal adenocarcinoma studies [26]. Similarly, the deposition of β -amyloid protein in human brain tissue slice, comprising the Alzheimer's diseases, have been investigated through FTIR spectroscopic imaging techniques [27].

The ATR-FTIR imaging technique is important in the biomedical field [28]. Many examples are available in the literature regarding ATR-FTIR in imaging techniques [25, 29]. Thus ATR-FTIR is the key for the potential characterization of biomedical samples in tissue engineering. In the ATR-FTIR mode, the sample preparation is very simple because the penetration depth of IR radiation does not depend on the sample thickness. For reliable and appropriate FTIR images, place the sample directly on the diamond ATR crystal which will result in good interaction of sample with the ATR crystal [30]. The biological tissue such as the aorta, small force is applied to the cross section of the aorta for better images [31]. The FTIR imaging of a brain tumor tissue section is indicated in the inset of Fig. 9.13.

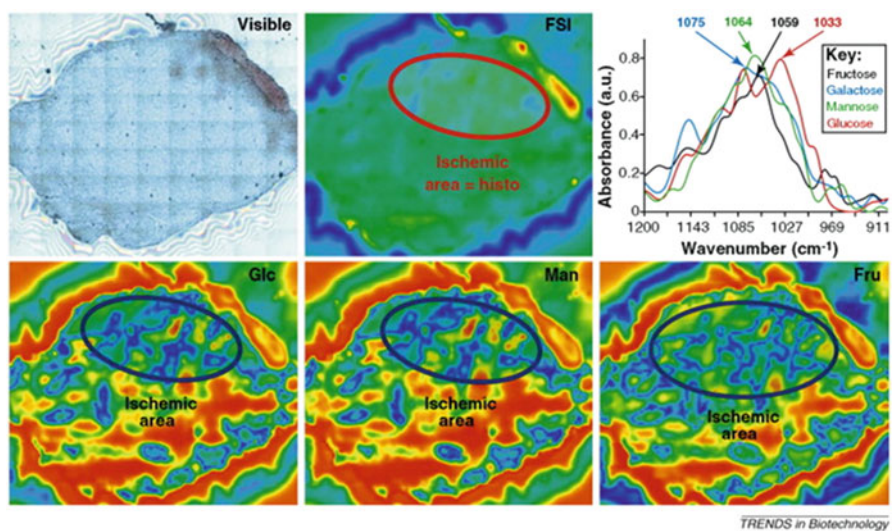


Fig. 9.13 FTIR imaging of a brain tumor tissue section, including full spectral image (FSI; 4000–500 cm^{-1} spectral integration) and chemical mapping of saccharides. The example provided shows that very similar results are obtained on chemical mapping with glucose absorption found at 1033 cm^{-1} (Glc), a mannose absorption band at 1064 cm^{-1} (Man), or a fructose absorption band at 1059 cm^{-1} (Fru) [32]

9.8.2 *FTIR in Proteins Study*

The infrared spectroscopy came into existence since the discovery of IR radiation in sunlight in 1800 by Sir William Herschel, an astronomer [33]. William Coblentz described the IR spectra of various sample in 1905 [34, 35]. After World War II, advancement occurred in double-beam dispersive IR spectrometer, and thereby IR spectroscopy was considering a common analytical apparatus for the researcher and had been applied in diverse scientific fields, including the characterization of protein molecules [36, 37].

In 1950, the structure of proteins was investigated by Ambrose and Eliot with the use of IR spectroscopy [38, 39]. Similarly, Miyazawa studied N-methylacetamide for the investigation of proteins molecule through IR spectroscopy [40, 41]. The structure of protein was investigated using X-ray crystallography; however, multidimensional NMR spectroscopy can help in the elucidation of protein structure determination. In many cases these techniques cannot be applied properly. In many cases the FTIR can be applied for the structural determination of protein. There are two major bands in the FTIR spectrum of protein known as amide I ($1600\text{--}1700\text{ cm}^{-1}$) and amide II. The amide I is the most intense band due to C=O stretching vibration, while amide II is due to the N-H bending vibration and C-N stretching vibration [42].

9.8.3 *Miscellaneous Applications of FTIR Spectroscopy*

FTIR is an extremely important tool for the detection of large range samples in different fields. For instance, resins, adhesives, paints, coatings, polymers, metal oxides, and large number of drugs can be analyzed with the help of this technique. For instance, different nature samples such as gummy materials, solids, liquids, and solution can be analyzed and identified with the help of FTIR. The identification of diverse range of organic and inorganic compounds can be analyzed through this technique. Polymers and polymer blends as well as indirect verification of trace organic contaminants on surfaces of various materials can be analyzed. Routine qualitative and quantitative analyses can be performed. With the help of FTIR adhesives, coatings and adhesion promoters or coupling agents as well as thin film can be easily analyzed. We can analyze stains and surface blemishes remnant from cleaning and degreasing processes through FTIR in combination with optical microscopy, SEM/EDX, XPS, and SIMS techniques. We can identify rubbers and filled rubbers through this technique, and the degrees of crystallinity in polymers can be determined through FTIR, for instance, low-density polyethylene (LDPE) and high-density polyethylene (HDPE) can be identified. Similarly, comparative chain lengths in organic molecules can also be differentiated through this method. We can also analyze the gaseous samples using a gas cell for the headspace analysis or environmental monitoring process.

9.9 Conclusion and Future Prospective

The advancement in the FTIR spectroscopy specifically for the characterization of materials is now well-known and is steadily increasing. The capability of FTIR to characterize chemical and biological materials is exponentially arising. In this chapter we provided the in-depth detail about the infrared spectroscopy. Spectral region with respect to infrared, instrumentation, and basic principal of FTIR has been discussed. Sample preparation techniques and various functional group ranges in organic compounds and nanomaterials are explained in detail. Finally, the application of FTIR in various scientific fields has been explored. This chapter will help the readers and scientific community about the detailed and advanced knowledge of infrared spectroscopy. In future prospect we will address the addition of novel accessories to the FTIR and will mechanistically explained the role of FTIR spectroscopy in the biological sample.

Acknowledgment The authors highly acknowledge the Chemistry Department and Center of Excellence for Advanced Materials Research King Abdulaziz University, Jeddah, Saudi Arabia and Department of Chemistry, University of Swabi, Anbar, Khyber Pakhtunkhwa, Pakistan for providing facility.

References

1. Shrivastava, N., Khan, L., Vargas, J., Ospina, C., Coaquira, J., Zoppellaro, G., Brito, H., Javed, Y., Shukla, D., & Felinto, M. (2017). Efficient multicolor tunability of ultrasmall ternary-doped LaF₃ nanoparticles: Energy conversion and magnetic behavior. *Physical Chemistry Chemical Physics*, *19*, 18660–18670.
2. Khan, L. U., Brito, H. F., Hölsä, J., Pirota, K. R., Muraca, D., Felinto, M. C., Teotonio, E. E., & Malta, O. L. (2014). Red-green emitting and superparamagnetic nanomarkers containing Fe₃O₄ functionalized with calixarene and rare earth complexes. *Inorganic Chemistry*, *53*, 12902–12910.
3. Herschel, W. (1800). XIII. Investigation of the powers of the prismatic colours to heat and illuminate objects; with remarks, that prove the different refrangibility of radiant heat. To which is added, an inquiry into the method of viewing the sun advantageously, with telescopes of large apertures and high magnifying powers. *Philosophical Transactions of the Royal Society of London*, *90*, 255–283.
4. Jacquinet, P. (1954). The luminosity of spectrometers with prisms, gratings, or Fabry-Perot etalons. *JOSA*, *44*, 761–765.
5. Fellgett, P. (1958). Equivalent quantum-efficiencies of photographic emulsions. *Monthly Notices of the Royal Astronomical Society*, *118*, 224–233.
6. Connes, J. R. (1961). Recherches sur la spectroscopie par transformations de Fourier, Éd. de la "Revue d'optique théorique et instrumentale.
7. Chamberlain, G. (1979). *Analysis of covariance with qualitative data*. Cambridge, MA: National Bureau of Economic Research.
8. Kauppinen, J., & Partanen, J. Frontmatter and index, fourier transforms in spectroscopy, i–ix.
9. Rubens, H., & Wood, R. (1911). XXVII. Focal isolation of long heat-waves. *The London, Edinburgh, and Dublin Philosophical Magazine and Journal of Science*, *21*, 249–261.

10. Rubens, H., & Von Baeyer, O. (1911). LXXX. On extremely long waves, emitted by the quartz mercury lamp. *The London, Edinburgh, and Dublin Philosophical Magazine and Journal of Science*, 21, 689–695.
11. Illingworth, K. (1927). A repetition of the Michelson-Morley experiment using Kennedy's refinement. *Physical Review*, 30, 692.
12. Camy-Peyret, C., Flaud, J.-M., Mandin, J.-Y., Chevillard, J.-P., Brault, J., Ramsay, D., Vervloet, M., & Chauville, J. (1985). The high-resolution spectrum of water vapor between 16500 and 25250 cm^{-1} . *Journal of Molecular Spectroscopy*, 113, 208–228.
13. Blakeney, A. B., Harris, P. J., Henry, R. J., & Stone, B. A. (1983). A simple and rapid preparation of alditol acetates for monosaccharide analysis. *Carbohydrate Research*, 113, 291–299.
14. Kauppinen, J. (1979). Working resolution of 0.010 cm^{-1} between 20 cm^{-1} and 1200 cm^{-1} by a Fourier spectrometer. *Applied Optics*, 18, 1788–1796.
15. Chen, Y., Zou, C., Mastalerz, M., Hu, S., Gasaway, C., & Tao, X. (2015). Applications of micro-fourier transform infrared spectroscopy (FTIR) in the geological sciences—a review. *International Journal of Molecular Sciences*, 16, 30223–30250.
16. Genzel, R., Lutz, D., Sturm, E., Egami, E., Kunze, D., Moorwood, A., Rigopoulou, D., Spoon, H., Sternberg, A., & Tacconi-Garman, L. (1998). What powers ultraluminous IRAS galaxies? *The Astrophysical Journal*, 498, 579.
17. Livingston, D. M. (1973). *The master of light: A biography of Albert Abraham Michelson*. Chicago: The University Press of Chicago.
18. Smith, B. C. (2011). *Fundamentals of fourier transform infrared spectroscopy*. Boca Raton: CRC press.
19. Johnston, S. F. (1991). *Fourier transform infrared: A constantly evolving technology*. New York: Ellis Horwood.
20. Ng, L. Y., Mohammad, A. W., Leo, C. P., & Hilal, N. (2013). Polymeric membranes incorporated with metal/metal oxide nanoparticles: A comprehensive review. *Desalination*, 308, 15–33.
21. Yao, H., Li, F., Lutkenhaus, J., Kotaki, M., & Sue, H.-J. (2016). High-performance photocatalyst based on nanosized ZnO-reduced graphene oxide hybrid for removal of rhodamine B under visible light irradiation. *AIMS Materials Science*, 3, 1410.
22. Khan, S. A., Khan, S. B., & Asiri, A. M. (2015). Core-shell cobalt oxide mesoporous silica based efficient electro-catalyst for oxygen evolution. *New Journal of Chemistry*, 39, 5561–5569.
23. Hidalgo, D., Bocchini, S., Fontana, M., Saracco, G., & Hernández, S. (2015). Green and low-cost synthesis of PANI-TiO₂ nanocomposite mesoporous films for photoelectrochemical water splitting. *RSC Advances*, 5, 49429–49438.
24. Thema, F., Beukes, P., Gurib-Fakim, A., & Maaza, M. (2015). Green synthesis of monteponite CdO nanoparticles by Agathosma betulina natural extract. *Journal of Alloys and Compounds*, 646, 1043–1048.
25. Kazarian, S., & Chan, K. (2006). Applications of ATR-FTIR spectroscopic imaging to biomedical samples. *Biochimica et Biophysica Acta (BBA) – Biomembranes*, 1758, 858–867.
26. Lasch, P., Boese, M., Pacifico, A., & Diem, M. (2002). FT-IR spectroscopic investigations of single cells on the subcellular level. *Vibrational Spectroscopy*, 28, 147–157.
27. Choo, L.-P., Wetzel, D. L., Halliday, W. C., Jackson, M., LeVine, S. M., & Mantsch, H. H. (1996). In situ characterization of beta-amyloid in Alzheimer's diseased tissue by synchrotron Fourier transform infrared microspectroscopy. *Biophysical Journal*, 71, 1672–1679.
28. Sommer, A. J., Tisinger, L. G., Marcott, C., & Story, G. M. (2001). Attenuated total internal reflection infrared mapping microspectroscopy using an imaging microscope. *Applied Spectroscopy*, 55, 252–256.
29. Kazarian, S. G., & Chan, K. A. (2006). Sampling approaches in fourier transform infrared imaging applied to polymers, *Characterization of polymer surfaces and thin films* (pp. 1–6). Springer. Berlin, Heidelberg.

30. Chan, K., & Kazarian, S. (2003). New opportunities in micro-and macro-attenuated total reflection infrared spectroscopic imaging: Spatial resolution and sampling versatility. *Applied Spectroscopy*, *57*, 381–389.
31. Colley, C., Kazarian, S., Weinberg, P., & Lever, M. (2004). Spectroscopic imaging of arteries and atherosclerotic plaques. *Biopolymers*, *74*, 328–335.
32. Petibois, C., & Desbat, B. (2010). Clinical application of FTIR imaging: New reasons for hope. *Trends in Biotechnology*, *28*, 495–500.
33. Herschel, W. (1801). Observations tending to investigate the nature of the sun, in order to find the causes or symptoms of its variable emission of light and heat; with remarks on the use that may possibly be drawn from solar observations. *Philosophical Transactions of the Royal Society of London*, *91*, 265–318.
34. Coblenz, W. W. (1905). *Investigations of infra-red spectra*. Washington, DC: Carnegie institution of Washington.
35. Smith, A. L. (1979). *Applied infrared spectroscopy: Fundamentals, techniques, and analytical problem-solving*. New York: Wiley.
36. Rothschild, K. J. (2016). The early development and application of FTIR difference spectroscopy to membrane proteins: A personal perspective. *Biomedical Spectroscopy and Imaging*, *5*, 231–267.
37. Derrick, M. R., Stulik, D., & Landry, J. M. (2000). *Infrared spectroscopy in conservation science*. Los Angeles: Getty Publications.
38. Elliott, A., & Ambrose, E. (1950). Structure of synthetic polypeptides. *Nature*, *165*, 921–922.
39. Elliott, A., Ambrose, E., & Robinson, C. (1950). Chain configurations in natures and denatured insulin: Evidence from infra-red spectra. *Nature*, *166*, 194–194.
40. Anderson, D., & Bellamy, L. J. (1975). *The infrared spectra of complex molecules*. London: Chapman and Hall xix+ 433 pp., price£ 8.00, Elsevier, 1976.
41. Miyazawa, T., & Shimanouchi, T. (1958). S.i. Mizushima, normal vibrations of N-methylacetamide. *The Journal of Chemical Physics*, *29*, 611–616.
42. Jabs, A. (2005). Determination of secondary structure in proteins by fourier transform infrared spectroscopy (FTIR), Jena Library of Biological Molecules [online][cited 16. 2. 2011]. Available online: http://www.imbjena.de/ImgLibDoc/ftir/IMAGE_FTIR.html.

Chapter 10

Rare Earth Luminescence: Electronic Spectroscopy and Applications



Latif Ullah Khan and Zahid U. Khan

Abbreviations

A	Acceptor
AD	Anno Domini
CAs	Contrast agents
CCD	Charge-coupled device
CET	Cooperative energy transfer
CFL	Compact fluorescent light
CIE	<i>Commission Internationale de l'Eclairage</i>
CRI	Color-rendering index
CT	Computed tomography
D	Donor
DCL	Down-conversion luminescence
ED	Electric dipole
EMU	Energy migration-mediated upconversion
ESA	Excited-state absorption
ET	Energy transfer
ETU	Energy transfer upconversion
FDG	18-Fluorodeoxyglucose
GaInN	Gallium indium nitride

L. U. Khan (✉)

Brazilian Nanotechnology National Laboratory (LNNano), Brazilian Center for Research in Energy and Materials (CNPEM), Campinas, SP, Brazil
e-mail: latif.khan@lnnano.cnpem.br

Z. U. Khan

Department of Immunology, Institute of Biomedical sciences-IV (ICB-IV), University of São Paulo, São Paulo, SP, Brazil
e-mail: zahidkhan@usp.br

GaN	Gallium nitride
LEDs	Light-emitting diodes
LMCT	Ligand-to-metal charge transfer
LPS lamps	Low-pressure sodium lamps
MCPs	Micro-channel plates
MD	Magnetic dipole
MH lamp	Metal halide lamp
MNPs	Magnetic nanoparticles
MRI	Magnetic resonance imaging
ms	Millisecond
NIR	Near-infrared
NPs	Nanoparticles
OPN	Osteopontin
PA	Photon avalanche
PAI	Photoacoustic imaging
PAM	Photoacoustic microscopy
PET	Positron emission tomography
PMT	Photomultiplier tubes
QDs	Quantum dots
RE	Rare earth
RGB	Red-green-blue
S	Singlet state
SPECT	Single-photon emission computed tomography
T	Triplet state
THP-1	Tamm-Horsfall protein-1
TTA	Thenoyltrifluoroacetate
UC	Upconversion
UCL	Upconversion luminescence
UCNPs	Upconversion nanoparticles
UV	Ultraviolet
YAG:Ce ³⁺	Y ₃ Al ₅ O ₁₂ :Ce ³⁺
α -CD	α -Cyclodextrin

10.1 Introduction

Luminescence, the emission of light by certain materials when they are relatively cool, has provoked the material researchers since the last century and been called as cold light [1] to differ from the emission owing to the incandescence (hot light) either firelight, candle, oil lamp, gas light, or modern incandescent lamps of the twentieth century. Recently, the solid-state white light-emitting diodes (LEDs) [2–5], based on luminescent materials, are considered the next-generation lighting devices for replacing the traditional incandescent and fluorescent lamps. The photoluminescence is characterized by emission of radiations at relatively low temperatures when the luminescent material is excited by absorption of photons.

The RE³⁺ ion-activated luminescent materials show excellent photostabilities, long luminescence lifetimes, large Stokes/anti-Stokes shifts, and narrow emission lines. Therefore, these luminescent materials have found a wide range of applications [6, 7], presently extend from laser physics to material sciences, agriculture, and medical diagnostics. Selected examples are phosphors for lighting and displays, lasers, cathode-ray tubes, radiation scintillations devices, optical telecommunications, security inks, anti-counterfeiting tags [7–9], probes for luminescent immunoassays, and bioconjugates for photodynamic treatment of cancer.

The trivalent lanthanide ions (Ln³⁺) show fascinating luminescent properties due to their abundant energy level structure in 4f configurations [10]. The rare earth compounds exhibit emissions in broad range of UV-visible to near-IR spectral regions, owing to the 4f energy levels of the RE³⁺ ions, which are sensitized through various energy transfer pathways. For the RE³⁺ organic complexes, the sensitization process can be achieved as an intramolecular energy transfer from the organic ligand to the rare earth ions (*antenna effect*) [11–17], whereas, for the luminescent RE³⁺ ion-doped inorganic materials, these phenomena take place as a result of the non-radiative transfer of excitation energy from a rare earth ion behaving as an energy donor (sensitizer) to another rare earth ion behaving as an energy acceptor (activator), including downshifting, quantum cutting, and upconversion processes [18]. In addition, the color of the emitted light depends on the RE³⁺ ion. For instance, Eu³⁺ emits in red, Tb³⁺ green, Sm³⁺ orange, and Tm³⁺ blue light. The Yb³⁺, Nd³⁺, and Er³⁺ are well known for their near-infrared luminescence [19]. In addition, the Pr³⁺, Sm³⁺, Dy³⁺, Ho³⁺, and Tm³⁺ ions also show transitions in the near-infrared region, and Gd³⁺ emits in the UV region.

The 4f energy levels of the RE³⁺ ions are slightly affected by the chemical environment due to the effective shielding of the 4f electrons by the filled 5s and 5p external subshells [11, 13]. Therefore, the absorption and emission spectra of the 4f intraconfigurational transitions of the RE³⁺ ions retain more or less their atomic character, irrespective of the host matrix or organic ligand [14, 20]. The 4f-4f transitions of the RE³⁺ ions are either achieved by electric dipole or magnetic dipole mechanisms. The magnetic dipole transitions are parity-allowed, whereas the electric dipole transitions are parity-forbidden (Laporte-forbidden); however the Laporte rule is slightly relaxed for these transitions due to the mixing of opposite parity electronic configurations, produced by the odd components of a non-centrosymmetric ligand field. Moreover, the ligand polarization effects have been shown to be of considerable importance for the 4f-4f transitions [11, 20]. This chapter presents a concise overview on the luminescence; key concept of electronic spectroscopy of rare earth ions, including 4f energy levels and luminescence spectra; as well as instrumentation and applications.

10.2 Luminescence

Luminescent phenomena have fascinated the mankind since the earliest times [1]. The light from the Aurora borealis, light of the sea, luminous animals of various kinds, luminescent wood, glow worms, and firefly bugs are all examples of naturally

occurring luminescence (Newton Harvey 1957) [21]. The term luminescence was first introduced in 1888 by a German physicist Eilhard Wiedemann that can be described as the emission of light by certain materials at relatively low temperatures (cold light), different from the emission owing to the incandescence (hot light) such as firelight, candles, oil lamps, and gas light [22]. The incandescence is usually produced by a direct heating of matter to high temperatures, which results in emitting light over a continuous range of energies (wavelengths) in correlation with temperature, whereas luminescence is the emission of radiations at normal lower temperatures when the luminescent materials are excited with often invisible energy sources such as ultraviolet light, electric fields, X-rays, energetic particles from radioactive decay, and so on. Therefore, on the basis of the nature of the exciting source, the luminescence is subdivided into a number of categories. Some of the most studied ones are given as follows [23]:

1. *Photoluminescence*: Emission after excitation by irradiation with electromagnetic radiation.
2. *Electroluminescence*: Emission by recombination of electrons and holes under the influence of an electric field.
3. *Radioluminescence*: Luminescence that results from bombardment of the materials by various particles other than light, such as electrons, alpha particles (ions), X-rays, γ -rays, etc.
4. *Cathodoluminescence*: Emission of light that observed after excitation with cathode rays.
5. *Chemiluminescence*: The nonthermal production of light by a chemical reaction.
6. *Triboluminescence*: The light observed by applying mechanical stress to crystals or by fracture of crystals. The solid materials that give luminescence are called phosphors or, latterly, luminescent materials.

10.2.1 History of Luminescence

The history of luminescence is well explained by the E. Newton Harvey in a book of 770 pages, entitled as *A History of Luminescence: From the Earliest Times until 1900* [21]. This book narrates interesting classical stories about the luminescence in the early ages from ancient cultures to modern times. One of the problems of the historian of luminescence is to sift the true from the false report. Stories of luminous jewels and luminous stones have been handed down from the earliest times, but in most cases, the light has been due to reflection rather than light emission. For example, the glowing eyes of cats are well known, and glowing eyes have also been observed in human beings. They were particularly mentioned by classic writers as characteristic of warriors during the heat of battle. The Greeks and Romans thought the ability to see at night was connected with this glowing of the eye (Newton Harvey 1957). Another phenomenon and a purely subjective one, the phosphene or apparent light that appears when the eyeball is pressed or struck, was known to Aristotle and has frequently been confused with real luminescent phenomena.

The earliest written account of a solid-state luminescent material comes from a Chinese text published in the Sung dynasty (960–1279 AD). It has been claimed that the Chinese had knowledge about artificial phosphors, although the evidence is not very convincing. The following story concerning a painting of the Emperor Tsi Tsung (976–998), of the Sung dynasty, was related by a Mr. MacGowan (Newton Harvey 1957) in a communication to the North China Herald and has been included by H. Rupp in her book *Die Leuchtmassen und ihre Verwendung* (Berlin 1937). The story has been traced by Professor Lien-Sheng Yang from Harvard University in old Chinese records, the miscellaneous notes by a Sung monk, which is titled as Hsiang-shan yeh-lu (eleventh century AD). This story is related to an interesting painting which was presented to the second emperor of the Sung dynasty (Newton Harvey 1957). This painting had a sketch of cow which appeared during the day as eating grass outside a pen, but at night in the dark, it was resting in the pen. When it was shown to the court, none of the officials could offer an interpretation. The monk Tsan-ning, however, said that the ink [or color] which was shown only in the night was mixed with drops from a special kind of pearl shell and the ink (or color) which was shown only during the day was made by grinding a rock which had fallen from a volcano to the sea shore. He claimed that the information came from a book by Chang Ch'ien *The Famous Envoy Sent to the Western Regions by Han Wu-ti* (reigned 140–88 BC). A scholar who consulted the imperial collections found the reference in a work dated from the six dynasties (the above is a summary of the story in the Hsiang-shan yeh-lu). In 1768 John Canton described a phosphor made from oyster shells, and it is possible (although improbable) that the Chinese prepared a luminous paint from the pearl oyster (Newton Harvey 1957).

Knowledge of luminescence in ancient India must not be concluded without the mention of the luminous cobra stone of India and Ceylon, although the date of the legend is unknown and the story sounds highly improbable but completely fascinating. The best account has been related by Professor H. Hensoldt (Newton Harvey 1957), who obtained one of the stones, called “Naja-Kallu,” during a stay at Point de Galle, Ceylon. It is narrated that about 1 cobra in 20 carries around in its mouth a small luminous stone that is placed in the grass at night to attract fireflies, which the cobra then proceeds to eat. Hensoldt caught 50 cobras without finding a stone, but one night in the field with a Tamil coolie, he saw a cobra resting by what he thought was a luminous spot. He wished to kill the cobra at once, but the Tamil implored him not to because the snake is alleged to be particularly dangerous when watching the Naja-Kallu (Newton Harvey 1957) or cobra stone (Naag-mani in Hindi). However, the next night the Tamil saw the cobra in the same place and obtained the stone by climbing a tree and throwing ashes over it. The ashes were collected and sifted after the snake had left. The stone was “a semitransparent water worn pebble of yellowish color, about the size of a small pea, which in the dark, especially when previously warmed, emitted a greenish phosphorescent light.” Chemically it was a fluorite, some varieties of which (chlorophane) are said to be sufficiently phosphorescent to shine all night long after exposure to the sun’s rays. The pebble no doubt existed but the part played by the cobra is reminiscent.

Among the true luminescence recognized by the ancients may be related to the Aurora borealis, the light of the sea, luminous animals of various kinds, phosphorescent wood and flesh, and ignis lambens, a silent electrical discharge in

air. The discovery of the Bologna stone in the year 1603 marked the beginning of modern luminescent materials. An Italian shoemaker named Vincenzo Cascariolo synthesized the famous Bologna stone by calcining a particular mineral from Monte Paderno close to Bologna, Italy [24]. This new material, later tentatively identified as BaS prepared from BaSO₄ (baryte), was described as being able to attract the “golden light of the Sun,” i.e., to emit light without heat, if illuminated prior by either sunlight or flames (Newton Harvey 1957). Today, this phenomenon is known as persistent luminescence, which is a special case of thermoluminescence (Chen and McKeever 1997) at room temperature. The Bologna stone was among the first luminescent materials and the first scientifically documented material to show persistent luminescence (Licetus 1640). Recently, Hölsä and coworkers [24] reported the preparation of the Bologna stone (BaS) from the natural baryte (Bologna, Italy) used by Cascariolo. They compared its properties, e.g., impurities (dopants) and their valences, luminescence, persistent luminescence, and trap structure, with those of the pure BaS materials doped with different transition metals (Cu, Ag, Pb) known to yield strong luminescence. Based on experimental result obtained, they constructed a plausible mechanism for the persistent luminescence from the Bologna stone with Cu⁺ as the emitting species and suggested that the puzzle of the Bologna stone can thus considered to be resolved after some 400 years of studies.

From the early years after Cascariolo’s discovery, the reasons behind the persistent luminescence aroused interest in the scientific community. Even the great Galileo joined the general discussion on the stone, though he never wrote anything on the subject [24]. It took almost 400 years for the discussion to heat up again, i.e., with the introduction of the modern persistent luminescent materials, such as SrAl₂O₄:Eu²⁺,Dy³⁺ and Sr₂MgSi₂O₇:Eu²⁺,Dy³⁺. These materials are capable of more than 24 h of persistent luminescence; therefore, their applications as non-radioactive phosphors in traffic signs and signals are remarkably increased. Numerous safety signs (exit signs, pedestrian walkway line markings, traffic signs, emergency signage), watches and clocks, textile printing, etc. require the use of persistent luminescent paints and afterglow phosphors. Currently, in 2015 Nissan has created luminous model of its leaf (glow-in-the-dark car) that glows for 10 h in the dark [25]. This motor company has become the first manufacturer in Europe to apply glow-in-the-dark car paint. The manufacturer is working with inventor Hamish Scott, creator of STARPATH, which is a spray-applied coating (persistent luminescent paint) that absorbs UV energy during the day so that it glows for between 8 and 10 h when the sun goes down.

In modern society, the use of phosphor-based technologies such as lightning and electronic display devices has key role in our daily life. We usually use fluorescent lamps (FL) as indoor lightning sources, which contain rare earth phosphors. In addition, in our information society, we read the various information of electronic media from the display devices, such as computers, laptops, mobile devices, flat-panel displays, traditional cathode-ray tube (CRT) television sets, etc., which contain various phosphors [26]. The luminescent materials have remarkable applications in modern technology, including radar screens, plasma video display screens, sensors, white light-emitting diodes (WLEDs), infrared detectors (upconversion phosphors), scintillators (detectors of X-rays and ionizing radiations), etc.

10.2.2 *Light and Lighting Technologies*

Light is part of electromagnetic radiation spectrum and a special class of radiant energy that is visible and perceivable by the normal human eye such as colors between red and violet, embracing wavelengths from 400 to 700 nm, which is also called visible light [1, 27]. The electromagnetic radiation occurs over an extremely wide range of wavelengths, from gamma rays (wavelengths less than 0.01 nm) to radio waves (wavelengths in meters). The wavelengths visible to human eyes occupy a very narrow region (400–700 nm) within the broad electromagnetic spectrum. On the lower energy side of visible light, the spectrum starts with radio waves, which are used to transfer images and sound, such as radio and television, followed by microwaves that are used in radar and microwave ovens. Further down the electromagnetic spectrum are infrared waves, which are perceived as heat. On the higher-energy side of the visible spectrum with shorter wavelengths are ultraviolet radiation, followed by X-rays that are used in medical diagnostic for bone imaging; the next are gamma rays and finally cosmic rays.

Light plays a vital role in our daily lives and has become an important tool according to the needs of our twenty-first century world. Light-based technologies protect health and safety, provide sustainable energy, enable space explorations, advance lighting options in rural areas, enable communication via the Internet, and hold the promise of limitless possibilities to improve the human condition and protect the earth. Before people knew how to use electricity, they planned their time around daylight hours [26]. They used fire for light at night as well as candles and stove fires to light the world. Later on, oil and gas were used as fuels to produce light.

In ancient days, the discovery of fire was a turn point in human civilization and used as an artificial lighting by early human being. The hollow rocks or shells were used to fill with animal fat and ignited to produce flame. Later on, wicks were added to control the rate of burning, which was also improved over time and made from paper, cotton, hemp, and flax. In the eighteenth century, the introduction of central burner was a major improvement in lamp design, which was invented by Ami Argand (Swiss Chemist). Further addition in the lamp was the use of the glass chimneys, which protected the flame and also control the flow of air to the flame. In addition, the application of coal, natural gas, and kerosene oil in lamps also became popular; thus the first commercial use of gas lighting began in 1792. The invention of electric incandescent light bulb has a history spanning from the early eighteenth century, which improved the artificial lighting and became popular for indoor illumination, to the twentieth century [27]. The history of the lighting technologies is well presented schematically in Fig. 10.1.

The name of the inventor, which will remain forever in the history of artificial lighting, is Thomas Edison, who carried out serious research efforts to develop a practical incandescent lamp and filed his first patent “Improvement in Electric Lights” (Patent No. US 214636 A) on October 14, 1878. However, he continued to analyze several types of materials in order to use and improve his original design

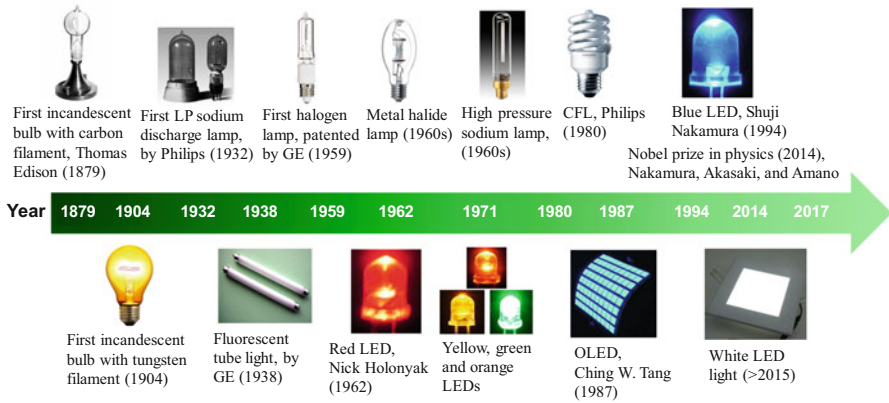


Fig. 10.1 The remarkable milestones in modern lighting technologies. (Prepared and updated by Latif U. Khan. Figure courtesy of source: <https://yikunliu.wordpress.com/2015/05/21/a-glance-of-modern-lighting-technologies/>)

metal filaments. Consequently, another US patent “electric lamp” (Patent No. US 223898 A) using a carbon filament or strip coiled and connected to platina contact wires was filed on November 4, 1879. The patent described several ways to create the carbon filament, including use of cotton and linen thread, wood splints, and papers coiled in various ways. After several months, Edison and his team discovered that a carbonized bamboo filament could last over 1200 h. This discovery marked the beginning of commercially manufactured light bulbs, and Thomas Edison’s company “Edison Electric Light Company” was made to market its new product in 1880.

Though carbon became the standard for the incandescent lamp and used nearly 30 years, however, it still possessed undesirable features. For example, its sublimation point is quite high, its vapor pressure is also high at operating temperature, and the bulb blackening was always a severed problem in the carbon filament lamps. Therefore, the search for better materials was continued, particularly in Europe for improved filament materials, which could be operated at higher temperature. The major parameter to be considered was the melting point of the material used in filament. Eventually, in 1906, William David Coolidge of General Electric Research Laboratory produced important result by introducing the incandescent bulbs with tungsten filaments. The tungsten is one of the most durable types of filaments used in light bulbs, because it has a high melting point and is able to withstand heat and corrosion after carbon arc.

The introduction of the incandescent tungsten filament was a crucial step in lighting technology, which proved a cornerstone for further major discoveries, including development of remarkable lighting sources, such as halogen lamps, metal

halide lamps, sodium vapor lamps, xenon arc lamps, fluorescent lamps, etc., because all these lamps use tungsten to certain extent as an important component such as electrode.

Halogen Lamp It is an advanced form of incandescent lamp that was developed by Elmer Fridrich and Emmet Wiley at General Electric Research Laboratory, Nela Park, Ohio, in 1955. Other research groups had also tried to produce the halogen lamps; however, they could not figure out how to stop the blackening of the lamp. Fridrich determined that the use of a small amount of iodine surrounding the tungsten filament could avoid the blackening of the lamp by producing a halogen cycle chemical reaction which redeposits evaporated tungsten to the filament, increasing its life and maintaining the clarity of the envelope.

General Electric Research Laboratory patented a practical lamp using iodine “Electric Incandescent Lamp” (Patent No. US 2883571 A) in 1959. Later on, the halogen lamp was improved by other engineers, so that it may be cheaper enough to be easily marketable. Therefore, the lamps have been made lighter in weight since 1980 and used in commercial and residential lightings, such as automotive head lamps, etc. Though the halogen lamp was low in cost to produce, does not use hazardous mercury, has better color temperature than standard tungsten, and has brightness close to sunlight, however on but this lamp had certain disadvantages, such as extremely hotness and possibility of explosion during glow. Therefore, the development of the economically viable, safe, and high luminous efficiency lamps was still important for the researchers working in the field of lighting technology.

Sodium Lamp The low-pressure sodium (LPS) lamps were invented in 1920 by Arthur H. Compton at Westinghouse Lamp Company, Pittsburgh, USA. The first lamp was a round shape bulb with two electrodes on each side. The solid sodium metal remained on the bottom center of the bulb, which was vaporized as the lamp heated up and consequently glowed yellow. The lamp was designed in a sphere shape; however, the tube design was more practical, similar to the neon lamp which had been already developed in 1920, but the problem with the tube would be the migration of the sodium toward its outer ends, which could be destroyed by the electrodes over time as well as the sodium which cannot get hot enough to vaporize. However, the commercially available LPS is usually in tube shape.

The major problem with Compton’s models was the highly corrosive sodium that could be attacked and blackened by regular silica glass. Marcello Pirani led the next major advancement in the low-pressure sodium lamp by developing a sodium-resistant glass in 1931 at Osram Lighting Company in Germany. The first low-pressure sodium lamps were released by Philips for commercial sale in 1932. Low-pressure sodium lamps are highly efficient electrical light sources, but their monochromatic yellow light (characteristic emission near 589 nm) restricts their outdoor applications such as street lighting, etc. and also inhibits color vision at night. Therefore, General Electric Research Laboratory later developed the first high-pressure sodium (HPS) lamps in Schenectady, New York, and Nela Park, Ohio. These lamps are further improvement in the LPS lamps and first lamp was released in the market at 1964. These lamps produce more acceptable color with broader

spectrum of light than the low-pressure lamps and mostly used for street lighting and industrial uses. However, they still have poorer color rendering than metal halide and halogen lamps.

Metal Halide Lamp This lamp was developed in the 1960s, which is also known as HID (high-intensity discharge) lamp, because it provides most of its light from the electric arc within a small discharge tube. The MH lamps are similar to mercury-vapor lamps; however, they contain additional metal halide compounds along with mercury in the quartz arc tube, which improve the efficiency and color rendition of the light. The lamps are worked in practical way as follows: (i) whenever the lamp turned on, the current is passed through the starting electrode and jumped at a short distance to the main electrode, through argon gas, which strikes an arc and heats up the quartz tube; (ii) the mercury is vaporized, and the arc traveled through mercury vapors from the starting electrode to the main electrode on the opposite side of the tube; and (iii) consequently, the metal halides are vaporized and dissociated to produce high-color-rendering light. The MH lamps are increasingly popular due to their good quality white light and good efficiency. The most prominent use of the MH lamps is in stadiums and sports fields. They are also used in car headlights and laboratory equipment, such as fluorescence microscopy.

Xenon Arc Lamp The other special type of lighting source is the xenon arc lamp, a gas discharge lamp that produces light by passing electricity through ionized xenon gas at high pressure. This lamp was invented in the 1940s by Osram and commercially used as a film projector lamp in the 1950s. The xenon arc lamps can be roughly divided into three categories: continuous-output xenon short-arc lamps, continuous-output xenon long-arc lamps, and xenon flash lamps. The xenon short-arc lamps are further divided into two distinct varieties: pure xenon, which contains only xenon gas, and xenon-mercury, which contains xenon gas and a small amount of mercury metal. The pulsed light sources, such as xenon flash lamps, can provide a very intense light output for several microseconds, about 1000 times higher than continuous-mode lamps. These lamps are still popular to be used in research laboratory instruments, such as ZEISS Microscopy, Horiba/Jobin Yvon FluoroLog-2 and 3 Spectrofluorometers, Varian Cary Eclipse Fluorescence Spectrophotometer, etc., as light sources. However, these modern equipments have also the facilities to use laser and light-emitting diodes (LEDs) as lighting sources.

Fluorescent Lamp The idea of the development of fluorescent lamp had been found in the history of lighting technology since the eighteenth century; however it took steady and long-time work over the decades to finally create a practical and commercially viable model. Though many inventors were involved in this work, Edmund Germer is credited by some historians as being the inventor of the first true fluorescent lamp. Edmund Germer (1901–1987) invented the high-pressure mercury-vapor lamp that was his development of the improved fluorescent lamp, which produced more economical lighting with less heat. Therefore, Edmund Germer, Friedrich Meyer, and Hans Spanner patented an experimental fluorescent lamp “Metal vapor lamp” (Patent No. US 2182732 A) in 1927, which was later purchased by the General Electric Company.

Meanwhile, George Inman led a group of General Electric scientists working on improved and practical fluorescent lamp, being under pressure from many competing companies; the team designed the first practical and viable fluorescent lamp, which was patented “Electric discharge lamp” (Patent No. US 2,259,040 A) in 1938. It should be noted that the introduction of phosphors, especially luminescent rare earth materials as a coating on the inside of the glass tube, led the commercialization of low-voltage fluorescent lamps for indoor and outdoor lighting with high luminous efficacy and energy-saving properties when compared to the incandescent lamps. Early phosphors were not especially efficient, and the first fluorescent lamps were in the form of tubes about 1 m in length. Improvements in the qualities of phosphors have made the efficiency greater; therefore, compact fluorescent lighting attracted attention and become commercially available in 1980.

Compact Fluorescent Lamp The important development in compact fluorescent light (CFL) is credited to Edward Hammer, who figured out in 1976 at General Electric Research Laboratory how to bend the fluorescent tube into a spiral shape, creating the first CFL bulb. Later on, Philips introduced its SL model in 1980, which was the first successful commercially available CFL bulb. Helical CFLs were also manufactured in China and became commercially available in 1995. Consequently, the sale of CFLs has been steadily increased and considered really popular lamps for house lighting till the recent age of 2016. The fluorescent lamps are more costly than incandescent lamps and classified as hazardous wastes due to the presence of mercury. Therefore, the improvement in the lamps was still continued after introducing the good luminous efficacy CFL bulbs. Recently, in 2016, General Electric tried to stop the CFL production, because the prices of light-emitting diodes (LEDs) have reasonably dropped; as a result, they are warmly attracting the attention of customers.

Light-Emitting Diodes These are semiconductor devices that emit visible light when an electric current pass through them (electroluminescent). The light in most of LEDs is usually monochromatic, occurring at a single wavelength, ranging from red ($\lambda = \sim 700$ nm) to blue-violet ($\lambda = \sim 400$ nm). The well-known LEDs are yellow-, green-, red-, and blue-emitting ones [28, 29]; in addition, some LEDs emit in infrared (IR) region ($\lambda = \geq 830$ nm); such a device is known as an *infrared-emitting diode* (IREM).

Nick Holonyak Jr. is considered the father of the visible light-emitting diodes (LEDs), because his first invention of visible red LED (1962) at General Electric, Syracuse, NY, attracted the broad use of III-V semiconductor alloy technology worldwide and well explored during several decades. The first commercial red-emitting GaAsP LED was offered by the General Electric (GE) Corporation in the early 1960s. However, the manufactured quantities of the product were low, probably due to the high price, which was 260 US dollars for a single LED [3]. The Monsanto Corporation was the first commercial company, which started the mass production of LEDs. The company had set up a factory in 1968, which produced low-cost GaAsP LEDs and sold them to customers. The long-life red LED was initially used for panel indicators, traffic lights, and automobile tail lights. The

key technical innovator and manager at Monsanto was M. George Craford, who made numerous contributions to LEDs, including the first demonstration of a yellow LED [29, 30]. The development of other colors, such as orange, green, blue, etc., broadened their applications in modern technologies, including lamps and display devices: computers, cellphones, television screens, etc.

The invention of bright blue light from the GaN semiconductor changed the history of lighting technology in the twenty-first century. Considerable research efforts were dedicated by Pankove and coworkers to make a marketable GaN LED in the 1960s, but could not manage. Therefore, the work on GaN was virtually stopped, and a single paper was published on GaN in 1982. However, Isamu Akasaki and coworkers in Nagoya, Japan, could not give up, and they demonstrated in 1989 the first true p-type doping and p-type conductivity in GaN. The stubborn Mg acceptors doped in GaN were activated by electron-beam irradiation, a method published by Hiroshi Amano, Isamu Akasaki, and coworkers [31]. It was later shown by Shuji Nakamura and coworkers that a high-temperature post-growth annealing of Mg-doped GaN also activates Mg dopants in GaN. These p-type doping breakthroughs opened the door to produce efficient p-n junction LEDs and laser diodes. Nowadays, Mg-doped GaN is the basis for all nitride-based LEDs and laser diodes.

A name closely associated with GaN LEDs and lasers is that of the Nichia Chemical Industries Corporation, Japan [2]. A team of researchers, which included Shuji Nakamura and Takashi Mukai, has made numerous contributions to the development of GaN growth, LEDs, and lasers. Their contributions include the demonstration of the first viable blue and green GaInN double-heterostructure LED that achieved efficiencies of 10% [32] and the demonstration of the first pulsed and continuous wavelength (CW) GaInN/GaN current injection blue laser operating at room temperature [29]. Therefore, Isamu Akasaki, Hiroshi Amano, and Shuji Nakamura were awarded with Nobel Prize in Physics (2014) in reward of the development of creditable blue-emitting LED. Red and green diodes had been around for a long time, but without blue light, white lamps could not be created that had remained a challenge for three decades. At last, Isamu Akasaki, Hiroshi Amano, and Shuji Nakamura succeeded, and their inventions were revolutionary. Incandescent light bulbs lit the twentieth century, and the twenty-first century will be lit by LED lamps.

10.2.3 Rare Earth Luminescence

The rare earth (RE) elements comprise of lanthanides, ranging from lanthanum to lutetium (Ln: La, Ce, Pr, Nd, Pm, Sm, Eu, Gd, Tb, Dy, Ho, Er, Tm, Yb, Lu) and scandium (Sc) and yttrium (Y). In nature, the yttrium and scandium occur in the same ore deposits as the lanthanides and exhibit similar chemical properties; therefore, they are usually referred to as rare earths [33, 34]. Though RE elements occurred as trace elements in the vast majority of geological environments, their

natural abundances in earth's crustal rocks, mostly ranging from hundreds of parts per billion (terbium, holmium, thulium, and lutetium) to tens of parts per million (lanthanum, cerium, and neodymium), are not exceptionally low compared to many other elements. Thus, despite their name, the rare earth elements (with exception of the radioactive promethium) are relatively plentiful in earth's crust.

The most common one is cerium, depending on the estimate, which is approximately the 27th most abundant element in the continental crust of the earth at 68 parts per million or as abundant as copper. These elements have similar physical and chemical properties [16, 35, 36]. These 17 RE elements are all electropositive metals with a remarkable uniformity of chemical properties. The similarity of the trivalent lanthanides to each other, especially each to its neighbors, as a consequence of their general adoption of the +3 oxidation state in aqueous solution caused their separation to be extremely difficult.

The names of the rare earth elements are closely associated with their discovery; most of them have been discovered in the nineteenth century, with the exception of yttrium (1794), lutetium (1907), and promethium (1943). Yttrium was discovered in 1794 by the Finnish mineralogist and chemist Johan Gadolin (Table 10.1), in a mineral that was later named gadolinite in his honor. The element gadolinium was named after the discovery of mineral gadolinite on the name of Johan Gadolin [37]. Another naturally occurring element is the samarium, which was indirectly named on the discoverer Vasilii Samarsky-Bykhovets (Russian mining engineer) after the discovery of mineral samarskite.

The rare earths are usually occurred in their compounds as RE^{3+} ions; other oxidation states are stable only when an empty ($4f^0$), half-filled ($4f^7$), or full ($4f^{14}$) subshell is produced. The predominant oxidation states are trivalent (Ln^{3+} , Sc^{3+} , Y^{3+}), also can be found the divalent (Sm^{2+} , Eu^{2+} , Tm^{2+} , Yb^{2+}) and tetravalent states (Ce^{IV} , Pr^{IV} , Tb^{IV}) [23, 35]. The electronic configuration of the RE^{3+} ions is represented by $[Xe]4f^N$, which shows a gradual increase in the number of electrons N with increasing the atomic numbers of the ions, ranging from $4f^0$ to $4f^{14}$ for the La^{3+} to Lu^{3+} ions.

The RE^{3+} ions exhibit a number of features in their chemistry that differentiate them from the d-block metals such as [35, 36]:

- (i) High coordination numbers (generally between 6 and 12).
- (ii) Coordination geometries are determined by ligand steric factors rather than ligand-field effects.
- (iii) They form labile "ionic" complexes that undergo facile exchange of ligand.
- (iv) Small ligand-field splitting and very narrow emission and absorption bands in comparison with the d-block metals.
- (v) They prefer anionic ligands with donor atoms even of high electronegativity (e.g., N, O, F).
- (vi) They readily form hydrated complexes (on account of the high hydration energy of the small Ln^{3+} ion).

Rare earth ions have been widely used in various research fields such as luminescent, steel, alloy, pigment, magnet, laser, and catalyst materials, because of

Table 10.1 The etymology of the names of the rare earth elements

Element	Symbol	Atomic number	Etymology
Scandium	Sc	21	After the Latin word, Scandia (Scandinavia), where the rare earth elements were first found
Yttrium	Y	39	After the village of Ytterby in Sweden, where the first ore of rare earth mineral “yttria” was discovered that was a source of yttrium (Y), erbium (Er), terbium (Tb), and ytterbium (Yb)
Lanthanum	La	57	From the Greek word “lanthanein,” meaning hidden
Cerium	Ce	58	After the dwarf planet Ceres, itself named after the Roman goddess of agriculture and motherly love
Praseodymium	Pr	59	From the Greek words “prasios,” or green, and “didymos,” meaning twin
Neodymium	Nd	60	From the Greek words “neos,” or new, and “didymos,” meaning twin
Promethium	Pm	61	After the Greek god of fire Prometheus
Samarium	Sm	62	After the mineral samarskite, in turn named after Vasili Samarsky-Bykhovets (1803–1870), discoverer of samarskite
Europium	Eu	63	After the continent of Europe
Gadolinium	Gd	64	After the mineral gadolinite, in turn named after Johan Gadolin
Terbium	Tb	65	After the village of Ytterby in Sweden
Dysprosium	Dy	66	After the Greek word “dysprositos,” meaning “difficult to catch”
Holmium	Ho	67	After the medieval Latin name for Stockholm (Holmia)
Thulium	Tm	68	After the mythological, most northern place on earth, Thule
Erbium	Er	69	After the village of Ytterby in Sweden
Ytterbium	Yb	70	After the village of Ytterby in Sweden
Lutetium	Lu	71	After Lutetia, the Latin name for Paris

Reproduced from Voncken [34] with permission from *Springer Nature*

their unique properties originating from their 4f intraconfigurational transitions [7, 9, 17]. Rare earth luminescence materials have a special status in photonics due to the unique spectroscopic properties of RE^{n+} ions with respect to light generation and amplification. Following the early applications in lighting at the end of the nineteenth century (Auer mantle, flint stones) [38], the discovery of the bright red-emitting phosphor $Y_2O_3:Eu^{3+}$ at the beginning of the twentieth century and the advent of the YAG:Nd³⁺ laser in 1964 elaborated further the importance of rare earths in modern lighting technologies.

The RE^{3+} ions show remarkable photoluminescence properties due to the abundant energy level structure (Fig. 10.2) in their 4f configurations. Some of these ions show luminescence in the visible or near-infrared spectral regions under UV irradiation lamp. The color of the emitted light depends on the RE^{3+} ion. For instance, Eu^{3+} emits in red, Tb^{3+} green, Sm^{3+} orange, and Tm^{3+} blue light [19].

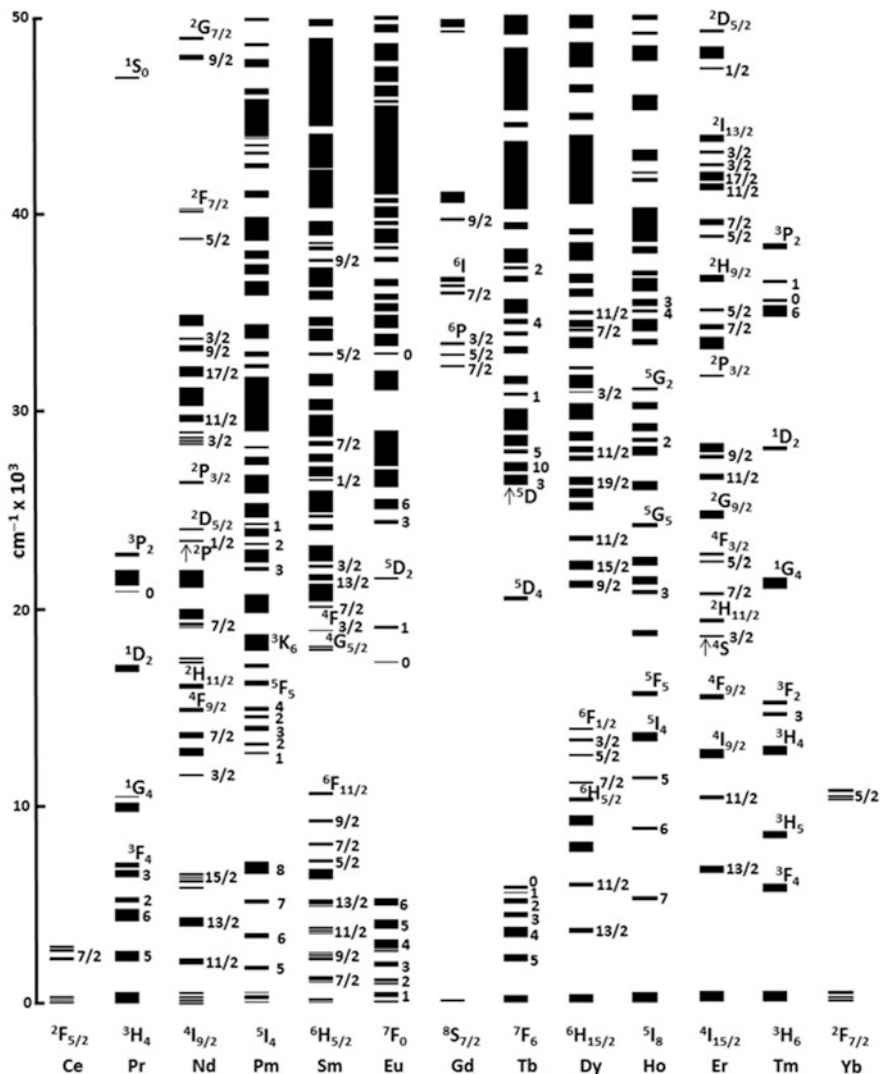


Fig. 10.2 Energy level structure of $\text{Ln}^{3+}:\text{LaF}_3$ based on computed crystal-field energies in the range of $0\text{--}50,000\text{ cm}^{-1}$ with labels of ^{2S+1}L and/or J , where the dominant character of the levels can be clearly assigned. (Reproduced from Khan and Khan [22] with permission from Springer Nature)

The Yb^{3+} , Nd^{3+} , and Er^{3+} are well known for their near-infrared luminescence. In addition, the Pr^{3+} , Sm^{3+} , Dy^{3+} , Ho^{3+} , and Tm^{3+} ions also show transitions in the near-infrared region, and Gd^{3+} emits in the UV region. While considering the 4f-4f luminescence of RE^{3+} ions, they can be divided into four groups depending on their photonic features [11, 39, 40]:

1. Sc^{3+} ($3d^0$), Y^{3+} ($4d^0$), La^{3+} ($4f^0$), and Lu^{3+} ($4f^{14}$) ions exhibit no luminescence because they contain no optically active electrons.
2. Gd^{3+} ($4f^7$) ion presents a special case, since there is a large energy gap between the $^8S_{7/2}$ ground state and first $^6P_{7/2}$ excited state ($\sim 32,000 \text{ cm}^{-1}$) that can emit in the ultraviolet region. In general, it cannot accept energy from the lower line excited states of the organic ligands via intramolecular ligand-to-metal energy transfer.
3. Sm^{3+} ($4f^5$), Eu^{3+} ($4f^6$), Tb^{3+} ($4f^8$), and Dy^{3+} ($4f^9$) ions have relatively large energy gaps between their excited and ground states. Complexes of these ions generally show strong luminescence because the excited energy levels of the ion lie just below that of the ligand triplet state.
4. Ce^{3+} ($4f^1$), Pr^{3+} ($4f^2$), Nd^{3+} ($4f^3$), Ho^{3+} ($4f^{10}$), Er^{3+} ($4f^{11}$), Tm^{3+} ($4f^{12}$), and Yb^{3+} ($4f^{13}$), the complexes of which usually show only weak 4f-4f luminescence, as a consequence of the small energy gap between their emitting and lower energy levels; this increases the probability of non-radiative transitions through coupling with vibrational modes in the ligands.

10.3 Electronic Spectroscopy of Rare Earth Ions

10.3.1 Energy Level Structure of the $[\text{Xe}]4f^N$ Configuration

The optical properties of the rare earth ions are fascinating and originate in the special features of the electronic $[\text{Xe}]4f^N$ configurations ($n = 0-14$). The more common oxidation states are +3, +2, and +4. However, the +3 oxidation state is characteristic for all rare earth ions which show a $4f^n$ configuration. These 4f configurations generate a rich variety of electronic levels, the number of which is given by $[(4l+2)!/(4l+2-n)n!]$, yielding to 3003 sublevels for Eu^{3+} and Tb^{3+} ions (Table 10.2). They are characterized by three quantum numbers, S , L , and J within the frame of Russell-Saunders spin-orbit coupling scheme [9, 20]. The energies of these levels are well defined due to the shielding of the 4f by the filled $5s^25p^6$ subshells, and they are little sensitive to the chemical environments in which the rare earth ions are placed.

Therefore, in RE^{3+} complexes the ligands in the first and second coordination sphere perturb and split the $^{2S+1}L_J$ energy levels of the RE^{3+} ions only slightly. This shielding is responsible for the specific properties of the rare earth luminescence [35], more particularly the narrow emission bands and the long lifetimes of the excited states due to forbidden 4f-4f transitions [41]. Moreover, especially the Ce^{3+} ion shows intense broad emission band due to the allowed f-d transitions; the position of the emission maximum strongly depends on the ligand environment of the Ce^{3+} ion [42]. The 4f-4f transitions are parity-forbidden; however the Laporte rule is slightly relaxed for these transitions due to the mixing of opposite parity electronic configurations, produced by the odd components of a non-centrosymmetric

Table 10.2 Number of terms, levels, and degeneracy of the f^N configurations of L_n^{3+} free ions

Configuration	L_n^{3+}	Terms ($2S + 1L$)			Number of terms	Number of J levels ($2S + 1L_J$)	Maximum number of crystal-field levels ($2S + 1L_{JM}$)
f^1 and f^{13}	Ce^{3+} , Yb^{3+}	2F			1	2	14
f^2 and f^{12}	Pr^{3+} , Tm^{3+}	1SDGI	3PFH		7	13	91
f^3 and f^{11}	Nd^{3+} , Er^{3+}	$^2PDFGHKL22.2.2$	4SDFGI		17	41	364
f^4 and f^{10}	Pm^{3+} , Ho^{3+}	$^1SDFGHKLN24.4.2.3.2$	$^3PDFGHKLM32.4.3.4.22$	5SDFGI	47	107	1001
f^5 and f^9	Sm^{3+} , Dy^{3+}	$^2PDFGHKLMNO457.6.755.3.2$	$^4SPDFGHKLM2.3.44.332$	6PFH	73	198	2002
f^6 and f^8	Eu^{3+} , Tb^{3+}	$^1SPDFGHKLMNQ4.6.4.8.473.4.2.2$	$^3PDFGHKLMNO6.5.97.966.33$	5SPDFGHKIL $^3.2.3.22$	119	295	3003
f^7	Gd^{3+}	$^2SPDFGHKLMNOQ257.101.09.9754.2$	$^4SPDFGHKLMN22.65.7.5533$	6PDFGHI 8S	119	327	3432

Reproduced from Sastri et al. [36] with permission from Elsevier

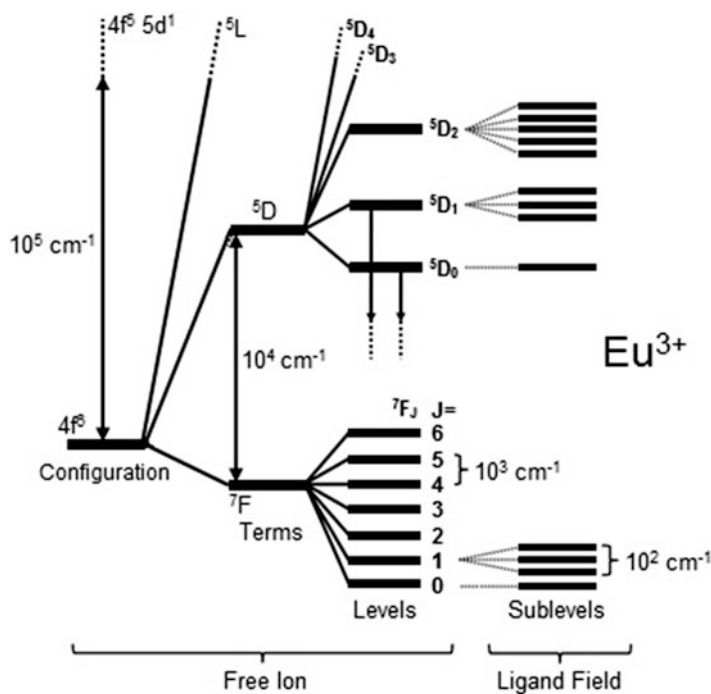


Fig. 10.3 Partial energy diagram of Eu^{3+} ($4f^6$) (left) showing the relative magnitude of the interelectronic repulsion (terms), spin-orbit coupling (levels), and crystal-field effects (sublevels). The downward arrows indicate the excited states $5D_0$ and $5D_1$ from which luminescence occurs. (Reproduced from Binnemans [20] with permission from Elsevier)

ligand field. Moreover, the ligand polarization effects have been shown to be of considerable importance for the $4f$ - $4f$ transitions.

The existence of different energy levels (Fig. 10.2) for the rare earth ions is a consequence of different interactions operating in the $4f^n$ electronic configuration of the ions. Depending on the number, the electrons can distribute in many ways over the $4f^n$ configurations; however some distributions are energetically more favorable. Each different electronic arrangement is called a *microstate*. For the systems with more than one $4f^n$ electrons, such as Eu^{3+} ion ($4f^6$) [20], the degeneracy of the $4f^n$ configuration is partly or totally lifted by several perturbations acting on the RE^{3+} ion: the electron repulsion, spin-orbit coupling, ligand-field perturbation, and eventually Zeeman effect (Fig. 10.3). The electron repulsion is the electrostatic interaction between the different electrons in the $4f$ subshell. The spin-orbit coupling results from the interaction between the spin magnetic moment and the orbital magnetic moment of the electron. The ligand-field effect is caused by the interactions between the $4f$ electrons and the electrons of the ligands. The Zeeman effect is the splitting of the energy levels by an external magnetic field.

The electrostatic repulsion splits the electronic configuration into spectroscopy terms labeled by “ ^{2S+1}L ” according to the spin multiplicity $2S+1$ and the total angular momentum L with a separation at around 10^4 cm^{-1} (Fig. 10.3). The terms are usually denoted by capital letters of the Latin alphabet: S ($L = 0$), P ($L = 1$), D ($L = 2$), F ($L = 3$), G ($L = 4$), H ($L = 5$), I ($L = 6$), K ($L = 7$), L ($L = 8$), M ($L = 9$), etc. Notice that the letter J is not used as a term label. The nomenclature for spin multiplicity is used as singlet, doublet, triplet, quartet, quintet, sextet, and septet for $2S + 1 = 1, 2, 3, 4, 5, 6,$ and 7 , respectively [20, 39]. The spin-orbit interaction (between two magnetic dipoles) removes the degeneracy of the ^{2S+1}L spectroscopy terms into J levels of the free ion characterized by $L, S,$ and J quantum numbers and labeled by $^{2S+1}L_J$ levels. These levels are relatively higher (10^3 cm^{-1}) because of the heavy rare earth nucleus (Fig. 10.3). The energy levels of *free ion* can be described by the $^{2S+1}L_J$ levels, where $2S+1$ represents the total spin multiplicity, L the total orbital angular momentum, and J the total angular momentum of the 4f electrons.

On placing the RE^{3+} ions in a chemical environment, such as organic ligands or inorganic matrices, the spherical symmetry of free ion is destroyed, and each spectroscopic level (J levels) further splits under the influence of the asymmetric electric field produced by the chemical environment, called as ligand field or crystal field. This interaction removes to a certain degree the degeneracy of the free-ion levels [39]. The magnitude of the splitting of the $^{2S+1}L_J$ energy levels has been first parameterized in the simplest way assuming a “Point Charge Electrostatic Model (PCEM)” generated by the chemical environment around of the rare earth ions. The ligand-field effect (H_{LF}) is further lifted the $(2J+1)$ degeneracy of the J levels in free ion, depending exclusively on the point of symmetry about the RE^{3+} ion (Table 10.3) [10], which are called as crystal-field levels (or Stark levels). The splitting of the energy levels by ligand-field effect is of the order of few hundred cm^{-1} (around 10^2 cm^{-1}).

Luminescence originating from the intraconfigurational d transitions is quite different from that of the 4f-4f ones. The spectra of d metals are much poorer in the number of observed pure zero-phonon transitions, since d^N configurations have less microstates by far than the $4f^n$ ones. The vibronic interaction is much stronger than in the case of 4f-4f transitions. In addition, for d-transition elements, the ligand-field interaction is at least one order of magnitude greater due to the non-screened and more extended d radial distribution. These facts produce very broad d-d transition bands [11]. Transition metal complexes have usually lower coordination numbers (four and six) than the f elements. In the case of fourfold tetrahedral coordination, d-p mixing relaxes Laporte rule allowing the d-d transitions, while in the case of octahedral coordination, Laporte rule is not relaxed, except for the vibronic interaction that instantaneously breaks down the center of inversion and allows the d-d transitions, with much weaker intensities than in the tetrahedral case. Ligand polarization effects on the d-d transitions, to our knowledge, have not yet been investigated.

Table 10.3 Number of sublevels of $^{2S+1}L_J$ (7F_J , $J = 0-6$) term of Eu^{3+} system for the different symmetry classes

Symmetry class	Point groups	$J = 0$	$J = 1$	$J = 2$	$J = 3$	$J = 4$	$J = 5$	$J = 6$
Icosahedral	I_h, I	1	1	1	2	2	3	4
Cubic	O_h, O, T_d, T_h, T	1	1	2	3	4	4	6
Octagonal	D_8, C_{8v}, S_8, D_{4d}	1	2	3	4	6	7	8
Hexagonal	$D_{6h}, D_6, C_{6v}, C_{6h}, C_6, D_{3h}, C_{3h}$	1	2	3	5	6	7	9
Pentagonal	$D_{5h}, D_5, C_{5v}, C_{5h}, C_5$	1	2	3	4	5	7	8
Tetragonal	$D_{4h}, D_4, C_{4v}, C_{4h}, C_4, S_4, D_{2d}$	1	2	4	5	7	8	10
Trigonal	$D_{3d}, D_3, C_{3v}, C_{3i} (=S_6), C_3$	1	2	3	5	6	7	9
Orthorhombic	D_{2h}, D_2, C_{2v}	1	3	5	7	9	11	13
Monoclinic	C_{2h}, C_2, C_s	1	3	5	7	9	11	13
Triclinic	C_1, C_i	1	3	5	7	9	11	13

Reproduced from Binnemans [20] with permission from Elsevier

10.3.2 Energy Transfer

The energy transfer is a process in which a donor ion, after excitation to an excited state as a result of absorption of certain energy $h\omega_{exc}$, transfers part of its excitation energy to a second neighboring acceptor ion (luminescent center) that may or may not show a weak absorption in the relevant wavelength range of the pumping band (excitation wavelengths) [43, 44]. Therefore, the luminescence of the acceptor ion is usually enhanced as a result of this energy transfer process, sometimes by several orders of magnitude, and the fluorescence of the excited donor ion is quenched. Energy transfer is a way to increase the luminescence efficiency of the rare earth materials by codoping one rare earth ion, e.g., Tb^{3+} (luminescence activator) together with the other rare earth ion, e.g., Ce^{3+} (luminescence sensitizer), in the solid host matrix (e.g., LaF_3) [45]. However, in the case of luminescent RE^{3+} complexes, the luminescence efficiency can be increased via intramolecular energy transfer from the organic ligands to rare earth ions (*antenna effect*) [15, 16, 19, 46], which overcome the problem of very low molar absorption coefficients ($1.0 \text{ M}^{-1} \text{ cm}^{-1}$) of transitions in 4f levels of these ions. In addition, this process of electronic energy transfer usually increased the population density of the emitting level of the luminescent center (e.g., RE^{3+} ion) that obviously improves the efficiency of the luminescent system, such as laser. Energy transfer may be radiative or non-radiative.

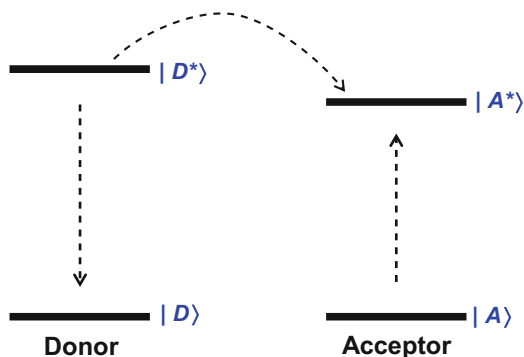
10.3.2.1 Radiative Energy Transfer

It is an excitation energy transfer process in which the donor ion (D) undergoes radiative deactivation and the neighboring acceptor ion (A) reabsorbs the emitted radiation of the donor ion. In this process, the energy-donating ion absorbs efficiently the excitation energy, showing efficient quantum yield, and the lifetime of the donor excited state is not changed [44]. The radiative energy transfer mechanism requires an overlap between the emission bandwidth or spectrum of the donor and the absorption bandwidth or spectrum of the neighboring acceptor ion. Therefore, photons emitted by D are reabsorbed by A, and consequently, emission from A is enhanced [47]. The radiative energy transfer is dominant when the distance between donor and acceptor is larger and their wave-function overlap is essentially negligible. The energy donor and acceptor ions are also called *sensitizer* and *activator*, which are denoted by S and A, respectively. Energy transfer sometimes occurs between similar ions, resulting in concentration-dependent fluorescence and self-quenching.

10.3.2.2 Non-radiative Energy Transfer

In this process, energy donor (D) absorbs the excitation energy efficiently and transfers it non-radiatively to the neighboring acceptor (A). In this case, the acceptor shows no or smaller absorption bands within the absorption spectral region of donor, while the donor shows no or smaller emission band in the emission spectral region of the acceptor. The process of non-radiative energy transfer is schematically shown in Fig. 10.4, where the donor and acceptor states are $|D\rangle$ and $|A\rangle$, respectively [47]. The interaction between the donor and the acceptor results in a decrease in the energy of the donor and an increase in the energy of the acceptor. It should be emphasized that no photons are emitted in such a process. However, non-radiative energy transfer is another deactivation channel, which is accompanied by a decrease in the lifetime of the excited state of the donor. The characteristic lanthanide ion luminescence (4f-4f

Fig. 10.4 Schematic representation of donor and acceptor states involved in the non-radiative energy transfer process. (Reproduced from Bettinelli and Flint [48] with permission from Elsevier)



luminescence) in rare earth compounds is a consequence of the strong absorption in the UV region by ligands (in the case of RE^{3+} complexes) or sensitizer ion (in the case of inorganic RE^{3+} materials) [49], which then transfers energy non-radiatively to the lanthanide ion that subsequently emits in the visible region.

The donor ions or molecules transfer energy non-radiatively to neighboring acceptor ones by a variety of mechanisms. A well-known mechanism for the transfer of energy from one site to another one in crystals (between dopants and defects in both semiconductors and insulators), amorphous materials, solutions, and biological systems is resonant energy transfer.

Resonant Energy Transfer This process occurred due to a weak electromagnetic coupling between the electrons on the energy donors and those on the acceptors [49], which are not to be confused with charged donors and acceptors in semiconductors. These energy donors and acceptors undergo only changes in their state of excitation (Fig. 10.4) not in their state of ionization. The resonant energy transfer mechanism was explained quantum mechanically by Forster in the dipole approximation for transfer between organic molecules. Dexter generalized the theory to higher-order interactions, including exchange interaction, and applied the theory to energy transfer between dopant ions in inorganic solids.

For ions or molecules separated by sub-nanometer distances, a direct energy exchange (Dexter energy transfer) resulting from wave-function overlap can occur [50, 51]. At larger distances when wave-function overlap is essentially negligible, the dominant process for resonant energy transfer is the Förster resonance energy transfer, which is associated with the Coulombic interactions that consist of long-range dipole-dipole interactions (Förster's mechanism) [44]. In resonant energy transfer, the donor ion in its excited electronic state equilibrates with the lattice modes before energy transfer occurs to the acceptor one. The theory was developed for donor and acceptor ions which are weakly coupled to each other but each, separately, strongly coupled to the lattice. For example, fluorescent lamps utilize resonant transfer between dopants in phosphors [49]. As a consequence of this strong electron-phonon interaction, energy can be conserved during the transfer. The transfer probability is found to depend on the overlap of the emission spectrum of the energy donor and the absorption spectrum of the energy acceptor. The basic interaction which drives the transfer is the electromagnetic coupling between the donor and acceptor. In the dipole approximation, it is essentially the same as the van der Waals interaction between gas molecules.

Resonant energy transfer provides an additional decay mechanism for the excited donor; therefore, the lifetime of the donor as measured by the decay of its characteristic fluorescence is decreased [52]. This clearly distinguishes this process from radiative transfer by sequential donor emission and acceptor absorption, which would not change the lifetime of the donor excited state. The dependence of the resonant energy transfer on the overlap of the donor emission and acceptor absorption contains evidence of the lattice relaxation before transfer. Therefore, conservation of electronic energy during the transfer distinguishes resonant transfer from nonresonant transfer. It is interesting to distinguish among radiative energy

transfer and nonresonant and resonant energy transfer [49]: in radiative transfer a real photon is created by the energy donor and is then absorbed by the energy acceptor; for nonresonant transfer phonons are created or annihilated as part of the transfer process, whereas for resonant transfer phonons are neither created nor destroyed.

Nonresonant Energy Transfer For the trivalent rare earth ions dopants with weak electron-phonon interactions and lack of overlap between the emission and absorption spectra of the donor and acceptor ion, the energy transfer may not be possible by the resonant energy transfer mechanism [49]. However, phonon-assisted energy transfer is possible, for moderately small energy mismatch may involve the creation and/or annihilation of a phonon at the sites of either or both the donor and the acceptor ion, and for large energy mismatch, many phonon processes may occur. For very small mismatch, the creation of one phonon and annihilation of another of a slightly different energy may be required. The latter, two-phonon processes can have a higher probability than a single-phonon process involving a low-energy phonon because of the low density of states of these latter phonons. In addition to phonon-assisted processes which create or annihilate real phonons, there are also phonon-assisted transfer processes involving virtual phonon exchange, in which a phonon is first annihilated/created at one site and then created/annihilated at the second site. Bettinelli and coworkers [48] have reported the nonresonant energy transfer from the 5D_4 energy level of Tb^{3+} to the 5D_0 energy level of Eu^{3+} ion for the $Cs_2NaTb_{1-x}Eu_xCl_6$ ($x = 0.01-0.15$) material, which involves the participation of one or more odd-parity phonons.

10.3.2.3 Intramolecular Energy Transfer Mechanisms in Rare Earths

Sensitization Processes in RE^{3+} Organic Complexes

Intramolecular energy transfer in rare earth complexes under excitation by near ultraviolet light has been the subject of major research investigations since last several decades, because the RE^{3+} ions show weak intense absorption bands due to very limited amount of radiation absorbed by direct excitation in the 4f-4f transitions. Therefore, the molar absorption coefficients ϵ of mostly transitions in the absorption spectra of the trivalent rare earth ions is lower than $10 \text{ L mol}^{-1} \text{ cm}^{-1}$ [11]. The luminescence intensity is not only proportional to the luminescence quantum yield but also to the amount of light absorbed; weak light absorption results in weak luminescence. The weak light absorption has been overcome by the development of the so-called antenna effect (or *sensitization*). Weissman discovered in 1942 that excitation of RE^{3+} complexes at wavelength corresponds to the absorption band of organic ligand results in intense metal-centered luminescence [19]. Part of the energy absorbed by the organic ligand is transferred to the RE^{3+} excited states (intramolecular energy transfer); consequently sharp intense emission bands, originating from the metal ion, are observed. This phenomenon is termed as sensitization of the metal-centered luminescence (also

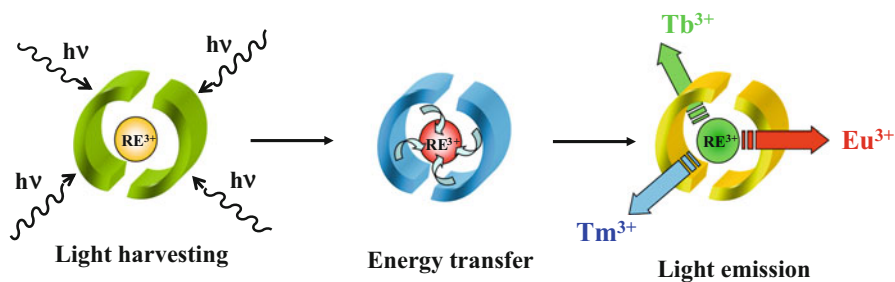


Fig. 10.5 Schematic representation of the sensitization process of rare earth luminescence via the surroundings of the metal ion. (Reproduced from Bünzli J-C, G. and Piguet, C. [17] with permission from The Royal Society of Chemistry)

referred to as *antenna effect*) [16], which proceeds in three distinct steps (Fig. 10.5): (i) light absorption by the surrounding chemical environment of the RE^{3+} ion via attached organic ligands (chromophores), (ii) energy transfer to the excited energy states of the metal ion, and (iii) de-excitation of the metal ion with its characteristic emission spectrum.

In this way, the emitting 4f level of the RE^{3+} ions is in general populated much more efficiently than by direct excitation of the RE^{3+} ion excited levels. Thus, the 4f-4f luminescence intensity is the result of a balance between strong absorption by the ligands, ligand-rare earth ion energy transfer rates, non-radiative decays, and radiative emission rates involved [12, 15, 53, 54]. Besides, the mechanism of the energy transfer from the organic ligand to the lanthanide ion has been investigated in the early 1960s and realized that the luminescent RE^{3+} complexes show potential as active components for amplification in polymer optical fibers and wave guides. Therefore, intense research activity has been going on in the field of luminescent materials based on rare earth complexes. The commonly accepted mechanism of energy transfer from the organic ligands to the rare earth ion (intermolecular energy transfer) and subsequent luminescent decay process has shown schematically in Fig. 10.6 that is detailed below.

Three pathways have been considered by which the excitation energy can be transferred to the rare earth ion [11, 13]: (i) The donor $|S_1\rangle$ state transfers energy to a higher excited 4f state $|4\rangle$ which then decays non-radiatively, finally populating the state $|2\rangle$. (ii) State $|4\rangle$ transfers energy back to a lower ligand triplet state $|T_1\rangle$ which then transfers energy to the lower 4f states $|3\rangle$ or $|2\rangle$. (iii) State $|S_1\rangle$ decays non-radiatively to the state $|T_1\rangle$, which then transfers energy to the states $|3\rangle$ or $|2\rangle$. In the case of Eu^{3+} and Tb^{3+} ions, there is experimental and theoretical evidence that process (iii) is dominant, although in some cases, direct energy transfer from singlet state $|S_1\rangle$ (process i) is of importance.

Trivalent europium ion is extremely useful in studying intramolecular energy transfer mechanism due to the special characteristics of its energy level structure. The energies of the excited 5D_J manifolds ($J = 0-4$) of the $4f^6$ configuration are sufficiently well separated from the ground state 7F_J manifolds ($J = 0-6$) and

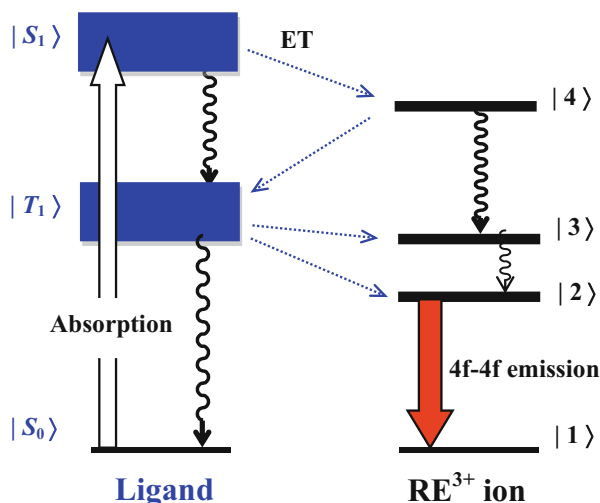


Fig. 10.6 Schematic energy level diagram showing the possible energy transfer processes in a RE^{3+} coordination compounds. Dashed arrows indicate energy transfer (ET), and wavy arrows indicate non-radiative decays. (Reproduced from Bünzli J-C, G. and Piguet, C. [17] with permission from The Royal Society of Chemistry)

usually present appropriate resonance conditions with excited states of the ligands. Therefore, for the sake of understanding, the non-radiative energy transfer pathway from the β -diketonate ligand (TTA, thenoyltrifluoroacetate) to Eu^{3+} ion has been shown in Fig. 10.7. Recently, Malta and coworkers [54] have reported that the main luminescence sensitization path in the $[\text{Eu}(\text{TTA})_3(\text{H}_2\text{O})_2]$ complex occurs through the energy transfer from the first T_1 excited state of the TTA ligand to the 5D_1 excited level of the Eu^{3+} ion.

Energy Transfer Between RE^{3+} Ions in Inorganic Solids

Trivalent rare earth ions doped in inorganic solids exhibit emissions in broad range of visible to near-infrared regions due to the 4f intraconfigurational transitions in their highly abundant energy level structure [16, 18]. The luminescence intensities of the various RE^{3+} ions are sometimes enhanced or quenched by the coexistence of other trivalent rare earth ions doped in the same host matrix. It has been concluded that these phenomena take place as a result of the non-radiative transfer of excitation energy from a rare earth ion behaving as an energy donor to another rare earth ion behaving as an energy acceptor [53, 55–57]. The mechanism which governs the energy transfer process between trivalent rare earth ions has been the subject of several papers [45, 57], which have been published earlier. Therefore, it has been concluded that electronic excitation of lanthanide ions in insulating host materials undergoes migration through resonant energy transfer and phonon-

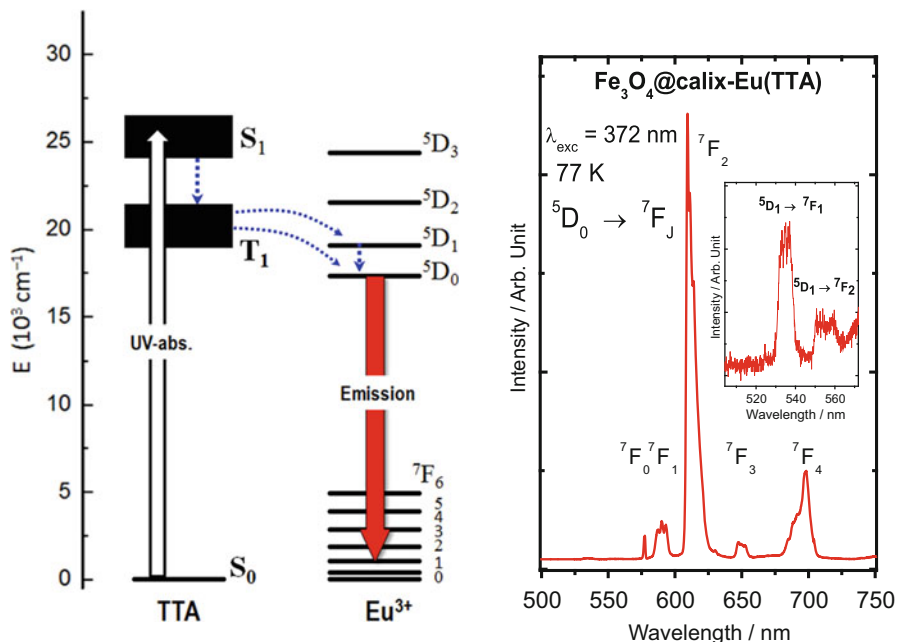


Fig. 10.7 Partial energy level diagram (left) of the $\text{Fe}_3\text{O}_4@\text{calix-Eu(TTA)}$ nanophosphor. The dashed arrows represent non-radiative decays; the red color arrow corresponds to the radiative decay of the Eu^{3+} ion, most probably intramolecular energy transfer processes from the TTA to Eu^{3+} ion. Room temperature emission spectrum (right) of the $\text{Fe}_3\text{O}_4@\text{calix-Eu(TTA)}$ under excitation at 372 nm which corresponds to the $S_0 \rightarrow S_1$ transition of the organic ligands. (Reprinted with permission from Khan et al. [14] Copyright 2018 American Chemical Society)

assisted nonresonant energy transfer processes, as a result of ion-ion interactions [16, 50, 51]. The latter is more important because ions imbedded in the lattice of host materials do not have exactly the same energy level in an excited state due to lattice stress and defects. As a result, the line widths of electronic transitions are homogeneously broadened, and resonant energy transfer becomes improbable. In addition, in case of the luminescence concentration quenching of the RE^{3+} ions, the resonant non-radiative cross-relaxation process usually occurred.

In order to be well understandable by readers, herein, we describe the example of the non-radiative energy transfer (ET) pathways among the Ce^{3+} , Gd^{3+} , and Tb^{3+} ions co-doped in LaF_3 host matrix, through the schematic energy level diagram, as shown in Fig. 10.8. A simplified energy transfer process among these ions is described as follows [45]: (i) a strong absorption from the $^2F_{5/2}$ ground state to the 5d excited state of the Ce^{3+} ion leading to a weak emission from 5d to $^2F_{5/2}$ states, (ii) non-radiative energy transfer pathway from the 5d state of the cerium ion to $^6I_{7/2}$ excited state of the Gd^{3+} ion that decays non-radiatively to $^6P_{7/2}$ emitting level resulting in weak UV emission assigned to the $^6P_{7/2} \rightarrow ^8S_{7/2}$ transition, and (iii) a direct energy transfer from the 5d (Ce^{3+}) and $^6P_{7/2}(\text{Gd}^{3+})$ states to the $4f^8$

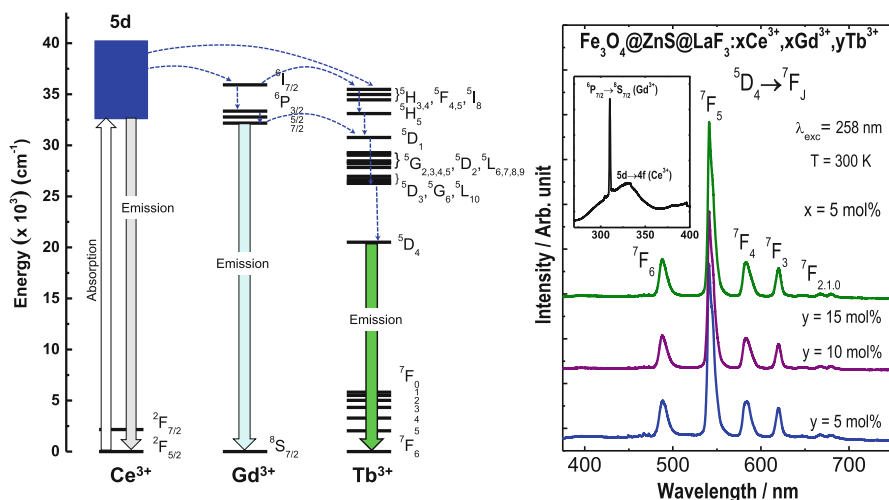


Fig. 10.8 Partial energy level diagram (left) of the $\text{Fe}_3\text{O}_4@ZnS@LaF_3:x\text{Ce}^{3+},x\text{Gd}^{3+},y\text{Tb}^{3+}$ nanophosphors presenting energy transfer (ET) processes from the sensitizer (Ce^{3+}) to the Gd^{3+} and Tb^{3+} activator ion. The dashed arrows represent *non-radiative* decays, and the gray, bluish, and green color downward arrows correspond to the radiative decay of the Ce^{3+} , Gd^{3+} , and Tb^{3+} ions, respectively. Room temperature emission spectra (right) of the $\text{Fe}_3\text{O}_4@ZnS@LaF_3:x\text{Ce}^{3+},x\text{Gd}^{3+},y\text{Tb}^{3+}$ under excitation at 258 nm which corresponds to the $4f(2F_{5/2}) \rightarrow 5d$ interconfigurational transition of the Ce^{3+} ion. (Reproduced from Shrivastava et al. [45] with permission from The Royal Society of Chemistry)

intraconfigurational excited states of the Tb^{3+} ion. In this energy transfer process, the Gd^{3+} ion provides another energy transfer pathway between sensitizer (Ce^{3+}) and activator (Tb^{3+}) ions.

Sensitization via ligand-to-metal charge transfer states or d-transition metal ions can also be envisaged. Charge transfer states essentially operate for Sm^{3+} , Eu^{3+} , and Yb^{3+} ; they are often used when these ions are inserted into inorganic matrices and their energy has to be carefully tuned. Indeed, if such LMCT states lie at high enough energy, they can transfer energy into the excited 4f states; however, when their energy is close to the energy of the emitting level, they act as efficient quenchers of the 4f luminescence.

Energy Transfer in Upconversion Luminescent RE^{3+} Materials

The upconversion is a nonlinear optical process that upconverts two or more low-energy near-infrared pump photons into a higher-energy output photon, ranging from the NIR to visible and even UV regions. This phenomenon was initially proposed by N. Bloembergen in 1959 [58]. Later on, extensive research efforts have been dedicated to enrich the family of UC luminescent materials and explain the mechanism of UC process. Most of the reported upconversion luminescent

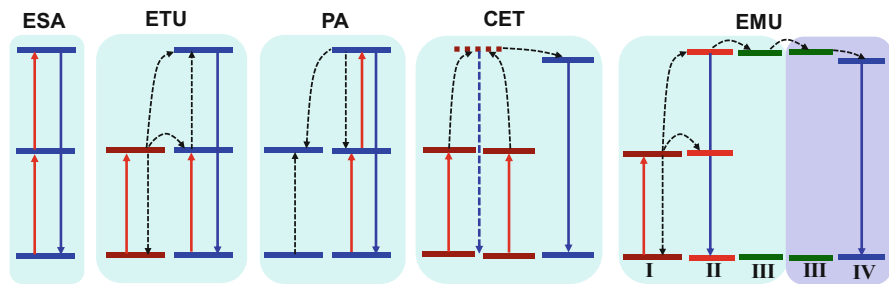


Fig. 10.9 Simplified energy level diagrams for reported anti-Stokes (UC) processes, ESA, ETU, PA, CET, and EMU (from left to right); upward (red) and downward (blue) full arrows represent direct excitation processes and radiative emission processes, respectively. The dashed arrows (black) correspond to the energy transfer processes. Note that non-radiative relaxations are not given here for clarity. The energy levels of sensitizers and activators ions are shown with dark red and blue colors, respectively, for the ETU, CET, and EMU processes, whereas, in case of the EMU, core and shell regions are highlighted with different background colors. (Reproduced from Dong et al. [18] with permission from The Royal Society of Chemistry)

materials contain rare earth ions as sensitizers and emitters (activators) because of the abundant energy level structure (Fig. 10.9) in 4f-electron configurations of these ions. Therefore, RE^{3+} ion-doped materials show unique upconversion luminescence properties including large anti-Stokes shifts of several hundred nanometers (even >600 nm, about 2 eV), sharp emission lines, long upconversion luminescence lifetimes (\sim ms), and remarkable photostability.

Generally, UC mechanisms are categorized into five classes, as described by Dong and coworkers in review article, which are given in detail as follows [16, 18, 59–63]:

- (i) *Excited-state absorption (ESA)*: This process (Fig. 10.9) is referred to a sequential absorption of two pump photons by a single rare earth ion of multiple energy levels, using a real intermediary energy level. As a result, the intermediate energy levels of the luminescent centers should be stable with adequate electron populations, which allow the sequential absorption of a second pump photon. The high pump power density and large absorption cross section facilitate ESA processes. The ESA is usually occurred in the upconversion luminescent rare earth materials, which contains simply one RE^{3+} ion as an activator doped in crystalline host matrix at low concentration, i.e., without sensitizer ion; consequently, interactions between the activators can be neglected, and ESA process is responsible for the upconversion. Furthermore, an ESA process is more likely to occur with a low-doping concentration ($<1\%$), as a high-doping concentration could lead to prominent non-radiative cross relaxations that deteriorate the emission intensity significantly.
- (ii) *Energy transfer upconversion (ETU)*: This is the most popular mechanism (Fig. 10.9), since it has a high efficiency (about two orders of magnitude higher

than ESA), and is less susceptible to external environment. The ETU usually occurred in upconversion materials, which contain two different types of rare earth ions, namely, a sensitizer and an activator, which are embedded in the upconversion unit. In ETU, the absorption cross section of the sensitizer is larger than that of the activator. Therefore, upon excitation of lower energy photons, both the sensitizer and the activator ions could be pumped to their excited states. Subsequently, the sensitizer ion non-radiatively transfers its excitation energy to the neighboring activator ion via a dipole-dipole resonant interaction that can emit from the high-energy levels. RE^{3+} ions with multiple excited states show great advantages for ETU processes. So far, most of the commonly used upconversion sensitizer and activator RE^{3+} ions pairs are $\text{Yb}^{3+}/\text{Er}^{3+}$, $\text{Yb}^{3+}/\text{Tm}^{3+}$, and $\text{Yb}^{3+}/\text{Ho}^{3+}$, which are all recognized to follow the ETU mechanism.

- (iii) *Photon avalanche (PA)*: This process was first proposed by Chivian et al. [64] in a Pr^{3+} -based infrared quantum counter in 1979. This mechanism occurred in the upconversion RE^{3+} materials, where the energy gap between the intermediate and ground states of the luminescent centers does not match the energy of the pump photon, as shown in Fig. 10.9. In this case, the luminescent centers may undergo an ESA process to populate a higher excited state (superexcited). In addition, if certain electrons are promoted to the intermediate state, then cross relaxation resonantly occurs between the superexcited ion and a neighboring ground state ion, leading to the occupation of the intermediate states of both ions. The repeating of such a process exponentially populates the intermediate states above the excitation threshold. The avalanche transitions are readily occurred as long as the consumption of superexcited ions is less than that of the ground state ions. The PA-related upconversion emissions are much less efficient. Therefore, limited reports are present in literature [18], e.g., PA-based upconversion emissions in LnVO_4 nanocrystals ($\text{Ln} = \text{Ce}, \text{Nd}$).
- (iv) *Cooperative energy transfer (CET)*: In this mechanism, both sensitizer and activator ions are important, similar to the ETU process. However, in a typical CET phenomenon, two sensitizer ions are cooperatively activated to a virtual excited state to fulfill a simultaneous energy transfer to a neighboring activator one, as shown in Fig. 10.9. In CET system, the low-efficiency cooperative UC emissions from the sensitizer ions can be also observed, in addition to the UC emission from the activators ions.
- (v) *Energy migration-mediated upconversion (EMU)*: This mechanism was first proposed by Liu and coworkers [62] for the upconversion luminescent lanthanide-doped $\text{NaGdF}_4@/\text{NaGdF}_4$ core-shell nanoparticle. The basic requirement for the EMU mechanism is the core-shell design nanostructure and four types of rare earth ions which participate in EMU process: sensitizers (I), accumulators (II), migrators (III), and activators (IV). The EMU process occurs via the following steps (Fig. 10.9):

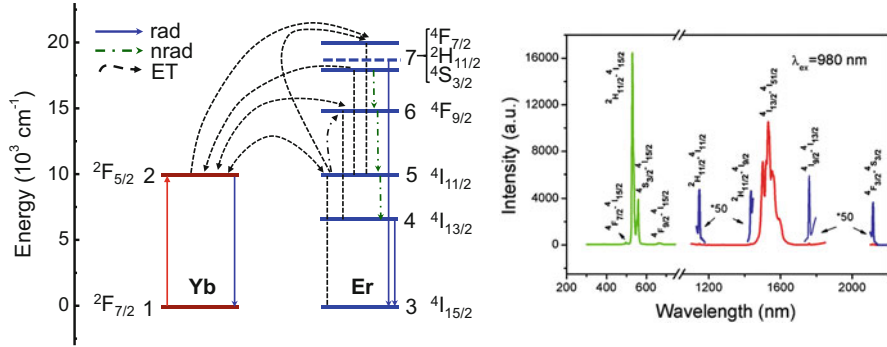


Fig. 10.10 Energy levels and processes (left) taken into account in the model: *rad.* refers to radiative transition, *nrad.* to non-radiative transition, and *ET* to energy transfer process; arrows point at the final levels of the acceptor, while the vertical dashed lines between the levels mark the transitions involved in the particular energy transfer process. (Reproduced from Shyichuk et al. [55] with permission from Elsevier). Room-temperature visible to IR emission spectra (right) of the $\text{YVO}_4:\text{Yb}^{3+}, \text{Er}^{3+}$ under 980 nm NIR excitation (300 mW). (Reproduced from Xu et al. [65] with permission from The Royal Society of Chemistry)

- (i) The sensitizer ion first absorbs the pump photons and subsequently transfers its excitation energy to an accumulator ion (population of excited state of accumulator ion) via an ETU process.
- (ii) The excited energy migrates from the high-lying excited state of the accumulator to the migrator ion.
- (iii) Then, followed by migration of excitation energy via the migrator ion sublattice through the core-shell interface, subsequently, the migrating energy is trapped by the neighboring activator ion.
- (iv) Radiative upconversion emissions from the activator and accumulator ions.

The energy transfer upconversion (ETU) between two neighboring ions is by far the most efficient process. Therefore, for the sake of understanding, the ETU process is described in a typical system of $\text{YVO}_4:\text{Yb}^{3+}, \text{Er}^{3+}$ through the energy level diagram, as shown in Fig. 10.10. The diagram shows the two-photon upconversion process involving Yb^{3+} ion (e.g., ${}^2\text{F}_{5/2} \rightarrow {}^2\text{F}_{7/2}$) as a sensitizer (donor) and Er^{3+} ion (e.g., ${}^4\text{I}_{15/2} \rightarrow {}^4\text{I}_{11/2}$, ${}^4\text{I}_{11/2} \rightarrow {}^4\text{S}_{3/2}$, and ${}^4\text{I}_{11/2} \rightarrow {}^4\text{F}_{9/2}$) as an activator (acceptor) [55, 65].

Cross Relaxation

The higher-energy level emissions of the rare earth ions are usually suppressed by two process [66]:

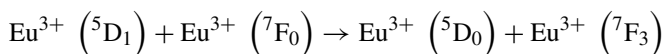
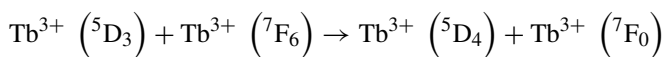
- (i) Multiphonon relaxation, which is only of importance if the energy difference between the involved levels of the RE^{3+} ion is less than about five times of the

highest vibrational frequency of the host lattice and it is independent of the concentration of the luminescent center. For example, in the case of $\text{YBO}_3:\text{Eu}^{3+}$ (0.1 mol%) materials, only $^5\text{D}_0$ emission is observed for the low Eu^{3+} ion concentration (0.1 mol%), since the higher-energy level emissions are quenched by multiphonon emission (highest borate lattice frequency $\sim 1050 \text{ cm}^{-1}$).

- (ii) The other one is the cross relaxation, which occurred above certain concentration of luminescent centers, because this process depends on the interaction between two luminescent centers and requires a high degree of resonance between two participating transitions in order to be efficient.

Most simply, the cross relaxation is a decay process in which a portion of excitation energy non-radiatively transfers from the excited level (populating through radiative absorption or energy transfer process) of one rare earth ion to the ground level of the other nearby ion in the same host matrix, consequently, which is promoted to the higher level (Fig. 10.11) and causes a decrease of the lifetime of the excited level of the RE^{3+} ion [45, 67]. For example, in the case of $\text{Y}_2\text{O}_3:\text{Eu}^{3+}$ phosphor, at low Eu^{3+} ion concentration (0.1 mol%), the emissions occurred from the $^5\text{D}_2$, $^5\text{D}_1$, and $^5\text{D}_0$ excited energy levels (highest lattice frequency $\sim 600 \text{ cm}^{-1}$) [66]. However, at high Eu^{3+} ion concentration (3 mol%), the emission spectrum of the $\text{Y}_2\text{O}_3:\text{Eu}^{3+}$ phosphor is dominated by the $^5\text{D}_0$ emission. In this case, the higher-energy level emission is quenched by cross relaxation in favor of the $^5\text{D}_0$ emission and causes a decrease of the lifetime of the excited level of the Eu^{3+} ion. This process usually occurred as the energy difference between the $^5\text{D}_1$ and $^5\text{D}_0$ excited levels matches approximately to the energy difference between the $^7\text{F}_0$ fundamental level and higher $^7\text{F}_3$ level. At high Eu^{3+} concentration, a portion of excitation energy difference, $^5\text{D}_1-^5\text{D}_0$ from the one Eu^{3+} ion (I), is non-radiatively transferred to the $^7\text{F}_0$ ground level of other nearby ones (II), which is promoted to the higher $^7\text{F}_0$ level. Therefore, the blue Eu^{3+} ion emission is quenched by cross relaxation in favor of the well-known red emission.

For the Eu^{3+} and Tb^{3+} ions, the cross relaxation may occur in the following way:



Similarly, for the Tb^{3+} ion, the energy difference between the $^5\text{D}_3$ and $^5\text{D}_4$ excited levels matches approximately to the energy difference between the $^7\text{F}_6$ fundamental level and higher $^7\text{F}_0$ level. Therefore, at higher Tb^{3+} ion concentration in host matrix, cross relaxation quenches the emission from the $^5\text{D}_3$ level in favor of emission originating from the $^5\text{D}_4$ one by transferring the portion of excitation energy difference, $^5\text{D}_3-^5\text{D}_4$ from the one Tb^{3+} ion (I) to the $^7\text{F}_0$ ground level of other nearby ones (II), consequently, which is promoted to the higher $^7\text{F}_0$ level (Fig. 10.11). This process implied that it is not usually possible to obtain blue Tb^{3+} emission in luminescent materials with higher Tb^{3+} concentrations.

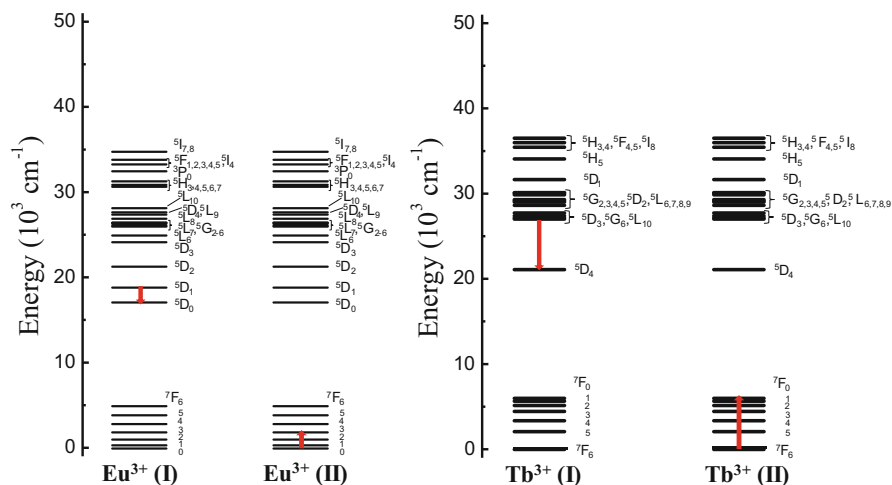


Fig. 10.11 Quenching of higher-energy level emission by cross relaxation. For Eu^{3+} ion (left), the ${}^5\text{D}_1$ emission of Eu^{3+} (I) is quenched by transferring the energy difference, ${}^5\text{D}_1$ - ${}^5\text{D}_0$ to the neighboring Eu^{3+} (II), which is promoted to the ${}^7\text{F}_3$ level. For Tb^{3+} ion (right), the ${}^5\text{D}_3$ emission of Tb^{3+} (I) is quenched by transferring the energy difference ${}^5\text{D}_3$ - ${}^5\text{D}_4$ to the other Tb^{3+} (II), which is promoted to the ${}^7\text{F}_0$ level. (Reproduced from Blasse and Grabmaier [66] with permission from Springer Nature)

10.3.3 Luminescence Spectra

The rare earth compounds absorb electromagnetic radiation, particularly in the UV-visible regions, exciting the RE^{3+} ions from their fundamental energy level to the higher levels in the partially filled 4f subshell [36]. Herein, the sensitization process (antenna effect) via intramolecular energy transfer is important to overcome the low molar absorption coefficients and populate the emitting level of the luminescent center (RE^{3+} ions), which radiatively decay to give corresponding emission color [10, 11, 13, 16, 19]. Therefore, with the exception of La^{3+} and Lu^{3+} , all the rare earth ions are luminescent and show narrow emission lines due to the 4f-4f intraconfiguration transitions, which cover the entire spectral regions, from UV (Gd^{3+}) to visible (e.g., Pr^{3+} , Sm^{3+} , Eu^{3+} , Tb^{3+} , Dy^{3+} , Tm^{3+}) and near-infrared (NIR, e.g., Pr^{3+} , Nd^{3+} , Ho^{3+} , Er^{3+} , Yb^{3+}) ranges.

The 4f-4f transitions are either achieved by electric dipole or magnetic dipole mechanisms. The magnetic dipole transitions are parity-allowed, whereas the electric dipole transitions are parity-forbidden (Laporte-forbidden); however the Laporte rule is slightly relaxed for these transitions due to the mixing of opposite parity electronic configurations, produced by the odd components of a non-centrosymmetric ligand field. Moreover, the ligand polarization effects have been shown to be of considerable importance for the 4f-4f transitions [20, 68]. The 4f-4f energy levels of RE^{3+} ions are only slightly affected by the chemical environment due to the

effective shielding of the 4f electrons by the filled 5s and 5p subshells. Therefore, the absorption and emission spectra of the intraconfigurational 4f transitions of the RE^{3+} ions retain more or less their similar atomic character irrespective of the host matrix.

10.3.3.1 Excitation Spectra

The excitation spectra of the luminescent rare earth materials are usually recorded, in order to determine the specific absorption wavelength of the characteristic electronic transition of the organic ligand (in case of RE^{3+} complexes), sensitizer ion, and ligand-to-metal charge transfer (LMCT) state (in case of inorganic RE^{3+} materials) that efficiently sensitize the luminescent center by intramolecular transfer process. Additionally, it also gives information about the 4f-4f energy levels, which efficiently transfer energy to the emitting level of the luminescent center. A transition is observed in the excitation spectrum only if this level is efficient in populating the emitting level and thus in generating luminescence [20, 35]. If an energy level is absent in the excitation spectrum, it means that this level is not efficient in absorbing the excitation energy and/or is not able in populating the emitting level. Therefore, the 4f-4f energy levels of the emitting RE^{3+} ion are also visible in the excitation spectra, in addition to the energy levels of the antenna ligands (Fig. 10.12), sensitizing ion, and LMCT transition. The comparative intensities of the 4f-4f transitions and $S_0 \rightarrow S_1$ transition of the organic ligands also give information about the efficiency of the luminescence sensitizations through intramolecular energy transfer from organic ligands to RE^{3+} ion. For example, the 4f-4f transitions are completely absent or negligibly smaller in the case of $\text{Fe}_3\text{O}_4@\text{SiO}_2\text{-(TTA-Eu-TTA)}$ and $\text{Fe}_3\text{O}_4@\text{SiO}_2\text{-(TTA-Eu-AMB)}$ nanophosphors (Fig. 10.12) [69], suggesting that the luminescence sensitizations through intramolecular energy transfer from TTA and AMB ligands to Eu^{3+} ion are more efficient.

The excitation spectra of the RE^{3+} materials are recorded by monitoring the emission of the higher-intensity transition of rare earth ion at fixed wavelength, and the excitation wavelength is scanned over the spectral region of interest. For example, the excitation spectrum of the Eu^{3+} complexes are recorded in spectral range of 200–550 nm, under the emission monitored at the ${}^5\text{D}_0 \rightarrow {}^7\text{F}_2$ hypersensitive transition of Eu^{3+} ion [14, 23, 69]. An excitation spectrum looks similar to an absorption spectrum, but there is no one-to-one relationship. The relative intensities of the transitions can be different, and there can be extra peaks present or peaks missing in comparison to the corresponding absorption spectrum. In fact, an excitation spectrum can be considered as being the product of an absorption spectrum and a plot of the quantum yield as a function of the wavelength. The main application of an excitation spectrum is to determine the optimum excitation wavelength for measuring an emission spectrum. In this regard, the wavelength that corresponds to the most intense peak or the maximum of the most intense band in the excitation spectrum is chosen.

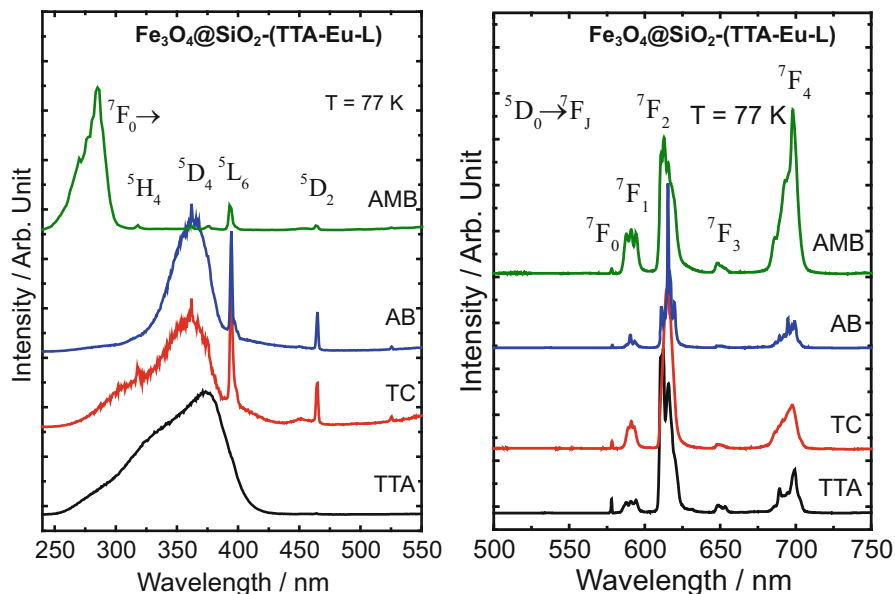


Fig. 10.12 Luminescence spectra of the $\text{Fe}_3\text{O}_4@\text{SiO}_2\text{-(TTA-Eu-L)}$, L: thenoyltrifluoroacetate (TTA), thioglycolate (TC), 4-aminobenzoate (AB), and 4-(aminomethyl)benzoate (AMB) nanophosphors recorded at low temperature (77 K), excitation spectra (left) of monitoring the emission of the ${}^5\text{D}_0 \rightarrow {}^7\text{F}_2$ hypersensitive transition and emission spectra (right) under excitation at 372, 360, 362, and 282 nm, which correspond to the $\text{S}_0 \rightarrow \text{S}_1$ transition of the TTA, TC, AB, and AMB ligands, respectively. (Reproduced from Khan et al. [69] with permission from Elsevier)

10.3.3.2 Emission Spectra

Emission spectra of the RE^{3+} materials are usually dominated by the presence of narrow emission bands, which are assigned to 4f-4f intraconfigurational transitions, arising from the radiative decay of the excited level (e.g., ${}^5\text{D}_0$ in case of Eu^{3+}) to the J levels of the ground term (e.g., ${}^7\text{F}_J$ in case of Eu^{3+}) [11, 20, 35]. In addition, these spectra may contain the emission band from the triplet state (T_1) of the ligands (in case of RE^{3+} organic complexes) or sensitizer ion (in case of inorganic rare earth materials), if the ligand-to-metal intramolecular energy transfer may not be efficient. However, this band is not observable in case of efficient ligand-to-metal intramolecular energy transfer process as shown in Fig. 10.12.

Generally, the luminescence spectra are recorded in a wavelength scale (expressed in nm). Therefore, it is suggested to plot the spectra in such a way that the shortest wavelength is at the left-hand side and the longest wavelength is at the right-hand side in order to facilitate the comparison between different spectra [20]. In the older literature, the opposite convention is often used. The emission spectra of the RE^{3+} materials are recorded by fixing the excitation wavelength, while the detection wavelength of the spectrofluorimeter is scanned over the spectral region of interest. The emission spectra of RE^{3+} compounds are more informative than the corresponding absorption spectra.

The significant observation in the emission spectra of the rare earth materials is the interval between the successive emission lines, which increases with increasing the J value. For example, in case of Eu^{3+} systems, the ${}^5\text{D}_0 \rightarrow {}^7\text{F}_1$ transition is very close to the ${}^5\text{D}_0 \rightarrow {}^7\text{F}_0$ transition, but the ${}^5\text{D}_0 \rightarrow {}^7\text{F}_6$ transition is lying more than 50 nm further to the infrared than the ${}^5\text{D}_0 \rightarrow {}^7\text{F}_5$ transition. Binnemans [20] has reported in the review article that this behavior can be explained by the fact that the splitting of the ${}^7\text{F}_J$ multiplet corresponds quite well to the Landé interval rule: the interval between successive energy levels is proportional to the larger of their total angular momentum values J (i.e., the splitting increases with increasing J values).

The majority of the transitions observed in the luminescence spectrum are induced electric dipole transitions (ED transitions). However, magnetic dipole transitions (MD transitions) can be also observed in the emission spectra of RE^{3+} ions [7, 13, 70, 71]. The electric dipole (ED) transition occurred due to the interaction of the Ln^{3+} ion with the electric field vector through an electric dipole. The intraconfigurational electric dipole transitions (e.g., s-s, p-p, d-d, or f-f transitions) are forbidden by the Laporte selection rule. This selection rule is strictly applied to the lanthanide ion in the gas phase (i.e., a centrosymmetric environment). However, it is slightly relaxed for the rare earth ions, which are embedded in a non-centrosymmetric chemical environment; consequently, the ED transitions can be partly allowed by vibronic coupling or due to the mixing of opposite parity electronic configurations into the 4f wave functions, which are produced by the odd components of a non-centrosymmetric ligand field. Therefore, the observed ED transitions are much weaker than ordinary electric dipole transitions. Therefore, they are often called “induced” electric dipole transitions (or “forced” electric dipole transitions), rather than just electric dipole transitions. The intensities of the ED transitions can be described by the Judd-Ofelt theory [11, 13, 14, 16, 46, 69, 70, 72–74].

The magnetic dipole (MD) transition is caused by the interaction of the lanthanide ion with the magnetic field component of the light via a magnetic dipole. The MD transitions are allowed by the Laporte selection rule, but their intensities are weak and comparable to those of the induced electric dipole transitions. They are largely independent of the chemical environment and can be considered in a first approximation to be constant. For example, in case of Eu^{3+} system, the ${}^5\text{D}_0 \rightarrow {}^7\text{F}_1$ transition has magnetic dipole character. Therefore, during the calculation of experimental intensity parameters (Ω_λ), also known as Judd-Ofelt parameters, the special character of the magnetic dipole which allowed ${}^5\text{D}_0 \rightarrow {}^7\text{F}_1$ transition is exploited for the experimental determination of the $A_{0 \rightarrow J}$ emission coefficients from the emission spectra of the Eu^{3+} compounds. This 4f-4f transition is formally insensitive to the chemical environment around the Eu^{3+} ion and, consequently, can be used as a reference [11, 13]. The detailed overview on the features of ${}^5\text{D}_0 \rightarrow {}^7\text{F}_J$ ($J = 0-6$) transitions for Eu^{3+} ion is summarized in a remarkable way in Table 10.4.

Table 10.4 Overview of the transitions observed in luminescence spectra of Eu^{3+} compounds

Transition ^a	Dipole character ^b	Wavelength range (nm)	Relative intensity ^c	Remarks
$^5\text{D}_0 \rightarrow ^7\text{F}_0$	ED	570–585	vw to s	Only observed in C_n , C_{nv} , and C_s symmetry
$^5\text{D}_0 \rightarrow ^7\text{F}_1$	MD	585–600	s	Intensity largely independent of environment
$^5\text{D}_0 \rightarrow ^7\text{F}_2$	ED	610–630	s to vs	Hypersensitive transition; intensity very strongly dependent on environment
$^5\text{D}_0 \rightarrow ^7\text{F}_3$	ED	640–660	vw to w	Forbidden transition
$^5\text{D}_0 \rightarrow ^7\text{F}_4$	ED	680–710	m to s	Intensity dependent on environment, but no hypersensitivity
$^5\text{D}_0 \rightarrow ^7\text{F}_5$	ED	740–770	vw	Forbidden transition
$^5\text{D}_0 \rightarrow ^7\text{F}_6$	ED	810–840	vw to m	Rarely measured and observed

Reproduced from Binnemans [20] with permission from Elsevier

^aOnly transitions starting from the $^5\text{D}_0$ level are shown

^bED induced magnetic dipole transition, MD magnetic dipole transition

^cvw very weak, w weak, m medium, s strong, vs very strong

10.3.4 Luminescence Decay Curves

The lifetime of the excited level of rare earth ions can be determined from their observed luminescence decay curves. The lifetime of an excited level is the combination of the radiative and non-radiative decay processes. There are three main processes which are usually operating in the relaxation or depopulation of the excited level of the rare earth ion, after being populated with radiative absorption or via energy transfer: (i) radiative decay, (ii) non-radiative decay through the transformation of excitation energy to vibrational quanta of the surroundings, and (iii) non-radiative energy transfer between two identical or nonidentical RE^{3+} ions present in the same host matrix, such as cross relaxation [11, 19, 20, 66]. The non-radiative decay rates via multiphonon relaxation are not directly observable. However, their presence and relative importance are determined by comparison of the observed lifetime of excited level with the total radiative lifetime, and the differences are attributed to the occurrence of non-radiative transitions. The radiative lifetime of an excited state can be determined by calculating the total spontaneous emission probability via the Judd-Ofelt theory or via direct calculation (vide infra).

The lifetime is usually defined as the time after which the population of an excited level of the emission center (RE^{3+} ion) has decayed to 1/e or 36.8% of the initial population. Two methods can be used to measure luminescence lifetimes: time-domain and frequency-domain [20]. In the time-domain method, the sample is excited with a pulse of light, and the width of the pulse is made as short as possible and should be ideally shorter than the lifetime of the excited

state. In the case of RE^{3+} compounds, typically a microsecond flash lamp is used to measure the luminescent decay curves, whereas the lifetime can be obtained by fitting the decay curve of the emission center (RE^{3+} ion), showing mono-exponential decay behavior with exponential function of $I(t) = I_0 \exp\left(-t/\tau\right)$, where $I(t)$ and I_0 are the luminescence intensities at time t and 0, respectively, as well as τ is the radiative decay time [45]. If the luminescent center occupies more symmetry sites and the luminescent decay curve displays bi-exponential decay behavior, then this curve is usually fitted with an exponential function of $I(t) = A_1 \exp\left(-t/\tau_1\right) + A_2 \exp(-t/\tau_2)$, and the average lifetime is calculated according to the Eq. $\tau_{\text{average}} = (A_1\tau_1^2) + (A_2\tau_2^2) / (A_1\tau_1 + A_2\tau_2)$ [69, 75], where τ_1 and τ_2 are short and long lifetimes, with corresponding intensity coefficients A_1 and A_2 .

10.3.5 CIE Coordinates

The emission colors of the rare earth phosphors are usually expressed with x and y color coordinates, using CIE chromaticity diagram (*Commission Internationale de l'Eclairage*), as a standard colorimeter [26, 69]. These x and y color coordinates are calculated as (i) uploading the emission spectrum of the luminescent material in CIE chromaticity diagram and (ii) generating the color coordinates that will give the values for x and y coordinates and will mark a spot in specific color region of the CIE diagram. The location of the spot represents the characteristic emission color of the luminescent material with the specific values of the x and y coordinates (Fig. 10.13). For example, the luminescent Eu^{3+} compounds usually give x and y an emission color coordinates in the red region of the CIE diagram due to the contribution of the high-intensity hypersensitive ${}^5\text{D}_0 \rightarrow {}^7\text{F}_2$ transition (612 nm) of the Eu^{3+} ion.

10.4 Instrumentation

10.4.1 Spectrofluorometer

The luminescence spectra and decay curves of the RE^{3+} compounds are usually recorded with a SPEX FL212 Fluorolog-2 spectrofluorometer and HORIBA Jobin Yvon Fluorolog-3 spectrofluorometer. The later one is the latest version, which is recently used in many photonic or photoluminescence research laboratories.

Generally, the spectrofluorometer consists of light source, excitation monochromator, sample compartment with sample holders, emission monochromator, and detectors (Fig. 10.14). This entire luminescence setup is fully controlled by spectroscopic computer program [76, 77]. The 450W xenon arc lamp is commonly used

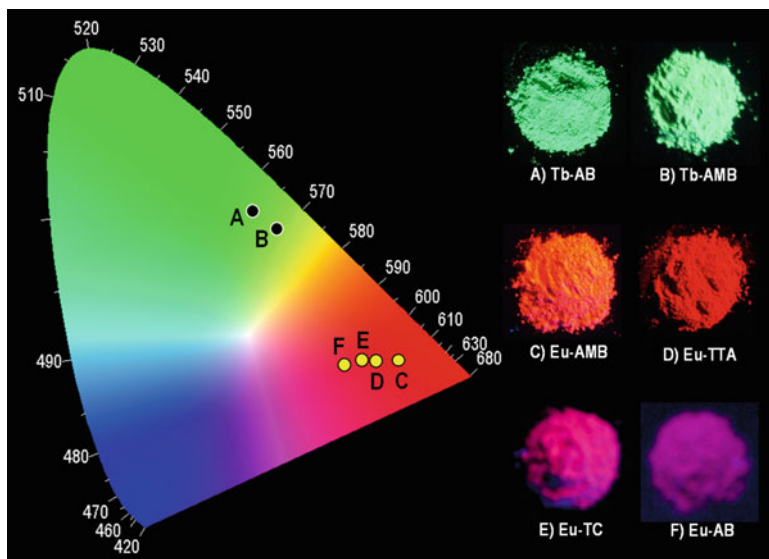


Fig. 10.13 CIE chromaticity diagram showing the (x,y) emission color coordinates for the $\text{Fe}_3\text{O}_4@\text{SiO}_2\text{-(TTA-Eu-L)}$ and $\text{Fe}_3\text{O}_4@\text{SiO}_2\text{-(TTA-Tb-L)}$, L: thenoyltrifluoroacetate (TTA), thioglycolate (TC), 4-aminobenzoate (AB), and 4-(aminomethyl)benzoate (AMB) nanophosphors irradiated at different wavelengths. The inset figures are photographs of nanomaterials taken with a digital camera displaying the green and red emissions under UV irradiation lamp at 254 and 365 nm. (Reproduced from Khan et al. [69] with permission from Elsevier)

as light source, which is already discussed in Sect. 10.2.2. However, other options also exist, including pulsed xenon lamp for phosphorimetry, a laser port for laser source, NanoLED solid-state pulsed sources, a triple-illuminator option to mount nanosecond or microsecond flash lamps, etc. Various detectors, such as a number of photomultiplier tubes (PMT) and CCD arrays, are used in the Fluorolog-3 to expand the range of detectable wavelengths from UV to the near-infrared region (longer than 800 nm). In addition, the Fluorolog-3 spectrofluorometer has facilities of fiberoptic probe that can be coupled to the sample compartment, and the spectroscopic measurements can be made remotely. The adjustable parameters for luminescent spectra measurement are excitation wavelength(s) and emission wavelength(s), excitation and emission slit widths, and sampling increment and integration time. Generally, the spectrofluorometer works on the basis of the following principles: (i) the light source produces photons; (ii) the excitation monochromator filters the coming beam of light from the light source and allows a single wavelength of light to reach the sample; (iii) in the sample compartment, the sample responds to the incoming radiation by emitting light after excitation with the selected wavelength, if the sample may luminescent; (iv) the resulting radiation coming from the sample is filtered by an emission monochromator that projects the signal to a detector (PMT or CCD); and finally (v) a spectrum is produced by recording the variation

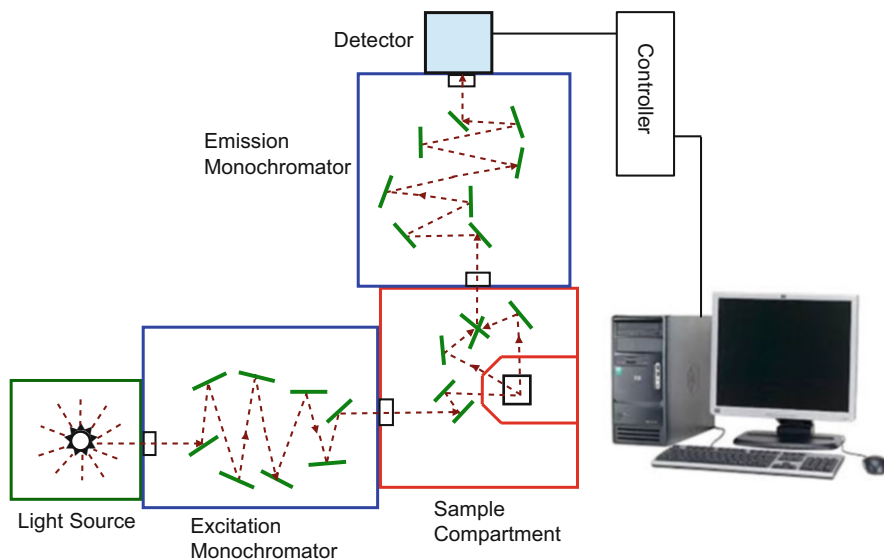


Fig. 10.14 Schematic illustration of the Fluorolog-3 spectrofluorometer, containing light source, excitation monochromator, sample compartment, emission monochromator, and detectors. (Prepared by Author Latif U Khan)

in intensity as a function of wavelength (nm). The spectrofluorometer components (monochromators, sample compartment, detector, accessories) are connected to a controller which, in turn, transfers information to the computer.

10.4.1.1 Monochromators

The monochromators, also known as monochromatic illuminators, are used to disperse the polychromatic or white light into the various colors or wavelengths. This dispersion can be achieved either by using prisms or diffraction gratings [77]. The spectrofluorometers usually used diffraction-grating monochromators rather than prism ones. The advantages of grating monochromators over prism ones are (i) linear wavelength dispersion, (ii) high aperture, and (iii) easy interchange of gratings for different spectral regions. However, the grating monochromator generally has higher scattered light, and the overlapping of orders can cause a problem. The most readily available and least expensive monochromator is the single-grating instrument, which is based on the Ebert-Fastie and Czerny-Turner configuration.

The Ebert-Fastie instrument [78, 79] consists of one large spherical concave mirror, one plane diffraction grating, and a pair of entrance and exit slits (Fig. 10.15). A portion of the mirror first collimates the light of source after passing from the entrance slit and falls upon the plane grating. Thereafter, a separate portion of the mirror focuses the dispersed light from the grating toward the exit slit, where it produces a monochromatic light of the entrance slit.

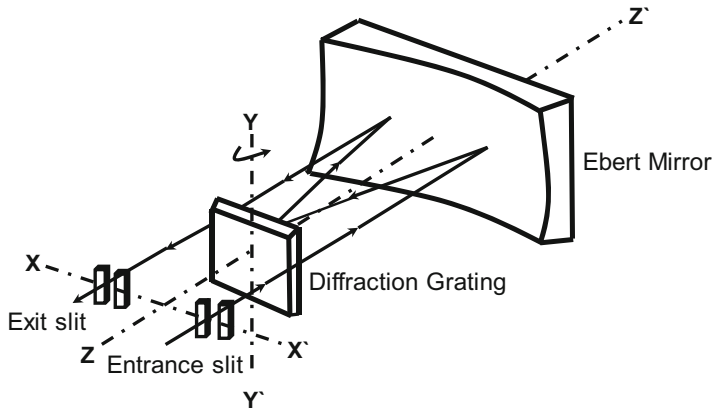


Fig. 10.15 Schematic illustration of the Ebert-Fastie monochromator. (Reproduced from Gaertner et al. [79] with permission from Elsevier)

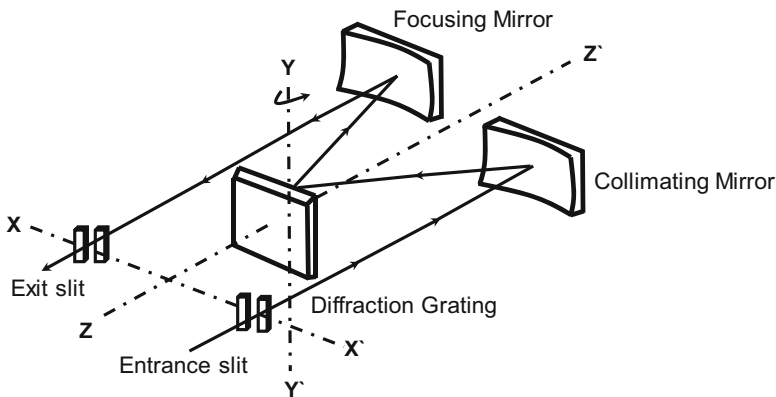


Fig. 10.16 Schematic illustration of the Czerny-Turner monochromator. (Reproduced from Gaertner et al. [79] and An et al. [82] with permission from Elsevier)

The Czerny-Turner (CZ) monochromator [80–81] is similar in principle to the Fastie-Ebert one but offers more flexibility in the design and positioning of the reflector mirror. It consists of two concave mirrors and one plan diffraction grating (Fig. 10.16). The two mirrors are working separately in the same way as the single spherical mirror of the Fastie-Ebert configuration. The collimating mirror first collimates the light source and then reflects toward the grating, thereafter, the focusing mirror is focused on the dispersed light from the grating toward the exit slit, where it produces a monochromatic image of the entrance slit. Generally, in a typical monochromator, the diffraction grating is rotatable and dispersed light by diffracting different wavelengths at different angles. The particular wavelength that passes through the monochromator is usually selected by rotating the angle

of the grating, but the mirror and slit positions are remained fixed. Therefore, the monochromator is designed to isolate a selective narrow portion of the spectrum from the source.

Two types of monochromators are used in Fluorolog-3 spectrofluorometers (Fig. 10.14), usually with Czerny-Turner configuration: (i) the excitation monochromator, which selects a narrow portion of the spectrum (bandpass) of a given light source and irradiates a sample, and (ii) the emission monochromator, which is used for analysis before the photosensitive detector and sequentially selects wavelengths for the detector to record the different components (spectrum) of the emitting light of the sample. Generally, the excitation monochromator is selected on the basis of principle that shows high efficiency in the ultraviolet region and an emission monochromator for high efficiency in the range of visible wavelengths.

The functional specifications of a monochromator include dispersion, efficiency, and stray light levels. Dispersion is usually given in nm/mm, whereas the slit width is sometimes expressed in mm. The monochromator for photoluminescence spectroscopy requires low stray light levels to avoid problems due to scattered or stray light. The stray light means the light of certain wavelength, which is transmitted by the monochromator different than the chosen wavelength and bandpass. Monochromators are also selected for high efficiency to maximize the ability to detect lower-intensity light. In typical monochromator of the spectrofluorometer, the slit (entrance and exit) widths are generally variable. Therefore, the light intensity that passes through a monochromator is approximately proportional to the square of the slit width. Larger slit widths produce higher-intensity signal levels and thus higher signal-to-noise ratios. Smaller slit widths yield higher resolution but at the expense of light or signal intensity.

10.4.1.2 Detectors

Two types of detectors are most commonly used in spectrofluorometers, which are described as below.

Photomultiplier Tube (PMT)

The photomultiplier is a vacuum tube that contain an input window, a photosensitive cathode (photocathode), a focusing electrode, a number of electron-multiplying dynodes, and an anode normally held at about +1000 volts relative to the photocathode (Fig. 10.17) [83, 84]. The most common photocathodes used for the visible spectral range are of bialkali, multialkali, and gallium arsenide (GaAs) or gallium arsenide phosphide (GaAsP) types, whereas the major secondary materials used for the dynodes are alkali antimonide, beryllium oxide (BeO), magnesium oxide (MgO), gallium phosphide (GaP), and gallium arsenide phosphide (GaAsP). These materials are coated on the substrate electrode made of nickel, stainless steel, or copper-beryllium alloy.

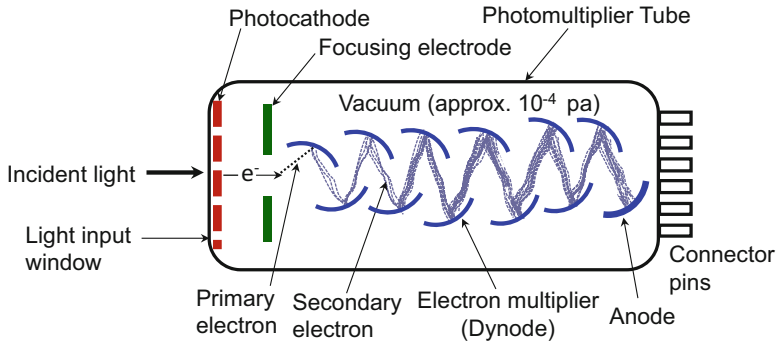


Fig. 10.17 Basic principle of a photomultiplier tube. Photons are converted to electrons by the photoelectric effect. The electrons are multiplied in a dynode chain and finally collected by an anode to provide an electrical output signal. (Reproduced from Kapusta et al. [83] with permission from Springer Nature)

The photomultiplier tube (PMT) worked on the basis of the following principle: a photon interacts with the photoelectric cathode material (e.g., potassium-cesium), causing emission of an electron by the photoelectric effect into the vacuum. This electron is directed by the focusing electrode toward the electron multipliers (dynodes), which is multiplied by means of secondary electron emission through interaction with various dynodes resulting in a cascade of millions of electrons reaching the anode. Thus, a light photon reaching the photocathode is converted to an electrical pulse at the anode. PM tubes can be operated into two modes: the first approach includes the generation of DC current as a consequence of the smoothing of the electrical pulses arrived at the anode, which is proportional to the number of photons reaching the photocathode. Another more sensitive approach is to count directly the single pulses generated from photons interacting with the PM cathode.

The quantum efficiency (conversion of photons into electric signal is called quantum efficiency) of the PMT depends on the wavelength and photocathode used. For example, bialkali types (e.g., EMI 9235) are sensitive in the spectral range between ~ 230 and 700 nm. They are most efficient at wavelengths below 500 nm, and their detection efficiencies reached up to 40% (ultra-bialkali) in this specific spectral range. The PMTs based on multialkali photocathodes are generally covered the broad spectral ranges from ~ 230 to 920 nm. However, they show lower detection efficiency that reaches about 15% between 400 and 700 nm. Moreover, the PMTs based on GaAs and GaAsP photocathodes are sensitive in the spectral range between 300 and 890 nm, especially the GaAsP that featured a higher detection efficiency about 40% at 600 nm when compared to the multialkali photocathodes. Several types of PMTs are commercially available with an extended sensitivity in the red region (S-20 cathode). However, the two PM tubes, especially 9235QB for UV/blue detection and Hamamatsu R943-02 for red/blue detection, are commonly used together to cover the required wide spectral range. The red-sensitive tube is normally cooled to ~ -10 °C to reduce the dark counts.

The micro-channel plates (MCPs) are compact and robust alternatives to the photomultiplier tubes. The MCP usually consists of a large number of closely packed channels and can be worked at similar principles as PMT with a suitable photocathode and anode. Each channel acts as an independent, continuous dynode photomultiplier. Total gain achieved is comparable to a PMT, but the performance is usually lower than the PMTs due to a relatively high chance of dark counts, which result from the large number of channels. In addition, these devices are susceptible to damage due to excess light exposure, vacuum leak, and vibration or shock.

CCD Detectors

These are one of the solid-state detectors, which are based on the principle that absorption of a photon generates pairs of charge carriers (electrons and holes) in a block of semiconducting material, and the migration of these carriers under voltage gives a pulse of current [83]. CCDs are widely used as sensors in digital cameras for imaging. However, these detectors are currently used in photoluminescence spectroscopy, especially Fluorolog-3[®] spectrofluorometer with high sensitive to UV-visible and near-infrared light, thus suitable for detection of luminescence or light in these spectral ranges. In addition, these detectors also allow multichannel operation, which means that the entire luminescence spectrum can be detected in a single acquisition in least possible time.

The CCD detectors are typically one-dimensional (linear) or two-dimensional arrays of thousands or millions of individual detector elements (also known as pixels). Each pixel interacts with light to produce a charge; the brighter the light and/or the longer the interaction, the more charge is accumulated. At the end of the measurement, the electronics readout device pulls the charge from the pixels, and each individual charge reading is measured. For example, in a typical Raman spectrometer, the Raman scattered light is dispersed using the diffraction grating, and this dispersed light is then projected onto the long axis of the CCD array. The first pixel will detect light from the low cm^{-1} edge of the spectrum, the second element will detect light from the next spectral position, and so on, whereas the last element will detect light from the high cm^{-1} edge of the spectrum. The main problem with the solid-state detectors (e.g., CCDs) is high dark count rates, which depends on the CCD temperature. Therefore, cooling systems are required to reduce or remove entirely the dark current. Recently, cooled CCDs are already available with thermoelectric cooling, showing few electron readout noise.

10.4.2 Sample Holders

The Fluorolog-2 and 3 spectrofluorometers are equipped with sample holders, depending on the physical nature of the sample used for photoluminescence spectroscopy measurement. The solid-sample holder is designed for solids, including

thin films, powders, pellets, and fibers. This holder consists of a base upon which a bracket and then spring clip are mounted. The powder samples are usually prepared by pasting the solid powders in the cavity of the sample block with the help of metallic rod and then clipped in the sample holder in an appropriate way (Fig. 10.18). In addition, other facilities for measurement of luminescence spectra, decay curves, and phosphorescence or delayed fluorescence of the powder sample at liquid nitrogen temperature (77K) are also present in the spectrofluorometers. In this case, a Dewar flask is used to freeze and maintain the temperature of the sample, which is mounted on the pedestal that can be fixed in the sample compartment of the Fluorolog-2 and 3 spectrofluorometers (Fig. 10.18). The powder sample is placed in the quartz tube to appropriate level and slowly immersed in the liquid nitrogen-filled Dewar.

The liquid sample holder, also called cuvette holder, is quite similar to the solid one, but it contains a specific chamber for the cuvette instead of spring clip as shown in Fig. 10.18. The liquid samples are filled in the cuvette and then placed in the cuvette holder.

10.5 Applications of Luminescent RE³⁺ Martials

10.5.1 Bioimaging

Luminescent imaging is a noninvasive diagnostic technique for visualizing and identifying various biological processes, which might be important for the pathogenesis and progression of many diseases [85]. While offering the high sensitivity and capacity of real-time monitoring, this technique has been adopted as an excellent approach to unearth the morphological, anatomical, and physiological details in tissues as well as the full range of bio-samples from cells to animals [86]. Moreover, imaging at cellular level offers an intuitionistic visualization of the physiological process at the cellular or subcellular level such as the interaction among cells, proteins, molecules, etc. As potential biomarkers, lanthanide nanoparticles have been widely exploited in bioimaging studies due to their tunable emission, high emission efficiency, long lifetime, low signal-to-noise ratio, deep tissue penetration, and low cytotoxicity [87].

Atherosclerosis and plaque rupture leading to stroke, myocardial infarction, and progression of peripheral artery have become the leading causes of death worldwide far surpassing the cancer and infectious diseases. Recently, monocytes and macrophages have been found to initiate and aggravate the atherosclerosis and cause the plaque instability and thrombogenicity. Therefore, these cells are considered an interesting target for the early diagnosis of atherosclerosis [88]. For instance, it has been shown that the rupture of vulnerable plaques leads to gruesome consequences; therefore identifying vulnerable plaques from stable plaques is a challenging phenomenon in clinic. Qia and coworkers [89] have selected

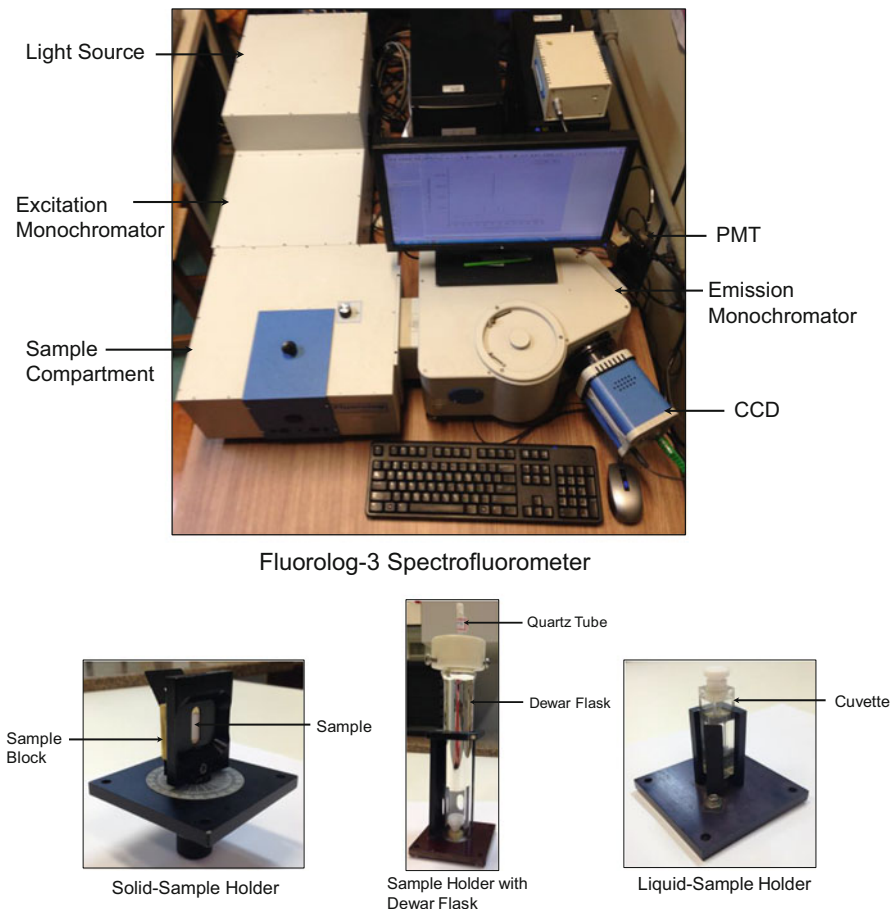


Fig. 10.18 Photographs of the Fluorolog-3 spectrofluorometer (top) and solid-sample holder with sample block, sample holder with Dewar flask, and liquid-sample holder with cuvette (bottom) taken with a digital camera (Facilities available at Laboratory of f-block elements, Institute of Chemistry, University of Sao Paulo, Brazil)

secreted biomarker osteopontin (OPN), associated with macrophages and foamy macrophages, as a target for identifying the vulnerable plaques. Moreover, they have developed a dual modality imaging probe by covalently attaching an OPN antibody to $\text{NaGdF}_4:\text{Yb}^{3+},\text{Er}^{3+}$ upconversion nanoparticles. The resulting probe was injected intravenously to mice, and optical imaging was performed to visualize the plaques. The imaging study showed that the signals of stable plaques and vulnerable plaques presented significantly different signal intensities, implying it as potentially useful tool for precise diagnostic of atherosclerosis plaques. Wang and coworkers [90] have synthesized $\text{NaYF}_4:\text{Yb}^{3+},\text{Er}^{3+}$ UCNPs coated with mesoporous silica shell. The UCNPs were also grafted with photosensitizer

covalently inside the mesoporous silica for photodynamic therapy. To perform the cellular imaging and photodynamic therapy, THP-1 macrophages were incubated with theranostic UCNPs for 0, 1, 2, and 4 h, respectively. Thereafter, they not only took images of THP-1 macrophages with the help of UCNPs, but the 660 nm red emission also activated photosensitizer to generate the singlet oxygen species that caused either apoptosis or necrosis of THP-1 macrophages.

10.5.1.1 Dual and Multimode Imaging

Multimodality imaging has become a common trend in the modern era to capture simultaneously visual information over many spatial scales. It is offering great advantages to acquire high-resolution anatomic morphology, to perform clinical diagnosis, or to evaluate functional processes such as gene and receptor expression, glucose distribution, pH value, and enzyme activity. Most dual and multimode imaging are based on the combination of luminescent imaging with one or more other imaging modalities, including X-ray computed tomography (CT), single-photon emission tomography (SPECT), positron emission tomography (PET), magnetic resonance imaging (MRI), and luminescence (optical) and photoacoustic imaging. Therefore, featured with unique optical and magnetic properties, lanthanide nanoparticles have been attracted immense interest as remarkable agents to integrate multiple imaging modalities to simultaneously capture visual information over many spatial scales.

Luminescent/MR Dual-Mode Imaging Magnetic resonance imaging (MRI) is a noninvasive and nondestructive medical diagnostic technique used to capture the detail of three-dimensional anatomical and functional images of sick or healthy individual body. In the current era, it has been successfully exploited in the medical field such as to (i) examine the brain, neck, and spinal cord injury and disease; (ii) identify bone and joint damage; (iii) explore tumors of soft tissue such as the brain, heart, and muscles; (iv) help in diagnosing central nervous system disorders, like stroke and multiple sclerosis; (v) reveal brain abnormalities in people with Alzheimer's disease and dementia, (vi) evaluate blood vessels to detect their blockage; and (vii) detect breast cancer and damage to soft tissue, etc. [91]. Moreover, MRI does not employ deleterious radiations like positron emission tomography (PET), single-photon emission tomography (SPECT), and computed tomography (CT) and has extremely high tissue penetration depth [92]. MRI operates on the basic principle of nuclear magnetic resonance, which typically depends on the spin-lattice relaxation and spine-spine relaxation time of protons contained in different tissues or organs to create imaging contrast. Different tissues have different relaxation times – T_1 and T_2 ; therefore MRI uses different contrast agents to produce enhancement in T_1 -weighted or T_2 -weighted images [93]. Among the lanthanide, Gd^{3+} ion is the most widely used contrast agent for T_1 relaxation enhancement. Other lanthanides (Nd, Dy, Er, and Yb) also show a smaller T_1 relaxation enhancement [87], but they have significant effect on T_2 relaxation.

Integration of luminescent/MRI techniques in one system is another improvement in medical field to provide more accurate physiological and pathological information with high sensitivity and specificity for disease diagnosis and therapy. Lanthanides nanoparticles have been widely exploited in luminescent/MRI dual-mode imaging. For instance, Zeng and coworkers [94] have been reported NaYbF₄:Tm³⁺/Gd³⁺ upconversion nanorods (UCNRs) that simultaneously show upconversion luminescence (UCL) and function as T_1/T_2 dual-weighted MRI contrast agents. These UCNPs have been investigated in mouse model that exhibited effectively real-time detection of tumor and even visualization of small malignant tumors (as small as 5 mm in diameter) with the help of UCL and T_1/T_2 dual-weighted MR imaging.

Ni and coworkers [96] have successfully developed NaYF₄:Yb/Tm³⁺/Gd³⁺ and NaYF₄:Yb³⁺/Tm³⁺/Gd³⁺@NaGdF₄ nanoprobe that was covalently linked to a targeting ligand Angiopep-2. This nanoprobe could cross the blood-brain barrier (BBB), target the glioblastoma, and then function as a simultaneous UCL/MRI bimodal imaging agent. The bimodal nanoprobe showed great potential in preoperative diagnosing and intraoperative positioning of the brain tumor by UCL/MR imaging. Jung and coworkers [95] have been reported the optical and magnetic europium-doped gadolinium sulfide (GdS:Eu³⁺) nanoparticles, where Eu³⁺ gave down-conversion luminescence (DCL) and Gd³⁺-based host matrixes worked as excellent T_1 -weighted MRI contrast agents. The GdS:Eu³⁺ showed enhanced luminescence in in vitro breast cancer cell imaging and T_1 -weighted imaging capability in MRI of the liver, kidney, and blood vessels (Fig. 10.19). The above results showed that both luminescent and MRI modalities can be integrated in a single system, using the lanthanide materials as multimodal agents that can diagnose more efficiently the disease, investigate the bioavailability, and monitor the real-time tracking of nanomedicine.

Luminescent/PET Dual-Mode Imaging Positron emission tomography (PET) is a chemical-based whole-body imaging technique, which fundamentally makes use of positron-emitting radionucleotide, including ¹¹C, ¹³N, ¹⁵O, ¹⁸F, ⁴⁴Sc, ⁶²Cu, ⁶⁴Cu, ⁸⁶Ga, ⁷²As, ⁷⁶Br, ⁸²Rb, ⁸⁶Y, ⁸⁹Zr, and ¹²⁴I [97], which emits γ -ray pairs to generate imaging contrast. The most common advantages of PET are its high sensitivity and unlimited penetration depth. In a general principle, the radiotracer is administered intravenously into the body, where it emits γ -ray pair, and special types of camera and computer system are fixed to detect the radiation and evaluate the tissue and organ functions. The radiotracer is typically incorporated into glucose, glucose analogue, or another compound. One of the most commonly used PET agents is radiolabeled glucose analogue, 18-fluorodeoxyglucose (FDG). After injection, the agent is accumulated in the region of interest where the PET measures its rate of consumption. The difference in the rate of consumption of glucose is used to distinguish between the benign and malignant tumors, because malignant tumor metabolizes glucose at faster rate than benign tumors. However, significance of the small radiotracers is limited by their quick clearance efficiency and exposure of patients to high ionizing radiations. Therefore, lanthanide nanoparticles have

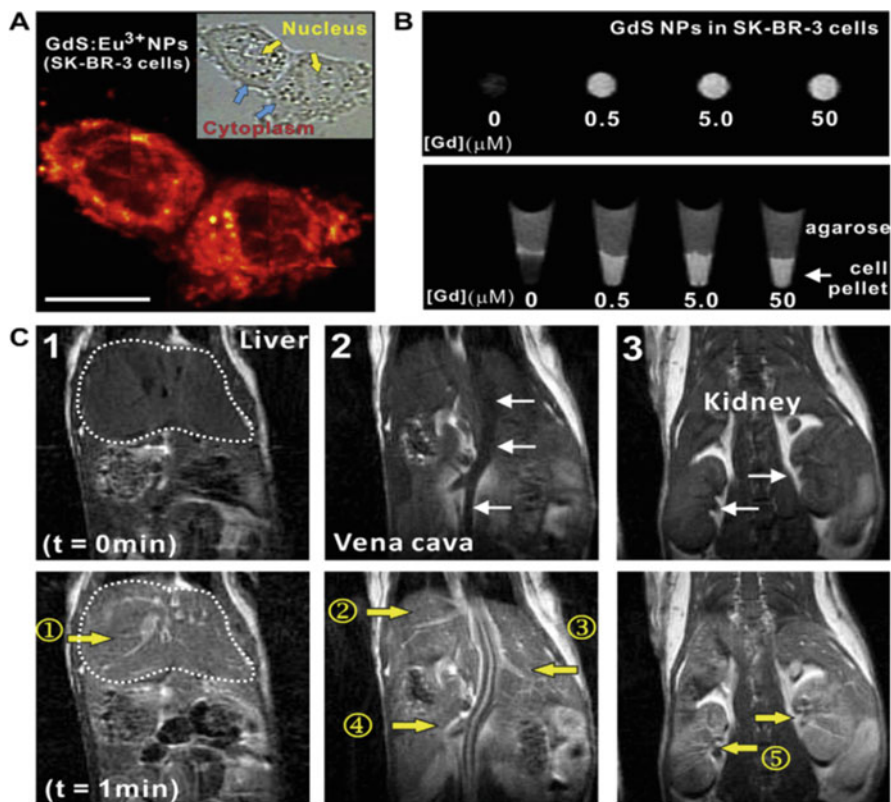


Fig. 10.19 (a) Confocal and phase contrast images of SK-BR-3 cells with GdS:Eu³⁺ NPs. (b) T_1 -weighted MR images of SK-BR-3 cell pellets with NPs. (c) T_1 -weighted MR images of mouse before (top: $t = 0$) and after (bottom: $t = 1$) injection of GdS:Eu³⁺ NP solution into the tail vein. Image areas were the liver (C1), the inferior vena cava (C2), and the kidneys (C3). Yellow arrows indicated branched blood vessels toward organs. (Reproduced from Jung et al. [95] with permission from Elsevier)

emerged as new approach for luminescent/PET imaging due to their improved bioavailability and target site accumulation. The radionuclide is either linked via functional group with the lanthanide or doped in lanthanide fluoride (such as ¹⁸F). For instance, Lee and coworkers [98] synthesized NaGdF₄:Yb³⁺,Er³⁺ nanoparticles and functionalized with tumor-specific dimeric cyclic arginine-glycine-aspartic acid (RGD) peptide. The (cRGDy_k)₂-UCNPs were radiolabeled with iodide (¹²⁴I) and evaluated as trimodal luminescent/PET/MRI probe against specific tumor angiogenesis-targeting properties. ¹²⁴I-radiolabeled-(cRGDy_k)₂-UCNPs showed in vitro and in vivo high specificity to angiogenesis tumor and exhibited remarkably both UCL/PET/MR imaging capabilities.

Liu and coworkers [99] reported ¹⁸F-NaYF₄:Yb³⁺,Er³⁺ nanoparticles and investigated their biodistribution with luminescent and PET imaging. An intense lumi-

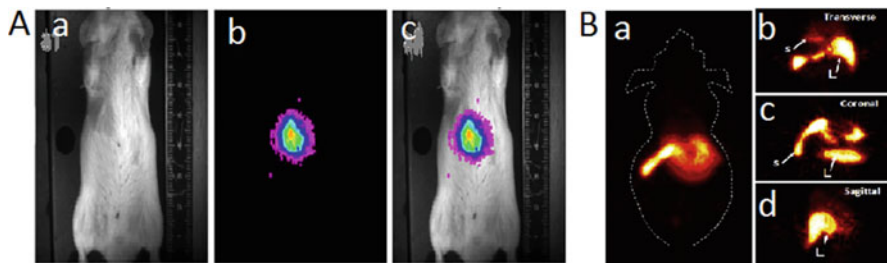


Fig. 10.20 $^{18}\text{F}\text{-NaYF}_4\text{:Yb}^{3+},\text{Er}^{3+}$ UCNPs nanoparticles for luminescent/PET dual-mode imaging. **a** (a–c): in vivo luminescent imaging of mouse at 5 min after intravenous injection of $^{18}\text{F}\text{-NaYF}_4\text{:Yb}^{3+},\text{Er}^{3+}$ UCNPs nanoparticles. **b** (a–d): in vivo micro-PET imaging of mouse from whole-body (a), transverse (b), coronal (c), and sagittal view (d) at 5 min after intravenous injection of $^{18}\text{F}\text{-NaYF}_4\text{:Yb}^{3+},\text{Er}^{3+}$ UCNPs nanoparticles. (Reproduced from Liu et al. [99] with permission from Elsevier)

nescent signal can be detected in the liver and spleen (Fig. 10.20), as these organs eliminate the foreign particles. Moreover, PET imaging also indicated the accumulation of nanoparticles in the liver and spleen, thus confirming the results of luminescent imaging. These results showed that $^{18}\text{F}\text{-NaYF}_4\text{:Yb}^{3+},\text{Er}^{3+}$ nanoparticles can be successfully employed for real-time tracking with high-sensitivity in vivo imaging. From these studies, it can be concluded that high-sensitivity, high-resolution, and 3D anatomical information can be obtained by applying the luminescent/PET dual-mode imaging techniques together, using luminescent rare earth materials as multimodal probes, which will be helpful for understanding the biodistribution and metabolism processes of nanoparticles in vivo and extended biotherapy studies.

Luminescent/SPECT Dual-Mode Imaging SPECT is a noninvasive medical imaging modality based on noncoincident γ -rays generated by radionuclides. The basic principle of SPECT is analogous to PET except in SPECT the radionuclides emit directly γ -photons and in PET give positron. The positron then interacts with electron, and the following annihilation makes a pair of γ -photons. The most important advantages of SPECT are its employment for the monitoring of biodistribution, pharmacokinetics, and target site accumulation due to their imaging sensitivity and penetration depth. However, the SPECT suffers the drawbacks of the lack of anatomical information and low spatial resolution [92]. The most commonly used radionuclides for SPECT include $^{99\text{m}}\text{Tc}$, ^{111}In , ^{123}I , ^{125}I , and ^{201}Tl . However, the ideal radionuclides should meet several criteria, such as relatively long physical half-life, suitable gamma energy range, and stable daughter radionuclides [100]. Lanthanide radionuclides exhibit different nuclear characteristics that could be used as SPECT imaging agents. The lanthanide radionuclides include the ^{153}Pm , ^{153}Sm , ^{166}Dy , ^{166}Ho , ^{175}Yb , and ^{177}Lu [101].

The exploitation of the rare earth materials at nanoscale level has made it easy to consolidate the luminescent and SPECT imaging in a single system for biomedical

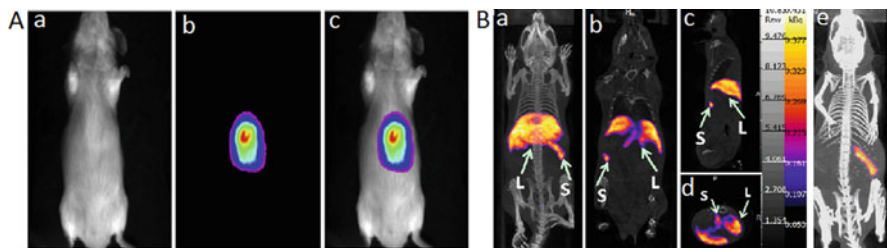


Fig. 10.21 **a**–**c**): in vivo images of mouse 1 h after tail vein injection of $\text{NaLuF}_4:^{153}\text{Sm}, \text{Yb}, \text{Tm}$ UCNPs. **b** **a**–**e**): in vivo SPECT images after intravenous injection of UCNPs, whole-body three-dimensional projection **a**), coronal **b**), sagittal **c**), and transversal images **d**) acquired at 1 h and whole-body three-dimensional projection **e**) acquired at 24 h, respectively. The arrows inset point to the liver (L) and spleen (S). (Reproduced from Yang et al. [102] with permission from Elsevier)

applications. For instance, Yang and coworkers [102] integrated the luminescent and radioactivity in $\text{NaLuF}_4:^{153}\text{Sm}, \text{Yb}, \text{Tm}$ nanoparticles for luminescent/SPECT dual-mode bioimaging. In medical areas, the biodistribution and bioavailability of drug are of major concern. Therefore, the biodistribution of radioactive nanoparticles were determined by using UPL/SPECT imaging techniques, indicating that the luminescent and radioactive nanoparticles were accumulated in the liver and spleen (Fig. 10.21). This concept showed that lanthanide radioactive nanoparticles serve as an in vivo next-generation probe for real-time tracking of nanomedicine and ultra-sensitive molecular imaging from the cellular scale to whole-body evaluation using luminescent/SPECT techniques.

Luminescent/X-Ray-CT Dual-Mode Imaging X-ray computed tomography was the first noninvasive radiological method to generate 3D anatomic images of a specific part of human body at higher spatial and temporal resolution without superimposition of adjacent structure. CT has become widely utilized in clinical diagnosis such as distinct anatomical visualization and high contrast imaging of several blood vessels, internal organs of the body, and muscles. In a general principle, a beam of X-ray photon is directed toward a specific part of the body; meanwhile some X-ray photons interact with the body by absorption or scattering, leading to attenuation of X-ray beam [92]. The contrast in CT images is then generated from the attenuation coefficients of X-ray in various tissues. Currently, two types of X-ray contrast agents (CAs) have been approved for human: water-soluble aromatic iodinated CAs and barium sulfate suspension. However, iodinated CAs have shown some drawbacks such as less efficient attenuation of X-ray, rapid renal clearance, and high toxicity in the kidneys [103]. Some other heavy metal elements such as Au, Pt, Bi, and Ta have been investigated as candidate for CT CAs. However, these CAs have short circulation lifetime and smaller X-ray attenuation coefficient [97]. Therefore, NPs of elements with large atomic number (high Z) have been extensively explored in the past decade, because these NPs can extend the circulation lifetime and enhance the aggregation at the site of interest [104]. Rare earth NPs have emerged as promising candidate for CT imaging, because lanthanides have larger atomic numbers, thus

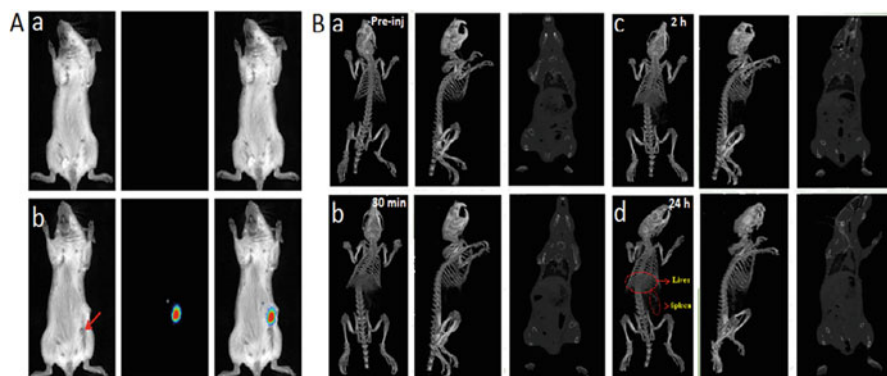


Fig. 10.22 **a** (a, b): in vivo UCL imaging of mouse (a), with subcutaneous injection of UCLNPs (b). The red arrow indicates the injected site; the panel from left to right denotes bright field UCL and overlays images. **b** (a–d): in vivo CT imaging of a mouse: pre-injection (a), 30 min (b), 2 h (c), and 24 h (d). The red circles indicate the liver and spleen. The left to right panels indicate the top view, the lateral view, and the maximum intensity projection of the mouse, respectively. (Reproduced from Li et al. [106] with permission from Elsevier)

big X-ray attenuation coefficient and good biocompatibility. Among trivalent lanthanide ions, Gd^{3+} and Yb^{3+} nanoparticles are the most extensively studied for CT CAs. Other RE^{3+} (such as La^{3+} , Dy^{3+} , Lu^{3+}) have also been explored for the CT CAs. Li and coworkers [105] fabricated multifunctional $NaYF_4:Yb^{3+}$, $Er^{3+}@NaGdF_4:Ce^{3+},Ln^{3+}(Eu^{3+},Tb^{3+},Sm^{3+},Dy^{3+})$ nanoparticles that showed up-down conversion dual-mode luminescent. The NPs exhibited high contrast in in vitro cell imaging and in vivo CT imaging, demonstrating great potential multiplexed luminescent biolabels and CT CAs. After intravenous injection, an enhancement of the signal of the heart could be observed within 15 min without an appreciable loss of contrast. However, the gradual enhancement of the liver and spleen continued for 1:30 h. This long-lasting liver-signal enhancement may be helpful in the identification of hepatic metastases. Moreover, Li and coworkers [106] used the multifunctional $BaYbF_3:Gd/Er$ nanoparticles as efficient agents for trimodal UCL/CT/MR imaging (Fig. 10.22).

Luminescent/Photoacoustic Imaging Photoacoustic imaging (PAI), also called optoacoustic imaging, is an emerging powerful biomedical imaging modality based on photoacoustic effect [107]. PAI hybridizes the merits of rich optical contrast and deeper tissue penetration while retaining high spatial resolution in biological tissue. It is featured with noninvasiveness, rapidness, accurate quantification, and cost-effectiveness as compared with other optical imaging modalities [108]. PAI primarily involves the irradiation of biological tissue with nonionizing laser pulses, during which some of the delivered light energy is absorbed and converted into heat, that subsequently generate the ultrasonic waves due to thermoelastic expansion. The produced ultrasonic waves propagate outside the tissues where they are detected by ultrasound transducer and then analyzed to generate the functional or structural

photoacoustic images [109]. PAI has emerged as promising approach especially in diagnosis of tumor pathophysiological status such as oxygen hypermetabolism, hemodynamics, and microvessel growth. Moreover, the penetration depth (~ 5 cm) of PA imaging is larger than the traditional near-infrared fluorescence imaging, due to the propagation characteristic of ultrasonic waves in tissues [110]. The hybridization of luminescence/PA dual-modal imaging is offering great advantages, because a cooperative synergy of the strength from both modalities is provided:

- (i) The capability of deep tissue imaging with high spatial resolution from PA imaging.
- (ii) The capability of rapid visualization from fluorescence imaging.
- (iii) It is safe and portable since no ionizing source is used [111].

Various contrast agents such as semiconductor quantum dots (QDs), carbon nanomaterials, lanthanides, and iron oxide NPs have been extensively investigated for PA imaging. For instance, Maji and coworkers [112] synthesized the $\text{NaYF}_4:\text{Yb}^{3+},\text{Er}^{3+}$ UCNPs functionalized with α -cyclodextrin (UC- α -CD) and investigated their PAI imaging capability. The UC- α -CD NPs exhibited intense luminescence quenching in water when excited at 980 nm. The luminescence quenching in aqueous solution was due to non-radiative relaxation that lead to an increase in thermal conductivity and subsequent PA signal enhancement. PAI imaging in vivo of an anesthetized mouse showed a good contrast enhancement localized on the kidney, demonstrating that at 980 nm excitation, UC- α -CD NPs could be used as efficient contrast agents for diagnostic purposes. Sheng and coworkers [110] developed $\text{NaYF}_4:\text{Yb}^{3+},\text{Er}^{3+}$ UCNPs coated with different surfactants (citric acid, ethylenediaminetetraacetic acid (EDTA), polyacrylic acid (PAA), and sodium citrate) and explored for dual modality PAI imaging in vitro and in vivo. To evaluate the PA properties in vitro, UCNPs were injected into polyethylene tubes, and the PA signals were measured under the dark-field confocal photoacoustic microscopy (PAM) system at the excitation of 520 and 975 nm. Among all the samples, sodium citrate-modified UCNPs showed the strongest PA signal. To further investigate for PA imaging in vivo, the sodium citrate-modified UCNPs were injected into the blood vessel of rat's brain around the superior sagittal sinus (SSS) and monitored with a PAM system for 30 min upon excitation 975 nm. The background signal from blood absorption was found to be 0.27 before the injection. The PA signal amplitude readily increased to 0.73 at 10 min after injection and was decreased slowly over the following 20 min to 0.46 which indicates a good blood circulation of sodium citrate-modified UCNPs. From the results, it can be concluded that sodium citrate-modified UCNPs could be employed as dual-modal imaging agents for both luminescence and PA imaging (Fig. 10.23) to achieve intrinsic high contrast, temporal, and spatial resolution reaching deeper depth.

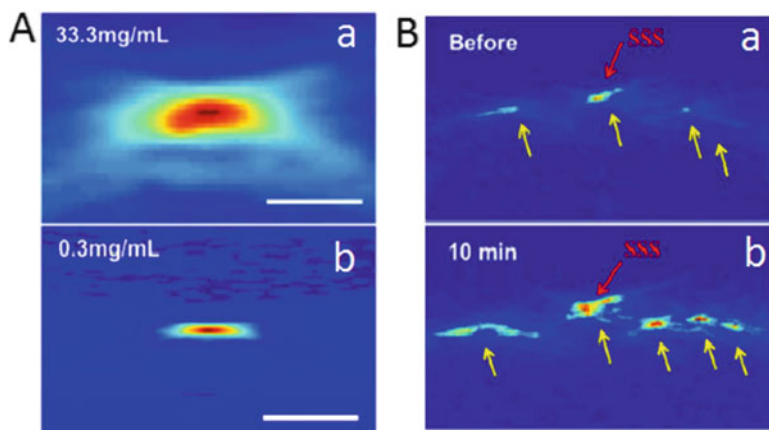


Fig. 10.23 **a** (a, b): PA images captured for sodium citrate-modified $\text{NaYF}_4:\text{Yb}^{3+},\text{Er}^{3+}$ UCNPs injected into polyethylene microtubings at two different concentrations. **b** (a, b): The cortical PA images (includes SSS blood vessel) before and 10 min after injection of UCNPs. (Reproduced from Sheng et al. [110] with permission from Elsevier)

10.5.2 Light-Emitting Diodes (LEDs)

The solid-state white light-emitting diodes have been attracted remarkable research interest as promising lighting devices, since the first commercially available LED was produced in 1996 by Nichia Chemical Co., using a blue InGaN LED chip coated with a yellow-emitting phosphor of yttrium aluminum garnet ($\text{Y}_{2.9}\text{Ce}_{0.1}\text{Al}_5\text{O}_{12}$, YAG: Ce^{3+}) [113]. The invention of bright blue light from the GaN semiconductor was a major development that changed the history of lighting technology in the twenty-first century. A team of researchers, which included Shuji Nakamura and Takashi Mukai, has made numerous contributions to the development of GaN growth, LEDs, and lasers. Their contributions include the demonstration of the first viable blue and green GaInN double-heterostructure LED, which achieved efficiencies of 10%, and the demonstration of the first pulsed and continuous wavelength (CW) GaInN/GaN current injection blue laser operating at room temperature [3, 29]. In reward of the development of creditable blue-emitting LED, Isamu Akasaki, Hiroshi Amano, and Shuji Nakamura were awarded with Nobel Prize in Physics (2014). This discovery was really crucial in lighting technology which opens a broad field to produce white light from blue-emitting LED. Therefore, white light-emitting diodes are considered the next-generation lighting devices for replacing the traditional incandescent and fluorescent lamps, owing to their energy-saving, robust, long lifetime, and environment-friendly features.

Generally, four different approaches are considered to generate the white light from LEDs [2]: (i) using a blue LED to excite a yellow phosphor, (ii) using an UV LED to excite red-green-blue (RGB) phosphors, (iii) using a blue LED to excite red-green (RG) phosphors, and (iv) mixing red, green, and blue, i.e., RGB, LEDs.

Among these methods, the first one is the most common and still an efficient method for fabrication of commercial white LEDs from a blue diode chip combined with $\text{Y}_3\text{Al}_5\text{O}_{12}:\text{Ce}^{3+}$ (YAG: Ce^{3+}) yellow phosphor. In fact, YAG: Ce^{3+} is still an excellent phosphor for blue-chip excitation with high luminescence quantum yield and good thermal stability [114]. However, due to the lack of red light component in the emission of YAG: Ce^{3+} , it is usually difficult to make warm white LEDs with high color-rendering index (CRI, $R_a > 80$) and low correlated color temperature (CCT < 4500 K), both of which are key requirements for some important applications such as indoor lighting. Therefore, extensive research interest has been dedicated to replace the conventional YAG: Ce^{3+} with low-cost phosphors to produce WLEDs, showing high luminescence quantum yield and color-rendering index (CRI), thus reducing the cost of the LEDs to the possible low level that can be easily commercially available.

The luminescent materials containing RE^{3+} ions exhibit well-defined narrow emission bands in different spectral ranges from visible to near-infrared with relatively long lifetimes and high quantum yields [7, 19, 72]. These characters make RE^{3+} materials efficient candidates for multidisciplinary photonic applications, recently extended from laser physics to optical markers, lighting, and display [8]. Several rare earth elements are used in phosphors for fluorescent and LED lighting. In 2012, a significant fraction of global demand for yttrium (40–60%), europium ($>70\%$), and terbium (40–60%) came from lighting applications. These materials were used primarily to produce red (Eu and Y), green (Tb), and blue (Eu) phosphors for fluorescent bulbs. However, with the introduction of solid-state lighting devices based on light-emitting diodes (LEDs), which are currently in the process of taking over the general illumination market [115], the yttrium and europium are also used in LED phosphors, but the quantities required are one to two orders of magnitude lower than what is needed to produce an equivalent amount of light using fluorescent bulbs. Therefore, this dynamic suggests that the rare earth oxides demand for lighting will be peaked and then might be declined off of current usage levels due to the gradual replacement of fluorescent lamp with LEDs. However, it is noteworthy that the role of rare earth ions, especially Ce^{3+} which emits a complementary color (yellow) of blue light, has central contribution to the development of white LEDs.

10.6 Conclusion

The rare earth (RE) elements are comprised of lanthanides: from lanthanum to lutetium (Ln: La, Ce, Pr, Nd, Pm, Sm, Eu, Gd, Tb, Dy, Ho, Er, Tm, Yb, Lu) and scandium (Sc) and yttrium (Y). Some of the RE^{3+} ions show characteristic emissions in the visible (from blue to red) and near-infrared spectral regions. The color of the emitted light depends on the nature of RE^{3+} ion. Therefore, rare earth materials show wide range of applications, from lighting (fluorescent lamps and LEDs) and displays, laser physics to material science, and agriculture and medical diagnostics (bioimaging). The present chapter is designed in simple

way to explain the luminescence, electronic spectroscopy, and applications of rare earth compounds. The chapter contains a detail on the luminescence and lighting technologies and electronic spectroscopy of rare earth ions: various intramolecular energy transfer mechanism in rare earth compounds, luminescence spectra, and their measurements and instrumental techniques. In addition, a considerable study on application of the rare earth compounds in designing luminescent probes for bioimaging, especially dual- and multimode imaging as well as LED phosphors, has also included. It is noteworthy that the content of the chapter is presented in an efficient way to be better understandable by the nonspecialized readers and fresh researchers.

Acknowledgments The authors are grateful for the financial support from the Coordenação de Aperfeiçoamento de Pessoal de Nível Superior (CAPES, Brazil) and Conselho Nacional de Desenvolvimento Científico e Tecnológico (CNPq, Brazil) and to The World Academy of Sciences (TWAS) for the advancement of science in developing countries and Fundação de Amparo à Pesquisa do Estado de São Paulo (FAPESP, Brazil).

References

1. Tilley, R. J. D. (2010). *Colour and the optical properties of materials*. Chichester: Wiley.
2. Sato, M., Kim, S. W., Shimomura, Y., Hasegawa, T., Toda, K., & Adachi, G. (2016). Rare earth-doped phosphors for white light-emitting diodes. In *Handbook on the physics and chemistry of rare earths* (Vol. 49, pp. 1–128).
3. Morrow, R. C. (2008). LED lighting in horticulture. *Hort Science*, *43*, 1947–1950.
4. Zhu, H., Lin, C. C., Luo, W., Shu, S., Liu, Z., Liu, Y., Kong, J., Ma, E., Cao, Y., Liu, R.-S., & Chen, X. (2014). Highly efficient non-rare-earth red emitting phosphor for warm white light-emitting diodes. *Nature Communications*, *5*, 4312.
5. Lin, C. C., & Liu, R. S. (2011). Advances in phosphors for light-emitting diodes. *Journal of Physical Chemistry Letters*, *2*, 1268–1277.
6. Liu, Y., Tu, D., Zhu, H., & Chen, X. (2013). Lanthanide-doped luminescent nanoprobes: Controlled synthesis, optical spectroscopy, and bioapplications. *Chemical Society Reviews*, *42*, 6924–6958.
7. Bünzli J-C, G., & Eliseeva, S. V. (2013). Intriguing aspects of lanthanide luminescence. *Chemical Science*, *4*, 1939–1949.
8. Bünzli, J. C. G. (2016). Lanthanide luminescence: From a mystery to rationalization, understanding, and applications. *Handbook on the Physics and Chemistry of Rare Earths*, *50*, 141–176.
9. Bünzli, J. C. G. (2010). Lanthanide luminescence for biomedical analyses and imaging. *Chemical Reviews*, *110*, 2729–2755.
10. Bünzli J-C, G. (2015). On the design of highly luminescent lanthanide complexes. *Coordination Chemistry Reviews*, *293–294*, 19–47.
11. Felinto Brito, H., Manoel Loureiro Malta, O., Claudia Franca Cunha Felinto, M., & Epaminondas de Sousa Teotonio, E. (2010). *Luminescence phenomena involving metal enolates*, *PATAI'S Chemistry of Functional Groups* (pp. 131–184). Chichester: Wiley.
12. Malta, O. L., & Gonçalves e Silva, F. R. (1998). A theoretical approach to intramolecular energy transfer and emission quantum yields in coordination compounds of rare earth ions. *Spectrochimica Acta Part A: Molecular Biomolecular Spectroscopy*, *54*, 1593–1599.

13. de Sá, G. F., Malta, O. L., de Mello, D. C., Simas, A. M., Longo, R. L., Santa-Cruz, P. A., & da Silva, E. F. (2000). Spectroscopic properties and design of highly luminescent lanthanide coordination complexes. *Coordination Chemistry Reviews*, *196*, 165–195.
14. Khan, L. U., Brito, H. F., Hölsä, J., Pirola, K. R., Muraca, D., Felinto, M. C. F. C., Teotonio, E. E. S., & Malta, O. L. (2014). Red-green emitting and superparamagnetic nanomarkers containing Fe₃O₄ functionalized with calixarene and rare earth complexes. *Inorganic Chemistry*, *53*, 12902–12910.
15. Kai, J., Felinto, M. C. F. C., Nunes, L. A. O., Malta, O. L., & Brito, H. F. (2011). Intermolecular energy transfer and photostability of luminescence-tuneable multicolour PMMA films doped with lanthanide- β -diketonate complexes. *Journal of Materials Chemistry*, *21*, 3796–3802.
16. Gschneidner, K. A., Bünzli, J.-C. G., & Pecharsky, V. K. (2007). *Handbook on the physics and chemistry of rare earths* (1st ed. pp. 1–511). North Holland: Elsevier.
17. Bünzli J.-C. G., & Piguet, C. (2005). Taking advantage of luminescent lanthanide ions. *Chemical Society Reviews*, *34*, 1048.
18. Dong, H., Sun, L.-D., & Yan, C.-H. (2015). Energy transfer in lanthanide upconversion studies for extended optical applications. *Chemical Society Reviews*, *44*, 1608–1634.
19. Binnemans, K. (2009). Lanthanide-based luminescent hybrid materials. *Chemical Reviews*, *109*, 4283–4374.
20. Binnemans, K. (2015). Interpretation of europium(III) spectra. *Coordination Chemical Reviews*, *295*, 1–45.
21. Harvey, N. E. (1957). *A history of luminescence: From the earliest times until 1900*.
22. Khan, L. U., & Khan, Z. U. (2017). Bifunctional nanomaterials: Magnetism, luminescence and multimodal biomedical applications. In *Complex magnetic nanostructures* (pp. 121–171). Cham: Springer International Publishing.
23. Khan, L. U. (2015). *Optical and magnetic nanomaterials containing Fe₃O₄ and SiO₂ matrices functionalized with calixarene and rare earth complexes*. São Paulo: University of Sao Paulo.
24. Lastusaari, M., Laamanen, T., Malkamäki, M., Eskola, K. O., Kotlov, A., Carlson, S., Welter, E., Brito, H. F., Bettinelli, M., Jungner, H., & Hölsä, J. (2012). The bologna stone: History's first persistent luminescent material. *European Journal of Mineralogy*, *24*, 885–890.
25. Anon. <http://www.dailymail.co.uk/sciencetech/article-2950494/Would-drive-glow-dark-car-Nissan-creates-luminous-model-Leaf-glows-10-hours-thanks-UV-paint.html> 2950494.
26. Virk, H. S. (2014). *Luminescence basic concepts, applications and instrumentation*. Switzerland: Trans Tech Publications Limited.
27. Kitsinelis, S. (2015). *Light sources*. Boca Raton: CRC Press Taylor & Francis Group.
28. Mottier, P. (2009). *LEDs for lightning applications* (1st ed.). UK: John Wiley & Sons.
29. Schubert, E. F. (2006). *Light-emitting diodes* (2nd ed.). UK: Cambridge University Press.
30. Craford, M. G., Shaw, R. W., Herzog, A. H., & Groves, W. O. (1972). Radiative recombination mechanisms in GaAsP diodes with and without nitrogen doping. *Journal of Applied Physics*, *43*, 4075–4083.
31. Amano, H., Kito, M., Hiramatsu, K., & Akasaki, I. (1989). P-type conduction in Mg-doped GaN treated with low-energy electron beam irradiation (LEEBI). *Japanese Journal of Applied Physics*, *28*, L2112–L2114.
32. Nakamura, S., Senoh, M., Iwasa, N., Nagahama, S. I., Yamada, T., & Mukai, T. (1995). Superbright green InGaN Single-Quantum-Well-Structure Light-Emitting Diodes. *Japanese Journal of Applied Physics*, *34*, L1332.
33. Atwood, D. A. (2005). *The rare earth elements: Fundamentals and applications*. Hoboken: Wiley.
34. Voncken, J. H. L. (2016). *The rare earth elements*. Cham: Springer International Publishing.
35. Cotton, S. (2005). Chap. 5 Electronic and magnetic properties of the lanthanides. In *Lanthanide and actinide chemistry* (pp. 61–87). England: John Wiley & Sons, Ltd.
36. Sastri, V. S., Bünzli, J.-C. G., Rao, V. R., Rayudu, V. R., & Perumareddi, J. R. (2003). *Modern aspects of rare earths and their complexes* (Elsevier B.V.).

37. Anon. (1968). J. Galissard de Marignac, P.E. Lecoq de Boisboudran, 1880, 1886 (<http://www.rsc.org/periodic-table/element/64/gadolinium#history>; Weeks 1968) 1886 1968.
38. Rodrigues, R. V., Marciniak, L., Khan, L. U., Matos, J. R., Brito, H. F., & Stręk, W. (2016). Luminescence investigation of Dy₂O₂S and Dy₂O₂SO₄ obtained by thermal decomposition of sulfate hydrate. *Journal of Rare Earths*, *34*, 814–819.
39. Reid, M. F. (2016). Theory of rare-earth electronic structure and spectroscopy. In *Handbook on the physics and chemistry of rare earths* (Vol. 50, pp. 47–64).
40. Chen, X., Liu, Y., & Tu, D. (2014). *Lanthanide-doped luminescent nanomaterials*. Berlin: Springer Berlin Heidelberg.
41. Khan, L. U., Zambon, L. F. M., Santos, J. L., Rodrigues, R. V., Costa, L. S., Muraca, D., Pirota, K. R., Felinto, M. C. F. C., Malta, O. L., & Brito, H. F. (2018). Red-emitting magnetic nanocomposites assembled from Ag-decorated Fe₃O₄@SiO₂ and Y₂O₃:Eu³⁺: Impact of iron-oxide/silver nanoparticles on Eu³⁺ emission. *Chemistry and Selection*, *3*, 1157–1167.
42. Dorenbos, P. (2002). Light output and energy resolution of Ce³⁺-doped scintillators. *Nuclear Instruments Methods Physics Research Section A Accelerators, Spectrometers, Detectors Associated Equipment*, *486*, 208–213.
43. Lakowicz, J. R. (2006). *Energy transfer, Principles of Fluorescence Spectroscopy* (pp. 443–475). Boston: Springer US.
44. Kalisky, K. (2006). *The physics and engineering of solid state lasers*.
45. Shrivastava, N., Khan, L. U., Khan, Z. U., Vargas, J., Moscoso-Londoño, O., Ospina, C., Brito, H. F., Javed, Y., Felinto, M. C. F. C., de Menezes, A. S., Knobel, M., & Sharma, S. K. (2017). Building block magneto-luminescent nanomaterials of iron-oxide/ZnS@LaF₃:Ce³⁺, Gd³⁺, Tb³⁺ with green emission. *Journal of Materials Chemistry C*, *5*, 2282–2290.
46. Zabicky, J., & Zabicky, J. (2009). *The chemistry of metal enolates, Part 1*.
47. Andrews, D. L. (1989). A unified theory of radiative and radiationless molecular energy transfer. *Chemical Physics*, *135*, 195–201.
48. Bettinelli, M., & Flint, C. D. (1990). Non-resonant energy transfer between Tb³⁺ and Eu³⁺ in the cubic hexachloroelpasolite crystals Cs₂NaTb_{1-x}Eu_xCl₆ (x=0.01–0.15). *Journal of Physics Condensed Matter*, *2*, 8417–8426.
49. Di Bartolo, B. (1984). *Energy transfer processes in condensed matter* (Vol. 114). Boston: Springer US.
50. Miyakawa, T., & Dexter, D. L. (1970). Phonon sidebands, multiphonon relaxation of excited states, and phonon-assisted energy transfer between ions in solids. *Physical Review B*, *1*, 2961–2969.
51. Dexter, D. L. (1953). A theory of sensitized luminescence in solids. *The Journal of Chemical Physics*, *21*, 836–850.
52. Soules, T. F., & Duke, C. B. (1971). Resonant energy transfer between localized electronic states in a crystal. *Physical Review B*, *3*, 262–274.
53. Malta, O. L. (2008). Mechanisms of non-radiative energy transfer involving lanthanide ions revisited. *Journal of Non-Crystalline Solids*, *354*, 4770–4776.
54. Faustino, W. M., Nunes, L. A., Terra, I. A. A., Felinto, M. C. F. C., Brito, H. F., & Malta, O. L. (2013). Measurement and model calculation of the temperature dependence of ligand-to-metal energy transfer rates in lanthanide complexes. *Journal Luminescence*, *137*, 269–273.
55. Shyichuk, A., Cámara, S. S., Weber, I. T., Carneiro Neto, A. N., Nunes, L. A. O., Lis, S., Longo, R. L., & Malta, O. L. (2016). Energy transfer upconversion dynamics in YVO₄:Yb³⁺,Er³⁺. *Journal of Luminescence*, *170*, 560–570.
56. Debasu, M. L., Ananias, D., Rocha, J., Malta, O. L., & Carlos, L. D. (2013). Energy-transfer from Gd(III) to Tb(III) in (Gd,Yb,Tb)PO₄ nanocrystals. *Physical Chemistry Chemical Physics*, *15*, 15565–15571.
57. Shrivastava, N., Khan, L. U., Vargas, J. M., Ospina, C., Coaquira, J. A. Q., Zoppellaro, G., Brito, H. F., Javed, Y., Shukla, D. K., Felinto, M. C. F. C., & Sharma, S. K. (2017). Efficient multicolor tunability of ultrasmall ternary-doped LaF₃ nanoparticles: Energy conversion and magnetic behavior. *Physical Chemistry Chemical Physics*, *19*, 18660–18670.

58. Bloembergen, N. (1959). Solid state infrared quantum counters. *Physical Review Letters*, *2*, 84–85.
59. Zhou, J., Liu, Q., Feng, W., Sun, Y., & Li, F. (2015). Upconversion luminescent materials: Advances and applications. *Chemical Reviews*, *115*, 395–465.
60. Liu, G. (2015). Advances in the theoretical understanding of photon upconversion in rare-earth activated nanophosphors. *Chemical Society Reviews*, *44*, 1635–1652.
61. Chen, G., Qiu, H., Prasad, P. N., & Chen, X. (2014). Upconversion nanoparticles: Design, nanochemistry, and applications in theranostics. *Chemical Reviews*, *114*, 5161–5214.
62. Wang, F., Deng, R., Wang, J., Wang, Q., Han, Y., Zhu, H., Chen, X., & Liu, X. (2011). Tuning upconversion through energy migration in core-shell nanoparticles. *Nature Materials*, *10*, 968–973.
63. Zheng, W., Huang, P., Tu, D., Ma, E., Zhu, H., & Chen, X. (2015). Lanthanide-doped upconversion nano-bioprobes: Electronic structures, optical properties, and biodetection. *Chemical Society Reviews*, *44*, 1379–1415.
64. Chivian, J. S., Case, W. E., & Eden, D. D. (1979). The photon avalanche: A new phenomenon in Pr³⁺-based infrared quantum counters. *Applied Physics Letters*, *35*, 124–125.
65. Xu, W., Chen, B., Yu, W., Zhu, Y., Liu, T., Xu, S., Min, X., Bai, X., & Song, H. (2012). The up-conversion luminescent properties and silver-modified luminescent enhancement of YVO₄:Yb³⁺, Er³⁺ NPs. *Dalton Transactions*, *41*, 13525.
66. Blasse, G., & Grabmaier, B. C. (1994). *Luminescent materials*. Berlin: Springer Berlin Heidelberg.
67. Lakshminarayana, G., Weis, E. M., Lira, A. C., Caldiño, U., Williams, D. J., & Hehlen, M. P. (2013). Cross relaxation in rare-earth-doped oxyfluoride glasses. *Journal of Luminescence*, *139*, 132–142.
68. Kurzen, H., Bovigny, L., Bulloni, C., & Daul, C. (2013). Electronic structure and magnetic properties of lanthanide 3+ cations. *Chemical Physics Letters*, *574*, 129–132.
69. Khan, L. U., Muraca, D., Brito, H. F., Moscoso-Londoño, O., Felinto, M. C. F. C., Pirota, K. R., Teotonio, E. E. S., & Malta, O. L. (2016). Optical and magnetic nanocomposites containing Fe₃O₄@SiO₂ grafted with Eu³⁺ and Tb³⁺ complexes. *Journal of Alloys and Compounds*, *686*, 453–466.
70. Malta, O. L., & Carlos, L. D. (2003). Intensities of 4f-4f transitions in glass materials. *Quim Nova*, *26*, 889–895.
71. Sá Ferreira, R. A., Nobre, S. S., Granadeiro, C. M., Nogueira, H. I. S., Carlos, L. D., & Malta, O. L. (2006). A theoretical interpretation of the abnormal 5D₀→7F₄ intensity based on the Eu³⁺ local coordination in the Na₉[EuW₁₀O₃₆]·14H₂O polyoxometalate. *Journal of Luminescence*, *121*, 561–567.
72. Borges, A. S., Dutra, J. D. L., Freire, R. O., Moura, R. T., Da Silva, J. G., Malta, O. L., Araujo, M. H., & Brito, H. F. (2012). Synthesis and characterization of the europium(III) pentakis(picrate) complexes with imidazolium counterions: Structural and photoluminescence study. *Inorganic Chemistry*, *51*, 12867–12878.
73. Barbosa, H. P., Kai, J., Silva, I. G. N., Rodrigues, L. C. V., Felinto, M. C. F. C., Hölsä, J., Malta, O. L., & Brito, H. F. (2015). Luminescence investigation of R³⁺-doped alkaline earth tungstates prepared by a soft chemistry method. *Journal of Luminescence*, *170*, 1–7.
74. Lourenço, A. V. S., Kodaira, C. A., Ramos-Sanchez, E. M., Felinto, M. C. F. C., Goto, H., Gidlund, M., Malta, O. L., & Brito, H. F. (2013). Luminescent material based on the [Eu(TTA)₃(H₂O)₂] complex incorporated into modified silica particles for biological applications. *Journal of Inorganic Biochemistry*, *123*, 11–17.
75. Murakami, S., Herren, M., Rau, D., & Morita, M. (2000). Photoluminescence and decay profiles of undoped and Fe³⁺, Eu³⁺-doped PLZT ceramics at low temperatures down to 10 K. *Inorganica Chimica Acta*, *300–302*, 1014–1021.
76. Anon. (2002). *Fluorolog[®] -3 operational manual* (Vol. 2). New Jersey: Horiba Jobin Yvon Inc.
77. Lakowicz, J. R. (2006). In J. R. Lakowicz (Ed.), *Principles of fluorescence spectroscopy*. Boston: Springer US.

78. Julien, C., & Hirlimann, C. (1980). Ebert-Fastie monochromator alignment. *Journal of Physics E*, *13*, 923–924.
79. Gaertner, A. A., Yoon, H. W., & Germer, T. A. (2014). Dispersive methods. *Experimental Methods in the Physical Science*, *46*, 68–95.
80. Simon, J. M., Gil, M. A., & Fantino, A. N. (1986). Czerny-turner monochromator: Astigmatism in the classical and in the crossed beam dispositions. *Applied Optics*, *25*, 3715.
81. Shafer, A. B., Megill, L. R., & Droppleman, L. (1964). Optimization of the Czerny-Turner spectrometer. *Journal of the Optical Society of America*, *54*, 879.
82. An, Y., Sun, Q., Liu, Y., Li, C., & Wang, Z.-Q. (2013). The design of astigmatism-free crossed czerny-turner spectrometer. *Optik – International Journal for Light and Electron Optics*, *124*, 2539–2543.
83. Kapusta, P., Wahl, M., & Erdmann, R. (2015). In P. Kapusta, M. Wahl, & R. Erdmann (Eds.), *Advanced photon counting* (Vol. 15). Cham: Springer International Publishing.
84. Hamamtsu. (2007). Basic principles of photomultiplier tubes. *Photomultiplier Tubes Basics Applications*, 13–19.
85. Gu, Z., Yan, L., Tian, G., Li, S., Chai, Z., & Zhao, Y. (2013). Recent advances in design and fabrication of upconversion nanoparticles and their safe theranostic applications. *Advanced Materials*, *25*, 3758–3779.
86. Wang, F., Banerjee, D., Liu, Y., Chen, X., & Liu, X. (2010). Upconversion nanoparticles in biological labeling, imaging, and therapy. *Analyst*, *135*, 1839–1854.
87. Dong, H., Du, S. R., Zheng, X. Y., Lyu, G. M., Sun, L. D., Li, L. D., Zhang, P. Z., Zhang, C., & Yan, C. H. (2015). Lanthanide nanoparticles: From design toward bioimaging and therapy. *Chemical Reviews*, *115*, 10725–10815.
88. Wang, T., Mancuso, J. J., Kazmi, S. M. S., Dwelle, J., Sapozhnikova, V., Willsey, B., Ma, L. L., Qiu, J., Li, X., Dunn, A. K., Johnston, K. P., Feldman, M. D., & Milner, T. E. (2012). Combined two-photon luminescence microscopy and OCT for macrophage detection in the hypercholesterolemic rabbit aorta using plasmonic gold nanorose. *Lasers in Surgery and Medicine*, *44*, 49–59.
89. Qiao, R., Qiao, H., Zhang, Y., Wang, Y., Chi, C., Tian, J., Zhang, L., Cao, F., & Gao, M. (2017). Molecular imaging of vulnerable atherosclerotic plaques in vivo with osteopontin-specific upconversion nanoprobe. *ACS Nano*, *11*, 6078–6084.
90. Wang, H., Zhu, X., Han, R., Wang, X., Yang, L., & Wang, Y. (2017). Near-infrared light activated photodynamic therapy of THP-1 macrophages based on core-shell structured upconversion nanoparticles. *Microporous and Mesoporous Materials*, *239*, 78–85.
91. Clarke, L. P., Velthuisen, R. P., Camacho, M. A., Heine, J. J., Vaidyanathan, M., Hall, L. O., Thatcher, R. W., & Silbiger, M. L. (1995). MRI segmentation: Methods and applications. *Magnetic Resonance Imaging*, *13*, 343–368.
92. Key, J., & Leary, J. F. (2014). Nanoparticles for multimodal in vivo imaging in nanomedicine. *International Journal of Nanomedicine*, *9*, 711–726.
93. Kircher, M. F., & Willmann, J. K. (2012). Molecular body imaging: MR imaging, CT, and US. part I. principles. *Radiology*, *263*, 633–643.
94. Xue, Z., Yi, Z., Li, X., Li, Y., Jiang, M., Liu, H., & Zeng, S. (2017). Upconversion optical/magnetic resonance imaging-guided small tumor detection and in vivo tri-modal bioimaging based on high-performance luminescent nanorods. *Biomaterials*, *115*, 90–103.
95. Jung, J., Kim, M. A., Cho, J. H., Lee, S. J., Yang, I., Cho, J., Kim, S. K., Lee, C., & Park, J. K. (2012). Europium-doped gadolinium sulfide nanoparticles as a dual-mode imaging agent for T1-weighted MR and photoluminescence imaging. *Biomaterials*, *33*, 5865–5874.
96. Ni, D., Zhang, J., Bu, W., Xing, H., Han, F., Xiao, Q., Yao, Z., Chen, F., He, Q., Liu, J., Zhang, S., Fan, W., Zhou, L., Peng, W., & Shi, J. (2014). Dual-targeting upconversion nanoprobe across the blood-brain barrier for magnetic resonance/fluorescence imaging of intracranial glioblastoma. *ACS Nano*, *8*, 1231–1242.
97. Li, X., Zhang, X.-N., Li, X.-D., Chang, J., Li, X., Zhang, X.-N., Li, X.-D., & Chang, J. (2016). Multimodality imaging in nanomedicine and nanotheranostics. *Cancer Biology and Medicine*, *13*, 339–348.

98. Lee, J., Lee, T. S., Ryu, J., Hong, S., Kang, M., Im, K., Kang, J. H., Lim, S. M., Park, S., & Song, R. (2013). RGD peptide-conjugated multimodal NaGdF₄:Yb³⁺/Er³⁺ nanophosphors for upconversion luminescence, MR, and PET imaging of tumor angiogenesis. *Journal of Nuclear Medicine*, *54*, 96–103.
99. Liu, Q., Chen, M., Sun, Y., Chen, G., Yang, T., Gao, Y., Zhang, X., & Li, F. (2011). Multifunctional rare-earth self-assembled nanosystem for tri-modal upconversion luminescence/fluorescence/positron emission tomography imaging. *Biomaterials*, *32*, 8243–8253.
100. Union, I., Pure, O. F., & Chemistry, A. (1991). Commission on radiochemistry and nuclear techniques * radiolabeling of monoclonal. *Radiolabeling of Monoclonal Antibodies with Metal Chelates* w : m : m : m : m : m : m : m : m, *63*, 427–463.
101. Misri, R., Saatchi, K., & Häfeli, U. O. (2012). Nanoprobes for hybrid SPECT/MR molecular imaging. *Nanomedicine (London, England)*, *7*, 719–733.
102. Yang, Y., Sun, Y., Cao, T., Peng, J., Liu, Y., Wu, Y., Feng, W., Zhang, Y., & Li, F. (2013). Hydrothermal synthesis of NaLuF₄: 153Sm, Yb, Tm nanoparticles and their application in dual-modality upconversion luminescence and SPECT bioimaging. *Biomaterials*, *34*, 774–783.
103. Yu, S.-B., & Watson, A. D. (1999). Metal-based X-ray contrast media. *Chemical Reviews*, *99*, 2353–2378.
104. Zhu, J., Lu, Y., Li, Y., Jiang, J., Cheng, L., Liu, Z., Guo, L., Pan, Y., & Gu, H. (2014). Synthesis of Au-Fe₃O₄ heterostructured nanoparticles for in vivo computed tomography and magnetic resonance dual model imaging. *Nanoscale*, *6*, 199–202.
105. Li, F., Li, C., Liu, J., Liu, X., Zhao, L., Bai, T., Yuan, Q., Kong, X., Han, Y., Shi, Z., & Feng, S. (2013). Aqueous phase synthesis of upconversion nanocrystals through layer-by-layer epitaxial growth for in vivo X-ray computed tomography. *Nanoscale*, *5*, 6950–6959.
106. Li, X., Yi, Z., Xue, Z., Zeng, S., & Liu, H. (2017). Multifunctional BaYbF₅ : Gd/Er upconversion nanoparticles for in vivo tri-modal upconversion optical, X-ray computed tomography and magnetic resonance imaging. *Materials Science and Engineering: C*, *75*, 510–516.
107. Beard, P. (2011). Biomedical photoacoustic imaging. *Interface Focus*, *1*, 602–631.
108. Prodi, L., Rampazzo, E., Rastrelli, F., Speghini, A., & Zaccheroni, N. (2015). Imaging agents based on lanthanide doped nanoparticles. *Chemical Society Reviews*, *44*, 4922–4952.
109. Theerthagiri, J., Senthil, R. A., Thirumalai, D., & Madhavan, J. (2015). *Handbook of ultrasonics and sonochemistry* (pp. 1–29).
110. Sheng, Y., Liao, L.-D., Thakor, N., & Tan, M. C. (2014). Rare-earth doped particles as dual-modality contrast agent for minimally-invasive luminescence and dual-wavelength photoacoustic imaging. *Scientific Reports*, *4*, 6562.
111. Sheng, Y., De Liao, L., Bandla, A., Liu, Y. H., Yuan, J., Thakor, N., & Tan, M. C. (2017). Enhanced near-infrared photoacoustic imaging of silica-coated rare-earth doped nanoparticles. *Materials Science and Engineering: C*, *70*, 340–346.
112. Maji, S. K., Sreejith, S., Joseph, J., Lin, M., He, T., Tong, Y., Sun, H., Yu, S. W. K., & Zhao, Y. (2014). Upconversion nanoparticles as a contrast agent for photoacoustic imaging in live mice. *Advanced Materials*, *26*, 5633–5638.
113. Nakamura, S., & Stephen Pearton, G. F. (2013). The blue laser diode. The complete story. *Springer Science Business Media*, *12*, 755–756.
114. George, N. C., Denault, K. A., & Seshadri, R. (2013). Phosphors for solid-state white lighting. *Annual Review of Materials Research*, *43*, 481–501.
115. Ku, A. Y., Setlur, A. A., & Loudis, J. (2015). Impact of light emitting diode adoption on rare earth element use in lighting: Implications for yttrium, europium, and terbium demand. *Electrochemical Society Interface*, *24*, 45–49.

Chapter 11

Raman Spectroscopy: A Potential Characterization Tool for Carbon Materials



Padmnabh Rai and Satish Kumar Dubey

11.1 Introduction

Raman spectroscopy technique is potentially utilized to identify the chemical bonding in molecules or solids and doping in semiconducting materials [1–5]. Even different forms of carbon materials could also be identified by this technique [1, 6–8]. Moreover, it determines the size and conductivity of nanoscale systems with high precision [1, 6]. It is a non-destructive technique unlike other techniques, such as temperature gravimetric analysis (TGA) and X-ray photoemission spectroscopy (XPS) [8, 9]. The current research in condensed matter physics and material science mainly focusses on exploring new nanomaterials and their applications in electronics, optoelectronics, plasmonics, and biosciences. Raman spectroscopy technique has become an important characterization tool for investigating the band structure and size of low-dimension materials such as carbon nanotube and graphene [1, 7]. However, Raman spectroscopy technique combined with plasmonics of nanomaterials (known as surface-enhanced Raman spectroscopy (SERS)) is an emerging technique to probe individual molecule and DNA structures [10, 11]. Recently the importance of directionality of SERS signals has been realized to explore the spectral and angular characteristics of the radiation pattern of Raman-active emitters by imaging the angular distribution of the signal in the Fourier plane of the microscope [12–15].

P. Rai (✉)

UM-DAE Centre for Excellence in Basic Sciences, Mumbai, India

Department of Physics and Astronomical Science, Central University of Himachal Pradesh, Dharamshala, India

e-mail: padmnabh.raai@cbs.ac.in

S. K. Dubey

Instrument Design Development Centre, Indian Institute of Technology Delhi, New Delhi, India

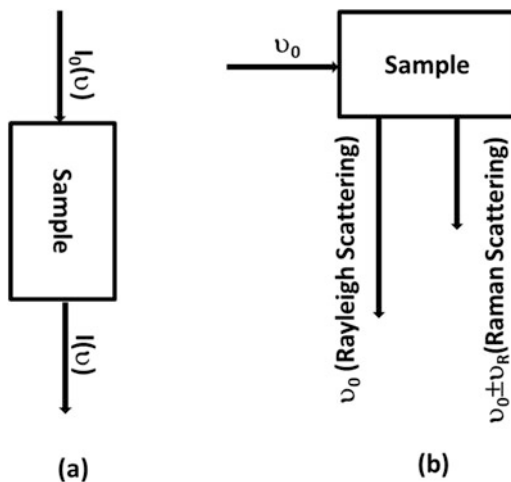
© Springer International Publishing AG, part of Springer Nature 2018

S. K. Sharma (ed.), *Handbook of Materials Characterization*,

https://doi.org/10.1007/978-3-319-92955-2_11

405

Fig. 11.1 Schematic diagram of (a) IR spectroscopy and (b) Raman scattering process for the given sample [5]



The vibrational transition can be observed in either Raman spectra or infrared (IR) spectra. In IR spectra, one measures the absorption of infrared light by the sample as a function of frequency. Figure 11.1a shows the schematic of IR spectroscopy. The intensity of IR absorption is given by the Beer-Lambert law:

$$I = I_0 \exp^{-\alpha cl} \quad (11.1)$$

where I_0 and I represent the intensity of incident and transmitted beams, respectively, α is the molecular absorption coefficient, c is the concentration of the sample, and l is the length of the cell (Fig. 11.1). In IR spectroscopy, the percentage transmission (T) is plotted against the wave number (ω):

$$T (\%) = (I/I_0) \times 100 \quad (11.2)$$

The Raman spectra originated through an entirely different mechanism as compared to IR spectra. When an intense light (laser) of frequency ν_0 is irradiated upon the sample, the scattered light is observed in perpendicular direction to the incident light (shown in Fig. 11.1b).

The scattered light can be categorized in two parts: (i) the Rayleigh scattering, which is having the same frequency (ν_0) as of the incident light, and (ii) the Raman scattering having the frequency $\nu_0 \pm \nu_R$, where ν_R is the frequency corresponding to molecular vibration. The $\nu_0 + \nu_R$ and $\nu_0 - \nu_R$ lines are called anti-Stokes and Stokes lines, respectively. Thus, in Raman spectroscopy, one measures the molecular vibration frequency (ν_R) as a shift from the incident frequency (ν_0). The energy level diagram for Stokes and anti-Stokes Raman scattering together with experimentally measured spectrum for Rhodamine 6G (well-known sample to calibrate Raman spectrum) is shown in Fig. 11.2.

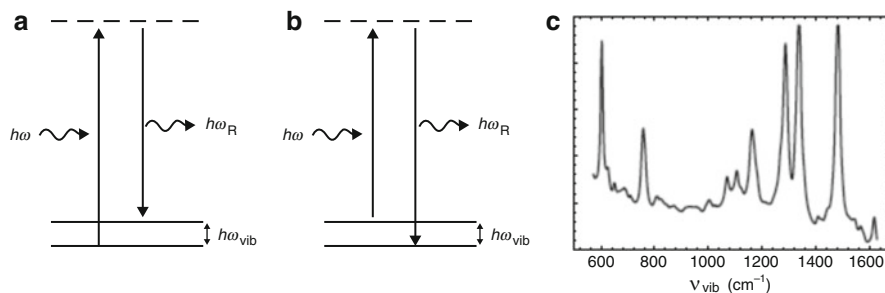


Fig. 11.2 Raman scattering process when (a) $\omega > \omega_R$ (Stokes Raman scattering), (b) $\omega < \omega_R$ (anti-Stokes Raman scattering). (c) Raman spectrum of Rhodamine 6G (RG6) molecule [16]

The contents of this chapter include as follows. Section 11.2 describes the sample preparation method and instrumentation of confocal scanning microscopy which deals the recording of Raman spectra of individual nanostructures. Section 11.3 discusses the geometrical structure, electronic band structure, phonon properties, and Raman spectra of single-walled carbon nanotubes (SWNTs). The Raman scattering of multi-walled carbon nanotubes (MWNTs) has also been discussed in Sect. 11.3. Section 11.3 presents the discussion on phonon properties and Raman scattering of graphene. In Sect. 11.4, the basic mechanism of surface-enhanced Raman spectroscopy (SERS) and its application to probe individual molecule are given. In Sect. 11.4, the momentum mapping of Raman scattering of individual nanostructures in the presence of optical nanoantenna is presented. Finally in Sect. 11.5, the summary and future aspects of this chapter are elaborated for the upcoming development in the field of Raman scattering of nanostructures.

11.2 Experimental Section

This section describes the confocal scanning microscopy technique in detail, such as configuration of optical microscope, confocal principle, and excitation source. Later, the sample preparation methods have been discussed. They are centred on CNT, graphene, and diamond materials for their Raman characterization.

11.2.1 Confocal Scanning Optical Microscope

Confocal scanning optical microscopy works on the confocal principle and employs far-field illumination and far-field detection system. The confocal arrangement in Raman spectrometer improves the positional accuracy of the nanomaterials and subsequently increases the signal-to-noise ratio. The simplest set-up of confocal

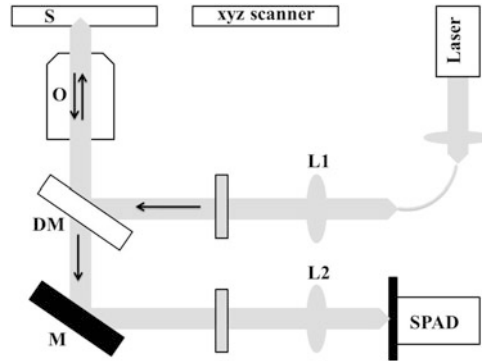


Fig. 11.3 The schematic of confocal scanning microscopy set-up. The laser light source is coupled to single-mode optical fibre and then passes through a lens to make the beam collimated. A dichroic mirror (beam splitter) reflects the light into objective of the microscope. The optical emissions generated by the nano-objects at the focus are collected by the same objective. The dichroic beam splitter transmits signal after filtering the selected region of wavelength onto another pinhole in front of a detector. Thus, images are obtained in the pixelated form by scanning the sample relative to focal plane of objective [16]

scanning microscope is shown in Fig. 11.3. In this configuration, the laser beam path is fixed, and the sample is raster scanned to record the image. The light from the laser source is passed through pinhole or a single-mode optical fibre and then coupled to the microscope objective with the help of couple of lenses. This mechanism of light coupling to microscope objective provides perfect Gaussian beam [16].

The diffraction-limited spot size (Δx) arises due to interaction of laser light at the entrance aperture which depends on numerical aperture (NA) of objective and the wavelength (λ) of laser used for illumination:

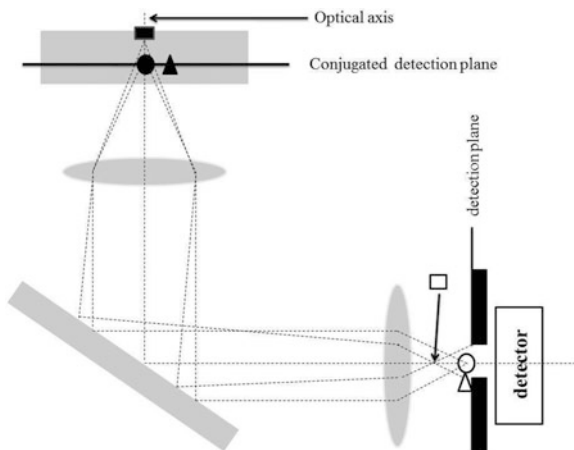
$$\Delta x = 0.61 \frac{\lambda}{NA} \quad (11.3)$$

With $NA = 1.49$, the lateral spot size for red light ($\lambda = 633 \text{ nm}$) is about 260 nm, which is slightly better than $\lambda/2$ (316 nm).

The reflected and scattered light is produced when laser light interacts with the nanostructure materials at the excitation wavelength and shifted wavelength relative to the excitation. The sample illumination and light capturing are obtained by the same microscope objective. The captured light is separated from the illuminated light by introducing a combination of optical filters, dichroic mirror, and notch filters in front of the collimated beam travelling towards charge-coupled device (CCD) detector having a pinhole at the entrance.

The motivation of using pinhole at the entrance of detector is to improve signal-to-noise ratio by collecting more signal from the focal plane. This is known as confocal principle (depicted in Fig. 11.4).

Fig. 11.4 There are three objects shown in the sample. Only one object (encircled), in the confocal plane and lying on the optical axis, is being captured at the detector plane. Signals other than that from this object are cut off by the pinhole configuration [16]



It is based on the detection principle that the light generated only from the focal plane is captured using the detector and rest of the light signal (stray signal in this case) coming from the region other than the focal area is filtered out using the pinhole unit and hence the stray signal does not reach the detector. The beams originating from points displaced along the optical axis will be defocused in the detection plane, and laterally displaced beams will be blocked by the pinhole placed in front of the detector. Therefore, the signal generated other than the object placed in the focal plane will be strongly attenuated.

11.2.2 Sample Preparation

Bundled CNT samples can be synthesized by different methods, such as chemical vapour deposition (CVD), arc discharge, laser ablation, and high-pressure carbon monoxide (HiPCO) method [17, 18]. The individual SWNTs are grown on Si/SiO₂ by CVD technique [19]. However, the density and length of SWNTs can be controlled by controlling the growth time. SWNT bundles are dispersed in sodium dodecyl sulphate surfactant solution by sonication and are subsequently processed by centrifugation [20–22].

Graphene is synthesized by mechanical exfoliation of graphite and CVD techniques [23–25]. However, the CVD growth of graphene is more versatile and applicable to wafer-scale requirements for electronics and photonics. In general, large-area graphene is synthesized on copper (Cu) foil by CVD technique and subsequently transferred on desired substrate after removing the Cu foil by Cu etchant (FeCl₃) [24].

Raman spectroscopy is commonly used for characterizing SWNT, graphene, and diamond samples because it has a potential to identify different phases and determine sizes and phonon dispersions of nanomaterials [1, 7, 25]. The simplicity

of Raman experiment makes it more versatile to perform the experiment at room temperature and under ambient pressure without destroying the samples in a quick response time. Raman spectroscopy becomes even more powerful to determine electronic and structural properties of individual SWNTs, graphene, diamond, and many more materials [1].

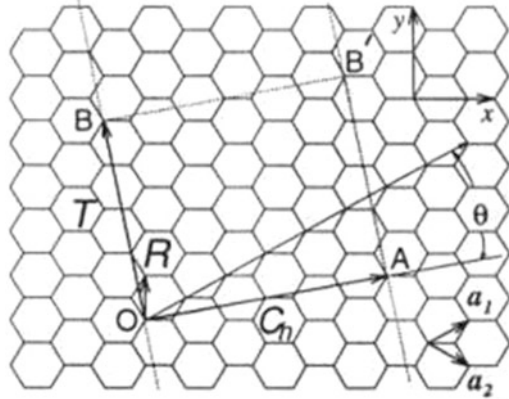
11.3 Raman Spectroscopy of Carbon Materials

The Raman scattering of carbon materials depends upon various aspects of the materials such as geometrical structure, electronic band structure, and phonon structure of the materials. Moreover, it is very powerful technique to disguise the different phases of the same material [1, 4, 7, 8]. Thus, by doing the Raman characterization of carbon materials, one can get the information about the size, conductivity, chemical doping, and phonon structure of the materials. In this section, we will discuss the potential applications of Raman spectroscopy for carbon nanotube and graphene.

11.3.1 Structure of Graphene and Carbon Nanotubes

The CNT can be conceptualized as a hollow cylinder formed by rolling two-dimensional (2D) graphene sheet. The bonding in nanotubes is of sp^2 nature. However, circular curvature causes quantum confinement and σ - π re-hybridization in which three σ bonds are slightly out of plane; for compensation, the π orbital is more delocalized outside the tube. This makes nanotubes mechanically stronger, electrically and thermally more conductive, and chemically as well as biologically more active than graphite. In addition, they allow topological defects such as pentagons and heptagons to be incorporated into the hexagonal network to form capped bent, toroidal, and helical nanotubes, whereas electrons will be localized in pentagons and heptagons because of redistribution of π electrons. A SWNT can be visualized as a hollow cylinder, formed by rolling over a graphene sheet, whereas a multi-walled nanotube (MWNT) consists of a group of coaxial SWNTs. There are an infinite number of possible atomic structures of a SWNT. Each structure is identified by its diameter and by the degree of the helical arrangement of carbon hexagons. To understand the structure (shown in Fig. 11.5), we first choose an origin, denoted by $(0,0)$, and then any lattice point (n,m) in the honeycomb structure of graphene sheet (Fig. 11.5), next we roll the graphene sheet such that the chosen lattice point (n,m) is superimposed to the origin $(0,0)$. In this way, we can construct a SWNT of chirality (n,m) . However we can use the two-dimensional lattice point of graphene as an index of the atomic structure of SWNT. Figure 11.5 shows how to generate a SWNT of helicity (n,m) . The resulting tube axis is normal to the line

Fig. 11.5 Chiral vector \vec{C}_h and chiral angle θ definition for a (4, 2) nanotube on graphene layer. \vec{a}_1 and \vec{a}_2 are the unit vectors of the two-dimensional hexagonal graphene sheet. The circumference of nanotube is given by the length of chiral vector. The chiral angle θ is defined as the angle between chiral vector \vec{C}_h and the zigzag axis [26]



$OA(\vec{C}_h)$ on the graphene sheet. The \vec{C}_h , known as chiral vector, can be expressed as a linear combination of the real-space unit vectors \vec{a}_1 and \vec{a}_2 of the graphene sheet as:

$$\vec{C}_h = n\vec{a}_1 + m\vec{a}_2 \quad (\text{where, } n, m \text{ are integers and } 0 \leq |m| < n) \quad (11.4)$$

In the x, y coordinates, the real-space unit vectors \vec{a}_1 and \vec{a}_2 of the hexagonal lattice of graphene are expressed as

$$\vec{a}_1 = \frac{3}{2}a_{cc}\hat{i} + \frac{\sqrt{3}}{2}a_{cc}\hat{j} \quad \text{and} \quad \vec{a}_2 = \frac{3}{2}a_{cc}\hat{i} - \frac{\sqrt{3}}{2}a_{cc}\hat{j} \quad (11.5)$$

It is noted here that \vec{a}_1 and \vec{a}_2 are not orthogonal to each other and the inner products between \vec{a}_1 and \vec{a}_2 yields

$$\vec{a}_1 \cdot \vec{a}_1 = \vec{a}_2 \cdot \vec{a}_2 = a^2, \quad \vec{a}_1 \cdot \vec{a}_2 = \frac{a^2}{2} \quad (11.6)$$

where the lattice constants $a = \sqrt{3}a_{cc}$, and $a_{cc} = 0.142$ nm is the nearest-neighbour distance between two carbon atoms in the graphene sheet.

Different types of SWNT are thus uniquely defined by the values of n and m . In general, there are three types of SWNT, each being defined by its chiral angle θ , where θ is defined as

$$\cos \theta = \frac{\vec{C}_h \cdot \vec{a}_1}{|\vec{C}_h| |\vec{a}_1|} = \frac{2n + m}{2\sqrt{n^2 + m^2 + nm}} \quad (11.7)$$

The value of θ lies in the range $0 \leq \theta \leq 30^\circ$, because of the hexagonal symmetry of the honeycomb lattice. Thus, the three types of SWNTs; zigzag, armchair, and chiral, correspond to $\theta = 0$, $\theta = 30$ and $0 < \theta < 30$, respectively. The diameter of a SWNT is equal to the magnitude of the chiral vector and can be written as

$$d_t = \frac{L}{\pi} = \frac{a\sqrt{n^2 + m^2 + nm}}{\pi} \tag{11.8}$$

As shown in the Fig. 11.5, \vec{T} is translational vector of unit cell of 1D SWNT, and is given by

$$\vec{T} = \frac{[(2m + n) \vec{a}_1 - (2n + m) \vec{a}_2]}{d_r} \tag{11.9}$$

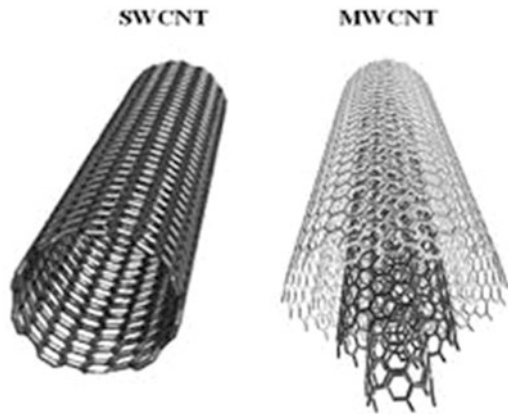
where d_r is the greatest common divisor of $(2m + n)$ and $(2n + m)$. That is, if d is the greatest common divisor of n and m , then d_r can be written as

$$d_r = d \text{ if } (n - m) \text{ is not a multiple of } 3d$$

$$d_r = 3d \text{ if } (n - m) \text{ is a multiple of } 3d$$

MWNTs contain at least two concentric graphene layers. The structure of SWNT and MWNT is shown in Fig. 11.6. The interplanar spacing in MWNTs is estimated to be approximately 0.334 nm [27] with successive tubes differing in circumference

Fig. 11.6 Geometrical structure of SWNT and MWNT generated by rolling the graphene sheet in tubular form



by $(2\pi \times 0.334) \text{ nm} \sim 2.1 \text{ nm}$. The interlayer spacing values are also reported in the range of 0.340–0.375 nm, with the interlayer distance increasing with a decrease in the tube diameter.

11.3.2 Electronic Band Structure of Graphene

The electronic properties of graphite are determined by its band structure and are highly anisotropic. Electron mobility within planes is high, as a result of overlap between the π orbitals on adjacent atoms. The mobility perpendicular to the planes is relatively low. Detailed structure of the electronic energy bands and Brillouin zones for the graphite was first developed by P.R. Wallace using the ‘tight-binding’ approximation [28].

The expression for energy (E_{2D}) dispersion relation of an electron in graphene sheet (2D) at a point defined by the wave vectors k_x, k_y is given by:

$$E_{2D}(k_x, k_y) = \pm \gamma_0 \left\{ 1 + 4 \cos\left(\frac{\sqrt{3}k_x a}{2}\right) \cos\left(\frac{k_y a}{2}\right) + 4 \cos^2\left(\frac{k_y a}{2}\right) \right\}^{1/2} \quad (11.10)$$

where γ_0 is the nearest-neighbour transfer integral and $a = 0.246 \text{ nm}$, is the in-plane lattice constant. Positive and negative signs correspond to the dispersion of the π (bonding) and π^* (antibonding) electrons, respectively, and k_x and k_y are x and y components of the momentum of an electron confined in the z -direction [28].

The hexagonal lattice of a graphene layer in real space consists of two carbon atoms, with lattice vectors $\vec{a}_1 = (\sqrt{3}a/2, a/2)$ and $\vec{a}_2 = (\sqrt{3}a/2, -a/2)$ and reciprocal lattice vectors $b_1 = (2\pi/\sqrt{3}a, 2\pi/a)$ and $b_2 = (2\pi/\sqrt{3}a, -2\pi/a)$, respectively. Carbon atoms have four valence electrons, three of which are used to form the sp^2 bonds with neighbour atoms in σ orbitals. They lie far below the Fermi level and do not contribute to the electrical conduction. The transport properties are determined by the fourth electron which occupies a π orbital resulting from a $2p_z$ bond.

The constant energy contour of conduction and valence band of a 2D graphene sheet is shown in Fig. 11.7a. The conduction and valence bands touch and are degenerate at the six K points in first Brillouin zone of graphene. The Fermi energy E_F is thus reduced to six points and is called Dirac points. Graphene layer is sometimes classified as zero-gap semiconductors because band gap is zero at the six K points. The energy contours for bonding band are drawn in first Brillouin zone as shown in Fig. 11.7b, and is similar for the antibonding band.

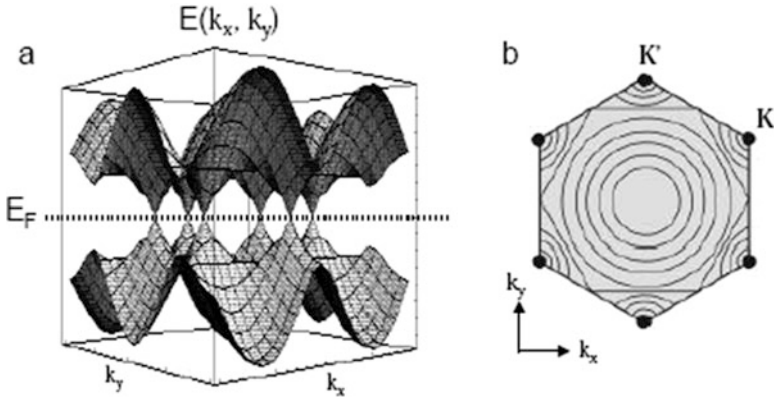


Fig. 11.7 (a) The energy dispersion of graphene layer (2D). The Fermi energy E_F is reduced to six points where the bonding and antibonding bands touch each other? (b) The hexagonal Brillouin zone of graphene layer with energy contours schematically drawn for the bonding band. The Fermi level is reduced to the six corner points, indicated by black dots [29]

11.3.3 Electronic Band Structure of Carbon Nanotube

The one-dimensional band structure of a SWNT can be derived from a 2D band structure of a graphene sheet by imposing periodic boundary conditions in the circumferential direction denoted by chiral vector \vec{C}_h . The allowed wave vectors, k , are obtained from the quantum condition:

$$\vec{k} \cdot \vec{C}_h = 2\pi q \tag{11.11}$$

where q is an integer.

The wave vectors along the direction of translational vector \vec{T} (i.e. along the nanotube axis) remain continuous for a nanotube of infinite length. The electrons are therefore free to move only in the direction of nanotube axis. Due to this quantization, a discrete number of parallel lines that represent the allowed modes of k values appear in the reciprocal space of graphene. These are shown as examples of armchair, zigzag, and chiral nanotubes in Fig. 11.8. The quantization of the wave vector allows us to characterize the expected transport properties of the nanotubes. From Eq. (11.11), it is expected that for a chiral (n, m) SWNT if $n - m = 3q$, nanotube should be metallic. On the other hand if $n - m \neq 3q$ it is expected to be semiconducting. Thus zigzag $(n,0)$ SWNTs will be metal when $n/3$ is an integer, and otherwise semiconducting. Armchair (n, n) SWNTs are expected to be truly metallic. The band gap of the semiconducting SWNTs depends inversely on diameter, which is given by

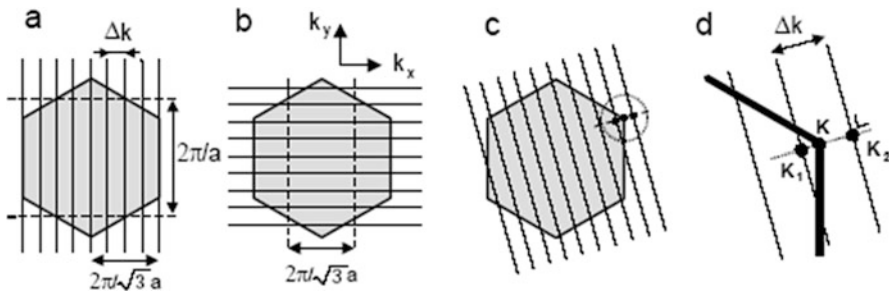


Fig. 11.8 Reciprocal space for an armchair (a), zigzag (b), and chiral (c and d) nanotube. The parallel lines represent the allowed values for the wave vector \vec{k} . In all cases the tube axis direction is along the lines. The circle in (c) encloses a region of states near the Fermi level for a chiral nanotube and is shown enlarged in panel (d). The points K_1 and K_2 are points of closest approach to the Fermi level at K in the two nearest allowed k -lines [29]

$$E_g = \frac{2\gamma_0 a_{cc}}{d_t} \quad (11.12)$$

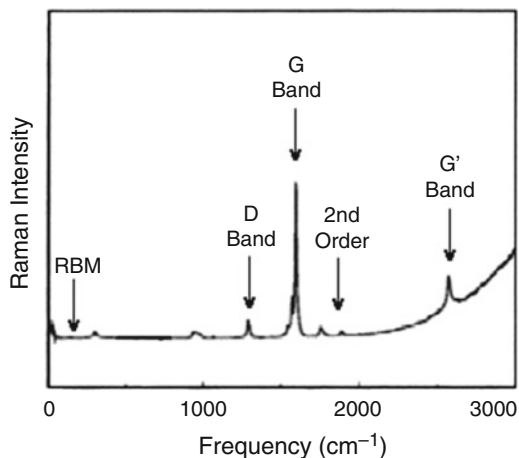
where γ_0 (2.7 eV) is the overlap integral for graphite, a_{cc} is the nearest-neighbour distance, and d_t is the diameter of nanotubes.

11.3.4 Raman Spectroscopy of Carbon Nanotube

Raman spectroscopy is used to study phonon dispersion relation, electronic band structure, and size of SWNTs. It relies on inelastic scattering, or Raman scattering of monochromatic light, usually from a laser in the visible, near-infrared, or near-ultraviolet range. The laser light interacts with phonons or other excitations in the system, resulting in the energy of the laser photons being shifted up or down. The shift in energy gives information about the phonon modes in the system. The unique optical and electronic properties observed in SWNT are largely due to one-dimensional (1D) confinement of electronic and phonon states. In combination with the unique 1D electronic structure, the resonantly enhanced Raman scattering intensity allows one to obtain detailed information about the vibrational properties of nanotubes, even at the isolated individual SWNT level. The Raman spectrum is normally obtained for wave numbers from 100 to 2000 cm^{-1} . Beyond this, higher-order modes are visible.

The spectral features of SWNTs can be divided into mainly three approximate parts: (1) radial breathing modes (RBMs) from 100 to 500 cm^{-1} , (2) disorder-induced D-band from 1300 to 1450 cm^{-1} , and (3) tangential modes (TM modes or G-band) from 1450 to 1600 cm^{-1} . A typical Raman spectrum of carbon nanotube sample is shown in Fig. 11.9 [30].

Fig. 11.9 Raman spectrum of SWNTs recorded in the frequency range $100\text{--}3000\text{ cm}^{-1}$ depicting the various bands [30]



11.3.4.1 Radial Breathing Mode (First-Order Raman Scattering)

The radial breathing mode (RBM) Raman features correspond to the coherent vibrations of C atoms in the radial direction (A_{1g} symmetry), as if the tube were ‘breathing’. The diameter of SWNTs or the inner diameter of MWNTs can be determined by the peaks in the RBM part of a Raman spectrum. This is called first-order Raman scattering because one phonon is involved in scattering process. The confinement in the radial axis is related to the diameter of the nanotube and hence is a function of the radial vibrational frequency. The diameter of SWNT in a bunch is given by the simple relation [31]:

$$w_{\text{RBM}} (\text{cm}^{-1}) = \frac{224}{d_t (\text{nm})} + A \quad (11.13)$$

where $A = 14\text{ cm}^{-1}$ when SWNT exists in bunches and zero for isolated SWNT, w is the wave number of the dominant peak, and d_t is the resultant diameter of the nanotube.

11.3.4.2 D-Band (Second-Order Raman Scattering)

The disorder-induced D-band Raman vibrational mode (A_{1g} symmetry), with highly dispersive spectral features, is also present in CNTs due to the collective in-plane vibrational movement of atoms towards and away from the centre of the hexagons formed by the covalently (sp^2) bonded carbon atoms. This is called second-order Raman scattering process because in this event one phonon and one elastic scattering by defect centres are involved. Thus a ratio of the intensities of the G- and D-bands would give a better understanding of the ‘quality’ of the CNTs.

11.3.4.3 G-Band (First-Order Raman Scattering)

The G-band Raman vibration modes (E_{2g} symmetry) are present due to in-plane vibrational movement of C atoms, which involves a combination of stretching and bending of C-C bonds. In this process, one phonon is involved in the scattering event process. The TM peak data can be used to determine the conductivity of the nanotubes. Depending on the shape of Raman spectrum and the energy of the exciting laser, the metallic or the semiconducting nature of the tubes can be predicted.

The number of emitted phonons before relaxation of the lattice can be one, two, and so on, which one may call one-phonon, two-phonon, and multi-phonon Raman process. However, the order of scattering events is defined as its number in the sequence of the total scattering events, including elastic scattering by a defect or an edge of the crystal. The schematic of first- and second-order Raman scattering process is described in Fig. 11.10.

The use of the resonance effect in Raman spectroscopy substantially increases the power of the technique. The intensity of Raman peak is enhanced when the incident or the scattered photon is in resonance with an electronic transition in the material. By studying the intensity of Raman peak as a function of the excitation laser energy (E_{laser}), one can obtain information about the electronic structure. In addition, variation of E_{laser} provides new power to the Raman technique, special for the study of one-dimensional carbon materials. SWNTs have been the focus of intensive work for fundamental studies. Different kinds of SWNTs, as determined by their tubular structures, i.e. diameter (d_t) and chirality (θ), exhibit different properties [26]. The structure of a given SWNT can be defined by the chiral vector \vec{C}_h , which spans

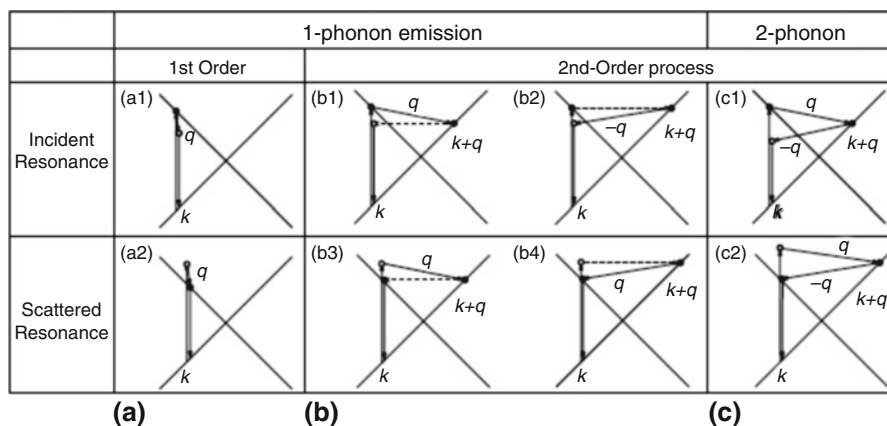


Fig. 11.10 (a) First-order, (b) second-order with one phonon, and (c) second-order with two-phonon, resonance Raman scattering process. The top one is incident resonance, and bottom one is scattered resonance Raman process. The phonon and elastic scattering process is shown by solid and dashed lines, respectively. The solid circle represents the resonance points [1]

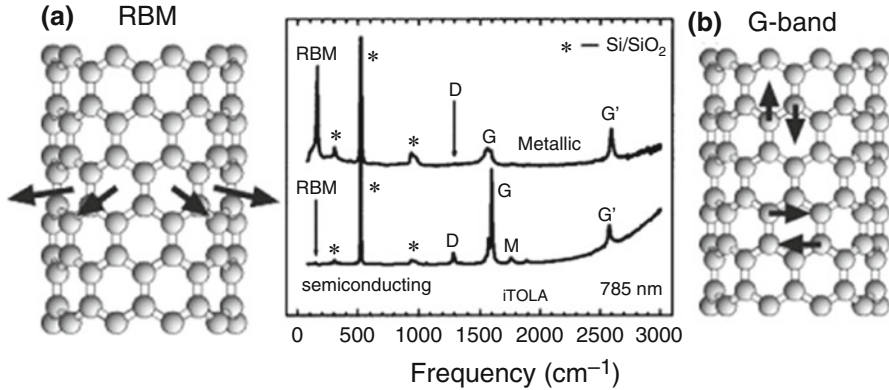


Fig. 11.11 Raman spectra from a metallic (top) and a semiconducting (bottom) SWNT showing the radial breathing mode (RBM), D-band, G-band, and G' -band features, in addition to weak double-resonance features associated with the M-band and the iTOLA second-order modes. Figures on the left and the right show, respectively, the atomic displacements associated with the RBM and G-band normal mode vibrations. The isolated carbon nanotubes are sitting on an oxidized silicon substrate which provides contributions to the Raman spectra denoted by "*" which are used for calibration purposes [32]

the circumference of the tube, and the vector \vec{C}_h can be denoted by a pair of indices (n,m) , which describes \vec{C}_h as a function of the graphene lattice unit vectors ($\vec{C}_h = n\vec{a}_1 + m\vec{a}_2$). The physical properties of carbon nanotubes depend strongly on (n,m) . Special attention should be given to the fact that SWNTs can be metallic if $(n-m)$ is a multiple of 3 or semiconducting otherwise. The characterization of nanotube structures, given by their indices (n,m) , is, therefore, of major importance for the development of carbon nanotube science and applications. The distinction between metallic and semiconducting SWNTs utilizes the different line shapes of the tangential mode vibrations, as shown in Fig. 11.11 [32]. This Raman feature is called the G-band, G denoting graphite-like in addition to weak double-resonance features associated with the M-band and the iTOLA (in-plane transverse optic (iTTo) and longitudinal acoustic (LA)) second-order modes. In graphite the feature has a single peak, since in-plane tangential vibrations are degenerate in the hexagonal sheet. In nanotubes this feature splits into up to six peaks due to the curvature of the graphene sheet and the quantum confinement along the tube circumference [33]. Raman spectroscopy can be used to determine the SWNT geometric structure by a direct evaluation of the (n,m) indices for individual SWNTs [32]. For the spectroscopic assignment of the SWNT indices (n,m) , experimental determination of properties of nanotube is necessary: the electronic transition $E_{ii}(i=1, 2, 3, \dots)$, giving the number of the electronic transition energy relative to the Fermi level of the unperturbed SWNT) and the nanotube radial breathing mode frequency (w_{RBM}). Therefore, once one measures a set of these two SWNT properties, a structural assignment can be made by using a model which directly relates the (E_{ii}, w_{RBM}) to

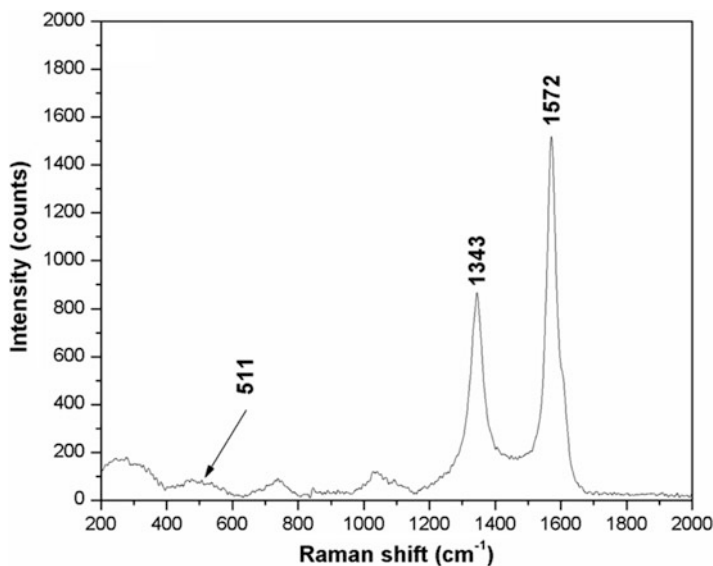


Fig. 11.12 Raman spectrum of MWNT sample indicating the presence of D- and G-bands and I_D/I_G ratio is 0.6

(n,m) . Because of the large diameter of the outer tubes for typical MWNTs, most of the characteristic differences that distinguish the Raman spectra in carbon nanotubes from that for graphite are not evident in MWNTs. The RBM from the large diameter tubes is usually too weak to be observable.

The Raman spectrum of MWNT sample is shown in Fig. 11.12. The spectrum is entirely different from SWNT as evident that no RBM peak is appearing, and splitting of G-band is also entirely different. The presence of the CNT intrinsic G-band and the disorder-induced D-band, indicative of inherent disorder, was observed in the sample. The I_D/I_G ratio is indicative of defects present into the sample.

11.3.5 Raman Spectroscopy of Graphene

Raman spectroscopy is a powerful tool to study the properties of graphene. It has been utilized to study various properties of graphene, such as number of layers, orientation, quality of edges, doping, disorder, and functional groups in the grapheme sample. Moreover, perturbation effects of electric and magnetic field can also be studied. As already described in the previous sections, graphene is a two-dimensional building block of sp^2 carbon allotropes of other dimensionality. It can be warped into zero-dimensional fullerene, rolled into one-dimensional carbon nanotube, and stacked to form three-dimensional graphite. So, it is at the centre of an ever-expanding research area of carbon materials [34–38]. The high mobility and

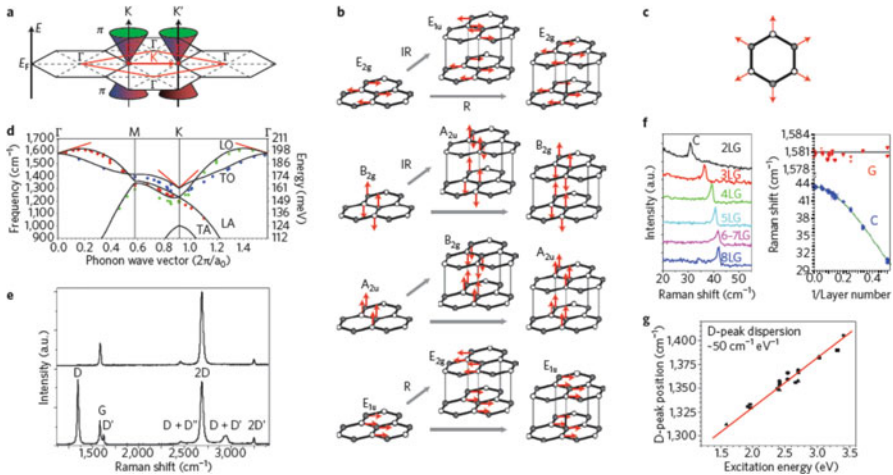


Fig. 11.13 Electron and phonon dispersion and Raman spectrum of two-dimensional (2D) graphene. **(a)** Electronic dispersion in first Brillouin zones of graphene. **(b)** Γ -point phonon-displacement pattern for graphene and graphite. Red and grey arrows show atom displacements and how each phonon mode in graphene gives rise to two-phonon modes of graphite, respectively. The labelling shows Raman-active (R), infrared-active (IR), and inactive (unlabelled) modes. **(c)** Atom displacement is shown by red arrows for the A_{1g} mode at K point. **(d)** The black curves represent the dispersion of phonon modes in graphene for Raman scattering. **(e)** Raman spectra of pristine (top) and defected (bottom) graphene sample. **(f)** The C peak as a function of number of layers in graphene sample. **(g)** The D-peak position as a function of excitation energy [7, 42–45]

near-ballistic transport makes it suitable for nanoelectronic devices working at high frequencies [39]. Additionally, its optical and mechanical properties are ideal for conductive electrodes and flexible photonics devices [34–37, 40, 41].

Figure 11.13a presents the plots of the electronic dispersion (Dirac cones) in first Brillouin zone of graphene. There are six normal modes (two being doubly degenerate) at the Brillouin zone centre (Γ): $A_{2u} + B_{2g} + E_{1u} + E_{2g}$ (shown in Fig. 11.13b), because graphene has two atoms per unit cell [42, 43]. The E_{2g} phonon is Raman active, whereas B_{2g} phonon is neither Raman active nor infrared active [42]. In the two inequivalent layers in graphite, the B_{2g} phonons are infrared active.

The E_{2g} phonon generates an infrared-active E_{1u} phonon and a Raman-active E_{2g} phonon in graphite. However, the B_{2g} phonon goes into an infrared-active A_{2u} phonon and an inactive B_{2g} phonon. The origin of D peak is due to the breathing modes of six-atom rings (Fig. 11.13c), and it requires a defect for its activation [46–48]. The optical phonon dispersions of SLG for the interpretation of the Raman spectra are depicted in Fig. 11.13d [43, 45, 49]. Three optical (O) phonon and three acoustic (A) phonon branches comprise in the phonon dispersion relation of single-layer graphene (SLG). The Raman spectrum of SLG is shown in Fig. 11.13e, which consists of distinct bands at $\sim 1350\text{ cm}^{-1}$ (D-band), $\sim 1580\text{ cm}^{-1}$ (G-band), ~ 1610 (D' -band), and $\sim 2700\text{ cm}^{-1}$ (2D-band). The mechanism for the source of D-band and G-band has already been discussed in the previous section of carbon nanotubes. The origin of D' -band is caused by double resonance that can also

happen as an intravalley process which involves two points on the same cone around K (or K'). The 2D- and 2D'-bands are the overtone of D- and D'-bands, respectively. No defects are required for the activation of 2D- and 2D'-bands; only momentum conservation by two phonons with opposite wave vectors is necessary for their origin. Thus they are always present in Raman scattering process of graphene [50, 51]. The Raman spectrum of multilayer graphene consists of two different sets of peaks, such as shear modes (C) and the layer breathing modes (LBMs) in addition to D-, G-, and 2D-bands compared to SLG [52–56]. The sensitivity of C-mode depends on interlayer coupling in multilayer, and the Raman scattering is displayed in Fig. 11.13f [52]. Thus the absence of C-mode in graphene sample is direct evidence of SLG. The peak position of C (P(C)) depends on the number of layers (N) in graphene sample is given by following expression [52]:

$$P(C)_N = \sqrt{\frac{2\alpha}{\mu}} \sqrt{1 + \cos\left(\frac{\pi}{N}\right)} \quad (11.14)$$

where $\alpha = 12.8 \times 10^{18} \text{ N m}^{-3}$ is the interlayer coupling and $\mu = 7.6 \times 10^{-27} \text{ kg } \text{\AA}^{-2}$ is the graphene mass per unit area. Figure 11.13g displays the dependence of D-band on the laser excitation energy. The D-band originates from TO phonons around the Brillouin zone corner K, is active by double resonance and is strongly dispersive with excitation energy due to a Kohn anomaly at K [44, 46–48].

The elementary steps of Raman scattering process involved for different bands in graphene is described in Fig. 11.14.

Electron dispersion, occupied states, and interband transitions neglecting the photon momentum accompanied by photon absorption are represented by solid black lines, shaded areas, and blue arrows, respectively, in Fig. 11.14. The emission lines, intraband transitions accompanied by phonon emission, and electron scattering on a defect are labelled by red arrows, dashed arrows, and horizontal dotted arrows, respectively, in Fig. 11.14.

In graphene, the C and G peaks appear due to involvement of one phonon in defect free samples. One-phonon modes can be Raman active only if their symmetry is correct and their wave vector is zero. The selection rule for two-phonon process obeys any pair of phonons with opposite wave vectors ($\mathbf{q}, -\mathbf{q}$). Thus, the matrix element has four contributions corresponding to process (i) both phonon emitted by the electron (ee), (ii) both phonon emitted by hole (hh), and (iii) one phonon emitted by electron and the other by hole (eh and he).

11.4 Surface-Enhanced Raman Spectroscopy

Surface-enhanced Raman spectroscopy (SERS) is a powerful technique that is used for the characterization of single molecules, proteins, or nanomaterial with a very small optical capture cross-section. Basically, it is a surface-sensitive technique that is used to enhance the Raman intensity signal by molecules adsorbed on the rough

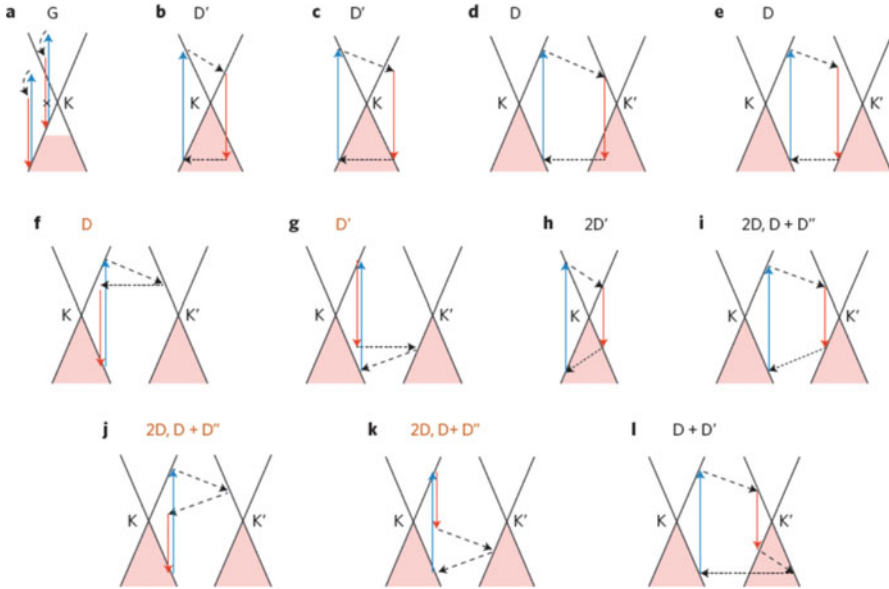


Fig. 11.14 Raman processes involved for different bands in graphene. (a) One-phonon processes responsible for the G peak. (b–g) In the presence of defects, the phonon wave vector need not be zero, producing the D' peak for intravalley scattering (b, c), and D peak for intervalley scattering (d–g). (h–k) For two-phonon scattering, momentum can be conserved by emitting two phonons with opposite wave vectors, producing the $2D'$ peak for intravalley scattering (h) and the $2D$ and $D + D''$ peaks for intervalley scattering (i–k). (l) With defects, one intravalley and one intervalley phonon can be emitted, producing the $D + D'$ peak [7]

surface of metal. Single molecule can also be detected by this technique because of large enhancement factor, i.e. 10^{10} – 10^{11} [57, 58]. Enhanced electric field is the main reason that is responsible for increase in Raman intensity. Localized surface plasmon resonances (LSPRs) get excited when the incident light strikes the rough surface of metal. This field enhancement is more when the excited Plasmon is in resonance with the incident radiation. This results into large signal intensity as an output [59]. Enhancement in the signal is fully dependent on resonance phenomena hence is not equal for all frequencies.

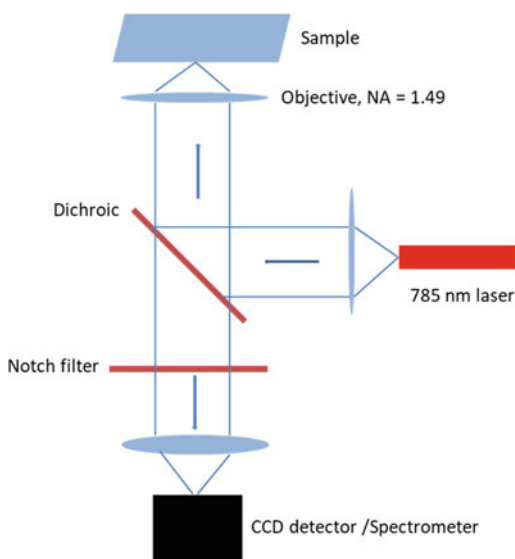
The improved interaction of light and matter mediated by optical antennas is the key in the current development of nanoscale optical spectroscopy [60–64]. Various optical antennas, such as nanorods, dimers, and more complex designs, have been employed for enhancing and redirecting the emission pattern of quantum emitters [61, 63]. These quantum emitters include fluorescent molecules, quantum dots, defect centres, and CNTs [61, 65–67]. Control of the emission pattern of quantum emitters is subject to intense research for directing light in well-defined region of the angular space [60–62]. The emission direction is strongly affected by the near-field interaction between the emitter and the optical antenna [60, 61].

Optical antennas are generally used in conjunction with carbon nanotubes for probing the vibrational properties of this one-dimensional structure by SERS [64]. The LSPRs, in metallic nanoscale objects, enhance the effectivity of light-matter interaction by increasing otherwise weak optical cross-sections. Much emphasis has been given on the design of antenna geometry enabling single-molecule SERS detection [68, 69]. Properly designed optical antennas, such as nanoscale gap antennas, confine light in deep subwavelength volume, thereby increasing the Raman signal of molecules. In such cases, the enhancement factor of SERS is proportional to the fourth power of electric-field enhancement [70].

11.4.1 Experimental Set-Up and Sample Preparation

The experimental set-up for the detection of SERS signal is shown in Fig. 11.15. We use an inverted optical microscope combined with an x, y -piezo position stage for raster scanning a microscope cover slide through a focus of a water immersion objective (NA = 1.2) and a linearly or circularly polarized laser emitting at $\lambda_{em} = 785$ nm for Raman excitation of CNTs or quantum emitters. The Raman signature is collected by raster scanning the sample through the focus of confocal microscope. The Stokes-shifted wavelengths are collected either with a spectrograph to disperse and identify the Raman lines or integrated by an avalanche photodiode to reconstruct a two-dimensional map of the response.

Fig. 11.15 Experimental set-up of inverted confocal optical microscope employed for SERS signal detection



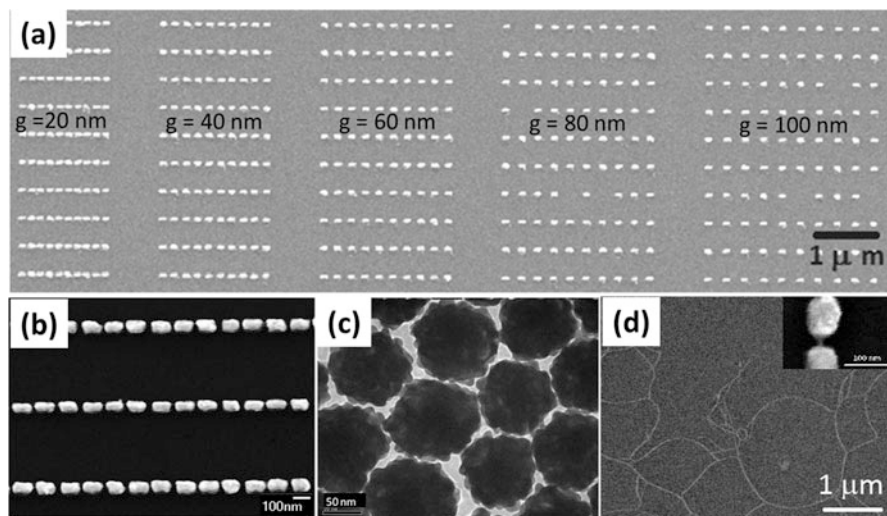


Fig. 11.16 SEM micrograph of (a) array of linear antenna chains of a gap ranging from 20 to 100 nm and (b) array of linear antenna chain of gap 20 nm. (c) TEM micrograph of nanoflowers. (d) SEM image of individual SWNT or thin ropes of SWNTs on pristine substrate and the inset is showing individual SWNT in between the gap of linear antenna chain [15]

Various types of substrates, such as linear antennas chains and self-assembled nanoflowers, are shown in Fig. 11.16. The linear antenna chains are fabricated by standard electron beam lithography (EBL) on ITO-coated cover glass slips. The linear chain consists of coupled Au nanorods of length (~ 110 nm), width (~ 55 nm), and thickness (50 nm of gold + 5 nm of chromium). The gap separating the antenna rods is varied from 20 to 100 nm (Fig. 11.16a). A high-magnification scanning electron microscopy (SEM) image of linear antenna chains with a gap of 20 nm is shown in Fig. 11.16b. The Au nanoflowers (size ~ 100 nm) are synthesized by solution-based reduction method [71], and a self-assembled monolayer is further deposited on ITO-coated cover glass substrate. The average diameter of the flower-shaped nanoparticles is estimated to be ~ 100 nm by using transmission electron microscopy (TEM) micrograph (Fig. 11.16c). High-pressure carbon monoxide (HiPCO) synthesized SWNTs (1 mg) are dispersed in per mL 1% wt. sodium dodecyl sulphate solution in water by sonication and are subsequently processed by centrifugation to remove bundles [20–22]. The nanotubes used in our experiment are ranging in diameter from 0.7 to 1.2 nm. After centrifugation, a diluted solution of SWNT is then spin-coated (Fig. 11.16d) on top of the SERS-active substrates. The density of individual SWNT or thin ropes of SWNTs on a pristine sample is estimated to be 1 SWNT or thin ropes of SWNTs/ μm^2 with the help of SEM image (Fig. 11.16d).

11.4.2 Theory of Surface-Enhanced Raman Scattering

To understand the SERS, let us consider the situation shown in Fig. 11.17. A molecule or nanomaterial located at \mathbf{r}_0 is placed in the vicinity of optical nanoantenna (located at position \mathbf{r}'_0) made of metal dimer or nanoparticles that act as local field-enhancing device.

The dipole moment associated with Raman scattering after interaction of incident field E_0 with the molecule is given by [16]

$$\mu(\omega_R) = \alpha(\omega_R, \omega) [E_0(\mathbf{r}_0, \omega) + E_s(\mathbf{r}_0, \omega)] \quad (11.15)$$

where ω is the frequency of exciting radiation and ω_R is the frequency of Raman-scattered radiation or vibrationally shifted frequency ($\omega_R = \omega \pm \omega_{\text{vib}}$). The polarizability α is modulated at the vibrational frequency ω_{vib} of the molecule and gives rise to the frequency mixing process. In the presence of metallic nanostructures, the molecule is interacting with local field $E_0 + E_s$, where E_0 is the local field in the absence of metal nanostructures and E_s is the enhanced field from the metal nanostructure. The E_s depends linearly on the incident field E_0 , and it can be represented as $f_1(\omega)E_0$, where f_1 represents the field enhancement factor.

The electric field radiated by induced dipole μ of the molecule due to influence of incident field is represented by the system's Green function G as [16]

$$E(\mathbf{r}_\infty, \omega_R) = \frac{\omega_R^2}{\epsilon_0 c^2} G(\mathbf{r}_\infty, \mathbf{r}_0) \mu(\omega_R) = \frac{\omega_R^2}{\epsilon_0 c^2} [G_0(\mathbf{r}_\infty, \mathbf{r}_0) + G_s(\mathbf{r}_\infty, \mathbf{r}_0)] \mu(\omega_R) \quad (11.16)$$

where G_0 and G_s represent the Green function corresponding to free space and scattered field due to interaction of molecule with metal nanostructure, respectively. We represent G_s as $f_2(\omega_R)G_s$, with f_2 being a second enhancement factor.

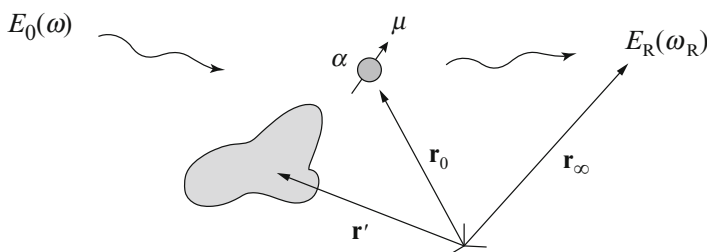


Fig. 11.17 Interaction of incident electromagnetic field E_0 with the molecule with polarizability α in the vicinity of metallic optical nanoantenna gives rise to scattered field E_R [16]

Using the relations $E_s = f_1(\omega)E_0$ and $G_s = f_2(\omega_R)G_0$ with intensity of Raman-scattered field $I \propto |E|^2$ yields [16]

$$I(\mathbf{r}_\infty, \omega_R) = \frac{\omega_R^4}{\varepsilon_0^2 c^4} [1 + f_2(\omega_R)] G_0(\mathbf{r}_\infty, \mathbf{r}_0) \alpha(\omega_R, \omega) [1 + f_1(\omega)]^2 I_0(\mathbf{r}_0, \omega) \quad (11.17)$$

Thus, the Raman-scattered intensity scales linearly with the excitation intensity I_0 , and it depends on the factor [16]:

$$|[1 + f_2(\omega_R)][1 + f_1(\omega)]|^2 \quad (11.18)$$

In the absence of metal nanostructures, the scattered intensity by setting $f_1 = f_2 = 0$. However, in the presence of the nanostructures, $f_1, f_2 \gg 1$ and overall Raman scattering enhancement becomes [16]

$$f_{\text{Raman}} = |f_2(\omega_R)|^2 |f_1(\omega)|^2 \quad (11.19)$$

Thus, the Raman scattering enhancement scales roughly with the fourth power of the electric-field enhancement. Despite of the described field enhancement mechanism, additional enhancement associated with SERS are a short-range chemical enhancement, which results from the direct contact of the molecule with the metal surface [16].

11.4.3 Surface-Enhanced Raman Scattering of Carbon Nanotube

Plasmon-enhanced Raman scattering of SWNT placed into near-field cavity or dimer antenna (gold) by dielectrophoretic method is displayed in Fig. 11.18 [64]. The plasmonic cavities enhance the Raman signal of a nanotube by a factor of 10^3 . The nanotube placed in the near-field cavity is excited by laser wavelengths 532 nm and 633 nm. The cavity dimensions are designed for resonance with 633 nm laser excitation. Hence, in Fig. 11.18a the signal of G-band of nanotube is maximum for laser polarization P_x , which is parallel to the nanotube axis. Figure 11.18b, c represents the near-field image corresponding to polarization P_y and P_x with respect to laboratory axis. The signal enhancement is found to be maximum for polarization (P_y) with laser wavelength 633 nm and minimum for P_x which corresponds to on or off state of the cavity, respectively. The corresponding near-field images are shown in Fig. 11.18e, f.

The Raman signal emitted by the molecule may be collimated by a directional antenna, which is known as beamed Raman scattering [72, 73]. The directionality has been employed to study the spectral and angular characteristics of the radiation

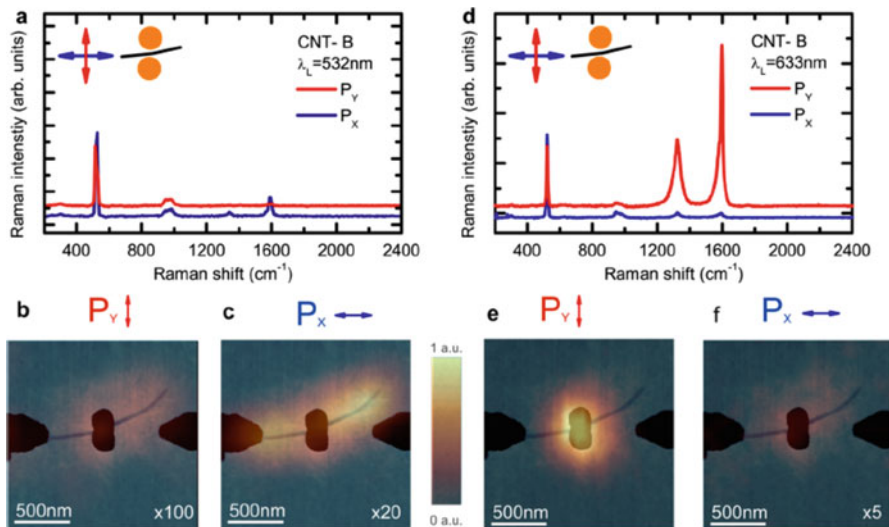
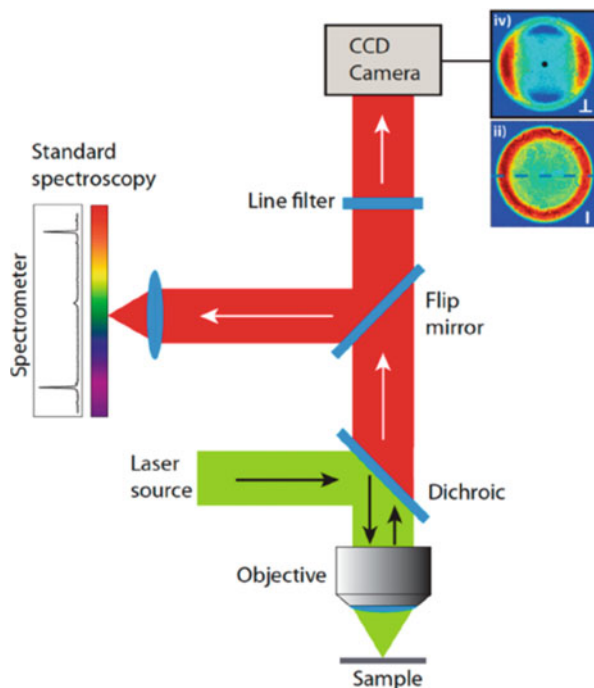


Fig. 11.18 (a) Raman spectra of nanotube with excitation wavelength 532 nm. (b) and (c) correspond to G-band Raman map for polarization P_y and P_x , respectively, with excitation wavelength 532 nm. (d) Raman spectra of nanotube with excitation wavelength 633 nm. (e) and (f) correspond to G-band Raman map for polarization P_y and P_x , respectively, with excitation wavelength 633 nm [64]

pattern of Raman-active emitters by imaging the angular distribution of the signal in the Fourier plane of the microscope [61, 63, 72, 73]. Thus, the Raman signal of nanotubes or molecules could be employed to understand the momentum-resolved selection rules in beamed scattering mode. The illustration to record Raman scattering in Fourier plane is shown in Fig. 11.19 [74].

The Raman scattering of thin ropes of SWNTs containing of few SWNTs is first located in the confocal plane by scanning confocal Raman microscopy. The hotspot generated by the interaction of nanotube and linear antenna chain is shown in Fig. 11.20a, whereas the hotspots generated by the nanotube randomly deposited on the nanoflowers are revealed in the confocal map of Fig. 11.20b. Figure 11.20c shows real-space Raman spectra of SWNTs recorded on substrate (pristine), linear antenna chains (20 nm gap), and nanoflowers, respectively. The radial breathing mode (RBM) at low frequency (~ 100 to 500 cm^{-1}), not shown here, is proportional to the SWNT diameter. We note that the tangential vibrating mode which is sensitive to the electronic band structure of SWNT (G-band) appears at ~ 1582 cm^{-1} . The M-band is found at (~ 1750 – 1850 cm^{-1}) (an overtone mode of out-of-plane transverse optical (oTO) mode at ~ 870 cm^{-1}) and iTOLA band is found at (1850 – 2050 cm^{-1}). This mode is a combination of in-plane transverse optical (iTO) and longitudinal acoustic (LA) mode in SWNTs [1]. The D- and M-bands are more marked in the case of the nanoflowers compared to the linear antenna chains. In addition, electron-phonon coupling and double-resonant Raman scattering which are explained in the

Fig. 11.19 Schematic diagram for recording the Raman scattering in Fourier plane, known as momentum-resolved Raman spectroscopy [74]



literature by the D- and D'-mode (D-mode for defect or disorder) are well observed in both samples between 1200 and 1400 cm^{-1} (D-modes) and at 1620 cm^{-1} (D' mode) with a heightened preference for nanoflowers. The short-scale irregularities formed on gold nanoflowers promote the local enhancement of the field, which excites some other modes in the molecule that are missing in normal Raman scattering [71].

The integrated SERS signals of G- (1595 cm^{-1}) and D (1300 cm^{-1})-bands of SWNT are plotted against the linear antenna chain gaps in Fig. 11.20d. It is expected from coupling-induced enhancement that the maximum SERS signal occurs for the lowest gap produced, here 20 nm gap, while there is no significant effect beyond 60 nm . This result is consistent with previous results on dimer antennas [62–64]. The chain geometry is designed such that it provides maximum enhancement for 785 nm laser excitation [63, 64]. In this case, laser light polarization is kept parallel to the chain axis for maximum coupling with the incident radiation. Usually the intensity ratio between G-mode and D-mode is around 10. The D-mode is then enhanced using SERS-active substrate.

The momentum-space Raman spectrum of SWNT was mapped on the two types of substrate, and the corresponding spectrum is displayed in Fig. 11.21. These spectra are recorded by translating the Fourier plane along the longitudinal direction (x -axis) of the inlet slit of the spectrometer [75]. For comparison purpose, we

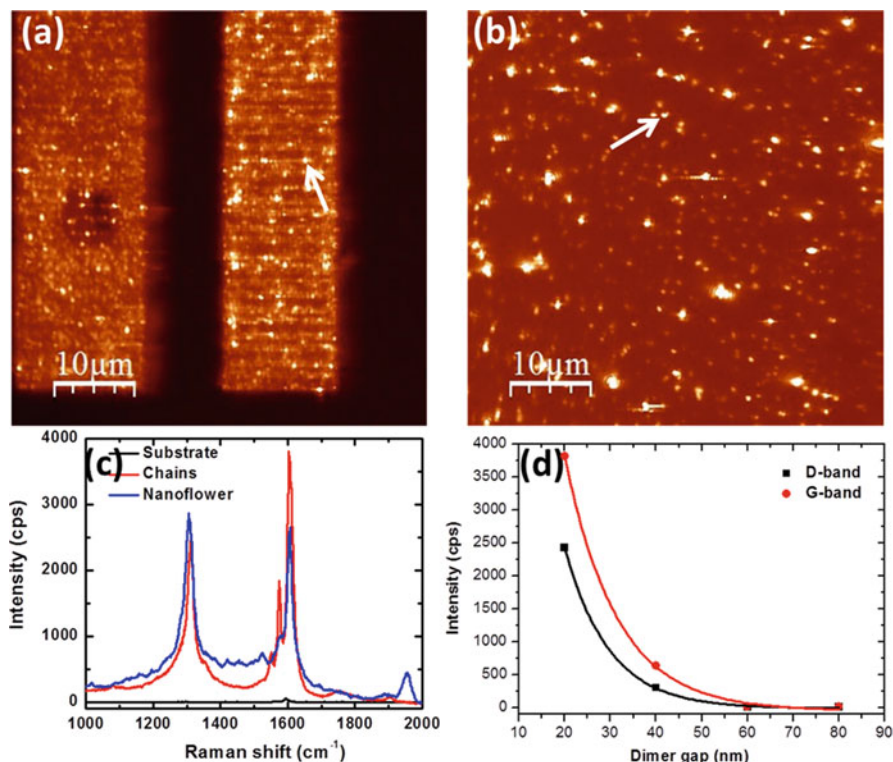


Fig. 11.20 Scanning confocal image of the integrated Raman intensity emitted from SWNTs dispersed over (a) linear antenna chains with a gap of 20 nm (right pad) and 40 nm (left pad), respectively, (b) nanoflower antenna, (c) comparison between Raman spectra of SWNTs dispersed over three different substrates (the ITO cover glass, linear antenna chains, and nanoflower), and (d) exponential variation of Raman signal of D- and G-band with the gap of linear antenna chains [15]

show in Fig. 11.21a a SERS spectra from a SWNT placed on the linear chain of coupled antennas recorded classically. The D-, G-, M-, and iTOLA-bands appear at 1300, 1590, 1750, and 1900 cm⁻¹, respectively, and the shoulder peak of G-band is positioned at 1560 cm⁻¹ (G⁻-band). This type of splitting of G-band is observed in semiconducting SWNTs [1]. Moreover, this implies that the SWNTs in the thin ropes are having uniform diameter. Figure 11.21b shows the SERS spectra now recorded at different in-plane momenta ($-1.2 \leq k_x/k_0 \leq 1.2$). We observe that all bands enhanced by the linear antenna chains do not depend on the momentum displayed in the Fig. 11.21b. The appearance of M- and iTOLA-bands at $k_x/k_0 = 0.0$ may be explained by radiation peaking as already observed at particular emission angle [63].

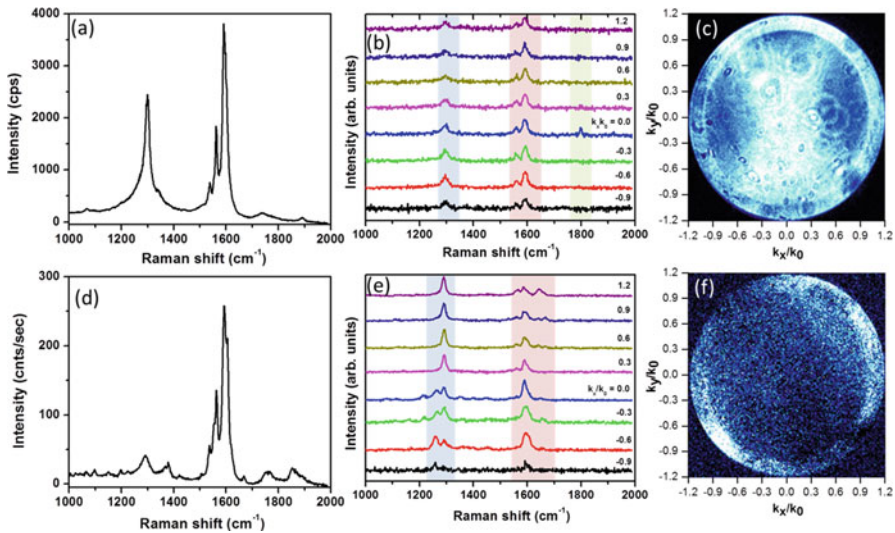


Fig. 11.21 Raman spectra of individual or thin ropes of only few SWNTs on linear chain of antennas recorded in (a) real space, (b) Fourier space at different longitudinal momenta (k_x), and (c) corresponding Fourier plane image. Raman spectra of SWNTs acquired on nanoflower antenna recorded in (d) real space, (e) Fourier space at different longitudinal momenta (k_x), and (f) corresponding Fourier plane image [15]

Figure 11.21d shows that the prominent Raman bands of SWNTs enhanced by the presence of nanoflower are present at 1290, 1360, 1560, 1590, 1655, 1760, and 1860 cm^{-1} . The amplitude and position of the peaks are now depending on the momentum. Other splitting such as D-, D⁺-, and D'-bands can be observed for large in-plane momenta. The D'-band is associated with the maximum in two-dimensional phonon density of states in graphene and commonly observed in the case of multi-walled carbon nanotube (MWNT) [76]. Interestingly, the shoulder peak of D-band is observed at the position of 1265 cm^{-1} (D⁻-band) at angular position $k_x = 0.0$. However, the D'-band is present at all angular position except $k_x = 0.3 k_0$. The observation of additional dispersive feature is caused by irregularities in the geometry of the nanoflowers [71]. The characteristic Raman features of SWNT, such as D-, G⁻-, and G-bands, present at all the longitudinal momentum measured in both linear antenna chains and nanoflower antenna. This result is consistent with the polarization measurement experiment, which explains the angular dependent of D-, G⁻-, and G-band because of characteristic peak of SWNT. However, other double-resonance (DR) peaks (D⁻, D⁺, D', M, and iTOLA) are not characteristic features of SWNT [1]. But these bands depend on the interaction between the object and the SWNT. The disorder bands vary from sample to sample due to the SWNT orientation towards the nanoflowers and also depend on excitation wavelength [77].

11.5 Summary and Future Aspect

In this chapter, we have reviewed the basics of Raman spectroscopy and SERS. Basic principal and optical resolution of confocal scanning optical microscope is discussed to explore its applicability for the characterization of nanomaterials. The structure of carbon nanotube and graphene has been reviewed to explore their electronic properties, phonon dispersion, and size, by Raman spectroscopy techniques. The Raman spectroscopy of carbon nanotubes enables the various information, such as structural assignment (n,m), diameter, electronic conductivity, and defect level in the samples. The Raman spectrum of graphene contains the information about the number of layers, type of edges, and defect level in the sample.

Linear chain of coupled Au antennas and Au nanoflowers has been applied to enhance the Raman scattering of SWNTs and to characterize the momentum sensitivity of the Raman bands. The in-plane mapping of momentum space generated by SERS of nanotubes reveals that the characteristic Raman bands of nanotube are uniformly distributed in momentum space using nanoantennas. DR bands appear at certain longitudinal momentum using localized SERS-active substrate such as nanoflowers.

Therefore, the Raman spectroscopy is a very powerful characterization tool to establish the basic theory of Raman scattering for zero-, one-, and two-dimensional materials, which can be applied to explore the new materials, such as boron nitride, MoS₂, and topological insulators.

Momentum angular mapping of enhanced Raman scattering explores the possibility to develop the experimental verification of selection rules of different Raman bands of molecules or nanostructures.

References

1. Dresselhaus, M. S., Dresselhaus, G., Saito, R., & Jorio, A. (2005). Raman spectroscopy of carbon nanotubes. *Physics Reports*, 409, 47.
2. Misra, A., Tyagi, P. K., Rai, P., & Misra, D. S. (2007). FTIR spectroscopy of multiwalled carbon nanotubes: A simple Approach to study the nitrogen doping. *Journal of Nanoscience and Nanotechnology*, 7, 1820.
3. Chen, G., Sumanshekera, G. U., Pradhan, B. K., Gupta, R., Eklund, P. C., Bronikowski, M. J., & Smalley, R. E. (2002). Raman-active modes of single-walled carbon nanotube derived from gas-phase decomposition of CO (HiPco process). *Journal of Nanoscience and Nanotechnology*, 2, 621.
4. Kumar, C. S. S. R. (2012). *Raman spectroscopy of nanomaterials characterization*. Berlin: Springer.
5. Ferraro, J. R., Nakamoto, K., & Brown, C. W. (2003). *Introductory Raman spectroscopy*. New York: Academic.

6. Rao, A. M., Richter, E., Bandow, S., Chase, B., Eklund, P. C., Williams, K. A., Fang, S., Subbaswamy, K. R., Menon, M., Thess, A., Smalley, R. E., Dresselhaus, G., & Dresselhaus, M. S. (1997). Diameter-selective Raman scattering from vibrational modes in carbon nanotubes. *Science*, 275, 187.
7. Ferrari, A. C., & Basko, D. M. (2013). Raman spectroscopy as a versatile tool for studying the properties of graphene. *Nature Nanotechnology*, 8, 235.
8. Raman spectroscopy: A simple, non-destructive way to characterize diamond and diamond-like materials. *Spectroscopy Europe*, 17, 10. (2005).
9. Kaufman, E. N. (2003). *Characterization of materials*. Hoboken, NJ: John Wiley & Sons, Inc.
10. Nie, S., & Emory, S. R. (1997). Probing single molecules and single nanoparticles by surface-enhanced Raman scattering. *Science*, 275, 1102.
11. Kneipp, K., Wang, Y., Kneipp, H., Perelman, L. T., Itzkan, I., Dasari, R. R., & Feld, M. S. (1997). Single molecule detection using surface-enhanced Raman scattering (SERS). *Physical Review Letters*, 78, 1667.
12. Zhu, W., Wang, D., & Crozier, K. B. (2012). Direct observation of beamed Raman scattering. *Nano Letters*, 12, 6235.
13. Chu, Y., Zhu, W., Wang, D., & Crozier, K. B. (2011). Beamed Raman: Directional excitation and emission enhancement in a plasmonic crystal double resonance SERS substrate. *Optics Express*, 19, 20054.
14. Ahmed, A., & Gordon, R. (2011). Directivity enhanced Raman spectroscopy using nanoantennas. *Nano Letters*, 11, 1800.
15. Rai, P., Singh, T., Brulé, T., Bouhelier, A., & Finot, E. (2017). Momentum angular mapping of enhanced Raman scattering of single-walled carbon nanotube. *Applied Physics Letters*, 111, 043104.
16. Novotny, L., & Hecht, B. (2006). *Principles of nano-optics*. Cambridge: Cambridge University Press.
17. Dresselhaus, M. S., Dresselhaus, G., & Avouris, P. (2001). *Springer series in topics in applied physics* (Vol. 80). Berlin: Springer.
18. Chen, G., Sumanasekera, G. U., Pradhan, B. K., Gupta, R., Eklund, P. C., Bronikowski, M. J., & Smalley, R. E. (2002). *Journal of Nanoscience and Nanotechnology*, 2, 621.
19. Hafner, J. H., Cheung, C. L., Oosterkamp, T. H., & Lieber, C. M. (2001). High yield fabrication of single-walled nanotube probe tips for atomic force microscopy. *The Journal of Physical Chemistry B*, 105, 743.
20. Hartmann, N., Piredda, G., Berthelot, J., Colas des Francs, G., Bouhelier, A., & Hartschuh, A. (2012). *Nano Letters*, 12, 177.
21. Rai, P., Hartmann, N., Berthelot, J., des Francs, G. C., Hartschuh, A., & Bouhelier, A. (2012). *Optics Letters*, 37, 4711.
22. Rai, P., Hartmann, N., Berthelot, J., Arocas, J., Colas des Francs, G., Hartschuh, A., & Bouhelier, A. (2013). *Physical Review Letters*, 111, 026804.
23. Novoselov, K. S., et al. (2004). *Science*, 306, 666.
24. Pandey, S., Rai, P., Patole, S., Gunes, F., Kwon, G.-D., Yoo, J.-B., Nikolaev, P., & Arepalli, S. (2012). *Applied Physics Letters*, 100, 043104.
25. Avouris, P., & Dimitrakopoulos, C. (2012). *Materialstoday*, 15, 86.
26. Saito, R., Dresselhaus, M. S., & Dresselhaus, G. (1998). *Physical properties of carbon nanotubes*. London: Imperial College Press.
27. Harris, P. J. F. (1999). *Carbon nanotubes and related materials: New materials for the twenty-first century*. Cambridge: Cambridge University Press.
28. Wallace, P. R. (1947). *Physics Review*, 71, 622.
29. Tans, S. J. (1998). Ph.D thesis, Delft University Press.
30. Dresselhaus, M. S., Dresselhaus, G., Jorio, A., Filho, A., & Saito, R. (2002). *Carbon*, 40, 2043.
31. Rao, A. M., Chen, J., Richter, E., Schlecht, U., Eklund, P. C., Haddon, R. C., Venkateswaran, U. D., Kwon, Y.-K., & Tomanek, D. (2001). *Physical Review Letters*, 86, 3895.
32. Jorio, A., Saito, R., Hafner, J. H., Lieber, C. M., Hunter, M., McClure, T., Dresselhaus, G., & Dresselhaus, M. S. (2001). *Physical Review Letters*, 86, 1118.

33. Jorio, A., Dresselhaus, G., Dresselhaus, M. S., Souza, M., Dantas, M. S. S., Pimenta, M. A., Rao, A. M., Saito, R., Liu, C., & Cheng, H. M. (2000). *Physical Review Letters*, 85, 2617.
34. Novoselov, K. S., et al. (2004). Electric field effect in atomically thin carbon films. *Science*, 306, 666.
35. Geim, A. K., & Novoselov, K. S. (2007). The rise of graphene. *Nature Materials*, 6, 183.
36. Charlier, J. C., Eklund, P. C., Zhu, J., & Ferrari, A. C. (2008). Electron and phonon properties of graphene: Their relationship with carbon nanotubes. *Topics in Applied Physics*, 111, 673.
37. Bonaccorso, F., Sun, Z., Hasan, T., & Ferrari, A. C. (2010). Graphene photonics and optoelectronics. *Nature Photonics*, 4, 611.
38. Bonaccorso, F., Lombardo, A., Hasan, T., Sun, Z., Colombo, L., & Ferrari, A. C. (2012). Production and processing of graphene and 2d crystals. *Materials Today*, 15, 564.
39. Lin, Y. M., et al. (2010). 100-GHz transistors from wafer-scale epitaxial graphene. *Science*, 327, 662.
40. Torrisi, F., et al. (2012). Inkjet-printed graphene electronics. *ACS Nano*, 6, 2992.
41. Sun, Z., et al. (2009). Graphene mode-locked ultrafast laser. *ACS Nano*, 4, 803.
42. Nemanich, R. J., Lucovsky, G., & Solin, S. A. (1977). Infrared active optical vibrations of graphite. *Solid State Communications*, 23, 117.
43. Reich, S., & Thomsen, C. (2004). Raman spectroscopy of graphite. *Philosophical Transactions of the Royal Society A*, 362, 2271.
44. Pocsik, I., Hundhausen, M., Koos, M., & Ley, L. (1998). Origin of the D peak in the Raman spectrum of microcrystalline graphite. *Journal of Non-Crystalline Solids*, 227–230, 1083–1086.
45. Maultzsch, J., Reich, S., Thomsen, C., Requardt, H., & Ordejon, P. (2004). Phonon dispersion in graphite. *Physical Review Letters*, 92, 075501.
46. Tuinstra, F., & Koenig, J. L. (1970). Raman spectrum of graphite. *The Journal of Chemical Physics*, 53, 1126.
47. Ferrari, A. C., & Robertson, J. (2000). Interpretation of Raman spectra of disordered and amorphous carbon. *Physical Review B*, 61, 14095.
48. Thomsen, C., & Reich, S. (2000). Double resonant Raman scattering in graphite. *Physical Review Letters*, 85, 5214.
49. Gruneis, A., et al. (2009). Phonon surface mapping of graphite: Disentangling quasi-degenerate phonon dispersions. *Physical Review B*, 80, 085423.
50. Ferrari, A. C., et al. (2006). Raman spectrum of graphene and graphene layers. *Physical Review Letters*, 97, 187401.
51. Basko, D. M., Piscanec, S., & Ferrari, A. C. (2009). Electron-electron interactions and doping dependence of the two-phonon Raman intensity in graphene. *Physical Review B*, 80, 165413.
52. Tan, P. H., et al. (2012). The shear mode of multilayer graphene. *Nature Materials*, 11, 294.
53. Lui, C., et al. (2012). Observation of layer-breathing mode vibrations in few-layer graphene through combination Raman scattering. *Nano Letters*, 12, 5539.
54. Lui, C. H., & Heinz, T. F. (2013). Measurement of layer breathing mode vibrations in few-layer graphene. *Physical Review B*, 87, 121404.
55. Sato, K., et al. (2011). Raman spectra of out-of-plane phonons in bilayer graphene. *Physical Review B*, 84, 035419.
56. Baranov, A. V., et al. (1987). Interpretation of certain characteristics in Raman spectra of graphite and glassy carbon. *Optics and Spectroscopy*, 62, 612.
57. Blackie, J. E., Le Ru, E. C., & Etchegoin, P. G. (2009). Single-molecule surface-enhanced Raman spectroscopy of nonresonant molecules. *Journal of the American Chemical Society*, 131, 14466.
58. Le Ru, E. C., et al. (2007). Surface enhanced Raman scattering enhancement factors: A comprehensive study. *The Journal of Physical Chemistry C*, 111, 13794.
59. Wang, D., et al. (2013). Directional Raman scattering from single molecules in the feed gaps of optical antennas. *Nano Letters*, 13, 2194.
60. Taminiau, T. H., Stefani, F. D., Segerink, F. B., & van Hulst, N. F. (2008). *Nature Photonics*, 2, 234.

61. Bohmler, M., Hartmann, N., Georgi, C., Hennrich, F., Green, A. A., Hersam, M. C., & Hartschuh, A. (2010). *Optics Express*, *18*, 16443.
62. Wang, D., Zhu, W., Best, M. D., Camden, J. P., & Crozier, K. B. (2013). *Nano Letters*, *13*, 2194.
63. Zhu, W., Wang, D., & Crozier, K. B. (2012). *Nano Letters*, *12*, 6235.
64. Heeg, S., Oikonomou, A., Fernandez-Garcia, R., Lehmann, C., Maier, S. A., Vijayaraghavan, A., & Reich, S. (2014). *Nano Letters*, *14*, 1762.
65. Kinkhabwala, A., Yu, Z., Fan, S., Avlasevich, Y., Mullen, K., & Moerner, W. E. (2009). *Nature Photonics*, *3*, 654.
66. Curto, A. G., Volpe, G., Taminiau, T. H., Kreuzer, M. P., Quidant, R., & van Hulst, N. F. (2010). *Science*, *329*, 930.
67. Le Ru, E. C., & Etchegoin, P. G. (2012). *Annual Review of Physical Chemistry*, *63*, 65.
68. Le Ru, E. C., & Etchegoin, P. G. (2006). *Chemical Physics Letters*, *423*, 63.
69. Kneipp, K., Wang, Y., Kneipp, H., Perelman, L. T., Itzkan, I., Dasari, R. R., & Feld, M. S. (1997). *Physical Review Letters*, *78*, 1667.
70. Nie, S., & Emory, S. R. (1997). *Science*, *275*, 1102.
71. Brule, T., Lelievre, H. Y., Bouhelier, A., Margueritat, J., Markey, L., Leray, A., Dereux, A., & Finot, E. (2014). *Journal of Physical Chemistry C*, *118*, 17975.
72. Chu, Y., Zhu, W., Wang, D., & Crozier, K. B. (2011). *Optics Express*, *19*, 20054.
73. Ahmed, A., & Gordon, R. (2011). *Nano Letters*, *11*, 1800.
74. Cañado, L. G., & Novotny, L. (2016). Observing the angular distribution of Raman scattered fields. *ACS Nano*, *10*, 1722.
75. Karaveli, S., Wang, S., Xiao, G., & Zia, R. (2013). *ACS Nano*, *7*, 7165.
76. Rao, A. M., Jorio, A., Pimenta, M. A., Dantas, M. S. S., Saito, R., Dresselhaus, G., & Dresselhaus, M. S. (2000). *Physical Review Letters*, *84*, 1820.
77. Chen, G., Sumanasekera, G. U., Pradhan, B. K., Gupta, R., Eklunf, P. C., Bronikowski, M. J., & Smalley, R. E. (2002). *Journal of Nanoscience and Nanotechnology*, *2*, 621.

Chapter 12

Photoelectron Spectroscopy: Fundamental Principles and Applications



Jagdish Kumar

12.1 Introduction

Spectroscopic techniques have played a vital role in understanding the internal structure of materials. The history of spectroscopy goes long back to sixteenth century when Sir Isaac Newton's experiments on light coined the term *spectrum* to refer to range of colours observed when white light was dispersed through prism [1]. In general, techniques of spectroscopy constitute the study of interaction of some radiations with matter and recording the response of matter. The techniques of spectroscopy have been a crucial platform in development of theory of quantum mechanics, whose roots lie in observations of phenomena such as black-body radiations, photoelectric effect and atomic spectra. A typical system in spectroscopy consists of some source of incident radiation, material under study (sample) and some detection system which measures outcome of interaction of radiation with matter.

The field of spectroscopy is classified according to various combinations of above-mentioned components. Based upon the type and frequency of incident radiation being used, different branches of spectroscopy are known as microwave spectroscopy [2], ultraviolet-visible spectroscopy [3, 4], infrared spectroscopy [5], X-ray [6] and gamma-ray spectroscopy [7]. The spectroscopic techniques also utilize particles as radiation source such as electrons/neutrons which utilize their de Broglie wavelength [8, 9]. Based upon nature of samples, spectroscopic techniques are known as *atomic spectroscopy* or *molecular spectroscopy* where interaction of radiation with atoms or molecules is studied. The atomic absorption and emission consists of electronic transitions in atoms and involves visible or ultraviolet

J. Kumar (✉)

Department of Physics and Astronomical Science, Central University of Himachal Pradesh,
Dharamshala, India

e-mail: jagdish@cuhimachal.ac.in

range of electromagnetic spectrum. The process of emission and absorption for a given element involves unique transitions among electronic states which lead to observation of *spectral lines*. The study of spectral lines has contributed a lot in understanding electronic structure of atoms and validation of quantum mechanical models of atoms and molecules. Similarly, in *molecular spectroscopy* in addition to electronic transitions, there are atomic vibrations or rotations which are studied under *infrared* and *Raman spectroscopy* [5].

Another classification of spectroscopic techniques can be based upon nature of interaction of radiation with matter. Some well-known branches of spectroscopy to study absorption spectrum of a material are *X-ray absorption spectroscopy (XAS)*, *X-ray absorption fine structure (XAFS)* and *X-ray absorption near-edge structure (XANES)* [10]. The study of emitted radiation or particles from a material comes under *emission spectroscopy*. Some of the emission spectroscopy techniques are *X-ray photoelectron spectroscopy (XPS)* [11], *atomic emission spectroscopy (AES)* [12] and *inductively coupled plasma-atomic emission spectroscopy (ICP-AES)* [13]. The emission spectroscopy can further be seen in terms of what is emitted as an outcome of radiation matter interaction. When electrons are emitted, the spectroscopic techniques are known as *photoelectron spectroscopy (PES)* and *Auger electron spectroscopy*.

Keeping in mind the vast area of spectroscopy, this chapter is dedicated to spectroscopic techniques based upon the study of emitted photoelectron from a material. Although there are many dedicated books and review articles on these techniques [11, 14, 18, 19], we aim to provide reader a concise overview of the technique and some applications to illustrate interpretation of results. The main objective of this chapter is to give intuitive understanding of the concepts and technology involved behind photoelectron-based spectroscopic techniques without employing much complexity. An exhaustive list of references has been provided at the end of this chapter for interested readers.

12.2 Overview of Photoelectron Spectroscopy (PES)

The origin of the wide range of properties observed in different materials lies in complex quantum mechanical behaviour being displayed by microscopic constituents at atomistic length scales. Most of the material phenomena such as magnetism, superconductivity, hardness, characteristic colour, piezoelectricity, thermoelectricity, conductivity, etc. are related to the energy changes in range from few milli-electron Volt (*meV*) to few electron volts (eV). Exciting a material with radiation sources in this energy range can reveal many secrets of the internal structure of the matter. The electrons in an atom can exist in quantized energy levels called *orbitals* and have spike-like density of states. When atoms combine together to form solid, the states of outer electrons merge together into closely spaced energy states called *energy bands*. The schematic energy level diagram of electrons in a solid is shown in Fig. 12.1. The photoelectron spectroscopy is

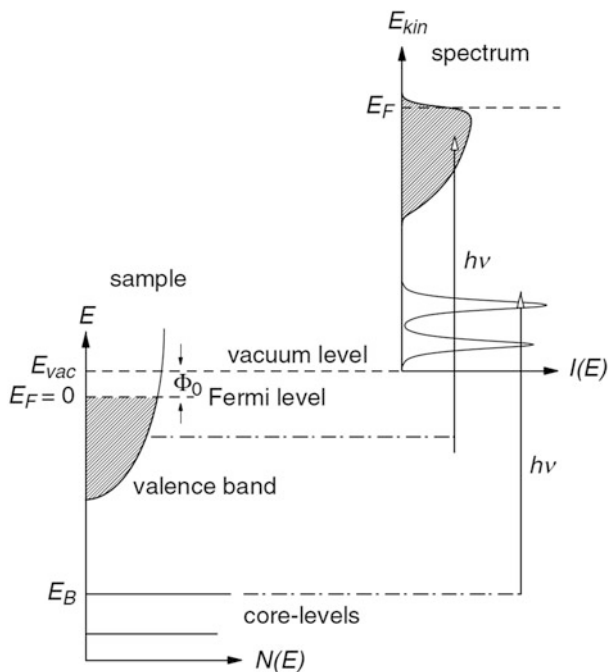


Fig. 12.1 Schematic energy level diagram for electrons in a solid [18]. [IOP Publishing Ltd and Deutsche Physikalische Gesellschaft]. (Reproduced by permission of IOP Publishing. Published under a CC BY-NC-SA licence (<http://creativecommons.org/licenses/by-nc-sa/3.0/>))

a technique which is based upon orbital picture of electrons in a material. This is although an approximation (independent electron approximation) for materials having more than one electron but works well for most of the cases [19].

When a material is illuminated with light of suitable frequency, the electrons from the occupied energy levels are ejected with some kinetic energy, and the phenomenon is known as *photoelectric effect*. The phenomenon of photoelectric effect is the basis of photoelectron-based spectroscopic (PES) techniques. Although the phenomenon of photoelectron ejection has been known for more than a century, its usage for spectroscopic techniques have come into practice from almost last 60 years [14]. The refined technologies for obtaining, processing and guiding monochromatic radiation beams have been key reason for usage of photoelectric effect for spectroscopic studies.

In photoelectron spectroscopy, a sample is illuminated with radiation of energy comparable to the energy required to remove electrons from energy states in the material. The study of ejected electrons provides the information of energy levels from where they have been ejected. When a radiation of frequency ν (greater than threshold frequency) falls on a material, the photoelectrons are ejected with some kinetic energy which is given by well-known Einstein equation:

$$E_{K.E.} = h\nu - h\nu_0 - \phi \quad (12.1)$$

where ν_0 is threshold frequency and ϕ is *work function* of the material. The threshold frequency for a particular electron depends upon the energy of orbital from where electron is ejected. Therefore, kinetic energy of the photoelectrons also depends upon the state from which they are ejected. In the simplest form, the probability of ejection of an electron from some state depends upon the number of electrons present in that energy state which is given by density of states corresponding to that energy. Therefore, measuring kinetic energy of photoelectrons provides the information of energy state from which they are ejected, and measure of number of electrons corresponding to some energy E provides the value of density of states $D(E)$. The work function is defined as the difference between the potential just outside the surface of the material (called vacuum state) and electrochemical potential (Fermi energy at 0K) of electron inside the material.

In general, the photoelectron current in a PES experiment is the function of multiple variables involving characteristics of incident photon and ejected electron. Incident photon is characterized by its energy ($E_{\text{ph}} = \omega$), polar (θ_{ph}) and azimuthal (φ_{ph}) angles to describe its direction, polarization of photon (p_{ph}). Similarly, the ejected electron also has some specific kinetic energy (E_{el}), polar (θ_{el}) and azimuthal (φ_{ph}) angles characterized by wavevector (k), and intrinsic property of spin (σ_{el}). Therefore, photoelectron current is a complicated function of these variables as given below:

$$I = F(E_{\text{ph}}, \theta_{\text{ph}}, \varphi_{\text{ph}}, p_{\text{ph}}; E_{\text{el}}, \theta_{\text{el}}, \varphi_{\text{el}}, p_{\text{el}}) \quad (12.2)$$

Different versions of photoelectron spectroscopic techniques use combination of different variables as varying parameters while keeping others fixed or integrating them out. For example, the technique known as energy-dispersive curve (EDC) measures intensity of photoelectrons (number of photoelectrons per unit area per unit time) as a function of energy and keeping all other parameters fixed. In the technique called angle-resolved photoelectron spectroscopy (ARPES), the angles θ_{el} , φ_{el} are resolved along with electronic energy. If spin of the electrons is also resolved, the technique is called spin-resolved photoelectron spectroscopy.

The schematic diagram of key components of a PES experiment is illustrated in Fig. 12.2. In a general photoelectron spectroscopy apparatus, the sample is illuminated by *radiation* of suitable energy which *ejects photoelectrons* giving rise to current (J_e) as given in Eq. (12.2). These ejected photoelectrons are guided with the help of *electron optics* into *electron energy analyser* which sorts the electrons as per their energy. The number of electrons with a specific energy is then detected with the help of *electron detectors* which converts the number of electrons into proportional photocurrent by using suitable electronics. One finally obtains photocurrent as a function of electron energy which provides information about interior energetics of the sample material.

The components of a photoelectron spectroscopy system are briefly described in the following subsections.

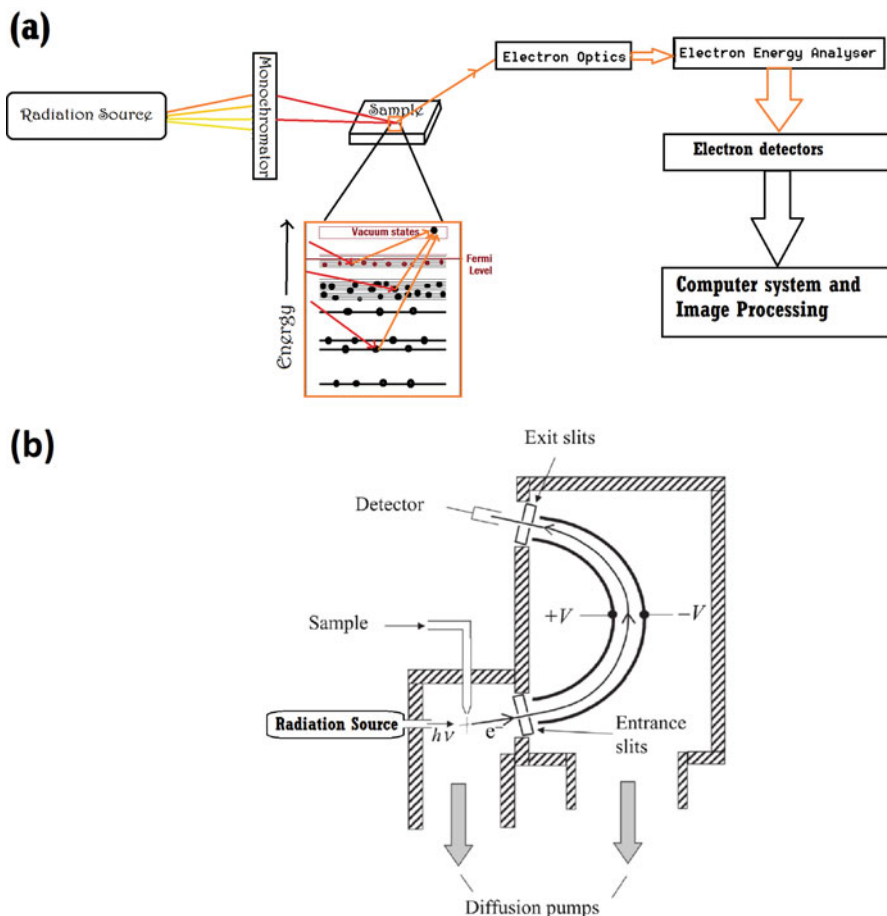


Fig. 12.2 (a) Block diagram and (b) schematic arrangement. ((Reproduced from [19] with permissions from Cambridge University Press) of components of a photoelectron spectroscopy system)

12.2.1 Radiation Sources

12.2.1.1 X-Rays

The nature of radiation source employed to perform photoelectron spectra depends upon the desired range of energy levels we want to study in a material. For example, to investigate the electron in core states having energies in keV range (typically 200–2000 eV), the source is X-rays (XPS). Some of the known sources of X-rays used are neon ($K\alpha = 848.6$ eV), Na ($K\alpha = 1040.9$ eV), magnesium ($Mg K\alpha = 1253.6$ eV), aluminium ($Al K\alpha = 1486.6$ eV) and copper ($Cu K\alpha = 8027.8$ eV) [15]. Mg $K\alpha$ and Al $K\alpha$ are most commonly used sources of X-rays in commercial XPS systems.

The energy of X-rays emitted from some source is the energy of transition of electron from higher to lower energy state. In above-mentioned cases, the given energy value is transition energy for electronic transition from L ($n = 2$) shell to innermost K ($n = 1$) shell. To obtain these transitions, the anode of element is bombarded with electrons coming from a cathode (electron source) which usually is a tungsten filament at high temperature. The electrons are accelerated to attain high energy by applying large external electric field between cathode and anode. When these high-energy electrons hit the target (anode), they can lose their energy mainly by two mechanisms. First they get retarded while approaching towards atomic nuclei of target and thus lose their energy by process known as *Bremsstrahlung radiation*. The second way they lose their energy is by the phenomenon called *X-ray fluorescence*. In X-ray fluorescence the high-energy electrons may eject some core electrons producing a vacant core state. This state then is filled with some electron from higher energy state resulting in emission of a photon with energy which is characteristic of the atoms of target. According to an empirical relation known as Moseley's law [16], the order of energy associated with $K\alpha$ transition for an element is:

$$E \cong 10.2(Z - 1)^2 \text{eV} \quad (12.3)$$

where Z is atomic number of an element.

12.2.1.2 Ultraviolet Radiation

To investigate the valence and conduction band states, the spectroscopy is known as ultraviolet photoelectron spectroscopy (UPS). The ultraviolet radiations can have energy between 3.10 and 124 eV. This energy range is perfect to investigate valence and conduction band electrons since their energy lies in same range. The ultraviolet radiation is further subdivided into different categories, namely, ultraviolet-A (UVA, 3.10–3.94 eV), ultraviolet-B (UVB, 3.94–4.43 eV), ultraviolet-C (UVC, 4.43–12.4 eV), middle ultraviolet (MUV, 4.13–6.20 eV) and vacuum ultraviolet (VUV, 6.20–124 eV) [17]. The main source of ultraviolet radiations in laboratories are gas discharge lamps, for example, helium ($\text{He-I}\alpha = 21.218 \text{ eV}$), ($\text{He-II}\alpha = 40.814 \text{ eV}$). The most commonly employed UV source in UPS experiments is He discharge lamps.

12.2.1.3 Synchrotron Radiation

Synchrotron is a cyclic particle accelerator and relativistic form of cyclotron. The charged particle having charge q in a synchrotron moves at relativistic speeds, and the magnetic field (\mathbf{B}) needs to be synchronized (hence name *synchrotron*) due to speed dependence of relativistic momentum according to the following equation of motion:

$$\frac{d}{dt} \left(\frac{mv}{\sqrt{1 - v^2/c^2}} \right) = q (\vec{v} \times \vec{B}) \quad (12.4)$$

Now since particle moving on circular path is accelerating and therefore should radiate energy at rate given by power which follows from relativistic Larmor's formula [20]:

$$P = \frac{2}{3} \frac{q^2 a^2}{c^3 \left(1 - v^2/c^2\right)^2} \quad (12.5)$$

where ' a ' is acceleration and v is velocity of particle. The intensity for spectrum of radiation emitted in synchrotron is given by [21]:

$$I(\nu) \propto \left\{ \begin{array}{l} (\nu/\nu_c)^{1/3} \text{ for } \nu \ll \nu_c \\ (\nu/\nu_c)^{1/2} e^{-\nu/\nu_c} \text{ for } \nu \gg \nu_c \end{array} \right\} \quad (12.6)$$

It can be obtained from the above formula that the peak of emission occurs at $0.29 \nu_c$ (where $\nu_c = \frac{3\gamma^2 eB}{2m_e c}$ is critical frequency) and decreases exponentially with increasing frequency. Practically a synchrotron can provide high-intensity radiation from few eV to few keV which is perfect for studies in photoelectron spectroscopy. From the spectrum being emitted from synchrotron, the radiation of desired wavelength may be selected with the help of monochromators (next section). However, due to limited availability and complexity, the synchrotron-based photoelectron systems are relatively expensive and are employed only in limited cases.

Other examples of radiation sources are argon and deuterium lamps, excimer lamp, ultraviolet LEDs and UV lasers, plasma and synchrotron sources. For obtaining good results, radiation source should have high intensity and narrow linewidth. In recent years, LASER-based methods for photoelectron spectroscopies have become popular and are much more sensitive to conventional photoelectron spectroscopic techniques [22].

12.2.2 Monochromators

The linewidth for radiation sources may be from few meV for discharge lamps and close to 1 eV for X-ray sources. This limits the precision of the measurements. *Monochromators* are employed to filter out undesired components from such source

and obtain nearly single wavelength (usually very narrow band of wavelengths) radiation. The name monochromators follows from Greek words, namely, *mono* (*single*) and *chroma* (*colour*). Although monochromators are employed in various areas such as optical imaging and spectroscopic devices, we shall mainly focus on ones used in photoelectron spectroscopy. *Dispersion* and *diffraction* are two main principles which can be employed to filter out undesired wavelengths from a spectrum and select a desired narrow band of wavelengths. Prism is the simplest example of monochromator based upon phenomenon of dispersion (employing wavelength dependence of refractive index of a material), which separates white light into spectrum of different colours at different angles. One can pick colour of desired wavelength from some specific angle.

The monochromators employed for X-rays are based upon diffraction phenomenon where X-rays of different wavelengths are directed on a crystal which produces diffraction pattern according to Bragg's law:

$$n\lambda = 2d \sin \theta \quad (12.7)$$

When X-rays having continuum of wavelengths are incident at same angle θ , only some specific wavelength will satisfy the condition for diffraction and can be obtained at a well-known angle as shown in Fig. 12.3. In this way we can filter out undesired components of wavelengths and select specific wavelength. Pyrolytic graphite (wide bandpass), silicon, germanium, quartz, LiF, InSb (narrow bandpass), etc. are few commonly used single crystals which are used as monochromators for X-rays. A crystal used in monochromator should be able to withstand X-ray intensity of incident beam and diffract high intensity of desired wavelength. A more interested reader may refer to this detailed article on X-ray monochromators [23].

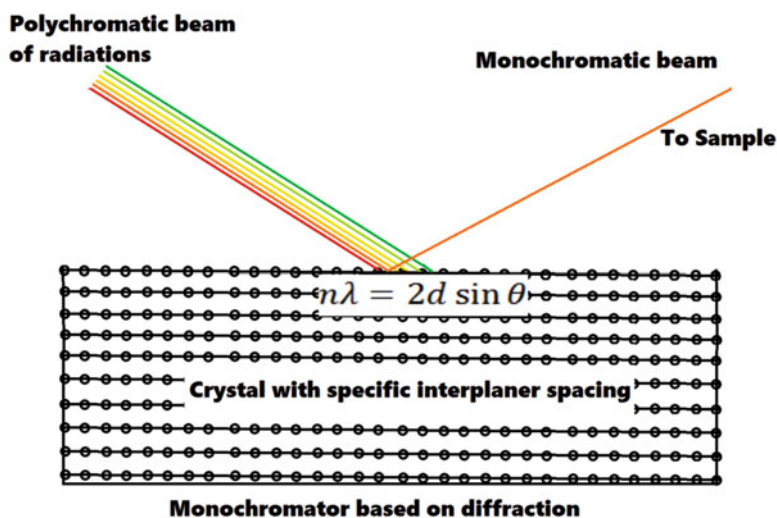


Fig. 12.3 Monochromator based upon diffraction (Colored online)

12.2.3 Electron Optics

The photoelectrons after getting ejected from the sample material are to be guided in a controlled way to reach electron energy analyser and then to electron detectors. Electron optics play crucial role in achieving this. Although the detailed description of electron optics is a vast field and has been presented nicely in a book by Grivet [24], we here shall restrict to basic ideas of electron optics. The electrons can be guided and focused by two types of mechanisms. Electric field, magnetic field or both can be used to apply force on an electron and thus can be used to guide and focus the electron beam. The mechanism to focus electron beam is called *electron lens*, and this acts in the same manner to guide electron beam in electron optics as the optical lenses act for beam of light waves. However, the two types of lenses are completely different in terms of their detailed mechanism used to produce lensing effect. Mainly, there are two mechanisms to produce lensing effect on electron beam. First is electrostatic lens (Einzel lens), which uses three consecutive apertures with outer ones being at ground potential and middle one at some potential which tend to pull the electrons towards optical axis. By varying potential of central plate, we can tune the lensing parameters.

In magnetic lens, the Lorentz force due to magnetic field is used to steer the electrons towards optical axis. A magnetic lens has copper wires (green circles in Fig. 12.4b) wound inside cylindrical shell (black solid lines) of some high permeability material (usually iron). For such arrangement the magnetic flux along optical axis is such that diverging electrons are forced towards from the optical axis (vertically downwards). The aberrations in electron lenses are far more pronounced than in optical lenses. The most critical aberrations are spherical aberration and chromatic aberration. The spherical aberration arises because outer region of lens has stronger force on electrons than inner zone which results into different focus

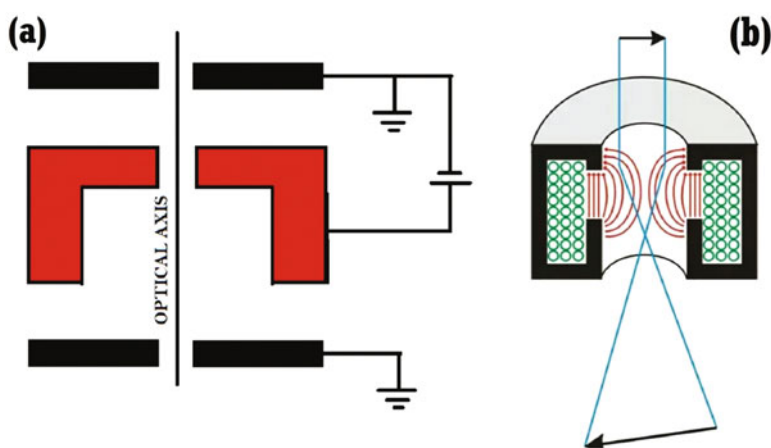


Fig. 12.4 Electron lensing mechanism (a) electrostatic Einzel lens [25] (b) magnetic lens [26]

points. The chromatic aberration arises due to broadening of electronic energies. Due to different energy values, the electrons get focused at different image planes. To overcome these aberration effects, the convergence angle is reduced which confine the electrons to the centre of the lens (i.e. towards optical axis). This, however, reduces the beam current, and one has to find optimization between beam current and convergence angle.

12.2.4 Electron Energy Analysers

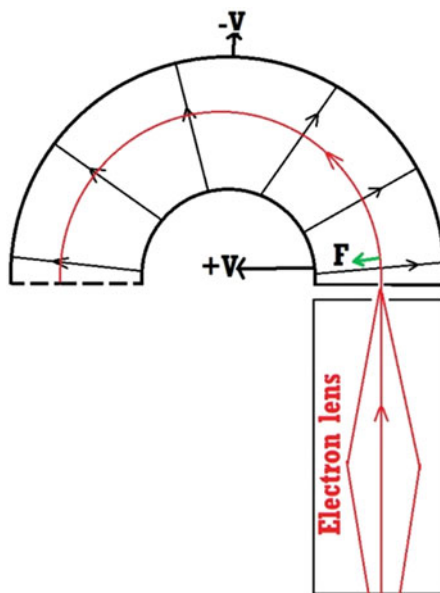
The basic purpose of the electron energy analyser is to sort the electrons with different kinetic energy according to their energy by employing electric or magnetic field. Based upon their basic principle, the electron energy analysers are broadly classified into two categories, namely, *retarding field analysers* and *deflection analysers*. The former are named so because they allow transmission of electrons with energy higher than their retarding potential [27]. In deflection-type analysers, the electrons with different kinetic energies (and hence velocities) are separated according to the path they follow based upon their velocities. There are different types of deflection analysers according to their physical geometry such as parallel plate analysers, cylindrical mirror analysers and hemispherical analyser. The hemispherical analysers are most commonly employed, and we shall restrict our discussion to this type of analysers. The hemispherical analysers consist of two concentric hemispherical electrode plates which are placed at equal and opposite potential with respect to entrance slit. The inner plate is kept at higher potential (+V) and outer plate at negative (-V). This sets up an electric field in the space between the plates in direction perpendicular to the plates and directed outwards (Fig. 12.5). Any electron entering the slit with velocity, \mathbf{v} (depending upon its kinetic energy), is acted upon by inward force given by $e\vec{E}$, where electric field \vec{E} depends upon the voltage applied ($\vec{E} = V\cdot\vec{d}$) to the plates. Due to this inward force, the electron path is changed from straight line and deflected as shown in Fig. 12.5.

For an electron to travel along circular path of radius r as shown in figure, the electric force should provide necessary centripetal force as given by the following condition:

$$\frac{mv^2}{r} = e\vec{E} \quad (12.8)$$

In case the velocity of electrons is either large or small, it will be over- or under-deflected by electric field and hence will not reach at exit slit. The voltage value on the hemispherical plates decides the energy of electrons that can pass through the slits and finally can be detected at the end. Assuming concentration of ejected

Fig. 12.5 Hemispherical electron energy analyser



electrons being small so that they behave like noninteracting free electrons and thus have only kinetic energy as given below¹:

$$\frac{1}{2}mv^2 = E \quad (12.9)$$

Substituting Eq. (12.9) in Eq. (12.8) and rearranging terms give:

$$\frac{E}{r} = e \vec{E}_r \quad (12.10)$$

The radial electrical field \vec{E}_r between two spherical shells kept at potential difference ΔV is given by [28]:

$$\vec{E}_r = \frac{ab}{(b-a)r^2} \Delta V \quad (12.11)$$

where b and a are radii of outer and inner sphere and r is radial distance of point of observation from the centre. Substituting this value of electrical field in Eq. (12.10) gives:

$$E = re \frac{ab}{(b-a)r^2} \Delta V \quad (12.12)$$

¹ E here refers to energy of the electron and \vec{E} to electric field between the hemispherical shells.

Equation (12.12) relates energy of electrons with dimensions of hemispherical analyser and applied voltage with energy of electrons that will be detected at the end. However, this expression cannot be used in a strict sense because the energy of the electrons is also affected by the presence of local charges on nearby surfaces around the path of the electron and also the contamination of inner walls of the spectrometer [19]. Because of this one is supposed to calibrate the obtained values of energy with samples of known energy spectrum.

A more practical formula for obtaining the energy of the electron is:

$$E = ek\Delta V \quad (12.13)$$

where k is called calibration constant and is given by 0.9375 [29].

To obtain the number of electrons with different energy values, full voltage scan is done, and the number of electrons detected at different voltage is measured. The electron lens is adjusted such that the energy of the electrons focusing at entrance slit of hemispherical analyser matches its pass energy. The combination of transfer lenses and hemispherical analyser can be operated into two different modes. The first mode is fixed analyser transmission (FAT) which is also known as constant analyser energy (CAE). In this mode the pass energy of analyser is kept fixed. The lens system retard the electron velocity so as to make their energy same as pass energy of the analyser. The second operation mode is called fixed retard ratio (FRR) also known as constant retard ratio (CRR). In CRR mode, the ratio of initial electron energy and analyser pass energy is kept constant. The resolution of detection system increases with increase in pass energy [29] as given below:

$$\Delta E = \frac{\Delta R}{R_{in} - R_{out}} E_{pass} \quad (12.14)$$

Therefore, by employing CRR mode, one can recover the low-intensity peaks at high energy. Moreover, at low energy, the resolution (accepted energy range) of detection system is limited, and thus high-intensity beam (which is not monochromatic) can be avoided to enter detection system. Key factors affecting energy resolution are diameter of analyser, pass energy and spread of X-ray spectrum. Localized charging of the sample may be another factor for broadening of lines.

12.2.5 *Electron Detectors*

Electron detectors are the devices used to detect electrons coming out from analyser. Since a single electron is very difficult to detect directly due to its small charge, therefore a huge amplification in electron number is required. This is usually achieved by employing two methods, namely, channel electron multiplier (CEM) or micro-channel plates (MCP). The CEMs also known as channeltrons are the detectors which are tube-shaped continuous electrode having high surface

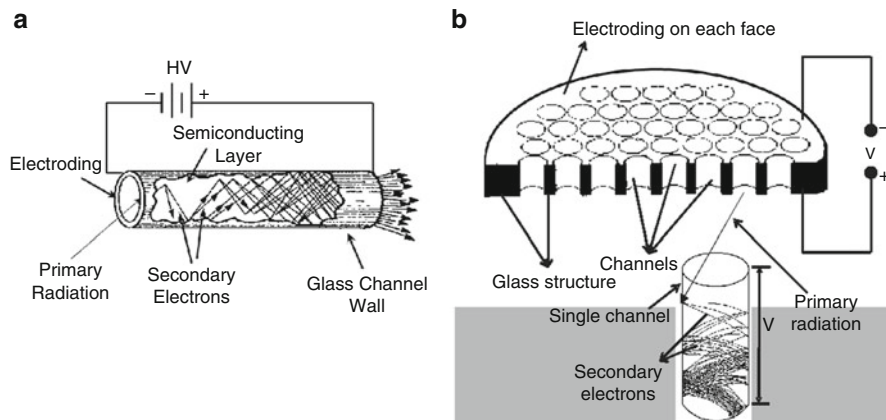


Fig. 12.6 (a) Channel electron multiplier (CEM) (b) micro-channel plates (MCP). (Taken from [30])

resistance. When potential is applied between input and output end, this behaves as a continuous electrode (dynode) and act as source of secondary electrons when some electron hits the inner surface. Those secondary electrons are further accelerated towards right end (as in Fig. 12.6) under influence of applied potential difference and strike on tube walls to produce further secondary electrons. In this way a large avalanche of electrons containing almost 10^8 electrons can be obtained within duration of almost 8 ns [30]. This corresponds to current of 2 mA which can easily be detected by employing suitable electronic circuit. A long straight channel may have unstable operation due to high electron density at the end of the channel which may cause ejection of ions whose movement in reverse direction can release further secondary electrons. To avoid this channels with curvature are used.

The second method to obtain electron gain is micro-channel plates (MCP) and is extremely useful for detecting single particles (Fig. 12.6b). The MCPs are actually an array of single channel multipliers, and this provides higher gain and good spatial and temporal resolution. The working principle of every channel is identical to channel electron multipliers as can be seen from Fig. 12.6b. Due to their multiple channels, they have the ability to resolve the position of the electrons and thus also known as position-sensitive detectors. The ion feedback may also be the challenging issue in MCPs which can be overcome by having a bias angle. The MCPs are used at the end of analyser in photoelectron spectroscopy experiment.

The electron flux obtained from electron multiplier tubes (MCPs) is hit on a phosphor plate which emits light in visible region which is recorded with the help of a charge-coupled device (CCD) camera. The CCD cameras are most commonly used nowadays specifically for research applications due to their high sensitivity for even low-intensity light signals and can produce high-resolution images [31].

12.2.6 Vacuum Chambers

The electrons must be able to travel the long path all the way from sample till detector. This needs that the electron should not have any scattering molecules on the way. The presence of air or other gas molecules/atoms may cause electrons to scatter and hence lose their path or energy. To avoid this it is required to have high vacuum throughout the sample and analyser chambers. The pressure of almost 10^{-5} [19] to 10^{-11} [29] millibar may be required and is achieved with the help of vacuum pumps. The area of vacuum technologies is vast, and many exclusive reports are available in literature [32, 33, 35, 36]. We shall here scan basic working principles of vacuum pumps. The vacuum pumps are broadly classified into the following main categories according to mechanism of their operation:

- Gas transfer vacuum pumps
- Entrapment vacuum pumps

The *gas transfer pumps* remove the gas particles from a chamber (to be vacuumed) by series of compression-expansion stages of pump/chamber volume (rotary pump, reciprocating positive displacement pumps) or by diffusion of gas molecules into gas-free high-speed vapour jet (diffusion-based pumps) or by lowering pressure in zone by employing a high-velocity fluid through a narrow Venturi nozzle (ejector pumps). The *entrapment vacuum pumps* employ different mechanism to take out the gas molecules out of chamber. In these pumps, the gas molecules are either condensed on some cold surface (cryopumps) or bonded by different means like chemisorption, absorption or adsorption (sorption pumps). Depending upon detailed mechanism of operation, the sorption pumps are classified into further categories as adsorption pumps (uses temperature-controlled adsorption) and getter pumps (gases form chemical compounds). These pumps are good for achieving ultra-high vacuum (UHV) and are used in series with other pumps. A complete systematic list of different types of vacuum pumps and their detailed working has been given in [36].

The vacuum region has been divided into four broad categories based upon pressure achieved as a result of pumping action. These are:

- *Rough vacuum* (atmospheric pressure to 1 mbar)
- *Medium vacuum* ($1-10^{-3}$ mbar)
- *High vacuum* ($10^{-3}-10^{-7}$ mbar)
- *Ultra-high vacuum* (lower than 10^{-7} mbar)

To attain ultra-high vacuum, one needs to use combination of pumps mentioned above in stages (Fig. 12.7). In stage 1, the rough vacuum is usually created with the help of positive displacement pumps such as rotary vane pumps. Once the rough vacuum is attained, then stage 2 is switched on, and after reaching medium vacuum, one goes for the next stage and so on. The roughing is mandatory step for attaining higher vacuum level, and depending upon desired vacuum and type of gases present in chamber, some stages shown in Fig. 12.7 may or may not be required. A detailed description of practical requirements as per various conditions has been presented in reference [36].

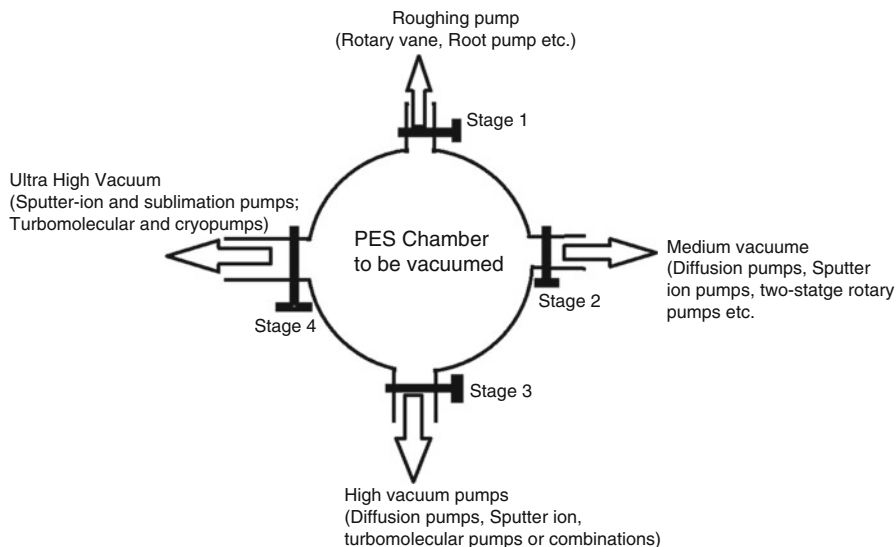


Fig. 12.7 Schematic diagram showing stage-wise usage of different vacuum pumps

12.3 Understanding Electronic States in Mono and Multiatomic Systems

From material science point of view, atoms are fundamental building block of any material. The crucial role of quantum mechanics for atomistic length scales is well accepted. The simplest model of atom by Bohr nicely demonstrates the quantization of atomic energy states and necessity of quantum numbers to describe those states. The quantum numbers act like address of the electron in an atom, molecule or material. When value of all the quantum numbers corresponding to an electron is defined, one can specify in which state electron is present. A detailed quantum mechanical description of atoms, molecules and solids requires one to solve well-known time-dependent Schrodinger equation as given below:

$$\hat{H}\Psi(x, t) = i\hbar \frac{\partial \Psi(x, t)}{\partial t} \quad (12.15)$$

where \hat{H} is Hamiltonian operator and for a multiatomic system is given by:

$$\hat{H} = \hat{H}_{k,N} + \hat{H}_{k,e} + \hat{H}_{p,N-N} + \hat{H}_{p,N-e} + \hat{H}_{p,e-e} \quad (12.16)$$

The terms on right-hand side of Eq. (12.16) are kinetic energy operator for nuclei, kinetic energy operator for electrons, nucleus-nucleus potential energy operator, nucleus-electron potential energy operator and electron-electron interaction energy operator, respectively. For obtaining the ground state electronic energy of a material,

one usually solves time-independent Schrodinger equation where right-hand side of Eq. (12.15) is energy times the wave function.

$$\hat{H}\Psi = E\Psi \quad (12.17)$$

Some simple cases have been discussed in the following sections.

12.3.1 Electronic States of Atoms

Although the quantum numbers appear while applying boundary to a particular problem when solving complex Schrodinger equation, these can be related to physical measurable properties of the system. Beginning with the simplest case, the electronic distribution in any atom is characterized by its electronic configuration which is based upon well-known *Aufbau principle*. Based upon Aufbau principle, one describes the electronic configuration of different elements in periodic table. For example, aluminium has electronic configuration $1s^2 2s^2 2p^6 3s^2 3p^1$. However, this simple description of electronic distribution has limited validity because Aufbau principle rests upon orbital approximation and assumes that energy of the orbitals remain unchanged irrespective of neighbouring orbitals. However, this is an approximation, and in actual practice, most atoms have more than one electron and do not have *one-electron solutions*, i.e. orbitals. They are represented by many-electron solutions such as Slater determinant used in Hartree-Fock approximation. Nonetheless, the orbital approximation is quite simple and powerful way to describe the state of electrons in an atom or solids. The quantum numbers are employed for describing an orbital in which electron is present. These are *principal quantum number* (n), *angular momentum quantum number* (l), *orbital magnetic quantum number* (m_l), *spin angular momentum quantum number* (s) and *spin magnetic moment quantum number* (m_s). The quantum numbers characterize state of an electron as given below. Principal quantum number refers to the main shell in which electron is present with values of n from 1, 2, 3, 4,..... corresponding to $K, L, M, N,.....$ shells, respectively. According to value of n , the average distance from nucleus and energy of electron increases. The outermost fully/partially occupied shells are called valence shells and play crucial role in determining physical and chemical properties of an atom. For a particular shell, the angular momentum quantum number l can assume any value between 0 and $n-1$ in integral steps and corresponds to subshell $s, p, d, f,...$ according to l being 0, 1, 2, 3,....., respectively. The value of l decides the magnitude of orbital angular momentum possessed by electron and is given by $\hbar\sqrt{l(l+1)}$. The magnetic moment quantum number m_l can assume $2l+1$ possible values from $-l$ to $+l$ in integral steps. The total angular momentum cannot align totally along z -direction due to uncertainty principle and thus the z -component of orbital angular momentum can assume integral values from $-m_l\hbar$ to $+m_l\hbar$. The direction of z -axis is arbitrary in free space, and in case of the interaction of particle moments with electric or magnetic field, the direction of field is considered as

z -axis also known as *axis of quantization*. The value of m_l also describes the spatial distribution of particular orbital (e.g. p_x , p_y , p_z , etc.). The magnetic moment ($\vec{\mu}$) and angular momentum (\vec{L}) for an electron are related by:

$$\vec{\mu} = -g \frac{e}{2m} \vec{L} \quad (12.18)$$

where value of ‘ g ’ for orbital case is 1 and for spin case is close to 2. According to Eq. (12.18), the orbital magnetic moment of the electron has *magnitude*:

$$\mu_l = \frac{e}{2m} \hbar \sqrt{l(l+1)} = \sqrt{l(l+1)} \mu_B \quad (12.19)$$

where $\mu_B = -\frac{e\hbar}{2m}$ is called Bohr magneton and is used as fundamental unit for describing magnetic moments of atoms and electrons. The z -component of orbital magnetic moment of an electron can assume values from $-m_l$ to $+m_l$ in integral steps.

The spin angular momentum quantum number (s) is related to intrinsic spin associated with the electron and can assume value $\frac{1}{2}$ for single-electron case. The absolute magnitude of spin angular momentum of an electron is given by $\hbar\sqrt{s(s+1)}$. The spin magnetic moment quantum number m_s can assume values $\pm\frac{1}{2}$ and thus electron is said to have two possible spin configurations *up* and *down*. The z -component of spin angular momentum of electron can take values $\pm\frac{1}{2}\hbar$, and spin magnetic moment can be either $+\mu_B$ or $-\mu_B$ (see Eq. (12.18)).

The situation discussed above refers to the case when spin and orbital angular momenta do not interact which is not the case practically. The interaction of spin and orbital angular momentum leads to coupling of angular momenta and to describe the actual experimental state of an atom; the total angular momentum quantum number j can assume values $l + s$, to $l - s$. For single-electron systems, j is $l \pm \frac{1}{2}$. The magnitude of total angular momentum is given by $\hbar\sqrt{j(j+1)}$. The z -component of total angular momentum can be $m_j\hbar$, where $m_j = -j, -j + 1, -j + 2, \dots, j - 1, j$.

The total magnetic moment of an atom is still given by Eq. (12.18) with g being replaced by g_L called Lende’s g factor, and it is given below [37]:

$$g_j = 1 + \frac{j(j+1) + s(s+1) - l(l+1)}{2j(j+1)} \quad (12.20)$$

12.3.1.1 Atomic States

As mentioned above, the electronic configuration describes the way electrons are distributed in an atom according to orbital approximation. However, in real atoms the orbital approximation breaks due to different interactions present in system. To take care of interactions without discarding the orbital approximation

completely, different approaches are followed. For example the electronic spin-spin, orbit-orbit or spin-orbit interaction may be important. Another case is electron-electron interaction which can be taken care in some average way like Hartree approximation where electron in many-electron system is supposed to interact with a mean Coulomb field of other electrons. Hartree-Fock approximation is another example where electrons are supposed to move independent of each other (orbital approximation) however, via Coulomb and exchange interactions. Considering the case of single atom, the spin angular momentum of the electron in an atom can interact with its own orbital angular momentum, spin angular momentum of other electrons and with orbital angular momentum of other electrons. The interaction of electron spin angular momentum with orbital angular momentum of other electrons is weak and can be neglected in most cases. The first two interactions refer to spin-orbit interaction and are considered using two well-known spin-orbital coupling schemes, namely, L - S coupling (also known as Russell-Saunders) or j - j coupling. The L - S coupling scheme is followed by the lighter atoms ($Z \leq 30$) where the electrostatic interaction among electrons is stronger than magnetism driven spin-orbit interaction for individual electrons. This leads to separate coupling of orbital angular momentum (orbit-orbit interaction) leading to $L = \sum_i l_i$ and spin angular momentum (spin-spin interaction) resulting $S = \sum_i s_i$. The total angular momentum quantum number L for a two-electron system having angular momentum l_1, l_2 can assume values from $l_1 + l_2, l_1 + l_2 - 1, l_1 + l_2 - 2, \dots, |l_1 - l_2|$. The resultant total angular momentum (L) and total spin angular momentum (S) also interact among themselves (spin-orbit coupling) leading to total angular momentum given by $J = L + S$. Due to L - S coupling among the electrons in atom, the resulting electronic states in an atom are represented by quantum number L, S and J by popular Russell-Saunders notations $^{2S+1}L_J$. The superscript $2S + 1$ is called *multiplicity*; resultant value of L is represented by symbols S, P, D, F,.... which correspond to $L = 0, 1, 2, 3, \dots$, and subscript J refers to total angular momentum quantum number. The possible values of total angular momentum quantum number are $L + S, L + S - 1, L + S - 2, \dots, |L - S|$. The Russell-Saunders notations are not unique to a particular atom and thus electronic configuration which results into particular R-S notation should be mentioned. While obtaining the *ground state* of atom, Hund's rules [38] are to be followed which are as follows:

1. *The total spin S of the electrons present in a shell should have maximum value as allowed by Pauli's exclusion principle.*
2. *The orbital angular momentum L should have maximum value consistent with condition 1 above.*
3. *The total angular momentum J is $|L - S|$ when a shell is less than half-filled and is $L + S$ when shell is more than half-filled. When the shell is exactly half-filled, the total angular momentum L is 0 and thus $J = S$.*

Some examples to illustrate the atomic states and R-S notations are shown in Table 12.1.

Table 12.1 Atomic states for elements in different configurations as per L-S coupling. Refer to selection rules and check for allowed and forbidden excited states mentioned below

Atom/ion	Configuration	l_1	l_2	l_3	L	s_1	s_2	s_3	S	$J= L-S $ $ L+S ^a$	Lowest energy state $2s+^1L_J$	Excited states
H	$1s^1$	0	-	-	0	$\frac{1}{2}$	-	-	$\frac{1}{2}$	$\frac{1}{2}$	$^2S_{1/2}$	$^2^2S_{1/2}, ^2^2P_{3/2}, ^2^2P_{1/2}, ^3^2S_{1/2}$, etc.
He	$1s^2$	0	0	-	0	$\frac{1}{2}$	$-\frac{1}{2}$	-	0^b	0	1S_0	$^3S_1, ^1P_1, ^3P_0, ^3P_1, ^3P_2$, etc.
He (excited)	$1s^1, 2s^1$	0	0	-	0	$\frac{1}{2}$	$\frac{1}{2}$	-	1	1	3S_1	$^1P_1, ^3P_0, ^3P_1, ^3P_2$, etc.
He (excited)	$1s^1, 2p^1$	0	1	-	1	$\frac{1}{2}$	$\frac{1}{2}$	-	1	2, 1, 0	3P_0	$^1P_1, ^3P_2, ^3P_1$, etc.
Be	$[He]2s^2$	0	0	-	0	$\frac{1}{2}$	$-\frac{1}{2}$	-	0	0	1S_0	$^3S_1, ^1P_1, ^3P_0, ^3P_1, ^3P_2$, etc.
B	$[He]2s^2, 2p^1$	0	0	1	1	$\frac{1}{2}$	$-\frac{1}{2}$	$\frac{1}{2}$	$\frac{1}{2}$	$\frac{3}{2}, \frac{1}{2}$	$^2P_{1/2}$	$^2P_{3/2}, ^4D_{7/2}, ^4F_{9/2}$, etc.
B (excited)	$[He]2s^1, 2p^2$	0	1	0	1	$\frac{1}{2}$	$\frac{1}{2}$	$\frac{1}{2}$	$\frac{3}{2}$	$\frac{5}{2}, \frac{3}{2}, \frac{1}{2}$	$^4P_{1/2}$	$^4P_{3/2}, ^4P_{5/2}, ^4D_{5/2}, ^4F_{9/2}$, etc.
Si	$[Ne]3s^2, 3p^2$	0(3s²)	1	0	1	0	$\frac{1}{2}$	$\frac{1}{2}$	1	2, 1, 0	3P_0	$^3P_1, ^3P_2$, etc.

(continued)

Table 12.1 (continued)

Atom/ion	Configuration	l_1	l_2	l_3	L	s_1	s_2	s_3	S	$J = L - S $	Lowest energy state	Excited states
Si (excited)	[Ne]3s ¹ , 3p ³	0	1	0-1 ^c	0 ($l_4 = 1$)	$\frac{1}{2}$	$\frac{1}{2}$	$\frac{1}{2}, \left(s_5 = \frac{1}{2}\right)$	2	$\frac{2}{2}$	5S ₂	
V	[Ar]3d ³ , 4s ²	2	1	0	3 ^d	$\frac{1}{2}$	$\frac{1}{2}$	$\frac{1}{2}$	$\frac{3}{2}$	$\frac{9}{2}, \frac{7}{2}, \frac{5}{2}, \frac{3}{2}$	4F _{3/2}	4F _{5/2} , 4F _{7/2} , 4F _{9/2} , etc.
Fe ³⁺	[Ar]3d ⁵	2, ($l_4 = -2$)	1, ($l_5 = -1$)	0	0	$\frac{1}{2}, \left(s_4 = \frac{1}{2}\right)$	$\frac{1}{2}, \left(s_5 = \frac{1}{2}\right)$	$\frac{1}{2}$	$\frac{5}{2}$	$\frac{5}{2}$	6S _{5/2}	States corresponding to other configurations
Co ²⁺	[Ar]3d ⁷	-2	-1	0	3	$\frac{1}{2}$	$\frac{1}{2}$	$\frac{1}{2}, -\frac{1}{2}$	$\frac{3}{2}$	$\frac{9}{2}, \frac{7}{2}, \frac{5}{2}, \frac{3}{2}$	4F _{9/2}	4F _{7/2} , 4F _{5/2} , 4F _{3/2} , etc.
		2 × 1	1 × 1			$\frac{1}{2}$	$\frac{1}{2}$					

^aThe underlined value of L , S and J corresponds to the lowest energy state as per Hund's rules

^bRefer to Hund's rules. The total spin S should be highest but consistent with Pauli's exclusion principle. For ground state of He, the two electrons cannot have parallel spins. Therefore $S = s_1 - s_2$

^c l_4, s_4

^d4s² has been ignored as they don't contribute

12.3.1.2 Selection Rules

The selection rules govern excitations of atom among various energy levels and are helpful in understanding the spectral lines as a result of transitions between these energy levels. For most of the cases, the transitions involve possibility of excitation of electron across different energy levels.

Transitions Among Electronic States

The orbital angular momentum quantum number must change by unity, i.e. $\Delta l \pm 1$. This is known as *Laporte selection rule* [39] which in general states that ‘The electronic transitions for atoms and centrosymmetric molecules only those transitions are allowed for which $\Delta l = \pm 1$ ’. That is why one should not expect the electronic transitions in an atom within particular subshell (say transition of electron from one *p/d* orbital to another *p/d*) or transition from any *s*-orbital to *d*-orbital.

Role of Coupling

L-S coupling

Due to coupling among the electronic states, the selection rules are redefined to accommodate additional constraints due to interaction. The selection rules for transitions among atomic states are as follows:

$$\Delta S = 0, \Delta L = 0, \pm 1, \Delta J = 0, \pm 1 (J = 0 \text{ to } J = 0 \text{ transitions not allowed}), \\ \Delta M_j = 0, \pm 1 (M_j = 0 \text{ to } M_j = 0 \text{ transitions not allowed}).$$

j-j coupling

In case the spin-orbit coupling among the individual electrons is stronger, they possess *j-j* coupling. The selection rules for transitions in this case are:

$$\Delta S = 0, \pm 1, \Delta l = 0, \pm 1, \Delta j = 0, \pm 1 \text{ (for electron undergoing transition)}, \\ \Delta j = 0, \pm 1 \text{ (for other electrons)} \Delta J = 0, \pm 1 (J = 0 \text{ to } J = 0 \text{ transitions not allowed}), \\ \Delta M_j = 0, \pm 1 (M_j = 0 \text{ to } M_j = 0 \text{ transitions not allowed}).$$

12.3.2 Electronic States of Solids

When atoms come together to form solid, the core atomic states remain almost unaffected, and states of valence electrons are affected the most. Therefore, the core electrons can be seen almost as if they are sitting in a free atom. The valence orbitals lead to band formation, and the energy states occupied by electron in solid are significantly redistributed. We shall limit our focus here to the crystalline solids only. The readers interested in molecules can refer to reference [19]. One of the most interesting features of crystalline solids is space periodicity. This periodicity enables one to write whole crystal in terms of a unit cell which when repeated in three dimensions can produce the whole crystal. It is due to this periodicity that apart from the mentioned quantum numbers for an atom, an additional quantum number called *wavevector* k enters in description of electron in periodic solid. As a simplest

example, consider case of free electron gas, which is limiting case of electrons in solids (best suited for metals). The electron is represented by plane wave $e^{ik \cdot r}$, where k is the wavevector. The energy of electrons in a solid is not only dependent upon n , l and m , but additional dependence on k also comes into play due to periodic nature of crystalline materials. This dependence of energy of an electron as a function of its wavevector is known as *band structure* of a material. For the simplest case of free electron gas, this dependence is given by $E(k) = \frac{\hbar^2 k^2}{2m}$. For a general case, the band structure can be complicated. There are two important characterizing measurable properties that can describe the valence electrons in bands:

12.3.2.1 Electronic Density of States

The electronic density of states (DOS) is the measure of number of electronic states available per unit energy range per unit volume. The density of states is described as function of energy $D(E)$ and measures the available states for electron at a particular energy value. The highest energy for which an electronic state is occupied at 0 K is known as *Fermi energy*. The electronic density of states provides many important clues about behaviour of a material. For example, when there is non-zero DOS at Fermi energy, the material will behave as metal, and when the DOS is zero at and around Fermi energy, the material will behave as semiconductor or insulator depending upon the gap over which DOS is zero. One may also predict about magnetic nature of material by looking at spin dependence of its DOS. When the DOS for spin-up and spin-down states are not the same over the whole energy range, the material will exhibit magnetic character.

12.3.2.2 Electronic Band Structure

The electronic band structure of a material describes the variation of energy of electron in material with its wavevector. The band structure gives the detailed information of energy states of the electron in Brillouin zone of a material. In principal, the band structure of a 3D material is a 4D diagram where three dimensions refer to the components of wavevector (k_x, k_y, k_z) and fourth dimension represents energy. However, it is difficult to visualize such 4D information and thus plot of energy as function of wavevector is plotted along certain desired directions along Brillouin zone. The electronic density of states at a particular energy value $D(E)$ is the total count of all the states in energy sphere between E and $E + dE$ in Brillouin zone. Figure 12.8 shows the electronic density of states, $D(E)$, and band structure of aluminium crystal in FCC structure calculated using *density functional theory* [40] which is one of the most popular approaches to theoretically calculate the electronic structure of a material.

The energy values are mentioned relative to *Fermi energy*. It can be seen that the states well below Fermi energy (below 20 eV) have almost no variation with

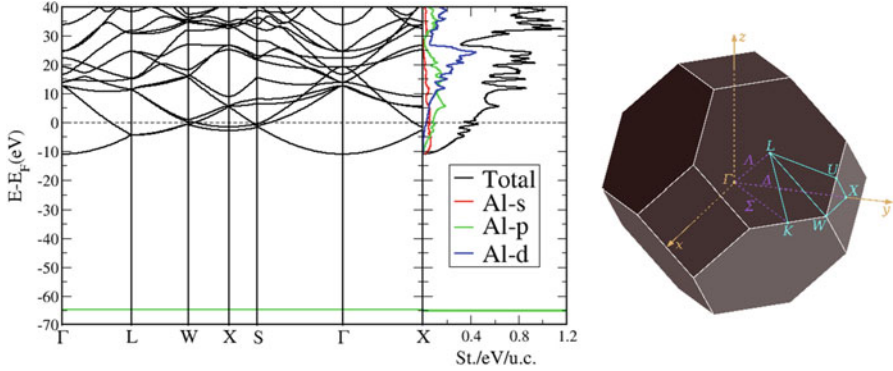


Fig. 12.8 Electronic density of states and band structure of *face centre cubic* (FCC) aluminium using density functional theory based on full-potential linearized augmented plane wave (FP-LAPW) method as implemented in ELK code [101]. The x -axis in band structure represents path along various directions in Brillouin zone (right most image [41]) of primitive cell of FCC lattice. Right portion of band structure figure shows electronic density of states which is the sum of all the states in Brillouin zone at a particular energy value

wavevector and are localized at almost a sharp energy value. This indicates that the deeply lying valence and core states are least affected because of bonding of atoms in crystal. It can be observed in band structure as well as in DOS plots. The electronic DOS for an individual atom consists of sharp spike-like peaks at the energy values equal to eigen-energy of electrons. The height of the peaks can be related to number of electrons present at that energy level. The number of electrons present between energy E_1 and E_2 at 0 K is given by:

$$N = \int_{E_1}^{E_2} D(E) dE \quad (12.21)$$

And the same expression for any finite temperature is given by:

$$N = \int_{E_1}^{E_2} D(E) f(E) dE \quad (12.22)$$

where $f(E)$ is a well-known Fermi-Dirac distribution function and is defined by:

$$f(E) = \frac{1}{1 + e^{\frac{E - E_F}{kT}}} \quad (12.23)$$

The total energy of all the electrons is given by:

$$E = \int_0^{\infty} D(E)E f(E) dE \quad (12.24)$$

The experimental technique to directly measure electronic density of states is X-ray (XPS for core and deep valence band) or ultraviolet (UPS for valence band states) photoelectron spectroscopy. The electronic band structure is measured via *angle-resolved photoelectron spectroscopy* (ARPES) techniques as discussed in the next sections. If one can also resolve the spin of the electron, the technique of photoelectron spectroscopy becomes much more informative specifically for magnetic systems. This technique is known as spin-resolved photoelectron spectroscopy. This technique has been discussed in Sect. 12.6.

12.4 Core Level Spectroscopy: X-Ray Photoelectron Spectroscopy (XPS)

The energy associated with X-rays ranges from few hundreds to few thousands electron volts. This range of energy belongs to core electrons of an atom, and therefore XPS is a tool to study deeply lying core states of atoms in solids. When X-rays of particular energy fall on a sample, the electrons can be ejected from any of the electronic states and shall possess kinetic energy as given by Eq. (12.1). The electrons sitting in valence states have higher energies (low-binding energy) and therefore possess the highest kinetic energy. On the other hand, the electrons sitting in deeply lying core states have very low energy (high-binding energy) which require large part of energy from incident X-rays to take electron out from material, and thus those electrons possess low kinetic energy. Therefore on the basis of kinetic energy of electrons being ejected from a material, one can obtain the value of binding energy (and hence energy of eigen state) of the electron by utilizing Eq. (12.1) as described below:

$$E_{B.E.} = h\nu - K.E. \quad (12.25)$$

The electronic states are characterized according to quantum numbers and corresponding notation of the subshell (as described in Table 12.1) in which electrons are present. In practice, one has to incorporate the work function of spectrometer Φ_{spec} which gives binding energy of electron as $E_{B.E.} = h\nu - K.E. - \Phi_{\text{spec}}$.

There are three main components of XPS data of any material:

- Intensity of peaks at binding energy of the electrons ejected from particular energy levels of an element
- Position of the peaks on energy axis
- Width/splitting of the peaks

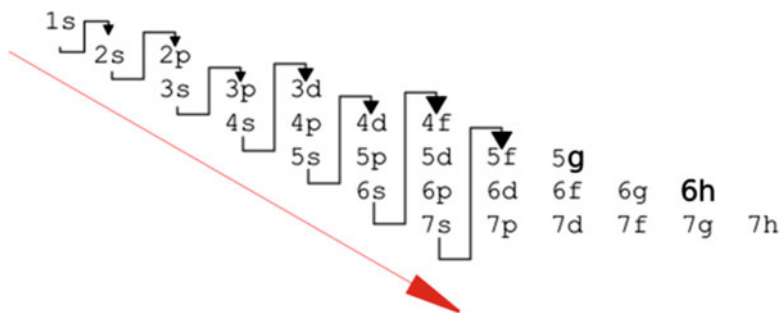


Fig. 12.9 Madelung rule for energy atomic orbitals [43]

By carefully analysing the above aspects of XPS data, one can tell about constituent elements, their percentage, nature of bonding and other interactions such as spin-orbit splitting.

The energy of electronic states² for the simplest case of hydrogen atom depends only on principal quantum number (n), and the electronic densities of states are well-defined lines at particular energy value as illustrated in Fig. 12.10a for the first few shells. The degeneracy of a particular energy level is $2n^2$ which means that each state can accommodate $2n^2$ electrons. The binding energy of the electron in the lowest energy state is 13.6 eV. As the atomic number increases, more and more charge is added to nucleus, and the number of electrons in atomic shells also increases. Due to raised nuclear charge, the attractive pull on electrons increases, and this raises their binding energy which can eventually reach few hundreds keV for heavy atoms. The presence of multiple electrons in the atomic shells adds more interactions such as electron-electron interaction and complex quantum mechanical interactions like exchange and correlation effects. Due to all such effects, the degeneracy of energy levels of atomic shells break, and the electronic shells split into subshells having different energies. On the basis of atomic spectra, Madelung in 1936 proposed an empirical rule to place the atomic orbitals according to rising energy as follows in Fig. 12.9. This is also known as Klechkowski rule which formally reads as follows:

- The orbitals having lower value of $n + l$ have lower energy.
- In case $n + l$ is same for any two orbitals, the orbitals having lower n have lower energy.

On the basis of the above rule, the atomic energy levels look as illustrated in Fig. 12.10b. The energy subshells may split further due to various interactions such as spin-orbit interaction, crystal field splitting, etc. The same has been illustrated for 3d subshells in inset of Fig. 12.10b. All such splitting can be measured experimentally using XPS experiments.

² $E_n = -\frac{13.6}{n^2}$.

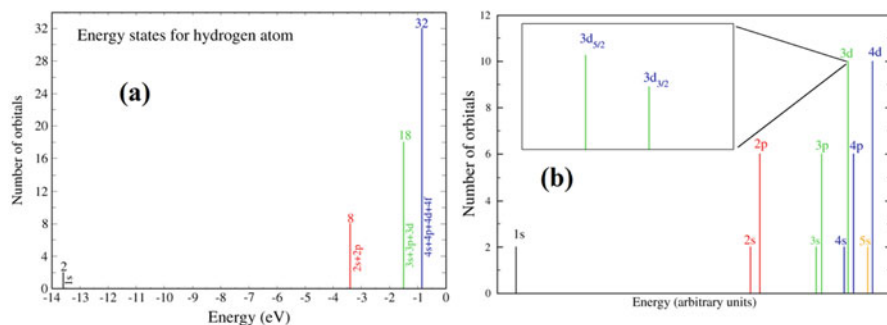


Fig. 12.10 Schematic representation of energy levels and degeneracy of (a) hydrogen atom and (b) any arbitrary atom. Inset of (b) shows splitting of electronic states due to interactions such as spin-orbit interaction or crystal field splitting

Whenever atoms come close, to form solids or molecules, the electrons in valence shells are redistributed significantly, and their energies are affected the most. The effect of atomic bonding is least on core electrons, and this idea is useful to detect the presence of a particular element in a material. For example, the presence of adventitious carbon can be found in almost any sample as the samples are exposed to atmosphere. This acts as a useful reference for XPS spectra of any material.

The binding energy peak of C-1s states can be found around 286 eV and can shift depending upon nature of contamination in samples. The common cases of contamination contain carbon in forms, C-O-C (286 eV), C-C (284.8 eV) or O-C=O (288.5 eV) [42]. The C-1s peak shifts towards higher energy if the carbon atom is bonded to a more electronegative atom. The C-1s peak for CF₂ is found at 292 eV and for CF₃ is found at 294 eV [42]. This is clearly evident from the fact that when outer electrons of carbon are attracted away from carbon by other species, the inner electrons are bound more strongly and hence rise in binding energy is observed. Therefore, the shifting of peak of core electrons gives the information about valence state of the atom. The electronic states broaden in energy due to different interactions, resolution of photoelectron spectrometer (a technical problem), presence of satellite peaks and intrinsic lifetime of core holes [11].

In crystalline solids, the valence electronic states of the atoms split in such a way that a continuum of energy levels is obtained around the atomic energy states and is known as energy bands. This has been illustrated schematically in Fig. 12.1 for a general case and in Fig. 12.8 for FCC aluminium. In Fig. 12.8, a horizontal line near -63 eV refers to core 2p-states of aluminium. The continuum of states around zero (Fermi energy) corresponds to bands formed due to bonding of valence 3s and 3p states. The integration of electronic density of states with respect to energy over a given energy range gives total number of the electrons (Eq. 12.22). The number of electrons coming out from states corresponding to a particular binding energy in XPS spectra depends upon the number of electrons present in corresponding energy level. The higher the number of electrons in a particular subshell, the intense will

be the peak at binding energy corresponding to that energy state. Moreover, due to atomic bonding and other interactions, the atomic energy states broaden, and therefore the intensity of peak also reduces significantly. Due to such broadening, the atomic states having more electrons may show less intensity than those having fewer electrons. Since the core states are least broadened, therefore usually the deep lying core states are observed with sharp peaks in XPS data. Along with this, the intensity of the peak corresponding to some elemental species in XPS spectra also depend upon the abundance of the element in region which is illuminated by X-rays, the depth up to which X-rays can penetrate (typically few nanometres), surface roughness and angle of sample to analyser. The electronic states of a particular element may also broaden due to difference in local environment around the element (inhomogeneity) in the samples. All these features make XPS spectra an ideal tool to investigate the actual details of any sample.

Along with characteristic peaks, additional peaks are also observed in XPS spectra due to other processes such as *Auger electron emission*, *satellite peaks*, *backscattered electrons*, etc. The Auger peaks being most prominent non-characteristic peaks occur due to emission of secondary electrons caused by *Auger effect*. In Auger effect, the X-rays eject electron from a low-energy orbital creating a vacant orbital there. This orbital is filled by an electron from a higher energy orbital with emission of a characteristic radiation of energy equal to energy difference of the two orbitals involved in transition. This secondary X-ray then ejects some other electron from atomic shell and is called *Auger electron*. Since Auger electrons ejected by an X-ray of different energy than the X-ray source being used in XPS, therefore their binding energy does not belong to expected energy levels of the atomic species. The binding energy of auger electrons can however be estimated by using Eq. (12.25) provided that the energy of photon is replaced with energy of radiation emitted during Auger process. In addition to Auger peaks, satellite peaks can also be observed when a non-monochromatic X-ray source is employed. Since the Auger peaks are not related to photon energy of X-ray source, these peaks do not have satellite peaks.

12.4.1 Charge Compensation

In XPS, the X-rays hit a neutral sample and eject the electrons out of the sample leaving nonneutral sample behind. In case the neutrality is not maintained, there will be additional positive charge left on the sample which provides additional pull to the ejected electrons providing extra binding energy. This will shift the XPS peaks from their actual position. Therefore, to maintain sample in its actual state, the ejected electrons have to be balanced by supply additional electrons. This can be done by making electrical connection of the sample to the instrument. However, this will work only for the case of conducting samples. In case of insulating samples, the neutrality is maintained by providing low-energy electron beam to the surface of the sample. The current of electron beam is adjusted to be the same as the current of photoelectrons ejected from the sample.

12.4.2 Depth Profiling

The XPS technique is surface sensitive, and one can get information of electronic structure of a material up to few nanometres deep from surface of the sample. However, the information of interior of the samples can be obtained by etching the surface layers of the sample using ion beam bombardment and recording XPS spectra after each etching cycle. Using this technique the internal inhomogeneities of a sample can be investigated.

12.4.3 Examples of XPS Spectra

Table 12.2 summarizes the data of binding energy peaks of different elements in various environments. It can be seen that the peaks may shift to higher or lower value depending upon the nature of local environment and bonding of the element. Below is specific example of MoS₂ and Mo in elemental form.

Ex1 There are a range of videos aimed at all ranges of XPS knowledge on the CasaXPS Casa Software YouTube channel. There is an example of MoS₂ within these videos as well as two videos looking at MoO₂ standard XPS spectra. Figure 12.11 shows:

- Molybdenum 3s peak have lower intensity than 3p peak indicating more number of electrons in 3p. Same feature can be noticed for sulphur 2s and 2p peaks. Intense peak of Mo 3d states reflect large degeneracy of d states in comparison to s and p states.
- The molybdenum 4s and 4p peaks are less intense and relatively broadened in comparison to 3s and 3p peaks indicating that core states are less affected due to bonding and valence states broaden to form energy bands. The same feature is observed for sulphur states.
- The sulphur 2p peak is more intense than Mo 3p peak indicating relatively more number of sulphur atoms as given by stoichiometry.
- The inset shows significant broadening of valence orbitals indicating formation of bands in MoS₂ crystal.
- The Madelung rule mentioned in Fig. 12.9 can be clearly seen in the binding energy values of different orbitals.

Ex2 Figure 12.12 shows the XPS spectra of molybdenum metal. The characteristic binding energy peaks for Mo 3s, 3p and 3d states are seen at almost same energy as in MoS₂. This shows that the core states are not affected by large extent when an atom changes from one material to other. There however may be shift in binding energy values and shape of the peaks depending upon the surrounding atoms. The binding energy values for Mo are also given in Table 12.2.

Table 12.2 Binding energy values for some selected elements

Sr. no.	Element	Chemical state	Binding energy (eV)
1.	H	Atomic hydrogen	13.6 [47] (1s)
2.	He	Atomic helium	24.6 [47] (1s) ^a
3.	Li	Atomic form	64.9 [47] (1s) ^b
			5.4 [47] (2s)
		LiF	56.1 [47] (1s)
		Li ₂ CO ₃	55.4 [47] (1s)
4.	Be	Atomic beryllium	119.3 [47] (1s)
			9.3 [47] (2s)
5.	B	Boron atomic form	200.1 [47] (1s)
			14.1 [47] (2s)
			8.3 [47] (2p) ^c
		ZrB ₂	187.8 [42] (1s)
6.	C	C atomic form	296.6 [47] (1s)
			17.8 [47] (2s)
			11.3 [47] (2p)
7.	Al (Al2p)	Al metal	72.6 [42]
		Aluminium oxide (Al ₂ O ₃)	74.6 [42]
		Aluminium oxide on Al foil	75.6 [42]
8.	Mg (Mg1s)	Magnesium metal	1303 [42]
		MgCO ₃	1305 [42]
9.	Si (Si2p)	Si (diamond structure)	99.4 [42]
		Si ₃ N ₄	101.7 [42]
		ZrSiO ₄	102 [42]
		SiO ₂	103.5 [42]
10.	Ca (Ca2p)	CaCO ₃	347.2 [42]
		Ca ₃ (PO ₄) ₂	347.4 [42]
11.	Cu (Cu2p)	Cu metal (FCC)	933 [42]
		Cu ₂ O	933 [42]
		CuO	933.5 [42]
		Cu (II) carbonate dihydroxide	934.7 [42]
12.	Mo	Mo metal	2867.1 (2s) [45]
			2626.0 (2p _{1/2}) [45]
			2521.2 (2p _{3/2}) [45]
			231.0 (3d _{3/2}) [46]

^aTaken under similar conditions, the peak for 1s states of He has intensity two times the intensity for H atom. This indicates presence of two electrons in 1s state of He

^bThe intensity of peak for 2s states is half the intensity for 1s states

^cThe intensity of 2p peak is half the other peaks indicating only one electron in 2p states. The peak intensity increases further as more electrons are added to 2p states as in C and N atoms

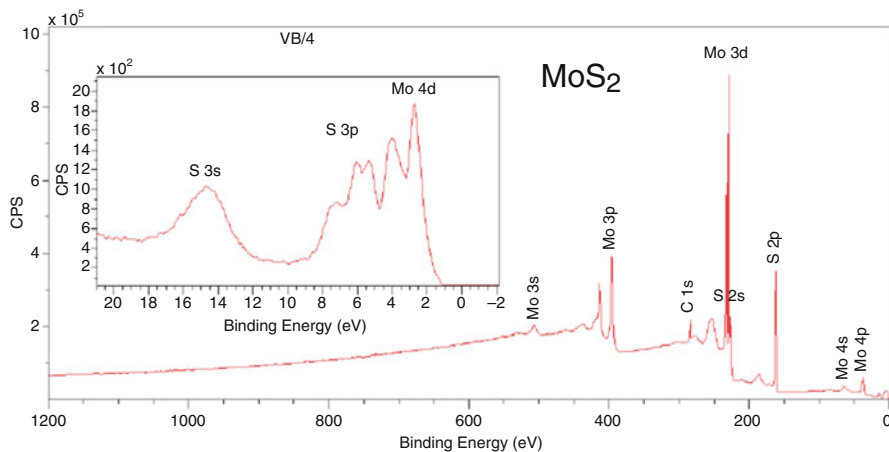


Fig. 12.11 XPS spectra of MoS₂ [44]. (Reproduced after permission from CasaXPS team)

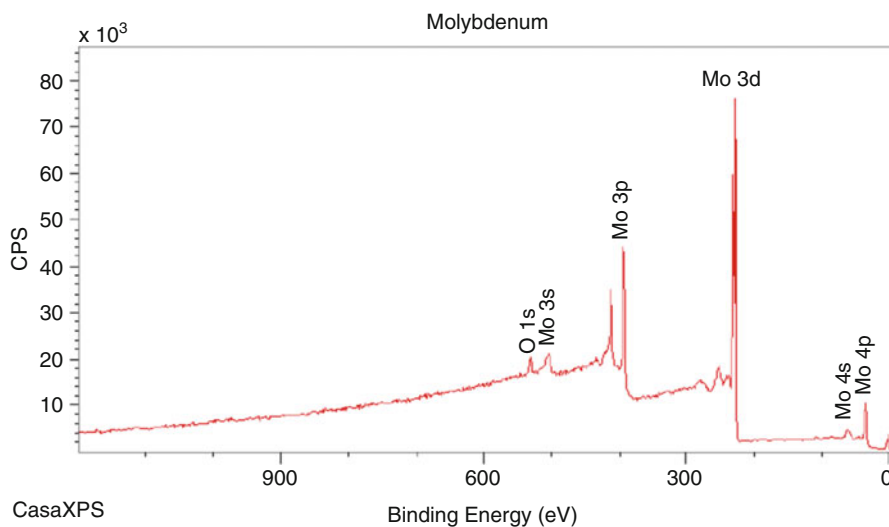


Fig. 12.12 XPS spectra of molybdenum [44]. (There are a range of videos aimed at all ranges of XPS knowledge on the CasaXPS Casa Software YouTube channel. There is an example of MoS₂ within these videos as well as two videos looking at MoO₂ standard XPS spectra.)

12.5 Valence Band Spectroscopy: Ultraviolet Photoelectron Spectroscopy (UPS) and Angle-Resolved Photoelectron Spectroscopy (ARPES)

The energy associated with X-rays is high enough so that they can eject the electrons from energy states over large range from strongly bound core states of the atoms to loosely bound valence electrons. The core states exist at well-defined energy values

and thus have large probability to get ejected and thus core states exhibit sharp peaks in BE curves in XPS experiments. On the other hand, due to bonding and other interactions, the energy states of valence electrons broaden (band formation), which leads to low-intensity peaks valence electrons broadened over energy range. The valence electrons ejected due to X-rays also have very high energies which limits accuracy of spectrometer for these electrons (refer to Eq. (12.14)). Therefore, XPS does not provide fine details of the valence band structure of a material. The energy of electrons in valence bands typically varies from few eV to few tens of eV. Due to this ultraviolet radiations (refer to Sect. 12.2.1.2) serve as a useful tool to study the details of valence band structure. Due to less energy, UV radiation cannot eject the electrons from core states, and only electrons from valence band are ejected and provide much refined information of the valence band states. The UPS technique provides useful experimental platform to verify most of the band structure calculation methods in solid-state physics.

12.5.1 Theoretical Overview

In case we do not change the relative positions/orientations of sample, detector and radiation source during a photoelectron spectroscopy measurement, we are measuring angle-integrated photoemission where integrated states over whole Brillouin zone have to be considered. Within the tree-step model (Sect. 12.7.1), one uses optical transitions among bulk electronic states which require the electron wavevector in reduced zone to be conserved. This allows one to consider only vertical electronic transitions in Brillouin zone, i.e. transitions having same value of wavevector for initial $E_i(\mathbf{k})$ and final $E_f(\mathbf{k})$ state. Thus, for some photon of energy $\hbar\omega$, there are many options for electronic excitations among $E_i(\mathbf{k})$ and $E_f(\mathbf{k})$ which are at energy difference of $\hbar\omega$. This consists of excitation of electrons from a surface in \mathbf{k} -space containing all the states having energy $E_i(\mathbf{k})$ to a surface of states having energy $E_f(\mathbf{k})$. All those transitions for which following equation is satisfied should be considered:

$$E_f(k) - E_i(k) - \hbar\omega = 0 \quad (12.26)$$

In case the detector, sample and radiation source are kept fixed with respect to each other during whole measurement (also called angle-integrated photoelectron spectroscopy), one obtain electrons from some energy state E depending upon total electronic density of states at that energy which is given by [11]:

$$D(E, \hbar\omega) = \int_{\text{BZ}} \delta[E_f(k) - E_i(k) - \hbar\omega] \delta[E - E_i(k)] d^3k \quad (12.27)$$

Equation (12.27) simply gives the sum of all those states in Brillouin zone for which initial energy $E_i(k)$ is fixed at some reference energy ($E = \hbar\omega - E_{\text{pass}}$) and

energy difference (for given value of k) between $E_f(k)$ and $E_i(k)$ is same as energy of radiation $\hbar\omega$. However, by measuring the direction of propagation of electron along with its kinetic energy, one can obtain the actual state in Brillouin zone (k -space) from which electron has been ejected. By doing measurements at different angles and different energies, one can therefore measure energy band structure of a material experimentally.

Assume that when radiation falls on the sample, some electron is ejected from energy state $E_i(k)$ to $E_f(k)$ and then is transported to surface without suffering inelastic scattering (three-step model Sect. 12.7.1). The kinetic energy of such photoelectron is given by:

$$E = \frac{\hbar^2 K^2}{2m} = \frac{\hbar^2 (K_{\perp}^2 + K_{\parallel}^2)}{2m} \quad (12.28)$$

where K_{\perp} and K_{\parallel} are components of ejected electron wavevector perpendicular and parallel to surface of material. If E_v is the energy of vacuum level and electron is ejected from state $E_f(k)$ on surface of the material, then kinetic energy in (12.28) is given as:

$$E = \frac{\hbar^2 (K_{\perp}^2 + K_{\parallel}^2)}{2m} = E_f(k) - E_v \quad (12.29)$$

From the above equation, one can obtain perpendicular component of electron kinetic energy as below:

$$\frac{\hbar^2 K_{\perp}^2}{2m} = [E_f(k) - E_v] - \frac{\hbar^2 (k_{\parallel} + G_{\parallel})^2}{2m} \quad (12.30)$$

where k_{\parallel} and G_{\parallel} , respectively, are electron wavevector and reciprocal lattice vector in reduced Brillouin zone of the sample and parallel to surface of sample. The reciprocal lattice vector appears because of Bloch-like nature of electron in periodic potential. Therefore, from Eq. (12.30) one can see that once we know the details of band structure, i.e. $E_f(k)$, and value of vacuum energy, the values of K_{\parallel} and K_{\perp} can be obtained. On the other hand, measuring the energies and directions of emitted electrons can deduce the information about band structure. For the electron in crystal, the parallel component of wavevector k_{\parallel} can be obtained from parallel component of ejected photoelectron K_{\parallel} using relation:

$$k_{\parallel} = K_{\parallel} - G_{\parallel} \quad (12.31)$$

Therefore, by measuring the polar angle Θ (as shown in Fig. 12.13), one can determine k_{\parallel} as given below:

$$k_{\parallel} = \frac{1}{\hbar} \sqrt{2mE} \sin(\Theta) \quad (12.32)$$

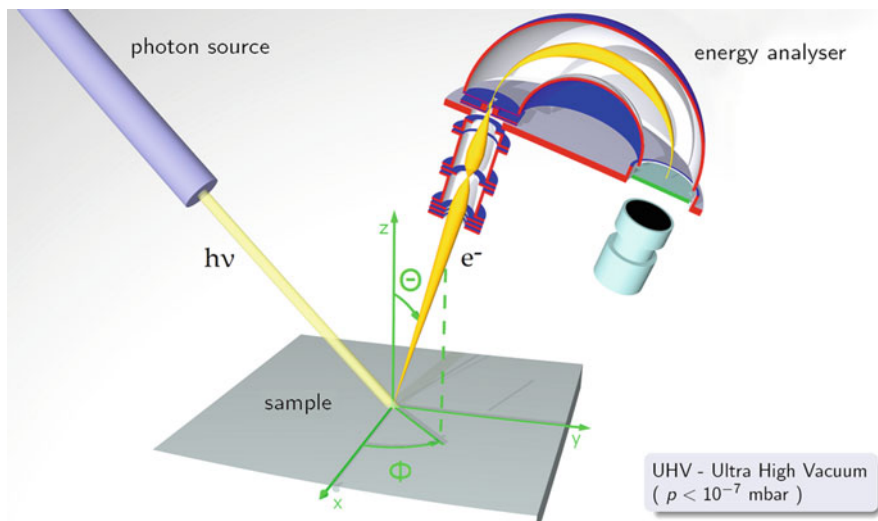


Fig. 12.13 Schematic diagram for angle-resolved photoelectron spectroscopy. (From [48])

No such relationship exists for perpendicular component of electron wavevector. This makes the task of obtaining the band structure for a general three-dimensional material difficult from angle-resolved measurements. However, by judiciously planning the experiment, one can still obtain reasonably meaningful information about band structure of a material for conditions mentioned below:

- (a) *Layered compounds*: In certain layered compounds such as MoS_2 , graphene and cuprate superconductors, there is weak interaction in certain direction leading to the negligible electronic dispersion along that direction. In such anisotropic materials, if one chooses the direction of weak electron dispersion as k_{\perp} , then the energy dispersion mainly depends upon k_{\parallel} and hence one need not bother about k_{\perp} .
- (b) *Normal emission*: In case one detects electrons only along direction perpendicular to surface, the parallel component k_{\parallel} will be zero. Therefore, by measuring electrons of different energies, information of electronic band structure $E(k)$ along specific direction (perpendicular to surface) can be obtained. By systematically varying the energy of incident photons, the band dispersion can be obtained along corresponding direction in Brillouin zone (refer to 12.5.3.1).
- (c) *Assuming free electron-like behaviour*: Another simplifying way to obtain k_{\perp} is to assume final electron state in crystal to be free electron-like. Due to this assumption, one can obtain k_{\perp} as follows [55]:

$$k_{\perp} = \frac{1}{\hbar} \sqrt{2m (E_{\text{kin}} \cos^2 \Theta + V_0)} \quad (12.33)$$

where V_0 is the band depth from vacuum and can be obtained by measuring electrons from normal emission.

(d) *Triangulation method* [57]: This method compares the energies of energy-dispersive curves from two different crystal surfaces in same plane of emission in Brillouin zone. The basic idea of this method is that the bands of any material at same point in Brillouin zone should be identical irrespective of scanning direction. Therefore, by comparing the energy bands obtained from scans obtained using different crystal surfaces, one can locate the absolute location of k -point (both k_{\perp} and k_{\parallel}) in Brillouin zone.

Once the information about k_{\perp} , k_{\parallel} and kinetic energy E_{kin} of the electron is obtained, one can locate the energy state in the Brillouin zone from where electron has been ejected and hence band structure $E(k)$ of a material is obtained. The value of azimuthal angle selects particular plane in Brillouin zone.

12.5.2 Experimental Setup

The schematic arrangement for any angle-resolved photoelectron system is given in Fig. 12.13. The system is exactly the same as that of an angle-integrated photoelectron system except for possibility to change relative positions and orientations of sample, radiation source and detector. For any system the k -space resolution is important characteristic which can be obtained by using Eq. (12.32) by taking the differential of the parallel component of wavevector one gets:

$$|\Delta k_{\parallel}| = \frac{1}{\hbar} \sqrt{2m E} \cos \Theta \Delta \Theta + \frac{1}{2\hbar} \sqrt{\frac{2m}{E}} \sin \Theta \Delta E \quad (12.34)$$

This gives us the k -space resolution of any ARPES system. It can be noticed from (12.34) that the k -space resolution of any system depends upon polar angle at which electrons detector is placed (see Fig. 12.13), angular ($\Delta \Theta$) and energetic (ΔE) resolution of the detector. Assuming the simplest case of measurement being done at direction perpendicular to surface, the k -space resolution only depends upon angular resolution. Assume that some experiment have detector with angular resolution of 4° (typical experimental situation). Then the k -space resolution at point perpendicular to surface comes out to be 0.07 \AA^{-1} which is fairly acceptable as typical Brillouin zone size for materials is more than 1 \AA^{-1} .

In ARPES system, it may be possible to move one or more components to obtain angular-dependent distribution of photoelectrons. Some of the systems consist of *movable analyser* which was developed by Lindau and Hagstrom [49]. In such system, the angle between perpendicular to sample surface and analyser can be

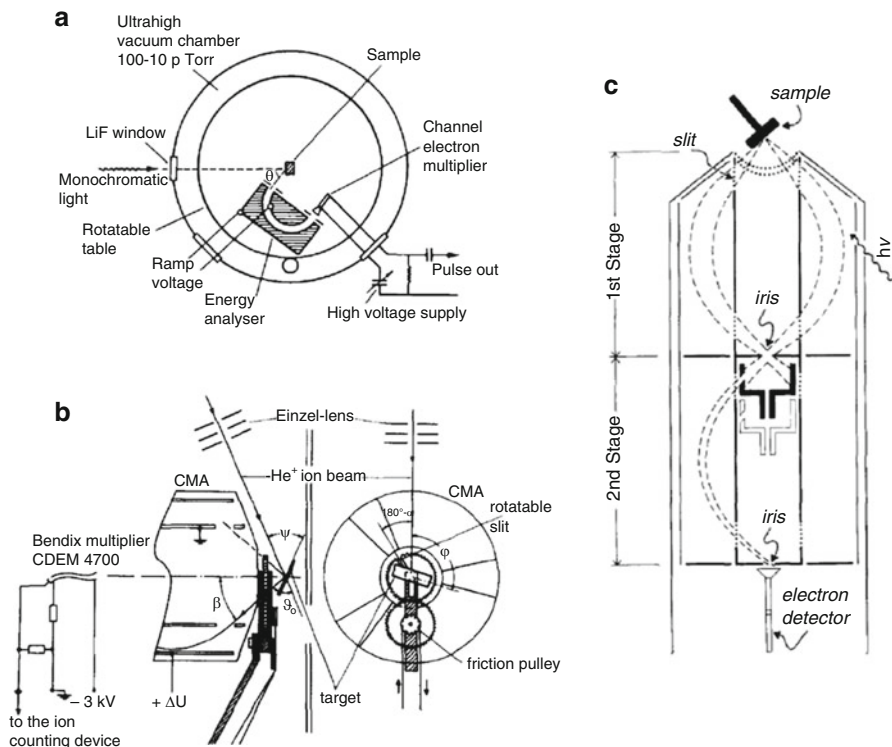


Fig. 12.14 Angle-resolved photoelectron spectroscopy (ARPES) systems. **(a)** A system with movable analyser [49] (© IOP Publishing. Reproduced with permission. All rights reserved), **(b)** modified CMA with external aperture. (Reproduced from [50], with the permission of AIP Publishing) and **(c)** modified two-stage CMA with internal drum. (Reproduced from [51], with the permission of AIP Publishing.)

varied by moving analyser (Fig. 12.14a). Other systems usually employ *cylindrical mirror analysers* (CMA) which can easily be modified for angle-resolved systems. One such modification was done by Niehus and Bauer [50] by placing a mask with aperture in external front part of the instrument. By rotating the mask, the angle of collection can be varied as illustrated in Fig. 12.14b. Another modification done to CMA was by Knapp and Lapeyre [51] who modified CMA by placing a movable internal drum (Y-shaped component shown in second stage) with small aperture in a two-pass analyser (Fig. 12.14c) which can be moved and also rotated about along the axis of cylinder to select desired angle and aperture for receiving the photoelectrons.

12.5.3 Some ARPES Studies

This section is devoted to very briefly illustrate the way ARPES data is presented and how band structure information is extracted from the same.

12.5.3.1 Normal Emission Spectra of GaAs (110) Surface

Figure 12.15a shows the energy distribution curves (EDC) in direction normal to (110) surface for GaAs at various energies of incident radiation [52]. The binding energy is given with respect to valence band maximum (VBM). The right panel of the figure shows the mapping of the bands in Brillouin zone along [110] direction

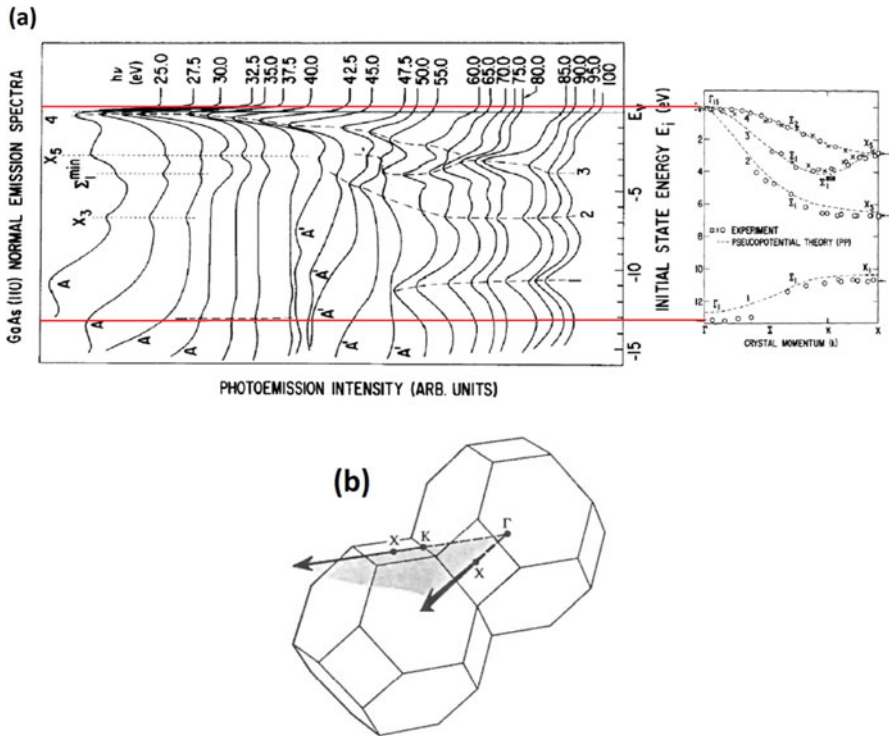


Fig. 12.15 Normal emission spectra of GaAs(110). The different curves refer to different photon energies. The corresponding band mapping along 110 direction in Brillouin zone is shown in right. (Reprinted from Publication [52], with permission from Elsevier). (b) Crystal structure (Figure created using XCRYSDEN software) and (c) Brillouin zone (Figure from [53]) for FCC lattice of GaAs and illustrating 110 direction in Brillouin zone

which refers to $\Gamma - K - X$ as illustrated in Fig. 12.15b. Each peak at certain binding energy in EDC refers to one point of band structure in Brillouin zone as shown by circles. To find the value of k_{\perp} , free electron-like dispersion (Eq. 12.30) $E(k_{\perp}) = \frac{\hbar^2 k_{\perp}^2}{2m} + E_0 = 3.81k_{\perp}^2 - 9.34$ eV has been employed by the authors [52]. The dashed lines refer to calculated band structure of GaAs (110) surface along $\Gamma - K - X$ direction using pseudopotential method [53]. By systematically scanning a peak at particular binding energy for different energies of incident radiation, one can construct various bands lines in Brillouin zone which can be compared with band structure calculations and in most cases shows reasonable agreement. The different band lines have been marked with 1, 2, 3 and 4 and have been shown in EDCs as well as band structure.

12.5.3.2 Au-110 Surface

By varying the polar angle Θ , Courths et al. have studied the angle-resolved photoelectron spectra for (110) and (111) surfaces of Cu, Ag and Au using ultraviolet light (ARUPS). Figure 12.16 shows results from same paper [56] showing the angle-resolved energy distribution curves (AREDCS) for Au (110) face obtained by varying polar angle Θ in $\Gamma - K - L - U - X$ plane of Brillouin zone. The right panel of the Fig. 12.16 shows the band dispersions $E_i(K_{\parallel})$ obtained from same data. The topmost energy distribution curve shows the normal dispersion of Au (111) surface and is used for locating the energy state in Brillouin zone by energy coincidence. The vertical arrows shown in right panel mark the transitions on Λ -line (a line between Δ and Σ points in Brillouin zone where the bands show extremal behaviour); horizontal arrows indicate corresponding energies in $\Theta = 0^\circ$ in angle-resolved energy-dispersive curves for (110) surface.

12.5.3.3 Electronic Structure of MoS₂ and MoSe₂

Figure 12.17 shows the electronic structure studies of two layered compounds MoS₂ and MoSe₂ performed by Mahatha et al. [58]. These two compounds have same hexagonal crystal structure having layers of X-Mo-X (X = S, Se). The interlayer interaction is weak and is mainly of van der Waals type. The main difference between these two compounds is their $\frac{c}{a}$ ratio which affects their interlayer interaction. Upper left (right) panel in Fig. 12.17 shows the experimental measurements of angle-resolved photoelectron spectra for MoS₂ (MoSe₂) along $\Gamma - M$ (marked by (a)) and $\Gamma - K$ (marked by (b)) directions. The brightness of the plots refers to the intensity of electrons and can be related to the number of electronic states available at that point in Brillouin zone. The zero on energy axis of these figures represents valence band maxima (VBM). The lower panel of Fig. 12.17 shows the comparison between calculated and experimental band structures for both the compounds. It can be seen that there is very good matching

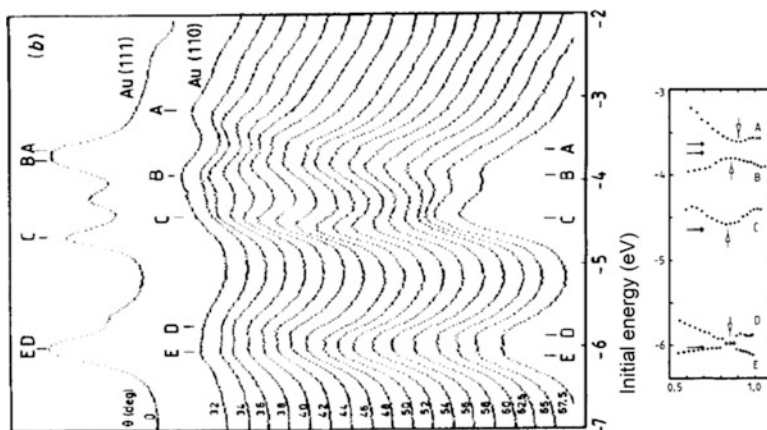


Fig. 12.16 AREDC for (110) surface of gold. Different curves refer to different values of polar angle. Corresponding mapping of bands in Brillouin zone is shown in right panel [56]. (© IOP Publishing. Reproduced with permission. All rights reserved)

in experiments and calculated results. These results demonstrate the precision and ability of experimental and theoretical techniques to characterize materials.

12.5.3.4 Electronic Structure of Bi_2Se_3

Bi_2Se_3 belongs to interesting class of modern materials known as topological insulators [60]. The most interesting part of this material is Dirac cone-like dispersions of surface electronic states near Fermi level. The energy versus photoelectrons shown in the left panel of Fig. 12.18 (Reproduced with permission from [59]) gives angle-integrated photoemission intensity and illustrates the low-lying core states in form of sharp peaks at well-defined energies. The middle figure in bottom row refers to the angle-resolved photoelectron spectra of valence band. The figure on the right shows the band structure calculations of the same region, and a good agreement between the experiment and theoretical calculations can be seen. The two plots on upper right panel of Fig. 12.18 shows the closer look on energy bands near Fermi level, and the linear Dirac-like dispersions can clearly be seen around Γ point.

12.6 Spin-Resolved ARPES

Apart from having electric charge, the electrons are endowed with another interesting property of *spin*. Many magnetism-related properties of a material result from this fundamental property associated with the electrons. Spin-resolved photoelectron spectroscopic technique provides additional dimension of exploring the

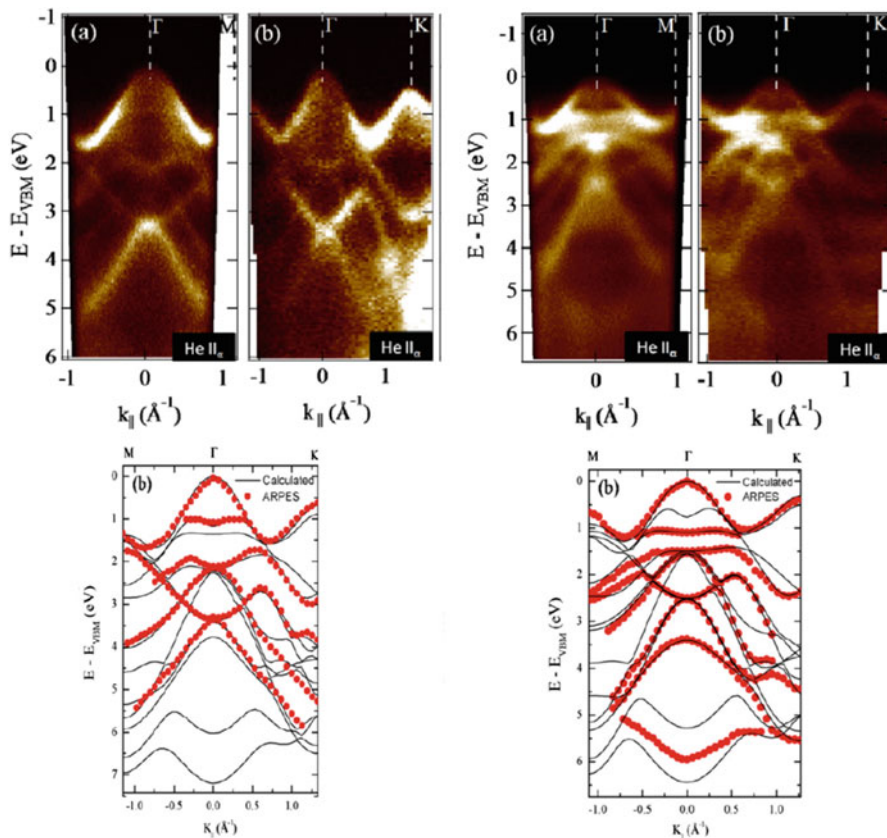


Fig. 12.17 Photoelectron spectra of (left) MoS₂ and (right) MoSe₂. The bottom panel shows the comparison of the experimental results with ab initio results obtained using density functional theory [58]. ((© IOP Publishing. Reproduced with permission. All rights reserved))

characteristics of a material based upon interplay of electronic spins in a material. The basic idea behind the spin based ARPES is that electronic spin is preserved in photoemission process. Therefore, by measuring the spin and energy of the photoelectron, one can measure spin-dependent band structure of material. The spin-dependent information of bands provides understanding of new physics of electronic spins inside a material. The understanding of such phenomenon leads to interesting new branches of technology known as *spintronics* [61], where electronic charge as well as spin is utilized for developing new electronic devices. Spin-dependent analysis of photoelectrons can give many insights of interior of material such as exchange splitting of energy bands (in ferromagnetic and antiferromagnetic materials) and half-metallic character (where material has metallic behaviour for one type of spins and shows band gap for other). Combined with XPS, one can obtain element-specific measure of local magnetism.

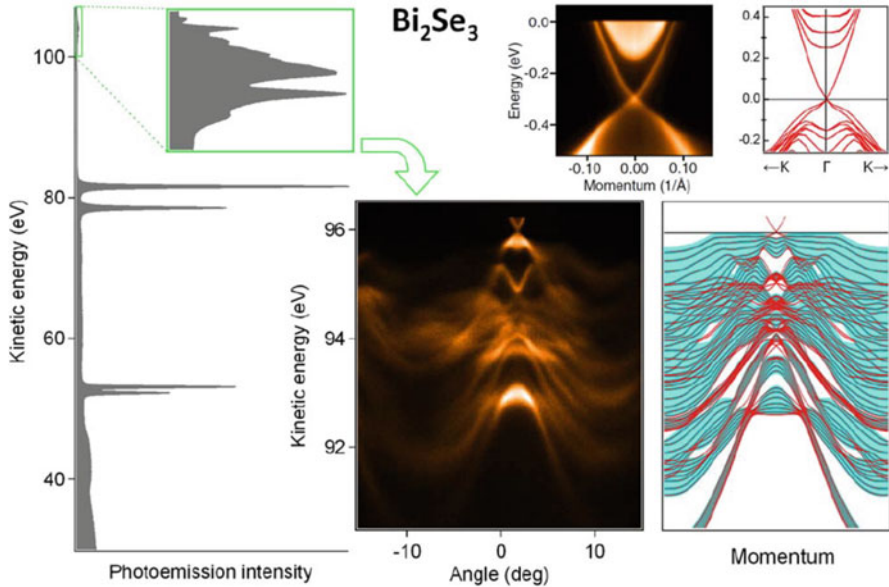


Fig. 12.18 Photoelectron spectrum for Bi_2Se_3 , a topological insulator. (Reproduced from [59], with the permission of AIP Publishing)

A simple ferromagnetic substance has majority electrons aligned along a particular direction and minority in opposite direction. This configuration is retained over significantly large region (few nanometres to hundreds of micrometres) called *magnetic domains*. The whole sample is divided into number of such regions with each oriented randomly with respect to others. Even a ferromagnetic material may not have net magnetization in such circumstances. When electrons from such sample are ejected, the average polarization of the photoelectrons may be zero, and no net information regarding spin configuration of sample can be obtained. There are two possible ways to eliminate this problem, first is to incident radiation on extremely small region of the sample so that the electrons are ejected from a single domain. This however requires well focused beam of radiation, large enough sized domains, stable and controllable position of radiation [62]. The second method is more practical and is used widely where one applies magnetic field on the sample so that all the domains merge into one and magnetization of whole sample is along one single direction. However, one challenge associated with this method is that in vacuum, the trajectories of most ejected photoelectrons (with velocities not along magnetic induction) spiral around the direction of magnetic induction due to Lorentz force $e(\vec{v} \times \vec{B})$. Due to this, the intrinsic spin information of ejected photoelectrons is lost. This is rectified by two approaches. In first, the magnetization outside the sample is minimized by magnetizing the sample along plane of photo-emitting surface (*transverse configuration*). The reduced magnetic induction reduces the Lorentz force and hence the spiralling effect. Another way to reduce spiralling of electrons is by magnetizing sample in direction perpendicular to photo-emitting

surface (*longitudinal configuration*) so that the electrons are ejected along magnetic induction leading to zero $\vec{v} \times \vec{B}$ and hence Lorentz force.

12.6.1 Polarimeters

The whole apparatus for spin-resolved photoelectron spectroscopy is similar to those discussed above except for additional detector (*polarimeters*) which detects spin of the electron. Therefore, a spin-ARPES apparatus combines a spin polarimeter with electron energy analyser. The polarimeters are the detectors which utilize spin-dependent interaction of the electrons with spin analyser. Most widely used polarimeters are based upon the spin-orbit interaction which introduces backscattering in opposite directions depending upon spin of incident electrons. Such polarimeters are known as *Mott polarimeters*. The scattering cross section due to spin-orbit interaction increases (decreases) for the electrons having parallel (antiparallel) spin with respect to normal \hat{n} to the scattering plane (the plane containing electron path and scattering nucleus). The Mott cross section for an electron is given by [62]:

$$\sigma(\theta) = I(\theta) [1 + S(\theta) P \cdot \hat{n}] \quad (12.35)$$

where $I(\theta)$ is given by [65]:

$$I(\theta) = |F(\theta)|^2 + |G(\theta)|^2 \quad (12.36)$$

$S(\theta)$ is called analysing power or Sherman function and depends upon electron energy, nature of material and angle of scattering and is defined as given below [62]:

$$S(\theta) = i \frac{F(\theta) G^*(\theta) - G(\theta) F^*(\theta)}{I(\theta)} \quad (12.37)$$

with $F(\theta)$ and $G(\theta)$ are spin-nonflip and spin-flip scattering amplitudes, respectively. P is polarization vector of incident electron. $\hat{n} = \hat{k}_1 + \hat{k}_2$, where \hat{k}_1 and \hat{k}_2 are wavevectors (unit magnitude) of incident and scattered electrons, respectively. The spin polarization of electron beam is measured by measuring spatial asymmetry A of scattered electrons which is given by [62]:

$$A = \frac{N_L - N_R}{N_L + N_R} \quad (12.38)$$

where N_L and N_R , respectively, are the number of the electrons scattered to left and right direction from the target. The detailed structure of a Mott polarimeter is described in Fig. 12.19. The spin-polarized electrons enter the system through

Wien filter which are further guided into Mott scattering chamber (shown in top-left) which is the most crucial part of the whole setup. When the polarized electrons enter the Mott chamber, they are scattered by one of the four gold foils (numbered 7) in target wheel (numbered 6). Depending upon their spin polarization, they are scattered to either of the two detectors (numbered 5). The details of other parts of the setup are discussed in [65, 66]. From Eqs. (12.35) and (12.38), the Mott asymmetry can be written as:

$$A = PS(\theta) \quad (12.39)$$

which depends upon Sherman function and which is named after N . Sherman who did accurate calculations $S(\theta)$ for gold, cadmium and aluminium [67, 68]. By using Eq. (12.39) the unknown polarization of the electron can be obtained by:

$$P = \frac{A}{S(\theta)} \quad (12.40)$$

The uncertainty in determining \mathbf{P} , spin polarization of an electron beam by a polarimeter is given by:

$$\Delta P = \frac{1}{\sqrt{JN_0}} \quad (12.41)$$

where $J = \eta S^2 = \frac{I}{I_0} S^2$ is the figure of merit of the spin analyser and N_0 is total number of electrons in the electron beam. I is the scattered intensity as appearing in Eq. (12.35), and I_0 is the beam intensity incident on the target. The figure of merit for spin analysers is typically of the order of 10^{-4} [62]. Therefore, by using this value in (12.39) and comparing the corresponding uncertainty in measuring intensity of the electrons $\Delta N = \frac{1}{\sqrt{N_0}}$, one can estimate that for $|P| < 1$, time required to measure the degree of spin polarization of electron beam is several times longer (may be as high as 10^4 times) [62] than to measure only the electron intensity. This time requirement is one of the key factors in deciding efficiency of an analyser. Depending upon the details of the instrument, there are different types of spin analysers, namely, *retarding type spin analysers*, *low-energy electron diffraction spin analyser* and *low-energy diffuse scattering spin analysers*. The details of their description have been given in [62] and references given there.

Recently, by combining polarimeter with a time-of-flight (TOF) spectroscopy analysis, a significantly high efficiency (almost 100 times) has been attained by Jozwiak et al. [69]. In this system, the spin resolution is provided by high efficiency low-energy exchange scattering (LEX) polarimeter, and energy is analysed using time of flight by employing parallel multi-channel detection which is a crucial step for improved efficiency of this system.

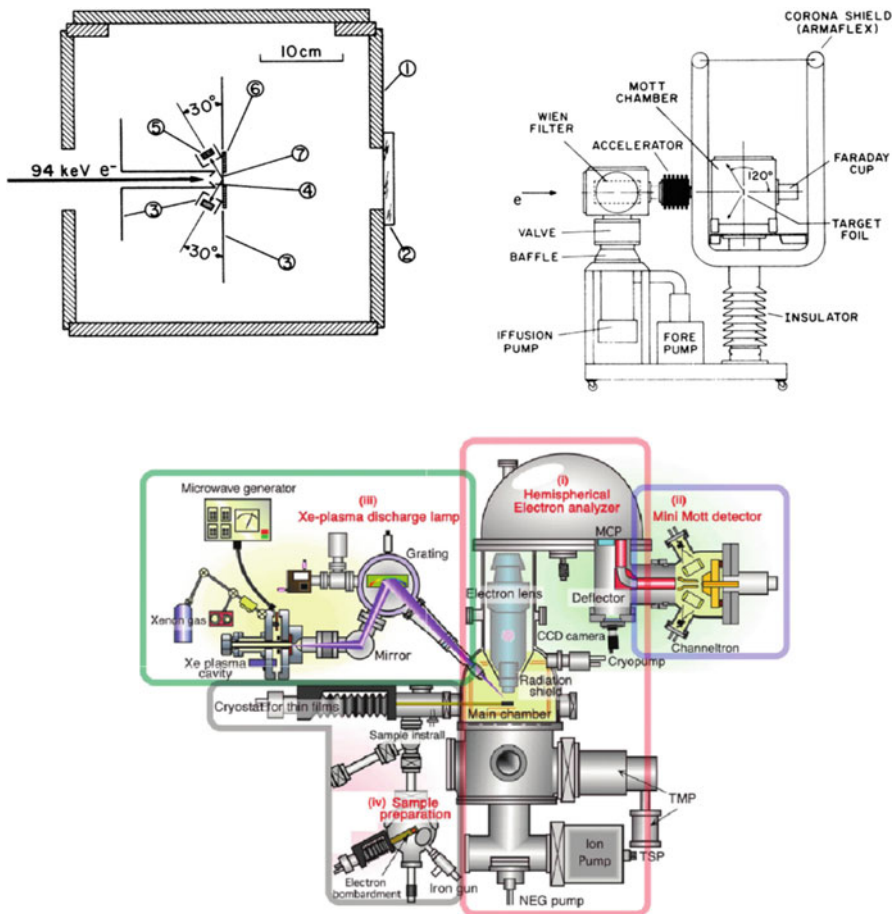


Fig. 12.19 Schematic representation of (top-left) Mott scattering region (Reprinted figure with permission from [65] Copyright (1986) by American Physical Society) and (top-right) Mott polarimeter (Reproduced from [66], with the permission of AIP Publishing) and (Bottom) schematic view of full assembly of a spin-resolved ARPES system (Reprinted with permission from [70])

12.6.2 Phase Space Considerations

In a spin-dependent angle-resolved system, a detector detects the energy and spin of the electron at some angle and therefore has limited volume of phase space. Therefore, phase space volume is important parameter for specifying the efficiency of the spin-resolved system. In context to the electron beam emitted from the sample, the phase space volume characterizes the real space co-ordinates and momenta of the electrons. The phase space volume for electron beam in longitudinal configuration is given by [62–64]:

$$2.17 \times 10^{-3} r^4 B_n^2 \text{mm}^2 \cdot \text{eV} \cdot \text{Steradian} \quad (12.42)$$

where r is the radius of the sample and expressed in millimetre. B_n is magnetic field expressed in gauss.

The phase space volume for energy analyser is related to its acceptance phase space (acceptance energy, area of acceptance) and resolving power and is given by [62–64]:

$$20R^2 \alpha^4 \Delta E \text{mm}^2 \cdot \text{eV} \cdot \text{Steradian} \quad (12.43)$$

where R is mean radius of beam path expressed in millimetre, α is half-angle of entrance to the hemisphere and expressed in radians. In case the phase space volume of the analyser is less than that of sample, some of the photoelectrons will be lost. Therefore, the two volumes should be comparable or analyser volume should be larger for an efficient system.

12.6.3 The Spin-Polarized ARPES Examples

12.6.3.1 Spin Resolved ARPES Spectra for Bi thin films

Figure 12.20 shows spin- and angle-resolved photoemission spectra for Bi(111) thin films studied by Takayama [70]. Figure 12.20 (a) indicates Fermi surface of Bi/Si(111) around Γ point. The lines marked by A–N in Fig. 12.20 (a) represent the regions of k-space where spin resolved energy dispersive curves (EDCs) shown in Figs. 12.20 (b–e) are shown. By employing spin-ARPES, anomalous Rashba effect (refer to original text [70] for details) has been investigated. Some of the important features noted were:

In Figure 12.20 (b) in-plane spin polarization in regions marked A and B is dominated by up spins. Regions C and D on the other hand have dominance of down spins, although the spin polarization is markedly suppressed (as seen from almost overlapping EDCs). The same is indicated with the help of value of magnitude of spin polarization $|\text{Py}|$ which is found 0.5 and 0.7 for A and B whereas suppresses to 0.3 and 0.2 for C and D, respectively. The same features can also be observed in other energy dispersive curves (EDCs) illustrated in Figs. 12.20 (c–e). X/Y represents in-plane and Z represents out-of-plane spin components.

12.6.3.2 Spin-Resolved Band Structure of BCC Fe

Figure 12.21 below shows the electronic band structure and density of states for BCC iron computed using density functional theory. It can be seen that there are clear signatures of spin dependence of electronic energy. The electronic density of states for majority and minority spins can clearly be differentiated from each other

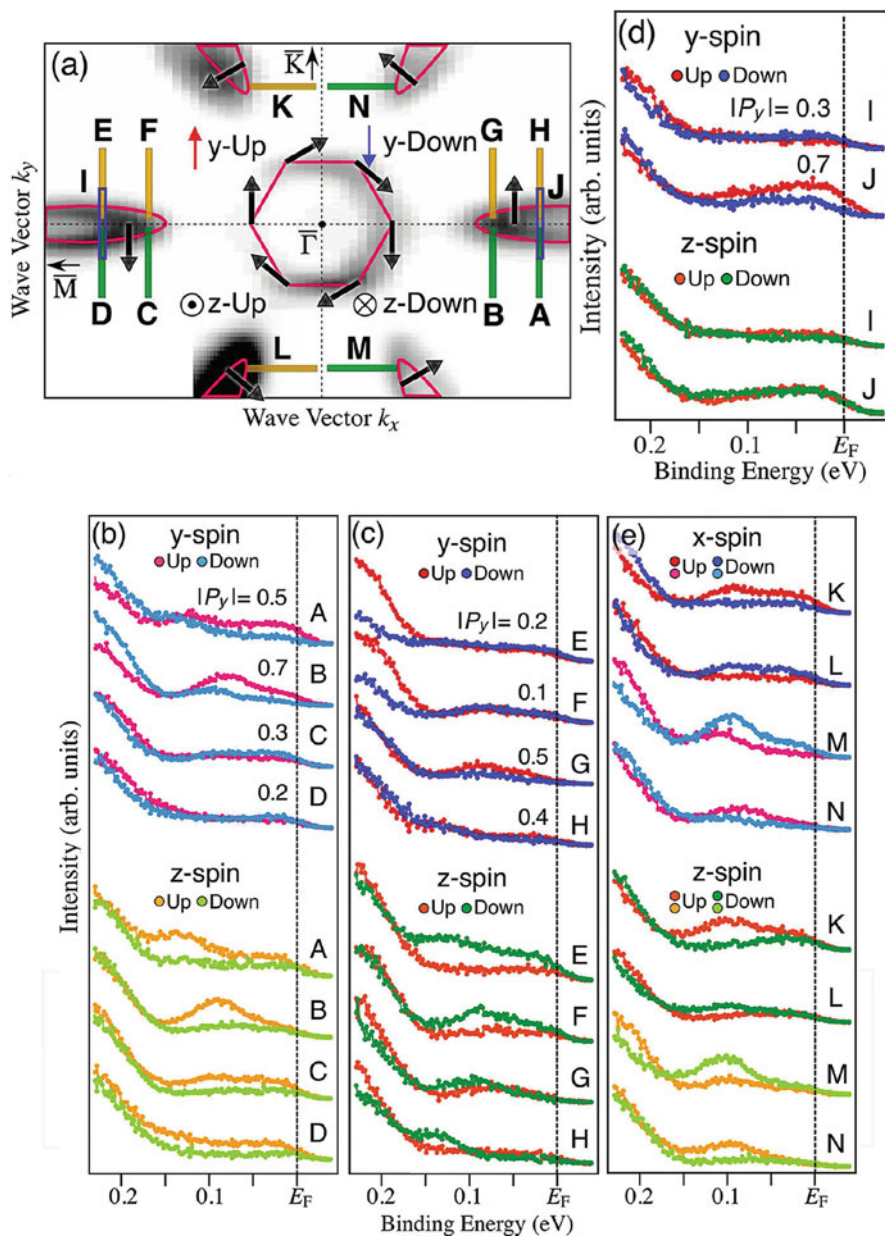


Fig. 12.20 Spin and angular resolved ARPES spectra of Bi(111) thin film. (a) represents Fermi surface of Bi(111) surface around Γ point. The lines marked by A, B, . . . N represent different regions in k -space for which spin resolved energy dispersive curves have been presented in figures (b–e). X/Y spins indicate in-plane spins and z indicates out-of-plane spins. $|P|$ represents magnitude of spin polarization along directions represented by subscript. (Figure produced after [70] with permissions.)

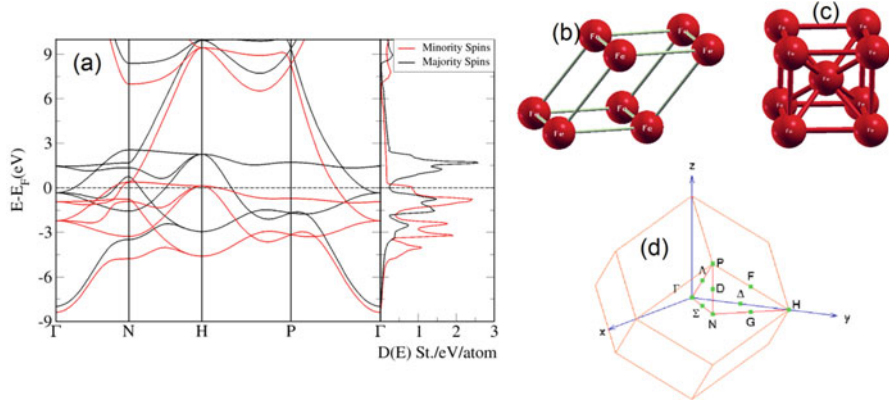


Fig. 12.21 (a) Spin-polarized electronic band structure and density of states of iron in BCC structure computed using density functional theory. The conventional BCC unit cell for iron is shown in (c), and (b) is corresponding primitive cell. The high symmetry points marked in band structure refer to the Brillouin zone corresponding to primitive cell as shown in (d)

indicating presence of magnetic interactions. The same distinction can be made between majority and minority spins in band structure as shown in (a). Such features of a material can be characterized using spin- and angle-resolved photoelectron spectroscopy as illustrated in previous example for WSe_2 .

12.7 Theoretical Aspects of Photoelectron Spectroscopy

The complete theoretical description of photoelectron spectroscopy requires detailed knowledge of ground state and excited state energy of a material, effect of time-dependent external potentials due to radiation on electronic structure, nature of surface, etc. This is extremely challenging task, and till date no method has been developed to determine the complete solution to this problem. Judicious approximation methods have been developed for solving this problem piecewise.

12.7.1 Three-Step Model

Berglund and Spicer [71] visualized the photoemission of the electron from a material in three simple processes: *excitation of the electron from their ground state energy state* and *their movement to surface of the solid* during which these electrons may lose their energy due to *inelastic scattering*. This analysis of photoelectron spectra is well known as the *three-step model* of photoemission. The electrons will be ejected from the surface of a material if after being excited from their ground state

energy level somewhere in interior of the sample, they are able to reach the surface of the material without losing much of their energy by suffering inelastic collisions and finally have sufficient energy to overcome the energy barrier when they reach at the surface. Those electrons after reaching surface finally escape from sample surface with some kinetic energy. In this model the intensity of the photoelectrons at some energy $I(E, \omega)$ consists of two components:

- Primary electrons $I_p(E, \omega)$, which suffers no inelastic scattering and thus have the highest kinetic energy among whole bunch of ejected electrons. In order to explore the electronic structure of a material, the primary electrons are of key interest in photoelectron spectroscopy.
- Secondary electrons $I_s(E, \omega)$, which suffer inelastic scattering during their transport to surface and hence have lost some of their energy. These electrons possess kinetic energy lower than primary electrons due to multiple scattering events and therefore constitute non-zero broad structureless background of primary peaks. However, due to strong *plasmon losses* [11, 71], one can obtain low-intensity broad peaks (of width not larger than 10 eV) which are well separated from primary electron intensities. Although the plasmon loss peaks of core electrons can be identified in the spectra, those for valence electrons are hard to identify as their broadening widths are of the order of valence band width.

The intensity of primary electrons $I_p(E, \omega)$ can further be obtained in terms of three functions, namely, *photoexcited electron distribution* $P(E, \omega)$, *transmission function* $T(E)$ and *escape function* $D(E)$ as follows:

$$I_p(E, \omega) = P(E, \omega) \times T(E) \times D(E) \quad (12.44)$$

$P(E, \omega)$ is related to excitation of the electron from low-energy occupied states to unoccupied high-energy vacant states. The electronic structure methods described in Sects. 12.7.3, 12.7.4, and 12.7.5 give a quick overview of theoretical techniques used to obtain electronic energy states. If inelastic scattering probability is supposed to be isotropic and characterized by electron mean-free path $\lambda_e(E)$, then transmission function $T(E)$ is given by [71]:

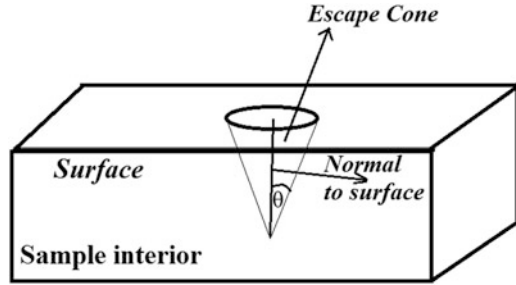
$$T(E) = \frac{\lambda_e(E)/\lambda_{ph}(\omega)}{1 + \lambda_e(E)/\lambda_{ph}(\omega)} \quad (12.45)$$

where $\lambda_{ph}(\omega)$ is the attenuation length of photons.

After the electrons have reached at surface without suffering any collisions, the component of electron crystal momentum should be perpendicular to surface of the crystal and must be higher than some critical value sufficient to overcome the potential energy barrier $E_F + \phi$. Assuming the excited photoelectrons to move like plane waves, one can obtain the condition for *escape cone* around a perpendicular surface along which the electrons can escape the surface of the material.

The opening angle relative to surface normal θ for escape cone can be obtained from the following expression [72]:

Fig. 12.22 Escape cone for electrons near surface



$$\cos(\theta) = \left(\frac{\phi + E_F}{E} \right)^{\frac{1}{2}} \quad (12.46)$$

The same has been illustrated in Fig. 12.22. For any electron approaching surface of the material at energy less than $E_F + \phi$, the escape function $D(E)$ will be zero as they do not have sufficient energy to overcome potential barrier. For those having energy greater than $E_F + \phi$ and approaching the surface of sample at an angle θ , the escape function (representing the fraction of electrons that escape the surface) will be related to θ . Those having θ zero, i.e. perpendicular to surface, will have the highest chance to escape, and those at parallel to surface will have least chance to escape. The escape function thus is defined as below:

$$D(E) = \begin{cases} \frac{1}{2} [1 - \cos(\theta)] & \text{for } E > E_F + \phi \\ 0 & \text{Otherwise} \end{cases} \quad (12.47)$$

where $\cos(\theta)$ is defined by Eq. (12.46).

Within the idea of three-step model, $P(E, \omega)$ is related to excitations of electrons within bulk-occupied electronic states (say E_n) to unoccupied states (say $E_{n'}$) as given below [11]:

$$P(E, \omega) \propto \sum_{n, n'} \int d^3k | \langle n' | p | n \rangle |^2 \delta [E_{n'}(k) - E_n(k) - \omega] \bullet \delta [E_{n'}(k) - E] \quad (12.48)$$

The integral in (12.48) extends over all occupied states in Brillouin zone. Moreover, to obtain the $P(E, \omega)$, one needs the knowledge of $E(k)$, i.e. band structure of a material in ground and excited states.

In the remaining part of the chapter, we shall present few of the most important approximations and methods that can be used to obtain electronic energy spectrum in a material and can evaluate $P(E, \omega)$. As given in Eq. (12.16), the Hamiltonian for a real material contain many terms which means that obtaining even ground state solution is a tedious task which although is achieved using many careful approximations described in following sections. Sections 12.7.2, 12.7.3, and 12.7.4 summarize the techniques and approximations to solve many-body problem for

time-independent Hamiltonian. The time-dependent part of Hamiltonian refers to interaction of many-electron system with external potential such as due to electromagnetic fields in photoelectron spectroscopy. Section 12.7.5 summarizes briefly the techniques available within density functional theory to obtain time-dependent interactions and excited states.

12.7.2 Born-Oppenheimer Approximation

The motivation behind Born-Oppenheimer approximation [73, 74] is heavy mass of atomic nuclei in comparison to electrons. Due to heavy mass, the nuclei respond almost negligibly to some external impulse such as applied electric field in comparison to electrons. Due to this important fact, the nuclear motion can be decoupled from electron motion and the Hamiltonian given by Eq. (12.16), and thus Schrodinger equation can be separated into two independent Schrodinger's equations, one for motion of nuclei and another for motion of electrons. Moreover, due to their heavy masses, in most of the cases, the motion of nuclei does not require quantum mechanical treatment and hence solving Schrodinger's equation. One can obtain nuclear kinetic energy and potential energy by simply writing classical expressions for them, which are far easier. The major challenge is obtaining solution of Schrodinger's for electronic part which looks as follows:

$$(\hat{\mathbf{H}}_{\mathbf{k},\mathbf{e}} + \hat{\mathbf{H}}_{\mathbf{p},\mathbf{N}-\mathbf{e}} + \hat{\mathbf{H}}_{\mathbf{p},\mathbf{e}-\mathbf{e}}) \Psi_e(X; x) = E_e(X) \Psi_e(X; x) \quad (12.49)$$

In the above equation, X is collective notation of positions of atomic nuclei, i.e. $X(X_1, X_2, \dots, X_M)$, if there are M nuclei in material. x represents position and spin co-ordinates of all the electrons, i.e. $x(x_1, \sigma_1; x_2, \sigma_2; \dots, x_N, \sigma_N)$, if there are total N electrons in material. The terms in Hamiltonian on left-hand side are, respectively, total kinetic energy of electrons, total potential energy of electrons due to their interaction with nuclei and total potential energy of electrons due to their interaction with each other. In operator form these terms are as given below:

$$\hat{\mathbf{H}}_{\mathbf{k},\mathbf{e}} = - \sum_{i=1}^N \frac{\hbar^2}{2m_e} \nabla_{\vec{\mathbf{r}}_i}^2 \quad (12.50)$$

$$\hat{\mathbf{H}}_{\mathbf{p},\mathbf{e}-\mathbf{e}} = \frac{1}{2} \sum_{i_1 \neq i_2=1}^N \frac{1}{4\pi\epsilon_0} \frac{e^2}{|\vec{\mathbf{r}}_{i_1} - \vec{\mathbf{r}}_{i_2}|} \quad (12.51)$$

$$\hat{\mathbf{H}}_{\mathbf{p},\mathbf{N}-\mathbf{e}} = - \sum_{\mathbf{k}=1}^M \sum_{i=1}^N \frac{1}{4\pi\epsilon_0} \frac{Z_{\mathbf{k}}e^2}{|\vec{\mathbf{R}}_{\mathbf{k}} - \vec{\mathbf{r}}_i|} \quad (12.52)$$

It is clear from the above equations that even after Born-Oppenheimer approximation, the solution for Schrodinger equation for even electronic part is a challenging. Even till date the efforts are going on to obtain the best possible solution. However, many judicious approximations have been proposed over the time by virtue of which we can obtain significantly precise solution to the mentioned equation for electrons in the materials.

12.7.3 Hartree-Fock Approximation

The most challenging term in Eq. (12.49) is electron-electron interaction in Hamiltonian. This is because electrons are microscopic particles, and uncertainty principle does not allow one to describe their accurate positions. Since the potential energy of any particles depends upon their positions, therefore, the description of this part of Hamiltonian is a difficult task. Moreover, the many particle wave function is a function of co-ordinates (position and spin) of all the electrons. This makes Eq. (12.49) as single-coupled equation for N electrons having $3N$ -independent variables. Imagine a real material containing 10^{23} atoms and electrons of almost the same order. Therefore, solving such an equation exactly is almost a formidable task till date even with the best possible computers. Hartree proposed a crucial approximation to break this single unsolvable problem for N electrons into N solvable problems for single electron [73].

Hartree [75] proposed that if one assumes the electrons to be moving independent of each other and write the many-electron wave function as product of single-electron wave functions, then the complicated problem can be split into set of many problems which are indeed solvable. The Hartree product is given by:

$$\Psi_e(x) = \varphi_1(x_1) \times \varphi_2(x_2) \dots \dots \times \varphi_N(x_N) \quad (12.53)$$

By substituting Hartree wave function into Eq. (12.49) and applying principle of variations, one obtains well-known Hartree equations given below:

$$\left[-\frac{\hbar^2}{2m_e} \nabla_{\vec{r}_i}^2 + V(\mathbf{r}) + V_H(\mathbf{r}) \right] \varphi_i(r_i) = \epsilon_i \varphi_i(r_i) \quad (12.54)$$

The terms $V(\mathbf{r})$ and $V_H(\mathbf{r})$ on left-hand side are, respectively, electron-nuclei interaction and Hartree potential describing electron-electron interaction.

$$V(\mathbf{r}) = \sum_{i=1}^M \frac{1}{4\pi\epsilon_0} \frac{Z_k e^2}{|\vec{\mathbf{R}}_k - \vec{\mathbf{r}}_i|} \quad (12.55)$$

$$\mathbf{V}_H(\mathbf{r}) = e^2 \int \frac{\mathbf{n}(\mathbf{r})}{|\vec{\mathbf{r}}_i - \vec{\mathbf{r}}|} d\mathbf{r} \quad (12.56)$$

One important difference in Eqs. (12.49) and (12.54) is that summations are not present in Hartree equations and many-electron wave function is replaced with single-electron wave functions. Hartree equations are set of \mathbf{N} -independent differential equations for \mathbf{N} electrons in the system. The Hartree potential appearing in above equations gives the potential which i th electron feels due to all other electrons as if they were present as a continuous distribution of charge. Then $\mathbf{n}(\mathbf{r})$ appearing in (12.56) is number density of electrons and can be obtained from single-particle wave functions as:

$$\mathbf{n}(\mathbf{r}) = \sum_{i=1}^N \varphi_i^*(\mathbf{r}) \varphi_i(\mathbf{r}) \quad (12.57)$$

One important challenge in obtaining solution of Hartree Eq. (12.54) is getting the Hartree potential as this requires knowledge of electron number density $\mathbf{n}(\mathbf{r})$ which further requires knowledge of single-electron wave functions as in (12.57) which indeed are to be obtained from solving Eq. (12.54). The Hartree equations can however be solved self-consistently where one begins with a trial guess of single-electron wave functions and constructs Hartree potential. This Hartree potential is then used in Hartree equations to obtain new set of single-electron wave functions. The Hartree potential is then constructed using these new wave functions, and the procedure is repeated till one obtain self-consistent solution, that is, the solutions do not change with further steps. Another serious flaw in Hartree approximation is with wave function which does not follow fundamental property of antisymmetric nature of many-particle wave function. This was overcome by using Slater determinant in Hartree-Fock approximation [76]. The Slater's [77] determinant is:

$$\Psi(x_1, x_2, \dots, x_N) = \frac{1}{\sqrt{N!}} \begin{vmatrix} \varphi_1(x_1) & \varphi_1(x_2) & \dots & \varphi_1(x_N) \\ \varphi_2(x_1) & \varphi_2(x_2) & \dots & \varphi_2(x_N) \\ \vdots & \vdots & \ddots & \vdots \\ \varphi_N(x_1) & \varphi_N(x_2) & \dots & \varphi_N(x_N) \end{vmatrix} \quad (12.58)$$

This leads to well-known Hartree-Fock equations which are as follows:

$$\left[-\frac{\hbar^2}{2m_e} \nabla_{\vec{\mathbf{r}}_i}^2 + \mathbf{V}(\mathbf{r}) + \mathbf{V}_H(\mathbf{r}) + \mathbf{V}_x(\mathbf{r}) \right] \varphi_i(r_i) = \epsilon_i \varphi_i(r_i) \quad (12.59)$$

Important to notice here is that Hartree-Fock equations are similar to Hartree equations except for an additional term $\mathbf{V}_x(\mathbf{r})$ which is called *exchange potential*. The exchange potential is purely due to quantum mechanical nature of the system

and has no classical analogue. Hartree-Fock approach is an important approach in dealing with multi-atomic systems such as molecules and solids.

12.7.4 Density Functional Theory

Density functional theory has become the most popular tool to calculate the ground state and excited state energies of real solids. The advantage of these methods is that they use electronic density, a function of three variables, to compute the ground state rather than many particle wave function which is a function of $3N$ variables. The area of density functional theory is vast, and we shall here restrict to a simple and formal introduction to technique of DFT. The Hamiltonian for electronic part of Schrodinger equation can be written broadly into two components as below:

$$H_e = H_{\text{int}} + V_{\text{ext}} \quad (12.60)$$

With H_{int} being Hamiltonian for electrons and their interaction among themselves and is given as:

$$H_{\text{int}} = T + V_{e-e} \quad (12.61)$$

T here is total kinetic energy, and V_{e-e} is electron-electron interaction energy. The interaction of electrons with nuclei is treated as external potential on electrons and is given by:

$$V_{\text{ext}}(\mathbf{r}) = \sum_{i=1}^M \frac{1}{4\pi\epsilon_0} \frac{Z_k e^2}{|\vec{\mathbf{R}}_k - \vec{\mathbf{r}}|} \quad (12.62)$$

The basic pillars of density functional theory are two fundamental theorems by Hohenberg and Kohn (HK) [79]. The first Hohenberg and Kohn theorem states that: *There is one to one correspondence between ground state electron density of an N electron system and external potential (potential due to atomic nuclei) acting on it.* The first Hohenberg-Kohn theorem established a one-to-one mapping between ground state wave function and ground state electron density of a material. This enables one to work in terms of electron density which is simpler entity than wave function.

The ground state energy thus can be written as functional of ground state electron density $E[n(\mathbf{r})]$. The Hohenberg-Kohn ground state energy functional is given by:

$$E^{\text{HK}}[n(\mathbf{r})] = T[n(\mathbf{r})] + V_{e-e}[n(\mathbf{r})] + \int V_{\text{ext}}(\mathbf{r}) n(\mathbf{r}) d\mathbf{r} \quad (12.63)$$

The second Hohenberg-Kohn theorem provides a pathway to obtain the ground state electron density via employing variational principle. The second Hohenberg-

Kohn theorem states that: *The electron density which minimizes overall energy functional is the true electron density corresponding to ground state wavefunction of Schrodinger equation.* The important point in above formalism is that the functional $\mathbf{F}[\mathbf{n}(\mathbf{r})] = \mathbf{T}[\mathbf{n}(\mathbf{r})] + \mathbf{V}_{e-e}[\mathbf{n}(\mathbf{r})]$ is universal and does not depend upon external potential. Therefore, once we know this universal functional, we can obtain ground state density and hence other properties of any system by simply plugging in external potential. Obtaining the true form of this universal potential is although not easy. However, many reasonable approximations have been employed to get acceptable form of this functional.

Kohn and Sham [80] devised a practical approach to obtain this universal functional and thus ground state electron density. They assumed a fictitious system of noninteracting quasiparticles (virtual noninteracting electrons) and decomposed the electron density $\mathbf{n}(\mathbf{r})$ of real system of interacting electrons as:

$$\mathbf{n}(\mathbf{r}) = \sum_i \varphi_i^*(\mathbf{r}) \varphi_i(\mathbf{r}) \quad (12.64)$$

where $\varphi_i(\mathbf{r})$ are Kohn-Sham orbitals and are solution of single-particle Kohn-Sham equations for system noninteracting electrons (quasiparticles). The Kohn-Sham equations are obtained by applying variational principle for a fictitious noninteracting system with assumption that it has same electron density as the real system. This simplification allows one to use simple functionals of a noninteracting system which are almost impossible to obtain for a real system. For example, one can use Thomas-Fermi [81] kinetic energy functional, $\mathbf{T}_{\text{TF}}[\mathbf{n}(\mathbf{r})] = \mathbf{C}_{\text{F}} \int \mathbf{n}^{\frac{5}{3}}(\mathbf{r}) d\mathbf{r}$, for Kohn-Sham system, whereas the exact form of the same for a real system is not known. This simplification however introduces a new challenging term called exchange and correlation energy which accounts for all complicated effects arising due to many-body effects and have not been incorporated in fictitious Kohn-Sham system. Using Kohn-Sham development, Hohenberg-Kohn functional (12.63) for a real system can be written as:

$$E^{HK}[\mathbf{n}(\mathbf{r})] = \mathbf{T}_{\text{TF}}[\mathbf{n}(\mathbf{r})] + \int \mathbf{V}_{\text{ext}}(\mathbf{r}) \mathbf{n}(\mathbf{r}) d\mathbf{r} + \mathbf{V}_{\text{H}}[\mathbf{n}(\mathbf{r})] + \mathbf{E}_{\text{xc}}[\mathbf{n}(\mathbf{r})] \quad (12.65)$$

The Kohn-Sham equations for system of noninteracting quasiparticles are given below:

$$\left[-\frac{\hbar^2}{2m_e} \nabla_{\mathbf{r}_i}^2 + \mathbf{V}(\mathbf{r}) + \mathbf{V}_{\text{H}}(\mathbf{r}) + \mathbf{V}_{\text{xc}}(\mathbf{r}) \right] \varphi_i(r_i) = \varepsilon_i \varphi_i(r_i) \quad (12.66)$$

The exchange-correlation potential appearing in Kohn-Sham equations can be obtained from $\mathbf{E}_{\text{xc}}[\mathbf{n}(\mathbf{r})]$ by taking its functional derivative with respect to electron density, i.e.

$$\mathbf{V}_{\text{xc}} = \frac{\delta \mathbf{E}_{\text{xc}}[\mathbf{n}(\mathbf{r})]}{\delta \mathbf{n}(\mathbf{r})} \quad (12.67)$$

To obtain $\mathbf{E}_{\text{xc}}[\mathbf{n}(\mathbf{r})]$ two popular approaches, namely, *local density approximation* (LDA) [82, 83] and *generalized gradient approximation* (GGA) [84, 85], are known. According to local density approximation, the exchange and correlation energy is given by:

$$\mathbf{E}_{\text{xc}}^{\text{LDA}}[\mathbf{n}(\mathbf{r})] = \int \varepsilon_{\text{xc}}(\mathbf{n}(\mathbf{r})) \mathbf{n}(\mathbf{r}) d\mathbf{r} \quad (12.68)$$

where the **function** $\varepsilon_{\text{xc}}(\mathbf{n}(\mathbf{r}))$ appearing in integral is exchange correlation energy per electron for interacting homogeneous electron gas. There are many studies on exchange and correlation effects of homogeneous electron gas, and this provides various forms of LDA that are available. One of the most popular forms of LDA is by Perdew and Zunger [87] who have employed Ceperley and Alder parameterization for $\varepsilon_{\text{xc}}(\mathbf{n}(\mathbf{r}))$ which refers to unpolarized homogeneous electron gas. Ceperley and Alder [88] have employed Quantum Monte Carlo calculations to study homogeneous electron gas and have obtained exchange and correlation energy as given below:

$$\varepsilon_{\text{xc}}(\mathbf{r}_s) = \varepsilon_x(\mathbf{r}_s) + \varepsilon_c(\mathbf{r}_s) \quad (12.69)$$

where the exchange energy is given by:

$$\varepsilon_x(\mathbf{r}_s) = -\frac{0.4582}{\mathbf{r}_s} \quad (12.70)$$

and correlation energy is given by:

$$\varepsilon_c(\mathbf{r}_s) = \begin{cases} \frac{-0.1423}{(1+1.0529\sqrt{\mathbf{r}_s}+0.3334\mathbf{r}_s)} & \text{for } \mathbf{r}_s \geq 1 \\ -0.0480 + 0.0311 \ln(\mathbf{r}_s) - 0.0116\mathbf{r}_s + 0.0020\mathbf{r}_s \ln(\mathbf{r}_s) & \text{for } \mathbf{r}_s \leq 1 \end{cases} \quad (12.71)$$

There are different flavours for local density approximation [89], depending upon how exchange and correlation energy has been estimated. In GGA, the exchange and correlation energy is considered not only to depend upon local value of electron density but also on its gradient. The general form for exchange and correlation energy functional for GGA is given by [86]:

$$\mathbf{E}_{\text{xc}}^{\text{GGA}}[\mathbf{n}(\mathbf{r})] = \int f(\mathbf{n}_{\uparrow}(\mathbf{r}), \mathbf{n}_{\downarrow}(\mathbf{r}), \nabla \mathbf{n}_{\uparrow}(\mathbf{r}), \nabla \mathbf{n}_{\downarrow}(\mathbf{r})) d\mathbf{r} \quad (12.72)$$

where $\mathbf{n}_{\uparrow}(\mathbf{r})$ and $\mathbf{n}_{\downarrow}(\mathbf{r})$ and electron densities for spin-up and spin-down electrons, respectively, such that total electron density at a point is $\mathbf{n}(\mathbf{r}) = \mathbf{n}_{\uparrow}(\mathbf{r}) + \mathbf{n}_{\downarrow}(\mathbf{r})$.

12.7.5 Time-Dependent Response of Electrons in Material

The electronic structure of the material obtained by the methods described above refers to the ground state of the system. The study of electronic structure using photoelectron spectra involves the time-dependent external potential due to external electromagnetic fields being incident on material sample. The excitonic effects also play important role specifically at high intensity of incident radiations. A brief summary of theoretical formalisms used to study such effects is described below.

12.7.5.1 Random Phase Approximation (RPA)

The idea of RPA was put forward by Bohm and Pines in series of papers during 1951 to 1953 [90–92]. According to RPA the Hamiltonian for electrons can be represented as [90]:

$$H = H_{\text{part}} + H_{\text{osc}} + H_{\text{part int}} \quad (12.73)$$

where H_{part} refers to kinetic energy, H_{osc} refers to external perturbing oscillating potential and $H_{\text{part int}}$ corresponds to screened interaction between electrons which is assumed to have significant values for distances shorter than minimum distance associated with oscillatory perturbation. For a particular frequency of external signal, the RPA method self-consistently [93] yields a dynamic dielectric function $\epsilon_{\text{RPA}}(k, \omega)$. A detailed description of systematic revisions and improvements in RPA has been summarized in [94] by Ren et al.

12.7.5.2 Time-Dependent Density-Functional Theory (TD-DFT)

Time-dependent density-functional theory is another tool to investigate the properties of many-electron systems in the presence of time-dependent potentials such as electric or magnetic fields. The foundation for TD-DFT was laid down by Erich Runge and E. K. U. Gross in 1984 [95] in the form of well-known Runge-Gross theorem which is time-dependent analogue of Hohenberg-Kohn theorem. The Hamiltonian for a time-dependent many-electron system looks similar to (12.60) except for the external potential being not only potential due to atomic nuclei but also time-varying term which may be arising from time-varying electric or magnetic field.

The RG theorem proved that *for a given initial state of the system, there is a unique mapping between time-dependent external potential $v(\mathbf{r}, t)$ and time-dependent electron density*. This important theorem opened up the possibility to work for time evolution of the system in terms of much simpler three-dimensional electron density rather than $3N$ -dimensional wave function. As in case of a time-independent system, variational principle can be applied for obtaining ground state of system; there is no such analogue for time-dependent system. Therefore, a

time-dependent analogue for Kohn-Sham system was desired which could result same time evolution of electron density as the real system. The density response function in RG formulation was symmetric in time and thus suffered from serious paradoxical conclusions according to which any change in potential at some time \mathbf{t} could change density at some earlier time. This problem was resolved by Robert van Leeuwen in 1998 [96] who employed Keldysh formalism [97] of complex-time path integrals.

12.7.5.3 GW Approximation

Another successful approach to study excited state properties is GW approximation. The experiments such as photoemission spectra and electronic transport properties yield information about quasiparticles (electrons or holes in excited state) of a system. The presence of many particle effects in system leads to self-energy of excited particles leading to significant changes in electron energy dispersion relations in comparison to independent-particle picture such as Kohn-Sham approach. Green's function formulation provides a systematic description of quasiparticle properties. The single-particle Green's function in orbital basis representation is given by [98]:

$$G(p, \tau) = -i \langle 0 | T \{ c_p(\tau) c_p^\dagger(0) \} | 0 \rangle \quad (12.74)$$

Here T is time-order operator, and $|0\rangle$ is many-electron ground state. Index p refers to quantum numbers for single-particle state such as band index (n) and wavevector (k). For many-particle Hamiltonian of the type given in (12.49), the single-particle Green's function satisfies the following equation [98]:

$$(\hbar\omega - H_0 - V_H) G(r, r'; \omega) - \int \Sigma(r, r'', \omega) G(r, r''; \omega) = \delta(r, r') \quad (12.75)$$

where $H_0 = \frac{p^2}{2m} + V_{\text{ion}}(r)$, V_H is Hartree potential and Σ is electron self-energy operator and is a functional of G . The solution of above equation can be expressed as [99, 100]:

$$G(r, r'; \omega) = \sum_{n,k} \frac{\psi_{nk}(r) \psi_{nk}^*(r')}{\omega - E_{nk} - i\delta_{nk}} \quad (12.76)$$

where E_{nk} and ψ_{nk} are the solutions to following equation for quasiparticles known as Dyson equations given below:

$$[E_{nk} - H_0(r) - V_H(r)] \psi_{nk}(r) - \int \Sigma(r, r', E_{nk}) \psi_{nk}(r') dr' = 0 \quad (12.77)$$

Therefore, given the self-energy Σ , the quasiparticle properties can be obtained by solving Eq. (12.77) which is similar to single-particle Kohn-Sham equations.

Within GW approximation [99], the self-energy is given by:

$$\Sigma(r, r', E) = i \int \frac{d\omega}{2\pi} e^{-i\delta\omega} G(r, r'; E - \omega) W(r, r'; \omega) \quad (12.78)$$

where $W(r, r'; \omega)$ is screened Coulomb interaction [100] and is given by:

$$W(r, r'; \omega) = \int \varepsilon^{-1}(r, r''; \omega) V_c(r'', r') dr'' \quad (12.79)$$

$V_c(r'', r')$ in the above equation is bare Coulomb potential, and $\varepsilon^{-1}(r, r''; \omega)$ is time-ordered dielectric response function of the system. Therefore, within GW approximation, the problem of computing quasiparticle properties is to obtain self-energy using operator given by Eq. (12.78) and using the same in Dyson equations (12.77) which can be solved to obtain quasiparticle energies E_{nk} and wave functions $\psi_{nk}(r)$.

12.8 Conclusion

In conclusion, this chapter provides a quick compilation of gist of vast literature available in photoelectron spectroscopy. An attempt is made to present the basic principles and experimental arrangement of different spectroscopic techniques based on photoelectron emission without incorporating much complexity. Simple conceptual interpretation of the results has been presented with the help of experimental results available in literature. A brief overview of theoretical methods to describe the photoelectron spectra and electronic structure of a material is also given. We hope this chapter is a good quick recipe for any beginner to understand basics of theoretical and experimental description of electronic structure of a material.

References

1. Darrigol, O. (2012). *A history of optics from Greek antiquity to nineteenth century*. New York: Oxford University Press.
2. Walter, G. (1948). Microwave Spectroscopy. *Rev. Mod. Phys*, 20, 668.
3. Tissue, B. M. (2002). *Ultraviolet and visible absorption spectroscopy*. New York: Wiley. <https://doi.org/10.1002/0471266965.com059>.
4. Owen, T. (2000). *Fundamentals of modern UV-visible spectroscopy*. Germany: Agilent Technologies.
5. Stuart, B. (2004). *IR spectroscopy: Fundamentals and applications*. Chichester: Wiley.
6. Chen, L. X., Zhang, X., & Shelby, M. L. (2014). Recent advances on ultrafast X-ray spectroscopy in the chemical sciences. *Chemical Science*, 5, 4136.

7. Gilmore, G. *Practical gamma-ray spectroscopy*. Wiley. <https://onlinelibrary.wiley.com/doi/book/10.1002/9780470861981>
8. Brundle, C. R., & Baker, A. D. (1978). *Electron spectroscopy: Theory, techniques and applications*. London: Academic.
9. Brooks, F. D., & Klein, H. (2002). Neutron spectrometry historical review and present status. *Nuclear Instruments and Methods in Physics Research A*, 476, 1–11.
10. Yano, J., & Yachandra, V. K. (2009). X-ray absorption spectroscopy. *Photosynthesis Research*, 102, 241.
11. Cardona, M., & Ley, L. (1978). *Photoemission in solids (Vol. I and II)*. New York: Springer-Verlag.
12. Bings, N. H., Bogaerts, A., & Broekaert, J. A. C. (2010). Atomic spectroscopy: A review. *Analytical Chemistry*, 82, 4653.
13. Dillane, S., Thompson, M., Meyer, J., Norquay, M., & Christopher O'Brien, R. (2011). Inductively coupled plasma atomic emission spectroscopy (ICP-AES) as a method of species differentiation of bone fragments. *Australian Journal of Forensic Sciences*, 43, 297.
14. Hufner, S. (2003). *Photoelectron spectroscopy: Principles and applications*. New York: Springer.
15. X-ray transition energies database NIST. <https://physics.nist.gov/PhysRefData/XrayTrans/Html/search.html>
16. Moseley, H. G. J. (1913). High frequency spectra of elements. *Philosophical Magazine*, 26, 1024.
17. Ultraviolet ISO data. http://www.spacewx.com/pdf/SET_21348_2004.pdf
18. Reinert, F., & Hufner, S. (2005). Photoemission spectroscopy—from early days to recent applications. *New Journal of Physics*, 7, 97.
19. Ellis, A., Feher, M., & Wright, T. (2005). *Electronic and photoelectron spectroscopy: Fundamentals and case studies*. Cambridge, UK: Cambridge University Press.
20. Griffiths, D. J. *Introduction to electrodynamic*. Cambridge University Press. <https://www.alibris.com/search/books/isbn/9781108420419>
21. Flynn, C. Lecture notes on “FFYS4346 Astrophysics II”, Lecture 4: Synchrotron Radiation. <http://www.astro.utu.fi/~cflynn/astroII/4.html>.
22. Kimura, K. (1999). Development of laser photoelectron spectroscopy based on resonantly enhanced multiphoton ionization. *Journal of Electron Spectroscopy and Related Phenomena*, 100, 273.
23. Ishikawa, T., Tamasaku, K., & Yabash, M. (2005). High-resolution X-ray monochromator. *Nuclear Instruments and Methods in Physics Research A*, 547, 42.
24. Grivet, P. *Electron optics*. Translated by P.W. Hawkes revised by A. Septier Pergamon Press, Oxford, New York, Toronto, Sydney.
25. McCord, M. A., & Rooks, M. J. (1997). In P. Rai-Choudhary (Ed.), *Handbook of microlithography, micromachining and microfabrication, volume 1, Microlithography*. SPIE Working Group <http://spie.org/Publications/Book/2035576?SSO=1>.
26. <http://www.microscopy.ethz.ch/lens.htm>
27. Hu, J., Rovey, J. L., & Zhao, W. (2017). Retarding field energy analyzer for high energy pulsed electron beam measurements. *The Review of Scientific Instruments*, 88, 013302.
28. Halliday, D., Resnick R., & Walker, J. *Fundamentals of physics*. Wiley. <https://www.wiley.com/en-to/Fundamentals+of+Physics+Extended%2C+10th+Edition-p-9781118230725>
29. Perriard, D. (2012). *Characterization of a novel spin detector based on spin diffraction on a crystal*. Master Thesis at ETH Zurich.
30. Wiza, J. L. (1979). Microchannel plate detectors. *Nuclear instruments & Methods*, 162, 587.
31. Boster, E. & Behm, T. (2010). “CCD Camera Operation and Theory” <http://instrumentation.tamu.edu/files/ccds.pdf>
32. Hablanian, M. (1997). *High-vacuum technology, a practical guide*. Marcel Dekker, Inc.

33. Marquardt, N. *Introduction to the principles of vacuum physics*. <http://www.chem.elte.hu/foundations/altkem/vakuumtechnika/CERN01.pdf>
34. https://en.wikipedia.org/wiki/Rotary_vane_pump#/media/File:Rotary_vane_pump.svg
35. Lindberg, V. (2008). Course on Lab Techniques, Rochester Institute of Technology, Chapter 6, Vacuum pumps. <https://people.rit.edu/vwlsps/LabTech/Pumps.pdf>.
36. Umrath, W. *Fundamentals of vacuum technology* https://www3.nd.edu/~nsl/Lectures/urls/LEYBOLD_FUNDAMENTALS.pdf
37. Zettili, N. *Quantum mechanics: Concepts and applications*. Wiley. <https://www.wiley.com/en-us/Quantum+Mechanics%3A+Concepts+and+Applications%2C+2nd+Edition-p-9780470026793>
38. Kittel, C. *Introduction to solid state physics*. Wiley. <https://www.wiley.com/en-us/Introduction+to+Solid+State+Physics%2C+8th+Edition-p-9780471415268>
39. Laporte, O., & Meggers, W. F. (1925). Some rules of spectral structure. *Journal of the Optical Society of America*, *11*, 459.
40. Capelle, K. (2006). A bird's-eye view of density-functional theory. arxiv:cond-mat/0211443.
41. [https://upload.wikimedia.org/wikipedia/commons/thumb/c/c1/Brillouin_Zone_\(1st,_FCC\).svg/2000px-Brillouin_Zone_\(1st,_FCC\).svg.png](https://upload.wikimedia.org/wikipedia/commons/thumb/c/c1/Brillouin_Zone_(1st,_FCC).svg/2000px-Brillouin_Zone_(1st,_FCC).svg.png)
42. <http://xpssimplified.com/periodictable.php>
43. https://upload.wikimedia.org/wikipedia/commons/3/30/Klechkowski_rule_2.svg
44. <http://www.casaxps.com/>
45. Huschka, W., Ross, D., Maier, M., & Umbach, E. (1988). Calibrated binding energies of some core levels in the energy range between 1.5–4keV. *Journal of Electron Spectroscopy and Related Phenomena*, *46*, 273.
46. Brox, B., & Olefjord, I. (1988). ESCA studies of MoO₂ and MoO₃. *Surface and Interface Analysis*, *13*, 3.
47. <http://cbc.arizona.edu/chemt/Flash/photoelectron.html>
48. https://en.wikipedia.org/wiki/Angle-resolved_photoemission_spectroscopy
49. Lindau, I., & Hagstrom, S. B. M. (1971). High resolution electron energy analyser at ultrahigh vacuum conditions. *Journal de Physique*, *E4*, 936.
50. Niehus, H., & Bauer, E. (1975). Low energy ion backscattering spectroscopy (ISS) with a commercial Auger cylindrical mirror analyzer (CMA). *The Review of Scientific Instruments*, *46*, 1275.
51. Knapp, J. A., Lapeyre, G. J., Smith, N. V., & Traum, M. M. (1982). Modification of cylindrical mirror analyser for angle resolved photoelectron spectroscopy. *The Review of Scientific Instruments*, *53*, 781.
52. Chiang, T. C., Knapp, J. A., & Eastman, D. E. (1979). Angle resolved photo-emission and valence band dispersions E(k) for GaAs: Direct vs indirect models. *Solid State Communications*, *31*, 917.
53. <http://image.sciencenet.cn/album/201404/23/151523b496kcef1enlzn.jpg>
54. Pandey, K. C., & Phillips, J. C. (1974). Nonlocal pseudopotentials for Ge and GaAs. *Physical Review B*, *9*, 1552.
55. Chiang, T. C., Knapp, J. A., Aono, M., & Eastman, D. E. (1980). Angle resolved photo-emission, valence band dispersion E(k) and electron and hole lifetimes for GaAs. *Physical Review B*, *21*, 3513.
56. Courths, R., Wern, H., Hau, U., Cord, B., Bachelier, V., & Hufner, S. (1984). Band structure of Cu, Ag and Au: Location of direct transitions on Λ line using angle-resolved photoelectron spectroscopy. *Journal of Physics F: Metal Physics*, *14*, 1559.
57. Kane, E. (1964). Implications of crystal momentum conservation in photoelectric emission for band structure measurements. *Physical Review Letters*, *12*, 97.
58. Mahatha, S. K., Patel, K. D., & Krishnakumar, S. R. M. (2012). Electronic structure investigation of MoS₂ and MoSe₂ using angle-resolved photoelectron spectroscopy and ab-initio band structure studies. *Journal of Physics: Condensed Matter*, *24*, 475504.
59. Kordyuk, A. A. (2014). ARPES experiment in fermiology of quasi-2D metals. *Low Temperature Physics*, *40*, 286.

60. Xia, Y., Qian, D., Hsieh, D., Wray, L., Pal, A., Lin, H., Bansil, A., Grauer, D., Hor, Y. S., Cava, R. J., & Hasan, M. Z. (2009). Observation of a large gap topological class with a single Dirac cone on the surface. *Nature Physics*, 5, 398.
61. Pulizzi, F. (2012). Spintronics. *Nature Materials*, 11, 367.
62. Pierce, D. T., Cellota, R. J., Kelley, M. H., & Unguris, J. (1988). Electron spin polarization analyzers for use with synchrotron radiation. *Nuclear Instruments and Methods in Physics Research*, A266, 550.
63. Pierce, D. T., Kuyatt, C. E., & Celotta, R. J. (1979). Spin and energy analyzed photoemission: A feasibility analysis. *The Review of Scientific Instruments*, 50, 1467.
64. Hughes, V. W., Long, R. L., Jr., Lubell, M. S., Posner, M., & Raith, W. (1972). Polarized electrons from photoionization of polarized alkali atoms. *Physical Review A*, 5, 195.
65. Fletcher, G. D., Gay, T. J., & Lubell, M. S. (1986). New insights into Mott-scattering electron polarimetry. *Physical Review A*, 34, 911.
66. Wainwright, P. F., Alguard, M. J., Baum, G., & Lubell, M. S. (1978). Application of a dc Fano effect polarized electron source to low-energy atom scattering. *Review of Scientific Instruments*, 49, 571.
67. Sherman, N. (1956). Coulomb scattering of relativistic electrons by point nuclei. *Physics Review*, 103, 1601.
68. Sherman, N., & Nelson, D. F. (1959). Determination of electron polarization by means of Mott-scattering. *Physics Review*, 114, 1541.
69. Jozwiak, C., et al. (2010). A high efficiency spin resolved photoemission spectrometer combining time-of-flight spectroscopy with exchange-scattering polarimetry. *Review of Scientific Instruments*, 81, 053904.
70. Takayama, A. *Anomalous Rashba effect of Bi thin film studied by spin-resolved ARPES*. Intech Open Books. <https://doi.org/10.5772/66278>.
71. Berglund, C. N., & Spicer, W. E. (1964). Photoemission studies of copper and silver: Theory. *Physics Review*, 136, A1030.
72. Smith, N. V. (1971). Photoemission properties of metals. *Critical Reviews in Solid State and Materials Sciences*, 2, 45.
73. Springborg, M. *Methods of electronic structure calculations: From molecules to solids*. Wiley. <https://www.wiley.com/en-us/Methods+of+Electronic+Structure+Calculations+%3A+From+Molecules+to+Solids-p-9780471979753>
74. Born, M., & Oppenheimer, J. R. (1927). On the quantum theory of molecules. *Annalen der Physik (Leipzig)*, 84, 457 Translated by S. M. Blinder with emendations by Brian Sutcliffe and Wolf Geppert.
75. Hartree, D. R. (1928). The wave mechanics of atom with a non Coulomb central field: Part-I theory and methods. *Mathematical Proceedings of the Cambridge Philosophical Society* 24, 89; Hartree, D. R. (1928). The wave mechanics of atom with a non Coulomb central field: Part-III Term values and intensities in series of optical spectra. *Mathematical Proceedings of the Cambridge Philosophical Society*, 24, 426.
76. Fock, V. (1930). *Zeitschrift für Physik*, 61, 126.
77. Slater, J. C. (1929). The theory of complex spectra. *Physics Review*, 34, 1293.
78. Jones, R. O., & Gunnarsson, O. (1989). Density functional formalism, its applications and prospects. *Rev Modern Physics*, 61, 689.
79. Hohenberg, P., & Kohn, W. (1964). Inhomogeneous electron gas. *Physics Review*, 136, B864.
80. Kohn, W., & Sham, L. J. (1965). Self-consistent equations including exchange and correlation effects. *Physics Review*, 140, A1133.
81. Thomas, L. H. (1927). Calculations of atomic fields. *Proceedings of the Cambridge Philosophical Society*, 23, 542; E. Fermi, *Zeitschrift für Physik* 48, 73 (1928).
82. Loos, P.-F. (2014). Generalized local density approximation and one-dimensional finite uniform electron gases. *Physical Review A*, 89, 052523.
83. Parr, R. G., & Yang, W. (1989). *Density functional theory of atoms and molecules*. New York: Oxford University Press.

84. Langreth, D. C., & Mehl, M. J. (1983). Beyond the local density approximation in calculations of ground state electronic properties. *Physical Review B*, 28, 1809.
85. Becke, A. D. (1988). Density-functional exchange-energy approximation with correct asymptotic behavior. *Physical Review B*, 38, 3098.
86. Perdew, J. P., Burke, K., & Ernzerhof, M. (1996). Generalized gradient approximation made simple. *Physical Review Letters*, 77, 3865 and “Erratum” *Phys. Rev. Lett.* 78, 1396 (1997).
87. Perdew, J. P., & Zunger, A. (1981). Self-interaction correction to density functional approximations for many electron systems. *Physical Review B*, 23, 5048.
88. Ceperley, D. M., & Alder, B. J. (1980). Ground state of the electron gas by stochastic method. *Physical Review Letters*, 45, 566.
89. Marques, M. A. L., Oliveira, M. J. T., & Burnus, T. (2012). LIBXC: A library of exchange and correlation functionals for density functional theory. *Computer Physics Communications*, 183, 2272.
90. Bohm, D., & Pines, D. (1951). A collective description of electron interactions-I magnetic interactions. *Physics Review*, 82, 625.
91. Pines, D., & Bohm, D. (1952). A collective description of electron interactions-II collective vs individual particle aspects of the interactions. *Physics Review*, 85, 338.
92. Bohm, D., & Pines, D. (1953). A collective description of electron interactions-III coulomb interaction in degenerate electron gas. *Physics Review*, 92, 609.
93. Ehrenreich, H., & Cohen, M. H. (1959). A self-consistent field approach to the many electron problem. *Physics Review*, 115, 786.
94. Ren, X., Rinke, P., Joas, C., & Scheffler, M. (2012). Random phase approximation and its applications in computational chemistry and material science. *Journal of Materials Science*, 47, 7447.
95. Runge, E., & Gross, E. K. U. (1984). Density functional theory for time dependent systems. *Physical Review Letters*, 52, 997.
96. van Leeuwen, R. (1998). Causality and symmetry in time dependent density functional theory. *Physical Review Letters*, 80, 1280.
97. Keldysh, L. V. (1965). Diagram technique for non-equilibrium processes. *Soviet Physics – JETP*, 20, 1018.
98. Louie, S. G., & Cohen, M. L. (2006). *Conceptual foundation of materials: A standard model for ground and excited states*. Amsterdam: Elsevier.
99. Hedin, L., & Lundqvist, S. (1969). Effects of electron-electron and electron-phonon interactions on the one electron states of solids. *Solid State Physics*, 23, 1.
100. Hybertsen, M. S., & Louie, S. G. (1986). Electron correlations in semiconductors and insulators: Band gaps and quasiparticle energies. *Physical Review B*, 34, 5390.
101. <http://elk.sourceforge.net/>

Chapter 13

Introduction to X-Ray Absorption Spectroscopy and Its Applications in Material Science



Aditya Sharma, Jitendra Pal Singh, Sung Ok Won, Keun Hwa Chae, Surender Kumar Sharma, and Shalendra Kumar

13.1 Basic Principle of X-Ray Generation and X-ray Absorption Spectroscopy

X-rays are photons with approximate wavelength of 0.01–10 nm, frequencies in the range of 30 petahertz to 30 exahertz (3×10^{16} – 3×10^{19} Hz), and energies in the range of 100 eV to 100 keV. X-rays are produced by interaction of accelerated electrons with metal target (e.g., Cu, Fe, Mo, W, etc.) within the X-ray tube as shown in Fig. 13.1. Generally, two types of radiation are generated from a typical X-ray generating tube: (i) characteristic radiation and (ii) bremsstrahlung (braking) radiation. Changing the X-ray tube current/voltage settings alters the properties of the X-ray beam. In the schematic of X-ray tube, in Fig. 13.1a, a small increase in the filament voltage (1) results in a large increase in tube current (2). It accelerates high-speed electrons from the hot filament negative cathode (3) within a high-vacuum tube, toward a positive tungsten target anode (4). The metallic anode is subjected to rotation to dissipate the heat generated. X-rays are generated within the tungsten anode, and an X-ray beam (5) is directed toward the window. In principle, X-rays are generated via interactions of the accelerated electrons with electrons of target metal atoms within the tube anode. The generation of characteristic X-rays is shown in Fig. 13.1b. When a high-energy electron (1) collides with an inner shell electron (2), both

A. Sharma (✉) · J. P. Singh · S. O. Won · K. H. Chae
Advance Analysis Center, Korea Institute of Science and Technology, Seoul, South Korea
e-mail: aditya16@postech.ac.kr

S. K. Sharma
Department of Physics, Federal University of Maranhão, São Luis, Maranhão, Brazil

S. Kumar (✉)
Department of Applied Physics, Amity School of Applied Sciences, Amity University Haryana,
Gurgaon, India

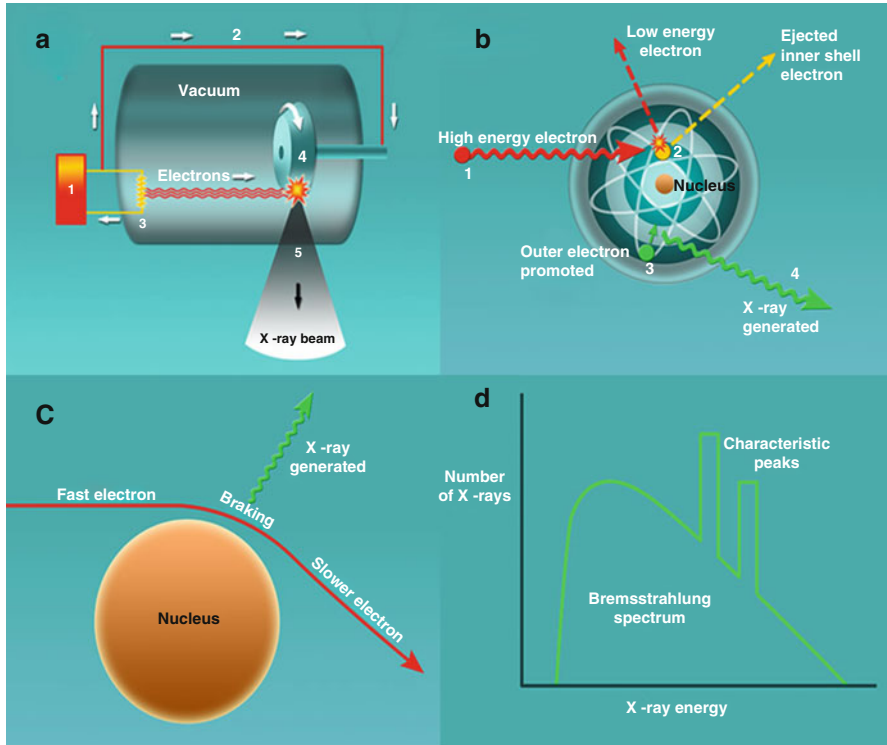


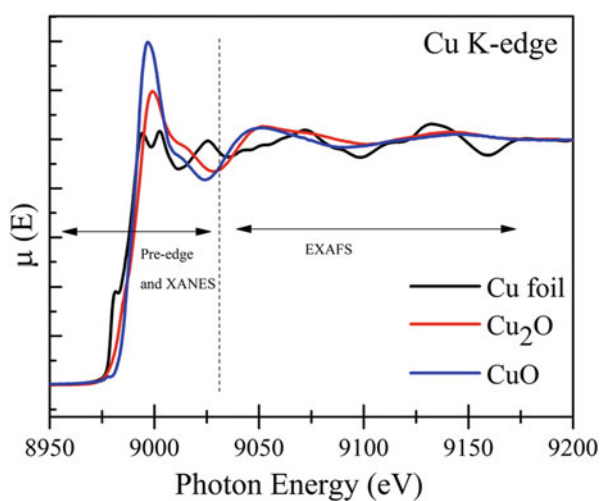
Fig. 13.1 (a) Schematic of X-ray generation tube, (b) schematic of characteristic X-ray generation, (c) schematic of bremsstrahlung X-ray generation and (d) a typical X-ray spectra from the X-ray generating tube. (Reproduced after the www.radiologymasterclass.co.uk, with permission)

are ejected from the target metal atom leaving a “hole” (or the vacancy of electron) in the electronic shell. This “hole” is filled by an outer shell electron (3) with a loss of energy emitted as an X-ray photon (4). The characteristic X-ray (e.g., K_{α}) is produced when the electron from $n = 2$ level (L shell) recombines with the “hole” at $n = 1$ level (K shell). Similarly, K_{β} characteristic X-rays can be produced, if the hole at $n = 1$ (K shell) is filled by the $n = 3$ level (M shell) electron. In a typical X-ray tube experiment, when the accelerated electrons pass through the target material, they slow down, and their path also deflects from their trajectory because of the positive charge of atomic nucleus (see Fig. 13.1c). The energy lost in slowing down and deflection of the electron is emitted as a bremsstrahlung X-ray photon. Bremsstrahlung radiation is also known as “braking radiation.” Approximately 80% of the produced X-rays, from the X-ray generator, consist of “braking radiation.” As a result of characteristic and bremsstrahlung radiation generation from an X-ray generator, a wide spectrum of X-ray energy is produced (see the Fig. 13.1d). This spectrum can be manipulated by changing the X-ray tube current/voltage settings or by adding filters to select out low-/high-energy X-rays.

Traditionally, the study of the electronic and optical properties of solids was performed with X-ray photons produced from the commercial X-ray tubes. But production of highly monochromatic X-rays with desirable photon flux was the issue to realize the practical application of X-rays in the fields of material science, chemistry, physics, metallurgy, biology, and other branches of science. Since the development of second-generation synchrotron radiation sources in the 1970s, the use of X-ray photons has expanded widely. Production of X-rays from a typical synchrotron accelerator will be discussed in the following section of the chapter. The most characteristic feature of an X-ray is that it excites a core electron; in other words X-ray spectroscopy has opened a new door to core-level spectroscopy [1, 2]. A direct implication is that the information on core-level spectroscopy is local and element specific. In order to interpret new experimental data, theoretical study of core-level spectroscopy has made continuous progress over the last 30 years and has made a major contribution to the physical understanding of spectroscopy.

More specifically, the X-ray absorption spectroscopy (XAS), with its two amendments, X-ray absorption near-edge structure (XANES) and extended X-ray absorption fine structure (EXAFS) or simply X-ray absorption fine structure (XAFS), deals with the modulation of an atom's X-ray absorption probability at energies near and above the binding energy of a core-level electron of an atom [3, 4]. Basically, the X-ray absorption coefficient $\mu(E)$ is measured in a typical XAFS measurement and explains how the X-rays are absorbed by the material as function of X-ray energy; for example, see Fig. 13.2 for the XAFS spectra of Cu metal and Cu oxides. In fact, the $\mu(E)$ of a material smoothly decreases with increasing the X-ray energy (\sim a factor of $1/E^3$) indicating penetrating nature of X-rays at high energies. However, at definite energy, which is a characteristic of the probing element in the material, there is an abrupt jump in $\mu(E)$, known as X-ray absorption edge. The absorption edge occurs when the X-ray photon has sufficient

Fig. 13.2 Cu K-edge XAFS spectra of Cu-foil, Cu_2O , and CuO which indicate the XANES and EXAFS regions in the spectra



energy to release electrons from the low-energy bound states of atoms. Therefore, the XAFS signal is originated from the physical and chemical state of the absorbing atom. XAFS spectrum of a certain compound/material is mainly sensitive to the valence state, bond distance, coordination number, and species of the material which surrounds the probed element [1–4]. An X-ray absorption spectrum is generally divided into two important sections as shown in Fig. 13.2, (i) pre-edge ($E < E_0$, where E_0 is the threshold energy of certain element edge) and XANES (where the energy of the incident X-ray beam is $E = E_0 \pm 10$ or 20 eV) and (ii) EXAFS, which starts approximately from $+30$ eV and continues up to 1000 eV above the edge [3, 4].

In most of the transition metal compounds, the metal K -edge spectra reflect the weak pre-edge peak due to the quadrupole-allowed but dipole-forbidden $1s \rightarrow 3d$ excitation (i.e., $\Delta l = \pm 2$) [3, 4]. The pre-edge region can be used to estimate the ligand field effects, spin state, and centrosymmetry of the probed element [1–4]. Metal K -rising-edge absorptions originate from the electric dipole-allowed ($\Delta l = \pm 1$) transitions [1–4]. The rising-edge region can be used to estimate the geometric structure, metal-ligand overlap via shakedown transitions, and charge on the metal center [1–4]. The XAFS signals are due to the interference events between the outgoing and reflected photoelectron waves from the central and surrounding atoms of a material. The XAFS can provide quantitative/qualitative structural information at an atomic scale about the local environment surrounding the central absorbing atom, i.e., bond distance, coordination number, and local symmetry. The XAFS is capable to investigate the local electronic/atomic structure of short-range materials, i.e., amorphous systems, liquid, and gases [1–4]. Because of the “local” sensitivity to the electronic/atomic structure of material, the XAFS provides a relatively straightforward and practical way to determine the chemical state and local electronic/atomic structure for a probed element and has been used routinely in a wide range of scientific fields, including material science, mineralogy, environmental science, catalysts research, and biology. In the following sections, basic principles and theoretical descriptions of the origin of XAFS spectra are provided.

X-Ray Absorption and Absorption Coefficient

X-rays are light photons with the wavelengths of ~ 25 to 0.25 Å or energies ranging from ~ 500 to 500 keV. In this energy regime, X-ray photons can be absorbed by the variety of materials through the *photoelectric effect*. An X-ray photon is absorbed by an electron in a tightly bound quantum core level (such as the $1s$ or $2p$ level) of an atom and results in an electronic transition to the continuum states, provided that the energy of the X-ray photon is higher than the binding energy of the bound electron, as shown in Fig. 13.3. If the energy of X-ray photon is less than the binding energy of the bound electron, the electron will not be perturbed from the well-defined quantum state and will not absorb the X-ray. In the X-ray absorption technique, we are mainly concerned with the absorption coefficient μ , which gives the X-ray absorption probability according to the Beer-Lambert law; $I_t = I_0 e^{-\mu t}$,

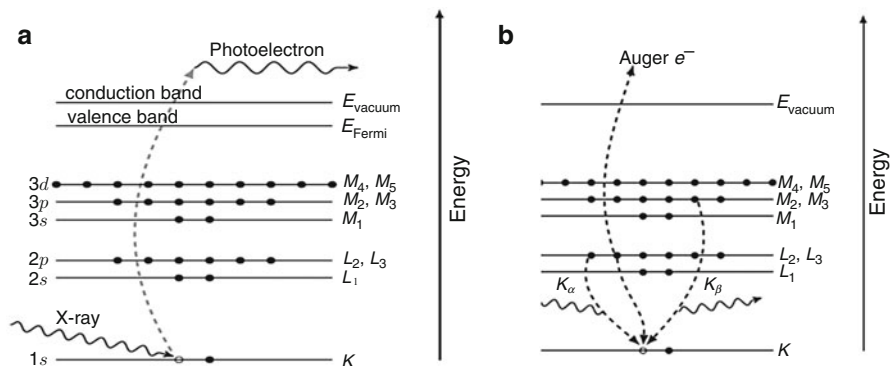


Fig. 13.3 (a) X-ray absorption by a core-level electron of an atom. A core-level electron is promoted out of the atom, creating a photoelectron and core hole. (b) Decay processes of the photoelectron either via fluorescence process (i.e., emission of K_{α} and K_{β} radiations) or via secondary electron emission (i.e., Auger's effect). (Adapted from the [3], with permission)

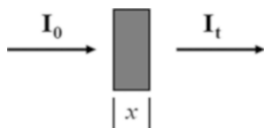


Fig. 13.4 X-ray absorption measurements: an incident beam of monochromatic X-rays of intensity I_0 passes through the sample of thickness, t , and the transmitted beam has intensity I_t

where I_0 , t , and I_t are the intensity of incident X-ray on the sample, sample thickness, and transmitted intensity through the sample, respectively, as shown in Figs. 13.3 and 13.4.

The absorption coefficient μ is a smooth function of energy and explicitly depends on the energy of incident X-rays E , sample density ρ , atomic mass A , and atomic number Z , roughly given as [3, 4]:

$$\mu \approx \rho Z^4 / AE^3 \quad (13.1)$$

Due to the Z^4 dependence of absorption coefficient of elements, the XAS can be applied to investigate the valence state and coordination chemistry of two close atomic number species in the same sample. For example, Cu and Zn coordination chemistry was precisely studied by the XAS from the $Zn_{1-x}Cu_xO$ solid solutions [5]. In fact, strong dependence of μ on both Z and E is a fundamental property of X-rays and makes the XAS useful for the medical and other imaging techniques such as X-ray computed tomography.

Following an absorption event, the atom is said to be in an excited state with one core hole and a photoelectron. The excited state is eventually decayed typically within a few femtoseconds of the absorption event. The decay process can be

completed either by the fluorescence effect (i.e., emission of X-rays of well-defined energies) or Auger's effect (i.e., ejection of secondary electrons), as presented in Fig. 13.3b. Either of these processes can be used to measure the X-ray absorption spectrum of a sample. In general, in the soft-energy regime, the Auger's process is dominant, but in the hard-energy regime, the fluorescence processes are likely to occur [3, 4]. In the following sections, we will discuss the modes of data collection either in total electron yield (TEY) mode or total fluorescence yield (TFY) mode.

13.2 Theoretical Description

13.2.1 Dipole and Quadrupole Approximation

The perturbation theory of quantum mechanics enlightens that the transition rates between the core and the final states are proportional to the product of the density of states, ρ , and squared modulus of the matrix element M and can be expressed as [2, 4]:

$$\mu \propto |M|^2 \rho \propto \langle f | H_p | i \rangle^2 \rho \quad (13.2)$$

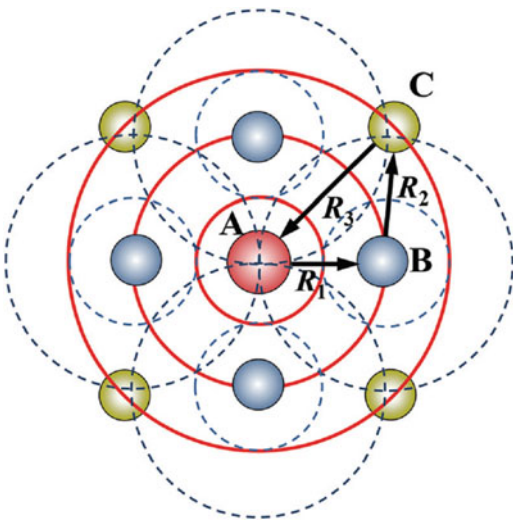
Here, $|f\rangle$ and $|i\rangle$ denote the final and initial states, respectively, and H_p represents the interaction Hamiltonian that causes the transition and is proportional to the scalar product of the electron momentum operator \vec{p} and vector potential \vec{A} of the X-ray:

$$H_p \propto \vec{A} \cdot \vec{p} \quad (13.3)$$

In an X-ray absorption event, the photoelectron is promoted to a free or continuum state and treated as outgoing wave which travels outward and undergoes multiple-scattering events with the neighbor atoms as presented in Fig. 13.5 [6].

Interference between the outgoing and scattered waves is directed by the wavelength of photoelectron and local environment of absorbing atom (i.e., atomic positions of neighboring atoms with respect to absorbing atoms, as shown in the Fig. 13.5 that the R_1 , R_2 , and R_3 are the dissimilar lengths). The wavelength of photoelectron is inversely proportional to the photoelectron momentum and therefore changes with photon energy. Thus, the final state in the X-ray absorption event is an energy-dependent superposition of outgoing and scattered waves [2–4]. By considering highly localized nature of initial states of the absorbing atom, the matrix element M , in Eq. 13.2, has to be dependent on the magnitude of the final-state wave function at the site of the absorbing atom [2, 4]. The constructive or destructive interference of outgoing and scattered waves thus increases or decreases the absorption probability, creating an energy-dependent fine structure

Fig. 13.5 A schematic presenting absorbing atom (red color, A) and first (blue, B) and second (green, C) neighboring atoms. An interference pattern can be created by the outgoing wave (red-colored solid lines) and reflected (blue-dotted lines) photoelectron waves. (Adapted from the [6], with permission)



of the absorption coefficient or the XAFS spectrum of a certain element which may be surrounded by the similar/diverse atomic species.

Indeed, this is a many-body problem where all electrons of the absorbing atom would have to be considered. In practice, however, it is generally assumed that only one electron is involved in the transition, and corrections due to many-body effects are added at a later stage. By using the single-electron approximation and dipole approximation, the quantity of Eq. 13.3 can give [4]:

$$\mu \propto \langle f | \hat{\varepsilon} \cdot \vec{r} | i \rangle^2 \rho \quad (13.4)$$

where $\hat{\varepsilon}$ denotes the X-ray polarization vector. Though, the dipole approximation is sufficient for low/middle Z elements; however, quadrupole interactions may become more important for the high Z elements and L -edges [4].

Practically, the synchrotron radiation is linearly polarized in the horizontal plane. The matrix element in Eq. 13.4 depends on the local orientation/geometry of the absorber and scattering atoms with respect to the X-ray polarization. The matrix element in Eq. 13.4 is also subject to the selection rules for the transitions from one quantum state to another, induced by electromagnetic radiation, i.e., $\Delta l = \pm 1$ and $\Delta m = 0, \pm 1$ for electric dipole interactions. Here, l and m denote the orbital angular momentum quantum number and its projection on the quantization axis, respectively [2, 4]. The initial core state of the electron is within the good approximation given by an atomic-like state with well-defined quantum numbers l and m . In contrast, the final state is usually a superposition of wave functions with different values of l and m , and only the fraction with the appropriate symmetry is of relevance for the transition [2, 4]. Thus, for K - and L_1 -edges (s states with $l = 0$), transitions occur only to final states containing p symmetry, while for L_2 - and L_3 -edges (p states with $l = 1$), transitions are only allowed to final states containing s or d symmetry.

13.2.2 Quasi-particle Model

In a typical X-ray absorption event, the initial state (i.e., an incident photon and core-level electron) is well approximated by an atomic-like state. But, the final state is an excited state and characterized by the presence of a core-hole and photoelectron wave. In the quasi-particle model, these final states, Ψ_f , are eigenstates of the Dyson equation, which is analogous to the Schrodinger equation for excited states [2, 4]:

$$h' \psi_f = \left[\frac{p^2}{2m} + V' + \sum (E_f) \right] \Psi_f = E_f \Psi_f \quad (13.5)$$

In Eq. (13.5), E_f denotes the energy of the photoelectron in the final state. The non-Hermitian Hamiltonian h' of the final state is characterized by the Coulomb potential V' calculated in the presence of a screened core hole and by the complex valued and energy-dependent self-energy $\Sigma(E_f)$ which incorporates many-body effects and extrinsic inelastic losses [2, 4]. The non-Hermiticity of h' is due to the complex nature of the eigenvalues E_f and is responsible for the finite lifetime of the final state [2, 4].

13.2.3 Multiple-Scattering Approach

In the multiple-scattering approach, we separate the potential of Eq. 13.5 into individual contributions, $v_{\vec{R}}$, which are localized at each atomic site \vec{R} [2, 4]:

$$V' + \sum (E_f) = \sum_{\vec{R}} v_{\vec{R}} (\vec{r} - \vec{R}) \quad (13.6)$$

The overall scattering not only depends on the energy of outgoing photoelectron waves (with energy of several eV or more above the threshold) but also depends on the potential in the core of neighboring atoms which is generally a spherical potential [2, 4]. In this regard, the ‘‘muffin-tin’’ approximation is well suited which assumes spherically symmetric atomic potentials out to a finite radius and a constant potential in between the atoms [2, 4, 7, 8]. This approximation is a good description for the close-packed structures but works less well for open structures. However, deviations are most prominent for small anisotropic systems close to the absorption threshold [2, 4]. Despite this approximation, the calculation of final states turns out to be computationally demanding and very often impractical. The multiple-scattering approaches therefore make use of the photoelectron Green’s function or propagator G in real space. Applying the identity [4, 7]

$$-\frac{1}{\pi} \text{Im } G = \sum_f |f\rangle \delta(E + E_i - E_f) \langle f| \quad (13.7)$$

where E and E_i denote photon energy and electron energy in the initial state, respectively, Eq. 13.4 can be written as [4, 7]

$$\begin{aligned} \mu &\propto \sum_f \langle i | \hat{\varepsilon} \cdot \vec{r}' | f \rangle \delta(E + E_i - E_f) \langle f | \hat{\varepsilon} \cdot \vec{r} | i \rangle \\ &\propto \text{Im} \langle i | \hat{\varepsilon} \cdot \vec{r}' G \hat{\varepsilon} \cdot \vec{r} | i \rangle \end{aligned} \quad (13.8)$$

The propagator \mathbf{G} can be treated as the sum of two contributions: (i) \mathbf{G}^{sc} due to multiple scattering from the surrounding elements and (ii) \mathbf{G}^{c} from the central atom, $\mathbf{G} = \mathbf{G}^{\text{c}} + \mathbf{G}^{\text{sc}}$. Based on these contributions, expression of μ can be given in terms of an atomic background μ_0 of the central absorber and the fine structure χ due to multiple scattering from the surrounding elements, i.e., $\mu = \mu_0(1 + \chi)$ [4, 7, 8]. Within this framework, the fine structure component can be written as

$$\chi = \text{Im } e^{i\delta} \left[1 - G^0 T \right]^{-1} G^0 e^{i\delta'} \quad (13.9)$$

where G^0 denotes the free particle propagator and T represents the scattering matrix, while δ and δ' are partial-wave phase shifts [4, 7, 8]. The matrix term in Eq. 13.9 can be written as a series expansion:

$$\left[1 - G^0 T \right]^{-1} G^0 = G^0 T G^0 + G^0 T G^0 T G^0 + \dots \quad (13.10)$$

The fine structure contribution can thus be understood as the sum of individual scattering contributions arising from all possible paths of the photoelectron from the absorbing atom and back. The first, second . . . terms in Eq. 13.10 correspond to single, double . . . scattering at surrounding atoms. The advantages of this multiple-scattering Green's function formalism lie in the fact that it treats XANES and EXAFS within the same unified theory, that it avoids explicit calculation of the final-state wave functions, and that it naturally incorporates inelastic losses and other quasi-particle effects [2, 4, 7, 8]. As an alternative to the path expansion, the fine structure contribution can also be expressed as the sum of irreducible n -body interactions which contain all scattering contributions due to a particular arrangement of n atoms including the absorber. This approach is directly related to the n -body distribution functions and is thus particularly suited for the study of highly disordered systems [2, 4, 7, 8].

13.2.4 Dipole Selection Rules and Transition Probabilities

Since the core state, from which the electron is removed, is known to be deeply bound and the dominating interaction exist between atomic nucleus and the electrons of the central or photo absorbing atom [1–4]. Consequently, the initial state can be approximated as an atomic-like state of well-defined quantum numbers, i.e., l and m , and the transition operator in the dipole approximation is proportional to the vector \vec{r} [1–4]. Contrary to the initial state, the spatial dependence of the final-state wave function is complicated. This is because of the fact that the final state is largely dependent on the potentials of the surrounding elements with respect to the central absorbing atom [1–4]. As mentioned in the above section, the final-state wave function can be expressed as a linear combination of functions with specific l and m , i.e., spherical harmonics centered on the absorbing atom, which are eigenfunctions of the operators L^2 and L_z [1–4]. Because of the orthogonality of spherical harmonics, the transition matrix element projects out only the part of the final-state wave function that has the appropriate symmetry for an allowed transition.

Electric dipole selection rules tell us that $\Delta l = \pm 1$ and quadrupole selection rules $\Delta l = \pm 2, 0$ [1–4]. For example, excitation of the 1s level ($l = 0$) only has nonzero dipole transition strength for transitions to the p symmetry ($l = 1$) part of the final-state wave function. The transition operator $x \pm iy$ causes transitions from $l = 0, m = 0$ to $l = 1, m = \pm 1$, while the transition operator z causes transitions to $l = 1, m = 0$ [1–4]. Dipole selection rules, therefore, imply that for K - and L_1 -edges, allowed transitions are to the states containing p symmetry. For L_2 - and L_3 -edges, allowed transitions are to the final states containing d and s symmetry. By applying these rules, it is important to realize that angular momenta are always referred to a specific origin. A p state centered on a neighboring atom is not a p state with respect to the central atom, although it can be expressed as a linear combination of different angular momentum states with respect to the central atom [1–4].

13.2.5 X-Ray Absorption Cross Section

X-ray absorption induced electronic transition probability, from the initial i state to final f state, is generally expressed in terms of X-ray absorption cross section σ_x . The σ_x is defined as the number of electrons excited per unit time divided by the number of incident photons per unit time per unit area [9–11]. The σ_x has the dimension of (length)². Basically, by applying dipole approximation and Fermi's golden rule, σ_x can be illustrated as [9–11]

$$\sigma_x = \frac{4\pi^2 h^2 e^2}{m^2} \frac{1}{hc E} \xi(E) |\langle f | e \cdot p | i \rangle|^2 \delta(E + E_i - E_f) \quad (13.11)$$

where e , m , E , $\xi(E)$, $\delta(E + E_i - E_f)$, and $|\langle f|e \cdot p|i\rangle|$ are the electron charge, electron mass, energy of incident photon, the energy density of final states, delta function for the conversion of energy, and the dipole matrix, respectively.

The presence of the dipole matrix term ($|\langle f|e \cdot p|i\rangle|$) reveals the importance of an effective interaction between the sum of the linear momentum operator of electrons, p , and the unit vector in the direction of the incident X-ray photons. The dipole matrix term is the theoretical basis for the polarization-dependent XAFS measurements that are often used for the determination of molecular orientation of adsorbates on surfaces [9]. In addition, the nature of the dipole transition also implies that the XAFS excitation should obey the dipole selection rule, which states that the change in angular momentum quantum number should be $\Delta l = \pm 1$ between the initial and final states. Therefore, for K -edge transitions (from an initial s state), the final states should have contributions from p orbitals. Similarly, for L -edge transitions (from an initial p state), the final states can be either s or d orbitals. The X-ray absorption cross section is proportional to the energy density of the final state $\xi(E)$, which qualitatively explains the direct correlations between a XAFS spectrum and the nature of the unoccupied states. However, more quantitative correlation can only be made by determining the exact form of $\xi(E)$, which depends on the normalization of wave functions.

In principle, the delta function in Eq. 13.11 is only valid for a final state with infinite lifetime. For a more quantitative analysis, it should be replaced by a Lorentzian to account for the finite lifetime of the final states [9]. This is an important point since the lifetime of a bound resonance state is often several orders of magnitude longer than a continuum resonance state [9–11]. The intensity for a resonance transition is often expressed by a dimensionless term, optical oscillator strength, f , which is related to the X-ray absorption cross section in Eq. 13.11 by [9]

$$\sigma_x = \frac{2\pi^2 h e^2}{m c} \frac{df}{E} \quad (13.12)$$

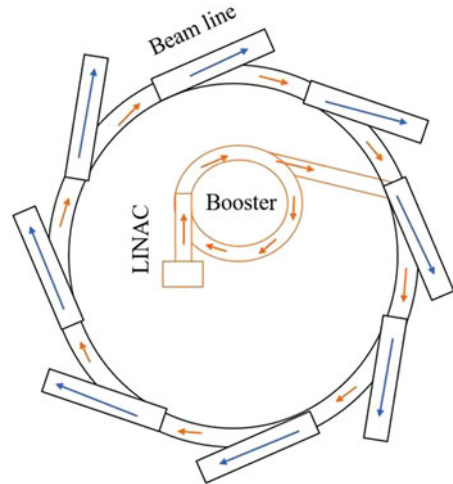
In other words, the resonance intensity (oscillator strength) in XAFS is the energy integral of the X-ray absorption cross section.

13.3 Experimental Aspects

13.3.1 Synchrotron Radiation Source

When electrons or other charged particles moving at relativistic speeds are forced by magnetic fields to follow curved trajectories, they emit electromagnetic radiation in the direction of their motion. This radiation is known as synchrotron radiation. In nature, cosmic rays are the sources of synchrotron radiation; however, manmade sources of this radiation are accelerators based on storage rings [1, 2, 12]. Pohang Accelerator Laboratory (PAL), South Korea, is a well-known synchrotron radiation

Fig. 13.6 Schematic planar view of a synchrotron radiation facility



facility among all the known synchrotron centers. A typical synchrotron radiation facility consists of circular evacuated pipes where the electrons are forced to follow circular paths (storage rings) under the action of magnetic field, produced by bending magnets placed along the circumference (Fig. 13.6). Before entering to storage rings, electrons have to pass through the following sections of synchrotron facility [1, 2, 12].

13.3.1.1 Linear Accelerator (LINAC)

Electrons are generated and accelerated by the LINAC section of synchrotron, and the typical energy of such accelerated electrons is the order of several MeV. Free electrons are generated in long pulses (several microseconds) at the cathode, which is a heated block of negatively charged metal. From this a shorter pulse (ca. 20 ns) is selected by application of an electrostatic field in the chopper and the beam and then narrowed down by a collimator. All this time they get accelerated toward the anode, which is a positively charged ring of metal, whose field guides the electron beam through it and toward the pre-buncher. This whole setup is called the “electron gun” [12]. In the pre-buncher the electron beam gets subdivided into bunches ca. 0.3 ns long. They then reach the actual LINAC, where the electron bunches get accelerated.

13.3.1.2 Booster Rings

These rings are used to boost the energy of these electrons to several GeV before entering to storage rings. Thus, combination of linear accelerator, booster rings, and storage rings is used to produce synchrotron radiation in the laboratory.

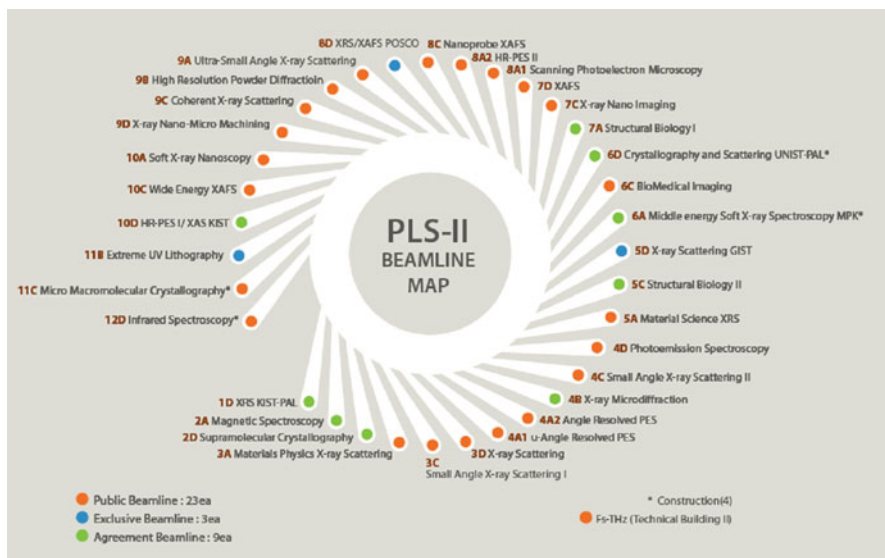


Fig. 13.7 Beamlines of Pohang Accelerator Laboratory (taken from www.pal.postech.ac.kr, with permission)

Radiation obtained from storage rings is carried out by a typical instrumentation to an experimental end station. This typical instrumentation is often termed as “beamline.” A synchrotron radiation center may consist of several beamlines depending upon applications and measurement requirements. For example, Pohang Accelerator Center, Pohang, South Korea, is a recognized synchrotron radiation facility in the world and consists of almost 34 beamlines (Fig. 13.7). (KIST) Korea Institute of Science and Technology 1D and 10D beamlines are among them which are dedicated to perform EXAFS and NEAXAFS measurements [13, 14].

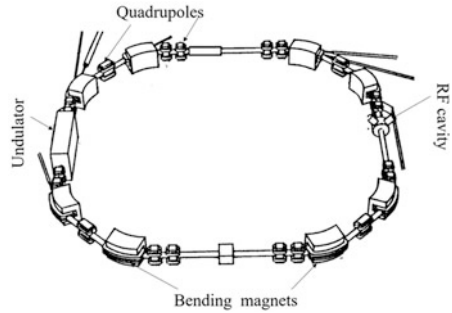
13.3.1.3 Storage Ring and Its Components

As described earlier storage rings in the accelerators play important role in achieving synchrotron radiation. This is done by a number of devices attached to the storage ring. In this section a short description is given for these devices. A schematic of actual storage ring is shown in Fig. 13.8.

RF System

The RF or radio frequency system is responsible for supplying energy to the electrons as they move around the storage ring. This is necessary since the synchrotron radiation generated for the experiments constantly drains the electrons’

Fig. 13.8 Typical schematic of storage ring with various components at PAL



energy [1, 2, 12]. All energy is supplied as electromagnetic radiation with a wavelength of about 0.1 m (which equates to a frequency of 3 GHz as before), i.e., as microwaves. The RF system is made up of three components:

Klystron – it is a powerful microwave amplifier, i.e., it takes a weak input signal and generates a strong output signal, which can then be used as energy in microwave form, which in this case is transferred to the electrons. Waveguides are coupled to the klystron as a means of transporting the radiation toward the cavity [12].

Waveguide – a waveguide in the general sense is a means of efficiently transporting electromagnetic radiation, for example, a coaxial cable for the TV signal or an optical fiber. In the example of the RF system, the waveguide consists of a hollow boxlike metal structure of approximated size of the radiation's wavelength [12].

Radio frequency cavity – the radiation then reaches the RF cavity, which is shaped to resonate at 3 GHz as well. Energy is transferred to the passing electrons as described for the LINAC. This makes up for the energy lost as synchrotron radiation during each cycle. The whole process has to be timed extremely accurately, since the wave package traversing the cavity every 200 ns needs to coincide precisely with a specific phase of the electromagnetic radiation to provide the necessary energy [12].

Bending Magnets

After leaving LINAC, the electron bunches then enter the storage ring, where all the actual research happens. To allow the electrons to circle the ring for many hours, they travel in a metal tube in which an ultrahigh vacuum is maintained. The air pressure in here is only about a hundred billionth of the outside pressure. The electrons are kept on their circular path with the help of strong magnetic fields (1.3 Tesla) applied by the bending magnets. To keep the electrons confined within the small vacuum chamber, elaborate electronics constantly refocus the beam. Also, the bending magnets are one of the sources of synchrotron light, where a narrow searchlight-like cone of radiation is emitted as the electrons pass the bend [12].

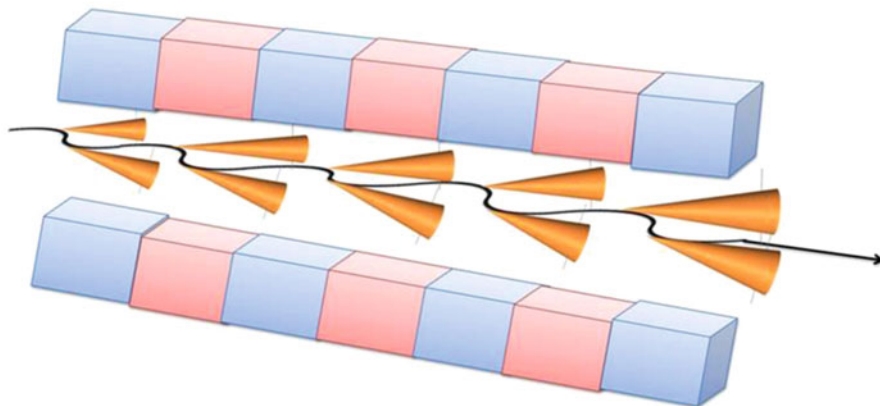


Fig. 13.9 Artistic view of the radiation beam emission from a multipole wiggler magnetic structure. There the yellow and green blocks are representing the magnetic poles (either S or N) [12]

Insertion Devices

Insertion devices (ID) are periodic magnetic structures installed in the straight sections of storage rings (Fig. 13.9). In these, the electrons are forced on a slalom course by an array of permanent magnets. Wigglers provide radiation with the same properties as bending magnets, only with an intensity enhanced by the number of magnet poles [12]. Insertion devices are of two kinds.

Wigglers

Basically, wiggler is a multipole magnet made up of a periodic series of magnets (N periods of length λu , the overall length being $L = N\lambda u$) [12], whose magnetic field forces the electrons to wiggle around the straight path. The alternating magnetic field is normally applied in the vertical direction, so the sinusoidal trajectory of the electron beam lies in the horizontal plane. Electrons follow in this way a curved trajectory with a smaller local radius of curvature with respect to the one of the dipole-bending magnet, because in a wiggler (Fig. 13.10), magnetic fields, higher than in a bending magnet can be used [12].

Undulators

These “insertion devices” use weaker magnetic fields and shorter magnets. The electrons move in weak undulations of short period, and the radiation cones generated in each period overlap in a way that they interfere and give the radiation special properties. In order to define undulators, a dimensionless parameter K is introduced based on Fig. 13.10. It is given by the ratio between the wiggling angle

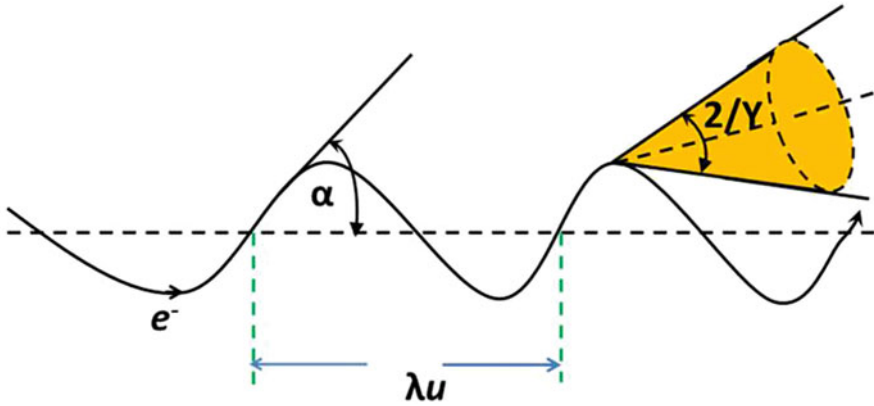


Fig. 13.10 Schematic view of the “wiggler” regime, where λu represents the period of the oscillations [12]

of the trajectory, α , and the natural angular aperture of synchrotron radiation, $1/\gamma$, $K = \alpha\gamma$. In a wiggler the transverse oscillations of the electrons are very large and the angular deviations, α , much wider than the natural opening angle $\psi = \gamma^{-1}$; therefore $K \gg 1$ [12]. In these large K devices, the interference effects between the emissions from different poles can be neglected, and the overall intensity is obtained by summing the contribution of the individual poles. An undulator is very similar to a wiggler, but its K value is less than 1, that means the wiggling angle α is smaller than, or close to, the photon natural emission angle γ^{-1} [12].

Quadrupoles

Quadrupole magnets have a group of four magnets laid out so that in the planar multipole expansion of the field, the dipole terms cancel, and the lowest significant terms in the field equations are quadrupole [12]. Quadrupole magnets are useful as they create a magnetic field whose magnitude grows rapidly with the radial distance from its longitudinal axis. The main function of quadrupoles is beam focusing inside storage ring.

13.3.2 X-Ray Beamlines

13.3.2.1 General Layout

A typical beamline consists of the following section for the smooth travel of synchrotron radiation up to the end station:

1. *Windows* are thin sheets of metal, often beryllium, which transmit almost the entire beam but protect the vacuum within the storage ring from contamination.
2. *Slits* control the physical width of the beam and its angular spread.
3. *Focusing mirrors* (one or more mirrors, which may be flat, bent flat, or toroidal) of the beamline are used to collimate (focus) the beam.
4. *Monochromators* are the devices based on diffraction by crystals which select particular wavelength bands and absorb other wavelengths which are sometimes tunable to varying wavelengths and sometimes fixed to a particular wavelength. A monochromator can filter out a single desired wavelength of radiation with a narrow bandwidth. Depending upon the energy of the radiation, perfect silicon one-crystal and grating monochromators are used.
5. *Spacing tubes* are the vacuum maintaining tubes which provide the proper space between optical elements and shield any scattered radiation.

These components are generally utilized in a typical beamline; however, their nature may differ depending upon the energy of radiation. To clarify this, examples of two beamlines are given below.

13.3.2.2 Soft X-Ray Beamline (KIST Beamline at Pohang Accelerator Laboratory, South Korea)

Optical Layout

Figure 13.11 shows the schematic optical layout of the soft X-ray beamline (10 D, KIST-PAL beamline). This beamline is designed to work at low energy. The energy range for this beamline is 200–1500 eV. The total length of the beamline from the light source is about 28 m. The beamline consists of three main parts: a pre-focusing mirror system (horizontal focusing mirror, HFM; vertical focusing mirror, VFM), a monochromator system (S1-CM-VLSPG-S2), and a refocusing mirror system (RFM). The pre-focusing mirror system focuses the beam horizontally and

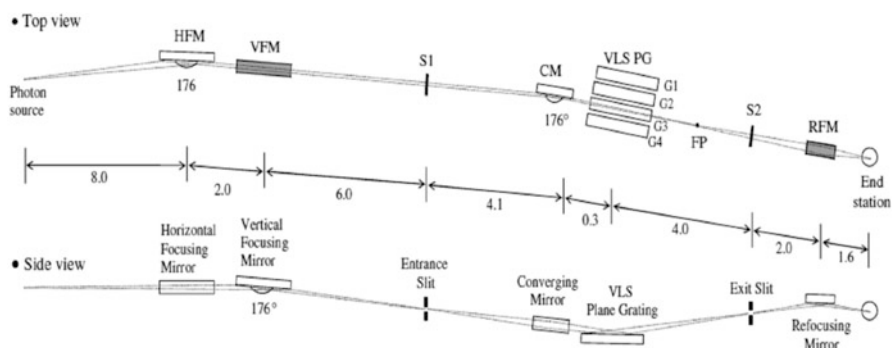


Fig. 13.11 Optical layout of 10D beamline at PAL (Adapted from Ref. [13], with permission)

Table 13.1 Characteristics of gratings

Gratings	Energy range (eV)	Groove density (grooves/mm)	Coating material
G1	100–250	400	Ni
G2	250–400	1000	Au
G3	400–800	1800	Au
G4	800–1400	2800	Au

vertically through two Au-coated spherical mirrors. The first mirror, a horizontal focusing mirror (HFM), focuses the radiation horizontally onto a focal point (FP) in Fig. 13.11. The second mirror, a vertical focusing mirror (VFM), focuses it vertically onto the entrance slit (S1). The mirrors maintain reflectivity over 60% for an incident angle of 88° in the photon energy range of 100–1800 eV. The monochromator system consists of the entrance slit (S1), a converging cylindrical mirror (CM), the VLSPGs, and the exit slit (S2). Although the gratings themselves can focus the diverging beam from the entrance slit, the CM is inserted in front of the VLSPGs to reduce the footprint at the gratings. It focuses the beam onto the exit slit by using its sagittal radius in combination with the VLSPGs and deflects horizontally the converging beam onto the VLSPGs at the same time.

The four interchangeable plane gratings are used to cover the energy range of 100–1800 eV. The gratings with 400, 1000, 1800, and 2800 grooves/mm are chosen to cover the energy ranges of 100–700, 300–1100, 500–1500, and 800–1800 eV, respectively. The characteristics of all the gratings and mirrors are summarized in Table 13.1. The openings of S1 and S2 can be controlled from 10 to 500 mm, and it determines the energy resolution. The HFM, VFM, S1, and VLSPGs are water cooled with copper sheets and tubes, where low-conducting water passes through. Finally, the refocusing mirror (RFM) focuses the monochromatic light from the monochromator onto the sample position efficiently. The 10 D beamline has two end stations: (i) high-resolution photoemission spectroscopy (HRPES) end station and (ii) soft X-ray absorption spectroscopy end station. The beam can be tuned to any of the end station by bending the RFM in tangential direction. Since it is possible to change the vertical focal point by bending the RFM in tangential direction, the beam can be focused on the sample positions of both HRPES and soft X-ray reflectivity end stations. Detailed implication and assembling of this beamline are reported elsewhere [13].

Experimental End Station

Figure 13.12 shows the layout of the end station for soft X-ray absorption spectroscopy measurements. The end station is for the measurement of NEXAFS with fluorescence yield detection. The base pressure of the chamber is low, about 10^{-8} torr. The sample stage and detector arm are rotated around the center of the chamber from 0 to 180° with a resolution of 0.001° . The rotations are

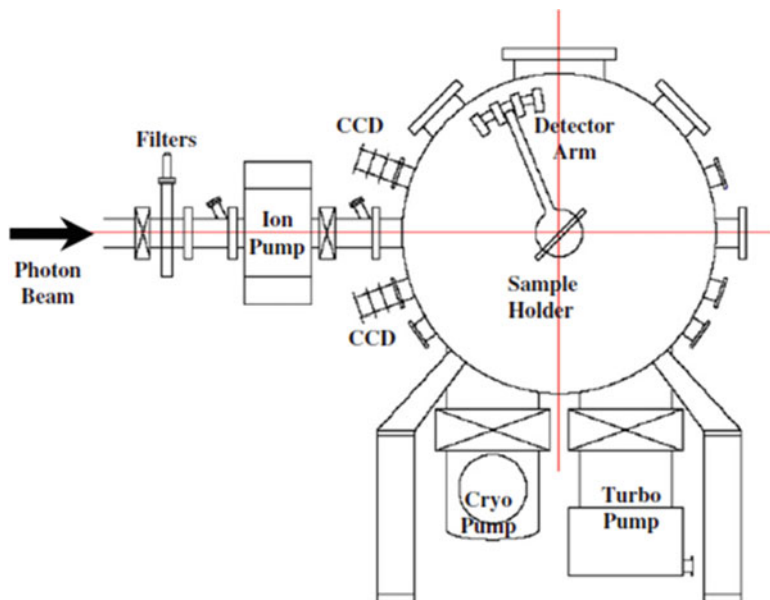


Fig. 13.12 Near-edge X-ray absorption fine structure measurements experimental end station of 10D beamline at PAL (Adapted from Ref. [13], with permission)

driven by the stepping motors attached outside the chamber through a two-axis coaxial ferrofluidic rotation feed through. The sample-detector distance is about 300 mm. On the detector arm, an electron detector using a double micro-channel plate for partial electron yield detection in NEXAFS, a Si p-i-n photodiode for fluorescence yield detection in NEXAFS, an AXUV photodiode with a slit for X-ray reflectivity/scattering, and an in-vacuum CCD camera for alignment are installed. To align the sample and the incident X-ray beam, the sample stage has also four degrees of freedom for X, Y, and Z motions with the resolution of 0.05 mm and tilt angle rotational motion. Moving ranges for each translational motions are 650 mm for X, 620 mm for Y, and 630 mm for Z. Thus, a sample as large as 100×60 mm can be installed and measured with the selection of sampling position. Data collection and the movement of the sample stage and detector are controlled by customized software programmed with LabViews. To facilitate NEXAFS measurements in both fluorescence yield mode along with electron yield mode, another experimental end station is also designed (Fig. 13.13).

Measurement Procedure

Incident photon flux (I_0) is measured by Au mesh placed in the path of beam. Samples are mounted on Cu holder with the help of carbon tape and placed in high vacuum (5×10^{-8} torr). Experimental setup allows NEXAFS measurements in both

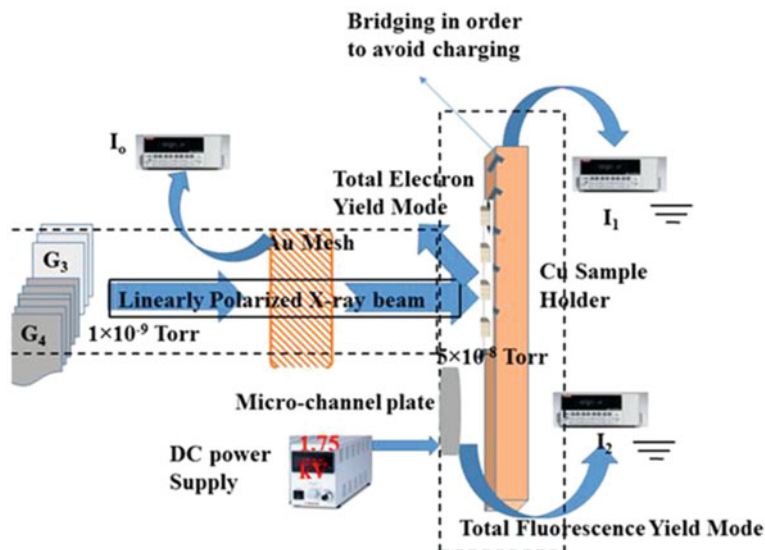


Fig. 13.13 Schematic of measurement setup at 10D-KIST beamline at PAL for simultaneous measurement at TEY and TFY modes

surface sensitive (total electron yield) and bulk sensitive (total fluorescence yield) modes.

Total Electron Yield Mode

During a typical X-ray absorption measurement, not only the Auger electrons but photoelectrons can also be emitted from the material provided that the energy of incident photon is larger than the binding energy of the electrons present in the different atoms of a probed compound. However, the kinetic energy of the emitted photoelectrons will be changed if the energy of incident photon is varied during the measurement. On the other hand, the kinetic energy of Auger electrons is independent of the incident photon energy and quite characteristic for a certain Auger transition from a specific element. Based on the kinetic energies, electron yield measurements in XAS can be carried out in three ways: (i) total electron yield (TEY), (ii) partial electron yield (PEY), and (iii) Auger electron yield (AEY). Details about the disadvantages and advantages, as well as the experimental setup, of the three methods are reported elsewhere [4, 12–14]. In the TEY method of data collection, all of the electrons (i.e., photoelectrons and Auger electrons) are collected with an electron channeltron multiplier. In this mode of data collection, the low-energy electrons (<20 eV, with large mean free path) are collected. TEY method is very effective for the topmost surface layers. In PEY method, a fraction of total electrons is collected by applying a retarding electric field in front of the electron detector. The disadvantage of PEY method is that it detects both photoelectrons and Auger electrons and also detects those electrons which undergo inelastic collisions with the substrate material (in case of thin films deposited on

a substrate). Consequently, the detection limit in PEY is not very well defined. Experimentally, PEY measurements can be carried out by using a standard retarding field double channel plate assembly or by placing two high transmission metal retarding grids in front of a channeltron multiplier. For a typical AEY measurement, an energy analyzer is needed at a specific Auger transition energy. Moreover, for thin films/substrate systems, the AEY method can be made much more sensitive than PEY by setting the energy window of the energy analyzer at an Auger transition of the thin films, therefore excluding contributions from photoelectrons/Auger electrons from the substrate. Predictably, the experimental setup for AEY is the most difficult among the three electron yield measurements because it requires an electron energy analyzer, such as a single-pass or double-pass cylindrical mirror analyzer.

Total Fluorescence Yield Mode

It is known that a core hole is created by excitation of core electrons by the X-ray photons. The energy gained by the annihilation of core vacancy can be released by either radiation of fluorescence photon or by Auger electrons. The rates of these two de-excitation processes are often, respectively, termed fluorescence yield (ω_f) and Auger yield (ω_a), and they satisfy the sum rule, $\omega_f + \omega_a = 1$. The relative ratios of the two decaying channels depend strongly on the atomic number of the element of interest. Similar to the TEY/PFY/AEY data collection, the XAS spectra can be collected in the TFY mode. TFY offers a higher signal-to-background ratio and applicability to insulating materials. However, it has not been considered to be suitable for concentrated samples, due to a self-absorption effect. Since, the fluorescence yield XAS represents a photon-in and photon-out technique, which has three main advantages over the TEY method: (1) It enables the XAS measurements to be carried out at non-UHV (up to torr range) conditions, allowing us to measure XAS for liquids in helium atmosphere. (2) It has a much larger information depth than the electron yield method providing an opportunity to probe bulk properties. (3) The detection of photon yield is insensitive to sample charging.

13.3.2.3 Hard X-Ray Beamline

Beamline Layout

The 1D beamline at PAL is a hard X-ray beamline covering 4–16 keV photon energy range. This beamline is equipped with a bending magnet as the X-ray source and is located at the Port No. 10B of PLS. The BL10B consists of a front end in the storage ring tunnel, a photon beam transfer line, and an experimental station in the experimental hall (Fig. 13.14).

The beamline optics is equipped with a double-crystal monochromator (DCM) and two mirror systems. The mirrors are made of silicon coated with 60 mm wide Ru (100 Å) over Pt (300 Å) along the beam direction. The angle of incidence is 4 mrad, which corresponds to a cutoff energy of 16 keV. The mirrors are placed

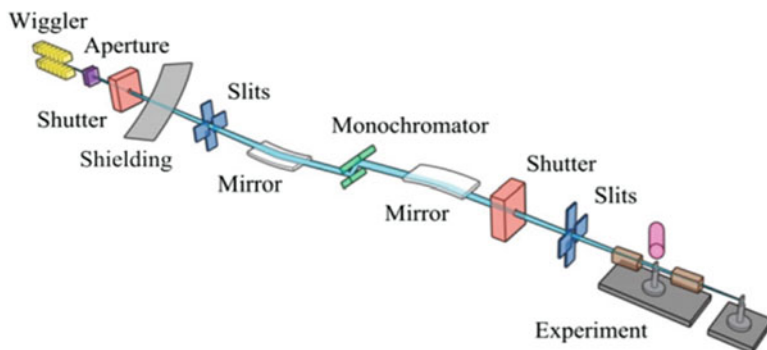


Fig. 13.14 Components of 1D beamline at PAL (taken from www.pal.postech.ac.kr, with permission)

in a cradle that is mounted kinematically onto the vessel base plate. A motorized six-strut movement system, which provides pitch, roll, yaw, height, lateral, and bendable motion, is mounted on the mirror vessel. The mirror vessel itself is fixed and decoupled from the motor motions via edge-welded bellows.

Experimental End Station

The experimental equipment is set up in an experimental hutch with dimensions of 5.2 m (length), 3.52 m (width), and 3.0 m (height) in which the sample position is located 27 m from the source. The beamline elements are located in radiation shielding enclosures, called hutches, which are the size of a small room (cabin). Its optical configuration allows high resolution and high brightness by passing a collimated beam through the DCM and by focusing the source on the sample position with unit magnification. The photon flux was measured by a calibrated AXUV-100G detector (International Radiation Detectors, Inc., USA) and a pico-ammeter (6517, Keithley, USA). The AXUV-100G detector transforms X-rays to current, and the pico-ammeter measures the current [2]. The unit for XAFS measurement is composed of a receiving slit, ionization chambers (IC SPEC, Oxford Danfysik, UK), partially depleted PIPS (passivated implanted planar silicon) detectors (Canberra Industries, USA), and a seven-element advanced hard X-ray LEGe detector array system (seven-element detector, Canberra Industries, USA). The incident beam is shaped by the receiving slit, the photon flux is monitored by the ionization chambers, and the fluorescent X-ray is measured by partially depleted PIPS detectors or seven-element detector. Schematic of EXAFS end station is shown in Fig. 13.15. Details of this beamline are reported in [14].

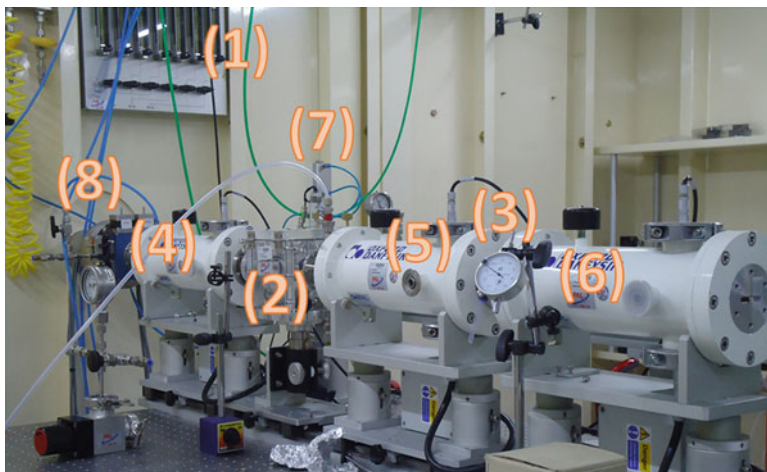


Fig. 13.15 EXAFS experimental setup at 1D KIST-PAL beamline

Measurement of Data from 1D Beamline

It consists of gas mixture system (1) which is used to fill inert gases to different chambers. Depending upon energy of the ion beam, inert gases are selected. Generally, chamber which is used for measuring incident beam current is filled with He. Chambers for measuring transmission and reference spectrum are filled with N_2 . For energy approaching to 16 keV, Ar gas or mixture of Ar and N_2 is preferred for these chambers; however, mixture of He and N_2 is filled when beam energy approaches to 4 keV. N_2 in transmission and reference chamber is best choice for measuring spectrum in the energy range 5–15 keV. In Fig. 13.15, sample is placed in a small chamber at position (2). This chamber is attached with a rotatory pump in order to isolate sample with environment. Position marked by (3) is used to place reference sample which enables simultaneous measurement of reference spectrum. Chambers for measuring incident current (I_0), transmission current (I_t), and reference current (I_r) are shown by nos. (4), (5), and (6). A fluorescence detector (7) is also attached with small chamber containing sample holder. In Fig. 13.15, (8) shows coupling from beamline to experimental station. Thus, this beamline facilitates measurement in both transmission and fluorescence mode by measuring transmission current and fluorescence current.

13.3.3 Other Lab-Source-Based XAFS Spectrometers

Besides, the synchrotron-based XAFS, lab-source-based XAFS machines are also available like *R-XAS looper* (Rigaku-Japan) and *easy-XAS-300 banc top spectrom-*

eter (USA). The lab-source-based machines are simply operated and do not require much instrumentation during their installation or functioning. By applying an appropriate target filament, detector, and monochromator arrangement, sustainable and monochromatic X-rays can be generated, and the XAS data can be collected with comparable quality to the second-/third-generation synchrotron-based XAS facility, though the energy range is limited in such machines and largely determined by the choice of *target filament* combination in the X-ray source section and selection of crystal, as a grating, in the monochromator section. Therefore, the XAFS data can be collected from certain elements only. However, the recent amendments such as accessibility of W-W and Mo-LaB₆ kinds of *target filament* combinations, various detectors (Ne, Ar, and Xe detectors), and presence of various monochromatic crystals (i.e., Ge(220), Ge(111), Ge(311), Ge(400), Ge(840), Si(400), and Si(620)) make easy access and detection of wide range of energy from such machines (i.e., 4–25 keV). This wide energy range from the lab-source machines makes them promising to scan *K*-edges and *L*-edges from a wide range of elements. The *R-XAS looper* machine at X-ray open laboratory, Korea Institute of Science and Technology, Seoul, South Korea, is capable of scanning *K*-edges from Ti to Ag and *L*-edges from the Xe to U elements in the periodic table. In the following section, we will provide a detailed description of X-ray generation, detection, and XAFS data collection from the *R-XAS looper*.

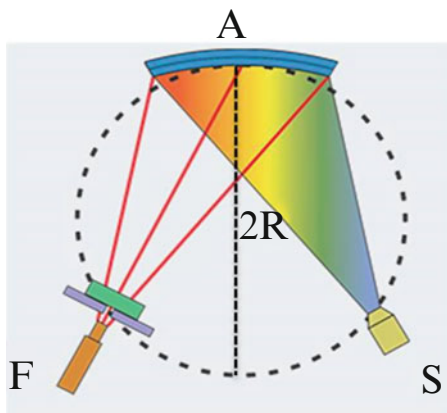
Principle of Measurement

Since highly monochromatic X-rays ($\Delta E < 5\text{--}10$ eV) are desired in a typical XAFS measurements, therefore, it is necessary to perform a crystal spectrometry. However, the ordinary spectrometry using a plane crystal utilizes only a small divergent angle, and therefore the intensity of X-rays is low, which would increase the time of XAS data collection. For this reason, the R-XAS looper machine adopts a special optical system that performs spectrometry and collection simultaneously using a Johannson-type curved crystal. In Fig. 13.16, S is an X-ray source, A is the center of monochromator crystal, and F is the receiving slit. These three points are arranged on a Rowland circle with radius R (320 mm for the R-XAS looper) in such a manner that the $SA = AF$ will be satisfied. The energy of the X-ray can be varied by controlling the distance. The monochromatic X-ray collected in this way is irradiated on to the sample, thereby measuring the intensity of X-ray before (I_0) and after (I_t) the passes from the sample. By determining the ratio between the I_0 and I_t , the absorption coefficient can be calculated as discussed in the above sections.

Configuration of Machine

The R-XAS looper is composed of two sections: (i) the spectrometer section and (ii) sample section. The spectrometer section consists of an X-ray generator, spectrometer (goniometer), divergence slit, receiving slit, and monochromator. The X-ray generator is a fixed-target tube of 3 kW. The spectrometer adopts the so-called linear spectrometer which employs stepping motors to exert control such that the distance from the X-ray source to the monochromator crystal and the distance from the crystal to the receiving slit remain equal, thereby allowing X-rays of

Fig. 13.16 Principle of focusing the optical system in R-XAS looper



any desired energy. The divergence slits and the receiving slits are variable slits driven by the stepping motors, with their widths controlled from the computer. The monochromator is provided with three axes, namely, omega, tilt, and Z. A Johannson-type monochromator crystal with a Rowland circle of 320 mm radius is mounted on the monochromator which is also controlled from the computer. The sample section consists of incoming X-ray intensity counter (I_0 -detector) which is a semi-transmission-type proportional counter with Be window on both sides and provides linearity of up to 1 million counts per seconds (cps) through combined use of high-speed electronic circuit. There are three types of I_0 -counter for the measurement of various elements, i.e., Ne, Ar, and Xe. After the I_0 -detector, sample holder is fixed with a rotating axis with respect to I_0 -detector. The rotating axis allows the users to tilt the sample with respect to the incident beam plane. After the sample holder, intensity monitor (I -counter) exists to collect the transmitted X-rays from the samples. Generally, I -counter is a high-speed scintillation counter and is capable of counting the X-rays with a high degree of detection efficiency over a broad range of energy levels. The following schematic layout of the machine shows various parts and their position (Fig. 13.17).

13.4 Data Analysis

13.4.1 XANES

The XANES data processing/analysis describes (qualitatively and nearly quantitatively) (i) the coordination chemistry (i.e., regular, distorted octahedral, tetrahedral, etc.), (ii) molecular orbitals and their hybridization (i.e., s-p/p-d hybridization, crystal field effects, etc.), (iii) band structure (i.e., the density of available occupied/unoccupied electronic states), and (iv) multiple scattering (i.e., multiple

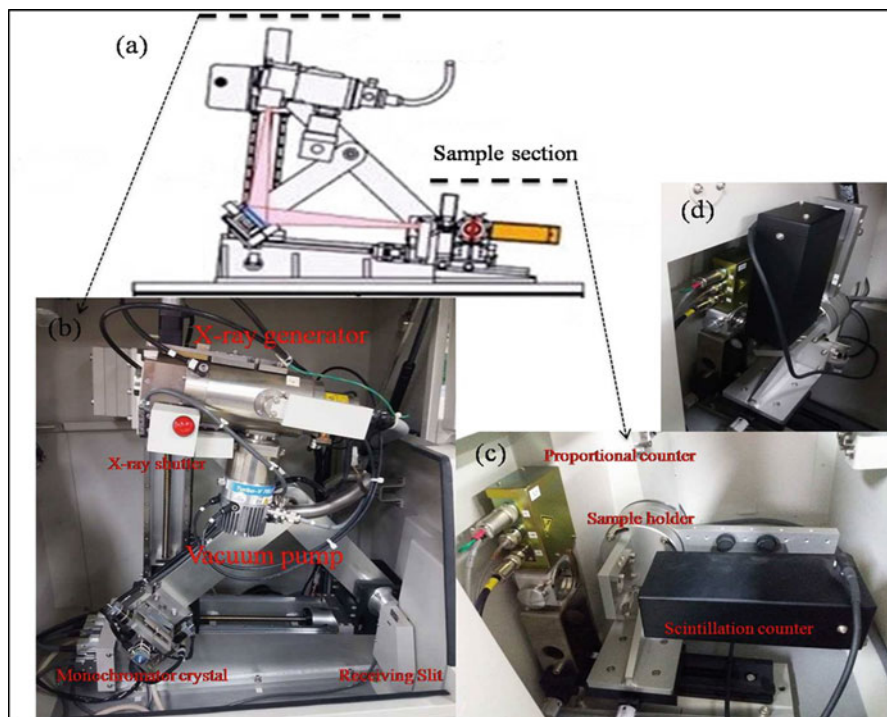


Fig. 13.17 (a) Shows the schematic layout of the machine, (b) shows the spectrometer section, (c) shows the sample section in the transmission data collection mode, and (d) shows the sample section in the fluorescence data collection mode

bounces of the photoelectrons) [1–10]. XANES and EXAFS provide the different information of the material; however, these two techniques are the part of same experiment and complement each other in the interpretation of results and data analysis. For XANES analysis, pre-edge and post-edge background subtraction, normalization, and finding the edge position (by using the derivative) are rather important and also very crucial for better EXAFS analysis. We are discussing these points in the following sections.

There are several methods for XANES/EXAFS data analysis like nonlinear least-square fittings, principal component analysis, and linear combination analysis. The data can be analyzed by a number of software packages that perform nonlinear least-square fittings and also report uncertainty in the results. Among them, IFEFFIT [7, 8], EXCURVE [15, 16], and GNXAS [17–19] are the popular XAS programs based on the ab initio calculations. In this chapter, most of the examples utilize the IFEFFIT program package which uses Demeter (Athena, Artemis, and Hephaestus) graphic user interfaces (<http://xafs.org/Software/Demeter>). Before the pre-edge/post-edge background removal, normalization, and data analysis, several other processes are required for refining the XANES/EXAFS data, for example,

(a) rebinning measured data points, (b) removal of bad data points which are clearly in the error (deglitching), (c) trimming the absorption spectra to the usable energy region (truncation), (d) changing the energy scale to align several scans, (e) averaging several scans to produce a high-quality spectrum for analysis, (f) considering the self-absorption effects, etc. [1–4]. After these preprocessing, the raw data is processed by the following steps.

13.4.1.1 Collection of $\mu(E)$ Raw Data

There are several, consecutive steps to be followed in the *Athena* to collect the $\mu(E)$ raw data from the measured intensities.

(a) After running the *Athena*, go to file > open file > select the desired XAS data file collected from the beamline. For example, the CuO file has been picked for analysis in the upper panel of Fig. 13.18. The right side of upper panel shows the details of energy steps, used beamline, synchrotron center, etc. After bringing the file, mark the columns for I_0 , I_t , and I_f . (Column numbers for I_t and I_f may be different in the file obtained from the different beamlines/synchrotron centers.) Plot the spectrum in $\mu(E)$. The resultant spectrum is presented in the lower panel of Fig. 13.18.

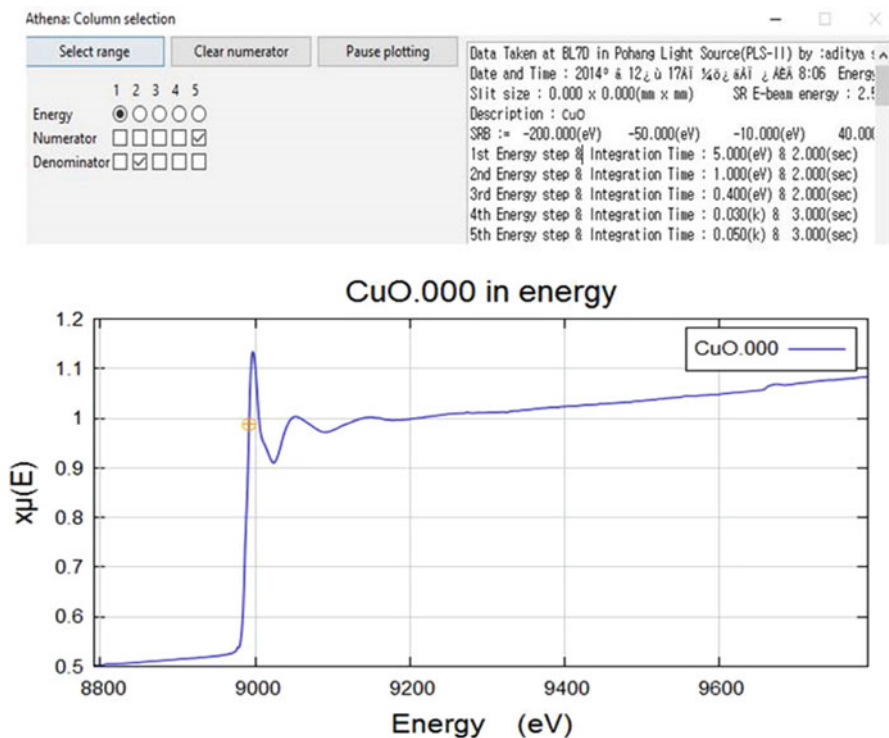


Fig. 13.18 Importing the data into *Athena* (upper panel) and plot in the $\mu(E)$ (lower panel)

- (b) For the better spectral features, it is desirable to collect several scans from the same sample and then bring them together in the *Athena*. Then plot them together. However, we need to align the data sets. For this, select the standard spectrum that we think there is no shift of energy, and the bad data points are already removed. Then select the other spectrum which is supposed to be aligning with the standard spectrum. For example, upper panel in Fig. 13.19, CuO-1 is aligned to the standard CuO. After alignment of the data set, it is important to merge all spectra. The merged spectrum may look like the lower panel of Fig. 13.19. One can rename the merged spectrum for his/her convenience and then save the *Athena* project somewhere in the computer.

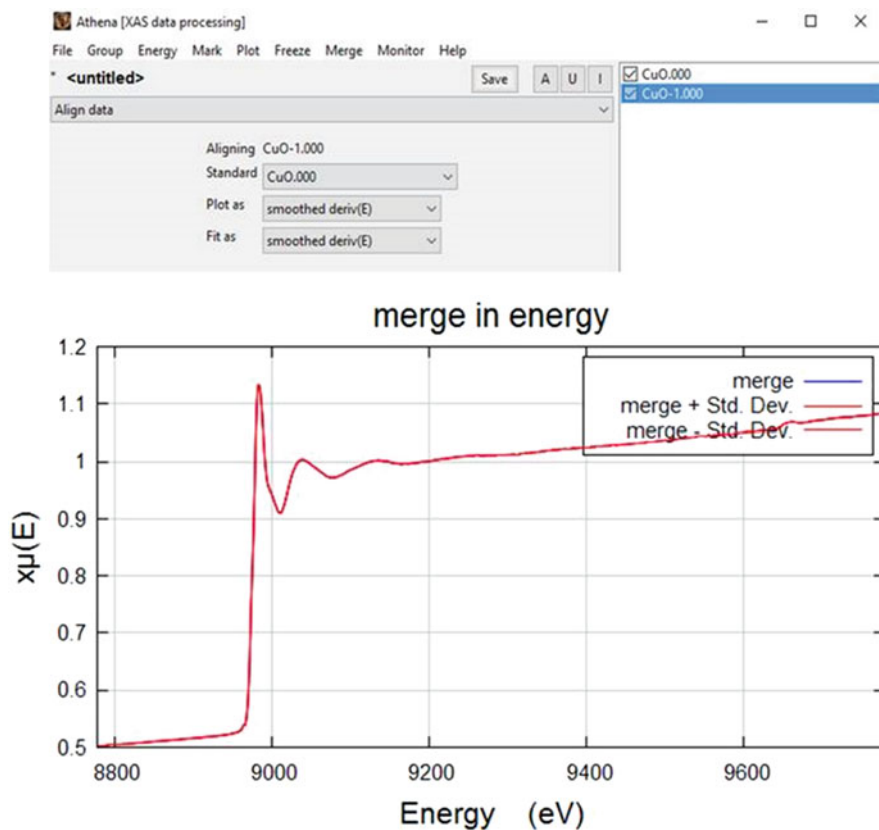


Fig. 13.19 Alignment of more than one data set (upper panel) and merge of data sets into one file (lower panel)

13.4.1.2 Selection of the Edge Energy (E_0)

The edge energy reference parameter (E_0), used for processing EXAFS data, is important for the alignment of the experimental spectrum to the theoretically calculated spectrum. Since a shift in E_0 is determined in the fit of theoretical spectra to the experimental spectra, therefore, systematic assignment of E_0 for all spectra is essential. The inflection point, i.e., the maximum in the first derivative or minimum in the second derivative of the absorption edge, is generally considered as a systematic choice [16]. Hence, the edge position is typically chosen at the inflection point with the help of the XANES and second-derivative XANES $\mu(E)$ spectra as illustrated in Fig. 13.20. The value of E_0 for Cu is generally taken as 8979.0 eV.

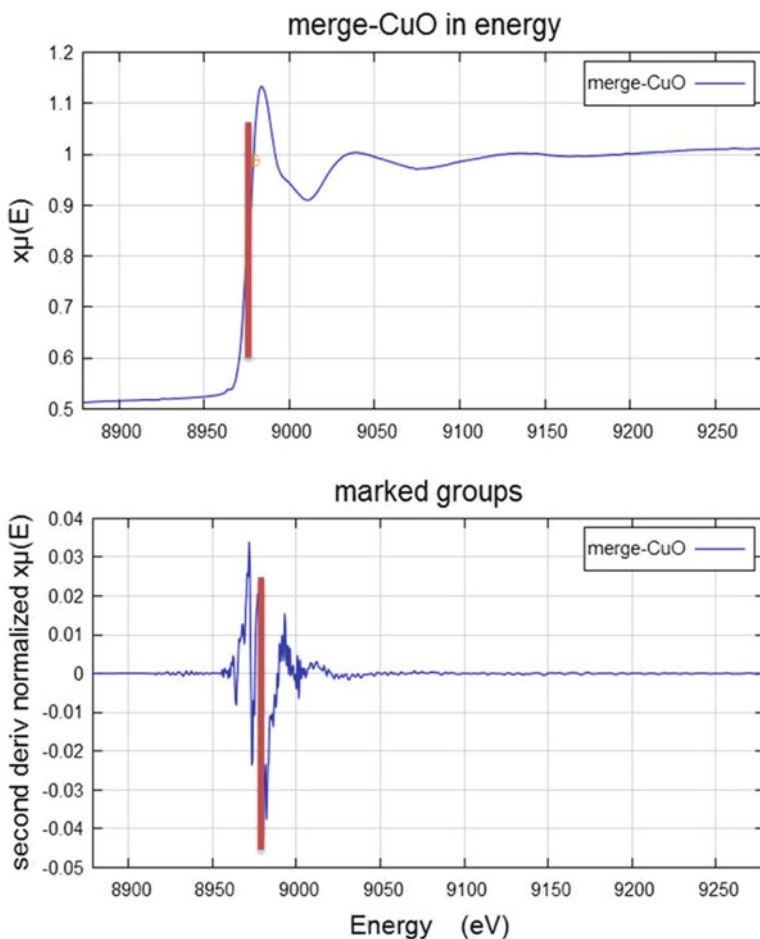


Fig. 13.20 The edge position E_0 has been typically chosen at the inflection point (red-colored marker, upper panel). The edge position, as defined in the upper panel, is determined as the minimum in the second-derivative spectra (lower panel)

13.4.1.3 Pre-edge/Post-edge Subtraction and Assignment of Edge Step

To get rid of any instrumental background and absorption from the other edges, it is important to subtract a smooth pre-edge function from $\mu(E)$. For the better pre-edge subtraction, it is also important to determine the edge jump ($\Delta\mu(E)$) [1–3]. The $\Delta\mu(E)$, at the threshold energy, should be determined in that manner which allows the $\mu(E)$ (pre-edge subtracted and normalized) to go from 0 (approximately) below the threshold energy to 1 well above the threshold energy. $\Delta\mu(E)$ and pre-edge and post-edge lines are shown in Fig. 13.21.

Generally, modified Victoreen [$\mu_{\text{pre-edge}}(\lambda) = C\lambda^3 - D\lambda^4$] [6, 20, 21] function is used to approximate the pre-edge and calculated by extrapolation of the pre-edge region in the data. Similarly, a linear/quadratic function is degenerated to the post-edge region [3, 6, 20, 21]. These lines are extrapolated to the absorption edge, E_0 , and the difference in absorption between these projected lines at E_0 is called the edge step ($\Delta\mu(E)$).

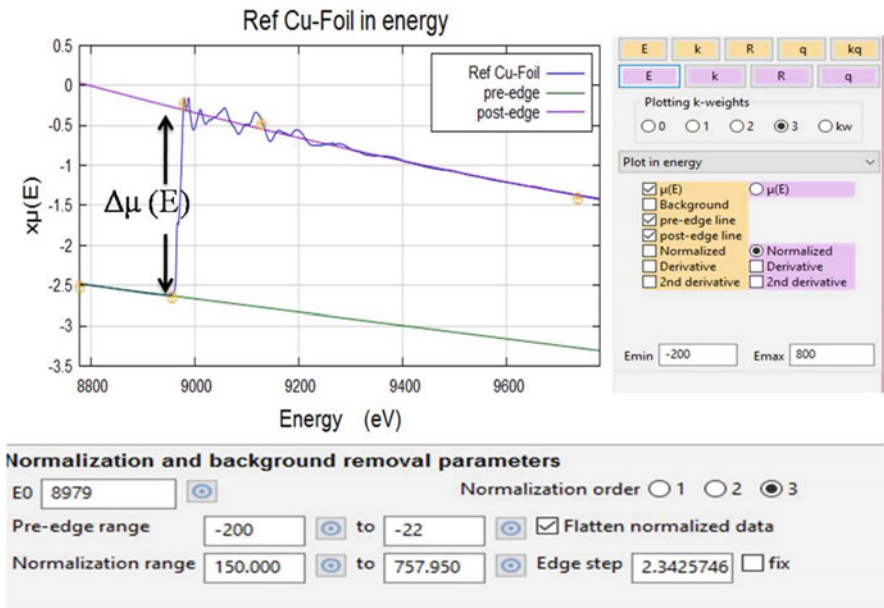


Fig. 13.21 $\Delta\mu(E)$ and pre-edge and post-edge lines in the left-side panel and the typical Athena window for the selection of pre-edge and post-edge lines. The lower panel shows the typical Athena window to select range of energy during the assignment of pre-edge and post-edges

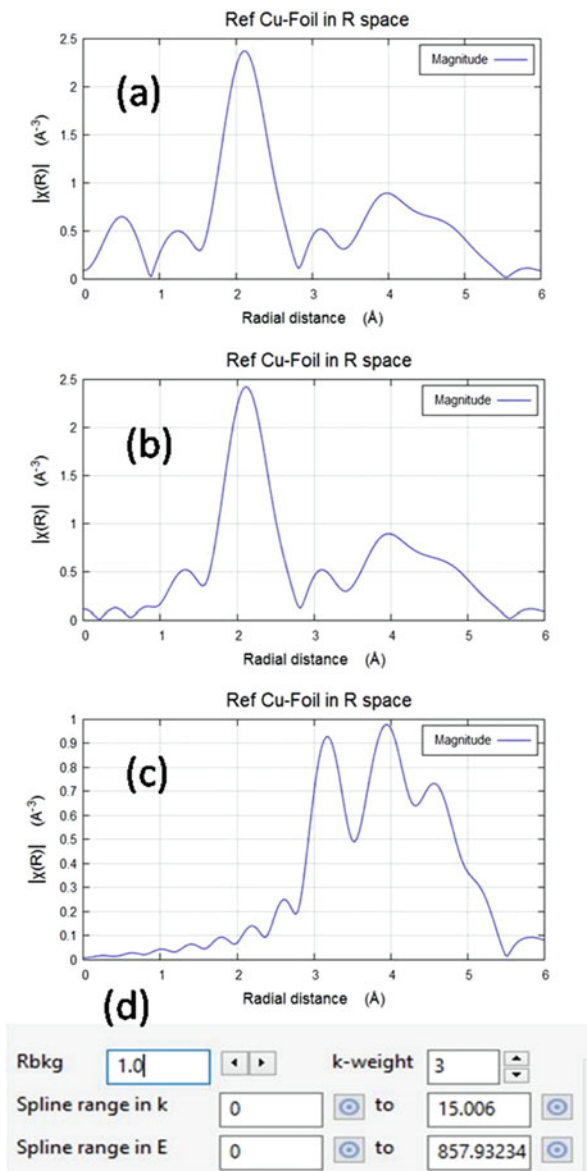
13.4.1.4 Background Subtraction and Normalization

The most fallible and puzzling step in the XAFS data analysis is the assignment and subtraction of the post-edge background function. Since $\mu_0(E)$ is the absorption coefficient from the individual absorbing atom without the presence of neighboring atom, we cannot measure this function separately from XAFS, even if the material is a gaseous system. We also do not try to measure an idealized $\mu_0(E)$ but determine it empirically by fitting a spline function to $\mu(E)$ [3, 6]. A spline is a piece-polynomial function that is designated to be adjustable enough to smoothly approximate an arbitrary waveform. This is certainly an ad hoc approach, without any real physical justification. Still it is widely used for the XAFS analysis. For determining the background $\mu_0(E)$, we want a smoothly varying spline function that removes the low R components of χ while retaining the high R components [3, 6, 20, 21].

The cubic spline function [3, 6, 20–22] is routinely used in the XAFS data analysis. The cubic spline function consists of four important parameters, R_{bkg} , weighing factor, start energy, and end energy. For a better spline function, selection of more data points is favorable which can be done by selecting the large energy range between the start and end energy (see Fig. 13.22d). It is also very important to take care of R_{bkg} and k -weighing factor. Generally the k^2 - or k^3 -weighing factor is recommended for the better emphasis of high k -portion of the data. The effect of low R_{bkg} values (low and high) is shown in Fig. 13.22a–c. The $|\chi(R)|$ vs R spectra are shown here for the same Cu foil with different R_{bkg} values. It is noticeable from the spectra that the very low value of R_{bkg} ($= 0.1$) giving oscillation in the lower R values. On the other hand, assignment of very high R_{bkg} ($= 3.0$) leads to diminished or elimination of the first two shells of Cu metal and leaving only the highest R components. But choice of R_{bkg} ($= 1.0$) gives Cu metal oscillation and also removed some of the lower R oscillations. Therefore, setting $R_{\text{bkg}} = 1$ or half of the near-neighbor distance is the suitable choice for the better spline.

Before $\chi(k)$ is obtained, the total absorption as obtained from experiment has to be normalized per absorber atom. Generally, spectra are normalized by division of the absorption data by the edge step at 50 eV after the absorption edge. Normalization is done by subtracting a regressed line determined by the pre-edge region from the entire spectra and dividing the measured spectra by the absorption step height at E_0 . The step height determines the amplitude of the EXAFS oscillations and is therefore correlated to the EXAFS parameters such as the amplitude reduction factor (S_0^2) and the coordination number (N). The final normalized Cu K -edge spectra of Cu foil and CuO are presented in Fig. 13.23.

Fig. 13.22 Effect of changing of R_{bkg} on the $|\chi(R)|$ vs R spectra (a) $R_{\text{bkg}} = 0.1$, (b) $R_{\text{bkg}} = 1.0$, (c) $R_{\text{bkg}} = 3.0$, and (d) spline parameters window in Athena



13.4.2 EXAFS

The aim of EXAFS data processing and analysis is to extract structural parameters (interatomic distances, coordination numbers, disorder degrees, etc.) in various coordination shells for the “unknown” sample. XANES/EXAFS data, either collected in the fluorescence or in transmission mode, the data reduction, and analysis

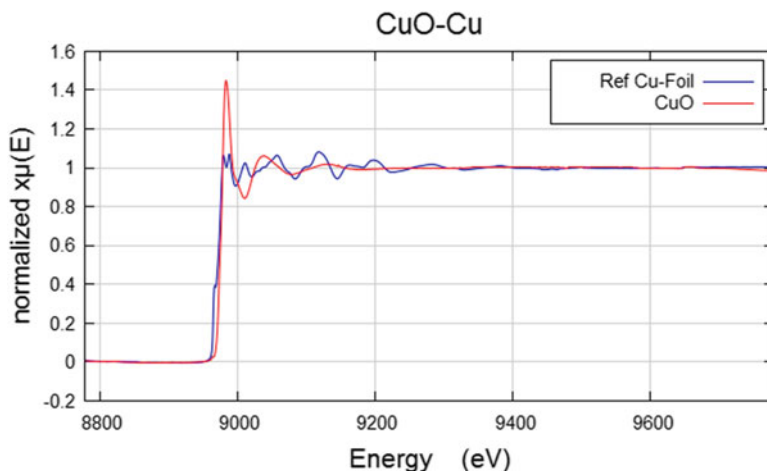


Fig. 13.23 Background subtracted and normalized XAFS spectra of CuO and Cu metal foil

(background subtraction, normalization, etc.) are essentially the same and have been discussed in the previous section. For getting the atomic structure information from the EXAFS data, several important steps are required: (i) convert χ from energy E to photoelectron wave number k , (ii) k -weight the XAFS $\chi(k)$, (iii) Fourier transform into R space, and (iv) EXAFS data modeling for obtaining the structural information from the material by simulating the desired structure.

13.4.2.1 Convert $\chi(k)$ from EXAFS Data

Conversion of $\chi(k)$ from the experimentally obtained μ_{total} [$\mu_{\text{total}} = \mu_{\text{atomic}} (1 + \chi)$] follows several consecutive steps which are explained in the previous sections (i.e., pre-edge/post-edge background removal, normalization, etc.). χ can be obtained after the atomic absorption is known using the following relation: $\chi = (\mu_{\text{total}} - \mu_{\text{atomic}}) / \mu_{\text{atomic}}$. The edge energy is used to determine k (\AA^{-1}) using the following relation $k = \sqrt{2m(E - E_0) / \eta^2}$ [3, 4, 6]. Thus calculated $\chi(k)$ is shown in Fig. 13.24a.

13.4.2.2 Weighed $\chi(k)$ Versus k Spectrum

To compensate for the decay of the waves with extended k , it is important to weigh the $\chi(k)$ data with some power of k^n ($n = 1, 2, 3$). Figure 13.24b–d shows the $k = 1, 2$, and 3 weighed $\chi(k)$ spectra for Cu foil. It is noticeable in the wave number range of 10–14 \AA^{-1} (Fig. 13.24b–d) that the oscillation strength is improved with increasing the k -weighted factor. However, it is also important to check the pre-

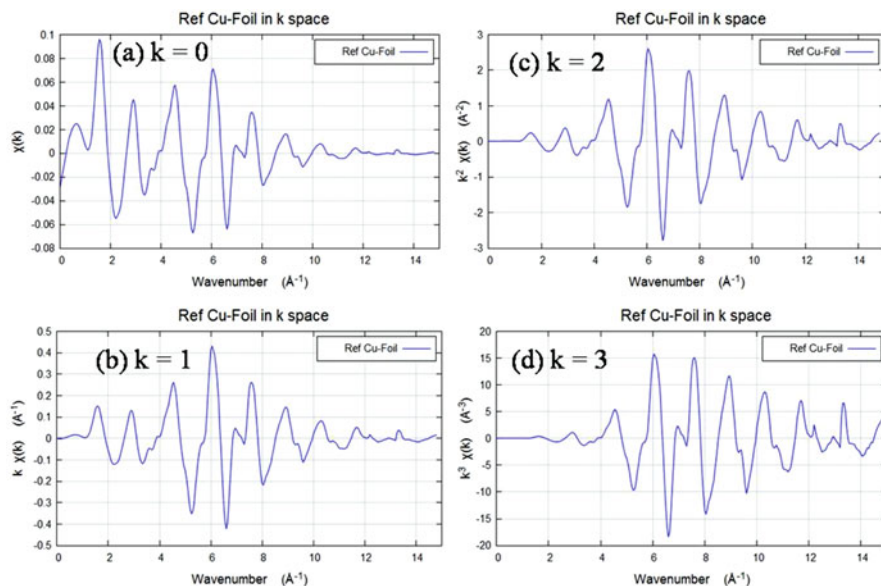


Fig. 13.24 $\chi(k)$ versus k spectrum of Cu foil: (a) $k = 0$, (b) $k = 1$, (c) $k = 2$, and (d) $k = 3$

edge/post-edge, normalization, and background removal (i.e., choice of R_{bkg}) before generating the $\chi(k)$ versus k spectrum from the experimental data.

13.4.2.3 Fourier Transformation of EXAFS Data

Fourier transform is very important step in the EXAFS data analysis. Since, the XAFS data is originated from the interference between the outgoing and incoming scattered photoelectron waves from the surrounding and central atoms [1–10]. Thus, a typical EXAFS data is the sum of consecutive constructive and destructive interference of waves and contains local structural information of surrounding atoms with respect to the central absorbing atom.

The process of Fourier transformation (FT) can be applied separately to each frequency component, in radial distance R , from the sum of several sine waves. Indeed, the FT separates the signals into its Fourier components, and each Fourier component is distinct by an amplitude and phase. However, the FT is a complex function and contains both the real and imaginary parts. The magnitude of FT is an envelope of the real and imaginary parts of the FT. Therefore, FT of EXAFS data can be used to isolate and identify the different coordination shells around the central absorbing atom. Moreover, the magnitude of FT-EXAFS or $|\chi(R)|$ almost looks like a radial distribution function [3, 6, 20]. A typical FT-EXAFS spectrum contains peaks in radial distance (R) and is known as the finger print of interatomic distance between the constituent atoms. All of the coordinating atoms which are

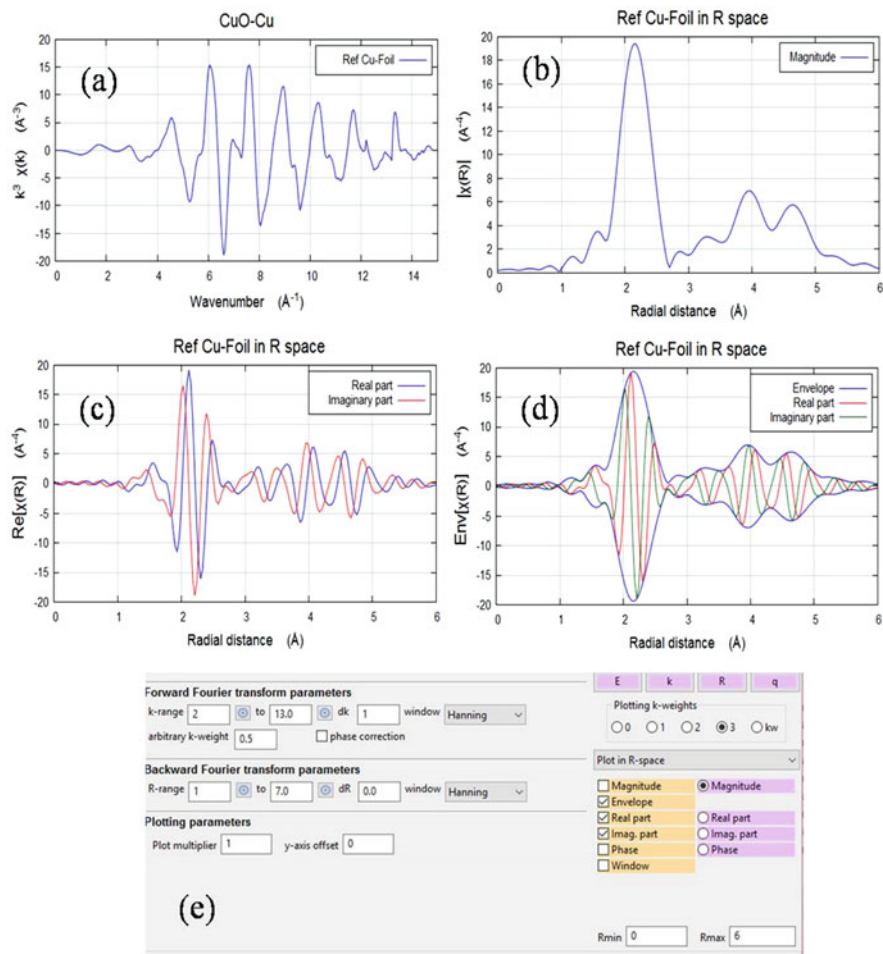


Fig. 13.25 (a) $k^3 \chi(k)$ versus k spectrum, (b) $|\chi(R)|$ versus R spectrum, (c) real and imaginary parts of FT-EXAFS, (d) envelope of $\chi(R)$ containing the real and imaginary parts, (e) the typical Athena window for changing the Fourier transformation parameters during the analysis. Here all the spectra are for Cu foil and the k -weighing factor was 3

at approximately the same radial distance from the absorber atom (a coordination shell) contribute to one peak in the magnitude of the FT. For example, we show k^3 -weighted FT-EXAFS of Cu foil in k and R space. Figure 13.25a shows the EXAFS $k^3 \chi(k)$ versus k spectrum, (b) the magnitude of $\chi(R)$ versus R spectrum, and (c) the real (blue color) and imaginary part (red color) of $\chi(R)$, (d) illustrates that the magnitude of $\chi(R)$ is envelope function of the real and imaginary parts of FT components, and (e) shows the typical window in *Athena* for Fourier transformation parameters.

13.4.2.4 EXAFS Data Modeling

Before going to EXAFS data modeling using the Artemis, it is important to discuss about the EXAFS equation and the parameters used in the EXAFS data fittings.

EXAFS Equation

Recent studies have shown that the amplitude reduction factor (S_0^2 ; will be discussed in the following section) may also depend on k , especially at low k values. Therefore, the modern EXAFS equation is written as [3, 6]

$$\chi(k) = \sum_z \frac{N_z S_0^2 f_z(k)}{k R_z^2} e^{-2k^2 \sigma_z^2} e^{-2R_z/\lambda_z(k)} \text{Sin} [2k R_z + \delta_z(k)] \quad (13.13)$$

In Eq. (13.13), N_z denotes the total number of atoms in the z th shell, λ is the mean-free path of photoelectron, and f_z is the backscattering amplitude. The above equation can be divided into two parts; the first part is considered as amplitude $A_z(k)$ and given as

$$A_z(k) = \sum_z \frac{N_z S_0^2 f_z(k)}{k R_z^2} e^{-2k^2 \sigma_z^2} e^{-2R_z/\lambda_z(k)} \quad (13.14)$$

Equation (13.14) not only contains the coordination term (N_z) and mean-free path term (λ) but also contains the disorder term (σ) which is the fluctuation in R_z due to structural disorder and temperature. The second part of the EXAFS equation represents the oscillation in the EXAFS data and is given as $\text{Sin} [2k R_z + \delta_z(k)]$. In the second term, $\delta_z(k)$ is the phase shift.

Parameters Used in the EXAFS Data Modeling

S_0^2 : S_0^2 is an overlap factor which includes the intrinsic losses due to inelastic effects in the EXAFS equation. One value of S_0^2 is often used for all paths included in the model. If there are more than one structure in the same model, then S_0^2 can be different. The S_0^2 values for the unknown sample can be determined by fitting the EXAFS spectrum of a standard sample (or metal foil) of known crystal structure measured under similar conditions as the unknown sample was measured. S_0^2 is assumed to be constant and generally kept to be $0.7 < S_0^2 < 1.0$ [3, 6, 20, 21]. S_0^2 is completely correlated with N in the EXAFS fittings. Theoretical calculations like FEFF 8.4 can also be used to determine S_0^2 .

N

“ N ” is an important fitting parameter in the EXAFS data simulation and known as “degeneracy of a path.” This parameter is generally determined from the coordination number of known atomic species in a known crystal structure. Degeneracy can be calculated, independently, for the single-scattering paths in the model of simulation. However, it is constrained for the multiple-scattering paths. Coordination numbers can also be constrained by considering the stoichiometry of a particular ligand attached to the absorbing atom [3, 6, 20, 21].

ΔR

“ ΔR ” parameter is known as “change in the path length” and can be determined independently for each path used in the fittings. The overall path length (R) of a shell (e.g., $M - O$ shell, where M is the metal element and O is the oxygen) is the sum of $R_{\text{eff}} \pm \Delta R$, where R_{eff} is determined by the used model for a certain path and ΔR is obtained by the simulation [3, 6, 20, 21].

ΔE_0

During the EXAFS data fittings, we need to define a value for E_0 , the threshold defining where $k = 0$. This is important because the determination of E_0 using the first derivative of $\mu(E)$ versus E spectra is ad hoc procedure. To achieve the E_0 value and uncertainty from the fit is important, as it is related with R . During the EXAFS data simulation, one value for the energy shift (ΔE_0) can be applied to all paths. This is the most common method of defining ΔE_0 . Two ΔE_0 values can be applied sometimes, where the value for the first path is different from the value for all other paths [3, 6, 20, 21].

σ^2

σ^2 is known as mean-squared displacement of the half path length. This parameter uses a Debye or Einstein model, with one or more characteristic temperatures. This parameter considers that the thermal and static disorders are similar in the coordination shells involving similar atoms and similar interatomic distances. During the fittings, each shell may contain unique σ^2 value. σ^2 values can be broken into two components to represent the structural and thermal disorder in the bond lengths [3, 6, 20, 21].

13.4.2.5 Example of EXAFS Data Fittings Using Artemis (Cu K-Edge Data from the Cu Foil)

In the following sections, we provide an example for EXAFS data simulation using Artemis. We have chosen Cu K-edge EXAFS data from the Cu foil. In Fig. 13.26a, a typical main window of Artemis (Demeter – 0.9.24) is shown describing various segments in the software. To import the desired EXAFS data, go to “Data sets” tab and click “Add.” It will import an Athena file (see Fig. 13.26b). Select the desired EXAFS data file, which you are willing to simulate. After selecting one of the files, a new window (known as data window) will appear (see Fig. 13.26c). This window

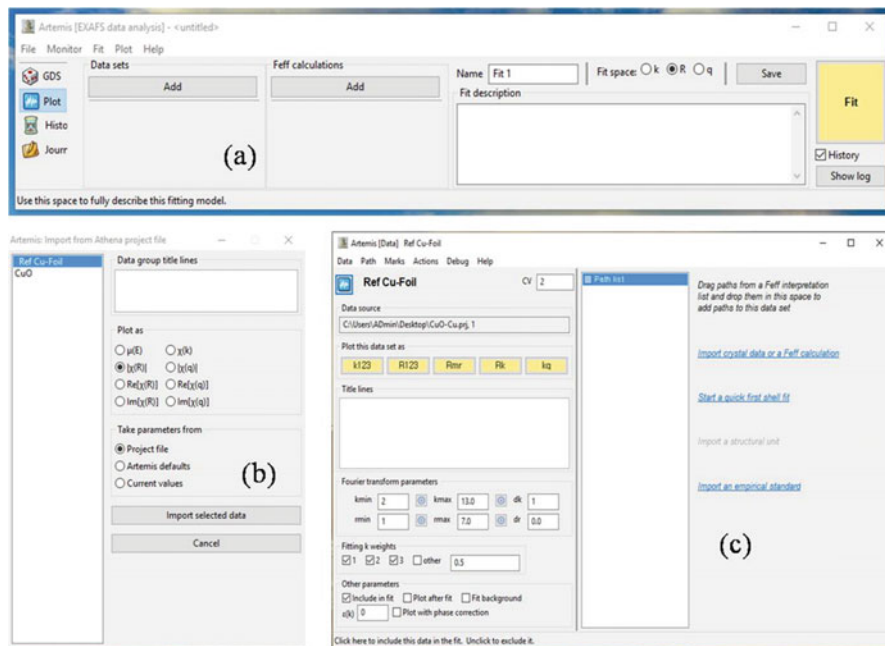


Fig. 13.26 (a) Typical main window of Artemis. (b) Importing data (Athena files) and (c) importing the “Feff files” for the simulation of desired data set

will ask you to import “Feff” file of certain structural information, which you are willing to simulate with the experimental EXAFS data. One can directly import “atoms.inp” or “feff.inp” files for the known standard samples/compounds from the ATOMS home page (the Atoms.inp Archive; <http://cars9.uchicago.edu/~newville/adb/>) or by generating the structure of the unknown element/compound using the ATOMS software.

An example of generating the “feff.inp” file using the ATOMS is shown in Fig. 13.27a for the Cu meal foil. First of all, one has to provide space group, lattice parameters, and position of the constituent atoms (if the compound contains more than one species then positions of all of the elements are necessary), and then click “Run Atoms.” ATOMS will produce “Feff” window which consists of a list of Cartesian coordinates for the atoms in the cluster and is written in the FEFF tab (Fig. 13.27b, c). After clicking the “Run Feff” button on the FEFF tab, the FEFF calculation is run. Once finished, a succinct summary of the calculation will be displayed on the Paths tab (Fig. 13.27d). To start the simulations, select paths (shown in Fig. 13.27d), and drag into the path list of data window (shown in Fig. 13.27c).

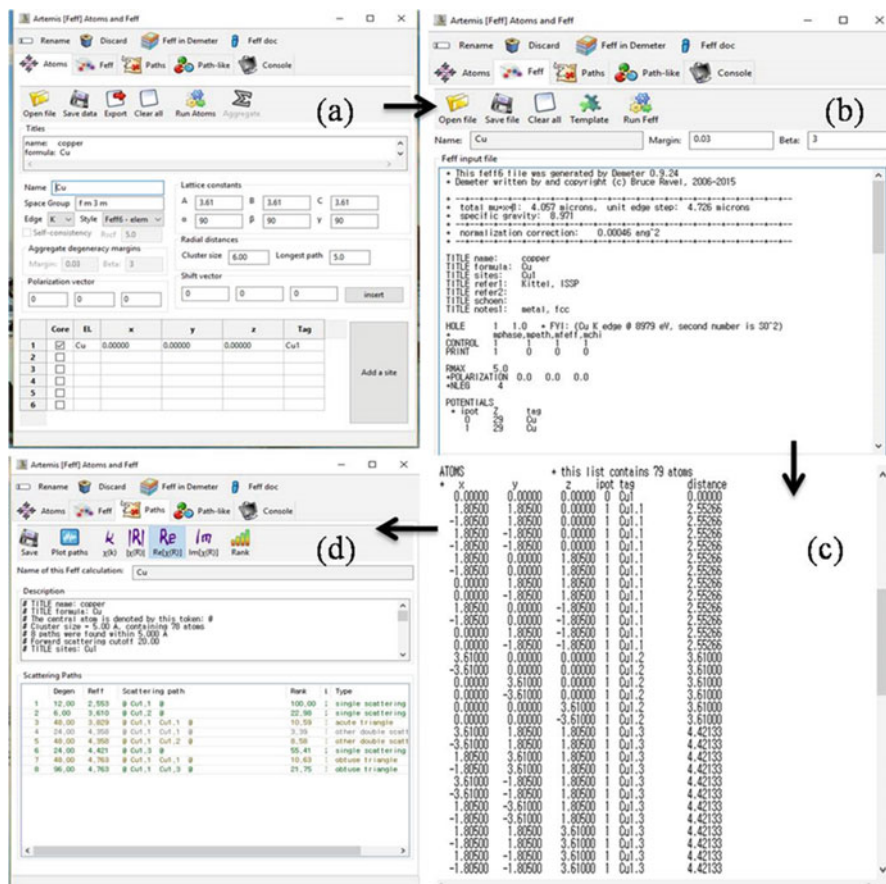


Fig. 13.27 (a) ATOMS page for assigning the space group and lattice parameters for a desired element/compound. (b, c) FEFF calculations, consisting of the list of Cartesian coordinates (d) Paths tab, consisting of a succinct summary of the calculations

Fitting of Single and Multiple Shells

Theoretically modeled data of Cu foil was fitted to the experimental EXAFS data in the R space (magnitude and real part), and the corresponding fits are shown in Fig. 13.28a. The data was fitted using k -weighting factor of 3. Fit was performed in the R ranges of 1–5 Å, with a window function between 1 and 5 Å. The R_{bkg} was fixed to 1. Since, the coordination number of Cu metal is well known therefore N was taken to its crystallographic value for the first shell and S_0^2 was used as fitting parameter. For the other multiple shells, we have fixed the value thus obtained. The S_0^2 value obtained for the present analysis is 0.81 and the ΔE_0 value obtained is 2.78 eV. The structural parameters, obtained from the EXAFS data fittings of Cu foil, are tabulated for the different shells in Table 13.2. Figure 13.28b, c shows the simulated EXAFS data in k -space and the typical window in Artemis for the goodness-of-fit

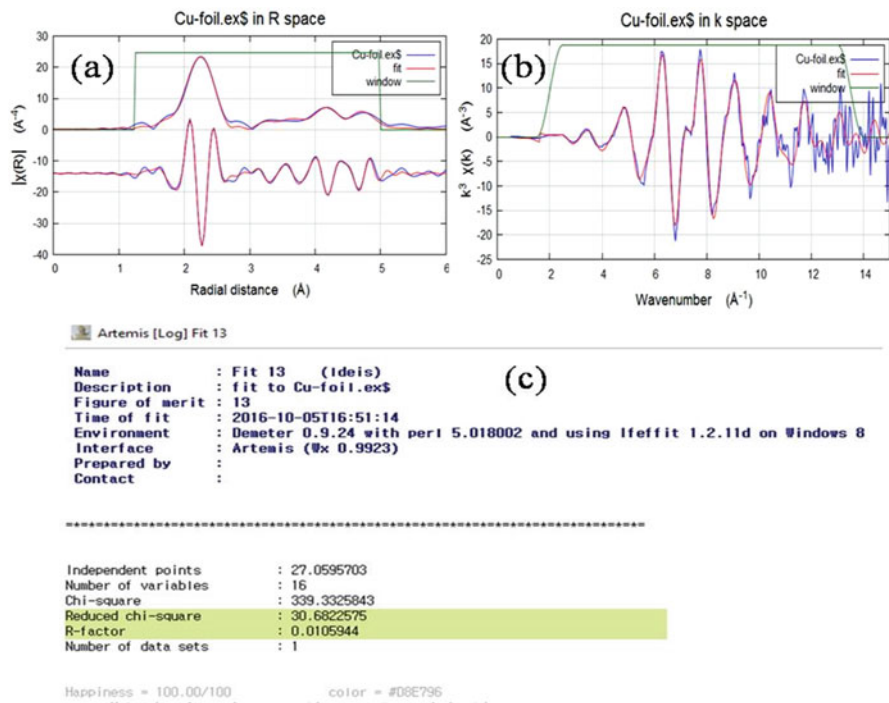


Fig. 13.28 (a) Simulated EXAFS data in r -space for Cu metal foil. (b) Simulated EXAFS data in k -space for Cu metal foil. (c) Typical Artemis window for the fitting parameters like goodness-of-fit (Chi-square) and r -factor of the simulations

Table 13.2 Local structural parameters for Cu foil obtained from the simulation of theoretical Cu structure to the experimental EXAFS data

$S_0^2 = 0.81$ and $\Delta E_0 = 2.78$ eV				
Shell	N	R (Å)	ΔR (Å)	σ^2 (Å ²)
1st shell	12	2.56	0.009	0.008
2nd shell	6	3.59	-0.017	0.012
3rd shell	24	4.43	0.015	0.025
4th shell	96	4.67	-0.13	0.004

and r -factor parameters of the fittings. From the simulations (either in k -space or in r -space), it is noticeable that the few number of paths from the FEFF calculations (four paths in this fitting) will give a very good approximation to the EXAFS with a suitably small number of adjustable parameters. It is not possible to fit more shells, beyond the $R_{\text{eff}} = 4.763$ Å, as the calculations are limited to this value (see Fig. 13.27d). Therefore, the experimental data should be good enough for getting a nice fit for more number of shells. The obtained parameters are also very close to the previously obtained structural parameters of Cu [20].

13.5 Applications of XAFS on Oxide Materials

In the last few decades, extensive research has been done by our group to understand diversifying phenomena of the various oxide materials, for example:

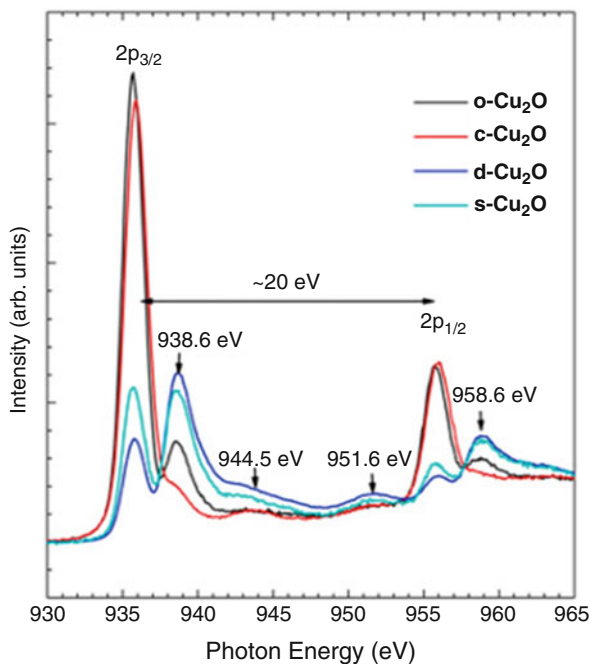
- (i) Determination of valence state of the doped elements in the various diluted magnetic semiconductors, multiferroic, and ferrite nanoparticles [23–27].
- (ii) Probing the local coordination chemistry of doped transition metal elements in the host SnO_2 and ZnO lattice [28, 29]
- (iii) Distinguishing the polymorphous phases (i.e., monoclinic, tetragonal, cubic, etc.) of HfO_2 and ZrO_2 [30, 31].
- (iv) Rutile and anatase phase justification in TiO_2 [5, 32].
- (v) Estimating the valence state of Cu in the $\text{CuO}/\text{Cu}_2\text{O}$ nanocomposites [32].
- (vi) Understanding the effect of aliovalent and isovalent element doping on the valence state and local atomic structure perturbation in catalyst nanoparticles of CeO_2 [33, 34].
- (vii) Investigating the local electronic structure properties, at/near the Fermi level, of the perovskite SrVO_3 thin films [35].

Besides such significant spectroscopy investigations by our group, in the following section, we provide much elaborated discussion on the few of other exciting findings on the oxide materials.

13.5.1 *Effect of Morphology on the Electronic Structure Properties of Cu_2O*

In many of the previous reports, the edge energy position of metal K -edge or L -edge XANES has been applied to distinguish the valence state of Cu which progressively shifts toward the higher energy with increasing the oxidation state of Cu [32, 36]. However, the effect of morphology of compound on the electronic structure aspect has not been investigated. Recently, the Cu_2O compound is synthesized with diversifying morphologies, i.e., cubic, octahedral, spheres, and truncated rhombic dodecahedral [36]. The conventional XRD results have shown preferred Cu_2O phase formation in all of the samples regardless the morphology variation. Figure 13.29 shows the Cu L -edge XANES of such morphologically diverse Cu_2O crystals. It is noticeable from Fig. 13.29 that the morphology of the Cu_2O crystal has strong influence on the hybridization of Cu (3d) and O (2p) orbitals. Since, the crystallographic structure of Cu_2O is symmetric (space group, Pn-3m) with six atoms per unit cell. The O atoms form a body-centered cubic lattice, and the Cu atoms are situated on the vertices of a tetrahedron around each O atom [32, 36]. Under this crystallographic symmetry, the Cu has $3d^{10}$ electronic configuration, and the Cu L -edge XANES features originate from the transitions of Cu $2p_{3/2}$ and $2p_{1/2}$ electrons into empty d states [32, 36]. The Cu d states have strong hybridization with the

Fig. 13.29 Copper *L*-edge XANES spectra of the Cu₂O nanocrystals. In the figure, o, c, d, and s stand for octahedral, cubic, dodecahedral, and spheres morphology, respectively. (Adopted from [36], with permission)



O 2p states, and, thus, the spectral features are very sensitive to the O concentration and local arrangement in crystal lattice. In case of cubic and octahedral morphology of Cu₂O crystals, the spectral features and edge energy positions are very similar but quite diverse with respect to the sphere and dodecahedral morphology. This indicates that the sphere and dodecahedral morphology obey higher valence state of Cu rather than Cu⁺¹ and may have diverse orientation of O atoms, at least partially [36].

13.5.2 Determination of Metal-Oxygen Metal Bond Length and Coordination in Oxide Nanoparticles

13.5.2.1 Site Occupancy of Cations in Ferrites

In most of the previous reports, on multielement systems, XAFS has been applied to investigate the valence state and hybridization of molecular orbitals which are influenced by the dissimilar surrounding element [34–37]. However, less attention has been paid to understand the site occupancy in the multifunctional materials like ferrites. In these systems the distribution of a certain element, at a specific lattice site of the unit cell, can alter the whole electronic structure properties and, consequently, applications of the compound [38–44]. Moreover, cation distribution

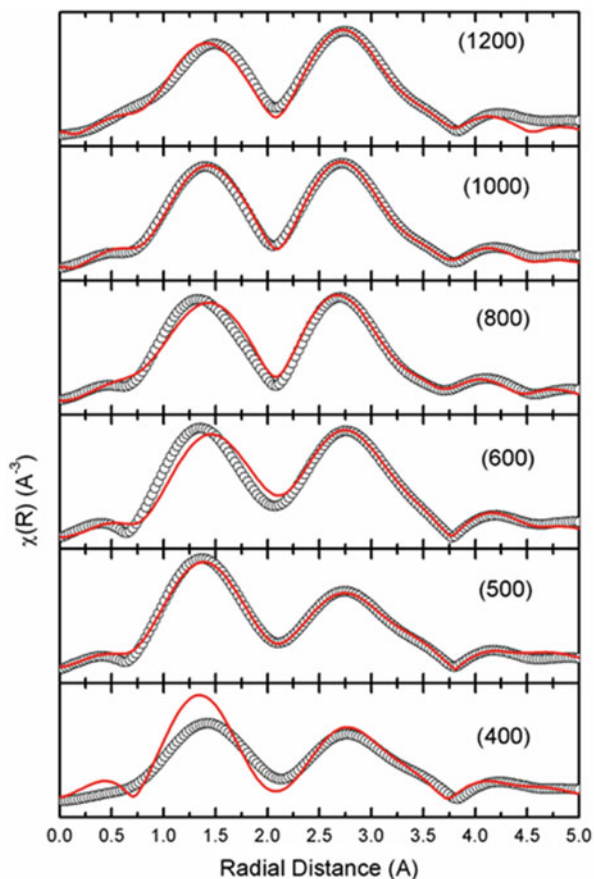
can be quite diverse in the small-sized nanoparticles, thin films, and bulk counterparts of the same compound and may offer intriguing properties/applications of the system. It is observed that ferrites synthesized under similar conditions sometimes exhibit a markedly different distribution of cations between the available sites in the spinel structure; this in turn causes significant differences in the magnetic properties of the samples [45]. Theoretical calculations of Zn *K*-edge and Fe *K*-edge X-ray absorption near-edge structures (XANES) using a first-principle method have been performed to evaluate the degree of cation disordering in spinel ZF (ZnFe_2O_4) thin film prepared by a sputtering method and ZnFe_2O_4 thin films annealed at elevated temperatures. The degree of cation disordering, x , defined as $[\text{Zn}_{1-x}^{2+}\text{Fe}_x^{3+}]_A[\text{Zn}_x^{2+}\text{Fe}_{2-x}^{3+}]_B\text{O}_4$, is estimated to be approximately 0.6 in the as-deposited film, which is consistent with the analysis of the extended X-ray absorption fine structure on the Zn *K*-edge [46]. It is found that low deposition pressures below 10^{-3} mbar cause iron super-occupation of tetrahedral sites without Zn^{2+} inversion, resulting in an ordered magnetic phase of ZnFe_2O_4 with high-room-temperature magnetic moment [47]. The overpopulation of cations in the octahedral sites was attributed to the ascendance in the importance of the ionic radii over the crystal energy and bonding coordination in determining which interstitial sites are occupied in this structurally disordered powder [48]. The nonequilibrium cation site occupancy in nanosized ZFs (~ 6 to 13 nm) with different degrees of inversion (~ 0.2 to 0.4) was investigated using Fe and Zn *K*-edge X-ray absorption near-edge spectroscopy (XANES) and extended X-ray absorption fine structure and magnetic measurements [49].

Thus, EXAFS is suitable to determine the cation distribution, coordination numbers, and metal-oxygen bond length in tetrahedral and octahedral environment under different synthesis conditions. Thus, this technique paves a new path for understanding the behavior of ferrites. In our group, cation inversion for MgFe_2O_4 nanoparticles is estimated from Fe *K*-EXAFS measurements. It is seen that cation inversion changes modify with change of annealing temperature. Figure 13.30 shows simulated Fe *K*-edge spectra for MgFe_2O_4 nanoparticles [50]. We have shown various parameters estimated from EXAFS simulation in Table 13.3. Fe *K*-EXAFS studies carried out on Dy-doped CoFe_2O_4 reveal that behavior of cation redistribution with Dy concentration is analogous to that estimated from Mössbauer and Rietveld refinement method [51].

13.5.3 Determination of Metal Oxidation in Biological and Environmental Applications

Environmental and biological applications of EXAFS are not less important [52–54]. This technique is effective to give experimental evidences to probable metal oxidation in various biological [55] and environmental applications [56]. Cellulose nanofiber (CNF) is one of the emerging green candidates for the various

Fig. 13.30 $\chi(R)$ spectra at Fe K -edge of materials synthesized at different annealing temperatures. (Adopted from [50], with permission)



domains due to its sustainability, abundance availability, and large surface area. However, its effectiveness in the environmental aspect of toxic heavy metal removal required improvement by tuning the interface between CNF and heavy metals by understanding removal mechanisms [57]. X-ray absorption spectra measured at the Cu K -edge were used to determine the oxidation states and chemical environments of Cu species in the whole-cell and peptidoglycan samples. In the whole-cell samples, most of the Cu retained at both pH values was coordinated by phosphate ligands. The whole-cell fractions contained significant concentrations of Cu(I) as well as Cu(II). An X-ray absorption near-edge spectrum analysis suggested that Cu(I) was coordinated by amine and thiol ligands [58].

Table 13.3 Interatomic distance (R), coordination numbers (N), Debye-Waller factors (σ^2), and correction to energy (ε_0) of main edge obtained by fitting the experimental Fe K -edge EXAFS spectra (Adapted from Ref. [50], with permission)

S.N.	Atoms	N	R	σ^2	Atoms	N	R	σ^2
A-site					B-site			
(400); ($x = 0.56$)								
1	O	4	1.86962	0.0013	O	6	2.08710	0.0051
2	Fe	12	3.87514	0.0053	Fe	6	3.04160	0.0113
3	$\varepsilon_0 = -3.7$				Fe	6	3.62771	0.0006
(500); ($x = 0.59$)								
1	O	4	1.89451	0.00100	O	6	2.07861	0.00600
2	Fe	12	3.61973	0.00100	Fe	6	3.01072	0.00600
3	$\varepsilon_0 = -3.2$				Fe	6	3.82953	0.00600
(600); ($x = 0.53$)								
1	O	4	1.89930	0.003	O	6	2.05073	0.003
2	Fe	12	3.61516	0.003	Fe	6	3.03648	0.003
3	$\varepsilon_0 = -2.8$				Fe	6	3.73780	0.003
(800); ($x = 0.54$)								
1	O	4	1.89134	0.003	O	6	2.05974	0.003
2	Fe	12	3.59051	0.003	Fe	6	3.03278	0.003
3	$\varepsilon_0 = -2.5$				Fe	6	3.70240	0.003
(1000); ($x = 0.59$)								
1	O	4	1.91525	0.003	O	6	2.04707	0.003
2	Fe	12	3.62107	0.003	Fe	6	3.05108	0.003
3	$\varepsilon_0 = -2.7$				Fe	6	3.47700	0.003
(1200); ($x = 0.71$)								
1	O	4	1.89175	0.003	O	6	2.04818	0.003
2	Fe	12	3.59563	0.003	Fe	6	3.03543	0.003
3	$\varepsilon_0 = -2.7$				Fe	6	3.74050	0.037

x is cation inversion estimated from Rietveld refinement

13.5.4 Other Applications

In addition to several above applications, this technique is able to give complete account of metal-oxygen interaction in materials of technological importance. Fe L -edge works as an important probe to identify presence of metal-oxygen interaction at MgO and Fe interface in Fe/MgO/Fe [59–61], Fe/MgO/Fe/Co multilayers [62], and MgO/Fe/MgO multilayers [63]. This technique is also able to give information about the change of valence state in Fe/MgO/Fe/Co multilayers under influence of intense irradiation [64]. Apart from this we carried out implantation of MgO using Zn and Fe. It is contemplated on the basis of NEXAFS measurements that no interaction occurs between implanted and host lattice [65].

S. Kumar et al. [66] studied the electronic structure of $\text{Mg}_{0.95}\text{Mn}_{0.05}\text{Fe}_{2-2x}\text{Ti}_{2x}\text{O}_{4\pm\delta}$ ($0 \leq x \leq 0.5$) ferrites at various edges such as at O K , Fe $L_{3,2}$, Fe K , and Ti $L_{3,2}$

using near-edge X-ray absorption fine structure (NEXAFS) spectroscopy. From the O *K*-edge spectra, they reported that the Fe 3d orbitals are considerably modified with the substitution of Ti ions. They observed that at $x \geq 0.3$, a new spectral feature originates (~ 532 eV) due to the transitions from oxygen 2p to Ti 3d orbitals and this spectral feature starts dominating the pre-edge spectra of the system. Both Fe $L_{3,2}$ - and Fe *K*-edge spectra suggest that iron Fe^{3+} ions convert into Fe^{2+} with the substitution of Ti ions. However, the Ti $L_{3,2}$ -edge NEXAFS spectra reveal that the valence state of Ti ions remains at 4+ for all the samples.

X-ray absorption spectroscopy is a very useful technique to know about the origin of ferromagnetism in dilute magnetic semiconductors. Various groups have used this technique to get information about the presence of oxygen vacancies, metal cluster formation, valence state, and site symmetry of the doped ions in a host semiconducting materials. S. Kumar et al. [67] reported the electronic structure of Co-doped CeO_2 nanoparticles using X-ray absorption fine structure spectroscopy. They performed NEXAFS measurements at spectra at Ce $M_{5,4}$, Ce L_3 , and O *K*-edge. Figure 13.31 represents the oxygen (O) *K*-edge NEXAFS spectra of Co-doped CeO_2 nanoparticles along with the reference spectrum of Ce_2O_3 . Three main features were observed as represented by $a_1(4f^0)$ at 530.0 eV, $b_1(5d-e_g)$ at 532.7 eV, and $c_1(5d-t_{2g})$ at 537.0 eV for pure and Co-doped CeO_2 nanoparticles. Broader and less intensive features were also found near 543.0 eV. It is well known that the O 1s NEXAFS spectra strongly depend on the Ce oxidation state. According to the dipole selection rules, the absorption must be from an s orbital into a p orbital. The excitation from the O 1s into the Ce 4f and Ce 5d levels becomes dipole allowed through the hybridization of the Ce orbitals with the O 2p orbitals [68, 69]. The spectral feature at 530.0 eV as labeled by a_1 (see Fig. 13.31) in CeO_2 is due to a transition from O 1s to Ce $4f^0$ state, which is the lowest unoccupied level. By comparing the O *K*-edge spectra of Co-doped CeO_2 with CeO_2 and Ce_2O_3 (see Fig. 13.31), it is observed that the spectral features of doped samples resemble with that of CeO_2 , which indicates that most of the Ce ions are in +4 state. Mullins et al. [69] also reported similar type of observations in the case of CeO_2 . However, in case of Ce_2O_3 , it is reported that a new spectral feature appeared at 535.0 eV and spectral feature at 530.0 eV disappeared. This new spectral feature originates at 535.0 eV which corresponds to a transition from $\text{O}1s^2\text{Ce}4f^1 \rightarrow \text{O}1s^1\text{Ce}4f^2$. However, they observed that all Co-doped CeO_2 nanoparticles show the absence of the spectral feature at 535.0 eV, and presence of strong peak at 530.0 eV indicates that Ce ions are in 4+ state.

From the EXAFS analysis, they found that the interatomic distance of Ce-O and Ce-Ce/Co decreases with Co doping, which shows a contraction of the lattice. The decrease in Ce-O distance also reflects that there is a formation of oxygen vacancies in CeO_2 matrix. They also performed the atomic multiplet calculations for Co $L_{3,2}$ -edge, in order to determine the valence state, symmetry, and field splitting. The results of atomic multiplet calculations was in good agreement with the experimental observation and show that Co-ions are in 2+ state and substituted at Ce-site with crystal field splitting of $10Dq = 0.57$ eV. The XAFS measurements

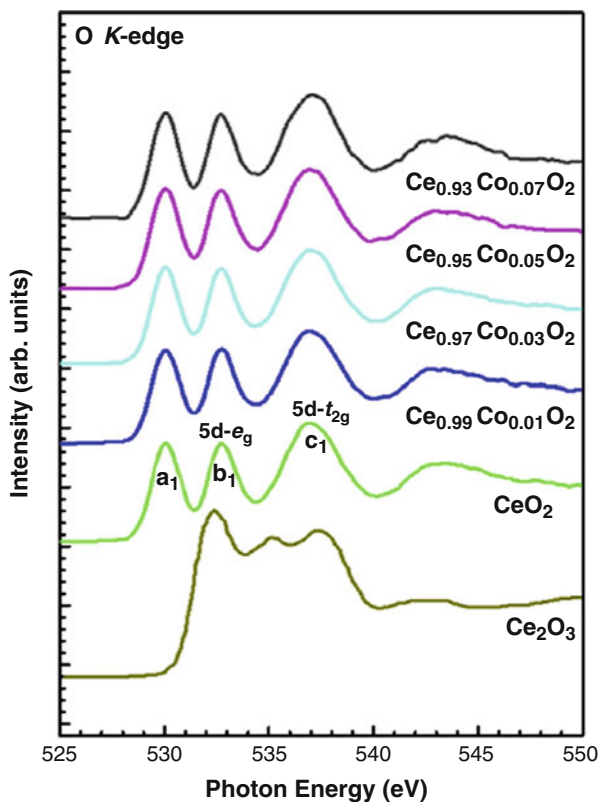


Fig. 13.31 O K-edge spectra of $\text{Ce}_{1-x}\text{Co}_x\text{O}_2$ ($0 \leq x \leq 0.7$) nanoparticles along with reference spectrum of Ce_2O_3 . (Adapted from the [66], with permission)

reveal that the Co-ions occupy the Ce position in the CeO_2 host matrix and create an oxygen vacancy.

Sharma et al. [70] reported the room-temperature ferromagnetism in pulsed laser deposition grown Fe-doped CeO_2 thin films. They used NEXAFS technique to study the electronic structure of these thin films. From the Fe $L_{3,2}$ -edge and Ce $M_{5,4}$ -edge NEXAFS spectra, they observed that Fe ions are in mixed valent $\text{Fe}^{2+}/\text{Fe}^{3+}$ states, while Ce ions are in 4+ state of Ce, throughout the doping. In order to understand the origin of ferromagnetism, they had performed X-ray magnetic circular dichroism (XMCD). The XMCD signal of thin films reveals the ferromagnetic ordering of substituted Fe ions in the ceria matrix, and they concluded that ferromagnetism is intrinsic to the ceria system and is not due to any secondary magnetic impurity.

Faheem Ahmed et al. [71] reported the morphological evolution between nanorods and nanosheets and room-temperature ferromagnetism of Fe-doped ZnO nanostructures. They study the origin of ferromagnetism in these materials using

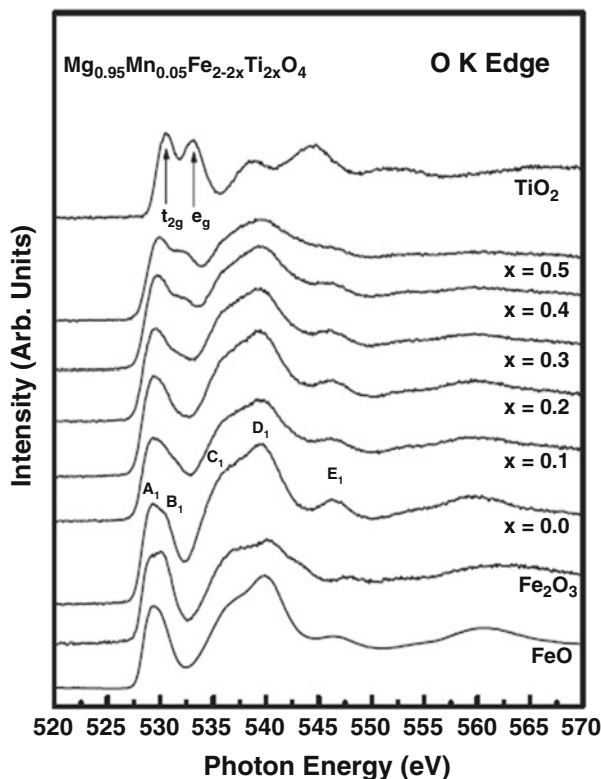


Fig. 13.32 Oxygen (O) K-edge NEXAFS spectra of FeO, Fe₂O₃, TiO₂ and Mg_{0.95}Mn_{0.05}Fe_{2-2x}Ti_{2x}O₄ samples. (Adapted from the Ref. [73], with permission)

the NEXAFS and EELS. The NEXAFS and EELS studies revealed the absence of metal clusters up to 5%, and Fe is found to be in a mixed (Fe²⁺/Fe³⁺) valence state with Fe²⁺ as the dominant state.

Electronic structure and magnetic properties of Co-doped TiO₂ thin films were studied using X-ray absorption spectroscopy by S. Kumar et al. [72]. They deposited thin films using the PLD method and then collected NEXAFS spectra at Ti L_{3,2} and Co L_{3,2} edges. From NEXAFS results they observed that Co and Ti ions are in 2+ and 4+ valence state, respectively. The atomic multiplet calculation performed at Co L_{3,2}-edge also supports the experimental observations and shows that Co ions are in 2+ valence state in O_h (octahedral) symmetry.

S. Kumar et al. [73] reported the structural, electrical transport, magnetic, and electronic structure studies of Mg_{0.95}Mn_{0.05}Fe_{2-2x}Ti_{2x}O₄ ferrite using X-ray diffraction, dielectric spectroscopy, DC magnetization, and near-edge X-ray absorption fine structure (NEXAFS) measurements (Fig. 13.32).

They had measured the NEXAFS spectra at various edges such as O K-, Fe L_{3,2}-, Fe K-, and Ti L_{3,2} edges to investigate the chemical states and the

electronic structure of the $\text{Mg}_{0.95}\text{Mn}_{0.05}\text{Fe}_{2-2x}\text{Ti}_{2x}\text{O}_4$ ($0 \leq x \leq 0.5$) system at room temperature.

The O *K*-edge spectra indicate that the Fe 3d orbitals are considerably modified with the substitution of Ti ions. They observed that at $x \geq 0.3$, a new spectral feature originates (~ 532 eV) which may be due to the transitions from oxygen 2p to Ti 3d orbitals and this feature starts dominating the pre-edge spectra of the system. From the electronic structure at both Fe $L_{3,2}$ - and Fe *K*-edge spectra, they found that iron Fe^{3+} ions convert into Fe^{2+} with the increase in the doping of Ti ions. The Ti $L_{3,2}$ -edge NEXAFS spectra reveal that the Ti remains in the 4+ state for all the samples. The observed experimental results have been explained on the basis of dilution of the magnetic sub-lattice by Ti substitution, which provides a strong interplay between electrical and magnetic properties along with their electronic structure.

13.6 Conclusions

This book chapter introduces and describes the generation of X-ray, fundamentals of XAS theory, experiment procedure, and data analysis. In this chapter, we have discussed in detail about the layout and working of the synchrotron facility. As this chapter demonstrates and reinforces the ever-expanding utilization of the XAS technique for the characterization of materials, therefore, this chapter will be very useful to readers, who utilize XAS technique for determining the fundamental physical and chemical properties of various complex materials. At the end of this chapter, various applications of XANES-EXAFS on several oxide materials have been discussed. The scientific cases presented in this chapter underline the strong complementarity of XANES/EXAFS with other spectroscopic techniques more traditionally employed in the study of defect, lattice distortion, and other structural information of the variety of material such as infrared absorption spectroscopy, X-ray diffraction, XPS, and electron paramagnetic resonance (EPR).

References

1. de Groot, F., & Kotani, A. (2008). *Core level spectroscopy of solids*. Boca Raton: CRC Press.
2. Bunker, G. (2010). *Introduction to XAFS*. Cambridge: Cambridge University Press, UK.
3. Newville, M. (2014). *Reviews in Mineralogy and Geochemistry*, 78, 33–74.
4. Schnorr, C. S., & Ridgway, M. C. (2015). *X-ray absorption spectroscopy of semiconductors*. Springer series in optical sciences. Springer-Verlag Berlin Heidelberg.
5. Sharma, A., Varshney, M., Shin, H. J., Lee, B. H., Chae, K. H., & Won, S. O. (2017). *Materials Chemistry and Physics*, 191, 129.
6. Sun, Z., Yan, W., Yao, T., Liu, Q., Xie, Y., & Wei, S. (2013). *Dalton Transactions*, 42, 13779.
7. Rehr, J. J., & Ankudinov, A. L. (2005). *Coordination Chemistry Reviews*, 249, 131.
8. Rehr, J. J., & Albers, R. C. (2000). *Reviews of Modern Physics*, 72, 621.
9. Chen, J. G. (1997). *Surface Science Reports*, 30, 1.
10. de Groot, F. (1994). *Journal of Electron Spectroscopy and Related Phenomena*, 67, 529.

11. Carra, P., & Altarelli, M. (1990). *Physical Review Letters*, *64*, 1286.
12. Balerna, A., & Mobilio, S. (2015). Introduction to synchrotron radiation. In: S. Mobilio, F. Boscherini, C. Meneghini (Eds.), *Synchrotron radiation-basics, methods and applications* (pp. 1–28). Heidelberg, New York, Dordrecht, London: Springer.
13. Hwang, H.-N., Kim, H. S., Kim, B., Hwang, C. C., Moon, S. W., Chung, S. M., Jeon, C., Park, C.-Y., Chae, K. H., & Choi, W. K. (2007). *Nuclear Instruments and Methods in Physics Research A*, *581*, 850–855.
14. Lee, I.-J., Yu, C.-J., Yun, Y.-D., Lee, C.-S., Seo, I. D., Kim, H.-Y., Lee, W.-W., & Chae, K. H. (2010). *Review of Scientific Instruments*, *81*, 026103.
15. Binsted, N., Strange, R. W., Hasnain, S. S. (1992). *Biochemistry*, *31*, 12117–12125.
15. Gurman, S. J., Binsted, N., & Ross, I. (1986). *Journal of Physics C*, *19*, 1845–1861.
16. Filipponi, A., DiCiccio, A., & Natoli, C. R. (1995). *Physical Review B*, *52*, 15122–15134.
17. Filipponi, A., & DiCiccio, A. (1995). *Physical Review B*, *52*, 15135–15149.
18. Diccio, A. (1995). *Physica B*, *209*, 125–128.
19. Gaur, A., Shrivastava, B. D., & Nigam, H. L. (2013). *Proceedings of the Indian National Science Academy*, *79*, 921–966.
20. Kelly, S. D., Hesterberg, D., & Ravel, B. (2008). *Methods of soil analysis part 5 mineralogical methods chapter 14*. Madison: Soil Science Society of America.
21. Koningsberger, D. C., Mojet, B. L., Van Dorssen, G. E., & Ramaker, D. E. (2000). XAFS spectroscopy; fundamental principles and data analysis. *Topics in Catalysis*, *10*, 143–155.
22. Thakur, P., Bisogni, V., Cezar, J. C., Brookes, N. B., Ghiringhelli, G., Gautam, S., Chae, K. H., Subramanian, M., Jayavel, R., & Asokan, K. (2010). *Journal of Applied Physics*, *107*, 103915.
23. Kumar, S., Kim, Y. J., Koo, B. H., Sharma, S. K., Vargas, J. M., Knobel, M., Gautam, S., Chae, K. H., Kim, D. K., Kim, Y. K., & Lee, C. G. (2009). *Journal of Applied Physics*, *105*, 07C520.
24. Kumar, S., Koo, B. H., Lee, C. G., Gautam, S., Chae, K. H., Sharma, S. K., & Knobel, M. (2011). *Journal of Nanoscience and Nanotechnology*, *11*, 396–401.
25. Kumar, Y., Singh, A. P., Sharma, S. K., Choudhary, R. J., Thakur, P., Knobel, M., Brookes, N. B., & Kumar, R. (2012). *Applied Physics Letters*, *101*, 112103.
26. Kumar, S., Vats, P., Gautam, S., Gupta, V. P., Verma, K. D., Chae, K. H., Hashim, M., & Choi, H. K. (2014). *Materials Research Bulletin*, *59*, 377–3814.
27. Sharma, A., Singh, A. P., Thakur, P., Brookes, N. B., Kumar, S., Lee, C. G., Choudhary, R. J., Verma, K. D., & Kumar, R. (2010). *Journal of Applied Physics*, *107*, 093918.
28. Kumar, R., Singh, A. P., Thakur, P., Chae, K. H., Choi, W. K., Angadi, B., Kaushik, S. D., & Patnaik, S. (2008). *Journal of Physics D: Applied Physics*, *41*, 155002.
29. Sharma, A., Varshney, M., Kang, S., Baik, J., Ha, T. K., Chae, K. H., Kumar, S., & Shin, H. J. (2016). *Advanced Materials Letters*, *7*, 17–22.
30. Sharma, A., Varshney, M., Shin, H. J., Kumar, Y., Gautam, S., & Chae, K. H. (2014). *Chemical Physics Letters*, *592*, 85–89.
31. Sharma, A., Varshney, M., Park, J. H., Ha, T. K., Chae, K. H., & Shin, H. J. (2015). *RSC Advances*, *5*, 21762–21771.
32. Sharma, A., Varshney, M., Shin, H. J., Park, Y. J., Kim, M. G., Ha, T. K., Chae, K. H., & Gautam, S. (2014). *Physical Chemistry Chemical Physics*, *16*, 19909–19916.
33. Sharma, A., Varshney, M., Park, J. H., Ha, T. K., Chae, K. H., & Shin, H. J. (2015). *Physical Chemistry Chemical Physics*, *17*, 30065–30075.
34. Sharma, A., Varshney, M., Lim, W. C., Shin, H. J., Singh, J. P., Won, S. O., & Chae, K. H. (2017). *Physical Chemistry Chemical Physics*, *19*, 6397–6405.
35. Khemthong, P., Photai, P., & Gridanurak, N. (2013). *International Journal of Hydrogen Energy*, *38*, 15992–16001.
36. Bagherzadeh, M., Mousavi, N., Amini, M., Gautam, S., Singh, J. P., & Chae, K. H. (2017). *Chinese Chemical Letters*, *28*, 1125–1130.
37. Singh, J. P., Kim, S. H., Won, S. O., Lim, W. C., Lee, I.-J., & Chae, K. H. (2016). *CrystEngComm*, *18*, 2701–2711.
38. Singh, J. P., Gautam, S., Srivastava, R. C., Asokan, K., Kanjilal, D., & Chae, K. H. (2015). *Superlattices and Microstructures*, *86*, 390–394.

39. Dixit, G., Singh, J. P., Chen, C. L., Dong, C. L., Srivastava, R. C., Agrawal, H. M., Pong, W. F., & Asokan, K. (2013). *Journal of Alloys and Compounds*, *581*, 178–185.
40. Kumar, H., Srivastava, R. C., Singh, J. P., Negi, P., Agrawal, H. M., Das, D., & Chae, K. H. (2016). *Journal of Magnetism and Magnetic Materials*, *401*, 16–21.
41. Gomes, J. A., Azevedo, G. M., Depeyrot, J., Mestnik-Filho, J., da Silva, G. J., Tourinho, F. A., & Perzynski, R. (2011). *Journal of Magnetism and Magnetic Materials*, *323*, 1203–1206.
42. Carta, D., Casula, M. F., Mountjoy, G., & Corrias, A. (2008). *Physical Chemistry Chemical Physics*, *10*, 3108–3117.
43. Yao, T. (1993). *Japanese Journal of Applied Physics*, *32*, 755–757.
44. Mishra, A., Mehjabeen, k., Jarabana, K. M., & Bisen, S. (2016). *Journal of Physics Conference Series*, *755*, 012044.
45. Calvin, S., Carpenter, E. E., Ravel, B., Harris, V. G., & Morrison, S. A. (2002). *Physical Review B*, *66*, 224405.
46. Nakashima, S., Fujita, K., Tanaka, K., Hirao, K., Yamamoto, T., & Tanaka, I. (2007). *Physical Review B*, *75*, 174443.
47. Torres, C. E. R., Golmar, F., Ziese, M., Esquinazi, P., & Heluani, S. P. (2011). *Physical Review B*, *84*, 06440.
48. Oliver, S. A., Harris, V. G., Hamdeh, H. H., & Ho, J. C. (2000). *Applied Physics Letters*, *76*, 2761.
49. Stewart, S. J., Figueroa, S. J. A., López, J. M. R., Marchetti, S. G., Bengoa, J. F., Prado, R. J., & Requejo, F. G. (2007). *Physical Review B*, *75*, 073408.
50. Singh, J. P., Won, S. O., Lim, W. C., Lee, I.-J., & Chae, K. H. (2016). *Journal of Molecular Structure*, *1108*, 444–450.
51. Kumar, H., Singh, J. P., Srivastava, R. C., Patel, R. P., & Chae, K. H. (2017). *Superlattices and Microstructures*, *109*, 296–306.
52. Parsons, J. G., Aldrich, M. V., & Gardea-Torresdey, J. L. (2002). *Applied Physics Reviews*, *37*, 187–122.
53. Zou, Y., Wang, X., Khan, A., Wang, P., Liu, Y., Alsaedi, A., Hayat, T., & Wang, X. (2016). *Environmental Science & Technology*, *50*, 7290–7304.
54. Que, L., Jr., & Tolman, W. B. (2008). Biologically inspired oxidation catalysis. *Nature*, *455*, 333–340.
55. Hummer, A. A., & Rompel, A. (2013). *Metallomics*, *5*, 597–614.
56. Tiemann, K. J., Gardea-Torresdey, J. L., Gamez, G., Dokken, K., Sias, S., Renner, M. W., & Furenlid, L. R. (1999). *Environmental Science & Technology*, *33*, 150–154.
57. Dwivedi, A. D., Sanandiy, N. D., Singh, J. P., Husnain, S. M., Chae, K. H., Hwang, D. S., & Chang, Y.-S. (2017). *ACS Sustainable Chemistry & Engineering*, *5*, 518–528.
58. Kretschmer, X. C., Meitzner, G., Gardea-Torresdey, J. L., & Webb, R. (2004). *Applied and Environmental Microbiology*, *70*, 771–780.
59. Singh, J. P., Gautam, S., Singh, B. B., Chaudhary, S., Kabiraj, D., Kanjilal, D., Chae, K. H., Kotnala, R., Lee, J.-M., Chen, J.-M., & Asokan, K. (2014). *Advanced Materials Letters*, *5*, 372–377.
60. Gautam, S., Asokan, K., Singh, J. P., Chang, F.-H., Lin, H.-J., & Chae, K. H. (2014). *Journal of Applied Physics*, *115*, 17C109.
61. Singh, J. P., Kaur, B., Gautam, S., Lim, W. C., Asokan, K., Kanjilal, D., & Chae, K. H. (2016). *Superlattices and Microstructures*, *100*, 560–586.
62. Singh, J. P., Gautam, S., Singh, B. B., Raju, M., Chaudhary, S., Kabiraj, D., Kanjilal, D., Lee, J.-M., Chen, J.-M., Asokan, K., & Chae, K. H. (2017). *Vacuum*, *138*, 48–54.
63. Singh, J. P., Lim, W. C., & Chae, K. H. (2015). *Superlattices and Microstructures*, *88*, 609–619.
64. Singh, J. P., Lim, W. C., Gautam, S., Asokan, K., & Chae, K. H. (2016). *Materials and Design*, *101*, 72–79.
65. Singh, J. P., Lim, W. C., Won, S. O., Lee, J., Lee, I.-J., & Chae, K. H. (2018). *Applied Surface Science*, *432*, 132–139.

66. Kumar, S., Gautam, S., Song, T. K., Chae, K. H., Jang, K. W., & Kim, S. S. (2014). *Journal of Alloys and Compounds*, *611*, 329–334.
67. Tsunekawa, S., Fukuda, T., & Kasuya, A. (2000). *Journal of Applied Physics*, *87*, 1318–1321.
68. Feng, X., Sayle, D. C., Wang, Z. L., Paras, M. S., Santora, B., Sutorik, A. C., Sayle, T. X. T., Yang, Y., Ding, Y., Wang, X., & Her, Y.-S. (2006). *Science*, *312*, 1504–1508.
69. Mullins, D., Overbury, S., & Huntley, D. (1998). *Surface Science*, *409*, 307–319.
70. Sharma, S. K., Thakur, P., Kumar, S., Shukla, D. K., Brookes, N. B., & Lee, C. G. (2010). *Thin Solid Films*, *519*, 410–413.
71. Ahmed, F., Kumar, S., Arshi, N., Anwar, M. S., & Koo, B. H. (2012). *CrystEngComm*, *14*, 4016–4026.
72. Kumar, S., Park, J. S., Kim, D. J., Lee, M. H., Song, T. K., Gautam, S., Chae, K. H., Kim, S. S., & Kim, M.-H. (2015). *Ceramics International*, *41*, S370–S375.
73. Kumar, S., et al. (2007). *Journal of Physics: Condensed Matter*, *19*, 476210.

Chapter 14

³¹P Solid-State NMR Spectroscopy of Adsorbed Phosphorous Probe Molecules: Acidity Characterization of Solid Acid Carbonaceous Materials for Catalytic Applications



Bhaskar Garg 

14.1 Introduction

The major source of energy for the present and foreseeable future of any nation is found in chemical bonds. Catalysis affords the means of changing the rates at which chemical bonds are formed and broken and thus allows chemistry of extreme specificity, making it possible to select a desired product over an undesired one. The reduced emissions from contemporary vehicles, the copiousness of fresh food, new pharmaceuticals for improving our health, and environmental remediation, all are made possible by chemical reactions controlled by the catalysts. Among catalysis of substantial interest, acid catalysis is quite prevalent and probably one of the most routine operations worldwide, in both industrial processes and academic settings. The petroleum, chemical, plastic, and pharmaceutical industries, essential to a healthy economy, rely heavily on acid catalysis. Not surprisingly, therefore, it lies at the heart of our quality of life.

In industrial petrochemical processes, homogeneous molecular acid catalysts such as sulfuric acid (H₂SO₄) and hydrofluoric acid (HF) have been well exploited (and will continue to be) over the past several decades. Indubitably, the distinctive spatial separation and self-similarity of structures between the active sites in these liquid acid catalysts perfectly allow consistent energetic interactions between each of active site and reaction substrate, enabling them as the catalyst of choice for most acid-catalyzed reactions. Nevertheless, the aforesaid toxic and corrosive catalysts suffer from their separation from the homogeneous reaction mixture, resulting in abundant non-recyclable acid waste, an issue of utmost importance to the international environmental community.

B. Garg (✉)

Department of Chemistry, Indian Institute of Technology Roorkee, Roorkee, Uttarakhand, India

In recent years, increasingly tight environmental regulations in conjunction with an emphasis on recoverability and reusability of catalysts have prompted researchers in stepping up efforts to embark eco-friendly solid acid catalysts, which are not only easier to separate and recover but also can be reused under appropriate conditions. In this milieu, a wide variety of solid acid catalysts, namely, cation-exchange resins, solid superacids, (supported) metal oxides/sulfides/triflates, zeolites, molecular sieves, silica, natural clays, and heteropolyacids, have been increasingly used in academic settings in a variety of acid-catalyzed reactions [1–14]. In line with this, some of these solid acid catalysts are routinely used in industrial settings as well.

The catalytic activity and product selectivity of solid acid catalysts, toward specific reaction, are usually evaluated by diversified features of acidic sites. Specifically, Lewis vs. Brønsted acid types, locations of acid sites either in the internal voids or on the external surfaces, their strength (strong vs. weak), and concentrations constitute the most prominent features of solid acid catalysts. Needless to say, a thorough and better understanding of these features is not only crucial for novel design but also for modification and exploration of practical yet newest applications of pre-existing solid acid catalysts. Taking this into account, a variety of analytical and spectroscopic techniques have been developed and explored extensively over the past few decades to dictate the acidity (-OH functions in most cases) of solid acid catalysts. In general, these conventional methods such as temperature-programmed desorption [15–17], titration [18, 19], microcalorimetry [20, 21], Fourier-transform infrared spectroscopy (FT-IR) [22–26], and solid-state nuclear magnetic resonance spectroscopy (SSNMR) [27–31] rely heavily on adsorption/desorption phenomena associated with the chemisorbed and/or physisorbed basic probe molecules (ammonia, pyridine, trimethylphosphine, etc.) on acidic sites, which in turn may be correlated to the overall acidity. All these conventional methods have their own distinct advantages as well as drawbacks w.r.t. diversified acidic features of acidic sites as mentioned above. This can be understood through IR spectroscopy based on the different interactions (coordination and H-bonding) between acidic sites and adsorbed pyridine as a basic probe molecule. Specifically, the appearance of characteristic stretching vibrations at 1540 cm^{-1} indicates that pyridine is adsorbed on Brønsted acid sites. On the other hand, adsorption of pyridine on Lewis acid sites gives band at 1455 cm^{-1} , distinguishing between both the acid types effectively. Despite this, this method does not provide any quantitative information about the concentration of acidic sites. Furthermore, the probe molecules used in indirect detection methods have also appeared too basic (at certain instances) to distinguish delicate differences in the locations of acidic sites, leading to an ambiguity in the interpretation of experimental results [32, 33].

Indubitably, the last decade has witnessed the substantial potential of SSNMR, a desirable and most versatile technique, in the acidity characterization of solid acid catalysts with high-resolution and quantitative capability [30, 31, 34]. In particular, ^1H NMR, ^{13}C NMR, and ^{31}P NMR are widely available and routinely accessible SSNMR techniques for acidity characterization. Among them, ^1H magic-angle-spinning (MAS) NMR can be used as a direct approach for the identification or detection of different types of acidic -OH groups in a solid acid catalyst.

For instance, the bridging hydroxyls in zeolites (Si-OH-Al; Brønsted acidic sites) usually exhibit their proton chemical shifts (δ ^1H) in the range of 3.6–5.6 ppm [29, 32, 35–37]. On the contrary, non- or weakly acidic terminal hydroxyls (Al-OH, Si-OH) can be identified at δ 1.5–2.0 ppm. Effective as the direct detection ^1H NMR method is, it cannot provide reliable information about the type, strength, and distribution of acid sites. The pursuit of alternative methods using ^1H MAS NMR or specific nucleus of interest capable of meeting some of aforesaid challenges has resulted in the development of a variety of absorbable probe molecules. Specifically, it has been reported that H-bonding interactions between pyridine- d_5 basic probe and Si-OH groups in zeolites, for instance, lead to higher proton chemical shifts (δ $^1\text{H} = 2$ –10 ppm), whereas a relatively higher downfield shift may be experienced (ca. 12–20 ppm) due to the adsorption of pyridine- d_5 on Si-OH-Al, resulting in the formation of pyridinium ion complexes ($\text{C}_5\text{D}_5\text{NH}^+$) [29, 38]. Aside from that of ^1H -pyridine- d_5 , the Brønsted acidity characterization of a solid acid catalyst may also be achieved by ^{13}C MAS NMR based on the couplings between acidic-H and carbonyl oxygen of isotopically labeled 2- ^{13}C -acetone, a hydrocarbon probe molecule [39, 40]. At this juncture, it is important to recall that the natural abundance of ^{13}C nucleus ($I = 1/2$) is quite low (1.07%), demanding highly expensive ^{13}C -enriched reagents for acidity characterization. On the other hand, despite having 99.98% natural abundance, the applicability of ^1H nucleus ($I = 1/2$) is limited due to relatively narrower chemical shift window (~ 20 ppm). Thus, in terms of resolution, sensitivity, and convenient handling, both ^1H and ^{13}C SSNMR with adsorbed probe molecules are less favorable.

Owing to its wide chemical shift range (>650 ppm) together with 100% natural abundance, ^{31}P NMR ($I = 1/2$) of adsorbed phosphorous-containing probe molecules, in particular trimethylphosphine (TMP) and trialkylphosphine oxides (R_3PO), by far, have been considered as a reliable technique having a self-assembly of very likable or ideal properties, and the scope of its utility has increasingly matured over the two decades for acidity characterization of a variety of solid acid catalysts [41–52]. Unlike ^1H and ^{13}C , ^{31}P MAS SSNMR with adsorbed R_3PO probe molecules can provide detailed information about acidic features including distribution, concentration, type, and strength of distinct acidic sites. However, since the focus of this book chapter strongly lies on discrimination between acid types and characterization of acidic strengths of recently employed carbonaceous solid acid catalysts in conjunction with their applications in acid-catalyzed reactions, we do not intend to cover other acidic features such as distribution/locations of acidic sites including the reaction mechanism. To get in-depth coverage or the corresponding productive details on these features, readers are suggested to consult the existing reviews or literature [29–31, 34, 53–55].

As such, this chapter will begin with a brief introduction about SSNMR, describing basic principle, different kinds of interactions, and instrumentation. Afterward, we shall move on the analysis strategies for ^{31}P MAS SSNMR using ^{31}P -TMP and ^{31}P - R_3PO approach. Lastly, the most significant and current state-of-the-art in the acidity characterization (acid type or strength) of different classes of carbonaceous solid catalysts as well as their catalytic applications (wherever

applicable) will be discussed. In this context, an emphasis will be placed on the characterization of Brønsted acidity and/or ^{31}P MAS SSNMR of adsorbed ^{31}P -TMP and ^{31}P -R₃PO on different carbonaceous catalysts.

14.2 Solid-State Nuclear Magnetic Resonance (SSNMR) Spectroscopy

SSNMR has long been heralded as a sensitive probe offering unique atomic-scale and element-specific insight into the structure, disorder, and dynamics of materials and, thus, makes a significant impact in different areas of science, including, but not limited to, industrial pharmaceutical chemistry, materials science, geochemistry, acid-base catalysis, polymer chemistry, and proteomics [47, 56–64].

14.2.1 Basic Concept

SSNMR is a kind of NMR spectroscopy, which is characterized by the presence of directionally dependent or anisotropic interactions such as chemical shift anisotropy (CSA) and internuclear dipolar coupling, to name but a few [61, 63, 65, 66]. To appreciate the role of anisotropy, it would be worthwhile to shed light on the basic difference between the spectra of samples recorded in both solution and solid state. To this end, the very first question which comes in mind is that what does the anisotropy really mean? Well, it may be understood by the following simple example.

Imagine a classroom with full of younger kids sitting in five or more rows for study. Needless to say, it would be much easier for the teacher of this class to move along the rows rather than moving across. Such movement of the teacher along the rows may be defined as velocity or motional anisotropy. Indeed, this is exactly the situation one frequently encounters in the solid materials. For instance, many properties of solid materials such as refractive index, electrical conductivity, etc. are anisotropic, and the magnitude of the relevant parameter is generally dependent on the direction of measurement w.r.t. to the crystal axis. At this juncture, it should be noted that besides externally applied magnetic field, the NMR resonance frequency also depends on other local factors including the presence of other randomly distributed nuclear spins in the vicinity. Thus, it may conclude that in the externally applied magnetic field, the resonance frequency of the nuclear spin, in the solid state, is direction dependent. For different orientations of the crystal in the magnetic field, the resonance frequencies are also different. Now, consider a situation where all kids in the classroom are randomly sitting in nearly all directions. In this case, the teacher will definitely face difficulties in moving toward any direction, and this situation may be defined as velocity isotropy, a phenomenon that can be seen in liquid

samples or solutions due to rapid and random motions (rotational and translational) of molecules. Consequently, the material properties become independent of the direction of measurement. Thus, in solution NMR, spectra consist of a series of very sharp transitions due to averaging of anisotropic interactions (by rapid Brownian motion of molecules) into isotropic interactions such as the isotropic chemical shift and J -coupling. Hence, in solution NMR, the high-resolution spectra can be easily recorded as such or over time and quite easy to interpret. On the contrary, the slow molecular motions cannot average the anisotropic terms to zero. Thus, the NMR spectra of powdered samples usually exhibit broad spectral lines, which result in the low-resolution characteristics, producing difficulties in the precise interpretation of non-equivalent nuclei. Despite this hindrance, the NMR spectrum of a solid sample is intrinsically rich in information as far as chemistry, structure, and dynamics are considered.

14.2.2 Interactions in SSNMR

As stated above, anisotropic interactions are orientation dependent and have a substantial influence on the behavior of a system of nuclear spins [63, 65, 67] in media with limited or no mobility. The powders, crystals, molecular aggregates, proteins, ceramics, resins, polymers, cements, metal and alloys, glasses, minerals, and large membrane vesicles constitute some of such media, while there are several ways for a nuclear spin to communicate with its surroundings in the solid state. Some important interactions associated with SSNMR are briefly discussed below.

14.2.2.1 Chemical Shift

It is well known that a nucleus is surrounded by an electron cloud and electrons are involved in bonding with neighboring atoms. These surrounding electrons produce an effective magnetic field at the site of the nucleus. As a result, the resonance frequency of the nucleus shifts away from that of a bare nucleus. This shift is known as the chemical shift, which describes the shielding effect of the electrons on the nucleus. Among a group of lines, the position of the resonance line of a nucleus serves as a fingerprint of the chemical environment of the nucleus. The corresponding Hamiltonian for the chemical shift term can be represented by the following equation [30].

$$\hat{H}_{\text{CS}} = \omega_0 \left[\delta_{\text{iso}} + \frac{1}{2} \delta_{\text{aniso}} \left(3\cos^2 \theta_{\text{CS}} - 1 + \eta \sin^2 \theta_{\text{CS}} \cos 2\phi_{\text{CS}} \right) \right] \hat{I}_z \quad (14.1)$$

where δ_{iso} is the isotropic chemical shift, δ_{aniso} is the anisotropic parameter, η is an asymmetric factor, and θ_{CS} and ϕ_{CS} are the polar angles of the external

magnetic field in chemical shift tensor (second-rank Cartesian tensors, which are 3×3 matrices).

In a solid single crystal sample, the position of the resonance line is influenced (shifted) by the anisotropy of chemical shift (CSA) according to the orientation of the molecule. In a solid powdered sample having a large number of randomly oriented crystals, the orientation of the molecules varies w.r.t. the external field, resulting in various chemical shifts due to the anisotropy of shielding effect. In other words, the acquired spectrum is an overlap of a large number of very closely spaced lines, which are often complex to analyze. In nutshell, the chemical shift term is closely related to the density of electron cloud surrounding the nucleus and directly proportional to the strength of the external magnetic field as described in Eq. 14.1 [30]. However, due to rapid molecular tumbling motion in the liquid state, only isotropic component of the chemical shift is considered (δ_{aniso} are averaged to zero over time; Eq. 14.1).

14.2.2.2 Dipole-Dipole Interaction

Being a magnetic dipole, the nuclear spin can also interact directly with the magnetic dipole of other nuclei, and this type of interaction is commonly referred as direct dipole-dipole interaction or dipolar coupling [65, 66]. Notably, one should not relate dipolar coupling with spin-spin coupling or J -coupling (as will be discussed later), which is generally small in the solid state and occurs due to the interaction between nuclear spins and electron cloud. The dipolar coupling causes the resonance line to split with the frequency separation between the split lines, providing a measure of the distance between the nuclear spins. The dipole-dipole interactions can be either homo- or heteronuclear based on the like and unlike spins, respectively. The dipolar interactions are directly proportional to the magnetogyric ratios (γ) of the nuclei and also depend on some special parameters, namely, internuclear distance ($1/r^3$) and the angle (θ) between the internuclear vector and the direction of the magnetic field, providing the nuclear spatial structural information. It would be worthwhile to mention here that in solid samples, the nuclei with high natural abundance (^1H , ^{19}F , ^{31}P , etc.) as well as high value of γ also have strong dipolar interactions, which result in the broadening of their NMR signals and, thus, producing the SSNMR spectra with poor resolution [65].

14.2.2.3 Quadrupole Interaction

It is well known that the nuclei with the spin quantum number $I = 1/2$ have a spherical distribution of electric charge. On the contrary, the nuclei with $I > 1/2$ such as ^2H , $^{6/7}\text{Li}$, ^{11}B , ^{14}N , ^{17}O , ^{23}Na , ^{25}Mg , ^{27}Al , ^{35}Cl , ^{39}K , ^{59}Co , $^{69/71}\text{Ga}$, and ^{93}Nb have an asymmetric distribution of nucleons giving rise to a non-spherical positive electric charge distribution. Such nuclei are termed as quadrupolar nuclei, which are of importance in a wide variety of materials and the compounds that make up

the inner layers of planet, Earth [30, 59, 61, 68–72]. Interestingly, for over 63% of the elements, the only NMR-active isotopes are quadrupolar, while over 74% of the nuclides in the periodic table have $I > 1/2$. The asymmetric charge distribution in the nucleus is defined by the nuclear electric quadrupole moment eQ , which is measured in barn ($\sim 10^{-28} \text{ m}^2$). Being an intrinsic property, eQ remains the same regardless of the environment. The quadrupole nuclei interact with the gradient in the electric field (EFG) [73] produced by the surrounding electrons and can have orientations with different energies. The quadrupole interaction is a ground state interaction similar to that of dipole-dipole interaction. However, it is dependent upon the distribution of electric point charges in the molecule as well as EFGs. The EFGs at the quadrupolar nucleus can be defined by the three components (symmetric traceless tensors), $|V_{XX}| \leq |V_{YY}| \leq |V_{ZZ}|$. Since the EFG tensor is traceless, isotropic tumbling in solution averages it to zero. Whereas the magnitude of the quadrupolar interaction is given by the nuclear quadrupole coupling constant C_Q ($C_Q = eQV_{ZZ}/h$ KHz or MHz), the asymmetry or shape of the quadrupole interaction is expressed by an asymmetry parameter η_Q ; $\eta_Q = (V_{XX} - V_{YY})/V_{ZZ}$, where $0 \leq \eta_Q \leq 1$. If $\eta_Q = 0$, the EFG tensor is axially symmetric. The quadrupole interactions can be as large as several MHz, with C_Q values of many hundreds of KHz to hundreds of MHz [73]. Despite this, in most cases, the quadrupole interactions remain smaller than the dominant Zeeman interactions.

14.2.2.4 Zeeman Interaction

Another interaction that manifests in the solid state is Zeeman interaction, an interaction between the applied magnetic field and the magnetic moment of the nucleus [74]. As the nuclear magnetic moment is proportional to the spin quantum number and γ , the Zeeman interactions become operative only with nuclei having $I > 0$, producing $2I + 1$ energy levels of separation. Furthermore, as γ is a constant for each specific nucleus, the frequency of each nucleus is also different at a specific applied magnetic field.

14.2.2.5 Indirect Dipole-Dipole or Spin-Spin Interaction or J -Coupling

J -coupling or indirect dipole-dipole interaction typically occurs between two non-equivalent nuclei, which are connected by three or less than three bonds in a single molecule. Its strength is usually less than 200 Hz. In the solid state, the J -coupling is relatively smaller than other type of interactions and is mostly neglected due to no obvious effect on the spectrum.

From the discussion in the preceding section, it is apparent that NMR resonance frequency varies with the relative orientation between the molecule and the external magnetic field. Due to the anisotropic terms, the NMR spectra in the solid state are intrinsically broad, leading to severely overlapped lines with poor spectral resolution. Consequently, in order to improve the spectral resolution, comparable to

what is available for the solution-state, a number of SSNMR techniques have been developed to minimize large anisotropic NMR interactions between the nuclei. The most important high-resolution SSNMR techniques are discussed below.

14.3 High-Resolution Solid-State NMR Techniques

14.3.1 Magic-Angle Spinning (MAS)

Magic-angle spinning (MAS) is one of the most standard and widely used techniques in solid-state NMR. Historically, this technique was independently discovered by both Andrew and Lowe in 1959 as a way to narrow the NMR lines by rapidly spinning the solid specimen (imposing a motion on the nuclei) [75, 76]. A few years later, in 1966, an alternative approach was developed by imposing a motion on the nuclei in spin space [77, 78]. In the early days, these two techniques were recognized as competitive approaches to line narrowing in solids. However, at present, they are seen very much as complementary methods. In particular, in MAS technique, the solid specimen is rapidly rotated around an axis oriented at an angle of 54.736° , the “magic angle,” w.r.t. the external magnetic field [61, 79] as depicted in Fig. 14.1. The solid samples are finely powdered and tightly packed into rotors of various diameters, which are then spun at maximum possible MAS rate, depending on the rotor size and type of the experiment under study. The smallest commercially available rotors with diameters of 0.75 mm can be rotated at rates of over 100 KHz [61]. However, in order to efficiently suppress the anisotropic interactions, the rate of MAS must be greater than or equal to the magnitude of the anisotropic interaction to average it to zero, i.e., $3 \cos^2\theta - 1 = 0$, when $\theta = 54.736^\circ$ or 54.74° . Notably, the CSA and many dipolar interactions can be correlated with the factor $3 \cos^2\theta - 1$.

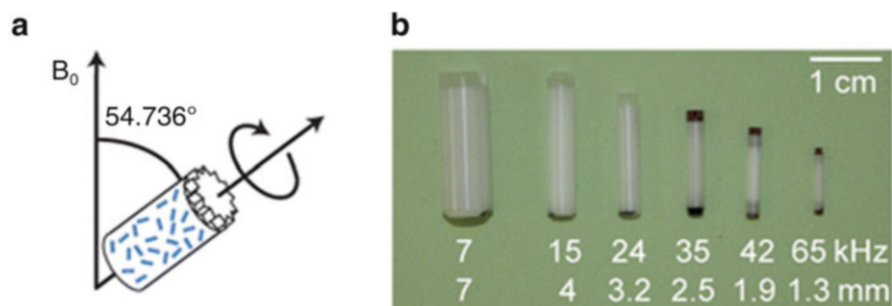


Fig. 14.1 (a) Schematic depiction of the MAS experiment, where a polycrystalline sample is rotated about an axis inclined at an angle of 54.736° with respect to the external magnetic field B_0 . (b) Rotors with various outer diameters and the maximum MAS rates that can be achieved with them. (Reprinted with permission from Ashbrook and Sneddon [61]. Copyright (2014) American Chemical Society)

Theoretically, the higher the spinning speed, the narrower the spectrum is. However, if the sample is spun at a rate less than the magnitude of the anisotropic interaction (for instance, quadrupole interaction), a manifold of spinning sidebands becomes visible [65, 79], which are separated by integer multiples of the spinning rate.

14.3.2 Cross-Polarization

Owing to the high value of magnetogyric ratios (γ) of protons, the solution-state NMR normally utilizes proton detection experiments. However, in SSNMR, the proton detection is less favorable due to the large number of homonuclear dipolar interactions. As a result, carbon detection is frequently used, which itself is a much less sensitive nucleus. Consequently, polarization-transfer technique serves as a key to enhance the signal of a less sensitive nuclei or spins such as ^{13}C or ^{15}N [80]. Specifically, in cross-polarization (CP) technique, pioneered by Pines [81], the abundant nucleus having high magnetogyric ratios (γ) such as ^1H or ^{19}F is excited, and its energy is transferred to the observed nucleus or dilute spins (^{13}C and ^{15}N) by using a long low-power pulse on both the channels under the so-called Hartmann-Hahn (H-H) matching conditions [82]. The radio-frequency power ratio of these pulses needs to be tuned so that the transition energy for both nuclei is the same, facilitating the effective polarization-transfer between the two spatial neighboring heteronuclei through the facile dipolar interaction. The visualization of this magnetization transfer as a matching of the energy levels is shown in Fig. 14.2. The H-H matching conditions for the static sample can be represented by Eq. 14.2.

$$\omega_{1S} = \omega_{1I} \quad (14.2)$$

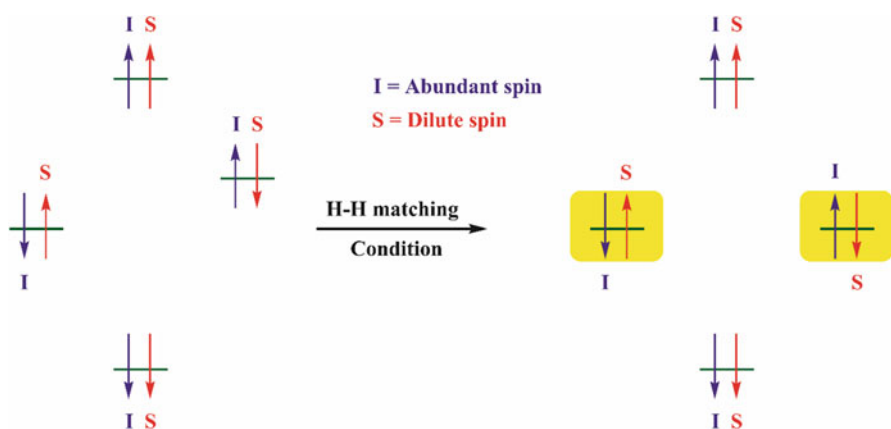


Fig. 14.2 A schematic for the visualization of magnetization transfer as a matching of the energy levels

However, depending upon the modulation of spinning rate, Eq. 14.2 is modified as:

$$\omega_{IS} = \omega_{IH} + \eta\omega_r \quad (14.3)$$

where $\eta = \pm 1, \pm 2$ and $\omega_r =$ sample spinning frequency. Since abundant spins are strongly coupled (dipolar interactions), they are subject to large fluctuating magnetic fields resulting from motion. This leads to rapid spin-lattice relaxation at the abundant nuclei (T_1 of the proton is usually shorter than ^{13}C). As such, one does not have to wait for slowly relaxing dilute nuclei to relax, providing CP as a time-saving technique. In other words, this method offers a much stronger signal than direct excitation, allowing faster repletion rate. When combined with MAS, this technique is termed as CPMAS NMR [83], decreasing the efficiency of polarization-transfer with increasing spinning speed. Nevertheless, at relatively high speed, some shaped pulses [84, 85] can be used to appreciate the H-H matching conditions in order to improve the efficiency of CP technique. However, the requirement of high-power irradiation is the major limitation of CP method that can deteriorate the probe or the sample at certain instances.

14.3.3 Dilution

Dilution is yet another technique, which is used to minimize the anisotropic interactions as well as to increase the signal-to-noise (S/N) ratio of NMR-active isotope(s) having a low natural abundance (^{13}C , 1.108%). Nevertheless, this method only works (to get high-resolution spectra) if there are no heteronuclear dipolar interactions such as with protons and/or fluorine. Moreover, the large anisotropic chemical shielding effects can also lead in the broadening of the spectra.

14.3.4 Heteronuclear Decoupling

The inherent poor resolution and associated sensitivity, due to the presence of strong anisotropic nuclear spin interactions (CSA and dipole-dipole interactions), are the major challenges in solid-state NMR for the determination of structure, parameters, and dynamics of molecular systems. Though MAS can lead to coherent averaging of CSA and dipole-dipole interactions (as described above), it is not sufficient to completely averaging out all the anisotropic interactions, which are present in complex and/or rigid spin systems. Consequently, radio-frequency pulse irradiation along with sample spinning on the high γ nuclei can be applied to eliminate the heteronuclear dipolar interactions. Such a line narrowing technique is referred as heteronuclear decoupling [86–89]. The simplest and conventional heteronuclear decoupling scheme involves high-power, continuous wave (CW) on resonance irradiation of the protons during the detection of the heteronuclei,

improving the linewidths. However, this method is not sufficient as the resonance offsets could lead to incomplete decoupling and residual line splitting [90, 91]. Nowadays, a great variety of heteronuclear decoupling methods (primarily for ^1H), namely, two-pulse phase modulation (TPPM) [86] and its variants such as frequency-swept TPPM ($\text{Sw}_f\text{-TPPM}$) [89], SPINAL [87] and xiX [92], DROOPY [93], and refocused continuous wave ($r\text{CW}$) [94], have been found to be particularly attractive. Interestingly, some of these methods such as SPINAL64, $\text{Sw}_f\text{-TPPM}$, and $r\text{CW}$ have shown similar performance as that for ^{19}F decoupling and can perform even better than the other techniques [95].

14.3.5 Multiple-Pulse Homonuclear Decoupling

Pioneered by three giants, namely, Waugh, Huber, and Haeberlen [96], the first multiple-pulse homonuclear decoupling technique, WAHUHA pulse sequence, came into existence for effective line narrowing in low-resolution SSNMR spectra. In multiple-pulse decoupling, the nuclear spin vectors are rendered time-dependent using radio-frequency irradiation. Whereas the time average of the homonuclear dipolar Hamiltonian in the first order is rendered zero, other interactions are partially retained. Nowadays, a variety of multiple-pulse techniques, including, but not limited to, MREV-8 [97], LG [98], DUMBO [99], and BLEW-12 [100], are successfully employed in SSNMR to eliminate certain deficiencies such as inhomogeneity in the radio-frequency field, phase errors, and high-order homonuclear dipolar Hamiltonian. When combined with MAS, these techniques are referred as combined rotation and multiple-pulse spectroscopy (CRAMPS) [101].

14.3.6 Recoupling Technique(s) in SSNMR

As the name suggests, recoupling denotes the reintroduction of afore-discussed NMR anisotropic interactions, which otherwise are eliminated or averaged out by means of MAS. Since these interactions are distance/orientation dependent (as mentioned above), their controlled reintroduction can furnish a lot of important structural information including distance or dihedral angle information. Though spinning the sample at relatively slow rate and extracting spin interaction parameters from spinning sideband amplitudes serve as a general way to yield information on spin interactions, nowadays recoupling techniques are commonly used to get the desirable high-resolution SSNMR spectra [102]. In general, the recoupling methods often rely on an averaging of the Hamiltonian theory [103], in which a time-dependent Hamiltonian is expressed as a time-independent effective Hamiltonian (Eq. 14.4).

$$H_{\text{eff}} = H^{(0)} + H^{(1)} + H^{(2)} + \dots \quad (14.4)$$

where $H^{(0)}$ stands for lowest-order term or the actual average Hamiltonian, $H^{(1)}$ is the first-order correction term, and so on. In other words, if radio-frequency pulses are applied in rotor-synchronized fashion, the averaging of spatial-dependent parameters (CSA or dipolar coupling) can be removed under MAS. The rotational echo double resonance (REDOR), firstly introduced in 1989 [104], represents the classical recoupling technique for heteronuclear spin systems. Herein, ^{13}C - ^{15}N as an example, the difference between the signal intensity of an acquired ^{13}C spectrum with and without a ^{15}N π pulse (that can selectively reintroduce the dipolar coupling) depends on the distance between the labeled nuclei. Needless to say, during signal acquisition, the dipolar couplings are removed by MAS producing the narrow signals [105]. However, it is to be noted that the radio-frequency pulses are only applied to the spin part of the dipolar Hamiltonian, while the MAS influences the spatial part. The transfer of populations in double resonance (TRAPDOR) [106], rotational echo adiabatic passage double resonance (REAPDOR) [107], and symmetry-based resonance echo saturation pulse double resonance (S-RESPDOR) [108] are some commonly used dipolar recoupling techniques for heteronuclear systems involving half-integer spins. Analogous to its heteronuclear variants in principle, the homonuclear recoupling technique is somewhat complicated in terms of the selective reintroduction of spin interactions. In this case, the selectivity is usually achieved by fine-tuning of the spinning frequency (rotor) to zero or double-quantum frequencies of the desired spin-pair, for instance, in rotational resonance [109].

14.4 Instrumentation

The current state-of-the-art NMR instruments typically use superconducting magnets that have a much higher magnetic field strength than their predecessors, with the sample inserted into the center bore as shown in Fig. 14.3 [110]. These spectrometers rely on computers allowing signal averaging followed by a mathematical calculation, which is known as Fourier transform (FT). Generally speaking, the basic components such as pulse programmer, data system, magnets, and observe and decoupler transmitters of the SSNMR instruments are the same as those of solution-phase instruments. It is, therefore, appropriate to briefly discuss the key components of a modern NMR spectrometer(s) being used to investigate the solid samples.

Owing to the large spectral widths as often encountered in SSNMR spectra, the intense radio-frequency pulses are needed to uniformly excite the entire spectral range and produce distortionless spectra. Furthermore, the direct dipole-dipole interactions are often significant (^1H) and demand large amount of radio-frequency energy to decouple as stated above. For these reasons, the use of high-power amplifiers is the key requirement to observe and decouple channels and a pneumatic spinning unit to achieve the necessary spin rate for MAS [111]. These amplifiers are capable of producing up to a KW of power. Normally, the observe channel for a ^{13}C

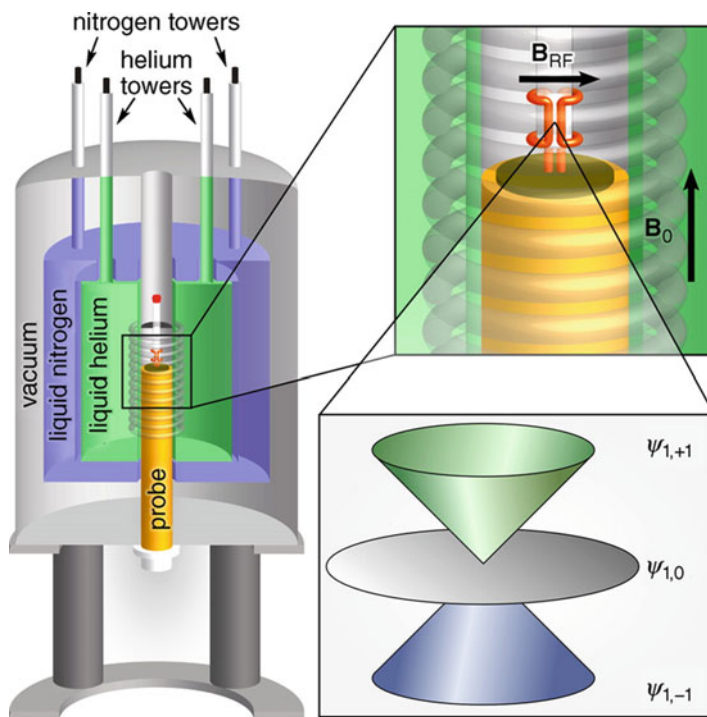


Fig. 14.3 A sample is placed in a strong magnetic field (B_0) oriented in the vertical direction to produce the Zeeman effect. When a magnetic field is present, the degeneracy of the spin angular momentum states of a spin-1 nucleus ($I = 1$ nucleus) is removed. A transverse radio-frequency pulse (B_{RF}) causes transitions between the Zeeman energy levels. The NMR signal is observed using the coil of the probe as the detector. (Reprinted with permission from Kinnun et al. [110]. Copyright (2012) American Chemical Society)

NMR experiment requires ca. 400 W of power under the instrumental conditions (5.87 T, 250 MHz) [110]. However, amplifiers should have triggering capabilities to amplify only the radio-frequency pulse in order to suppress the background noise in the recorded spectral data. On another front, in carbon experiment, the decoupler amplifier must produce the radio-frequency signal at one-fourth the power level of the observe channel.

The analogue-digital converters (ADCs) are the advantageous components in the modern-pulsed FT-NMR spectrometers as the signals are recorded in analogue form, i.e., the superposition of various damped harmonic oscillations. However, the signals in analogue form must be digitized by computer in order to access the FT. The “maximum sampling rate” is very prominent parameter feature of an ADC defining the maximum resonance frequency range, which can be digitized effectively, and, thus, the largest spectral window. Typically, in modern NMR instruments, 16–18-bit digitizers are used. This implies that the most intense signal

can be digitized as 2^{18} . However, the trade-off for such fast sampling rate in an ADC is a reduced dynamic range as the signals with $\leq 1/2^{18}$ of the signal amplitude cannot be distinguished in intensity [111]. Consequently, the receiver gain or the signal amplification should be adjusted so that the most intense signal could almost fill the amplifier completely.

It is an undeniable fact that most of today's research in the field of SSNMR rely heavily on MAS at which the spatial dependencies of many NMR interactions are averaged to their isotropic values. However, sample spinning at a precisely defined speed and angle is quite challenging and places stringent design requirements on SSNMR spectrometers. Thanks to the MAS speed controller, a vital part in SSNMR instrumentation, which not only supplies the spinning gases but also helps in monitoring and controlling the spinning speed. In most cases, the compressed dry air is used in the routine experiments. However, N_2 gas is, by far, the best alternative for temperature-dependent experiments, especially, to avoid oxidation at high temperatures. Notably, in the more advanced MAS experiments, two separate gas streams can be used effectively, bearing gas to support the sample and drive gas for spinning the sample. In line with the current developments in MAS controller, the ability to spin samples automatically at a desired speed is quite appreciating, but does not work well with dense powdered samples or half-full rotors. In such cases, it is preferred to control the spinning manually. In line with this, inserts or inert powders may be used to fill rotors for getting stable spinning [111].

Recall that high-resolution SSNMR relies upon the ability to rapidly rotate the sample about the magic angle (57.74°), relative to the magnetic field. Taking this into account in conjunction with the magnitude of the radio-frequency energy involved, it is of no surprise that probes for SSNMR experiments are somewhat more complex and different than their solution-phase counterparts. This complexity results in greater space requirements for probe design, and, therefore, a traditional SSNMR spectrometer works on wide-bore superconducting magnets having a bore diameter of ca. 89 mm [111]. Notably, the SSNMR probes are engineered to handle much higher radio-frequency power, which is required to excite and decouple the frequency bandwidths, a necessary condition for SSNMR. Specifically, the most common probe used in SSNMR experiment is a double-resonance probe that includes the standard irradiation and receiver electronics, yet capable of performing CP and MAS experiments. Normally, a double air-bearing design is used for MAS, which can permit a high-speed spinning (3.5–5 KHz) at variable temperature (~ 77 –400 K), with the ability for multinuclear data acquisition [63]. The samples are loaded into a small rotor, with sealed caps on both ends. The rotors are typically made of zirconium oxide (ZrO_2) for performing the experiments at ambient temperature. However, silicon/boron nitride-made rotors are used for variable temperature experiments. The rotor is inserted into the stator assembly, and compressed air or N_2 gas passes through tiny holes to float the sample on a bearing of gas. Mechanistically, the NMR probe delivers a transmitter-induced radio-frequency pulse to the nuclei. This rotates the net magnetization about an axis transverse to the main magnetic field. The spins precess consistently and relax

back to the equilibrium. As a result, they become out of the phase, generating a decaying signal in the probe coil. This decay is referred as free induction decay (FID). Finally, a fast FT (FFT) of the FID is performed computationally to record the NMR spectrum [110].

14.5 ^{31}P SSNMR Versus Adsorbed Probe Molecules

As stated above, ^{31}P nuclei with a wide chemical shift range (>430 ppm) and γ value are much more sensitive than ^{13}C nuclei in terms of the natural abundance (400-fold higher). Accordingly, phosphorous compounds are preferred than hydrocarbon probes as far as acidity characterization of solid acids by SSNMR is considered. The use of phosphorous compounds as probes such as TMP [112–114] not only leads to a highly sensitive spectrum but also avoids an isotope-enriched sample.

In an elegant work, Lunsford and co-workers [112, 115] discovered that TMP can be used as an efficient probe molecule in ^{31}P NMR to characterize the acidity of H-Y zeolite. This study set the new trend and opened the door for probing the acidic features of a wide range of solid acid catalysts such as microporous zeolites [29, 114, 116], mesoporous aluminosilicate molecular sieves [117], 12-tungstophosphoric acid [118], and sulfated and mixed metal oxides [119]. The adsorption of TMP on the surface of solid catalysts (as mentioned above) can be understood based on the three different interaction models as shown in Fig. 14.4.

1. Physisorption of TMP on less acidic $-\text{OH}$ groups through weak H-bonding interaction, leading a ^{31}P chemical shift of ca. -55 ppm.
2. Chemisorption of TMP on Lewis acid centers formed by metal cations, with a relatively wider ^{31}P chemical shift range of -20 to -60 ppm. Such large chemical shift window can be attributed to the formation of M-P bond through electron pair sharing of LUMO of metal center (M) with P atom of TMP.
3. Chemisorption of TMP on Brønsted acidic sites, resulting in the formation of TMPH^+ ionic complexes, giving rise to ^{31}P chemical shift in the range of ca. -2 to -5 ppm.

With reference to the interaction mode (3), it should be noted that an effective proton transfer occurs from solid acid surface (bridging hydroxyl group(s)) to adsorbed TMP molecule as revealed by a DFT study [120]. In particular, the greater the extent of proton transfer, the greater is the strength of acid site, resulting in an alight increase in ^{31}P chemical shift. Besides identifying the Lewis acid sites, one can also get the qualitative information of the acidic strength using ^{31}P -TMP approach. For instance, when TMP was adsorbed on ZrO_2 , the ^{31}P NMR spectrum exhibited three distinct resonances at δ -30.3 (sharp), -42.2 (weak shoulder), and -50.1 (most intense and sharp) ppm, which corresponded to the three types of Lewis acidic sites [121] with varying acidic strength (Fig. 14.5). However, the absence of any resonance for TMPH^+ ionic complex clearly indicated that ZrO_2

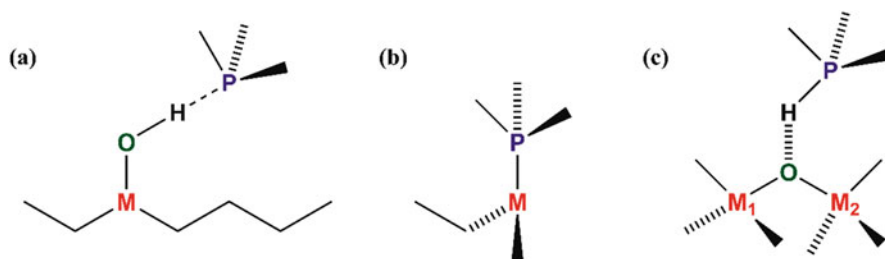


Fig. 14.4 Different interaction modes of adsorbed TMP on the surfaces of solid acid catalysts: (a) Physisorbed TMP on hydroxyls (H-bonding interaction). (b) Chemisorbed TMP on Lewis acidic sites (usually a metal cation). (c) Chemisorbed TMP on Brønsted acid sites

does not contain any Brønsted acidic sites [121]. In contrast to what was seen for bare ZrO_2 , the adsorption of TMP on mixed metal oxides such as $\text{MoO}_x/\text{ZrO}_2$ and WO_x/ZrO_2 exhibited two major ^{31}P resonances at $\delta -3.3$ and 57.8 ppm and a relatively weak resonance (broad) at $\delta -48$ ppm. Based on the appearance of a resonance signal at $\delta -3.3$ ppm, it was concluded that the introduction of MoO_x or WO_x can induce the formation of Brønsted acidic $-\text{OH}$ groups, protonating the adsorbed TMP into TMPH^+ ionic complex. Aside from that of $\delta -3.3$ ppm resonance, the two resonances at $\delta 57.8$ and -48 ppm were attributed to TMPO and TMP , respectively. In this milieu, it would be worthwhile to comment here that TMP is a pyrophoric and toxic molecule and can be easily oxidized, especially when exposed to oxygen [112], during sample treatment. Furthermore, being volatile in nature under ambient atmospheric conditions, the use of TMP as a probe molecule is somewhat inconvenient and requires more attention during experimental handling.

The superiority of sulfated metal oxide, in terms of inducing new Brønsted acidic sites as well as increasing Lewis acidic strength, over bare metal oxides has also been demonstrated by ^{31}P -TMS SSNMR acidity characterization scheme. For example, the adsorption of TMP on pristine TiO_2 resulted only a single sharp ^{31}P resonance at $\delta -35$ ppm. Nevertheless, the resonance peak at $\delta -35$ ppm experienced a significant downfield shift ($\delta = -8$ ppm) after surface modification of TiO_2 by sulfonating agent affording $\text{SO}_4^{2-}/\text{TiO}_2$ (Fig. 14.6) [122]. The appearance of ^{31}P peak at $\delta -27$ ppm in $\text{SO}_4^{2-}/\text{TiO}_2$ clearly indicated a reasonable increase in Lewis acidity.

In a relevant yet other work, the adsorption of TMP on the surface of pristine Al_2O_3 and $\text{SO}_4^{2-}/\text{Al}_2\text{O}_3$ catalysts afforded ^{31}P signals at $\delta -51$ and -49 ppm. The appearance of an additional small peak in the ^{31}P SSNMR spectrum of pristine Al_2O_3 at $\delta \sim 34$ ppm could be ascribed due to the presence of TMPO [123]. It is noteworthy that ^{31}P SSNMR spectra of both $\text{SO}_4^{2-}/\text{TiO}_2$ and $\text{SO}_4^{2-}/\text{Al}_2\text{O}_3$ were accompanied by a resonance at $\delta -3 \pm 1$ ppm, presumably, due to the interaction of TMP with Brønsted acidic $-\text{SO}_4^{2-}$ groups (Fig. 14.7). These results are consistent with the notion that sulfonation of metal oxides not only increases the Lewis acidity but also promotes the formation of new Brønsted acidic sites ($-\text{SO}_4^{2-}$).

Fig. 14.5 ^{31}P single-pulse MAS NMR spectra (with proton decoupling) of TMP loaded on mesoporous materials: (a) zirconia, (b) $\text{MoO}_x/\text{ZrO}_2$, and (c) WO_x/ZrO_2 . Asterisks denote spinning sidebands. (Reprinted with permission from Xu et al. [121]. Copyright (2006) American Chemical Society)

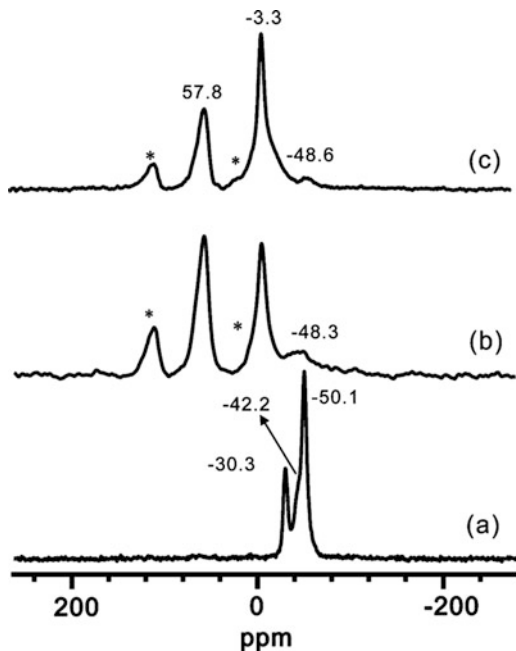
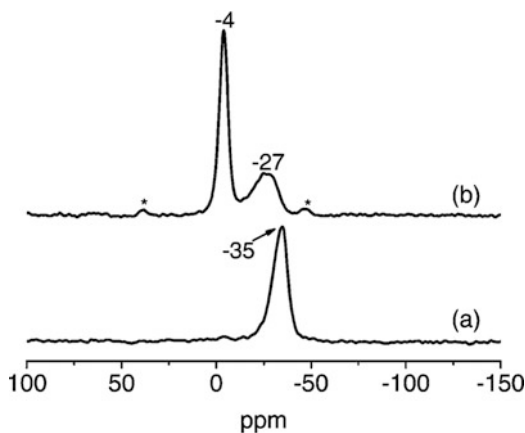
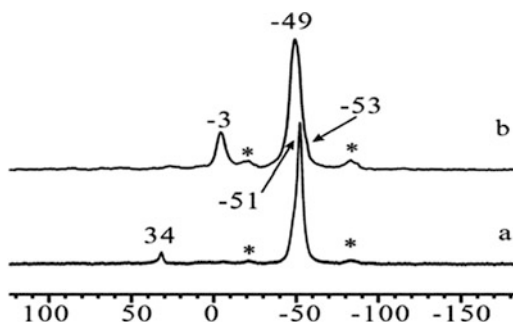


Fig. 14.6 ^{31}P MAS NMR spectra of TMP loaded on TiO_2 (a) and $\text{SO}_4^{2-}/\text{TiO}_2$ (b). Asterisks denote spinning sidebands. (Reprinted with permission from Zhang et al. [122]. Copyright (2008) American Chemical Society)



To investigate the possible interactions between Al metal and TMP, Grey and co-workers [124] relied on the use of $^{31}\text{P}/^{27}\text{Al}$ TRAPDOR (transfer of populations in double resonance) technique. In a typical work, the adsorption of TMP on H-Y zeolite exhibited two ^{31}P resonance signals at δ -32 and -46 ppm in conjunction with resonances at δ -3 (TMPH⁺) and -60 ppm (physisorbed TMP). However, a noticeable TRAPDOR effect was experienced only with resonance at δ -46 ppm, revealing that TMP binds to Al centers predominately as also verified by ^{27}Al - ^{31}P INEPT (insensitive nuclei enhanced by polarization-transfer) method [125].

Fig. 14.7 ^{31}P single pulse with ^1H decoupling MAS spectra of TMP adsorbed on (a) $\gamma\text{-Al}_2\text{O}_3$ and (b) $\text{SO}_3/\text{Al}_2\text{O}_3$. The weak signal at 34 ppm in (a) is due to trimethylphosphine oxide. (Reprinted with permission from Yang et al. [123]. Copyright (2003) Royal Society of Chemistry)



In yet another work, Grey [126, 127] and Larsen [54] adopted a new protocol, in which TMP was replaced by a series of diphenyldiphosphine or bisphosphane ($\text{Ph}_2\text{P}(\text{CH}_2)_n\text{PPh}_2$; $n = 1, 3,$ and 6) probes for probing the Brønsted acidity and spatial distribution of acidic sites in a variety of solid acid catalysts by making the use of ^{31}P MAS and ^{31}P two-dimensional double-quantum (2D DQ) NMR experiments [128]. In this way, the resonance positions, internuclear distances between two P atoms, and concentration of various phosphine molecules/ions could be assigned in different adsorption systems with ease.

Lewis vs. Brønsted acidity features can also be described for pure and sodium ion-exchanged CeO_2 catalysts using ^{31}P -TMP SSNMR approach as deduced by Xu, Wang, and co-workers [129]. For instance, the adsorption of TMP on both bare- and cation-exchanged CeO_2 catalysts gave a singlet ^{31}P resonance at $\delta -19.3$ ppm, indicative of the presence of only Lewis acidic sites. Interestingly, when catalyst was treated at high temperature (180°C), the signal at $\delta -19.3$ ppm remained intact, describing the water-tolerant character of CeO_2 catalyst.

Aside from those of many experimental studies, the ^{31}P -TMP SSNMR approach has also been used to rank Lewis acid strength by making use of a series of theoretical Lewis models having different metallic centers (B, Al, and Ti) [114]. In such studies, the binding energy value, as calculated from the adsorbed TMP on Lewis acidic sites, was used as an evaluating parameter to know the strength of Lewis acidity. Indeed, a linear correlation was observed between binding energy and calculated δ values for different Lewis acid systems with different metallic centers, facilitating the usefulness of aforesaid approach for the quantitative characterization of Lewis acidic strength.

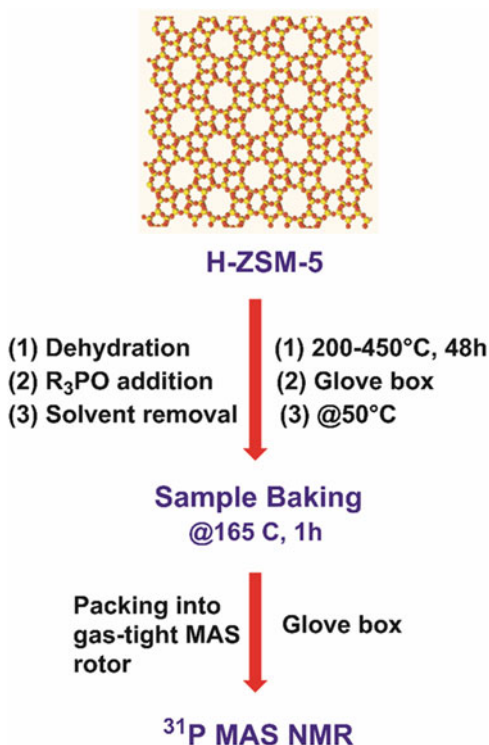
In light of the above discussion, it is evident that ^{31}P -TMP SSNMR approach is quite useful in authenticating the Lewis acidity in different solid acid catalysts. However, the same approach is less suitable in probing the Brønsted acidity, due to the much narrower ^{31}P chemical shift window (ca. $\delta -2$ – 5 ppm) as observed for TMPH^+ ionic complexes [120]. In this context, the use of the oxidized derivatives of trialkylphosphine (R_3PO) such as TMPO, triethylphosphine oxide (TEPO), tributylphosphine oxide (TBPO), and trioctylphosphine oxide (TOPO) as probe molecules has appeared to be more practical for characterizing the Brønsted acidic sites [13, 14, 41–45, 48, 53, 64, 130–133]. This is due to the fact that the electron

density around P atom in R₃PO molecules can be changed easily through the facile interaction between the Brønsted acidic sites and oxygen atom of the probe molecule (formation of R₃POH⁺ complexes). This results in the significant downfield shifting of ³¹P resonances over a wide range (ca. δ 50–105 ppm), depending on the acid strength. Among different R₃PO homologues, TMPO is perhaps the most studied base (probe molecule) capable of spanning over a wide range of ³¹P resonances (ca. 50–98 ppm) after adsorption on Brønsted acidic sites. However, the ³¹P resonances of crystalline bulk and physisorbed TMPO usually occur at ca. δ 39 and 30–45 ppm, respectively [30, 31, 34, 134].

The frequent use of TMPO in acidity characterization methods is mainly due to its suitable molecular size (kinetic diameter (KD) = 0.55 nm), capable of characterizing not only the strength but also the locations of acidic sites in solid acid catalysts [134]. For instance, consider the case of microporous H-ZSM-5 zeolite catalyst, which is known to consist of 10-membered ring (10-MR) channels with an average pore diameter of ca. 0.6 nm. Thus, the adsorption of TMPO on H-ZSM-5 may provide the information pertaining both extracrystalline and intracrystalline acidic sites. However, owing to its larger KD (0.82 nm), TBPO cannot diffuse into the pore channels of H-ZSM-5 and, thus, can only interact with acid sites present on the external surface. As such, this approach provides a powerful mean of differentiating external and internal acidic sites in a variety of solid acid catalysts [134, 135]. At this juncture, it would be worthwhile to shed light on the standard operating scheme being developed by Liu and co-workers [30, 34] for ³¹P-R₃PO SSNMR or ³¹P-TMPO/TBPO SSNMR, in particular. In a typical experiment, the solid acid catalyst (H-ZSM-5 zeolite) was first dehydrated at 473–723 K for 2 days under $\leq 10^{-5}$ torr vacuum. The dehydrated catalyst was placed in a vessel inside the glove box, and a known amount of TMPO in anhydrous CH₂Cl₂ was introduced into the vessel. Next to this, the TMPO-loaded catalyst was allowed to heat at 50 °C under vacuum for efficient solvent removal. The homogeneous distribution of probe molecules on acidic sites of zeolite catalyst was further ascertained by heating the adsorbate-loaded catalyst above the melting point of TMPO (165 °C; TMPO's m.p. = 140 °C) for ca. 1 h. In the final step, the sample was packed into a gas-tight MAS NMR rotor in the glove box. The standard operation procedure for the acidity characterization of H-ZSM-5 using ³¹P-TMPO/TBPO SSNMR approach is shown in Scheme 14.1. It is noteworthy that some catalysts tend to adsorb CH₂Cl₂ as strongly as that of TMPO, generating some unwanted ³¹P relic. Based on the experimental observations, it was generalized that the adequate thermal pretreatment of the adsorbate-loaded catalyst is crucial to warrant a homogeneous distribution of probe molecule. In this context, the literature report authored by Kojima and Hayashi [136] sheds light on the effect of residual CH₂Cl₂ during adsorption of probe molecule (TMPO) on solid acids. Aside from that, an alternative method for TMPO loadings onto zeolites has also been reported, describing the use of anhydrous THF and agitation treatment [113].

Following the standard protocol of TMPO adsorption, the extensive investigations have been made over the past several years for acidity characterization of a range of diversified solid acid catalysts such as microporous zeolites [29, 35, 41,

Scheme 14.1 Standard operation procedure for ^{31}P -R₃PO approach



45 130, 131, 134, 135, 137, 138], HPAs [133, 139], molecular sieves [134, 135, 137], and supported/sulfated metal oxides [140, 141]. For instance, with the added advantage of theoretical DFT calculations, Deng and co-workers [142] explored the distribution of Brønsted acidic sites in zeolite, H-MCM-22. Specifically, it was found that in H-MCM-22, the potential Brønsted acidic sites reside at extracrystalline side pockets or intracrystalline supercages (12-MR, $(0.71 \times 0.71 \times 1.82 \text{ nm})$ connected by 10-MR windows of $0.4 \times 0.54 \text{ nm}$ in size) on the external surfaces, while 2D sinusoidal channels (10-MR, $0.4 \times 0.59 \text{ nm}$) were not found to have any such sites, providing an insight into reaction selectivity of H-MCM-22 for catalytic applications. In similar yet another work, ^{31}P -TMPO SSNMR approach was applied to characterize acidic sites in HTaMoO₆ and Nb_xW_(10-x) oxides, which represent the layered nanosheet and mesoporous structures, respectively [143, 144]. In the latter case, the adsorption of TMPO on Nb_xW_(10-x) oxides resulted a gradual downfield shifting of the main ^{31}P resonance from δ 67 ppm ($x = 7$) to 70 ($x = 5$) to 75 ppm ($x = 3$), suggesting an increase in the acidity with a sequential decrease in the loadings of Nb (x). However, the ^{31}P SSNMR spectra of TMPO-loaded Nb₃W₇ ($x = 3$) was also accompanied with a distinct sharp small peak at $\delta \sim 86 \text{ ppm}$, inferring the presence of superacidity features [44]. Thus, a correlation between Nb/W ratio vs. acidic strength of Nb_xW_(10-x) could be established, which was also found in accordance with the observed catalytic activities.

Given the 100% natural abundance and much wider chemical shift of ^{31}P as compared to ^{13}C as well as relatively a higher basicity of TMPO than acetone, ^{31}P -TMPO SSNMR is somewhat more superior than $2\text{-}^{13}\text{C}$ -acetone approach for acidity characterization as far as the variations in the concentration and strength of Brønsted acidic sites are considered. For example, five different Brønsted acidic sites with varying acidic strength ($\delta = 53, 63, 67, 75,$ and 86 ppm) could be identified in the ^{31}P SSNMR spectra of TMPO-loaded H-ZSM-5 (Si/Al = 15) [134]. Likewise, TMPO-loaded H-Y exhibited ^{31}P resonances at $\delta 55$ and 65 ppm for Brønsted acidic sites in supercages and sodalite, respectively [145]. On the contrary, adsorption of $2\text{-}^{13}\text{C}$ -acetone on the Brønsted acidic sites of H-ZSM-5 and H-Y exhibited only a singlet ^{13}C peak at $\delta 223$ and 220 ppm, respectively [39, 146]. This may be attributed to the easy alteration of electron density around P atom of TMPO unlike acetone, forming TMPOH^+ ion complexes. Notably, the TMPOH^+ complexes (protonated by Brønsted acidic sites) are not affected by water, while the metallic center of Lewis acidic sites tends to react easily with a water molecule, generating weak Brønsted acidic sites. This feature has been put in a good use too for differentiating Brønsted and Lewis acidic sites in solid acid catalysts following ^{31}P -TMPO SSNMR approach. For example, the ^{31}P MAS SSNMR spectrum of TMPO-loaded dehydrated ZrO_2 catalyst exhibited four resonances at $\delta 34, 41, 53,$ and 62 ppm. Among these, the resonances at $\delta 34$ and 41 ppm could be assigned to mobile and physisorbed TMPO with ease. However, to ascertain the origin of the other two resonances, the TMPO-loaded ZrO_2 catalyst was progressively exposed to humidity. Interestingly, with increasing water content, the intensities of both resonances at $\delta 53$ and 62 ppm decreased, while their chemical shift values remained intact, attributable to the two different Lewis acidic sites with varying acid strength [140]. When ZrO_2 was sulfonated, the TMPO-loaded SZ- $x\text{N}$ ($x = 0.5, 1.0,$ and 2.0) samples or sulfated ZrO_2 exhibited both Brønsted (^{31}P $\delta = 68$ and 87 ppm) and Lewis (^{31}P $\delta = 63$ and 90 ppm) acidic sites. Specifically, the resonances at $\delta 90$ and 87 ppm were attributed to the strong Lewis and Brønsted acidic sites, respectively. These results clearly indicate that sulfonation reactions of bare solid catalysts have positive effect on acidic strength [140]. In this regime, it should be noted that larger ^{31}P chemical shift value, for instance, at $\delta 90$ ppm in sulfated ZrO_2 , represents TMPO adsorbed on Lewis acidic centers with stronger acid strength as also inferred by DFT calculations [120]. Effective as the progressive hydration treatment is, it certainly requires a sophisticated or even a tedious experimentation in distinguishing Lewis and Brønsted acidity. Taking this into account, Chan and co-workers [147] developed a straightforward NMR spectrum-editing technique capable of directly identifying both Lewis and Brønsted acidic sites in solid catalysts, for example, zeolites. In particular, this could be achieved by utilizing a selective ^1H excitation pulse in conjunction with the Lee-Goldburg cross-polarization (LG-CP) method [148, 149]. Notably, the latter can effectively suppress the homonuclear dipole-dipole interactions.

Based on many experimental studies (as described above), it can be generalized that the ^{31}P chemical shift values of adsorbed phosphorous probe molecules

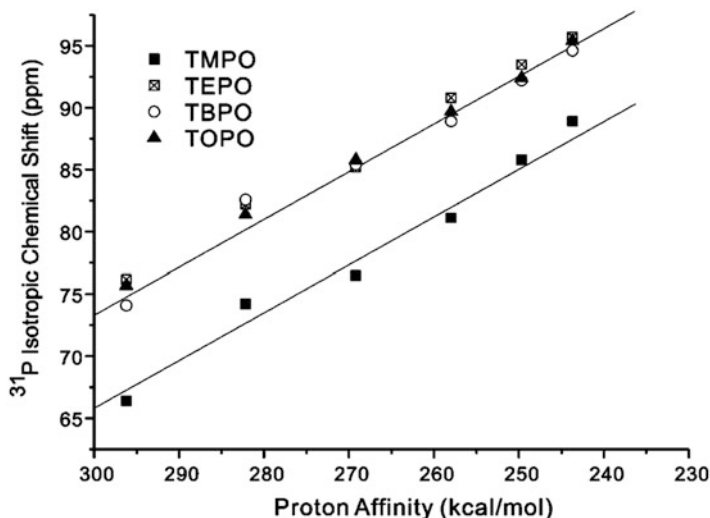


Fig. 14.8 Optimized structures of (a) TMPOH^+ , (b) TEPOH^+ , (c) TBPOH^+ , and (d) TOPOH^+ adsorption complexes for an 8T cluster model with Si-H bond length of 2.00 Å. Selected interatomic distances (Å) are indicated. (Reprinted with permission from Zheng et al. [44]. Copyright (2008) American Chemical Society)

increase with increasing strength of Brønsted acidic sites [41, 42]. However, the observed ^{31}P chemical shifts w.r.t. acidic strengths can not only be taken as a “hallmark”, producing an ambiguity in the interpretation of acidic strength(s) at certain instances. In order to fill this gap, Liu, Deng, and co-workers [44, 150] carried out a systematic DFT calculation to establish the correlation between the Brønsted acidic strength and ^{31}P chemical shifts of adsorbed R_3PO molecules on acid sites. As such, the adsorption structures and ^{31}P chemical shift values of adsorbed R_3PO molecules were derived based on a typical 8T zeolite cluster model [150] by varying the distance of Si-H bond. As shown in Fig. 14.8, linear correlations between the proton affinities (the energy required to tear off the protons from Brønsted acidic sites) and R_3PO molecules were observed. Taking TMPO as a representative case, these correlations may be expressed by Eq. 14.5.

$$\delta^{31}\text{P} = 182.866 (\pm 5.314) - 0.3902 (\pm 0.020) \times \text{proton affinity} \quad (14.5)$$

$$(R^2 = 0.9913).$$

It is apparent from Fig. 14.8 that ^{31}P chemical shift values for TEPO, TBPO, and TOPO nearly overlap with one another, suggesting that the variations in the length of alkyl chain in R_3PO molecules have no obvious effect on ^{31}P chemical shift values. Nevertheless, an average and consistent downfield offset of ca. $\delta^{31}\text{P} 8 \pm 2$ ppm was recognized for adsorbed R_3PO molecules, relative to that of TMPO. Based on the proton affinity of ca. 250 kcal/mol as inferred by DFT calculations, a ^{31}P chemical

shift value of ~ 86 ppm was set as the superacidity threshold for TMPO. As such, this study can facilitate the direct assessment of acidity features of a variety of solid acid catalysts.

14.6 ^{31}P SSNMR Versus Acidity Characterization of Carbonaceous Materials and Their Composites for Catalytic Applications

Indubitably, the metal-free catalysis is the key in developing an efficient and sustainable chemistry for both academic research and possible technological applications. As the 15th most abundant natural element and the 4th most abundant element by mass, carbon has appeared as an attractive “green” option for catalytic transformations in both liquid and gas phase. In particular, the catalysis involving heterogeneous carbon materials for the transformation or synthesis of (in)organic substrates is typically known as carbon catalysis or carbocatalysis. Nevertheless, it is worth commenting here that at certain instances, carbocatalysis can act as a bridge toward homogeneous catalysis owing to the presence of indefinitely persistent colloidal dispersions of carbocatalysts (distinguishable from supported metal catalysts). In such cases, the process should be referred as “pseudo-homogeneous” as the catalyst remains ostensibly in the same phase during the reaction as those of reactants and products but can be recovered by means of membrane filtration or centrifugation after the reaction [151].

Although exceptional, carbon is truly ubiquitous as it can be derived from abundant precursors through simple processes. Compared to traditional metals or metal oxides, well-structured carbon materials exhibit unique physicochemical properties with relatively a high surface area. The discovery of carbon-based solid acid catalysts, in particular carbon materials bearing sulfonic acid groups [152], has greatly whetted researchers’ interest in solid acid carbocatalysis. Indeed, over the past two decades, the emergence of novel nanofabrication techniques and the rapid pace of research at the interface of nanotechnology and materials science both with classical carbon materials (graphite, amorphous carbon, etc.) and nanocarbons (fullerenes, carbon nanotubes, and graphene) have only strengthened these efforts and opened up new research directions for the development of highly efficient functional carbonaceous materials and/or their composites for a variety of acid-catalyzed reactions [8–10, 151–162]. However, it should be noted that carbonaceous materials are usually built not only of elemental carbon but also of a variety of heteroatoms, which are generally present as surface functional groups, for instance, graphene (as will be discussed later). For this reason, the surface chemistry of carbonaceous materials is as important as carbon texture for catalytic applications.

In principle, the sulfonation of incompletely carbonized organic matter (sugars, starch, cellulosic materials, and polymers) serves as the most promising and widely accepted route for the synthesis of sulfonated carbon, especially, amorphous carbon

[163]. However, the catalytic performances of the materials prepared by this method largely depend upon the carbonization temperature. Interestingly, unlike many solid acid catalysts such as sulfonated ZrO_2 , sulfonated WO_2 , and HPAs, the sulfonated carbon-based solid acid catalysts only display Brønsted acidity, providing relatively an easy interpretation of acidic features through ^{31}P SSNMR of adsorbed phosphorous probe molecules. This section will deal with the most significant and recent advancement being made in the acidity characterization of a variety of carbon-based solid acid catalysts using ^{31}P MAS SSNMR of adsorbed TMP and R_3PO probe molecules. In line with this, the different synthetic routes and catalytic applications of these carbonaceous and composite materials have also been explored, wherever applicable.

In an elegant work, Hara and co-workers [164] prepared a functionalized amorphous carbon material by carbonization of D-glucose at 573–723 K followed by sulfonation. In a typical procedure, the pyrolysis of D-glucose, accompanied by dehydration and dissociation of $-\text{C}-\text{O}-\text{C}-$, led to the formation of polycyclic aromatic carbon rings in conjunction with an amorphous carbon structure (at relatively high temperature). The $-\text{SO}_3\text{H}$ groups were then introduced into the aromatic carbon rings by treatment with fuming sulfuric acid (15 wt % SO_3) to afford a material containing phenolic hydroxyl and carboxylic acid groups as well. The ^{31}P MAS NMR spectrum of as-prepared sulfonated carbon (at 673 K) exhibited a broad asymmetric peak at δ 80 ppm, similar to that of H-ZSM-5, after TMPO adsorption (Fig. 14.9a). Therefore, the acid strength of the sulfonated carbon (673 K) could be estimated equivalent to that of concentrated H_2SO_4 as was also verified by colorimetry experiment. This indicated that the as-prepared sulfonated carbon material can exhibit much stronger acidity than sulfoaromatic acids such as benzene

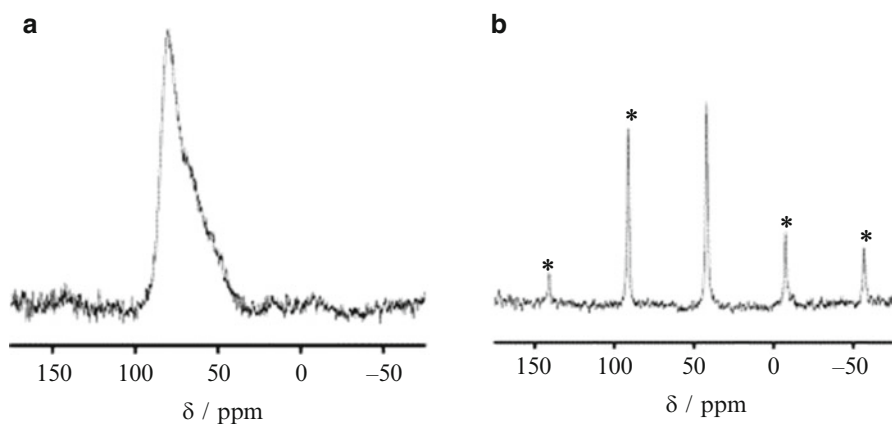
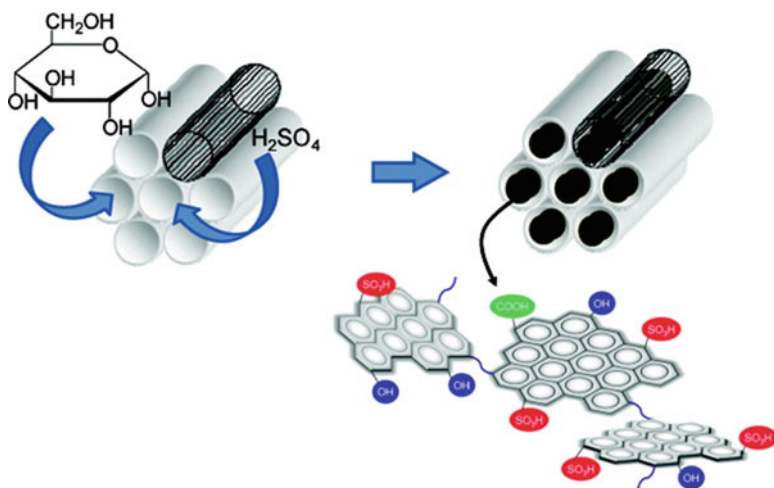


Fig. 14.9 ^{31}P MAS NMR spectra for the sulfonated (a) 673 K and (b) 823 K carbon samples after exposure to TMPO (0.75 and 0.19 mmol of TMPO, respectively, per 1 g of the carbon sample). Asterisks denote spinning sidebands (SSB). (Reprinted with permission from Okamura et al. [164]. Copyright (2006) American Chemical Society)

sulfonic acid and *p*-toluene sulfonic acid ($H_0 \sim -2$). Furthermore, the absence of any resonance peak (usually sharp) at δ 41 ppm for TMPO crystal indicated the complete adsorption of TMPO on the active sites of sulfonated carbon without any surface aggregation. In contrast to what was seen for 673 K sulfonated carbon, the ^{31}P MAS NMR spectrum of 823 K sulfonated carbon exhibited only one peak due to TMPO crystal at ca. δ 41 ppm (Fig. 14.9b), which indicated the surface aggregation of TMPO rather than the adsorption on the active sites. The sulfonated carbons prepared at 723 K or below were regarded as “soft” carbon materials (composed of flexible polycyclic aromatic carbon with different functional groups) and could be used in the hydration of 2,3-dimethyl-2-butene and esterification of acetic acid in aqueous solutions. In contrast, the sulfonated carbon prepared at 873 K adsorbed much less water, which indicates that the reactants cannot reach most of the SO_3H groups in the material and thus largely decrease the catalytic performances due to the growth of less flexible carbon network.

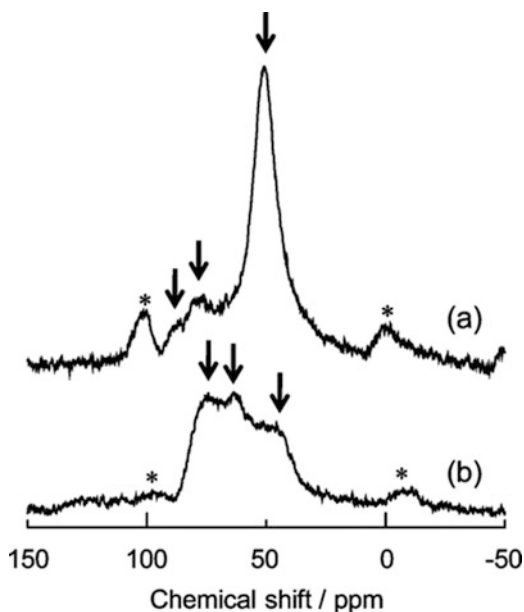
In their successive work [165], the group reported the preparation of carbon/SBA-15 composite, a mesoporous silica-supported sulfonated carbon material, by D-glucose loading into the mesopores of SBA-15 followed by pyrolytic carbonization (823 K) and sulfonation with concentrated sulfuric acid (96 wt%) at 423 K (Scheme 14.2). The as-obtained black powder was thoroughly washed with hot distilled water (> 353 K) in order to completely remove any residual sulfate anions.

The acid strength of as-prepared carbon (20 wt%)/SBA-15 material and carbon obtained by silica removal from carbon (20 wt%)/SBA-15 was examined using ^{31}P -TMPO SSNMR approach. Typically, samples were dehydrated at 423 K and soaked

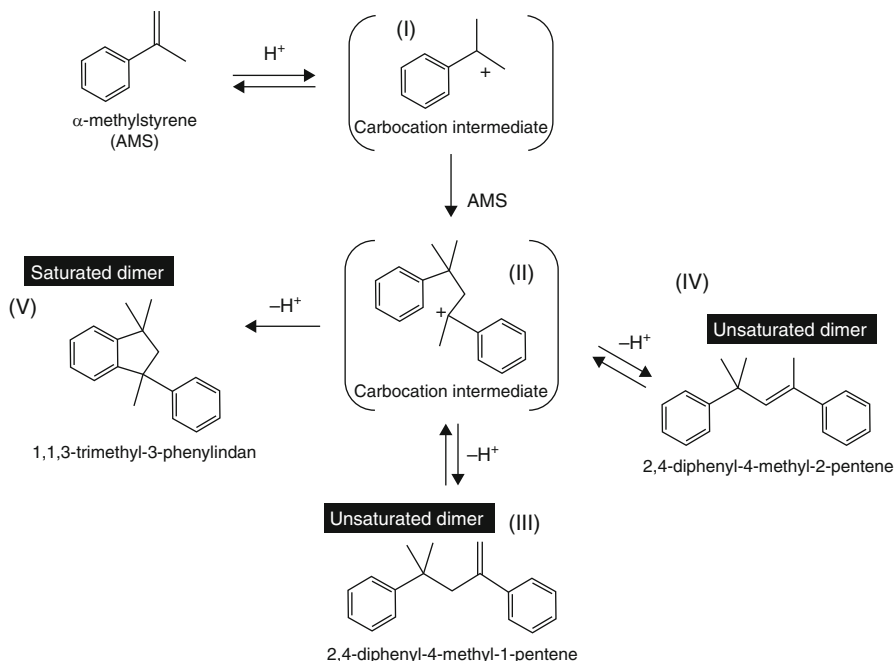


Scheme 14.2 A schematic for the synthesis of $-\text{SO}_3\text{H}$ -bearing amorphous carbon-silica composites. (Reprinted with permission from Nakajima et al. [165]. Copyright (2009) American Chemical Society)

Fig. 14.10 ^{31}P MAS NMR spectra for (a) carbon (20 wt%)/SBA-15 and (b) carbon obtained by silica removal from carbon (20 wt%)/SBA-15 after TMPO adsorption. The $\text{SO}_3\text{H}/\text{TMPO}$ ratio of samples is 2. * denotes a spinning sideband. (Reprinted with permission from Nakajima et al. [165]. Copyright (2009) American Chemical Society)



in THF solution containing an adequate amount of TMPO at room temperature for 2 days in a glove box under an inert argon atmosphere. After removal of THF, the TMPO-adsorbed samples were packed into a rotor in a glove box under nitrogen atmosphere, prior to analysis. As shown in Fig. 14.10a, the ^{31}P MAS NMR spectrum of carbon (20 wt%)/SBA-15 displayed three distinct resonances at δ 51, 79, and 86 ppm. Among them, the strong resonance at δ 51 ppm was assigned due to the adsorption of TMPO on the silanol (Si-OH), which indeed can be overlapped with the resonances for adsorbed TMPO on carboxylic and phenolic acidic sites [164]. The other two signals at higher chemical shifts could be reasonably attributed to $-\text{SO}_3\text{H}$ groups. The absence of any signal at δ 40 ppm indicated that TMPO can diffuse in the nano-spaces of the carbon-silica composite material with ease and were completely adsorbed on acidic sites. Interestingly, the appearance of a resonance at δ 86 ppm further indicated that as-prepared carbon-silica composite had stronger Brønsted acidic sites than that of bulky sulfonated carbon prepared from D-glucose (δ 80 ppm) as observed previously [164]. In contrast, the ^{31}P MAS NMR spectrum of carbon obtained by silica removal from carbon (20 wt%)/SBA-15 was significantly broadened and exhibited three resonances centered at δ 45, 64, and 75 ppm, which were correspondingly assigned for physisorbed TMPO, TMPO adsorbed on $-\text{COOH}$ or $-\text{OH}$ sites, and TMPO adsorbed on $-\text{SO}_3\text{H}$ acidic groups (Fig. 14.10b). Nevertheless, no resonance corresponding to strong Brønsted acidic sites, for instance, δ 80 or 86 ppm, was observed. The ^{31}P MAS NMR were further verified by conventional color-producing reagents, confirming that carbon-silica composite exhibits a comparable acidity to that of concentrated H_2SO_4 ($pK_a = -11$ to -8).



Scheme 14.3 The reaction mechanism for AMS dimerization. (Reprinted with permission from Nakajima et al. [165]. Copyright (2009) American Chemical Society)

The catalytic performances of as-prepared carbon-silica composite in conjunction with H_2SO_4 , amberlyst-15, Nafion-NR50, Nafion-SAC13, and a conventional D-glucose-derived carbon-based solid acid were demonstrated in the dimerization of α -methyl styrene (AMS) at 323 K, producing a mixture of unsaturated dimers III (2,4-diphenyl-4-methyl-1-pentene) and IV (2,4-diphenyl-4-methyl-2-pentene), and a saturated dimer V (1,1,3-trimethyl-3-phenylindan) as presented in Scheme 14.3. In contrast to the conventional polymer-based strong solid acid catalysts, the carbon/SBA-15 exhibited remarkable catalytic performance with greater than 85% and 95% AMS conversion and dimeric pentene selectivity, respectively. Interestingly, the estimated turnover frequency (TOF) for carbon (20 wt%)/SBA-15 was found significantly larger (9.8 min^{-1}) than that of carbon (38 wt%)/SBA-15 (5.4 min^{-1}), which indicated a decrease in effective surface $-\text{SO}_3\text{H}$ acidic groups for the reaction with an increase in the carbon particle size. It was confirmed that the SBA-15 support has no catalytic activity, which indicated that silanol functions do not participate in the reaction. Unlike polymer-based acid catalysts, the bulky glucose-derived carbon or physical mixtures of bulky carbon materials did not show any catalytic activity due to the inability of the same to incorporate hydrophobic AMS into the bulk structure with small surface area. The selective production of unsaturated dimers over the carbon/SBA-15 composite was attributed to blocking of the intramolecular Friedel-Crafts alkylation on $-\text{SO}_3\text{H}$ -bearing carbon with

large surface area. The carbon-silica composite could be readily recovered after the reaction and reused for up to three runs without any loss of catalytic activity.

In 2011, Hara's group further developed a series of $-\text{SO}_3\text{H}$ -bearing mesoporous carbon materials (RF-573, RF-673, RF-773, and RF-973) by sulfonation of carbonized resorcinol-formaldehyde (RF) resin at varying temperatures (573 K, 673 K, 773 K, and 973 K) [166]. The acidic properties of functionalized solid acid carbon materials were examined using ^{31}P -TMPO SSNMR approach in a similar fashion as reported previously [164]. The as-prepared mesoporous acidic carbon (RF-773) having a large surface area of ca. $433\text{ m}^2\text{ g}^{-1}$ and high densities of $-\text{SO}_3\text{H}$ (0.9 mmol g^{-1}) and phenolic $-\text{OH}$ (2.0 mmol g^{-1}) groups exhibited excellent catalytic activity for the selective dimerization of AMS (>99% selectivity for unsaturated dimers). The high catalytic performance of the solid acid was attributed to the large surface area and mesoporosity (ca. 10 nm), providing high accessibility of hydrophobic reactants to $-\text{SO}_3\text{H}$, while a high density of phenolic OHs prevented side reactions such as intramolecular Friedel-Crafts alkylation.

In other work, $-\text{SO}_3\text{H}$ groups were introduced into the aromatic carbon ring of the amorphous carbon sheet following electrophilic aromatic substitution to afford mesoporous carbon Starbons-300 (300 refers the pyrolytic temperature) as solid acid catalysts [167]. Whereas the ^{31}P MAS NMR spectrum of TEPO-adsorbed Starbons-300 showed a signal at δ 53.89 ppm, corresponding to the interaction of $-\text{OH}$ groups with TEPO, the ^{31}P MAS NMR spectrum of Starbons-300- H_2SO_4 -15 was accompanied with a downfield shift to 63.3 ppm together with a small shoulder at δ 85.30 ppm attributable to the strong Brønsted acidic site. The sulfonated carbon Starbons-300 displayed a high catalytic activity and selectivity in the esterification of free fatty acids. However, from the integral (ca. 20%) of signal at δ 85.30 ppm, it can be estimated that only 10% of the strong acid sites would be accessible to TEPO under the experimental conditions, presumably, due to the problems associated with the diffusion in the ultra-micropores. By making use of ^{31}P -TEPO SSNMR approach on sulfonated hydrothermal carbon (SHTC), Fraile and co-workers [168] demonstrated that microporosity is not permanent, and accessibility could be changed depending upon the solvent under study. In their work, when TEPO (0.55 eq w.r.t the total amount of sulfonic sites) was adsorbed on SHTC from a solution in hexane, the ^{31}P MAS NMR spectrum exhibited only one intense signal at ca. δ 58 ppm, typical for weak silanol groups. However, the adsorption of TEPO (0.8 eq w.r.t the total amount of sulfonic sites) on SHTC in methanol afforded a strong resonance at δ 86 ppm corresponding to the arylsulfonic acid groups. In addition, the appearance of a minor broad signal at δ 65 ppm was attributed to the $-\text{COOH}$ groups. From the integrals of both signals, it was estimated that ca. 65% of the sulfonic acidic sites were accessible to TEPO under the experimental conditions. These results clearly indicate that the solvent can play a key role in improving the accessibility to the catalytic active sites and the probable flexible nature of the pore structure in SHTCs. Very recently, the hydrothermal sulfonation method has been used in the synthesis of flower-like carbon sphere solid acid catalysts from D-glucose [169] for esterification reaction. The ^{31}P -TMPO SSNMR spectrum of these sulfonated spheres exhibited a small resonance at δ 83 ppm in conjunction with the

signals at 45 (very strong), 55, and 71 ppm, which were correspondingly assigned for TMPO adsorbed on $-\text{SO}_3\text{H}$, physisorbed TMPO, and TMPO adsorbed on $-\text{OH}$ and $-\text{COOH}$ groups.

Pinna, Valente, and co-workers [170] developed carbon (CT-1) and carbon-silica composites (CST-R; $0 \leq R \leq 1$) as catalysts by the chemical activation of a sulfonic acid organic precursor at low temperature. The acidic strength and relative amount of acidic sites of as-prepared composites were assessed by ^{31}P MAS NMR spectroscopy of adsorbed TEPO. The spectra exhibited diverse profile for each material, indicating that the acid properties were significantly influenced by the preparation conditions. Specifically, the ^{31}P spectra and deconvolution values for the CST-0, CST-0.1, CST-0.4, and CST-1 composites revealed that the chemical shift values and peak intensities of certain signals changed across the series. For instance, the most abundant acid sites in CST-0.1 and CST-1 were recognized at δ 61 and 88 ppm, respectively. However, CST-0.1 and CST-1 exhibited respective signals at δ 97 and 100 ppm attributable to the strongest acidic sites (Fig. 14.11). These results suggested that not only the amount of acidic sites increased with increasing R values but also the overall acidity became stronger. With the added advantage of FT-IR and XPS results, the ^{31}P resonances at δ 61 and 72 ppm could be, respectively, assigned for weaker $-\text{OH}$ and $-\text{COOH}$ groups, and those at higher chemical shifts were attributed to the stronger $-\text{SO}_3\text{H}$ groups. Most importantly, the resonance at ca. 97–100 ppm was supposed to be due to the interaction of TEPO with sulfuric ester groups, which remained unidentified by both FT-IR and XPS analysis. In the case of CST-0 material, an intense and narrow signal at δ 80 ppm

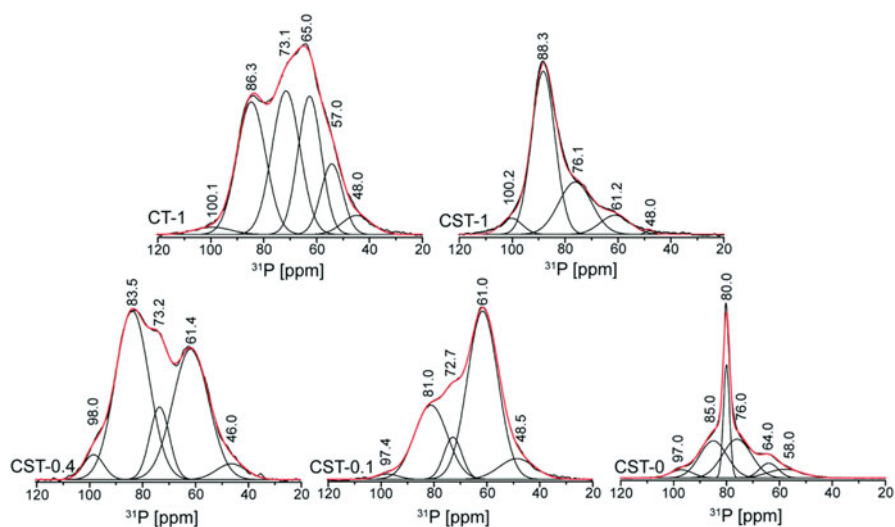


Fig. 14.11 ^1H -decoupled ^{31}P MAS NMR spectra and spectral deconvolutions of the CT-1 and CST- R materials after adsorption of TEPO. (Reprinted with permission from Russo et al. [170]. Copyright (2014) Royal Society of Chemistry)

was ascribed to TEPO interacting with the carbon precursor. Among all prepared composite materials, the CST-1 was found to possess not only the strongest acidity but also the greatest amount of stronger acidic sites. By comparing the ^{31}P NMR spectra of CT-1 and CST-1, it was revealed that the combination of carbon with silica material can generate relatively a higher amount of stronger acidic sites and thus a stronger solid acid.

The chemically activated composite materials were proved as effective solid acid catalysts in the reactions of biomass-derived 5-hydroxymethyl-2-furaldehyde (HMF) and furfuryl alcohol (FA) with ethanol affording furanic ethers and levulinate esters (bioEs), as well as in the integrated conversion of fructose to bioEs as depicted in Fig. 14.12. In their successive work [171], the group adopted the similar strategy to prepare mesoporous composites by the activation of *p*-toluenesulfonic acid deposited on the ordered mesoporous silica MCF (mesostructured cellular foam) and SBA-15, where *p*-toluenesulfonic acid served both as the carbon and $-\text{SO}_3\text{H}$ groups' source. The as-prepared mesoporous (SO_3H)-functionalized carbon-silica composites with large pores and high amounts of acid sites (up to 2.3 mmol g^{-1}) could be applied as versatile solid acid catalysts in the production of bioEs from fructose, HMF and FA effectively.

In yet another work [172], sulfonated mesoporous benzene and biphenylene bridged periodic mesoporous organosilica (PMO) materials having the crystal-like pore walls were prepared for the catalytic dehydration of fructose to HMF. The acidic strengths of TEPO-adsorbed propylsulfonic acid PMO materials containing different acid loadings (PMO-1a-c) were evaluated by ^{31}P NMR spectroscopy as shown in Fig. 14.13. In particular, a large distribution of ^{31}P chemical shifts (from δ 60 to 95 ppm) was observed for PMO-1a-c, which indicated a broad distribution of Brønsted acidic sites in distinct local environments. Compared to the $-\text{SO}_3\text{H}$ -free Ph-PMO material, the ^{31}P resonance associated with the silanol acid sites in PMO-1a-c experienced a slight downfield shifting ($\sim \delta$ 2 ppm), presumably, due to the introduction of $-\text{SO}_3\text{H}$ groups. However, the resonance at δ 60.4 ppm was unambiguously assigned for silanol acidic sites using a reference sample material, Si-PMO-1c. Regardless of the acid loading, all functionalized PMO materials were accompanied by a minor broad resonance at ca. 94 ppm due to the stronger Brønsted acidic sites. Interestingly, the intensity of the resonance at 72.9 ppm increased significantly upon increasing the proton loadings (from 0.36 to 1.11 mmol g^{-1}) in PMOs. The maximum intensity at δ 72.9 ppm was recognized for PMO-1a, which was attributed to the main $-\text{SO}_3\text{H}$ acid population. Despite this, the PMO-1a exhibited the lowest TOF in the dehydration of fructose. The authors hypothesized that this may be due to the influence of other parameters such as solvation and the problems associated with the accessibility of the acidic sites.

Petroleum cokes are one of the massive by-products in petroleum industry and can serve as readily available raw materials for the preparation of solid acids. Given its high carbon content (ca. 90%) and low ash content, Zheng and co-workers [173] developed a solid acid catalyst from petroleum coke by KOH activation followed by sulfonation with concentrated H_2SO_4 . The acidity of as-prepared material together with pristine petroleum coke was derived following ^{31}P -TMP/TMPO SSNMR approach as shown in Fig. 14.14. In detail, the ^{31}P MAS NMR spectrum of TMP-

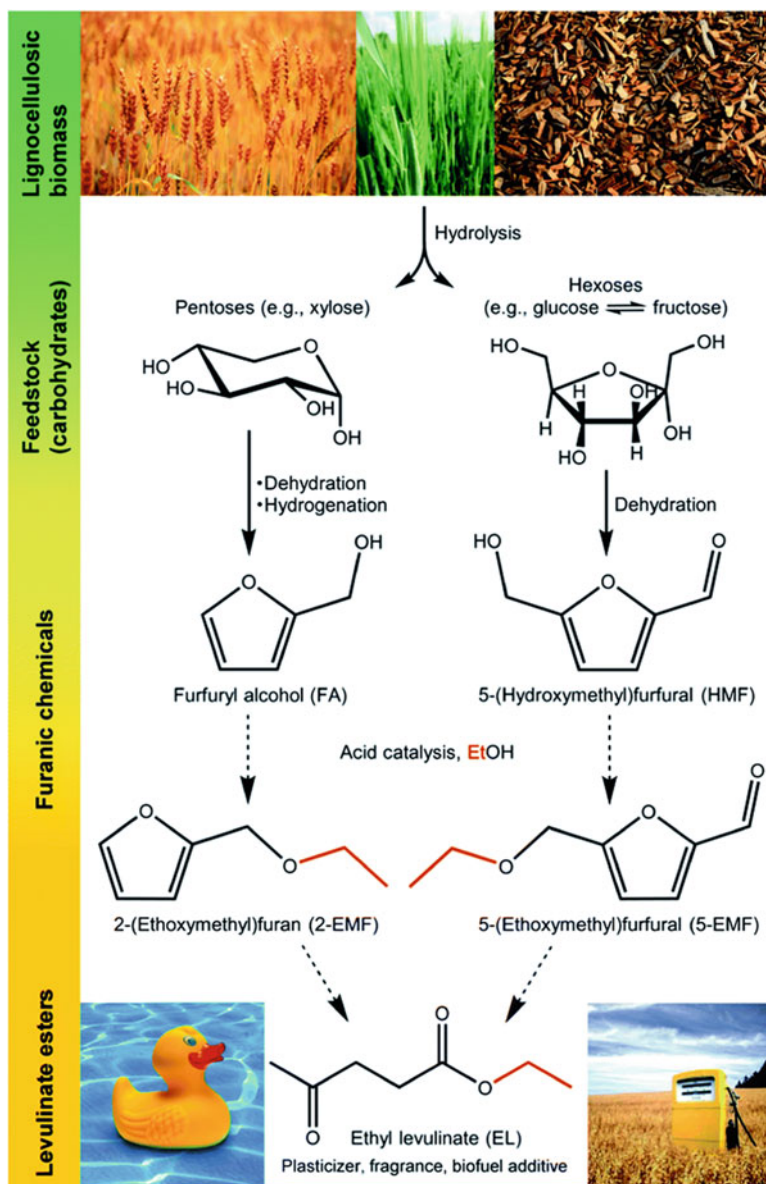


Fig. 14.12 Carbohydrate biomass conversion to useful bioproducts. (Reprinted with permission from Russo et al. [170]. Copyright (2014) Royal Society of Chemistry)

loaded petroleum coke exhibited only one major peak at $\delta -60$ ppm due to the physisorbed TMP (Fig. 14.14a), indicating that neither Lewis nor Brønsted acidic sites were present in the pristine petroleum coke. However, two sharp resonances at $\delta -4$ and -60 ppm were recognized in the ^{31}P MAS NMR spectrum of TMP-

Fig. 14.13 ^{31}P MAS NMR spectra of TEPO probe molecules adsorbed on PMO-1a, PMO-1b, PMO-1c, Si-PMO-1c, and Ph-PMO. (Reprinted with permission from Bispo et al. [172]. Copyright (2014) Royal Society of Chemistry)

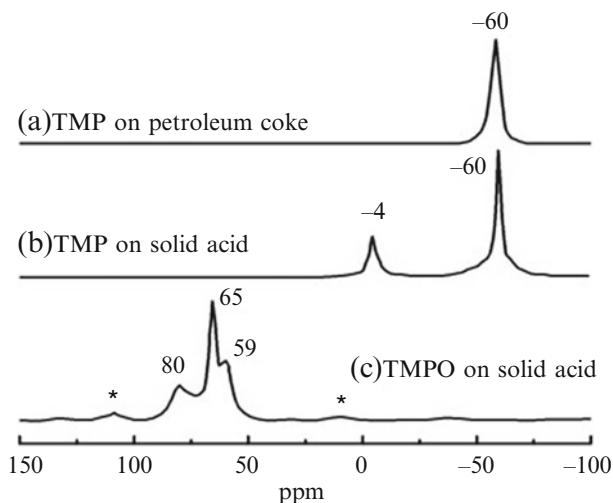
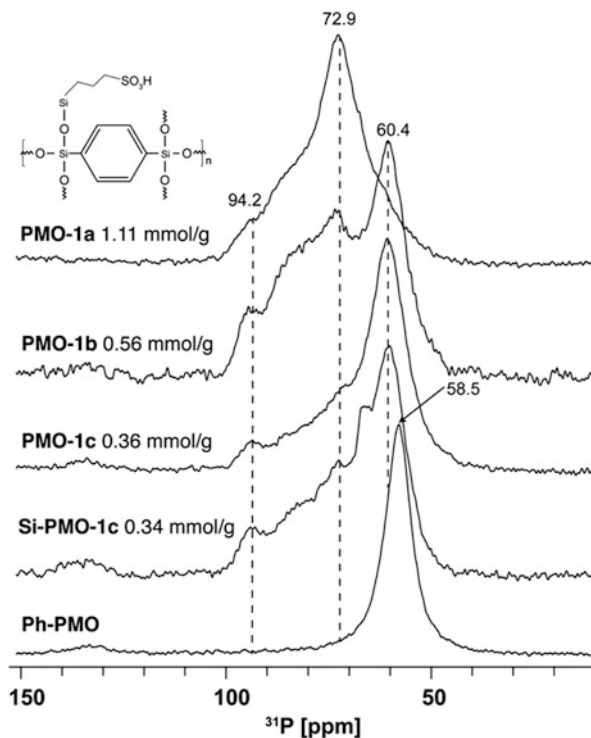
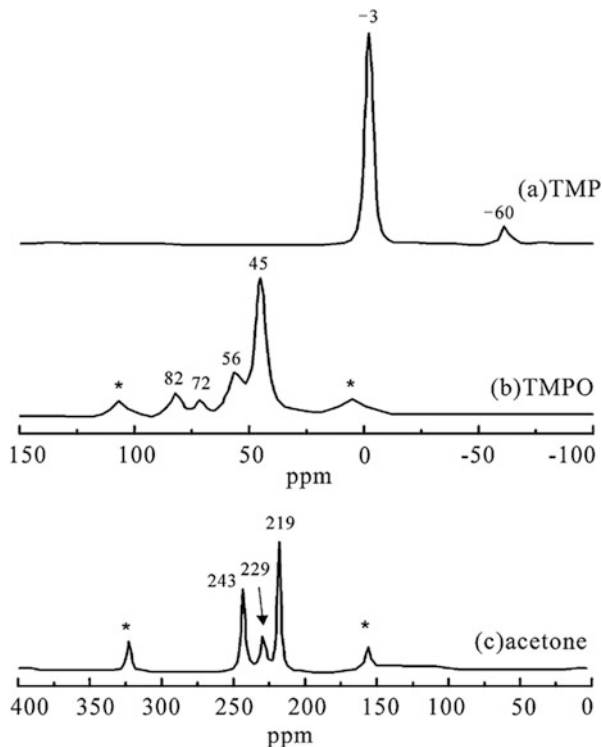


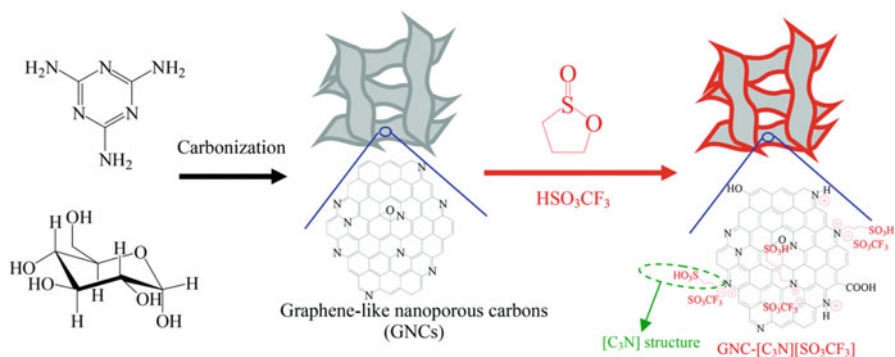
Fig. 14.14 ^{31}P single pulse with ^1H decoupling MAS spectra of TMP adsorbed on (a) petroleum coke and (b) solid acid and (c) TMPO adsorbed on solid acid. The asterisk denotes spinning sidebands. (Reprinted with permission from Zeng et al. [173]. Copyright (2013) Elsevier B. V)

Fig. 14.15 ^{31}P single pulse with ^1H decoupling MAS spectra of (a) TMP and (b) TMPO adsorbed on the solid acid; (c) ^{13}C CP/MAS NMR spectra of 2- ^{13}C -acetone (0.2 mmol/g) adsorbed on the solid acid. The asterisk denotes spinning sidebands. (Reprinted with permission from Zeng et al. [174]. Copyright (2013) Elsevier B. V)



loaded solid acid. The appearance of a new peak at $\delta -4$ ppm (Fig. 14.14b) clearly indicated that the solid acid possessed only Brønsted acidic sites. In contrast to what was seen with TMP, the ^{31}P NMR spectrum of TMPO-loaded solid acid displayed three resonances at δ 59, 65, and 80 ppm (Fig. 14.14b), which were correspondingly identified for $-\text{OH}$, $-\text{COOH}$, and $-\text{SO}_3\text{H}$ Brønsted acidic sites as also verified by FT-IR data. The carbon-based solid acid catalyst could be used in the esterification of oleic acid with quite high TOF (46 h^{-1}) than those of sulfated zirconia (36 h^{-1}) and H-ZSM-5 (28 h^{-1}).

In another work [174], Zeng's group produced a carbon-based solid acid by sulfonation of the partially carbonized agricultural biowaste, peanut shell. The ^{31}P single-pulse spectrum acquired after TMP adsorption onto the surface of solid acid was accompanied by two resonances at $\delta -3$ and -60 ppm (Fig. 14.15a) corresponding to adsorbed TMP on the Brønsted acidic sites and physisorbed TMP, respectively. On the other hand, the ^{31}P NMR spectrum of TMPO-loaded solid acid exhibited three signals at δ 56, 72, and 82 ppm (Fig. 14.15b) attributable to the weakly acidic $-\text{OH}$, $-\text{COOH}$, and $-\text{SO}_3\text{H}$ groups, respectively. The resonance at 45 ppm was ascribed to the physisorbed TMPO. The type and strength of acid sites as deduced by ^{31}P MAS NMR spectroscopy was further confirmed by ^{13}C CP/MAS spectroscopy (Fig. 14.15c). The catalytic activity of solid acid was demonstrated in the transesterification reaction of cottonseed oil with methanol.



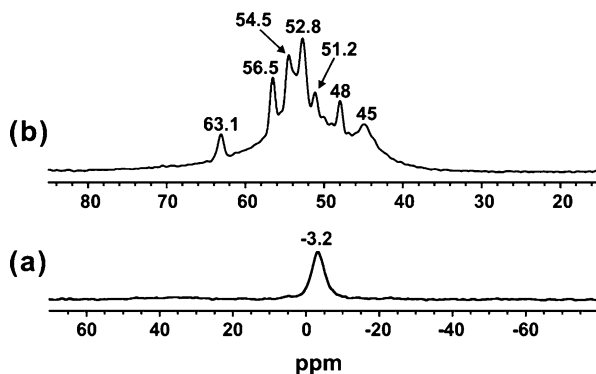
Scheme 14.4 A schematic for the synthesis of GNC-[C₃N][SO₃CF₃] material. (Reprinted with permission from Liu et al. [177]. Copyright (2015) Royal Society of Chemistry)

The highest conversion of 90.2% could be achieved under optimized conditions. The catalyst could be reused up to five runs; however, the conversion rate decreased significantly from 90.2% to 50.3% during five runs, due to the decrease in the total acid density from 6.85 to 3.42 mmol g⁻¹. After five runs, the spent solid acid catalyst was treated with ether, H₂SO₄, and deionized water and dried. The as-regenerated solid acid could be reused with original activity, indicating that most of the acid sites were recovered by the regeneration process, achieving a total acid density of 6.12 mmol g⁻¹.

Owing to their nonvolatility, heat resistance, non-corrosiveness, and negligible vapor pressure, Brønsted acidic ionic liquids (AILs) have emerged as revolutionary candidates and green alternative to conventional liquid and solid acid catalysts [175, 176]. Taking this into account, Zheng, Qi, and co-workers [177] synthesized AILs and sulfonic group bifunctional graphene-like nanoporous carbons (GNC-SO₃H-ILs) by treating nitrogen-containing graphene-like nanoporous carbons (GNCs) with 1,3-propane sultone through quaternary ammonization reaction followed by ion exchanging with strong acids such as H₂SO₄ or HSO₃CF₃. The GNC supports could be synthesized from carbonization of a mixture of dicyandiamide or melamine and glucose without using any additional template. The schematic for the overall synthesis of GNC-SO₃H-ILs is depicted in Scheme 14.4.

The acidity properties of as-prepared GNC-[C₃N][SO₃CF₃] (where C₃ stands for 1,3-propane sultone and [SO₃CF₃] stands for the anion of trifluoromethanesulfonic acid) were evaluated through ³¹P-TMP/TMPO SSNMR approach. As shown in Fig. 14.16, the TMP-loaded GNC-[C₃N][SO₃CF₃] showed only single resonance at δ -3.2 ppm attributable to the reaction of TMP with only the Brønsted acidic sites as discussed above. However, TMPO-loaded GNC-[C₃N][SO₃CF₃] exhibited multiple signals at δ ca. 45, 48, 51.2, 52.8, 54.5, 56.6, and 63.1 ppm, indicating the presence of various Brønsted acidic sites with different acidic strength. Whereas the weakly acidic sites (δ 45 and 48 ppm) were attributed to the presence of -COOH or -OH groups in GNC-[C₃N][SO₃CF₃], the remaining signals were assigned due to

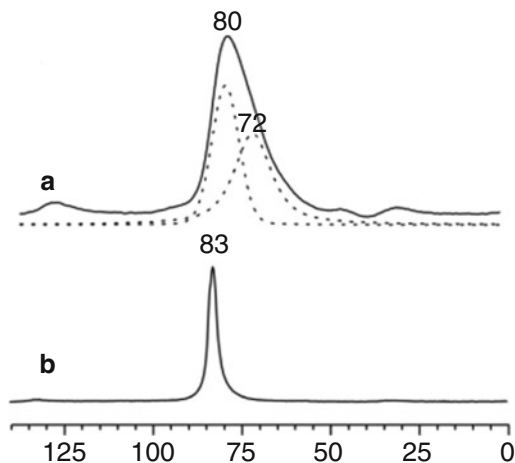
Fig. 14.16 Room temperature ^{31}P MAS NMR spectra of adsorbed (a) TMP acquired with proton decoupling and (b) TMPO of GNC-[C₃N][SO₃CF₃]. (Reprinted with permission from Liu et al. [177]. Copyright (2015) Royal Society of Chemistry)



the ILs, $-\text{SO}_3\text{H}$ groups, and protonated structure (GNC-[N⁺H][SO₃CF₃]) located in the outer and inner surfaces of GNC-[C₃N][SO₃CF₃]. It was hypothesized that the protonated structure should be formed by protonation of N atom in GNC by HSO₃CF₃. However, this is in contrast to the earlier reports where the presence of strongest acidic sites (mostly $-\text{SO}_3\text{H}$ groups) were unambiguously identified by ^{31}P resonances at δ 80–86 ppm or even more. The catalytic activity of GNC-SO₃H-ILs was demonstrated in biomass transformations, for instance, in the production of biodiesel and depolymerization of crystalline cellulose into sugars, and was found comparable to those of homogeneous ILs and mineral acids. The group further extended the quaternary ammonization strategy in the synthesis of porous carbonaceous solid acid catalysts (with controllable acid sites) from N-rich porous carbon [178] for catalyzing the synthesis of biofuels and fine chemicals. Recently, a similar approach has been used in the preparation of porous carbon from farm animal waste in catalyzing biomass transformations [179].

Liu, Zheng, and co-workers [180] developed mesoporous polydivinylbenzene (PDVB)-based strong solid acids (PDVB-SO₃H-SO₂CF₃) by grafting of strong electron-withdrawing group of $-\text{SO}_2\text{CF}_3$ onto the network of PDVB-SO₃H, which could be synthesized from sulfonation of super hydrophobic mesoporous PDVB or copolymerization of DVB with sodium *p*-styrene sulfonate. The distribution and strength of acid sites in PDVB-SO₃H and PDVB-SO₃H-SO₂CF₃ catalysts were determined using ^{31}P -TMPO SSNMR approach. As shown in Fig. 14.17a, the ^{31}P MAS NMR spectrum of TMPO-loaded PDVB-SO₃H showed two resonances at δ 72 and 80 ppm with a relative concentration of 40% and 60%, respectively. Based on the range of ^{31}P chemical shift, these two resonances were ascribed due to TMPO adsorbed on Brønsted acidic sites with varied extent of protonation. In contrast, only one uniform ^{31}P resonance at δ 83 ppm was detected in the case of PDVB-SO₃H-SO₂CF₃ indicative of homogeneously distributed Brønsted acidic sites (Fig. 14.17b). Interestingly, the resonance at δ 83 ppm was found close to the superacidity threshold. According to the relationship between proton affinity and ^{31}P chemical shift, the calculated proton affinities for ^{31}P chemical shift at 72, 80, and 83 ppm were estimated to be 284, 264, and 256 kcal/mol, respectively. It is clear

Fig. 14.17 Solid-state ^{31}P MAS NMR of adsorbed TMPO on (a) PDVB-SO₃H and (b) PDVB-SO₃H-SO₂CF₃. (Reprinted with permission from Liu et al. [180]. Copyright (2013) Elsevier B. V)



that the acidic strengths of PDVB-SO₃H can be dramatically enhanced by HSO₃CF₃ treatment. The PDVB-SO₃H-SO₂CF₃ exhibited excellent catalytic activities and good recyclability in biomass transformation toward transesterification to biodiesel and depolymerization of crystalline cellulose to sugars when compared with those of PDVB-SO₃H, Nafion NR50, and sulfated zirconia. The excellent catalytic activity and good recyclability of PDVB-SO₃H-SO₂CF₃ may be attributed to its ultra-strong acid strength, large surface area, and tunable hydrophobic-oleophilic and stable network.

The electronic “boom” that the world has experienced during the last decade is only due to one specific material, namely, graphene. Graphene can be defined as a single-atom-thick 2D sheet of sp^2 -hybridized carbon atoms with a hexagonal packed lattice structure. Owing to its exceptional physicochemical properties, graphene and its derivatives such as graphite oxide, graphene oxide (GO), and reduced graphene oxide (rGO) have been increasingly used for a variety of technological applications including acid catalysis [10, 151, 181–187]. In graphene-based acid catalysis, the fabrication of graphene with –SO₃H groups affording sulfonated graphene is of crucial importance and increasingly used for a variety of acid-catalyzed reactions [10, 151]. Ling and co-workers [188] developed an upscale and energy-efficient protocol for oleum (fuming H₂SO₄)-assisted sulfonation of graphene following the concept of green chemistry. The acid strength of resultant sulfonated graphene (GSO₃H) in conjunction with GO, rGO, and amberlyst-15 was evaluated using ^{31}P -TEPO SSNMR approach as shown in Fig. 14.18. In detail, the ^{31}P NMR spectrum of rGO exhibited a broad resonance centered at δ 55.5 ppm corresponding to the TEPO adsorbed on residual –OH and –COOH groups on the surface of rGO. The GSO₃H shared a resonance at nearly same chemical shift (δ 58.3 ppm) as that of rGO and was found in accordance with the earlier report [189]. However, a relatively high intensity of this signal than rGO was attributed to the reintroduction of oxygen functionalities during sulfonation treatment. Aside from that resonance

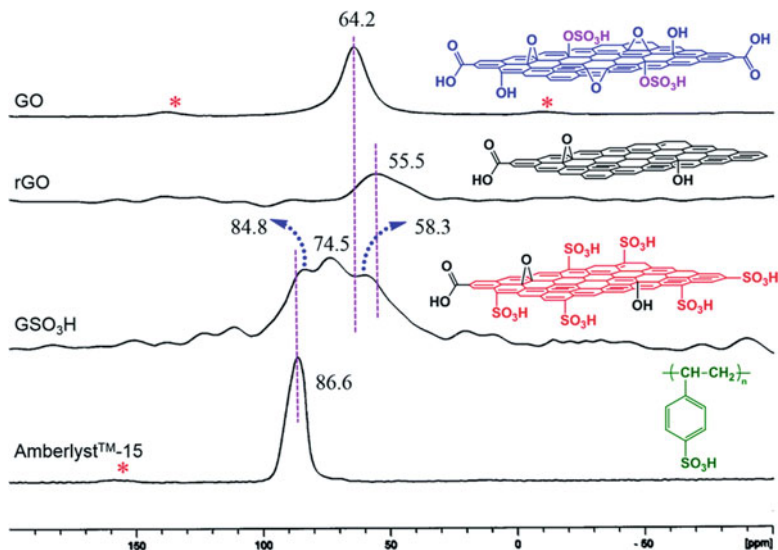


Fig. 14.18 ^{31}P NMR spectra of TEPO chemically adsorbed onto GO, rGO, GSO₃H, and Amberlyst™-15. The asterisks mark spinning sidebands. (Reprinted with permission from Garg et al. [188]. Copyright (2014) Royal Society of Chemistry)

at δ 58.3 ppm, the ^{31}P NMR spectrum of GSO₃H was accompanied with two overlapping but strong signals at δ 74.5 and 84.8 ppm, authenticating the successful grafting of strong Brønsted acidic $-\text{SO}_3\text{H}$ groups on rGO surface. The authors postulated that just by simple switching in the experimental conditions, highly acidic sulfonated graphene can be obtained with ease. Indeed, this has proved to be the case where TEPO-loaded sulfonated graphene can display a single sharp ^{31}P resonance at δ 78.5 ppm in the scalable synthesis [190]. The catalytic activity of GSO₃H was demonstrated in the efficient synthesis of (biodegradable) ester plasticizers, industrially important fine chemical, and biodiesel production. The superior catalytic performance of GSO₃H over traditional homogeneous acids, amberlyst-15, and AILs was attributed to the presence of highly acidic and stable $-\text{SO}_3\text{H}$ acid groups within the 2D graphene domain, which synergistically work for high mass transfer in the reaction.

14.7 Conclusions

As with many other technical fields, the research on carbon-based solid acid catalysis has seen dramatic advancement recently and is significantly influencing the current state of the art in the fields of both analytical chemistry and materials science. Among a variety of available analytical tools, the solid-state ^{31}P MAS

NMR spectroscopy of adsorbed phosphorous probe molecules has appeared as a unique, practical, and most reliable technique for the precise characterization of acidity features (type, strength, distribution, and concentration) of a diversified range of solid acid catalysts. In this book chapter, we have shed light on the most significant as well as current development being made in the acidity characterization of a variety of carbonaceous materials and/or their composites (including graphene) by making the use of ^{31}P SSNMR of adsorbed phosphorous probe molecules such as TMP, TMPO, and TEPO. Certainly, however, the growing or unusual interest of researchers in carbon-based solid acid catalysis has resulted “an unsweet smell” of conceptual vagueness as far as acidity characterization is concerned. We believe that this book chapter may provide a strong foundation over the subject and stimulate further work, leading to the development of new advancement in the field for wide technological applications.

Acknowledgements Dr. B. Garg is thankful to the Science and Engineering Research Board (SERB), New Delhi, Government of India (YSS/2015/002036), for financial support. B. Garg additionally thanks to all the publishers for providing permissions in reusing the figures and schemes.

References

1. Chauhan, S. M. S., Garg, B., & Bisht, T. (2007). Synthesis of calix[4]pyrroles by Amberlyst-15 catalyzed cyclocondensations of pyrrole with selected ketones. *Molecules*, *12*, 2458–2466.
2. Yamato, T. (1998). Recent developments of perfluorinated resin sulfonic acid (Nafion-H). *Recent Research Development in Pure & Applied Chemistry*, *2*, 297–310.
3. Mizuno, N., & Misono, M. (1998). Heterogeneous catalysis. *Chemical Reviews*, *98*, 199–217.
4. Okuhara, T. (2002). Water-tolerant solid acid catalysts. *Chemical Reviews*, *102*, 3641–3666.
5. Harmer, M. A., Farneth, W. E., & Sun, Q. (1996). High surface area nafion resin/silica nanocomposites: A new class of solid acid catalyst. *Journal of the American Chemical Society*, *118*, 7708–7715.
6. Suwannakarn, K., Lotero, E., Goodwin, J. G., Jr., & Lu, C. (2008). Stability of sulfated zirconia and the nature of the catalytically active species in the transesterification of triglycerides. *Journal of Catalysis*, *255*, 279–286.
7. Onda, A., Ochi, T., & Yanagisawa, K. (2008). Selective hydrolysis of cellulose into glucose over solid acid catalysts. *Green Chemistry*, *10*, 1033–1037.
8. Wang, X., Liu, R., Waje, M. M., Chen, Z., Yan, Y., Bozhilov, K. N., & Feng, P. (2007). Sulfonated ordered mesoporous carbon as a stable and highly active protonic acid catalysts. *Chemistry of Materials*, *19*, 2395–2397.
9. Yu, H., Jin, Y., Li, Z., Peng, F., & Wang, H. (2008). Synthesis and characterization of sulfonated single-walled carbon nanotubes and their performance as solid acid catalyst. *Journal of Solid State Chemistry*, *181*, 432–438.
10. Garg, B., & Ling, Y.-C. (2013). Versatilities of graphene-based catalysts in organic transformations. *Green Materials*, *1*, 47–61.
11. Weckhuysen, B. M., & Yu, J. (2015). Recent advances in zeolite chemistry and catalysis. *Chemical Society Reviews*, *44*, 7022–7024.
12. Patil, M. K., Prasad, A. N., & Reddy, B. M. (2011). Zirconia-based solid acids: Green and heterogeneous catalysts for organic synthesis. *Current Organic Chemistry*, *15*, 3961–3985.

13. Wada, E., Kitano, M., Yamamoto, K., Nakajima, K., Hayashi, S., & Hara, M. (2016). Synthesis of niobium-doped titanate nanotubes as solid acid catalysts. *Catalysis Science & Technology*, *6*, 4832–4839.
14. Jiang, J., Gándara, F., Zhang, Y.-B., Na, K., Yaghi, O. M., & Klemperer, W. G. (2014). Superacidity in sulfated metal-organic framework-808. *Journal of the American Chemical Society*, *136*, 12844–12847.
15. Niwa, M., Suzuki, K., Isamoto, K., & Katada, N. (2006). Identification and measurements of strong Brønsted acid site in ultrastable Y (USY) zeolite. *The Journal of Physical Chemistry B*, *110*, 264–269.
16. Corma, A. (1995). Inorganic solid acids and their use in acid-catalyzed hydrocarbon reactions. *Chemical Reviews*, *95*, 559–614.
17. Knözinger, H., Kriltlenbrink, H., & Ratnasamy, P. (1977). 2,6-Disubstituted pyridines as probe molecules for surface acid sites-an infrared spectroscopic study. *Journal of Catalysis*, *48*, 436–439.
18. Benesi, H. A. (1956). Acidity of catalyst surfaces. I. Acid strength from colors of adsorbed indicators. *Journal of the American Chemical Society*, *78*, 5490–5494.
19. Moscou, L., & Moné, R. J. (1973). Structure and catalytic properties of thermally and hydrothermally treated zeolites: Acid strength distribution of REX and REY. *Journal of Catalysis*, *30*, 417–422.
20. Cardona-Martinez, N., & Dumesic, J. A. (1992). Applications of adsorption microcalorimetry to the study of heterogeneous catalysis. *Advances in Catalysis*, *38*, 149–244.
21. Drago, R. S., Dias, S. C., Torrealba, M., & de Lima, L. (1997). Calorimetric and spectroscopic investigation of the acidity of HZSM-5. *Journal of the American Chemical Society*, *119*, 4444–4452.
22. Bhan, A., Allian, A., Sunley, G., Law, D., & Iglesia, E. (2007). Specificity of sites within eight-membered ring zeolite channels for carbonylation of methyls to acetyls. *Journal of the American Chemical Society*, *129*, 4919–4924.
23. Zecchina, A., Spoto, G., & Bordiga, S. (2005). Probing the acid sites in confined spaces of microporous materials by vibrational spectroscopy. *Physical Chemistry Chemical Physics*, *7*, 1627–1642.
24. Lavalley, J.-C., Anquetil, R., Czyzniewska, J., & Ziolk, M. (1996). Use of pyridine as a probe for the determination, by IR spectroscopy, of the Brønsted acid strength of M^+HNaY zeolites. *Journal of the Chemical Society, Faraday Transactions*, *92*, 1263–1266.
25. Busca, G. (1999). The surface acidity of solid oxides and its characterization by IR spectroscopic methods. An attempt at systematization. *Physical Chemistry Chemical Physics*, *1*, 723–736.
26. Busca, G. (1998). Spectroscopic characterization of the acid properties of metal oxide catalysts. *Catalysis Today*, *41*, 191–206.
27. Sulikowski, B., Datka, J., Gil, B., Ptaszynski, J., & Klinowski, J. (1997). Acidity and catalytic properties of dealuminated zeolite Y. *The Journal of Physical Chemistry B*, *101*, 6929–6932.
28. Peng, L., Liu, Y., Kim, N., & Readman, J. E. (2005). Detection of Brønsted acid sites in zeolite HY with high-field ^{17}O -MAS-NMR techniques. *Nature Materials*, *4*, 216–219.
29. Hunger, M. (1997). Brønsted acid sites in zeolites characterized by multinuclear solid-state NMR spectroscopy. *Catalysis Reviews: Science and Engineering*, *39*, 345–393.
30. Zheng, A., Hung, S.-J., Wang, Q., Zhang, H., Deng, F., & Liu, S.-B. (2013). Progress in development and application of solid-state NMR for solid acid catalysis. *Chinese Journal of Catalysis*, *34*, 436–491.
31. Zheng, A., Liu, S.-B., & Deng, F. (2013). Acidity characterization of heterogeneous catalysts by solid-state NMR spectroscopy using probe molecules. *Solid State Nuclear Magnetic Resonance*, *55-56*, 12–27 and references there in.
32. Kotrla, J., Kubelkova, L., Lee, C. C., & Gorte, R. J. (1998). Calorimetric and FTIR studies of acetonitrile on H-[Fe]ZSM-5 and H-[Al]ZSM-5. *The Journal of Physical Chemistry B*, *102*, 1437–1443.

33. Farneth, W. E., & Gorte, R. J. (1995). Methods for characterizing zeolite acidity. *Chemical Reviews*, *95*, 615–636.
34. Zheng, A., Hung, S.-J., Liu, S.-B., & Deng, F. (2011). Acid properties of solid acid catalysts characterized by solid-state ^{31}P NMR of adsorbed phosphorous probe molecules. *Physical Chemistry Chemical Physics*, *13*, 14889–14901 and references therein.
35. Hunger, M., Ernst, S., Steuernagel, S., & Weitkamp, J. (1996). High-field ^1H MAS NMR investigations of acidic and non-acidic hydroxyl groups in zeolites H-Beta, H-ZSM-5, H-ZSM-58 and H-MCM-22. *Microporous Materials*, *6*, 349–353.
36. Peng, L., Huo, H., Liu, Y., & Grey, C. P. (2007). ^{17}O magic angle spinning NMR studies of Brønsted acid sites in zeolites HY and HZSM-5. *Journal of the American Chemical Society*, *129*, 335–346.
37. Pfeifer, H., & Ernst, H. (1994). NMR studies of zeolites. *Annual Reports on NMR Spectroscopy*, *28*, 91–187.
38. Xu, M., Arnold, A., Buchholz, A., Wang, W., & Hunger, M. (2002). Low-temperature modification of mesoporous MCM-41 material with sublimated aluminum chloride in vacuum. *The Journal of Physical Chemistry B*, *106*, 12140–12143.
39. Barich, D. H., Nicholas, J. B., Xu, T., & Haw, J. F. (1998). Theoretical and experimental study of the ^{13}C chemical shift tensors of acetone complexed with Brønsted and Lewis acids. *Journal of the American Chemical Society*, *120*, 12342–12350.
40. Haw, J. F., Nicholas, J. B., Xu, T., Beck, L. W., & Ferguson, D. B. (1996). Physical organic chemistry of solid acids: Lessons from in situ NMR and theoretical chemistry. *Accounts of Chemical Research*, *29*, 259–267.
41. Rakiewicz, E. F., Peters, A. W., Wormsbecher, R. F., Sutovich, K. J., & Mueller, K. T. (1998). Characterization of acid sites in zeolitic and other inorganic systems using solid-state ^{31}P NMR of the probe molecule trimethylphosphine oxide. *The Journal of Physical Chemistry B*, *102*, 2890–2896.
42. Osegovic, J. P., & Drago, R. S. (2000). Measurement of the global acidity of solid acids by ^{31}P MAS NMR of chemisorbed triethylphosphine oxide. *The Journal of Physical Chemistry B*, *104*, 147–154.
43. Margoese, D., Melero, J. A., Christiansen, S. C., Chmelka, B. F., & Stucky, G. D. (2000). Direct syntheses of ordered SBA-15 mesoporous silica containing sulfonic acid groups. *Chemistry of Materials*, *12*, 2448–2459.
44. Zheng, A., Huang, S.-J., Chen, W.-H., Wu, P.-H., Zhang, H., Lee, H.-K., de Ménorval, L.-C., Deng, F., & Liu, S.-B. (2008). ^{31}P chemical shift of adsorbed trialkylphosphine oxides for acidity characterization of solid acid catalysts. *The Journal of Physical Chemistry A*, *112*, 7349–7356.
45. Seo, Y., Cho, K., Jung, Y., & Ryoo, R. (2013). Characterization of the surface acidity of MFI zeolite nanosheets by ^{31}P NMR of adsorbed phosphine oxides and catalytic cracking of decalin. *ACS Catalysis*, *3*, 713–720.
46. Zhang, X., Xiao, B., Chen, J., Guo, M., & Yang, Q. (2016). Adjusting the acid strength of hybrid solid acids in confined nanospace. *Topics in Catalysis*, *59*, 1748–1756.
47. Zheng, A., Li, S., Liu, S.-B., & Deng, F. (2016). Acidic properties and structure-activity correlations of solid acid catalysts revealed by solid-state NMR spectroscopy. *Accounts of Chemical Research*, *49*, 655–663.
48. Wiper, P. V., Amelse, J., & Mafra, L. (2014). Multinuclear solid-state NMR characterization of the Brønsted/Lewis acid properties in the BP HAMS-1B (H-[B]-ZSM-5) borosilicate molecular sieve using adsorbed TMPO and TBPO probe molecules. *Journal of Catalysis*, *316*, 240–250.
49. de Mattos, F. C. G., de Carvalho, E. N. C. B., de Freitas, E. F., Paiva, M. F., Ghesti, G. F., de Macedo, J. L., Dias, S. C. L., & Dias, J. A. (2017). Acidity and characterization of 12-tungstophosphoric acid supported on silica-alumina. *Journal of the Brazilian Chemical Society*, *28*, 336–347.

50. Koito, Y., Nakajima, K., Hasegawa, R., Kobayashi, H., Kitano, M., & Hara, M. (2014). Lewis acid properties of some metal salts for lactic acid formation in water: ^{31}P NMR spectroscopy with trimethylphosphine oxide as a molecular probe. *Catalysis Today*, 226, 198–203.
51. Hu, Y., Guo, B., Fu, Y., Ren, Y., Tang, G., Chen, X., Yue, B., & He, H. (2015). Facet-dependent acidic and catalytic properties of sulfated titania solid superacids. *Chemical Communications*, 51, 14219–14222.
52. Peng, Y.-K., Ye, L., Qu, J., Zhang, L., Fu, Y., Teixeira, I. F., McPherson, I. J., He, H., & Tsang, S. C. E. (2016). Trimethylphosphine-assisted surface fingerprinting of metal oxide nanoparticle by ^{31}P solid-state NMR: A zinc oxide case study. *Journal of the American Chemical Society*, 138, 2225–2234.
53. Kitano, M., Kobayashi, H., Hayashi, S., & Hara, M. (2017). Acid properties of protonated titanate nanotubes. *Journal of the Japan Petroleum Institute*, 60, 113–120.
54. Kanthasamy, R., Mbaraka, I. K., Shanks, B. H., & Larsen, S. C. (2007). Solid-state MAS NMR studies of sulfonic acid-functionalized SBA-15. *Applied Magnetic Resonance*, 32, 513–526.
55. Li, S.-H., Li, J., Zheng, A.-M., & Deng, F. (2017). Solid-state NMR characterization of the structure and catalytic reaction mechanism of solid acid catalysts. *Acta Physico-Chimica Sinica*, 33, 270–282.
56. Beckonert, O., Coen, M., Keun, H. C., Wang, Y., Ebbels, T. M. D., & Holmes, E. (2010). High-resolution magic-angle-spinning NMR spectroscopy for metabolic profiling of intact tissues. *Nature Protocols*, 5, 1019–1032.
57. Geppi, M., Borsacchi, S., Mollica, G., & Veracini, C. A. (2008). Applications of solid-state NMR to the study of organic/inorganic multicomponent materials. *Applied Spectroscopy Reviews*, 44, 1–89.
58. Brown, S. P. (2012). Applications of high-resolution ^1H solid-state NMR. *Solid State Nuclear Magnetic Resonance*, 41, 1–27.
59. Laws, D. D., Bitter, H.-M. L., & Jerschow, A. (2002). Solid-state NMR spectroscopic methods in chemistry. *Angewandte Chemie, International Edition*, 41, 3096–3129.
60. Dracinsky, M., & Hodgkinson, P. (2015). Solid-state NMR studies of nucleic acid components. *RSC Advances*, 5, 12300–12310.
61. Ashbrook, S. E., & Sneddon, S. (2014). New methods and applications in solid-state NMR spectroscopy of quadrupolar nuclei. *Journal of the American Chemical Society*, 136, 15440–15456.
62. Ader, C., Schneider, R., Seidel, K., Etzkorn, M., & Baldus, M. (2007). Magic-angle-spinning NMR spectroscopy applied to small molecules and peptides in lipid bilayers. *Biochemical Society Transactions*, 35, 991–995.
63. Bugay, D. E. (1993). Solid-state nuclear magnetic resonance spectroscopy: Theory and pharmaceutical applications. *Pharmaceutical Research*, 10, 317–327.
64. Obenaus, U., Dybala, M., Lang, S., Scheibe, M., & Hunger, M. (2015). Generation and properties of Brønsted acid sites in bifunctional Rh-, Ir-, Pd-, and Pt-containing zeolites Y investigated by solid-state NMR spectroscopy. *Journal of Physical Chemistry C*, 119, 15254–15262.
65. Apperley, D. C., Harris, R. K., & Hodgkinson, P. (2012). *Solid state NMR: Basic principles and practice*. New York: Momentum Press.
66. MacKenzie, K. J. D., & Smith, M. E. (2002). *Multinuclear solid-state NMR of inorganic materials*. Oxford: Pergamon Press.
67. Nelson, B. N., Shieber, L. J., Barich, D. H., Lubach, J. W., Offerdahl, T. J., Lewis, D. L., Heinrich, J. P., & Munson, E. J. (2006). Multiple-sample probe for solid-state NMR studies of pharmaceuticals. (2006). *Solid State Nuclear Magnetic Resonance*, 29, 204–213.
68. Ashbrook, S. E., & Duer, M. J. (2006). Structural information from quadrupolar nuclei in solid state NMR. *Concepts in Magnetic Resonance*, 28A, 183–248.

69. Ashbrook, S. E., & Smith, M. E. (2006). Solid state ^{17}O NMR—an introduction to the background principles and applications to inorganic materials. *Chemical Society Reviews*, 35, 718–735.
70. Chapman, R. P., Widdifield, C. M., & Bryce, D. L. (2009). Solid-state NMR of quadrupolar halogen nuclei. *Progress in Nuclear Magnetic Resonance Spectroscopy*, 55, 215–237.
71. Freitas, J. C. C., & Smith, M. E. (2012). Chapter 2 – recent advances in solid-state ^{25}Mg NMR spectroscopy. *Annual Reports on NMR Spectroscopy*, 75, 25–114.
72. Bräuniger, T., & Jansen, M. Z. (2013). Solid-state NMR spectroscopy of quadrupolar nuclei in inorganic chemistry. *Anorg Allg Chem*, 639, 857–879.
73. Vega, A. J. (2010). Quadrupolar nuclei in solids. *eMagRes*. <https://doi.org/10.1002/9780470034590.emrstm0431.pub2>.
74. Iwahara, N., Vieru, V., Ungur, L., & Chibotaru, L. F. (2017). Zeeman interaction and Jahn-Teller effect in the Γ_8 multiplet. *Physical Review B*, 96, 064416–064427.
75. Andrew, E. R., Bradbury, A., & Eades, R. G. (1959). Removal of dipolar broadening of nuclear magnetic resonance spectra of solids by specimen rotation. *Nature*, 183, 1802–1803.
76. Lowe, I. J. (1959). Free induction decays of rotating solids. *Physical Review Letters*, 2, 285–287.
77. Mansfield, P., & Ware, D. (1966). Nuclear resonance line narrowing in solids by repeated short pulse r.f. irradiation. *Physical Review Letters*, 22, 133–135.
78. Ostroff, E. D., & Waugh, J. S. (1966). Multiple spin echoes and spin locking in solids. *Physical Review Letters*, 16, 1097–1098.
79. Polenova, T., Gupta, R., & Goldbourt, A. (2015). Magic angle spinning NMR spectroscopy: A versatile technique for structural and dynamic analysis of solid-phase systems. *Analytical Chemistry*, 87, 5458–5469.
80. Vieth, H.-M., & Yanconi, C. S. (1993). Cross polarization in solid state NMR spectroscopy. Efficient polarization transfer via the non-Zeeman reservoir. *Chemical Physics Letters*, 205, 153–156.
81. Pines, A., Gibby, M. G., & Waugh, J. S. (1972). Proton-enhanced nuclear induction spectroscopy. A method for high resolution NMR of dilute spins in solids. *The Journal of Chemical Physics*, 56, 1776–1778.
82. Hartmann, S. R., & Hahn, E. L. (1962). Nuclear double resonance in the rotating frame. *Physics Review*, 128, 2042–2053.
83. Wu, G., & Wasylishen, R. E. (1992). Applications of two-dimensional ^{31}P CP/MAS NMR techniques for studying metal phosphine complexes in the solid state. *Organometallics*, 11, 3242–3248.
84. Metz, G., Wu, X., & Smith, S. O. (1994). Ramped-amplitude cross polarization in magic-angle-spinning NMR. *Journal of Magnetic Resonance, Series A*, 110, 219–227.
85. Hediger, S., Meier, B. H., & Ernst, R. R. (1995). Adiabatic passage Hartmann-Hahn cross polarization in NMR under magic angle sample spinning. *Chemical Physics Letters*, 240, 449–456.
86. Bennett, A. E., Rienstra, C. M., Auger, M., Lakshmi, K. V., & Griffin, R. G. (1995). Heteronuclear decoupling in rotating solids. *The Journal of Chemical Physics*, 103, 6951–6958.
87. Fung, B. M., Khitrin, A. K., & Ermolaev, K. (2000). An improved broadband decoupling sequence for liquid crystals and solids. *Journal of Magnetic Resonance*, 142, 97–101.
88. Paëpe, G. D., Sakellariou, D., Hodgkinson, P., Hediger, S., & Emsley, L. (2003). Heteronuclear decoupling in NMR of liquid crystals using continuous phase modulation. *Chemical Physics Letters*, 368, 511–522.
89. Thakur, R. S., Kurur, N. D., & Madhu, P. K. (2006). Swept-frequency two-pulse phase modulation for heteronuclear dipolar decoupling in solid-state NMR. *Chemical Physics Letters*, 426, 459–463.
90. Reich, H. J., Jautelat, M., Messe, M. T., Weigert, F. J., & Roberts, J. D. (1969). Nuclear magnetic resonance spectroscopy. Carbon-13 spectra of steroids. *Journal of the American Chemical Society*, 91, 7445–7454.

91. Ernst, M. (2003). Heteronuclear spin decoupling in solid-state NMR under magic-angle sample spinning. *Journal of Magnetic Resonance*, *162*, 1–34.
92. Detken, A., Hardy, E. H., Ernst, M., & Meier, B. H. (2002). Simple and efficient decoupling in magic-angle spinning solid-state NMR: The XiX scheme. *Chemical Physics Letters*, *356*, 298–304.
93. Paëpe, G. D., Lesage, A., & Emsley, L. (2003). The performance of phase modulated heteronuclear dipolar decoupling schemes in fast magic-angle-spinning nuclear magnetic resonance experiments. *The Journal of Chemical Physics*, *119*, 4833–4841.
94. Vinther, J. M., Nielsen, A. B., Bjerring, M., van Eck, E. R. H., Kentgens, A. P. M., Khaneja, N., & Nielsen, N. C. (2012). Refocused continuous-wave decoupling: A new approach to heteronuclear dipolar decoupling in solid-state NMR spectroscopy. *The Journal of Chemical Physics*, *137*, 214202–214215.
95. Vinther, J. M., Khaneja, N., & Nielsen, N. C. (2013). Robust and efficient ¹⁹F heteronuclear dipolar decoupling using refocused continuous-wave rf irradiation. *Journal of Magnetic Resonance*, *226*, 88–92.
96. Waugh, J. S., Huber, L. M., & Haeberlen, U. (1968). Approach to high-resolution nmr in solids. *Physical Review Letters*, *20*, 180–182.
97. Rhim, W.-K., Elleman, D. D., & Vaughan, R. W. (1973). Enhanced resolution for solid state NMR. *The Journal of Chemical Physics*, *58*, 1772–1773.
98. Vinogradov, E., Madhu, P. K., & Vega, S. (1999). High-resolution proton solid-state NMR spectroscopy by phase-modulated Lee-Goldburg experiment. *Chemical Physics Letters*, *314*, 443–450.
99. Sakellariou, D., Lesage, A., Hodgkinson, P., & Emsley, L. (2000). Homonuclear dipolar decoupling in solid-state NMR using continuous phase modulation. *Chemical Physics Letters*, *319*, 253–260.
100. Burum, D. P., & Bielecki, A. (1991). An improved experiment for heteronuclear-correlation 2D NMR in solids. *Journal of Magnetic Resonance*, *94*, 645–652.
101. Ryan, L. M., Taylor, R. E., Paff, A. J., & Gerstein, B. C. (1980). An experimental study of resolution of proton chemical shifts in solids: Combined multiple pulse NMR and magic-angle spinning. *The Journal of Chemical Physics*, *72*, 508–515.
102. Baldus, M. (2007). ICMRBS founder's medal 2006: Biological solid-state NMR, methods and applications. *Journal of Biomolecular NMR*, *39*, 73–86.
103. Haeberlen, U., & Waugh, J. S. (1968). Coherent averaging effects in magnetic resonance. *Physics Review*, *175*, 453–467.
104. Schaefer, J. (2011). Development of REDOR rotational-echo double-resonance NMR by Terry Gullion and Jacob Schaefer [J. Magn. Reson. *81* (1989) 196–200]. *Journal of Magnetic Resonance*, *213*, 421–422.
105. Thompson, L. K. (2002). Solid-state NMR studies of the structure and mechanisms of proteins. *Current Opinion in Structural Biology*, *12*, 661–669.
106. Grey, C. P., & Vega, A. J. (1995). Determination of the quadrupole coupling constant of the invisible aluminum spins in zeolite HY with ¹H/²⁷Al TRAPDOR NMR. *Journal of the American Chemical Society*, *117*, 8232–8242.
107. Gullion, T. (1995). Measurement of dipolar interactions between spin-1/2 and quadrupolar nuclei by rotational-echo, adiabatic-passage, double-resonance NMR. *Chemical Physics Letters*, *246*, 325–330.
108. Chen, L., Lu, X., Wang, Q., Lafon, O., Trébosch, J., & Amoureux, J.-P. (2010). Distance measurement between a spin-1/2 and a half-integer quadrupolar nuclei by solid-state NMR using exact analytical expressions. *Journal of Magnetic Resonance*, *206*, 269–273.
109. Raleigh, D. P., Levitt, M. H., & Griffin, R. G. (1988). Rotational resonance in solid state NMR. *Chemical Physics Letters*, *146*, 71–76.
110. Kinnun, J. J., Leftin, A., & Brown, M. F. (2013). Solid-state NMR spectroscopy for the physical chemistry laboratory. *Journal of Chemical Education*, *90*, 123–128.

111. Bryce, D. L., Bernard, G. M., Gee, M., Lumsden, M. D., Eichele, K., & Wasylshen, R. E. (2001). Practical aspects of modern routine solid-state multinuclear magnetic resonance spectroscopy: One-dimensional experiments. *Canadian Journal of Analytical Sciences and Spectroscopy*, *46*, 46–82.
112. Lunsford, J. H., Rothwell, W. P., & Shen, W. (1985). Acid sites in zeolite Y: A solid-state NMR and infrared study using trimethylphosphine as a probe molecule. *Journal of the American Chemical Society*, *107*, 1540–1547.
113. Kao, H.-M., Yu, C.-Y., & Yeh, M.-C. (2002). Detection of the inhomogeneity of Brønsted acidity in H-mordenite and H-b zeolites: A comparative NMR study using trimethylphosphine and trimethylphosphine oxide as ^{31}P NMR probes. *Microporous and Mesoporous Materials*, *53*, 1–12.
114. Yang, G., Zhuang, J., Ma, D., Lan, X., Zhou, L., Liu, X., Han, X., & Bao, X. (2008). A joint experimental-theoretical study on trimethylphosphine adsorption on the Lewis acidic sites present in TS-1 zeolite. *Journal of Molecular Structure*, *882*, 24–29.
115. Rothwell, W. P., Shen, W., & Lunsford, J. H. (1984). Solid-state phosphorus-31 NMR of a chemisorbed phosphonium ion in HY zeolite: Observation of proton-phosphorus-31 coupling in the solid-state. *Journal of the American Chemical Society*, *106*, 2452–2453.
116. Zhang, W., Han, X., Liu, X., & Bao, X. (2003). Characterization of the acid sites in dealuminated nanosized HZSM-5 zeolite with the probe molecule trimethylphosphine. *Journal of Molecular Catalysis A: Chemical*, *194*, 107–113.
117. Luo, Q., Deng, F., Yuan, Z., Yang, J., Zhang, M., Yue, Y., & Ye, C. (2003). Using trimethylphosphine as a probe molecule to study the acid sites in Al-MCM-41 materials by solid-state NMR spectroscopy. *The Journal of Physical Chemistry B*, *107*, 2435–2442.
118. Yang, J., Janik, M. J., Ma, D., Zheng, A., Zhang, M., Neurock, M., Davis, R. J., Ye, C., & Deng, F. (2005). Location, acid strength, and mobility of the acidic protons in Keggin $12\text{-H}_3\text{PW}_{12}\text{O}_{40}$: A combined solid-state NMR spectroscopy and DFT quantum chemical calculation study. *Journal of the American Chemical Society*, *127*, 18274–18280.
119. Yu, H., Fang, H., Zhang, H., Li, B., & Deng, F. (2009). Acidity of sulfated tin oxide and sulfated zirconia: A view from solid-state NMR spectroscopy. *Catalysis Communications*, *10*, 920–924.
120. Chu, Y., Yu, Z., Zheng, A., Fang, H., Zhang, H., Huang, S. J., Liu, S. B., & Deng, F. (2011). Acidic strengths of Brønsted and Lewis acid sites in solid acids scaled by ^{31}P NMR chemical shifts of adsorbed trimethylphosphine. *Journal of Physical Chemistry C*, *115*, 7660–7667.
121. Xu, J., Zheng, A., Yang, J., Su, Y., Wang, J., Zeng, D., Zhang, M., Ye, C., & Deng, F. (2006). Acidity of mesoporous $\text{MoO}_x/\text{ZrO}_2$ and WO_x/ZrO_2 materials: A combined solid-state NMR and theoretical calculation study. *The Journal of Physical Chemistry B*, *110*, 10662–10671.
122. Zhang, H., Yu, H., Zheng, A., Li, S., Shen, W., & Deng, F. (2008). Reactivity enhancement of 2-propanol photocatalysis on $\text{SO}_4^{2-}/\text{TiO}_2$: Insights from solid-state NMR spectroscopy. *Environmental Science & Technology*, *42*, 5316–5321.
123. Yang, J., Zhang, M., Deng, F., Luo, Q., Yi, D., & Ye, C. (2003). Solid state NMR study of acid sites formed by adsorption of SO_3 onto $\gamma\text{-Al}_2\text{O}_3$. *Chemical Communications*, *7*, 884–885.
124. Grey, C. P., Veeman, W. S., & Vega, A. J. (1993). Rotational echo $^{14}\text{N}/^{13}\text{C}/^1\text{H}$ triple resonance solid-state nuclear magnetic resonance: A probe of ^{13}C - ^{14}N internuclear distances. *The Journal of Chemical Physics*, *98*, 7711–7724.
125. Morris, G. A., & Freeman, R. (1979). Enhancement of nuclear magnetic resonance signals by polarization transfer. *Journal of the American Chemical Society*, *101*, 760–762.
126. Peng, L., Chupas, P. J., & Grey, C. P. (2004). Measuring Brønsted acid densities in zeolite HY with diphosphine molecules and solid state NMR spectroscopy. *Journal of the American Chemical Society*, *126*, 12254–12255.
127. Peng, L., & Grey, C. P. (2008). Diphosphine probe molecules and solid-state NMR investigations of proximity between acidic sites in zeolite HY. *Microporous and Mesoporous Materials*, *116*, 277–283.
128. Schnell, I. (2004). Dipolar recoupling in fast-MAS solid-state NMR spectroscopy. *Progress in Nuclear Magnetic Resonance Spectroscopy*, *45*, 145–207.

129. Wang, Y., Wang, F., Song, Q., Xin, Q., Xu, S., & Xu, J. (2013). Heterogeneous ceria catalyst with water-tolerant Lewis acidic sites for one-pot synthesis of 1,3-diols via Prins condensation and hydrolysis reactions. *Journal of the American Chemical Society*, *135*, 1506–1515.
130. Huang, S.-J., Zhao, Q., Chen, W.-H., Han, X., Bao, X., Lo, P.-S., Lee, H.-K., & Liu, S.-B. (2004). Structure and acidity of Mo/H-MCM-22 catalysts studied by NMR spectroscopy. *Catalysis Today*, *97*, 25–34.
131. Zheng, A., Han, B., Li, B., Liu, S.-B., & Deng, F. (2012). Enhancement of Brønsted acidity in zeolite due to an intermolecular solvent effect in confined micropores. *Chemical Communications*, *48*, 6936–6938.
132. Kitano, M., Wada, E., Nakajima, K., Hayashi, S., Miyazaki, S., Kobayashi, H., & Hara, M. (2013). Protonated titanate nanotubes with Lewis and Brønsted acidity: Relationship between nanotube structure and catalytic activity. *Chemistry of Materials*, *25*, 385–393.
133. Han, X., Kuang, Y., Xiong, C., Tang, X., Chen, Q., Hung, C.-T., Liu, L.-L., & Liu, S.-B. (2017). Heterogeneous amino acid-based tungstophosphoric acids as efficient and recyclable catalysts for selective oxidation of benzyl alcohol. *Korean Journal of Chemical Engineering*, *34*, 1914–1923.
134. Zhao, Q., Chen, W.-H., Huang, S.-J., Wu, Y.-C., Lee, H.-K., & Liu, S.-B. (2002). Discernment and quantification of internal and external acid sites on zeolites. *The Journal of Physical Chemistry B*, *106*, 4462–4469.
135. Zhao, Q., Chen, W.-H., Huang, S.-J., & Liu, S.-B. (2003). 39 qualitative and quantitative determination of acid sites on solid acid catalysts. *Studies in Surface Science and Catalysis*, *145*, 205–209.
136. Kojima, N., & Hayashi, S. (2011). Undesorbed dichloromethane in zeolites studied by solid-state NMR. *Bulletin of the Chemical Society of Japan*, *84*, 1090–1095.
137. Kao, H.-M., Chang, P.-C., Liao, Y.-W., Lee, L.-P., & Chien, C.-H. (2008). Solid-state NMR characterization of the acid sites in cubic mesoporous Al-MCM-48 materials using trimethylphosphine oxide as a ³¹P NMR probe. *Microporous and Mesoporous Materials*, *114*, 352–364.
138. Kao, H.-M., Liu, H., Jiang, J.-C., Lin, S.-H., & Grey, C. P. (2000). Determining the structure of trimethylphosphine bound to the Brønsted acid site in zeolite HY: Double-resonance NMR and ab initio studies. *The Journal of Physical Chemistry B*, *104*, 4923–4933.
139. Han, X., Chen, K., Du, H., Tang, X.-J., Hung, C.-T., Lin, K.-C., & Liu, S.-B. (2016). Novel Keggin-type H₄PVMO₁₁O₄₀-based ionic liquid catalysts for *n*-caprylic acid esterification. *Journal of the Taiwan Institute of Chemical Engineers*, *58*, 203–209.
140. Chen, W.-H., Ko, H.-S., Sakthivel, A., Huang, S.-J., Liu, S.-B., Lo, A.-Y., & Tsai T-C Liu, S.-B. (2006). A solid-state NMR, FT-IR and TPD study on acid properties of sulfated and metal-promoted zirconia: Influence of promoter and sulfation treatment. *Catalysis Today*, *116*, 111–120.
141. Li, S., Zhou, H., Jin, C., Feng, N., Liu, F., Deng, F., Wang, J.-Q., Huang, W., Xiao, L., & Fan, J. (2014). Formation of subnanometer Zr-WO_x clusters within mesoporous W-Zr mixed oxides as strong solid acid catalysts for Friedel-Crafts alkylation. *Journal of Physical Chemistry C*, *118*, 6283–6290.
142. Zheng, A., Chen, L., Yang, J., Zhang, M., Su, Y., Yue, Y., Ye, C., & Deng, F. (2005). Combined DFT theoretical calculation and solid-state NMR studies of Al substitution and acid sites in zeolite MCM-22. *The Journal of Physical Chemistry B*, *109*, 24273–24279.
143. Tagusagawa, C., Takagaki, A., Takanabe, K., Ebitani, K., Hayashi, S., & Domen, K. (2010). Layered and nanosheet tantalum molybdate as strong solid acid catalysts. *Journal of Catalysis*, *270*, 206–212.
144. Tagusagawa, C., Takagaki, A., Iguchi, A., Takanabe, K., Kondo, J. N., Ebitani, K., Hayashi, S., Tatsumi, T., & Domen, K. (2010). Highly active mesoporous Nb-W oxide solid-acid catalyst. *Angewandte Chemie, International Edition*, *49*, 1128–1132.
145. Karra, M. D., Sutovich, K. J., & Mueller, K. T. (2002). NMR characterization of Brønsted acid sites in faujasitic zeolites with use of perdeuterated trimethylphosphine oxide. *Journal of the American Chemical Society*, *124*, 902–903.

146. Li, S., Zheng, A., Su, Y., Zhang, H., Chen, L., Yang, J., Ye, C., & Deng, F. (2007). Brønsted/Lewis acid synergy in dealuminated HY zeolite: A combined solid-state NMR and theoretical calculation study. *Journal of the American Chemical Society*, *129*, 11161–11171.
147. Huang, S.-J., Tseng, Y.-H., Mou, Y., Liu, S.-B., Huang, S.-H., Lin, C.-P., & Chan, J. C. C. (2006). Spectral editing based on selective excitation and Lee-Goldburg cross-polarization under magic angle spinning. *Solid State Nuclear Magnetic Resonance*, *29*, 272–277.
148. van Rossum, B.-J., de Groot, C. P., Ladizhansky, V., Vega, S., & de Groot, H. J. M. (2000). A method for measuring heteronuclear (^1H - ^{13}C) distances in high speed MAS NMR. *Journal of the American Chemical Society*, *122*, 3465–3472.
149. Ladizhansky, V., & Vega, S. (2000). Polarization transfer dynamics in Lee-Goldburg cross polarization nuclear magnetic resonance experiments on rotating solids. *The Journal of Chemical Physics*, *112*, 7158–7168.
150. Zheng, A., Zhang, H., Lu, X., & Liu S-B Deng, F. (2008). Theoretical predictions of ^{31}P NMR chemical shift threshold of trimethylphosphine oxide absorbed on solid acid catalysts. *The Journal of Physical Chemistry B*, *112*, 4496–4505.
151. Garg, B., Bisht, T., & Ling, Y.-C. (2014). Graphene-based nanomaterials as heterogeneous acid catalysts: A comprehensive perspective. *Molecules*, *19*, 14582–14614.
152. Hara, M., Yoshida, T., Takagaki, A., Takata, T., Kondo, J. N., Hayashi, S., & Domen, K. (2004). A carbon material as a strong protonic acid. *Angewandte Chemie, International Edition*, *43*, 2955–2958.
153. Stellwagen, D. R., van der Klis, F., van Es, D. S., de Jong, K. P., & Bitter, J. H. (2013). Functionalized carbon nanofibers as solid-acid catalysts for transesterification. *ChemSusChem*, *6*, 1668–1672.
154. Zhang, M., Li, C., Hua, W., Yue, Y., & Gao, Z. (2014). Preparation and catalytic performance of perfluorosulfonic acid-functionalized carbon nanotubes. *Chinese Journal of Catalysis*, *35*, 1874–1882.
155. Wang, L., Dong, X., Jiang, H., Li, G., & Zhang, M. (2014). Phosphorylated ordered mesoporous carbon as a novel solid acid catalyst for the esterification of oleic acid. *Catalysis Communications*, *56*, 164–167.
156. Sun, Y., Hu, J., An, S., Zhang, Q., Guo, Y., Song, D., & Shang, Q. (2017). Selective esterification of glycerol with acetic acid or lauric acid over rod-like carbon-based sulfonic acid functionalized ionic liquids. *Fuel*, *207*, 136–145.
157. Chang, B., Guo, Y., Yin, H., Zhang, S., & Yang, B. (2015). Synthesis of sulfonated porous carbon nanospheres solid acid by a facile chemical activation route. *Journal of Solid State Chemistry*, *221*, 384–390.
158. Zhao, J., Zhou, C., He, C., Dai, Y., Jia, X., & Yang, Y. (2016). Efficient dehydration of fructose to 5-hydroxymethylfurfural oversulfonated carbon sphere solid acid catalysts. *Catalysis Today*, *264*, 123–130.
159. Ngaosuwan, K., Goodwin, J. G., Jr., & Prasertdham, P. (2016). A green sulfonated carbon-based catalyst derived from coffee residue for esterification. *Renewable Energy*, *86*, 262–269.
160. Zhou, Y., Niu, S., & Li, J. (2016). Activity of the carbon-based heterogeneous acid catalyst derived from bamboo in esterification of oleic acid with ethanol. *Energy Conversion and Management*, *114*, 188–196.
161. Zhou, L., Dong, B., Tang, S., Ma, H., Chen, C., Yang, X., & Xu, J. (2013). Sulfonated carbon catalyzed oxidation of aldehydes to carboxylic acids by hydrogen peroxide. *Journal of Energy Chemistry*, *22*, 659–664.
162. Poonjarernsilp, C., Sanoa, N., & Tamon, H. (2014). Hydrothermally sulfonated single-walled carbon nanohorns for use as solid catalysts in biodiesel production by esterification of palmitic acid. *Applied Catalysis B: Environmental*, *147*, 726–732.
163. Nakajima, K., & Hara, M. (2012). Amorphous carbon with SO_3H groups as a solid Brønsted acid catalyst. *ACS Catalysis*, *2*, 1296–1304.
164. Okamura, M., Takagaki, A., Toda, M., Kondo, J. N., Domen, K., Tatsumi, T., Hara, M., & Hayashi, S. (2006). Acid-catalyzed reactions on flexible polycyclic aromatic carbon in amorphous carbon. *Chemistry of Materials*, *18*, 3039–3045.

165. Nakajima, K., Okamura, M., Kondo, J. N., Domen, K., Tatsumi, T., Hayashi, S., & Hara, M. (2009). Amorphous carbon bearing sulfonic acid groups in mesoporous silica as a selective catalyst. *Chemistry of Materials*, *21*, 186–193.
166. Suganuma, S., Nakajima, K., Kitano, M., Kato, H., Tamura, A., Kondo, H., Yanagawa, S., Hayashi, S., & Hara, M. (2011). SO₃H-bearing mesoporous carbon with highly selective catalysis. *Microporous and Mesoporous Materials*, *143*, 443–450.
167. Aldana-Pérez, A., Lartundo-Rojas, L., Gómez, R., & Niño-Gómez, M. E. (2012). Sulfonic groups anchored on mesoporous carbon Starbons-300 and its use for the esterification of oleic acid. *Fuel*, *100*, 128–138.
168. Fraile, J. M., García-Bordejé, E., Pires, E., & Roldán, L. (2014). New insights into the strength and accessibility of acid sites of sulfonated hydrothermal carbon. *Carbon*, *77*, 1157–1167.
169. Li, Y., & Zeng, D. (2017). Synthesis and characterization of flower-like carbon spheres solid acid from glucose for esterification. *Materials Letters*, *193*, 172–175.
170. Russo, P. A., Antunes, M. M., Neves, P., Wiper, P. V., Fazio, E., Neri, F., Barreca, F., Mafrá, L., Pillinger, M., Pinna, N., & Valente, A. A. (2014). Solid acids with SO₃H groups and tunable surface properties: Versatile catalysts for biomass conversion. *Journal of Materials Chemistry A*, *2*, 11813–11824.
171. Russo, P. A., Antunes, M. M., Neves, P., Wiper, P. V., Fazio, E., Neri, F., Barreca, F., Mafrá, L., Pillinger, M., Pinna, N., & Valente, A. A. (2014). Mesoporous carbon-silica solid acid catalysts for producing useful bio-products within the sugar-platform of biorefineries. *Green Chemistry*, *16*, 4292–4305.
172. Bispo, C., Vigier, K. D. O., Sardo, M., Bion, N., Mafrá, L., Ferreira, P., & Jérôme, F. (2014). Catalytic dehydration of fructose to HMF over sulfonic acid functionalized periodic mesoporous organosilicas: Role of the acid density. *Catalysis Science & Technology*, *4*, 2235–2240.
173. Zeng, D., Liu, S., Gong, W., Wang, G., Qiu, J., & Tian, Y. (2013). Acid properties of solid acid from petroleum coke by chemical activation and sulfonation. *Catalysis Communications*, *40*, 5–8.
174. Zeng, D., Liu, S., Gong, W., Wang, G., Qiu, J., & Chen, H. (2014). Synthesis, characterization and acid catalysis of solid acid from peanut shell. *Applied Catalysis A: General*, *469*, 284–289.
175. Garg, B., & Ling, Y.-C. (2014). One-pot green synthesis of azides from alcohols using Brønsted acidic ionic liquid [HMIM][BF₄] as solvent and catalyst. *Journal of the Chinese Chemical Society*, *61*, 737–742.
176. Garg, B., & Ling, Y.-C. (2012). Highly efficient synthesis of N-confused meso-tetraspirocyclohexyl calix[4]pyrrole using Brønsted acidic ionic liquids as catalysts. *Tetrahedron Letters*, *53*, 5674–5677.
177. Liu, F., Kong, W., Wang, L., Yi, X., Noshadi, I., Zheng, A., & Qi, C. (2015). Efficient biomass transformations catalyzed by graphene-like nanoporous carbons functionalized with strong acid ionic liquids and sulfonic groups. *Green Chemistry*, *17*, 480–489.
178. Liu, F., Li, B., Liu, C., Kong, W., Yi, X., Zheng, A., & Qi, C. (2016). Template-free synthesis of porous carbonaceous solid acids with controllable acid sites and their excellent activity for catalyzing the synthesis of biofuels and fine chemicals. *Catalysis Science & Technology*, *6*, 2995–3007.
179. Noshadi, I., Kanjilal, B., & Liu, F. (2016). Porous carbonaceous solid acids derived from farm animal waste and their use in catalyzing biomass transformation. *Applied Catalysis A: General*, *513*, 19–29.
180. Liu, F., Zheng, A., Noshadi, I., & Xiao, F.-S. (2013). Design and synthesis of hydrophobic and stable mesoporous polymeric solid acid with ultra strong acid strength and excellent catalytic activities for biomass transformation. *Applied Catalysis B: Environmental*, *136-137*, 193–201.
181. Garg, B., Sung, C.-H., & Ling, Y.-C. (2015). Graphene-based nanomaterials as molecular imaging agents. *WIREs Nanomedicine and Nanobiotechnology*, *7*, 737–758.

182. Garg, B., Bisht, T., & Ling, Y.-C. (2015). Graphene-based nanomaterials as efficient peroxidase mimetic catalysts for biosensing applications: An overview. *Molecules*, *20*, 14155–14190.
183. Ke, Y., Garg, B., & Ling, Y.-C. (2016). A novel graphene-based label-free fluorescence 'turn-on' nanosensor for selective and sensitive detection of phosphorylated species in biological samples and living cells. *Nanoscale*, *8*, 4547–4556.
184. Garg, B., Bisht, T., & Ling, Y.-C. (2016). Graphene-based nanomaterials: Versatile catalysts for carbon-carbon bond forming reactions. *Current Organic Chemistry*, *20*, 1547–1566.
185. Garg, B., & Bisht, T. (2016). Carbon nanodots as peroxidase nanozymes for biosensing. *Molecules*, *21*, 1653.
186. Garg, B., & Ling, Y.-C. (2016). Chapter 10: The richness of graphene-based materials in biomimetic applications. In M. Aliofkhazraei, N. Ali, W. I. Milne, C. S. Ozkan, S. Mitura, & J. L. Gervasoni (Eds.), *Graphene science handbook: Applications and industrialization* (pp. 125–142). Taylor & Francis/CRC Press, Boca Raton.
187. Garg, B., Bisht, T., & Thomas, K. R. J. (2017). Chapter 9: Magnetic graphene nanocomposites for multi-functional applications. In S. K. Sharma (Ed.), *Complex magnetic nanostructures-synthesis, assembly and applications* (pp. 317–357). Cham: Springer International Publishing AG.
188. Garg, B., Bisht, T., & Ling, Y.-C. (2014). Sulfonated graphene as highly efficient and reusable acid carbocatalyst for the synthesis of ester plasticizers. *RSC Advances*, *4*, 57297–57307.
189. Antunes, M. M., Russo, P. A., Wiper, P. V., Veiga, J. M., Pillinger, M., Mafra, L., Evtuguin, D. V., Pinna, N., & Valente, A. A. (2014). Sulfonated graphene oxide as effective catalyst for conversion of 5-(hydroxymethyl)-2-furfural into biofuels. *ChemSusChem*, *7*, 804–812.
190. Oger, N., Lin, Y. F., Labrugère, C., Grogneq, E. L., Rataboul, F., & Felpin, F.-R. (2016). Practical and scalable synthesis of sulfonated graphene. *Carbon*, *96*, 342–335.

Index

A

- Abbe's equation, 155
- Aberration correction model, 150
- Absorption, inorganic materials, 295–296
- Accelerating voltages, 121, 126
- Additive process, 236
- AFM, *see* Atomic force microscopy
- Airy discs, 117, 154
- Alzheimer's disease, 340
- α -methyl styrene (AMS), 575
- Analogue-digital converters (ADCs), 561
- Angle-resolved energy distribution curves (AREDCS), 471
- Angle-resolved photoelectron spectroscopy (ARPES), 438, 468, 469
 - Au-110 surface, 471
 - Bi₂Se₃, electronic structure of, 472
 - GaAs (110) surface, normal emission spectra of, 470–471
 - MoS₂ and MoSe₂, electronic structure of, 471–472
 - spin-resolved ARPES
 - BCC Fe, 478
 - Bi thin films, 478
 - ferromagnetic substance, 474
 - longitudinal configuration, 475
 - Lorentz force, 474
 - magnetic domains, 474
 - phase space considerations, 477–478
 - polarimeters, 475–477
 - transverse configuration, 474
- Arlunya image processor, 225
- Atomic emission spectroscopy (AES), 436
- Atomic force microscopy (AFM), 241
 - atomic resolution images, 270
 - attractive and repulsive forces, 268
 - biological samples, imaging of, 264, 270
 - cantilever with sharp tip/probe, 264, 269, 270
 - conducting mode AFM, 264, 281, 283
 - contact mode, 267
 - advantages and disadvantages, 271–272
 - Ar beam-induced ripple formation, on InP surface, 280, 282
 - force-distance curve, 271
 - repulsive force, 271
 - SPM controller, functions, 271
 - Co thin films and nanoparticles (*see* Cobalt (Co) thin films and nanoparticles)
 - feedback mechanism, 270
 - Hooke's law, 268
 - laser diode, 269
 - limitations, 272, 290
 - for liquid samples, 264
 - multimode, 264
 - non-biological materials, surfaces of, 264
 - nonconducting materials, 250
 - non-contact mode, 272
 - optical lever, 268–269
 - position-sensitive photodetector, 270
 - probe-sample separation, 267
 - probe/tip attached to flexible cantilever, 268
 - static and dynamic mode, 270
 - tapping (intermittent) mode
 - advantages and disadvantages, 272
 - biological samples, imaging of, 283
 - gold films, nanoring formation in, 281, 282
 - topographic images, 270
- Atomic number, 121

- Atomic probe microscopy, 229
 Atom manipulation process, 232–233
 ATOMS software, 534, 535
 Attenuated total reflectance (ATR), 297, 335–336
 Aufbau principle, 450
 Auger electron emission, 461
 Auger electron spectroscopy, 436
 Auger electron yield (AEY), 516, 517
 Auger spectroscopy, 229
 Autocorrelation function, Co nanoparticles
 exponential correlation model, 286, 287
 height-height correlation function, 286
 lateral correlation length, 286
 one-dimensional autocorrelation function, 285
 pristine and ion-irradiated thin films, 287–289
 AXUV-100G detector, 518
- B**
- Background spectrum, 331, 332
 Backscatter coefficient, 123
 Backscattered electrons (BSEs), 119, 122–124, 461
 Band gap energy, 301, 303
 BasIreps program, 26–28
 Beaucage model, 65
 Beer-Lambert law, 406, 500
 Beer's law, 307, 320
 Bending vibration, 325
 1,3,5-Benzenetribenzoic acid (BTB)
 molecules, 240–241
 Bias-dependent surface imaging, 231
 Bias voltage, 231
 Bioimaging
 atherosclerosis, 388
 dual and multimode imaging, 390–397
 lanthanide nanoparticles, 388
 LEDs, 397–398
 luminescent imaging, 388
 osteopontin, 389
 THP-1 macrophages, 390
 UCNPs, 389–390
 vulnerable plaques, rupture of, 388
 Biomedical imaging, 339–340
 Bismuth oxyhalides (BiOX), 303, 304
 Blackbody effect, 293
 Bohr magneton, 451
 Bologna stone (BaS), 350
 Bolometers, 333
- Bolt press and gas cell holders, 334
 Boltzmann constant, 294
 Bomem instruments, 322
 Bonse-hart instruments, 70
 Bragg equation, 10–11
 Bragg's law, 154, 442
 Bremsstrahlung radiation, 440
 Brønsted acidic sites, 563, 564, 566, 567
 Brownian motion, 81, 553
- C**
- Cadmium oxide (CdO), 339
 C-AFM, *see* Conducting atomic force microscopy
 Carbon materials, Raman spectroscopy
 CNTs, electronic band structure of, 414–415
 D-band, second-order Raman scattering, 416
 first-order Raman scattering
 G-band, 417–419
 RBM, 416
 graphene
 B_{2g} phonon, 420
 Brillouin zone of, 420
 CNTs, structure of, 410–413
 E_{2g} phonon, 420
 electronic band structure, 413–414
 Kohn anomaly, 421
 LBMs, 421
 SLG, 420
 CasaXPS Casa Software YouTube channel, 462
 Catalytic applications, 302–307
 Cathodeluminescence (CL), 171
 Cathode-ray tube (CRT), 350
 Cathodoluminescence, 348
 CCD, *see* Charge-coupled device
 CDW, *see* Charge density wave
 Cellulose nanofiber (CNF), 539, 540
 Centerburst, 330
 Channel electron multiplier (CEM), 446, 447
 Channeltrons, *see* Channel electron multiplier
 Charge-coupled device (CCD), 173, 387, 408
 camera, 447
 detectors, 71
 Charge density wave (CDW), 243–246
 Chemical mapping, 201–203
 Chemical shift anisotropy (CSA), 552
 Chemical vapour deposition (CVD), 409

- Chemiluminescence, 348
Closed structure (CS), 236
Cobalt oxide (Co₃O₄), 338–339
Cobalt (Co) thin films and nanoparticles
 atomic force microscopy
 irradiated films, 277–279
 pristine films, 275–277
 magnetic force microscopy
 irradiated films, 277–279
 pristine films, 275, 276, 278, 279
 surface correlation (*see* Surface correlation,
 Co nanoparticles)
Cold-field emission, 166
Combined rotation and multiple-pulse
 spectroscopy (CRAMPS), 559
Compact fluorescent light (CFL), 355
Complementary metal-oxide-semiconductor
 (CMOS), 72
Compound microscope, 263
Compton, Arthur H., 353
Computed tomography (CT), 390, 394
Computerized tomography, 204
Conductance imaging, 226
Conducting atomic force microscopy
 (C-AFM), 264, 281, 283
Conduction band (CB), 295, 296
Confocal scanning microscopy, 407
Constant analyser energy (CAE), 446
Constant current mode, 224, 267
Constant height mode, 224, 225, 266–267
Constant retard ratio (CRR), 446
Constructive interference, 328
Contact mode AFM, 267
 advantages and disadvantages, 271–272
 Ar beam-induced ripple formation, on InP
 surface, 280, 282
 force-distance curve, 271
 repulsive force, 271
 SPM controller, functions, 271
CONTIN regularization, 86
Continuous wave (CW), 356, 558
Contrast agents (CAs), 394
Cooperative energy transfer (CET), 373
Coulomb potential, 491
Cross-polarization (CP) technique, 557–558
Cryopumps, 171
Cubic spline function, 527
Cumulant method, 83–85
Cyclic voltammetry, 241
Cylindrical mirror (CM), 514
Cylindrical mirror analysers (CMA), 444,
 468
Czerny–Turner (CZ) monochromator, 383–385
- D**
DIB layout, 18–19
 de Broglie relation, 155
 de Broglie’s equation, 5
Debye formulation, 55
Debye model, 533
Debye–Scherrer geometry, 3
Deflection analysers, 444
Deformation vibration, *see* Bending vibration
Density functional theory (DFT), 229–230,
 456
Density of states (DOS), 224
Destructive interference, 328
Detection quantum efficiency (DQE), 173
Deuterated TGS (DTGS) detector, 333
Dewar flask, 388
Dexter energy transfer, 366
Diamond, 336
10-Dicyanoanthracene (DCA), 240
Diffraction contrast, 159, 161, 162
Diffuse reflectance measurements, 298
Diffusion pumps, 170
Diode array, 312
Dirac delta function, 6
Dissolved organic matters (DOMs), 95
Double-crystal monochromator (DCM), 517,
 518
Dual and multimode imaging
 luminescent/MR dual-mode imaging,
 390–391
 luminescent/SPECT dual-mode imaging,
 393–394
 luminescent/X-Ray-CT dual-mode
 imaging, 394–395
 PAI, 395–397
Dual-pellet holder, 334
Dual wavelength, 309, 311
Dynamic light scattering (DLS)
 “black-box” tool/technique, 78
 data, interpretation of
 particle size distribution, 88–90
 PDI, 87–88
 Z-average, 86–87
 vs. electron microscopy’s size, 100–102
MNP-based researches
 FOQELS, 98
 functionalized layer, thickness of,
 90–94
 particle concentration determination
 tool, 97–98
 particle’s colloidal stability, 94–96
 thermoresponsive, particle size of,
 96–97

Dynamic light scattering (DLS) (*cont.*)
 particle concentration, role of, 102–104
 sedimentation energy, 104–105
 TEM, 78
 working principle of
 Brownian motion, 81
 CONTIN regularization, 86
 cumulant method, 83–85
 intensity profiles of, 79–80
 linear fit, 82–83
 normalized electric field correlation
 function, 81
 normalized intensity correlation
 function, 82
 polarized light beam, 79
 Seigert equation, 81
 Stokes-Einstein equation, 81
 time-averaged intensity, 80
 Z-average size, 78
 Dyson equations, 490, 491, 504

E

Ebert-Fastie monochromator, 383, 384
 EdPCR program, 29
 EELS, *see* Electron energy-loss spectroscopy
 EFTEM, *see* Energy-filtered transmission
 electron microscope
 Einstein model, 533
 Electric dipole (ED) transition, 379
 Electric discharge lamp, 355
 Electric field microscopy (EFM), 264
 Electrochemical etching, 222, 229
 Electrochemical polishing, 229
 Electroluminescence, 348
 Electromagnetic lenses, 166–167
 Electromagnetic spectrum, 293–294
 Electron beam evaporation method, 287
 Electron beam lithography (EBL), 424
 Electron detectors, 171
 DQE, 173
 modern CCD detectors, 173
 scintillator-photomultiplier detector,
 175–176
 semiconductor detectors, 174–175
 Electron diffraction, 229
 Electron energy-loss spectroscopy (EELS),
 148, 150, 198, 199, 205
 Electron gun
 field emitters, 125–129
 thermionic emitters, 125–126
 Electronic density of states (DOS), 456
 Electronic energy transfer process
 CIE coordinates, 381

intramolecular energy transfer mechanisms,
 rare earths
 cross relaxation, 374–376
 inorganic solids, RE³⁺ ions in, 369–371
 sensitization processes, RE³⁺ organic
 complexes, 367–369
 in upconversion luminescent RE³⁺
 materials, 371–374
 luminescence decay curves, 380–381
 luminescence spectra
 emission spectra, 378–380
 excitation spectra, 377–378
 4f-4f intraconfiguration transitions, 376
 ligand polarization effects, 376
 magnetic dipole transitions, 376
 sensitization process (antenna effect),
 376
 non-radiative energy transfer
 donor and acceptor states, 365
 nonresonant energy transfer, 367
 resonant energy transfer, 366–367
 radiative energy transfer mechanism, 365
 Electronic spectroscopy, rare earth ions
 CIE coordinates, 381
 energy transfer (*see* Electronic energy
 transfer process)
 luminescence decay curves, 380–381
 luminescence spectra, 376–380
 [Xe]4f^N configurations, 360–364
 Electronic states
 of atoms, 450–455
 of solids
 DOS, 456
 electronic band structure, 456–458
 Electron lensing mechanism, 443
 Electron microscope
 vs. optical microscope, 147, 152–154
 TEM (*see* Transmission electron
 microscopy)
 Electron microscopy (EM), 113, 263
 Electron-phonon interactions, 247
 Electron repulsion, 362, 363
 Electron spin resonance, 249
 Electrostatic Einzel lens, 443
 Electrostatic forces, 230
 Energy-dispersive curve (EDC), 438, 471, 478
 Energy-dispersive spectroscopy (EDS), 192,
 195, 197
 Energy-dispersive X-ray spectroscopy (EDX),
 124, 138, 148
 Energy-filtered transmission electron
 microscope (EFTEM), 198–201
 Energy migration-mediated upconversion
 (EMU), 373–374

- Energy transfer upconversion (ETU), 372–374
- Entrapment vacuum pumps, 448
- Environmental electron microscopy, energy-filtered TEM (EFTEM), 150
- Environmental remediation, 305
- Environmental secondary electron detector (ESED), 139
- EXAFS measurement, 509, 518, 519, 539
- Excitation energy transfer process, 365
- Excited-state absorption (ESA), 372
- EXCURVE program, 522
- Exponential correlation model, 286, 287
- Extended X-ray absorption fine structure (EXAFS)
- Artemis (Cu *K*-Edge data from Cu Foil), 533–535
 - $\chi(k)$ conversion, 529
 - Fourier transformation, 530–531
 - modeling, 532–533
 - weighed $\chi(k)$ vs. *k*spectrum, 529–530
- F**
- Face centre cubic (FCC), 457
- Fast FT (FFT), 563
- Feedback circuit, 218, 219, 223, 224
- constant height mode, 225
 - spectroscopic measurement, 232
- Fermi-Dirac distribution function, 457
- Fermi energy, 456
- Fermi level, 220, 221, 230, 231
- Fermi's pseudo-potential, 5
- Fermi's rule, 506
- Ferrites, 538–539
- Fiber-optic quasi-elastic light scattering (FOQELS), 98
- Field emission guns (FEG), 125–129, 138, 164–165
- Field emission scanning electron microscope (FESEM), 126, 138
- vs. SEM, 139–140
- Field evaporation process, 229
- Fixed analyser transmission (FAT), 446
- Fixed retard ratio (FRR), 446
- Floating-layer technique, 229
- Fluorescent lamps (FL), 350
- 18-Fluorodeoxyglucose (FDG), 391
- Force-distance (F-D) curve, 271
- Förster resonance energy transfer, 366
- Fourier transformation (FT), 530–531, 560
- Fourier transform infrared spectroscopy (FTIR)
- absorption spectrum, 319, 320
 - applications
 - biomedical imaging, 339–340
 - proteins study, 341
 - basic principle of, 325–326
 - electromagnetic spectrum, 318–319
 - gaseous samples, 341
 - history of, 322
 - hydrogen fluoride, 318
 - instrumentation
 - bolometers, 333
 - infrared red radiation sources, 333
 - interferogram to spectrum, 331–332
 - interferometer and interferogram, 328–330
 - photon detectors, 332
 - pyroelectric detectors, 333
 - sample holders, 334
 - sample preparation, 334–335
 - thermal detectors, 332–333
 - IR-ATR, 335–336
 - materials characterization
 - nanomaterials, 338–339
 - organic compounds, 336–338
 - matter-energy interaction, 323–325
 - net dipole moment, 319
 - organic and inorganic compounds, 341
 - percent transmittance, 321
 - wavenumbers, 320
 - zero dipole moment, 318
- Fractal aggregate (FA) model
- fractal aggregate architecture, 62
 - Gaussian size distribution, 62–63
 - mass fractal aggregate, 62
 - mass fractal structure, 60
 - N* primary nanoparticles, 59
 - pair-distribution function, 61
 - Porod law, 60
 - surface fractals, 60
- Free induction decay (FID), 563
- Fridrich, Elmer, 353
- FullProf, 2
- FullProf Studio, 31–33
- Furfuryl alcohol (FA), 578
- G**
- GaAsP LED, 355
- Gadolinium, 357
- Gallium arsenide (GaAs), 385, 386
- Gallium arsenide phosphide (GaAsP), 385, 386
- Gas transfer vacuum pumps, 448
- Gatan imaging filter (GIF), 176
- Gaussian distributions, 50, 83, 85

General Electric (GE) Corporation, 355
 General Electric Research Laboratory, 353
 Generalized gradient approximation (GGA), 488
 Germanium, 336
 Germer, Edmund, 354
 GNXAS program, 522
 Gold (Au) thin films, 281, 282
 Graphene, 409–410
 B_{2g} phonon, 420
 Brillouin zone of, 420
 CNTs, structure of, 410–413
 E_{2g} phonon, 420
 electronic band structure, 413–414
 Kohn anomaly, 421
 LBMs, 421
 SLG, 420
 Graphene-like nanoporous carbons (GNCs), 582
 Graphene nanoribbons (GNR), 232
 Graphene-superconductor (GS) interface, 226
 Graphite, imaging of HOPG, 234–236
 Green's function, 425, 490, 504, 505
 GSAS, 2
 Guinier average approach, 48
 Guinier law, 44
 Cartesian coordinate system, 45
 concentrated nanoparticle solution, 46
 distributed properties, 47
 experimental SAXS curves, 46
 Guinier average approach, 48
 percolated samples, 46
 radius of gyration, 47
 scattering intensity, 45

H

HAADF-STEM, *see* High-angle annular dark-field scanning transmission electron microscopy
 Hamiltonian theory, 559
 Hammer, Edward, 355
 Hard X-ray beamline
 experimental end station, 518
 layout, 517–518
 1D beamline, data measurement, 519
 Hartmann-Hahn (H-H) matching conditions, 557
 Heavy-duty magnetic film holder, 334
 Hemispherical electron energy analyser, 444, 445
 Hexagonal boron nitride (h-BN), 227
 HgCdTe detectors, 332

High-angle annular dark-field scanning transmission electron microscopy (HAADF-STEM), 192–194
 High-density polyethylene (HDPE), 341
 Highest occupied molecular orbital (HOMO), 323
 High-intensity discharge (HID) lamp, 354
 Highly oriented pyrolytic graphite (HOPG), 234–236
 High-pressure carbon monoxide (HiPCO) method, 409, 424
 High-pressure sodium (HPS) lamps, 353
 High-resolution photoemission spectroscopy (HRPES), 514
 High-resolution transmission electron microscopy (HRTEM), 147, 190–192
 High-temperature superconductors (HTS), 245
 ^1H magic-angle-spinning (MAS), 550
 Hohenberg-Kohn theorem, 486–487, 489
 Holographic grating, 308
 Homonuclear recoupling technique, 560
 Hooke's law, 268, 271, 336
 HORIBA Jobin Yvon Fluorolog-3 spectrofluorometer, 381
 Horizontal focusing mirror (HFM), 513, 514
 Hot-field emission, 166
 HRTEM, *see* High-resolution transmission electron microscopy
 Hubbard model, 243–244
 Hund's rules, 452
 Huygens principle, 7
 Hydrogen fluoride (H-F), 318, 324
 5-Hydroxymethyl-2-furaldehyde (HMF), 578

I

IFEFFIT program package, 522
 Incident radiation, 297
 Inductively coupled plasma-atomic emission spectroscopy (ICP-AES), 436
 Infrared-emitting diode (IRED), 355
 Infrared spectroscopy, 229
 In-plane bending vibration, 325
 In-plane transverse optic (iTo), 418, 427
 Insensitive nuclei enhanced by polarization-transfer (INEPT), 565
 Insertion devices (ID), 511
 Institut laue-langevin (ILL), 18–19
 Integrating sphere, 298
 Interference writing, 330
 International Tables of Crystallography, 13
 Ion pumps, 170–171

Ion scattering, 229

Iron oxide, 339

J

Johannson-type curved crystal, 520

Judd-Ofelt theory, 379, 380

K

Keldysh formalism, 490

Klechkowski rule, 459

Klystron, 510

Kohn-Sham equations, 487, 490

Korea Institute of Science and Technology (KIST), 509

Kubelka-Munk theory, 297

L

Lab-source-based XAFS spectrometers

configuration of machine, 520–521

easy-XAS-300 banc top spectrometer, 519–520

principle of measurement, 520

R-XAS looper, 519, 520

target filament combination, 520

Landé interval rule, 379

Lanthanum hexaboride (LaB₆), 138

Laplace transform formula, 86

Laporte rule, 347, 360, 363, 379

Laporte selection rule, 455

Larmor frequency, 249

Larmor's formula, 441

Lateral correlation length, 286–288

Lateral manipulation (LM), 233

Layer breathing modes (LBMs), 421

Lead perovskite, 301

Le Bail method, 24–25

Lee-Goldburg cross-polarization (LG-CP) method, 569

Lende's *g* factor, 451

Lewis acid, 563, 564

Lift mode, MFM

fullerene films, magnetic domains in, 280–281

ion irradiation experiments, 275

magnetic information, 274–275

topography measurement, 274, 275

Ligand-field effect (H_{LF}), 363

Ligand-to-metal charge transfer (LMCT) state, 377

Light and lighting technologies

artificial lighting, 351

carbon filament, 352

CFL, 355

electromagnetic radiation, 351

fluorescent lamp, 354–355

halogen lamp, 353

incandescent tungsten filament, 352

LEDs, 355–356

metal filaments, 352

metal halide lamp, 354

sodium lamp, 353–354

wavelengths, 351

xenon arc lamp, 354

Light-emitting diodes (LEDs), 354–356, 397–398

Light microscope vs. electron microscope, 147, 152–154

Linear accelerator (LINAC), 508

Linear fit, 82–83

Local barrier height (LBH), 245

Local density approximation (LDA), 488

Local density of states (LDOS), 226, 230, 231

Localized surface plasmon resonances (LSPRs), 422

Logarithmic amplifier, 223

longitudinal acoustic (LA) (iTOLA), 418, 427

Loop technique, 229

Lorentz force, 443

Low-density polyethylene (LDPE), 341

Low-energy diffuse scattering spin analysers, 476

Low-energy electron diffraction spin analyser, 476

Low-energy exchange scattering (LEX), 476

Lower critical solution temperature (LCST), 96

Lowest unoccupied molecular orbital (LUMO), 323

Low-pressure sodium (LPS) lamps, 353

L-S coupling, 452, 455

Luminescence

history of, 348–350

light and lighting technologies, 351–356

rare earth elements, 356–360

Lutetium, 357

M

Maclaurin series, 84

Macroscopic work function, 227

Madelung rule, 459, 462

- Magic-angle spinning (MAS), 556–557
 Magnesium oxide (MgO), 298
 Magnetic dipole (MD) transition, 379
 Magnetic film/pellet holder, 334
 Magnetic force microscopy (MFM), 264, 290
 Co thin films and nanoparticles
 irradiated films, 276–279
 pristine films, 275–277, 279
 high imaging resolution, 273
 lift mode
 fullerene films, magnetic domains in,
 280–281
 ion irradiation experiments, 275
 magnetic information, 274–275
 topography measurement, 274, 275
 magnetic probe, 273
 operating principle of, 273–274
 Magnetic lens, 443
 Magnetic resonance imaging (MRI), 390
 Magnetic scattering
 atomic scattering factor, 13
 Fourier series, 15
 helical magnetic structures, 15
 magnetic form factor, Nd^{3+} , 13–14
 magnetic interaction, 12–13
 magnetic ordering, 12
 magnetic structure factor, 15
 magnetization, 13, 14
 neutron diffractogram, 12
 Magnetization, 13, 14
 Mass thickness contrast, 159–161
 “Maximum sampling rate”, 561
 Mesoscopic work function, 227
 Mesostructured cellular foam (MCF), 578
 Metal halide lamp, *see* High-intensity
 discharge lamp
 Metal phthalocyanine (MPc), 239, 240
 Metal vapor lamp, 354
 Metoprolol tablets, 299
 Meyer, Friedrich, 354
 MFM, *see* Magnetic force microscopy
 Mg-doped GaN, 356
 Michelson interferometer, 322, 327–330
 Micro-channel plates (MCPs), 387, 446, 447
 Micro-electromechanical system (MEMS), 205
 Microstate, 362
 Mie theory, 89
 Monochromator system, 308, 309
 Monsanto Corporation, 355
 Moseley’s law, 440
 Mössbauer refinement method, 539
 Mott polarimeters, 475
 Movable analyser, 468
 “Muffin-tin” approximation, 504
 Multimode, 264
 Multiphonon relaxation, 374–375
 Multipole lenses, 156
 Multi-walled carbon nanotubes (MWNTs),
 407, 416, 430
N
 Nanolithography, 253
 Nanomachining, 253
 Nanometer patterning technique, 253
 NEAXAFS measurement, 509, 514, 515
 Neutron diffraction
 applications, 16–17
 elastic neutron scattering, 10–11
 ILL, 18–19
 magnetic interaction, 2
 magnetic scattering
 atomic scattering factor, 13
 Fourier series, 15
 helical magnetic structures, 15
 magnetic form factor, Nd^{3+} , 13–14
 magnetic interaction, 12–13
 magnetic ordering, 12
 magnetic structure factor, 15
 magnetization, 13, 14
 neutron diffractogram, 12
 magnetic structure
 BasIreps program, 26–28
 Cartesian/spherical components, 29–31
 double perovskite $\text{A}_2\text{BB}'\text{O}_6$, 19–21
 FullProf Studio, 31–33
 FullProf Suite, 19
 K_Search program, 21–23
 Le Bail method, 24–25
 magnetic peaks identification, 21–23
 Mag.pcr file, 27–29
 Rietveld analysis, 19
 Sr_2YRuO_6 , 19–20
 WinPLOTR-2006 program, 21, 23
 neutrons and phonons, 2
 nuclear scattering
 absolute value of b , 8–9
 atomic nucleus, 5
 atomic scattering factor, 7–8
 average kinetic energy, 3
 de Broglie’s equation, 5
 De Broglie wavelength, 3
 Debye–Scherrer geometry, 3
 Dirac delta function, 6
 Fermi’s pseudo-potential, 5
 Huygens principle, 7
 Maxwell–Boltzmann velocities, 3
 monochromatic beam, 3–4

- particle accelerators, 4
 - scattering wave, 5
 - values of b , 8
 - wave amplitude, 7
 - X-ray scattering, 6–7
 - polycrystalline materials, 2
 - X-and gamma-type photons, 1
 - Neutron powder diffraction (NPD), 19
 - NIR spectrometry, 300
 - NMR spectroscopy, 341
 - Non-contact AFM (NC-AFM), 272
 - Nuclear scattering
 - absolute value of b , 8–9
 - atomic nucleus, 5
 - atomic scattering factor, 7–8
 - average kinetic energy, 3
 - de Broglie's equation, 5
 - De Broglie wavelength, 3
 - Debye–Scherrer geometry, 3
 - Dirac delta function, 6
 - Fermi's pseudo-potential, 5
 - Huygens principle, 7
 - Maxwell–Boltzmann velocities, 3
 - monochromatic beam, 3–4
 - particle accelerators, 4
 - scattering wave, 5
 - values of b , 8
 - wave amplitude, 7
 - X-ray scattering, 6–7
 - Nujol mull, 335
 - Numerical aperture (NA), 155, 408
- O**
- One-molecule-at-a-time basis method, 232
 - Open structure (OS), 236
 - Optical microscopy (OM), 114, 254
 - vs. electron microscope, 147, 152–154
 - reflection and refraction of light, principles of, 263
 - Optical path difference (OPD), 328, 329, 331
 - Optical spectroscopy, inorganic materials
 - catalytic applications, 302–307
 - electromagnetic spectrum, 293–294
 - instrumentation
 - detectors, 311–312
 - dispersion device, 307–309
 - radiation source, 307
 - UV-Vis spectrophotometer configuration, 309–311
 - materials
 - absorption, 295–296
 - reflectance, 296–298
 - transmittance, 298–300
 - solar cell applications, 300–302
 - Oscillation frequency, 274
 - Osram Lighting Company, 353
 - Osteopontin (OPN), 389
 - Out of plane bending vibration, 325
- P**
- Parallel plate analysers, 444
 - Partial electron yield (PEY) mode, 516, 517
 - Particle system, 88
 - Passivated implanted planner silicon (PIPS), 518
 - Pauli's exclusion principle, 220
 - Periodic mesoporous organosilica (PMO) materials, 578
 - Perovskite, 301, 302
 - Perturbation technique, 232
 - Phonon detection, 247–248
 - Photoacoustic imaging (PAI), 395–397
 - Photoacoustic microscopy (PAM), 396
 - Photocatalysis process, 302–306
 - Photodegradation process, 303
 - Photodiode, 333
 - Photoelectric effect, 500
 - Photoelectron emission methods, 229
 - Photoelectron spectroscopy (PES)
 - atomic/molecular spectroscopy, 435
 - Born-Oppenheimer approximation, 483–484
 - core level spectroscopy
 - atomic bonding effect, 460
 - charge compensation, 461
 - crystal field splitting, 459
 - depth profiling, 462
 - energy atomic orbitals, 459
 - energy bands, 460
 - spin-orbit interaction, 459
 - XPS data, 458, 461
 - XPS spectra, 460–464
 - X-rays, 458, 461
 - de Broglie wavelength, 435
 - density functional theory, 486–488
 - EDC, 438
 - Einstein equation, 437
 - ejected electrons, 437, 438
 - electron detectors, 438, 446–447
 - electron energy analyser, 444–446
 - electron optics, 443–444
 - energy bands, 436
 - Hartree-Fock approximation, 484–486
 - incident photon, 438

- Photoelectron spectroscopy (PES) (*cont.*)
 incident radiation, 435
 independent electron approximation, 437
 infrared and Raman spectroscopy, 436
 molecular spectroscopy, 436
 mono and multiatomic systems, electronic states in
 atoms, 450–455
 quantum numbers, 449
 Schrodinger equation, 449
 solids, 455–458
 monochromators, 441–442
 photoelectric effect, 437
 quantum mechanics theory, 435
 radiation sources
 synchrotron radiation, 440–441
 ultraviolet radiation, 440
 X-rays, 439–440
 spectral lines, 436
 spin-resolved ARPES
 BCC Fe, 478
 Bi thin films, 478
 ferromagnetic substance, 474
 longitudinal configuration, 475
 Lorentz force, 474
 magnetic domains, 474
 phase space considerations, 477–478
 polarimeters, 474–477
 transverse configuration, 474
 three-step model, 480–482
 threshold frequency, 438
 time-dependent response of electrons in material
 GW approximation, 490–491
 RPA, 489
 TD-DFT, 489
 vacuum chambers, 448–449
 valence band spectroscopy
 angle-integrated photoemission, 465
 ARPES data, 469–472
 Brillouin zone, 465
 electron wavevector, 466
 experimental setup, 468–469
 free electron-like behaviour, 467–468
 layered compounds, 467
 normal emission, 467
 reciprocal lattice vector, 466
 triangulation method, 468
 UPS technique, 465
 work function, 438
 Photoemission from absorbed xenon (PAX)
 technique, 227
 Photoexcitation process, 296
 Photoluminescence, 348
 Photomultiplier, 309, 311, 312
 Photomultiplier tubes (PMT), 382, 385–387
 Photon detectors, 332
 Phototubes, 311, 312
 Piezo-scanner, 224
 Pinhole-collimated instruments, 69–70
 Planar tunneling, 230
 Planck's constant, 318
 Pohang Accelerator Laboratory (PAL), 507, 509
 Point charge electrostatic model (PCEM), 363
 Poly(N-isopropylacrylamide) (PNIPAAm), 96
 poly(N-vinylcaprolactam) (PNVCL), 96
 poly(oligo(ethylene glycol)-methacrylate) (POEGMA), 96
 Polycrystalline method, 10
 Polydispersity index (PDI), 51, 65, 87–88
 Polydivinylbenzene (PDVB), 583
 Polytetrafluoroethylene (PTFE), 298
 Polyvinyl alcohol (PVA), 68
 Porod law, 44, 48–49
 Position-sensitive detector (PSD), 18
 Positron emission tomography (PET), 390, 391
 Press-on demountable cell holders, 334
 Prism, 442
 Promethium, 357
³¹P Solid-state nuclear magnetic resonance spectroscopy (SSNMR)
 acid catalysis, 549
 adsorbed phosphorous probe molecules
 ²⁷Al-³¹P INEPT, 565
 Brønsted acidic sites, 563, 564, 566–570
 2-¹³C-acetone approach, 569
 H-ZSM-5 zeolite catalyst, 567
 interaction modes, 563, 564
 Lewis acidic sites, 563, 564, 566, 569
 LG-CP method, 569
 ³¹P chemical shift values, 570
 proton transfer, 563
 ³¹P-R₃PO approach, 568
 ³¹P-TMP SSNMR approach, 566
 solid acid catalysts, 563, 564, 566
 sulfated metal oxide, 564
 superacidity features, 568
 TMP, 563, 564
 TMPO, 567, 569, 570
 TRAPDOR effect, 565
 8T zeolite cluster model, 570

- anisotropic interactions
 - chemical shift, 553–554
 - dipole-dipole interaction, 554
 - indirect dipole-dipole/spin-spin interaction/*J*-coupling, 555–556
 - quadrupole interaction, 554–555
 - Zeeman interaction, 555
 - carbonaceous materials, acidity
 - characterization of
 - AMS dimerization, 575
 - Brønsted acidic sites, 574, 581
 - carbohydrate biomass conversion, 579
 - carbon catalysis/carbocatalysis, 571
 - carbon-silica composite, 574–577
 - colorimetry experiment, 572
 - furfuryl alcohol, 578
 - GNC-[C₃N][SO₃CF₃] material, 582, 583
 - graphene, 584, 585
 - HMF, 578
 - hydrothermal sulfonation method, 576
 - intramolecular Friedel-Crafts alkylation, 575, 576
 - metal-free catalysis, 571
 - PDVB-SO₃H-SO₂CF₃ catalysts, 583, 584
 - petroleum cokes, 578, 580
 - PMO materials, 578
 - SHTC, 576
 - SO₃H groups, 572–574, 576, 585
 - solid acid, 580, 581
 - sulfonated carbons, 572, 573
 - surface functional groups, 571
 - TEPO, 576, 577, 580, 585
 - TMP adsorption, 580, 581
 - TMPO, 573, 574, 577, 580
 - TOF, 575
 - CSA, 552
 - high-resolution solid-state NMR techniques
 - cross-polarization, 557–558
 - dilution, 558
 - heteronuclear decoupling, 558–559
 - MAS, 556–557
 - multiple-pulse homonuclear decoupling, 559
 - recoupling techniques, 559–560
 - ¹H MAS NMR, 550, 551
 - instrumentation, 560–563
 - internuclear dipolar coupling, 552
 - isotropic chemical shift, 553
 - J*-coupling, 553
 - Lewis vs. Brønsted acid, 550
 - non-recyclable acid waste, 549
 - petrochemical process, 549
 - pyridine, 550
 - pyridine-*d*₅, 551
 - resonance frequency, 552
 - TMP and trialkylphosphine oxides, 551
 - Pyroelectric detector, 333
- Q**
- Quantum dots (QDs), 396
 - Quantum effects, 141
 - Quantum Monte Carlo calculations, 488
- R**
- Radial breathing mode (RBM), 416, 418, 419, 427
 - Radiation-matter interaction, 293
 - Radio frequency cavity, 510
 - Radioluminescence, 348
 - Raman spectroscopy
 - carbon materials
 - carbon nanotube, electronic band structure of, 414–415
 - D-band, second-order Raman scattering, 416
 - G-band, first-order Raman scattering, 417–419
 - graphene, 410–414, 419–421
 - RBM, first-order Raman scattering, 416
 - CNTs, 426–430
 - confocal scanning optical microscopy, 407–409
 - IR spectra, 406
 - momentum angular mapping, 407, 431
 - sample preparation, 409–410
 - SERS signals, 405
 - experimental set-up and sample preparation, 423–424
 - LSPRs, 422, 423
 - nanoscale optical spectroscopy, 422
 - optical antennas, 422, 423
 - theory of, 425–426
 - TGA, 405
 - vibrational transition, 406
 - XPS, 405
 - Random phase approximation (RPA), 489
 - Rare earth (RE)
 - electronic spectroscopy, rare earth ions
 - CIE coordinates, 381
 - energy transfer, 364–376
 - luminescence decay curves, 380–381
 - luminescence spectra, 376–380
 - [Xe]4f^{*N*} configurations, 360–364

- Rare earth (RE) (*cont.*)
 4f energy levels, 347
 instrumentation
 sample holders, 387–388
 spectrofluorometer, 381–387
 LEDs, 346
 luminescence (*see* Luminescence)
 luminescent RE³⁺ materials, applications of
 bioimaging, 382–397
 LEDs, 397–398
 phosphors, 347
 trivalent lanthanide ions, 347
 Rashba effect, 478
 Raster scanning, 423
 Rayleigh criterion, 117
 Rayleigh law, 98
 Rayleigh scattering, 89, 406
 Reactive nanoscale iron particles (RNIP), 94
 Reflectance, inorganic materials, 296–298
 Refocused continuous wave (*r*CW), 559
 Refocusing mirror system (RFM), 513, 514
 Retarding field analysers, 444
 Retarding type spin analysers, 476
 Rhodamine 6G, 406–407
 Richardson's law, 163
 Rietveld method, 2, 28
 Rietveld refinement method, 539
 Rotary pump, 163
 Rotational echo adiabatic passage double
 resonance (REAPDOR), 560
 Rotational echo double resonance (REDOR),
 560
 Russell-Saunders notations, 452
 Russell-Saunders spin-orbit coupling scheme,
 360
- S**
 SAED, *see* Selected area electron diffraction
 Samarskite, 357
 Sample-to-detector distance (SDD), 39
 SAS software package, 43
 Satellite peaks, 461
 Scanning electron microscopy (SEM), 100,
 250, 424
 applications of, 140
 composition, 116
 development in, 138–139
 electron beam, importance of, 117–118
 vs. FESEM, 139–140
 FESEM operation, 132–134
 human chromosomes, imaging of, 282, 283
 instrumentation
 apertures, 131
 condenser lens, 129–130
 electron gun (*see* Electron gun)
 FESEM, 125
 lenses and apertures, 129
 objective lens, 130
 scanning coils, 130
 specimen chamber, 131–132
 stigmator coils, 131
 morphology, 116
 nanomaterials characterization, 140–143
 OM and EM, 114–115
 operator control
 accelerating voltage, 134
 astigmatism, 136
 charging, 137
 emission current, 134
 focus and alignment, 135
 high-resolution imaging, 136–137
 objective apertures size, 135
 probe diameter, 134–135
 scan-square method, 137–138
 specimen damage, 138
 tilting, 136
 working distance, 135
 principles of
 accelerating voltages, 121
 atomic number, 121
 BSEs, 119
 carbon tap, 118
 inelastic and elastic interaction,
 119–120
 photons, 119
 primary electrons, 118, 119
 secondary electrons, 118
 tilt, 121–124
 vs. TEM, 115–116
 topography, 116
 Scanning force microscopy (SFM), 250
 Scanning probe microscopy (SPM)
 definition, 263
 MFM (*see* Magnetic force microscopy)
 STM (*see* Scanning tunneling microscopy)
 surface scanning, 217
 Scanning transmission electron microscopy
 (STEM), 44, 139, 150, 191–194
 Scanning tunneling microscopy (STM)
 advantages, 253–254
 atomic resolution capability, 264
 biology and organic chemistry, application
 in, 250–251

- electrochemical applications, 252
- electron spin resonance, 249
- imaging process
 - spectroscopic imaging, 231–232
 - topographical process, 230–231
- instrumental operation of, 223
- limitations/drawbacks, 254, 264, 267
- liquid and gaseous media, scanning in, 218
- nanolithography and nanomachining, 253
- nonconducting materials, application in, 250
- operational modes of
 - constant current mode, 224, 267
 - constant height mode, 224, 225, 266–267
 - potentiometry, 228
 - spectroscopic mode, 225–226
 - work function measurement, 226–228
- quantum mechanical tunneling, 265
 - one-dimensional potential barrier, 218–219
 - from sample to tip, 220–221
 - from tip to sample, 220–222
 - transmission coefficient, 219–220
- schematic of, 265, 266
- as sensing device, 249
- single atoms/molecules manipulation, 232–233
- STM tip, geometry of, 222–223
- surface scanning, 217
- surface science, application in, 217
 - adsorbate covered surface, 241–243
 - charge density wave, 243–246
 - graphite, 234–237
 - inhomogeneous material, 247, 248
 - irregular structures, 241
 - metals, 239–241
 - phonon detection, 247, 249
 - semiconductors, 236–239
 - spin-polarized tunneling, 249
 - superconductors, 245–246
- tip-material influence, 228–230
- tip-sample separation, 265
- tribology, application in, 253
- tunneling current, 218, 265, 266
- Scanning tunneling potentiometry (STP), 228
- Scanning tunneling spectroscopy (STS), 225–226, 231–232
- Scattering coefficient, 297
- Schrodinger equation, 449, 450, 483, 486, 504
- Schrödinger's equation, 219
- Schultz-Zimm distributions, 50
- Scintillator-photomultiplier detector, 175–176
- Secondary electrons (SE2), 123
- Selected area electron diffraction (SAED), 194–196
- Self-assembled monolayers (SAMs), 241
- Semiconductor detectors, 174–175
- Semiconductors, STM application, 236–239
- S-glutamic acid, 250
- Sherman function, 476
- Siebert equation, 81, 86
- Signal-to-noise (S/N) ratio, 558
- Silicene, 237–238
- Silicon diode, 312
- Silicone-like reconstruction (SLR), 238–239
- Silicon phthalocyanine dichloride (SiPcCl₂), 240
- Single-layer graphene (SLG), 420
- Single-pellet holder, 334
- Single-photon emission tomography (SPECT), 390
- Single-walled carbon nanotubes (SWNTs), 407, 409, 415, 416, 430
- Skating mode, *see* Constant height mode
- Slit-collimated instruments, 69
- SLR, *see* Silicone-like reconstruction
- Small-angle X-ray scattering (SAXS)
 - absorption and scattering, 39
 - anisotropic systems, 43
 - autocorrelation function, 42
 - basic schematic setup, 39
 - correlated particles, 55
 - FA and Beaucage models, application of, 66–68
 - FA model (*see* Fractal aggregate model)
 - monodisperse system, 58
 - Ornstein-Zernike integral, 58, 59
 - scattering amplitude, 58
 - total scattering intensity, 58
 - unified exponential/power law model, 64–65
 - correlation function, 42
 - 1-D/2-D scattering pattern, 43
 - diluted sets of nano-objects
 - scattering intensity, 52
 - simple geometrical shape, 55–57
 - uncorrelated spherical nanoparticles, 52–54
 - dispersion intensity, 41
 - electron density, 42
 - Fourier transformation, 40, 42
 - heat and/or fluorescence radiation, 39

- Small-angle X-ray scattering (SAXS) (*cont.*)
 instrumentation
 beam stop, 71
 bonse-hart instruments, 70
 CCD detectors, 71
 imaging plates detectors, 71–72
 pinhole-collimated instruments, 69–70
 sample holder, 70
 slit-collimated instruments, 69
 solid-state detectors, 72
 TEM, 72–73
 X-ray source, 69
 isotropic and non-fixed nano-objects
 Guinier law, 44
 high- q regime, 48–49
 intermediate- q regime, 49–52
 low- q regime (*see* Guinier Law)
 Porod law, 44
 scattering intensity, 44
 nanoparticle, mean size of, 38
 neutron diffraction techniques, 38
 pair-distribution function, 42
 Patterson function, 41
 SAS software package, 43
 scattering amplitude, 40, 42
 scattering intensity, 42, 43
 Soft X-ray beamline (KIST Beamline)
 experimental end station, 514–515
 measurement procedure
 NEXAFS, 515
 TEY method, 516–517
 TFY mode, 517
 optical layout, 513–514
 Solar cell applications, 300–302
 Solid-state epitaxy process, 238
 Spanner, Hans, 354
 Spectrofluorometer
 detectors
 CCD, 382, 387
 PMT, 382, 385–387
 Fluorolog-3, 382, 389
 monochromators, 383–385
 450W xenon arc lamp, 381
 Spectrophotometers, 307
 SPEX FL212 Fluorolog-2 spectrofluorometer,
 381
 Spin-polarized scanning tunneling microscope
 (SP-STM), 248–249
 Spintronics, 474
 SPM, *see* Scanning probe microscopy
 STM, *see* Scanning tunneling microscopy
 Stokes-Einstein equation, 81, 83
 Stokes-shifted wavelengths, 423
 Stretching vibration, 324–325
 STS, *see* Scanning tunneling spectroscopy
 Subtractive process, 236
 Sulfonated hydrothermal carbon (SHTC), 576
 Superconductors, STM application, 245–246
 Superior sagittal sinus (SSS), 396
 Surface barrier detector, 174
 Surface correlation, Co nanoparticles
 autocorrelation function
 exponential correlation model, 286, 287
 lateral correlation length, 285–286
 one-dimensional autocorrelation
 function, 285
 pristine and ion-irradiated thin films,
 287–289
 height-height correlation function,
 286–289
 surface roughness, 284–285
 Surface-enhanced Raman spectroscopy
 (SERS), 405, 407
 Surface tunneling spectroscopy, 225
 Symmetric traceless tensors, 555
 Symmetry-based resonance echo saturation
 pulse double resonance
 (S-RESPDOR), 560
 Synchrotron radiation source
 booster rings, 508–509
 cosmic rays, 507
 electromagnetic radiation, 507
 LINAC, 508
 storage ring and components
 bending magnets, 508, 510
 insertion devices, 511
 quadrupole magnets, 512
 radio frequency system, 509–510
 undulators, 511–512
 wigglers, 511
- T**
 Tapping (intermittent) mode AFM
 advantages and disadvantages, 272
 biological samples, imaging of, 281–283
 gold films, nanoring formation in, 281, 282
 TEM, *see* Transmission electron microscopy
 Temperature gravimetric analysis (TGA), 405
 Tersoff-Hamann model, 222, 223, 230, 231
 Thermal detectors, 332–333
 Thermal magnetic noise, 157
 Three-dimensional (3-D) tomography,
 203–204
 Tight-binding model, 230
 Tilt, 121–124
 Time-dependent density-functional theory
 (TD-DFT), 489–490

- Time-dependent perturbation theory, 222
- Time-of-flight (TOF) spectroscopy, 477
- Tip crash technique, 218, 233
- Tip-sample interaction, 229, 230
- Tip-sharpening techniques, 222, 229
- Titanium oxide (Ti-O), 339
- Total electron yield (TEY) mode, 502, 516–517
- Total fluorescence yield (TFY) mode, 502, 517
- Transfer of populations in double resonance (TRAPDOR), 560
- Transmission coefficient, 219–220, 232
- Transmission electron microscopy (TEM), 54, 72–73, 78, 100, 114, 250
- aberration correction model, 150
 - apertures, 177
 - applications, 150–151
 - electromagnetic lenses, 166–167
 - electron
 - advantages of, 157
 - detectors, 171, 173–176
 - discovery of, 157
 - field emission guns, 164–165
 - field emission source, 162, 164, 166
 - limitation, 157
 - properties of, 157–159
 - thermionic emission source, 162–164
 - thermionic gun, 164, 165
 - EMCD, 205
 - environmental TEM, 205
 - filters, 176–177
 - historical developments, 148–150
 - imaging and spectroscopy
 - chemical mapping, 201–203
 - in conventional TEM, 188–190
 - EDS, 195, 197
 - EELS, 198, 199, 205
 - EFTEM, 198–201
 - HRTEM, 190–192
 - SAED, 194–196
 - STEM, 191–194
 - 3-D tomography, 203–204
 - imaging contrast mechanisms
 - bright-field and dark-field imaging, 159, 160
 - diffraction/amplitude contrast, 159, 161, 162
 - mass thickness, 159–161
 - phase contrast, 159, 161, 162
 - liquid-cell TEM, 205
 - neutron source, 157
 - operational and alignment procedures, 177–180
 - purpose of, 150
 - resolution and limitations, 154–157
 - sample preparation
 - abrasion mechanism, 182–183
 - aim of, 180
 - artifact eliminations, 186–187
 - basic criterion, 181
 - biological sample preparation, 181
 - bulk sample, steps for, 181, 182
 - chemical and electrochemical dissolution, 184
 - ionic abrasion principles, 184–185
 - nanoparticles, 185–187
 - optical images of, 186
 - vs. SEM, 115–116
 - vacuum systems
 - definition, 168
 - high vacuum, 169
 - history, 168
 - low vacuum, 169
 - principle purposes for, 168
 - ultrahigh vacuum, 168, 169
 - vacuum pumps, 163, 168–172
 - vacuum units, 168–169
 - X-rays, 157
- Transmission electron microscopy (TEM) micrograph, 424
- Transmittance, inorganic materials, 298–300
- Tribology, 253
- Triboluminescence, 348
- Tributylphosphine oxide (TBPO), 566
- Triglycerine sulfate (TGS) detector, 333
- Trimethylphosphine (TMP), 551
- Trioctylphosphine oxide (TOPO), 566
- Trip-atom interaction, 233
- Trivalent europium ion, 368
- Tunneling effect, 218
- one-dimensional potential barrier, 218–219
 - from sample to tip, 220–221
 - from tip to sample, 220–222
 - transmission coefficient, 219–220
- Tunneling resistance, 233
- Tunneling spectroscopy, 245
- Turbo-molecular pump, 170
- Turnover frequency (TOF), 575
- 2D Fourier transform (2DFT), 244
- Two-pulse phase modulation (TPPM), 559
- U**
- UC mechanisms
- CET system, 373
 - EMU process, 373–374
 - ESA, 372
 - ETU, 372–373
 - photon avalanche process, 373

UCNPS, 389, 390, 396
 Ulbricht sphere, *see* Integrating sphere
 Ultra-high vacuum (UHV), 448
 Ultraviolet photoelectron spectroscopy (UPS), 440
 Ultraviolet-visible spectrophotometers, 298, 300, 301
 Ultraviolet-visible spectroscopy (UV-vis), 304, 309–311
 Universal sample holder, 334

V

Vacuum systems
 definition, 168
 high vacuum, 169
 history, 168
 low vacuum, 169
 principle purposes for, 168
 ultrahigh vacuum, 168, 169
 vacuum pumps, 163, 168–172
 vacuum units, 168–169
 Valence band (VB), 295, 296
 Valence band maximum (VBM), 470, 472
 Van der Waals forces, 230, 268
 Vertical focusing mirror (VFM), 513, 514
 Vertical manipulation technique, 233
 Vibrational spectrometry, 299
 Vibrations modes, 323–325
 Visible-light microscope, 152
 Voltage-dependent imaging, 226

W

WAHUA pulse sequence, 559
 Water splitting process, 303, 306
 Wave function, 219
 Waveguide, 510
 Westinghouse Lamp Company, 353
 White light-emitting diodes (WLEDs), 350
 Wiley, Emmet, 353
 Wings, 330
 WinPLOT-2006 program, 21
 Work function, 220, 221
 measurement of, 226–227

X

X- and gamma-type photons, 1
 XANES, 505

X-ray absorption fine structure (XAFS), 436, 499, 500, 505, 507
 oxide materials
 Cu₂O, morphology effect of, 537–538
 metal oxidation, biological and environmental applications, 539–541
 metal-oxygen metal bond length and oxide nanoparticles, 538–539
 MgO and Fe interface, 541
 NEXAFS measurements, 541–545
 oxygen (O) *K*-edge spectra, 542–545
 X-ray absorption near-edge structures (XANES), 436, 499
 background subtraction and normalization, 527–529
 edge energy reference parameter, 525
 EXAFS analysis, 522
 IFEFFIT program package, 522
 $\mu(E)$ raw data collection, *Athena* project, 523
 nonlinear least-square fittings, 522
 pre-edge/post-edge subtraction and assignment, 524
 X-ray absorption spectroscopy (XAS), 436, 499, 501, 517
 beamlines
 general layout, 512–513
 hard X-ray beamline, 517–519
 lab-source-based XAFS spectrometers, 519–521
 soft X-ray beamline (KIST Beamline), 513–517
 cross section, 506–507
 dipole and quadrupole approximation, 502–503
 dipole selection rules and transition probabilities, 506
 EXAFS data
 Artemis (Cu *K*-Edge data from Cu Foil), 533–535
 $\chi(k)$ conversion, 529
 Fourier transformation, 530–531
 modeling, 532–533
 weighed $\chi(k)$ vs. *k* spectrum, 529–530
 multiple-scattering approach, 504–505
 quasi-particle model, 504
 synchrotron radiation source
 bending magnets, 508, 510
 booster rings, 508–509
 cosmic rays, 507

- electromagnetic radiation, 507
 - LINAC, 508
 - storage ring and components, 509–512
 - XAFS, oxide materials
 - Cu₂O, morphology effect of, 537–538
 - metal oxidation, biological and environmental applications, 539–541
 - metal-oxygen metal bond length and oxide nanoparticles, 538–539
 - MgO and Fe interface, 541
 - NEXAFS measurements, 541–545
 - oxygen (O) *K*-edge spectra, 542–545
 - XANES data
 - background subtraction and normalization, 527–529
 - edge energy reference parameter, 525
 - EXAFS analysis, 522
 - IFEFFIT program package, 522
 - $\mu(E)$ raw data collection, *Athena* project, 524
 - nonlinear least-square fittings, 522
 - pre-edge/post-edge subtraction and assignment, 526
 - X-ray generation, basic principle of and absorption coefficient, 500–502
 - bremsstrahlung (braking) radiation, 497, 498
 - characteristic radiation, 497, 498
 - core-level spectroscopy, 499
 - filament voltage, 497
 - XAFS, 500
 - X-ray photons, 499
 - X-ray crystallography, 341
 - X-ray diffraction (XRD), 44
 - X-ray energy-dispersive detectors, 197
 - X-ray free-electron lasers (XFEL), 71
 - X-ray magnetic circular dichroism (XMCD), 205
 - X-ray optics, 253
 - X-ray photoelectron spectroscopy (XPS), 436
 - X-ray photoemission spectroscopy (XPS), 405
- Y**
- Yttrium, 357
- Z**
- Z-average, 86–87, 105
 - Zeeman effect, 362
 - Zeeman interaction, 555, 561
 - Zero path difference (ZPD), 328
 - Zero separation theorem-based closure (ZSEP), 59
 - Ziegler-Nichols method, 224
 - Zinc oxide (ZnO), 338
 - Zinc selenide (ZnSe), 336
 - Zirconium oxide (ZrO₂), 562